

Tom Proulx *Editor*

Experimental and Applied Mechanics, Volume 6

Proceedings of the 2011 Annual Conference on
Experimental and Applied Mechanics



 Springer

Conference Proceedings of the Society for Experimental Mechanics Series

For other titles published in this series, go to
www.springer.com/series/8922

Tom Proulx
Editor

Experimental and Applied Mechanics, Volume 6

Proceedings of the 2011 Annual Conference on Experimental
and Applied Mechanics

Editor

Tom Proulx
Society for Experimental Mechanics, Inc.
7 School Street
Bethel, CT 06801-1405
USA
tom@sem1.com

ISSN 2191-5644 e-ISSN 2191-5652
ISBN 978-1-4614-0221-3 e-ISBN 978-1-4614-0222-0
DOI 10.1007/978-1-4614-0222-0
Springer New York Dordrecht Heidelberg London

Library of Congress Control Number: 2011928691

© The Society for Experimental Mechanics, Inc. 2011

All rights reserved. This work may not be translated or copied in whole or in part without the written permission of the publisher (Springer Science+Business Media, LLC, 233 Spring Street, New York, NY 10013, USA), except for brief excerpts in connection with reviews or scholarly analysis. Use in connection with any form of information storage and retrieval, electronic adaptation, computer software, or by similar or dissimilar methodology now known or hereafter developed is forbidden.

The use in this publication of trade names, trademarks, service marks, and similar terms, even if they are not identified as such, is not to be taken as an expression of opinion as to whether or not they are subject to proprietary rights.

Printed on acid-free paper

Springer is part of Springer Science+Business Media (www.springer.com)

Preface

Experimental and Applied Mechanics represents one of eight volumes of technical papers presented at the Society for Experimental Mechanics Annual Conference & Exposition on Experimental and Applied Mechanics, held at Uncasville, Connecticut, June 13-16, 2011. The full set of proceedings also includes volumes on Dynamic Behavior of Materials, Mechanics of Biological Systems and Materials, Challenges in Mechanics of Time-Dependent Materials and Processes in Conventional and Multifunctional Materials, MEMS and Nanotechnology; Optical Measurements, Modeling and, Metrology; Experimental and Applied Mechanics, Thermomechanics and Infra-Red Imaging, and Engineering Applications of Residual Stress.

Each collection presents early findings from experimental and computational investigations on an important area within Experimental Mechanics. Experimental and Applied Mechanics was organized by: Carlos E. Ventura, *University of British Columbia*; Hugh A. Bruck, *University of Maryland*; Wendy C. Crone, *University of Wisconsin–Madison*

Experimental and Applied Mechanics covers the wide variety of subjects that are related to the broad field of experimental or applied mechanics. It is SEM's mission to disseminate information on a good selection of subjects. To this end, research and application papers relate to the broad field of experimental mechanics. The current volume on Experimental and Applied Mechanics includes studies on:

- Fracture and Fatigue
- Fatigue and Failure of Non-traditional Materials
- Composite Materials
- Composite Damage
- Characterizing Composite Materials
- Modal Analysis: Measurement Techniques
- Modal Analysis: Analytical Methods
- Dynamic Phenomena
- Measurements and Modeling

The Organizers would like to thank the presenters, authors and session chairs for their participation.

The opinions expressed herein are those of the individual authors and not necessarily those of the Society for Experimental Mechanics, Inc.

Bethel, Connecticut

Dr. Thomas Proulx
Society for Experimental Mechanics, Inc

Contents

1	A Rocking Spalling Test to Characterise the Crack velocity in concrete	1
	P. Forquin, R. Cheriguene, Laboratory of Physics and Mechanics of Materials	
2	Crack Growth Behavior in Preloaded Metallic Nested-angle Plates Under Flight Load Spectrum	3
	M. Haile, T.-K. Chen, M. Shiao, D. Le, U.S. Army Research Laboratory	
3	Experimental and Finite Element Analysis (FEM) of Bioceramics	13
	D. Katundi, Supmeca/LISMMA - Paris; F. Ayari, Supmeca/LISMMA - Paris/College of Science & Technology; E. Bayraktar, Supmeca/LISMMA - Paris; A. Tosun-Bayraktar, P. Vauqelin	
4	Damage Analysis of the Ceramic Reinforced Steel Matrix Composites Sheets: Experimental and Numerical Study	21
	E. Bayraktar, Supmeca -Paris/CNAM, Arts et Métiers; D. Katundi, F. Ayari, Supmeca -Paris; J.-P. Chevalier, CNAM, Arts et Métiers; F. Bonnet, ARCELOR – Research	
5	Dynamic Mechanical Properties of Polymeric Materials Aged in PEM Fuel Cell Conditions	31
	C.-W. Lin, National Sun Yat-Sen University/University of South Carolina; T. Cui, University of South Carolina; C.-H. Chien, National Sun Yat-Sen University; J. Tan, Nanjing University of Technology; Y.-J. Chao, J.W. Van Zee, University of South Carolina	
6	Mechanical Characterization and Modeling of Solid Oxide Fuel Cells and Stacks	37
	R. Berke, M.E. Walter, Ohio State University	
7	The Impulse Imparted Upon Monolithic Metal Plates due to Blast Loading	45
	J. Wright, E. Wang, A. Shukla, University of Rhode Island	
8	Investigation in Shear Behavior of Intermetallic Composites Using V-notched Beam Test Method	53
	Y. Yuan, Baker Hughes Incorporated; C. Feng, ION Geophysical Co.; Z. Xu, Baker Hughes Incorporated; H.-P. Li, Aker Solutions	
9	The Influence of Sample Thickness on the DCDC Fracture Test	61
	C. Nielsen, A.V. Amirkhizi, S. Nemat-Nasser, University of California, San Diego	
10	Analysis of Hysteresis Damage Accumulation and the Effect on Fatigue Life	65
	O. Scott-Emuakpor, T. George, C. Cross, Air Force Research Laboratory; M.-H. Herman Shen, The Ohio State University	

11 Fatigue Improvement of Welded Elements by Ultrasonic Impact Treatment Y. Kudryavtsev, Structural Integrity Technologies Inc.	75
12 Delamination Between Functionalized Silicon Surfaces S.R. Na, A. Hassan, K.M. Liechti, M.J. Krische, The University of Texas at Austin	89
13 Failure and Fracture Behavior of Brittle Polymer Foam A. Kidane, G. Ravichandran, California Institute of Technology	91
14 Crack Growth in Three-point Bend Specimens Made of Polymeric Foams E.E. Gdoutos, G. Papakaliatakis, Democritus University of Thrace	99
15 Reliability Evaluation of Conformal Coatings for Tin Whisker Failure Mitigation in Accelerated Testing Conditions K.H. Mahan, B. Han, S. Han, M. Osterman, University of Maryland	107
16 Investigation of Manganese Cobalt Oxide (MCO) Coatings on Fuel Cell Interconnects S. Akanda, M.E. Walter, Ohio State University	109
17 Extracting Crack-tip Field Parameters in Anisotropic Elastic Solids From Full-field Measurements Using Least-squares Method and Conservation Integrals F. Hou, S. Hong, Michigan State University	119
18 Velocity Measuring Approaches for the Determination of Ballistic Limits of GLARE 5 Fiber-metal Laminate Plates A. Seyed Yaghoubi, M.F. Chow, B.M. Liaw, The City College of New York	129
19 Underwater Explosive Loading of Curved Composite Plates: Experimental and Computational Comparisons J. LeBlanc, Naval Undersea Warfare Center; A. Shukla, University of Rhode Island	139
20 Adhesion Strength in Metal/Polymer Composites B.O. Calcagno, University of Puerto Rico-Mayagüez; K.R. Hart, W.C. Crone, University of Wisconsin-Madison	149
21 Modal-parameter Identification From Nonstationary Ambient Vibration Data D.-Y. Chiang, C.-S. Lin, National Cheng Kung University	157
22 High-speed Digital Image Correlation Measurements of Random Nonlinear Dynamic Response T. Beberniss, S. Spottswood, T. Eason, U.S. Air Force Research Laboratory	171
23 Experimental Modal Analysis of an Inflatable, Self-rigidizing Toroidal Satellite Component M. Danesh Pazhooh, M.A. Dokainish, S. Ziada, McMaster University	187
24 Selective Excitation Using Phase Shifted Ultrasound Radiation Force From Focused Transducers in air T.M Huber, N. Beaver, J. Helps, Gustavus Adolphus College	201
25 The Steelpan as a Tool to Incite Interest in Engineering Education S.E. Maloney, University of Cambridge; N.L. Williams, University of Bedfordshire Business School	207
26 Non-contacting Strain Measurement in Dynamic Tensile Testing D. Zhu, McGill University; B. Mobasher, S.D. Rajan, Arizona State University	209

27 Quantification of Micro-crack Density for Fiber Based Composites	217
V.P. Mills, J.A. Gilbert, T.K. Ooi, University of Alabama in Huntsville	
28 Dynamic Shear Response of a Polymer Bonded Explosive Using a Modified Hopkinson bar Apparatus	223
P.D. Zhao, F.Y. Lu, Y.L. Lin, R. Chen, L. Lu, National University of Defense Technology	
29 Shock Testing Accelerometers With a Hopkinson Pressure bar	229
J.T. Foster, Sandia National Laboratories; D.J. Frew, Dynamic Systems and Research; M.J. Forrestal, Forrestal Consulting; E.E. Nishida, Sandia National Laboratories; W. Chen, Purdue University	
30 Effect of Residual Stresses on Spallation of the Film Under Impact by Coated Bullet	239
C.-W. Wu, Chinese Academy of Sciences	
31 Fracture Testing of Simulated FRP Repairs	253
T. Chawla, M.N. Cavalli, University of North Dakota	
32 Hybrid Nano/Microcomposites for Enhanced Damage Tolerance	259
I.M. Daniel, J.S. Fenner, Northwestern University	
33 Drop-weight Impact Studies of GLARE 5 Fiber-metal Laminates	267
A. Seyed Yaghoubi, Y.X. Liu, B.M. Liaw, The City College of New York	
34 Finite Element Modal Analysis of an Inflatable, Self-rigidizing Toroidal Satellite Component	281
M. Danesh Pazhooh, M.A. Dokainish, S. Ziada, McMaster University	
35 Experimental and Finite Element Modal Analysis of the Flexible Wings of Micro Munition Vehicles	289
U.K. Chakravarty, U.S. Air Force Research Laboratory	
36 Numerical Analysis Study of the Failure Mechanism of Transparent Materials During low Velocity Impact Used in Protective Systems	295
C.G. Fountzoulas, R.E. Brennan, J.M. Sands, U.S. Army Research Laboratory	
37 Effects of End Restraint on Eyebar Behavior in Bridges	301
D.F. Mazurek, U.S. Coast Guard Academy	
38 Three-dimensional Mechanics of Microcellular Solids Using Scanning Confocal Microscopy	309
R.P. McCaffrey, P.B. Matthews, D.S. Gianola, University of Pennsylvania	
39 Characterization of the Mechanical Properties of Surface Nanocrystallized Materials	311
J.D. Gale, J. Marshall, A. Achuthan, Clarkson University	
40 Variation of Compression of Seals in PEM Fuel Cells	319
C.-H. Chien, C.-W. Lin, National Sun Yat-Sen University; Y.-J. Chao, C. Tong, J. Van Zee, University of South Carolina; T.-H. Su, National Sun Yat-Sen University	
41 Neutron Emission Evidences in Natural Materials Under Monotonic, Cyclic, and Vibrational Loading	329
A. Carpinteri, G. Lacidogna, A. Manuello, Politecnico di Torino; O. Borla, Politecnico di Torino/Istituto Nazionale di Fisica Nucleare	
42 Acoustic Emission and Electrical Properties of Quasi-brittle Materials Under Compression	343
G. Lacidogna, A. Carpinteri, A. Manuello, Politecnico di Torino; G. Niccolini, A. Agosto, Istituto Nazionale di Ricerca Metrologica INRIM; O. Borla, Politecnico di Torino/Istituto Nazionale di Fisica Nucleare	

43 Temperature Effect on Tensile Testing of Hybrid and Non-hybrid Composites	351
Y. Budhoo, Vaughn College of Aeronautics and Technology; F. Delale, B. Liaw, The City College of New York	
44 Studies on Fracture Performance of Bio-fiber-silica-glass Fiber Reinforced Epoxy Hybrid Composites	363
A.K. Chaudhary, P.C. Gope, V.K. Singh, G.B. Pant, University of Agriculture & Technology	
45 Mechanical Behavior of Bio-inspired Sandwich Composites	369
S. Haldar, J.K. Imo, H.A. Bruck, University of Maryland	
46 Characterization of Mechanical Behavior of Kevlar 49 Fabrics	377
D. Zhu, McGill University; B. Mobasher, S.D. Rajan, Arizona State University	
47 Identification of the Tensile Properties of Composite Material Under Variable Strain Rates	385
V.K. Singh, P.C. Gope, M. Tewari, G.B. Pant University of Agriculture & Technology	
48 Compression/Shear Response of Honeycomb Core	393
M.W. Czabaj, W.R. Tubbs, A.T. Zehnder, Cornell University; B.D. Davidson, Syracuse University	
49 Light Guide Component in Efficiency Enhancement of DSSC	399
C.-H. Chien, M.-L. Tsai, National Sun Yat-Sen University; C.-H., Hsieh, National Kaohsiung First University of Science and Technology; Y.-H. Li, T.-H. Su, F.-I. Su, Y.-L. Chung, C.-I. Chen, C.-W. Lin, National Sun Yat-Sen University	
50 Sign Support Structures Tested by means of Guided Waves	409
X.P. Zhu, P. Rizzo, University of Pittsburgh; J. Bruck, Pennsylvania Department of Transportation	
51 Reliability-based Design of Structures Under Seismic Loading: Application to Timber Structures	417
H. Riahi, R. Moutou Pitti, P. Bressolette, A. Chateauneuf, E. Fournrly, Université Blaise Pascal	
52 Progress in Developing a Standard for Dynamic Strain Analysis	425
E. Hack, EMPA Duebendorf; G. Lampeas, University of Patras; J. Mottershead, E.A. Patterson, University of Liverpool; T. Siebert, Dantec Dynamics GmbH; M. Whelan, European Commission DG Joint Research Centre	
53 Polymers in Biaxial States of Stress at Various Loading Rates	431
N.G. Ohlson, The Royal Institute of Technology	
54 Parametric Study to Optimize Aluminum Shell Structure Under Various Conditions	439
F. Ayari, College of Science and Technology/Supméca/LISMMA-Paris; E. Bayraktar, Supméca/LISMMA-Paris	
55 A Force Domain Analog-to-Digital Converter Applied in Micro and Nanoscale Tensile Tests	451
W.-F. Yeh, J.. Wang, University of Washington	
56 Distributed Fiber Optic Strain Measurement Using Rayleigh Scatter in Composite Structures	461
E.E. Sanborn, A.K. Sang, Luna Technologies; E. Wesson, Non-Metallic Resources (RPS); D.E. Wigent, III, 3TEX, Inc.; G. Lucier, North Carolina State University	
57 Diamond Sensors With Silicon Technologies for Sensing in Harsh Environments	471
T. Sanders, G. Hess, AET Inc.; J. Davidson, W.P. Kang, Vanderbilt University; T. Ooi, A. Corder, Missile Defense Agency	

58 The Influence of Restraint Systems on Panel Behavior	477
D.C. Jegley, NASA Langley Research Center	
59 Burst Strength of Pipeline Test Specimens Containing Longitudinal or Circumferential Corrosion Defects	487
J.L.F. Freire, Pontifical Catholic University of Rio de Janeiro; A.C. Benjamin, Petrobras R&D Center; R.D. Vieira, Pontifical Catholic University of Rio de Janeiro; J.L.C. Diniz, Fluke Engineering	
60 A Comparative Analysis of Two Full-scale MD-500 Helicopter Crash Tests	495
J. Littell, ATK Space Systems	
61 Structural Integrity Assessment of Blade's Subcomponents Using Acoustic Emission Monitoring	511
D. Zarouchas, Free University of Brussels; A. Antoniou, F. Sayer, Fraunhofer Institut für Wind Energy and Energy System Technology; D. Van Hemelrijck, Free University of Brussels; A. Van Wingerde, Fraunhofer Institut für Wind Energy and Energy System Technology	
62 Measurement of Cohesive Parameters of Craze in Polystyrene Films	519
C.K. Desai, A.S.. Kumar, S. Basu, V. Parameswaran, Indian Institute of Technology Kanpur	
63 Delamination Growth Using Cohesive Zone Model for Adhesive Bonding Under Compression	527
M.M. Islam, R.K. Kapania, Virginia Polytechnic Institute and State University	
64 Simulation of Stable Tearing Crack Growth Using the Cohesive Zone Model Approach	537
X. Chen, X. Deng, M.A. Sutton, University of South Carolina	
65 Experimental and Numerical Results for Diffusion Bonded Joints	545
A.H.M.E. Rahman, M.N. Cavalli, University of North Dakota	
66 Modeling of Stable Tearing With Crack Tunneling in Specimens of Different Thickness	553
J. Yan, M.A. Sutton, X. Deng, University of South Carolina	
67 Fatigue Modeling of Collagenous Soft Tissues	561
C. Martin, W. Sun, University of Connecticut	
68 An <i>in-situ</i> Experimental-numerical Approach for Interface Delamination Characterization	569
J.P.M. Hoefnagels, Eindhoven University of Technology; M. Kolluri, Eindhoven University of Technology/Materials Innovation Institute (M2i); J.A.W. van Dommelen, M.G.D. Geers, Eindhoven University of Technology	
69 Interface Integrity in Stretchable Electronics	577
J. Neggers, J.M. Hoefnagels, Eindhoven University of Technology; O. van der Sluis, Philips Applied Technologies; O. Sedaghat, M. Geers, Eindhoven University of Technology	
70 A Miniaturized Contactless Pure-bending Device for in-situ SEM Failure Analysis	587
J.P.M. Hoefnagels, C.A. Buizer, M.G.D. Geers, Eindhoven University of Technology	
71 Study of Propagation of a Pre-existing Crack Under Different Boundary Conditions for Fatigue Loading	597
M. Tewari, V.K. Singh, A.K. Chaudhary, G.B. Pant University of Agriculture & Technology	
72 Stochastic Model for Estimation of Probability-confidence Bounded a-N Curves	607
P.C. Gope, G.B. Pant University of Agriculture & Technology	

73 Waveforms and Frequency Spectra of Elastic Emissions due to Macrofractures in Solids	613
A. Schiavi, G. Niccolini, P. Tarizzo, INRiM - National Institute of Metrological Research; A. Carpinteri, G. Lacidogna, A. Manuello, Politecnico di Torino	
74 Failure Characteristics of Spot Welds of AHSS Under Quasi-static Conditions	623
J. Ha, H. Huh, Korea Advanced Institute of Science Technology; H. Lee, K.S. Kim, POSCO Global R&D Center	
75 Characterization of Adaptive Reinforced Concrete Structures	631
K.R. Biszick, Optechnology, Inc.; J.A. Gilbert, H. Toutanji, University of Alabama in Huntsville; T. Lavin, Soems, Inc.; M.T. Britz, R.K. Bommu, University of Alabama in Huntsville	
76 Bulk Waves for the Nondestructive Inspection of Immersed Structures	643
E. Pistone, P. Rizzo, P. Werntges, University of Pittsburgh	
77 Assault Rifle Bullet-experimental Characterization and Computer (FE) Modeling	651
L. Carbajal, J. Jovicic, H. Kuhlmann, DuPont Engineering Research & Technology	

A rocking spalling test to characterize the crack velocity in concrete

Pascal FORQUIN and Rachid CHERIGUENE

LEM3, Université Paul Verlaine - Metz, Ile du saulcy, 57045 Metz Cedex 01

Keywords: Dynamic cracking, Ultra-high speed camera, Digital Image Correlation, Spalling test.

Abstract

The dynamic crack velocity is a key-parameter involved in the micro-mechanics based modelling of the tensile damage of geomaterials under impact loading. However, because of technical difficulties, very few experimental methods have been proposed in the literature. In this work, a new set-up is presented based on spalling tests. A compressive pulse is transmitted to a parallelepipedic specimen by means of a Hopkinson bar. It is reflected as a tensile wave on the opposite free surface of the sample. A short notch is used to trigger a single crack whereas a larger notch provides a rocking effect of the rear part of the specimen. This experimental configuration has been optimized using numerical simulation analysis. Finally, a series of tests have been conducted on dry and wet concrete. Crack gauges and ultra-high speed camera coupled to Digital Image Correlation have been used to determine the crack speed in this material.

Experimental set up

A gas gun launches a projectile made of aluminium alloy 65 mm in length and 45 mm as diameter that hits the Hopkinson bar of the same diameter and 1200 mm length, Fig.1-right. The pulse is then transmitted to the specimen which has been put in contact with the bar. An ultra-high speed camera is used to visualize the crack propagation during the test. This camera has a 312x260 pp resolution and is able to acquire 102 images with an inter-frame time up to 1 micro-second. In addition, because of the rocking effect of the specimen two lasers interferometer are placed pointing on the rear edge of the specimen, one on the top of the rear edge and the other on the bottom. A series of numerical modeling has been conducted to optimize the design of the specimen and the projectile velocity with the aim to increase the stress intensity factor for triggering the crack without damaging the target. The specimen, Fig.1-left, is parallelepipedic $120 \times 60 \times 20 \text{ mm}^3$. Each sample is pre-notched to favour the crack initiation. Also, a high density random pattern is applied to the filmed face of the specimen in order to perform a Digital Image Correlation post-treatment [1]. Moreover, a strain gauge is placed close to the contact edge for recording the transmitted pulse and a crack gauge is stucked on the opposite face close to notch tip, where the crack initiation is expected, to characterize the crack propagation.

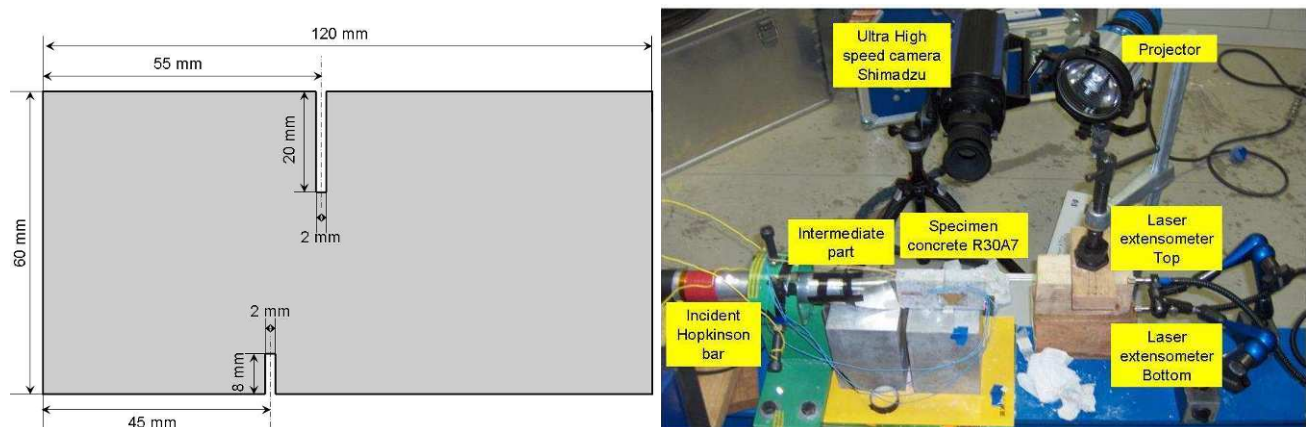


Fig.1: Optimized specimen geometry used in the rocking spalling tests (left). Experimental set up used for dynamic crack propagation testing (right).

Experimental results

Seven tests have been performed with two sets of sample: water saturated specimens and dried specimens. The dried specimens others were stored at 65°C until they reached a stabilized mass. Two results are plotted in Fig.2 for dry and wet specimens. Both tests show a gap in time regarding the crack initiation between the crack gauge signal and the DIC results. It is supposedly due to a lack of resolution of the crack gages. Nevertheless, a consistent value of crack propagation velocity has been found out (1300 ms^{-1}).

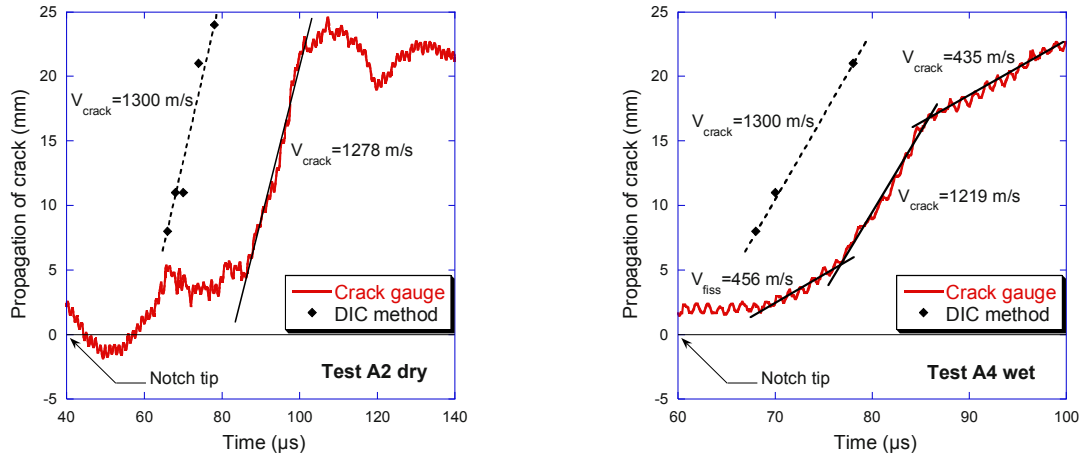


Fig.2: Crack velocity in R30A7 concrete: comparison between crack gauge and DIC results for dry specimen (left) and wet specimen (right).

Crack propagation with DIC is determined from an analytical method [2] based on the Crack Opening Displacement measurements. This method allows evaluating the crack tip position (Fig.3) and cracking velocity, (Fig.2).

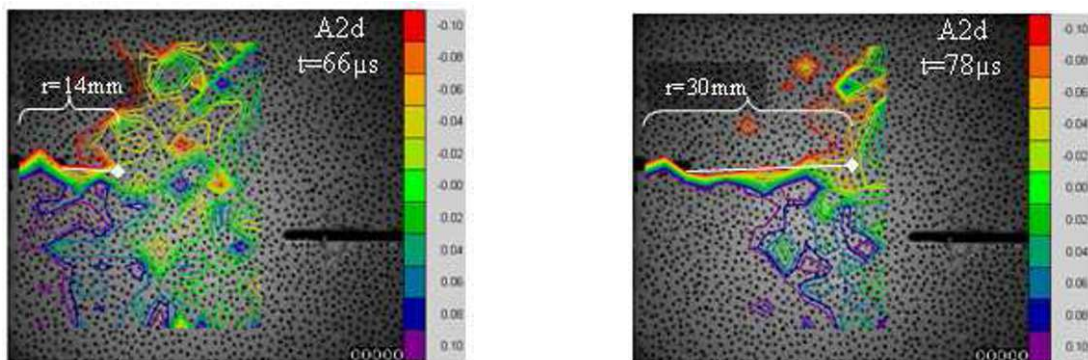


Fig.3: Axial displacement field (vertical orientation on figure) in pixel measured by DIC for dry specimen A2 (Correli Q4 software, 1 pixel = 0.1923 mm). Estimation of the crack tip position for $t = 66 \text{ μs}$ and $t = 78 \text{ μs}$.

Conclusion

This work presents a new experimental methodology named Rocking Spalling test performed to determine the crack propagation velocity in concrete materials. Technical difficulties related to single crack initiation problems have been analysed numerically. Crack velocity has been measured by crack gauge and Digital Image Correlation. The latter gives more accurate results for this material.

References

- [1] P. Forquin, L. Rota, Y. Charles and F. Hild, *International Journal of Fracture* **125** (2004), pp.171-187.
- [2] Pascal Forquin. *Endommagement et fissuration de matériaux fragiles sous impact balistique, rôle de la microstructure*. Thèse doctoral (LMT n°2003/15), 2003.

Crack growth behavior in preloaded metallic nested-angle plates under flight load spectrum

Mulugeta Haile*, Tzi-Kang Chen, Michael Shiao, and Dy Le

US Army Research Laboratory, Vehicle Technology Directorate
Aberdeen Proving Ground
Maryland

*mulugeta.a.haile@us.army.mil

ABSTRACT

Numerical and experimental results are presented from a project aimed at predicting the fatigue life of a rotorcraft airframe component subjected to flight load spectrum. The airframe component is a riveted joint used on cabin frame cap splices of several civilian and military helicopters which hereafter is modeled as lap-joined nested-angle plates. This component is fatigue sensitive due to the highly cyclic and vibratory rotorcraft mission spectrum and as such prediction of its fatigue life is an important part of the design cycle. This paper presents a systematic approach that combines 3D finite element simulation in ABAQUS and 2D damage analysis in NASGRO to estimate the life of the component. In the numerical analysis, fatigue crack growth rates for through-the-thickness crack initiating from fastener holes is computed using 2D standard and weight function models with the crack plane stress field obtained from 3D FEA analysis. Effect of load interaction due to tensile overload is included using strip-yield retardation model. Finally, results of the numerical simulations are compared with representative experimental data obtained under similar spectrum loading condition.

1 Introduction

Fatigue crack growth prediction albeit being a relatively old subject, over 150 years, is still an empirical science rather than a theoretical one. In the early days, SN curves were used to design fail-safe structures for infinite life[1, 2]. The empirical constants of SN curves, however, are derived from constant amplitude cyclic tests and hence are not representative of the random spectrum load that many airframe structures are exposed to. Moreover, it has been determined that [3, 4] the experimental fatigue lives of specimens and components subjected to random amplitude loading can be well below the fatigue lives predicted by the SN data. Hence a better design strategy is required.

With the advent of fracture mechanics, the damage tolerance design philosophy begins to evolve mainly in the aerospace industry. Fundamental to the damage tolerant approach is an understanding of structural performance in the presence of cracks or damage[5, 6] where emphasis was on determination of critical flaw size in a give time and usage condition. Hence models for crack growth prediction have to be formulated. Paris (1961) [7] was the first to develop a relationship to describe the crack progression rate or da/dN and the cyclical component ΔK of the Irwin stress (or stress intensity factor). Paris power law is give by,

$$\frac{da}{dN} = C \cdot \Delta K^n \quad (1)$$

where C and n are empirical parameters determined from curve fitting of experimental data. The Paris law, although the most popular model among the material science and fracture mechanics community [6] doesn't describe the experimentally observed threshold and critical growth behaviors. Moreover, Equation(1) predicts the same fatigue life regardless of the mean-stress history of the spectrum. Walker (1970) [8] re-formulated Paris' law by including effects of mean-stress through the use of a load ratio, R , where $R = \sigma_{min}/\sigma_{max}$ or K_{min}/K_{max} . The Walker equation is give by,

$$\frac{da}{dN} = C \left[\frac{\Delta K}{(1-R)^{1-m}} \right]^n \quad (2)$$

where C , n and m are again empirical parameters determined from a curve fit to a set of fatigue crack growth (FCG) experimental data. Different values of m are required in eq.(2) depending on whether R is greater than or less than zero. Forman (1972) [9] further modified the Paris' power law by introducing a factor depending on $(1-R)$ instead of R where $R = \sigma_{min}/\sigma_{max}$,

$$\frac{da}{dN} = \frac{C \Delta K_{rms}^n}{(1-R_{rms})K_c - \Delta K_{rms}} \quad (3)$$

here ΔK_{rms} and R_{rms} are the RMS (Root Mean Square) stress intensity factor range and stress ratio, n and c are curve fitting constants. The above three crack growth equations (eqs.(1),(2),(3) or Paris, Walker, and Forman) doesn't take into account crack retardation phenomenon and hence are not very accurate for estimation of crack growth in spectrum loaded components.

A more ambition predictive model comes from Forman and Newman (1984) [10] who modified the power law by including effects of plasticity-induced crack closure using what they called *crack opening function*. They developed what is now known as the NASGRO equation [11]. The NASGRO (or Nasgro) equation is a full-range crack model that mathematically represents all the three regions of the FCG curves while taking into account mean stress and crack closure effects. It is given by,

$$\frac{da}{dN} = C \left[\left(\frac{1-f}{1-R} \right) \Delta K \right]^n \frac{\left(1 - \frac{\Delta K_{th}}{\Delta K} \right)^p}{\left(1 - \frac{\Delta K_{max}}{\Delta K_c} \right)^q} \quad (4)$$

where ΔK is the applied stress-intensity factor range, and R is the stress ratio; ΔK_{th} is the fatigue threshold, K_{max} is the stress-intensity factor corresponding to the peak applied load, and K_c is the critical stress intensity factor; p and q are curve fitting constants that control the shape of the fitting in the threshold and critical crack growth regions respectively; and f is Newman's crack opening function. The constants C and n , which are the main fitting parameters are determined by minimizing the curve fitting error equation given by,

$$e_i = \log \left(\frac{da}{dN} \right) - \log(C) - n \log \left[\left(\frac{1-f}{1-R} \right) \Delta K \right]_i - \log \left[\frac{\left(1 - \frac{\Delta K_{th}}{\Delta K} \right)^p}{\left(1 - \frac{\Delta K_{max}}{\Delta K_c} \right)^q} \right]_i \quad (5)$$

Equation (4) estimates crack growth behavior in near threshold and critical growth regimes better than any other model and is probably the most accurate empirical model currently available [11]. It is also good to note that the Nasgro equation may be reduced to the Paris law eq.(1) by setting parameters p and q to zero and ignoring the effect of crack closure, i.e. by setting $f = R$ for $0 < R < 1$.

This paper uses the NASGRO equation with stress gradients obtained from 3D finite element analysis (ABAQUS) to predict spectrum crack growth in preloaded nested-angled plates. The 3D FEA stress gradient is the result of the combined action of fastener preload, bearing contact load and friction shear forces acting on the plates. The numerical predictions so obtained are compared with experimental data from fatigue tests of two nominally identical nested-angle specimens.

2 Experiments

The goal of the experimental study was to determine fatigue crack growth in nested angle specimens under loads that simulate the various flight regimes of a typical rotorcraft. All tests are performed in ambient laboratory conditions using a servo-hydraulic test frame which applies a predetermined spectrum load at a constant frequency. The test specimens are made of aerospace grade Al 7075-T6 alloy angle-plates with thickness of 0.063in. Schematics of the nested-angle plates is shown in Fig.(1). The two plates shown in the figure are lap joined using stainless-steel fasteners with a bolt-load of 800lbf. The fastener holes are uniformly spaced in intervals of 1.12in and are drilled and rimmed to a nominal diameter of $\phi = 0.1875$ in. Detailed description of the experimental setup is available in [12, 13, 14]

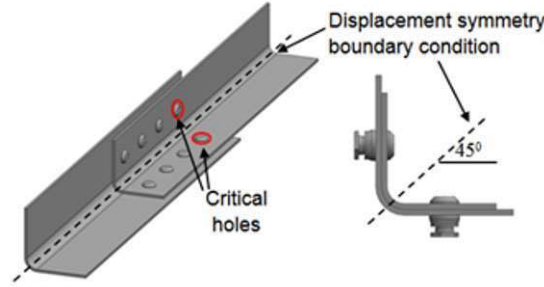


Fig. 1: Geometry of the nested angle test specimen. The two plates are made from Al 7075-T6 and the fasteners are stainless steel. The critical holes are the locations of maximum principal stresses where crack will most likely initiate. The broken lines show the displacement symmetry plane in the FEA model.

The first test specimen (specimen-A) is run at a constant load amplitude of 3350lbf and a stress ratio $R=0.1$ until it fails by fracture. The remaining two specimens (B & C) were tested under variable flight load spectrum that peak at $P_{max}=2500$ lbf and 3000lbf respectively. The flight spectrum used to test specimens B and C is developed from a representative mission profile of a UH-60 type class helicopter undergoing predefined maneuvers. The spectrum cycles are then constructed from recorded strain gage data where internal loads (or stresses) at control points are available for a combination of velocity, load factor and flight maneuvers. During individual specimen tests the flight spectrum is scaled by the peak test load and is input to the servo-hydraulic test frame controller. Fig.(2) shows a segment of the normalized UH-60 single flight mission spectrum used in this experiment.

3 Numerical simulations

3.1 Stress analysis

The numerical analysis conducted herein involves full 3D finite element simulation of the constant spectrum test (specimen-A) at its peak load $P_{max}=3350$ lbf. Stress analysis for the variable spectrum specimens were obtained by scaling the stress values of specimen-A by the load ratios i.e. the stress distribution for specimen-B is calculated by multiplying the stress distribution of specimen-A by $2500/3350$ likewise for specimen-C it is $3000/3350$ times stresses on specimen-A, assuming linear behavior.

The purpose of the 3D stress analysis is two-fold. First, the analysis is used to calculate the crack plane stress gradient resulting from the combined action of the applied load, contact load, and surface

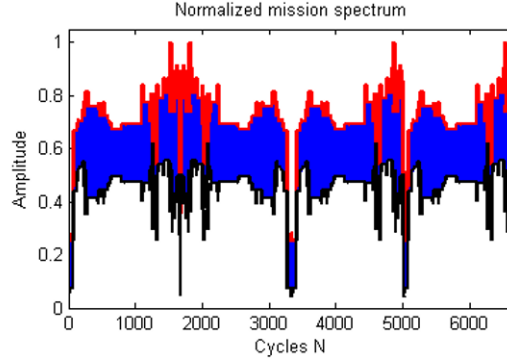


Fig. 2: A segment of the normalized flight mission spectrum (see also [12]). This spectrum is scaled by $P_{scale}=2500$ for specimen-B and $P_{scale}=3000$ for specimen-C.

shear forces resulting from friction contact pairs. Second, the analysis is used to calculate the stress intensity factors at the peak load to verify if the 3D FEA obtained stress intensity factors (SIF) correlate to the one obtained from the damage tolerance analysis code (NASGRO). It is agreed upon that the stress intensity factors computed using the 3D finite element analysis would give a better estimate of the crack tip intensity as it takes full account of the stress field near the crack tip arising from friction and contact interactions. Close correlation of the FEA SIF values with NASGRO SIF is generally taken as an indication to the accuracy of the 2D life prediction methodology of NASGRO. The finite element model is also required to identify the location of the maximum tensile stress (or hot spots) near the critical fastener hole. This is where cracking will very likely initiate.

Using Abaqus, a nonlinear, static, large deflection finite element model with contact and friction was developed using the displacement symmetry model shown in Fig.(1). The symmetry model enables to refine the mesh and also to simplify the geometry into a form that is readily compatible with Nasgro's simple library models. Surface-to-surface contact with friction was included to represent the part-to-part interaction between the two plates and the stainless-steel fasteners. A frictionless contact was later simulated and compared with the frictional contact to see if introduction of friction has any effect on the predicted fatigue life of the specimen.

We applied the FEA loads into simulation steps. The first load step was used to resolve fastener clamp-up (bolt-load of 800lbf) and establish contact throughout the model. In the second step, the remote load is ramped up to its final magnitude of 3350lbf. Analyses sanity checks (such as mesh convergence and load equilibrium) were performed to ensure that the finite element model performs well.

3.2 Finite element results

Figure (3) shows the maximum principal stress contour near the critical hole of the small leg specimen (the smaller of the two nested plates shown in Fig.(1) for cases $\mu=0.6$ and $\mu=0$ upper and lower figures respectively. For the case where $\mu=0.6$, the peak value of the principal tensile stress is 45.5 ksi and this stress is located at the faying surface between the two plates away from the critical hole (see Fig.(1) for critical hole). For the second case where $\mu=0$, the hot spot is located at the usual location near the edge of the critical hole in the 3 and 9 o'clock directions with the maximum principal stress being 77.6 ksi.

As can be seen, the maximum principal stress (magnitude and location) is affected by the introduction of contact friction. Moreover, the load transfer by each of the eight fasteners also depends on the extent of the friction coefficient μ . In the extreme case where a higher friction coefficient is assumed, most of the load transfer between the plates is through surface shear and the contribution of the load transfer through fastener shank is minimal. For $\mu=0.6$, large amount of load is transferred

by each fastener through friction contact between fastener heads and the plates. For $\mu=0$, the load transfer is mainly between fastener shank and the hole. Figure (4) shows the principal normal stress contour in the symmetry model.

As noted earlier, the finite element analysis is the first step of the damage tolerance analysis and its purpose is to calculate the stress fields that are needed by NASGRO library models. Fig.(4) shows sections on the plate where stress distributions are required to run NASGRO code. The cross section stress at sections 1 and 2 (Sec.1 and Sec.2) are used as inputs to NASGRO's TC03 model whereas the stress at section 3 (Sec.3) is used as an input to run model TC13.

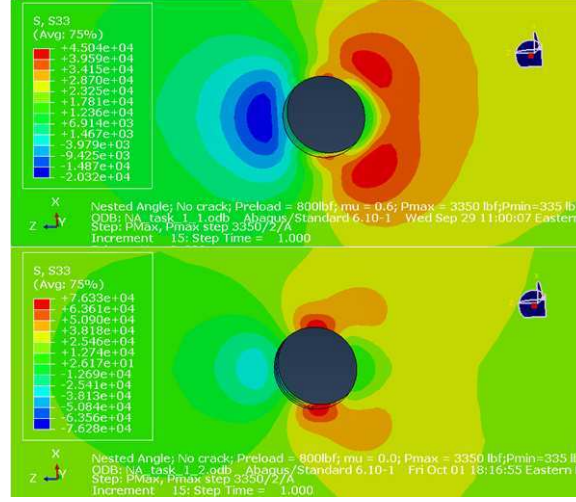


Fig. 3: Principal tensile stress contours around the critical fastener hole. The upper figure shows the stress contours for simulation case 1 where $\mu = 0.6$, $P_{max} = 3350\text{ lbf}$, $Boltload = 800\text{ lbf}$, $\sigma_{max} = 45.5\text{ ksi}$ and the lower figure shows the stress contours for simulation case 2 where $\mu = 0$, $P_{max} = 3350\text{ lbf}$, $Boltload = 800\text{ lbf}$, $\sigma_{max} = 77.6\text{ ksi}$. Note that the location of the hot-spot do not coincide on the figures.

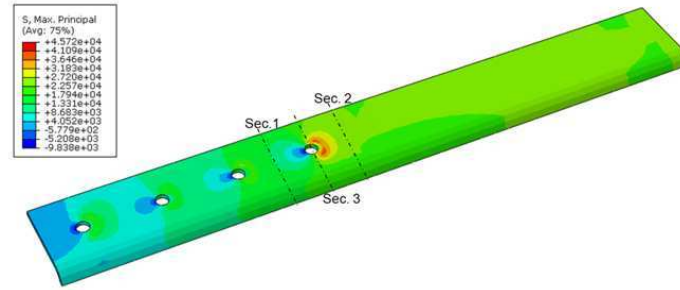


Fig. 4: Principal stress contours on the small-leg symmetry model for simulation case 1. Sec.1 and Sec.2 are planes where normal stresses are extracted for input into NASGRO's TC03 model. Sec.3 is the section stress input into TC13.

3.3 Fatigue crack growth predictions

Fatigue crack growth prediction for the constant and mission spectrum loads are conducted using Nasgro. Since Nasgro doesn't have a library crack geometry that models the nested-angle configu-

ration some assumptions are needed. First, the half symmetry angle specimen is modeled as flat (or 2D) assuming that the edge radius doesn't significantly alter the stress distribution near crack tip throughout the loading cycle. Second, contact friction is represented implicitly within bearing and bypass stresses as there is no field in Nasgro GUI that allows for friction input.

We used two library crack models for the life estimation. The weighted function stress intensity model TC13 shown in Fig.(5) was used since it allows modeling of a through crack at an offset-hole in a finite plate with a nonlinear stress gradient input. The stress gradient information for frictional and frictionless contact cases are obtained from the 3D stress analysis as depicted by Sec.3 in Fig.(4). Figure (5) shows the principal stress distribution used as Nasgro inputs for the friction and frictionless cases.

A second simulation was conducted using the classical library model TC03 shown in Fig.(6). TC03 requires the remote stress field and bearing load be specified at the critical fastener hole locations. The remote stress field was again obtained from FE simulation by mapping the principal stresses across sections 1 and 2 as shown in Fig.(6). Since part of the load is transferred through friction, the resultant of the stresses from sections 1 and 2 and bearing load P in TC03 model won't satisfy equilibrium. Hence contact friction has to be included indirectly as discussed below.

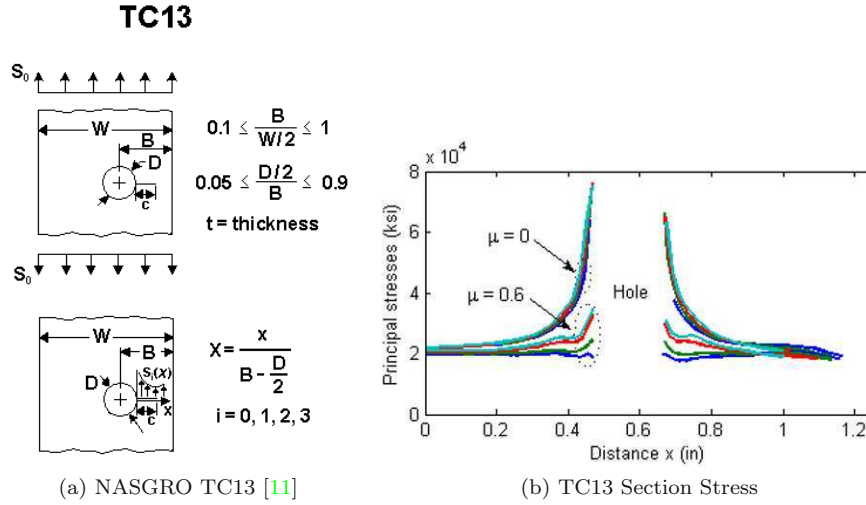


Fig. 5: NASGRO TC13 library model and the corresponding crack plane stress inputs for $\mu = 0.6$ and $\mu = 0$. The various curves on the graph show the stress distribution at certain depth through the plate thickness at Sec.3. Note that the principal stress near the hole are maximum for $\mu = 0$ in addition the difference in principal stress between the two cases becomes small away from the hole.

3.4 Including effects of friction

The crack plane stress gradient input into Nasgro's TC13 has the friction effect included in it and hence doesn't require further consideration. However this is not the case for TC03. As shown in the FEA analysis (see Fig.(5)), the large bolt preload used to clamp-up the two nested plates and the high friction coefficient resulted in a significant surface shear between the plates and fastener heads. This shear force has shown to alter the magnitude and location of the maximum principal stress and the likely location of crack initiation point on the plates(Fig.(3)). A logical question that needed to be addressed was whether or not this friction induced shear force will affect the fatigue life of the specimens. Also how may friction shear stress be included in Nasgro's TC03 model? To address these questions a parametric study has been conducted. The study involves partitioning the FEA calculated friction forces and adding a certain fraction of it into the bearing load (P) and bypass

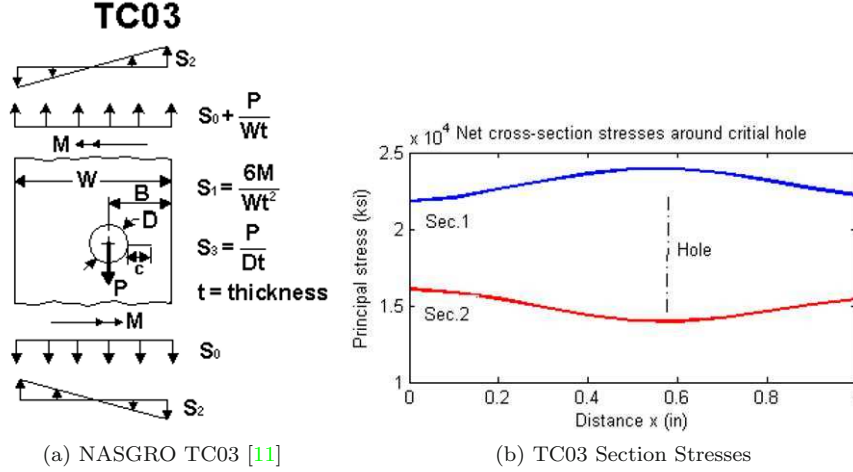


Fig. 6: NASGRO TC03 library model and the corresponding section stresses for $\mu = 0.6$. The stress at Sec.2 corresponds to the bypass stress S_0 on TC03. The bearing load P is also obtained from the finite element analysis.

stress (S_0) of Nasgro's TC03 while maintaining force equilibrium of the model. Four analysis cases were considered: (1). TC03-1 all the friction force is added onto the bearing hole P , (2). TC03-2 half of the friction force is added onto bearing load P and the other half is added onto the bypass stress S_0 , (3). TC03-3 half of the friction force is added onto the bearing load and the other half is ignored (thrown away), (4). TC03-4 all the friction force is ignored. These four cases were simulated with the scaled flight spectrum loads and results are compared with experimental data.

4 Results and discussions

Figure (7) presents crack size vs. log-cycles for the spectrum load specimens (B&C) considered in this work. In each life prediction plots are five curves consisting of TC13 and the four cases of TC03 discussed above. Simulation results for strip-yield interaction model are also shown.

In all TC03 cases, the simulations considering any portion of the friction shear stress resulted in highly conservative life estimates. The 50-50 approach (case 2), i.e., dividing the friction into two and adding it into bearing and bypass stresses has resulted in insignificant life change compared to the 100% on-bearing (case 1). A big jump, however, is observed when half of the friction is added into the bypass stress and the other half is ignored. Better TC03 correlation with the experimental data was observed when the effect of friction shear stress is ignored altogether. This observation seems to contradict the finite element simulations that have shown significant stress field around the fastener holes as seen in Fig.(5). One possible explanation for this disparity could be made by observing that; the friction shear forces do cancel each other i.e. the friction shear distribution above and below the crack plane act in the same direction so that one half of these force aids the crack opening force whereas the other half tends to close the crack with the same magnitude. These actions resulted in a net zero crack plane displacement as verified by the good correlation of TC03-4 with the experimental data. The crack retardation models (strip-yield) in general have resulted in the prediction curves to shift slightly to the right. This is always true since the crack opening stress K_{open} is higher when crack advances in the wake of plastically deformed material[?]. Figure (8) compares the stress intensity factors calculated by the 3D FEA analysis and the 2D Nasgro simulation. The observed close correlation between FEA SIF and TC13 and TC03-4 SIF values justified the accuracy of the 2D assumption made at the beginning of the analysis.

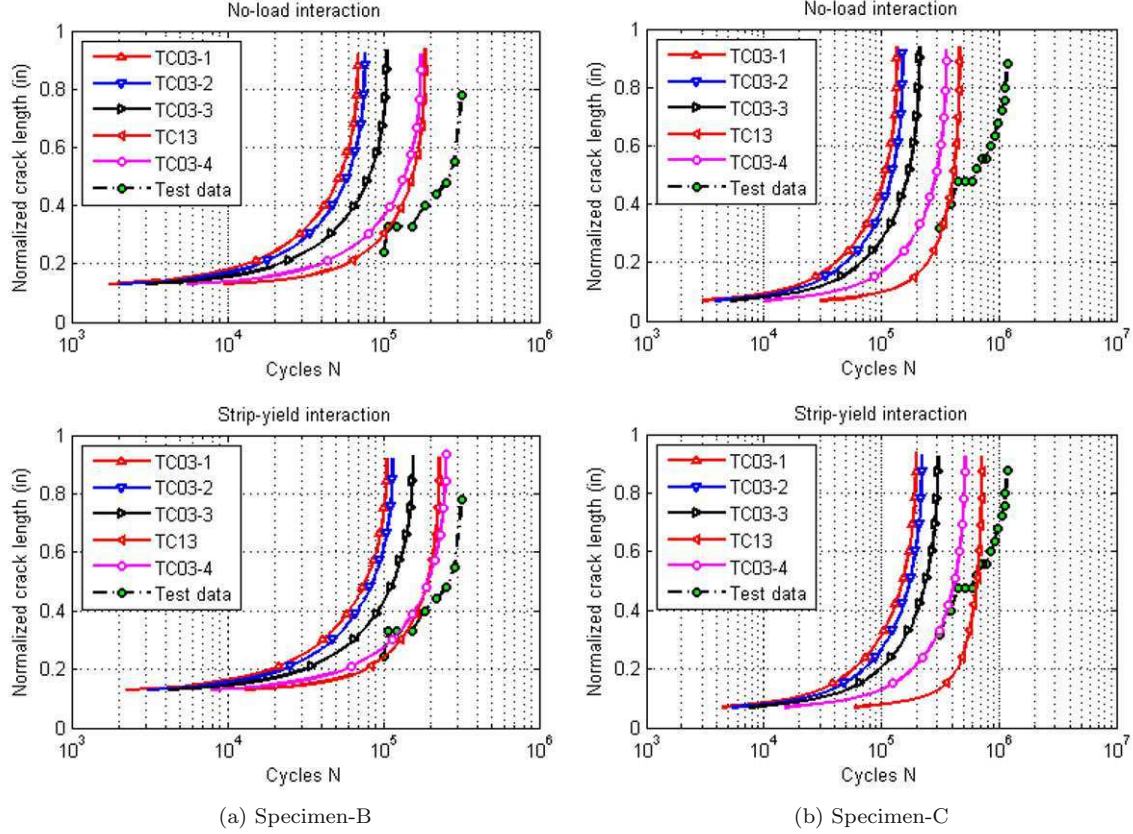


Fig. 7: Comparison of numerical simulations and experimental data for specimen-B (left two plots) and specimen-C(right two plots). The four cases of friction are shown as TC03-1 through -4. The upper plots show crack length vs. cycle without considering load interaction (load history) and the lower two plots show results for strip-yield interaction model. Better correlation with experimental data is observed for TC13 and TC03-4 simulations with strip-yield interaction option engaged.

5 Conclusions

Numerical fatigue crack growth analysis on a representative rotorcraft structural component has been presented. The later is a riveted joint used on cabin frame splice of several military and civilian rotorcrafts. The stress field around the critical hole resulting from the combined action of applied load, fastener preload and friction are obtained using 3D finite element analysis. Fatigue crack growth and life prediction is performed using Nasgro TC03 and TC13 library models with and without load interactions. In general, Nasgro crack growth prediction using TC13 (with craze plane stress gradient input from 3D FEA) shows a better agreement with the experimental data. TC03 predictions without the inclusion of contact friction also provided a well correlated life estimate. However, inclusion of any portion of friction stress in the analysis has resulted in a highly conservative life prediction by the model. Effort is still underway to further refine the analysis with more experimental data.

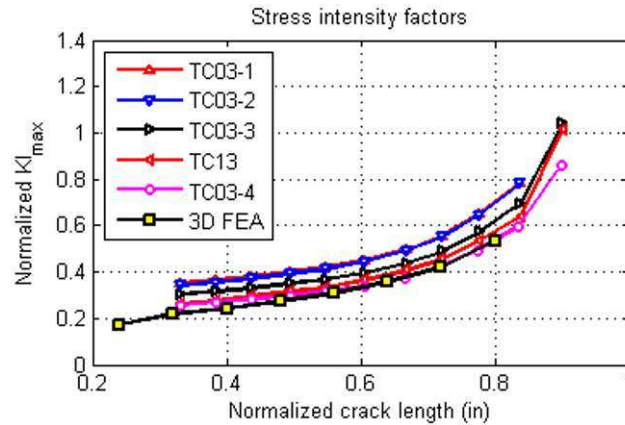


Fig. 8: Comparison of stress intensity factors calculated by 3D finite element analysis and NASGRO's 2D models TC13 and the four cases of TC03.

References

- [1] Schutz W *A history of fatigue* Eng. Frac. Mech. 54 263-300 (1996)
- [2] Lombardo D.C. *Helicopter structures - A review of loads, Fatigue design techniques and usage* Defense science and technology organization aeronautical research laboratory, Commonwealth of Australia (1993)
- [3] Hudson, C.M. and Hardrath, H.F. *Investigation of the Effects of Variable Amplitude Loadings on Fatigue Crack Propagation Patterns* TND-1803, NASA (1963)
- [4] Christensen, R.H. *Fatigue Crack, Fatigue Damage and their Detection* J. Metal Fatigue, McGraw-Hill, New York (1959)
- [5] Reddick H.K. *Safe-life and Damage-Tolerant design approach for Helicopter structures* Applied Technology Laboratory, US Army Research and Technology Laboratories (AVRADCOM), Virginia
- [6] Pugno N, Ciavarella M, Cornetti P, Carpinteri A., *A generalized Paris' law for fatigue crack growth* J. of the Mechanics and Physics of Solids, Issue 54 (2006)
- [7] Paris, P. and Erdogan, F. *A Critical Analysis of Crack Propagation Laws* J. of Basic Engineering, Volume 85 (1963)
- [8] Walker, K. *The Effect of Stress Ratio During Crack Propagation and fatigue for 2024-T3 and 7075-T6 Aluminum* American Society for Testing and Materials, (1970)
- [9] Forman, R. G. *Study of fatigue crack initiation from flaws using fracture mechanics theory* Engineering Fracture Mechanics. 4(2), pp 333-345 (1972)
- [10] Newman, Jr., J. C. *A Crack Opening Stress Equation for Fatigue Crack Growth* J. of Fracture, Volume 24, No. 3, (1984)
- [11] *NASGRO Fracture Mechanics and Fatigue Crack Growth Analysis Software* Version 5.2, NASA-JSC and Southwest Research Institute (2008)
- [12] Urban, M.R. *Spectrum loading and surface effects in AL 7075-T6*, 65th AHS annual forum, Grapevine, TX (2009)
- [13] Urban, M.R., Bauer, G., Meyer T.G., Goshal A., Welsh G.S., and Bordick N., *Integrated statistical stress life analysis methodology utilizing local stress field*, 66th AHS annual forum, Phoenix, AZ (2010)
- [14] Urban, M.R. *Analysis of the fatigue life of riveted sheet metal Helicopter airframe joints*, Int. J. of Fatigue, Elsevier Ltd. pp 1013-1026 (2003)

Experimental and Finite Element Analysis (FEM) of Bioceramics

D. Katundi^a F. Ayari^{a, b} E. Bayraktar^{a*} and A. Tosun-Bayraktar^c

^aSupmeca/LISMMA - Paris, School of Mechanical and Manufacturing Engineering France

^bLaboratory of Mechanics, College of Science & Technology, 1008 Montfleury, Tunis, Tunisia

^cChemical Processing Department - P. Vauquelin, 21, Av. Bouteux 75013 Paris France

*Corresponding author: bayraktar@supmeca.fr

ABSTRACT

Hydroxyapatite (HAP) displays very excellent biocompatibility in the body and is for the most part used in biomedical applications thanks to well biocompatibility for replacement of bone. In fact, Boron and Ti containing HAP are the bioactive materials and it can incorporate into bone structures, supporting bone in-growth without breaking down or dissolving, and it interacts with the living tissue due to the presence of free calcium and phosphate compounds. Boron containing HAP are also extensively useful for the manufacturing of bio-ceramics in order to improve the physical and chemical properties of biomaterials. Boron nowadays used in HAP applications is a very successful candidate material for bioceramic engineering. Generally, Al_2O_3 powder is added to HAP powder in order to obtain high fracture toughness. Al_2O_3 has good mechanical properties as compared with HAP, and exhibits extremely high stability with human tissues. In this paper, the effect of microwave sintering temperature on the relative density, hardness, and phase purity of compacted bovine Hydroxyapatite (BHA) powder was reported. This research is a comprehensive attempt to develop Hydroxyapatite bio composite ceramics reinforced with alumina - Al_2O_3 , pure metallic titanium and pure pulverised boron powders. A Finite Element (FEM) analysis is also used to simulate the macroscopic behaviour of this material, taking into account the relevant microscopic scales. Generally, microwave-sintered samples showed much small grain size and a uniform microstructure. For this reason, the behaviour of bio ceramics in case of rapid heating in microwave was also discussed. Recent results revealed that microwave processing was a promising method for sintering porous bio ceramics thanks to clean and shorter sintering time regarding to conventional sintering methods.

Keywords: HAP Bio ceramics; Microwave sintering; FE analysis; Interface; Boron; Titanium

1. Introduction

Biomaterials are designed and fabricated for implantation within or incorporation with a living system to replace or repair the living tissues or organs which form an interface between the living and non-living parts [1, 2]. Biomaterials are based on polymers, metals, ceramics, or composites of these [3]. Hydroxyapatite (HAP), $\text{Ca}_{10}(\text{PO}_4)_6(\text{OH})_2$ is a very well known phosphate in the biologically active phosphate ceramic family by virtue of its similarity to natural bone mineral. Synthetic and naturally produced hydroxyapatite finds a variety of biological applications and brings out the formation of an apatite layer at the interface with bone tissue [4, 7, 8]. This property makes HAP extremely attractive and widely used as a material for bone implants. Nevertheless, fracture strength and toughness of this ceramic are low, and it cannot endure practical use. For this reason, HAP is usually reinforced with various biocompatible materials that can improve the strength of the pure HAP. Titanium is a successful biocompatible material that is extensively used for biomedical applications, especially for bone-anchoring systems, such as dental, orthopaedic implants and osteosynthesis applications. It has advantageous bulk mechanical properties such as a low modulus of elasticity, a high strength-to-weight ratio, and passive surface properties i.e. excellent corrosion resistance and low rates of ion release as well as a high degree of biocompatibility which is largely attributed to an inert surface oxide film. Alumina, another material used to make implantable orthopaedic devices, is a very well tolerated material with minimum tissue reaction after implantation. It exhibits high mechanical strength and minimum wearing. Therefore, it is frequently used in high load-bearing sites such as hip prostheses and dental implants [3-8, 10-16].

Additionally, Paraffin is very successful additive in HAP for creating micro porosity in the structure. During the heating, Paraffin is burned and leaved its place as micro porosity homogeneously distributed in the structure. Paraffin was used in this study as a well substitution of naphthalene that is irritant material. Concerning borohydroxyapatite compounds (Boron containing HAP), they are extensively useful for the manufacturing of bio-ceramics in order to improve the physical and chemical properties of biomaterials. Boron very often used in HAP application, is a very successful candidate material for bioceramic applications. Recent scientific researches indicate that Boron will be more useful with other materials in future bioceramic applications.

In this paper, a net shape microwave sintering procedure was used in the frame of the "Bioceramic" research project by using pure metallic titanium and pure pulverised boron powders and a few percent of paraffin to create a micro porous structure that was well replaced the other materials to create porous structure. A special attention was given for the microstructural evolution with recently developed compositions to give practical significance for the application of the biomaterials.

2. Experimental study

In this preliminary study, a new microwave sintering method (lower energy costs and shorter processing times) has been carried out for manufacturing of bio composite materials that all the details were given in former paper [2]. The compacts geometry was prepared based on the fixed matrix natural HAP + 10% alumina (Al_2O_3) reinforced with pure metallic titanium and pure pulverised boron with Yttrium and Zirconia (VWR-France). Before process, alumina was doped with MgO (1%). Then, the blended powders homogenized by ball milling during one hour were compacted by uniaxial cold isostatic pressing with a green compact pressure of 300 MPa, intending to produce an initial green density ranging 90%. The aspect ratio of this geometry was between 0.9-1. Cylindrical test specimens were prepared (Height=11mm, Diameter=11mm) according to the British Standards-BS 7253, and then sintered for a short time (up to 30 min) in microwave oven. At the second stage, micro hardness and quasi static compression tests were performed on the sintered samples to study the influence of microstructure and phase composition on the micro-mechanical behaviour of the recently formed compositions. For etching, acetic and lactic acids were used for microstructural surface analysis. For evaluation of fracture surfaces of the specimens, failed during the compression test have been analysed in Scanning Electron Microscope and chemical analysis by “EDS” analysis. Some of the specimens were analyzed by XRD to distinguish the possible phases that can be occurred in high temperatures during sintering. Experimental results were used for a Finite Element (FEM) analysis to create a simple and for an easy understandable model the behaviour of the bioceramic materials during the deformation.

2.1. Microwave - Sintering

The application of microwave energy to the processing of various materials such as ceramics, metals and composites offers several advantages over conventional heating methods. Microwave heating results in lower energy costs and decreased processing times for many industrial processes. These advantages include unique microstructure and properties, improved product yield, energy savings, reduction in manufacturing cost and synthesis of new materials.

At the beginning of the test, some of the specimens were sintered in an electrical - conventional furnace (High Temperature Furnace) in order to compare the microstructural evolution regarding to the sintered specimens in microwave oven. In this project, the primary aim, however is to use a house type microwave oven in laboratory conditions. For this reason, a house type (2.45 GHz) microwave oven was used by converting some of the conditions of the microwave oven. Temperature measurement system was adapted to the microwave by using a special thermocouples covered with safety insulating cables to prevent the electrical contact of the thermocouples when microwave works. The accuracy of temperature measurement with this device was determined to be within -10°C of the temperature measured.

The thermo couples were inserted inside of the alumina crucible that it was very close (2-3 mm) to the specimens. All of the details for this sintering method in former papers [6, 7, 9]. Compared to the conventional sintering, there was a slight increase in density of the specimens sintered using microwave conditions. Since the microwave sintering took much shorter time, densification rate in the microwave sintering process may be considered to be higher than in the conventional sintering. For effective sintering time for these samples were chosen 20 minutes.

3. Results and Discussion

3.1. Experimental part

Natural HAP was obtained from calcinated fresh - young bovine bones by following the method developed formerly in SUPMECA/LISMMA-Paris [6, 7-8]; after cutting, the femurs were undergone deproteinized with NaOH treatment. After repeated washing, they were heat treated at 850°C . The treated HAP powder (particle sizes of 1-2 μm) was one by one mixed in different percentages. Figures 1 and 2 show the microstructure natural HAP taken from the SEM image with “EDS” analysis, containing 5% and 10% pure pulverised metallic boron powder that was distributed homogeneously in the structure. The average grain size measured of this mixture varies from 1 to 5 μm . This structure verifies that the microwave sintering gives a clean, lower energy costs and shorter processing times for these materials.

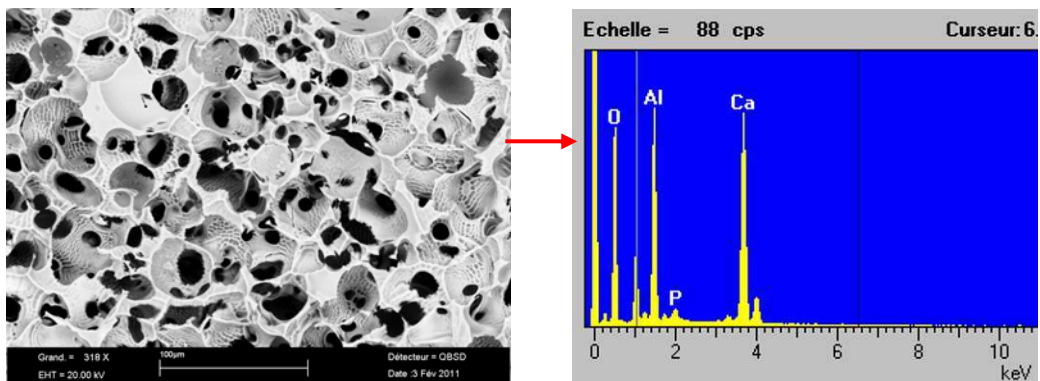


Fig. 1a. Microstructure of the sample containing only 5%B

Figure 1b shows the distribution map (SEM-cartography) of main elements resulting from Figure 1a. The diffusion of Alumina and Calcium show very uniform distribution, it means that much more improvement has been carried out in the compositions containing boron powder from 5% volume fraction. In reality, alumina shows an easy diffusion even if it does not show high thermodynamic tendency. Doping of Alumina with MgO before sintering process facilitates to react easily with HAP matrix. Looking at the illuminated areas in the back-scattering (BS) SEM images of Figure 1b, it is noted that the Alumina-associated phases were uniformly distributed in the bulk of composite materials.

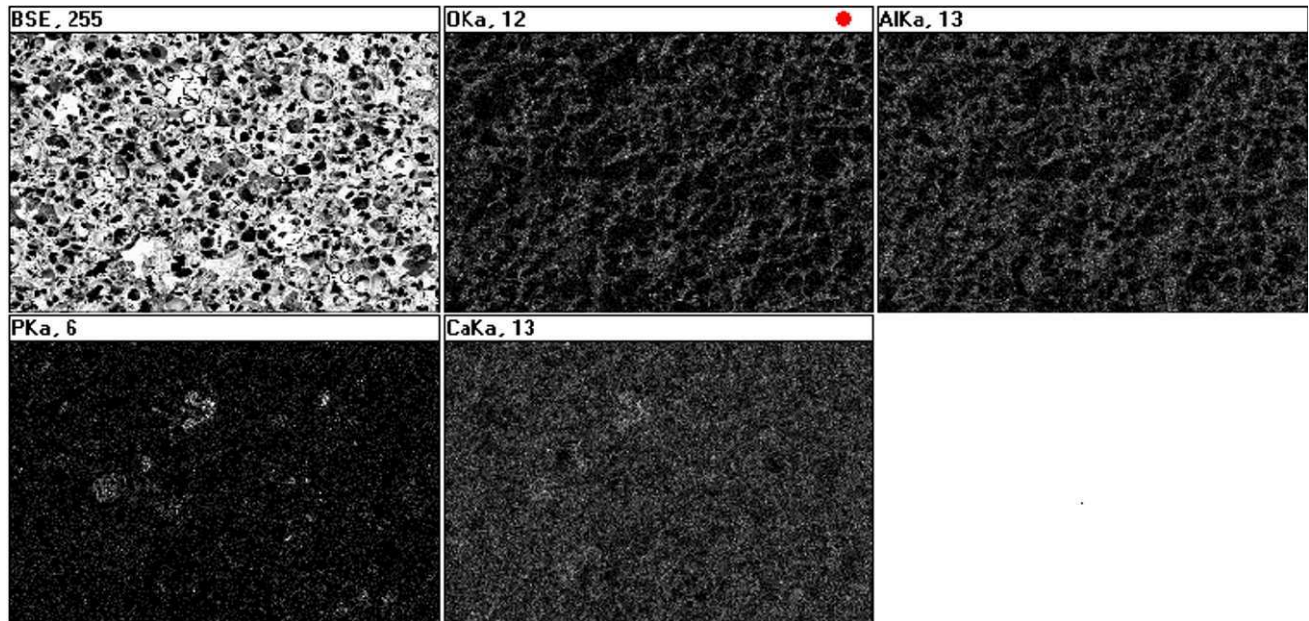


Fig.1b. Distribution map (SEM) of main elements resulting from Figure 1a (sample containing 5%B)

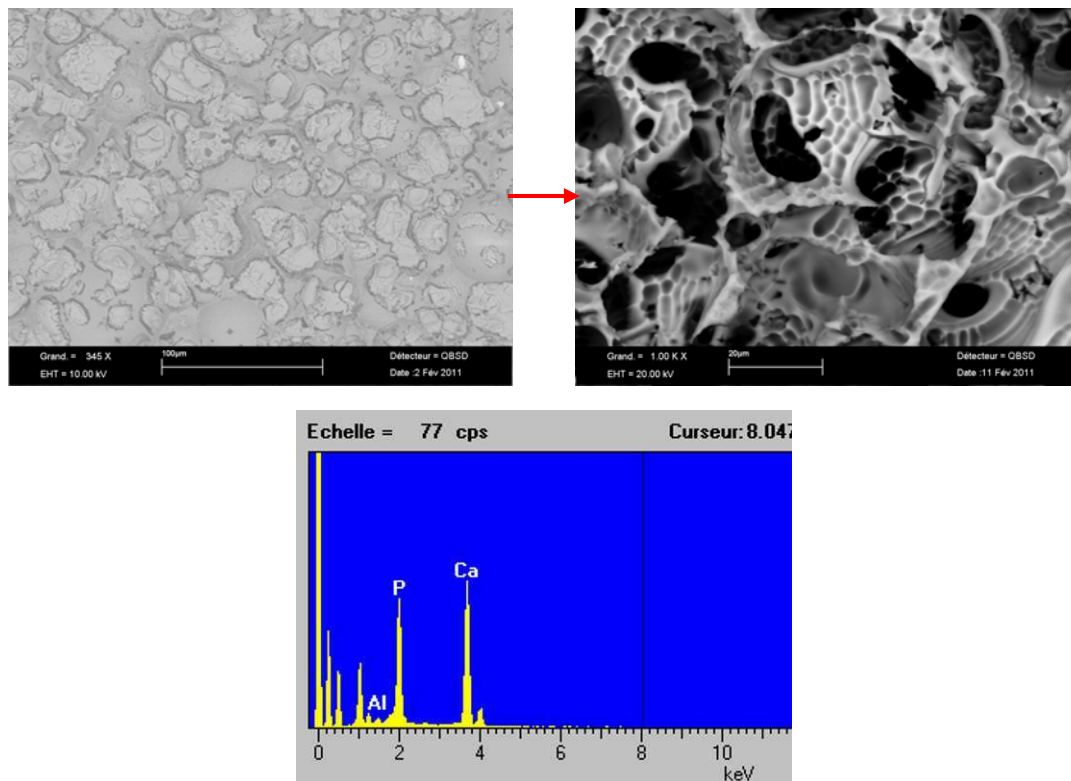


Fig. 2. Microstructure of the sample containing only 10%B

The SEM images shown in the Figures 3 and 4 indicate SEM micrograph of the sample containing 20%B+15%Ti and 20%B+20%Ti respectively. Very perfect sintering has occurred with these composition with very hard structure (see Table 1), and also the formation of certain amount of a glassy phase was identified. Ti always shows a high thermodynamic tendency to diffuse and then to react with HAP matrix easily.

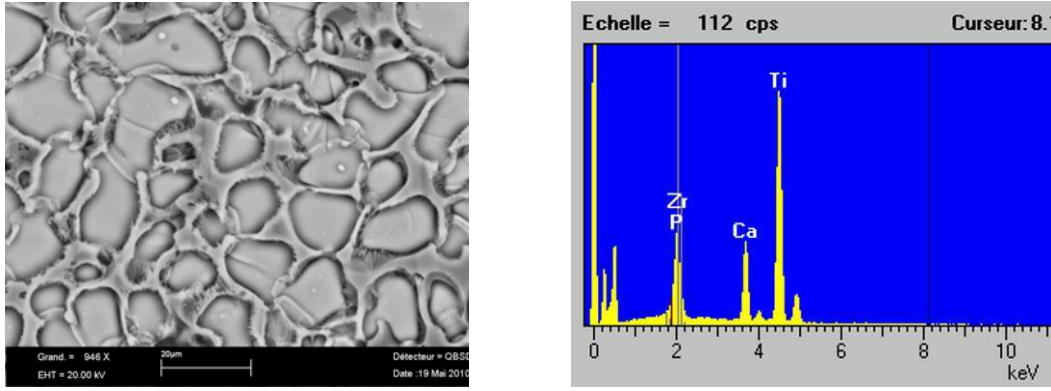


Fig. 3. SEM micrograph containing 20%B+15%Ti+3%Yi₂O₃+3%ZrO₂

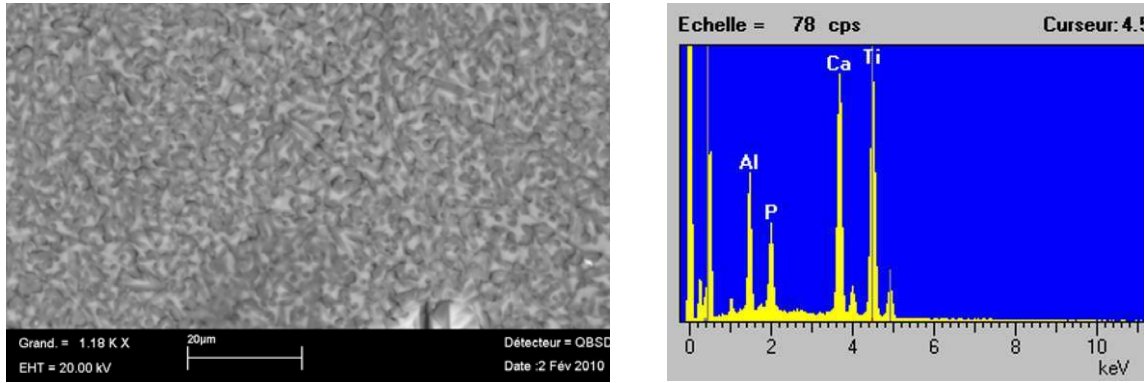


Fig. 4. SEM micrograph containing 20%B+20%Ti+3%Yi₂O₃+3%ZrO₂

The phases containing titanium elements were distributed uniformly in the structure even if there are an excess of Ti at the grain boundaries. Finally, a well fusion was observed in the structure and some of the specimen showed a regular micro porosity in the matrix. The diffusion of Ti is much more even inside the matrix compared to Al. As explained in the section of experimental conditions, these compositions have been processed with Yttrium and Zirconium. It seems that both of these elements give a fine and stable structure and noticeable effect on the homogenous distribution of the additional elements in the structure.

More interesting structure has been obtained in the samples containing 40%B having a very high hardness values. They have been processed with natural HAP and they were stabilised by doping with 1% MgO. However, many of the specimens with this composition showed microcracks and also micro porosities in the structures after sintering. From these Figures, it is concluded that the samples containing boron were considerably crystallized at all boron containing compositions. In fact, all the compositions given in this paper indicate that the densification was highly improved. Recently, to evaluate of the machining of the samples containing boron, some of the samples were machined by drilling and turning. The preliminary results have shown that manufacturing of these materials in different shape is possible; they do not show brittleness during machining that have been evaluated in former study [17].

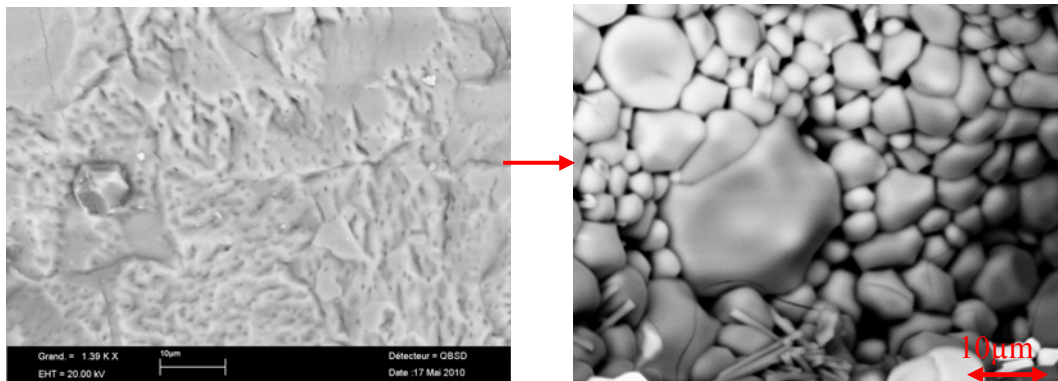


Fig. 5. SEM Micrograph and fracture surface of the sample containing only 40%B

Figure 6 shows SEM Microstructure of the samples containing a) 15%TiO₂ and b) 20%TiO₂ respectively. These samples have been manufactured for obtaining a micro porous structure by adding 10% paraffin and 3%Yi₂O₃+3%ZrO₂).

In practical point of view, additions of Y_2O_3 and ZrO_2 stabilise the microstructure by making fine grain and homogeneous structure. By using paraffin, the natural micro porosity is greatly improved (up to 20%) and homogenous distribution of the natural micro porosity in the structure. It means that an artificial porosity was well created by using Similar results have been obtained in the structures given in Figure 7 that indicates SEM Micrograph of the sample containing 20% TiO_2 +10% paraffin+3% Y_2O_3 +3% ZrO_2 .

Paraffin wax has a very smooth effect on the size and distribution of the artificial porosity. These results original and gives successfully new results on the bio ceramics containing pure Ti and pure Boron with additive of paraffin.

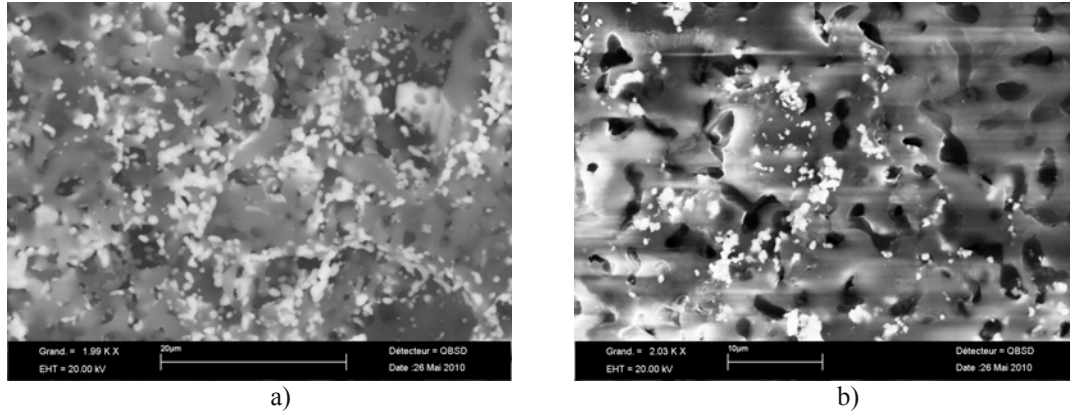


Fig. 6. a) Microstructure of the sample containing a) 15% TiO_2 +10% paraffin and b) 20% TiO_2 +10% paraffin

Experimental results of compressive strength and microhardness of the samples with different compositions (volume fraction) were summarised in Table 1.

At least five specimens were tested for each composition and mean values have been considered. Compressive strength values of high boron containing (>10%) are better than the other composition. For the sake of simplicity, only limited experimental results were used for a FEM study has been carried out to give a practical idea for the manufacturing of bioceramics. Naturally, we could not give more detail on the FEM carried out in the frame of this project going on due to limited page of the SEM proceedings

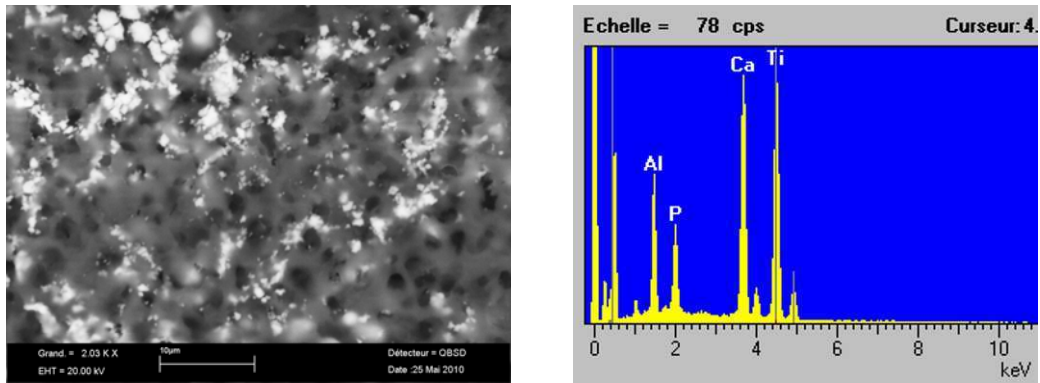


Fig. 7. SEM Microstructure of the sample containing 20% TiO_2 +10% paraffin+3% Y_2O_3 +3% ZrO_2

3.2. A microstructural model and FE simulations

The idealized microstructure considered in this study consists of a random arrangement of cylindrical inclusions embedded in a continuous HAP bio composites, matrix. The volume fraction of inclusions is varied from 10% to 20% and the micro-macro transition schemes are evaluated in many case. However, when the volume fraction increases, nearby inclusions start to interact and this affects the overall mechanical behaviour. The generation of the random distribution follows cylinders filled with identical and aligned cylindrical inclusions. The RVE microstructure is periodic along the 3 directions, allowing us to apply periodic boundary conditions to the external faces of the specimens. The inclusion positioning is constrained by the practical limitation of generating an acceptable FE mesh. A criterion is applied to the minimal distance between each inclusion surface and the external faces of the specimen. The volume of one particular cell inclusion is less than 1 mm^3 .

The representative cells are meshed with quadratic tetrahedral. FE simulations are performed using ABAQUS (2008) and the whole volume is meshed using 4-node C3D4 tetrahedral in ABAQUS), enabling us to better capture the strain gradients in the matrix. Convergence study was successfully conducted by comparing the predictions (effective response and average inclusion response) to those obtained with finer meshes. Figure 8a show typical meshes for a composite with various % of inclusions and variable geometry of specimen are used. The macroscopic stress predicted by the FE analysis is computed from a volume average of the stress tensor given at each integration point over the RVE of domain i:

$$\bar{\sigma} = \frac{1}{V(i)} \sum_{k=1}^{N_k} \sigma_k V_k \quad (1)$$

3.2.1. Numerical procedure

It is aimed to compute the macroscopic stresses and strains using a homogenization procedure. The procedure consists on defining the deformation state at each integration point, in the FE model, as well as the current matrix average state that depends on the corresponding state at the previous step time. FE analysis provides an alternative approach for estimating material properties. A FE model for the heterogeneous test is constructed in which the material parameters to be determined are considered as variable. The simulation is performed and results are compared to data from a comparable experiment data set. The agreement between the model predictions and the data is quantified and judged to be adequate or not. If the agreement is not adequate, the parameter values are updated, a new FE model is created and run, and the process continues till obtaining satisfactory results.

3.2.2. Boundary conditions and material properties

The boundary condition is so set that at the bottom border $U_x, U_y, U_z = 0$ and at the upper face of the specimen is imposed a negative displacement load U_y in y-direction to make via the rigid plate indenter. A static step with small step time is used to assess the gradual evolution of stresses and strains in the elements model, the equivalent reaction force is calculated and used to furnishes the maximum load, when the deformation at the contact zone riches comparable value with the considered limited experimental one.

The mechanical HAP bio composite material properties are derived from the particles inclusions properties. Hydroxyapatite bio composite ceramics reinforced with alumina - Al_2O_3 , pure titanium and pure pulverised boron powder. The inclusion material is assumed to be linearly elastic with elastic modulus $E_p = 390\text{GPa}$ and Poisson's ratio $\nu = 0.33$. Pure titanium with high purity fraction is selected to be the metallic matrix with elastic modulus $E_m = 114\text{GPa}$, Poisson's ratio $\nu = 0.34$.

The FE solution used to simulate two-phase composites consisting of an elasto-plastic matrix reinforced by linear elastic inclusions. Uniaxial compressive loading are successively applied to the multi particle cells embedded in the ceramic matrix. The average of the macroscopic strain over a RVE computed at each time step provides the loading history for the corresponding FE models.

Average equivalent stress in the inclusions of two phase composite materials is determined for different volume fractions of the reinforcing phase. Multiparticles, FE predictions (FE with 25% volume fraction) correspond to a uniaxial compression test. For comparison, the predictions of the compressive results, by mean of deformation and maximum loading were presented for uniaxial compression (Figures 8b, c and 9 and also Table 1). The average volume fractions for particles were indicated in the same table. Only results due to compressive tests using a rigid plate are presented here.

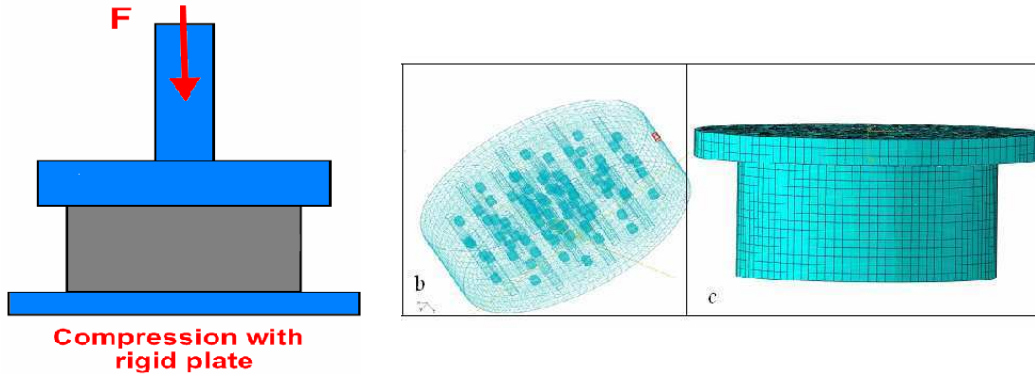


Fig. 8. a) Experimental setup scheme for modelling under compression with plate indenter and b, c) FEM

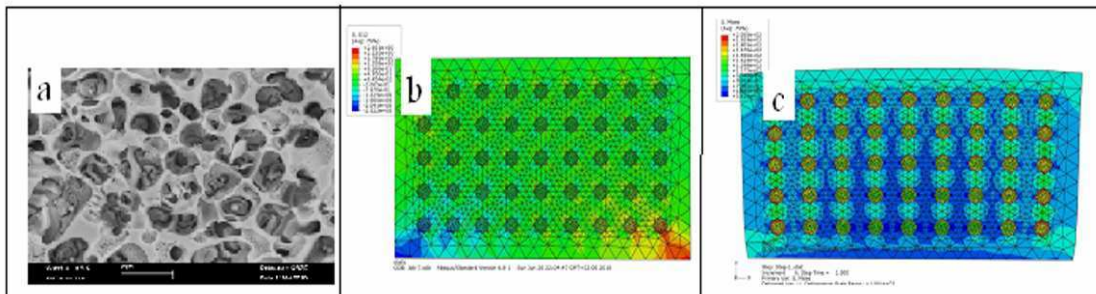


Fig. 9. a) Microstructure of the sample containing 20% Boron (b) details of sheet and plate indenter and c) FEM

Table 1. Physical and mechanical properties with different aspect ratio of the HAP composites

Composition Matrix→(HAP+10%Al₂O₃)	Aspect ratio, (H/D)	Mean HV_{0,2}	σ_{compressive} Exp (MPa)	σ_{compressive} FEM (MPa)	Density (g/cm³)
10%Ti	1	111	15±6	37	1,81
15%Ti	1	137	39±5	48	1,84
20%Ti	0,95	114	43±7	45	1,89
20%Ti+3%Y+3%Zr	1	124	45±13	54	1,91
5%B	0,95	145	59±5	105	1,86
10%B	0,9	420	85±12	119	1,85
20%B	0,9	519	65±15	171	1,79
10%Ti+10%B	1	620	135±15	167	1,92
15%TiO ₂ +10%B	0,89	700	205±15	250	1,94
20%B+15%Ti+3%Y ₂ O ₃ +3%ZrO ₂	0,9	740	265±15	278	1,94
20%B+20%Ti+3%Y ₂ O ₃ +3%ZrO ₂	0,9	734	245±15	275	1,90
40%B	0,85	745	260±10	300	1,93

4. Conclusions

This preliminary study revealed that the addition of the pure metallic boron (atomic pulverised) and pure titanium powders improve the structure and mechanical behaviour of the samples produced by microwave sintering. The hardness and compressive strength were greatly achieved. Addition of the Paraffin gives very smooth porous structure. Compressive strength values of the higher boron containing samples were demonstrated the superiority of mechanical properties for all cases after microwave sintering.

As for FEM, the reaction of the inclusions in the HAP matrix can be predicted based on the solution of inclusions in a finite medium having the properties of the matrix. Here only a simple FEM allowing heterogeneous field was proposed to solve an equivalent inclusion problem. Macroscopic deformation histories corresponding to the non-monotonic uniaxial and the plane strain compression were consecutively considered. Here, a simple prediction has made by using a simple FEM Naturally, development of HAP biocomposites needs more investigations to attempt a high accuracy between experimental results and their equivalent FE predictions.

Acknowledgement

The authors would like to thank “LISMMA research foundation” for the going-on research project. Technical help and useful scientific discussion of Professor D. Toueix head of the department of chemical processing- P. Vauquelin is gratefully acknowledged

References

1. L.L. Hench and J. Wilson, (1993), "An introduction to bioceramics" World Scientific Publishing, Co. Pte. Ltd., Singapore, p. 406
2. S.V. Bhat, "Biomaterials, "Kluwer Academic Publishers", (2002), Netherlands, p. 253
3. J.B. Park, and J.D. Bronzino, (2003), "Biomaterials: Principles and applications" CRC Press, Boca Raton, Florida.
4. R. Xin, Y. Leng, J. Chen, (2005), Biomaterials, **26** (33) 6477-6486
5. M.K. Herliansyah and M. Hamdi et al., Mat. Sci. and Eng. MSE C 29 (2009) 1674-1680
6. E. Bayraktar, D. Katundi, “Manufacturing of new metal matrix composites”, Int. J. of A. in Mat. and Manuf. Eng., (2010) JAMME, vol. 38/1, 7-14
7. E. Bayraktar, “HAP production-simple method”, (2008), p. 15-22, Paris - France
8. A. Chiba, S. Kimura, et al., Mat. Sci. and Eng. MSE A350 (2003) 179- 183
9. Z. Belghazi, MS Thermal Project, p.35, Supmeca/Paris, Dept of Materials Science, 2010
10. D. E. Clark, “Ceramics”Annu. Rev. Mater. Sci. 1996, 26: 299-331
11. S. Salman et al. Ceramics International 35 (2009) 2965–2971
12. X. W. Li · H. Y. Yasuda · Y. Umakoshi, J Mater Sci: Mater Med (2006) 17: 573–581
13. Y. ZHANG, J. M. STEWART, B. MOROSIN and C.R., HUBBARD, in “ceramic transactions, Vol. 1, Ceramic Powder, Science IIB”, edited by G. L. Messing, E. R. Fuller and H. Hausner (The American Ceramic Society, Westerville, OH, 1988) p. 1192

13. Hing K.A, Gibson I.R, Di-Silvio L, Best S.M, and Bonfield W. Effect of Variation in Ca:P Ratio on Cellular Response of Primary Human Osteoblast-like Cells to Hydroxyapatite-based Ceramics. *Bioceramics*. 11:293, 1998
14. Groot K, Klein C.P.A.T, Wolke J.G.C, and de Blieck-Hogervorst J. Chemistry of Calcium Phosphate Bioceramics. pp. 3-15 in *Handbook of Bioactive Ceramics, Vol.II*. Edited by Yamamuro T, Hench L.L, and Wilson J. 1990
15. Damien C.J, and Parsons J.R. Bone Graft and Bone Graft Substitutes: A Review of Current Technology and Applications. *J. Appl. Biomater*. 2:187-208, 1991
16. Oonishi H, Hench L.L, Wilson J, Sugihara F, Tsuji E, Kushitani S, and Iwaki H. Comparative Bone Growth Behavior in Granules of Bioceramic Materials of Various Sizes. *J. Biomed Mater Res*. 44:31-43, 1999
17. Katundi D., Ayari F., Bayraktar E., Design of Natural Hydroxyapatite Biocomposites: Experimental and Numerical Study, American Institute of Physics; Journal, Materials Physics and Applications, vol. 1, no. 1, pp. 235-241, ed. AIP Conference Proceedings 1315, 2011, ISSN ISBN 978-0-7354-0871-5

Damage Analysis of the Ceramic Reinforced Steel Matrix Composites Sheets: Experimental and Numerical Study

E. Bayraktar^{1,2*}, D. Katundi¹, F. Ayari¹, J-P. Chevalier², F. Bonnet³

¹Supmeca -Paris, School of Mechanical and Manufacturing Engineering, France

²Chair of Industrial Materials, CNAM, Arts et Métiers, 75141 Paris 03 –France

³ARCELOR – Research, Paris, France

*bayraktar@supmeca.fr

ABSTRACT

This paper reports damage analysis of TiB₂ (ceramic particles) reinforced steel matrix composite sheets. This new steel composite receives much attention as potential structural materials due to their high specific strength and stiffness. The goal of the research described in this paper is to study the usage of this new steel family in the manufacture of light structures. Therefore, titanium diboride TiB₂ reinforced steel matrix composite sheets were characterized by optical and scanning electron microscopes after the mechanical tests carried out on the base metal and welded specimens under dynamic and static test conditions. However, the non homogeneity of the structure in this type of composites makes deeply complexity of their numerical and analytical modelling to predict their damage during the loading. For example, the interfaces essentially play a key role in determining mechanical and physical properties. A Finite Element (FEM) analysis is also used for modelling to simulate the macroscopic behaviour of this material, taking into account the relevant microscopic scales.

Keywords: Steel matrix composites; Ceramic particles-TiB₂; Crash test; Welding; Weldability

1. Introduction

Metal Matrix Composites (MMCs) have recently received considerable attention in manufacturing engineering as potential structural materials due to their high specific strength and stiffness [1-6, 8-12]. While most work on MMCs is directed towards producing novel and lightweight engineering materials, there is also considerable interest in developing iron and steel matrix composites. Iron and steel matrix composites reinforced with TiB₂/TiC ceramic particulates have been the focus of intensive investigation due to their ease of fabrication, low costs and isotropic properties. These materials potentially have good wear resistance with an excellent combination of low density and high toughness values [1, 4, 5]. For this reason, MMCs with fresh, ultrafine and stable ceramic reinforcements can demonstrate outstanding mechanical properties [6]. Among various ceramic particulates, titanium carbide (TiC) and titanium diboride (TiB₂) are good candidate materials because of their excellent properties such as high hardness, low density, high melting temperature, high modulus, good wear and corrosion resistance [5, 7, 10-12]. These materials are highly attractive for automotive applications, because their lightness and high toughness make them conducive to the production of environmentally friendly cars. However, several limitations associated with the use of pure TiC and TiB₂ were found in the literature [5-7, 9-12].

The first theme concerns the microstructural evolution of the composite sheets as base and welded structures due to their potential use in the automotive industry. The second theme is the relationship between microstructural and mechanical properties, notably weldability and the ductile brittle transition temperature of these steel matrix composite (TiB₂-RSMCs) sheets recently invented and developed by the ARCELOR Research Group in France [1]. Introducing these new composite steels in cars will reduce the total vehicle weight. This is a major topic of interest in support of the general goal of reducing fuel consumption and CO₂ emissions in future car designs.

2 Experimental conditions

Initially, the plate materials with a thickness of 2, 2.5 and 3mm were made of special continuous casting and hot and cold rolling (classical steel manufacturing method) by ARCELOR Research Group-France. The values of carbon and manganese are 0.04% and 0.40% respectively. Some of the steel sheets were welded only one fusion weld line by Gas Tungsten Arc (GTAW) process. Basically TiB₂ ceramic particulates were used as reinforced materials in the iron matrix. All other details can be found easily in the documents [1, 2].

First of all, a detail metallographic analysis has been carried out. Evolution of TiB₂ ceramic particulates were observed in the welded and base-metal parts. Secondly, micro hardness tests have been done on the polished metallographic specimens. In order to evaluate the toughness properties of the TiB₂-RSMCs, impact –crash-tensile tests (ITT) have been carried out at different temperatures on the test specimens with a special geometry containing a smooth part (BM) and notched part (WM) with a special device mounted on an impact pendulum

[7, 8]. Finally, static compressive tests, under a rigid spherical indenter with fixed radius ($r = 3\text{mm}$) have been carried out and the results were compared with that of the numerical analysis carried by using ABAQUS Code. Fracture and deformed surfaces of the sheet specimens were analysed by means of Scanning Electron Microscope (SEM) for understand the damage behaviour of the TiB_2 -RSMCs specimens under crash and static compression tests.

3 Results and Discussion

3.1 Microstructural evaluation

Different mechanisms due to the reinforcements in steel matrix were effective in the microstructure. This evaluation indicates the size effect and distribution of the ceramic particulates in the matrix. The morphology of the ceramic particulates and the matrix has been evaluated in metallurgical point of view. This information has allowed understanding the cohesion and wetability of the ceramic particulates with matrix. Generally, TiB_2 ceramic particulates grew in hexagonal prismatic or rectangular shape. The micrograph given in Figure 1 shows the morphology and distribution of TiB_2 reinforcements produced in steel matrix and eutectic structure in the weld bead. The details of microstructure evolution in Weld Metal - WM, and Heat Affected Zone, HAZ were discussed in former papers [2].

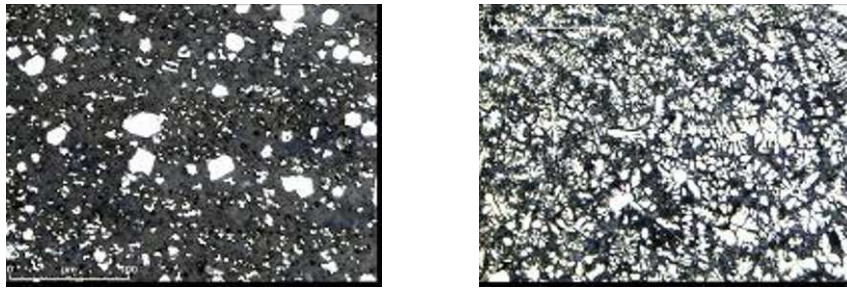


Fig. 1. Evolution of the microstructure of TiB_2 -RSMCs specimens in base metal (left) and weld bead (right)

In fact, solubility of iron in the TiB_2 remains less than 4 % it means that system Fe/TiB_2 keeps intact the mechanical properties of TiB_2 . In the system Fe-B-Ti , TiB_2 precipitates in steel by eutectic solidification (this avoids the primary precipitation of borides in the liquid metal). (Volume fraction is around 15 %, eutectic composition). These values were found with the surface percentages of the TiB_2 ceramic particulates calculated by image analysis. Weld Bead, after solidification, gives regularly a dendritic structure. This type of structure is always developed around the ferrite nuclei.

3.2 Evaluation of micro hardness and impact tensile test behaviour

Micro hardness measurement was given in the Figure 2 as the mean values for three different zones (BM, HAZ, and WM). The values for the new steel sheets, without welding (only base metal), has been added in this diagram. The population of TiB_2 particles distributed in the matrix plays an important role on the hardness evolution in the steel sheets.

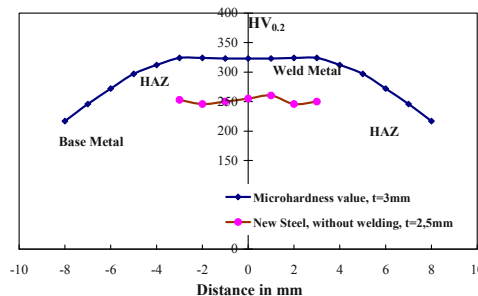


Fig. 2. Hardness evolution in different parts of the steel sheets (WM, HAZ and Base metal)

Impact tensile tests results were given in the Figure 3. All the details with this special test technique can be found in former works [2]. As indicated in the ductile – brittle transition behaviour of the test specimens are deeply

different. As the base metal (without welding specimens in Figure 3a) gives a satisfaction transition values (around -80°C) the welded specimens show a transitions varying between -40 and -10°C depending on the thickness and also steel grades (Figure 3a and 3b). However, these results are very successful results for a steel matrix reinforced ceramic particles.

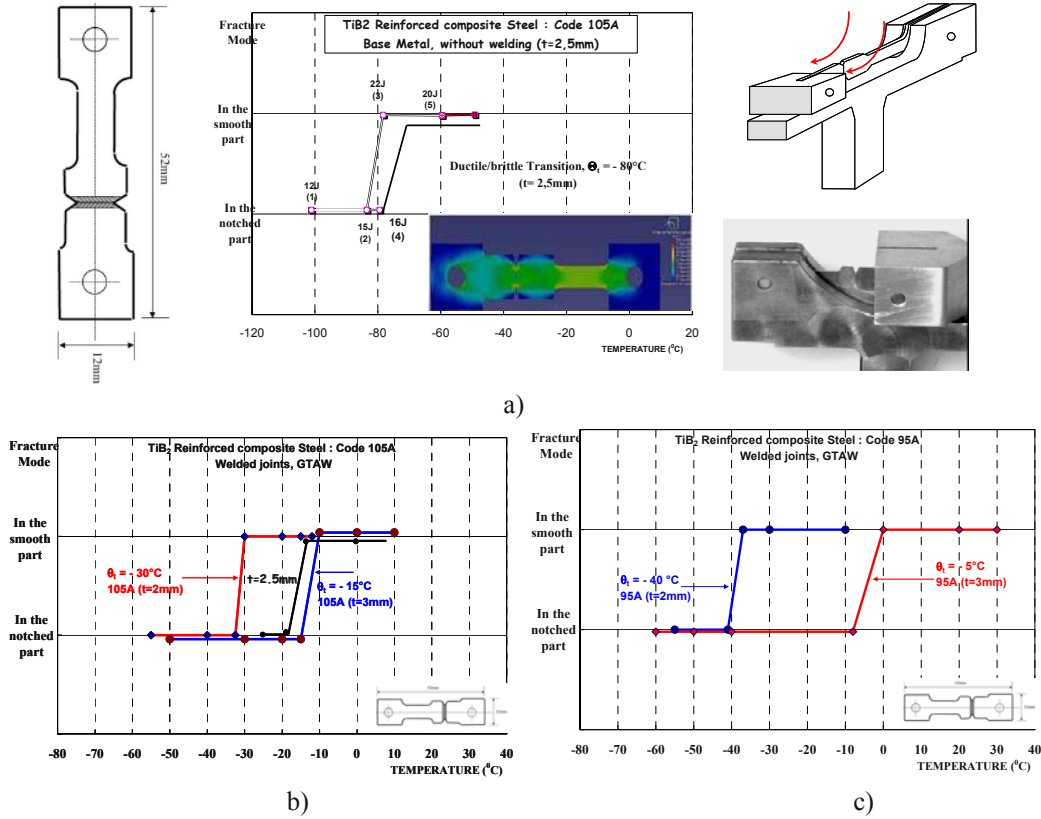


Fig. 3. Impact Tensile Test (ITT) results for the base metal and welded specimens with test device and developed specimen geometry and also FE stress distribution model with Abaqus stress analysis

Evidently, fracture surfaces of these specimens verify these experimental results in case of the ductile and brittle failure conditions as indicated in Figure 4.

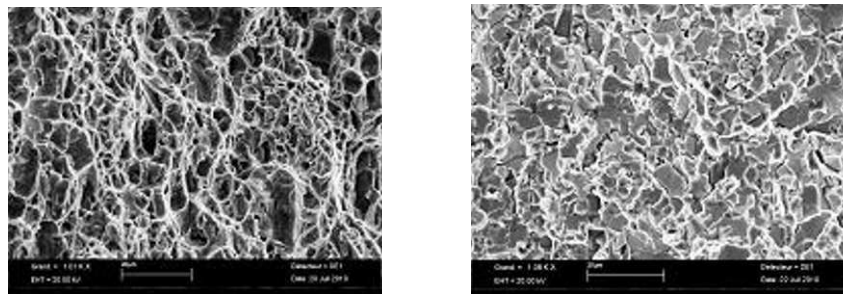


Fig.4. Impact tensile test results for the specimen failed in ductile (left) and brittle (right) fracture conditions

3.3. Compressive tests, under a rigid spherical indenter

Static compression tests have been carried out under a rigid spherical indenter ($r=3\text{mm}$) and deformed zone areas were measured for each test specimen (only base metal) and fractographic analysis were also made for each specimen. This test is a typical damage test to understand the behaviour of the steel sheets containing ceramic reinforcements (Figure 5). The development of this product requires a better understanding of the relationship between crack propagation and microstructure. For this reason, a finite element based model was build which is inspired from the microstructure of the material. The micro hardness testing and the compressive tests are thus selected to compare between performances of this material based on experimental tests results and also

numerical macro FE structural study. The dispersion of TiB_2 particles in iron matrix is somewhat heterogeneous containing relatively regular shape of TiB_2 particles.

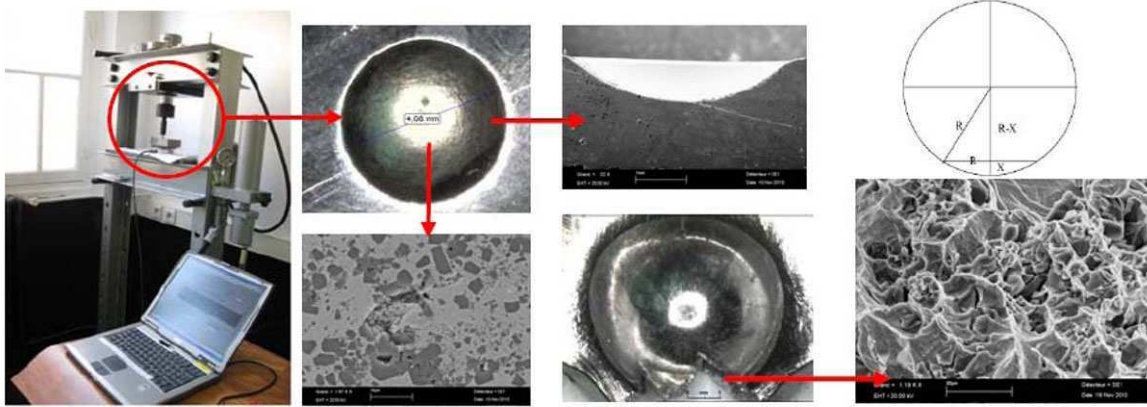


Fig. 5. Static compression test under a rigid spherical indenter: deformed area on the sheet and fracture surface after deformation

Naturally, ITT and compression test carried out here as similar to the deep drawability tests cannot be positioned on the same plane. In other words, ITT characterises a ductile–brittle transition mode in fracture in dynamic loading conditions. So, it is sensitive to the physical parameters, which play a role on the cleavage (grain size, other defects, etc.). However, static compression test, of which ultimate stage is mostly the plastic failure, is mainly sensitive to the flow rule of materials during the deformation and also to the presence of particles of the second phase as indicated in these sheets reinforced with TiB_2 ceramic particles. Meanwhile, to make a correlation between these two different test variables should be considered as an indicative presentation, because both of these tests reflect micro-structural parameters which influent both of these two type of tests. These parameters give practical information about the damage behaviour of these materials.

4. Microstructural Model and Finite Element (FE) simulations

In order to understand well the stress strain mechanism of steel matrix composites reinforced with TiB_2 ceramic particles, a finite element model (FEM) based on the actual microstructures was build. This model is stimulated from the micromechanical composition of the Fe-TiB_2 as MMC material. Also, this model can provide the distribution of von Mises effective stress, strain and the maximum principal stress in the matrix and particles. The model is used to perform a comparison between experimental results and numerical results of compression tests. Figure 6 describes schematically the conditions of experimental compression tests, under a rigid spherical indenter with fixed radius ($r = 3\text{mm}$). Geometric variables were illustrated used in this model and the geometry and mesh parameters were also used to analyse these experimental tests.

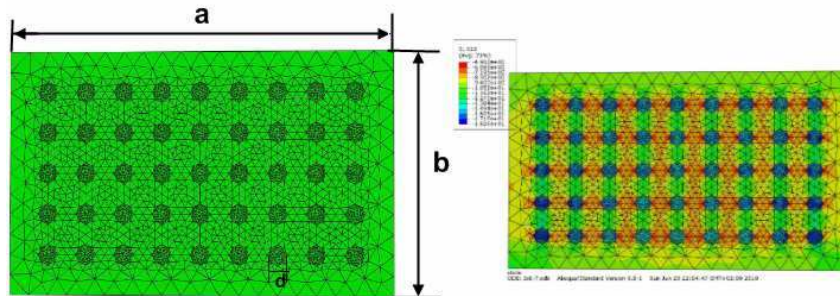


Fig. 6. Two-phases of steel matrix reinforced with TiB_2 ceramic particles under deformation

The ideal microstructure considered in this study consists of a random arrangement of cylindrical inclusions (quasi hexagonal) embedded in a continuous steel matrix containing low carbon (Figure 7). The volume fraction of inclusions can vary from 10% to 20% and the micro-macro transition schemes are evaluated in many cases. However, when the volume fraction increases, nearby inclusions start to interact and this case influences the overall mechanical behaviour. Simulations must then be performed on a Representative Element Volume (REV) of the microstructure. Indeed, the spread of the macroscopic response for several distributions of various

inclusions is lower than 5%. The generation of the random distribution follows rectangular cylinders filled with identical and aligned cylindrical inclusions. The RVE microstructure is periodic along the 3 directions, allowing us to apply periodic boundary conditions to the external faces of the specimens.

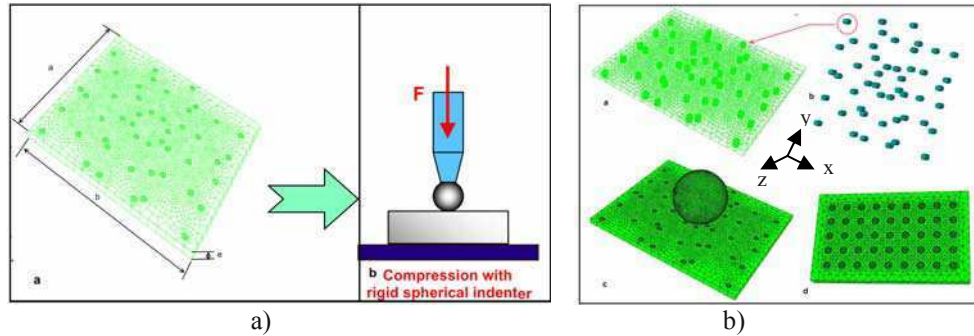


Fig.7. MMC Fe-TiB2 under compressive test a) FE model, b) the compressive scheme and c) different model parts and mesh representation

The inclusion positioning is constrained by the practical limitation of generating an acceptable FE mesh. A criterion is applied to the minimal distance between each inclusion surface and the external faces of the specimen. The volume of one particular cell inclusion is less than 1 mm^3 .

The representative cells are then meshed with quadratic tetrahedral elements. FE simulations are performed using ABAQUS (2008) and the whole volume is meshed using 4-node C3D4 tetrahedra in ABAQUS, enabling us to better capture the strain gradients in the matrix [12-14]. After that, a convergence study was successfully conducted by comparing the predictions (effective response and average inclusion response) to those obtained with finer meshes. The macroscopic stress predicted by the FE analysis is computed from a volume average of the stress tensor given at each integration point over the REV of domain “i”:

$$\bar{\sigma} = \frac{1}{V(i)} \sum_{k=1}^{N_k} \sigma_k V_k \quad (1)$$

4.1. Numerical procedure

The macroscopic stresses and strains values were aimed to compute using a homogenization procedure according to the Mori-Tanaka (M-T model) [12]. In fact, the computations of the matrix average stress and the macroscopic stresses are identical to the M-T model. The procedure is fully history-dependent, the deformation state at each integration point in the FE discretization as well as the current matrix average state depends on the corresponding state at the previous step time. Therefore, for any loading condition, even non-monotonic or non-proportional may be considered. The Mori-Tanaka scheme coupled with a FE solution of the equivalent inclusion problem. FE analysis provides an alternative approach for estimating the material properties. A FE model for the heterogeneous test is constructed in which the material parameters to be determined are considered as variable. The simulation is then performed and results are compared to data from a comparable experiment data set. The agreement between the model predictions and the data is quantified and judged to be sufficient or insufficient. If the agreement is not adequate, the parameter values are updated, a new FE model is created and run, and the process continues. Development of an effective parametric FE procedure requires automation of model creation, submission, results extraction, and comparison with experimental data. Within the context of Abaqus, the Python scripting language allows for such automation. The inclusion average stress may be directly extracted from the FE simulation using a Python script file. The computation of the average stress in each phase affects only the effective response of the composite, not the prediction of the stress-strain partitioning. This holds provided that all components of the macroscopic strain are given.

Here, a combination of tools was used to drive the optimization process. A Matlab interface was developed to create the Abaqus input file with all the necessary geometries, material parameter assignments, and also FE results acquisition. Python scripts were used to extract reaction forces, displacements and other variables from the output database, which were fed back into the Matlab process for comparison with the experimental data.

The FE solution is used to simulate two-phase composites consisting of an elasto-plastic matrix reinforced by linear elastic inclusions. The predictions of the mean-field models are compared to reference results from FE computations on representative cells containing a random arrangement of multiple inclusions (Figure 7). Uniaxial and plane strain loading are successively applied to the multi-particle cells. The average of the macroscopic strain over a representative equivalent volume (REV) computed at each time step provides the

loading history for the corresponding MF models. Therefore, results corresponding to the same macroscopic strain history, consistently with a strain homogenization procedure.

Average equivalent stress in the inclusions of two phase MMC material is determined for different volume fractions of the reinforcing phase. The multi-particle, FE predictions (FE with 20% volume fraction) correspond to a uniaxial compression test, while the predictions of the FE model are obtained imposing the same strain history as in the multi particle simulation.

4.2. Boundary conditions and material properties

The boundary condition is so set that at the bottom border as $U_x, U_y, U_z = 0$ and at the upper face of the specimen is imposed a negative displacement load U_y in y-direction via the rigid spherical or the plate indenter. A static step with small step time is used to assess the gradual evolution of stresses and strains in the elements model, the equivalent reaction force is calculated and used to furnishes the maximum load, when the deformation at the contact zone riches comparable value with the considered limited experimental one.

The mechanical Fe-TiB₂ MMC material properties are derived from the particle inclusion properties of the TiB₂ and those of pure iron as matrix. The inclusion material is assumed to be linearly elastic with elastic modulus $E_p=300$ GPa and Poisson's ratio $\nu = 0.3$. In the same way, iron is selected to be the metallic matrix with elastic modulus $E_m=210$ GPa, Poisson's ratio $\nu= 0.33$. The inclusion average stress may be directly extracted from the FE simulation using a Python script file. The computation of the average stress in each phase influences only the effective response of the composite, not the prediction of the stress-strain partitioning. This holds provided that all of the components of the macroscopic strain are given. At this stage, a combination of tools was used to drive the calculation process.

4.3. Results

The FE solution used to simulate two-phase composites consisting of an elasto-plastic matrix reinforced by linear elastic inclusions. The predictions of the mean-field models are compared to the reference results from FE computations on representative cells containing a random arrangement of multiple inclusions. Uniaxial compressive loading are successively applied to the multi particle cells embedded in the metal iron matrix. The average of the macroscopic strain computed at each time step provides the loading history for the corresponding FE models.

Average equivalent stress in the inclusions of two phase MMC material is determined for 2 volume fractions of the reinforcing phase 10 % and 20%. For comparison, the predictions of the compressive results, by mean of deformation and maximum loading are shown for uniaxial compression [Figures 8, 9](#) and [Table 1](#). The average volume fraction for specimens in [Table 1](#) is taken to be 15 %. Only the results due to compressive tests using a rigid sphere are presented here.

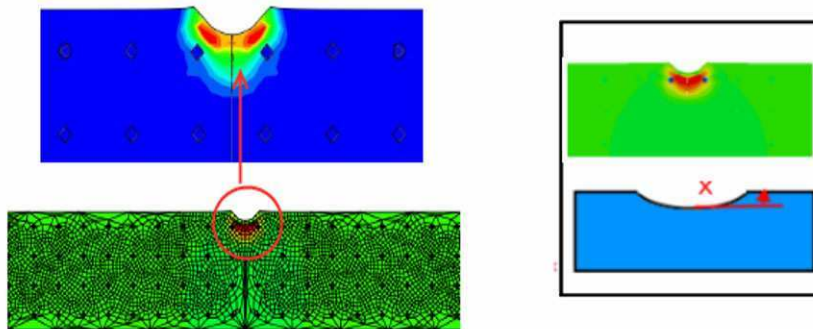


Fig. 8. FEM measurements of the deformation depth under compression of the MMC under compressive tests (Equivalent plastic strain distributions in the contact area)

In fact, [Figure 9](#) gives comprehensive evaluation of the deformation behaviour of this material as noted from experimental and FEM variation of the compressive load as a function of displacement under compressive tests. However, interesting results have been obtained from hardness measurements carried out in vertical and horizontal direction under the deformed area due to compression test (experimental) and also very similar results were obtained from variation of the stress σ_2 as a function of displacement due to compression test (FEM). These results show clearly that a strain hardening mechanism does not occur in this material what ever the deformation level (from small stress levels up to stresses induced failure);

First of all, the structure of the matrix is similar that of the pure iron. It contains very low carbon and the microstructure contains very low dislocation density that does not increase during the deformation even if the microstructure with small grain size. Most probably, the hardness values around the deformed area and also variation of the stress σ_2 as a function of displacement do not change during the deformation and the materials does not show a noticed work hardening phenomenon.

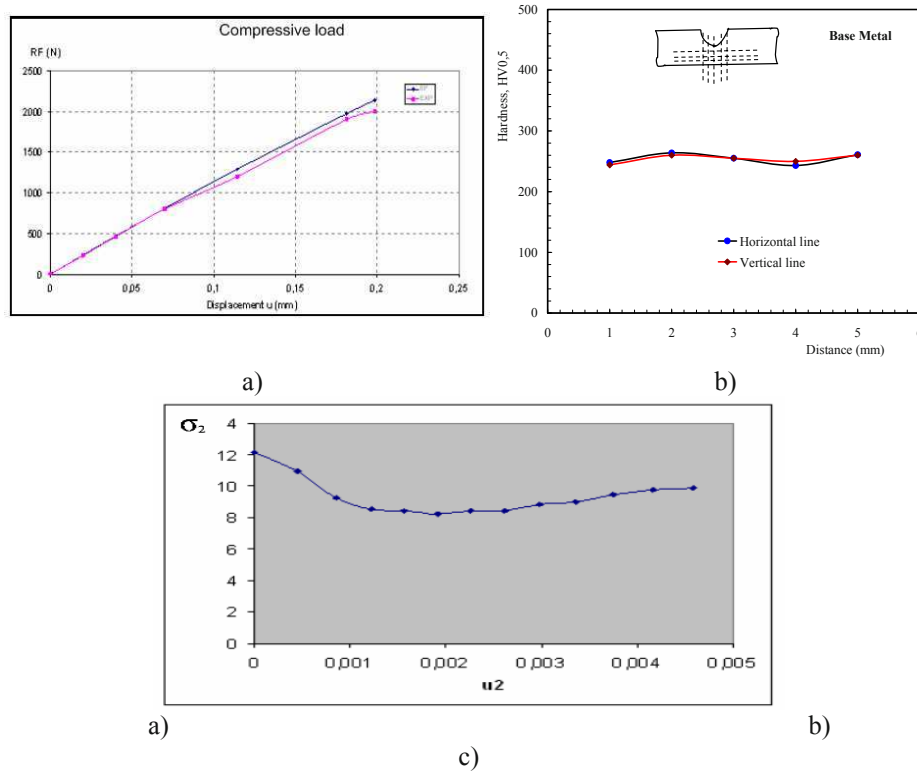


Fig. 9. a) Experimental and FEM variation of the compressive load as a function of displacement of the MMC under compressive tests and b) Hardness evolution in different direction after compression test (experimental) and c) FEM variation of the stress σ_2 as a function of displacement of the MMC under compressive tests

4.4. Partial Discussion of FE results

The inclusions response is predicted based on the solution of inclusions in a finite medium having the properties of the matrix. This equivalent inclusion problem is solved by the FE method, allowing field heterogeneities to take place in the made up matrix. In this model the scheme of Mori-Tanaka model is used, the average of the strain in the actual matrix of the composite is taken as far-field strain. The new method is applied to this composite made of an elasto-plastic iron matrix reinforced by spherical or cylindrical elastic TiB_2 inclusions. Macroscopic deformation histories corresponding to non-monotonic uniaxial and plane strain tension/compression are successively considered. In all cases, predictions of the approaches are compared to reference results obtained by FE simulations on cells containing inclusions.

This FE study showed that the M-T assumption is able to simulate the effective response of such composites almost for less than 20% of inclusion volume fraction. However, the predicted inclusion response is, in general, less accurate than the macroscopic real one so that the stress level in low inclusion fraction is underestimated by the mean-field model, this fact was well discussed in a number of previous works [15-17]. This effect is due to a certain extent, compensated by the matrix prediction which raises the stress level in the effective response. This is due to a slight overestimation of the matrix average strain combined with the present comparison material for the matrix. For higher volume fractions (from 20 %) the single inclusion modelling yields very poor predictions of the inclusion response. This can be explained by plastic localization taking place between inclusions in the real composite, which is overlooked by the FE model (Figure 9).

Figure 10 illustrates the history of energy for the same plate, both total energy and strain energy figure 17 a and c show the same shape at the loading step, then the energy falls to low values and this sharp drop can join the experimental results obtained with Charpy choc test as the energy transition was dropped sharply from the ductile to the brittle zone. This sudden jump is due to the repartition and the size of the TiB_2 particles.

Development of a new iron matrix, composite reinforced with TiB_2 , needs more investigations to attempt a high accuracy between experimental results and their equivalent FE predictions. The best choice of the volume fraction and the size particle is a competitive compromise that could be defined accordingly to the industrial

destination of the MMC material. In fact, a larger investigation in the development of these materials can lead to the development of a smart strategy that can be easily used in the future to design smart MMC materials that can be adapted to the functionality of this latter. So that the material composition and the geometry design of the phase distribution in the MMC matrix could be monitored from an application to other.

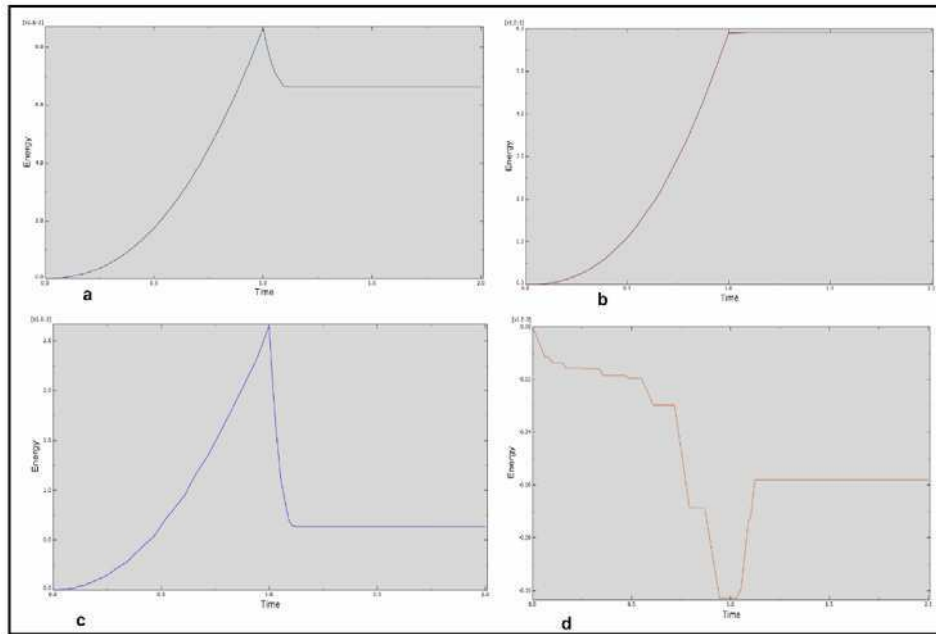


Fig. 10. FEM variation of the stress energy history of the MMC under compressive tests

Table1. General evaluation to compare experimental and FE results form compression test

Test n°	N° of specimen	Specimen size (mm)	FE. Max force (N)	Exp. max force (N)	R	Rayon R ₁ mm	FE. x (mm)	Exp x (mm)
1	AC-x	25x30x3			3	2,04	0,82	0,80036367
2	AC-1	24x28x2	31104	31025,4	3	2,15	0,91	0,9077524
3	AC-2	21x21x2	29800	29038,5	3	2,03	0,78	0,79113151
4	AC-3	25x30x3	31600	31570,4	3	2,3	1,14	1,07386397
5	AC-4	21x7x3	25700	25636,2	3	2,97	2,56	2,57679792
6	AC-5	28x26x2	26800	26735,6	3	2,01	0,771	0,77291671
7	AC-6	12x27x2	24400	24334,6	3	2,17	0,95	0,92850296
8	AC-7	25x30x3	14400	14334,5	4,75	1,74	0,33	0,33016969

5. General Conclusion

Some of the conclusions can be driven from partial results of this study;

- TiB₂ particulate reinforced MMC_s sheets were successfully manufactured as proposed in the Patent.
- Weldability of this new steel family has a big potential success in manufacturing engineering (Formability of tailored welded blanks, TWBs)
- Weld bead shows finer structure
- There is no abnormal evolution in HAZ during the welding (e.g. grain growth)
- The weld bead shows a fine eutectic structure.
- There is no abnormal evolution in the HAZ (e.g., grain growth).
- Preliminary work suggests that this product (originally developed for the car industry) should find other applications for all of the structures designed by stiffness (ex: energy domain, road transport and railway)
- A finite element model of the MMC material has been developed using a specimen with specific geometry and material properties. Accurate determination of material parameters is an integral component of developing a Fe - TiB₂ MMC. For most direct estimation, parameters would be determined using standard experimental test techniques (e.g. uniaxial tension or compression). For intention of modelling MMC iron composites, preparation of excised samples presents a number of difficulties. If insertion of inclusion particles is not well designed, it could affect the final result of simulation and it can induce false correlation between external and internal variables. Finally, even if uniaxial properties are precisely measured, the applicability of such data, and resulting

material parameters, need a robust simulation to reach the satisfactory conclusions about the mechanical behaviour of those materials.

- In general, the development of this MMC material is enhanced for many causes, in particular as far as we are looking for improving some roughness properties, we can associate particular attention to the grain size, because when it is reduced at a large scale, the presence of stresses and imperfections introduced by mechanical alloying enhance the roughness property; the overall roughness property is a competition between decrease in grain size and increase in strain. An enhancement of the numerical model to a nano scale can be with a great utility to bring more light and answers on the mechanical improvement of this material.

Acknowledgement

This study contains partial results of “ANR-ADRERA” project that is going on. Technical and financial support from ARCELOR-MITTAL Research Group, France is gratefully acknowledged.

References

- [1] ARCELOR Research group; Patent EP 1 897 963 A1, Bulletin 2008/11, 20p, 2008
- [2] Bayraktar E., Kaplan D., Buirette C. and Grumbach M., Application of Impact tensile testing to the welded thin sheets, *Journal of Materials Processing Technology - JMPT*, 145, I, 27-39, 2004
- [3] Akhtar F., Askari S. J., Shah K. A., Xueli Du, Guo S., Microstructure, mechanical properties, electrical conductivity and wear behavior of high volume TiC reinforced Cu-matrix composites, *Materials Characterization*, 60, 4, 327-336, 2009,
- [4] Yang Y., Wang H., Liang Y., Zhao R., Jiang Q., Fabrication of steel matrix composites locally reinforced with different ratios of TiC/TiB₂ particulates using SHS reactions of Ni-Ti-B₄C and Ni-Ti-B₄C-C systems during casting, *Materials Science and Engineering: A*, 445-446, 398-404, 2007
- [5] Jiang Q.C., Ma B.X., Wang H.Y., Wang Y., Dong Y.P., Fabrication of steel matrix composites locally reinforced with in situ TiB₂-TiC particulates, *Composites Part A: Applied Science and Manufacturing*, 37, 1, 133-138, 2006
- [6] Wang Y., Zhang Z.Q., Wang H.Y., Ma B.X. and Jiang Q.C., Effect of Fe content in Fe-Ti-B system on fabricating TiB₂ particulate locally reinforced steel matrix composites, *Materials Science and Engineering A* 422, 339-345, 2006
- [7] Ziębowicz B., Szewieczek D., Dobrzański L.A., New possibilities of application of composite materials with soft magnetic properties, *Journal of Achievements in Materials, and Manufacturing Engineering, JAMME*, 20/1-2, 207-210, 2007
- [8] Narayanasamy R., Ramesh T. and Pandey K.S., Some aspects on cold forging of aluminium-iron powder metallurgy composite under triaxial stress state condition *Materials and Design* 29, 891-903, 2008
- [9] Tang F., Anderson I.E., Gnaupel -Herold T., and Prask H., Pure Al matrix composites produced by vacuum hot pressing: tensile properties and strengthening mechanisms, *Materials Science and Engineering A* 383, 362-373, 2004
- [10] Grabowski A., Formanek B., Sozanska M., Janicki D., Nowak M., Laser remelting of Al-Fe-TiO powder composite on aluminium matrix, *Journal of Achievements in Materials and Manufacturing Engineering, JAMME*, 33/1, 2009
- [11] Duraes L., Costa B. F. O., Santos R., Correia A., Campos J and Portugal A., Fe₂O₃/aluminum thermite reaction intermediate and final products characterization, *Materials Science and Engineering A* 465, 199-210, 2007
- [12] Mori, T., Tanaka, K., 1973. Average stress in matrix and average elastic energy of materials with misting inclusions, *Acta Metall.* 21, 571, 574
- [13] Doghri I., Tinel L., Micromechanical modelling and computation of elasto-plastic materials reinforced with distributed-orientation fibers, *International Journal of Plasticity* 2005; 21:1919-1940
- [14] Lu L, Lai MO, Su Y, Teo HL, Feng CF. In-situ TiB₂ reinforced Al alloy composites. *Scripta Mater* 2001; 45 (9):1017-23
- [15] Gorsse S, Miracle DB. Mechanical Properties of Ti-6Al-4V/TiB composites with randomly oriented and aligned TiB reinforcements. *Acta Mater* 2003; 51 2427-42
- [16] Giraud A., Huynh Q.V., Hoxha D., Kondo D. , Effective poro-elastic properties of transversely isotropic rock-like composites with arbitrarily oriented ellipsoidal inclusions, *Mechanics of Materials* 2007; 39: 1006-1024
- [17] Fukasawa T, Ando M, Ohji T, Kanzaki S. Synthesis of porous ceramics with complex pore structure by freeze-dries processing. *J. Am. Ceram. Soc.* 2001; 84(1): 230-232

Dynamic Mechanical Properties of Polymeric Materials Aged in PEM Fuel Cell Conditions

Chih-Wei Lin^{a,b}, Tong Cui^b, Chi-Hui Chien^a, Jinzhu Tan^c, Yuh-Jin Chao^{b*}, and J.W. Van Zee^d

^aDepartment of Mechanical and Electro-Mechanical Engineering, National Sun Yat-Sen University, Kaohsiung, 804, Taiwan ROC

^bDepartment of Mechanical Engineering, University of South Carolina, Columbia, SC29208, USA

^cCollege of Mechanical and Power Engineering, Nanjing University of Technology, Nanjing, Jiangsu 210009, China

^dDepartment of Chemical Engineering, University of South Carolina, Columbia, SC29208, USA

ABSTRACT Gaskets/seals in PEM fuel cells are exposed to acidic, humid air, mechanical compressive pressure and cyclic temperature environment. Chemical degradation of three elastomeric gasket materials in a simulated and an aggressive accelerated fuel cell solution at 80°C up to 63 weeks was investigated in this work using dynamic mechanical analysis (DMA) which assesses the change of dynamic mechanical properties of the three material samples as they aged. The three materials tested are copolymeric resin (CR), liquid silicone rubber (LSR), and fluorosilicone rubber (FSR).

Keywords: DMA, glass transition temperature, elastomeric gasket material, PEM fuel cell

1. INTRODUCTION

Gaskets in PEM fuel cells are typically made of elastomeric materials and are exposed to acidic liquid solution, humid air and hydrogen, as well as subjected to mechanical stress. The long-term stability and durability of the gaskets materials are therefore critical to both sealing and the electrochemical performance of the fuel cells. In this study, three polymeric materials that are or have potential to be used as gasket or seals in PEM fuel cells were first aged in a simulated or an accelerated fuel cell environment solutions at 80°C which is close to the PEM fuel cell operating temperature. The dynamic mechanical characteristics of the virgin and aged materials were then studied using a DMA (TA Instruments, RSA-III).

2. EXPERIMENT DESCRIPTIONS

2.1 Materials and Simulated Fuel Cell Environment Solutions

* Corresponding Author. Tel.: +1 803 7775869, fax: +1 803 7770106, E-mail address: chao@sc.edu

Three elastomeric sealing materials, namely, Copolymeric Resin (CR), Fluorosilicone Rubber (FSR), and Liquid Silicone Rubber (LSR), are, among others, currently been used, or are considered to use, in PEM fuel cells as the gasket/seal.

Two solutions were used to age the three materials. The first is an accelerated durability test (ADT) solution. The final composition is 1M H_2SO_4 , 10ppm HF and reagent grade water having 18Mega Ohm resistances. The pH value is less than one. The second solution is termed a "Regular" solution. Chemical composition of the solution is 12ppm H_2SO_4 and 1.8ppm HF with reagent grade water having 18Mega Ohm resistances.

2.2 Aging and Characterization Methods

Rectangular-shaped specimens were prepared and exposed to either the ADT or the Regular solution. The dimensions of the specimens are 70mm in length, 20mm in width, and 2.0mm in thickness, except Copolymeric Resin (CR) which has a thickness of 1.5mm. The samples were submerged in the ADT and Regular solutions in different bottles placed in an oven at a temperature of 80°C. The aged samples were taken out of the test bottles at selected times for observation and tests. The process completed in 63weeks.

3. RESULTS AND DISCUSSIONS

3.1 Material Properties from DMA

3.1.1 Copolymeric Resin (CR)

The CR samples at different aging weeks were used to reveal the dynamic mechanical properties. Fig. 1(A) presented the storage modulus (E') and the loss modulus (E''). Fig. 1(B) is the $\tan \delta$ versus temperature for the samples aged in the Regular solution. Fig. 2 is for CR in the ADT solution.

Figs. 1 and 2 show that the glass transition temperature (T_g) is about -48°C and no change after aging. T_g is identified in Fig. 1 as the temperature where sharp decrease in E' or the peak in Fig 2 occurs.

In the Regular solution (see Fig. 1(A)), the E' and E'' increased slightly as the samples aged; but in the ADT solution (see Fig. 2(A)) they tend to decrease as it ages.

Both E' and E'' are stable and maintain a nearly constant value for temperatures higher than T_g for both virgin and aged samples. Note that in our previous work [1], the surface chemistry of CR changed notably after exposure to the environment (particularly in the ADT solution), see the FTIR results in [1]. CR material in Regular solution is more chemically stable than in ADT solution under current test conditions. The current data shows however that the bulk, dynamic mechanical properties of the material is affected very little by aging in the environments.

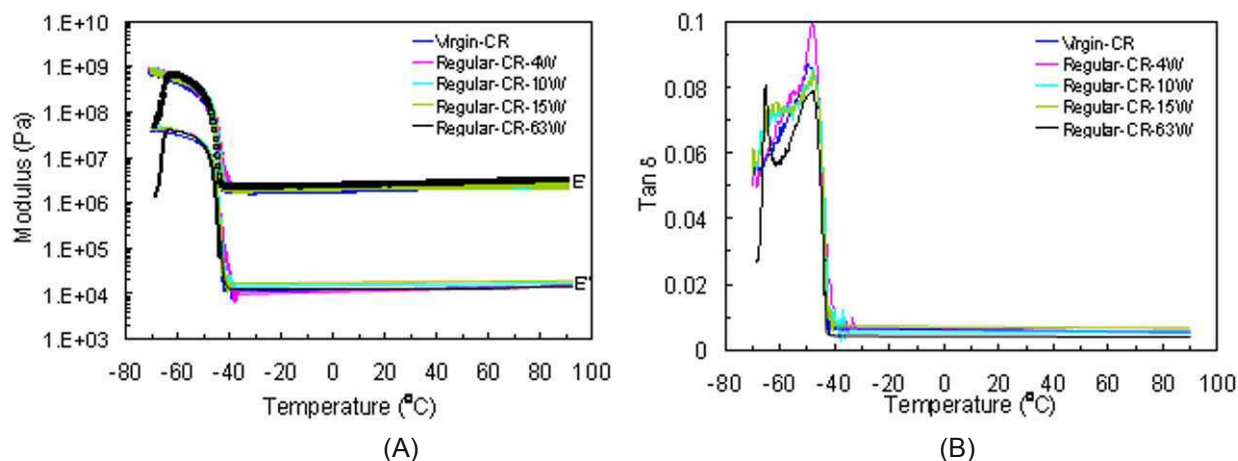


Fig. 1. (A) Storage modulus E' and loss modulus E'' , and (B) tangent delta versus temperature of virgin and aged CR samples exposed to the Regular solution

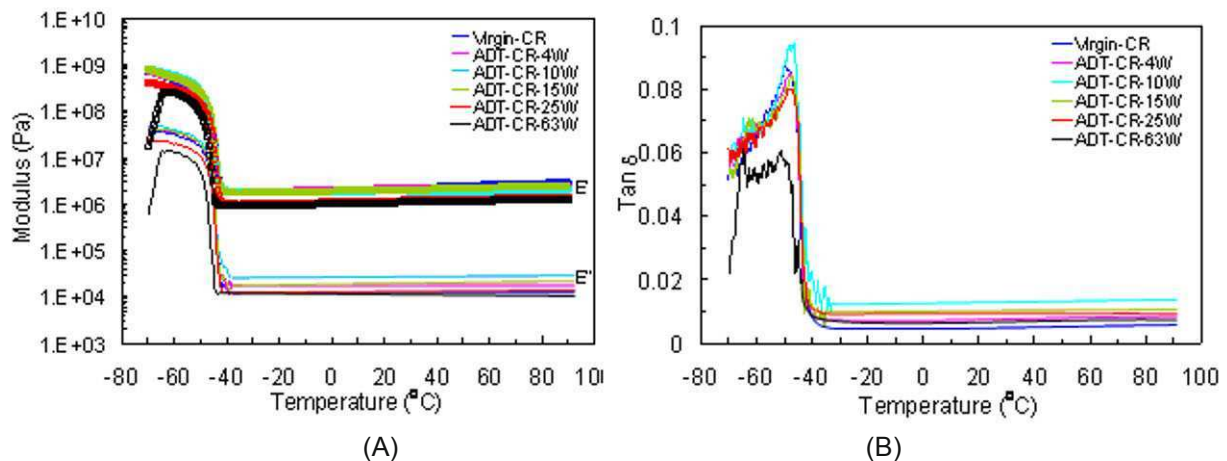


Fig. 2. (A) Storage modulus E' and loss modulus E'' , and (B) tangent delta versus temperature of virgin and aged CR samples exposed to the ADT solution. The optical pictures show the surface conditions of the virgin and 63-week aged specimens.

3.1.2 Fluorosilicone Rubber (FSR)

Test data for FSR samples are shown in Figs. 3 and 4 in the Regular and the ADT solution, respectively. Figs. 3(A) and 4(A) present the storage modulus (E') and the loss modulus (E''). Figs. 3(B) and 4(B) are the $\tan \delta$ versus temperature.

Figs. 3 and 4 show that the glass transition temperature (T_g) is about -50°C and has no change after aging. Above T_g , both E' and E'' decrease fast between T_g and room temperature and slowly after room temperature. The aging appears to increase the modulus slightly.

Note that in our previous study [1], no FTIR spectrum change was observed for FSR in either Regular or ADT solution. FSR appeared to be the most stable materials among the three tested in FTIR tests.

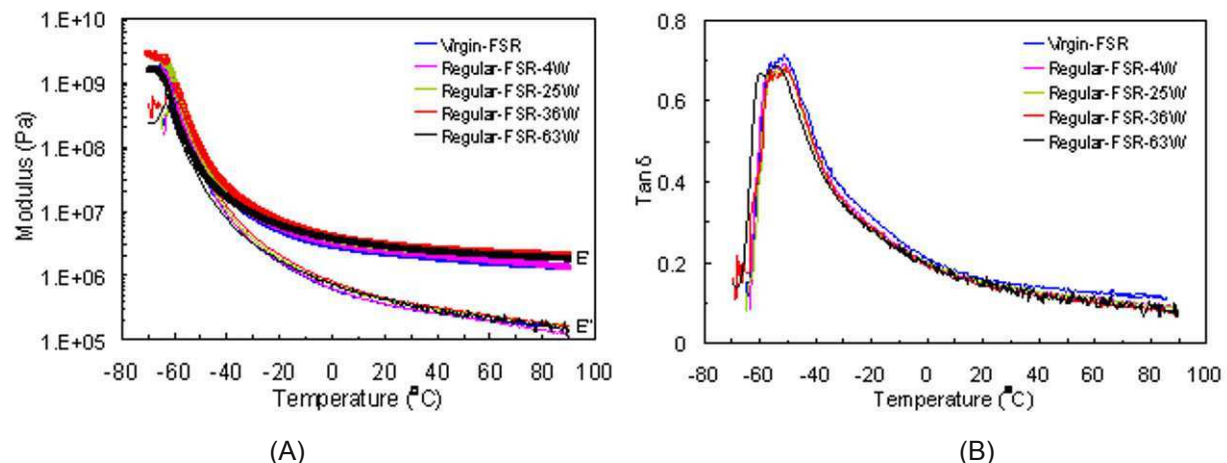


Fig. 3. (A) Storage modulus E' and loss modulus E'' , and (B) tangent delta versus temperature of virgin and aged FSR samples exposed to the Regular solution

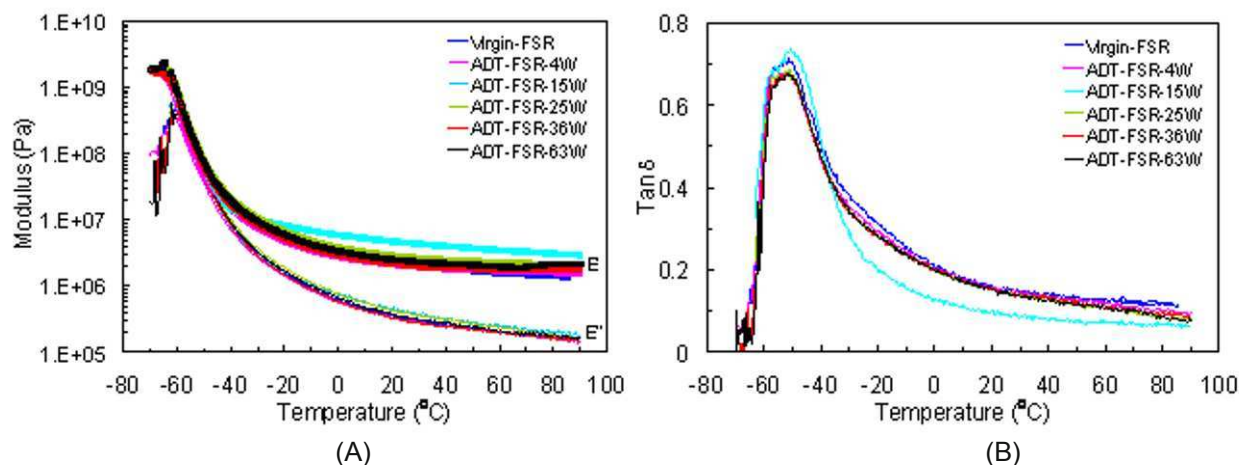


Fig. 4. (A) Storage modulus E' and loss modulus E'' , and (B) tangent delta versus temperature of virgin and aged FSR samples exposed to the ADT solution

3.1.3 Liquid Silicone Rubber (LSR)

Test data for LSR samples are shown in Figs. 5 and 6 in the Regular and the ADT solution, respectively. Figs. 5(A) and 6(A) present the storage modulus (E') and the loss modulus (E''). Figs. 5(B) and 6(B) are the $\tan \delta$ versus temperature.

Figs. 5 and 6 show that the glass transition temperature (T_g) is about -42°C and has no change after aging. The T_g is consistent with our previous data reported in [1]. Above T_g , E' is nearly constant, but E'' gradually decreases with temperature. The aging appears to increase the modulus slightly in both solutions.

Note that surface appearance of the LSR in ADT changed from black to white after 63 weeks (see the discussion in [1]). It was concluded in [1] that there are significant surface chemical changes for LSR samples exposed to ADT solution at 80°C over time. The chemical degradation is likely due to de-crosslinking and chain scissoring in the rubber backbone in the environment. However, the bulk, dynamic mechanical properties of the LSR material had very little change aged in both solutions according to the current test data.

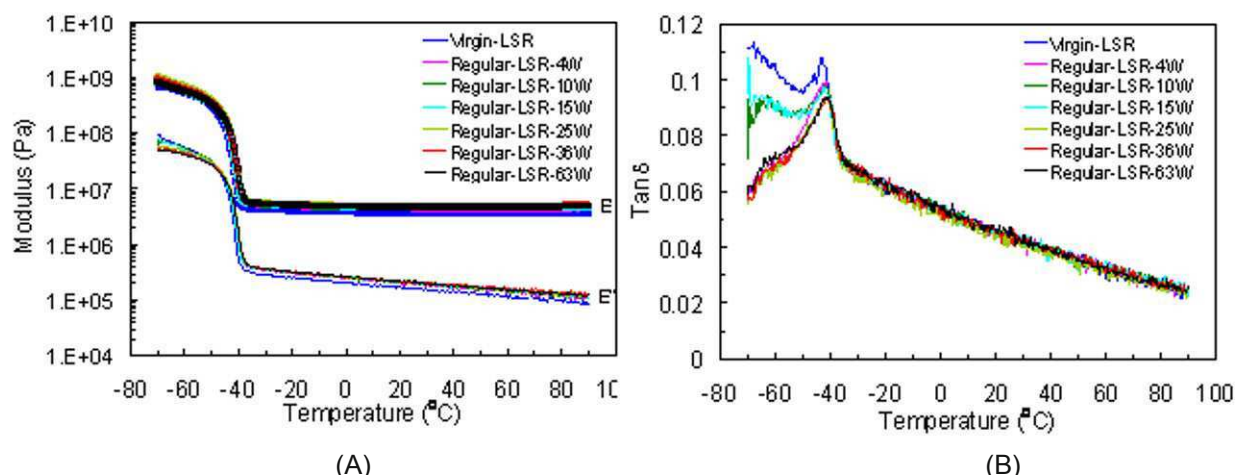


Fig. 5. (A) Storage modulus E' and loss modulus E'' , and (B) tangent delta versus temperature of virgin and aged LSR samples exposed to the Regular solution

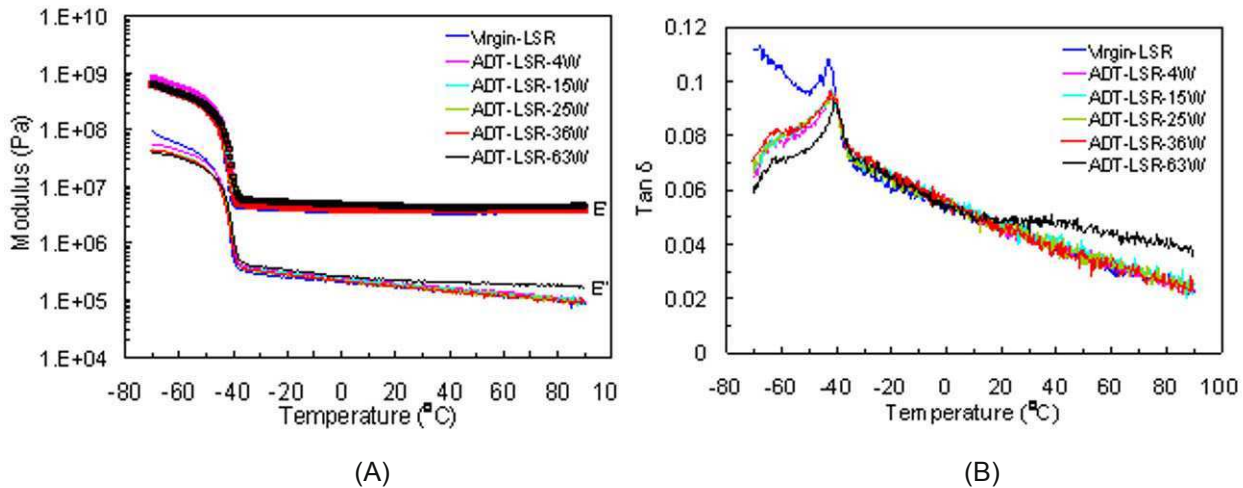


Fig. 6. (A) Storage modulus E' and loss modulus E'' , and (B) tangent delta versus temperature of virgin and aged LSR samples exposed to the ADT solution. The optical pictures show the surface conditions of the virgin and 63-week aged specimens

4. CONCLUSIONS AND FUTURE STUDY

From the DMA data and discussions above, it appears that CR, LSR and EPDM are good candidates for PEM fuel cell applications, in terms of both T_g and the storage modulus E' . Among the three, EPDM seems to be the best, as

- (a) In ADT solution, CR showed cracks and both CR and LSR lost weights to about 45% after ageing [1].
- (b) CR and LSR had significant amount of silicone leachants in ADT solution [1].
- (c) CR and LSR had chemical degradation in ADT solution as shown by our FTIR analysis [1].

Note that in the Regular solution, all three materials performed equally well in our chemical degradation studies [1,2].

ACKNOWLEDGEMENTS

This study is sponsored by Graduate Students Research Abroad Program (Grants no.97-2917-I-110-108) from National Research Council, Taiwan, and National Sun Yat-Sen University Study Abroad Scholarship Award to the first author. In addition, support from the US Department of Energy (DE-FC36-06G086041 and DE-FG36-08GO88116) to the University of South Carolina Research Foundation, the NSF Industry/University Cooperative Research Center for Fuel Cells at the University of South Carolina (EEC-0324260 and IIP-0856055), and Natural Science Foundation of Jiangsu Province in China (BK2009362) is greatly appreciated. Materials in this study were kindly provided by Dow-Corning and Dana Corporation.

REFERENCE

- [1] Lin C.W., Chien C.H., Tan J., Chao Y. J., and Van Zee J.W. Chemical Degradation of Five Elastomeric Seal Materials in a Simulated and an Accelerated PEM Fuel Cell Environment, *Journal of Power Sources* 2011; 196(4): 1955-66.
- [2] Cui T., Lin C.W., Chien C.H., Chao Y.J., Van Zee J.W. Service life estimation of liquid silicone rubber seals in polymer electrolyte membrane fuel cell environment, *Journal of Power Sources* 2011; 196(3):1216-21

Mechanical Characterization and Modeling Of Solid Oxide Fuel Cells and Stacks

Ryan Berke¹ and Mark E. Walter

The Ohio State University, Department of Mechanical and Aerospace Engineering
201 W. 19th Ave., Columbus, OH 43210

ABSTRACT

Planar Solid Oxide Fuel Cells (SOFCs) are made up of repeating sequences of thin layers of cermet electrodes, ceramic electrolytes, seals, and current-collectors. For electro-chemical reasons it is best to keep the electrolyte layers as thin as possible. However, for electrolyte-supported cells, the thin electrolytes are more susceptible to damage during production, assembly, and operation. The latest-generation electrolyte-supported SOFCs employ a honeycomb-type support structure that includes both thick and thin regions within the electrolyte. The thin regions are more electro-chemically efficient, while the thick regions provide mechanical support.

The performance of the electrolyte within the context of a mechanically and thermally loaded stack is being investigated. Temperature profiles are obtained from CFD models. Mechanical and thermal material properties are obtained from experiments with individual components. Single-component models are used to further characterize components with complex geometries, particularly the electrolyte and the compliant, electrically conducting metal foams. A 2-D stack model uses the data from experiments and single-component models to evaluate the mechanical response of the cells to loads comparable to those experienced in assembly and operation. The model is run both at room temperature and at operating temperature to determine which parameters can best reduce the demands on the brittle electrolyte without sacrificing electro-chemical efficiency.

I. INTRODUCTION

Fuel cells are electro-chemical devices which consist of an electrolyte and two electrodes which enable reactions in fuel and oxidant to produce energy. Solid Oxide Fuel Cells (SOFCs) in particular are characterized by a solid electrolyte which is electrically non-conducting and impermeable to gas diffusion, but permits ions to migrate through it. When brought up to their operating temperatures, the anode strips electrons from the fuel to form oxygen ions, which pass through the electrolyte to the cathode. The stripped electrons, which cannot pass through the electrolyte, are routed to the cathode through an external circuit, thus providing electrical power. Electrons arriving at the cathode combine with oxygen ions and with hydrogen in the fuel to produce water [1],[2] .

SOFCs are generally characterized by both their geometric configuration, most commonly tubular or planar, and by which of the ceramic layers provides the primary mechanical support, generally the anode or the electrolyte. Tubular cells have the advantage of being much easier to seal against cross-contamination of gases, but planar cells are generally preferable due to the potential for increased power density, for easier cell-to-cell interconnection, and significantly reduced manufacturing costs.[3]. Electrolyte-supported cells are advantageous over anode-supported cells because they are less susceptible to failure due to anode reoxidation or cathode reduction. However, the thicker electrolyte results in higher resistance and requires higher operating temperatures to minimize ohmic losses [4]. Electrolyte-support is also preferable because the porous anodes are generally harder to seal.

¹ Contact Author: berke.13@osu.edu

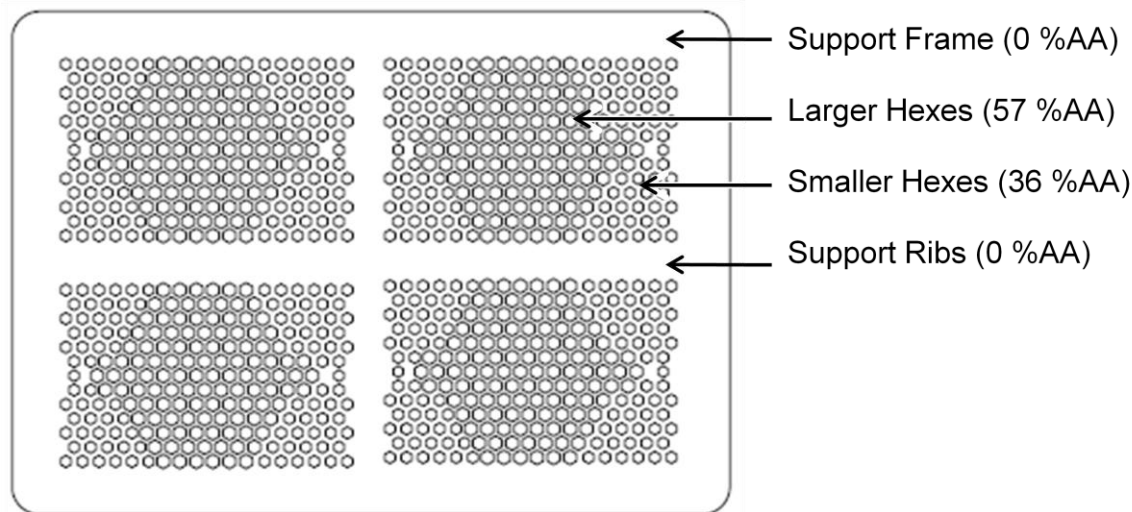


Fig. 1: In-plane geometry of a FlexCell Electrolyte

For electro-chemical reasons, it is best to keep the electrolyte as thin as possible. Thinner electrolytes can allow for lower operating temperatures and have lower resistive losses [5]. However, it remains important to maintain sufficient thickness that the electrolyte is mechanically robust enough to provide mechanical support.

In order to produce cells which are mechanically robust while electro-chemically efficient, NexTech Materials Ltd. has developed a new planar, electrolyte-supported SOFCs which it calls the FlexCell™ [6]. The design incorporates an electrolyte layer made up of alternating regions of thin, “active” regions supported by a thicker, hexagonal mesh, as shown in Fig. 1. The thin regions, which are approximately 40 microns in thickness, allow for more electrochemically efficient energy production, while the thicker regions, approximately 200 microns, provide mechanical support. The cells are produced in layers which are on the order of 100-1000 square centimeters in area, making them upwards of 2500 times larger in length in-plane than they are through the thickness.

To ensure robust, efficient designs, the ability to model the cells using finite element analysis is desirable. Previous work, which focused solely on the electrolyte, employed a two-scale modeling approach. Small-scale local geometry was studied with a full 3-D unit-cell model, and large-scale effects were studied with a shell-element model that did not require prohibitively many elements [7]. To study the performance of the electrolyte in the context of a full SOFC stack, further modeling and experiments have been run to characterize the surrounding SOFC components.

II. SOFC STACK COMPONENTS

Aside from the electrolyte, a number of other components must be considered in order to model a full stack. Figure 2 is a schematic of a generic stack and shows all the different components down to the cell level. A porous anode and cathode are bonded to either side of the electrolyte, forming an energy-producing assembly that is often referred to as positive electrode-electrolyte- negative electrode, or PEN for short [8]. On either side of the electrodes, compliant, metal foams are used to direct current from the electrodes to the interconnect, while allowing gases to diffuse to and from the PEN layer. The steel interconnects form a separation between cells, as well as contain channels to direct the flow of gases. Additionally, seals are needed at the edges of cells to prevent the cross-contamination of fuel and oxidant from one side of the PEN to the other.

III. REPEATING CELL MODEL

To begin to model the stack, the repeating unit shown in Fig. 2 is modeled. To simplify the model, the electrolyte was treated as a solid layer with uniform thickness and equivalent mechanical properties that account for the effects of the thin regions. Finite element modeling was used previously to show that for any linear elastic

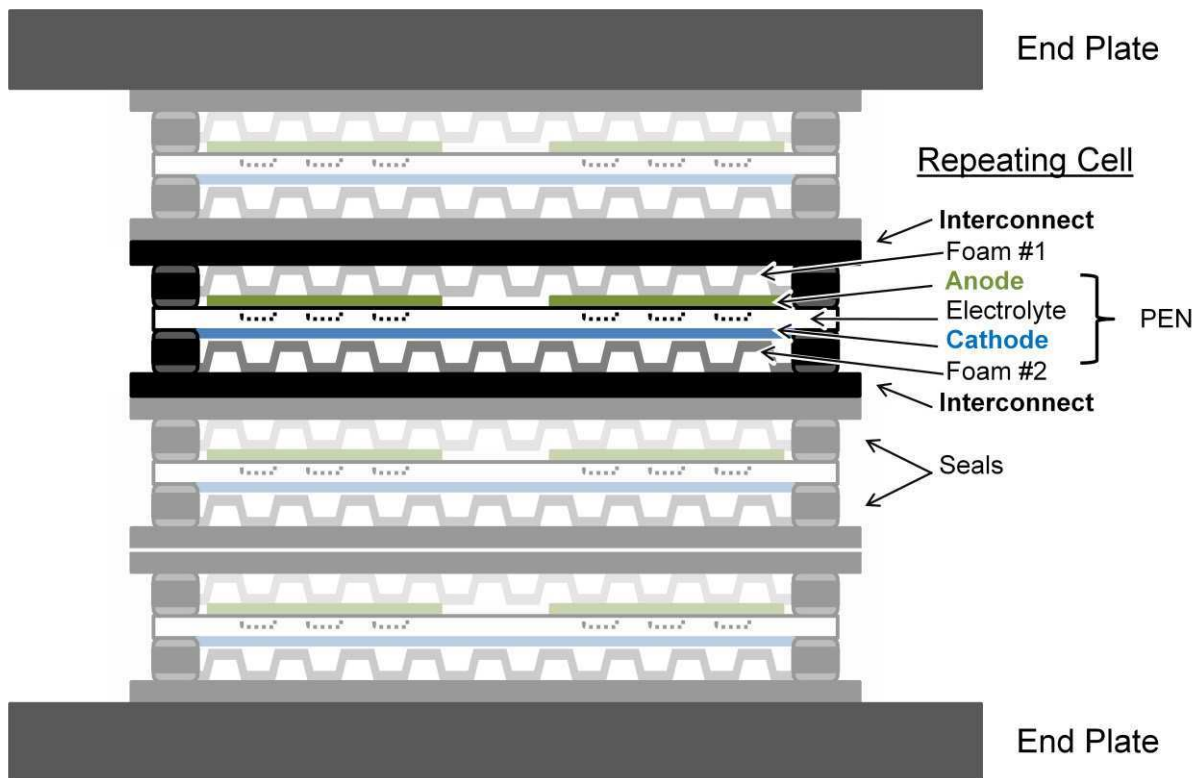


Fig. 2: Schematic of a Planar SOFC Assembly

material, the reduction in stiffness of a FlexCell electrolyte is dependent on the percentage of 'active area' devoted to thinner, active hexes. Percent active area is defined as follows:

$$\%AA = \frac{\text{Area of Hexes}}{\text{Total Area of Region}} \times 100\% \quad (1)$$

For example, the electrolyte shown in Fig. 1 contains a combination of larger and smaller hexes. The large hexes are 4.5 mm across and are spaced 1.5 mm apart, taking up about 57% of their surrounding area. The small hexes, which are 3.0 mm across and spaced 3.0 mm apart, take up about 36%. The frame and ribs contain no hexes, so their %AA is zero.

The equivalent stiffness, E_{eq} for FlexCell geometries of varying thicknesses is written as follows:

$$\%E_{eq} = \frac{t_s + f(\%AA)t_m}{t_s + t_m} \times 100\% \quad (2)$$

where t_m is the thickness of the active membrane, t_s is the additional thickness added in the support regions, and $f(\%AA)$ is determined by a curve fit of 35 finite element simulations:

$$f(\%AA) = 100 - 1.8847 (\%AA) + .90538 * (\%AA)^2 \quad (3)$$

To further simplify the repeating cell model, it has also been assumed that the mechanical effects of the anode and cathode are minimal when compared to the effect of the electrolyte itself. The anode and cathode are porous cermets which are much softer than the electrolyte. In addition, the electrodes are applied in much thinner layers than the electrolyte, thus further reducing any strength. By neglecting the electrodes in the stack model, the model avoids having to devote many tiny elements to their region, which would be computationally prohibitive. Other researchers have shown that in electrolyte-supported cells, the difference in stress on the electrolyte between an electrolyte by itself and a full PEN assembly is only around 10% [9].

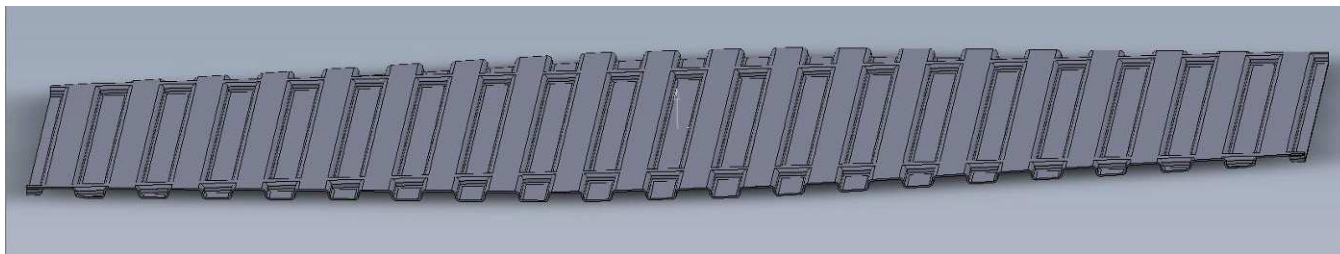


Fig. 3: 3-D Geometry of a Current Collector

In most of the stack components, the geometry is simple and the material properties are available in the literature. The electrolyte is typically made from Yttria-Stabilized Zirconia (YSZ), which has a Young's Modulus of around 200 GPa [10]. As described above, in active regions of the FlexCell the equivalent stiffness is by definition lower. The interconnect layers are made typically from Crofer® 22 APU [11],[12]. The seals are each three layers: a steel shim sandwiched between two glass-ceramic seals which attach to the electrolyte frame and interconnect, respectively [13]. With the exception of the metal foams, all component geometries are able to be modeled as rectangles in a 2-D cross-sectional representation of the stack.

As shown in Fig. 3, the foam on the anode side is a nickel foam which is stamped into a corrugated pattern. The cathode side foam is Crofer which has been formed into sheets of expanded metal mesh and then stamped into a similar corrugation pattern. Mechanical properties for the nickel foam are obtained from existing literature [14], and the mechanical behavior of the expanded metal configuration is determined below.

IV. MECHANICAL RESPONSE OF CATHODE-SIDE FOAM

Samples of the expanded metal were compressed from an initial thickness of 1.5mm to a final thickness of 0.1 mm, resulting in the load-displacement data in Fig. 4. The samples were pressed between two cylindrical rods which were 31.75 mm in diameter. The recorded loads were divided by the rods' cross-sectional area to determine a contact pressure. This contact pressure is later used with a finite element simulation. The experiments were performed at room temperature, although there are plans to repeat the measurements at the SOFCs' operating temperature of up to 850 °C.

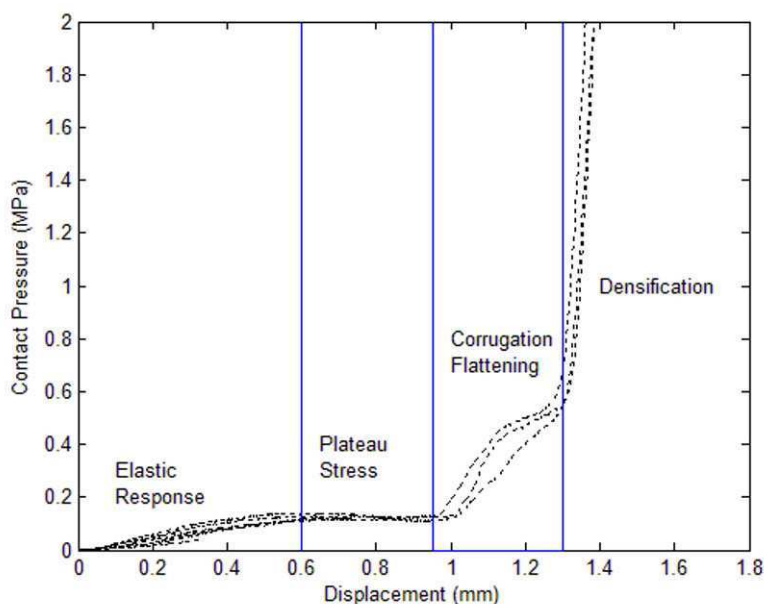


Fig. 4: Load-Displacement Response of Corrugated Expanded Metal

Like many foams found in literature, the deformed material initially exhibits a linearly elastic response, followed by a plateau stress in which the deformation is believed to be dominated by small-scale failure by buckling and/or plastic yielding [15]. After a plateau, traditional foams enter a stage called densification, in which the voids in the foam have compressed to the extent that opposite faces come into contact. Foams undergoing densification exhibit stress-strain behavior with slopes much steeper than the initial elastic response. The corrugated expanded metal appears to exhibit an analogous slope, but there is an additional unexplained behavior between the plateau stress and densification. Because this material is not a “true” foam, it is believed that this extra region may correspond to the flattening of the corrugation structure as both faces of the material in each of the flat regions come into contact with both load rods.

Based on the experimental data, a single-component model of the expanded metal current collector was generated in ANSYS. The model used a 2-D cross-section of the corrugated pattern as its geometry and is treated as a generic, isotropic, plastically-deformable solid. For boundary conditions, the nodes along the bottom surface of the foam were all fixed in place vertically, while the top surface nodes were subjected to incremental displacements downward. The model underwent compression with the same range of deformation as the samples

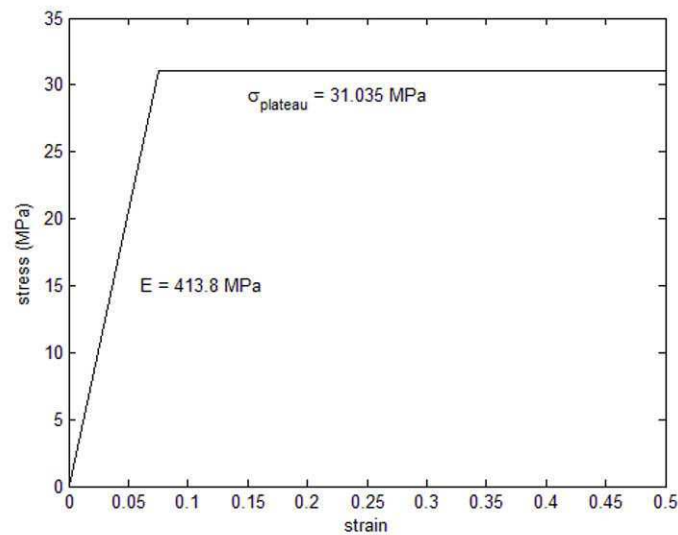


Fig. 5: Material Behavior Determined by Model

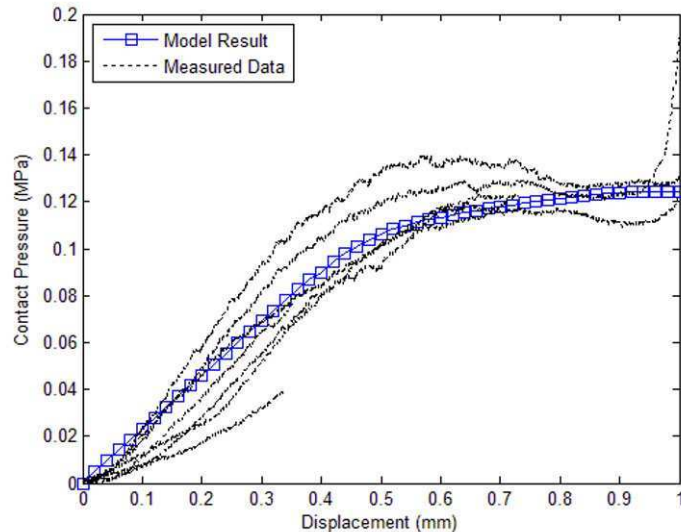


Fig. 6: Load vs. Displacement in Linear and Plateau Regions

loaded in the experiments. The material parameters in the model were modified over several iterations until the reaction forces reported by the displaced nodes agreed with the contact pressures measured by the load frame. The final stress-strain curve for the modeled material is given in Fig. 5. Simulations which used the material data from Fig. 5 resulted in the pressure vs. displacement data given in Fig. 6.

V. DISCUSSION OF RESULTS

As is shown in Fig. 6, the model was able to replicate the load-displacement response in the elastic and plateau regions. However, the model was unable to reproduce the response of the later regions, regardless of the material properties that were defined. There are a number of possible reasons for this discrepancy. In conventional foams the expected response assumes that the foam is uniformly dense and undamaged throughout the material, whereas the stamped corrugations imply plastic yielding and collapse of the foam in and around the folds of the corrugation pattern. Whatever residual stresses or damage may have occurred in the folds is not accounted for in the finite element model. Regardless of prior damage or yielding, the presence of the folds in the model represents possible sites for stress concentration and plastic hinges. A sample stress contour, which shows the development of stress concentrations, is shown in Fig. 7.

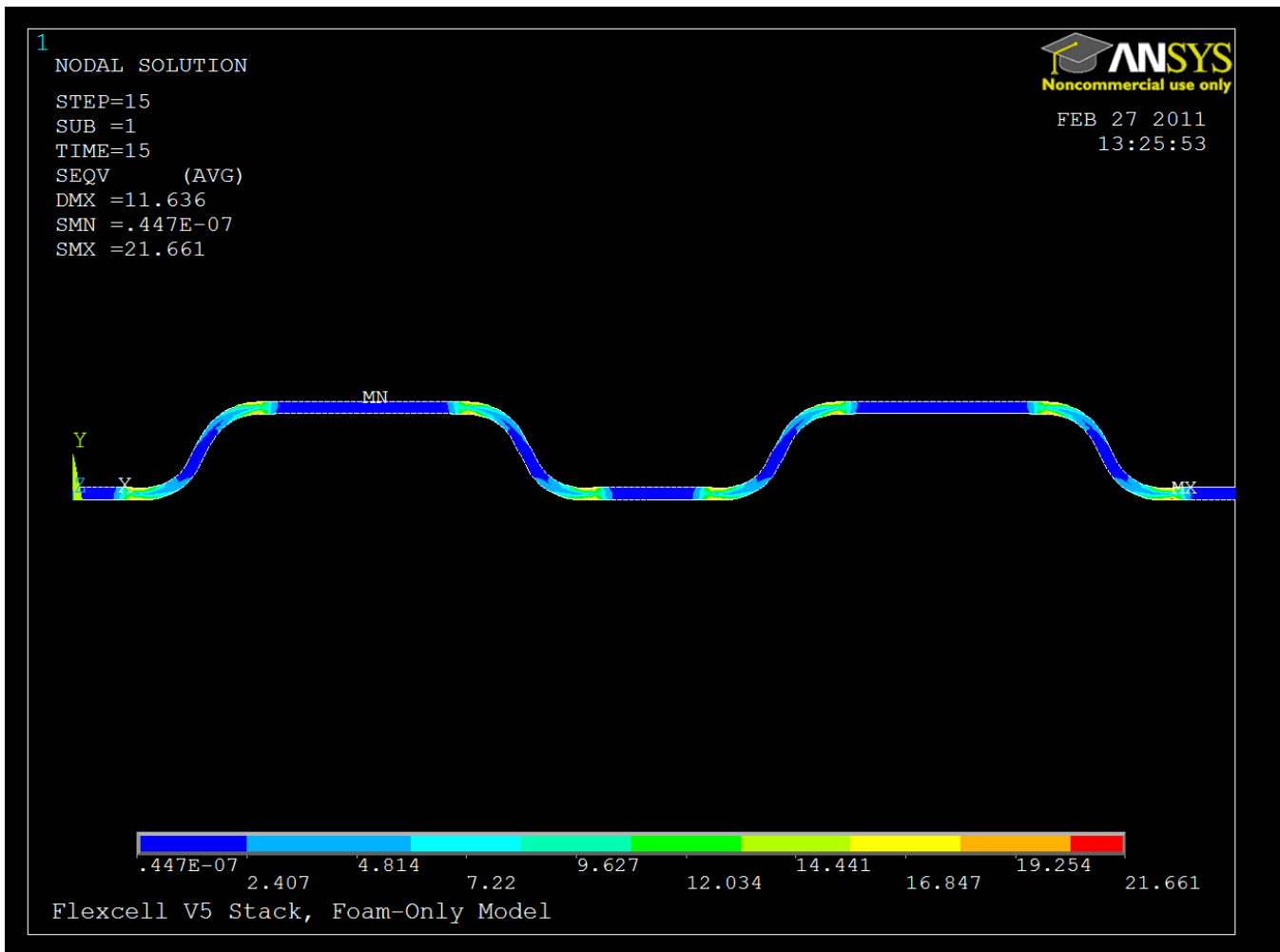


Fig. 7: Stress Contours Present in Compressed Foam

For the purposes of building a full stack model, the ability to model the current collectors in the higher displacement regimes is not expected to be critical. What matters most is the amount of force transferred from the foam to the electrolyte under a given displacement. Because of the way that the material properties have been identified, the desired forces are automatically produced. Within the context of the surrounding stack, it is expected that by the time the foam reaches its flattening and densification regimes, it will already have undergone considerable displacement and the damage to the electrolyte will likely have already compromised the cell.

VI. CONCLUSIONS

In order to produce a full stack model for the FlexCell design, characterization of the surrounding components must be performed. Many of the components exhibit simple geometries with well-understood properties, but a few, including the patterned, metal foam current-collectors, do not. To evaluate the impact on the electrolyte, it is critical to understand how loads and displacements are transferred between components. Since it is not important to understand the material response of the actual components, effective properties can usually be used.

There is still further work to be done in evaluating the mechanical performance of the FlexCell. The above characterization needs to be repeated at higher temperature, and the results need to be incorporated into a model which includes the rest of the stack. Figure 8 shows a region of a cell containing both foams and seals. The stack model itself is computationally complex, containing nonlinear behaviors associated with materials and components which deform plastically, have sliding contact between components, and have coupled thermal-structural responses.

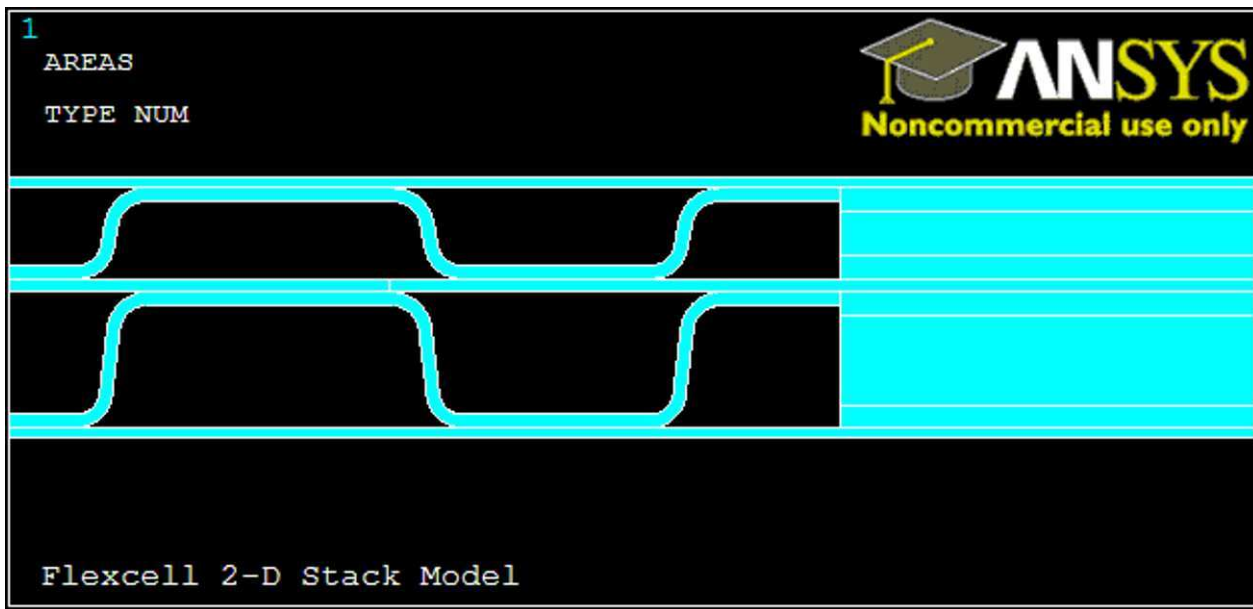


Fig. 8: Representative Segment of Stack Model

REFERENCES

- [1] S. M. Haile, "Fuel cell materials and components ,," *Acta Materialia*, vol. 51, no. 19, pp. 5981-6000, Nov. 2003.
- [2] R. M. Ormerod, "Solid oxide fuel cells," *Chemical Society Reviews*, vol. 32, no. 1, pp. 17-28, 2003.
- [3] P. Singh and N. Q. Minh, "Solid Oxide Fuel Cells: Technology Status," *International Journal of Applied Ceramic Technology*, vol. 1, no. 1, pp. 5-15, 2005.
- [4] N. Q. Minh, "Solid oxide fuel cell technology--features and applications," *Solid State Ionics*, vol. 174, no. 1, pp. 271-277, Oct. 2004.
- [5] N. Sammes, A. Smirnova, and O. Vasylyev, Eds., "Intermediate-Temperature SOFC Electrolytes," in *Fuel*

- Cell Technologies: State and Perspectives*, vol. 202, Berlin/Heidelberg: Springer-Verlag, 2005, pp. 19-34.
- [6] "NexTech unveils largest SOFC tech platform," *Fuel Cells Bulletin*, vol. 2009, no. 8, p. 1, Aug. 2009.
 - [7] R. Berke, A. Suresh, and M. E. Walter, "Mechanical Characterization and Modeling of Electrolyte Membranes in Electrolyte-Supported SOFCs," presented at the SEM 2010 Annual Conference, Indianapolis, IN, 2010.
 - [8] C. Lin, T. Chen, Y. Chyou, and L. Chiang, "Thermal stress analysis of a planar SOFC stack," *Journal of Power Sources*, vol. 164, no. 1, pp. 238-251, Jan. 2007.
 - [9] A. Selçuk, G. Merere, and A. Atkinson, "The influence of electrodes on the strength of planar zirconia solid oxide fuel cells," *Journal of Materials Science*, vol. 36, no. 5, pp. 1173-1182, 2001.
 - [10] A. Selçuk and A. Atkinson, "Strength and Toughness of Tape-Cast Yttria-Stabilized Zirconia," *Journal of the American Ceramic Society*, vol. 83, no. 8, pp. 2029-2035, 2004.
 - [11] F. Smeacetto, M. Salvo, M. Ferraris, J. Cho, and A. Boccaccini, "Glass-ceramic seal to join Crofer 22 APU alloy to YSZ ceramic in planar SOFCs," *Journal of the European Ceramic Society*, vol. 28, no. 1, pp. 61-68, 2008.
 - [12] Thyssenkrupp VDM, "Material Data Sheet No. 4046 for Crofer 22 APU," Jun-2006. [Online]. [Accessed: 28-Feb-2011].
 - [13] J. Milhans, D. Li, M. Khaleel, X. Sun, and H. Garmestani, "Mechanical properties of solid oxide fuel cell glass-ceramic seal at high temperatures," *Journal of Power Sources*.
 - [14] V. Paserin, S. Marcuson, J. Shu, and D. S. Wilkinson, "The chemical vapor deposition technique for Inco nickel foam production—manufacturing benefits and potential applications," in *Cellular Metals and Metal Foaming Technology*, 2003.
 - [15] M. Ashby, "The properties of foams and lattices," *Philosophical Transactions of the Royal Society A: Mathematical, Physical and Engineering Sciences*, vol. 364, no. 1838, pp. 15 -30, Jan. 2006.

The Impulse Imparted upon Monolithic Metal Plates due to Blast Loading

Jefferson Wright, Erheng Wang and Arun Shukla

Dynamic Photomechanics Laboratory, Dept of Mechanical, Industrial and Systems
Engineering

The University of Rhode Island, 92 Upper College Rd, Kingston, RI 02881, USA

ABSTRACT

The impulse imparted onto a structure is a major component in the study of fluid-structure interactions during a blast loading event. A better understanding of the impulse transferred to a structure will lead to an improved evaluation of an object's blast performance. However, limited experimental studies have been performed to determine the impulse imparted to a structure during a blast event. In this study, a comprehensive experimental study on the impulse imparted to free standing monolithic plates under blast loading is conducted. A series of aluminum and steel cylindrical plates were subjected to various experimental loading conditions using a shock tube apparatus. The motion of the specimens was captured using a high speed camera, Photron SA1, to determine their velocity and momentum. The relationship between the impulse transferred to the specimens and the shock wave pressures was analyzed. These results were compared with the theories developed by Xue and Hutchinson, 2004 and Kambouchev, et al, 2006, 2007. The comparisons show that the current fluid-structure model needs to be modified in air blast when the compressibility of the fluid cannot be ignored.

INTRODUCTION

The impulse imparted onto a structure is a major component in the study of fluid-structure interactions during a blast loading event. A better understanding of the impulse transferred to a structure will lead to an improved evaluation of an object's blast performance. This in turn will help direct the design of new structures with greater blast resistance.

The momentum imparted into a structure during a blast event is typically calculated via fluid-structure interaction. This problem was first solved by Taylor [2] who calculated the solution for a one dimensional wave impinging and reflecting on a solid plate to derive the momentum transmitted into the plate. From this, the momentum transmitted to a plate during a blast loading was found to derive from the density of the fluid, the wave speed, the blast decay time and the areal density of the plate. This fluid structure interaction during a blast loading has been continuously studied for the many years [2-8] and in particular Taylor's solution has been used to evaluate the blast resistance of sandwich composites with different core topologies [5-7]. However these researchers did not include the non-linear compressibility of the fluid in their studies. Due to the non-linear compressibility of air during blast loading events the results have been questioned [11]. In addition, Kambouchev, et al [3-4] revised Taylor's model by including the compressibility of the air. This compressibility however, was for waves under the acoustic limit which means that they are governed by the linear wave equation with a constant wave speed. This may be valid for a low intensity air blasts but for high intensity air blasts, one for which there is a noticeable difference between the velocities of the incident and reflected shock wave [1] further considerations may be needed. Some researchers [9-10] used pendulum experiments to estimate the impulse transmitted to the structures from a blast loading. This method can only estimate the final impulse transmitted to the structures and shows neither the impulse redistribution behavior nor the imparted impulse history during the blast event.

In this paper, a series of well-designed shock wave loading experiments were conducted on free-standing monolithic flat plates to simulate the one-dimensional shock wave loading status using a shock tube apparatus.

The specimen momentum history was obtained from both the high-speed photography technique and the measured pressure-time profiles. The experimental results were carefully analyzed and compared with the theoretical prediction from the existing models.

2. EXPERIMENT SETUP

2.1 MATERIALS AND SPECIMENS

The metallic cylindrical plates used were 6061 T6 aluminum and 1018 steel of dimensions 77.8 mm in diameter, which is slightly larger than the inner diameter of the shock tube (76.2 mm), and 6.4 mm thick with masses of 81.5 g and 232 g respectively. Cylindrical plates were used to ensure that any loading on the specimens was limited to the area of the muzzle opening, to (as close as possible) maintain the conditions for a one dimensional uniform blast loading.

2.2 EXPERIMENTAL PROCEDURE

A shock tube apparatus was utilized in the present study to generate a controlled blast loading. It consisted of both a driver and driven section which had an overall length of 8 m. These two sections were separated by a destructible diaphragm. A picture of the shock tube can be seen in Figure 1. The driver section was pressurized with high pressure Helium gas which created a pressure difference across the diaphragm. When this difference became great enough the diaphragm ruptured quickly releasing the gas. This gas then traveled down the driven section and created a planar shock wave which imparted an impulse upon the specimen. Two pressure transducers (PCB102A) were mounted at the end of the muzzle section to record the incident and reflected pressure profiles. The first pressure sensor was mounted 20 mm away from the muzzle and the second was mounted 180 mm away (160 mm separation from the first pressure sensor). The final muzzle diameter was 76.2 mm. Figure 2 shows a typical measured pressure profile. Four incident peak pressures of the shock waves were chosen in the current study: .44, .76, 1.03, and 1.35 MPa in the present study.



Fig.1. Shock tube apparatus

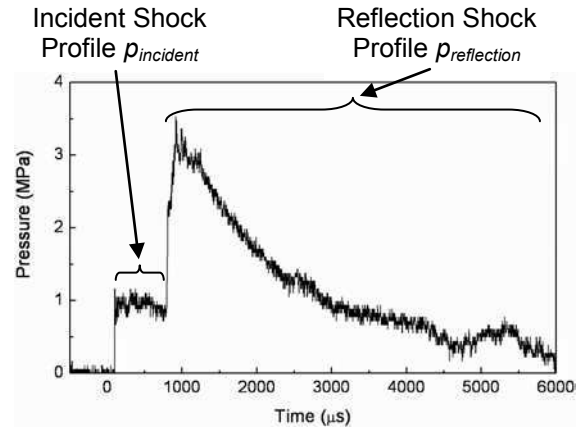
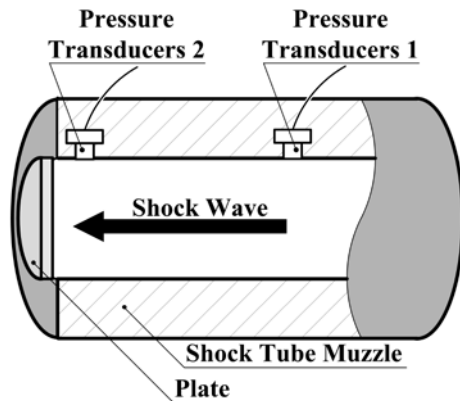


Fig. 2 Typical experimental pressure profile

The specimen was placed on a stand created to ensure placement and a freestanding boundary condition of the specimen, while imparting minimal frictional forces upon the specimen during loading. The flat face of the specimen was set normal to the axis of the shock tube with the face completely covering the opening. A diagram of this set up can be seen in Figure 2. At least two specimens of each type were tested at each incident pressure to ensure reliability.

A high speed photography system was utilized to capture the motion of the specimens in order to determine their velocity and momentum. The lens axis of the camera was set perpendicular to the shock tube and direction of motion of the as shown in figure 3. The distance between the camera and the plate was chosen to be approximately 2 m, which is more than 20 times that of the plate's dimension (~ 0.1 m) and 10 times that of the plate displacement in the images (~ 0.2 m), to avoid image distortion during plate propagation. In addition, the side of all of the specimens was painted white to give good contrast between the object and the background. The

camera was a Photron SA1 high-speed digital camera which has the ability to capture images at a framing rate of 40,000 fps with an image resolution of 512x256 pixels for a 2 second time duration.



(a) Diagram of the muzzle



(b) Real muzzle setup

Fig. 2 The muzzle setup

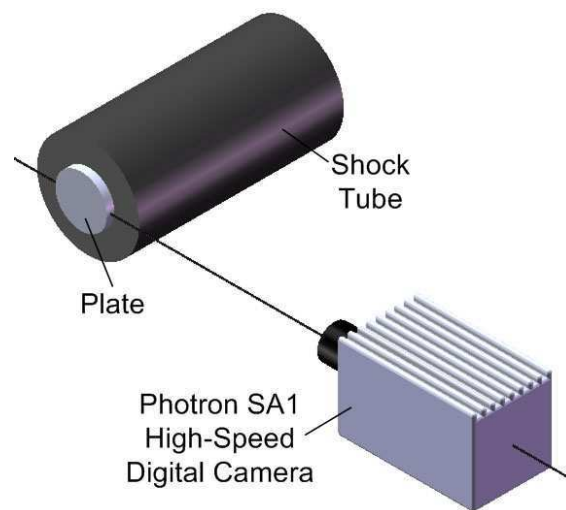


Fig. 3 orientation of camera to shock tube and specimen

3. EXPERIMENTAL RESULTS AND DISCUSSION

3.1 HIGH-SPEED SIDE-VIEW IMAGES

The real time observation of the motion of the aluminum specimens at different initial overpressure is shown in [figure 5](#). On the right side of the each image is the shock tube and the shock wave impinges upon the plate from this side. The images show that the circular plate moves linearly away from the shock tube near the time of impact and then rotates slightly as it travels away from the muzzle. This rotation may be due to the reflection of the expanded gas from the boundaries of the dump tank. From the high-speed images, it can be clearly seen that under higher incident pressure, the plate moved faster (with larger distance to the muzzle at the same time).

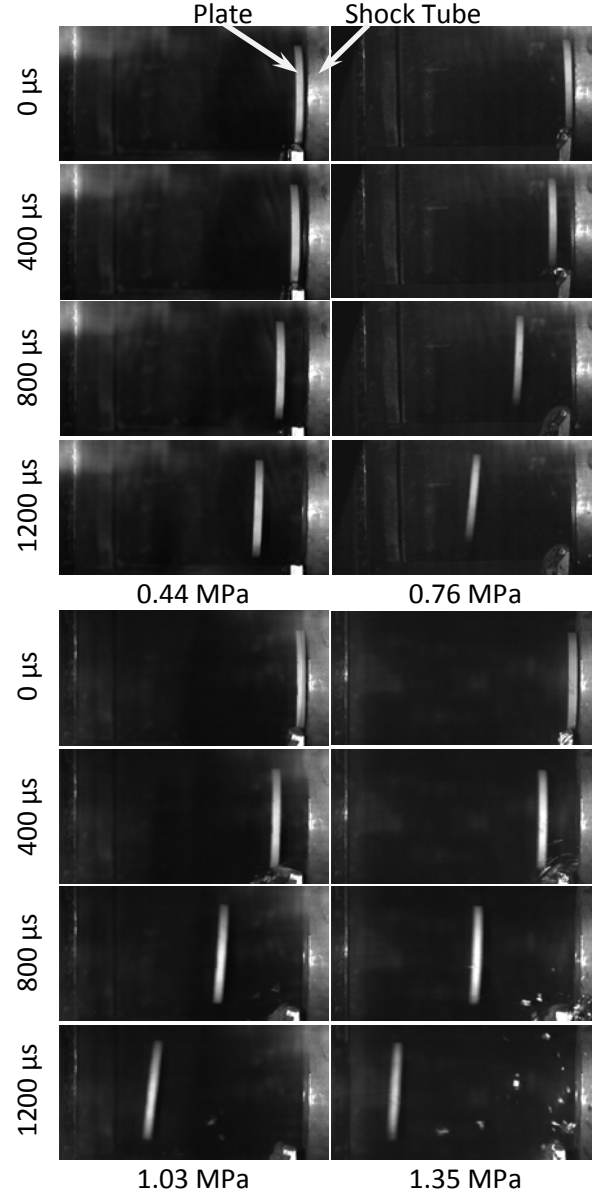


Fig. 5 High-speed side-view images of aluminum plates for different shock loadings

3.2 MOMENTUM OF PLATE FROM HIGH SPEED IMAGES

The momentum of the plates can be obtained from the high-speed images shown in Figure 5. A close-view of the typical high-speed side-view image is shown in Figure 6. Curve fitting methods, such as cubic spline curve fitting, can be used to pick up the position of the front face of the specimen. An example of the 7-point cubic spline curve fitting is shown in Figure 6. Since the specimen did not show any compression during the shock wave loading process, this curve can be used to represent the position of the specimen. Then the displacement profile of each point on the specimen can be obtained by correlating the position of the specimen in each image to that in the image at time $t = 0$. The differential of this displacement profile with respect to the time gives the velocity profile. The momentum of the plate can be evaluated from the velocity profile and the areal density of the plate. It can be expressed as:

$$\text{Horizontal momentum: } I_x^{plate} = \int_S m_s u_x ds \quad (1)$$

where, u_x is the x direction (horizontal) velocity and ds is the areal element of the plate.

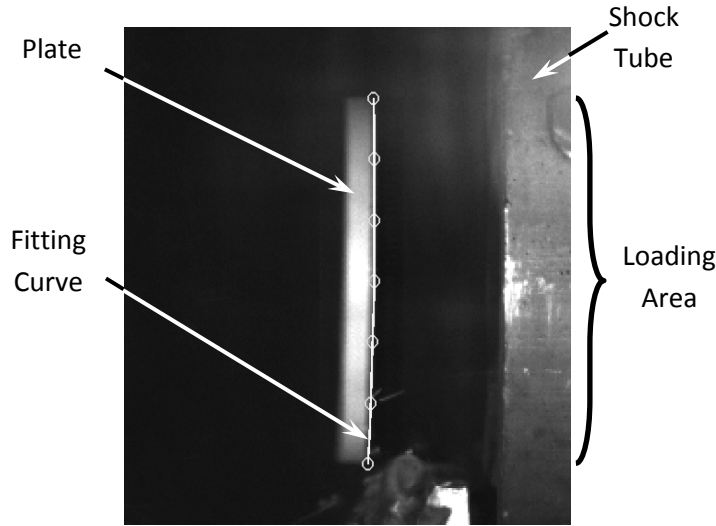


Fig. 6 Specimen under blast load with cubic spline

3.3 MOMENTUM OF PLATE FROM MESURED PRESSURE PROFILES

The momentum of the plates can be also obtained from the measured pressure profiles. Figure 7 shows the measured reflected pressure profiles of the aluminum plates for different shock loadings. These pressure profiles are considered to be the same as the pressure applied upon the plates. Since the cross-sectional area of the muzzle is known. The pressure impulse applied on the plates can be calculated as,

$$I_{pressure} = \int_0^{t_1} (p_{reflected} - p_0) S dt \quad (2)$$

where, p_0 is the atmospheric pressure.

Consider the momentum conservation during the one dimensional shock wave loading, the momentum of the plate should be identical to the pressure impulse applied to it. Figure 8 shows the momentum of the plates measured from the high-speed images and the pressure impulse of aluminum plates for different shock wave loadings. It can be seen that the momentums measured from the high-speed images agree with the pressure impulses very well. This verifies that the momentum is conserved during the loading process.

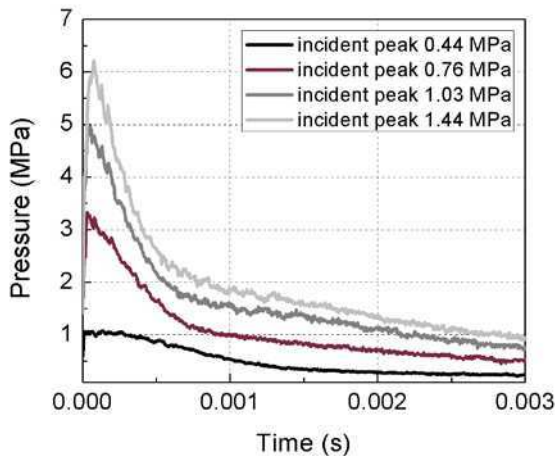


Fig. 7 Reflected pressure profiles of the aluminum plates for different shock loading

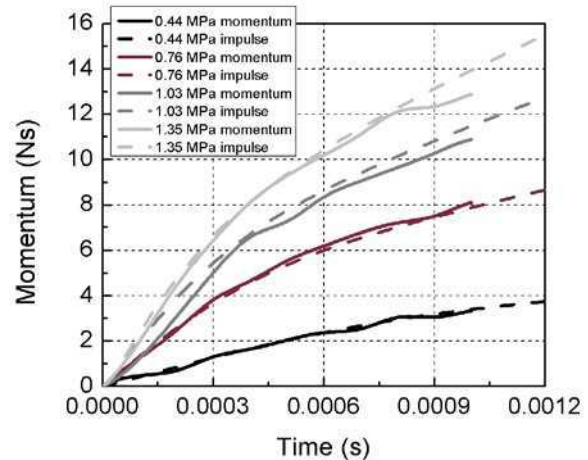


Fig. 8 Comparison between the measured momentums and the pressure impulses

3.4 COMPARISON WITH THEORETICAL PREDICTION

The reflected pressure profile has been theoretical predicted by Taylor [2]. Though Kambouchev, et al [3-4] have claimed to have extended Taylor's model to consider the compressibility of the gas, their results are compatible with Taylor's model under the acoustic limit. Therefore, only Taylor's model is given here. Assume the expression of an ideal incident pressure profile as following,

$$p_{incident}(t) = p_{incident_peak} e^{-\frac{t}{\theta}}, \quad 0 \leq t \leq \infty \quad (3)$$

where, p_{peak} is the peak pressure and θ is the time constant.

Through the analysis in Taylor's classic paper [2], the reflected pressure profile can be calculated as,

$$p_{reflected}(t) = 2p_{incident_peak} e^{-\frac{t}{\theta}} - \frac{2p_{incident_peak}\psi}{\psi - 1} \left[e^{-\frac{t}{\theta}} - e^{-\frac{\psi t}{\theta}} \right] \quad (4)$$

where, $\psi = (\rho_0 c_0 \theta) / \rho_s$ is a non-dimensional parameter. c_0 is the wave speed in the gas. ρ_0 And ρ_s are the densities of the gas and the specimen, respectively. Thus, when $t=0$, the reflected pressure reach its peak value,

$$p_{reflected_peak} = 2p_{incident_peak} \quad (5)$$

Then, the impulse imparted on the specimen can be calculated as,

$$I_{impart} = \int_0^{t_+} p_{reflected}(t) S dt \quad (6)$$

The relation between the peak reflected pressure and the peak incident pressure is shown in Figure 9. It can be seen that the prediction is close to the experimental result when the peak incident pressure is very low. However, when the incident shock wave is very intense, there are large differences between the predicted and experimental results. This indicates that the compressibility of the gas will play a crucial role in a highly intensive shock wave loading process.

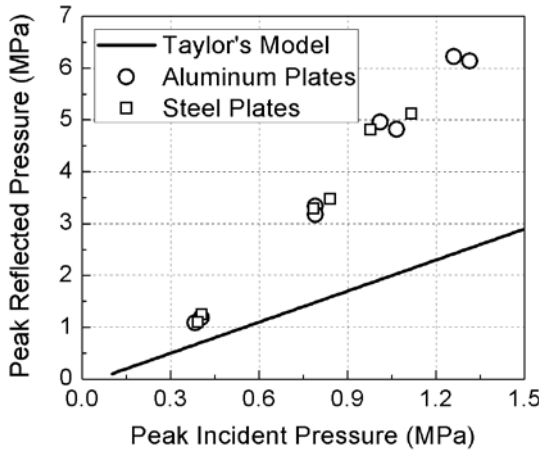


Fig. 9 The relation between the peak reflected pressure and peak incident pressure

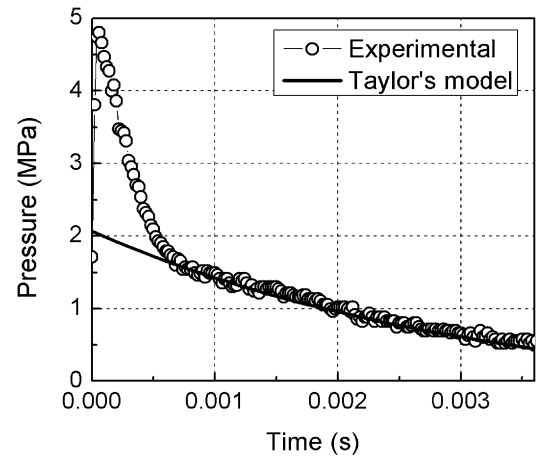


Fig. 10 Comparison between the experimental and predicted reflected pressure profile

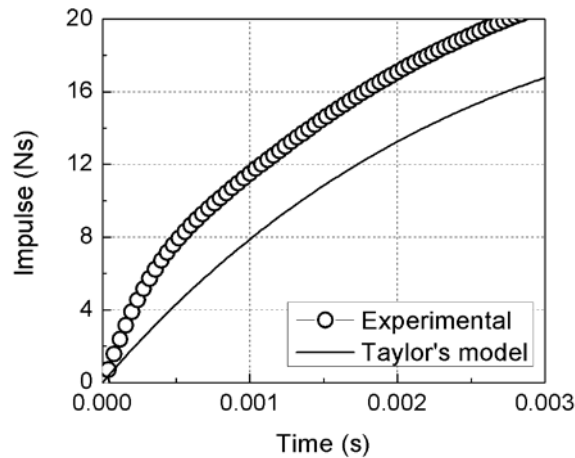


Fig. 11 The relation between the peak reflected pressure and peak incident pressure

The experimental and predicted pressure profiles of an aluminum plate under a shock loading with a 1.03 MPa incident peak pressure are plotted in Figure 10. In the first 750 μ s, which is the most important region for the fluid structure interaction, the predicted pressure profile is completely different than the experimental one no matter the amplitude or shape. It shows that it will induce a large error if the compressibility of the gas in a shock wave loading process is ignored. It should be noted that after 750 μ s, the prediction agrees with experimental results very well. This is due to the experimental setup. From Figure 5, it can be seen that the gap between the specimen and muzzle was very large, compared to the specimen's dimensions. The gas can escape from this gap and the pressure transducer, which is located on the muzzle, is far from the specimen. Therefore, the gas at the pressure transducer is not disturbed too much by the specimen. The compressibility of the gas can thus be ignored for these times/distances. Figure 11 shows the impulses calculated from the pressure profiles in Figure 10 and Eq. (6). It can be clearly seen that Taylor's model under predicted the impulse imparted to the plates.

5. CONCLUSIONS

In this paper, a series of shock wave loading experiments on free-standing monolithic plates was conducted using a shock tube apparatus. The impulses imparted onto the plates were calculated from the measured reflected pressure profile and verified by the momentum of the plates measured from the high speed images. These experimental pressure and impulse results were compared with the results predicted by existing theoretical models [2-8]. The results show that in the early time of the shock loading process, which is the most important region for the fluid-structure interaction, the existing theoretical model cannot predicted the experimental results no matter the peak reflected pressure or the pressure and momentum profiles. This indicates that the compressibility of the gas must be considered in future models especially in the very early region of a shock wave loading process.

ACKNOWLEDGEMENT

The authors kindly acknowledge the financial support of the Office of Naval Research (Dr. Y.D.S. Rajapakse) under grant no. N000140410268, and of the Department of Homeland Security under Cooperative Agreement No. 2008-ST-061-ED0002.

REFERENCES

- [1] E. Wang and A. Shukla, Analytical and Experimental Evaluation of Energies during Shock Wave Loading, Int. J. Impact. Eng. 37: 1188-1196, (2010).

- [2] G.I. Taylor, The pressure and impulse of submarine explosion waves on plates. In: Bachelor GK, Editor, The Scientific Papers of Sir Geoffrey Ingram Taylor, volume III: Aerodynamics and the mechanics of Projectiles and Explosions, Cambridge University Press, pp. 287-303 (1963).
- [3] N. Kambouchev, Analysis of blast mitigation strategies exploiting fluid-structure interaction, PhD dissertation, Massachusetts Institute of Technology, (2007).
- [4] N. Kambouchev, L. Noels and R. Radovitzky, Nonlinear compressibility effects in fluid-structure interaction and their implications on the air-blast loading of structures, *Journal of Applied Physics*, 100(6), 063519, (2006).
- [5] Z. Xue, J.W. Hutchinson, A comparative study of impulse-resistant metal sandwich plates, *Int. J. Impact. Eng.* 30, 1283-1305 (2004) .
- [6] N.A. Fleck and V.S. Deshpande, The resistance of a clamped sandwich beams to shock loading, *J. Appl. Mech.* 71, 386-401 (2004).
- [7] V.S. Deshpande and N.A. Fleck, One-dimensional response of sandwich plates to underwater shock loading, *Journal of the Mechanics and Physics of Solids*, 53, 2347-2383, (2005).
- [8] J.G. Hetherington and P.D. Smith, Blast and ballistic loading of structures, ISBN 10: 0750620242, ISBN 13: 9780750620246 (1994).
- [9] G.N. Nurick, G.S. Langdon, Y. Chi and N. Jacob, Behavior of sandwich panels subjected to intense air blast: part 1- Experiments. *Compos. Struct.* 91, 433-441 (2009).
- [10] J. Shen, G. Lu, Z. Wang and L Zhao, Experiments on curved sandwich panels under blast loading, *Int. J. Impact. Eng.* 37, 960-970 (2010).
- [11] P.J. Tan, S.R. Reid and J.J. Harrigan, Discussion: "The resistance of clamped sandwich beams to shock loading" *Journal of Applied Mechanics* 72, 978-979 (2005).

Investigation in Shear Behavior of Intermetallic Composites Using V-Notched Beam Test Method

Yusheng Yuan, Baker Hughes Incorporated, 14990 Yorktown Plaza, Houston, TX 77040
Chuanyu Feng, ION Geophysical Co., 2105 City West Blvd., Houston, TX 77042
Zhiyue Xu, Baker Hughes Incorporated, 14990 Yorktown Plaza, Houston, TX 77040
Hung-Peng Li, Aker Solutions, 3010 Briarpark Dr., Suite 500, Houston, TX 77042

ABSTRACT

Nano-engineered intermetallic composites have been recently developed and identified as an emerging technology for a number of breakthrough downhole applications at Baker Hughes. This type of intermetallic composite is composed of particulate metallic phases with specifically designed intermetallic intergranular interphases, which may behave very differently from conventional metal-based composites and alloys. The customized design of these materials yields unique mechanical and chemical properties preferred for various downhole applications.

To characterize the shear properties of the material that often needs special attention, a proven shear test method, the V-notched beam or Iosipescu shear test method (ASTM D5379), was used for the targeted materials. However, when this test method was applied to the selected intermetallic composite, complicated off-axial two-path fractures, rather than a desired pure shear failure mode, were observed. To investigate the failure mechanism and the effectiveness of the ASTM testing method, a full 3-D finite element model was created and investigated using an extended finite element method (XFEM). Based on the finite element analysis results and the additional shear tests of a reference alloy with similar base metal composition, the true material system-dependent failure mechanisms were identified and the test method was further validated. A special mechanical design guideline for this innovative nano-engineered intermetallic composite material was also recommended.

KEYWORDS

Intermetallic Composites, V-notched Beam or Iosipescu Shear Test Method, Failure Mechanisms, XFEM, Crack Initiation and Propagation

INTRODUCTION

A variety of service tools and critical components such as removable or drillable tools used in oilfield downhole operations require only a temporary setting or a limited lifetime in the wellbores. After the services are completed, these tools or components need to be removed or dispersed from the wellbores to recover fluid paths for hydrocarbon production. The conventional removal technologies such as retrieving, drilling or milling operations require additional trips into the deep well. These steps usually involve various intervention tools and heavy surface equipment. These operations are usually time consuming and very expensive.

Furthermore, in hydraulic fracturing operations, a series of molded plastic or fiber-reinforced plastic tripping balls with varied sizes is commonly used as flow and pressure control means for fracturing operations. After the fracturing treatment for the formation, the frac balls are intended to be flowed back to the surface with well fluids. Frac ball technology has been commonly used in fracturing operations, but there is still a big concern about limitations of strength, stiffness and operating temperature of the currently used frac balls as well as the ball flow-back uncertainty.

An ideal solution for such service tools and components is to have a specially designed "smart" material that would have high mechanical strength in the initial operating state, but with the ability to degrade or dissolve after a certain period of exposure to wellbore conditions. This will eliminate all the expensive interventional operations and the concerns and uncertainty in current hydraulic fracturing operations.

To solve this problem, a series of nano-engineered intermetallic composite materials (ICM) with high mechanical strength and stiffness and a controlled dissolution rate was developed to provide such smart performance for various critical downhole applications. The ICM is commonly composed of particulate metallic phases with specifically designed intermetallic intergranular interphases. Due to the special material design, this material may behave very differently from the conventional metal-based composites and alloys. In order to understand the mechanical behavior of the material better and use it in various downhole applications, detailed mechanical and chemical properties must be characterized to provide design guidelines. In this paper, the shear mechanical properties of the intermetallic composite material are investigated using the V-notched beam method.

The V-notched beam or Iosipescu shear test method was first proposed by N. Iosipescu in 1967 [1] and became ASTM standard shear test method D5379 for composite materials in 1995 [2,3]. This test method has been known as a proven shear test method and used extensively for composite and other material systems because a nearly uniform pure shear stress state is presented in the notched gage section of the test specimen under a shear load. However, when this test method was applied to a selected intermetallic composite material, complicated off-axis two-path fractures, rather than a desired pure shear failure, were observed.

This observation may suggest two possible mechanisms for such an undesirable failure mode: (1) improper geometry of the test specimen or test method resulted in a different failure mode, or (2) special inherent material behavior of the new intermetallic composite imposed the change in the failure mode. To investigate the failure mechanism behind the undesirable failure mode and to further evaluate the V-notched beam test specimen design, a 3-D finite element model was created using Abaqus™ advanced modeling technique, the extended finite element method (XFEM). By using the XFEM technology, crack initiation and propagation was investigated for different specimen designs. Also, additional V-notched beam shear tests were further conducted with the same test specimen geometry for a reference metal alloy with similar base metal composition. Based on the finite element analysis and additional shear test results, the true material system-dependent failure mechanisms were identified and the test method was further validated.

EXPERIMENTAL

Material: The material under investigation is a specially designed intermetallic composite material (referred as Baker ICM hereon). It is composed of the particulate metal phases and the intermetallic intergranular phases as shown in Figure 1. The nano-engineered intergranular interphases are designed to achieve preferred mechanical and chemical properties. The overall intermetallic composite properties are then governed by both the particulate metal phases and the intermetallic intergranular interphases.

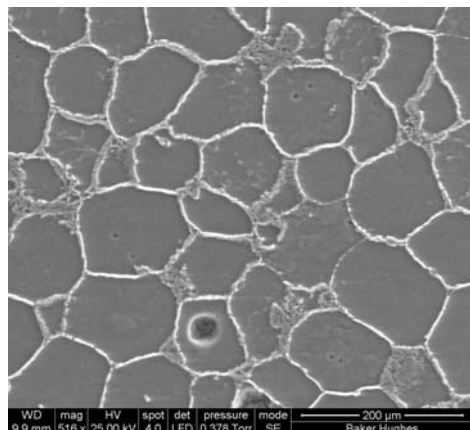


Fig. 1 SEM micrograph showing typical microstructure of the Baker ICM with metallic particulate phases and the intermetallic intergranular interphases.

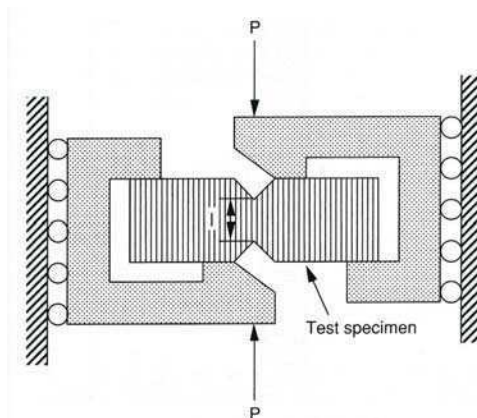


Fig. 2 Schematic of loading fixture for the V-notched beam shear test.

V-Notched Beam Shear Test: The shear test method used in this study is the ASTM standard test method D5379, the V-Notched Beam Method [3]. In this shear test method, a standard V-notched beam test specimen is mounted at two end sections in a specially designed test fixture as shown in Figure 2. Under shear loading, a nearly uniform shear stress is generated in the center plane of the notched gage section of the specimen as illustrated in the literature [3].

The standard test fixture used in this study was provided by Wyoming Test Fixture (WTF) Inc. A photograph of this test fixture with a test specimen installed in place is presented in Figure 3. The geometry of a standard V-notched beam test specimen is illustrated in a sketch shown in Figure 4a and a wire-EDM machined V-notched beam test specimen of Baker ICM is shown in Figure 4b.

The shear tests were conducted using a servo hydraulic MTS test frame equipped with a 10 kip load cell. To apply shear load, the actuator is moved at 2 mm/min under displacement control mode until fracture of the test specimen occurs. A digital video camera is set to capture the fracture process for supplemental information. For comparison, additional V-notched beam shear tests were also conducted for a reference standard metal alloy with similar base metal composition as in the ICM, and referred as Base Alloy hereon.



Fig. 3 ASTM D5379 standard test fixture with a standard V-notched beam shear test specimen installed.

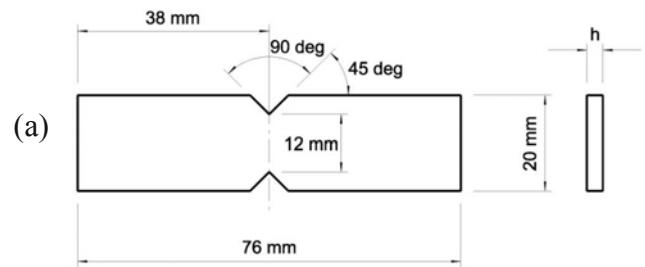


Fig. 4 (a) Standard geometry of a D5379 V-notched beam test specimen and (b) a machined standard test specimen of Baker ICM.



Fig. 5 V-notched beam specimen of Baker ICM failed in an off-axis two-path fracture under shear loading.

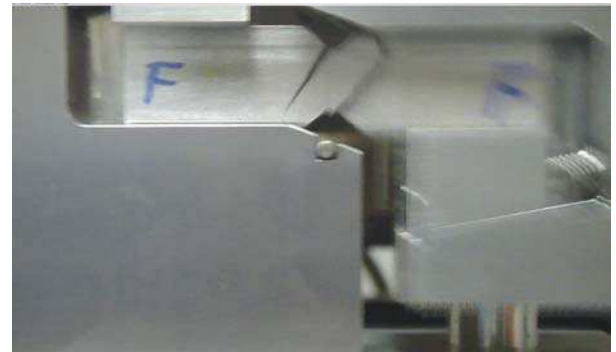


Fig. 6 Digital camera video picture caught the crack propagation direction in the Baker ICM beam specimen in the test fixture during the shear test.

Test Results and Discussion: Three V-notched beam shear tests were conducted on the MTS test frame using the WTF D5379 standard test fixture as described previously. Rather than a desired pure shear failure across the notched gage section, all the test specimens were actually fractured in an off-axis two-path mode as shown in

Figure 5. The shearing process was not recorded using a true high-speed camera, but the video recorded was enough to identify the crack propagation direction as shown in **Figure 6**.

From the observed fracture pattern of the broken specimen as well as the recorded video, it is concluded that the crack was initiated at the upper or lower notch surfaces near the roots of the notches and then propagated along the direction nearly 45° from the principal axis. For comparative purpose, four additional standard V-notched beam test specimens of the Base Alloy were prepared and tested under the same testing procedure, at the same displacement speed and using the same test fixture per ASTM D5379. With all the Base Alloy specimens, the desired true shear failure mode across the notched sections was indeed observed as shown in **Figure 7**.

To make the test data more intuitive in comparison without exposure of the company's proprietary technical information, the stress data of the Baker ICM and the Base Alloy were normalized by the critical shear yield strength of the Base Alloy. Typical normalized average shear stress across the center plane of the notched cross section versus displacement curves from both the Baker ICM and the Base Alloy specimens are plotted in **Figure 8**, respectively. The normalized mechanical properties of the Base Alloy and the Baker ICM are presented in **Table 1** based on our test results and manufacturer published data.



Fig. 7 V-notched beam specimen of base alloy failed in a true shear failure mode under shear loading.

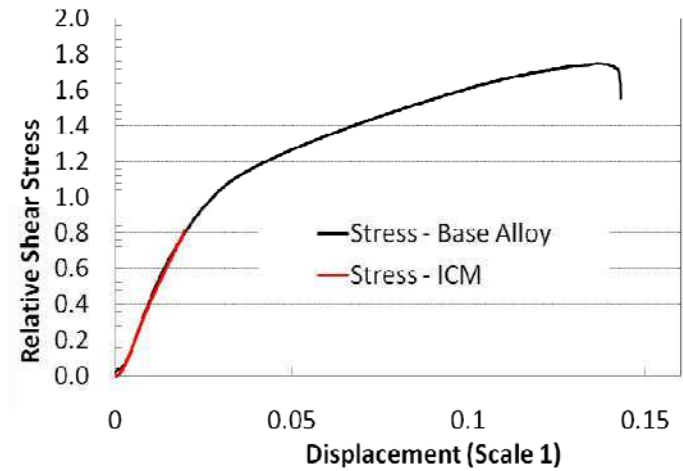


Fig. 8 Normalized average shear stress across the notched cross section versus displacement curves for Baker ICM and the Base Alloy specimens.

Table 1. Comparison of Mechanical Properties of Baker ICM with Base Alloy
(Stress data are normalized by the shear yield strength of the Base Alloy)

	Tensile Strength	Tensile Yield Strength	Shear Stress at failure	Shear yield Strength	Tensile Modulus initial	Tensile Elongation
Base Alloy	3.06	2.59	1.75	1.0	1.00	1.00
Baker ICM	2.12	1.62	0.82	-	1.09	0.22

From the normalized average shear stress versus displacement curves presented in **Figure 8** and the normalized test results presented in **Table 1**, we can see that the average shear stress of the Base Alloy specimen was running through its yield point and reached its ultimate shear stress at a normalized value of 1.75. This corresponds to an ultimate shear strength of the alloy that is within the range of the manufacturer published values for the alloy.

In contrast, the average maximum shear stress in the notched gage section of the Baker ICM specimen is found to be only at a normalized value of 0.82, with an off-axial two-path fracture mode indicating an unacceptable premature failure of the Baker ICM specimen before reaching its shear yield point. To understand this undesired failure mode and failure process, it is important to uncover the failure mechanisms behind them. The following are some of our considerations on the possible failure mechanisms.

It is noted that when the V-notched beam specimen is under shear loading in the standard test fixture, a nearly uniform pure shear stress is generated in the center plane of the notched gage-section. The shear stress direction is parallel to the shear loading direction or the vertical direction. While the pure shear stress is distributed in the center plane, the principal stresses in tension and compression are also distributed and applied to the gage section of the specimen in the direction of $\pm 45^\circ$ correspondingly. Besides this, bending moments at the off-the-center-plane locations also generate certain tensile stresses in the notched sectional area.

It is also noted from Table 1 that the tensile yield strength and the ultimate tensile strength of the Baker ICM are relatively low. When the maximum principal tensile stress along the 45° direction in the notched section of the specimen reaches or approaches the tensile strength of the material, a small crack may be initiated at that location, especially in the brittle interphase areas. The crack may propagate thereafter before the shear stress in the notched gage section reaches its failure level. In contrast, the Base Alloy shows more ductile feature with much higher tensile yield strength and ultimate tensile strength. Therefore, the tensile-failure induced off-axial fracture does not occur when the shear stress reaches its shear strength. These result in a true shear failure mode in the notched Base Alloy specimen. To fully and clearly understand the fracture mechanism of the Baker ICM material and further validate the V-notched beam test method, a series of finite element analyses were performed.

FINITE ELEMENT ANALYSIS OF V-NOTCHED BEAM TEST

XFEM Model and Material Modeling: Due to the complexity of the shearing process, a 3D finite element model was used to fully investigate the fracture mechanism. Because of the difficulty in predicting the failure mode in the notched Baker ICM test specimen and how the crack will initiate and propagate, it is preferable to use a simulation technology that does not require a pre-defined crack path. The newly developed Abaqus 6.10 software [4] is equipped with an advanced new feature, the extended finite element method (XFEM). It uses enriched features to handle crack initiation and propagation automatically, based on the pre-defined material properties including fracture toughness. XFEM technology is a perfect tool to simulate crack initiation and propagation for the Baker ICM notched beam shear test.

Figure 9 shows the established 3D model based on the standard notched beam shear test method. During the simulation, the notched section width of the specimen is of interest, and investigation of failure mode versus different widths was conducted. With XFEM, the first-order brick and tetrahedron elements are required. Since our target is the specimen, enriched feature is only applied to the specimen. As for the material properties, they were obtained from previous experiments, and the fracture toughness was estimated based on the mechanical test results.

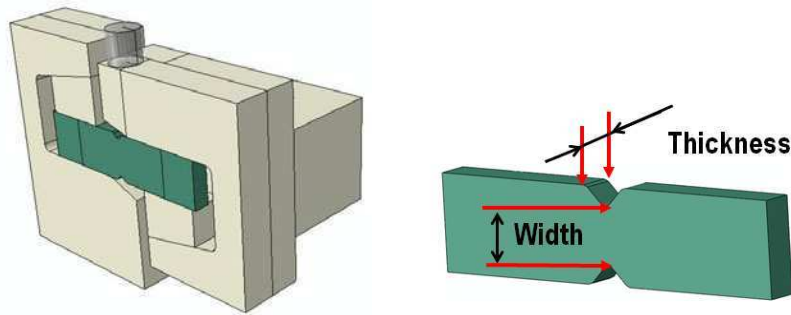


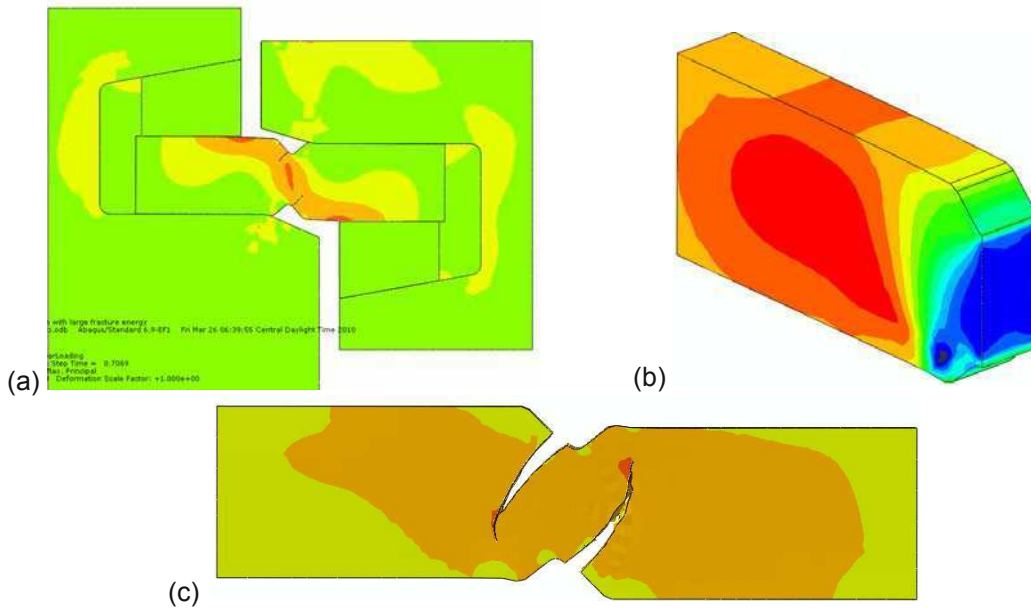
Fig. 9 Full 3D model and specimen designation

XFEM Results and Discussion: Detailed finite element analyses were conducted for the specimens with five different notched-section widths, specifically 50%, 75%, 100% and 120% of the standard width, and one additional without a notch. The standard specimen with 100% of the standard width was first investigated as a benchmark to check the fidelity of the simulation.

Figure 10a and 10c show crack initiation at the notch surface near the root and crack propagation through the specimen in nearly 45° off axial directions, respectively, based on the analysis defined in the maximum principal stress field. As shown in these two figures, the simulated fracture mechanics process matches closely with the experimental result as shown in the photo presented in Figure 5. This confirmed our considerations on fracture mechanisms for the Baker ICM specimens in the tests.

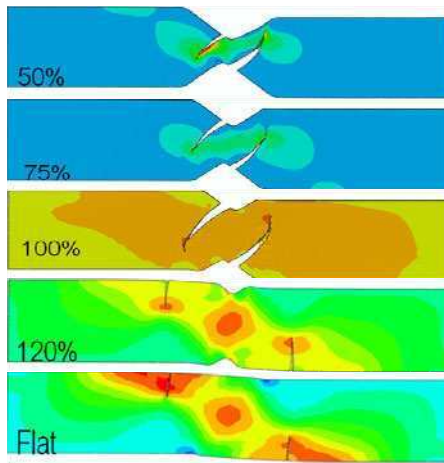
With the fracture process matching closely the experimental results, it is reasonable to correlate the shear stress from the simulation. It is thus noticed that the corresponding pure shear stress distribution in the center plane of the notched gage-section is as expected, nearly uniform, as shown in Figure 10(b).

As soon as the fidelity of the model was verified, we wanted to know how the notched section width of specimen would affect the fracture mode. In other words, was it possible to obtain true shear failure for this type of material? Figure 11a shows crack initiation and propagation for all five different geometry configurations defined in the maximum principal stress field. As the width gets smaller, the only difference is that the calculated average shear stress at fracture is getting smaller, but the fracture pattern remains the same. This corrected some of our initial thinking of forcing the specimen to be fractured in shear mode by reducing the width of the specimen's notched section. Figure 11b shows the calculated average shear stresses in the notched gage section of the specimens with different gage-section widths, normalized by the maximum principal stress limit. It shows that for the standard specimen, the average shear stress reaches almost the maximum value. This partially demonstrates the standard V-notched specimen design is at its optimized geometry.

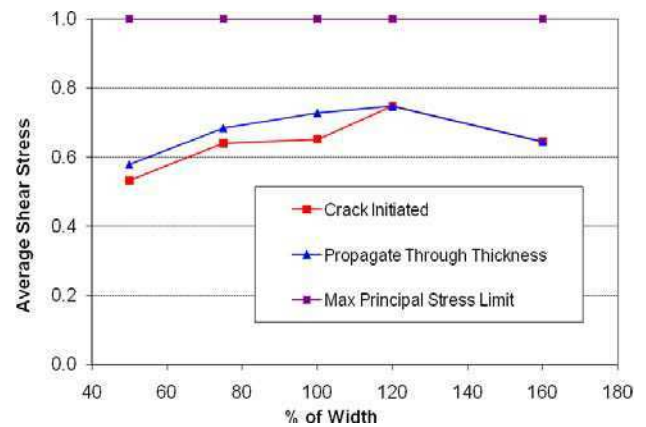


(a) Crack initiation during shear loading defined in maximum principal stress field; (b) Shear stress distribution in the center plane of the notched gage section; (c) Crack propagated to closely match the experimental results defined in maximum principal stress field.

Fig. 10 XFEM results for standard specimen geometry.



(a) Crack initiation and propagation of the specimens with different gage-section widths defined in maximum principal stress field



(b) Relative average shear stress in the notched gage section normalized by maximum principal stress limit of the specimens with different gage-section widths

Fig. 11 FEA results for five specimen geometry configurations.

CONCLUSIONS AND RECOMMENDATION

Based on the experimental results of the V-notched beam shear tests from both the Baker ICM and the Base Alloy and the XFEM analysis results for the V-notched beam test, it is concluded that:

1. The V-notched Baker ICM shear specimens under shear loading failed in an off-axial two-path fracture mode rather than a desired pure shear failure mode in the plane between the two notches. Finite element analysis results indicate the off-axial fracture was initiated from a maximum principal stress-induced tensile failure near the root of the notches and propagated along the principal stress direction even after reducing the notched section width. However, using the same test method for the Base Alloy test specimens, a true shear failure mode was obtained.
2. The V-notched beam shear test method, in general, is a valid shear test method and the geometry of the standard V-notched beam test specimen is in optimized condition because a nearly uniform pure shear stress state is generated in its notched gage section under a shear load. Since this test method could not generate a true shear failure mode with the current Baker ICM material, we recommend not using this test method for determining its shear strength. However, this test method is still a valid method for shear modulus determination of this ICM material and for shear property determination of other materials so long as it can generate a true shear failure mode.
3. In component design and analysis with the current Baker ICM material, if the major loading condition involves shear, it is recommended to consider examining the maximum principal stresses and identifying possible tensile failure based on the measured tensile properties of the material.

ACKNOWLEDGEMENT

The authors would like to thank the Baker Hughes Completions and Production Technology for its permission to publish this paper. The authors would also like to express sincere appreciation to Bennett Richard, Jim Goodson, Mike Johnson and Gaurav Agrawal for their direction and constant support for this research project.

Abaqus is a trademark or registered trademark of Dassault Systèmes or its subsidiaries in the United States and/or other countries.

REFERENCES

- [1] Iosipescu, N., "New Accurate Procedure for Single Shear Testing of Metals," Journal of Materials, Vol. 2, No. 3, September 1967, pp. 537-566.
- [2] Walrath, D.E. and Adams, D.F., "The Iosipescu Shear Test Method as Applied to Composite materials," Experimental Mechanics, Vol. 23, 1983, pp.105-110
- [3] ASTM D5379M-98, "Standard Test Method for Shear Properties of Composite materials by the V-Notched Beam Method, Annual Book of ASTM Standards, Vol. 15.03
- [4] Abaqus version 6.10 User Manual, 2010

The Influence of Sample Thickness on the DCDC Fracture Test

Christian Nielsen¹, Alireza V. Amirkhizi¹ and Sia Nemat-Nasser^{1,*}

¹ Center of Excellence for Advanced Materials, Dept of Mechanical and Aerospace Engr,
University of California at San Diego, 9500 Gilman Drive, La Jolla, CA 92093-0416, USA

* sia@ucsd.edu

ABSTRACT

The double cleavage drilled compression (DCDC) fracture test uses axial compression to drive stable cracks in glasses and brittle polymers. The cracks are generated by regions of tension in a rectangular column of material containing a central hole. The observed relationship between crack length and the applied axial stress is fitted with a two-dimensional finite element model to estimate fracture toughness. The model is applied to previous DCDC experimental results for poly(methyl methacrylate) (PMMA) samples of varying thicknesses. Both plane stress and plane strain cases are considered. Three dimensional finite element models of the DCDC test indicate plane stress analysis is the most applicable condition and suggest explanations for the effect of sample thickness.

Keywords: DCDC, PMMA, fracture, healing, toughness, finite element

INTRODUCTION

The double cleavage drilled compression (DCDC) fracture test uses uniaxial compression to generate large cracks in a brittle material [1]. The DCDC sample is a tall, rectangular column with a central, through-thickness hole ([Figure 1a](#)). Under compression, regions of tension at the apex and base of the hole create and propagate symmetric mode I cracks. The length of the cracks is controlled by the axial compression. Several models have been proposed to correlate the relationship between applied stress and crack length with fracture toughness, a quantitative measure of the material's resistance to fracture.

The influence of DCDC sample height, width, and hole size on the observed fracture behavior has been previously studied and factored into proposed fracture toughness models [2]. Here, we examine our DCDC experiments on samples with different thicknesses, noting the thicker samples require more stress to propagate long cracks. We use two- and three-dimensional finite element calculations to investigate this thickness effect.

EXPERIMENTAL

DCDC tests were conducted on poly(methyl methacrylate) (PMMA) samples with thicknesses of 3, 4, 5, 8, and 11 mm [3]. The samples were 50 mm tall and 12 mm wide with a 3 mm diameter central hole. The thinnest samples (3, 4, and 5 mm) were loosely fitted with a brace to prevent out-of-plane buckling. After initiating the cracks, uniaxial compression was applied under displacement control at 0.5 $\mu\text{m}/\text{sec}$. The crack length was measured every 30 seconds and correlated with the applied load. Increasing sample thickness was found to increase the axial stress required to propagate long cracks (cracks longer than the diameter of the hole).

COMPUTATIONAL

A two-dimensional finite element calculation was developed [3] to estimate PMMA fracture toughness using the DCDC experimental data. One quarter of the DCDC geometry was modeled with shell elements and a linear elastic material model ([Figure 1b](#)). The boundary conditions were correlated with experimental observations (applied force and crack length). Extending the crack in the calculation yielded a change in internal energy, an energy release rate, and a critical stress intensity factor.

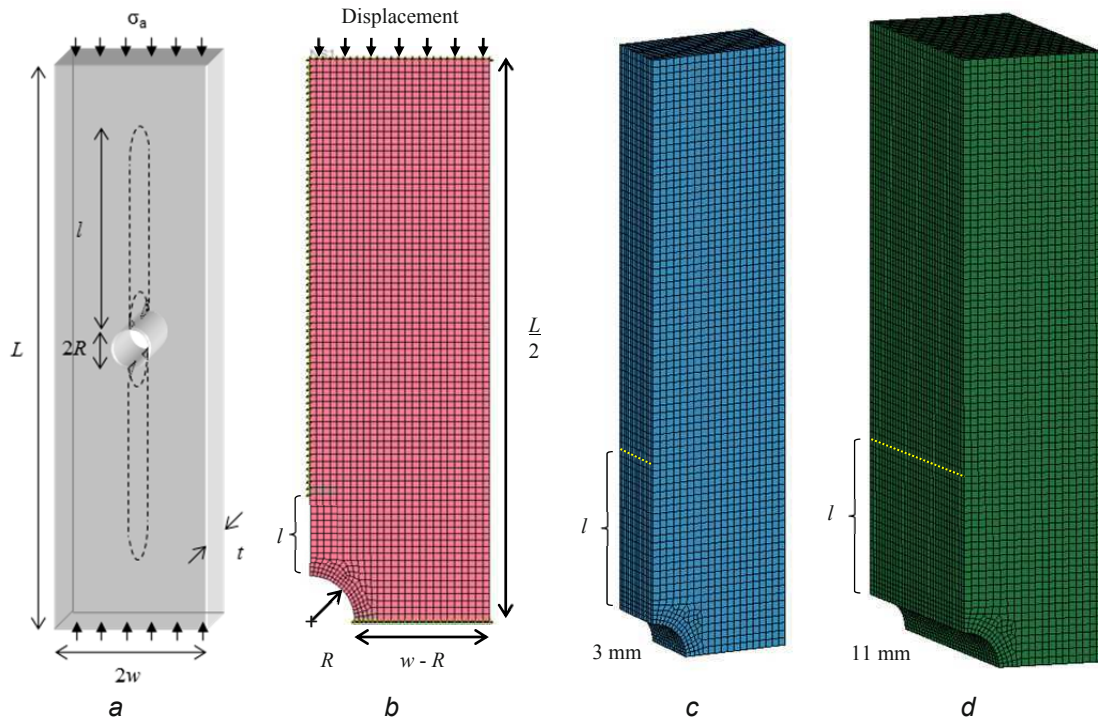


Figure 1. (a) DCDC geometry. (b) 2D finite element model. (c) 3D 3 mm thick finite element model. (d) 3D 11 mm thick finite element model.

Plane stress and plane strain conditions in this 2D calculation were compared as an approximation of the effect of thickness. The pronounced thumbnail shape of the cracks in the thicker samples suggested an internal stress state closer to plane strain. It was initially assumed that plane strain and plane stress represent the extreme cases of thick and thin DCDC geometries. The calculations, however, do not indicate a significant difference in axial stress at the same crack opening stress between plane stress and plane strain cases.

New, three-dimensional finite element models were developed to better study the influence of sample thickness on the DCDC test. The 3 and 11 mm geometries were modeled (Figures 1c and 1d) following a similar approach to the 2D case, although the crack lengths were fixed at twice the hole diameter. The results show that the samples are generally in plane stress in both cases, and the thumbnail crack tip shape is due to localized variations in the stress state. Out-of-plane tensile stresses were observed in both geometries, an effect not captured by the 2D calculations. At the same average crack opening stress along the crack tip, the 11 mm thick geometry required more axial stress than the 3 mm thick geometry. The increase in axial stress is less than half of the difference observed experimentally, but the discrepancy can be attributed to simplifying assumptions, including a linear elastic material model, straight crack tip, and unconcentrated mesh at the crack tip.

CONCLUSIONS

Double cleavage drilled compression (DCDC) fracture tests of PMMA show thicker samples require more axial stress to propagate long cracks. Two-dimensional finite element calculations using plane strain and plane stress assumptions do not identify the reason. Three-dimensional finite element calculations yield out-of-plane tensile stresses and higher axial stresses for thicker samples. These results indicate that increasing DCDC sample thickness increases the overall constraint on the deformation of the sample. This constraint necessitates more axial stress to propagate the cracks.

ACKNOWLEDGEMENTS

This work was conducted with the support of Air Force Office of Scientific Research grant FA9550-08-1-0314 to UC San Diego.

REFERENCES

- [1] Janssen C, 'Specimen for fracture mechanics studies on glass', 10th International Congress on Glass, Kyoto Japan, Ceramic Society of Japan, 1974.
- [2] Plaisted T, Amirkhizi AV, and Nemat-Nasser S, 'Compression-induced axial crack propagation in DCDC polymer samples: experiments and modeling', *Int J Fract*, 141, 447-457, 2006.
- [3] Nielsen C, Amirkhizi AV, and Nemat-Nasser S, 'Geometric effects in DCDC fracture experiments', SEM Annual Conference & Exhibition on Experimental and Applied Mechanics, Albuquerque New Mexico USA, Society for Experimental Mechanics, 2009.

Analysis of Hysteresis Damage Accumulation and the Effect on Fatigue Life

Onome Scott-Emuakpor*, Tommy George, & Charles Cross
Air Force Research Laboratory
Wright-Patterson AFB, OH 45433

M.-H. Herman Shen
Department of Mechanical Engineering
The Ohio State University
Columbus, OH 43210

ABSTRACT

In order to validate an existing energy-based fatigue life prediction understanding, the strain energy accumulation for interrupted loading cycles was analyzed. The life prediction method being validated was developed based on the understanding that strain energy density accumulated during monotonic fracture is a physical damage quantity that is equal to total cumulative hysteresis strain energies in a fatigue process. If this understanding is true, it is possible to suspend cyclic loading for long periods during a fatigue procedure, and then resume the procedure to failure, resulting in the same fatigue life as if the fatigue test was conducted continuously to failure. This assumption, along with critical analyses such as surface roughness and loading frequency, is tested empirically on Titanium 6Al-4V (Ti64) axial tension-compression specimens in the lifetime regime of 5×10^3 and 6×10^4 . The failure results are compared, with encouraging results, to the aforementioned energy-based prediction method, thus validating the theory and the prediction capability.

1. INTRODUCTION

Fatigue life behavior is one of the most critical material properties required for gas turbine engine component design. The widely used design tools for characterizing fatigue life are the modified Goodman diagram and a Stress versus Fatigue Life (S-N) curve [1, 2]. For an accurate characterization of fatigue life, tens to hundreds of experimental results are required to construct Goodman diagrams and S-N curves. Depending on the desired lifing limit, significantly long time periods could be necessary to gather these experimental results. Therefore, a fatigue life prediction method that would require considerably less data and time than conventional empirical fatigue data would be an improvement to the aforementioned design tools.

In order to reduce the amount of empirical data necessary to construct a fatigue life design tool, the discovery of a physical fatigue damage quantity was required. The simplest way to attain a damage quantity that is cumulative with fatigue cycles is by exploring the correlation between fatigue life and energy. This correlation was studied as early as 1923 by Jasper [3]; however extensive/successful research on energy/failure correlation was not conducted until the second half of the 20th century. In 1955, Enomoto validated that under cyclic loading there exists a critical energy value where failure occurs, thus validating the existence of a physical damage quantity for fatigue [4]. This critical energy value was defined in later research efforts as the following: the accumulation of hysteresis plastic energy during fatigue, and the strain energy accumulated during monotonic fracture [5, 6, 7]. Both of these physical damage quantities have been used to predict fatigue life of materials such as steel, aluminum and 60Sn/40Pb solder [8, 9, 10, 11]. Also, modifications to the method proposed by Stowell has provided an energy-based fatigue life prediction method capable of determining fatigue life of uniaxial bending and tension-compression at various stress ratios [12, 13]

Based on the definition of the fatigue life damage quantity, it is fair to say that cumulative hysteresis damage is irreversible; thus, if cyclic loading is suspended for a significant time frame during fatigue testing, fatigue life will not be affected. This theory was tested for uniaxial tension-compression loading of Ti64 at two distinct fully-reversed stress amplitude values. Also analyzed was the acceptability of the variation in the empirical fatigue life results

* Corresponding author. Tel.: +1-937-255-6810; fax: +1-937-656-5532
E-mail address: onome.scott-emuakpor@wpafb.af.mil (Onome Scott-Emuakpor)

associated with each of the two stress amplitudes. The results of the finding are presented in the proceeding sections.

2. EXPERIMENTAL PROCEDURE

Cyclic loading experiments on Ti64 were conducted on two different specimens: (1) a continuous radius specimen and (2) a uniform gage-section specimen, both shown in Figure 1 [14]. The continuous radius specimen is used for acquiring fatigue results because it is less susceptible than the uniform gage-section specimen to buckling at higher compressive stress magnitudes. The uniform gage-section, however, is more compatible with a MTS (Material Testing Systems) 634.12E-24 model extensometer because they both have the same gage length (25.4mm); thus, it is used for low frequency, cyclic testing to acquire precise hysteresis stress-strain results.

Both the continuous radius and the uniform gage-section specimens were machined via waterjet on a 3.175mm thick Ti64 plate, where the geometry is based on recommendations from ASTM E466 standard for load controlled fatigue testing [14]. The chosen grain direction of each specimen was designated to be perpendicular to the eventual loading axis. No delicate post-machine polishing or stress relieving procedure was conducted on any specimen after the waterjet cut. The effect of this decision is analyzed later in the manuscript.

The fatigue tests were conducted on an axial MTS servohydraulic load frame with a 100kN load capacity. The load frame was controlled using a MTS TestStarII model controller, which stores load, displacement, and also strain via a MTS 634.12E-24 model extensometer mounted on the specimen; however, the only data required by the TestStarII during fatigue testing was load amplitude and cycles to failure. The tension-compression loads applied during the cyclic tests were fully-reversed at an operating frequency between the range of 5-15Hz, where the frequency is chosen based on the allowable stroke distance and load amplitude of the 100kN load frame performance chart [15].

Low frequency, cyclic tests were conducted on the same 100kN MTS load frame as the fatigue tests. The tension-compression loads applied during the cyclic tests were fully-reversed at an operating frequency of 0.1Hz. This frequency was chosen because it provides the optimal rate for accurate hysteresis strain energy calculation without the effects of anelasticity [16]. The TestStarII controller was used to acquire time, load, strain and displacement data during testing at a rate of 2 points per second, which is 20 points per cycle.

Monotonic fracture results are a critical part of the energy-based life prediction method. These results were attained from specimens that were waterjet cut, with no post-machine polishing or stress relieving procedure, from a 3.175mm thick Ti64 plate according to the recommendations by ASTM E8 standard for tension testing of metals [17]. Tests were conducted on the 100kN MTS load frame. Experiments were carried out at a displacement control rate of 0.0254 mm/sec. Data was acquired at a rate of 0.5 data points per second.

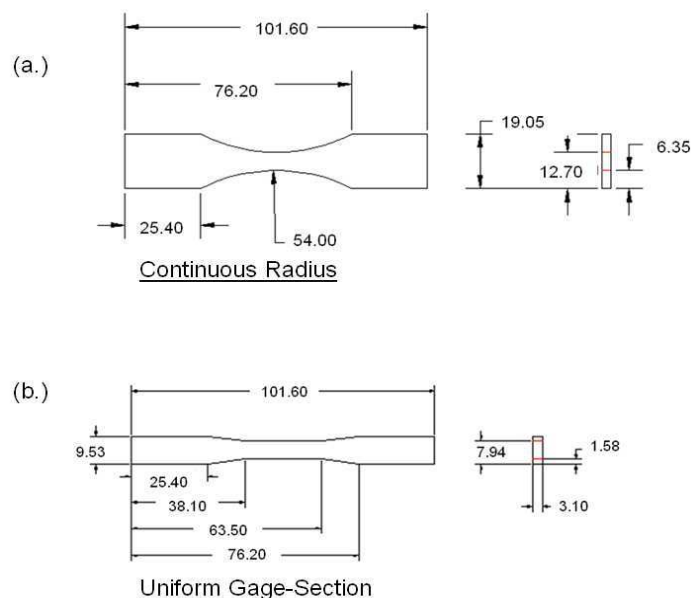


Figure 1. ASTM fatigue specimen dimensions (mm): (a.) Continuous radius, (b.) uniform gage-section.

3. FATIGUE LIFE ANALYSIS

Unlike Aluminum 6061-T6 results from previous research [12, 13], Ti64 has a wide fatigue life scatter. Therefore, the effects of several material behaviors and trends, due to test setup, on fatigue life were analyzed. Though most of these trends were previously observed for Al 6061-T6, it was important to show that the material behavior of Ti64 showed a consistent scatter and validated irreversible plastic energy accumulation during cyclic loading.

Frequency Effect: The first testing effect observed was the MTS load frame frequency versus fatigue life. This effect was observed for the fully-reversed stress-amplitudes of 534MPa and 724MPa. These stress levels were chosen for two reasons: 1.) the values were high enough to avoid the region where the endurance limit phenomenon occurs, and 2.) time constraints prevented testing the theory of irreversible cumulative hysteresis damage at higher cycle counts. The energy-based life prediction calculation determined that the expected life for stress-amplitudes of 534MPa and 724MPa was approximately 4600 and 39000 cycles, respectively, and it was assumed that fatigue failure of each stress level would occur around those values regardless of the loading frequency. The analyzed frequencies were 15Hz, 10Hz and 5Hz for 534MPa, and 10Hz and 5Hz for 724MPa. These frequencies were chosen based on the allowable stroke distance of the 100KN load frame performance chart [15]. The result for each stress level is shown in the plots of Figure 2. Also, statistical results are shown in Table 1. Though the results of this analysis shows a wide scatter, primarily the 18% relative standard deviation of the 534MPa results, there is no noticeable trend based on loading frequency. Therefore, fatigue results at stress amplitudes above 700MPa, which are run at 10Hz or less, can be plotted with fatigue results at stress levels below 500MPa, which are conducted at 15Hz.

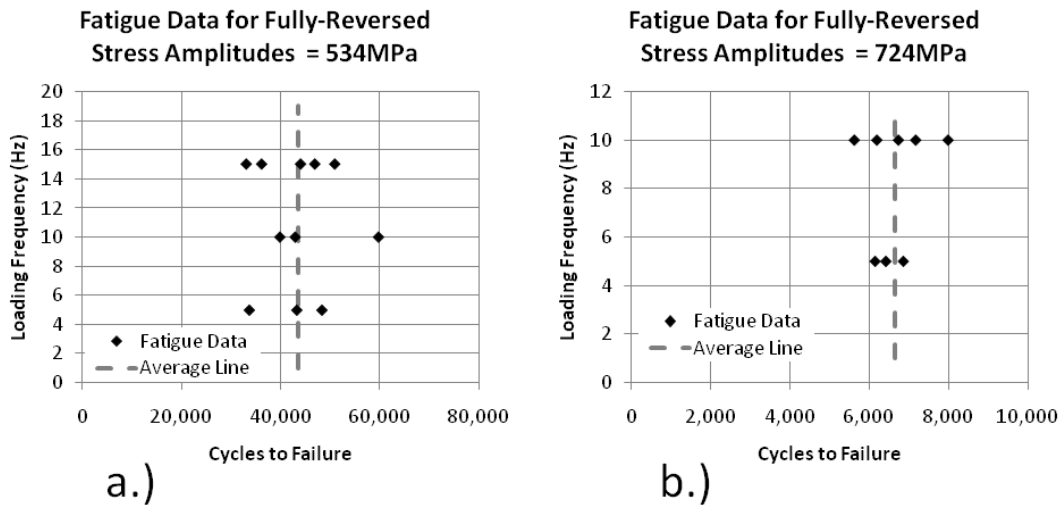


Figure 2. Frequency versus failure cycles: a.) 534MPa and, b.) 724MPa.

Table 1. Statistical results of frequency effect.

	534MPa	724MPa
Lifetime STD =	7859	724
Lifetime Mean =	43545	6643
Rel. STD (%) =	18.05	10.91

Load Effect: The applied stress amplitude for fatigue experiments are determined by measuring the cross-sectional area of the specimen being tested. Based on variation with the waterjet machine tolerance ($\pm 0.127\text{mm}$), the $\pm 0.2032\text{mm}$ manufacturer tolerance of the Ti64 plate thickness and slight variance in hand measurements, the possibility of a fatigue life trend with respect to the applied load amplitude was likely. This trend was observed for 534MPa and 724MPa. The graphical observation is shown on the plots of Figure 3, and the statistics are in Table 2. Like the frequency effect analysis, these results cannot verify that there is a fatigue life trend based on loading values.

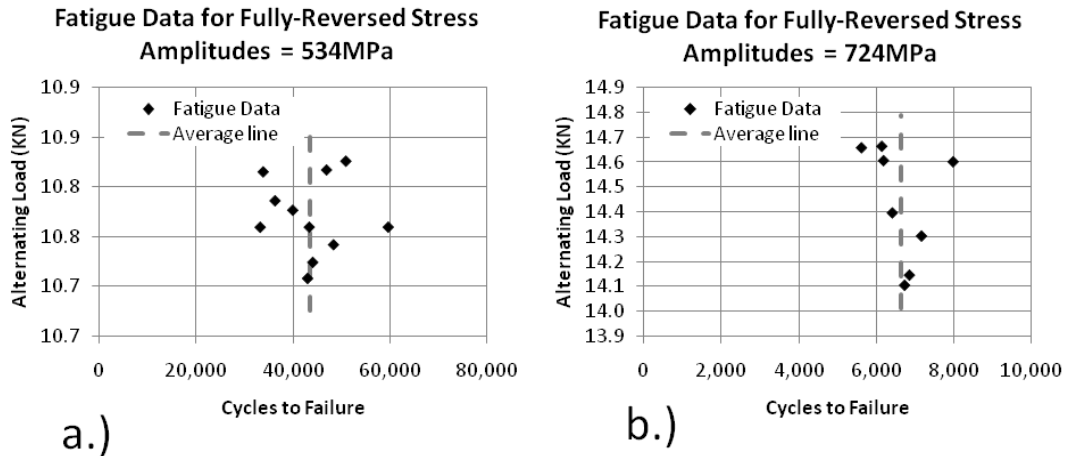


Figure 3. Load amplitude versus failure cycles: a.) 534MPa and, b.) 724MPa.

Table 2. Statistical results of load effect.

	534MPa	724MPa
Load STD (KN) =	0.039	0.231
Load Mean (KN) =	10.77	14.44
Rel. STD (%) =	0.358	1.599

Surface Roughness Effect: Ti64 is a more sensitive material than Al 6061-T6, which is the material the energy-based life prediction method was developed upon. Though previous research shows there is no correlation between fatigue performance and surface roughness, this analysis was conducted by comparison with two post-machining surface polishing techniques and does not regard a non-polished surface roughness [18]. Since there is no post-waterjet polish or LSG (Low Stress Grind) process for the fatigue specimens in this study, the surface roughness of each specimen have a higher probability of lacking consistency. Furthermore, handling the specimens (delivery, storage, etc.) could also induce unwanted residual stresses. Therefore, fatigue results of the three different batches of Ti64 specimens were compared; note, the batches are from the same Ti64 plate stock and are designated as specimens machined at three different times. The results, which are compared on the S-N plot of Figure 4, show a consistent trend for fatigue behavior.

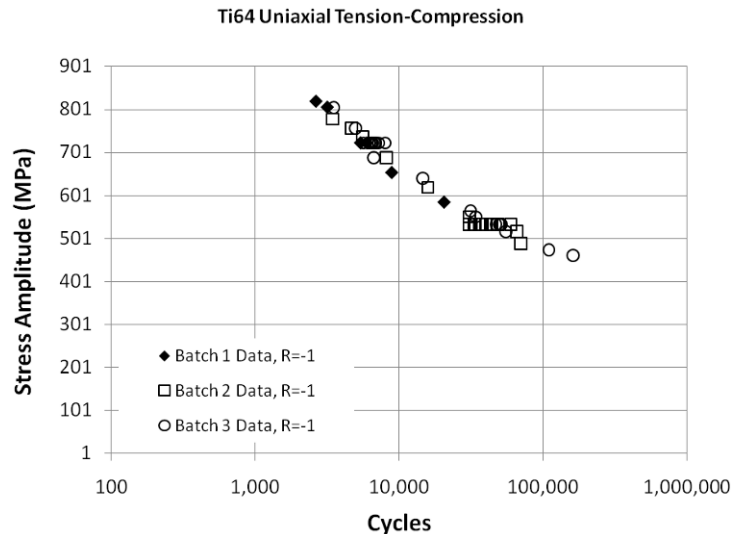


Figure 4. Fatigue results for Ti64.

Loading Delay Analysis: Previously stated, the energy-based fatigue life prediction method was developed based on the understanding that a physical damage quantity exists for fatigue failure. The damage quantity is accumulated plastic strain energy from hysteresis loading, which is irreversible. In order to validate this

understanding, fatigue analysis was conducted at the same stress amplitude values used in the previous analysis (534MPa and 724MPa). The scope of the analysis was to see if suspending cyclic loading during fatigue testing would affect fatigue life. The analysis was conducted to answer two key questions: 1.) will suspending cyclic loading present a noticeable trend between fatigue life and loading delay time, and 2.) will the fatigue life results from the delayed tests fall within the scatter of continuous cyclic loaded fatigue results? To answer the first question, empirical Ti64 results were viewed on the plots of Figure 5 for 534MPa and 724MPa. The results show no trend for both stress levels and minimal variation at 724MPa.

In order to see if fatigue life results fell within acceptable Ti64 scatter, all fatigue data was plotted on the normal distribution constructed by fatigue data of continuous cyclic loading results [19]. Since fatigue life shows no noticeable trend with respect to loading frequency, fatigue data at different frequencies were used in the construction of the normal distribution. The results for both stress levels are shown on the plots of Figure 6 and 7. Both stress levels show that all but one of the time delayed fatigue life data falls within one-sigma of the distribution. Therefore, this validates that suspending cyclic loading for significant time frames during fatigue testing will not affect fatigue life and the notion of a physical damage quantity for fatigue still holds true.

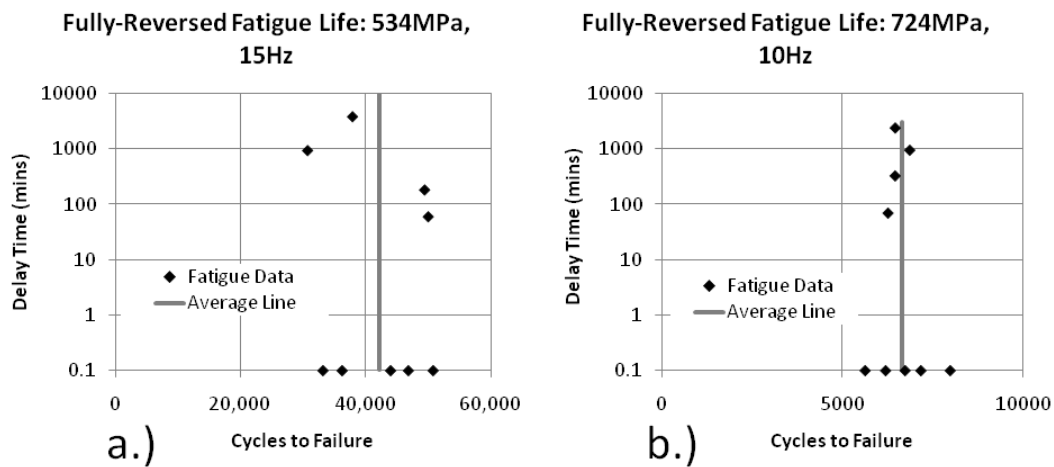


Figure 5. Ti64 fatigue life comparison with load delays: a.) 534MPa and, b.) 724MPa.

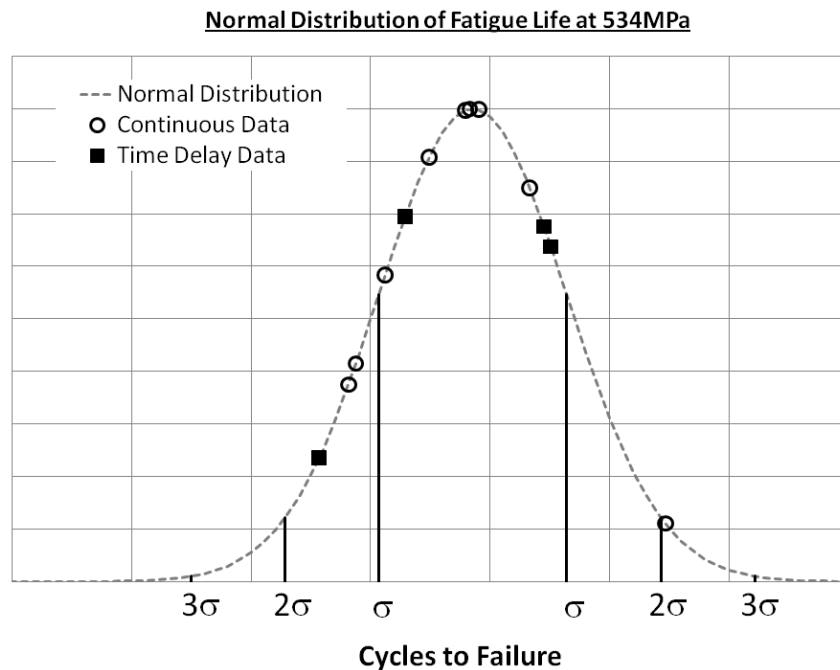


Figure 6. Normal distribution of fatigue life at 534MPa.

Normal Distribution of Fatigue Life at 724MPa

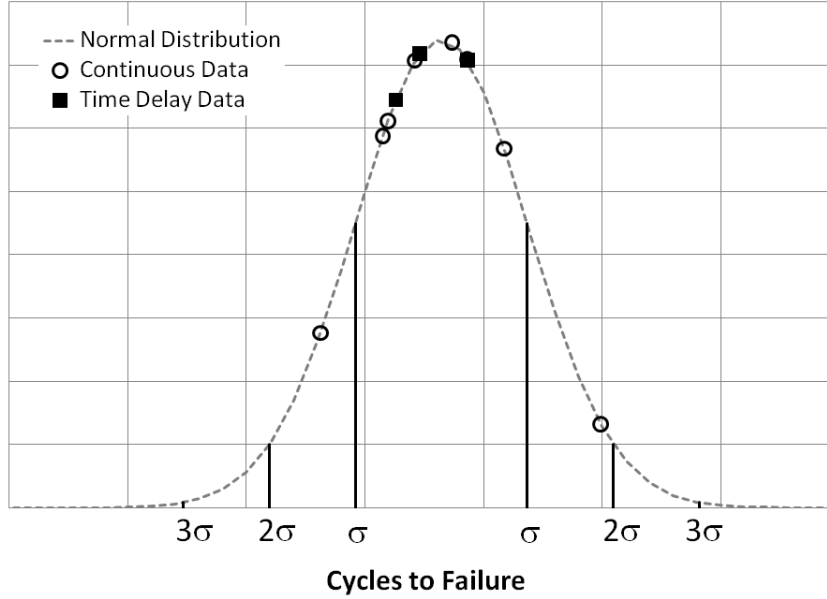


Figure 7. Normal distribution of fatigue life at 724MPa.

4. ENERGY-BASED LIFE PREDICTION

Data from the fatigue analysis section is used here to validate the capability of the energy-based fatigue life prediction method. This method was developed from the stress-strain representations of Equation (1) - (3) [7, 12]. Equation (1) represents the monotonic stress-strain relationship, Equation (2) represents the expression for the parameter σ_o in Equation (1), and Equation (3) is the expression for the cyclic strain. Equation (3) was created based on a simplified coordinate system, where the horizontal versus vertical axes represents peak-to-peak strain versus peak-to-peak stress, respectively. On this coordinate system, shown in Figure 8, the origin is defined as the minimum fully-reversed point of a hysteresis loop; in other words, both the stress and the strain values are read from zero to peak-to-peak magnitudes.

$$\varepsilon = \frac{\sigma}{E} + \varepsilon_o \sinh\left(\frac{\sigma}{\sigma_o}\right) \quad (1)$$

$$\sigma_o = \frac{\sigma_n - \sigma_y}{\ln\left(\frac{\varepsilon_n}{0.002}\right)} \quad (2)$$

$$\varepsilon_{cycle} = \frac{\sigma_{pp}}{E} + \frac{1}{C} \sinh\left(\frac{\sigma_{pp}}{\sigma_c}\right) \quad (3)$$

The parameters for Equation (1) - (3) are defined as follows: σ is the nominal applied monotonic stress value, ε is the strain corresponding to the applied monotonic stress, σ_{pp} is the generalized/peak-to-peak stress value corresponding to the generalized/peak-to-peak cyclic strain ε_{cycle} ($2\sigma_a$ replaces σ_{pp} in Equation (3) after all necessary derivations), σ_f is the fracture stress, ε_f is the ductility, σ_y is the yield stress, E is the modulus of elasticity, and the variables σ_c , σ_o , ε_o , and C are curve fit parameters [12]. The curve fit parameters for the cyclic and monotonic representations are statistically acquired by comparison between the equations and the respective experimental results [20, 21].

The energy-based prediction method calculates fatigue life by dividing the total monotonic strain energy density by the strain energy density for one cycle. The total strain energy density accumulated during a monotonic process is determined as the area underneath the curve constructed by Equation (1), and the strain energy density for one cycle is represented by the area within the hysteresis loop formed by Equation (3). Calculating the monotonic strain energy density from experimental results is a straightforward task, whereas the strain energy

density in one cycle is determined by making an assumption that the tensile stress-strain behavior of the hysteresis loop is the same as the compressive behavior. This assumption is a simplification for the strain energy density per cycle calculation because Bauschinger effect shows that the tensile and compressive behaviors in a hysteresis loop are not identical [22]. The resulting hysteresis strain energy regarding the simplification, which is calculated by Equation (4), shows a minor deviation with Al 6061-T6 data when compared with the correlating strain energy that incorporates Bauschinger Effect on Figure 9.

The energy-based fatigue life calculation is represented by Equation (5) [23], where σ_a is the applied stress amplitude. Using the material parameters in Table 3, Equation (5) results compare well to the empirical Ti64 fatigue results in Figure 10.

$$W_{cycle} = \sigma_{pp} \epsilon_{cycle} - 2 \int_0^{\sigma_{pp}} \epsilon_{cycle} d\sigma_{pp} \quad (4)$$

$$N = C \frac{\sigma_f \left(\epsilon_f - \frac{\sigma_f}{2E} \right) - \epsilon_o \sigma_o \left[\cosh \left(\frac{\sigma_f}{\sigma_o} \right) - 1 \right]}{2\sigma_c \left\{ \frac{\sigma_a}{\sigma_c} \sinh \left(\frac{2\sigma_a}{\sigma_c} \right) - \left[\cosh \left(\frac{2\sigma_a}{\sigma_c} \right) - 1 \right] \right\}} \quad (5)$$

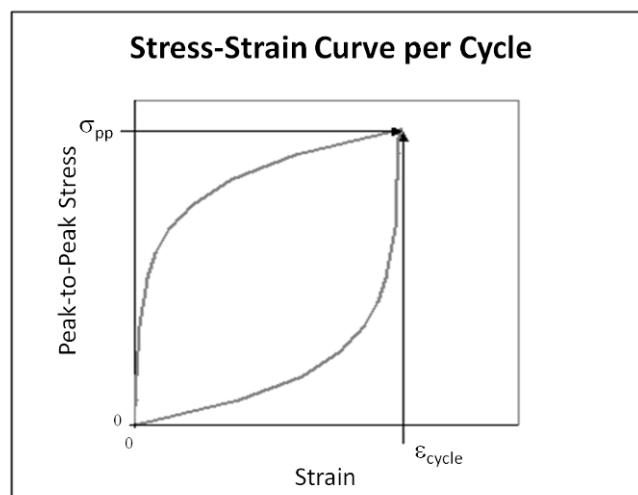


Figure 8. Energy-based hysteresis loop schematic.

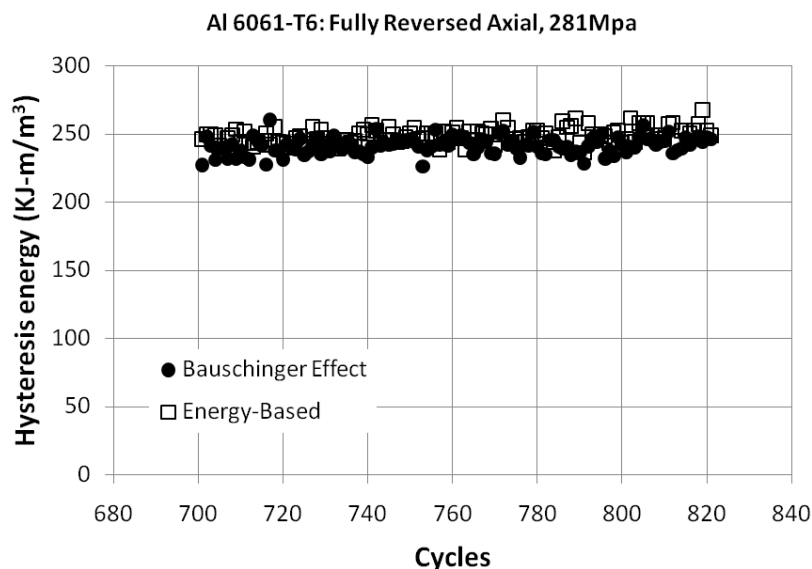


Figure 9. Hysteresis energy comparison.

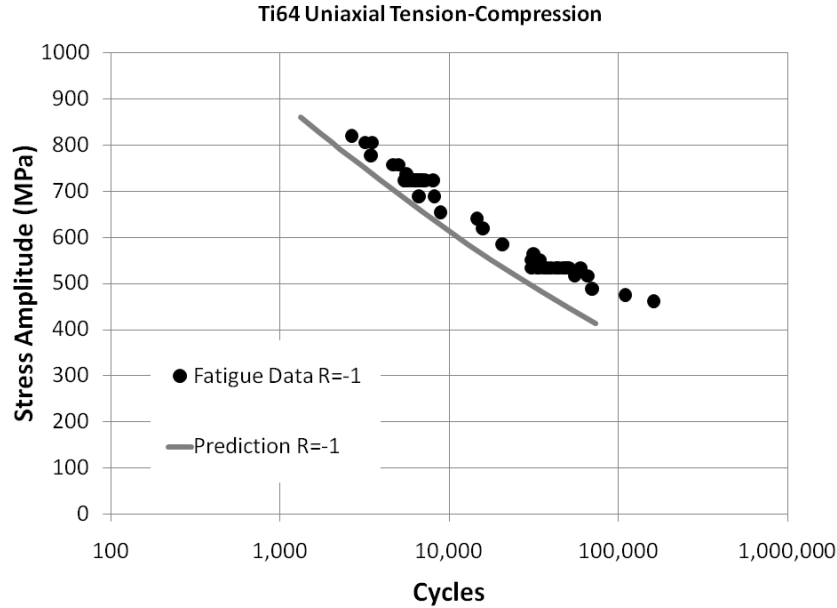


Figure 10. Energy-based life prediction comparison for Ti64.

Table 3. Material parameters for Ti64.

$C (mm/mm)$	$= 1.80E+05$
$E (GPa)$	$= 113.6$
$\varepsilon_o (mm/mm)$	$= 6.94E-10$
$\varepsilon_f (mm/mm)$	$= 4.53E-01$
$\sigma_c (MPa)$	$= 345.7$
$\sigma_f (MPa)$	$= 1161$
$\sigma_o (MPa)$	$= 66.24$
$\sigma_v (MPa)$	$= 1029$

5. CONCLUSION

It has been proven that hysteresis strain energy density is irreversible due to the analysis showing that suspending cyclic loading during fatigue testing of Ti64 does not affect the expected fatigue life in the lifetime regime of $5 \times 10^3 - 6 \times 10^4$. Other effects that do not show a noticeable trend on fatigue life are surface roughness and loading frequency. Although these assumptions, along with the omission of Bauschinger effect, have been used in energy-based theory prior to this manuscript, validating the assumption and constructing a well-compared energy-based life prediction for Ti64 fatigue has been encouraging for the future direction of energy/failure correlation studies.

Acknowledgements

The authors would like to thank the Air Force Research Laboratories (AFRL), specifically the Turbine Engine Fatigue Facility (TEFF) and the Air Force Office of Scientific Research (AFOSR) for their funding and support.

REFERENCE

- [1] Goodman, J., 1899, *Mechanics Applied to Engineering*, Longmans, Green, and Co., London.
- [2] Wöhler, A., "Wöhler's experiments on the strength of metals," *Engineering*, Paris Exposition, 1867, Vol. 4, pp.160-161.

- [3] Jasper, T.M., "The Value of the Energy Relation in the Testing of Ferrous Metals at Varying Ranges of Stress and at Intermediate and High Temperatures," *Philosophical Magazine*, Series. 6, Oct. 1923; 46: 609-627.
- [4] Enomoto, N., "On Fatigue Tests Under Progressive Stress," *Proc. ASTM*, 1955, Vol. 55, pp. 903-917.
- [5] Morrow, J., "Cyclic Plastic Energy and Fatigue of Metals," *Internal Friction, Damping and Cyclic Plasticity*, ASTM, 1964, ASTM STP 378, pp. 45-87.
- [6] Feltner, C.E., and Morrow, J.D., "Microplastic Strain Hysteresis Energy as a Criterion for Fatigue Fracture," *Journal of Basic Engineering Transactions*, ASME, 1961, Vol. 83, pp. 15-22.
- [7] Stowell, E., "A Study of the Energy Criterion for Fatigue," *Nuclear Engineering and Design*, 1966, Vol. 3, pp. 32-40.
- [8] Sarihan, V., "Energy Based Methodology for Damage and Life Prediction of Solder Joints Under Thermal Cycling," *Transactions on Components, Packaging, and Manufacturing Technology*, IEEE, 1994, Vol. 17, No. 4, pp. 626-631.
- [9] Solomon, H., "Low-Frequency, High Temperature Low-Cycle Fatigue of 60Sn/Pb Solder," *Low Cycle Fatigue*, ASTM STP 942, Solomon, H., Halford, G., Kaisand, L., and Leis, B., Eds., ASTM International, West Conshohocken, PA, 1988, pp. 342-369.
- [10] Chang, C.S., Pimbley, W.T., Conway, H.D., "An analysis of metal fatigue based on hysteresis energy," *Journal of Experimental Mechanics*, 1968, Vol. 8, Issue 3, pp. 133-137.
- [11] Cheng, G., and Plumtree, A., "A Fatigue Damage Accumulation Model Based on Continuum Damage Mechanics and Ductility Exhaustion," *International Journal of Fatigue*, 1998, Vol. 20, No. 7, pp. 495-501.
- [12] Scott-Emuakpor, O., Shen, M.-H.H., George, T., Cross, C., and Calcaterra, J., "Development of an Improved High Cycle Fatigue Criterion," *Journal of Engineering for Gas Turbines and Power*, ASME, 2007, Vol. 129, Issue 1, pp. 162-169.
- [13] Scott-Emuakpor, O., Shen, M.-H.H., George, T., and Cross, C., "An Energy-Based Uniaxial Fatigue Life Prediction Method for Commonly Used Gas Turbine Engine Materials," *Journal of Engineering for Gas Turbines and Power*, ASME, 2008, Vol. 130, Issue 6, pp. 1-15.
- [14] American Society for Testing and Materials, "E466-07: Standard Practice for Conducting Force Controlled Constant Amplitude Axial Fatigue Tests of Metallic Materials," *ASTM Book of Standards*, 2009, Vol. 03.01, ASTM International, West Conshohocken, PA.
- [15] Material Testing Systems, "MTS Landmark Testing Solutions," MTS Systems Corporation, 2010, Eden Prairie, MN.
- [16] Ozaltun, H., Shen, M-MH, George, T., Cross, C. "An Energy Based Fatigue Life Prediction Framework for In-Service Structural Components," *Journal of Experimental Mechanics*, 2010.
- [17] American Society for Testing and Materials, "E8M-09: Standard Test Methods for Tension Testing of Metallic Materials," *ASTM Book of Standards*, 2009, Vol. 03.01, ASTM International, West Conshohocken, PA.
- [18] Guilherme, A., Henriques, G., Zavanelli, R., and Mesquita, M., "Surface Roughness and Fatigue Performance of Commercially Pure Titanium and Ti-6Al-4V Alloy after Different Polishing Protocols," *Journal of Prosthetic Dentistry*, 2005, Vol. 93, Issue 4, pp. 378-385.
- [19] Montgomery, D., and Runger, G., "Applied Statistics and Probability for Engineers," John Wiley and Son, Inc., New York, NY, 2003, 3rd Edition.

- [20] Scott-Emuakpor, O., George, T., Cross, C., and Shen, M.-H.H., "Analysis of Strain Energy Behavior throughout a Fatigue Process," *Journal of Experimental Mechanics*, 2011.
- [21] Krige, D., "A Statistical Approach to Some Basic Mine Valuation Problem on the Witwatersrand," *Journal of the Chemical, Metal and Mining Society of South Africa*, 1951, Vol. 52, Issue 6, pp. 119-139.
- [22] Panontin, T., and Sheppard, S., "Fatigue and Fracture Mechanics," ASTM, STP-1332, 1999, Vol. 29, ASTM International, West Conshohocken, PA.
- [23] Letcher, T., Shen, M.-H.H., Scott-Emuakpor, O., George, T., and Cross, C., "An Energy Based Critical Fatigue Life Prediction Method," *ASME/IGTI Turbo Expo*, Vancouver, BC, Canada, 2011, Paper number: GT2011-45443.

Fatigue Improvement of Welded Elements by Ultrasonic Impact Treatment

Y. Kudryavtsev

Structural Integrity Technologies Inc., Markham, Ontario, Canada

E-mail: ykudryavtsev@sintec.ca

ABSTRACT

The ultrasonic impact treatment (UIT) is one of the new and promising processes for fatigue life improvement of welded elements and structures. In most industrial applications this process is known as ultrasonic peening (UP). The beneficial effect of UIT/UP is achieved mainly by relieving of harmful tensile residual stresses and introducing of compressive residual stresses into surface layers of a material, decreasing of stress concentration in weld toe zones and enhancement of mechanical properties of the surface layers of the material. The UP technique is based on the combined effect of high frequency impacts of special strikers and ultrasonic oscillations in treated material. Fatigue testing of welded specimens showed that UP is the most efficient improvement treatment as compared with traditional techniques such as grinding, TIG-dressing, heat treatment, hammer peening and application of LTT electrodes. The developed computerized complex for UP was successfully applied for increasing the fatigue life and corrosion resistance of welded elements, elimination of distortions caused by welding and other technological processes, residual stress relieving, increasing of the hardness of the surface of materials. The UP could be effectively applied for fatigue life improvement during manufacturing, rehabilitation and repair of welded elements and structures. The areas/industries where the UP process was applied successfully include: Shipbuilding, Railway and Highway Bridges, Construction Equipment, Mining, Automotive, Aerospace. The results of fatigue testing of welded elements in as-welded condition and after application of UP are considered in this paper. It is shown that UP is the most effective and economic technique for increasing of fatigue strength of welded elements in materials of different strength. These results also show a strong tendency of increasing of fatigue strength of welded elements after application of UP with the increase in mechanical properties of the material used.

1. Introduction

The ultrasonic impact treatment (UIT) is one of the new and promising processes for fatigue life improvement of welded elements and structures [1-7]. In most industrial applications this process is also known as ultrasonic peening (UP) [8-12]. The beneficial effect of UIT/UP is achieved mainly by relieving of harmful tensile residual stresses and introducing of compressive residual stresses into surface layers of materials, decreasing of stress concentration in weld toe zones and enhancement of mechanical properties of surface layers of the material. The fatigue testing of welded specimens showed that the UP is the most efficient improvement treatment when compared with such traditional techniques as grinding, TIG-dressing, heat treatment, hammer peening, shot peening and application of LTT electrodes [1, 13, 14].

The UP technique is based on the combined effect of high frequency impacts of special strikers and ultrasonic oscillations in treated material. The developed system for UP treatment (total weight - 11 kg) includes an ultrasonic transducer, a generator and a laptop (optional item) with software for optimum application of UP - maximum possible increase in fatigue life of parts and welded elements with minimum cost, labor and power consumption. In general, the basic UP system shown in [Figure 1](#) could be used for treatment of weld toe or welds and larger surface areas if necessary.



Figure 1. Basic ultrasonic peening system for fatigue life improvement of welded elements and structures [6]

The most recent design of the UP equipment is based on "Power on Demand" concept. Using this concept, the power and other operating parameters of the UP equipment are adjusted to produce the necessary changes in residual stresses, stress concentration and mechanical properties of the surface layers of materials to attain the maximum possible increase in fatigue life of welded elements and structures.

The effects of different improvement treatments, including the UP treatment, on the fatigue life of welded elements depend on the mechanical properties of used material, the type of welded joints, the parameters of cyclic loading and other factors. For effective application of UP, depending on the above-mentioned factors, a software package for Optimum Application of UP was developed that is based on original predictive model. In the optimum application, a maximum possible increase in fatigue life of welded elements with minimum time/labor/cost is thought [15].

The developed technology and computerized complex for UP were successfully applied for increasing of the fatigue life of welded elements, elimination of distortions caused by welding and other technological processes, relieving of residual stress, increasing of the hardness of the surface of materials and surface nanocrystallization. The areas/industries where the UP was applied successfully include: Railway and Highway Bridges, Construction equipment, Shipbuilding, Mining, Automotive and Aerospace to name a few.

2. Principles, Technology, Equipment for UP

2.1. Freely Movable Strikers

The UIT/UP equipment is based on known technical solutions from the 40's of last century of using working heads with freely movable strikers for hammer peening. At that time and later on, a number of different tools based on using freely movable strikers were developed for impact treatment of materials and welded elements by using pneumatic [16, 17] and ultrasonic [18-24] equipment. A more effective impact treatment is provided when the strikers are not connected to the tip of the actuator but could move freely between the actuator and the treated material. Figure 2 shows a standard set of easy replaceable working heads with freely movable strikers for different applications of UP.



Figure 2. A set of interchangeable working heads for UIT/UP [7]

2.2. Ultrasonic Impact and Effects of Ultrasound

The UP technique is based on the combined effect of high frequency impacts of the special strikers and ultrasonic oscillations in treated material. Some specific features of the ultrasonic impact treatment of metals are described in [16] where it is shown that the operational frequency of the transducer and the frequency of the intermediate element-striker are not the same.

During the ultrasonic treatment, the striker oscillates in the small gap between the end of the ultrasonic transducer and the treated specimen, impacting the treated area [18-21]. This kind of high frequency movements/impacts in combination with high frequency oscillations induced in the treated material is typically called the ultrasonic impact.

There are a number of effects of ultrasound on metals that are typically considered: acoustic softening, acoustic hardening, acoustic heating, etc. In the first of these (acoustic softening that is also known as acoustic-plasticity effect), the acoustic irradiation reduces the stress necessary for plastic deformation. In general, the effect of ultrasound on the mechanical behavior could be compared with the effect of heating on a material. The difference is that acoustic softening takes place immediately when a metal is subjected to ultrasonic irradiation. Also, relatively low-amplitude ultrasonic waves leave no residual effects on the physical properties of metals after acoustic irradiation is stopped [25].

2.3. Technology and Equipment for Ultrasonic Peening

The ultrasonic transducer oscillates at a high frequency, with 20-30 kHz being typical. The ultrasonic transducer may be based on either piezoelectric or magnetostrictive technology. Whichever technology is used, the output end of the transducer will oscillate, typically with amplitude of 20 – 40 μm . During the oscillations, the transducer tip will impact the striker(s) at different stages in the oscillation cycle. The striker(s) will, in turn, impact the treated surface. The impact results in plastic deformation of the surface layers of the material. These impacts, repeated hundreds to thousands of times per second, in combination with high frequency oscillations induced in the treated material result in a number of beneficial effects of UP.

The UP is an effective way for relieving of harmful tensile residual stresses and introducing of beneficial compressive residual stresses in surface layers of parts and welded elements. The mechanism of residual stress redistribution is connected mainly with two factors. At a high-frequency impact loading, oscillations with a complex frequency mode spectrum propagate in a treated element. The nature of this spectrum depends on the frequency of ultrasonic transducer, mass, quantity and form of strikers and also on the geometry of the treated element. These oscillations lead to lowering of residual welding stresses. The second and the more important factor, at least for fatigue improvement, is surface plastic deformation that leads to introduction of the beneficial compressive residual stresses.

In the fatigue improvement, the beneficial effect is achieved mainly by introducing of the compressive residual stresses into surface layers of metals and alloys, decrease in stress concentration in weld toe zones and the enhancement of the

mechanical properties of the surface layer of the material. The schematic view of the cross section of material/part improved by UP is shown in Figure 3 with the attained distribution of the stresses after the UP. The description of the UP benefits is presented in Table 1.

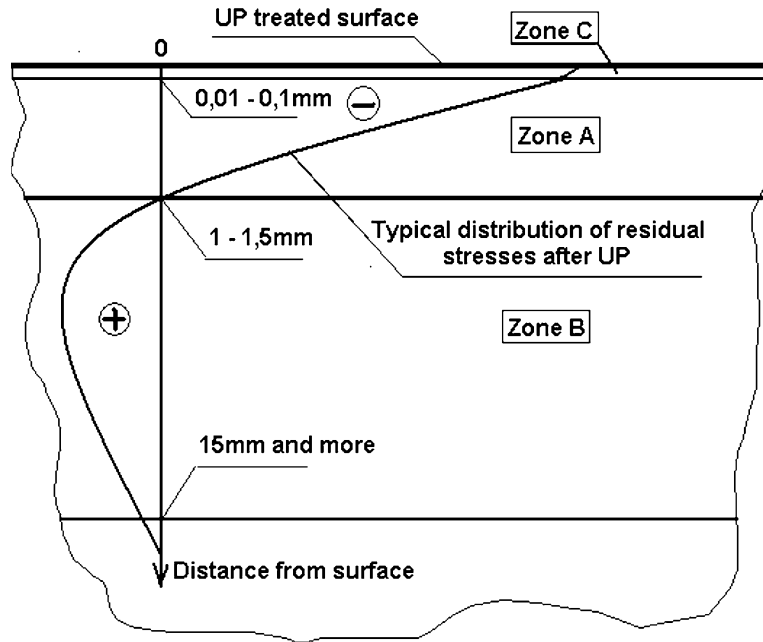


Figure 3. Schematic view of the cross section of material/part improved by Ultrasonic Peening [9]

Table 1. Zones of Material/Part Improved by Ultrasonic Peening [9] (see Figure 3 for illustration of the zones)

Zone	Description of zone	Distance from surface,	Improved characteristics
A	Zone of plastic deformation and compressive residual stresses	1 – 1.5 mm	Fatigue, corrosion, wear, distortion
B	Zone of relaxation of welding residual stresses	15 mm and more	Distortion, crack propagation
C	Zone of nanocrystallization (produced at certain conditions)	0.01 – 0.1 mm	Corrosion, wear, fatigue at elevated temperature

Figure 4 illustrates the concept of the fatigue life improvement of welded elements by UP. In case of welded elements, it is enough to treat only the weld toe zone – the zone of transition from base metal to the weld, for a significant increase of fatigue life. A so-called groove, shown in Figures 4 and 5, characterized by certain geometrical parameters is produced by UP [2, 4].

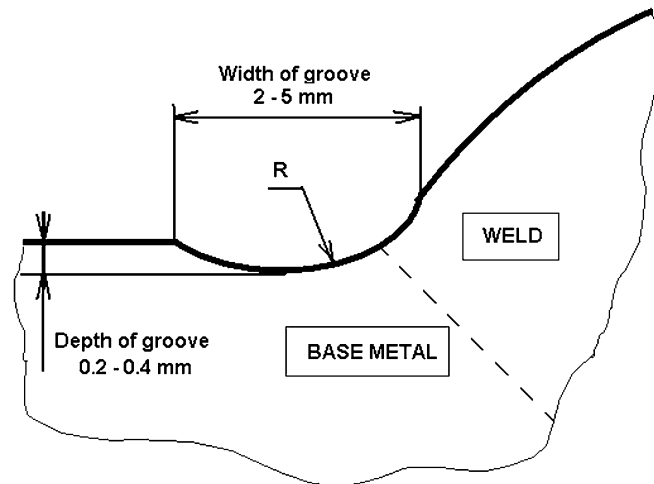


Figure 4. Profile of weld toe improved by Ultrasonic Peening [9]

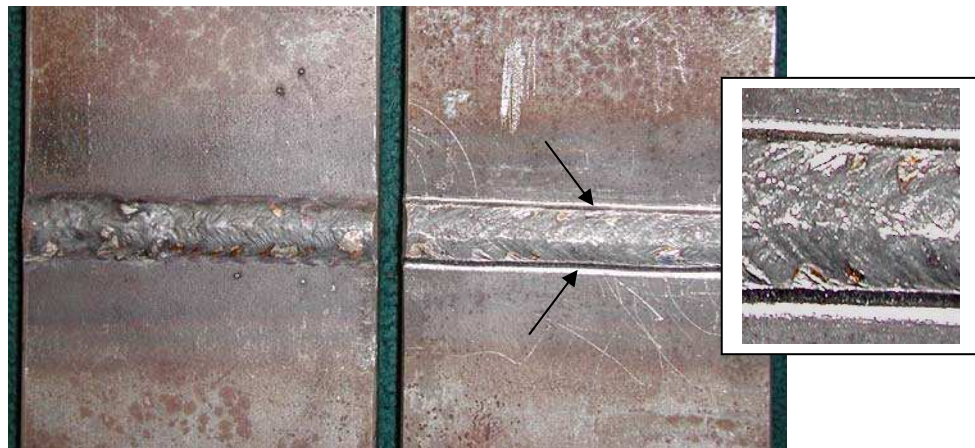


Figure 5. The view of the butt welds in as-welded condition (left side sample) and after application of UP (right side sample) [7]. Notice the formation of a uniform, shiny groove along the weld toe marked with arrows and shown in greater details in the insert.

3. Application of UP for Fatigue Improvement

The UP could be effectively applied for fatigue life improvement during manufacturing, rehabilitation and repair of welded elements and structures. Examples of all three applications will be described below.

3.1. Manufacturing and Rehabilitation

Three series of large-scale welded samples, designed as shown in Figure 6, were subjected to fatigue testing to evaluate the effectiveness of UP application to the existing welded structures: 1 – in as welded condition, 2 – UP was applied before fatigue testing, 3 – UP was applied after fatigue loading with the number of cycles corresponding to 50% of the expected fatigue life of samples in as-welded condition [9].

The results of fatigue testing of the large-scale welded samples imitating the transverse non-load-carrying attachments (Fig. 6) with UP applied to specimens in as-welded condition and also after 50% of expected fatigue life are presented in Figure 7.

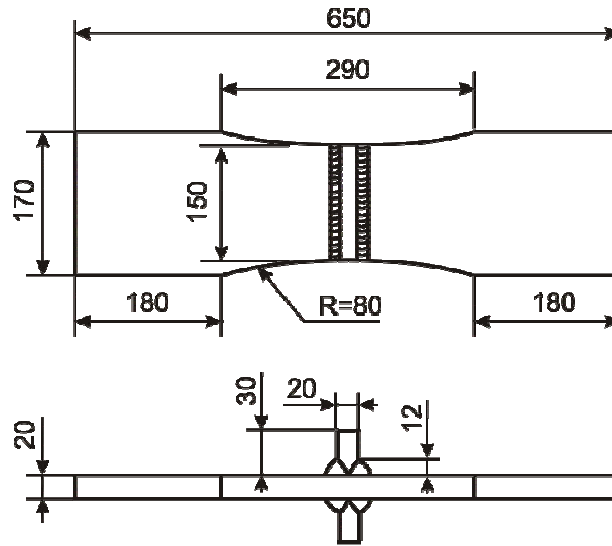


Figure 6. The general view of welded sample for fatigue testing

The UP caused a significant increase in fatigue strength of the considered welded element for both series of UP treated samples. The increase in limit stress range at $N=2 \cdot 10^6$ cycles of welded samples is 49% (from 119 MPa to 177 MPa) for UP treated samples before fatigue loading and is 66% (from 119 MPa to 197 MPa) for UP treated samples after fatigue loading, with the number of cycles corresponding to 50% of the expected fatigue life of the samples in as-welded condition. The higher increase of fatigue life of UP treated welded elements for fatigue curve #3 could be explained by a more beneficial redistribution of residual stresses and/or “healing” of fatigue damaged material by UP in comparison with the fatigue curve #2.

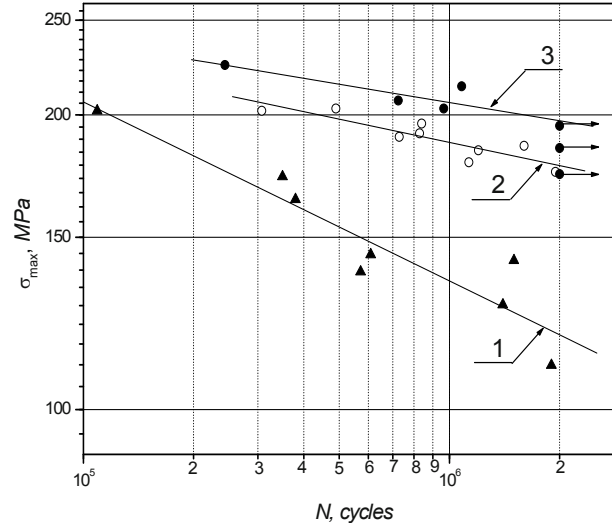


Figure 7. Fatigue curves of welded elements (transverse non-load-carrying attachment: 1 – in as welded condition, 2 – UP was applied before fatigue testing, 3 – UP was applied after fatigue loading with the number of cycles corresponding to 50% of expected fatigue life of samples in as-welded condition.

3.2. Weld Repair

In this paper the rehabilitation is considered as a prevention of possible initiation of fatigue cracks in existing welded elements and structures that are in service. The UP could also be effectively used during the weld repair of fatigue cracks [7, 10].

Figure 8 shows the drawing of a large-scale welded specimen containing non-load carrying longitudinal attachments designed for fatigue testing [7]. Such specimens were tested in as-welded condition and after weld repair with and without application of UP.

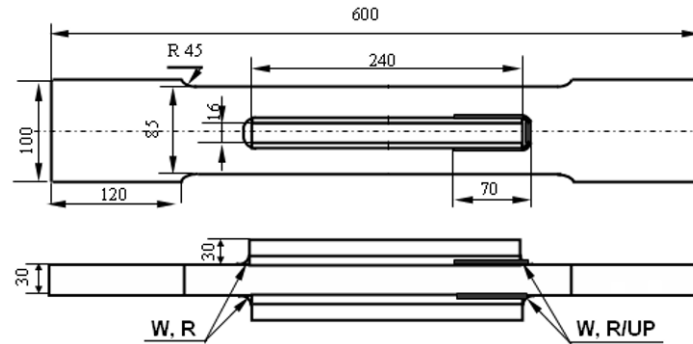


Figure 8. Drawings of welded specimens for fatigue testing at different conditions:
W – as-welded condition; R - repair by gouging and welding; R/UP – repair by gouging, welding and UP

The testing conditions were zero-to-tension stress cycles ($R=0$) with different level of maximum stresses. The fatigue testing was stopped and the number of cycles was recorded when the length of fatigue crack on surface reached 20 mm. Then, the fatigue crack was repaired by gouging and welding and the fatigue test was continued. After repair, a number of samples were subjected to UP. The weld toe of the “new” weld was UP treated. The results of fatigue testing of welded specimens in as-welded condition and after weld repair of fatigue cracks are presented in Figure 9.

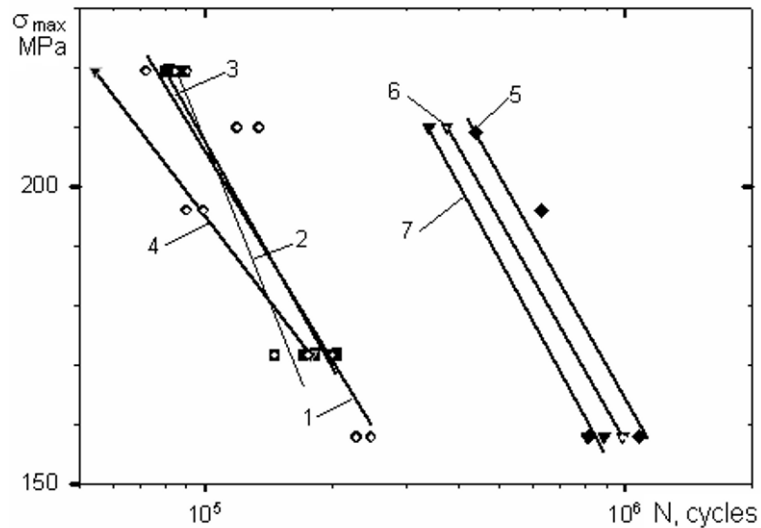


Figure 9. Results of fatigue testing of welded elements: 1 - as-welded condition, 2, 3 and 4 – after first, second and third weld repair, 5, 6 and 7 - after first, second and third weld repair with application of UP

The fatigue testing of large scale specimens showed that the repair of fatigue cracks by welding is restoring the fatigue strength of welded elements to the initial as-welded condition. Second and third repair of fatigue cracks also practically restored the fatigue life of repaired welded elements to initial as-welded condition.

The application of UP after weld repair increased the fatigue life of welded elements by 3-4 times. Practically the same significant fatigue improvement of repaired welded elements by UP is observed also after second and third repair of fatigue cracks in welded elements.

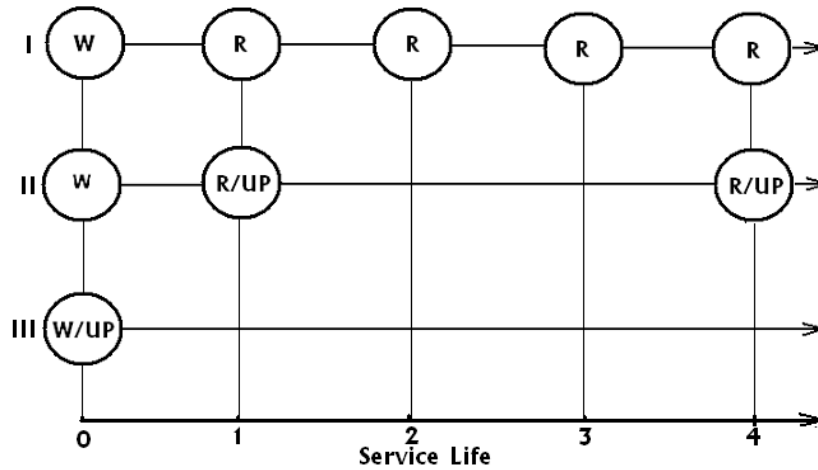


Figure 10. Diagram showing the endurance of welded elements: Line I - fatigue crack is repaired by gouging and welding, Line II - fatigue crack is repaired by gouging, welding and UP, Line III – UP is applied before/during the first phase of service life, W – as-welded condition, R - repair by gouging and welding, R/UP – repair by gouging, welding and UP, W/UP- welding and UP

A comparison of the efficiency of weld repair of fatigue cracks with and without application of UP is presented in Figure 10. This diagram illustrates the fatigue behavior of the same welded elements in cases when UP is not applied (I), when UP is applied after weld repair (II) and UP is applied before/during the first phase of service life (III). Here, 1 unit of service life corresponds to ~ 240,000 cycles of loading at the stress range 158 MPa and to ~ 75,000 at the stress range 220 MPa. Every circle, marked R or R/UP, in Fig.10 starting from the number 1 on service life axis indicates a fatigue fracture and a repair of the welded element. As can be seen from Fig.10, the benefit from application of UP for weld repair and rehabilitation of welded elements is obvious.

4. Ultrasonic Peening of HSS Welded Elements

4.1. 700 MPa yield strength steel

Four series of large-scale welded samples were subjected to fatigue testing to evaluate the effectiveness of UIT/UP application for fatigue life improvement of welded elements made from 350 MPa and 700 MPa yield strength steels [13]. The fatigue specimens were designed as 80 mm wide by 8 mm thick steel plates with longitudinal non-load carrying fillet welded attachments, as shown in Figure 11.

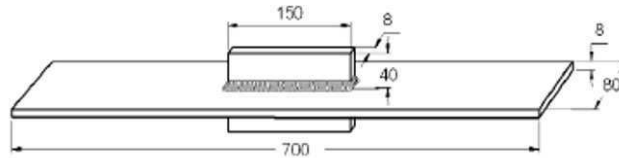


Figure 11. Welded specimen for fatigue testing of 350 and 700 MPa yield strength steel welded elements [13]

All testing has been conducted under constant amplitude axial tension in servo-hydraulic fatigue testing machines. The applied stress ratio has been $R=0.1$, with test frequencies varying from 2 to 6 Hz depending on load levels. Failure is defined to have taken place upon complete separation of the specimen. The results of fatigue testing are presented in Figure 12.

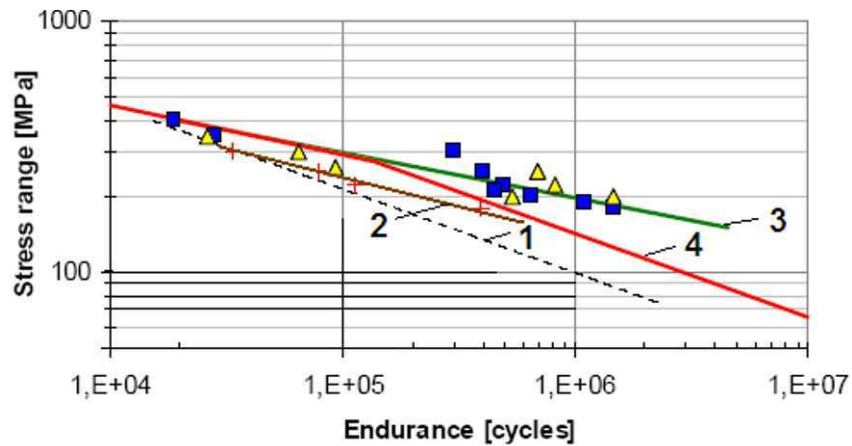


Figure 12. Fatigue test results for 350 and 700 MPa yield strength steel welded specimens [13]:
 1- in as-welded condition, 350 MPa and 700 MPa yield strength steels, 2 - after UIT, 350 MPa yield strength steel,
 3- after UIT/UP, 700 MPa yield strength steel, 4- FAT 112 design curve

As can be seen from Figure 12, the UIT/UP provided significant increase in fatigue performance of considered welded element for 700 MPa yield strength steel. The increase in limit stress range at 2 millions cycles of loading was 81% for welded samples treated by UIT/UP in comparison with as-welded condition, while TIG-dressing provided a 36% increase in limit stress range of welded element (see Table 2).

TABLE 2. INCREASE IN LIMIT STRESS RANGE OF WELDED ELEMENT
 AT 2 MILLIONS CYCLES OF LOADING [13]

S-N curve	Slope m	FAT value [MPa]	Improvement at FAT value [%]
As-welded S355 and S700	-3 (fixed)	71.3	-
UIT/UP S700	-5 (fixed)	129.4	81
Robotized TIG-dressing S700	-3 (fixed)	97.0	36.0

4.2. 960 MPa yield strength steel

Four series of large-scale welded samples were subjected also to fatigue testing to evaluate the effectiveness of UIT/UP application for fatigue life improvement of welded elements made from 960 MPa yield strength steel [14]. The fatigue specimens were designed as 50 mm wide by 6 mm thick steel plates with longitudinal non-load carrying fillet welded attachments, as shown in Figure 13.

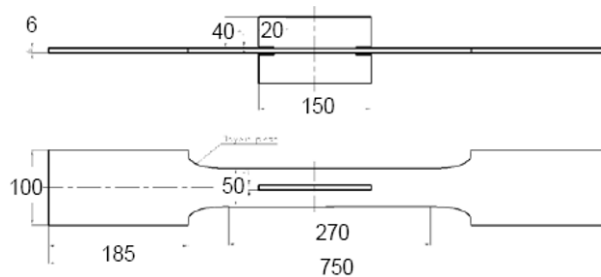


Figure 13. Specimen geometry for fatigue testing of 960 MPa yield strength steel welded elements [14]

The testing has been conducted under constant amplitude using $R = -1$. All of the as-welded specimens failed at the weld toe at the end of the longitudinal stiffeners. For the improved by UIT/UP welds, tested using constant amplitude loading, a variety of other failure modes were observed. The results of fatigue testing are presented in Figure 14.

As can be seen from Figure 14, the UIT/UP treatment with an instrument based on piezoelectric transducer provided the highest increase in fatigue performance of considered welded element for 960 MPa yield strength steel in comparison with the efficiency of application of magnetostrictive transducer and LTT electrodes.

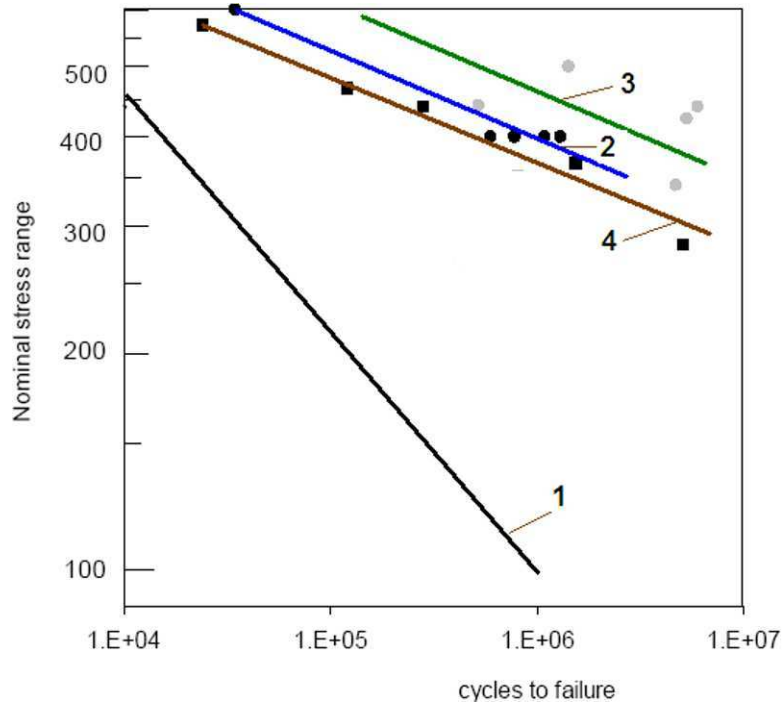


Figure 14. Fatigue test results for 960 MPa yield strength steel welded specimens [14]: 1- in as-welded condition, 2 and 3 - after UIT/UP based on using magnetostrictive and piezoelectric transducers respectively, 4- after application of LTT electrodes

5. Industrial Applications of UP

As was demonstrated, the UP could be effectively applied for fatigue life improvement during manufacturing, rehabilitation and repair of welded elements and structures. The UP technology and equipment were successfully applied in different industrial projects for rehabilitation and weld repair of parts and welded elements. The areas/industries where the UP was applied successfully include: Railway and Highway Bridges, Construction Equipment, Shipbuilding, Mining, Automotive and Aerospace.

An example of application of UP for repair and rehabilitation of welded elements subjected to fatigue loading in mining industry is shown in Figure 15. Around 300 meters of welds, critical from fatigue point of view, were UP treated to provide improved fatigue performance of large grinding mills.



Figure 15. Application of UP for rehabilitation of welded elements of a large grinding mill

Based on the fatigue data and the solution described in [10], the UP was also applied during the rehabilitation of welded elements of a highway bridge over the Ohio River in the USA.

The bridge was constructed about 30 years ago. The welded details of the bridge did not have macroscopic fatigue cracks. The motivation for application of the UP for fatigue life improvement of this bridge was the fatigue cracking in welded elements and failure of one of the spans of another bridge of approximately the same age and design. The stages of preparation for UP treatment of the bridge and the process of UP treatment of one of the welded vertical stiffeners are shown in [Figures 16 and 17](#). More than two thousand and five hundred welded details of the bridge structure that were considered to be fatigue critical were UP treated.



Figure 16. Ultrasonic Peening of a welded bridge: preparation for UP treatment (two UP systems/lifts)



Figure 17. Ultrasonic Peening of a welded bridge: UP of the end of one of welded vertical stiffeners

6. Conclusions

1. Ultrasonic Impact Treatment (UIT/UP) is a relative new and promising technique for fatigue life improvement of welded elements and structures in materials of different strength including HSS with the yield strength of 700-1000 MPa. The results of fatigue testing show a strong tendency of increasing of fatigue strength of welded elements after application of UP with the increase in mechanical properties of the material used. It allows using to a greater degree the advantages of the HSS in welded elements, subjected to fatigue loading.
2. The fatigue testing of welded specimens also showed that the UP is the most efficient improvement treatment as compared with traditional techniques such as grinding, TIG-dressing, heat treatment, hammer peening, shot peening or application of LTT electrodes.
3. The developed computerized complex for UP was successfully used in different applications for increasing of the fatigue life of welded elements, elimination of distortions caused by welding and other technological processes, relieving of residual stress, increasing of the hardness of material surfaces and surface nanocrystallization. The areas/industries where the UP was applied successfully include: Railway and Highway Bridges, Mining, Construction Equipment, Shipbuilding, Automotive and Aerospace.

References

1. V. Trufyakov, P. Mikheev and Y. Kudryavtsev. Fatigue Strength of Welded Structures. Residual Stresses and Improvement Treatments. *Harwood Academic Publishers GmbH. London. 1995. 100 p.*
2. Y. Kudryavtsev, V. Korshun and A. Kuzmenko. Improvement of Fatigue Life of Welded Joints by Ultrasonic Impact Treatment. *Paton Welding Journal. 1989. No. 7. p. 24-28.*
3. V. Trufyakov, P. Mikheev, Y. Kudryavtsev and D. Reznik. Ultrasonic Impact Peening Treatment of Welds and Its Effect on Fatigue Resistance in Air and Seawater. *Proceedings of the Offshore Technology Conference. OTC 7280. 1993. p. 183-193.*
4. Y. Kudryavtsev, P. Mikheev and V. Korshun. Influence of Plastic Deformation and Residual Stresses Created by Ultrasonic Impact Treatment on Fatigue Strength of Welded Joints. *Paton Welding Journal. 1995. No. 12. p. 3-7*
5. V. Trufyakov, P. Mikheev, Y. Kudryavtsev and E. Statnikov. Ultrasonic Impact Treatment of Welded Joints. *International Institute of Welding. IIW Document XIII-1609-95. 1995.*

6. Y. Kudryavtsev and J. Kleiman. Fatigue Improvement of Welded Elements and Structures by Ultrasonic Impact Treatment (UIT/UP). *International Institute of Welding. IIW Document XIII-2276-09. 2009.*
7. Y. Kudryavtsev and J. Kleiman. Increasing Fatigue Strength of Welded Elements and Structures by Ultrasonic Impact Treatment. *International Institute of Welding. IIW Document XIII-2318-10. 2010.*
8. Patent of USA # 6467321. 2002. Device for Ultrasonic Peening of Metals.
9. Y. Kudryavtsev, J. Kleiman, L. Lobanov et al. Fatigue Life Improvement of Welded Elements by Ultrasonic Peening. *International Institute of Welding. IIW Document XIII-2010-04. 2004. 20 p.*
10. Y. Kudryavtsev, J. Kleiman, A. Lugovskoy et al. Rehabilitation and Repair of Welded Elements and Structures by Ultrasonic Peening. *International Institute of Welding. IIW Document XIII-2076-05. 2005. 13 p*
11. Y. Kudryavtsev, J. Kleiman, A. Lugovskoy et al. Fatigue Life Improvement of Tubular Welded Joints by Ultrasonic Peening. *International Institute of Welding. IIW Document XIII-2117-06. 2006. 24 p.*
12. Y. Kudryavtsev, J. Kleiman and Y. Iwamura. Fatigue Improvement of HSS Welded Elements by Ultrasonic Peening. *Proceedings of the International Conference on High Strength Steels for Hydropower Plants, July 20-22, 2009. Takasaki, Japan.*
13. P. Haagensen. Progress Report on IIW WG2 Round Robin Fatigue Testing Program on 700 MPa and 350 MPa YS Steels. *International Institute of Welding. IIW Document XIII-2081-05. 2005.*
14. G. Marquis and T. Björk. Variable Amplitude Fatigue Strength of Improved HSS Welds. *International Institute of Welding. IIW Document XIII-2224-08. 2008.*
15. Y. Kudryavtsev. Residual Stress. *Springer Handbook on Experimental Solid Mechanics. Springer – SEM. 2008. P. 371-387.*
16. Patent of USA No. 2,356,314. 1944. Scaling Tool. Reo D. Grey and James R. Denison.
17. Patent of USA No. 3,349,461. 1967. Descaling Tool. Joseph F. Niedzwiecki.
18. Krilov N. A., Polishchuk A. M. Using of ultrasonic apparatus for metal structure stabilization. *Physical background of industrial using of ultrasound. Part I. LDNTP. Leningrad..- P. 70-79. 1970. (in Russian)*
19. Patent of USA No. 3,609,851. 1971. Metal Working Apparatus and Process. Robert C. McMaster and Charles C. Libby.
20. Patent of USA No. 3,595,325. 1971. Intermediary Impact Device. Charles C. Libby and William J. White.
21. C. Feng and K. Graff. Impact of a Spherical Tool against a Sonic Transmission Line. *The Journal of the Acoustical Society of America. Volume 52, Number 1 (Part 2), 1972. pp. 254-259.*
22. I. Polozky, A. Nedoseka, G. Prokopenko et al. Relieving of welding residual stresses by ultrasonic treatment. *The Paton Welding Journal. 1974. № 5.- p. 74-75. (in Russian)*
23. Author's Certificate (USSR) # 472782. 1975. Ultrasonic head for strain hardening and relaxation treatment. E. Statnikov, L. Zhuravlev, A. Alexeyev, Yu. Bobylev, E. Shevtsov, V. Sokolenko and V. Kulikov. (in Russian)
24. Author's Certificate (USSR) # 601143. 1978. Ultrasonic multiple-strikers device. G. Prokopenko and V. Krivko. (in Russian)
25. B. Langenecker. Effects of Ultrasound on Deformation Characteristics of Metals. *IEEE Transactions on Sonics and Ultrasonics. Vol. SU-13, No. 1, March 1966, pp. 1-8.*

DELAMINATION BETWEEN FUNCTIONALIZED SILICON SURFACES

S. R. Na¹, A. Hassan², K. M. Liechti¹ and M.J. Krische²

¹Aerospace Engineering and Engineering Mechanics

²Chemistry and Biochemistry

The University of Texas at Austin

Austin, TX 78712

kml@mail.utexas.edu

The paper describes the development of an experiment with associated analysis to determine the toughness of a molecular adhesive formed by bringing together two functionalized silicon surfaces. Si (111) surfaces were coated with amine and carboxy-terminated self-assembled monolayers (SAMs). The areal density of these termini was varied in order to modulate the bonding interactions between the two surfaces. The silicon beams were pressed together to form miniature laminated beam beam specimens and then fractured in high vacuum using a specially developed fracture tester. Normal crack opening displacements were measured using infra red crack opening interferometry.

The fracture toughness of the specimens was measured as a function of the areal density of bonds. Traction-separation laws were extracted from the measurements of crack opening displacements. Interesting differences are being noted in mode 1 and mixed-mode in these highly controlled experiments.

Failure and Fracture Behavior of Brittle Polymer Foam

Addis Kidane and Guruswami Ravichandran
Graduate Aerospace Laboratories (GALCIT)
California Institute of Technology
1200 E California Blvd. Pasadena CA 91125

ABSTRACT

Experimental study was performed to investigate the fracture behavior of relatively brittle polymer foam. A single notch bending specimen made of a PVC core cell foam A-series, A 800 and A 1200, are used for the investigation. To measure the strain around the defect section, a 2D digital image correlation (DIC) technique was used. The fracture initiation toughness was calculated from the load displacement curve and a strain fields obtained from DIC technique. Furthermore a study was performed to investigate the failure behavior of foam core with sharp cracks, notch and circular hole. To reduce the size effect, the net cross-sectional areas of the specimen for all the geometries considered are kept constant. An Instron tensile loading machine was used and the tensile load was measured directly through the load cell. The full strain field around the section was measured using DIC and the data points at the interest location were extracted. The result was compared with the dog-bone tensile experiment of intact specimen. It was observed that, the net section strength for specimen with cracks, notch and circular hole is higher than that of the intact foam core.

INTRODUCTION

Lightweight structures with superior blast mitigation and impact resisting behavior are currently attracting the attention of Aerospace, Navy and other related industries. Sandwich structures with layer of composites as face sheets and foam material as core are widely used in such applications. Polymer foams have shown promising results as a core material for sandwich structures due to their high energy absorption capabilities, especially in the case of impact loading [1, 2]. There are well documented studies on the compressive properties and energy absorbing behavior of these materials [3]. It is shown that the structural response of polymer foam strongly depends on the foam density, cell microstructure and solid polymer properties [3]. Recent developments in manufacturing processes of polymer foams make the material available to be used in different shapes and sizes. Some of the applications of this material require these materials to have cuts and holes in them. It is well understood that, in the case of a fully dense material, the presence of a cracks, notches and holes in structures results in a stress concentration and thus leading to fracture. Understanding the tensile strength, the effect of notches and cracks and fracture behavior of foams is important to design structures using this material.

There exist a few studies on the tensile properties of open and closed cell foams with a presence of notches and holes. Andrews and Gibson [4], present a finite element analysis on the influence of defect size and cell size on the tensile strength of ductile two-dimensional cellular structures. Based on their study, they have concluded (a) the net section strength of a honeycomb with a circular hole is equal to the tensile strength of the intact honeycomb, (b) The net section strength of a honeycomb with a crack (defect width smaller than the cell size) is greater than the tensile strength of the intact honeycomb and the strengthening becomes more significant as the normalized cell size is increased, (c) the net section strength of a honeycomb with a notch (defect width greater than the cell size) is greater than the tensile strength of the intact honeycomb and the strengthening effect is independent to the normalized cell size.

In a different study, Andrews and Gibson [5] investigated, experimentally and numerically, the influence of crack-like defects on the tensile strength of open cell aluminum foam. They concluded that, the net section strength increased with an

increasing notch size, indicating a notch strengthening effect. On the other hand, Paul et al. [6], experimentally studied the tensile strength of a closed cell Aluminum foam in the presence of notches and holes. They observed that, the net strength decreases with an increase in the notch length or holes diameter when the notch root or hole diameter is larger than the cell size.

Besides these few studies presented in literature, the effect of holes, cracks and notches in foam materials is not well understood. A detailed investigation on the failure of polymer foam and the effect of hole and cracks on the tensile strength of this material is essential. It is also observed that, foam cracking is one of the main failure modes in sandwich structures and understanding the fracture properties this material is important. Usually, in sandwich structures, the cracks starts at the core material and propagates to the faces and results in delamination.

In this paper, an experimental investigation on the tensile properties of PVC foam with a presence of crack, notches and holes is presented. Furthermore, a fracture behavior of this material is investigated. An INSRON tensile testing machine in conjunction with a 2D digital image correlation (DIC) technique is used. It is observed that the net section tensile yield strength in the presence of holes, notches and cracks is higher than that of the intact specimen. It is also observed that, the defected specimen failed at a lower strain compared to the intact specimen, indicating a presence of a strain concentration around the defects section.

MATERIAL AND SPECIMEN GEOMETRY

The foam materials used in the present study is Corecell™ A series styrene foams, which are manufactured by Gurit SP Technologies specifically for marine sandwich composite applications. The material properties for A800 and A1200 Corecell™ foam that were used in the present study are listed in Table 1.

For the tensile experiments, four different specimen geometries, as shown in Fig.1, were considered; Dog-bone specimen without a defect (DB), with a center crack (CC), with an edge crack (EC) and with a center hole (CH). To avoid the size effect, the net cross sectional area were kept constant for all the specimens with defects considered. The gage lengths were 134 mm, widths were 25.4 mm, effective widths were 18 mm, and thicknesses were 6 mm.

Table 1 Selected mechanical properties of foam

Material	Nominal density (kg/m ³)	Shear modulus (MPa)	Shear Elongation (%)
A800	150	47	50
A1200	210	76	46

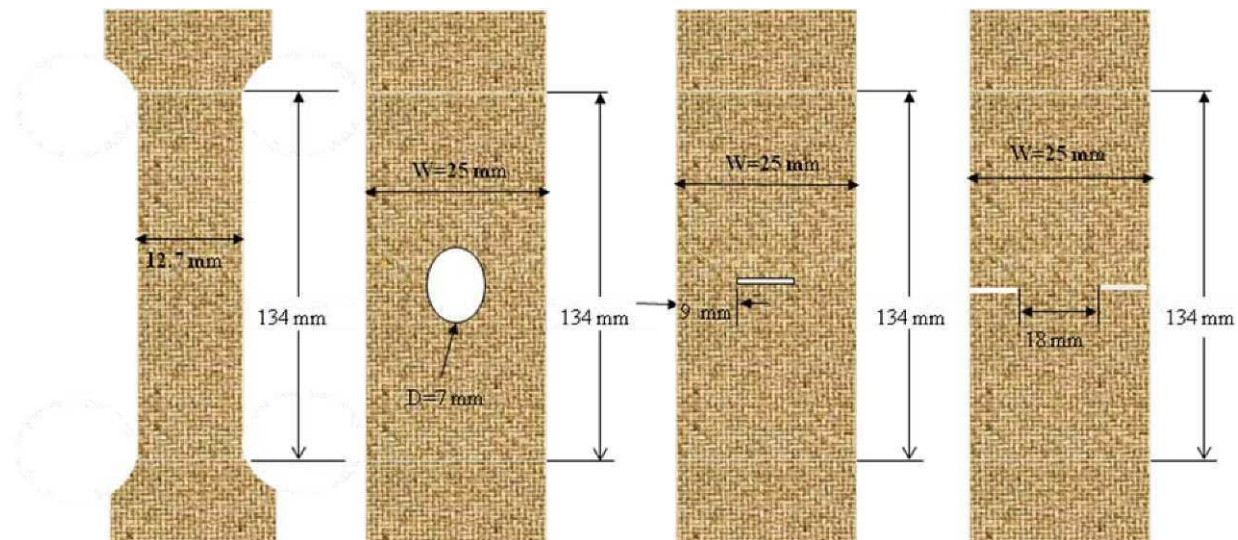


Fig 1 Schematic drawing and geometry of tensile specimens, (a) Dog-bone specimen without a defect (DB), (b) with a center hole (CH), (c) with a center crack (CC), (d) with an edge crack (CH)

For the fracture experiment, single edge notched bend (SENB) specimens, as shown in Fig.2, were prepared from A1200 foam sheet according to ASTM E3999. The span length was 50 mm, the width was $w=14$ mm, the thickness was $B=7$ mm and the initial crack length was $a=7$ mm. The crack was first machined with 1 mm thick blade and later the artificial crack was extended with razor blade.

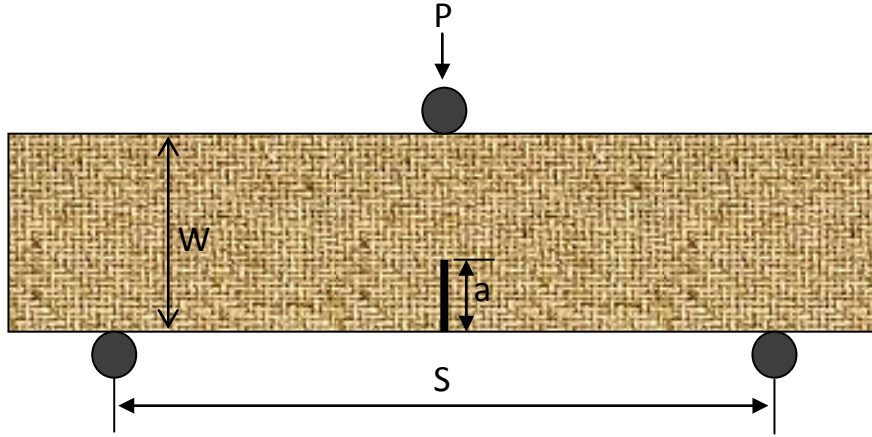


Fig 2 Schematic drawing of a single edge notched bend (SENB) specimen

EXPERIMENTAL SETUP

TENSILE STRENGTH

An INSTRON machine was used in a displacement control mode at a speed of 1mm/min and the tensile load was recorded directly by the load cell. To measure the strain fields around the required area, a 2D DIC technique was used. Digital images of the sample at several deformation steps were taken using a high speed CCD camera. The resolution of the images was 2048×2048 pixels. First, the displacement and strain field around the gage length were calculated and later the strains on the required field were extracted

FRACTURE BEHAVIOR

The fracture surfaces of tensile specimens of the polymer foam considered in this study show no evidence of gross yielding or necking. Hence the foam is relatively brittle and stress intensity factor was used as a parameter to determine the fracture behavior. There are different techniques developed for determining the stress intensity factors for brittle materials. In the present study, the stress intensity factor K_I was obtained experimentally using a three point single notched bending experiment. An INSTRON machine was used in a displacement control mode at a cross head speed of 1mm/min and the load-displacement data was recorded directly by the load cell. Digital images of the sample at several deformation steps were taken using a high speed CCD camera. A 2D DIC technique was used to obtain the displacement and strain fields. The stress intensity factor K_I was calculated using three different techniques; critical load in the load-displacement curve using the linear elastic fracture mechanics theory, the stress intensity factor formulation using a single strain data point with a three parameter solution described by Dally and Sanford [7] and the modified multipoint strain method presented by Berger and Dally [8].

The detailed analysis of the above techniques can be obtained in the literature and only a brief description is presented below.

LOAD-DISPLACEMENT

The stress intensity factor K_I is calculated from the critical load in the load displacement curve using the linear elastic fracture mechanics given by Eq (1).

$$K_I = \frac{PS}{BW^{3/2}} \left[2.9 \left(\frac{a}{W} \right)^{1/2} - 4.6 \left(\frac{a}{W} \right)^{3/2} + 21.8 \left(\frac{a}{W} \right)^{5/2} - 37.6 \left(\frac{a}{W} \right)^{7/2} + 38.7 \left(\frac{a}{W} \right)^{9/2} \right] \quad (1)$$

Where P is the critical load, a is the crack length, B is the thickness, W is the width, and S is the span.

SINGLE POINT THREE-TERM SOLUTION

A method for determining the mode I stress intensity factor by using a strain gage was first proposed by Dally and Sanford (1985). In this method a single or two strain gages will be placed on a region where the strain fields can be described by a three or four term of series. In the case of three-term series representation, only a single strain gage is required positioned near to the crack tip and oriented at a specific direction. The orientation angle α , of the strain gage is a function of material Poisson's ratio (ν) and can be given as,

$$\cos(2\alpha) = -(1 - \nu)/(1 + \nu) \quad (2)$$

The location of the strain gage from the crack tip direction can be represented by the radius (r) and angle (θ). This angle is unique and related to α as shown below

$$\tan(\theta/2) = \cot(2\alpha) \quad (3)$$

The stress intensity factor can be given as

$$K_I = \frac{1}{\cos(\theta/2)} \left[\frac{E(1 + \nu)\epsilon_{rr}}{A_0 r^{-1/2}} + (1/2)\sin\theta \sin(3\theta/2)\cos 2\alpha - (1/2)\sin\theta \cos(3\theta/2)\sin 2\alpha \right] \quad (4)$$

Where, E and ν are the Young's modulus and Poisson's ratio of the material and ϵ_{rr} is the strain in the radial direction

The Poisson's ratio of the foam used for the current experiment was determined from uniaxial tensile test. A dog-bone specimen was loaded uniaxially and using the DIC technique the three strain components; ϵ_x , ϵ_y and ϵ_{xy} , at the center of the gage length were determined and these value were used to obtain the poisson's ratio using equation below.

$$\nu = -\frac{\epsilon_y}{\epsilon_x} \quad (5)$$

DIGITAL IMAGE CORRELATION

Usually a single strain gage positioned in a specific direction is used to determine the fracture stress intensity factor using a three term solution [7]. However it is very difficult to put a strain gage on foam materials and get a correct strain signal. Furthermore, the strain gage only gives a single data point and it is very sensitive to the direction of the gage position. To avoid this problem a digital image correlation technique is used. In these fracture tests, the foam specimen only undergoes small amount of deformation before failure and the out-of-plane deformation is negligible. Therefore, the tests are considered as a 2-D and only a single camera is used to record the images. Digital images of the sample at several deformation steps were taken using a high speed CCD camera. A 2D digital image correlation (DIC) technique was used to obtain the displacement and strain fields.

In the case of a single strain gage technique, usually a prior knowledge of the plastic zone is required to accurately determine stress intensity factor from a single point value. However, in the current study, a series of single points are considered, and hence knowledge of the plastic zone prior to the experiment was not important. First the full strain field around the crack tip was generated, and then strain data at different radius were considered and used to calculate the stress intensity factor.

MULTIPLE POINT MANY-TERM SOLUTION

An overdeterministic approach to determine the stress intensity factor from many-term solution by using multiple strain gages proposed by Berger and Dally [1988] was adapted and used in the present study in conjunction with multiple strain values obtained from the DIC. The technique allows considering a larger number of strain points at a location far from the crack-tip where the plastic-zone correction is negligible and many terms in order to account for the higher order terms.

Unlike multiple strain gages, the DIC technique is full field and makes choosing strains at any location easy. Furthermore, since the three direction strain fields can be obtained at each point, a transformation of the strain field equations to the radial direction is not required. In the present study, a six term series expression of strain field was considered. The stress intensity factor is given by the relation

$$K_I = A_0 \sqrt{2\pi r} \quad (6)$$

Where A_0 , is the first order coefficients

A large number of points were considered and the unknowns were solved using a least-squares approach.

RESULTS AND DISCUSSIONS

TENSILE STRENGTH

The tensile load measured directly through the load cell was used to calculate the tensile strength and the average of strains along the defect section obtained from the DIC was used to calculate the corresponding strain. The net section strength, in the case of a specimen with sharp cracks, a notch and a hole, is defined as the tensile load divided by the remaining intact area in the section with the defect. A typical strain field near the circular hole under a tensile load is shown in Fig. 3. The strain time plot at different points along the cross-section of the specimen with center hole is shown Fig. 4. The average of these strains along the diameter of the hole is used in the strain-stress plot.

Typical stress-strain plot for all the specimen geometries considered are plotted in Fig. 5. The result was compared with the dog-bone tensile experiment of the intact specimen. From the figure it is clear that, the specimens without defect showed a typical strain-stress plot of a soft material, yielding followed by hardening and failure. The entire specimens with discontinuity shows a similar trend and result irrespective of the type of defects considered. In the case of specimens with defects, the failure takes place before any hardening effect is observed. It can also be seen that, the specimens with defects show a higher tensile yield strength compared to the intact specimen. This could be due to the relocation of failure from the weak plane in the case of cracks with defects. The failure stress is about the same for the both case, with defects and without but the failure strain decrease in the case of specimen with defects compared to specimen without defect. The failure strain in the case of specimen without any defect is about 10 % and the failure strain for specimens with defects is about 3 %.

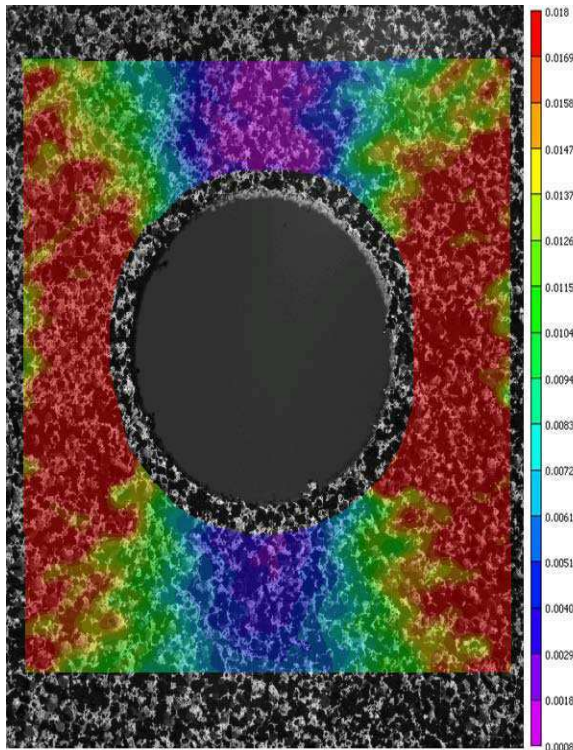


Fig 3 A typical DIC strain field for tensile specimen With a center hole (CH) under tension

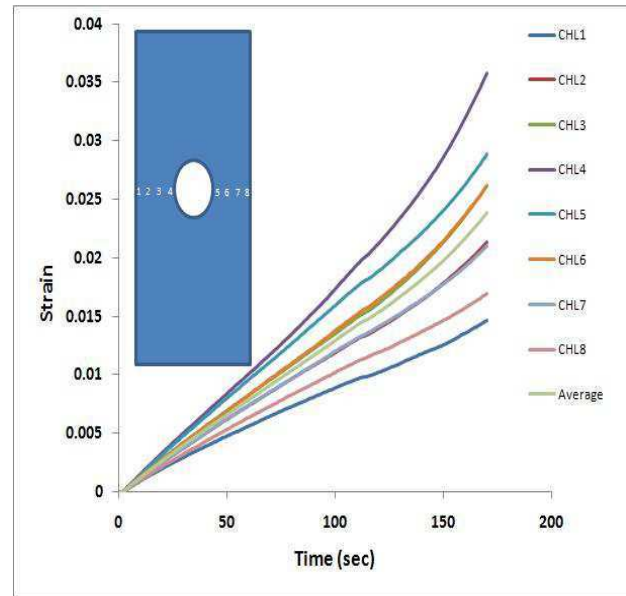


Fig 4 Strain-time plots along the midline of the hole in tensile specimen with a center hole (CH) under tension

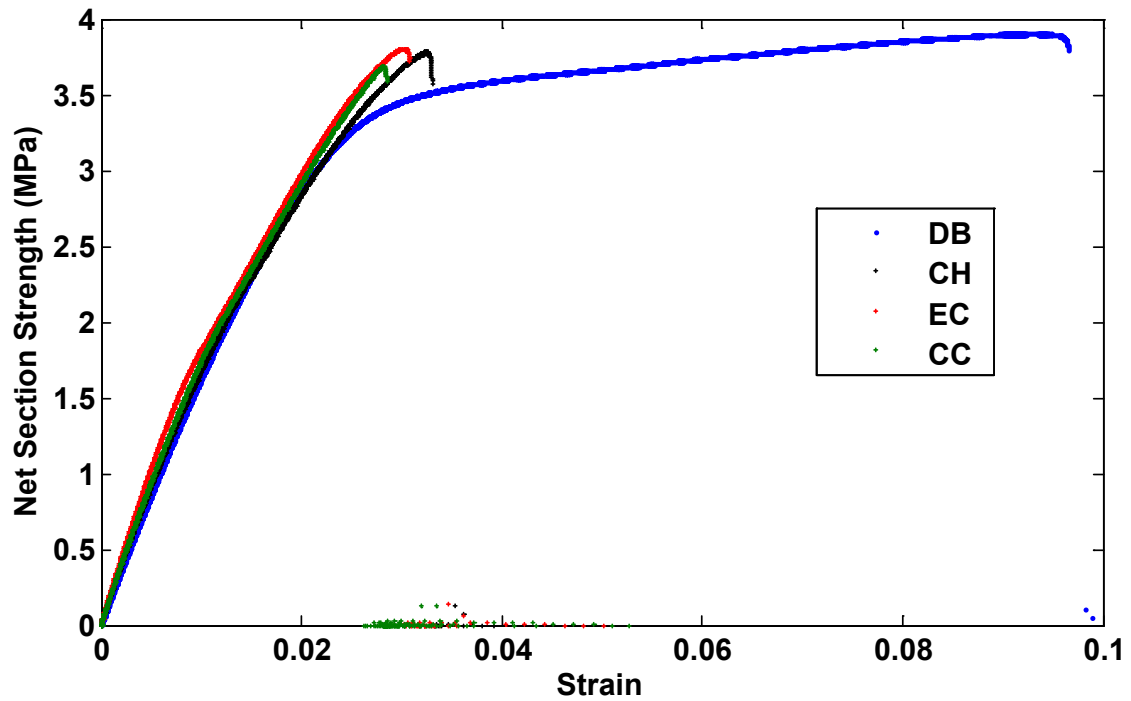


Fig 5 Net section strength-strain plot for different tensile specimen geometries

STRESS INTENSITY FACTOR

A typical load - deflection curve obtained from SENB experiment is plotted in Fig.6. The stress intensity factor was calculated using Eq. 1 and the critical load from the load-deflection curve. The average value of K_I obtained from the critical load measurement is $0.39 \text{ MPa m}^{1/2}$ with in an error of -0.011 to $+0.028$.

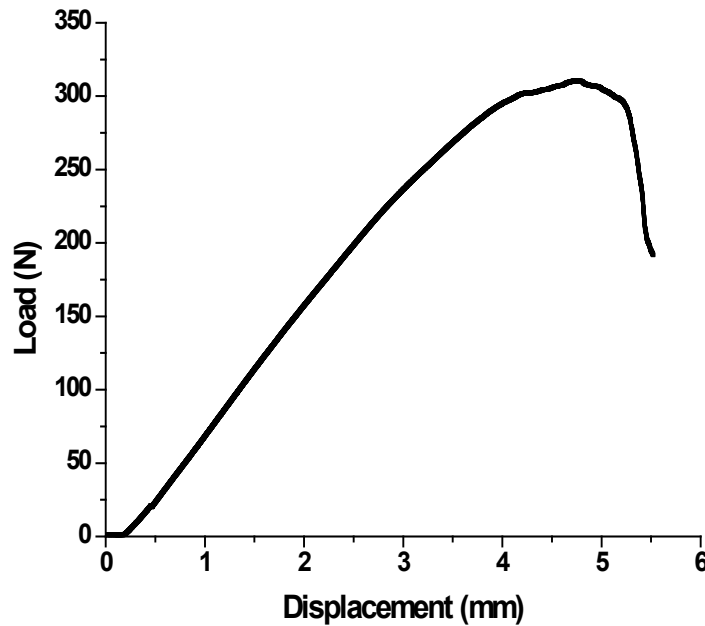


Fig 6 Typical load displacement curve for three-point bend test

The displacement and strain fields around the crack tip were calculated from the acquired image using vic2D software provided by correlated soln. inc. Fig. 7(a) shown a typical spackled pattern of three-point bend testing specimen, and Fig. 7(b) shows the strain contour around the crack before the crack propagates. The strain fields are used to calculate K_I using Eq. 5 and Eq. 6.

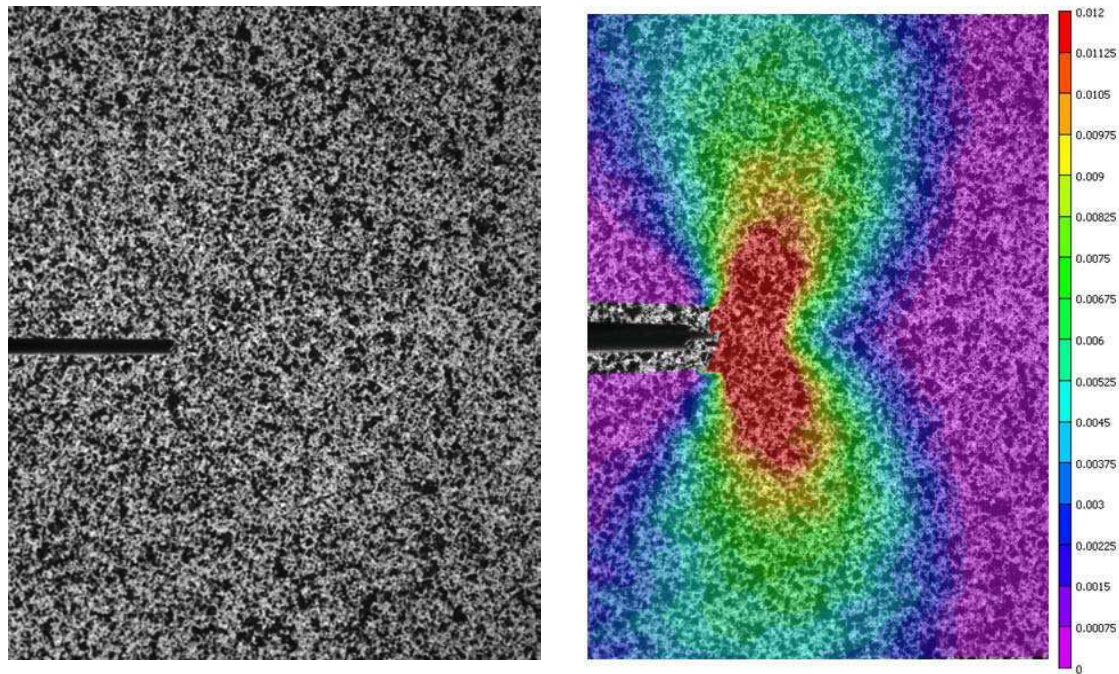


Fig 7 A typical three point bending specimen (a) DIC speckle pattern, (b) strain field near the crack tip

The Poisson's ratio for the foam material considered is 0.22 and results in $\alpha = 64.68$ and $\theta = 78.65$. Using these two angles, multiple points at different radius were considered and Eq. 5 was used to calculate the stress intensity factor.

Eq. 7 was also used to calculate the stress intensity factor from the multiple strain points. The value of K_I is very close to the one obtained in the above two cases, with average value of $K_I = 0.39 \text{ MPa m}^{1/2}$. Using the calculated stress intensity factor and constants, the strain field was generated as shown in Fig. 8. It is clearly seen that, the strain field, e_{yy} regenerated from the calculated K_I and the corresponding coefficients matches well with the original strain field directly obtained from the DIC Fig. 7 (b).

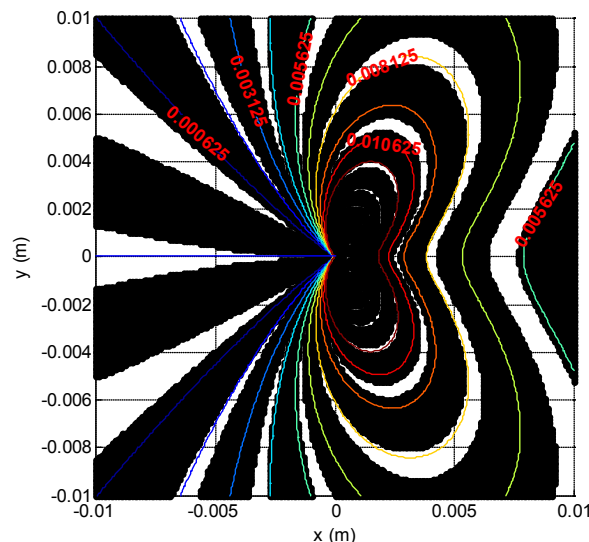


Fig 8 Opening mode strain field regenerated from calculated K_I and corresponding coefficients

CONCLUSION

An experimental investigation on the effects of holes, cracks and notches on tensile strength of polymer foam is performed. For specimens with cracks, notches and circular holes, the net section strength showed a notch-strengthening effect, the net section strength is higher compared with the specimen without defect. Though the failure stress is about the same, specimens with discontinuity failed at a lower strain compared with the intact specimen, indicating a presence of a strain concentration around the defects sections. The presence of discontinuity in polymer foam decreases the failure strain and the energy associated with it. Currently, because of their good energy absorption mechanism, foams are used in sandwich structures. Hence using strains in characterizing failure criteria will be appropriate. Furthermore fracture experiments have been performed and the stress intensity factor was obtained.

ACKNOWLEDGMENT

This work was supported by the Office of Naval Research (Dr. Y. D. S Rajapakse, Program Manager) and is gratefully acknowledged.

REFERENCES

- [1] Md. E. Kabir, M.C. Saha, S. Jeelani, "Tensile and fracture behavior of polymer foams", *Material Science and Engineering A*, 429, 225-235 (2006).
- [2] Erheng Wanga, Nate Gardner and Arun Shukla, "The blast resistance of sandwich composites with stepwise graded cores", *International Journal of Solids and Structures*, 46 (18-19), 3492-3502 (2009).
- [3] L.J. Gibson. M.F Ashby, "Cellular Solids: structure and properties", 2nd ed., Cambridge University Oxford, 1997.
- [4] E.W. Andrews and L. J. Gibson, "The influence of cracks notches and holes on the tensile strength of cellular solids", *Acta Materialia*, 49, 2975-2979 (2001).
- [5] E.W. Andrews and L. J. Gibson, "The influence of crack-like defects on the tensile strength of an open-cell aluminum foam", *Scripta Materialia*, 44, 1005-1010 (2001).
- [6] A. Paul, T. Seshacharyulu and U. Ramamurty, "Tensile strength of closed-cell al foam in the presence of notches and holes", *Scripta Materialia*, 40 (7), 809-814 (1999).
- [7] J.W. Dally and R.J. Sanford, "Strain-gage methods for measuring the opening-mode stress-intensity factor, k ," *Experimental Mechanics*, 27 (4), 381-388, (1987).
- [8] J.R. Berger and J.W. Dally, "An overdeterministic approach for measuring k , using strain gages" *Experimental Mechanics*, 28 (2), 142-145 (1988).

Crack Growth in Three-Point Bend Specimens Made of Polymeric Foams

E.E. Gdoutos and G. Papakaliatakis

Office of Theoretical and Applied Mechanics of the Academy of Athens
School of Engineering, Democritus University of Thrace
GR-671 00 Xanthi, Greece
egdoutos@civil.duth.gr

ABSTRACT

The problem of crack growth in a three-point bend specimen made of polymeric foams is investigated. Polymeric foams are anisotropic materials and cracks, generally, propagate under mixed-mode loading. The axes of material anisotropy are inclined with respect to the crack plane. Due to the anisotropy of the material crack kinking occurs even though the applied load is symmetrical with respect to the crack plane. The study will take place within the frame of linear elastic fracture mechanics of anisotropic media. The strain energy density criterion will be used for the determination of the critical load of crack initiation and crack growth path under mixed-mode loading. The opening-mode and sliding-mode stress intensity factors are determined by a finite element program. A special circular core element surrounding the crack tip with 19 nodes is used. The core element is joined to the conventional 12-node quadrilateral element by requiring that the displacement at the nodes on the circumference of the core element match the corresponding singular solution. Results are obtained for the critical load of crack initiation and crack growth trajectories as a function of the orientation of the axes of material symmetry and the anisotropy of the material.

Introduction

Cellular materials have extensively been used in sandwich construction due to their excellent properties, such as high specific modulus and strength, low weight, good thermal insulation and low cost. The mechanical behavior of cellular materials has been studied in [1-4]. It was found that the compressive stress-strain behavior of PVC cellular foams consists of an initial relatively small and stiff elastic regime, an extended stress plateau regime and a final regime in which densification of the material takes place. In the stress plateau regime the cells of the foam collapse, while the average stress remains almost constant during the instability spread through the material. Axial compression produces little lateral spreading resulting to almost zero Poisson's ratio. When all of the cells collapse the material is densified and its stiffness increases. As a consequence of such behavior foams change their volume during plastic compression. This is contrary to dense solids which are incompressible during plastic deformation. On the contrary, the uniaxial stress-strain behavior in tension is nonlinear elastic without any identifiable yield region.

The objective of this work is to study the problem of crack growth in a three-point bend specimens in a cross-linked polymeric foam under the commercial name Divinycell H250 with a density of 250 Kg/m^3 . The problem is analyzed by finite elements. The results of stress analysis are coupled with the strain energy density theory to obtain crack growth trajectories for various values of the angle of orientation of the axes of anisotropy of the material with respect to the loading direction.

Mechanical Characterization of Foam Materials

The study will include many types of fully cross-linked PVC closed-cell foams under the commercial name Divinycell H80, H100, H160, H250 with densities of 80, 100, 160 and 250 kg/m³, respectively, and balsa wood. Figure 1 shows the stress-strain curves of Divinycell H250 in tension and compression. Note that the uniaxial stress-strain behavior in tension is nonlinear elastic without any identifiable yield region. In uniaxial compression the material is nearly elastic-perfectly plastic in the initial stage of yielding. Mechanical properties of materials studied are shown in Table 1. All Divinycell H80, H100, H160 and H250 materials exhibit axisymmetric anisotropy with much higher stiffness and strength in the cell (3-direction) than the in-plane direction. The ratio of the stiffness in the cell (e-direction) to the in-plane direction is of the order of 1.5. The anisotropy of balsa wood is more pronounced with the above ratio equal to 42. All materials display different behavior in tension and compression with tensile strengths much higher than corresponding compressive strengths.

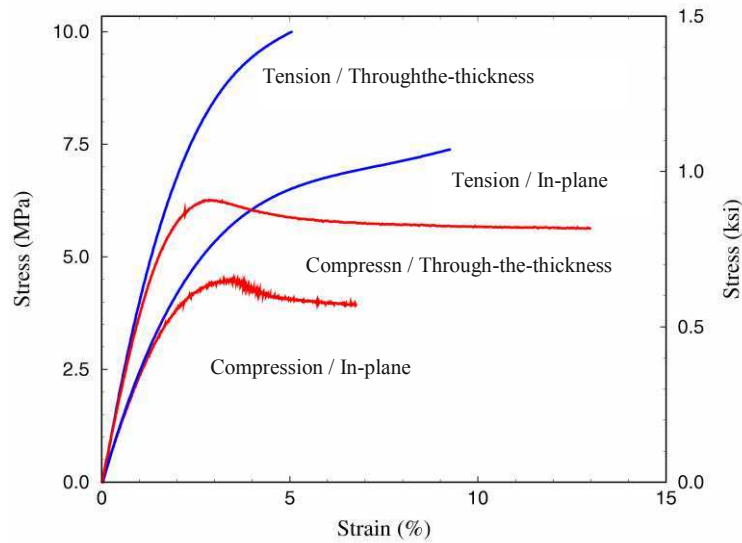


Fig. 1: Stress-strain curves of Divinycell H250 PVC foam, in tension and compression.

Strain Energy Density Criterion

The basic quantity in the strain energy density theory for crack problems is the strain energy density function dW/dV , which can be put in the form [5-7]:

$$\frac{dW}{dV} = \frac{S}{r} \quad (1)$$

where S is the strain energy density factor and r is the distance measured from the crack tip.

For plane elastic problems under conditions of plane stress the strain energy density function is given by

$$\frac{dW}{dV} = \frac{1}{2} (\sigma_x \epsilon_x + \sigma_y \epsilon_y + \tau_{xy} \gamma_{xy}) \quad (2)$$

where σ_x , σ_y , τ_{xy} are the stress and ϵ_x , ϵ_y , γ_{xy} are the strain components.

The strain energy density factor S is given by [5-7]:

$$S = A_{11}k_1^2 + 2A_{12}k_1k_2 + A_{22}k_2^2 \quad (3)$$

where

$$A_{11} = \frac{1}{4} [\alpha'_{11}A^2 + \alpha'_{22}C^2 + \alpha'_{66}E^2 + 2\alpha'_{12}AC + 2\alpha'_{16}AE + 2\alpha'_{26}CE] \quad (4a)$$

$$A_{12} = \frac{1}{4} [\alpha'_{11}AB + \alpha'_{22}CD + \alpha'_{66}EF + \alpha'_{12}(AD + BC) + \alpha'_{16}(AE + BE) + 2\alpha'_{26}(CE + DE)] \quad (4b)$$

$$A_{22} = \frac{1}{4} [\alpha'_{11}B^2 + \alpha'_{22}D^2 + \alpha'_{66}F^2 + 2\alpha'_{12}BD + 2\alpha'_{16}BF + 2\alpha'_{26}DF] \quad (4c)$$

with

$$A = \operatorname{Re} \left[\frac{s_1 s_2}{s_1 - s_2} \left(\frac{s_2}{z_2} - \frac{s_1}{z_1} \right) \right], \quad B = \operatorname{Re} \left[\frac{1}{s_1 - s_2} \left(\frac{s_2^2}{z_2} - \frac{s_1^2}{z_1} \right) \right] \quad (5a)$$

$$C = \operatorname{Re} \left[\frac{1}{s_1 - s_2} \left(\frac{s_1}{z_2} - \frac{s_2}{z_1} \right) \right], \quad D = \operatorname{Re} \left[\frac{1}{s_1 - s_2} \left(\frac{1}{z_2} - \frac{1}{z_1} \right) \right] \quad (5b)$$

$$E = \operatorname{Re} \left[\frac{s_1 s_2}{s_1 - s_2} \left(\frac{1}{z_1} - \frac{1}{z_2} \right) \right], \quad F = \operatorname{Re} \left[\frac{1}{s_1 - s_2} \left(\frac{s_1}{z_2} - \frac{s_2}{z_1} \right) \right] \quad (5c)$$

and

$$k_1 = \frac{K_1}{\sqrt{\pi}} \quad k_2 = \frac{K_2}{\sqrt{\pi}}. \quad (6)$$

In the above equations α_{ij} are the compliance coefficients of the anisotropic material relating stress and strain, K_1 and K_2 are the stress intensity factors which dictate the stress field in the neighborhood of the crack tip, $z_1 = x_1 + iy_1$, $z_2 = x_1 - iy_1$ are complex numbers, and the other coefficients are related to the anisotropic behavior of the material [4-6].

Consider a plate with a through-the-thickness crack of length $2a$ that is subjected to a uniaxial stress σ perpendicular to the crack plane. The axis x' of orthotropy of the material makes an angle φ with the crack axis, x (Fig. 1). The compliance coefficients α'_{ij} referred to the system $x'y'$ (Fig. 1) are related to the coefficients a_{ij} referred to the system xy by the following equations [5-7]

$$\begin{aligned} \alpha'_{11} &= \alpha_{11} \cos^4 \varphi + (2\alpha_{12} + \alpha_{66}) \sin^2 \varphi \cos^2 \varphi + \alpha_{22} \sin^4 \varphi + (\alpha_{16} \cos^2 \varphi + \alpha_{26} \sin^2 \varphi) \sin 2\varphi, \\ \alpha'_{22} &= \alpha_{11} \sin^4 \varphi + (2\alpha_{12} + \alpha_{66}) \sin^2 \varphi \cos^2 \varphi + \alpha_{22} \cos^4 \varphi - (\alpha_{16} \cos^2 \varphi + \alpha_{26} \cos^2 \varphi) \sin 2\varphi, \end{aligned}$$

$$\begin{aligned}
\alpha'_{12} &= \alpha_{12} + (\alpha_{11} + \alpha_{22} - 2\alpha_{12} - \alpha_{66})\sin^2 \varphi \cos^2 \varphi + \frac{1}{2}(\alpha_{26} - \alpha_{16})\sin 2\varphi \cos 2\varphi, \\
\alpha'_{66} &= \alpha_{66} + 4(\alpha_{11} + \alpha_{22} - 2\alpha_{12} - \alpha_{66})\sin^2 \varphi \cos^2 \varphi + 2(\alpha_{26} - \alpha_{16})\sin 2\varphi \cos 2\varphi, \\
\alpha'_{16} &= [\alpha_{22} \sin^2 \varphi - \alpha_{11} \cos^2 \varphi + \frac{1}{2}(2\alpha_{12} + \alpha_{66})\cos 2\varphi]\sin 2\varphi + \alpha_{16} \cos^2 \varphi (\cos^2 \varphi - 3\sin^2 \varphi) \\
&\quad + \alpha_{26} \sin^2 \varphi (3\cos^2 \varphi - \sin^2 \varphi), \\
\alpha'_{26} &= [\alpha_{22} \sin^2 \varphi - \alpha_{11} \sin^2 \varphi - \frac{1}{2}(2\alpha_{12} + \alpha_{66})\cos 2\varphi]\sin 2\varphi + \alpha_{16} \sin^2 \varphi (3\cos^2 \varphi - \sin^2 \varphi) \\
&\quad + \alpha_{26} \cos^2 \varphi (\cos^2 \varphi - 3\sin^2 \varphi),
\end{aligned} \tag{7}$$

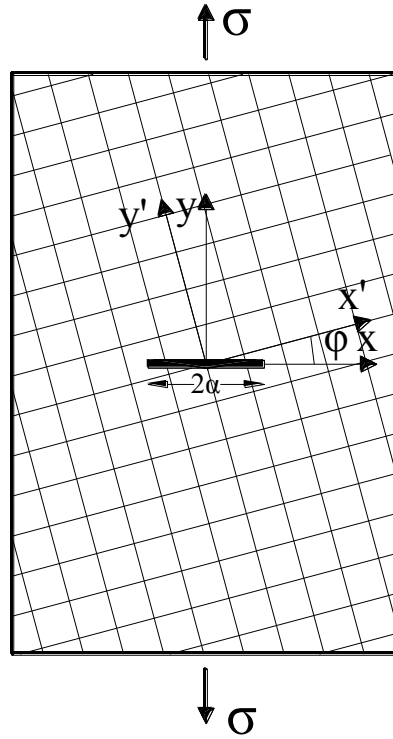


Fig.2 A cracked plate with a crack perpendicular to the applied load at an angle with the direction of the axis of material orthotropy of the material

According to the strain energy density theory unstable crack growth takes place in the radial direction along which S becomes minimum. This condition is mathematically put in the form:

$$\frac{\partial S}{\partial \theta} = 0, \quad \frac{\partial^2 S}{\partial \theta^2} > 0. \tag{8}$$

This equation is used for the determination of the critical angle θ_c of initial crack growth.

Unstable crack growth occurs when $S_{\min}(\theta_c)$ takes its critical value S_c which is an intrinsic material parameter, that is,

$$S_{\min}(\theta_c) = S_c. \quad (9)$$

Equations (8) and (9) will be used for the determination of the critical quantities at crack instability for the case of Fig. 1.

Results

Results were obtained for a three-point bend specimen with a symmetrical crack (Fig. 3). The axis of material symmetry made an angle φ with respect to the crack axis (Fig. 2). The stress analysis of the plate was performed by the ABACUS computer program. Figs 4 and 5 present the finite element idealization of the specimen in the vicinity of the crack tip. Fig. 6 presents the variation of strain energy density function dW/dV along the circumference of a circle centered at the crack tip for $\varphi = 0, 30^\circ$ and 60° . The values of θ at which dW/dV presents local minima are the critical values of the angle of initial crack growth.

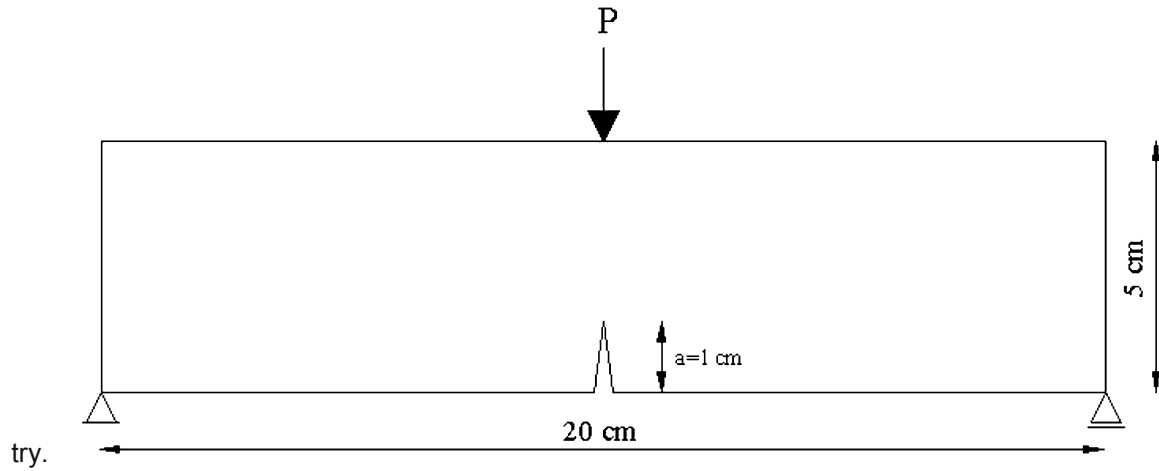


Fig. 3 A three-point bend specimen with a symmetrical crack

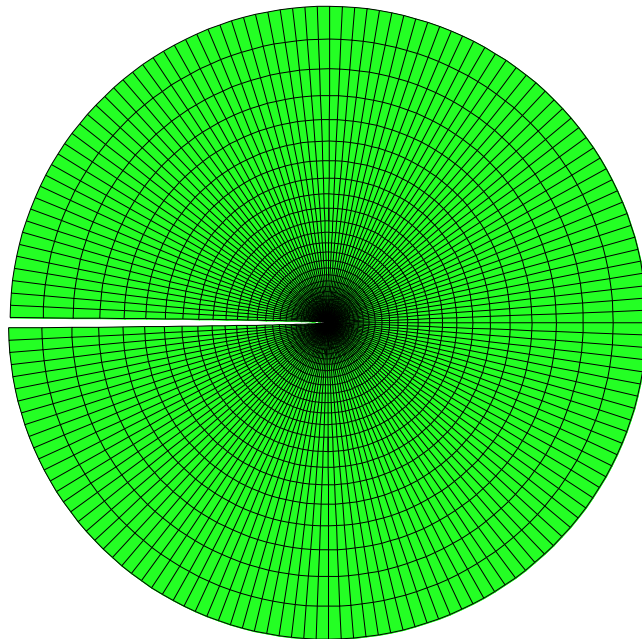
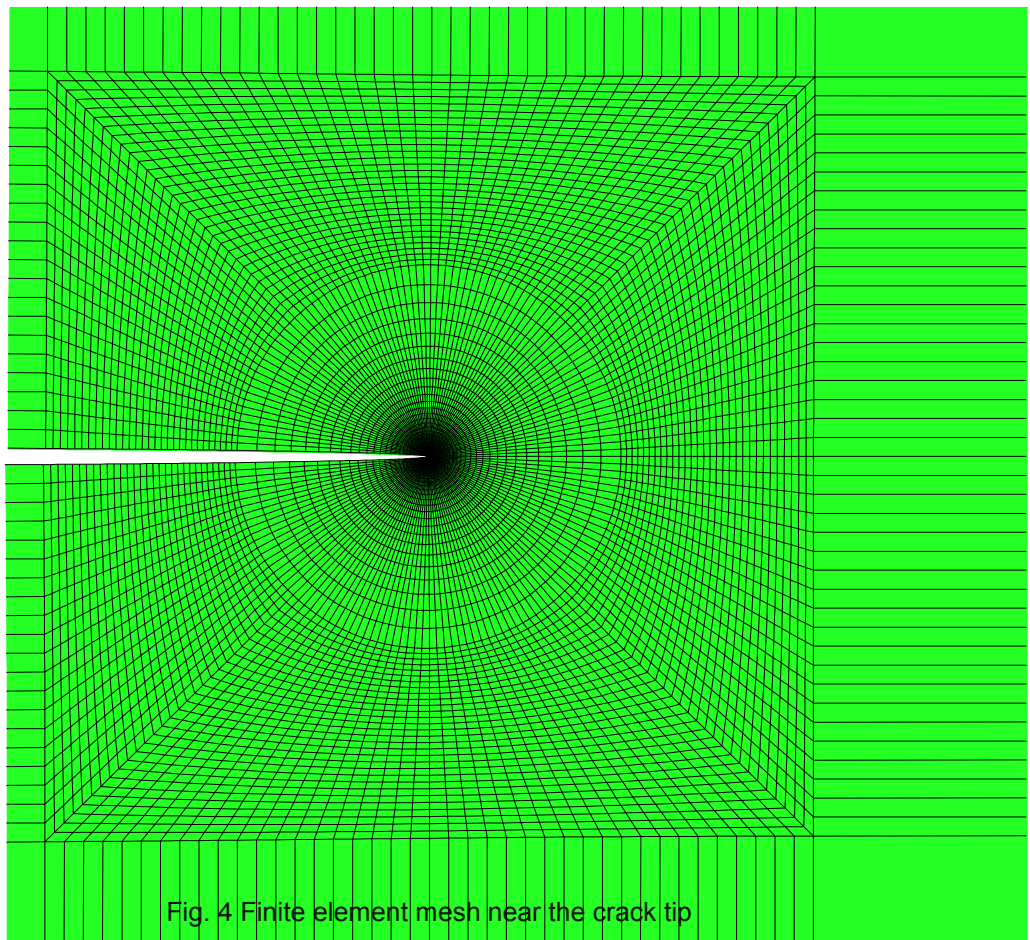


Fig. 5 Detailed mesh

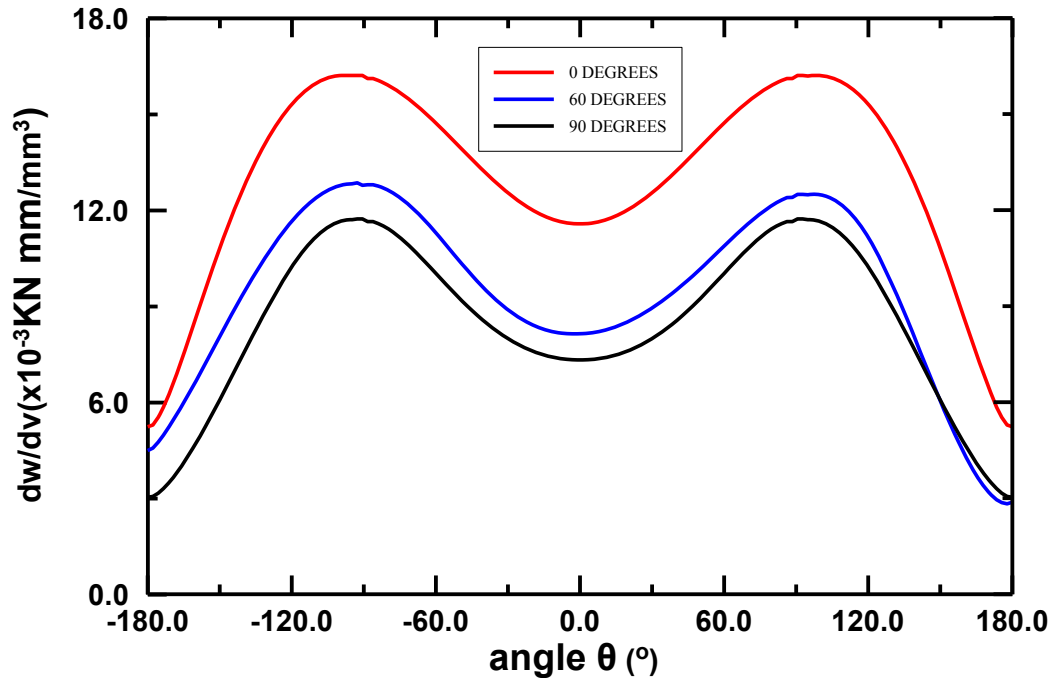


Fig. 6 Variation of strain energy density function dW/dV versus polar angle θ around the circumference of a circle surrounding the crack tip at a distance of 0.012 mm from the crack tip for $\phi = 0, 30^\circ$ and 60° . Crack grows in the direction of local minimum of strain energy density function

Conclusions

The crack growth in polymeric foams which present mechanical anisotropic behavior was studied. The case of a three-point bend specimen with the axes of material anisotropy at an angle with respect to the crack plane is analyzed. From the results of stress analysis in conjunction with the strain energy density theory the mixed-mode crack growth behavior of the plate was obtained. Results for the angle of initial crack growth for various orientations of the axes of anisotropy of the material with respect to the loading direction were reported.

References

- [1] Gibson L.J. and Ashby, M.F., "Cellular Solids," Cambridge University Press (1997).
- [2] Gdoutos, E.E., Daniel, I.M. and Wang, K.-A. "Multiaxial Characterization and Modelling of a PVC Cellular Foam," *J. Therm. Comp. Mat.* **14**, 365-373 (2001).
- [3] Gdoutos, E.E., Daniel, I.M. and Wang, K.-A., "Failure of Cellular Foams under Multiaxial Loading," *Comp Part A*, **33**, 163-176 (2002).
- [4] Gdoutos E.E. and Abot, J.L., "Indentation of a PVC Cellular Foam," In: *Recent Advances in Experimental Mechanics - In Honor of Isaac M. Daniel*, Kluwer Academic Publishers pp. 55-64 (2002).
- [5] Gdoutos, E.E., "Problems of Mixed-Mode Crack Propagation," Martinus Nijhoff Publishers (1984).
- [6] Gdoutos, E.E., "Fracture Mechanics Criteria and Applications," Kluwer Academic Publishers (1990).
- [7] Gdoutos, E.E., "Fracture Mechanics – An Introduction," Second Edition (2005).

Reliability Evaluation of Conformal Coatings for Tin Whisker Failure Mitigation in Accelerated Testing Conditions

K. H. Mahan, B. Han, S. Han, M. Osterman
Department of Mechanical Engineering
University of Maryland

Abstract

Tin whisker growth has become a reliability concern during the course of Pb-free solder transition. A common mitigation strategy is to use conformal coatings to prevent electrical shorts by tin whiskers. However, recent research indicates that under elevated temperature and humidity, or in areas of thin covering, whiskers can grow and penetrate conformal coatings. Additionally, for long environmental exposure, the effectiveness of conformal coatings may be compromised.

The main objective of this work is thus to develop a test procedure (1) to determine the initial adhesive and cohesive strengths of an applied coating and (2) to subsequently assess the rate of degradation under accelerated testing conditions for long-term evaluation.

We propose a blister-type test method to assess both the adhesive and cohesive strengths of conformal coatings. The proposed approach offers unique advantages. The testing method mimics actual tin whisker growth and allows for a quantitative comparison of the adhesive and cohesive strengths of the coating. In addition, blister test specimens can be subjected to harsh environments, which make this test perfect for accelerated testing.

In the typical blister test of adhesive strength, pressure is applied through a hole in a substrate. As the pressure is increased, the coating layer on top of the substrate will begin to bulge out like a blister. The blister will continue to grow until it reaches a maximum blister height, at which point delamination will occur [1]. In a modified blister test for cohesive strength, a thin film coating will be fixed between two copper substrates. A ramp pressure will be applied to the hole in the lower substrate until the blister reaches a critical height, at which point the film will fail due to rupture.

The typical blister tests of coating layers are marred by the presence of large scatter in their results, making the quantitative assessment of adhesion difficult, and the ability to distinguish the effects of environmental exposure even more challenging. In the proposed study a novel concept to create a pre-defined initial crack diameter is proposed and implemented to reduce deviation in test results.

Two common conformal coatings, silicone rubber and urethane, were selected for testing. Preliminary experimental results indicate that silicone coating samples fail due to the limited

cohesive strength of the coating, while urethane coating samples fail either cohesively or adhesively due to weak adhesion between the coating and the tin-coated substrate. Each conformal coating was tested before and after subjecting it to two accelerated testing conditions. The first accelerated testing condition is a high temperature and humidity chamber maintaining the specimens at 55°C/85%RH for a 2000 hour period. Adhesion and cohesion testing was then performed every 1000 hours. The second accelerated testing condition is a temperature cycling chamber which cycled the temperature from -55°C to 125°C for 1000 cycles. Testing was performed for every 500 cycles in the T/C chamber. From the blister test for adhesive strength, the critical pressure is determined, and an analytical equation developed by Gent and Lewandowski [2] is applied to determine the adhesion strength. From the cohesive blister test, the maximum blister height is determined, and a finite element model is employed to determine the cohesive strength.

The effectiveness of the proposed test procedure is reviewed by using the experimental data of initial properties. The results from the accelerated testing are followed to evaluate the key parameters of two conformal coatings for long-term reliability.

References:

1. Williams, M. L. (1969). "The Continuum Interpretation for Fracture and Adhesion." J. Appl. Pol. Sci. **13**: 29-40.
2. Gent, A. N. and L. H. Lewandowski (1987). "Blow-off Pressures for Adhering Layers." J. Appl. Pol. Sci. **33**: 1567-1577.

Investigation of Manganese Cobalt Oxide (MCO) Coatings on Fuel Cell Interconnects

S. Akanda and Mark E. Walter,
Department of Mechanical Engineering
The Ohio State University, Columbus, OH 43210

ABSTRACT

Planar Solid Oxide Fuel Cells (SOFCs) are composed of repeating cathode-electrolyte-anode units separated by electrically conductive interconnects. With the reduction in fuel cell operating temperature to approximately 800°C, it has become possible to use chromium-based, ferritic stainless steel or Crofer for interconnects. These interconnects must survive the high temperature oxidizing and reducing environments while maintaining electrical conductivity. Unfortunately the formation of chromium oxide scale poisons the cell by significantly reducing cathodic activity. Chromium scale formation can be inhibited by applying an electrically conductive manganese cobalt oxide (MCO) spinel coating to the interconnect prior to its installation in the fuel cell. The most cost-effective way to apply protective coatings to interconnects involves spray coating. To investigate the quality of the coatings and the coating adhesion, four-point bend experiments were undertaken at room temperature. Tensile cracking patterns on the convex surfaces of the bend specimens were used to determine the interfacial shear strengths of the coatings. SEM images of the cracked coating surfaces were processed to analyze the interface failure mechanisms, the crack spacing, and areas that spalled at higher strains. These investigations were able to show distinct differences between coatings formed with different processes parameters.

Introduction

With high efficiencies and harmless by-products, planar SOFCs have the potential to radically alter the production and distribution of electricity. Although SOFCs operate at temperatures of 700-850°C, SOFCs have several advantages over other fuel cell types. The principal advantage is fuel flexibility. Because the ceramic membrane is an oxygen ion conductor, oxygen partial pressure gradients create the voltage that allows cell operation. Thus both H₂ and CO can be consumed as fuel, allowing a range of reformed hydrocarbon fuels to be considered. The high operating temperatures create advantages both by enabling catalysis of the fuels without special, expensive materials and by paving the way to enhanced efficiency within combined cycle systems (e.g., [1]). Another important advantage is the enhanced tolerance of SOFCs to fuel impurities. CO, which poisons proton exchange membrane (PEM) fuel cells, is a *fuel* for SOFCs. H₂S, another common contaminant in hydrocarbon and some biomass-derived hydrogen fuels, is tolerated in SOFCs currently being developed; competing fuel cell systems require large desulfurizers which reduces overall system efficiency. SOFCs are not without their own challenges, however. In particular, SOFC materials selection, cell and stack design, manufacturing, conditioning, sealing, and degradation/failure are active subjects for research and development.

Individual fuel cells are connected in series through metallic interconnects (ICs) to construct a fuel cell stack. In addition to acting as electrical conductors for adjacent cathodes and anodes, interconnects also act as separators between anode-side fuel flow and cathode-side air flow. Interconnects should be electrically conductive, creep resistant, thermally conductive, chemically inert in oxidizing and reducing environments, low cost, and easy to

fabricate. For the following reasons, chromium based alloys such as ferritic stainless steels (17%Cr) or Crofer (23%Cr) are the most promising materials for interconnects in SOFCs: gas-tightness, low electrical resistivity, matched coefficient of temperature expansion (CTE), ease of fabrication, and cost effectiveness [2-3].

One major limitation of chromium-based interconnects is chromium migration to the cathode which is known as chromium degradation or chromium poisoning. Chromium alloys result in the formation and evaporation of chromium trioxide CrO_3 and chromium hydroxide $\text{CrO}_2(\text{OH})_2$, depending on the cathode side inlet atmosphere. Upon migration to the cathode active area, where oxygen is reduced to its oxide ions, these chromium based compounds may reduce back to Cr_2O_3 . As a result, the effective active area is decreased which in turn will significantly drop the efficiency of SOFCs. Also the formation of oxide scales on the surfaces of interconnects can lower the efficiencies of SOFCs because Cr_2O_3 is highly electrically resistive and it increases the contact area specific resistance (ASR).

Thus it is important for cathode-side metallic interconnects in high temperature fuel cell applications to inhibit chromium migration and to resist the oxidizing and corrosive environment. One way to achieve the necessary chemical inertness is to perform bulk surface modification by developing a thin, dense protective coating on the surface of the relatively thick interconnects. The protective layer acts as a diffusion barrier to the chemical reaction between interconnects and corrosive environment and thus slows the rates of chromium oxide scale formation.

Generally pervoskite materials with a chemical structure of $(\text{AB})_2\text{O}_3$, where A and B are metallic cations, are used as protective coatings. The most commonly used pervoskite materials are lanthanum-manganese oxide and lanthanum-cobalt/chromium oxide. One important drawback to using pervoskite materials is the lack of sufficient thermo-mechanical stability due to poor adhesion to interconnects and mismatched CTEs. Also, investigation by several researchers has indicated the reduction of chromium degradation by factor of 3 only while using pervoskite materials. This may still results in a significant amount of degradation of cell performance [4].

A promising alternative of pervoskite type composite is spinel structure material of $(\text{AB})_3\text{O}_4$ where A and B are again metallic cations. Other researchers have also recently used spinel manganese cobalt oxide as a protective layer in SOFC interconnects. Larring *et al* observed increased capability of $(\text{Mn},\text{Co})_3\text{O}_4$ to prevent chromium evaporation compared to that of pervoskite composites. In addition, the $(\text{Mn},\text{Co})_3\text{O}_4$ spinel protective layer showed well matched mechanical and thermal properties with that of substrate alloys. Moreover with iron (Fe) doping in the spinel manganese cobalt oxide, it was possible to achieve excellent electrical conductivity. The MCO protective layer can be screen printed or sprayed on the surfaces of interconnects prior to operation [4].

In practice, the mechanical integrity of protective coatings on interconnects is affected by complex thermo-chemical-mechanical conditions. The diffusion barrier which prevents the chemical attack can be severely damaged by the mechanical stress generated during oxide scale growth, by thermal cycling, and by mechanical loads associated with fuel cell operation.

The Pilling-Bedworth Ratio (PBR) is defined as the ratio of the volume of oxide to the metal consumed and is used to model stress generation during oxide scale growth [6]. The PBR term is alternatively defined by the ratio of the volume per metal ion in the oxide to the volume per metal atom in the metal. The PBR is successful in determining the qualitative nature of stress in the oxide scale during inward growth. When oxygen diffuses into the metal substrate, the oxide scale experiences compressive stresses for PBRs greater than 1 and tensile stresses for PBRs less than 1. The PBR is not able to predict stresses in oxide scales that grow through outward diffusion of the metal.

An important source of growth stress is epitaxial constraints. Differences between lattice parameters of the oxide and substrate cause stresses to become maximum in oxide-metal phase boundaries. The stresses fall off toward

the oxide surface. Borie *et al* [7] employed X-ray techniques to reveal that thin oxide films on copper are strained because of the epitaxial relationship between the oxide and underlying material. Epitaxial stresses are only important for thin oxide scale as they are inversely related to the oxide scale thickness.

Appleby *et al* [8] studied the effect of microstructural composition of oxide scale on growth stresses. Their study revealed that the transition of initially formed scale on the surface of $(\text{Cr,Fe})_2\text{O}_3$ to a scale with increasing Cr and decreasing Fe content caused tensile stresses to develop. A decrease in atomic volume associated with the transition is the apparent explanation for the tensile stress development.

The formation of fresh oxide inside the scale itself can be an important source of compressive stresses in oxide scales. Jaenicke *et al* [9] found that in the oxidation of copper, micro-cracking induced by the growth stresses provides pathways for gas migration. The availability of copper molecules resulted in the formation of fresh oxide in the scale. Since the new oxide has higher volume than the cracked volume, significant compressive stresses are developed and there is the further development of compressive stresses.

Disparity of Coefficient of Thermal Expansion (CTE) between oxide and substrate is arguably the most significant reason for residual stresses in the scale and substrate. These residual stresses form when cooling from oxidation temperature to room temperature. Mismatched CTEs also cause stress development during thermal cycling. Moreover with temperature changes, phase transformation in both the oxide scale and substrate can result in stress development.

Christl *et al* [10] incorporated acoustic emission techniques to detect thermal cycling-induced oxide scale cracking on low alloy steel. The oxidization temperature was 600°C and the alloy was cyclically cooled by 300°C . With AE analysis, it was possible to distinguish between different failure modes during cooling. Through-scale cracking led to many AE events with high amplitudes. During buckling and delamination of the scale, lower amplitude AE events were observed.

Zhang *et al* [11] analyzed AE data for 304 stainless steels which were oxidized in pure oxygen at 800°C for 20 hours and then cooled to room temperature by two different methods. In their first method, the test specimens were furnace cooled directly to room temperature and in the second method the specimens were cooled to an intermediate temperature, held at that temperature for 24 hours and then cooled to room temperature. If the specimen was cooled to room temperature directly, it cracked and spalled more extensively. When the cooling was interrupted at higher temperatures, creep relaxation of residual stresses caused the total number of AE events on further cooling to decrease. If the cooling was interrupted at lower temperatures and after extensive cracking and spalling, the scale fracture process stopped once the hold temperature had stabilized. An analysis of the AE data revealed that conditions for scale cracking follow a log-normal distribution with respect to average scale stress.

In different work, Zhang *et al* [12] monitored the scale cracking and spalling of Ni-30Cr alloys which were oxidized at 1000°C and then cooled to room temperature either by furnace cooling or constant rate cooling. Their AE results indicated the starting of cracking and spalling at a critical temperature. Cracking continued over a range of temperatures, indicating that there was a distribution of critical fracture stress throughout the scale. SEM analysis of the morphology of the fractured area showed that the interface between scale and substrate was relatively weak. Cooling led to first buckling and through thickness crack development and then final spallation of oxide scale.

In summary, oxide coatings are brittle in nature and exhibit little or no ductility. Growth stresses superimposed with thermal stresses can create complex stresses in the coating layer. These growth stresses usually result in coating fracture and failure. For weaker coating-substrate interfaces, oxide scales first buckle under high

compressive stresses and then spall if through-thickness cracks develop. For relatively stronger interfaces, shear cracks can form in the coating, which causes shear sliding in the cracked segment and finally spallation in the protective coating [13]. For SOFCs, when the protective coating layer fails, uncoated interconnect metal is exposed to the corrosive operating environment. The resulting damage and degradation to interconnect can cause significant degradation of the electrochemical performance of the SOFC.

With SOFCs operating in a complex thermo-chemical–mechanical environment, it becomes necessary to better understand the response of protective coatings on SOFC interconnects. Therefore, it is very important to characterize relevant SOFC coating-interconnect interfaces. Understanding the failure mechanisms in the interface will have positive impact in assessment of reliable interconnects for high temperature applications.

Several researchers have incorporated different experimental methods to characterize coating-interconnect interface systems in SOFCs. sun *et al* [14] performed stair stepping indentation tests to quantify the interfacial shear strength of oxide-Crofer systems in SOFCs along with finite element simulation. Critical load at which the scale spallation occurred was used to quantify the interfacial shear strength. However, indentation creates a plastically deformed zone beneath the surface which limits the depth of indentation to be less than coating thickness.

To investigate the coating-interconnect interfaces, four point bend experiments were performed at room temperature in the present work. The experimental set up was designed in such a way as to placing the brittle coating under tensile stresses. The strains required for coating failure/spallation were such that the ductile interconnect exceeded its elastic limit. The spacing between the resulting saturated parallel cracks in the coating surface was incorporated in the shear lag model to quantify interfacial shear strength. Fracture mechanics analysis was performed to obtain interfacial fracture energy from the strain at onset of spallation.

Experimental

The interconnect-MCO coating specimen were supplied by NexTech Materials Ltd. Fig.1 shows the necessary steps of developing the coating on the interconnect surface. Either SS441 (17% Cr) or Crofer (23% Cr) are used as interconnects. The $\text{Mn}_{1.5}\text{Co}_{1.5}\text{O}_4$ powder is synthesized to a slurry or ink by using an appropriate binder system. In the next step, the slurry or ink is sprayed to the interconnect surface at room temperature. In order to remove organic binders from the MCO coating, the coated samples are heat treated at high temperature in a reducing environment. For a final step, the spinel layer may be exposed to subsequent oxidation at high temperature. In the present analysis four types of specimen are considered. Type 1: Oxidized coating-Crofer substrate, Type 2: Reduced coating-Crofer substrate, Type 3: Oxidized coating-SS441 substrate, Type 4: Reduced coating-SS441 substrate. The specimen substrates were 80 mm in length, 10 mm in width, and 3 mm thick. The coating thickness ranged from 15 – 30 μm .

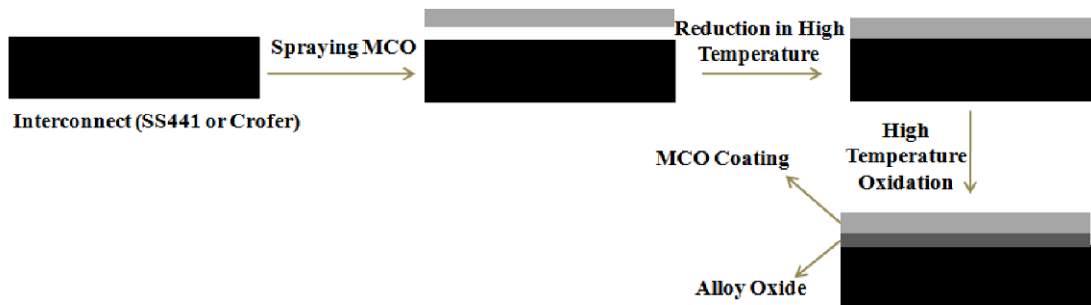


Fig.1 Flow chart of developing MCO coating on interconnects by NexTech Materials Ltd.

The four point bend fixture was mounted in a table-top servo-electric load frame from TestResources. The inner loading span was set to 20 mm while outer supporting span was set to 60 mm. AE was monitored using a Vallen-System AMSY-4. The AE sensor was placed on the specimen during the experiment. The transient stress wave generated from scale cracking and other failure phenomena was detected by the sensor. The signal was pre-amplified by 34 dB, and the signal threshold was set to 40 dB. The load frame data and AE data were synchronized for subsequent analysis of failure mechanisms.

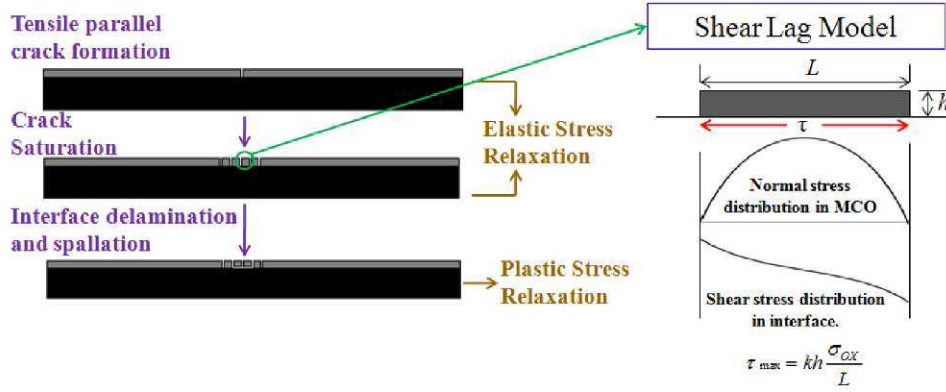


Fig. 2 Mechanism of elastic and plastic stress relaxation during experiment.

Fig.2 schematically illustrates the failure of the coating under tensile loading. Initial cracks are produced in the coating when the tensile stresses exceed the tensile strength of the brittle coating. During the rest of the experiment, tensile stresses are not transferred to the segments of coating directly from bend fixture. However the tensile stresses are transferred from the ductile substrate to the coating segments through interface as interfacial shear stress (shear-lag). As a consequence of transfer of stresses, tensile stresses continue to develop in the coating layer, creating further parallel cracks. The formation of multiple parallel cracks can be modeled as an elastic stress relaxation and cracking continues with strain until saturation. From the shear lag model, the shear stress at the interface can be calculated from the following equation [15], [16]:

$$\tau_{max} = kh \frac{\sigma_{ox}}{L} \quad (1)$$

where σ_{ox} is the tensile oxide strength, τ is the interfacial shear stress, h is the oxide thickness, L is crack spacing, and k is an integration constant which depends on the shear stress distribution along the interface. A sinusoidal shear stress distribution is assumed in the present analysis which results in $k = \pi$. Upon measuring the saturation crack spacing, it is possible to calculate the interfacial shear strength using Equation (1). The tensile oxide strength is calculated from the strain at which the oxide scale first cracks. The first energetic AE hit is assumed to correspond to the failure strain of the coating.

At higher strains (greater than 0.5%) the ductile substrate begins to undergo plastic deformation. The plastic stress relaxation can be modeled as interfacial slip and delamination and substrate yielding at the base of the parallel coating cracks [13]. Also at higher strain the coating spalls due to the effect of Poisson ratio which introduces compressive stress normal to the applied stress on the substrate. In the present work, it is assumed that the coating is perfectly adhered to the interconnect and is elastically strained during the experiment. This leads to the developing of elastic energy storage in the coating. Beyond a certain point, it is energetically favorable to release the stored elastic energy as interfacial fracture, resulting coating spallation. The interfacial fracture energy, G can be calculated from the relation [17]

$$G = Wh \quad (2)$$

where W is stored elastic energy in the coating per unit volume and h is coating thickness. W is a function of residual stress and stress-strain evolution on coating during the experiment. During the elastic deformation of the substrate, the compressive stress generated in the coating is calculated by

$$\sigma_c = \frac{E_c}{(1-\nu_c^2)} (\nu_c - \nu_s) \varepsilon_c \quad (3)$$

During the plastic deformation of the metal interconnect; the compressive stress is increased by the following relation:

$$\sigma_c = \frac{E_c}{(1-\nu_c^2)} \left[\varepsilon_c + \nu_c \left(\frac{1}{(1+\varepsilon_c)^2} - 1 \right) \right] \quad (4)$$

where E is elasticity, ν is Poisson ratio, and ε is strain. Subscript 'c' stands for coating and subscript 's' stands for substrate. Finally the stored elastic energy in the coating, W is calculated from the simple relation

$$W = \int \sigma d\varepsilon \quad (5)$$

During the plastic stress relaxation the crack spacing remains constant (saturated) as the shear stress at the interface exceeds the shear strength of the interface.

Results and Discussion

Figure 3 presents a typical stress-strain curve of a coating-interconnect composite system obtained from the load-frame data along with characteristic synchronized AE data for each specimen type. The AE data provides indication of cracking events. In Fig.3, for each type of specimen, cumulative AE data is observed to increase with imposed composite strain up to approximately 0.1% strain. The increasing nature of AE data in this phase denotes the formation of transverse parallel cracks on the coating as a consequence of stress transfer from substrate to the coating according to shear-lag theory. This phase is modeled as elastic stress relaxation. The flatness of AE nature in the next phase indicates the saturation of parallel cracks due to interface slipping or yielding. Measuring the spacing between parallel cracks in this phase, it is possible to calculate interfacial shear strength from equation 1. Interfacial shear strength indicates the capability of load transfer from substrate to coating through interface. The stronger the bond between coating and interconnect, the more the load is transferred through interface.

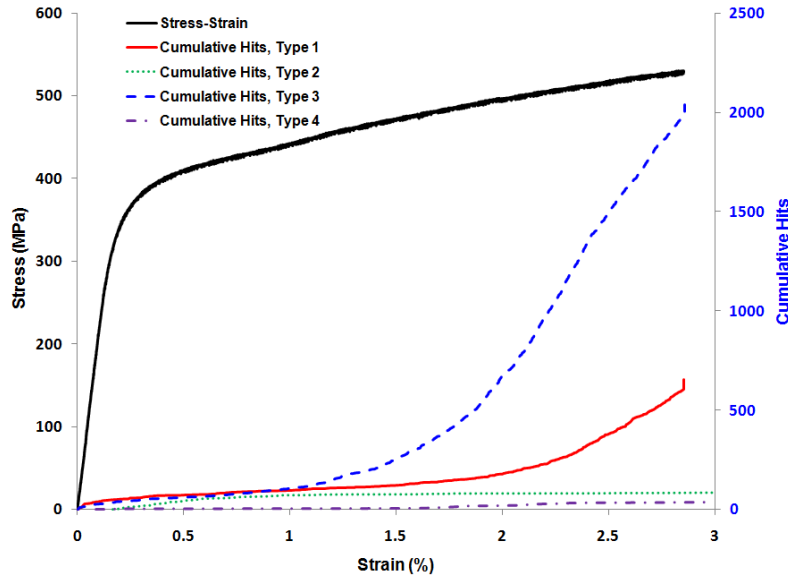


Fig.3 Stress-strain curve with synchronized AE data.

A distinct phase of AE data is seen when considering oxidized specimens (Type 1 and Type 3) during plastic stress relaxation (about 1.5-2% strain). In this phase, a sharp increase in the rate of AE events with strain is occurred. This sudden increase of AE events is not present for reduced specimens (Type 2 and Type 4). The higher rate of AE hits with strain indicates extensive interface delamination and spallation of oxidized specimens. Analyzing the AE data in this phase reveals decreased interfacial adhesion due to oxidation. Depending on the alloy composition of interconnects; different alloyed oxides are formed between MCO coatings and interconnect which are brittle in nature. The brittleness of alloyed oxide promotes more interfacial fracture and spallation as compared to reduced specimens.

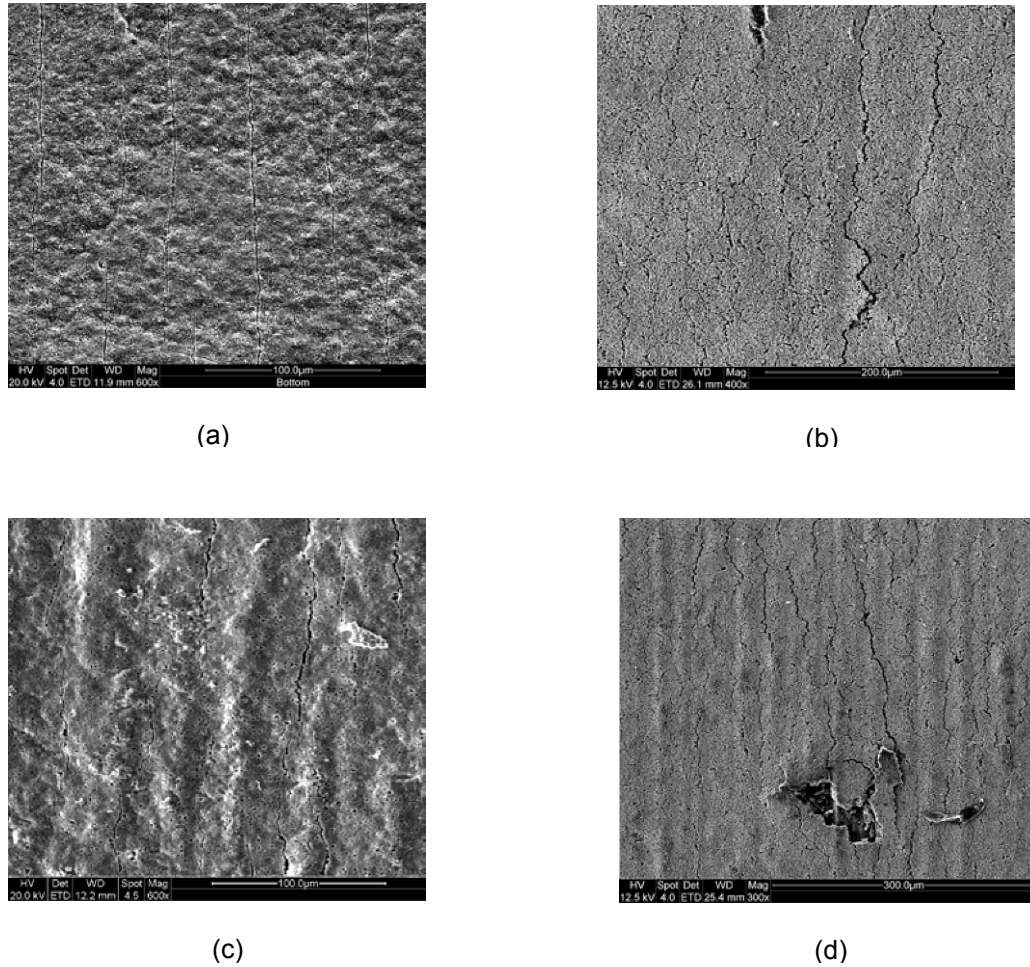


Fig.4 SEM images of transverse parallel cracks at approximately 3% strain. (a) Type 1 (b) Type 2 (c) Type 3 (d) Type 4.

Table 1: Average interfacial shear strength for each type of specimen.

Case	Minimum Shear Strength (MPa)	Maximum Shear Strength (MPa)	Mean Shear Strength (MPa)	Standard Deviation (MPa)
1. Oxidized MCO-Crofer	1.27	6.64	2.25	0.9114
2. Reduced MCO-Crofer	500.88	620.7	905.27	242.36
3. Oxidized MCO-SS441	1.854	36.63	18.49	7.0565
4. Reduced MCO-SS441	382.38	1234.3	751.81	182.26

Fig.4 shows the SEM micrographs of saturated transverse parallel cracks formed in each type of specimens. Using crack spacing measurements, the interfacial shear strength was calculated from equation 1 and tabulated in Table 1. The interface between Crofer substrate and MCO in the oxidized condition has the lowest interfacial shear strength and in the reduced condition has the strongest interfacial shear strength. It is also observed from Table 1 that Type 1 specimens have more uniform shear strength at the interface as indicated by their lowest standard deviation whereas shear strength is least uniform for Type 2 specimens.

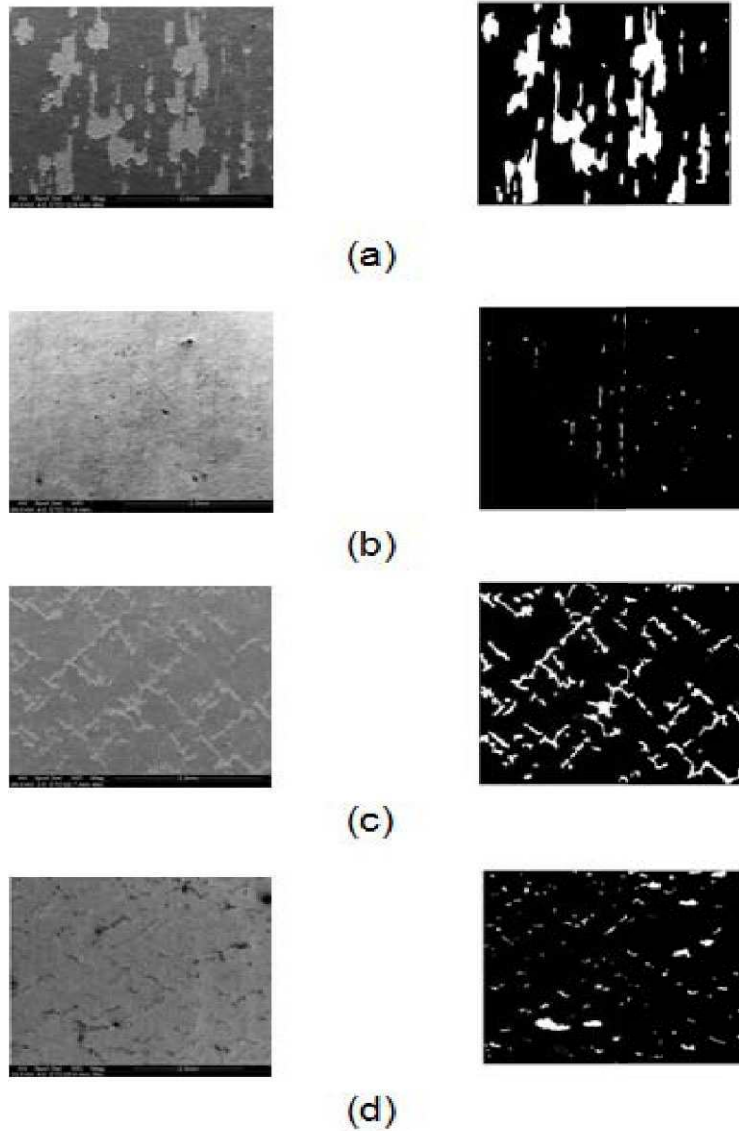


Fig 5 SEM (left) and processed (right) images of spalled surfaces at 3% strain (a) Type 1 (b) Type 2 (c) Type 3 (d) Type 4.

Scanning Electron Microscopy (SEM) was performed on the cracked coating surfaces for each type of specimen. The SEM images were processed to measure the percentage of total spallation area. In Fig.5, the SEM images and their corresponding processed images are presented for each type. In the processed images, the white portions denote spalled areas whereas the black portions indicate the unspalled coating. The measured values of percentage of spallation area and fracture energy are tabulated in Table 2. From Table 2, it can be concluded that

oxidized MCO-Crofer substrate has the lowest interfacial fracture energy with maximum spallation whereas the reduced MCO-Crofer system shows the strongest adhesion with minimum spallation.

Table 2: Interfacial fracture energy for each type of specimen.

Type	Onset of Spallation Strain (%)	Interfacial Fracture Energy (J/m ²)	% Spallation Area
1. Oxidized MCO-Crofer	2.4	9.2-17.45	18.88
2. Reduced MCO-Crofer	1.6	11.29-81.84	0.66
3. Oxidized MCO-SS441	1.5	21.13-85.05	9.43
4. Reduced MCO-SS441	1.6	15-71.16	3.23

Conclusions

Four point bend experiments were performed on both oxidized and reduced spinel MCO coated Crofer and SS441 SOFC interconnects. The present analysis reveals the significant impact of oxidation on both interfacial shear strength and interfacial fracture energy. The formation of brittle alloyed oxide weakens the interface. As a result, interface can transfer lesser load which is verified by lower interfacial shear strength compared to that of reduced specimen. Similar trend is found in case of adhesion of interface. Oxidized specimens show significantly decreased interfacial fracture energy than that of reduced specimen.

In reduced condition, Crofer interconnect shows to have stronger interface in both interfacial shear and adhesion due to possessing more chromium than that of SS441. Chromium contents strengthen the interface more. On the other hand, in oxidized condition formation of chromium oxide weakens the interface than that of SS441.

Future work involves the study of effect of residual stress on interfacial fracture energy and shear strength. Residual stress is an important factor for both reduced and oxidized interconnects. X-ray diffraction methods will be incorporated to validate the analytical residual stress calculations. Finally, high temperature experiments will be performed to assess the impact of temperature on interfacial shear strength and fracture energy.

Acknowledgement

This project is financially supported by National Science Foundation (NSF) CMMI grant no. 0825558. Technical support, above and beyond GOALI expectations, from NexTech Materials Ltd is also acknowledged.

References

- [1] Haile S.M., Fuel cell materials and components, Acta Materialia, vol. 51, pp. 5981-6000, 2003
- [2] Sun X, Liu W.N., Stephen E. and Khaleel M.A., Determination of interfacial adhesion strength between oxide scale and substrate for metallic SOFC interconnects, Journal of Power Sources, vol. 176, pp. 167-174, 2008
- [3] Wincewicz K.C. and Cooper J.S., Taxonomies of SOFC material and manufacturing alternatives, Journal of Power Sources, vol. 140, pp. 280-296, 2005.
- [4] Puranen A. and Lagerbom J., The structure and properties of plasma sprayed Iron oxide doped Manganese Cobalt Spinel Coatings for SOFC Interconnects. Journal of Thermal Spray and Technology, 2010
- [5] Schutze M., Protective Oxide Scale and Their Breakdown, The Institute of Corrosion wiley series on corrosion and protection.
- [6] Philling N.B. and Bedworth R.E., The Oxidation of Metals at High Temperatures, J. Inst. Met, vol. 29, pp. 529-591, 1923.
- [7] Borie B., Sparks C.J. and Cathcart J.V., Epitaxially induced strains in Cu₂O films on copper single crystals--I X-ray diffraction effects, Acta Materialia, vol. 10, pp. 691, 1962.
- [8] Appleby W.K., Tylecote R.F., Stresses During Gaseous Oxidation of Metal, Corros. Sci., vol. 10, pp. 325, 1970.
- [9] Jaenicke W., Leistikow W. and Stadler A., Mechanical Stresses during the Oxidation of Copper and Their Influence on Oxidation Kinetics. III, J. of Electrochem. Soc., vol. 111, pp. 1031, 1964.
- [10] Christl W., Rahmel A. and Schutze M., Application of Acoustic Emission Technique for the detection of oxide scale cracking during thermal cycling, J. of Electrochem. Soc., vol. 141, pp. 1255-1260, 1994.

- [11] Zhang Y., Leistikow W. and Shores D. A., Cracking and Spalling of Oxide Scale from 304 Stainless Steel at High Temperatures, J. of Electrochem. Soc., vol. 141, pp. 1255-1260, 1994.
- [12] Zhang Y. and Shores D.A., Study of Cracking and Spalling of Cr_2O_3 Scale Formed on Ni-30Cr Alloy, Oxidation of Metals. vol. 40, pp. 529-553, 1993.
- [13] Nagl M.M., Saunders S.R.J., Evans W.T. and Hatt D.J., The Tensile Failure of Nickel Oxide Scales at Ambient and At Growth Temperatures, Corrosion Science. vol. 35, pp. 965-977, 1993.
- [14] Sun X. Liu W.N. Stephen E. and Khaleel M.A., Determination of interfacial adhesion strength between oxide scale and substrate for metallic SOFC interconnects, Journal of Power Sources, Vol 176, pp .167-174,2007
- [15] Nagl M.M.,Saunders S.R.J, Evans W.T. and Hatt D.J., An in situ Investigation of the tensile failure of oxide scales. Oxidation of Metals. vol. 42, pp. 431-449, 1994.
- [16] Evans H.E. and Lobbs R.C., Experimental Data on the Spallation of Protective Oxide, Corros. Sci, vol. 24, pp. 209-222, 1984.
- [17] Ambhorn S.C. Toscan F. Wouter Y. Galarie A. and Dupeux A., Determination of mechanical adhesion energy of thermal oxide scales on AISI 430 Ti alloy using tensile test. Material Science and Technology, Vol. 23, Issue 4, pp. 497-501, 2007

Extracting Crack-tip Field Parameters in Anisotropic Elastic Solids From Full-field Measurements Using Least-squares Method and Conservation Integrals

Fang Hou and Soonsung Hong
Department of Mechanical Engineering, Michigan State University,
East Lansing, Michigan 48824

ABSTRACT:

This paper presents parameter-estimation methods developed to determine crack-tip field parameters in anisotropic elastic solids from full-field experimental data. The crack-tip field parameters of interest include not only stress intensity factors but also effective crack-tip positions. Two approaches that are based on least-squares method and conservation integrals were presented. In the approach based on the least-squares method, the Stroh representation of anisotropic elasticity was used to determine the coefficients in the asymptotic expansion of crack-tip fields in anisotropic solids. On the other hand, conservation integrals in fracture mechanics, such as J-integral, M-integral, Interaction integrals, were also used to extract the parameters including the effective crack-tip position. Both approaches were employed to analyze crack-tip displacement fields obtained by using Digital Image Correlation technique during translaminal fracture test of a fiber-reinforced polymer matrix composite. The applicability of homogeneous isotropic plane-elasticity models to translaminal fracture processes in laminated composite materials is also discussed.

1. INTRODUCTION

Fiber-reinforced composite materials have been widely used in aerospace, automotive and other industries owing to their high strength-to-weight ratio. However, it is well known that heterogeneous microstructures in composite materials introduce a variety of failure mechanisms and damage modes, which makes it difficult to develop reliable theoretical models to describe and predict such failure processes. Therefore, research efforts to understand the complexity of fracture processes in composites heavily relies on experimental observations and measurements. Up until recently, most of the experimental investigations of composite fracture are based on measuring far field loads and overall deformations during mechanical tests. Then, the crack-tip field parameters, such as stress intensity factors, are inferred through analytical formula or numerical calibrations in order to characterize fracture behaviors of composites.

On the other hand, owing to the advances in full-field optical measurement techniques, the crack-tip field quantities, such as stress intensity factors, can be directly determined from measured near-tip deformation fields. Thus, the applications of optical techniques to investigate fracture behavior of engineering materials have become routine tasks. Nevertheless, a relatively fewer number of investigations based on optical techniques were conducted to investigate fracture processes of fiber reinforced composite materials. This is because the extraction and interpretation of the crack-tip field parameters in composite require special considerations on material heterogeneity and anisotropic behavior, when compared to homogeneous isotropic materials.

In this study, we integrated the digital image correlation technique into conventional fracture tests to provide better insight to the progression of fracture processes in composite materials during the tests. Firstly, the description of asymptotic crack-tip fields in anisotropic elastic solids was presented following Stroh representation [1, 2] of general anisotropic elasticity. Based on the asymptotic expansion of crack-tip fields, two approaches to determine the crack-tip field parameters from near-tip deformation fields were presented, namely the least-squares method [3, 4] and the conservation integrals [5-7]. Special considerations were made to determine not only the stress intensity factors but also the effective position of a propagating crack-tip, so that crack growth resistance-curve (R-curve) can be constructed solely from the optical measurements. Both approaches were employed to characterize translaminal fracture behavior of a fiber-reinforced polymer matrix composite.

2. ESTIMATION OF THE CRACK-TIP FIELD PARAMETERS IN ANISOTROPIC ELASTIC SOLIDS

2.1 Asymptotic expansion of crack-tip fields in anisotropic solids

In order to describe the present study for in-plane deformation in anisotropic solid, the 2-D anisotropic elasticity based on Stroh representation [1], which is well documented in the work of Suo [2], is briefly reviewed here.

Consider an in-plane elastic field of a general anisotropic solid. Then, the in-plane displacement components $u_k(x,y)$ can be represented by using the Stroh formalism of anisotropic elasticity as follows,

$$u_k = 2 \operatorname{Re} \left[\sum_{\alpha=1}^2 A_{k\alpha} f_{\alpha}(z_{\alpha}) \right] \quad (1)$$

where the functions $f_{\alpha}(z_{\alpha})$ are analytic functions of complex variables, $z_{\alpha} = x + p_{\alpha}y$, and the 2×2 matrix, $A_{k\alpha}$, depends only on the elastic stiffness tensor, C_{ijkl} . Each column of the matrix $A_{k\alpha}$ and the characteristic complex root p_{α} are the eigenvector and the eigenvalue of the following eigenvalue equation, respectively

$$\sum_{k=1}^2 [C_{i1k1} + p_{\alpha}(C_{i1k2} + C_{i2k1}) + p_{\alpha}^2 C_{i2k2}] A_{k\alpha} = 0 \quad (2)$$

Then, the stress components σ_{i2} can be represented as

$$\sigma_{i2} = 2 \operatorname{Re} \left[\sum_{\alpha} L_{i\alpha} f'_{\alpha}(z_{\alpha}) \right] \quad (3)$$

where, the matrix $L_{k\alpha}$ is given by

$$L_{i\alpha} = \sum_{k=1}^2 (C_{i2k1} + p_{\alpha} C_{i2k2}) A_{k\alpha} \quad (4)$$

A general form of crack-tip fields in a semi-infinite crack problem with the origin at the crack tip can be expressed using the Stroh formalism. From the traction-free boundary condition at the crack plane located in the negative real axis, the eigenfunction expansion of the elastic fields can be obtained from Hilbert arc problem as

$$\mathbf{L} \mathbf{f}'(z) = \frac{1}{2} \left[\frac{\mathbf{F}(z)}{\sqrt{z}} + i \mathbf{G}(z) \right] \quad (5)$$

where $\mathbf{F}(z) = \sum_{n=0}^{\infty} \mathbf{f}_n z^n$ and $\mathbf{G}(z) = \sum_{n=0}^{\infty} \mathbf{g}_n z^n$, and both \mathbf{f}_n and \mathbf{g}_n are column vectors with two real-number elements. In this

expression, the stress intensity vector defined as $\mathbf{k} = \{K_{II} \ K_I\}^T$ is related to the \mathbf{f}_0 as follows,

$$\mathbf{k} = \sqrt{2\pi} \mathbf{f}_0 \quad (6)$$

where mode-I and mode-II stress intensity factors are K_I and K_{II} , respectively. In this representation, the displacement and stress fields including the higher order terms are represented as eigenfunction expansions similar to Williams-type expansion for the isotropic case.

2.2 Least squares method

Least squares method (linear and non-linear) is the most commonly-used data-fitting method. The best fit in the least-squares sense minimizes the sum of squared residuals, a residual being the difference between an observed value and the fitted value provided by a model.

In the present study, the full-field displacements around the crack tip are obtained by DIC. The analytical eigenfunction expansions for displacement components around the crack tip are known in terms of Stroh representation. If we also consider the rigid body translation in the results obtained by DIC, the expansions for the displacements around the crack tip can be rewritten in more general forms as

$$u = \sum_{n=-1}^{2N+1} A_n(x,y) h_n \quad (7)$$

$$v = \sum_{n=-1}^{2N+1} B_n(x,y) h_n \quad (8)$$

or in the matrix notation

$$u = \mathbf{A} \mathbf{h} \quad (9)$$

$$v = \mathbf{B} \mathbf{h} \quad (10)$$

Here x and y are the coordinates in the coordinate system with origin at the crack tip, N represents the number of terms in the expansion used in calculation (theoretically $N = \infty$), and h_n are constants related to F_n and G_n in Stroh representation, which need to be determined in the least-squares.

Then the sum of squared residuals of the displacements for points can be presented as

$$E = \frac{1}{2} \sum_{i=1}^m (\|u_i - \tilde{u}_i\|^2 + \|v_i - \tilde{v}_i\|^2) = \frac{1}{2} \sum_{i=1}^m (\|\mathbf{A}\mathbf{h} - \tilde{u}_i\|^2 + \|\mathbf{B}\mathbf{h} - \tilde{v}_i\|^2) \quad (11)$$

Here \tilde{u}_i and \tilde{v}_i are the experimental results of data i obtained by DIC. The minimum value of E occurs when the gradient is zero, i.e.

$$\frac{\partial E}{\partial \mathbf{h}} = 0 \quad (12)$$

Then the following linear equations are obtained as:

$$\left(\sum_{i=1}^m \mathbf{A}^T \mathbf{A} + \mathbf{B}^T \mathbf{B} \right) \mathbf{h} = \sum_{i=1}^m \mathbf{A}^T \tilde{u}_i + \mathbf{B}^T \tilde{v}_i \quad (13)$$

It is known that u and v are linear functions with respect to the coefficients h_n and non-linear functions with respect to the coordinates x and y . If the crack tip position is known (so are the coordinates x and y), linear least-squares method can be used to get the unknowns by solving the above equations directly [3].

However, in the present study of composite, a damage zone usually occurs in front of the crack tip. The crack tip position is not easy to be determined visually. Thus we use the non-linear least-squares which treat the crack tip positions as unknowns as well [4]. However, the non-linear least squares method has one problem that sometimes it can not converge to reasonable values especially when the higher order terms of the eigenfunction expansions are included in the calculation. A possible solution is to combine the linear and non-linear least-squares. The method is also based on an iteration procedure. The visible crack tip position is firstly used as the initial guess. Then the other unknowns are obtained by linear least-squares method. Secondly the obtained unknowns are back substituted into the nonlinear least-squares part to get the crack tip position. Then this obtained crack tip position is used as the guess for the next iteration step. The procedure keeps moving until it finds a convergent result. In the present study, the linear least squares method is combined with the nonlinear least-squares method called Levenberg-Marquardt algorithm. Another thing which is worth mentioning here is that it has been reported that the number of the terms can influence the accuracy of the calculation [3, 4]. Generally, it is found from our analysis to the artificially constructed analytical displacement field that more number of the terms should be included in the calculation to get a convergent result with smaller error.

2.3 Conservation integrals.

There are various conservation integrals (path independent integral) in Fracture Mechanics such as J and M integrals [5-8]. J integral is the most famous conservation integral because it represents the strain energy release rate and is related to the stress intensity factors. The explicit expressions of J and M are:

$$J = \int_{\Gamma} (w dy - T_i \frac{\partial u_i}{\partial x} ds), \quad (14)$$

$$M = \int_{\Gamma} (w x_i n_i - T_k u_{k,i} x_i) d\Gamma \quad (15)$$

Here w is the strain energy density, $w = \frac{1}{2} \sigma_{ij} \epsilon_{ij}$ in linear elasticity. T_i are the components of the traction vector, $T_i = \sigma_{ij} n_j$, n_j are the components of the unit vector normal to Γ . Γ is a path connecting any two points on the opposite sides of the crack surface and enclosing the crack tip. ds is an element of arc length along Γ . u_i are the displacement components.

It has been derived by Suo [2] that J is related to the stress intensity factors in anisotropic solids in terms of the following relations:

$$J = \frac{1}{4} \mathbf{k}^T \mathbf{H} \mathbf{k} \quad (16)$$

Here

$$\mathbf{k} = \begin{Bmatrix} K_{II} \\ K_I \end{Bmatrix} \text{ and } \mathbf{H} = -2 \operatorname{Im}(\mathbf{A} \mathbf{L}^{-1}) \quad (17)$$

\mathbf{A} and \mathbf{L} are both 2×2 matrices defined in Stroh representation. \mathbf{H} is a 2×2 symmetric matrix.

Another important conservation integral is the J-based interactional integral [8], which is firstly introduced to separate mode I and Mode II stress intensity factors in the mixed mode problems. Suppose two independent elastic states “A” and “B” for the plane problems, which represent the unknown and auxiliary field respectively. Now consider a superposed state “A+B”, the J integral of this state is

$$J_r[A+B] = J_r^{\text{int}}[A,B] + J_r[A] + J_r[B] \quad (18)$$

Here $J_r^{\text{int}}[A,B]$ is defined as the J-based interactional integral, which has the explicit expression as

$$J_r^{\text{int}}[A,B] = \int_r w^{(A,B)} dy - (T_i^{(A)} \frac{\partial u_i^{(B)}}{\partial x} + T_i^{(B)} \frac{\partial u_i^{(A)}}{\partial x}) ds \quad (19)$$

Here

$$w^{(A,B)} = C_{ijkl} u_{i,j}^{(A)} u_{k,l}^{(B)}. \quad (20)$$

Based on the relation of $J = \frac{1}{4} \mathbf{k}^T \mathbf{H} \mathbf{k}$, the relation between the interactional integral $J_r^{\text{int}}[A,B]$ and the stress intensity factors for the two states \mathbf{k}^A and \mathbf{k}^B can be obtained as

$$J_r^{\text{int}}[A,B] = \frac{1}{4} [(\mathbf{k}^A)^T \mathbf{H} \mathbf{k}^B + (\mathbf{k}^B)^T \mathbf{H} \mathbf{k}^A] = \frac{1}{2} (\mathbf{k}^A)^T \mathbf{H} \mathbf{k}^B. \quad (21)$$

To get $\mathbf{k}^A = \begin{Bmatrix} K_{II}^A \\ K_I^A \end{Bmatrix}$ for the unknown field, two auxiliary field ‘B1’ and ‘B2’ with $\mathbf{k}^{B_I} = \begin{Bmatrix} K_{II}^{B_I} \\ K_I^{B_I} \end{Bmatrix} = \begin{Bmatrix} 1 \\ 0 \end{Bmatrix}$ and

$\mathbf{k}^{B_{II}} = \begin{Bmatrix} K_{II}^{B_{II}} \\ K_I^{B_{II}} \end{Bmatrix} = \begin{Bmatrix} 0 \\ 1 \end{Bmatrix}$ are constructed using Stroh representation with the same material properties. Then the corresponding

interactional integrals $J_r^{\text{int}}[A,B_I]$ and $J_r^{\text{int}}[A,B_{II}]$ can be obtained by the explicit expression respectively.

Then \mathbf{k}^A can be obtained by the following equations:

$$\mathbf{k}^A = \begin{Bmatrix} K_{II}^A \\ K_I^A \end{Bmatrix} = 2 \mathbf{H}^{-1} \begin{Bmatrix} J_r^{\text{int}}[A,B_I] \\ J_r^{\text{int}}[A,B_{II}] \end{Bmatrix}. \quad (22)$$

For a semi-infinite crack, if the coordinate of the crack tip in y direction is assumed to be zero, then the coordinate of the crack tip in x direction is $x_0 = M/J$ with respect to an arbitrary origin.

3. EXPERIMENT

3.1 Experiment procedure

The composite material investigated in this study is Cyply 1002, a glass-fiber reinforced epoxy laminate, manufactured by Cytec Engineered Materials. A cured composite panel of that has 0/90 cross-ply laminates are used. Each composite panel has 13 plies of 3.3mm thickness. The composite laminate has 13 plies in the arrangement of cross-ply [(0/90)₆/0] lay-ups. The elastic properties of the composite panel were measured in this study following ASTM D3518 and Mill handbook MIL-HDBK-17-1F. The lay-up sequences and measured material properties of the specimen are shown in the following table.

Table 1. Elastic properties of the composite material

Lay-up	Transverse Young's modulus E_x	Longitudinal Young's modulus E_y	Shear modulus G_{xy}	Poisson ratio
$[(0/90)_6/0]_T$	22.39Gpa	22.14Gpa	3.172Gpa	0.127

Translaminar fracture tests were conducted using the extended compact tension (ECT), also known as eccentrically loaded single-edge-notch specimen (ESET) following ASTM E1922-04 [9]. The specimen geometry is shown in Fig.1 (a). The specimens with an initial notch of 0.20 mm width were machined using an abrasive water jet cutter. The crack length-to-width ratio (a/W) was 0.5. In order to minimize delamination of surface plies, the fiber direction in the surface plies was parallel to the initial notch direction. This led to self-similar crack growth in the composite laminates without extensive delamination as shown in Fig.1 (c). The fracture tests were conducted at an extension rate of 1 mm/sec using MTS servo-hydraulic mechanical test frame. The applied load and loading-point displacement were recorded with 10 Hz sampling rate.

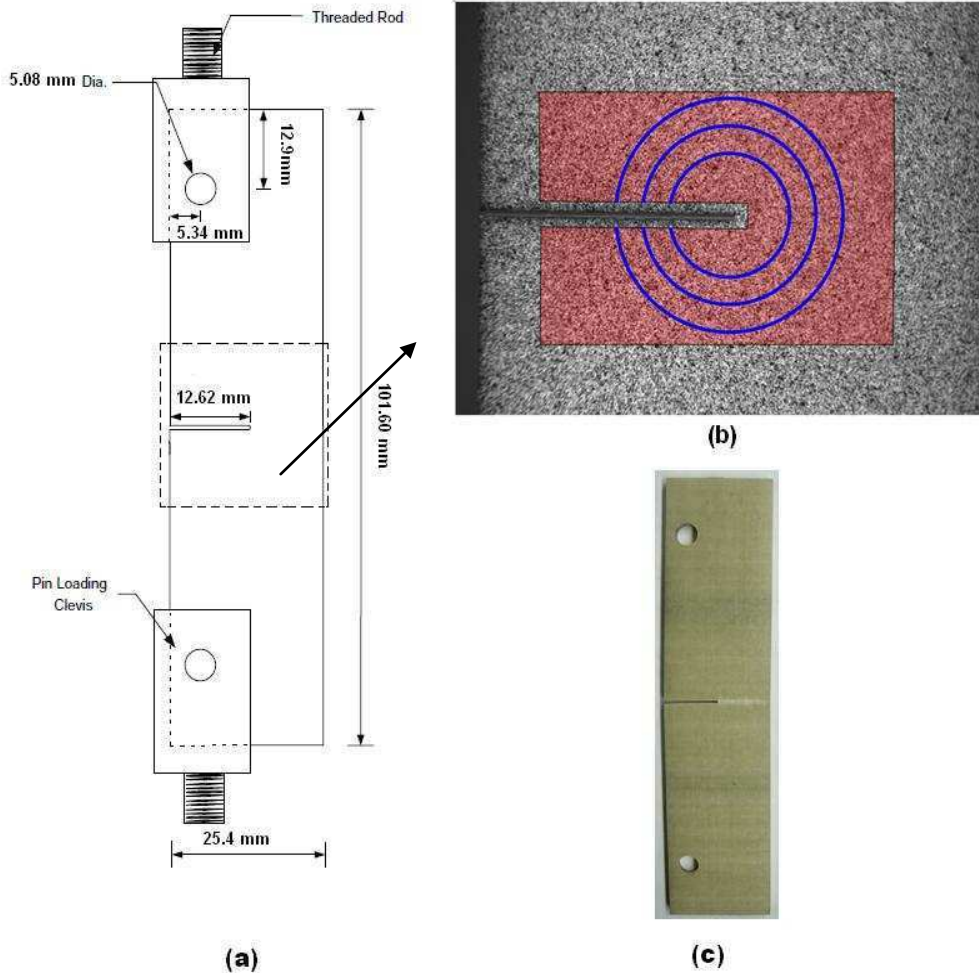


Fig.1 (a) Geometry of specimen, (b) Speckle patterns, data field used in calculation (red area) and integral paths (blue contours). (c) Self-similar crack growth.

To achieve full-field measurements using DIC, random speckle patterns were spray-painted on the composite specimens. During the fracture tests, a series of digital images (1280 x 960 pixels) were acquired with a frame rate of 1 Hz. The size of the field-of-view was 19.1 mm x 13.5 mm (22.5 $\mu\text{m}/\text{pixel}$) centered on the initial notch. A typical image of the speckle pattern is shown in Fig.1 (b). The displacement fields near the notch tip were obtained from the images using a custom-built DIC software. The parameters for the DIC analysis included a subset-size of 41 x 41 pixels and a subset spacing of 10 pixels.

3.2 Experiment result and discussion.

A typical load-displacement relation is plotted in Fig. 2. It shows that the linear part is up to more than 80% of the peak load, excluding the small nonlinear part at the beginning when the load is small. It is also observed that $\Delta V/V$ is less than 10%, which represents that relatively small damage zone occurs around the crack tip during fracture. So the formula provided in ASTM E1922-04 can be used to get the applied stress intensity factor as well as the fracture toughness.

Fig. 3 shows a typical result of the contour maps of the displacement fields around the crack tip obtained by digital image correlation at the 70th second. A length of 1 millimeter corresponds to about 44.5 pixels in the images processed by digital image correlation. It is observed that the obtained displacement fields are smooth. The fluctuation happens only near the crack face. Actually, the displacement data in this area are invalid. Since the subset used in DIC overlap the crack face, the displacements are determined by areas on both sides of the crack surface, which have opposite displacement. Therefore, the data near the crack face should be eliminated in the post processing. In the present study, data within 30 pixels near the crack face, which is equal to the summation of the half length of the subset and the width of the notch (crack), are excluded. In addition, these nearly symmetric displacement fields reflect the mode I loading in the fracture test.

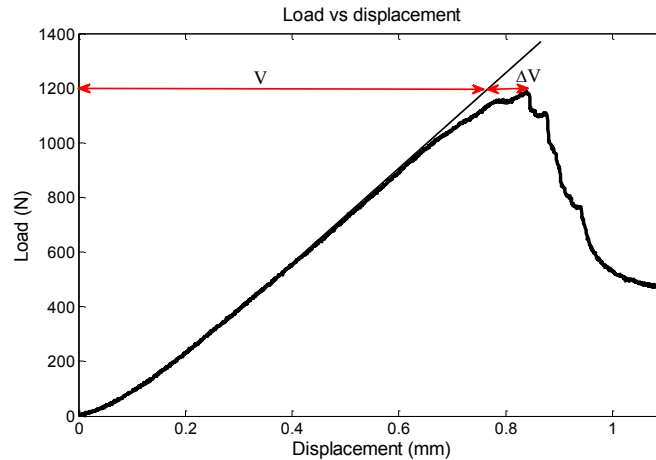


Fig.2 Load-Displacement diagram

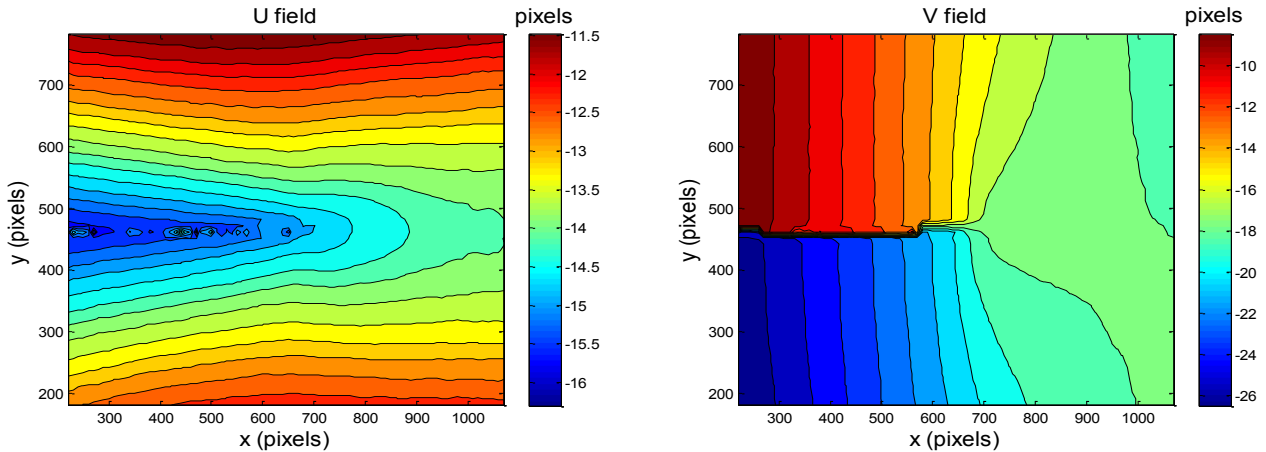


Fig.3 Example of the displacement fields around the crack tip obtained by digital image correlation.

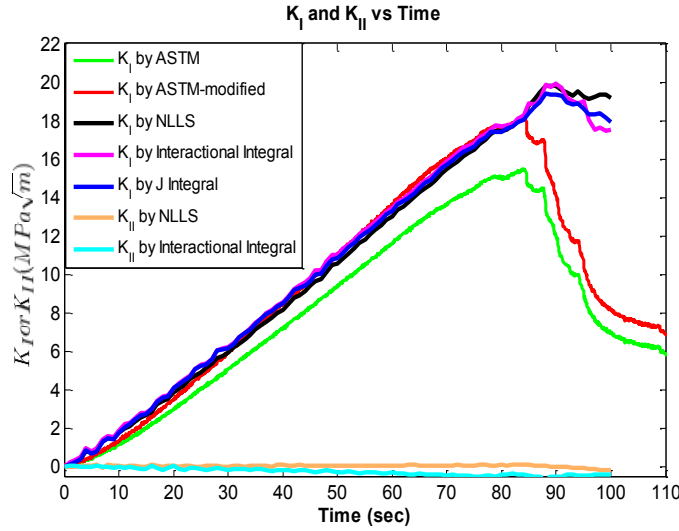


Fig. 4 Comparison of mode I and mode II stress intensity factors obtained by different methods during the fracture test.

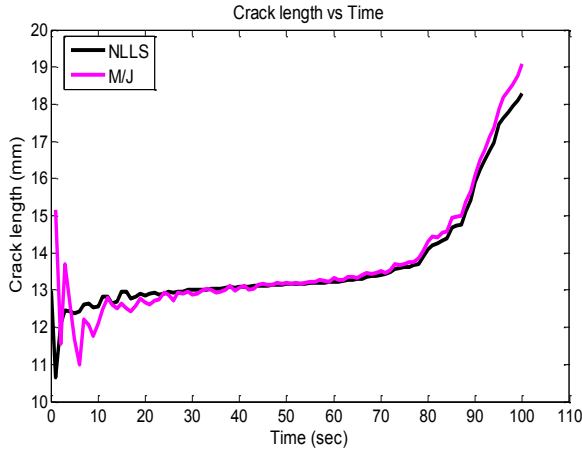


Fig.5 Variation of crack length during the test.

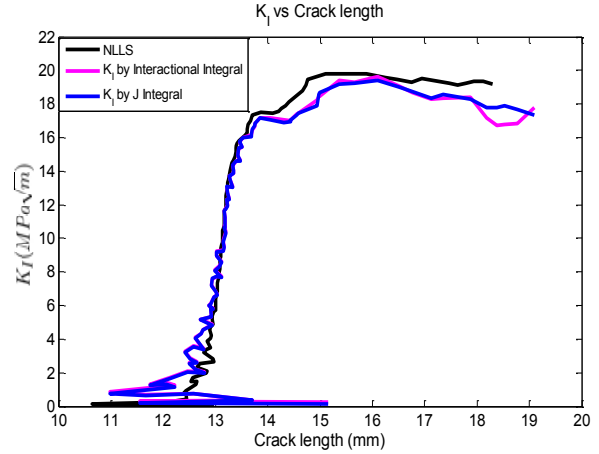


Fig.6 R curve.

Fig. 4 shows the results of mode I and mode II stress intensity factors extracted by different methods during the whole fracture test. Five different methods are used to get K_I in the present study. The terms “ K_I by ASTM” and “ K_I by ASTM modified” in the legend represent the results obtained by the formula in ASTM E 1922-04 which is derived based on the isotropic elasticity and its modified version which brings a constant corrected factor considering the influence of the orthotropy [10], respectively. The formula provided in ASTM 1922-04 is shown as:

$$K_I = \frac{P}{BW^{1/2}} F(a/W) \quad (23)$$

where

$$F(a/W) = \alpha^{1/2} \frac{[1.4 + \alpha]}{[1 - \alpha]^{3/2}} [3.97 - 10.88\alpha + 26.25\alpha^2 - 38.9\alpha^3 + 30.15\alpha^4 - 9.27\alpha^5] \quad (24)$$

P is the applied load at the pins, B is the specimen thickness, W is the width of the specimen, a is the original crack length, and $\alpha = a/W$. If the influence of material orthotropy is considered, a corrected factor $Y(\rho)$ is introduced into the previous formula as follows:

$$K_I = \frac{P}{BW^{1/2}} Y(\rho) F(a/W) \quad (25)$$

where

$$Y(\rho) = 1 + 0.1(\rho - 1) - 0.016(\rho - 1)^2 + 0.002(\rho - 1)^3 \quad (26)$$

ρ is defined as a constant related to the orthotropic material properties

$$\rho = \frac{(E_1 E_2)^{1/2}}{2G_{12}} - (\nu_{12} \nu_{21})^{1/2} \quad (27)$$

The terms “ K_I by NLLS” and “ K_I by Interactional Integral” represent the results obtained by the non-linear least squares methods and interactional integral described in “Methodologies” section, respectively. Since mode I loading is dominant in the test, K_I can also be obtained directly by the relation between J and K_I , assuming K_{II} is zero. The result is shown by term “ K_I by J Integral”.

Firstly, it is observed that the difference between the results of “ K_I by ASTM” and “ K_I by ASTM modified” is about 16% at the maximal load, which means the influence of the orthotropic material properties is relatively large. Secondly, the results of terms “ K_I by ASTM modified”, “ K_I by NLLS”, “ K_I by Interactional Integral” and “ K_I by J Integral” are very close to each other before reaching the maximal load, which can inversely verify the validity of the parameter-extraction methods for the present study. In addition, it is noteworthy that the values of K_I of the terms “ K_I by NLLS”, “ K_I by Interactional Integral” and “ K_I by J Integral” keep increasing for a little while after reaching the maximal load, opposite to the immediately decrease of that of “ K_I by ASTM modified”. It is due to the fact that the formula provided in ASTM (both original and modified versions) are based on two assumptions that the damage zone (process zone) occurs in front of the crack tip is negligible, and crack length is constant during the whole test. For the first assumption, the damage zone size before crack propagation in the present study has been pointed out to be relatively small and thus the assumption of constant crack length before crack propagation exists. It explains the consistence of “ K_I by NLLS”, “ K_I by Interactional Integral”, “ K_I by J Integral” and “ K_I by ASTM modified” before reaching the maximal load. However, the crack length as well as the damage zone size will increase after reaching the maximal load. So the ASTM formula is not valid any more after the maximal load. Generally, K_I is a combination of the applied load and the crack length, with a general form as follows:

$$K_I = YF\sigma\sqrt{\pi a_{eff}}.$$

Here Y and F are both corrected factors only related to orthotropic material properties and specimen geometry, respectively. At the beginning of the crack propagation, the effective crack length a_{eff} , which is defined as the sum of the actual crack size and a process zone correction, keep increasing while the applied stress σ decreases a little. The combination of the two variables will cause the applied stress intensity factors to keep increasing for a little while until the crack propagate unstably. So the least-squares method and conservation integrals which can reveal this phenomenon show superiority over ASTM in accurately measuring the fracture toughness K_{IC} in the present study for fiber-reinforced composite. The terms “ K_{II} by NLLS” and “ K_{II} by Interactional Integral” in Fig. 4 represent the results of K_{II} obtained by non-linear least squares methods and interactional integral. Comparing to K_I , K_{II} is negligible. It is consistent with the fact that K_I is dominant in this test.

Fig.5 shows the variation of the crack length in the fracture test. The results obtained by two different methods show good agreement with each other, except the beginning part where the displacements are very small and the accuracy of the calculation is influenced significantly by the noise in the data. It can be seen that the crack length starts to significantly increase at the 70th second. It is also the time when the plot of “ K_I by ASTM” and “ K_I by ASTM modified” starts to deviate from the linear part, corresponding to the time when the increase of load deviates from linearity. There is a little increasing jump of the crack length which is consistent with the decreasing jump of “ K_I by ASTM” and the load around 80

second. It is observed from the captured images that the bridging fibers in the damage zone suddenly break at this moment. After the crack reaches about 14 millimeters at the 80 second, the crack grows rapidly.

Fig.6 shows the extracted R curve, which reflects the material resistance to crack extension. Strictly speaking, the present fiber-reinforced composite has a rising R curve rather than a flat one. The rising R curve reflects the increase of the resistance. To understand the shape of the R curve, it is better to study the fracture process of the studied fiber-reinforced composite, which can be described briefly as follows [11]. The matrix of the composite ruptures at first, then the load is carried by the fibers. It will then cause a mechanism called fiber bridging, where the propagating crack leaves fibers intact. The fibers do not fail at the same time, because the fiber strength is subject to statistical variability. Consequently, the material exhibits quasi ductility, where damage accumulates gradually until final failure. In other words, a damage zone at the crack tip increases in size as the crack grows. Thus the driving force must increase to maintain the crack growth. After the crack reaches a relatively long length, the R curve reaches steady-state with further growth. The critical crack length in the present study when the crack grows unstably is nearly 14 millimeters, corresponding to the 80th second.

4. CONCLUDING REMARKS

Until recently, research efforts in fracture mechanics of composite materials have been mainly based on a continuum analysis for homogeneous anisotropic linear elastic materials that contains a flaw of known length. This is an extension of conventional LEFM concepts to account for anisotropic constitutive responses. Nevertheless, the applications of LEFM principles to fiber reinforced composite have been less successful due to the complexity of the crack-extension process in micromechanical point of view. On the other hand, even after extensive studies on micromechanical models to account for various failure mechanisms, such as fiber pull-out, matrix cracking, fiber/matrix debonding and interlaminar delamination, it is still illusive that this bottom-up approach will provide a capability to predict macroscopic crack growth in fiber-reinforced composite materials.

In this study, an experimental investigation method based on full-field optical deformation measurements are presented as a way to characterize subcritical and steady-state crack advances as well as stress intensity factors during fracture tests. The experimental analysis method still relies on the fracture mechanics theories in anisotropic elasticity under the assumption of homogeneous approximation. Nonetheless, for some limited cases, self-similar and collinear crack advances in composite materials can be experimentally investigated to account for the crack-tip damage zone in a similar way to Irwin's plastic-zone correction factor and R-curve. Furthermore, the method is expected to provide a foundation for top-down approach to multiscale analysis of fracture in heterogeneous solids.

5. REFERENCES

- [1] A. N. Stroh. Dislocation and Cracks in Anisotropic Elasticity. *Philos. Mag.* 3, 625–46. 1958.
- [2] Suo. Z. Singularities, interfaces and cracks in dissimilar anisotropic media. *Proc R Soc Lond A* 427, 331–358. 1990.
- [3] McNeill S.R., Peters W.H. and Sutton M.A. Estimation of stress intensity factor by digital image correlation. *Engng Fract Mech.* 28(1), 101–112. 1987.
- [4] Yoneyama S, Ogawa T, Kobayashi Y. Evaluating mixed mode stress intensity factors from full-field displacement fields obtained by optical methods. *Eng Fract Mech* 74, 1399–1412. 2007.
- [5] Rice, J.R., A path independent integral and the approximate analysis of strain concentration by notches and cracks. *J. Appl. Mech. Trans. ASME* 35, 379–386. 1968.
- [6] Budiansky, B. and Rice, J.R., Conservation laws and energy-release rates. *J. Appl. Mech. Trans. ASME* 40, 201–203. 1973.
- [7] Knowles, J.K. and Sternberg, E. On a class of conservation laws in linearized and finite elastostatics. *Arch. Rat. Mech.* 44, 187. 1972.
- [8] Chen, F.H.K. and Shield, R.T. Conservation laws in elasticity of the *J*-integral type. *J. Appl. Math. Phys.* 28, 1–22. 1977.
- [9] ASTM E1922-04, "Standard test method for translaminar fracture toughness of laminated and pultruded polymer matrix composite materials". Annual Book of ASTM Standards 03.01, American Society for Testing and Materials, 1159–1163. 2003.
- [10] Bao G, Ho S, Suo Z, Fan B. The role of material orthotropy in fracture specimens for composites. *Int J Solids Struct* ;29(9):1105–16. 1992.
- [11] T.L. Anderson, Fracture mechanics: fundamentals and applications (3nd ed.), CRC Press. 2005.

Velocity Measuring Approaches for the Determination of Ballistic Limits of GLARE 5 Fiber-Metal Laminate Plates

A. Seyed Yaghoubi, M.F. Chow, B.M. Liaw

*Department of Mechanical Engineering, The City College of New York,
Convent Avenue and 138th Street, New York, NY 10031, USA*

ABSTRACT

In this study, 152.4 mm by 101.6 mm (6"×4") GLARE 5 plates with various thicknesses were impacted by a 0.22 caliber bullet-shaped projectile using a high-speed gas gun. Velocities of the projectile along the ballistic trajectory were measured at different locations throughout the test using (1) a pair of laser-beam optoelectronic paths near the gun muzzle, (2) two sets of chronographs before and after the specimen, and (3) a high speed camera for recording the trajectory history of the projectile. The high speed camera yielded the most reliable way of measuring the projectile speed and could record the projectile orientation before and after the impact. It was experimentally detected that the measured speed of the projectile at the muzzle of the barrel was less than the actual impact speed of the projectile. The phenomenon can be explained by the well-known intermediate ballistics. The incident projectile impact velocity versus the residual velocity was plotted and numerically fitted according to the classical Lambert–Jonas equation for the determination of ballistic limit velocity, V_{50} . The results showed that V_{50} varied in a parabolic trend with respect to the metal volume fraction (MVF) and the specimen's thickness.

INTRODUCTION

GLARE 5 is a fiber–metal laminate (FML) made of interlacing layers of 2024-T3 aluminum alloy sheets and S2-glass/epoxy laminates. By combining the beneficial properties of monolithic metals and fiber-reinforced composites, FMLs provide drastically improved mechanical properties compared to conventional polymer matrix composites or aluminum alloys [1,2]. They have gained wide attention in the aerospace and space industries [3] for many advantages such as low density, high strength, higher damage tolerance to fatigue crack growth and impact damage caused by foreign objects or blast loading, corrosion prevention, fire retardation, etc. [3-11].

Ballistic impact response of S2-glass fiber/toughened epoxy composite beams was examined by Sevkat et al. [12]. Their approach was based on both experimental and numerical techniques to assess damage in the composite beams. They estimated ballistic limit velocity, V_{50} , with sufficient accuracy by combining results obtained from ballistic tests and finite element predictions. Gellert et al. [13] studied the effect of target thickness on the ballistic perforation of glass fiber reinforced plastic composites. They concluded that thicker targets are more ballistically efficient, especially against blunt projectiles. Langdon et al. [14] studied the behavior of FMLs subject to localized blast loading. Their experiments were based on samples of varying thickness and material distribution, and they investigated the influence of stacking configuration. They concluded that the size and shape of the front and back face damage regions depended on the thickness of the panels. Cortes et al. [15] investigated the impact properties of high-temperature fiber-metal laminates. They concluded that under high velocity impact conditions, glass fiber-reinforced poly-ether-imide laminates offered the highest specific perforation energy among the laminates they had considered. They also reported that interlaminar and interfacial delaminations appeared to be the primary mechanisms for absorbing and dissipating energy during the impact event in those laminates. Hoo Fatt et al. [16] studied the ballistic impact on GLARE fiber-metal laminates. They derived analytical solutions based on test results to predict the ballistic limit and energy absorption of fully clamped GLARE panels subjected to ballistic impact by a blunt titanium cylinder. It was illustrated that ballistic limit varied linearly with panel thickness. Their result showed the deformation energy due to bending and membrane accounted for 84-92% of the total energy absorbed. However, the energy dissipated in delamination represented 2-9% of the total absorbed energy and the remaining absorbed energy, about 7%, was

attributed to tensile fracture energy of both glass/epoxy and aluminum. Furthermore, based on their study, thinner panels absorbed a higher percentage of deformation energy than thicker panels since it was easier for them to bend and stretch before fracture. Meanwhile, the thinner panels absorbed lower percentage of delamination energy than the thicker panels since they had fewer plies to delaminate. The main objective of this study was to examine different velocity measuring approaches for the determination of ballistic limits of GLARE 5 fiber-metal laminate plates and to investigate the effects of thickness and metal volume fraction (MVF) of the GLARE 5 panels on its ballistic impact velocity V_{50} .

EXPERIMENTAL PROCEDURES

All GLARE panels considered in this study consist of 2024-T3 aluminum alloy with a thickness of 0.305mm (0.012") per layer and S2-glass/epoxy laminated layers, each with a thickness of 0.508 mm (0.020"). Each S2-glass/epoxy layer has a layup orientation of $[0^\circ/90^\circ]_s$. GLARE 5 panels with various thicknesses were cut into rectangular specimens with dimensions of 152.4 mm x 101.6 mm (6" x 4"). The configuration of GLARE 5 panels with different thicknesses and typical mechanical properties of constituents are described in [Tables 1](#) and [2](#), respectively [17-19]. In [Table 1](#), the term MVF represents metal volume fraction and is defined as the ratio of the sum of the thicknesses of all aluminum layers over the total thickness of the fiber-metal laminate [20]:

$$MVF = \frac{\sum t_{\text{aluminum}}}{t_{\text{FML}}} \quad (1)$$

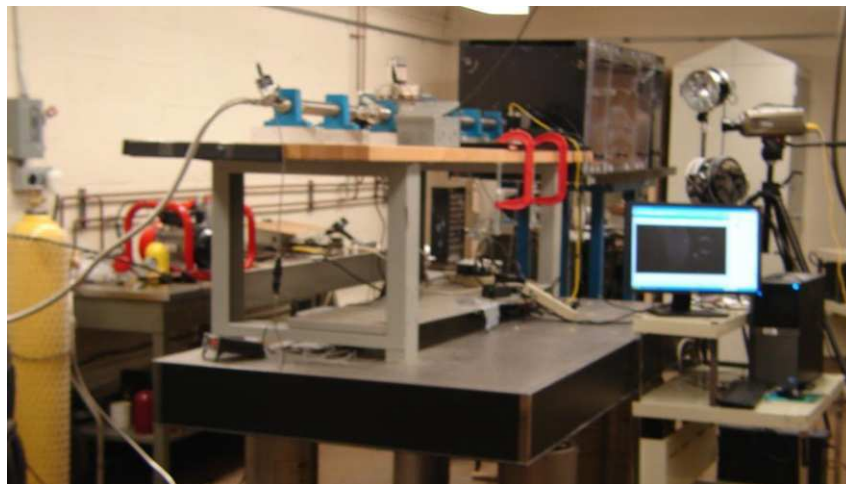
Table 1. GLARE 5 panels tested in this study with different thicknesses.

Lay-up Configuration (m/n)	Prepreg Plies & Orientation	Total Thickness	MVF
2/1	<div>[0° / 90° / 90° / 0°]</div> <div>cross-ply</div>	1.117mm (0.044")	0.546
3/2		1.930mm (0.076")	0.474
4/3		2.743mm (0.108")	0.445
5/4		3.556mm (0.140")	0.429
6/5		4.368mm (0.172")	0.419
The configuration notation <i>m/n</i> means the panel is composed of <i>m</i> aluminum-alloy layers interlaced with <i>n</i> fiber-reinforced epoxy layers.			

Table 2. Typical values of mechanical properties.

Mechanical property	Aluminum 2024-T3	UD S2 Glass/FM 94 Epoxy Prepreg
Tensile ultimate strength (MPa)	L 455	1900
	T 448	57
Tensile yield strength (MPa)	L 359	–
	T 324	–
Tensile modulus (Gpa)	L 72	54
	T –	9.4
Ultimate strain (%)	L 19	3.5
	T –	0.6
Compressive yield strength (MPa)	L 303	–
	T 345	–
Compressive modulus (GPa)	L 74	54.4
	T –	11
Density (g/cm ³)	2.79	2.00
The symbols, L and T, stand for longitudinal (the rolling direction for the metal) and transverse directions, respectively.		

The ballistic impact tests were conducted at room temperature using a high-pressure gas gun. The pictures of the gas gun setup and the specimen container are shown in Fig. 1. Helium was used as the propellant. The specimen was secured in place by clamping 25.4 mm (1”) of each end, as depicted in Fig 2. The composite plate specimen was impacted by a 0.22 caliber copper projectile at the center. Once high-pressure gas was released by a fast acting solenoid valve, a 0.22 caliber copper bullet accelerated through the 1.016 m (40”) gun barrel to the desired speed.

**(a)**

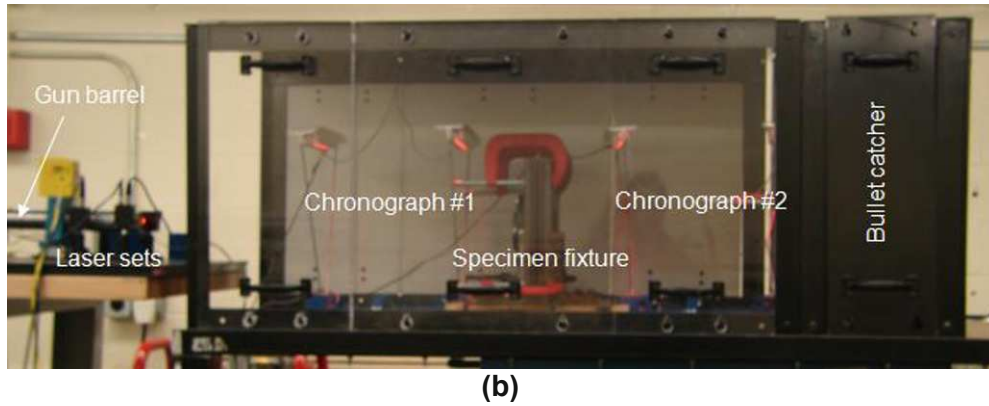


Figure 1. The high-speed gas gun setup for ballistic impact tests (a), specimen container (b).

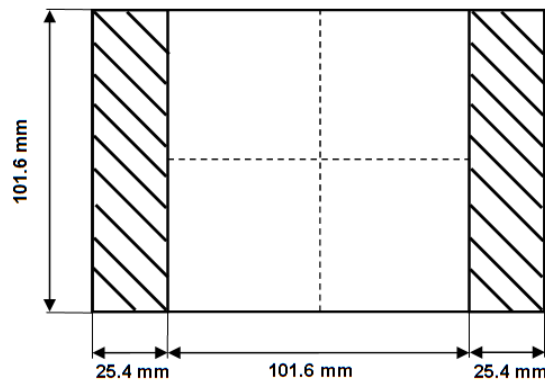


Figure 2. A composite plate specimen clamped at the two ends.

The speed of the projectile was measured in three distinct ways. A pair of diode-lasers/amplified-photodiodes, separated by 101.6 mm (4"), was located near the exit of the gun barrel, forming two optical gates to measure the speed of the projectile at the gun muzzle. For the second measurement, two pairs of chronographs were used to measure the projectile speed before and after impact; one pair was located in front of the target, while the second was located behind the target. Last, a high-speed camera was used to monitor the bullet motion during the test. Using the captured high-speed video, the bullet speed was then determined before and after the impact. Figure 3 shows a typical way of measuring the bullet speed from high-speed camera. A schematic picture of the setup is shown in Fig. 4.

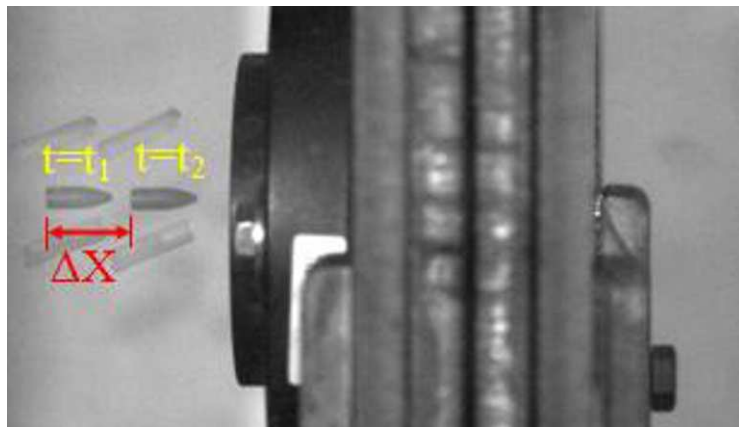


Figure 3. Typical way of measuring the bullet speed from the high-speed camera.

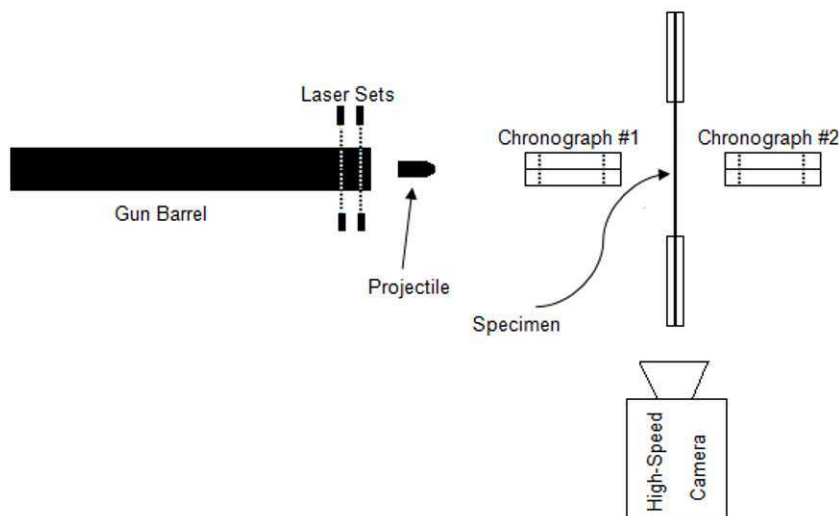
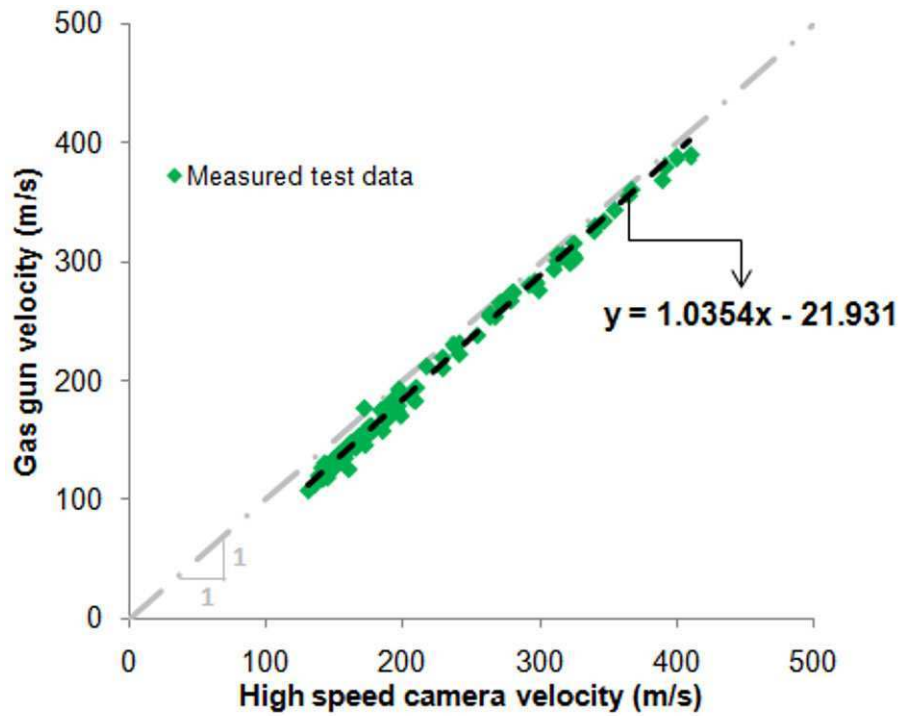


Figure 4. Schematic of the experimental setup.

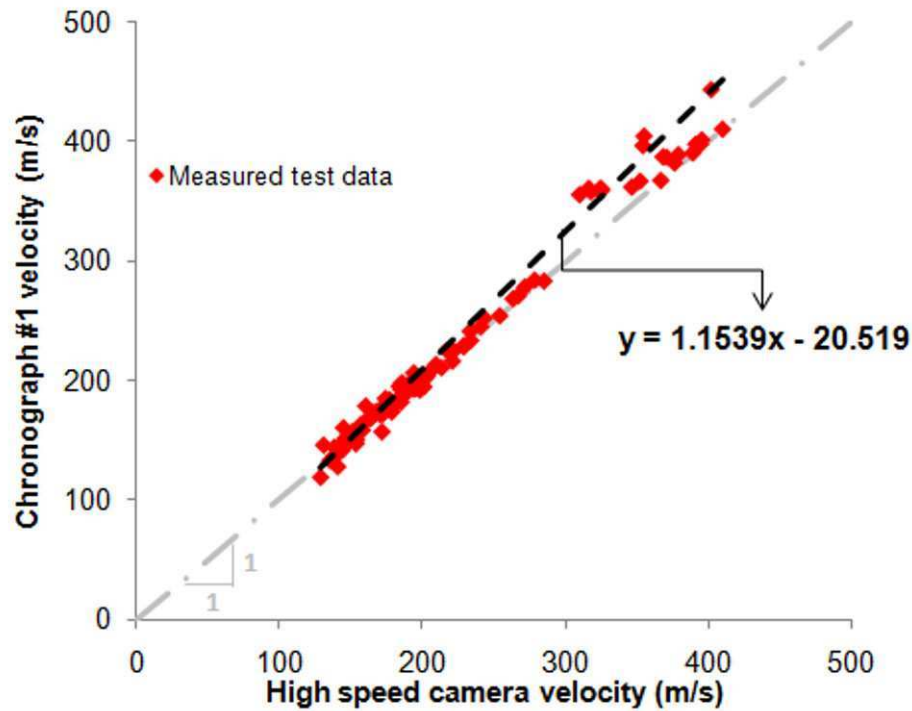
RESULTS AND DISCUSSION

Measuring a projectile velocity is a crucial factor in order to study the behavior of a specimen under impact. Several tests were conducted on the GLARE 5 specimens with different thicknesses (Table 1) and corresponding velocities were measured based on the three distinct methods that mentioned earlier. Figure 5 shows the comparison of the incident speed of the bullet measured from the gun and the chronograph versus the high-speed camera. As it is obvious from Fig. 5(a), the measured test data suggested that the bullet speed obtained from the high-speed camera was higher than the one measured from the gun by a small magnitude. In other words, it could be stated that the exited bullet from the gun barrel was further accelerated along the bullet trajectory before hitting the target. This phenomenon can be explained by intermediate ballistics, which is defined as the study of the transition from internal to external ballistics occurred in the vicinity of the gun muzzle [21]. The resultant trend line in Fig 5(b) implies that the bullet's strike speed determined by the chronograph was higher than that achieved from the high-speed camera. Furthermore, most portion of the test data were along the bisector line, i.e. $y=x$; implying that both high-speed camera and chronograph techniques yielded in approximately close values in measuring the bullet speed. However, scattering of the results obtained from the chronography suggests that chronography is not always trustable.

Figure 6 illustrate shock wave formation before and after projectile exit. As the projectile accelerated along the bore, it pushed ahead of it a column of air augmented by any leakage of propellant gases past the projectile. A shock wave formed just ahead of the projectile, traveled along the bore, and was released as a near-spherical precursor blast shock at the muzzle, as shown in Fig. 6(a). Once the outflowing air velocity was sufficient, a small bottle shock would form about the muzzle [21]. The projectile would then emerged, and once the projectile gas seal had passed the muzzle, the high pressure propellant gases would be released into the atmosphere generating a powerful blast shock, which was initially highly non-spherical due to the presence of the projectile and the high velocity flow of the propellant gases. The propellant gases rapidly expanded, accelerating to velocities much greater than that of the projectile, so that shock waves formed around the base of the projectile, rather as though the projectile was moving backwards (Fig. 6(b)). This apparent reverse gas flow provided slight additional acceleration of the projectile for several calibers distance beyond the muzzle [21].



(a)



(b)

Figure 5. Comparison of the Projectile-speed measurements: (a) Gas gun vs. High speed camera, (b) Chronograph #1 vs. High speed camera. In the equations, X stands for high speed camera velocity while y stands for gas gun velocity in (a) and chronograph #1 velocity in (b).

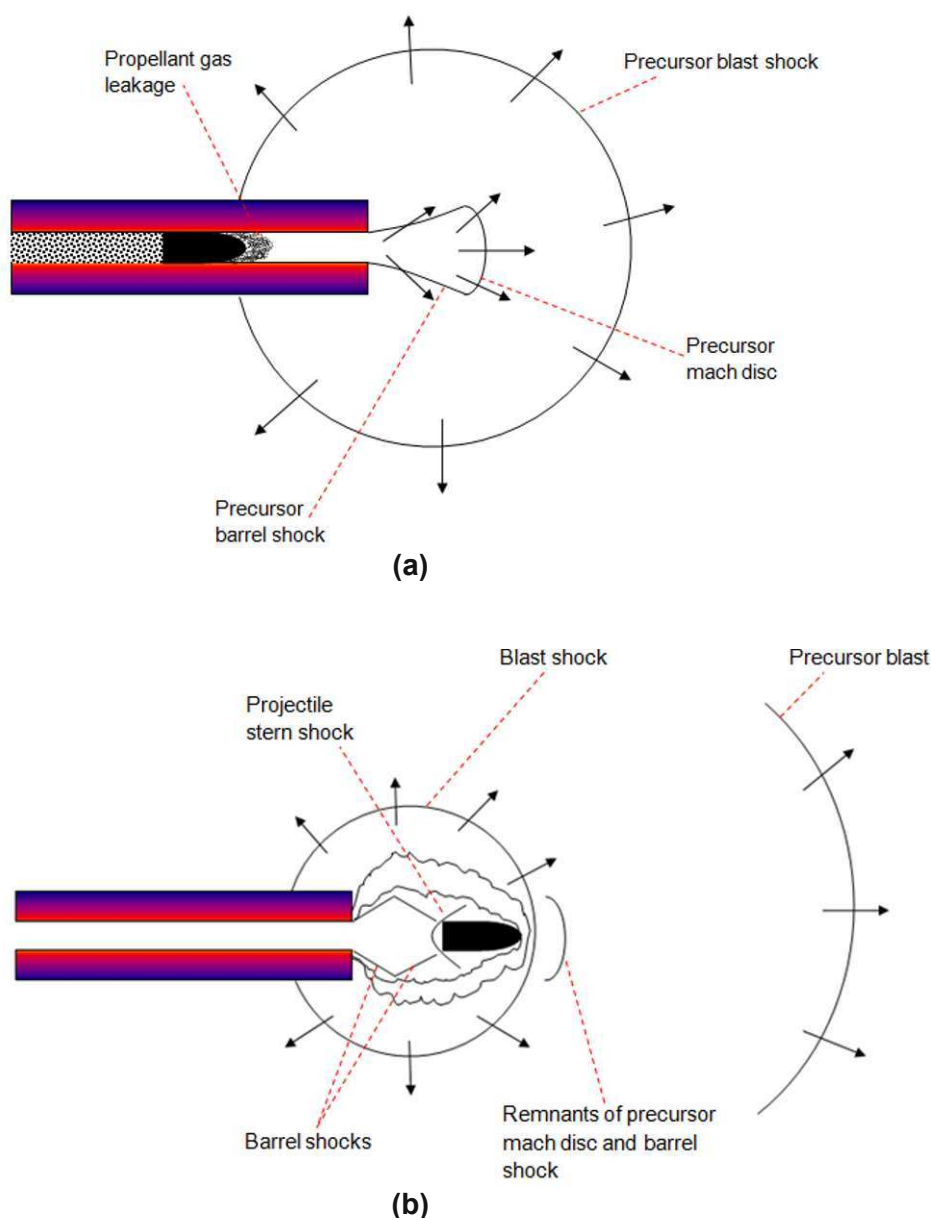


Figure 6. Shock wave formation before projectile exit (a), the initial formation of shock waves shortly after projectile exit (b).

Bullet residual velocity was determined by the high-speed camera and the chronograph#2 which was located after the target. However, chronograph #2 failed in measuring the speed of the bullet in 90% of the cases. This was mainly due to the triggering of the chronograph caused by some suspensions, e.g. dust, rather than the bullet. Hence, high-speed camera was the only reliable source in obtaining the velocity of the bullet. In the case of bullet rebounding off the target, chronograph #1 would fail in measuring the speed of the bullet since it was already triggered by measuring the incident speed of the bullet. On the other hand, if it had the capability of triggering, the results obtained would not be always reliable. There are three reasons for this. First, if the bullet's rebounding speed was not enough, then the bullet could not traverse the chronograph's infrared optical gates and hence the chronograph would not trigger. Secondly, a particle rather than the bullet might cause the triggering of the chronograph. Thirdly, the rebounding motion of the bullet is not always along a straight line, e.g. it could be tilted, tumbled, dropped steeply, moved along a curved path due to the gravity, etc. Thus, regardless of what the motion of the bullet was, the chronograph would only measure the speed of the bullet as it passed through its infrared optical gates. Thus other velocity components, i.e. transitional or rotational, could not be measured by chronography in which they are very

important in determining the residual kinetic energy of a projectile. Therefore, monitoring the projectile motion becomes very important. As a consequence, high-speed camera would be very helpful in such situations.

After determining the speed of the bullet before and after impact, the incident projectile impact velocity was plotted versus the residual velocity for each type of the specimens listed in Table 1. The experimental data could then be fitted by least-square regression according to the classical Lambert-Jonas equation [22] for the positive residual velocity values:

$$V_R^P = A(V_I^P - V_{50}^P) = A \cdot V_I^P - B \quad (2)$$

where A and B are two regression coefficients and P is the power. V_R and V_I are residual and incident velocities of the projectile, respectively, while V_{50} is the ballistic limit velocity.

For each specimen type, several P values were tried according to its V_R vs. V_I experimental trend. Subsequently, ballistic limit velocity, i.e. V_{50} , was determined based on the specimen experimental trend and classical Lambert-Jonas equation. V_{50} is defined as the velocity required for a projectile to perforated a piece of armor 50% of the time. With current gas gun facility, achieving low velocity range, i.e. lower than 140 m/s, was very difficult and almost impossible. Therefore, Lambert-Jonas equation becomes very useful for determining the V_{50} . Figure 7 depicts variation of ballistic limit with respect to the panel thickness for the cross-ply GLARE 5 specimens. In the plot, the average ballistic limit and its variation range is denoted by a solid diamond and a deviation bar for each individual panel thickness. It is apparent that by increasing the panel thickness, ballistic limit also increased with a parabolic trend. Metal volume fraction versus ballistic limit for the cross-ply GLARE 5 specimens with different thicknesses is given in Fig. 8. It is worth noting that as the number of prepreg laminated layers increased, the ballistic limit also escalated.

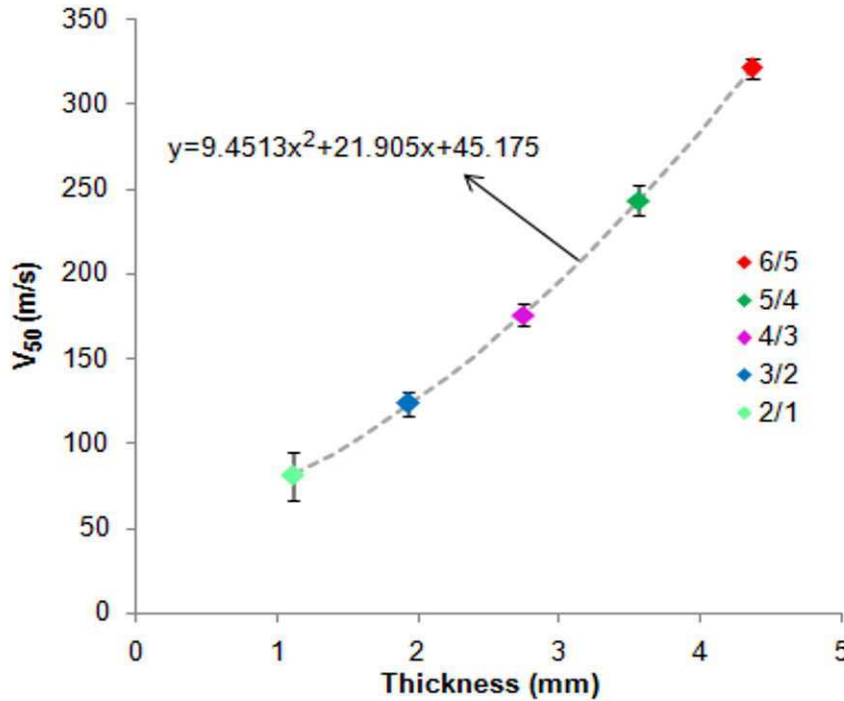


Figure 7. Variation of ballistic limit with thickness for the cross-ply GLARE 5 specimens. In the equation x stands for thickness and y for V_{50} .

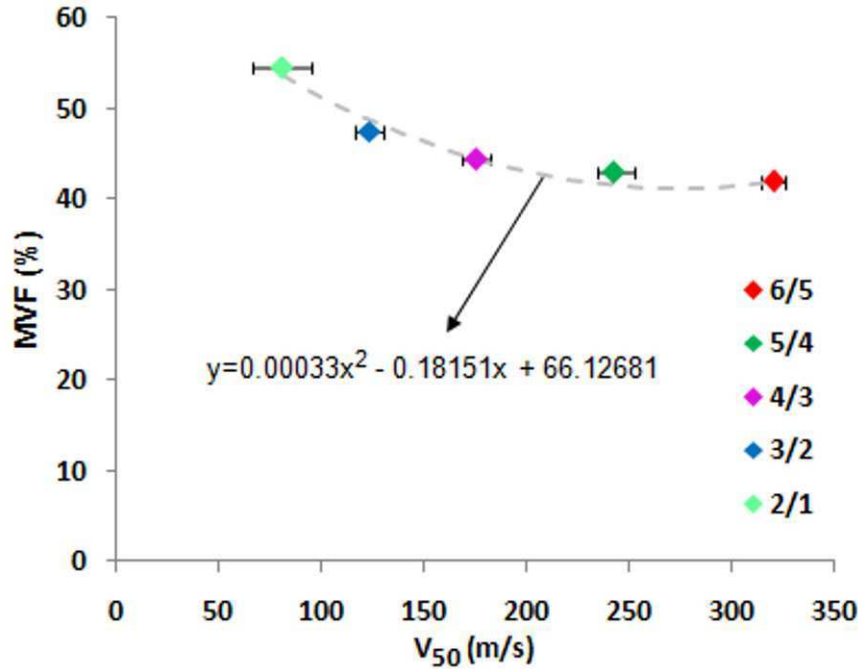


Figure 8. Variation of metal volume fraction with ballistic limit for the cross-ply GLARE 5 specimens with different thicknesses. In the equation x stands for V_{50} and y for MVF.

CONCLUSIONS

This study presents an experimental investigation on different approaches for measuring the velocity of a projectile in order to determine the ballistic limits of GLARE 5 fiber-metal laminate plates with various thicknesses. The following remarks can be concluded from this study.

- ❖ The projectile was further accelerated along the ballistic trajectory after emerging from the gun barrel. As a result, the projectile speed and in general ballistic limit would be underestimated based on the speed obtained from the gun.
- ❖ In general, chronography did not give consistent and reliable results for measuring the speed of a projectile.
- ❖ With the possibility of different projectile's motions either after perforation or rebounding off the target, monitoring the projectile motion became important in the calculation of the residual kinetic energy.
- ❖ Based on this study, the high-speed camera technique yielded in the most reliable and accurate results in measuring the projectile's speed. On the contrary, chronographs failed most of the time to accurately measure the projectile's speed; while the laser-based technique gave lower estimates of impact velocity.
- ❖ Ballistic limit velocity increased parabolically as panel thickness increased and also increased as the metal volume fraction decreased.

ACKNOWLEDGMENTS

This study was supported by NASA Faculty Award for Research (FAR) under Grant No. NAG3-2259, and by ARO under Grant No. DAAD19-03-1-0086. Dr. Kenneth J. Bowles and Dr. John P. Gyekenyesi were the Technical Monitors of the NASA grant. Dr. Bruce LaMattina was the Program Manager of the ARO grant.

REFERENCES

1. Vlot A., Glare-History of the development of a New Aircraft Material, Kluwer, Dordrecht: Kluwer Academic Publishers, 2001.
2. Vermeeren C.A.J.R., Beumler T., De Kanter J.L.C.G., Van Der Jagt O.C., Out B.C.L., Glare design aspects and philosophies. *Appl. Compos. Mater.*, 10, 257-276, 2003.
3. Vogeslang L.B., Volt A., Development of fibre metal laminates for advanced aerospace materials. *J. of Mater. Processing Technol.* 103, 1-5, 2000.
4. Vlot A., Impact loading on fiber metal laminates. *Int. J. Impact Eng.*, 18 (3) , 291-307, 1996.
5. Alderliesten R., Rans C., The meaning of threshold fatigue in fibre metal laminates. *Int. J. Fatigue*, 31, 213-222, 2009.
6. Sun C.T., Dicken A., Wu H.F., Characterization of impact damage in ARALL laminates. *Compos. Sci. Technol.*, 49, 139-144, 1993.
7. Abdullah M.R., Cantwell W.J., The impact resistance of polypropylene-based fibre-metal laminates. *Compos. Sci. Technol.*, 66, 1682-1693, 2006.
8. Langdon G.S., Nuricka G.N., Cantwell W.J., The response of fibre metal laminate panels subjected to uniformly distributed blast loading. *Eur. J. Mech. A, Solids*, 27, 107-115, 2008.
9. Vasek A., Polak J., Kozak V., Fatigue crack initiation in fiber-metal laminate GLARE 2. *Mater. Sci. Eng.*, A234-236, 621-624, 1997.
10. Kawai M., Hachinohe A., Takumida K., Kawase Y., Off-axis fatigue behaviour and its damage mechanics modelling for unidirectional fibre-metal hybrid composite: GLARE 2. *Compos. Part A*, 32, 13-23, 2001.
11. Castrodeza E.M., Bastian F.L., Perez Ipiña J.E., Critical fracture toughness, J_C and δ_{5C} , of unidirectional fiber-metal laminates. *Thin-Walled Struct.*, 41, 1089-1111, 2003.
12. Sevkate E., Liaw B., Delale F., Raju B.B., A combined experimental and numerical approach to study ballistic impact response of S2-glass fiber/toughened epoxy composite beams. *Compos. Sci. and Technol.*, 69(7-8), 965-982, 2009.
13. Gellert E.P., Cimpoeru S.J., Woodward R.L., A study of the effect of target thickness on the ballistic perforation of glass-fiber-reinforced plastic composites. *Int. J. Impact Eng.*, 24, 445-456, 2000.
14. Langdon G.S., Lemanski S.L., Nurick G.N., Simmons M.C., Cantwell W.J., Schleyer G.K., Behaviour of fiber-metal laminates subjected to localized blast loading: Part I-experimental observation. *Int. J. Impact Eng.*, 34, 1202-1222, 2007.
15. Cortes P., Cantwell W.J., The impact properties of high-temperature fiber-metal laminates. *J. Compos. Mater.*, 41(5), 613-632, 2007.
16. Hoo Fatt M.S., Lin C., Revilock Jr. D.M., Hopkins D.A., Ballistic impact of GLARETM fiber-metal laminates. *Compos. Struct.*, 61, 73-88, 2003.
17. Data sheets. Aviation Equipment Structures, Inc., Costa Mesa, California, 1998.
18. QA Reports B0319B-2, B1008B-1, B0904A-3. Structural Laminates Company, New Kensington, Pennsylvania, 1994.
19. Alloy 7475 Plate and Sheet, ACRP-053-B. Alcoa Mill Products, Bettendorf, Iowa.
20. Vlot A., Gunnink J.W. (Eds.). *Fiber Metal Laminates, an Introduction*. Dordrecht, the Netherlands: Kluwer Academic Publishers, 2001.
21. Farrar C.L., Leeming D.W., *Military Ballistics-A Basic Manual (Battlefield Weapons Systems & Technology)*. Brassey's Defence Publishers, Volume X, 1983.
22. Lambert J.P., Jonas G.H., Towards standardization of in terminal ballistics testing: velocity representation. Ballistic Research Laboratories, Aberdeen Proving Ground, Maryland, Report No. BRL-R-1852, 1976.

Underwater Explosive Loading of Curved Composite Plates: Experimental and Computational Comparisons

James LeBlanc^{a*}, Arun Shukla^b

^a Naval Undersea Warfare Center (Division Newport), 1176 Howell Street, Newport, RI, 02841

^b University of Rhode Island, 92 Upper College Rd., Kingston, RI 02881

* Corresponding author: Telephone: (401) 832-7920
Email: JAMES.M.LEBLANC@Navy.mil

ABSTRACT

The effect of underwater shock loading on an E-Glass / Vinyl-Ester composite material has been studied. The work consists of experimental testing, utilizing a water filled conical shock tube and computational simulations, utilizing the commercially available LS-DYNA finite element code. The plates consist of elliptically curved geometry with 0/90 biaxial laminates. The plates are held with fully clamped boundary conditions and are subjected to underwater explosive (UNDEX) loading. The transient response of the plates is captured in real time through the use of a Digital Image Correlation (DIC) system. The DIC data and computational results show a high level of correlation for both the plate deformation and velocity histories using the Russell error measure. The finite element models are also shown to be able to simulate the onset of delamination mechanisms.

1. INTRODUCTION

Composite materials have been widely used in a variety of applications in the marine, automotive, and transportation industries. These materials offer the advantages of high strength to weight ratios, reduced maintenance costs, and improved corrosion resistance. Recently, there has been an increased interest in composite materials for use in military applications including land vehicles (structural components and armor solutions), advanced ship hull designs, and submarine components. The use of these materials in wartime environments requires that they not only be able to withstand the loads produced by everyday use but also those imparted from explosions and high speed projectile impacts. Currently, the response of these materials at static and quasi-static loading rates is well understood. However, the response at the high strain rates that shock and ballistic events can induce is not well understood. This leads to an inherent conservative approach to be taken when these structures are designed and constructed. Typically this results in structures which do not fully realize the weight savings afforded by these materials. The focus of the current research is on the response of composite materials subjected to underwater explosions, UNDEX.

The response of materials subjected to shock and impact loading has been studied over a wide range of loading rates. The effect of shock loading on stainless steel plates subjected to underwater impulsive loads has been presented by Espinosa et al [1]. Nurick et al [2,3] have studied the effects of boundary conditions on plates subjected to blast loading and identified distinct failure modes depending on the magnitude of the impulse and standoff. The response of E-Glass and Carbon based composite laminates under shock and explosive loading has been presented by Tekalur et al [4]. LeBlanc et al [5] have studied the effects of shock loading on three-dimensional woven composite materials. Recently, there has been an increased interest in the study of the effect of shock loading on sandwich structures. These studies include the effects of shock and impact loading conditions (Jackson et al [6], Schubel et al [7]).

The finite element modeling of damage in composites has been performed primarily on models simulating strain rates up to those representing drop test experiments with some work performed at the high strain rate regimes expected in shock loading. Material models are continually being implemented and refined in existing commercial finite element codes (O'Daniel et al [8], McGregor et al [9]). Recent publications involving computational modeling of damage progression in composites have utilized Ls-Dyna and the Mat_162 (Mat_Composite_OPTION) material model which simulates fiber breakage, matrix cracking and delamination damage. Batra and Hassan [10] studied the response of composites to UNDEX loading through numerical simulations; however, there are no comparisons to experimental results. LeBlanc et al. [11] have

presented a modeling methodology which simulates composite plates subjected to underwater explosive loading with comparisons to both the transient strain response as well as post mortem damage.

2. COMPOSITE MATERIAL

The material used in this study is an E-Glass / Vinyl ester composite with a 0° - 90° biaxial layup. The glass fabric is a balanced construction of 0° and 90° fibers with the two layers being stitched together rather than woven. The panels which are utilized in the study consist of 3 plies of the fabric. The finished part thickness is 1.37 mm (0.054 in.) and has a fiber content of 62% by weight.

The geometry of the plates consists of a curved midsection with a flat boundary as shown in [figure 1](#). The convex face of the plate represents the mold line in the manufacturing and has a radius of curvature of 18.28 cm (7.2 in.), an outer diameter of 26.54 cm (10.45 in.), and the curved portion of the plate is 22.86 cm (9 in.) in diameter.

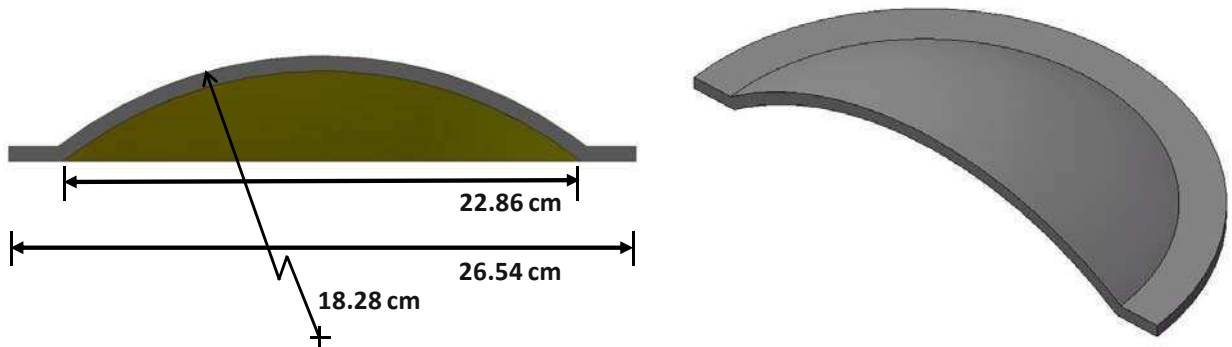


Fig. 1 Composite Plate Geometry (Section View)

3. SHOCK LOADING APPARATUS

A conical shock tube (CST) facility located at the Naval Undersea Warfare Center, Division Newport was utilized in the shock loading of the composite materials. The shock tube is a horizontally mounted, water filled tube with a conical internal shape, [Figure 2](#). The tube geometry represents a solid angle segment of the pressure field that results from the detonation of a spherical explosive charge. In an open water environment the pressure wave expands from the charge location as a spherical wave. In the shock tube the rigid wall acts to confine the expansion of the pressure wave in a manner that simulates a conical sector of the pressure field. Further discussion on the development and history of the water filled conical shock tube is provided by references 12 and 13.

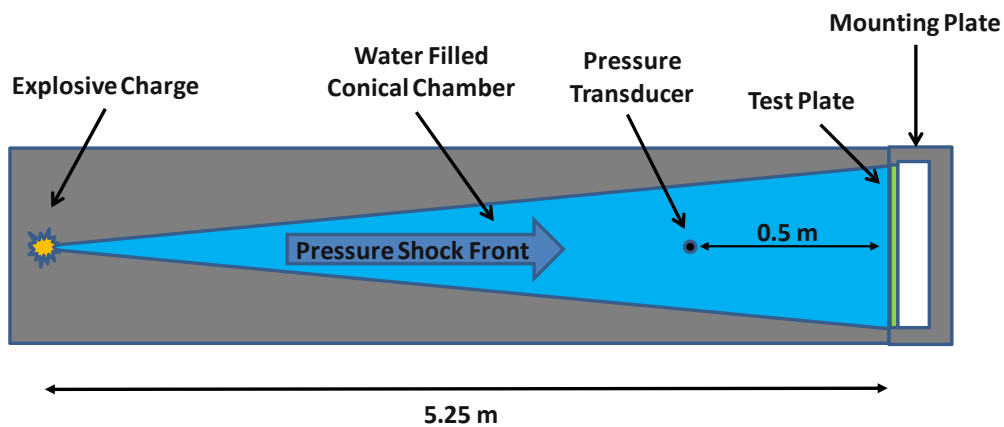


Fig. 2 Conical Shock Tube Schematic (not to scale)

A mounting fixture has been designed so the test specimens are air backed with fully clamped edges. The mounting arrangement is shown in [figure 3](#). The specimens are mounted with the convex surface towards the incoming shock fronts. This is chosen so that the test will represent geometries commonly used in underwater applications with curved surfaces typically facing into the fluid (i.e. submersible vehicle hull forms).

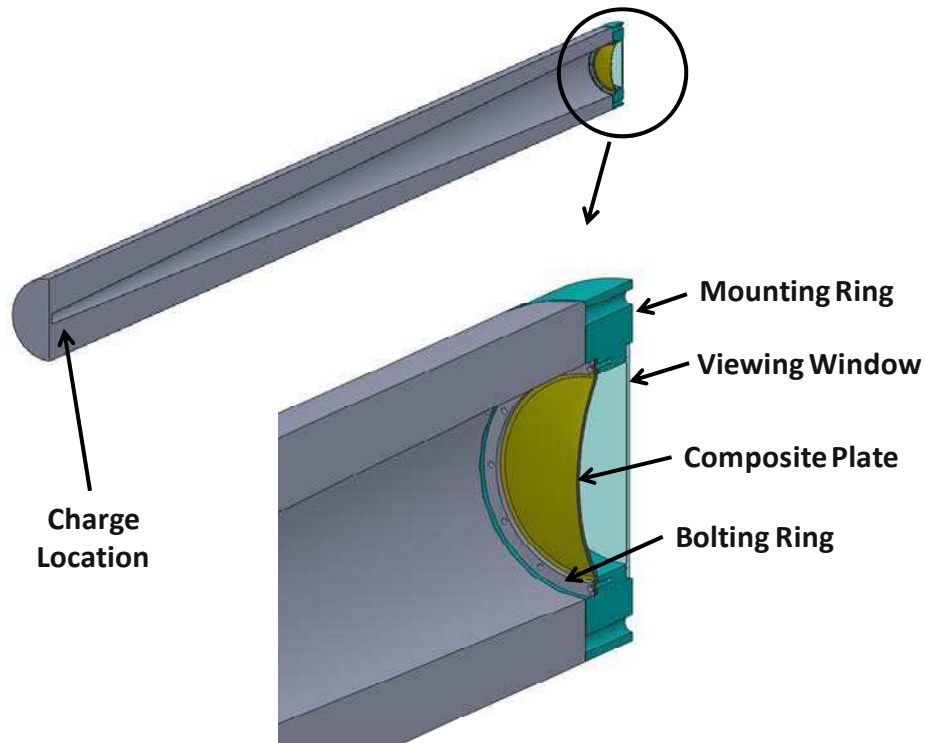


Fig. 3 Shock Tube Mounting Configuration

4. EXPERIMENTAL PROCEDURE

Shock testing of the composite material has been performed with the CST. High speed photography coupled with a 3D digital image correlation system is utilized to capture the back face transient response during the shock event. This system offers the advantage that it is a noncontact measurement technique which gives whole field information. The explosive charge used in the study is an M6 blasting cap with a net TNT equivalence of 1.32grams. This yields peak pressures at the sensor location (.508 m in front of the test specimen) of approximately 10.3 MPa (1500 lb/in²).

The Digital Image Correlation (DIC) technique is used to capture the transient response of the back face (dry) of the plates. DIC is a non-intrusive, optical technique for capturing the full field, transient response of the panels through the use of high speed photography and specialized software. Prior to testing, the back face of the sample is painted white and then coated with a randomized speckle pattern, [Figure 4](#). The post processing is performed with the VIC-3D software package which matches common pixel subsets of the random speckle pattern between the deformed and un-deformed images. Two high speed digital cameras, Photron SA1, are positioned behind the shock tube, [figure 4](#). The use of two cameras allows for the out-of-plane behavior to be captured. If a single camera is utilized the data would be limited to the in-plane results. A frame rate of 20,000 was used with an inter-frame time of 50 μ s.

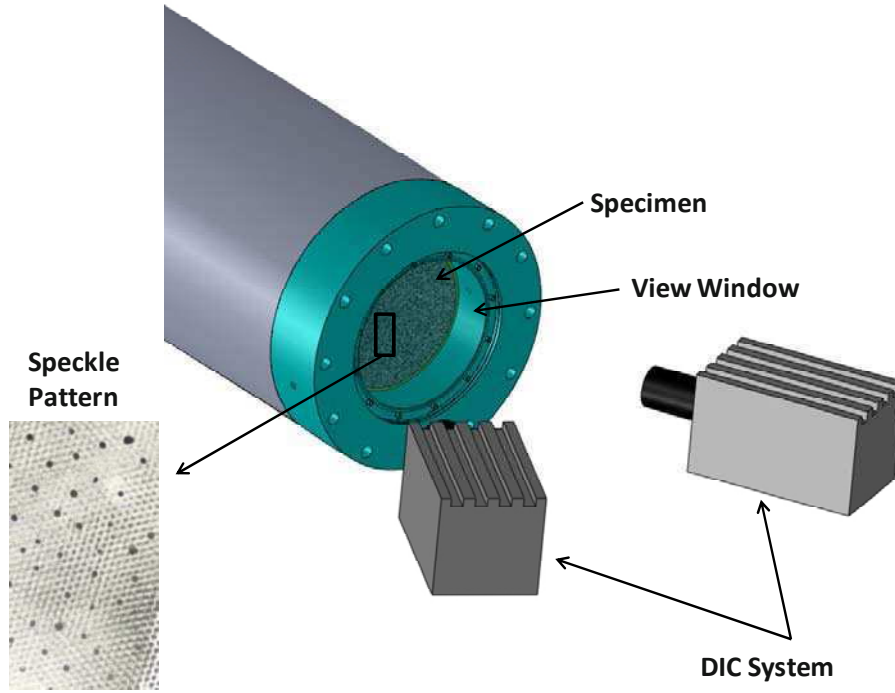


Fig. 4 Digital Image Correlation Schematic

5. FINITE ELEMENT MODELING

Finite element modeling of the experiment has been performed utilizing the Ls-Dyna code available from the Livermore Software Technology Corporation (LSTC). All simulations are generated with Version 971, Release 4.2 and are run in double precision mode. The composite plate in the simulations is modeled using shell elements with a fully integrated element formulation (Type 16). The model of the 1.37 mm (0.054 in.) plate consists of 3 layers of shell elements. Each layer represents a 0° and 90° combined ply with a thickness of 0.457 mm (0.018 in.). The in-plane element edge lengths are approximately 2.54 mm (0.1 in.) and the maximum element aspect ratio is 2.7:1.

The Ls-Dyna material model utilized in this work is Mat_Composite_Failure_Option_Model (Mat_059, Option=Shell). This is an orthotropic material definition capable of modeling the progressive failure of the material due to any of several failure criterion including tension / compression in the longitudinal and transverse directions, compression in the through thickness direction, and through thickness shear. The material model inputs are derived from static tensile testing with no modifications for strain rate effects. It was seen that the static properties provide reasonable results for shock loading conditions. The DIC strain measurements made during this study show that the in-plane strain rates are on the order of 10-50/s. Although the through thickness strain rate was not measured it is expected to be higher than the in-plane strain rate. Similar observations were made by Chan et al [14] for the ballistic impact problem and by LeBlanc et al for shock loading of flat composite plates [11].

Delamination damage is considered and is taken into account through the use of a surface-to-surface tiebreak contact definition. Using this approach, each ply is modeled as a shell layer of elements representing the mid-surface of each ply and the shell layers are offset by the ply thickness. The tie break definition initially ties the nodes between plies together to inhibit sliding motion. The force at each node is monitored by the software and the corresponding normal and shear stresses are computed. Failure is defined by the following formula:

$$\left(\frac{\sigma_N}{NFLS}\right)^2 + \left(\frac{\sigma_S}{SFLS}\right)^2 \geq 1 \quad (1)$$

where: σ_N and σ_S are the computed normal and shear stresses, respectively
 NFLS and SFLS are the failure normal and shear stresses, respectively

The complete finite element model of the CST test setup is shown in [figure 5](#). The model consists of the internal fluid of the shock tube and the composite test sample. The fluid within the tube is considered in the simulation so as to capture the fluid structure interaction (FSI) at the interface of the fluid and test plate. Only the first 1.01 m (40 in.) of the fluid extending from the test sample towards the charge location is modeled. This was deemed to be acceptable for 2 reasons: (1) the fluid is loaded with the pressure profile measured 0.508 m (20 in.) from the test sample and (2) a non-reflecting boundary layer is applied at the charge side boundary of the fluid domain. The fluid is modeled with solid elements and a null material definition. The use of the null material allows for the material to be defined with a linear polynomial equation of state (EOS) which only the bulk modulus and density of the water is defined. The pressure load is applied as a plane wave at the location of the test pressure transducer. The pressure profile that was measured for the test is applied to the model. The fluid-structure interaction is handled through the use of a tied-surface-to-surface (Ls-Dyna keyword *Contact_Tied_Surface_To_Surface) contact definition. The mounting plate is simulated by a nodal constraint set that forces the nodes in the clamped area of the plate to have zero displacement.

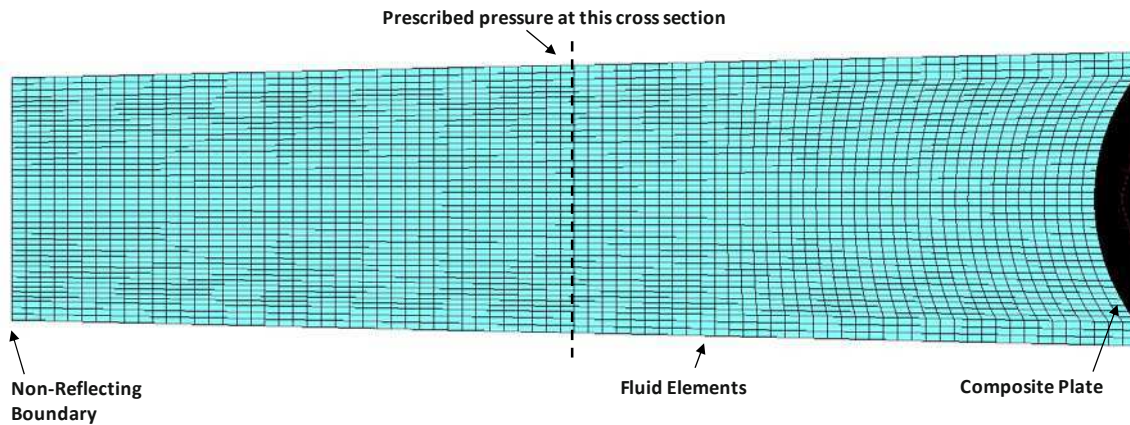


Fig. 5 Finite Element Model of CST

6. FINITE ELEMENT SIMULATION RESULTS

The finite element simulation of the shock tube testing allows for a visual full field representation of the interaction between the pressure wave and the composite plate. The pressure field in the fluid as it interacts with and loads the plate is shown in the left side of [figure 11](#). The associated plate response is shown in the right side of the figure. Although the pressure wave is uniform prior to its impact with the test plate, the loading on the plate itself is complex and not uniform. The loading of the plate and the associated response can be separated into two distinct time regimes. Where the pressure wave interacts with the plate over 0.2 ms, the plate does not start to deform until the wave is nearly fully reflected and takes approximately 5.5 ms to complete.

The plate deformation in the current study can be described as a full inversion, taking approximately 5.5 ms to complete. At 1 ms, a hinge forms at the outer edge of the plate at the clamped boundary. This hinge then continues to propagate towards the center of the plate as seen in the deformation progression images in [figure 6](#). The deformation is completed when the plate has fully inverted itself at 6.5 ms.

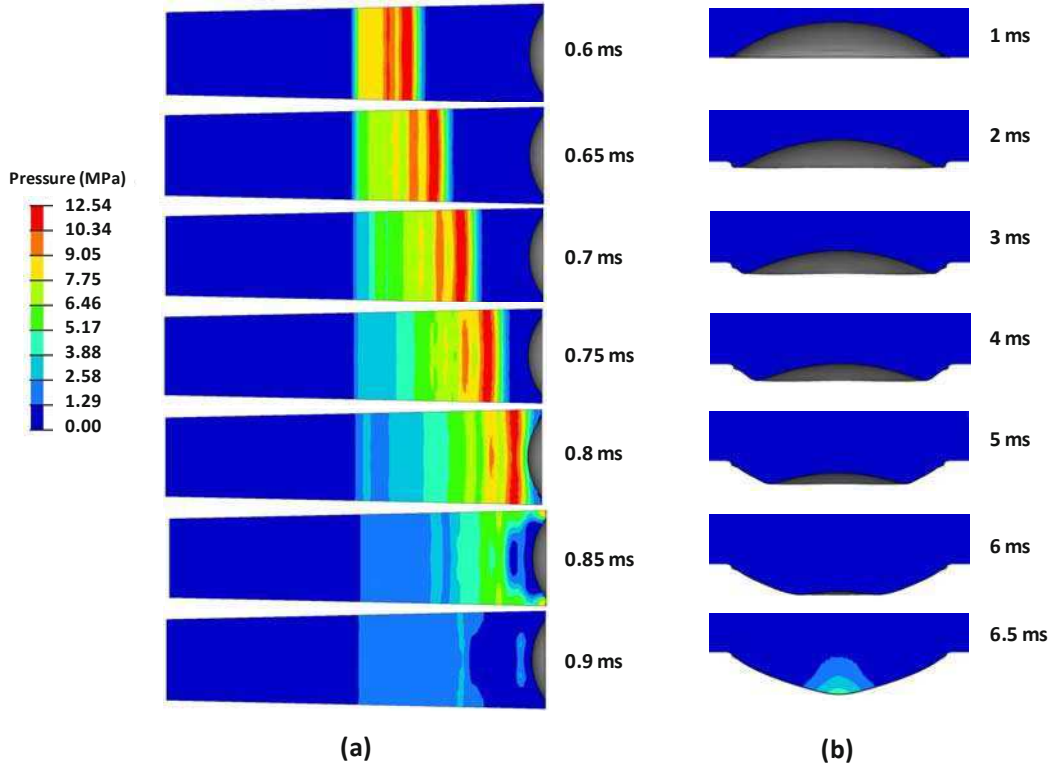


Fig. 6 (a) Fluid Structure Interaction, (b) Plate Deformation Progression

7. SIMULATION CORRELATION TO TEST

The displacement and velocity data that was captured during the experiments is used as a basis to correlate and validate the finite element model results. The quality of the correlation between the test data and numerical results in this study is quantified using the Russell Comprehensive Error measurement. The full derivation of the error measure is provided by Russell [15] with the phase, magnitude, and comprehensive error measures respectively given as:

$$RP = \frac{1}{\pi} \cos^{-1} \left(\frac{\sum c_i m_i}{\sqrt{\sum c_i^2 \sum m_i^2}} \right) \quad (2)$$

$$RM = \text{sign}(m) \log_{10}(1 + |m|) \quad (3)$$

$$RC = \sqrt{\frac{\pi}{4} (RM^2 + RP^2)} \quad (4)$$

Excellent, acceptable, and poor correlation using the Russell error measure is given as: Excellent - $RC \leq 0.15$, Acceptable - $0.15 < RC \leq 0.28$, and Poor $RC > 0.28$. The definition of these criteria levels are the result of a study that was undertaken to determine the correlation opinions of a team in support of a ship shock trial. A summary of the process used to determine the criteria is presented by Russell [16].

The DIC technique allows for the extraction of a large amount of data from the surface of the plates. The two variables that are used for correlation of the simulations to the experiments are the out of plane displacement and velocity. Time histories are extracted from the DIC data for the center of the plate. The displacement and velocity comparisons are shown in figure 7. From these graphical comparisons and error summary it is seen that there is a high level of correlation between the experimental results and the computational simulations.

The displacement comparison shows that the experiment and simulation results agree nearly exactly until 2.5 ms at which point the displacement in the experiment occurs slightly faster than the simulation. In the velocity comparison, it is

seen that there is an initial out-of-plane velocity of just less than 20 m/s which then settles to about 10 m/s for the remaining duration of the event. It is seen that the simulation is able to capture the peak velocities seen in the experiments. Overall, it is shown that the Russell error for the displacement comparison is excellent and the velocity correlation is acceptable.

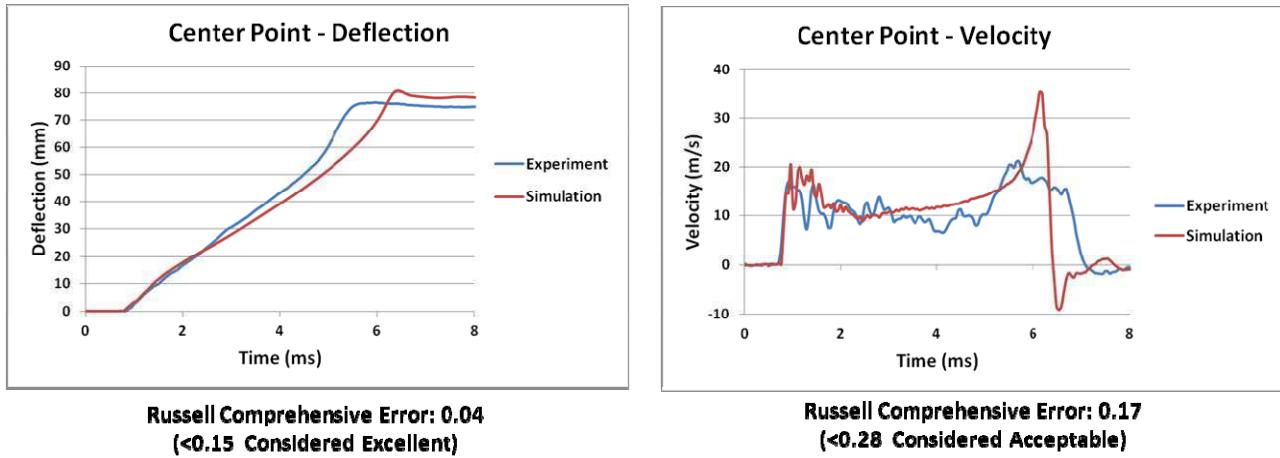


Fig. 7 Deformation and Velocity Comparison of Experiment and Simulation

In addition to the point wise time histories, full field comparisons are made between the experiment and simulations. A comparison of the full field, out of plane displacement evolution is shown in [figure 8](#). From this figure, it is seen that the experiment and simulation show good correlation in terms of the displacement evolution. Overall, the displacements over the surface of the plate correlate well between the experiment and the simulation.

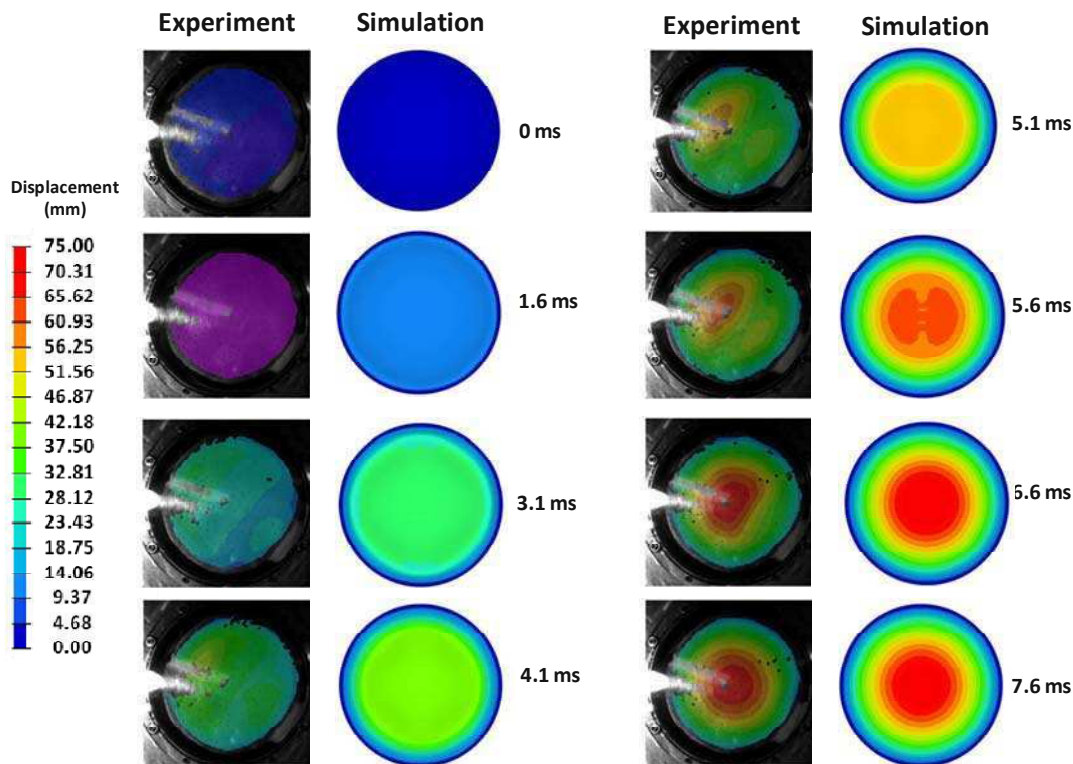


Fig. 8 Full Field Deformation Comparison of Experiment and Simulation

In addition to the transient response correlations, the relationship between the material damage observed during the test and the damage level predicted by the simulations is of interest. In the experiment the main damage mechanism that was observed is delamination between the plies. The final damage state from the shock test is shown in [figure 9a](#). Here it is seen that the extent of the delamination ranges from approximately 1.27 cm (0.5 in.) in the lower left region of the plate to 5.08 cm (2 in.) at the 3 O'clock position. In the corresponding computational model, [figure 9b](#), the delamination area is highlighted by the black area at the edge of the plate and propagates inwards from the edge 1 cm (0.4 in.). In the simulation results there are also 4 larger delamination zones at the 45° directions. These areas indicate the weaker material directions (fibers run in the 0° and 90° directions) and extend 3.81 cm (1.5 in.) from the edges. Although the amount of delamination is somewhat larger in the experiment than is observed in the computational model, it is encouraging that the model is able to predict the onset of the delamination itself and propagate it to a comparable distance

In the current model the choice of a delamination criterion was taken to be 36 MPa (5250 lb/in²) for both tensile and shear stresses. The delamination criterion is set to approximately one-half of the tensile strength of the vinyl ester based on prior work by LeBlanc et al [11]. The degradation by ½ of the tensile strength accounts for voids, and interfacial defects / flaws between the layers of fibers during the manufacturing of the material. Therefore the failure criteria was set to 36 MPa (5,250 lb/in²) based on testing performed on pure resin samples.

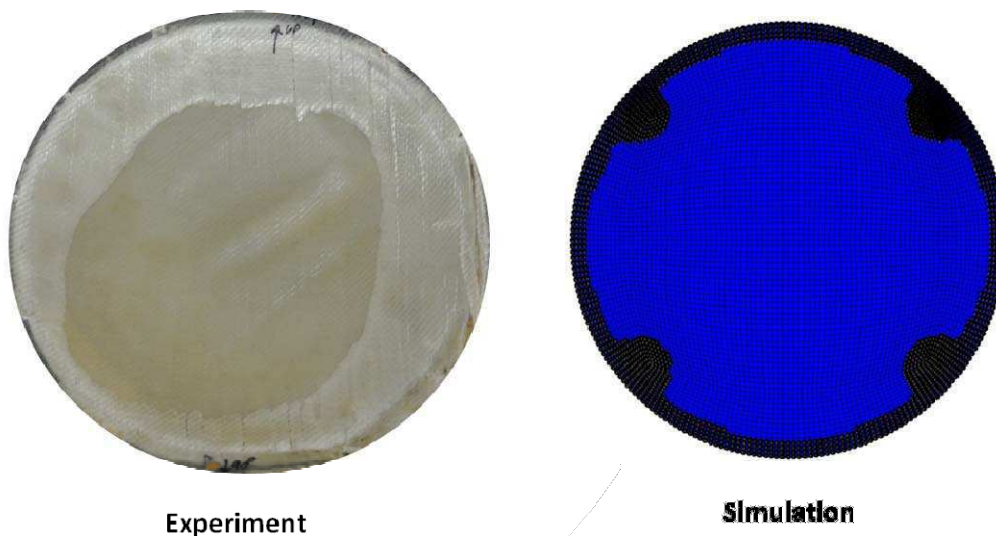


Fig. 9 (a) Material Damage during Test, (b) Material Damage from Simulation

8. CONCLUSIONS

A conical shock tube has been used to study the response of curved E-Glass / Vinyl ester composite panels subjected to underwater shock loading. The material is a bi-axial laminate with fibers balanced in the 0 and 90 degree directions. The round plates are curved in shape with the convex surface oriented towards the incoming shock front with fully clamped boundaries. A 3D Digital Image Correlation system is used to capture the full field, transient response of the back (dry) surface of the plates. This allowed for real time recording of the displacement and velocity history of this surface. The displacement and velocity data for the center point and a point halfway between the center and boundary are correlated to the computational models by utilizing the Russell error. The Russell error value for the deflection correlation at these two points is excellent. The velocity correlation at the point halfway between the center and the boundary is also excellent, while the center point velocity has acceptable correlation. The full field displacement evolution is also shown to agree between the experiment and the simulations. The computational model was also able to predict the onset of delamination damage and predict its growth to a reasonable degree. This work has shown the ability of the Ls-Dyna material model `Mat_Composite_Failure_Option_Model` to realistically model the behavior of a composite material under shock loading conditions. This work has served to show that computational tools can serve to support experimental test results and show promise for use as an alternative to testing to support structural designs utilizing composite materials.

9. ACKNOWLEDGEMENTS

The financial support of the Naval Undersea Warfare Center (Division Newport) In-house Laboratory Independent Research program (ILIR) directed by Dr. Anthony Ruffa is greatly acknowledged. Arun Shukla would like to acknowledge the support of Office of Naval Research under ONR Grant No. N00014-10-1-0662 (Dr. Y.D.S. Rajapakse) to the University of Rhode Island. Bruce Booker, Steve Morin, and Brian Ploutz are thanked for their operation of the shock tube facility. The assistance of Nate Gardner and Nicholas Heeder with the DIC setup is acknowledged.

10. REFERENCES

- [1] Espinosa, H.D., Lee, S., Moldovan, N., “A Novel Fluid Structure Interaction Experiment to Investigate Deformation of Structural Elements Subjected to Impulsive Loading”, *Experimental Mechanics*, 46, 805-824, 2006
- [2] Nurick, G., Olson, M., Fagnan, J., Levin, A., “Deformation and Tearing of Blast Loaded Stiffened Square Plates”, *International Journal of Impact Engineering*, 16, 273–291, 1995
- [3] Nurick, G., Shave, G., “The Deformation and Tearing of Thin Square Plates Subjected to Impulsive Loads - An Experimental Study”, *International Journal of Impact Engineering*, 18, 99–116, 1996
- [4] Tekalur, A.S., Shivakumar, K., Shukla, A., “Mechanical Behavior and Damage Evolution in E-Glass Vinyl Ester and Carbon Composites Subjected to Static and Blast Loads”, *Composites: Part B*, 39, 57-65, 2008
- [5] LeBlanc, J., Shukla, A., Rousseau, C., Bogdanovich, A., “Shock Loading of Three-Dimensional Woven Composite Materials”, *Composite Structures*, 79, 344-355, 2007
- [6] Jackson, M., Shukla, A., “Performance of Sandwich Composites Subjected to Sequential Impact and Air Blast Loading”, *Composites: Part B*, Article in Press, 2010
- [7] Schubel, P.M., Luo, J., Daniel, I., “Impact and Post Impact Behavior of Composite Sandwich Panels”, *Composites: Part A*, 38, 1051-1057, 2007
- [8] O’Daniel, J. L., Koudela, K. L., Krauthammer, T., “Numerical Simulation and Validation of Distributed Impact Events”, *International Journal of Impact Engineering*, 31, 1013–1038, 2005
- [9] McGregor, C. J., Vaziri, R., Poursartip, A., Xiao X., “Simulation of Progressive Damage Development in Braided Composite Tubes under Axial Compression”, *Composites: Part A*, 38, 2247–2259, 2007
- [10] Batra, R.C., Hassan, N.M., “Response of Fiber Reinforced Composites to Underwater Explosive Loads”, *Composites: Part B*, 38, 448–468, 2007
- [11] LeBlanc, J., Shukla, A., Dynamic Response and Damage Evolution in Composite Materials Subjected to Underwater Explosive Loading: An Experimental and Computational Study”, *Composite Structures*, 92, 2421-2430, 2010
- [12] Poche, L., Zalesak, J., “Development of a Water-Filled Conical Shock Tube for Shock Testing of Small Sonar Transducers by Simulation of the Test Conditions for the Heavyweight MIL-S-901D (Navy)”, *NRL Memorandum Report* 7109, 10 October 1992
- [13] Coombs, A., Thornhill, C.K., “An Underwater Explosive Shock Gun”, *Journal of Fluid Mechanics*, 29, 373-383, 1967
- [14] Chan, S., Fawaz, Z., Behdinan, K., Amid, R., “Ballistic Limit Prediction using a Numerical Model with Progressive Damage Capability”, *Composite Structures*, 77, 466–474, 2007
- [15] Russell, D.M., “Error Measures for Comparing Transient Data, Part I: Development of a Comprehensive Error Measure, Part II: Error Measures Case Study”, *Proceedings of the 68th Shock and Vibration Symposium*, November 3-6, 1997
- [16] Russell, D.M., “DDG53 Shock Trial Simulation Acceptance Criteria”, *69th Shock and Vibration Symposium*, October 12-19, 1998

Adhesion Strength in Metal/Polymer Composites

Barbara O. Calcagno*

Dept. of General Engineering, University of Puerto Rico-Mayagüez

Kevin R. Hart

Engineering Mechanics Program, University of Wisconsin-Madison

Wendy C. Crone

Dept. of Engineering Physics, University of Wisconsin-Madison

*Corresponding Author:

Call Box 9000

Mayagüez, PR 00681-9000

barbara.calcagno@upr.edu

ABSTRACT

A load applied to a composite is transferred from the matrix to the dispersed phase through their shared interface. The performance of the composite depends strongly on the interfacial adhesion between the constituents. Shear strength, resistance to delamination, and effective load transfer between the matrix and the inclusion are improved when the interfacial bond is optimized. The interfacial adhesion strength between the metallic inclusions, titanium (Ti) and a nickel titanium shape memory alloy (NiTi), and different polymeric matrices, namely polycarbonate (PC), polypropylene (PP), and high-density polyethylene (HDPE), was measured using pullout testing. The adhesion strengths were determined by dividing the force needed to produce debonding of the interface of the polymer/metal strip over the embedded strip area. Results show that PC exhibits the highest adhesion with no difference for either NiTi or Ti. Comparison of the adhesion strength values for PP/Ti and PP/NiTi show a higher and very distinct value for the PP and Ti. In the case of HDPE, the interfacial bonding between the polymer and the NiTi is stronger than with the Ti but the difference is not as big as the one found for the PP composites.

INTRODUCTION

The shear lag or load transfer theory, developed by Cox [1], predicts how an uniaxial tensile load applied to a continuous cylindrical fiber embedded in a weak matrix is redistributed when there is a strong adhesion between the two phases. Assuming no-slip between the interfaces of both constituents, and using elasticity theory, equations for the shear stress distribution and the tensile stress distribution in the fiber were developed. This theory was modified by Kelly [2] and used extensively to predict composites mechanical behavior [3, 4]. Several modifications to the load transfer theory have been introduced, which include: the effect of the load transferred to the end of the fiber to consider the effect of short fibers in the magnitude and distribution of stresses [5]; the potential existence of stress concentration in the matrix due to neighboring fibers [6]; and the incorporation of different inclusion geometries to take into account the fiber shape, such as conical [7] or rectangular layers [8]. In all cases a strong interfacial bonding between the surfaces of the inclusion and the matrix of the composite is assumed.

The mechanisms that are believed to play a role in the adhesion between two surfaces are molecular bonding, mechanical coupling, and thermodynamic adhesion [9]. Molecular bonding is due to intermolecular forces such as chemical bondings (metallic, covalent, and ionic), dipole-dipole interactions, and van der Waals forces. The mechanical coupling, known also as interlocking, is due to surface roughness, which increasing the surface area allows a greater molecular bonding interaction. The thermodynamics mechanism of adhesion is based on an optimization of the interfacial tension at the interface, which could occur when the surface free energy of the polymer is minimized. All these mechanisms are heavily dependent on the surface condition of the materials involved.

A variety of methods have been used to characterize the interfacial adhesion strength in composite materials. Peel test, lap shear, fiber pullout, fragmentation, and microindentation are some of them [9-14]. These tests each provide a mean for comparison of the interfacial strength but do not give a fundamental property measure.

In the peel test [9] adhesive tape is pressed against the surface of the sample with a rubber cylinder and quickly pulled off. The delamination toughness is calculated using the average peel force and the width of the sample. The lap shear test [14] uses an overlap configuration where two samples are bonded over a region and separated by using a tensile force. The fiber pullout test [10-13] has been used extensively to measure the force needed to pull a fiber of a known length out from a matrix. This test requires a tensile stress to pullout the fiber lower than its ultimate tensile stress. The embedded fiber length should be less than the critical length to ensure that the tensile stress inside the fiber does not reach the tensile strength producing fracture of the fiber. In the fragmentation test [10-13], a fiber embedded in a matrix is loaded with a tensile force producing multiple fractures in the fiber. The test ends when the fracture segments reach the critical length for load transfer. The microindentation test [11, 12] consists in applying a compressive stress to embedded single fibers perpendicular to a cut surface. The test aims to produce debonding and/or slippage of the fibers.

The pullout method has been used extensively to study the behavior of interfacial adhesion strength between the shape memory alloy NiTi and polymeric matrices. Paine et al. [15] used pullout tests to measured the interface adhesion between NiTi and a graphite/epoxy thermoset matrix, and a thermoplastic matrix after treating the surface of the NiTi wires using acid etching, hand sanding, polymer coating and sandblasting. They reported the maximum force on the pullout curve as the force needed for adhesion failure. Paine et al. found that the adhesion strength depends upon the matrix used and the preparation and roughness of the metallic surface. The strongest adhesion was reported for the sandblasted wires. They also reported that the embedded length does not have an effect on the interfacial shear strength.

Jonalagadda et al. [16] correlated the NiTi/polymer adhesion with the local displacements induced by stresses produced by NiTi shape memory wires embedded in an epoxy matrix. Pullout tests were carried out on samples with different surface treatments: acid etched, hand sanded and sandblasted. The results for the roughest surface, corresponding to the sandblasted wires, exhibited the lower wire displacements; the highest debond stress and the highest shear stresses in the matrix. The debond stresses were calculated using the maximum pullout force and the interfacial work of fracture following the work by Penn and Lee [17]. For the shear stresses, a shear-lag solution derived by Tyson and Davies [18] was used. Smith et al. [19] used pullout tests to compare the adhesion strength of untreated and treated NiTi surfaces with silane coupling agents. The adhesion strength was determined measuring the maximum force required to pullout the NiTi wire from the PMMA matrix divided by the length of the wire embedded in the polymer.

Al-Sheyyab et al. [20] used a different testing geometry to investigate the influence of surface coating pre-treatment on the bonding between plastic and metal (steel, and aluminum). Samples with double overlapping between polymer and metal were manufactured to measure the adhesion strength using tensile-shear test. The ratio between the metal thickness and the overlap length with the plastic was 1:5. The coated metal sheets were placed in a mold, where the polymer was fed by injection molding. The average shear stresses were calculated by dividing the total applied shear force over the contact area. Using a simulation software based on the finite elements method, they obtained the stress distribution over the contact area and identified the location with maximum local stresses. They reported that maximum stresses occurred at the sides of the overlapping area.

The study presented in this paper is part of a broader investigation to establish the key factors in the fracture of an inclusion within a polymer/metal-alloy composite during calendaring [21]. Two metal inclusion materials were chosen, titanium and the shape memory alloy NiTi, and were tested in combination with three polymers, polycarbonate (PC), polypropylene (PP), and high-density polyethylene (HDPE). Our prior work has shown that the deformation and fracture behavior of the inclusion depends on the processing parameters and factors such as interfacial adhesion, the dimensions and the mechanical properties of the constituents, the deformation behavior of the polymeric matrices, and finally on how the load is transferred from the rollers to the samples. In a prior study the interfacial adhesion strength between NiTi, and three different polymers, polycarbonate, polypropylene, and high-density polyethylene [22] used in the cold rolling tests was studied by using pullout tests of a wire embedded in a polymeric matrix. The NiTi wires (0.032 in diameter) embedded in the polymers were tested at a crosshead speed of 5 mm/min. Results showed that the adhesion strength between the NiTi and the HDPE had the highest value, followed by the PC. The NiTi/PP exhibited the lowest interfacial adhesion strength. Tests

performed with Ti wires of the same diameter were unsuccessful due to yielding of the wire during the pullout test. An alternative geometry was sought in order to characterize the adhesion strength between the material combinations of interest. The configuration chosen for the pullout sample was similar to the cold rolling samples to capture not only the effect of the bonding between the two surfaces in contact and avoid yielding of the embedded material, but also the effect of the shape and size of the inclusion.

EXPERIMENTAL METHODS

Tensile pullout tests were performed to measure the adhesion strength between polymers and NiTi, and Ti. The polymers used were polycarbonate, polypropylene, and high-density polyethylene, (McMaster, #8742K131, #8574K24, #8619K421, size 12" x 12" x 1/16"). Pseudoelastic NiTi, (Nitinol Devices & Components, NiTi foil, Alloy type SE 508, pseudoelastic at room temperature, 55.6 at% Ni, 0.0127 mm, and 0.6 mm thick), and Ti (Alfa Aesar, Ti foil, 99%, 0.0127 mm, and 0.5 mm thick), were used as the metal inclusions.

The strip pullout samples were made following the same procedure and process parameters used for the sandwich cold rolling samples described by Calcagno [22, 23]. Rectangular grooves 5 mm wide were cut into the stainless steel molds used to prepare cold rolling samples. Grooves with a depth of 1.02 mm were made on either side of the open 50 mm square near the center. These grooves housed the strips while the plastic was melted. The etched NiTi or Ti, approximately 50 mm long and 5 mm wide, were placed between two polymer rectangles in the molds such that roughly 20 mm of the metal was exposed in one of the grooves on the sides of the molds. This procedure was followed to make the pullout samples with thin and thick strips.

For the pullout test of the strip samples, a sample holder used to measure the adhesion between a wire and polymer interface minimizing the compressive stress to the polymer was used [24]. Such device consists of a 1" NPS stainless steel pipe nipple, and a pipe cap with a centered hole as shown in [Figure 1](#).

For the tests of the strip pullout sample, the hole was enlarged to give the strip some degree of freedom during sample positioning to avoid torsion during the test. The sample was inserted inside the pipe with the strip going through the hole in the center of the pipe cap as seen in [Figure 1\(b\)](#). Two half wood cylinders were cut and placed inside the pipe nipple to keep the sample from curling, avoiding lateral compressive stress on the samples during test.

The pullout tests were performed in an Instron 5566 with a constant crosshead speed of 5 mm/min. The adhesion strength between the metal or alloy and the polymer interface was calculated by dividing the maximum force needed to produce debonding during a pullout tensile test over the embedded strip surface area.

RESULTS AND DISCUSSION

Calcagno [22] was successful in obtaining adhesion strength results for the pullout of NiTi wires (0.031 in diameter) embedded in PP, PC, and HDPE. However during the pullout tests of Ti wires (0.0313 in diameter) in PP, the wire yielded, and it fractured with PC or HDPE as matrices. In subsequent work Ti wires with a thicker diameter (0.0625 in) were used, but plastic deformation was also observed. At this point a different configuration for the pullout samples was sought. Two main factors that could affect the bonding were taken into consideration: similar surface roughness of the inclusion to the one used in the cold rolling samples, and a stress distribution during the pullout similar to the cold rolling. The double overlapping configuration used by Al-Sheyyab et al. [20] was chosen with the modification of having a strip of 5 mm wide embedded in the polymer as shown in [Figure 1\(a\)](#). The PP samples with thin NiTi strip were tested successfully, however during the tests of the PP/Ti samples, most of the thin Ti strips yielded, and torsion was observed during the pullout tests. This problem was overcome using thicker strips for both, Ti and NiTi. The surface of all strips was subjected to the same etching treatment applied to the cold rolling strips.

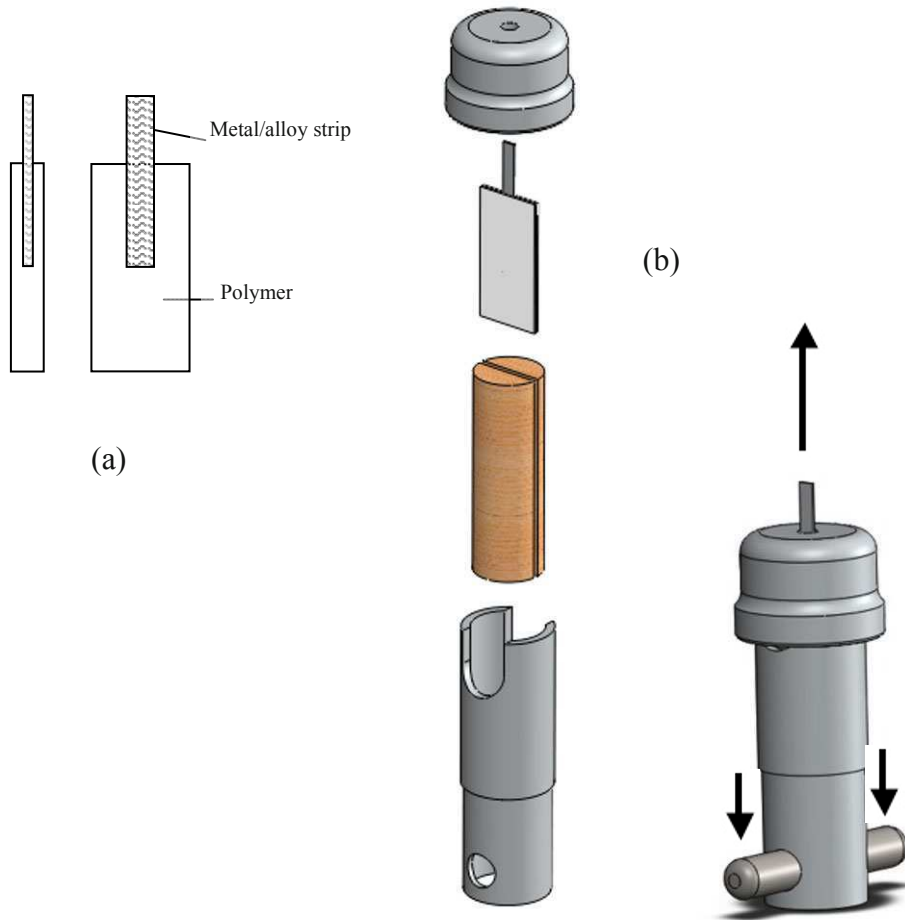


Figure 1: (a) Sketch of a pullout sample, lateral and frontal view. (b) Sketch of the sample holder for the pullout test, exploded and compressed view with applied load.

Typical stress/extension data obtained during pullout tests of PP/Ti, PC/Ti, and HDPE/Ti strip samples are shown in Figure 2. Upon continued loading, the force needed to induce failure of the polymer/strip interface is attained. That force is represented by the maximum in the curve, which in the case of PP/Ti corresponds to 2.34 N/mm^2 for a strip with an embedded length of 12.11 mm. The PC/Ti sample debonded at the highest value of the three cases with adhesion strength of 4.57 N/mm^2 and embedded strip length of 12.1 mm. For the HDPE/Ti the maximum strength is 2.00 N/mm^2 for a strip with an embedded length of 10.3 mm. After this point, only friction opposes the sliding of the strip [3, 25, 26]. The load required to overcome the interfacial adhesion between both materials is much lower than the load needed to induce deformation in the strips of Ti, thus the adhesion strength was calculated by dividing this force over the surface area of the embedded strip.

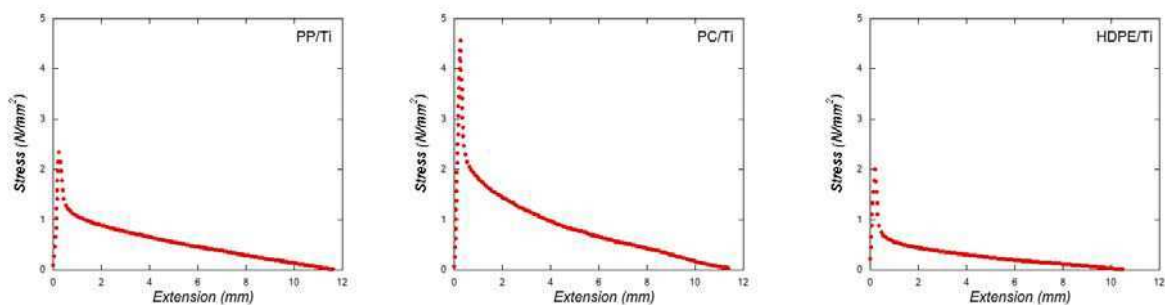


Figure 2: Adhesion Stress vs. Displacement for PP/Ti, PC/Ti, and HDPE/Ti strips pullout samples

Similarly, Figure 3 portrays typical stress/extension data for pullout tests of PP/NiTi, PC/NiTi, and HDPE/NiTi strip samples. In the case of PP/NiTi the stress needed to induce debonding between the polymer and the strip, was 1.52 N/mm^2 for a strip with an embedded length of approximately 10.88 mm. The PC/NiTi sample debonded at the highest value of the three cases with adhesion strength of 4.15 N/mm^2 and embedded strip length of 10.48 mm. The adhesion strength obtained for the HDPE/Ti was 1.8 N/mm^2 for a strip with an embedded length of 8.63 mm.

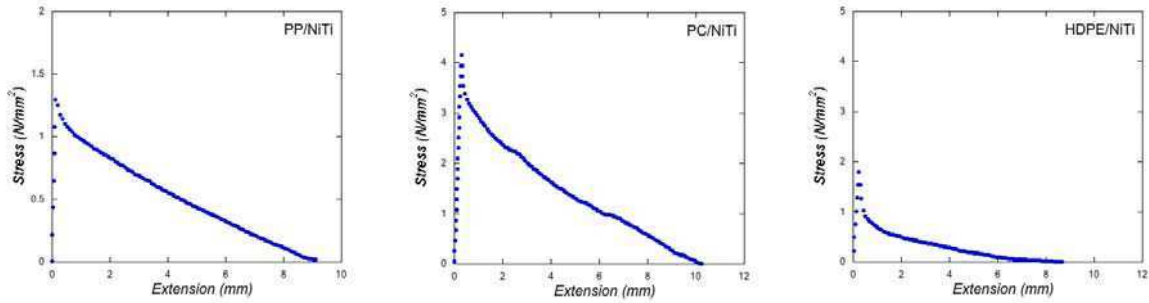


Figure 3: Adhesion Stress vs. Displacement for PP/NiTi, PC/NiTi, and HDPE/NiTi strips pullout samples.

Sample preparation and pullout tests for the PP/Ti, and PP/NiTi were performed as planned. In the case of the HDPE/Ti and HDPE/NiTi, the results of few samples were discarded due to bending of the strip during the test caused by incorrect placing of the sample in the grips. Some of the PC/Ti and PC/NiTi samples contained bubbles in the polymer, which occurred during the manufacture of the samples. Results for these samples were also excluded from the adhesion strength computations. Further information for all the NiTi and Ti samples tested is included in reference [21]. The results of all pullout tests are summarized in Table 1.

A comparison of the adhesion strength values obtained for the six materials combinations tested is provided in Figure 4. The interfacial bonding strength for each polymeric matrix and metallic inclusion has very low standard error for each condition. The PC exhibits the highest adhesion with no difference between NiTi and Ti. Comparison of the adhesion strength values for PP/Ti and PP/NiTi show a higher and very distinctly different value for the PP and Ti. In the case of HDPE, the interfacial bonding between the polymer and the NiTi is stronger than with the Ti but the difference is not as big as the one founded for the PP composites.

Table 1: Summary for the average adhesion strength, and standard deviations for all strip pullout samples.

Constituent	NiTi		Ti	
	Adhesion Strength (N/mm ²)	Standard deviation (N/mm ²)	Adhesion Strength (N/mm ²)	Standard deviation (N/mm ²)
PC	4.42	0.17	4.48	0.27
PP	1.44	0.11	2.32	0.12
HDPE	2.26	0.31	1.75	0.15

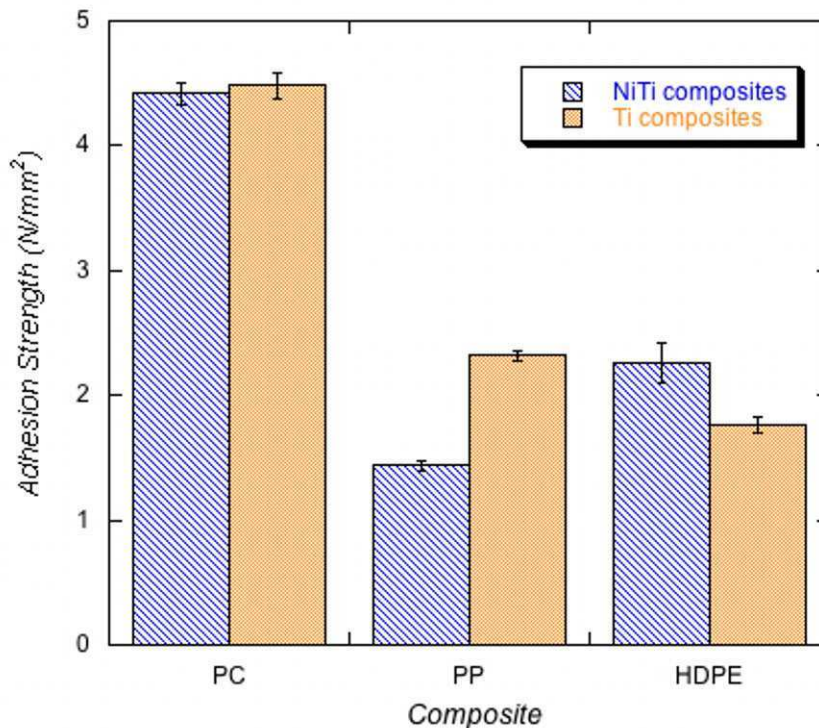


Figure 4: Comparison of Adhesion Strength for all NiTi and Ti composites.

CONCLUSION

The modified overlapping configuration sample for the pullout tests was successfully used to characterize the interfacial bonding strength for all the combinations of matrix/inclusion considered. The adhesion strength was reported as the maximum force attained to debond the two surfaces divided by the contact surface area. Comparison between the adhesion strength between the NiTi and Ti with each of the polymers used was performed. Results show that the PC exhibits the highest adhesion with no difference between NiTi and Ti. Comparison of the adhesion strength values for PP/Ti and PP/NiTi depict a higher and very different value for the PP with Ti inclusions.

ACKNOWLEDGEMENTS

The authors acknowledge the funding support from the AFOSR Grant (FA 9550-04-1-0109), the National Defense Science and Engineering Graduate fellowship (NDSEG), and the University of Puerto Rico at Mayaguez, from which B. Calcagno was on leave of absence.

REFERENCES

1. Cox, H.L., The elasticity and strength of paper and other fibrous materials. *British Journal of Applied Physics*, 1952. 3: p. 72-79.
2. Kelly, A. and W.R. Tyson, Tensile Properties of Fibre-Reinforced Metals - Copper/Tungsten and Copper/Molybdenum. *Journal of the Mechanics and Physics of Solids*, 1965. 13(6): p. 329-8.
3. Gray, R.J., Analysis of the Effect of Embedded Fiber Length on Fiber Debonding and Pull-out from an Elastic Matrix .1. Review of Theories. *Journal of Materials Science*, 1984. 19(3): p. 861-870.
4. Matikas, T.E., Analysis of load transfer behaviour and determination of interfacial shear strength in single-fibre-reinforced titanium alloys. *Advanced Composites Letters*, 2007. 16(5): p. 181-192.
5. Nardone, V.C. and K.M. Prewo, On the Strength of Discontinuous Silicon-Carbide Reinforced Aluminum Composites. *Scripta Metallurgica*, 1986. 20(1): p. 43-48.

6. Nair, S.V. and H.G. Kim, Modification of the Shear Lag Analysis for Determination of Elastic-Modulus of Short-Fiber (or Whisker) Reinforced Metal Matrix Composites. *Journal of Applied Mechanics-Transactions of the Asme*, 1992. 59(2): p. S176-S182.
7. Ji, S.C. and P.L. Zhao, Location of Tensile Fracture within Rigid-Brittle Inclusions in a Ductile Flowing Matrix. *Tectonophysics*, 1993. 220(1-4): p. 23-31.
8. Lloyd, G.E., C.C. Ferguson, and K. Reading, A Stress-Transfer Model for the Development of Extension Fracture Boudinage. *Journal of Structural Geology*, 1982. 4(3): p. 355-372.
9. Awaja, F., et al., Adhesion of polymers. *Progress in Polymer Science*, 2009. 34(9): p. 948-968.
10. Zhandarov, S.F. and E.V. Pisanova, The local bond strength and its determination by fragmentation and pull-out tests. *Composites Science and Technology*, 1997. 57(8): p. 957-964.
11. Favre, J.P., G. Desarmot, and P. Sigety, Fibre/polymer tests at the fibre scale: Tools for analysing and optimizing the composite response to mechanical loads, in *Interfacial Effects in Particulate, Fibrous and Layered Composite Materials*. 1996. p. 133-152.
12. Herrerafranco, P.J. and L.T. Drzal, Comparison of Methods for the Measurement of Fiber Matrix Adhesion in Composites. *Composites*, 1992. 23(1): p. 2-27.
13. Narkis, M., E.J.H. Chen, and R.B. Pipes, Review of Methods for Characterization of Interfacial Fiber-Matrix Interactions. *Polymer Composites*, 1988. 9(4): p. 245-251.
14. Court, R.S., M.P.F. Sutcliffe, and S.M. Tavakoli, Ageing of adhesively bonded joints-fracture and failure analysis using video imaging techniques. *International Journal of Adhesion and Adhesives*, 2001. 21(6): p. 455-463.
15. Paine, J.S.N., W.M. Jones, and C.A. Rogers, Nitinol actuator to host composite interfacial adhesion in adaptive hybrid composites. *AIAA; 33rd Structural Dynamics and Materials Conference*, 1992: p. 556-65.
16. Jonnalagadda, K., G.E. Kline, and N.R. Sottos, Local displacements and load transfer in shape memory alloy composites. *Experimental Mechanics*, 1997. 37(1): p. 78-86.
17. Penn, L.S. and S.M. Lee, Interpretation of Experimental Results in the Single Pull-out Filament Test. *Journal of Composites Technology & Research*, 1989. 11(1): p. 23-30.
18. Tyson, W.R. and G.J. Davies, A Photoelastic Study of Shear Stresses Associated with Transfer of Stress During Fibre Reinforcement. *British Journal of Applied Physics*, 1965. 16(2): p. 199-&.
19. Smith, N.A., et al., Improved adhesion between nickel-titanium shape memory alloy and a polymer matrix via silane coupling agents. *Composites Part a-Applied Science and Manufacturing*, 2004. 35(11): p. 1307-1312.
20. Al-Sheyyab, A., I. Kuehnert, and E. Schmachtenberg, Insert coating as a pre-processing approach for improvement of adhesive bonding in plastic-metal hybrid structures. *Society of Plastics Engineers Annual Technical Conference: Plastics Encounter at ANTEC 2007, Conference Proceedings*, 2007. 2: p. 996-1000.
21. Calcagno, B.O., Deformation and Fracture in Multilayer Systems during Calendaring Processes. University of Wisconsin-Madison; PhD. Thesis, 2010.
22. Calcagno, B.O., Fracture of a Shape Memory alloy in polymer composites induced by cold rolling. Master Thesis, University of Wisconsin - Madison. 2008.
23. Calcagno, B.O., et al., Fracture induced by cold rolling in metal/polymer composites. *Society for Experimental Mechanics - SEM Annual conference and Exposition on Experimental and Applied Mechanics 2009*, 2009. v 4: p. p 2357-2364.
24. Antoun, G.G., Improving to adhesion between a NiTi wire and polymer matrix for composite applications and mechanical fabrication of nanometer-sized shape memory alloy NiTi particles from bulk by rolling and folding. Master Science Thesis. 2003, Wisconsin: Madison.
25. DiFrancia, C., T.C. Ward, and R.O. Claus, The single-fibre pull-out test .1. Review and interpretation. *Composites Part a-Applied Science and Manufacturing*, 1996. 27(8): p. 597-612.
26. Desarmot, G. and J.P. Favre, Advances in Pull-out Testing and Data-Analysis. *Composites Science and Technology*, 1991. 42(1-3): p. 151-187.

Modal-Parameter Identification From Nonstationary Ambient Vibration Data

Dar-Yun Chiang* and Chang-Sheng Lin†

Department of Aeronautics and Astronautics, National Cheng Kung University

No.1, Ta-Hsueh Road, Tainan 701, Taiwan

ABSTRACT

Identification of modal parameters from response data only is studied for structural systems under nonstationary ambient vibration. By assuming the ambient excitation to be nonstationary white noise in the form of a product model, the modal parameters of a system could be identified through the correlation method in conjunction with a technique of curve-fitting. However, the error involved in the approximate free-decay response would generally lead to a distortion in the modal parameters of identification. It is shown that, under appropriate conditions, the ambient response corresponding to nonstationary input of various types can be approximately expressed as a sum of exponential functions, so that we can use the Ibrahim time-domain method in conjunction with a channel-expansion technique to directly identify the major modes of a structural system without any additional treatment of converting the original data into the form of free vibration. To further distinguish the structural modes from non-structural modes, the concept of mode-shape coherence and confidence factor is employed. Numerical simulations, including one example of using practical excitation data, confirm the validity and robustness of the proposed method for identification of modal parameters from general nonstationary ambient response.

Keywords: Ibrahim time-domain method, Nonstationary ambient vibration, Channel-expansion technique, Mode-shape coherence and confidence factor

1. Introduction

Modal-parameter identification from ambient vibration data has gained considerable attention in recent years [1,2]. A variety of methods have been developed for extracting modal parameters from structures undergoing ambient vibration. Ibrahim [3] applied the random-decrement technique coupled with a time-domain parameter identification method [4] to process ambient vibration data. James *et al.* [5] developed the so-called natural excitation technique using the correlation technique coupled with time-domain parameter extraction. It was shown that the cross correlation between two response signals of a linear system with classical normal modes and subjected to stationary white-noise inputs is of the same form as free-vibration decay or impulse response. Chiang and Cheng [6] proposed a correlation technique for modal-parameter identification of a linear, complex-mode system subjected to stationary ambient excitation. Chiang and Lin [7] applied the correlation

* Professor

†Ph.D. candidate, e-mail: p46914151@yahoo.com.tw

technique coupled with Eigensystem Realization Algorithm to identify modal parameters of a system subjected to realistic ambient excitation.

In the previous studies of modal-parameter identification from ambient vibration data, the assumption usually made is that the input excitation is a broadband stochastic process modeled by *stationary* white or filtered white noise. In the present paper, it is shown that if the input signals can be modeled as nonstationary white noise, which is a product of white noise and a deterministic time-varying function, the practical problem of insufficient data samples available for evaluating nonstationary correlation can be approximately resolved by first extracting the amplitude-modulating function from the response and then transforming the nonstationary responses into stationary ones. The correlation functions of the stationary response are treated as free vibration response, and so the Ibrahim time-domain method can then be applied to identify modal parameters of the system. However, the error involved in the approximate free-decay response would generally lead to a distortion in the modal parameters of identification. Furthermore, we propose a technique to extend the ITD method for modal-parameter identification from nonstationary ambient vibration data without using input data or any additional treatment of converting the original forced-vibration data into the form of free vibration. It is shown that the ambient response corresponding to nonstationary input of various types can be approximately expressed as a sum of exponential functions, so that we can use the ITD method to directly identify the major modes of a structural system. For the purpose of improving the accuracy of modal-parameter identification, a channel-expansion technique is also employed. Numerical simulations, including one example of using practical excitation data, will be performed to confirm the validity and robustness of the proposed method for identification of modal parameters from general nonstationary ambient vibration data.

2. Correlation Technique

James *et al.* [5] developed the so-called Natural Excitation Technique (NExT) using the correlation technique. It was shown that the cross-correlation between two response signals of a linear system with classical normal modes and subjected to white-noise inputs is of the same form as free vibration decay or impulse response. In combination with a time-domain parameter extraction scheme, such as the ITD method, this concept becomes a powerful tool for the identification analysis of structures under stationary ambient vibration. When a system is excited by stationary white noise, the cross-correlation function $R_{ij}(\tau)$ between two stationary response signals $x_i(t)$ and $x_j(t)$ can be shown to be [5]:

$$R_{ij}(\tau) = \sum_{r=1}^n \frac{\phi_{ir} A_{jr}}{m_r \omega_{dr}} \exp(-\zeta_r \omega_r \tau) \sin(\omega_{dr} \tau + \theta_r) \quad (1)$$

where ϕ_{ir} denotes the i -th component of the r -th mode shape, A_{jr} a constant, and m_r the r -th modal mass. The result above shows that $R_{ij}(\tau)$ in Eqn. (1) is a sum of complex exponential functions (modal responses), which is of the same mathematical form as the free vibration decay or the impulse response of the original system. Thus, the cross-correlation functions evaluated of responses data can be used as free vibration decay or as impulse response in time-domain modal extraction schemes so that measurement of white-noise inputs can be

avoided. It is remarkable that the term $\phi_{ir} A_{jr}$ in Eqn. (1) will be identified as the mode-shape components. In order to eliminate the A_{jr} term and retain the true mode-shape components ϕ_{ir} , all the measured channels are correlated against a common reference channel, say x_j . The identified components then all possess the common A_{jr} component, which can be normalized out to obtain the desired mode shape ϕ_{ir} .

3. Practical Treatment of Nonstationary Data

The practical problem for evaluating non-stationary correlation is that usually very limited data samples are available in engineering practice. The problem can be resolved by first extracting the modulating function from the response if the excitation can be modeled approximately as the product model. If the excitation can be modeled as non-stationary white noise as represented by the product model with a slowly-time-varying amplitude-modulating function, according to our theoretical derivation, then the responses of the system can also be modeled approximately as a product model with the same amplitude-modulating function as that associated with the excitation itself. With the modulating function extracted, the original non-stationary responses can be transformed into stationary ones. To extract the modulating function out of the non-stationary response histories, we employ the technique of curve fitting. The time-varying standard deviation of the response histories is firstly determined using interval average and then applied curve fitting. This gives us the deterministic envelope function which describes the slow variation in the amplitude of the ambient excitations. We can thus acquire the approximate stationary responses by dividing the non-stationary responses of each DOF with the associated modulating functions obtained by curve fitting. Then the correlation functions of the stationary response data can be obtained, which are in turn treated as the free decay responses corresponding to each DOF. The modal parameters of the system can then be obtained via a time-domain mode identification method, such as the Ibrahim time-domain method (ITD).

4. Extension of Ibrahim Time-Domain Method for Modal-parameter Identification from Ambient Vibration Data

As mentioned above, by assuming the ambient excitation to be nonstationary white noise in the form of a product model, the modal parameters of a system could be identified through the correlation method in conjunction with a technique of curve-fitting. However, the error involved in the approximate free-decay response would generally lead to a distortion in the modal parameters of identification. In the following, we are going to extend the ITD method to identify modal parameters of a structure solely and directly from forced response data, i.e., without using input data or any additional treatment of converting responses into the form of free vibration. It is remarkable that the essence of the ITD method is to utilize the free-decay responses which are expressible as linear combinations of exponential functions, so that extraction of modal parameters can be performed using different time-delayed sampled responses. In light of this concept, we come up with a new idea that if the ambient vibration data can be approximated directly as a linear combination of exponential functions, then the ITD method may be used for modal-parameter identification directly from ambient response data. In the

following, we will show that, under appropriate conditions, nonstationary ambient responses can be approximately expressed as a linear combination of exponential functions.

4.1 Modeling of Ambient Excitation

In this paper, we consider that the ambient excitation can be modeled as a nonstationary process, which is represented by a proper composition of stationary process and a deterministic time-varying function. We start by considering that a stationary process $W(t)$ can be approximately expressed as [8]

$$W(t) \approx \text{Re} \left\{ \sum_{k=1}^{N_\omega} \psi_k e^{i\omega_k t} \right\}, \quad (2)$$

where $\psi_k = \sqrt{4S_{WW}(\omega_k) \Delta\omega} e^{-i\varphi_k}$, $\omega_k = k \cdot \Delta\omega$, $S_{WW}(\omega)$ is the power spectral density function of $W(t)$ (if $W(t)$ is white noise, S_{WW} is a constant), and φ_k , $k=1 \sim N_\omega$, are a set of independent random variables (phases) uniformly distributed over $(0, 2\pi)$. Note that, for each k , $\psi_k e^{i\omega_k t}$ has a similar form to vibration behavior of a mode, so herein we call it a “mode” of excitation, and the corresponding ψ_k can thus be viewed as a component of “mode shape” of excitation (corresponding to a certain degree of freedom). Eq.(2) is originally used to simulate stationary Gaussian processes and to generate sample functions with prescribed power spectra. It is noted that a stationary sample function $W(t)$, as described in Eq.(2), can be approximately expressed as a linear combination of $e^{i\omega_k t}$, which is of a similar form to the undamped, free vibration of a discrete linear system.

To describe the time-varying nature of ambient excitation in practice, we consider the excitation to be a nonstationary process. In general, a nonstationary process can be expressed, on the basis of a stationary process $W(t)$, as follows:

1. Product model :

$${}_p f(t) = {}_p \Gamma(t) W(t), \quad (3)$$

where ${}_p \Gamma(t)$ is a deterministic envelope function (or amplitude-modulating function) used to describe the time-varying amplitude (variance) of a nonstationary process.

2. Additive model :

$${}_a f(t) = {}_a \Gamma(t) + W(t), \quad (4)$$

where ${}_a \Gamma(t)$ is a deterministic trend function used to describe the time-varying mean of a nonstationary process.

The time-varying functions ${}_p \Gamma(t)$ and ${}_a \Gamma(t)$ mentioned above could be further approximated as

$$\Gamma(t) \approx \sum_{k=1}^n a_k e^{\alpha_k t}. \quad (5)$$

By utilizing the above formulation as well as choosing appropriately the values of n , a_k , and α_k , we can describe a wide variety of nonstationary behavior in reality. Substituting both Eqs.(2) and (5) into Eqs.(3) and (4), respectively, the models can be expressed as follows:

$${}_p f(t) = \text{Re} \left\{ \sum_{k=1}^{N_\omega} \left(\psi'_{1k} \cdot e^{(\alpha_1 + i\omega_k)t} + \dots + \psi'_{nk} \cdot e^{(\alpha_n + i\omega_k)t} \right) \right\}, \quad (6)$$

$${}_a f(t) = \sum_{k=1}^n a_k e^{\alpha_k t} + \text{Re} \left\{ \sum_{k=1}^{N_\omega} \psi_k e^{i\omega_k t} \right\}, \quad (7)$$

where $\psi'_{nk} = a_n \psi_k$. It is apparent from Eqs.(6) and (7) that a nonstationary process in the form of either a product model or an additive model can also be approximately expressed as a linear combination of exponential functions. In the following, we are going to analyze the responses of a system subjected to nonstationary inputs discussed above.

4.2 Analysis of Ambient Response

Consider an N -degree-of-freedom (DOF), discrete-time, linear system subjected to ambient excitation resulting from a single source, which is assumed to be a nonstationary process in the form of either Eq.(6) or (7). The displacement response, either ${}_p \mathbf{x}(t)$ or ${}_a \mathbf{x}(t)$, which is a vector of displacement corresponding to different DOF of a system can be obtained by combining the complementary solution and the particular solution as follows:

$${}_p \mathbf{x}(t) = \sum_{k=1}^{2m+n \cdot N_\omega} {}_p \boldsymbol{\phi}_k e^{\lambda_k t} = {}_p \boldsymbol{\Phi} {}_p \boldsymbol{\Lambda}, \quad (8)$$

where m is the number of (real) modes of the system, and ${}_p \boldsymbol{\Phi}$ is an $N \times (2m + n \cdot N_\omega)$ matrix, which is the complex “modal” matrix composed of ${}_p \boldsymbol{\phi}_k$ for $k=1 \sim 2m + n \cdot N_\omega$, including the $2m$ mode shapes of the structure as well as the $n \cdot N_\omega$ “mode shapes” of the nonstationary excitation in the form of Eq.(6). ${}_p \boldsymbol{\Lambda}$ is a $(2m + n \cdot N_\omega) \times 1$ matrix composed of $e^{\lambda_k t}$ for various k .

$${}_a \mathbf{x}(t) = \sum_{k=1}^{2m+n \cdot N_\omega} {}_a \boldsymbol{\phi}_k e^{\lambda_k t} = {}_a \boldsymbol{\Phi} {}_a \boldsymbol{\Lambda}, \quad (9)$$

where the roles of ${}_a \boldsymbol{\phi}_k$, ${}_a \boldsymbol{\Phi}$, and ${}_a \boldsymbol{\Lambda}$ are similar to those in Eq.(8). Note that, in Eqs.(8) and (9), some λ_k 's are associated with structural modes, while the others may be associated with the excitation. Eqs.(8) and (9) show that both ${}_p \mathbf{x}(t)$ and ${}_a \mathbf{x}(t)$ can be expressed as a linear combination of exponential functions, which signifies that the forced-response data can be put into the form of free-vibration without any additional treatment, and the major modes of a structural system can then be obtained via a time-domain modal-identification method, such as the ITD method, as described next.

4.3 ITD Extraction

In the following, we will extend the ITD method to identify modal parameters of a structure from forced-response data. Recall that in the conventional ITD analysis, which uses free-decay responses of a structure to identify its modal parameters in complex form [4], we define a system matrix \mathbf{A} , such that

$$\mathbf{A} \mathbf{X} = \mathbf{Y}, \quad (10)$$

where \mathbf{Y} is a response matrix obtained from time-shifting of a data-expansion matrix \mathbf{X} . Eq. (10) implies that the system matrix \mathbf{A} can be determined from \mathbf{X} and \mathbf{Y} by using the least-squares method when the

number of sampling points is larger than the number of measurement channels. The order of the system matrix \mathbf{A} is chosen to be at least twice of the number m of (real) modes of interest. If the number of measurement channels does not actually reach the number of modes of interest, we may employ the technique of channel expansion [4], which uses time-delayed responses as additional response channels, such that the total number of measurement channels reaches the desired order of the system matrix \mathbf{A} . In the present paper, the ITD method is extended for modal-parameter identification directly from the force response data. Thus, the noise due to excitation would generally lead to a distortion in identifying modal parameters of a system. To take advantage of the property of consistency in the theory of system identification for improving the effectiveness of the extended ITD method, we tend to use more measurement data in the analysis, which can be practically achieved by extending the sampling period and/or by performing channel expansion. In performing channel expansion, we usually construct a data-expansion matrix \mathbf{X} with more measurement channels to have richer information of structural modes, as follows:

$$\mathbf{X} = \begin{bmatrix} {}_0\mathbf{X} \\ {}_\tau\mathbf{X} \end{bmatrix}, \quad (11)$$

where ${}_\tau\mathbf{X}$ is obtained from τ -time shifting of the original response data matrix ${}_0\mathbf{X}$. It follows from almost the same procedure as used in ITD to solve the eigenvalue problem associated with the corresponding system matrix \mathbf{A} determined by using the least-squares method, and then the major modes of a structural system can be identified. Note that the well-known least-squares method is a classical strategy to find solutions for over-determined systems, usually interpreted as a method of fitting data. It can be shown [9] that estimates obtained by the least-squares method also have optimal statistical properties of being unbiased, efficient, and consistent. Based on the concept mentioned above, the higher-order \mathbf{A} will lead to more complete and accurate modal parameters of a system. Note that the eigenvalues of \mathbf{A} are directly related to the natural frequencies and the damping ratios of the original vibrating system, and the eigenvectors of \mathbf{A} correspond to the mode shapes of the system [4].

It should be mentioned that, however, the modes identified by the extended ITD method directly from the forced response data will generally include the vibrating modes of a structural system, the “modes” of excitation (as mentioned above), and possibly some fictitious modes due to numerical noise. In the following, we are going to show how to extract the structural modes from the identified modes. Recall that it is apparent from Eqs.(8) and (9) that the nonstationary response in the form of either a product model ${}_p\mathbf{x}(t)$ or an additive model ${}_a\mathbf{x}(t)$ can be approximately expressed as a linear combination of exponential functions. The time-delayed responses obtained from τ -time shifting of ${}_p\mathbf{x}(t)$ and ${}_a\mathbf{x}(t)$, denoted respectively as ${}_p\mathbf{x}(t+\tau)$ and ${}_a\mathbf{x}(t+\tau)$, can be derived as follows:

$${}_p\mathbf{x}(t+\tau) = \sum_{k=1}^{2m+n+N_\omega} {}_p\phi_k e^{\lambda_k t}, \quad (12)$$

$${}_a\mathbf{x}(t+\tau) = \sum_{k=1}^{2m+n+N_\omega} {}_a\phi_k e^{\lambda_k t}, \quad (13)$$

where ${}^\tau\phi_k = {}_p\phi_k e^{\lambda_k \tau}$ and ${}^\tau\phi_k = {}_a\phi_k e^{\lambda_k \tau}$. According to Eqs.(12) and (13), as well as the aforementioned relationship between ${}_0\mathbf{X}$ and ${}_\tau\mathbf{X}$ in Eq.(11), a typical eigenvector ϕ_i of \mathbf{A} corresponding to the i th eigenvalue λ_i can be expressed as

$$\phi_i = \begin{bmatrix} {}_0\phi_i \\ {}_\tau\phi_i \end{bmatrix}, \quad (14)$$

where we can show that

$${}_\tau\phi_i = {}_0\phi_i e^{\lambda_i \tau}, \quad (15)$$

provided that ${}_0\phi_i$ is the mode-shape vector of a structure mode or excitation mode [cf. Eqs.(12) and (13)]. This is because that vibration of each “mode” demonstrates exponentially decayed harmonic behavior. Based on the concept mentioned above, to further extract the structural modes from the identified modes, we can employ the mode-shape coherence and confidence factor (MSCCF) [10], which is defined as

$$\text{MSCCF}({}_0\phi_i, {}_\tau\phi_i) = \frac{{}_0\phi_i^T {}_\tau\phi_i^* e^{\lambda_i \tau}}{{}_\tau\phi_i^T {}_\tau\phi_i^*}, \quad (16)$$

where the superscripts $*$ and T denote the complex conjugate and matrix transpose respectively. When the MSCCF value of an identified mode shape is approximately equal to 1, it implies that the mode shape represents a mode shape associated the structure or the excitation. Identification results are then sorted as either structural parameters or input-force characteristics through computing the MSCCF values.

Furthermore, to distinguish the vibrating modes of the structural system from a excitation, we can use the modal assurance criterion (MAC) [11], which is originally used to check for agreement between the identified mode shapes as well as exact shapes, and has been extensively used to confirm the vibrating modes of a structural system in experimental modal analysis. The definition of the MAC is

$$\text{MAC}(\phi_{iA}, \phi_{jX}) = \frac{|\phi_{iA}^T \phi_{jX}^*|^2}{\phi_{iA}^T \phi_{iA}^* \phi_{jX}^T \phi_{jX}^*}, \quad (17)$$

where ϕ_{iA} and ϕ_{jX} denote the i th theoretical and the j th identified mode shape, respectively. The value of MAC varies between 0 and 1. When the MAC value is equal to 1, the two vectors ϕ_{iA} and ϕ_{jX} represent exactly the same mode shape. On the other hand, when two mode shapes are orthogonal with each other, the MAC value is zero. Verification of the vibrating modes of a structural system can thus be performed through computing the MAC values. If the mass matrix or the stiffness matrix of a structural system is available, we can distinguish the structural modes from the excitation modes or the fictitious modes according to the orthogonality conditions of mode shapes with respect to the stiffness matrix or to the mass matrix. If neither the exact information of the structural modes nor the mass matrix (or the stiffness matrix) of the structural system is available, the structural modes can usually be identified by observing identified damping ratios, due to that the “excitation modes” are related to the steady-state responses corresponding to persistent (in contrast to shock or

impulse) excitation and the corresponding damping ratios are generally close to zero (i.e., showing no decay), while the damping ratios corresponding to the vibrating modes of damped structures are normally non-zero.

5. Numerical Simulation

To demonstrate the effectiveness of the proposed method, we first consider a linear 6-DOF chain model with viscous damping. The mass matrix \mathbf{M} , stiffness matrix \mathbf{K} , and the damping matrix \mathbf{C} of the system are given as follows :

$$\mathbf{M} = \begin{bmatrix} 2 & 0 & 0 & 0 & 0 & 0 \\ 0 & 2 & 0 & 0 & 0 & 0 \\ 0 & 0 & 2 & 0 & 0 & 0 \\ 0 & 0 & 0 & 2 & 0 & 0 \\ 0 & 0 & 0 & 0 & 3 & 0 \\ 0 & 0 & 0 & 0 & 0 & 4 \end{bmatrix} \text{ N} \cdot \text{s}^2 / \text{m}, \quad \mathbf{K} = 600 \cdot \begin{bmatrix} 1 & -1 & 0 & 0 & 0 & 0 \\ -1 & 2 & -1 & 0 & 0 & 0 \\ 0 & -1 & 2 & -1 & 0 & 0 \\ 0 & 0 & -1 & 2 & -1 & 0 \\ 0 & 0 & 0 & -1 & 3 & -2 \\ 0 & 0 & 0 & 0 & -2 & 5 \end{bmatrix} \text{ N / m}, \quad \mathbf{C} = 0.05\mathbf{M} + 0.001\mathbf{K} + 0.2 \begin{bmatrix} 1 & \dots & 1 \\ \vdots & \ddots & \vdots \\ 1 & \dots & 1 \end{bmatrix}_{6 \times 6} \text{ N} \cdot \text{s / m}.$$

Note that because the damping matrix \mathbf{C} cannot be expressed as a linear combination of \mathbf{M} and \mathbf{K} , the system has non-proportional damping (and so complex modes in general). Consider that the ambient vibration input is modeled as nonstationary white noise, as represented by the product model or the additive model, given by Eqs.(2) and (3), respectively. Using Eqs.(2) and (3), the stationary white noise simulated is multiplied and added, respectively, by an amplitude-modulating function ${}_p f(t) = 4 \cdot (e^{-0.002t} - e^{-0.004t})$ and a trend function ${}_a f(t) = 50 \cdot (e^{-0.002t} - e^{-0.004t})$ to obtain the nonstationary white noise inputs, which act on the sixth mass of the system. Note that the stationary white noise, whose bandwidth extends well past all the frequencies of interest, is generated using the spectrum approximation method [8] as a zero-mean band-pass noise, for which the power spectral density constant is $0.02 \text{ m}^2 / (\text{s}^3 \cdot \text{rad})$ with a frequency range from 0 to 50 Hz. The sampling interval is chosen as $\Delta t = 0.01 \text{ s}$, and the sampling period is $T = 1310.72 \text{ s}$. The time signal of a simulated sample of the nonstationary white noise is shown in Fig.1.

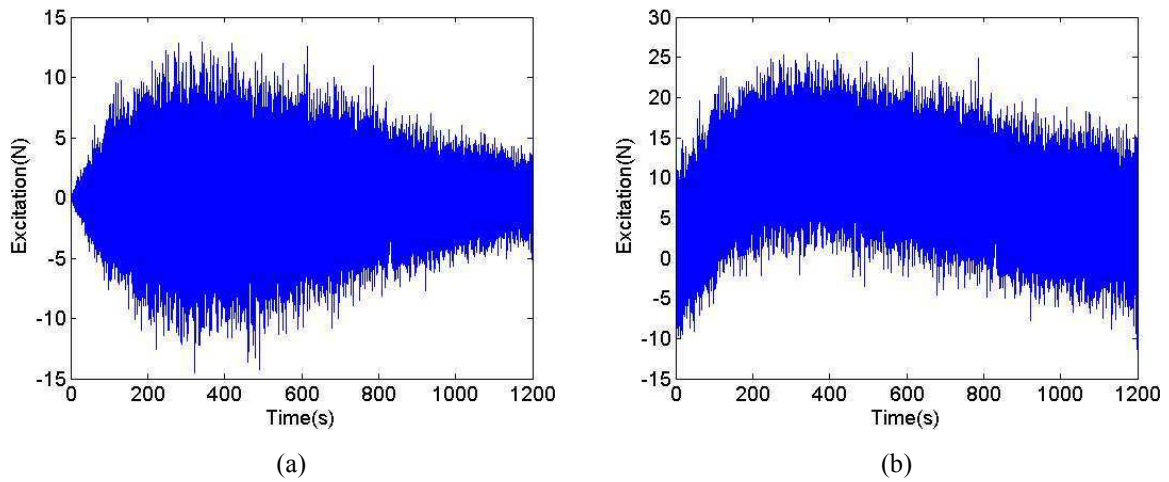


Fig. 1 Sample function of non-stationary white noise with a slowly-varying amplitude-modulating function or trend function,
a) product model, b) additive model

The displacement responses of the system were obtained using Newmark's method. The Ibrahim time-domain method is then applied to identify the modal parameters of the system. By examining the Fourier spectrum associated with each of the response channels, we chose the response of the sixth channel $X_6(t)$, which contains rich overall frequency information, as the reference response to compute the correlation functions of the system. According to the theory presented in a previous section, the nonstationary problem may reduce to a stationary problem if we can extract the amplitude-modulating function from the original nonstationary data in the form of a product model. Therefore, we can follow the same procedures as those for stationary problems, and the correlation functions thus obtained are treated as free-vibration data. The Ibrahim time-domain method could then be applied to identify modal parameters of the system.

Furthermore, because the nonstationary white-noise input can be expressed as a sum of exponential functions, according to the theory presented in another previous section, we can thus use the Ibrahim time-domain method in conjunction with the channel-expansion technique to identify the major modes of a structural system solely and directly from the ambient response data. The results of modal-parameter identification of the 6-DOF system subjected to nonstationary white-noise input in the form of a product model are summarized in Tables 1 and 2, which shows that the errors in natural frequencies identified are less than 1 % and the error in damping ratios are less than 10%. Note that the "exact" modal damping ratios listed in Table 1 and 2, as well as the exact mode shapes, are actually the equivalent values obtained by using ITD from the simulated free-vibration data of the nonproportionally damped structure. The concepts of MSCCF and MAC can be employed to further confirm the vibrating modes of the structural system, and the results are also listed in Tables 1 and 2. In general, when the MAC values are larger than 0.9 and the MSCCF values are closer to 1, the identified results can be referred to as "accurate". The errors of identified damping ratios and mode shapes are somewhat higher, which may be due to the fact that the system response generally has lower sensitivity to these modal parameters than to the modal frequencies.

Table 1 Results of modal-parameter identification of a 6-DOF system subjected to nonstationary white-noise input in the form of a product model through the correlation method in conjunction with a technique of curve-fitting

Mode	Natural Frequency (rad/s)			Damping Ratio (%)			MAC
	Exact	ITD	Error(%)	Exact	ITD	Error(%)	
1	5.03	5.03	0.06	5.24	5.12	2.29	1.00
2	13.45	13.43	0.16	1.07	1.06	0.93	1.00
3	19.80	19.74	0.28	1.13	1.09	3.54	1.00
4	26.69	26.53	0.60	1.43	1.41	1.40	0.98
5	31.66	31.41	0.80	1.66	1.65	0.60	0.94
6	33.73	33.38	1.03	1.74	1.70	2.30	0.95

Table 2 Results of modal-parameter identification of a 6-DOF system subjected to nonstationary white-noise input in the form of a product model through the ITD method in conjunction with a channel-expansion technique

Mode	Natural Frequency (rad/s)			Damping Ratio (%)			MSCCF	MAC
	Exact	ITD	Error(%)	Exact	ITD	Error(%)		
1	5.03	5.06	0.66	5.24	5.32	1.56	1.01	0.99
2	13.45	13.42	0.23	1.07	1.14	6.64	1.01	0.99
3	19.80	19.77	0.16	1.13	1.11	1.49	1.01	0.99
4	26.69	26.51	0.69	1.43	1.32	8.04	1.01	0.99
5	31.66	31.43	0.73	1.66	1.72	3.55	1.02	0.99
6	33.73	33.40	0.99	1.74	1.81	3.88	1.02	0.99

The results of modal-parameter identification of the 6-DOF system subjected to nonstationary white-noise input in the form of an *additive* model are summarized in Table 3. It can be observed that the result of identification is still satisfactory. Note in the present method that it is significant to have sufficiently long measurement data in order to reduce the error due to noise effect in the process of modal-parameter identification, especially for the identification of damping ratios. In addition, to improve the effectiveness of the extended ITD method, we can use a data-expansion matrix \mathbf{X} with more measurement channels. The corresponding system matrix \mathbf{A} determined by using the least-squares method will lead to more complete and accurate modal parameters of a system. Based on numerical studies of this paper, the results of modal-parameter identification using the extended ITD are satisfactory with the selection of the number of measurement channels of \mathbf{X} being as $16m$.

Table 3 Results of modal-parameter identification of a 6-DOF system subjected to nonstationary white-noise input in the form of an additive model through the ITD method in conjunction with a channel-expansion technique

Mode	Natural Frequency (rad/s)			Damping Ratio (%)			MSCCF	MAC
	Exact	ITD	Error(%)	Exact	ITD	Error(%)		
1	5.03	5.12	1.79	5.24	5.29	0.95	1.03	1.00
2	13.45	13.44	0.07	1.07	0.90	15.89	1.02	1.00
3	19.80	19.77	0.15	1.13	1.06	6.19	1.03	1.00
4	26.69	26.49	0.75	1.43	1.27	11.19	1.04	1.00
5	31.66	31.45	0.66	1.66	1.59	4.22	1.05	1.00
6	33.73	33.24	1.45	1.74	2.06	18.39	1.06	1.00

To further examine the effectiveness of the proposed method, we consider the previous 6-DOF chain model excited by a vibration practically recorded at Sun-Moon Lake on the 21th September, 1999, when the Chi-Chi Earthquake of a moment magnitude 7.6 occurred in central Taiwan. The sampling interval and period of this seismic record are $\Delta t = 0.005\text{ s}$ and $T = 59.995\text{ s}$, respectively. A sample of the seismic record, which serves as the excitation input acting on the sixth mass of the model, is shown in Fig. 2. The displacement responses of the system were obtained using Newmark's method, then we perform the modal-parameter identification using the simulation responses, and results obtained are summarized in Table 4. From Table 4, we see that the identification results are good. It indicates that when the practical ambient excitation, such as earthquakes, can be approximately expressed as the composition of exponential functions, the proposed method is applicable to identify the modal parameters of a structural system subjected to realistic excitation.

Table 4 Results of modal-parameter identification of a 6-DOF system subjected to a recorded sample of the Chi-Chi Earthquake through the ITD method in conjunction with a channel-expansion technique

Mode	Natural Frequency (rad/s)			Damping Ratio (%)			MSCCF	MAC
	Exact	ITD	Error(%)	Exact	ITD	Error(%)		
1	5.03	5.16	2.66	5.24	6.68	27.54	1.07	0.98
2	13.45	14.47	7.61	1.07	1.22	13.90	1.00	1.00
3	19.80	19.95	0.76	1.13	1.25	10.98	1.03	1.00
4	26.69	26.74	0.19	1.43	1.02	28.64	1.03	0.98
5	31.66	32.73	3.38	1.66	1.40	15.52	1.05	0.99
6	33.73	33.01	2.15	1.74	1.87	7.32	1.08	1.00

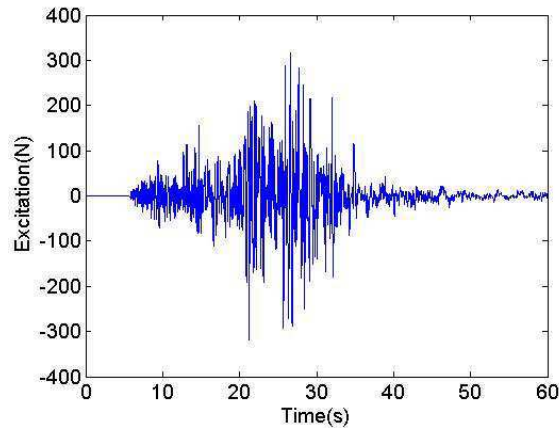


Fig. 2 A recorded sample of the Chi-Chi Earthquake

Recall that in the correlation technique, to improve the accuracy of identified modal parameters, it is important to choose a proper reference channel for computing correlation functions. The richer frequency content the reference channel has, the better results of modal-parameter identification can be achieved. By using the

extended ITD method proposed in the present paper, we can avoid computing correlation functions to convert forced responses into free vibration. Furthermore, we show that the present method is valid for general nonstationary input, and the restriction can be avoided of the product model, which was employed for modeling ambient excitation assumed to be nonstationary white noise.

4. Conclusions

In the present paper, by assuming the ambient excitation to be nonstationary white noise in the form of a product model, the modal parameters of a system could be identified through the correlation method in conjunction with a technique of curve-fitting. However, the error involved in the approximate free-decay response would generally lead to a distortion in the modal parameters of identification. Furthermore, we propose a technique to extend the Ibrahim time-domain method for modal-parameter identification directly and solely from nonstationary ambient vibration data, i.e., without using input data or any additional treatment of converting the original forced-vibration data into free vibration. It is shown that, under appropriate conditions, the ambient vibration responses corresponding to various nonstationary inputs can be expressed as a sum of exponential functions, so that we can use the Ibrahim time-domain method in conjunction with the channel-expansion technique to identify the major modes of a structural system. To confirm the validity of the proposed method, numerical simulations have been performed for various cases in which the systems subjected to nonstationary white-noise input in the forms of a product and an additive model, respectively. Furthermore, to improve the effectiveness of the extended ITD method, we use a data-expansion matrix with more measurement channels such that the corresponding system matrix determined by using the least-squares method will lead to more complete and accurate modal parameters of a system. By using the extended ITD method proposed in this paper, we can avoid computing correlation functions to convert forced responses into free vibration. Through numerical examples, including one example of using practical excitation data, we show that the present method has been shown to be valid for general nonstationary ambient input, and the restriction can be avoided of the product model for modeling ambient excitation assumed to be nonstationary white noise.

Acknowledgements

This research was supported in part by National Science Council of the Republic of China under the grant NSC-96-2221-E-006-188.

References

- [1] Ventura, C. E., Liam Finn, W.D., Lord, J.-F., and Fujita, N., "Dynamic Characteristics of a Base Isolated Building from Ambient Vibration Measurements and low level earthquake shaking," *Soil Dynamics and Earthquake Engineering*, **23** (4) (2003), pp. 313-322.
- [2] Ren, W.-X., Zatar, W., and Harik, I. E., "Ambient Vibration-Based Seismic Evaluation of a Continuous Girder Bridge," *Engineering Structures*, **26** (5) (2004), pp. 631-640.

- [3] Asmussen, J. C., Ibrahim, S. R. and R. Brincker, "Random Decrement and Regression Analysis of Bridges Traffic Responses", *Proceedings of the 14th International Modal Analysis Conference*, **1** (1996), pp. 453-458.
- [4] Ibrahim, S. R. and Mikulcik, E. C., "A Method for the Direct Identification of Vibration Parameters from Free Response", *Shock and Vibration Bulletin*, **47** (4) (1977), pp. 183-198.
- [5] James, G. H., Carne. T. G. and Lauffer, J. P., "The Natural Excitation Technique for Modal Parameter Extraction from Operating Wind Turbines", *SAND92-1666. UC-261, Sandia National Laboratories, 1993*.
- [6] Chiang, D.Y. and Cheng, M. S., "Modal Parameter Identification from Ambient Response", *AIAA Journal*, **37** (1999), pp. 513-515.
- [7] Chiang, D. Y. and Lin, C. S., "Identification of Modal Parameters from Ambient Vibration Data Using Eigensystem Realization Algorithm with Correlation Technique", *Journal of Mechanical Science and Technology*, **24** (12) (2010), pp. 2377-2382.
- [8] Shinozuka, M., "Simulation of Multivariate and Multidimensional Random Processes", *Journal of the Acoustical Society of America*, **49** (1) (1971), pp. 357-367.
- [9] Hsia, T. C., "Least-Squares Theory", *System Identification: Least-Squares Methods*, Lexington Books, Lexington, Massachusetts, 1977, pp.17-32.
- [10] Gao, Y. and Randall, R. B., "The ITD Mode-Shape Coherence and Confidence Factor and Its Application to Separating Eigenvalue Positions in the Z-Plane", *Mechanical Systems and Signal Processing*, **14** (2) (2000), pp. 167-180.
- [11] Allemang, R. L. and Brown, D. L., "A Correlation Coefficient for Modal Vector Analysis", *Proceedings of the 1st International Modal Analysis Conference*, Society for Experiment Mechanics, Bethel, CT, 1983, pp. 110-116.

High-Speed Digital Image Correlation Measurements of Random Nonlinear Dynamic Response

Timothy Beberniss, Aerospace Structures Engineer, Structural Sciences Center, Air Vehicles
Directorate, Air Force Research Laboratory, Wright-Patterson AFB, OH 45385
Email address: timothy.beberniss@wpafb.af.mil

Michael Spottswood, Senior Aerospace Structures Engineer, Structural Sciences Center, Air Vehicles
Directorate, Air Force Research Laboratory, Wright-Patterson AFB, OH 45385

Thomas Eason, Senior Aerospace Structures Engineer, Structural Sciences Center, Air Vehicles
Directorate, Air Force Research Laboratory, Wright-Patterson AFB, OH 45385

ABSTRACT

Future United States Air Force (USAF) high-speed vehicles will require innovative, non-contacting full-field measurement techniques to validate analysis and design practices. In this experimental investigation, the authors explore the feasibility of using high-speed 3D digital image correlation (DIC) to measure the geometrically nonlinear and stochastic response of a compliant panel representing thin-gauge aircraft-like structure. Existing measurement techniques typically employed for this application include laser vibrometry, accelerometers, and discrete strain gages. However, these approaches are limited to a few points or direct contact resulting in altered structural response. The possibility of full-field noncontact displacement and strain measurement is an attractive alternative for this type of dynamic response testing, particularly as one is not limited to predetermined sensor location. The technical challenges of using DIC for this application include extending the technique from quasi-static or extremely short duration transient dynamic measurement technique to steady-state, long-duration (seconds of data) random response. Multiple, long-time sample records are desired for ensemble averaging, and correspondingly high sample rates generate appreciable volumes of digital images never before attempted with this type of analysis. DIC displacement and strain results are compared to the more traditional measurement methods to establish accuracy. Results demonstrate the feasibility of using DIC for nonlinear dynamic displacement and strain response measurements. The ability to obtain full-field displacement data was beneficial towards identification and differentiation of the dynamic panel response from the inherent dynamic response of the experimental facility.

INTRODUCTION & BACKGROUND

High-speed, extreme-environment air vehicle designs require structures that can withstand intense loading. Examples include vehicles exposed to launch, sustained hypersonic velocities, re-entry, and stealth aircraft with buried engines and ducted exhaust. These structural designs will experience extremely hot, transient surface temperatures and thermal gradients, significant dynamic pressure fluctuations, and long-duration exposure to these environments [1]. Challenges in predicting the response of structures in extreme environments include: the coupling between thermal-fluid-structural response; the computational cost and complexity of large models; material nonlinearity, temperature dependence and degradation; the spatial variation of material and structural properties; the uncertainty in loads, material properties, and geometry and boundary conditions. Compounding these analysis and design challenges are the failure modes of high-speed vehicle structures. These structures can fail in high-cycle fatigue due to severe aero-acoustic and mechanical vibration loading, in low-cycle fatigue due to thermal and mechanical loading, and by material degradation or oxidation due to the extreme thermal environment [2].

The AFRL Air Vehicles Directorate, Structural Sciences Center (SSC) seeks to identify those characteristics of high-speed vehicle structures at the panel level and corresponding extreme-environments that necessitate a multi-disciplined analysis. A multi-discipline, coupled capability will be necessary for certain vehicle applications and structural configurations in order to accurately predict the response and life. In particular, it will be advantageous to understand where one or two-way domain coupling is required (or not) to better understand and expand the design space. The design of these extreme environment structures is driven by the trajectory and mission requirements, the selection of a particular vehicle, and the specific location on that vehicle. Arriving at an efficient design is difficult because the analysis and design methods used in industry are

typically single-discipline and often rely on superposition. That is, the worst-case loading scenarios from each domain are superposed resulting in structures that are many times over-built. For this class of vehicles, overly conservative structural designs correspondingly pare back performance and oftentimes for hypersonic vehicle programs, result in programs being canceled. Perhaps the most important factor to facilitate a better understanding for the design process is a series of progressively more complex experiments designed to reproduce the critical and potentially damaging characteristics of high-speed flight. A technical challenge to overcome in this type of experimentation is adequate instrumentation resolution to thoroughly capture the important phenomena while also not interfering and perhaps even contaminating the results.

One of the focuses of this study is to present and discuss a novel use of 3D DIC in a dynamic, extreme-environment setting as a means to address the instrumentation technical challenge. Specifically, the experimental full-field DIC based displacement and strain response of a compliant panel representing aircraft-like thin-gauge panel to the effects of high-speed flow will be demonstrated for long time records. Full-field displacement, strain and load measurements are desired in experiments, but are oftentimes not available. Those experiments that do take advantage of full-field measurements are usually quasi-static or very short-duration vibratory or transient events [3,4,5,6]. For those dynamic experiments that do require long time record measurements for data processing in the frequency domain, and to make stochastic process assumptions like stationarity/ergodicity [7], single point measurements are traditionally made using accelerometers and laser vibrometry. The use of DIC for full-field, structural panel-scale measurements for finite time records is very challenging due to the inordinate amounts of data processing involved. Avitabile *et. al.* successfully used DIC to measure structural mode shapes, and compared the technique and results to traditional modal testing techniques [8]. They note that optical techniques, unlike more traditional modal testing techniques, can have noise-floor issues for higher-frequency modes of vibration as the displacements are quite small. Siebert and Crompton [9] used DIC for vibration and transient testing. They demonstrate the ability to capture operational deflection shapes for several different structures excited at resonance.

In order to study the full-field structural response to an extreme-environment, a joint experiment is being conducted between the AFRL SSC and the Propulsion Directorate's large scale supersonic combustion research facility[10] abbreviated herein as RC-19 test facility. The RC-19 test facility is a continuous-flow wind tunnel designed to study the mechanisms that govern the mixing and combustion process for realistic supersonic combustor geometries. For this set of experiments, the 5 inch by 6 inch test section with the Mach 2 nozzle was utilized along with the large optical access sidewalls. This feature was advantageous for visualizing the flow environment and for obtaining the spatial and temporal pressure loads over the surface of the compliant panel using a fast response pressure sensitive paint [11] on the flow side. The purpose of this RC-19 experiment is two-fold: 1) to investigate the high-speed flow effects, including shock impingement, on the response of a flexible, thin-gauge metallic panel, and 2) to explore and extend where necessary, full-field measurement techniques in order to capture the dynamic loading and nonlinear response of the panel in this high-speed flow environment. The overarching issues to be addressed in this experimental program include: 1) the turbulent boundary layer and shock impingement/oscillation effects on a thin panel, 2) a measure of the flow-induced pressure correlation across the panel, and 3) a measure of the impact on the loading (if any) due to the introduction of a flexible panel into the flow.

EXPERIMENTAL

The RC-19 test facility provides an opportunity to study the effects of a turbulent boundary layer and shock impingement on the dynamic response of the plate for a substantial duration of time. A sectional view of the tunnel and arrangement of the compliant panel and shock generator is shown in [figure 1](#). For the compliant panel test the normal top wall of the tunnel's test section was replaced with three sections. The first section is located at the inflow and contains pressure ports before the compliant panel. The second section contains the compliant panel while the third section terminates the top wall to the exhaust and contains ports to a cavity located behind the panel. The shock generator that is placed in the bottom wall of the tunnel, shown in block 3 of [figure 1](#), turns the flow in a continuous fashion between 0 and 10 degrees. The turbulent boundary layer without the shock generator develops naturally within the tunnel. When the shock generator turns the flow, a shock is impinged on the opposite wall at a location determined by the shock generator's angle and placement in the various block locations. The turbulent boundary layer and shock impingement imparts a random fluctuating pressure load on the panel exciting it dynamically. This dynamic response, at sufficiently high levels can result in high cycle fatigue in thin skinned aircraft structures. A full investigation of the compliant panel's dynamic response requires careful characterization of the incoming loads as well as the dynamic characteristics of the panel. While this paper is focused on the use of digital image correlation to obtain the dynamic response of a compliant panel with random excitation, a brief overview of additional measurements is given below to characterize the loads introduced into the compliant panel.

There were three primary sources of load introduction to the compliant panel: 1) the background mechanical vibrations from the tunnel, 2) the fluctuating pressure from the shock impingement/boundary layer, and 3) the thermally generated load from the temperature variance between the compliant panel and its frame. In order to assess the mechanical vibrations from the tunnel, 15 single axis accelerometers and 2 tri-axial accelerometers were spatially distributed along the top and side walls of the tunnel. This distribution of accelerometers was determined from modal characterization of the tunnel. Before the introduction of airflow, a combination of a roving instrumented hammer and laser vibrometer was used to measure the tunnel modal characteristics. During testing, and to characterize the fluctuating pressure on the compliant panel, a fast response pressure sensitive paint was applied to the flow side. Additionally, static and dynamic pressure measurements were obtained upstream of the panel as well as in the back-side cavity of the compliant panel. Temperature was monitored at one location on the compliant panel and one corresponding location on the compliant frame throughout the test using K type thermocouples.

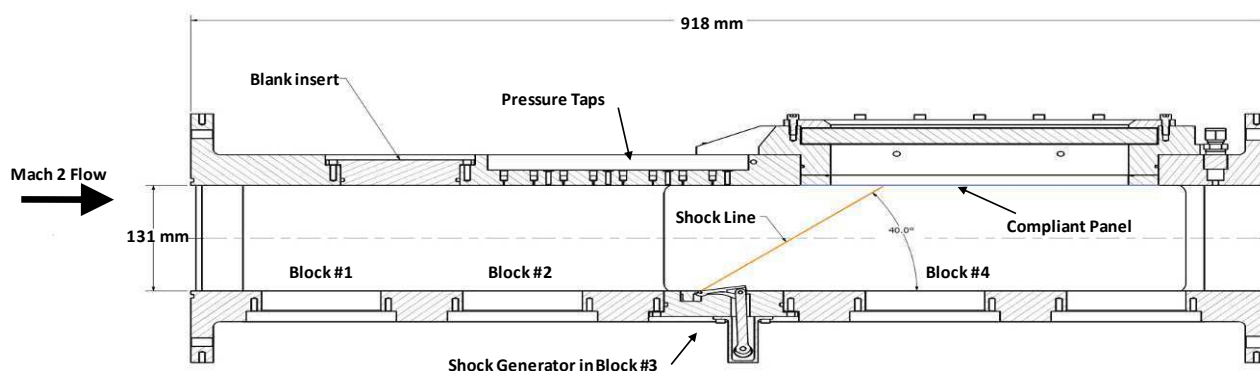


Fig. 1 Section view of tunnel with the shock generator shown in block #3

TEST ARTICLE AND INTEGRATION INTO TUNNEL WALL

In order to directly expose the compliant panel to the fluctuating pressure of the tunnel, the panel formed a section of the tunnel top wall. This posed some design challenges in terms of the tunnel start-up conditions, operating conditions, desired panel dynamic response, and minimization of step transitions between the top wall and panel leading edge. On tunnel start-up, the exhaust section reduces the pressure to approximately 0.2 atm. The tunnel is then started by allowing an inflow of air. The large pressure differential created between normal atmospheric pressure on the back side and vacuum conditions on the flow side would yield the test panel even before the introduction of the desired fluctuating pressures. Therefore a cavity was designed on the back side of the panel and vented to the tunnel pressure through ports located in the third top wall section positioned, just downstream of the compliant panel. A 19 mm thick quartz window (GE 124) was used on the top wall of the cavity to allow proper field of view by the DIC cameras and laser vibrometer. An assembly view of the middle portion of the test section top wall is shown in figure 2. When the tunnel is operating without the shock generator, the pressure differential between the top and bottom of the panel is negligible. When the flow is turned with the shock generator, the pressure upstream of the shock line remains nearly constant but increases downstream of the shock line, with a corresponding increase in pressure in the cavity behind the panel. This pressure differential directly influences the deformed shape that the compliant panel vibrates about. In the initial design of the compliant panel, tunnel start-up and shock impingement were critical load cases from a static yield strength perspective. Tunnel start-up issues were mitigated through the use of the cavity to equalize the front and back side pressure on the plate. The desired dynamic response of the plate was guided by what is traditionally thought of as sonic fatigue issues that can occur in aircraft structures. High-cycle or sonic fatigue occurs in thin, lightly damped aircraft structures with vibrational modes below 500 Hz - these modes represent greater deflection and stress states. Therefore, the compliant panel was designed to contain three modes below 500 Hz. Satisfying this requirement in the space available in the width of the top wall of the tunnel constrained the panel length and thickness. Step height transitions were minimized by making the top wall insert shown figure 2 vertically adjustable with jackscrews to bring the compliant panel flush with the other sections of the top wall. Additionally the panel was bonded to the compliant panel frame using Hysol EA-9394 structural paste adhesive to avoid further disturbing the flow from fasteners. The compliant panel is 305 mm long by 152 mm constructed from AISI 4130 chromoly steel sheet 0.635 mm thick. The bonding area between the compliant panel and frame reduce the effective vibration area to 254 mm long by 127 mm wide.

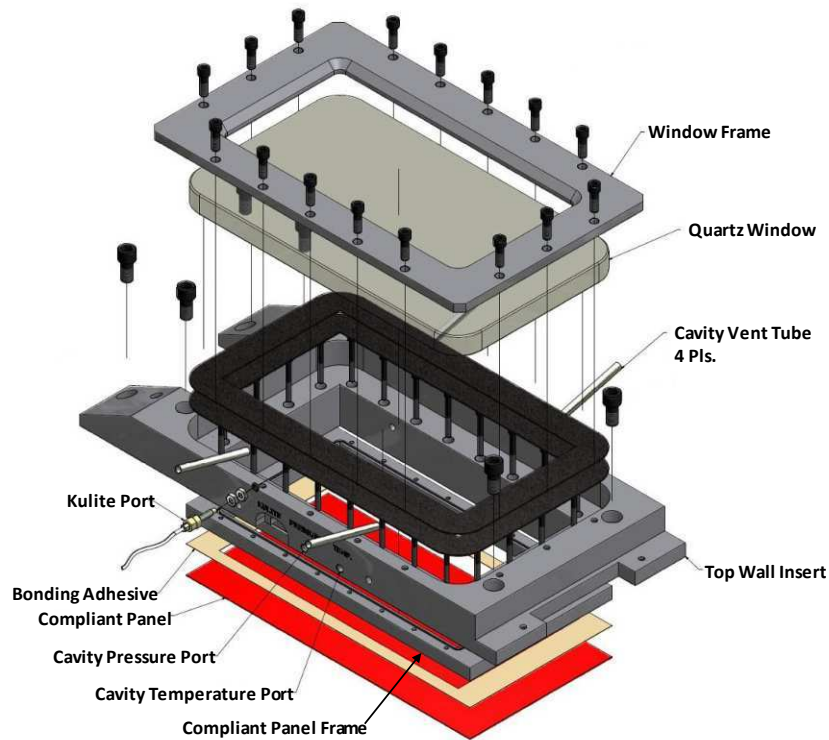


Fig. 2 Top wall middle section assembly

EXPERIMENTAL SET-UP AND PROCEDURE

The dynamic response of the compliant panel was measured primarily using 3D DIC and laser vibrometry, shown in relation to the tunnel in [figure 3](#). Additionally, a strain gage was placed mid way down the length of the plate near the edge to monitor the load conditions at the bond line. The 3D DIC system consists of two Photron Fastcam SA5 high-speed cameras with 32 GB of internal memory each for the optical hardware. ARAMIS, a commercial 3D DIC software by Trilion Quality Systems, was used to calibrate and analyze the images. The calibration followed the procedure recommended by ARAMIS using a 250 x 200 mm calibration panel at a standoff distance of 533 mm. The calibration summary reported that the cameras were angled at 15 degrees with respect to panel's normal with a measuring volume of 400 by 415 by 415 mm and a deviation of 0.025 pixels. A frame rate of 5000 fps was used with an image resolution of 640 by 352 pixels allowing for 20.8 seconds of images to be recoded using Photron Fastcam viewer software version 3.27. As is standard, a TTL trigger was used to synchronize the cameras. To minimize unwanted external heating of the compliant panel, two LED light systems were used. The primary light source was a LED panel light from Litepanels model 5600K 1x1 bifocus variable flood. A banner white high intensity area light model LEDRA70D4-XQ was also used to minimize shadows from the cavity walls on the panel. A Polytec Laser Vibrometer with the OVF 552 Fiber Optical Interferometer head and OFV 5000 controller was used to measure plate velocity. The vibrometer system was used in single point absolute mode with the tracking filter off and sensitivity set at 1000 mm/s/V. The laser fiber head was attached to the tunnel top-wall in an effort to make relative measurements, and cancel out tunnel vibration effects on the panel velocity measurement. A laser retro-reflective target was placed at the panel $\frac{1}{4}$ -point so as to observe most modes below 1000 Hz.

The experimental procedure began with tunnel start-up as described previously, and by setting the inlet total pressure to 2.65 atm. This resulted in a static pressure on the panel of 0.34 atm with the shock generator at 0 degrees. The inflowing air was not heated creating a static temperature of -112 °C. This resulted in a panel equilibrium temperature of 0.5 °C. Test measurements did not begin until the frame, initially at room temperature, and panel temperature differential reached 6.5 °C. This temperature difference resulted in a tensile preload on the panel, slightly altering the dynamic response. Once a stable temperature difference was achieved, the cameras were triggered and images were recorded for 20.8 seconds. At the same time, the laser vibrometry data and strain gage data were recorded on a separate data acquisition system for 60 seconds of time at a sampling rate of 10 kHz. The shock generator angle was increased in 2 degree increments, and the process was repeated until the shock generator reached 10 degrees.

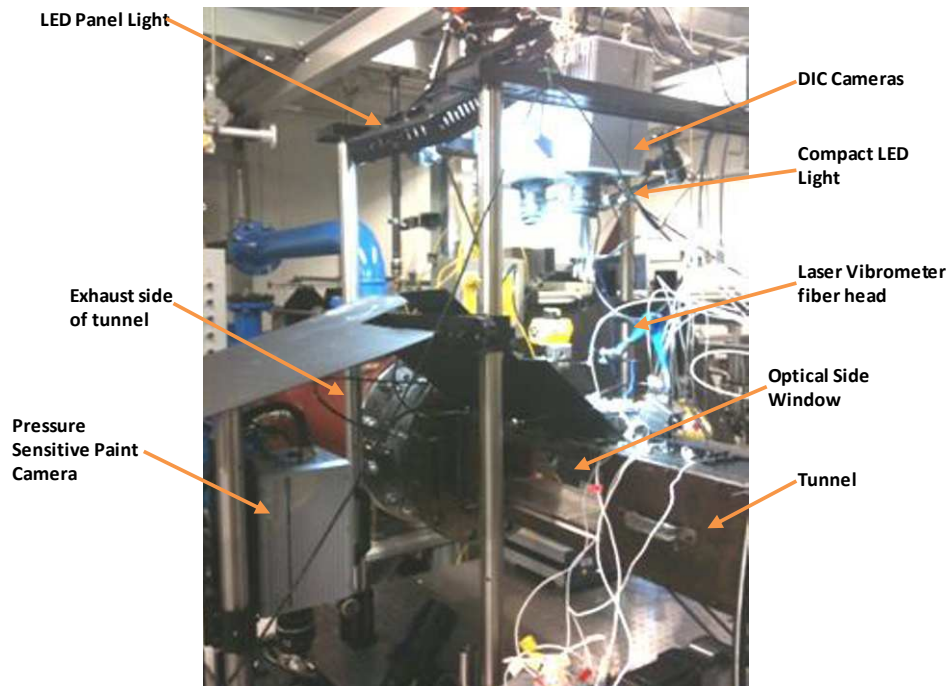


Fig. 3 Overview of the experimental set-up

HIGH-SPEED 3D DIGITAL IMAGE CORRELATION PROCEDURE

Due to the stochastic nature of the Mach 2 turbulent flow across the face of the compliant panel specimen resulting in potential nonlinear transverse response, long time records are required for sufficient averaging as previously discussed. For these reasons traditional 2D low-speed DIC is completely ineffective, and the more recent 3D high-speed DIC developments have generally been grossly inefficient. A search of the literature reveals little to no high-speed DIC application in the realm of random, nonlinear dynamic response. Therefore, the technical challenges associated with generating tens or even hundreds of thousands of image files needed to create a sufficiently long time record while also achieving accuracy levels on the order of the displacements associated with high cycle fatigue vibrations is a difficult prospect at best. Given the 0.635 mm thickness of the panel specimen, purely linear out-of-plane peak response levels are on the order of 0.1 mm or less. Unfortunately, the out-of-plane noise floor achievable with high-speed DIC is typically upwards of 40 μm [8]. These relatively high noise levels are often less than a full order of magnitude below typical linear out-of-plane vibration response of a clamped thin plate. One of the largest contributors to optical measurement techniques accuracy is the type and quality of visual tracking medium employed [3,12]. Therefore, for the current study several types of speckle patterns and optical targets were investigated for the lowest attainable noise floor.

When the endeavor of high-speed 3D DIC for random nonlinear response was initiated for the current study the true full-field displacement and strain typical of DIC was not the goal. Instead a grid pattern of discrete points that could be used for a more traditional multi-input, multi-output (MIMO) modal test was desired. This somewhat more traditional technique minimized what could be viewed as the inordinate amount of unnecessary data considering the sheer volume of measurement points created when the full-field of view is used. The DIC analysis software package, ARAMIS, uses overlapping facets with the size and degree of overlap selectable by the user, across the entire selected area. This blanketing of measurement points is perhaps ideal for coupon sized specimens however, on the scale of an entire panel this process can become cumbersome. Another optical measurement technique software package, PONTOS, uses retro-reflective target dots on a flat black background for multiple discrete point measurement and could be considered a more traditional photogrammetry method. Using yet another software tool developed for real-time DIC analysis that combines the capabilities of both the ARAMIS and PONTOS systems, a load server was developed at the request of AFRL to facilitate processing the thousands and even hundreds of thousands of high-speed images that would be required for nonlinear random response.

The early attempts at high-speed 3D DIC for this study, which concentrated on an array of discrete photogrammetry type targets, can be seen in [figure 4](#). The retro-reflective material used for the photogrammetry targets are essentially identical to those used for laser vibrometry. The possibility of measuring displacement with photogrammetry and velocity with a laser

vibrometer at a coincident point makes comparison between the two methods considerably more direct. However, two significant issues arose with the photogrammetry approach. First the noise floor achieved was not appreciably below the response levels of the plate during initial low-level modal testing [0, 1000 Hz]. Secondly, the DIC algorithm employed to visually track the target shared with the laser vibrometry system was essentially confused by the laser footprint on the target. Subsequently, the photogrammetry system attempted to track the laser reflection and not the actual target area negating the desired coincident point comparison. A study to compare the effectiveness of photogrammetry and several different speckle patterns for dynamic DIC was therefore undertaken.



Fig. 4 Compliant panel specimen with photogrammetry targets

Digital image correlation, especially in the 2D low-speed configuration, has been implemented and refined for fracture mechanics over the span of the last two decades. Typically a multilayered coating of black and white flat paint is applied to create a relatively fine random gray scale. Recent work in dynamic DIC has tended to gravitate to a more coarse black and white random pattern achieved with white paint base and small black permanent marker dots with random spacing [8]. To investigate the various types of DIC patterns, three distinctly different 3 by 3 cm speckle patterns were applied to a spare compliant panel specimen as seen in [figure 5](#). On the left is the more traditional quasi-static type multilayered pattern. In the center is the coarser black marker speckle pattern and on the right is a very fine single layer black on white pattern created by spattering with a fine bristle brush. The goal was to attempt a coarse, medium, and fine speckle pattern and determine through a single simultaneous test of the three, which pattern best suited the linear random vibration response noise floor requirements for modal testing.

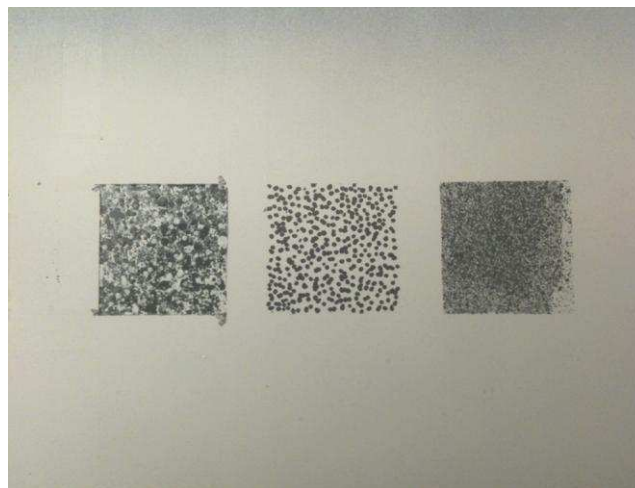


Fig. 5 DIC speckle patterns investigated (a) multilayered black and white spattered; (b) white base with black permanent marker dots; (c) single coat of finely sprayed black on white background

A low-level random response test was then conducted on the compliant panel specimen as it was suspended from the corners of the frame to create a clamped-clamped boundary condition on the plate, and a free-free condition on the frame. Low-level random acoustic excitation was applied to the panel from 0 to 1000 Hz. Response was measured with the SA5 high speed cameras at a resolution of 512 x 360 pixels and a rate of 5000 frames per second. This camera configuration generated 124,252 frames equating to 25 seconds. To decrease the time required to download such a large number of images, the data was left in a binary format until it could later be converted to a usable format. Since the system is stereoscopic, reducing the time required to offload the images even further was accomplished by using two computers to download from the cameras simultaneously. Despite these time-saving techniques, a single test run at the above settings still required 30 minutes of image download time. The binary images were then converted to 8 bit TIFFs at a later date so multiple test runs could be recorded in a relatively short period of time. For the photogrammetry case, the 21 points seen in [figure 4](#) were discretely analyzed for out-of-plane displacement. For the DIC cases, each speckle pattern had a single 15 by 15 pixel facet analysis area within the 3 cm square. The calculated noise floor for the cases was then compared. The photogrammetry had a noise floor of approximately 40 μm . The very fine pattern on the right and typical quasi-static pattern on the left in [figure 5](#) both had a noise floor on the order of 20 μm . The course pattern in the middle achieved a noise floor of 10 μm and was therefore deemed the most accurate for this application. A modal identification test of the compliant panel specimen was actually attempted with the photogrammetry test data using the 21 discrete points to construct panel mode shapes; however, the panel response was not sufficiently above the noise floor. Therefore, the same reflective targets were instead used in combination with the laser vibrometer to construct the first six panel mode shapes seen in [figure 6](#). It is believed with the proper test parameters a low-level, linear, full modal identification test from 0-1000 Hz could ultimately be achieved with high speed DIC and is a subject for future exploration.

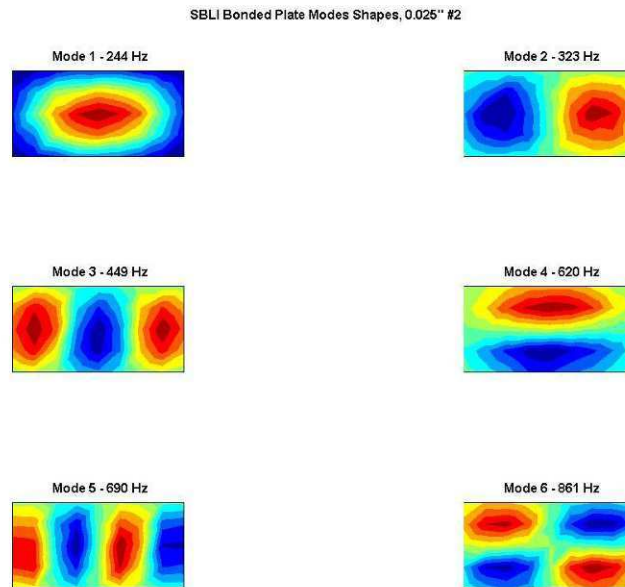


Fig. 6 Compliant panel specimens experimentally measured first six mode shapes

Based on the information gained from the DIC speckle pattern study it was determined the more course black marker on white paint background pattern would produce the most accurate results for the RC-19 compliant panel wind tunnel experiment. To avoid an unnecessary increase in an already time consuming and computationally intensive measurement process, the entire panel was not patterned. For instance, the displacement near the panel boundary is small compared to the center region and therefore much closer the known noise floor limitations of DIC. Therefore, 21, 1 by 1 cm discrete speckle areas were applied to the center region of the panel as seen in [figure 7](#). The speckle pattern was applied in discrete areas to facilitate data reduction and ease of processing while still providing sufficient levels of spatial resolution to identify excited deflected shapes during the wind-tunnel tests. A photogrammetry target was placed at a strategic point where most plate modes below 1000 Hz could be measured with a laser vibrometer and potentially directly compared to photogrammetry displacement at that point. The strain gage location was also given a speckle pattern for a direct comparison of the strain gage and DIC computed strain. For the discussion of results, it should be noted the long edge of the panel is considered the

x-axis and the short edge is the y-axis. Therefore, the pattern in the lower left corner of [figure 7](#) is considered point 1 and point 2 is directly to the right. The pattern in the upper right corner is then considered point 21.



Fig. 7 Compliant panel specimen installed in RC-19 test section with (a) discrete speckle pattern regions and (b) photogrammetry target

TEST RESULTS

The preliminary compliant panel tests in the RC-19 wind tunnel used only the strain gage and the single vibrometer point to monitor and record panel response. The lack of spatial resolution this created, combined with the varying temperature difference between the frame and panel and little-understood dynamic pressure across the face of the plate, proved overwhelming when plate mode identification under these conditions was first attempted. The spatial resolution achievable with DIC, although never before attempted under these conditions, ultimately proved invaluable to understanding the complex plate response.

As mentioned previously, the most difficult hurdle in the implementation of 3D high-speed DIC measurement of a compliant panel subjected to such an extreme environment is the combination of resolution, sample rate, and length of time record required. Traditional DIC only requires perhaps a few hundred images for processing fracture tests which is achievable with low-speed cameras. Transient dynamic analysis requires high-speed imaging, but is typically limited to several thousand images over the span of milliseconds. Until recently, the sheer volume of images required for the current application was simply insurmountable. As an example a 1-second snapshot, 2-second snapshot, and full 20.8 second time record of panel displacement measured with DIC for a steady-state run condition in the RC-19 tunnel is presented in [figure 8](#). At 5000 frames per second and a resolution of 640 x 352 pixels, the 1-second snapshot required the storage, download, conversion, and analysis of 5000 image files. This volume of images is already at or even more likely beyond what is typically attempted with DIC analysis software. As can be seen in [figure 8\(a\)](#) the lack of sufficient averages, needed due to the stochastic nature of the panel response, results in little-to-no useful information obtained from the power spectral density (PSD).

Until just recently the limit of a high-end, high-speed camera memory was about 4 GBs of storage capacity. Therefore, the length of the time record snapshot can be increased to 2-seconds and the result for this approximate maximum time record for a 4 GB camera is shown in [figure 8\(b\)](#). There is a slight improvement in the resolution of panel response; however, the amount of information that can be gleaned from these results is still marginal. Major peaks can be seen and are assumed to be the first 4 modes of the panel, but the room for error in mode identification is still well above acceptable levels. [Figure 8\(c\)](#) shows the full 20.8 second time record achieved with 32 GBs of memory per camera available with the SA5. Distinctive peaks are now visible and lower amplitude response not seen before is now able to be evaluated.

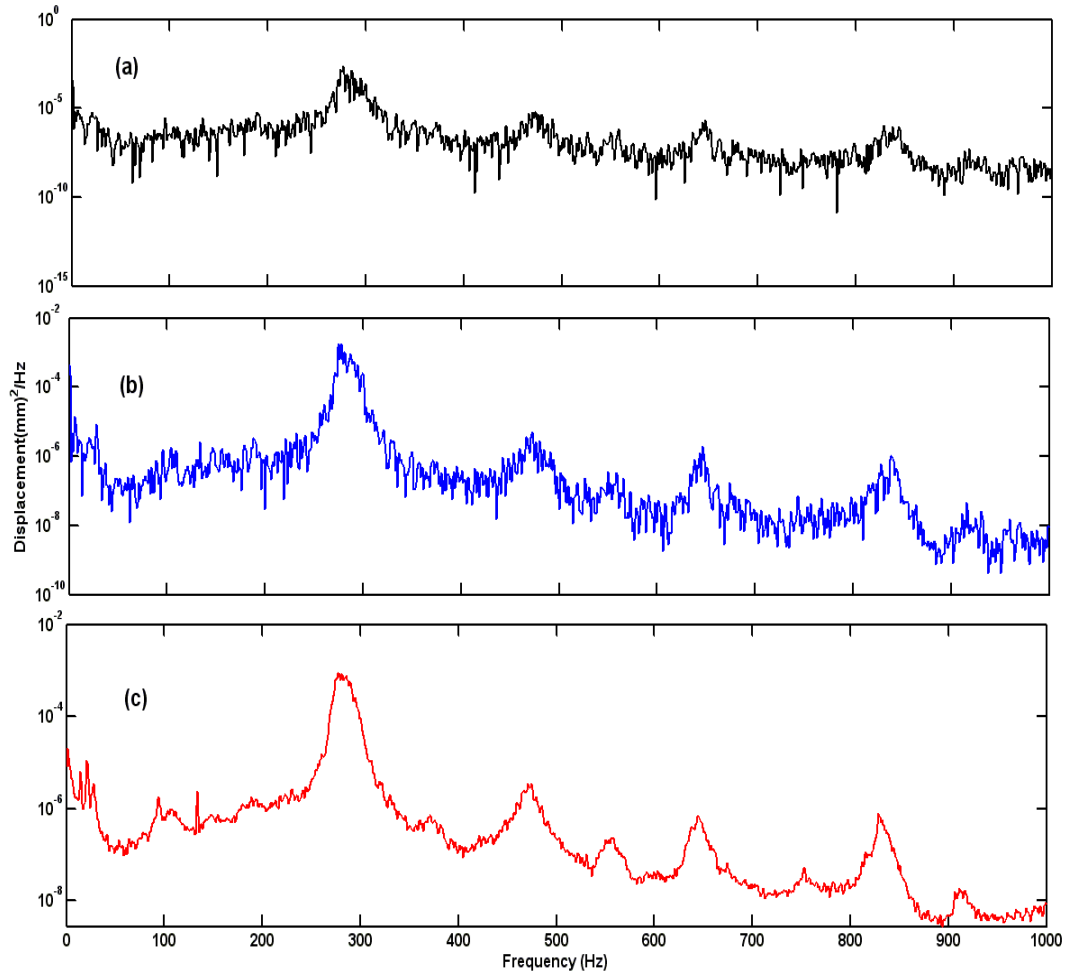


Fig. 8 DIC displacement PSD from (a) 1 second 5000 frame time record (b) 2 second 10,000 frame time record and (c) 20.8 second 101,661 frame time record

Armed with an appropriately averaged PSD of panel displacement response at several points across the plate center region, the question of DIC data reliability must be addressed. The response from the strain gage along the plate edge for a 60-second time record can be seen in [figure 9](#). Unfortunately, the DIC speckle pattern over the strain gage was below the noise floor when attempts were made to evaluate it for either displacement or strain. An attempt was then made to evaluate strain at panel point 4 and the results are shown in [figure 10](#). Even at this point where displacement at each facet is able to be evaluated and remains well above the noise floor, the difference in displacement is below the noise floor once again. Strictly for comparison of general trends to verify the measured response with DIC, the displacement at point 4 is shown in [figure 11](#). The trend of the data between the strain gage in [figure 9](#) and DIC displacement in [figure 11](#) is clearly very similar despite being almost 2 cm apart across a high gradient region. The strong similarity between the two readings supports the validity of the DIC displacement results.

The laser vibrometer measurement at the retroreflective marker and the DIC displacement from point 10 can be seen in [figure 12](#). The vibrometer velocity has been integrated and is presented as displacement. Again bearing in mind these data are at slightly different points on the panel, the similarity in general trends and even amplitudes further increases the confidence in the DIC measurements. The amplitude of the largest peak in the response of the DIC data is only slightly higher than that of the vibrometer data. This slight increase would be expected since the DIC measurement point is about 1 cm further inward from the panel edge where displacement goes to zero. As with previous attempts at direct comparison, the DIC analysis software was unable to track the photogrammetry target with the vibrometer laser reflection making a direct comparison unsuccessful. It is believed in the future the laser light could be filtered out of the DIC image to overcome the interference.

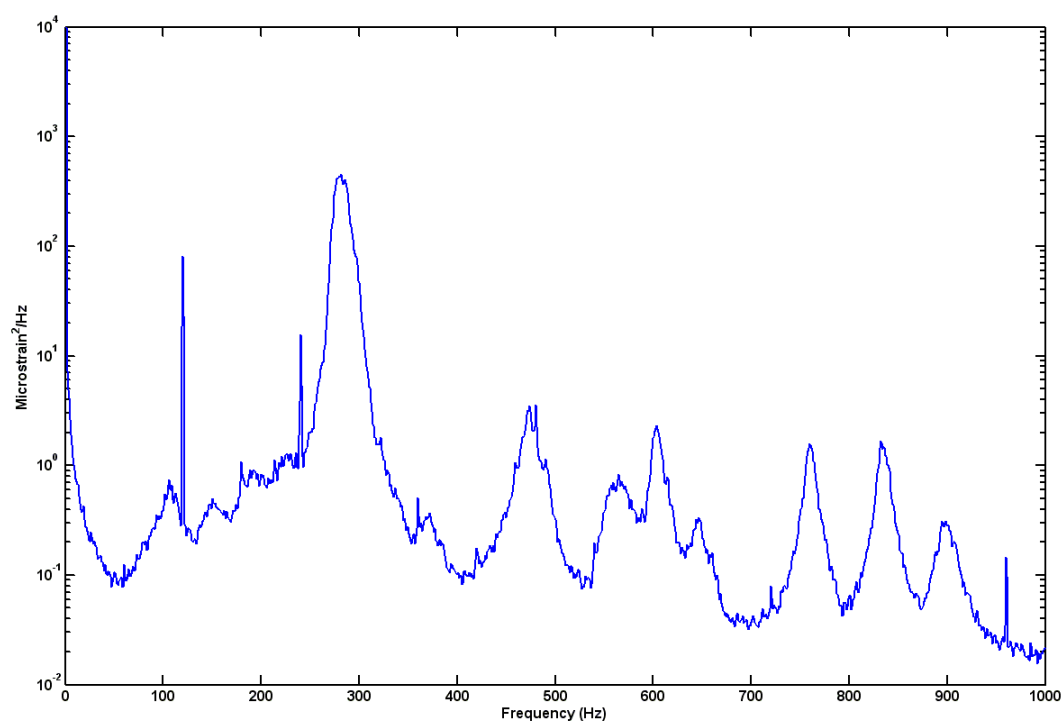


Fig. 9 Uni-axial strain gage measurement PSD at center of plate, long edge

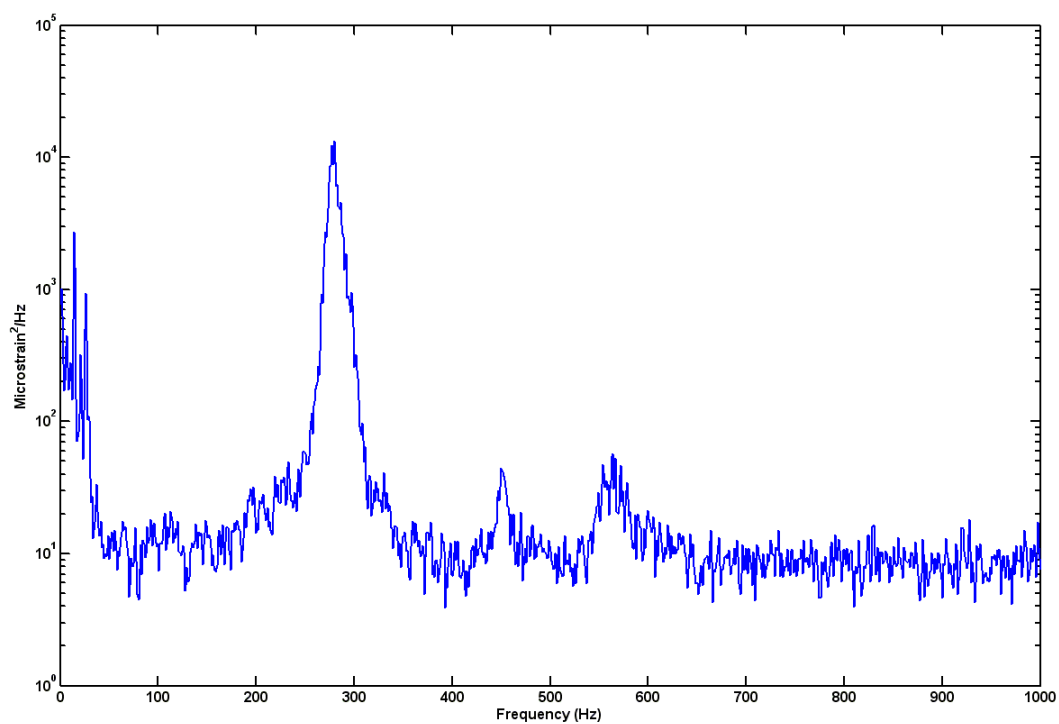


Fig. 10 DIC strain measurement PSD at speckle point 4

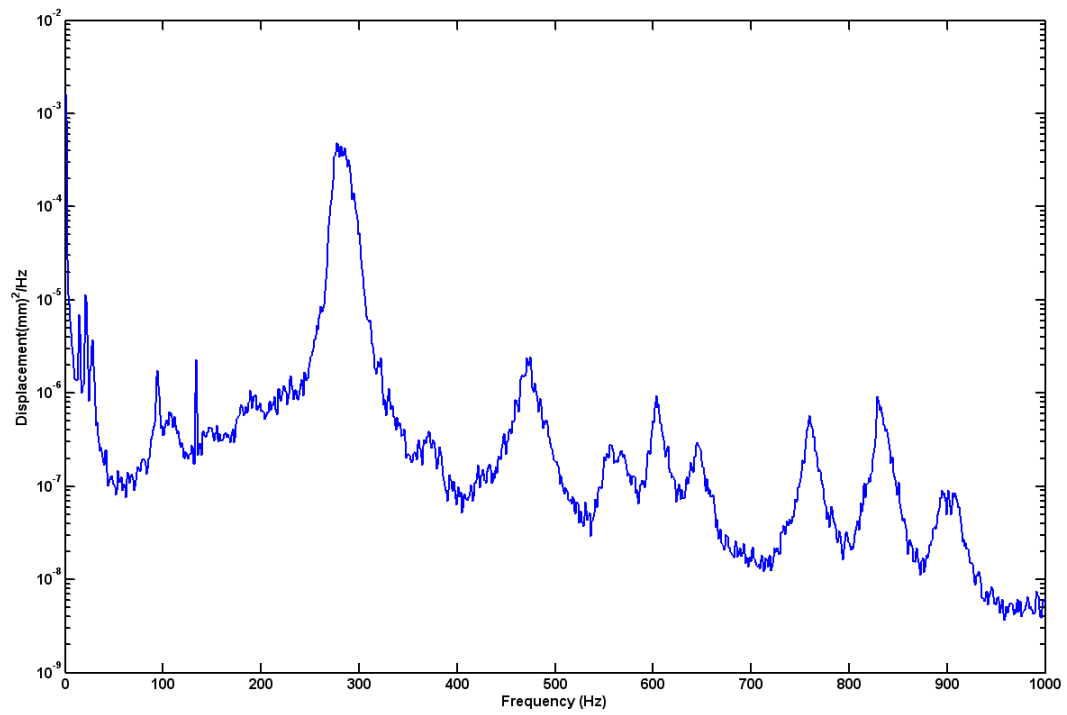


Fig. 11 DIC displacement measurement PSD at speckle point 4

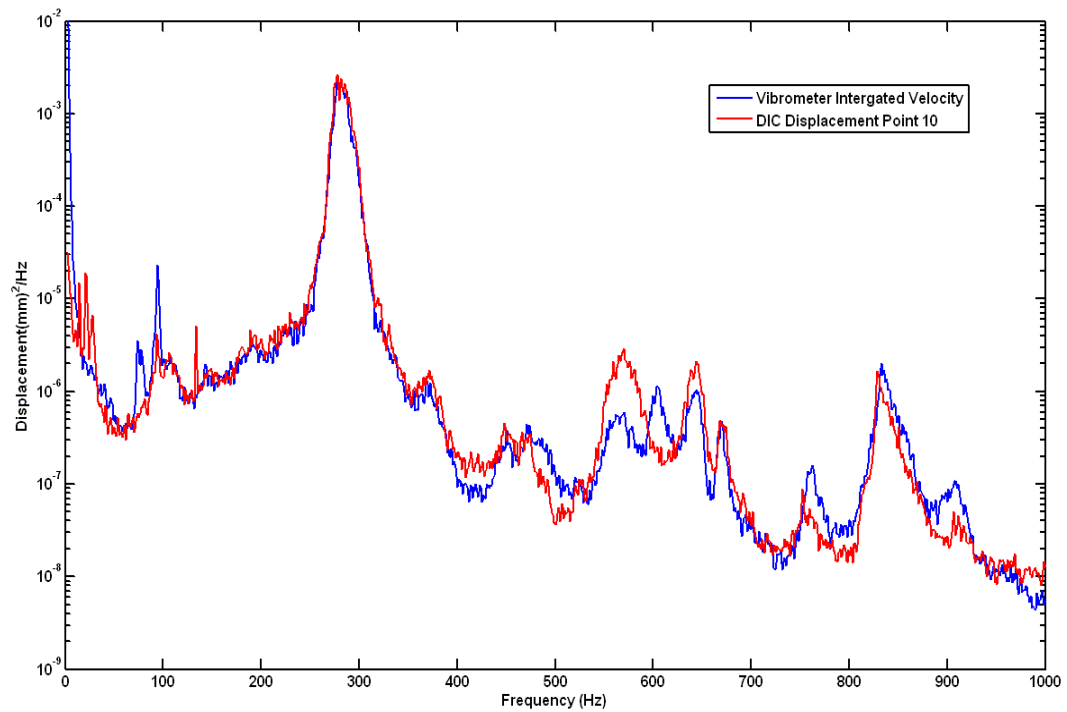


Fig. 12 PSD of integrated vibrometer velocity (—) and DIC displacement measurement at point 10 (—)

With confidence that the DIC measurements have at least been indirectly supported by both the laser vibrometer and strain gage measurements, the next task was to actually interpret the panel response. With all 21 points of displacement response data across the center region of the panel successfully evaluated for all test runs, adequate and consistent spatial resolution was achieved. Since at the time of this publication the varying pressure load on the face of the plate was not yet known, modal identification of the panel while under the various wind tunnel conditions had to be attempted with only the panel response. One means to shed light on the spatial distribution of the various peaks of the DIC displacement PSDs is to systematically march along one of the line of points on the panel and note the amplitude of the response at that point with respect to the points surrounding it. Beginning with a few points along the plate centerline in the x direction in [figure 13](#) there are several characteristics to note. First, the amplitude of the largest peak at 265 Hz increases from point 8, closest to the short edge on the left, to the plate center at point 11. The response then decreases again at point 14 nearest the short edge on the right side. This general trend of increasing and decreasing response towards a peak at the center, coupled with the panel modal results before installation in the RC-19 test section in [figure 6](#), would indicate that this is the panel first mode. The increase of about 20 Hz between the initial modal results and the RC-19 test results can most likely be attributed to the aforementioned 6.5 °C temperature difference between the panel and frame. This negative temperature delta would effectively pre-stress the panel and increase the frequencies. Also of note is the response peak at approximately 360 Hz. The response at the panel center point drops out almost completely at this frequency indicating that it is likely located at a node line. Furthermore, the points on either side of the node line have nearly identical amplitude. Again, looking at the initial modal results in [figure 6](#) and the center node line behavior represented in the displacement PSD, this is clearly the panel second mode. The third major peak at about 515 Hz in [figure 13](#) would then be the third panel mode as each measurement point is predictably at each of the three regions of highest displacement for this mode. The fourth panel mode should not be seen in this figure as all points fall on the node line. At just over 700 Hz, a mode with a node line along the center can once again be seen indicating this is likely the fifth panel mode.

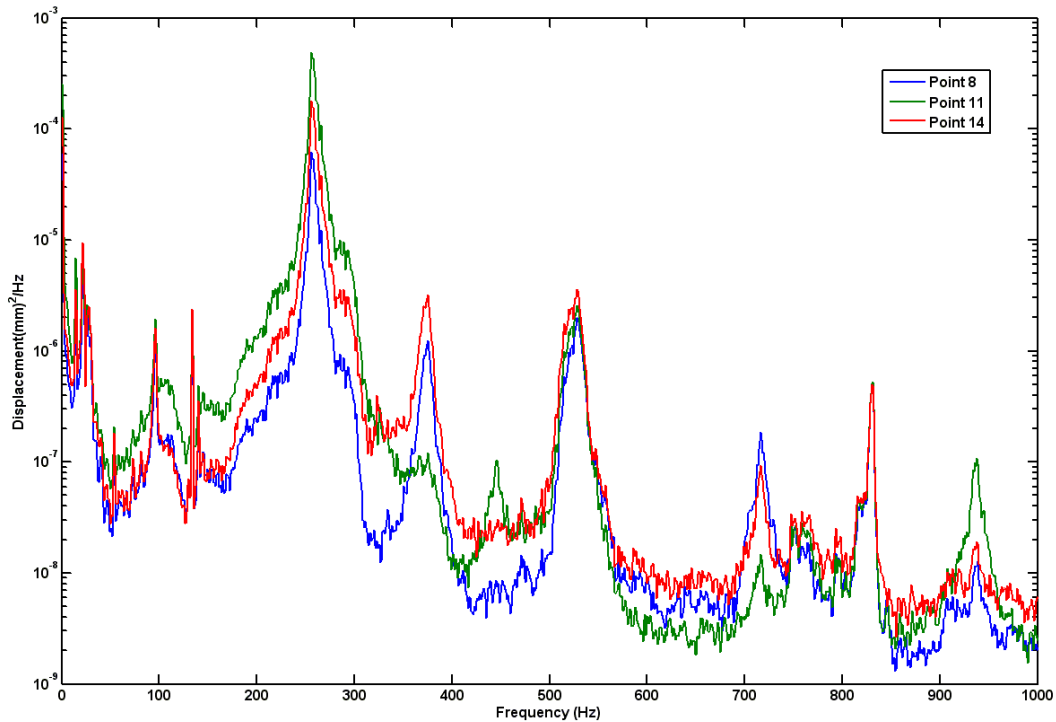


Fig. 13 DIC displacement measurements PSD along the panel center line, x direction

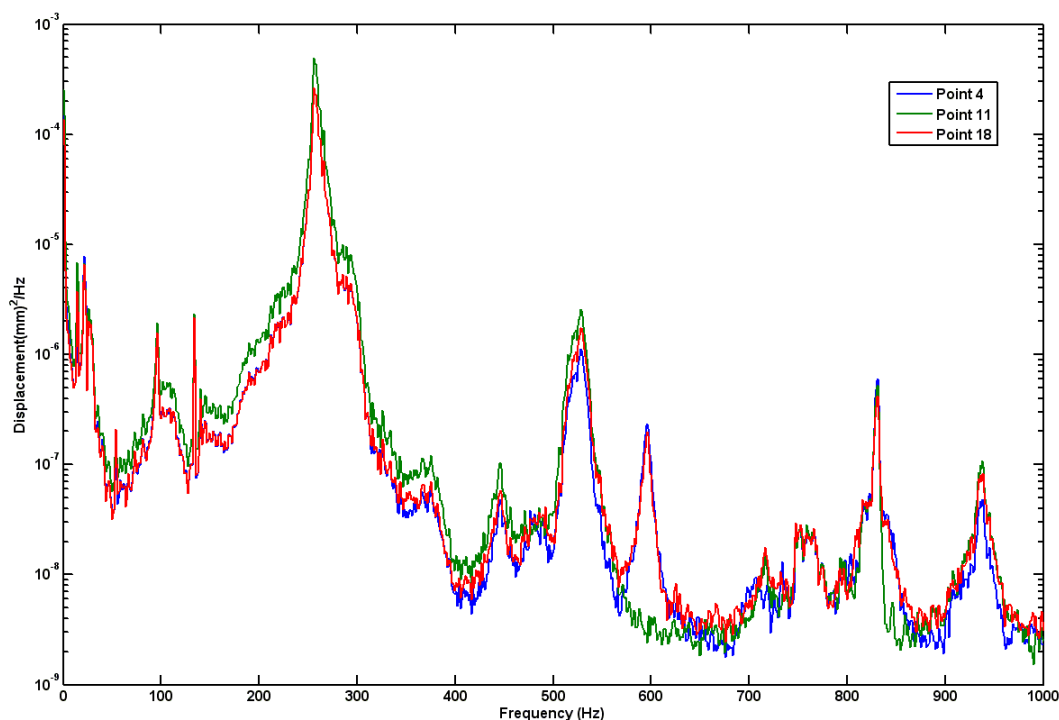


Fig. 14 DIC displacement measurement PSD along panel centerline, y direction

Figure 14, representing the three points along the panel centerline in the y-direction, further supports the conclusions drawn from the previous figure. The first peak at 265 Hz once again has peak amplitude at the center and slightly lower and equal amplitude above and below. The peak at 360 Hz is essentially gone representing the node line of the second mode. The peak at 515 Hz is once again seen at nearly equal amplitude at all three points with the highest at the center due to the center anti-node of the third mode. At 600 Hz the fourth mode can now be clearly seen and the expected node line at the center point where the amplitude disappears. The fifth mode at 715 Hz is now no longer visible due to the vertical node line at the center. To add further spatial information, in figure 15 are three points along the bottom edge in the x direction. The center node line is once again seen in the second (360 Hz) and fifth (715 Hz) modes as the response amplitude greatly decreases further supporting the conclusions drawn from the previous two figures. Nearly all the points along the centerline in the x direction are shown in figure 16 to add yet more support to the mode identification with even greater spatial resolution. Amplitudes increase and then decrease as you move along the length of the panel as expected and mode four (600 Hz) is predictably not present at every point.

The importance of the spatial resolution generated by DIC for panel mode identification while subjected to the RC-19 running conditions can also be noted by the various smaller peaks around 100 Hz, 450 Hz, and 850 Hz. Any one of these peaks could have potentially been mistaken for panel mode response due to the fluctuating pressures from the turbulent flow when in fact they are largely artifacts of the chaotic environment created by a continuous flow Mach 2 wind tunnel. Understandably RC-19 was not originally designed with vibration testing in mind. For instance the peak just below 100 Hz is the tunnel's first bending mode as seen with the array of accelerometers attached to the outer tunnel walls. The sharp peak at about 120 Hz is actually flicker in the LCD lights from the AC power source. Attempts will be made in future tests to eliminate this noise through the use of battery powered LEDs. The peak at 850 Hz is actually a mode in the apparatus used to suspend the two cameras above the test section as seen in the acceleration data from a tri-axial accelerometer mounted to the camera crossbar.

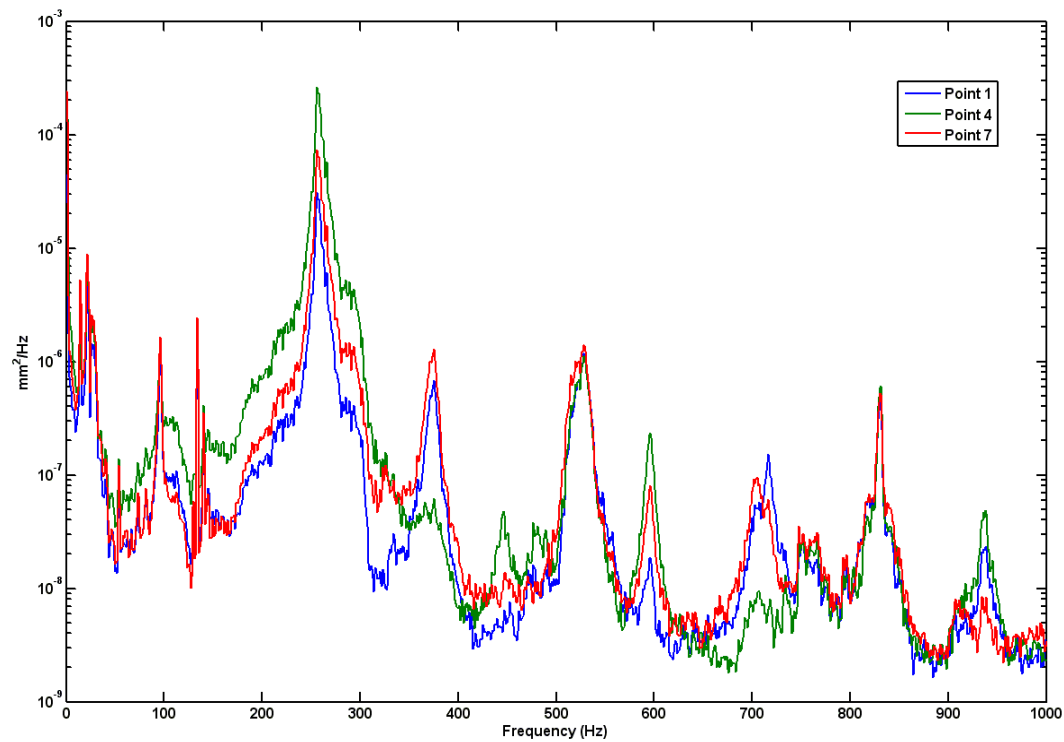


Fig. 15 DIC displacement measurement PSD along panel bottom edge, x direction

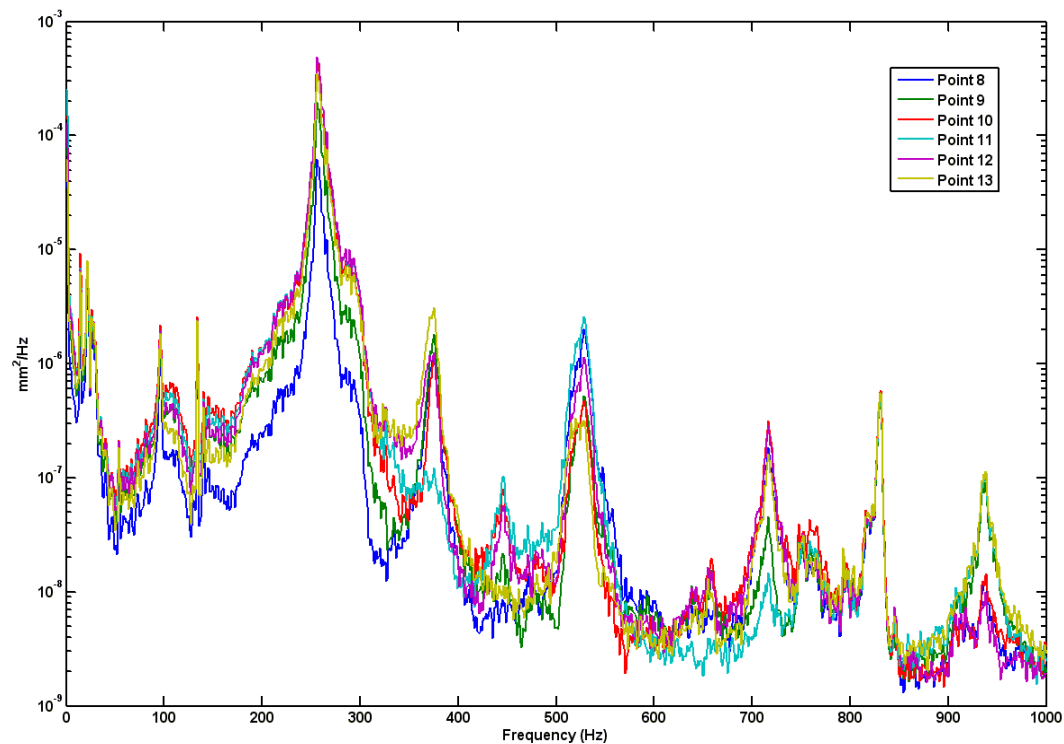


Fig. 16 DIC displacement measurement PSD along panel center line, x direction

Finally, with confidence in the identification of the plate modes while under fluctuation pressure loads from the Mach 2 flow of the wind tunnel, some insight can now be gained into the effect of a shock impinging on the plate with the use of the variable-angle shock generating wedge. Looking at [figure 17](#) the blue line is the baseline condition with the wedge at 0 degrees. The first mode peak at 265 Hz is relatively sharp and could be considered generally linear. The peak displacement for the 0 degree case is 0.29 mm which is just under half a plate thickness. The green line is the plate response when the shock generating wedge is raised to 10 degrees. Using Schlieren shock visualization techniques in preliminary tests it was seen that this shock wedge angle produced a shock impingement at about the panel quarter point in the x-direction. The most notable conclusion from these results is the significant change in panel response induced by the shock impingement. Consider the first mode response in particular. The displacement response was linear, or nearly so for the 0 degree case, while at the 10 degree shock generator angle the first mode peak has both increased and broadened in frequency. This response is the hallmark of acoustic fatigue, and is associated with a transition to a hard-spring Duffing-type nonlinear response. Furthermore, the peak panel displacement for the 10 degree case increased from 0.29 mm to 0.63 mm, which is nearly a plate thickness. A rule of thumb employed to determine nonlinearity, is displacement response equal to or above one plate thickness. These initial experimental results, intended to determine the validity of DIC for these test conditions, are encouraging. This measurement technique will be very useful in studying shock boundary layer interaction (SBLI) on a compliant panel investigation for future RC-19 experiments.

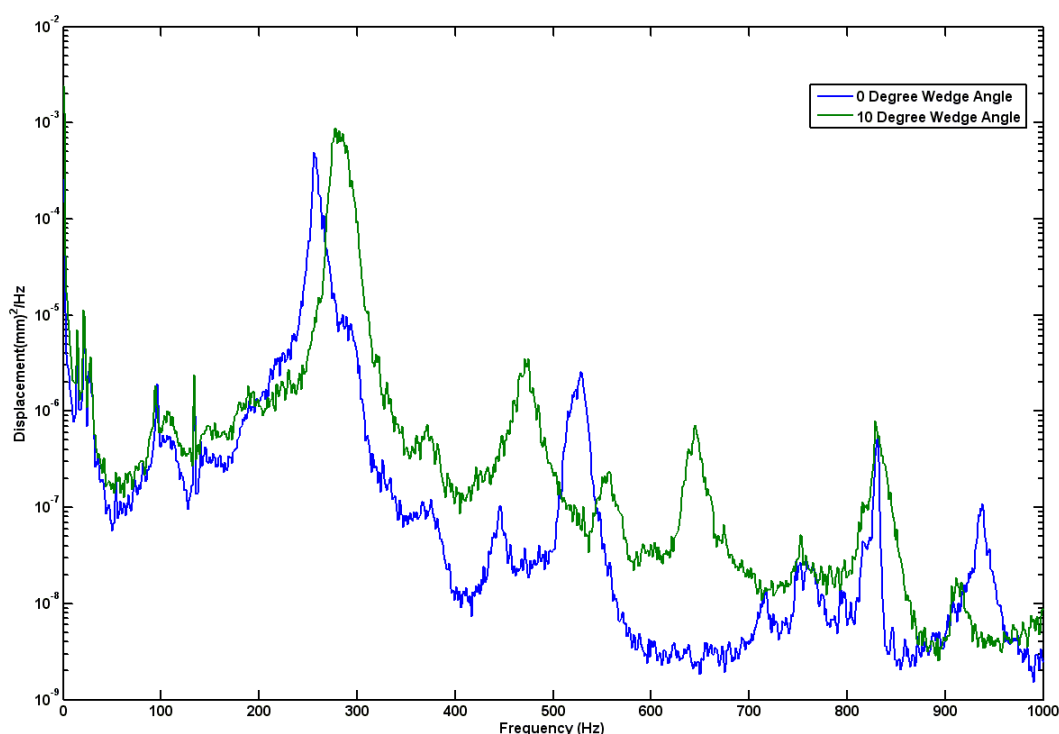


Fig. 17 DIC displacement measurement PSD at panel center (—) 0 degree shock wedge angle and (—) 10 degree wedge angle

CONCLUSIONS

Extreme environment experimentation produces many challenges in the measurement of representative thin-gauge aircraft panel dynamic response. Validating computational response prediction tools is difficult when only one or two discrete measurement points are available. The expected nonlinear structural response adds complexity to the problem, further necessitating full-field measurement techniques. Abundant and reliable information describing panel response due to shock boundary layer interaction will be required to design durable yet lightweight hypersonic aircraft structure. This information could be realized given robust full-field measurement techniques. DIC offers intriguing measurement possibilities assuming the numerous technical challenges can be overcome.

Determining which DIC specific parameters best suit the current application is critical. Tradeoffs between resolution, frame rate, and length of required time record must be considered. Various measurement “targets” have both advantages and

disadvantages for different conditions. For the current study, the time record length and measurement location preparation proved to be the most critical for the refinement of random displacement response and noise floor considerations respectively. Both were successfully achieved for simultaneous displacement measurement of 21 points on a compliant metallic panel specimen, which replaced a portion of a supersonic wind tunnel test section wall during continuous Mach 2 flow operation. DIC trends compared well to both discrete vibrometry and strain gage measurements. Spatial resolution was achieved to a degree that the identification of panel vibratory modes was possible at both linear and nonlinear response levels. With the capability to identify panel modes under various conditions, a shock boundary layer interaction investigation can successfully proceed. However, to date DIC strain measurement at or near the panel root was not successful for current test conditions, and further noise floor refinement will be required.

Future work will include more investigations into methods to increase DIC measurement accuracy. Specimen preparation, camera equipment selection and configuration, lighting techniques, and test environment integration all have a profound effect on the quality of DIC results. Further refinement of the processes involved in storing, downloading, converting, and analyzing massive quantities of image files also needs to be addressed to enable a sufficient number of runs during a single wind tunnel test. While real-time high-speed 3D DIC data analysis is unlikely soon, it would be beneficial to analyze portions of the DIC data during testing.

REFERENCES

- [1] J.D. Leatherwood, S.A. Clevenson, C.A. Powell, E.F. Daniels, "Acoustic Testing of High-Temperature Panels," *Journal of Aircraft* 29 (1992) 1130 - 1136.
- [2] R.D. Blevins, I. Holehouse, "Thermoacoustic Loads and Fatigue of Hypersonic Vehicle Skin Panels," *Journal of Aircraft* 30 (1993) 971-978.
- [3] T. Siebert, T. Becker, K. Spilthof, I. Neumann, R. Krupka, "High-speed Digital Image Correlation: Error Estimations and Applications," *Optical Engineering* 46(5):051004 (2007).
- [4] M.S. Kirugulige, H.V. Tippur, T.S. Denney, "Measurement of Transient Deformations Using Digital Image Correlation Method and High Speed Photography: Application to Dynamic Fracture," *Applied Optics*, 46 (2007) 5083-5096.
- [5] P. Lall, D.R. Panchagade, D.Iyengar, S. Shantaram, H. Schrier, "High Speed Digital Image Correlation for Transient-Shock Reliability of Electronics," *IEEE Transactions on Components and Packaging Technologies*, 32 (2009) 378-395.
- [6] V. Tiwari, M.A. Sutton, S.R. McNeill, S. Xu, X. Deng, W.L. Fournery, D. Bretall, "Application of 3D image correlation for full-field transient plate deformation measurements during blast loading," *International Journal of Impact Engineering* 36 (2009) 862-874.
- [7] A. Chaudhary, S.M. Spottswood, X.Q. Wang, M.P. Mignolet, "Estimation of Time to Stationarity in Geometrically Nonlinear Structural Responses," *Proceedings of the Tenth International Conference on Recent Advances in Structural Dynamics*, University of Southampton, 2010.
- [8] P. Avitabile, C. Niezrecki, M. Helfrick, C. Warren, P. Pingle, "Noncontact Measurement Techniques for Model Correlation," *Journal of Sound & Vibration*, 44 (2010) 8-13.
- [9] T. Siebert, M.J. Crompton, "Application of High Speed Digital Image Correlation for Vibration Mode Shape Analysis," *Proceedings of the SEM Annual Conference*, June 7-10, 2010, Indianapolis, Indiana, USA.
- [10] Gruber, M. R. and Nejad, A. S., "Development of a Large-Scale Supersonic Combustion Research Facility," 32nd Aerospace Sciences Meeting & Exhibit, Reno, NV, AIAA 94-0544, (1994) 1-11.
- [11] J. Crafton, A Forlines, S. Palluconi, Kuang Hsu, C. Carter, and M. Gruber, "Investigation of Transverse Jet Injections in a Supersonic Crossflow Using Fast Responding Pressure-Sensitive Paint," AIAA
- [12] P. Zhou and K. E. Goodson, "Sub-pixel Displacement and Deformation Gradient Measurement Using Digital Image-Speckle Correlation," *Optical Engineering*, 40(8) 1613-1620, (2001).

Experimental Modal Analysis of an Inflatable, Self-rigidizing Toroidal Satellite Component

M. Danesh Pazhooh, M.A. Dokainish, S. Ziada
McMaster University, Department of Mechanical Engineering, JHE 316, Hamilton,
Ontario, Canada

ABSTRACT

Modal testing of an extremely flexible self-rigidizing inflatable torus with regular pattern of hexagonal domes was carried out. For the first time the feasibility of using a non-contact in-house fabricated electromagnetic excitation in modal testing of such an ultra-flexible inflatable structure was investigated. Non-contact transducers, laser displacement sensors, were used in this study. Non-contact excitation and measurement technique were used to avoid frequency shift problems due to inertial loading on the structure. Within the frequency bandwidth of 1-25 Hz, four in-plane and four out of plane modes' damped natural frequencies were extracted and compared with prior studies.

1. Introduction

The antenna design requirements for satellites drove their size to dimensions that could not be deployed into space using solid parts. This problem introduced a revolutionary change in satellite design. It was suggested that inflatable portions be used instead of large rigid antennas.

Inflatable structures, also known as Gossamer or membrane structures have attracted much interest in space applications such as large telescopes, antennas, solar sails, sun shields, and solar thermal propulsion. These structures possess many advantageous properties such as ultra-lightweight, small stowage volume (packing efficiency), high strength-to-mass ratio, low overall space program cost, design flexibility, and on-orbit deployability [1, 2]. Inflatable structures can also reduce the total system mass. Since they have very few mechanical components, they are of lower deployment complexity, and thus higher reliability [2, 3].

The three main components of several gossamer communication or imaging satellites are inflatable struts, an inflatable torus as the structural support components and some sort of lens, aperture, or array housed inside the torus boundary. The circular or elliptical torus provides the boundary for any housed membrane or lens, and it ties together the satellite or craft supporting struts [4, 5]. Fig. 1 shows the In-Space Technology Experiments Program (IN-STEP) of Inflatable Antenna Experiment (IAE) which was performed in 1996 by L'Garde and NASA JPL together [6].

It is anticipated that the harsh environment of space, intense temperature differentials and micrometeorite bombardment, will most likely threaten the pressurized satellite components. Typically, the gossamer structures need to maintain their internal pressure to keep their structural stiffness. Though, chances that meteoroid or other objects impact the structure are very low, it is desirable that the structure become rigidized after deployment. Hence, there would be no need to maintain the internal pressure to keep the structural shape.

Addressing the rigidization issue, United Applied Technologies (Huntsville, AL, USA) designed and manufactured a new thin film casting process for toroidal satellite component, which once inflated could support

its own structural shape even when its internal pressure was released. The flat thin sheets of Kapton 300JP[®] were formed into curved thin films with regular pattern of hexagonal domes. The inflated self-rigidizing torus, SRT, could support its own structural shape even when there was no internal pressure, due to the additional stiffness provided by the pushed out hexagonal domes.

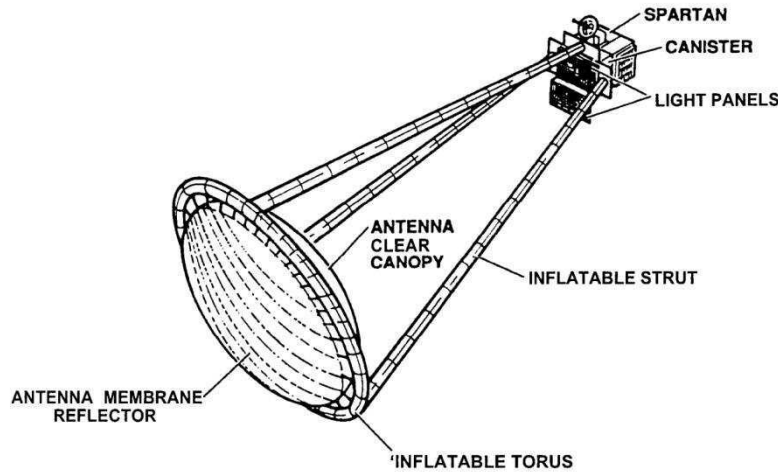


Fig. 1 Experimental orbital configuration of inflatable antenna used in IAE [6]

The inflated antenna must maintain a desired surface accuracy in order to focus all the incoming light and microwave on a receiver. The vibration of satellite distorts the antenna surface, thus making it dysfunctional for a certain amount of time. Attenuating these disturbances is crucial to maintaining the satellite performance. Besides using mechanisms to maintain the antenna surface accuracy, one possible way to attenuate the inflatable antenna overall vibration is to control the vibration of its main support system, i.e., the inflated torus.

Many investigations have been performed on the pressurized inflatable satellite components, particularly the toroidal one [7-17]. The research on unpressurized satellite components, such as the SRT, is limited only to the two following works.

In 2004, Ruggiero et al. [18] performed experimental modal analysis of a SRT, using an electromagnetic shaker and two sets of accelerometer, single input multiple outputs (SIMO). They measured three out-of-plane and one in-plane mode frequencies. In 2006, Song et al. [19] used a subwoofer to acoustically excite the SRT structure. The torus' displacement response was acquired by laser displacement sensor, SISO. They captured three out-of-plane and two in-plane modes. In both previous studies on the SRT, the inflation nozzle was left open to the atmospheric pressure which made the SRT opt to wrinkle and sag in the gravity force presence.

There are a number of unresolved issues in the existing experimental modal analysis techniques related to the excitation and sensing methodologies. Previous modal experiments of the SRT were not successful in detecting all of the first three in-plane modes. Considerable improvements in the modal experiment can be achieved by employing non-contacting excitation and sensing transducers, which is precisely the case in the present research.

2. Experimental setup

2.1. Test structure

Three SRT prototypes were designed and manufactured at the United Applied Technologies (Huntsville, Alabama). The first two SRT were used by Ruggiero et al. [18] and Song et al. [19], respectively. The structure which is used in this research is the third SRT prototype.

The tested structure was an extremely flexible self-rigidizing inflatable torus. The 181cm ring diameter and 22 cm tube diameter torus was constructed of thin films of Kapton 300JP[®]. The flat 76 micrometer thick Kapton[®] sheets were formed into curved 46 micrometer thin films with regular pattern of hexagonal domes of 32.5 micrometer thickness, Fig. 2(a). The top and bottom of the torus, which each were constructed from seven joined segments at shear seams, were joined together at the inner and outer peel seams (flaps) to form the complete torus, Fig. 2(b). The "3M scotch-weld epoxy adhesive 2216 B/A translucent[®]" was used to join these 14 segments.

Ideally, in the absence of the gravity force, the inflated torus, due to the additional stiffness provided by the pushed out hexagonal domes, could support its own structural shape even when there was no internal pressure. The geometric properties of the SRT are provided in Table 1.

The test structure was suspended horizontally from the lab's ceiling at six equally spaced points using 3.3 meter long suspension systems, as shown in Fig. 2(a). A very soft spring suspension system was used to provide the lowest possible rigid body frequencies while having the strength to suspend the test article above the floor. Each suspension, which consisted of a series of one slinky, two soft springs and two rubber bands, was attached to the torus through holes located in the outer circumferential peel seams (flaps). The measurements were performed after the rubber bands were allowed to creep for more than two weeks.

Once suspended, the torus was inflated by a small aquarium pump. Using a pressure regulator, the pressure was maintained below 1379 Pa. The amount of pressure was monitored by a monometer. Thereafter, the supply pump was removed and the inflation nozzle was left open to the atmospheric pressure to allow the internal pressure to become equal to the atmospheric pressure. Leaving the air nozzle open to the atmospheric pressure had challenges. The inflatable torus hardly could maintain its shape long enough for one continuous set of measurement, i.e., due to the earth's gravity, it rapidly wrinkled and sagged. Hence, using the regulator, a very small internal pressure of 149.3 Pa could be maintained during the experiment to prevent the sag and wrinkle of the torus. The leakage flow rate was slow enough to allow useful measurement.



Fig. 2 The self-rigidizing inflatable torus, (a) Complete torus; (b) Peel and shear seams

The pendulum and plunge (bouncing up and down) frequencies of the test structure were found to be 0.27Hz and 0.29Hz, respectively. It was expected that the first natural frequency would be between 2.0 to 3.0 Hz [18, 19]. Hence, the suspension frequencies were less than ten percent of the first natural frequency and therefore in an acceptable range. To reduce the mass loading effect of the air tube, the tube was suspended freely from a stand. In order to minimize the effect of the air current disturbance over the SRT, all the air ventilation ducts of the lab were blocked, and the air conditioner was turned off during the measurements.

Table 1 Geometric properties of the SRT

Property	Value
Film thickness	46×10^{-6} m
Ring radius	0.907 m
Tube radius	0.111 m
Average shear seam width	0.021 m
Average peel seam width	0.051 m
Average shear and peel seam thickness	2.88×10^{-4} m
Average overlapped shear and peel seam thickness	4.48×10^{-4} m
Hexadome width (major radius)	7×10^{-3} m
Hexadome height	3×10^{-3} m
Hexadome thickness	32.5×10^{-6} m
Gap between the adjacent hexadomes	1×10^{-3} m
Mass	0.560 kg

2.2. Excitation and Sensing Setup

Considering the low stiffness and high flexibility of inflatable structures, the choice of suitable sensing and actuation systems in the dynamic testing was limited. The extremely flexible nature of the SRT caused point excitation to result in only local deformation; hence the excitation method should be cautiously selected.

Using the contact excitation systems would have had drawbacks. For instance, had an electromagnetic shaker as the excitation system been used and the input energy is not properly distributed throughout the structure, the shaker could have pierced or ripped the membrane [20]. Considering the very low mass of the SRT, employing smart materials as actuators or sensors would have caused frequency shift. The same reasoning applies with the application of accelerometer as a sensor. Therefore, a noncontact actuation and sensing system was employed in the present study.

2.2.1. Excitation Setup

The test structure was excited via a non-contacting electromagnetic exciter. An in-house fabricated electromagnet was made out of four layers of 28 gauge copper wire on an iron core. The core had a 4.5 mm diameter and was 47 mm long. The electromagnet was placed close to the test structure where a strong permanent Rare Earth magnet was attached to the torus. In order to reduce the effect of local deformation of the very flexible membrane of the SRT, the 9.54 mm in diameter magnet was attached to the torus by means of a 2.5cm by 3.5 cm double sided exterior mounting tape. By this modification, the excitation energy was distributed to a larger area of the SRT surface and the global bending modes of the structure

were excited without causing local excitation (deformation.) The magnet had 5 mm thickness, and weighed 2.69 grams, which was approximately 0.5% of the torus weight. The configuration of the electro-magnetic excitation system is illustrated in Fig. 3.

A time-changing current applied to the electromagnetic exciter resulted in a time-changing magnetic field. Hence the excitation system, without even coming into contact with the SRT, applied significant forces to it. Since the deflected modes were in a different orthogonal direction, the magnet was attached at the outer surface of the torus at an approximate 45 degree angle with respect to the peel seam, Fig. 2(b), to excite all the modes. While it was impossible to keep the distance between the solenoid and magnet constant at all time, an effort was done to maintain this gap at approximately 3 cm.

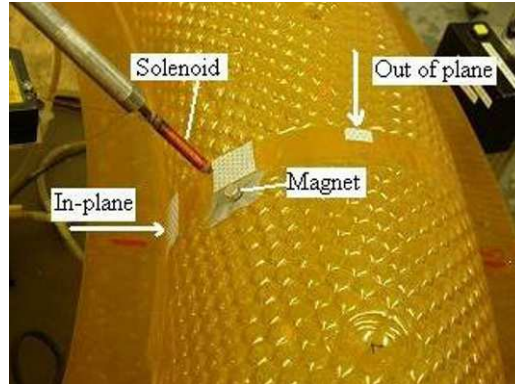


Fig. 3 Electromagnetic excitation setup

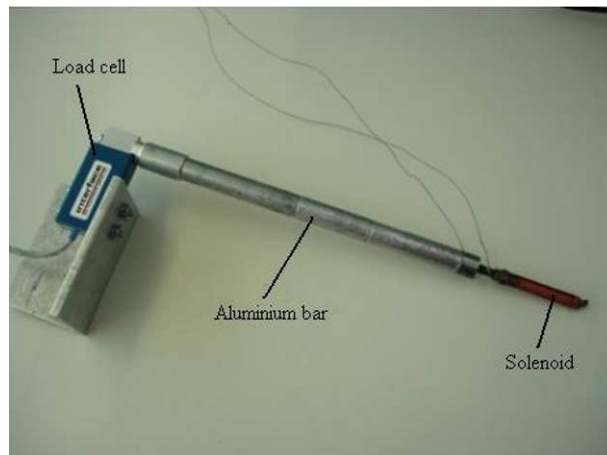


Fig. 4 Electromagnetic exciter and load cell ensemble

2.2.2. Sensors

As noncontact measurement transducers, laser displacement sensors were used to avoid the stiffness of instrumentation wiring as well as frequency shift problem associated with the inertial loading and damping on the structure. The laser measurement system was very versatile, which allowed easy changing of the location and number of the measurement points.

Two Keyence laser triangulation displacement sensor head LK-G82 and a common controller LK-G3001 were used. Since measurement of the force applied to the torus was impossible, the reaction of the force on

the core of electromagnet was measured using an Interface MB-5 Miniature Beam load cell. The strain gage based load cell was isolated from the electromagnetic field of the solenoid by an 18 cm aluminium bar, Fig. 4. The load cell was placed between the isolation aluminium bar and an aluminium bracket. The bracket was clamped to a rigid stand.

In order to capture the scaled mode shapes, drive point measurement was necessary. The modes of interest were ring modes, i.e., in-plane and out-of-plane motions of the torus. The directions of the in-plane and out of plane measurements are shown in Fig. 3. For each of the in-plane and out-of-plane measurements, displacement was measured by roving the laser displacement sensors at 14 evenly spaced points along the inner surface and top of the structure, respectively, Fig. 5. The drive point measurement was taken at location 1.

Response measurements on the surface of the SRT were complicated by the fact that the Kapton[®] film is optically transparent, which allowed much of the laser light to pass through the test article. Preliminary test proved that by attaching reflective tape at the measurement points, a better coherence could be achieved. Henceforth, reflective tapes were used at all measurement points which added a total of approximately 8 grams to the mass of the torus, which was 1.4% of the torus mass.

3. Noncontact Testing and Data Analysis

3.1. Experimental Procedure

Careful selection of excitation signal (specific length and bandwidth) was found to be critical for a flexible inflatable torus when trying to obtain reliable vibratory responses with reasonable accuracy.

Since by narrowing down the bandwidth, sufficient input energy could be provided to the entire structure and the global modes would be excited, a periodic chirp signal was used for the input signal. The periodic chirp signal could characterize the nonlinearity and it is leakage free (self-windowing) and had the best signal to noise ratio characteristic when compared to other type of excitation signals.

The analog chirp signal of 1 to 25 Hz was generated using Matlab Signal Processing Toolbox for periods of 10 seconds. The chirp signal was fed to a National Instrument card PCI-6024E. Thereafter, the signal was fed to a power amplifier, Panasonic RAMSA WP-1200, and the voltage-adjusted signal, 3.4 V, was sent to the electromagnetic exciter. This voltage was selected based on the experimental study that a voltage above 3.4 V would have burned the solenoid. The data collected from the laser displacement sensors and load cell were sent back into the National Instrument card, and the signal processing was performed with Matlab Signal Processing Toolbox. The cut-off frequency for the low pass filters of displacement sensors was 30 Hz. To remove the effect of the rigid body modes, a fourth order digital high pass Butterworth filter with the cut off frequency of 1 Hz was used.

The internal pressure was maintained at approximately 149.3 Pa, with the room temperature being kept at approximately 26 degrees Celsius during the experiment. There was no control on the humidity.

The frequency of the pump diaphragm was measured at 60 Hz. Any effect of the pump on the frequency response functions would therefore have appeared at 60Hz, which was above the desired frequency range of 1 to 25 Hz. In a preliminary test, no noticeable effect of pump noise and the air flow into the structure was found on the measurement of frequency response function.

Owing to the current-squared nature of the generated magnetic force, even a single frequency sinusoidal input signal to the electromagnet, results in a complex periodic force signal [21]. All frequency response function measurements were estimated using the H_1 estimation algorithm, which cancels noise at the output. The measurement sampling frequency was 2000 Hz and no windowing was used.

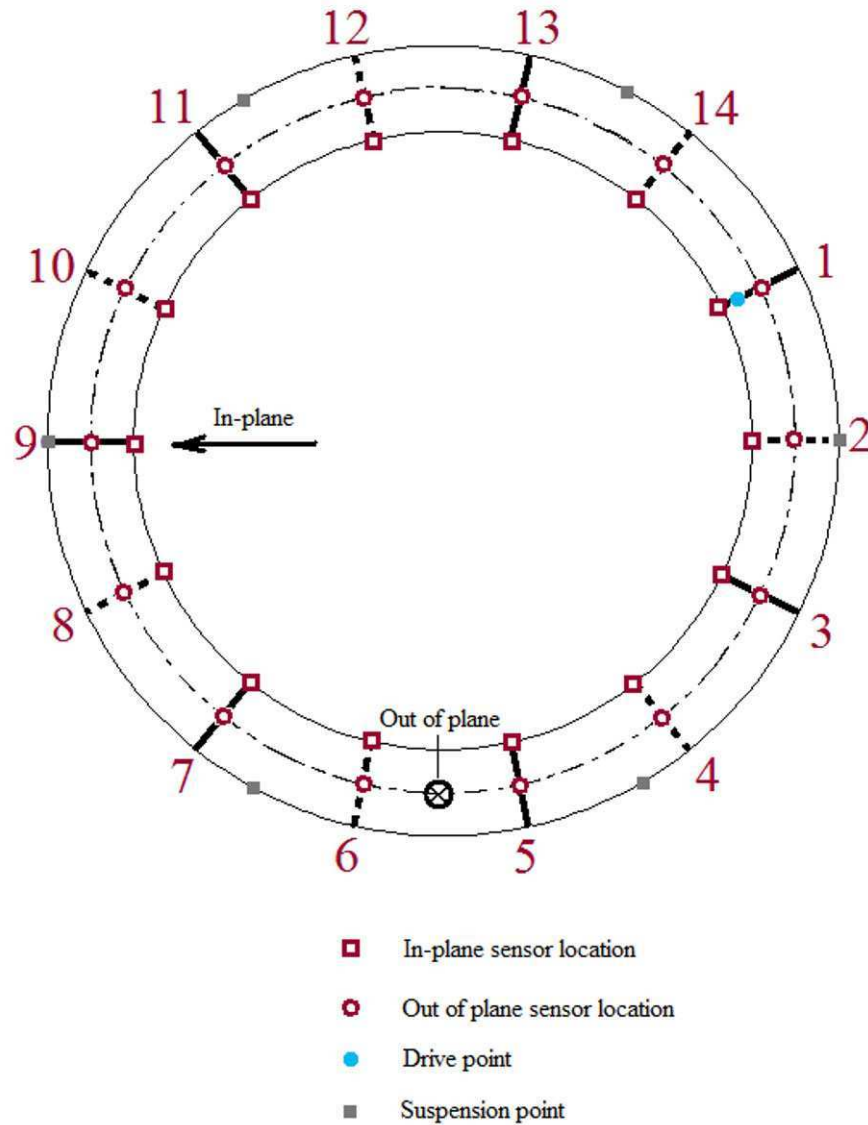


Fig. 5 A sketch of the SRT, showing the 14 locations of the sensors as well as the suspension points around the perimeter. The solid and dashed radial lines are the connection shear seams in the top half and bottom half of the SRT, respectively

In the signal processing phase, both cyclic (linear) and power spectra averaging was used. In each measurement, one block of excitation took place without acquiring the associated input and output data, i.e., one delay block. This caused the transient response to any start or change in the periodic excitation to decay out of the response signals, so both the input and outputs signals would be periodic within the observation period [22]. Each delay block was equal to the observation period, 10 seconds. To reduce the possible leakage error, cyclic averaging of the time domain data was employed. After the delay block, four continuous blocks of time data, i.e., excitation and responses, were captured and linearly averaged. Hence, the total test time for each cyclic average was five continuous blocks of data.

In the estimation of the frequency response function, linear (stable) spectral averaging was performed to remove the variance error due to extraneous random noise and randomly excited nonlinearities. Twelve ensemble of delay and captured data blocks were used in the spectral averaging of the cross and auto power spectra.

Coherence function was used to determine the effectiveness of the excitation in these tests. The coherence was examined for each data block. Any broadband drop in coherence denoted poor excitation. When this occurred, the measurement was discarded and repeated.

3.2. Nonlinearity Detection

The inflatable torus was assumed to be nonlinear. While keeping the internal pressure at approximately 149.3 Pa, the lightly pressurized torus was excited at two different levels of excitation of 1.8 and 3.4 V. The excitation level of 1.8 V was the lowest voltage that could excite the torus globally, i.e. 180 degree from the drive point about the torus ring section. As mentioned in the previous section, the 3.4V excitation was the highest voltage could be used without burning the solenoid.

Fig. 6 shows the frequency response functions for the out-of-plane and in-plane measurements of sensor location 1. Any deviation between the two curves indicates some sort of nonlinear behaviour. For a linear system, increasing the input by a factor should increase the output by the same factor. For nonlinear modes, the frequency and width of the modal peak vary by the level of excitation. By overlaying the two frequency response functions, for each in-plane and out of plane measurements, it is observed that the response of the SRT displays weak nonlinear system behavior. This means that not only the estimated frequency but also the corresponding damping of some modes was valid only at the level of excitation (3.4 V) used in the test.

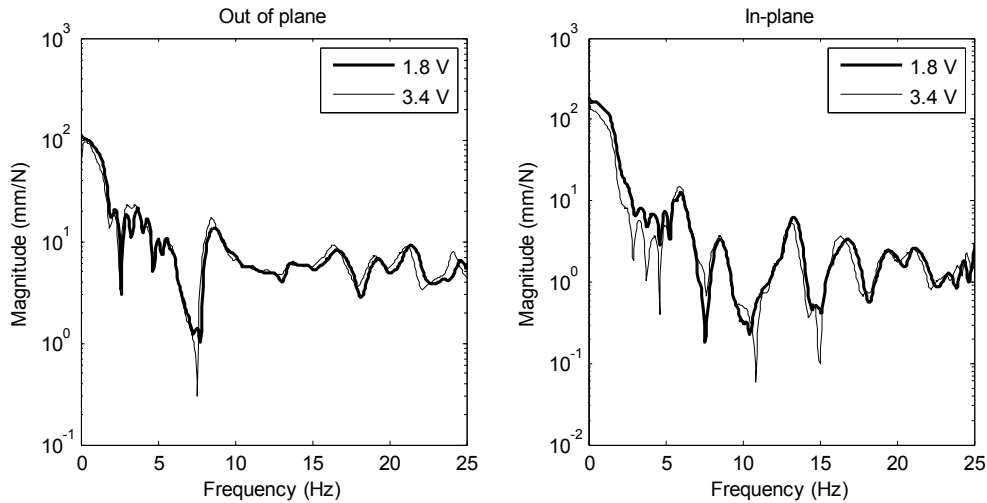


Fig. 6 Nonlinearity detection: out-of-plane and in-plane frequency response functions of location 1

3.3. Modal Parameter Identification

After completing the data measurements, the collected frequency response functions were analyzed using the STAR Modal software from Spectral Dynamics, Inc.

The curve fitting was done by Global Curve Fitting method. This method splits the curve fitting process up into two steps. In the first step, using all the measurement data, the frequency and damping are estimated.

The second step uses a second estimation process to obtain the residues (mode shapes) from the known and fixed values for the frequency and damping. Since the frequency and damping estimates can be obtained by processing all the frequency response functions and not a single measurement, these modal parameter estimates are more accurate than the estimates by curve fitters that fit frequency response functions one at a time. The second advantage of the Global Curve Fitting is that since the damping is known from the first step, the mode shapes are generally more precisely estimated in the second step [23].

The identified natural frequencies of both in-plane and out of plane modes of this study and prior work done by Ruggiero et al. [18] and Song et al. [19] on a similar SRT are summarized in Table 2.

The identified mode shapes of the first four in-plane and out of plane modes are shown in Figs. 7 and 8, respectively. The numbers on the deformed shape of the SRT stand for the measurement points. The in-plane modes have the oval, triangle, square and pentagon shape for the first, second, third and fourth modes, respectively. The out of plane modes resemble the bending mode of a free-free beam.

Table 2 Comparison between non-rigid body frequencies determined by the present study and prior work done by Ruggiero et al. [18] and Song et al. [19]; The asterisk indicates a split mode pair

Mode	Non-rigid body frequencies (Hz)					
	In-plane			Out of plane		
	Present study	Ruggiero et al.	Song et al.	Present study	Ruggiero et al.	Song et al.
1	4.68	3.0	5.07	3.21	2.0	2.88
1*	6.07	---	---	---	---	---
2	8.43	---	13.02	8.12	4.9	9.51
2*	9.46	---	---	---	5.5	---
3	13.32	---	22.08	12.79	11.2	14.61
4	17.21	---	---	17.55	---	---

4. Discussion

The method of fabrication, as well as the extensive repair that was done on the flaps, resulted in thickness variations along the joined regions. This contributed to non-uniform stiffness and mass distributions in both the torus and the flaps, affecting the modal parameters of the SRT. Besides, the flaps were not completely flat and had wrinkles at various locations. The mass imbalance and boundary conditions created modal asymmetry in this axisymmetric structure and consequently divided some resonant frequencies in two well separated frequencies. In Table 2 the split mode pairs are indicated by asterisks.

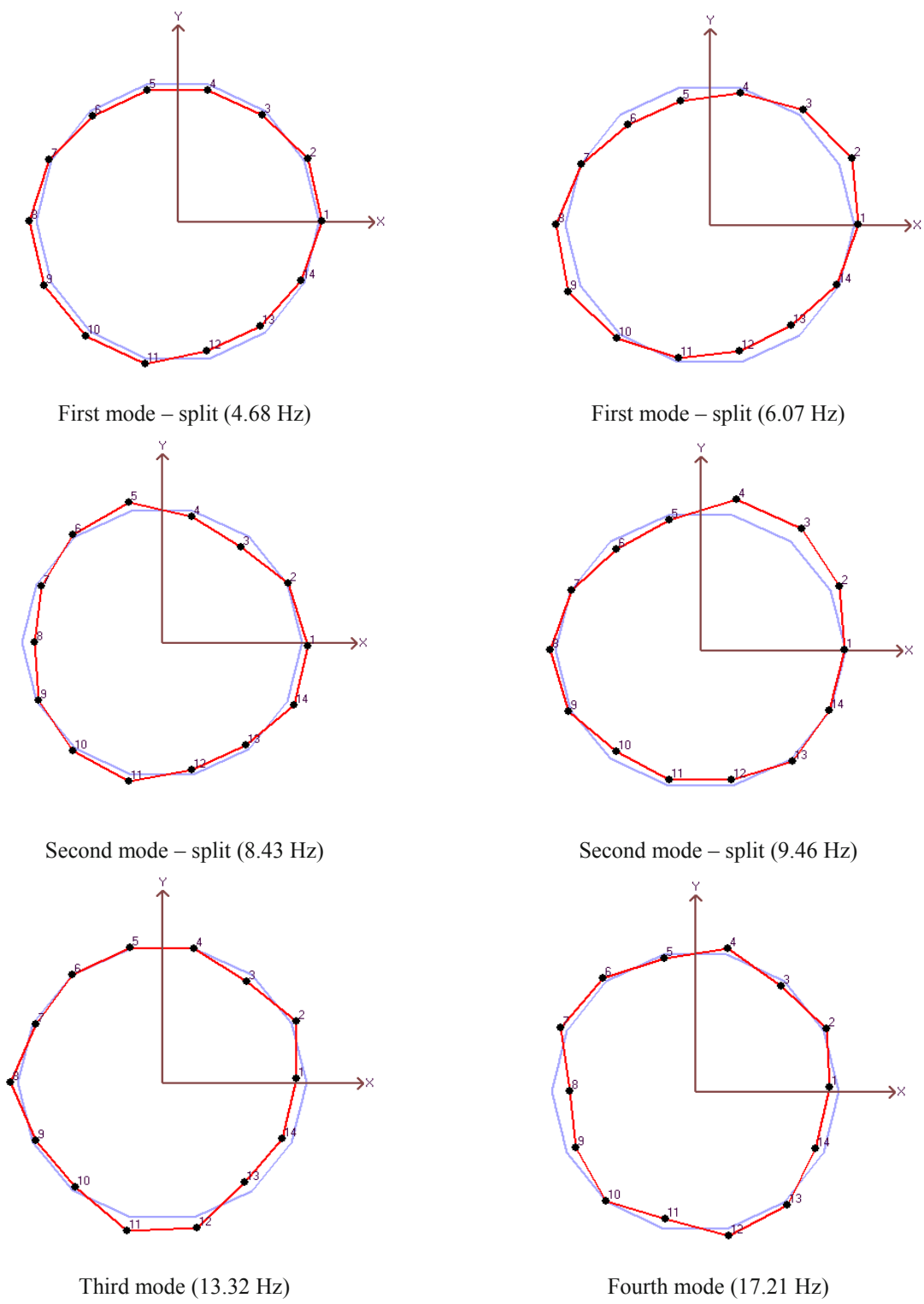


Fig. 7 Experimentally identified the first four in-plane mode shapes

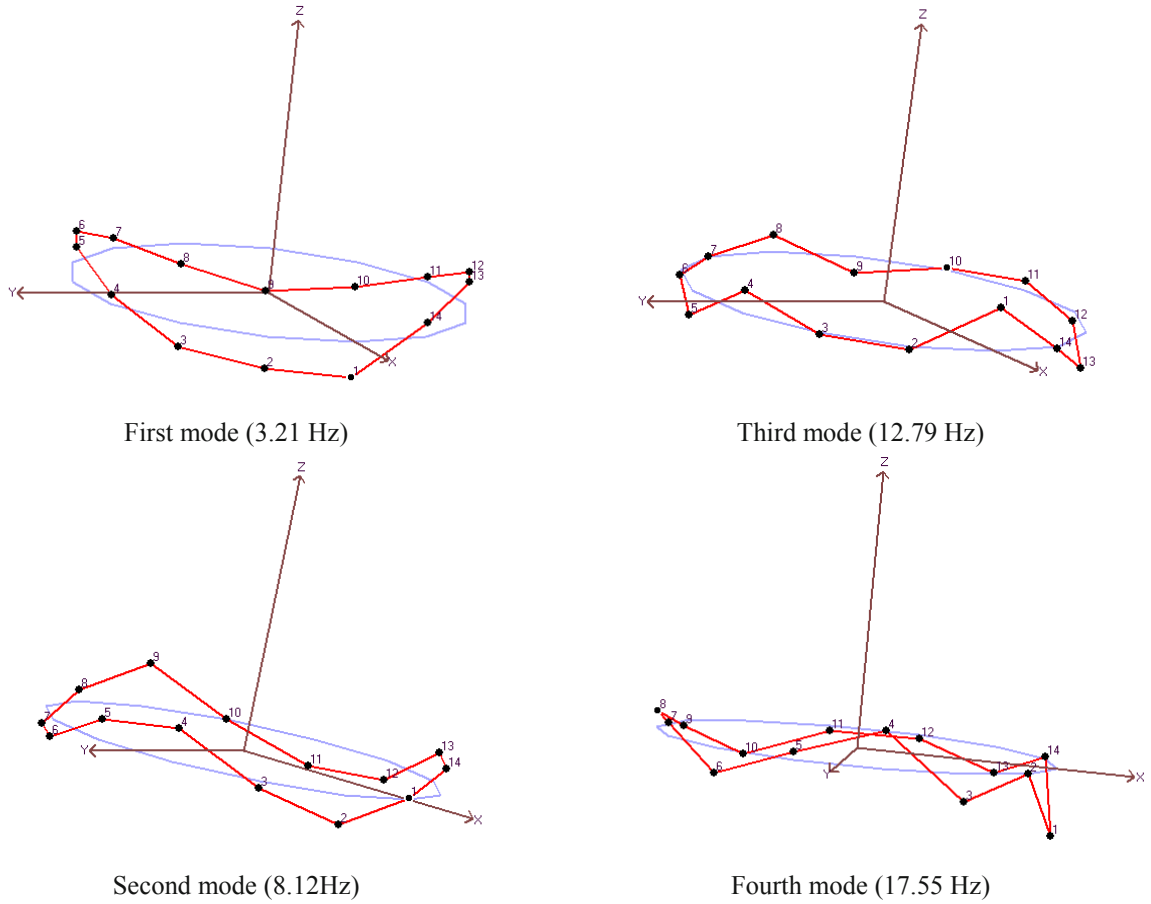


Fig. 8 Experimentally identified the first four out of plane mode shapes

The measured frequencies by Ruggiero et al. are lower than those obtained in the present study, [Table 2](#), indicating the higher stiffness of the current structure. In the present study, the SRT was pressurized at a very low pressure, while in the Ruggiero et al. study the inflation nozzle was left open to the atmospheric air, which allowed the SRT to wrinkle. Though in their study, the SRT was suspended vertically, lack of internal pressure, though small, could have reduced the stiffness and consequently reduced the identified frequencies of the SRT. Increasing the pressure increases the stiffness of the structure and consequently the identified frequencies [8-10]. The second possible cause for this trend is the use of accelerometer in their modal experiment. The contact measurement transducers, due to inertial loading on the structure, might have caused frequency shift toward lower frequencies. In the Ruggiero et al. study, the SRT was suspended vertically from the ceiling using two rubber wires causing a pendulum frequency of approximately 3.5 Hz, which was greater than the first natural frequency of 2 Hz extracted by this team, ([Table 2](#)). It is known that suspension frequencies greater than 10% of the first natural frequencies lead to inaccurate frequency identification. There was no information available regarding the plunge frequency of the SRT in that study.

In the study by Song et al., only the first two in-plane modes exhibited the expected classical mode shape. The third in-plane mode had the oval shape of the first mode. Their measured frequencies are higher than those obtained in the present study, [Table 2](#), indicating the high stiffness of their structure. In their study, the SRT was suspended at three points by 3.2 meter long monofilament lines with pendulum frequency of 0.28 Hz. These suspension lines could have presented stiffness in the

out of plane direction and depending on the location of the suspension points and the vibration nodes, the suspension lines could have affected the modal parameter identification. The monofilament lines generally should not introduce a significant stiffness in the in-plane direction. Though, in the in-plane deformation, the structure might have deformed in the out of plane direction as well, and the added stiffness by the support might have increased the identified frequencies and could have changed the mode shapes of the structure. In the Song et al. study, similar to the Ruggiero et al. tests, the inflation nozzle was also left open to the atmospheric air which made the SRT wrinkle and sag in the presence of the gravity force. This could have affected the stiffness of the SRT as well. But the most important difference between the results of their study and the present work lies in the method of excitation and collection of data. They had used the acoustic excitation. Besides, in the calculation of the frequency response function instead of the actual acoustic signal, the white noise signal from the signal generator was used as the input signal.

The modal experiment of the SRT proved that dynamic testing of this structure was very challenging. It was impossible to keep the electromagnet and the permanent magnet exactly at the same distance even in one set of measurements. The drive point measurement was very challenging due to spatial limitation. The width of the shear seam was 2.1 cm, and it was not possible to accommodate the laser sensor head and the electromagnet support in this small area, in such a way that both displacement measurement and excitation are performed exactly at the same point and direction. Also, since maintaining the internal pressure was done manually, it was less likely to achieve the same pressure at all times. Variable pressure contributed to variable stiffness which might have altered the modal parameters of the structure. Owing to the presence of very small punctures in the SRT, the air leakage made the distribution of pressure non-uniform in the torus.

The torus was suspended from the ceiling by very soft and long springs. The suspension frequencies were less than ten percent of the first natural frequency, 3.21 Hz, and it is not expected to affect the modal parameters directly. While during the experiments all the air ventilation ducts of the lab were blocked and the air conditioner was turned off, still the effect of the air current disturbance over the SRT was observed to produce pendulum movement of the SRT.

5. Conclusions

In this paper, experimental modal analysis of the SRT was presented. An in-house fabricated non-contacting electromagnetic exciter and two laser displacement sensors were employed. The sensors clearly picked up the signal within 180° of the actuator, which indicated that the excitation system was able to excite the torus' global modes.

First, it was shown that the SRT had a weak nonlinear behaviour. Hence, the identified natural frequencies and modal damping were valid at the level of excitation used in the testing, 3.4V. Then, the first four in-plane and out of plane damped natural frequencies were identified and compared with prior studies of similar SRTs.

The identified frequencies of the present study were higher than the measured frequencies by Ruggiero et al. (2004b) and lower than those obtained by Song et al. (2006), as presented in Table 2. This indicated the higher stiffness of the current structure than the former study and its lower stiffness than the latter one.

Being able to identify the first four in-plane and out of plane modes, particularly the in-plane ones, as well as decipher the modal asymmetry proved that the present experimental approach is sufficiently accurate to use in future studies.

Acknowledgments

The authors would like to thank Shirley Bradford of the United Applied Technologies, Inc. (Huntsville, AL) for kindly donating the self-rigidizing torus for experimentation. Mitra Danesh Pazhooh would also like to thank NSERC for the scholarship.

References

- [1] Jenkins, C.H.M., Gossamer Spacecraft: Membrane and Inflatable Structures Technology for Space Application, Progress in Astronautics and Aeronautics 191, American Institute of Aeronautics and Astronautics, Inc, 2001.
- [2] Cadogan, D., Scheir, C., Dixit, A, Ware, J., Cooper, E., Kopf, P., Intelligent Flexible Materials for Deployable Space Structures (InFlex), 47th AIAA/ASME/ASCE/AHS/ASC Structures, Structural Dynamics and Materials Conference, pp. 3705-3721, 2006.
- [3] Peng, F., Hu, Y.R., Ng, A., Active Control of Inflatable Structure Membrane Wrinkles Using Genetic Algorithm and Neural Network, Collection of Technical Papers - AIAA/ASME/ASCE/AHS/ASC Structures, Structural Dynamics and Materials Conference, pp. 3386-3394, 2004.
- [4] Griffith, D.T., Main, J.A., Experimental Modal Analysis and Damping Estimation for an Inflated Thin-Film Torus, Journal of Guidance, Control, and Dynamics 25 (4), pp. 609-617, 2002.

- [5] Lewis, J.A., Inman, D.J., Finite Element Modeling and Active Control of an Inflated Torus Using Piezoelectric Devices, *Journal of Intelligent Material Systems and Structures* 12, pp. 819-833, 2001.
- [6] Freeland, R.E., Bilyeu, G.D., Veal, G.R., Validation of a Unique Concept for a Low-Cost, Lightweight Space Deployable Antenna Structure, IAF Paper 93-I.1.204, presented at the 44th Congress of the International Astronautical Federation, 1993.
- [7] Main, J.A., Carlin, R.A., Garcia, E., Peterson, S.W., Straus, A.M., Dynamic Analysis of Space Based Inflated Beam Structure, *Journal of the Acoustical Society of America* 97 (2), pp.1035-1045, 1995.
- [8] Griffith, D.T., Main, J.A., Modal Testing of an Inflated Thin Film Polyimide Torus Structure, *Proceedings of IMAC XVIII*, pp. 1035–1041, 2000.
- [9] Slade, K.N., Tinker, M.L., Lassiter, J.O., Engberg, R., Comparison of Dynamic characteristics for an Inflatable Solar Concentrator in Atmospheric and Thermal Vacuum Conditions, *Collection of Technical Papers – the 41st AIAA/ASME/ASCE/AHS/ASC Structures, Structural Dynamics and Materials Conference and Exhibit*, pp. 64-75, 2000.
- [10] Slade, K.N., Dynamics of an Inflatable Structure in Vacuum and Ambient Conditions, *AIAA Journal* 39 (5), pp. 894–901, 2001.
- [11] Park, G., Kim, M.H., Inman, D.J., Integration of Smart Materials into Dynamics and Control of Inflatable Space Structures, *Journal of Intelligent Material Systems and Structures* 12 (6), pp. 423–433, 2002.
- [12] G. Park, E. Ruggiero, D.J. Inman, Dynamic Testing of an Inflatable Structure using Smart Materials, *Smart Materials and Structures* 11 (1), pp. 147–166, 2002.
- [13] Park, G., Sausse, M., Inman, D.J., Main, J.A., Vibration Testing and Finite Element Analysis of an Inflatable Structure, *AIAA JOURNAL* 41 (8), pp. 1556-1563, 2003.
- [14] Ruggiero, E., Park, G., Inman, D.J., Wright, J., Multi-input multi-output modal testing techniques for a gossamer structure, *American Society of Mechanical Engineers, Aerospace Division (Publication) AD 67, Adaptive Structures and Materials Systems*, pp. 167-175, 2002.
- [15] Ruggiero, E.J., Park, G., Inman, D.J., Multi-input multi-output vibration testing of an inflatable torus, *Mechanical Systems and Signal Processing* 18, (5), pp. 1187-1201, 2004.
- [16] Sodano, H.A., Park, G., Inman, D.J., An investigation into the performance of macro-fiber composites for sensing and structural vibration applications, *Mechanical Systems and Signal Processing* 18, pp. 683–697, 2004.
- [17] Ruggiero, E.J., Inman, D.J., A comparison between SISO and MIMO modal analysis techniques on a membrane mirror satellite, *Journal of Intelligent Material Systems and Structures* 16 (3), pp. 273-282, 2005.
- [18] Ruggiero, E.J., Tarazaga, P.A., Inman, D.J., Modal Analysis of an Ultra-Flexible, Self-Rigidizing toroidal Satellite Component, *Proceeding of IMECE04, 2004 ASME International Mechanical Engineering Congress and Exposition*, pp. 671-677, 2004.
- [19] Song, H., Weaver Smith, S., Main, J.A., Dynamic Testing of an Inflatable, Self-Supporting, Unpressurized Thin-Film Torus, *Journal of Guidance, Control, and Dynamics* 29 (4), pp. 839-845, 2006.
- [20] Ruggiero, E.J., Inman, D.J., Gossamer Spacecraft: Recent Trends in Design, Analysis, Experimentation, and Control. *Journal of Spacecraft and Rockets* 43 (1), pp. 10-23, 2006.
- [21] Ewins, D.J., *Modal Testing: Theory, practice and application*, 2nd ed. Baldock, Hertfordshire, England: Research Studies Press Ltd, 2000.
- [22] Allemang, R.J., *Vibrations: Experimental Modal Analysis*, Cincinnati: Structural Dynamics Research Lab, University of Cincinnati, 1999.
- [23] Richardson, M.H., Formenti, D.L., Global Curve Fitting of Frequency Response Measurements using the Rational Fraction Polynomial Method. 3rd IMAC Conference (1985).

Selective excitation using phase shifted ultrasound radiation force from focused transducers in air

Thomas M. Huber, Nathaniel Beaver, Justin Helps

Department of Physics, 800 College Avenue, Gustavus Adolphus College, Saint Peter, MN 56082

ABSTRACT

In recent years, it has been demonstrated that the ultrasound radiation force can be used as a noncontact technique for modal excitation. A novel capability of this method is the ability to perform selective excitation. A phase shift is imparted between the modulation signals emitted from a pair of ultrasound transducers focused at different positions on an object. When there is no phase difference between the radiation force produced by each transducer, they push in unison on the object, which induces symmetric eigenstates. When there is a 180° phase shift between the radiation force from the transducers, they will excite antisymmetric or torsional eigenstates. We describe some of the first demonstrations of this selective excitation using high-frequency focused ultrasound transducers.

I. INTRODUCTION

Modal analysis of structures requires an excitation source as well as a method for detecting vibration. In the past, both of these tasks were performed using mechanical transducers, such as a mechanical shaker for modal excitation and an accelerometer to detect vibration. In recent years, the introduction of laser Doppler vibrometers [1] has allowed non-contact measurements of vibration. However, in most cases, it was not possible to perform fully non-contact modal testing because there were few methods to perform non-contact excitation.

A promising technique for non-contact modal excitation is the use of the ultrasound radiation force.[2] In this technique, a pair of ultrasound frequencies are incident on the object under study. The excitation is caused by the non-linear interaction at the surface that causes a radiation force at the difference frequency between the two ultrasound frequencies. This ultrasound radiation force excitation method has a number of unique advantages relative to conventional excitation sources. One of the primary advantages is the non-contact nature of the excitation; this removes limitations such as the requirement for physically attaching a shaker and the resulting mass load. Another advantage is the wide bandwidth available for excitation – the transducers used for the current experiment have been used for excitation of structures at frequencies below 100 Hz to in excess of 300 kHz. As will be detailed in this paper, by using a focused transducer the ultrasound radiation force technique also allows selective excitation by using the phase shift in the modulation frequency between two transducers. This offers capabilities that are generally not possible using conventional mechanical excitation or non-contact excitation techniques.

Previous studies[3] have demonstrated that the ultrasound radiation force can be used to selectively excite brass cantilevers and hard drive suspensions. However, these studies used a diverging pair of 40 kHz transducers. The long wavelength and diverging output meant that it was difficult to spatially isolate the radiation force from the two ultrasound transducers. The current experiment used a pair of focused transducers in air with a central frequency of about 550 kHz and a 2 mm diameter

focus. This transducer pair, along with a scanning laser Doppler vibrometer, allowed non-contact excitation and measurements of a simple brass cantilever as well as an acoustic guitar.

II. THEORY

A. Ultrasound Radiation Force Excitation

Previous papers have described in detail the mechanism for ultrasound radiation force excitation.[4] If an object is ensonified with a pair of sinusoidal waveforms with frequencies f_a and f_b , the velocity potential $\phi(t)$ is

$$\phi(t) = A \cos[2\pi f_a t - \phi/2] + A \cos[2\pi f_b t + \phi/2] \quad (1)$$

where ϕ is a phase constant. The acoustical radiation force is proportional to the square of this velocity potential, which leads to a static radiation force as well as a dynamic radiation force at the difference frequency $\Delta f = f_b - f_a$ and high-frequency components at $2f_a$, $2f_b$, and $f_a + f_b$. In the current experiment, each ultrasound transducer was driven with a dual sideband, suppressed carrier (DSB-SC) waveform consisting of the sum of a pair of sine waves with frequencies of $f_a = f_c - f_m/2$ and $f_b = f_c + f_m/2$ that were symmetric about the central frequency f_c . In the current experiment, the goal was to excite audio-range resonances in structures, so the modulation frequency was between about 150 Hz and 2 kHz. For the carrier frequency of $f_c \sim 550$ kHz, the high frequency components were above 1 MHz, and thus were far above the resonance frequencies of the structures under test. Audio frequency excitation will only result from the radiation force component $F(t)$ at the difference frequency (alternately named the modulation frequency) $f_m = (f_b - f_a)$,

$$F(t) = F_0 \cos[2\pi f_m t + \phi]. \quad (2)$$

The magnitude F_0 of this ultrasound radiation force depends on a number of factors including the magnitude of the intensity of the ultrasound incident on the surface, as well as specific characteristics of the surface. The phase of this radiation force can be changed by adjusting the phase constant ϕ .

It is important to note that the radiation force given in Equation 2 does not explicitly depend on the carrier frequency. However, the intensity of the ultrasound at the surface can significantly change as a result of standing wave interference due to reflections back to the transducers. As discussed in Ref. 5, because of standing waves, minor changes in carrier frequency, room temperature or transducer position can cause substantial variability in the radiation force. To mitigate these standing waves effects, the carrier frequency was randomly varied using the algorithm described in detail in Ref. 5. A carrier frequency in the range from 500 kHz to 600 kHz was randomly selected and this same carrier frequency was maintained for 10 cycles of the carrier. After these 10 cycles, another random carrier frequency was selected. This method of randomly varying the carrier frequency eliminates the possibility of standing wave formation, which substantially improves the stability and repeatability of the measurements.

B. Selective Excitation Using Phase Shifted Transducer Pair

To perform selective excitation, a pair of ultrasound transducers was focused at two different locations on the structure under test. These transducers were separately driven by DSB-SC waveform using Eq. 1. Both transducers were driven with the same modulation frequency, f_m , even though the central carrier frequency was different for the two transducers. Therefore, both transducers caused a radiation force excitation $F(t)$ at the same frequency. The program generating the waveforms allowed a phase difference ϕ to be introduced between the pair of transducers. When the two transducers were driven with the modulation frequency in phase, the resulting radiation force from both transducers was in phase; this tends to enhance the excitation of vibrational modes that are symmetric relative to the two focus points while suppressing modes that are antisymmetric. In contrast, when there was a phase difference near 180° between the radiation force produced by the two transducers, they tended to reinforce modes that were antisymmetric while suppressing symmetric modes. Thus, by merely changing the phase difference of the between the two transducers, it was possible to selectively enhance or suppress different vibrational modes.

III. EXPERIMENTAL SETUP

In the current experiment, a pair of Microacoustics[6] ultrasound transducers were used in air. These transducers have a focal length of 70 mm, and a 2 mm diameter focal spot. To generate the waveforms that were used for excitation, a 60 MSample/second Strategic Test Digital-to-Analog Converter (DAC) card[7] was used. A Visual C++ program generated a DSB-SC waveform using Eq. 1 with a carrier frequency randomly being varied between 500 and 600 kHz. The resulting waveforms were amplified using ENI-240L and ENI-2100 amplifiers to obtain signals with amplitudes of about 70Vrms into the 50 Ω impedance transducers. The amplitude of the velocity of these devices were measured using a Polytec PSV-400 Polytec PSV-400 scanning laser Doppler vibrometer.[8]

A. Ultrasound excitation of brass cantilever

To demonstrate the capability of selective excitation a simple brass cantilever was used. This cantilever was clamped at one end, and had dimensions of 0.35mm x 7.85 mm x 26.2 mm.

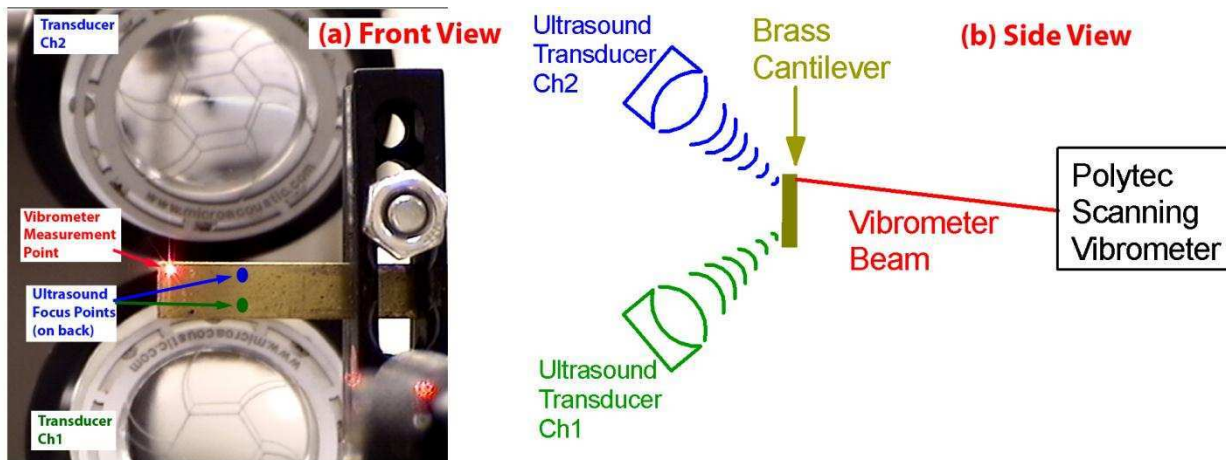


Figure 1: Setup used for ultrasound excitation of brass cantilever. (a) front view showing the vibrometer measurement point on the cantilever and the transducers positioned behind; (b) side view showing the relative orientation of the transducers and vibrometer.

As shown in Figure 1, a pair of ultrasound transducers was directed at the back of this cantilever at about a 30° angle relative to the normal; because the transducers were mounted at an angle, the ultrasound spot size was roughly 2mm wide by 3mm high and were centered roughly 1cm from the free end of the cantilever. To measure vibration, the vibrometer beam was directed at the front of the cantilever; for the single point measurements shown in Figures 2 and 3, the vibrometer measurement point was located near a corner on the free end of the cantilever as shown in Figure 1a. For comparison with conventional mechanical base excitation, a Bruel & Kjaer 4810 mechanical shaker was placed in contact with the support that held the cantilever.

The analog output of the laser Doppler vibrometer was sampled at 128 ksamples/second, and an FFT was performed on the data set. For each modulation frequency f_m , the amplitude and phase was extracted from the FFT data set. Operational deflection shapes were determined by animating

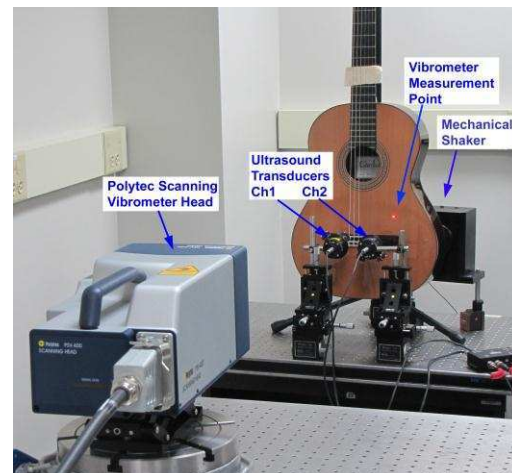


Figure 2: Apparatus used for ultrasound excitation of classical guitar showing Polytec PSV-400 vibrometer, and two ultrasound transducers Ch1 and Ch2 focused at opposite sides of the bridge of the guitar.

the amplitude and phase measured at many points on the surface.

B. Ultrasound excitation of guitar

A Cordoba 45R classical guitar[9] was hung from the bottom of the headstock. As shown in Figure 2, string vibrations were damped with a piece of felt wedged between the strings and the neck of the guitar. The pair of ultrasound transducers was focused on either side of the bridge. To compare the results with conventional base excitation, the Bruel & Kjaer 4810 mechanical shaker was placed in contact with the back of the guitar.

Because the amplitude of the vibrometer signal was very small, a Stanford Research System SR830 lock-in amplifier was used to extract the vibration signal from the noise. The reference signal was a sinusoidal waveform at the modulation frequency f_m that was generated using the Strategic Test DAC card. Further details can be found in Ref. 10.

IV. RESULTS

A. Selective excitation of Brass Cantilever

The brass cantilever used for this experiment has a fundamental frequency of 267 Hz for the 1st transverse mode. Fig. 3a, shows the response in the region from 1665-1705 Hz obtained by the vibrometer when the cantilever was excited using a mechanical shaker. Apparent in this plot are a pair of resonances at about 1677 Hz and 1690 Hz. Using the scanning laser vibrometer, it was determined that these correspond to the 2nd transverse mode and 1st torsional mode; animations of the measured deflection shapes of these resonances can be found online.[11] Because of the strong overlap of these two modes, when excited with a mechanical shaker, the measured deflection shapes are combinations of both modes; the deflection shape at 1677 Hz is primarily a 2nd transverse deflection shape, but has torsional characteristics, and vice versa.

Fig. 3b shows the response when ultrasound radiation force from single transducers Ch1 or Ch2 was separately used to excite the cantilever. It is clear that the resonance frequencies determined using the ultrasound radiation force from a single transducer are nearly identical to the frequencies obtained using a conventional mechanical shaker.

Fig. 3c illustrates the novel capability for selective excitation that results from using the pair of ultrasound transducers either in phase or 180 degrees out of phase.

The process can be understood by considering the symmetry characteristics of the 2nd transverse and 1st torsional modes – the 2nd transverse mode is symmetric across the width of the cantilever, whereas the 1st torsional mode is antisymmetric. When the transducers were driven with the same phase (▼), the resonance near 1677 Hz was enhanced, while the resonance near

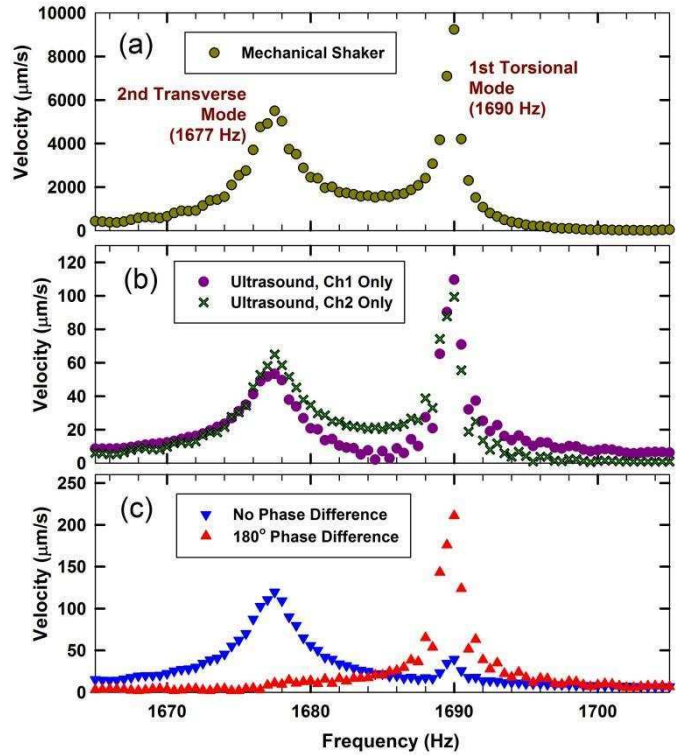


Figure 3: Doublet of resonances for a brass cantilever. (a) excitation using a mechanical shaker and (b) single ultrasound transducers have substantial overlap of these two resonances. (c) By varying the phase difference between the transducers, it is possible to isolate the resonances because the 2nd transverse mode is symmetric relative to the centerline and the torsional mode is antisymmetric.

1690 Hz was suppressed. This happens because driving the transducers in phase will tend to suppress the torsional mode that is antisymmetric across the width of the cantilever. In contrast, when the transducers were driven with a 180° difference in modulation phase (\blacktriangle), the radiation force from the two transducers will be out of phase with each other. Because the torsional mode near 1690 Hz is antisymmetric, these out-of-phase driving forces will tend to enhance the torsional mode while suppressing the symmetric 1677 Hz 2nd transverse mode.

The result of varying the phase difference can be seen more clearly in Fig. 4. This shows the result when the modulation frequency was kept at either 1677 Hz (\blacksquare) or 1690 Hz (\blacklozenge) while varying the phase. As expected for a symmetric mode, the 1677 Hz response is maximized when the two transducers were driven in phase, near 0° or 360° , and is minimized near 180° . The opposite response was obtained for the antisymmetric 1690 Hz mode, where the maximum response is observed near 180° with minimum near 0° . These results show the effectiveness of using the phase difference between the transducers to effectively enhance or suppress one of the resonances. Because the distance between the transducers and the surface are not precisely the same, the minima and maxima were shifted slightly from exactly 0° or 180° .

B. Ultrasound excitation of guitar

As an illustration of a more complicated set of overlapping resonances, Fig. 5 shows the results for measurements of an acoustic guitar in the region from 620 Hz to 745 Hz. Fig. 5a shows the response obtained by the vibrometer using a mechanical shaker. This plot seems to show three different resonances that are strongly overlapping. Fig. 5b shows the corresponding response curves when the ultrasound transducers Ch1 and Ch2 were used to excite the guitar separately – the same overlapping modes are apparent in the ultrasound driven spectra as are apparent in the mechanically driven spectrum.

Fig. 5c illustrates that these resonances can be resolved by using a pair of ultrasound transducers. When the transducers were driven with no phase difference between them (\blacktriangledown), the resonance near 660 Hz was enhanced, while the resonances near 680 Hz and 705 Hz were suppressed. In contrast, when the transducers were driven with a 180° difference in modulation phase (\blacktriangle) the 660 Hz resonance was suppressed while enhancing the upper two resonances. Therefore, even without measuring the deflection shapes, there is strong evidence that the mode at 660 Hz is symmetric about the midline of the guitar, whereas the mode near 680 Hz and 705 Hz are antisymmetric. The real power of the technique becomes apparent when measurements of the deflection shapes are

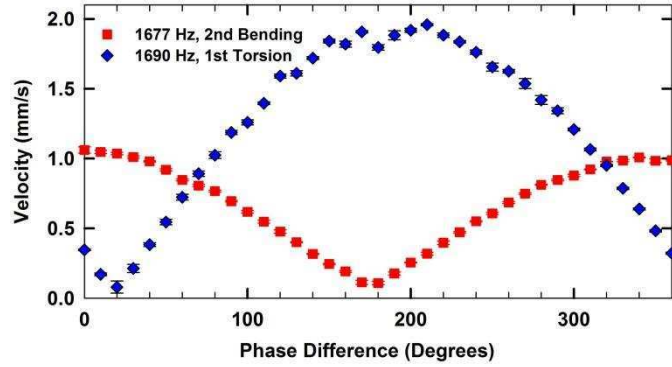


Figure 4: Response of cantilever as a function of the phase difference between transducers. The 1677 Hz 2nd transverse mode peaks when the transducers are driven in phase, and the 1690 Hz torsional mode peaks when they are out of phase.

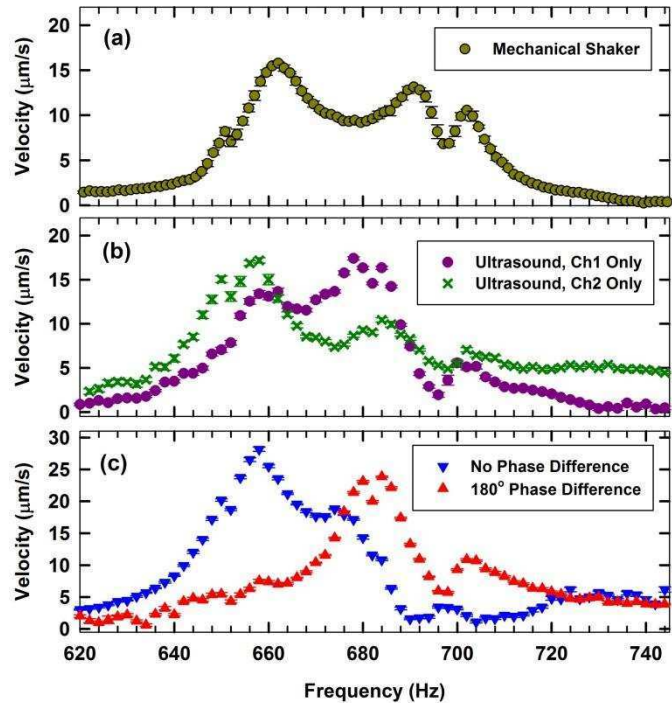


Figure 5: Frequency response of the face of an acoustic guitar in the region from 620 to 745 Hz showing several overlapping modes when excited using (a) a mechanical shaker and (b) two individual ultrasound transducers. In (c) these resonances are resolved by using the pair of ultrasound transducers driven either in phase or with a 180 degree phase difference.

measured. When a mechanical shaker, or single ultrasound transducer is used, the deflection shapes at 660 Hz and 680 Hz are complicated linear combinations of two overlapping modes. By using the transducer pair it allows these to be decoupled. Animation of these deflection shapes can be viewed online.[12]

V. CONCLUSIONS

The results of this study indicate that the ultrasound radiation force can be used for selective excitation of a brass cantilever and a guitar. The guitar is several orders of magnitude more massive than the cantilever, but the same selective excitation mechanism works for both.

ACKNOWLEDGMENTS

The authors would like to thank R. Mark French of Purdue University, for valuable discussions as well as the loan of the Cordoba guitar used in the current study.

REFERENCES

- [1] Polytec Incorporated; www.polytec.com
- [2] M. Fatemi, and J.F. Greenleaf, J.F., "Ultrasound stimulated vibro-acoustic spectrography," *Science* 28, pp. 82-85, 1988; T.M. Huber, M. Fatemi, R.R. Kinnick, and J.F. Greenleaf, "Noncontact modal analysis of a pipe organ reed using airborne ultrasound stimulated vibrometry," *J. Acoust. Soc. Am.* 119, pp. 2476-2482, 2006.
- [3] T.M. Huber, S.D. Hagemeyer, E.T. Ofstad, M. Fatemi, R.R. Kinnick, and J.F. Greenleaf, "Noncontact mode excitation of small structures in air using ultrasound radiation force," in *Proceedings of 2007 Society for Experimental Mechanics Annual Conference*, June 4, 2007; T.M. Huber, D. Calhoun, M. Fatemi, R.R. Kinnick, J.F. Greenleaf, "Noncontact modal testing of hard-drive suspensions using ultrasound radiation force," *Proceedings of International Modal Analysis Conference (IMAC XXIV)* February 2, 2006
- [4] G.T. Silva, S. Chen, J.F. Greenleaf, and M. Fatemi, "Dynamic ultrasound radiation force in fluids," *Phys. Rev. Lett.* 71, 056617, 2005; P.J. Westervelt, "Theory of steady force caused by sound waves," *J. Acoust. Soc. Am.* 23, pp. 312-315, 1951.
- [5] T.M. Huber, N. Beaver, J. Helps, "Elimination of standing wave effects in ultrasound radiation force excitation in air using random carrier frequency packets", submitted to *J. Acoust. Soc. Am.*
- [6] MicroAcoustics Instrument Inc., Broadband Air-Coupled Transducer (BAT), <http://microAcoustic.com>, Canada.
- [7] Strategic Test UF2e-6022; <http://www.strategic-test.com/eng/Instruments/Arbitrary-Waveform-Generators2/PCI-Express-X1/14-bit-D-A/100-MS-s/UF2e-6022>
- [8] <http://www.polytecpi.com/PDF/PSV-400DataSheet1003.pdf>
- [9] <http://www.cordobaguitars.com/74.php>
- [10] T.M. Huber, N. Beaver, J. Helps, "Noncontact Modal Excitation of a Classical Guitar using Ultrasound Radiation Force Excitation", submitted to *Exp. Tech.*
- [11] <http://physics.gac.edu/~huber/animations/cantilever>.
- [12] http://physics.gac.edu/~huber/guitars/ultrasound_cordoba.

The Steelpan as a tool to incite interest in Engineering Education

S. E. Maloney^a and N. L. Williams^b

^aUniversity of Cambridge, Institute for Manufacturing
Alan Reece Building, 17 Charles Babbage Road, Cambridge, CB3 0FS, United Kingdom
sem73@cam.ac.uk

^bUniversity of Bedfordshire Business School,
Luton campus, Vicarage Street, Luton, Bedfordshire, LU1 3JU, United Kingdom
nigel.williams@beds.ac.uk

ABSTRACT

There is an economic imperative to increase the level of innovative activities in developed and developing countries. Universities have been encouraged to increase the number of science and technology graduates. One of the approaches used by universities is the encouragement of minority students, in particular, Black African-American and African-Caribbean students into undergraduate engineering. However, to realize the potential of these students, programs need to build understanding of engineering principles in a manner that appeal to multiple learning styles. The steelpan, a percussion instrument invented in Trinidad and Tobago, can provide a possible solution. The steelpan also known as the pan or steel drum is produced by creatively deforming metal sheet. The pan is a unique musical device and offers an opportunity to teach engineering concepts using an instrument that is a part of the cultural heritage of some of these students. The technology of the steelpan is multidisciplinary and requires knowledge in the areas of materials science, production processes, acoustics, vibrations and music. By decomposing the production of the instrument into these underlying bodies of knowledge, it provides an ideal opportunity to explain and demonstrate engineering principles at low cost. This presentation demonstrates options for courses that use the steelpan to encourage elementary and high school students into the engineering profession.

INTRODUCTION

Science and technology education is seen as critical to the future economic growth of the UK economy [1]. Highly skilled engineers are seen as essential to creating innovative products and services, positioning the UK as a global manufacturing leader [2]. However, in the UK, interest in undergraduate degrees in Engineering is in decline [3]. The UK government has expended considerable effort in reversing this trend with a number of interventions aimed at increasing interest and access to engineering education [4]. One particular grouping, Afro-Caribbean males, has been a target of many of these efforts. These students perform poorly at secondary school science and exhibit little interest in undergraduate programs [5]. This tends to limit their access to professional and entrepreneurial opportunities. Stimulating interest in engineering programs in this group can bring economic and social benefits [6], however, the way in which it is taught excludes many students [7]. Courses fail to stimulate interest in engineering by establishing its relevance to student's personal interest [8]. This presentation demonstrates how the pan can be used as a tool to incite interest in the pursuit of engineering programs.

ENGINEERING EDUCATION AND LEARNING STYLES

Educators need to be aware of how students acquire engineering subject knowledge. Learning of science and engineering concepts takes place in two steps: reception and processing of information [9]. During reception, internal and external information becomes available to students who then select the information they deem important. Processing may take several forms incorporating memorization, reasoning, reflection or action [10]. The first basis of classification for learning styles is the type of information that the student prefers to receive either perceived through sensory means or interpreted through intuitive means. The second is the most effective mode through which sensory information is received either visual or verbal. The third is the way in which

information is organized, either inductive in which empirical observations are given and engineering principles are inferred or deductive in which principles are given and outcomes are determined. The fourth is the way in which the student prefers to work with information either actively or reflectively. Finally, the last dimension is how students build understanding either through incremental steps or sequentially or through larger, global stages. The learning styles of many students are incompatible with how engineering concepts are taught and demonstrated [11]. Many of these students are visual, sensing, inductive, and active, while others with strong design skills are global rather than sequential. However, most engineering education is auditory, abstract (intuitive), deductive, passive, and sequential. To improve student performance, active, team based activities have been recommended to introduce students to the practice of engineering. In particular, programs that integrate theoretical concepts and practical applications have improved retention rates in minority engineering students [12].

SUMMARY

There is a need therefore to design interventions to meeting the objectives of technology education that engage a wider range of learning styles. A solution may be found in the steelpan. The instrument has been adopted by educators primarily to teach music in schools [13]. The integrative nature of the pan making process which links materials, metallurgy and vibrations offers significant promise for science and technology education. Further, the familiarity of Afro-Caribbean students with the instrument could make it a stimulus to which they will pay attention. Educational objectives can be designed that align with all domains of learning, unlike most engineering programs, an approach that educators have been recommending for some time [14]. These aspects provide an ideal opportunity for introducing engineering concepts that is both comprehensive and appealing. This presentation would be used to demonstrate how the steelpan can be used to introduce basic engineering science concepts while simultaneously appealing to different learning styles.

REFERENCES

- [1] Bils, M. and P. J. Klenow. "Does Schooling Cause Growth?" *The American Economic Review* 90(5): 1160-1183 (2000).
- [2] Frenz, M. and G. Ietto-Gillies. "The impact on innovation performance of different sources of knowledge: Evidence from the UK Community Innovation Survey." *Research Policy* 38(7): 1125-1135 (2009).
- [3] Bowen, E., J. Prior, et al. *Engineering more engineers - bridging the mathematics and careers advice gap* (2008).
- [4] Melville-Ross, T. and A. Langlands. *Strategic plan 2006-11*. H. E. F. C. f. England. Bristol, Higher Education Funding Council for England: 1-57 (2009).
- [5] Osborne, J., S. Simon, et al. "Attitudes towards science: a review of the literature and its implications." *International Journal of Science Education* 25: 1049-1079 (2003).
- [6] Barrett, G. A., T. P. Jones, et al. "Ethnic Minority Business: Theoretical Discourse in Britain and North America." *Urban Stud* 33(4-5): 783-809 (1996).
- [7] Tobias, S. "Some Recent Developments in Teacher Education in Mathematics and Science: A Review and Commentary." *Journal of Science Education and Technology* 8(1): 21-31 (1999).
- [8] Locke, W. "Higher Education policy in England: missed opportunities, unintended consequences and unfinished business." *Journal of Access Policy and Practice* 5: 180-204 (2008).
- [9] Felder, R. "Reaching the Second Tier: Learning and Teaching Styles in College Science." *Journal of College Science Teaching* 23(5): 286-290 (1993).
- [10] Cagiltay, N. E. "Using learning styles theory in engineering education." *European Journal of Engineering Education* 33: 415-424 (2008).
- [11] Lumsdaine, M. and E. Lumsdaine. "Thinking Preferences Of Engineering Students: Implications For Curriculum Restructuring." *Journal of Engineering Education*(April): 194-204 (1995).
- [12] Carlson, L. and J. Sullivan. "Hands-on Engineering: Learning by Doing in the Integrated Teaching and Learning Program." *International Journal of Engineering Education* 15(1): 20-31 (1999).
- [13] Svaline, J. M. (1995). "Why Not Start a Steel Band?" *Music Educators Journal* 82(3): 22-25 (1995).
- [14] Howard, R. A., C. A. Carver, et al. "Felder's learning styles, Bloom's taxonomy, and the Kolb learning cycle: tying it all together in the CS2 course." *SIGCSE Bull.* 28(1): 227-231 (1996).

Non-Contacting Strain Measurement in Dynamic Tensile Testing

Deju Zhu¹, Barzin Mobasher², S.D. Rajan³

¹ Postdoctoral fellow, Department of Mechanical Engineering, McGill University, Montreal, QC, Canada, E-mail: Deju.Zhu@mail.mcgill.ca

² Professor, Ph.D., P.E., Department of Civil, Environmental and Sustainable Engineering, Arizona State University, Tempe, AZ, 85287, corresponding author, E-mail: Barzin@asu.edu

³ Professor, Ph.D., Department of Civil, Environmental and Sustainable Engineering, Arizona State University, Tempe, AZ, 85287, E-mail: S.Rajan@asu.edu

ABSTRACT

This paper presents the development of a test procedure and application of non-contacting strain measurement in dynamic tensile testing. The strain time histories of test specimens measured by a laser extensometer were derived by a phase-shift technique based on zero-crossing method. The accuracy of proposed procedure was verified by comparing the strain values measured by the laser extensometer with the actuator measurement of a servo-hydraulic high speed machine using aluminum alloy (AA) 6061-T6, and then applied to Alkaline Resistant (AR) glass fabric reinforced cement composite. Comparison between these two measurements shows a good agreement. The strain rate effect on the mechanical properties of AR-glass fabric-cement composite was found. The failure behavior of the composite was also discussed using the images captured by high speed camera.

Keywords: dynamic tensile testing; laser extensometer; phase-shift; cement composites.

1. Introduction

Understanding the mechanical properties of engineering materials at high strain rates is an area of interest for various applications including structures, military, and sports. Materials loaded at high strain rates exhibit mechanical characteristics that are different from those obtained under quasi-static loading. The strain rate dependency of various materials has been known since the 19th century and mechanical responses under high strain rate, blast, or shock have been investigated throughout years of research. A number of experimental techniques exist in investigating high strain rate material properties: split Hopkinson bar devices, falling weight devices, flywheel facilities, hydraulic machine, etc. [1-7]. Measurement of deformation plays an important role in establishing the dynamic behavior of materials and the direct measurement of strain is challenging at high strain rates. Traditional strain measuring techniques rely on the use of extensometers and strain gages, both of which must be specialized for a specific specimen configuration, testing temperature, rate of loading and range of strain. Each of these variables constrains the range of applicability for a particular extensometer. Strain gages are more cost effective but are limited in the maximum allowable strain, require careful alignment and bonding techniques for a single use, and are also limited in their temperature range. The use of a non-contacting strain measuring technique is preferred in many situations. Methods such as laser extensometer [8], digital laser speckle technique [9], rotating drum of high speed camera [10], diffraction-grating technique [11] and image analysis [12-14] are currently in use for non-contacting strain measurement. The present work describes a data reduction procedure for the high speed function of a laser extensometer and its application in dynamic tensile testing at moderately high strain rates. The laser extensometer used in the present work is manufactured by Optrix Inc. (Model 3000). A phase-shift method based on zero-crossing detection is used in the processing of raw data for calculation of displacement and strain. The proposed procedure is firstly applied to dynamic tensile testing using aluminum alloy (AA) 6061-T6 on a servo-hydraulic high speed testing machine. Then Alkaline Resistant (AR) glass fabric-cement composite specimens are tested on the same machine. At last the failure behavior and stress-strain response of the AR-glass fabric-cement composite were discussed and compared with its response under static loading.

2. Basic Principles

Fig. 1(a) shows the optical layout of laser extensometer. The incoming laser beam is comprised of two collinear, orthogonally polarized components which differ in frequency by 250 kHz. The laser beam goes through a calcite beam splitter (A) and divides into two beams one of which passes through a half wave plate (B). The half wave plate rotates the polarization vector by 90 degrees, thus allowing it to interfere with the unaltered beam to create an interference pattern on the surface of the object. Both laser beams go through 50/50 beam splitter (C) which transmits one polarized beam, and reflects the other thus separating the two frequency components based on their orthogonal polarization. Mirrors (D) are used to make the transmitted and reflected beams parallel to one another. The beams reflected by the mirror intersect at one location on specimen surface where a moving fringe is formed. The beams reflected by 50/50 beam splitter also intersect on specimen surface and form moving fringe. The lights scattered from both locations of specimen surface are detected by optical detectors (E) which generate independent signals characterizing the displacement of the test specimen at the point of measurement. Both detectors are connected to a control and display unit. A digital phase-meter in the control and display unit keeps track of the relative phase difference between each detected signal and a reference signal. Surface displacement is measured for each of the two locations and the differential displacement (removing rigid body motions) is converted to an average strain measure between the points [15]. The displacement measurement at each point is facilitated by interference of two beams of the laser light that meet at the sample surface at a fixed angle (Figure 1(b)). Interference fringe patterns are formed where the two beams overlap, due to the differential distance travelled by each beam. The fringe spacing is given by

$$D_{fringe} = \lambda / (2 \sin \phi) \quad (1)$$

where ϕ is the half angle between the two incoming beams and λ is the laser wavelength.

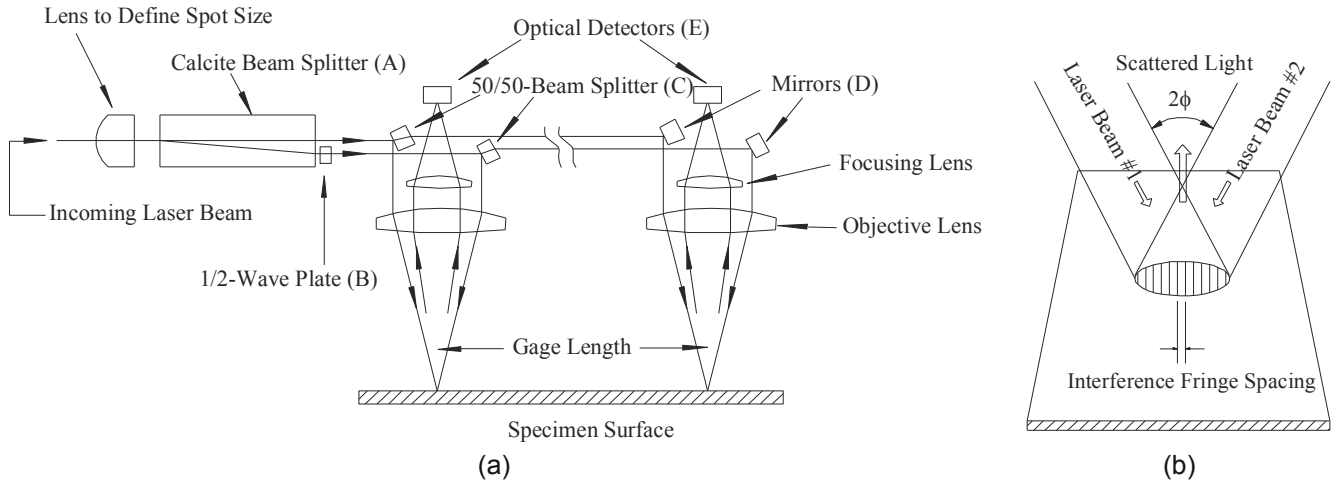


Fig. 1 (a) Optical layout of laser extensometer and (b) interference fringe

To facilitate data processing, a stabilized 2-frequency laser is used so that beams 1 and 2 differ in frequency by precisely 250 kHz. This causes the fringes to move relative to a stationary surface at a rate equal to the difference in the frequencies. The laser extensometer detector, located between the two incoming beams, senses light scattered from the test specimen. The detected signal, viewed on an oscilloscope, consists of a large DC signal plus a superimposed AC signal at a frequency close to 250 kHz. If the specimen surface is fixed relative to the extensometer, the AC signal will have a frequency of precisely 250 kHz. This frequency however will change due to the movement of the specimen. This frequency f can be expressed as a function of the surface velocity by the following equation

$$f = f_0 + (V / D_{fringe}) \quad (2)$$

where f_0 is the difference in frequencies (250 kHz), V is the velocity of the surface, and D_{fringe} is the fringe spacing (17.4 micron).

The phase of the detected signal is compared to the laser reference signal of 250 kHz. By comparing the relative phase of these two signals, the direction and distance of the surface movement can be determined. When the

surface moves a distance equal to fringe spacing (D_{fringe}), the relative phase increases by as much as one sinusoidal wave cycle. The movement of the fringe pattern is oriented so that only axial displacement is detected while the measurement is insensitive to small changes in surface reflectivity. In applications conducted under normal speed mode, the electronic control and display unit can convert the optical signals of laser extensometer into one analog or digital voltage output that is collected by a data acquisition device. The maximum data rate is 125 kHz, and maximum extension rate (strain rate) is 0.2 s^{-1} . However, in high speed mode applications, the control and display unit is unable to process the signals continuously to convert the optical signals into analog or digital outputs. In this case, a two-step process of high speed data acquisition followed by post processing is adopted. A high speed accessory is necessary to convert optical signals to electronic signals in the form of sinusoidal waves and transfer them through high speed data acquisition to a digital recording format. The sinusoidal signals are post-processed to obtain the displacements at both points. The procedure is discussed in the following sections.

3. Phase Shift Based on Zero-Crossing Method

The detectors in the laser extensometer head measure two 250 kHz sinusoidal waves when the specimen is stationary. When the specimen deforms under loading, these sinusoidal wave signals will change their frequencies. A MATLAB code was developed to calculate the phase shift between each of sinusoidal waves and the reference signal of 250 kHz using zero-crossing method. Fig. 2 indicates the basic concept of phase shift based on zero-crossing method – a change in phase of a periodic signal with respect to a reference. The zero-crossing is defined by

$$\begin{aligned} x(i)x(i+1) &\leq 0 \quad \text{unbiased zero-crossing} \\ x(i+1) - x(i) &> 0 \quad \text{ascending} \\ x(i+1) - x(i) &< 0 \quad \text{descending} \end{aligned} \quad (3)$$

where $x(i)$ is the voltage of current time step, $x(i+1)$ represents the voltage of next time step.

These zero-crossing locations are shown with an asterisk in Fig. 2. The phase shift between the reference signal and laser signal can be calculated as follows

$$\theta_i = \frac{2\pi(T_{i+1} - T_i)}{T_{ref}} \quad (4)$$

In this equation, θ_i is the phase shift, T_i and T_{i+1} are the time when zero-crossing is detected by eqn. (3), and T_{ref} is the period of reference signal (1/250 ms). The phase shifts of both signals can be obtained with respect to the reference signal. The displacement of measurement point is directly proportional to the number of phase shift cycles and fringe spacing as follows

$$D_i = \frac{\theta_i}{2\pi} D_{fringe} = \frac{(T_{i+1} - T_i)}{T_{ref}} D_{fringe} \quad (5)$$

where D_i is the displacement of the measurement point on specimen surface, θ_i is the phase shift at current time step, and D_{fringe} is the fringe spacing.

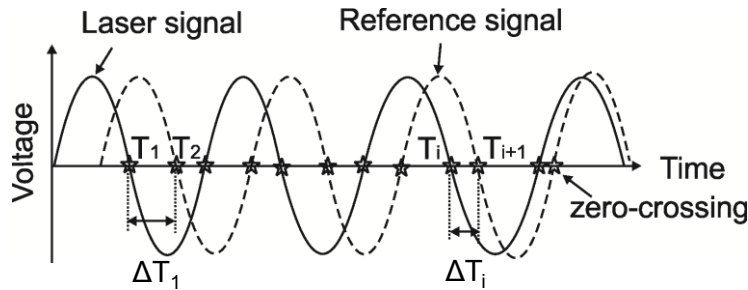


Fig. 2 Phase shift between reference signal and second signal

4. Experimental Program

4.1 Aluminum Alloy (AA) 6061-T6

AA6061-T6 is ductile, heat treated and artificially aged, containing magnesium and silicon as its major alloying element. It exhibits elastic-plastic behavior with large failure strain. The aluminum specimens with dimensions of $18 \times 75 \times 1.6$ mm are shown as Fig. 3. The gage length is 25 mm.

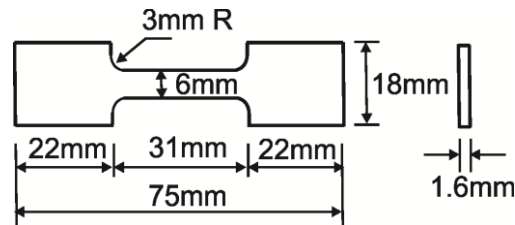


Fig. 3 AA6061-T6 test specimen

The dynamic tensile tests are conducted using a MTS servo-hydraulic high rate testing machine in open-loop control. The development and application of this test method have been addressed in our earlier work [16, 17]. The setup of the dynamic tensile testing is presented in Fig. 4. A tensile specimen is placed into the upper and lower grips. Proper alignment of laser extensometer is achieved to obtain valid signals for strain measurement. The dynamic load is introduced to the lower grip through a slack adaptor. In this work, the load is measured by a piezoelectric load washer (Kistler 9041A) with a capacity of 90 kN. A high speed digitizer is used to collect the signals from load washer, laser extensometer and actuator at a sampling rate of 10 MHz. When operating at its maximum sampling rate of 10 MHz, the digitizer is able to collect transient 250 kHz signals from the laser extensometer without signal aliasing. The data is acquired from a variety of sources – two from laser extensometer, one from piezoelectric load washer, and one from the actuator. The actuator signal is filtered by low-pass filter with a cutoff frequency of 3 kHz to eliminate high frequency noise. This allowed a direct comparison of the actuator measurement with the laser extensometer data.

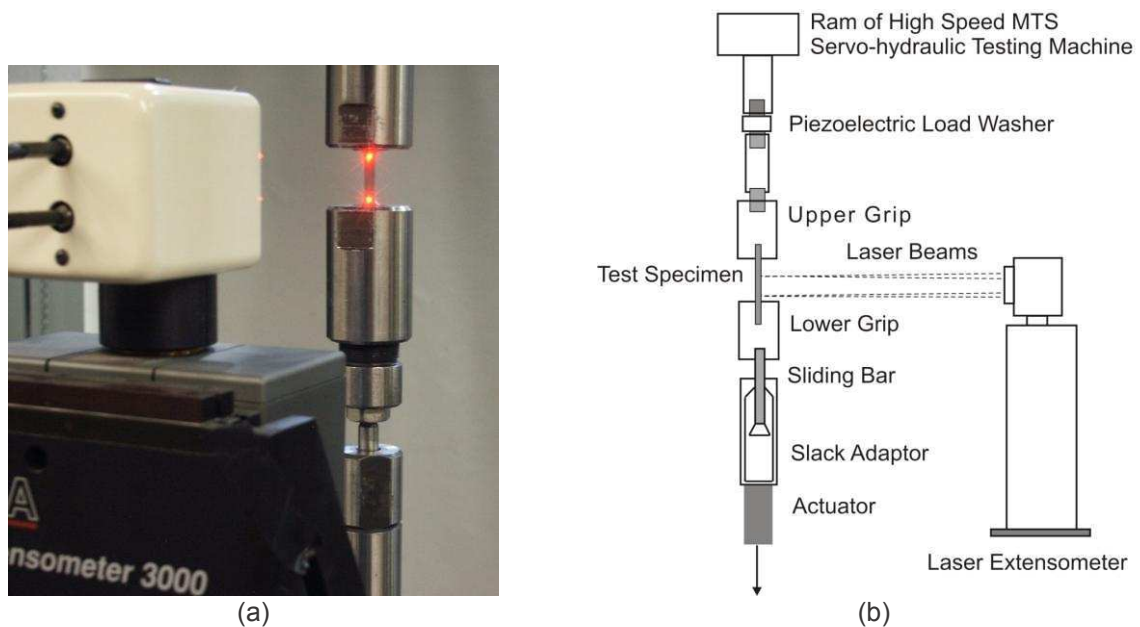


Fig. 4 The setup of dynamic tensile test: (a) snapshot, (b) schematics

Fig. 5 shows the comparison of strain time history measured by laser extensometer and actuator for AA6061-T6 specimens. Note that the strain values measured by actuator are not a linear function of time although high frequency noises are filtered out by low-pass filter. At strain rates of 161, 206 and 214 s^{-1} , the strain time history

curves obtained by these two measurements agree very well and the maximum strain values are almost identical. At the strain rate of 138 s^{-1} , the difference between these two measurements was large (0.028 mm/mm). This is due to the poor quality of the acquired laser signals. Overall, the strain time histories of specimens derived from laser extensometer agreed with actuator measurement for most of tests. But one should be aware of that the accuracy of the laser measurement depends on the quality of the acquired signals.

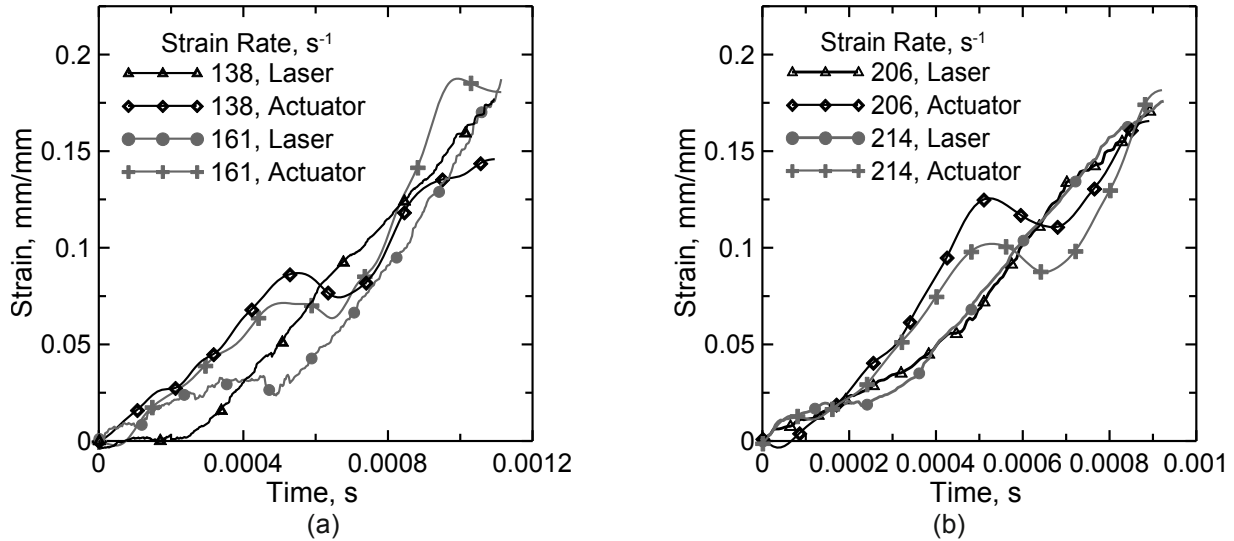


Fig. 5 Comparison of actuator and laser extensometer measurement for AA6061-T6 at different strain rates: (a) 138 and 161 s^{-1} (average value = 150 s^{-1}), (b) 206 and 214 s^{-1} (average value = 210 s^{-1})

4.2 AR-glass Fabric-cement Composite

Test Specimens

The AR-glass fabric-cement composites in this study are prepared using the pultrusion process. In this process, the fabric passes through a slurry infiltration chamber to get coated, and then is pulled through a set of rollers to squeeze the paste in between the fabric openings while removing excessive paste [18]. The fabric-cement composite are then formed on a plate shaped mandrel resulting in laminated sheets with $250 \times 300 \text{ mm}$ and thickness of about 10 mm . Cement boards are made with 4 layers of fabrics. The reinforcing yarns in the composite of each fabric are placed along the pultrusion direction. After forming the samples, constant load of about 50 N was applied on the surface of the fabric-cement sheet to improve penetration of the matrix in between the yarn and fabric openings. All boards are cured in water at room temperature for 28 days and then cut into pieces with dimensions of $25 \times 150 \times 10 \text{ mm}$ (width \times length \times thickness). Aluminum plates of dimensions of $25 \times 50 \times 1 \text{ mm}$ (width \times length \times thickness) were glued onto the gripping edges of the composite specimen to minimize localized damage and provide better load transfer in the grips. The gage length of the composite specimen is 50 mm . The mix design for the composite was 42% cement, 5% silica fume, 0.1% superplasticizer and 50% water by volume and the water/cement ratio by weight was 0.4.

Failure Behavior

The failure behavior of the composite was recorded using a high speed digital camera (Phantom v.7) at a sampling rate of 10,000 fps. Typical images were chosen to present the cracking pattern of the composite, as shown in Fig. 6. Note that there are three stages in the failure of the composite during the loading process. Fig. 6(a)-(c) represents the developing of the multiple cracking process. The behavior of successive cracking was indicative of stress transfer mechanism at the fabric-cement interface to be sufficient for load transfer and composite action. After this stage, the strain increased and cracks opened uniformly until a point of bifurcation where one of the cracks becomes the dominant one that continues to open, while the load begins to decrease. Only this dominant crack was observed and all other cracks closed and were not visible anymore (Fig. 6(d)-(e)). The main crack continues to widen under load for the duration of the test. At this point the forces were mainly carried by the fabric until all its yarns were completely broken (Fig. 6(e)), leading to a complete failure of the composite.

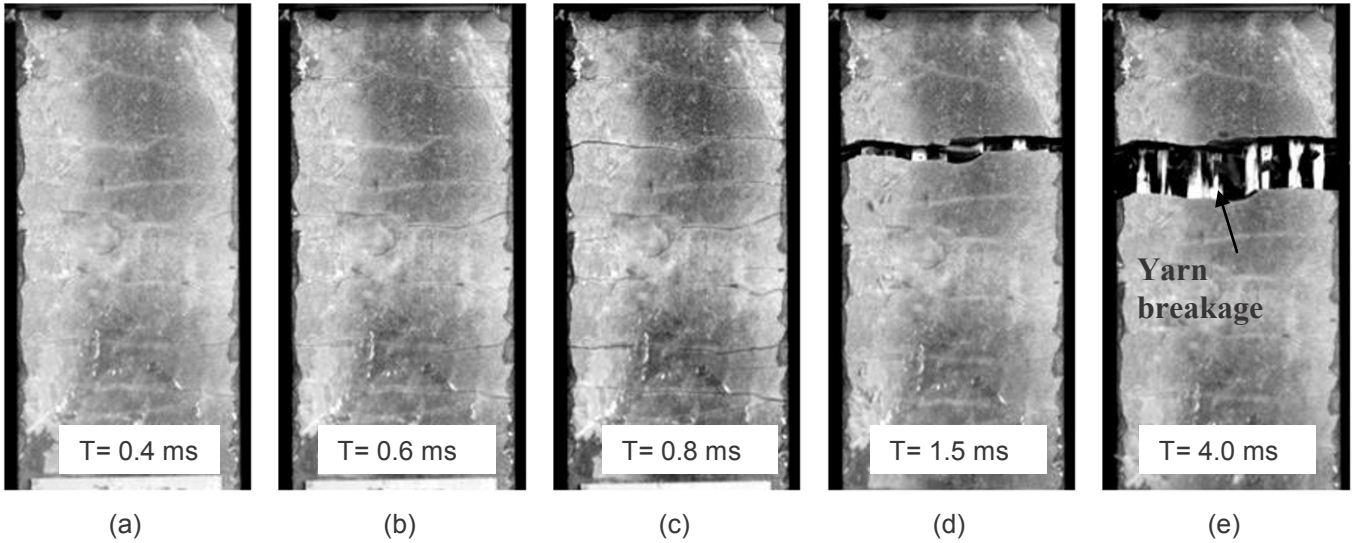


Fig. 6 AR glass composites: (a)-(c) multiple micro-cracking, (d) main crack widening and other micro-cracks closing, and (e) complete failure

Fig. 7 shows the comparison of strain time histories of two tests (test no. 1 and 4) for the composite measured by actuator and laser extensometer. It should be noted that the strain time history curves of the composite specimens also have a wavy pattern as those of AA6061-T6 specimens. Each strain time history curve indicates a good agreement in strain values measured by laser extensometer and actuator. One should point out again that the accuracy of laser measurement depends on the quality of signals. If the surface of composite specimen has large defects, the quality of signals can be influenced significantly causing inaccurate strain measurement.

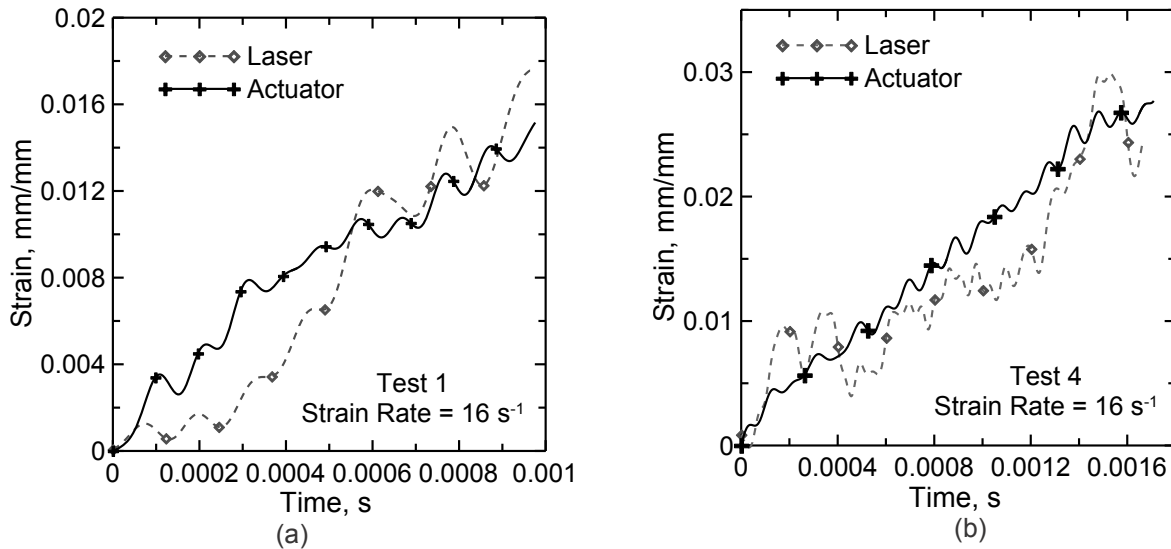


Fig. 7 Comparison of strain time histories of AR-glass fabric-cement composites measured by the laser extensometer and actuator: (a) test 1, and (b) test 4

Strain Rate Effect

The stress-time and stress-strain curves of these four tests are shown in **Fig. 8**. The response of individual specimens is not same, and two of the tests show a different trend. The test durations are less than 0.1 ms and there is only one peak in the stress time history, indicating the 4 layers of AR glass fabric broke simultaneously. However, for the rest of specimens, there are multiple peaks on the stress-strain curves, indicating separated failure of fabric layers. The dynamic material properties of the fabric-cement composite are summarized in Table 1. The Young's modulus is 790 ± 161 MPa, tensile strength is 6.20 ± 0.99 MPa, and the toughness (the area under stress-strain curve) is 0.080 ± 0.041 MPa.

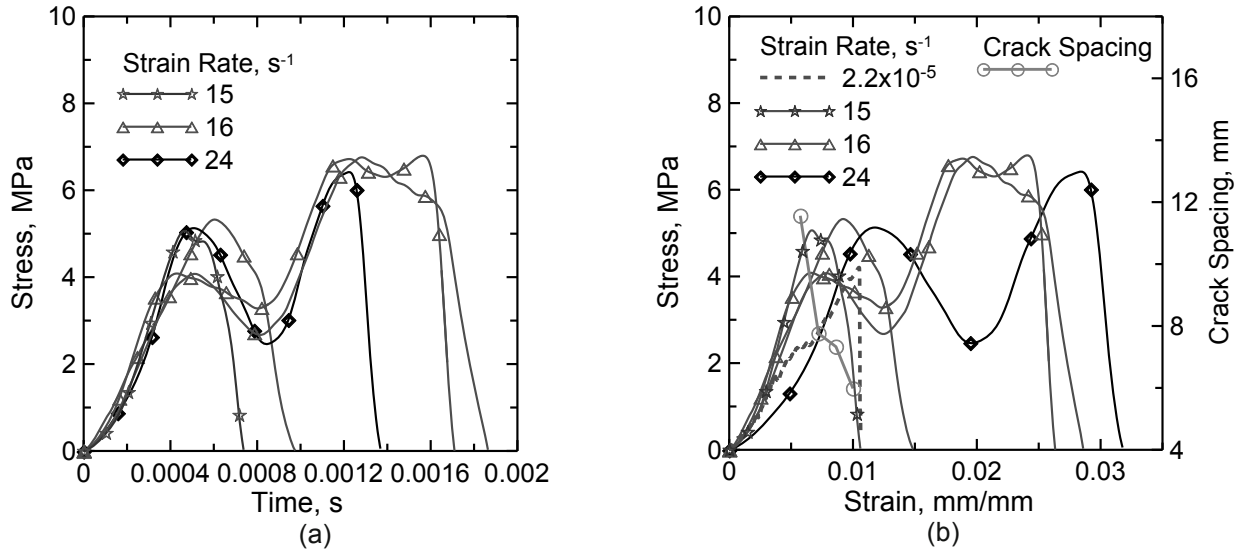


Fig. 8 Response of AR-glass fabric-cement composite: (a) stress-time, and (b) stress-strain and crack spacing

The typical stress-strain response of the composite under quasi-static loading was also plotted in Fig. 8(b). Note that the strength of the composite under dynamic loading performed about 21.3 % stronger than quasi-static condition. The maximum strain was approximately two times larger than that under quasi-static loading. On the other hand, there was a significant difference between the two loading conditions in toughness. The composite under dynamic loading exhibited significantly higher toughness, almost three times higher than that under quasi-static loading. The averaged static properties of the composites were also included in Table 1. The calculated crack spacing based on captured images at a strain rate of 15 s^{-1} (test no. 5) was correlated with the applied strains and plotted together with the stress-strain responses in Fig. 8(b). The average crack spacing value decreased from 11.56 mm to 5.98 mm when the strain increased from 0.006 to 0.01, indicating the progressive development of cracks during the loading process.

Table 1 Dynamic and static material properties of AR-glass fabric-cement composite

Loading Condition	Test No.	Strain Rate (s^{-1})	Young's Modulus (MPa)	Tensile Strength (MPa)	Toughness (MPa)	Max. Strain (mm/mm)
Dynamic	1	16	639	5.32	0.044	0.0152
	2	24	660	6.42	0.109	0.0323
	3	16	767	6.76	0.110	0.0302
	4	16	831	7.42	0.111	0.0277
	5	15	1054	5.06	0.028	0.0106
	Avg.	17	790	6.20	0.080	0.0232
	Std. Dev.	4	167	0.99	0.041	0.0098
Static	Avg.	2.2×10^{-5}	376	5.11	0.024	0.0103
	Std. Dev.	-	16.5	0.25	0.002	0.0007

5. Conclusions

In this paper, the high speed mode of the laser extensometer from Optra Inc. has been successfully used for AA6061-T6 and AR-glass fabric-cement composite at moderately high strain rates using a high speed accessory, a high speed digitizer and phase-shift technique. The following conclusions are advanced.

- 1) The proposed non-contacting strain measurement procedure using phase-shift technique is applicable to dynamic tensile testing for brittle cement-based composites and ductile AA6061-T6 material with maximum strain varying from 0.01 to 0.2.

- 2) The strain time histories of AA6061-T6 specimens at two nominal strain rates (150 and 210 s^{-1}), and AR-glass fabric-cement composite specimens at one nominal strain rate (17 s^{-1}) measured by the laser extensometer in high speed mode agree well with those measured by the actuator at the strain rates investigated.
- 3) The progressive developing of cracks during loading process indicates sufficient stress transfer at the fabric-cement interface. The AR-glass fabric-cement composite is sensitive to strain rate. The Young's modulus, tensile strength, maximum strain, and toughness under dynamic loading are higher than those under quasi-static loading.

Acknowledgements

The authors wish to thank William Emmerling, Donald Altobelli and Chip Queitzsch of the Federal Aviation Administration's Aircraft Catastrophic Failure Prevention Research Program for their support and guidance. Funding for this effort was provided by the FAA. The authors would like to thank Dr. Alva Peled for providing the AR-glass fabric-cement composites.

Reference

- [1] Nicholas T. Tensile testing of material at high rates of strain. *Experimental Mechanics*, 21(5), 177-185, 1981.
- [2] Zhu D, Gencoglu M and Mobasher B. Low velocity impact behavior of AR glass fabric reinforced cement composites in flexure. *Cement and Concrete Composites*, 31(6), 379-387, 2009.
- [3] Kenneth GH. Influence of strain rate on mechanical properties of 6061-t6 aluminum under uniaxial and biaxial states of stress. *Experimental Mechanics*, 6(4), 204-211, 1966.
- [4] Zhu D, Peled A and Mobasher B. Dynamic tensile testing of fabric-cement composites. *Construction and Building Materials*, 25(1), 385-395, 2011.
- [5] Silva FA, Zhu D, Mobasher B, Soranakom C, Toledo Filho RD. High speed tensile behavior of sisal fiber cement composites. *Materials Science & Engineering: A*, 3(15), 544-552, 2010.
- [6] Silva FA, Butler M, Mechtcherine V, Zhu D and Mobasher B. Strain rate effect on the tensile behaviour of textile-reinforced concrete under static and dynamic loading. *Materials Science and Engineering: A*, 528(3), 1727-1734, 2011.
- [7] Mechtcherine V, Silva FA, Butler M, Zhu D, Mobasher B, Gao S and Mäder E. Behaviour of strain-hardening cement-based composites under high strain rates. *Journal of Advanced Concrete Technology*, 9(1), 51-62, 2011.
- [8] Bastias PC, Kulkarni SM, Kim KY and Gargas J. Non-contacting strain measurements during tensile tests. *Experimental Mechanics*, 36(1), 78-83, 1996.
- [9] Anwender M, Zagar BG, Weiss B and Weiss H. Non-contacting strain measurements at high temperatures by the digital laser speckle technique. *Experimental mechanics*, 40(1), 98-105, 2000.
- [10] Verleysen P and Degrieck J. Optical measurement of the specimen deformation at high strain rate. *Experimental mechanics*, 44(3), 247-252, 2004.
- [11] James FB. On the direct measurement of very large strain at high strain rate. *Experimental mechanics*, 7(1), 8-14, 1967.
- [12] Aydilek AH, Guler M and Edil TB. Use of image analysis in determination of strain distribution during geosynthetic tensile testing. *Journal of Computing in Civil Engineering*, 18(1), 65-74, 2004.
- [13] Zhu D, Mobasher B and Rajan SD. Dynamic tensile testing of Kevlar 49 fabrics. *ASCE Journal of Materials in Civil Engineering*, in press ([http://dx.doi.org/10.1061/\(ASCE\)MT.1943-5533.0000156](http://dx.doi.org/10.1061/(ASCE)MT.1943-5533.0000156)), 2010.
- [14] Zhu D, Mobasher B and Rajan SD. Image Analysis of Kevlar 49 Fabric at High Strain Rate. *Society for Experimental Mechanics - 11th International Congress and Exhibition on Experimental and Applied Mechanics*, v2, p.986-991, 2008.
- [15] Laser Extensometer 3000 Operation & Maintenance Manual, OPTRA, Inc.
- [16] Zhu D, Rajan SD, Mobasher B, Peled A and Mignolet M. Modal analysis of a servo-hydraulic high speed testing machine and its application to dynamic tensile testing at an intermediate strain rate. *Experimental Mechanics*, in press (<http://dx.doi.org/10.1007/s11340-010-9443-2>), 2010.
- [17] Zhu D, Mobasher B, Silva FA and Peled A. High Speed Tensile Behavior of Fabric-Cement Composites. *Proceedings pro075: Material Science - 2nd ICTRC - Textile Reinforced Concrete*, v1, p. 205-213, 2010.
- [18] Peled A, Mobasher B. Pultruded fabric-cement composites. *ACI Materials Journal*, 102(1), 15-23, 2005.

Quantification of Micro-Crack Density for Fiber Based Composites

V. Pete Mills

Doctoral Student in Mechanical Engineering
Department of Mechanical and Aerospace Engineering
University of Alabama in Huntsville
Huntsville, AL 35899

John A. Gilbert

Professor of Mechanical Engineering
Department of Mechanical and Aerospace Engineering
University of Alabama in Huntsville
Huntsville, AL 35899

Teng K. Ooi

Adjunct Associate Professor
Department of Mechanical and Aerospace Engineering
University of Alabama in Huntsville
Huntsville, AL 35899

ABSTRACT

This paper describes a method for quantifying defects in fiber based composite materials created during the fabrication process. The defects include voids that arise during manufacturing, micro-cracks produced during cure, and delaminations which occur between lamina.

In this method, photomicrography technology is used in conjunction with computer aided design (CAD) software. The photomicrographs, stored as bitmap images, provide a visualization of the bond behavior between the fiber and the resin materials. The CAD software transforms each bitmap image into a two-dimensional work space where the areas of the defects are computed by tracing them using a closed polygon feature. Micro-crack density measurements are made by dividing the sum of the individual micro-crack areas by the total specimen area.

The approach is applied to measure the micro-crack densities in materials used for ablative nozzle applications.

INTRODUCTION

Micro-cracks may result in a composite material during fabrication. The latter may lead to material shrinkage and high residual stresses which produce defects in the material. These anomalies compromise structural integrity and affect service life. In such cases, the determination of the micro-crack density provides insight into the probability of failure. Moreover, quantitative measurements of this parameter can form a basis for making comparisons regarding the structural performance of different materials.

An example of this involves an ongoing search to find a suitable replacement for the Rayon/SC-1008 composites currently used in ablative nozzle applications. The problem is that Rayon is no longer produced locally in the United States, primarily due to environmental considerations. The material is available from suppliers located overseas but, for military purposes, there is a pressing need to eliminate foreign dependence.

In 1989, Canfield and Koenig [1] discussed the historical background and efforts spent to replace Rayon with PAN in ablative composites contained within strategic and tactical launch systems. After designers working on the Orion solid motor stage 1 nozzle tried to make this substitution by using a composite system consisting of PAN fiber cured with a phenolic resin (91LD), researchers at ATK reported that various nozzle components were susceptible to cracking which could result in a catastrophic failure of the overall system [2]. They introduced evidence to demonstrate that delaminations initiated at the surface of the PAN due to high residual stresses created by material shrinkage as volatile loss occurred. The sources of the residual stress were attributed to curing and part cool down. In addition, it was found that moisture loss over time led to shrinkage sufficient to cause delamination (crack) flaw initiation followed by continued crack propagation.

In contrast, a recent study indicated that a PAN/SC-1008 constituent/matrix could be manufactured that met or exceeded the characteristics of the Rayon-based constituent/matrix; thereby establishing a new source of composite materials for ablative nozzle fabrication and/or military applications [3]. This conclusion was reached in part by using the method of photomicrography with CAD to compare the micro-crack densities of specimens cut from Rayon/SC-1008 and PAN/SC-1008 composite plates.

This paper outlines this procedure and shows typical results found during this investigation.

PHOTOMICROGRAPHY

Methods typically used to identify micro-cracks include ultrasonic testing (UT), computer regulation thermography (CRT), and non-destructive testing methodologies such as X-ray methods. But these methods are mainly used to identify isolated cracks, making it difficult to characterize the micro-crack density. Photomicrography, on the other hand, allows an investigator to visualize and characterize the extent to which cracking occurs in a matrix.

A photomicrograph is a photograph of an object as seen through an ordinary lighted microscope with a camera that is either attached to the normal eyepiece of the microscope or, more commonly, integrated by modifying the image train of the device. Applications include visualization of opaque objects and structures, such as metals and stones that are ground smooth or etched chemically.

A LEICA MZ 16A Microscope equipped with an LEICA digital camera was used to record photomicrographs of the Rayon and PAN configurations described below. [Figure 1](#) shows a photograph of the equipment.

MICRO-CRACK DENSITY MEASUREMENT

The photomicrographs recorded during this study were captured at 20X magnification and stored in bitmap format using Microsoft Paint software. The images were transferred to the drawing screen of a CADopia software package that transformed each bitmap into a two-dimensional work space where the areas of defects were computed by tracing them using a closed polygon feature.

After closed polygons were traced around the micro-crack areas and the full microphotograph, the pertinent areas were computed. Micro-crack density measurements were made by dividing the sum of the individual micro-crack areas by the total specimen area.

Overall, this relatively simple approach provided a numerical methodology for data collection and the capability to quantify the micro-crack density of each constituent resin system so that comparisons could be made and conclusions drawn.

SPECIMEN FABRICATION

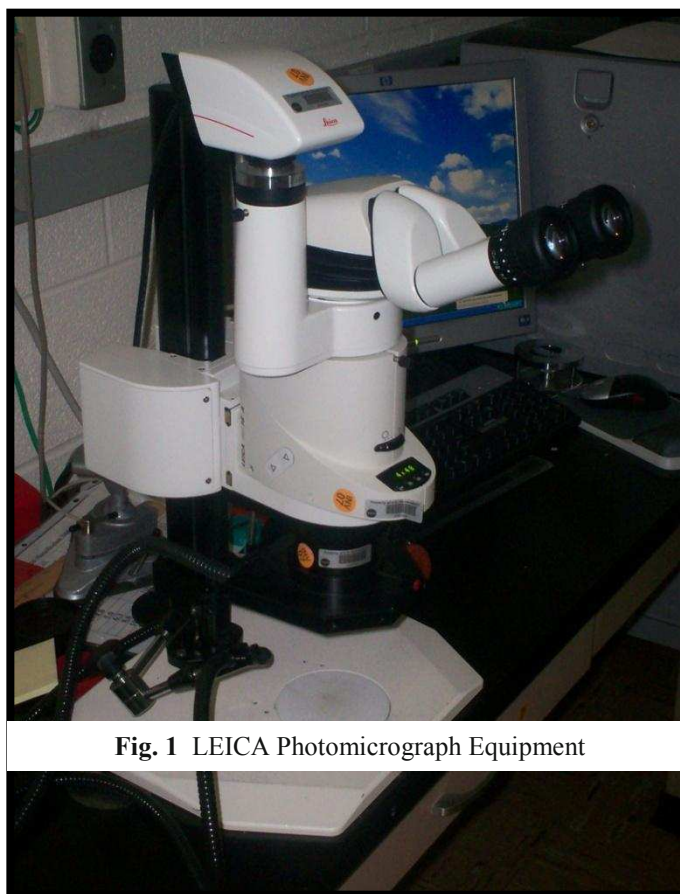


Fig. 1 LEICA Photomicrograph Equipment

Although the majority of applications associated with Rayon rely on the use of pre-impregnated materials, comparisons were made during the study at hand by using wet hand lay-ups, mainly because PAN composites were not readily available in a pre-impregnated form. The woven cloths were manufactured with fibers having the properties described in [Tables 1 and 2](#).

Table 1 Rayon Material Properties

	Carbon NARC Rayon
Carbon Assay (%)	99
Density (g/cc)	1.5
Tensile Strength (ksi)	100
Tensile Modulus (Msi)	6
Thermal Conductivity (W/m-K)	4
Coefficient of Thermal Expansion (in/in/°F)	13×10^{-6}

Table 2 PAN Material Properties

	PAN T300 Carbon Fiber
Carbon Assay (%)	92
Density (g/cc)	1.76
Tensile Strength (ksi)	530
Tensile Modulus (Msi)	33
Thermal Conductivity (W/m-K)	13
Coefficient of Thermal Expansion (in/in/°F)	-0.23×10^{-6}

Durite® SC-1008 was used to bond the layers of cloth together. It is a laminating phenolic liquid resin produced by Borden Chemicals and consists of a laminating varnish in isopropyl alcohol. Applications include the manufacturing of glass cloth laminates designed to withstand extended exposures at temperatures up to 500°F. [Table 3](#) shows its mechanical properties.

Table 3 SC-1008 Resin Material Properties

Specific Gravity	1.2759
Poisson's Ratio	0.375
Tensile Strength at Failure	8900 psi
Elongation at Failure	1.7 %
Tensile Modulus	5.7×10^5 psi
Shear Modulus	2.4×10^5 psi

Aluminum molds were assembled and prepared prior to performing the hand lay-up of the fabric. Components consisted of a base plate, four side bars, screws to secure the rectangular mold configuration, and a top plate. After the mold was cleaned with acetone, Kapton® tape was applied to prevent leakage. A mold release was sprayed onto the configuration to facilitate removal of the panels.

One panel was fabricated with the Rayon cloth and another with the PAN. The general process used to manufacture each test panel was to cut out layers of the cloth fiber, combine the layers, and apply resin to the stacked configuration in the mold. The next steps were to seal the composite with bagging material, cure it at the specified temperature and pressure, and then remove the final cured panel from the mold.

The panels themselves measured 15.2 cm (6 in.) in the warp direction and 33.0 cm (13 in.) in the fill direction and layers were stacked until the panels had a thickness of 1.9 cm (0.75 in.). Each panel was designed so that the fiber cloth comprised 60 percent of the configuration while the SC-1008 neat resin comprised 40 percent. The desired volumetric proportions were accomplished by weighing the fabric and resin.

Once the proper amount of resin was obtained, each lamina was coated and placed in the mold. This procedure was repeated until the desired thickness was met while, at the same time, ensuring that all plies were aligned in the warp direction. [Figure 2](#) illustrates the lay-up process while [Fig. 3](#) shows a fully cured test panel.

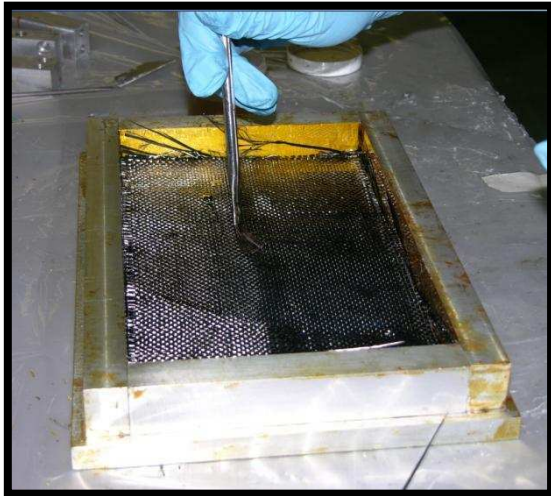


Fig. 2 Wet Hand Lay-Up Process



Fig. 3 Fully Cured Panel

Once the panels had cured, a number of 25.4 mm (1 in.) by 25.4 mm (1 in.) specimens were extracted from them by cutting parallel to the warp and fill directions. Photomicrographs were taken of both edges so that the micro-crack density could be determined.

PHOTOMICROGRAPHS

Figure 4 shows a typical photomicrograph corresponding to a cross sectional view of a cured composite panel. Salient features are identified, such as tool serrations, fiber cloth, and micro-cracks (voids).

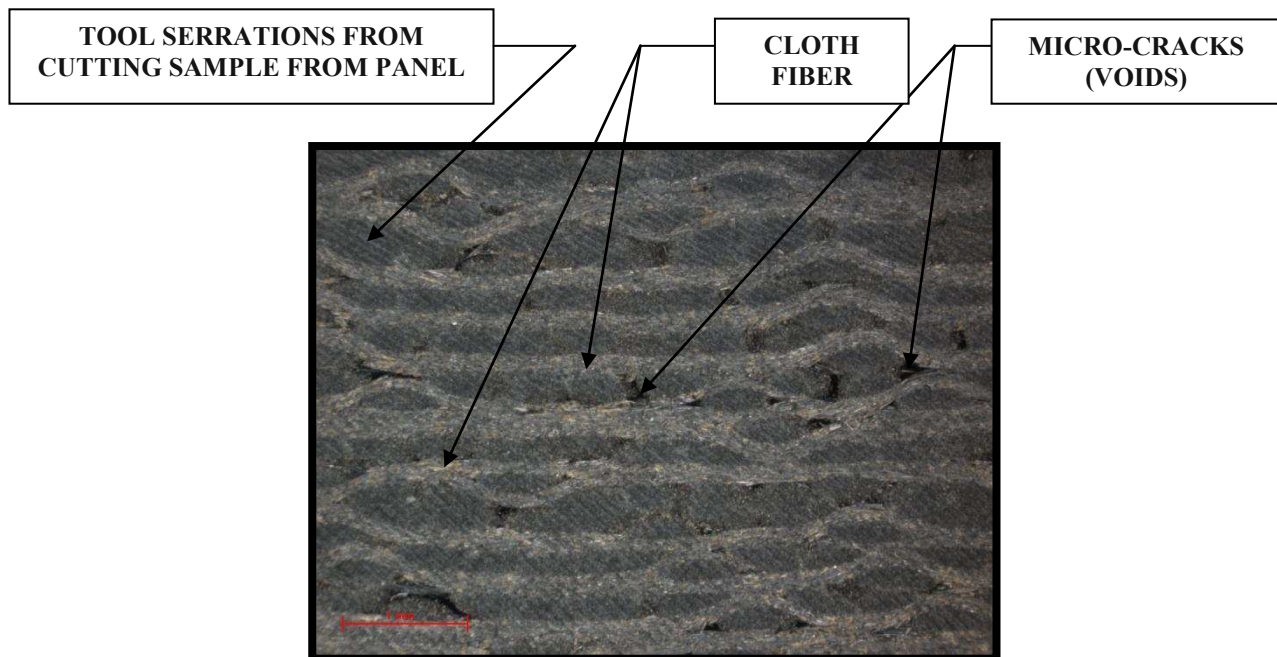


Fig. 4 Typical Cured Composite Cross Section View

Tool serrations correspond to the diagonal lines. These were produced by the tool that was used to cut the specimens from the cured composite panel. The cloth fiber corresponds to the light gray and whitish areas while micro-cracks (voids) correspond to the black (darkened) areas. In the latter, the adhesive resin did not adhere to the cloth fiber. Resin is not readily viewable because it is cohesive with the cloth fiber.

RESULTS

Figures 5-8 show typical photomicrographs recorded and processed using the CADopia software to visualize and quantify micro-cracks in the Rayon/SC-1008 and PAN/SC-1008 samples. The photographs include both fill and warp sections; red areas correspond to the defects.

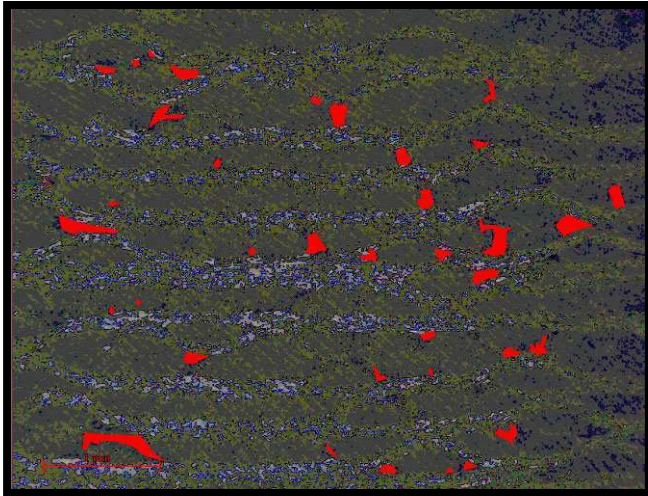


Fig. 5 Rayon/SC-1008 Fill Micro Cracks

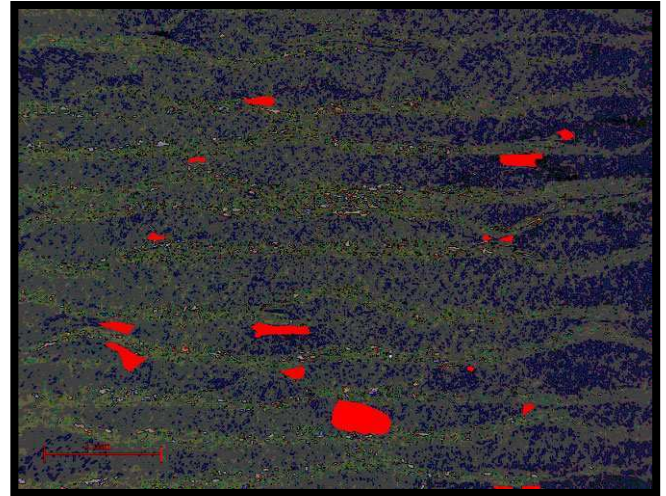


Fig. 6 Rayon/SC-1008 Warp Micro Cracks

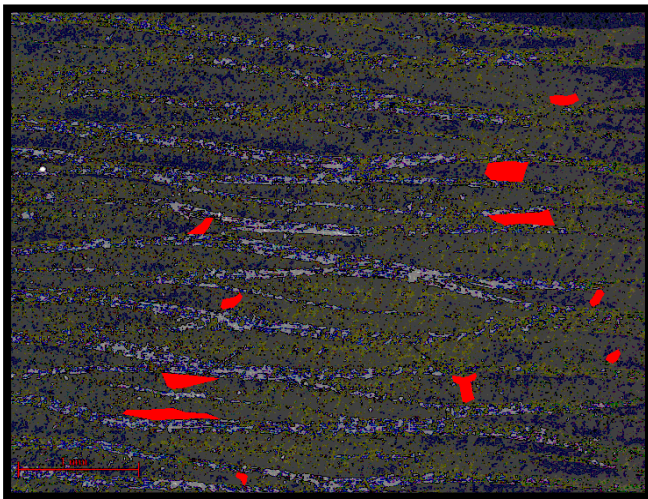


Fig. 7 PAN/SC-1008 Fill Micro Cracks

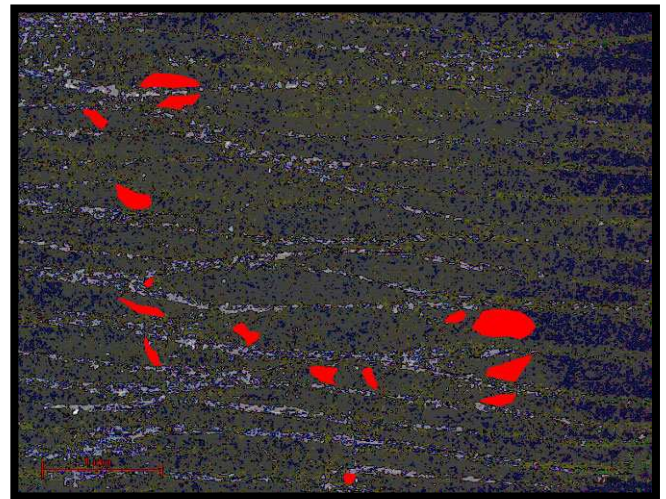


Fig. 8 PAN/SC-1008 Warp Micro Cracks

There was an average of 28 micro-cracks in the Rayon/SC1008 baseline specimens which had an average percent micro-crack density of 1.97. The PAN/SC-1008 specimens had an average of only 13 micro-cracks per specimen with a substantially lower average percent micro-crack density of 1.16. Thus, the PAN outperformed the Rayon baseline.

CONCLUSION

A method was described to measure micro-crack density in which photomicrograph technology was used in conjunction with computer aided design (CAD) software. Photomicrographs, stored as bitmap images, provided a visualization of the bond behavior between different fiber and resin materials. The CAD software allowed the areas associated with defects to be computed by tracing them using a closed polygon feature. Micro-crack density measurements were made by dividing the sum of the individual micro-crack areas by the total specimen area so that relative comparisons related to structural integrity and service life could be made.

REFERENCES

1. A. Canfield A., Koenig, J., "Development of PAN Precursor Materials for Solid Propellant Rocket Motor Nozzles," AIAA/ASME/SAE/ASEE Joint Propulsion Conference & Exhibit, Monterey, California, 10-12 July 1989.
2. "Orion Stage 1 Vectorable Nozzle Separations," ATK Technical Interchange Meeting, 12 September 2005.
3. Mills, V.P., "Variable Viable Rayon Composite Replacement: Micro-cracking in Polyacrylonitrile-Based Carbon-Phenolic Composites," Ph.D. Dissertation, University of Alabama in Huntsville, Huntsville, Alabama, 2008.

Dynamic shear response of a polymer bonded explosive using a modified Hopkinson bar apparatus

P.D. Zhao¹, F.Y. Lu^{1}, Y.L. Lin¹, R. Chen¹, L. Lu²*

1. College of Science, National Univ. of Defense Technology, 410073 Changsha, China

2. College of electronic science and engineering, National Univ. of Defense Technology, 410073 Changsha, China

Abstract: An innovative Hopkinson pressure bar system for testing the shear response of materials at high strain rates has been developed. A novel single-lap specimen of a polymer bonded explosive (PBX) is used. Instead of strain gauges mounted on the bars, one quartz force transducer is sandwiched between the clamp and the transmission bar to directly measure the weakly loading forces. A laser gap gauge is employed to monitor the shear strain of the specimen, which is based on the luminous flux method. Finite element code ANSYS is used to analyze the stress state in the specimen. Experimental results show that this new method is effective and reliable for determining the shear stress-strain responses of the soft materials at high strain rates.

INTRODUCTION

Safety assessments of energetic materials for accidental impacts have received considerable attention in recent years. Damage caused by the dynamic loading increases the sensitivity of energetic materials and plays an important role in the initiation and the violence of reaction during the low level mechanical threats. For the polymer bonded explosive (PBX), the compression strength is much larger than the tension and shear strength[1, 2]. It implies that most of damages of PBX in practice application are incurred by the tension stress and shear stress. A number of previous authors have reported the dynamic compression behaviors of polymer bonded explosives[3-5]. Some researchers also applied the dynamic Brazilian testing to investigating the tension responses of polymer bonded explosives[6]. The experiments focused on studying the dynamic shear properties of PBX, however, are few relatively.

Even though quasi-static loading the design of a specimen which achieves a uniform shear stress on the test effective area is not easy. An additional difficulty under dynamic loading is the requirement that force equilibrium should be satisfied within very short time range. It's the obstacle that prevents some standard quasi-static test from being transformed into the dynamic shear test. The split Hopkinson pressure bar technique (SHPB)[7-9] is widely used for determining the mechanical properties of materials under high strain-rate loading ($10^2 \sim 10^4 \text{ s}^{-1}$). Various designs of specimens[10-12] have been used to test the interlaminar shear strength or failure strength of composite materials with SHPB. Hallett et al[13] pointed out that in all these designs of specimens, the single-lap design easily achieves uniform shear stress with the very low normal (peeling) stress.

Conventional SHPB analysis employs strain gauges mounted on the incident bar and transmitted bar to measure the stress wave profiles. In the dynamic tests of low strength materials, the transmitted signal is too small to be measured with the strain gauge because of the enormous mechanical impedance difference (the product of the acoustic impedance and cross-sectional area) between that of the bar and the specimen. This will lead to inaccuracy of the specimen stress history. In dynamic single-lap shear experiments [13], a strain gauge rosette was mounted on the specimen to measure the shear strain of the specimen. For the small specimen, the size of strain gauge should be smaller than that of the gauge section. It will increase the difficult of the experimental operation. Meanwhile, the shear strain is blank after the strain gauge failure, which is useful for getting more details of the shear stress-stain relationship. And for low shear strength materials such as PBX, this work focused on, the influences of the bond on the test results should be considered discreetly.

In this work, we modified a SHPB system to investigate the shear response of a PBX at high strain rates. An optimized single-lap design of specimen is employed. The traditional strain gauges are no longer used in our modified system. We use one quartz transducer that is sandwiched between the transmission bar and the clamp to directly measure the dynamic loading forces[14]. A laser gap gauge is employed to monitor the strain of the specimen. As there is no strain gauge used in the experiment, we could ignore the wave dispersion in the bar.

EXPERIMENT

Specimen and testing apparatus

The schematic of the specimen design is shown in Fig. 1(a). Fig. 2(b) shows a photograph of an actual specimen. Specimens were made by molding, with mass density of 1.7g/cm^3 . The thickness of the specimen is 10mm. For eliminating the stress concentrations, we using the large radius of the corner in notch region. It's also convenient to removing mold without the sharp edge of the specimen. The length of effective test region should be less than that of the lap, as shown in Fig.1. Otherwise, the strain in the lap would exceed the elastic limitation with localized damage before the specimen appearing shear failure.

The apparent feature of the specimen is that the corners in notch region are not thoroughly symmetrical. The effect of the special notch position is a compressive stress in the shear region, which can compensate for the tensile stress caused by elastic deformation of the specimen adjacent to the shear region. In fact, if the notches are placed symmetrically, the stress state in the shear region is a combination of shear and tension.

We modified a 20 mm diameter SHPB system to investigate the shear response of a PBX under high strain rates (Fig.2). Two clamps were design to load the specimen, which were respectively agglutinated on the ends of the incident and transmission bars. The bars are made with 7075 aluminum. The incident (input) bar is 1800 mm long and the transmitted (output) bar is 1200 mm long. The slope of the incident pulse is small enough to ensure the specimen achieving force equilibrium before shear failure occurring. The schematic diagram of the modified Hopkinson bar system is shown in Fig. 2.

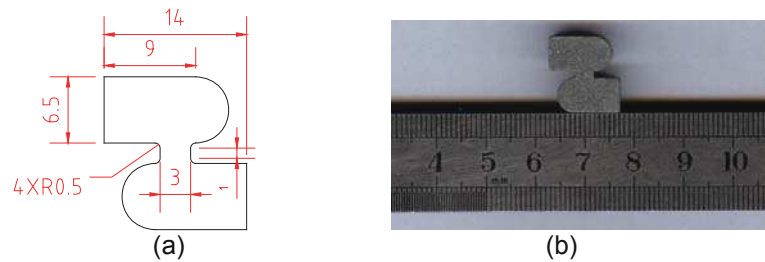


Fig.1 (a) Schematic of the specimen; (b) photograph of the specimen used in this study

Measurement techniques

The method of measuring the shear strain of the specimen with strain gauge[13], isn't suitable for this work. A laser gap gauge (LGG) is employed to monitor the strain of the specimen. The LGG system consists of a diode line laser, a laser holder, a collecting lens and a light detector. The schematic

The laser operates at 670 nm with a 5 mW output power. It has a large field depth and minimal variations in thickness across the line length. The line is $30\text{ }\mu\text{m}$ thick at 185 mm away, and the divergence angle is 5° . The light detection part consists of a collecting lens and a photodiode light detector. The collecting lens focuses the incoming laser light into the photodiode detector, which is placed near its focus. A narrow-band-pass filter centered at 670 nm is placed in front of the detector window. The photodiode detector output is pre-amplified, and the optoelectronics and the preamplifier together have a bandwidth of 1.5 MHz. The output voltage of the detector is proportional to the total amount of laser light collected. The whole system has a noise level less than 0.4 mV.

We use a set of high precision gauges to partly block the probe laser to calibrate the LGG. The blocking width ranges from 0 to 10 mm at a step of 0.01 mm. Because of the high uniformity of the laser sheet, the light-blocking width Δd is linear with the amount of output voltage ΔU :

$$\Delta d = k\Delta U \quad (1)$$

where $k=4.08$ mm/V is the calibration parameter of the LGG system. Denote the standard deviation as σ , and the uncertainty of the system follows from equation (2) as:

$$\sigma_{\Delta d} / \Delta d \approx \sqrt{(\sigma_k / k)^2 + (\sigma_{\Delta U} / \Delta U)^2} \quad (2)$$

Here $\sigma_k=0.03$ mm/V, and $\sigma_{\Delta U}=0.4$ mV. As an example, for $\Delta U = 0.25$ V, $\Delta d = 1.02$ mm and the uncertainty is about 0.01mm. Thus the relative error of the displacement measurement is around 0.8 %.

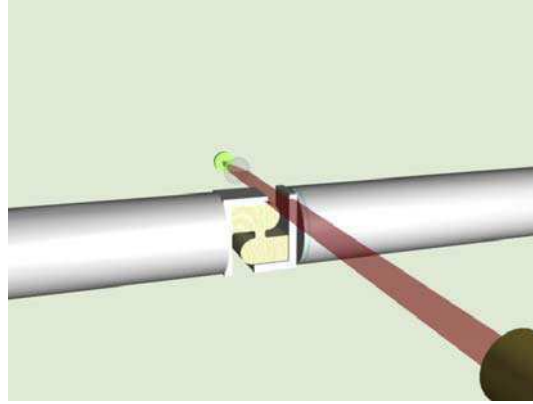


Fig.2 Schematic diagram of the modified Hopkinson bar system

The X-cut quartz is widely used in SHPB experiments[14, 15], which is much more sensitive in detecting forces in its X -direction than the indirect surface strain gage method. The acoustic impedance of the self-generating quartz transducer is also very close to the mechanical impedance of the aluminum bar, which ensures that introduction of the quartz disks do not affect the one-dimensional wave propagation in the bar. We use a quartz force transducer which is sandwiched between the clamp and the transmission bar to directly measure the dynamic loading forces.

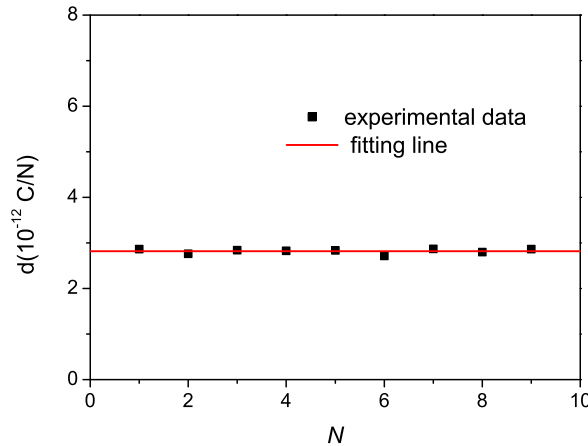


Fig.3 Calibration results of the piezoelectric constant

In our work, a 2 mm thick shim of the same diameter of the quartz crystal is used as the positive pole between quartz crystal and the clamp. We made use of the traditional SHPB apparatus with strain gauge to calibrate the quartz transducer. As result of the calibration experiment, the piezoelectric constant is $2.82 \times 10^{-12} \pm 0.05$ C/N, shown in Fig. 3.

Stress state analysis

The numerical analysis is carried out using the commercial finite element code ANSYS (Release 10.0, Ansys Inc.). The geometry model of the specimen is the same as the actual one. A total of 323528 elements of SOLID185 are used to mesh the specimen. The specimen material is assumed to be elastic. The density of the specimen is respectively 1.7g/cm^3 ; the Young's modulus is 1GPa for the specimen; The Poisson's ratio is 0.33. A key assumption that the mechanical property of the material is strain-rate independent is made for simplifying the question. Both sides of the specimen are constrained with no transverse displacements. It is to simulate the clamp-effect.

Fig. 4 shows the contour maps of the specimen. The stress state in the specimen is complex as expected. The shear stress in the gauge section, however, is rather uniform as shown in Fig. 4(a). The peeling stress is also relative uniform in Fig. 4(b). It indicates that the gauge section of specimen is dominated by the shear loading, meanwhile, with the low peeling stress (less than 10 percent of the shear stress in the gauge section). Fig. 5 is the comparison of the stress state in the section gauge and the computed shear stress. The curved surface is the shear stress in the gauge section. The X-axis and Y-axis respectively correspond to the transverse and vertical orientations of the specimen. The plane face is the calculated average shear stress (ratio of the loading force to the area of shear section) in Fig. 5. One can observe that the main part of the curved surface is flat, and it is close to the plane. It indicates that the calculated shear stress can approximate the shear stress in the gauge section well.

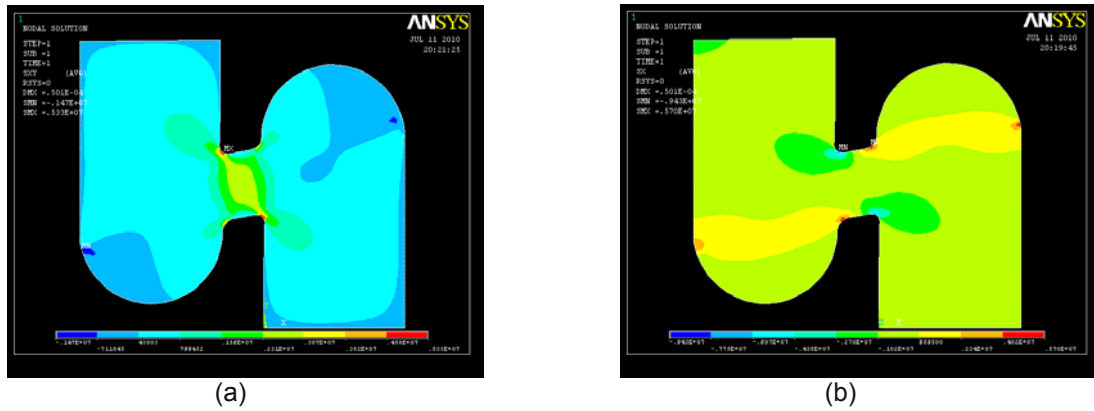


Fig.4 Contour map of the specimen: (a) shear stress; (b) peeling stress

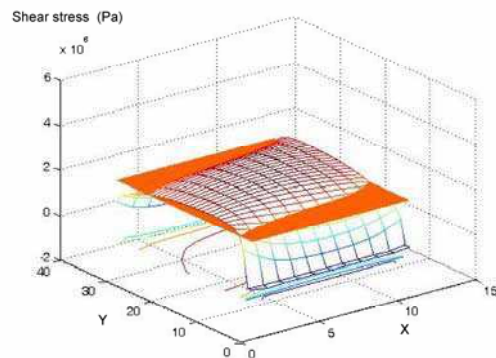


Fig.5 Comparison of the shear stress in the specimen and the computed one

RESULTS AND DISCUSSION

The photo of the retrieved specimen is shown in Fig. 6. The failure of the specimen occurs at the gauge section as expected. Typical compression stress-strain curves obtained at high strain rates are shown in Fig. 7. Average pressure strain rates at three main levels are 300, 400 and 500s^{-1} . From the Fig. 7, we know that the PBX specimens are not very sensitive to shear

strain rates. At shear strain rates 300s^{-1} , the peak compression stress is about 1.45MPa . And the average failure stress is about 1.4MPa at the shear strain rates 500s^{-1} . The rate hardening effect is not obvious.

The shapes of shear strain-stress curves are not identical with each other. At strain rates 300 and 370 s^{-1} , the curves drop sharply, after reaching the peaks. However, the curves decrease slowly with a flat after reaching the peaks at higher strain rates. It may be relate with the friction effect in the shear failure surface. When the loading is low, the friction in the specimen is not obvious. The instability of the specimen is sudden. With the loading increasing, the friction effect is prominent, which prevents the specimen losing stability. Thus the strain increases and the stress decreases a few.

Fig.8 shows the changing of the failure stress and strain with the shear strain rates. The failure stress varies little as shown in Fig. 8(a), and the average failure stress is about 1.39MPa . The failure strain rises with the strain rate increasing. It indicates that the rate hardening effect affect parameters differently. Compared with the failure stress, the failure strain is sensitive to the strain rates. The strain rate increase from 300s^{-1} to 500s^{-1} , and the failure strain rises from 0.82 to 0.11 .



Fig.6 Typical retrieved specimen

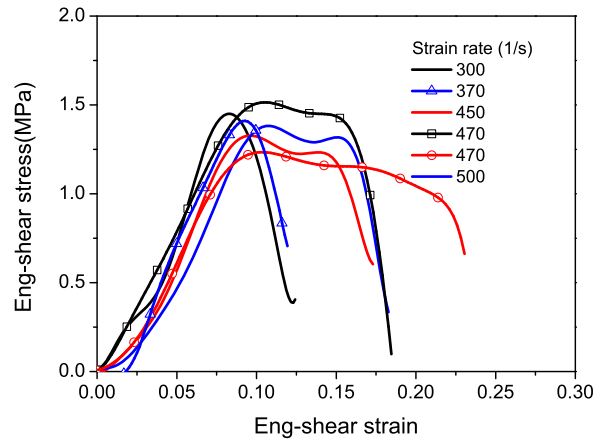


Fig.7 Typical Stress-strain curves

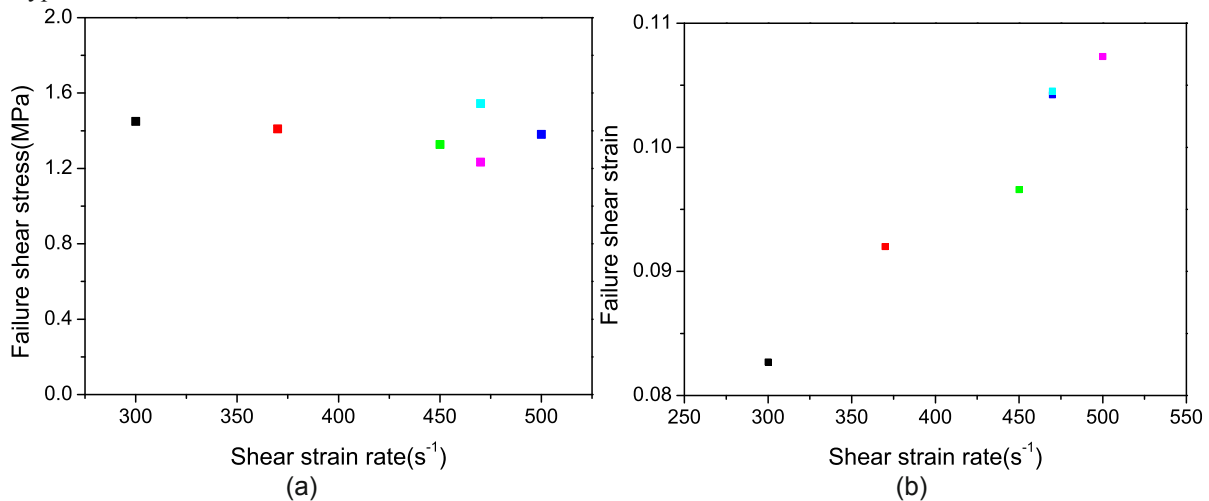


Fig. 8 (a) Results of the failure strain with strain rate; (b) Results of the failure stress with strain rate

CONCLUSION

We propose a modified SHPB apparatus to measure the responses of the PBX under shear loading at high strain rates. In this method, Instead of strain gages mounted on the bars, one quartz force transducers is sandwiched between the clamp and the transmission bar to directly measure the weakly loading forces. A laser gap gauge is employed to monitor the shear strain of the specimen. The experimental results show that the failure strain is sensitive to the strain rate, but the failure stress is independent on the strain rate. This technique is readily implementable and can be applied to investigating the dynamic shear behaviour of the soft materials.

ACKNOWLEDGMENTS

This work was supported by the Natural Science Foundation of China (NSFC) through Grant No. 10672177 & 10872215 and 10902100. And we would like to acknowledge the support of National Key Laboratory Foundation under grant NO.9140C670902090 and Science Foundation of CAEP under grant NO.2009A0201008.

REFERENCES

- [1] Wiegand D.A. and Reddingius B., "Mechanical properties of plastic bonded composites as a function of hydrostatic pressure", *Shock Compression of Condensed Matter*. 812-815 (2003).
- [2] Balzer J.E., Siviour C.R., Walley S.M., et al., "Behaviour of ammonium perchlorate-based propellants and a polymer-bonded explosive under impact loading", *Proceedings of the Royal Society of London Series a-Mathematical Physical and Engineering Sciences*. 460(2043): 781-806 (2004).
- [3] Blumenthal W.R., Gray G.T., Idar D.J., et al., "Influence of temperature and strain rate on the mechanical behavior of PBX 9502 and Kel-F 800 (TM)", *Shock Compression of Condensed Matter-1999*, Pts 1 and 2. 505: 671-674 (2000).
- [4] Bonthoux F. and Girodon A., "Adaptation of a Hopkinson-Kolsky Apparatus in the Study of Mechanical-Behavior of Explosive Materials Based on Temperature", *Journal De Physique*. 46(Nc-5): 639-644 (1985).
- [5] Cady C.M., Blumenthal W.R., Gray G.T., et al., "Mechanical properties of plastic-bonded explosive binder materials as a function of strain-rate and temperature", *Polymer Engineering and Science*. 46(6): 812-819 (2006).
- [6] Grantham S.G., Siviour C.R., Proud W.G., et al., "High-strain rate Brazilian testing of an explosive simulant using speckle metrology", *Measurement Science & Technology*. 15(9): 1867-1870 (2004).
- [7] Song B. and Chen W., "Dynamic stress equilibration in split Hopkinson pressure bar tests on soft materials", *Experimental Mechanics*. 44(3): 300-312 (2004).
- [8] Song B., Chen W., Antoun B.R., et al., "Determination of early flow stress for ductile specimens at high strain rates by using a SHPB", *Experimental Mechanics*. 47: 671-679 (2007).
- [9] Zhao H., Gary G., and Klepaczko J.R., "On the use of a viscoelastic split Hopkinson pressure bar", *International Journal of Impact Engineering*. 19(4): 319-330 (1997).
- [10] Werner S.M. and Dharan C.K.H., "The dynamic response of graphite fibre-epoxy laminate at high shear strain rate.", *J Composite Mater*. 20: 365-374 (1986).
- [11] Bouette B., Cazeneuve C., and Oytana C., "Effect of strain rate on interlaminar shear properties of carbon/epoxy composites", *Composite Science and Technology*. 45: 313-321 (1992).
- [12] Dong L. and Harding J., "A single-lap shear specimen for determining the effect of strain rate on the interlaminar shear strength of carbon-fibre reinforced laminates", *composites*. 25: 129-138 (1994).
- [13] Hallett S.R., Ruiz C., and Harding J., "The effect of strain rate on the interlaminar shear strength of a carbon/epoxy cross-ply laminate : comparison between experiment and numerical prediction", *Composite Science and Technology*. 59: 749 (1999).
- [14] Chen W., Lu F., and Zhou B., "A quartz-crystal-embedded split Hopkinson pressure bar for soft materials", *Experimental Mechanics*. 40(1): 1-6 (2000).
- [15] Song B., Ge Y., Chen W., et al., "Radial inertia effects in kolsky bar testing of extra-soft specimens", *Experimental Mechanics*. 47: 659-670 (2007).

Shock testing accelerometers with a Hopkinson pressure bar

John T. Foster
Sandia National Laboratories
Terminal Ballistics Technology Dept.
PO Box 5800, MS 1160
Albuquerque, NM 87185
jtfoste@sandia.gov

Danny J. Frew
Dynamic Systems and Research

Micheal J. Forrestal
Consultant

Erik E. Nishida
Terminal Ballistics Technology Dept.
Sandia National Laboratories

W. Chen
Purdue University
School of Aeronautics and Astronautics

ABSTRACT

The electronic industry continues to dramatically reduce the size of electrical components. Many of these components are now small enough to allow shock testing with Hopkinson pressure bar techniques. However, conventional Hopkinson bar techniques must be modified to provide a broad array of shock pulse amplitudes and durations. For this study, we evaluate the shock response of accelerometers that measure large amplitude pulses, such as those experienced in projectile perforation and penetration tests. In particular, we modified the conventional Hopkinson bar apparatus to produce relatively long duration pulses. The modified apparatus consists of a steel striker bar, annealed copper pulse shapers, an aluminum incident bar, and a tungsten disk with mounted accelerometers. With these modifications, we obtained acceleration pulses that reached amplitudes of 10 kG and durations of 0.5 ms. To evaluate the performance of the accelerometers, acceleration-time responses are compared with models that use independent stress and strain measurements. Comparisons of data from all three measurements are in good agreement.

1 Introduction

A major goal for our penetration technology program is to obtain a fundamental understanding of the penetration process for concrete targets. For many applications [1, 2], the projectile nose does not erode and the projectile has relatively small deformations. In those cases, rigid-body deceleration data from data recorders mounted within the projectile provide a close measure of net force on the projectile nose. Because tests with projectiles that are large enough to contain an acceleration data recorder are expensive, it seems prudent to conduct inexpensive performance evaluation experiments on the accelerometers prior to penetration tests. As pointed by Togami et al. [3], there are no standard calibration methods for high-G accelerometers, so performance evaluation prior to penetration tests adds to the confidence of the penetration data.

In a previous study [4], we presented a Hopkinson bar technique to examine the performance of accelerometers and reported durations to about 0.1 ms. In this study, we make modifications to the apparatus in [4] and report durations to about 0.5 ms. In particular, we use a longer steel striker bar and two annealed copper pulse shapers. Experimental details are explained in the next section. Next, we present models of the acceleration response of the tungsten disk and mounted accelerometers. We conclude with a comparison of the measured acceleration and models that predict acceleration from independent stress and strain measurements. Comparisons of data from all three measurements show good agreement.

2 Experimental apparatus and procedure

Figures 1 and 2 show the modified Hopkinson bar apparatus. A maraging steel (C350) striker bar impacts the double,

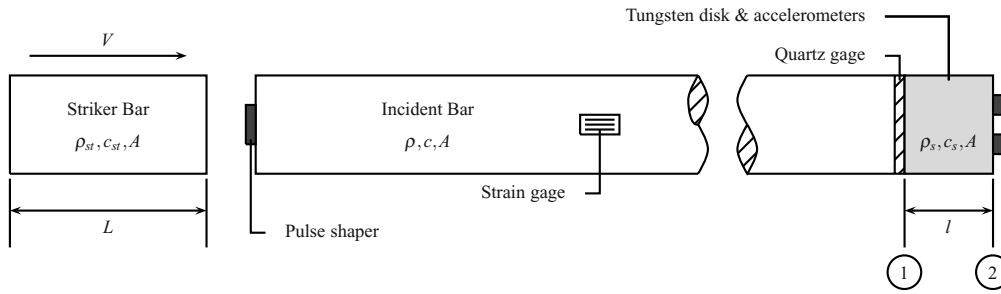


Fig. 1 Schematic of modified Hopkinson apparatus.

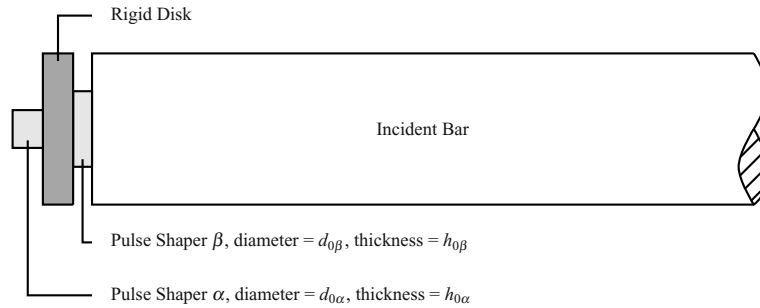


Fig. 2 Schematic of pulse shaper design.

annealed copper (C11000) pulse shaper that is attached to the 7075-T651 aluminum incident bar. The pulse shaper produces a nondispersive, compressive stress wave that propagates in the aluminum incident bar and eventually interacts with the tungsten disk at the end of the bar. Strain gages are attached to the incident bar, a quartz stress gage is placed between the end of the incident bar and the disk, and two accelerometers from different suppliers are mounted to the end of the disk. In a previous study [4], we reported acceleration-time durations of about 0.1 ms. To achieve durations of about 0.5 ms, we use a longer ($L = 0.914$ m) steel striker bars and the double pulse shaper [5, 6] shown in Fig. 2. The disk is attached to the incident bar with a plastic shrink tube that allows the disk to separate from the incident bar when the interface stress becomes tensile. Thus, we achieve a single pulse loading.

We now have several analytical models that help us design our experiments without many unnecessary experimental trials. In [5, 6], we presented models that predict incident stress pulses for single and double pulse shapers. We show in a subsequent

section that predictions and measured incident strain pulses are in good agreement. Next we performed a stress wave analysis in the tungsten disk [4] and show that rise time of the incident stress pulse is long enough and the tungsten disk length is short enough that the disk response can accurately be approximated as rigid-body motion. Since we measure stress at the aluminum bar-tungsten disk interface with the quartz gage, we can calculate rigid-body acceleration of the tungsten disk from Newton's Second Law and the stress gage data. Thus, we have a direct comparison with the measured acceleration-time pulse. In addition, we use the measured incident strain pulse as input to a model [4] that calculates rigid-body acceleration of the disk. These models and measurements are used to evaluate the performance of the accelerometers.

The experimentally verified model for the rigid-body acceleration of the disk shows that the shape of the acceleration-time pulses are dominated by the slopes of the incident stress wave. Thus, shaping the incident stress with the pulse shaper shown in Fig. 2 is a critical item for this modified Hopkinson bar technique. We use the high impedance tungsten disk, so that the incident bar-disk interface remains in compression with multiple wave transits in the disk.

3 Tungsten disk response

Figure 1 shows the tungsten disk in contact with the aluminum incident bar. We use pulse shaping techniques [5, 6] to propagate nondispersive stress waves in the aluminum incident bar that eventually interact with the disk. The disk has a larger impedance than the incident bar so that stresses at the bar-disk interface remain in compressive for multiple wave transits in the disk. In [3], we performed a stress-wave, interaction analysis on the incident bar and disk and present equations for the particle velocities v_1 , v_2 at stations 1 and 2 shown in Fig. 1. When v_1 and v_2 were nearly equal, we concluded that the disk could be modeled accurately as a rigid body. During this study, we recognized that we could easily obtain particle accelerations at stations 1 and 2 in Fig. 1. The only time-dependent term in the equations for v_1 and v_2 in [3] is the incident stress $\sigma_i(t)$. Then to obtain a_1 and a_2 , we simply replace $\sigma_i(t)$ with $d\sigma_i(t)/dt$.

In addition to the stress wave analysis, we present an equation of motion that assumes the disk is a rigid body. From [3], the rigid body motion, $y(t)$, of the mass m is governed by

$$\frac{d^2y}{dt^2} + \lambda \frac{dy}{dt} = \frac{2A}{m} \sigma_i \quad (1a)$$

$$\lambda = \frac{A\rho c}{m}, \quad \sigma_i = E\epsilon_i \quad (1b)$$

where σ_i is the incident stress pulse. For a ramp incident pulse

$$\sigma_i = E = \gamma_1 t, \quad (2)$$

and

$$a(t) = \frac{d^2y}{dt^2} = \frac{2\gamma_1}{\rho c} [1 - e^{-\lambda t}]. \quad (3)$$

For a parabolic incident pulse

$$\sigma_i = \gamma_1 t + \gamma_2 t^2, \quad (4)$$

and

$$a(t) = \left(\frac{2\gamma_1}{\rho c} - \frac{4\gamma_2}{\lambda \rho c} \right) [1 - e^{-\lambda t}] + \frac{4\gamma_2}{\rho c} t. \quad (5)$$

For more terms in the expression for σ_i , we use the polynomial expression

$$\sigma_i = \gamma_1 t + \gamma_2 t^2 + \dots + \gamma_N t^N. \quad (6)$$

The acceleration of the rigid mass for Eq. (6) is

$$\begin{aligned} a(t) = & \sum_{n=1}^N \left[(-1)^{n-1} \frac{2n! \gamma_n}{\rho c \lambda^{n-1}} (1 - e^{-\lambda t}) \right] \\ & + \sum_{m=1}^N \sum_{n=1}^{m-1} \left[(-1)^{n+m-1} \frac{2m! \gamma_m}{n! \rho c \lambda^{m-n-1}} t^n \right]. \end{aligned} \quad (7)$$

In the next section, we show that a_1 and a_2 from the wave equations bracket and closely approximate $a(t)$ from the rigid-body analysis. Thus, we can calculate the rigid-body disk acceleration, $a(t)$, from Newton's Second Law and data from the stress gage. Thus,

$$a(t) = \frac{\sigma(t)A}{m} \quad (8)$$

where $\sigma(t)$ is the stress gage time history, A is the cross-sectional area of the incident bar and disk, and m is the mass of the disk and mounted accelerometers. Therefore, acceleration calculated with the stress gage data can be compared with measurements from the accelerometers.

In [3], we also derive an equation that predicts the rigid-body acceleration of the disk in terms of the measured incident stress. From [3],

$$a(t) = \frac{d^2y}{dt^2} = \frac{2A}{m} \left[\sigma_i(t) - \lambda \exp(-\lambda t) \int_0^t \sigma_i(\tau) \exp(\lambda \tau) d\tau \right] \quad (9)$$

In summary, we first show that for our design parameters the disk motions can be closely approximated as rigid-body motion. Then, we compare the acceleration-time measurements with models that use independent stress and strain measurements. We show in the next section that data from all three measurements are in good agreement.

4 Results

Pulse shaping techniques were used to achieve two distinct load levels called Load Level 1 and Load Level 2 throughout this section. A pulse shaping design code was used to accurately predict the materials and geometries of the pulse shapers required to achieve these loads, thus eliminating many experimental trials. Figures 3 and 4 show comparisons of the predicted incident stress pulses to representative incident stresses measured in the experiments. Note that the unloading portion of the incident

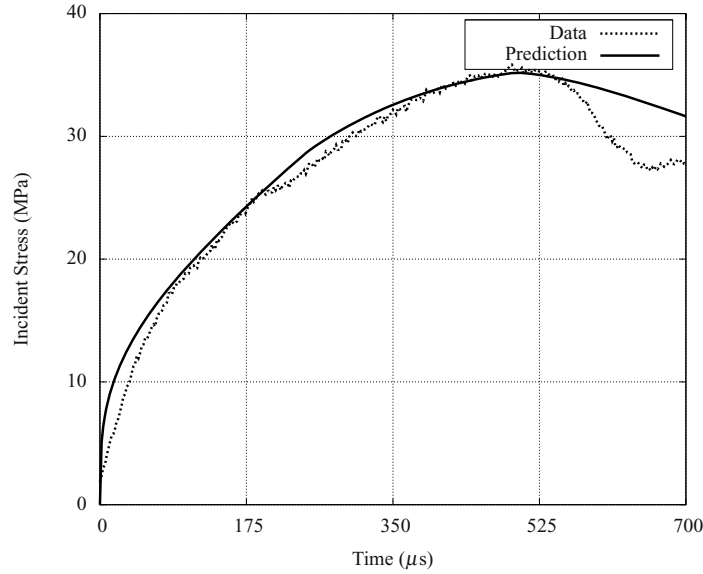


Fig. 3 Comparison of pulse shaper design code prediction to experimental incident pulse for Load Level 1

stresses are not well predicted by the pulse shaper design code because the pulse shapers are modeled via their plastic responses in the code whereas they will unload elastically after plastic deformation in the experiment. This is understood and acceptable because the portion of the incident stress of interest here is the loading portion. From the analysis in the previous section it is observed that the acceleration of the tungsten disk is dominated by the slope of incident stress upon loading.

To demonstrate the accuracy of our analysis in the previous section we will compare model predictions to data collected from quartz gages in the experiments at Load Levels 1 and 2. At Load Level 1, we approximate the incident stress by two curves. First, we approximate the incident stress as a 2-term polynomial as in Eq. (4), we also approximate it as a 12-term polynomial as in Eq. (6). Least squares curve fits were done in each case to determine the γ_n 's. We use the γ_n fit parameters in Eq. (7) along with the material properties to predict the acceleration of the tungsten disk. For a 19.05 mm diameter, 7075-T6 aluminum incident bar we used $\rho = 2710 \text{ kg m}^{-3}$ and $c = 5040 \text{ m s}^{-1}$. The total mass, m , of the tungsten disk and two

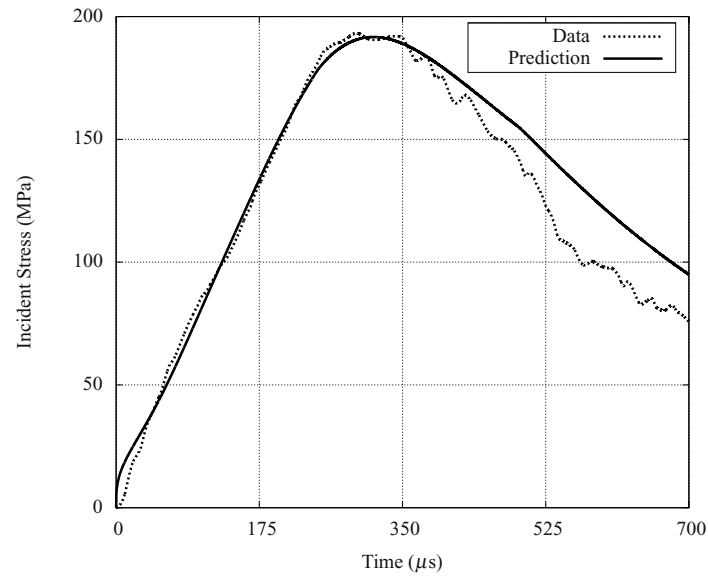


Fig. 4 Comparison of pulse shaper design code prediction to experimental incident pulse for Load Level 2

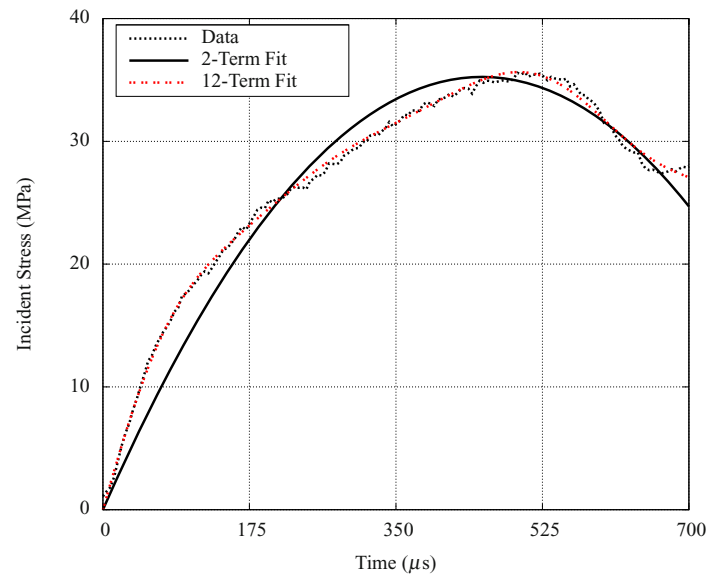


Fig. 5 Comparison of experimental incident pulse with 2-term and 12-term least square fits of data for Load Level 1

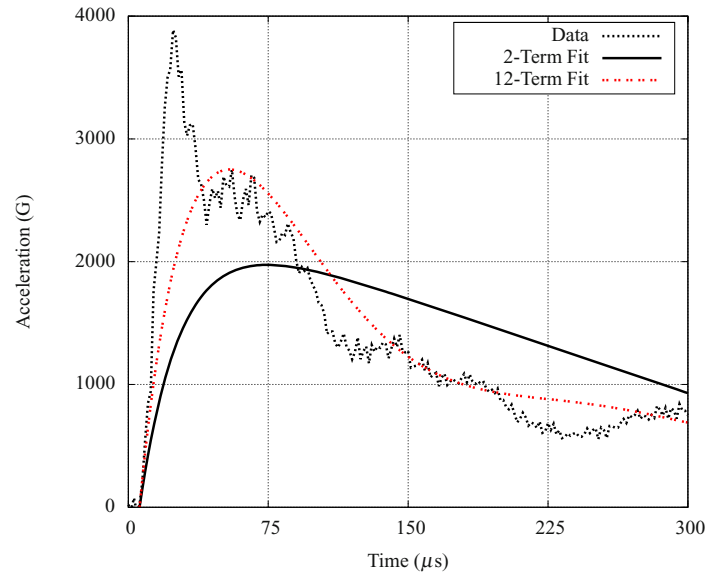


Fig. 6 Comparison of quartz crystal acceleration with 2-term and 12-term incident pulse fit model predictions for Load Level 1

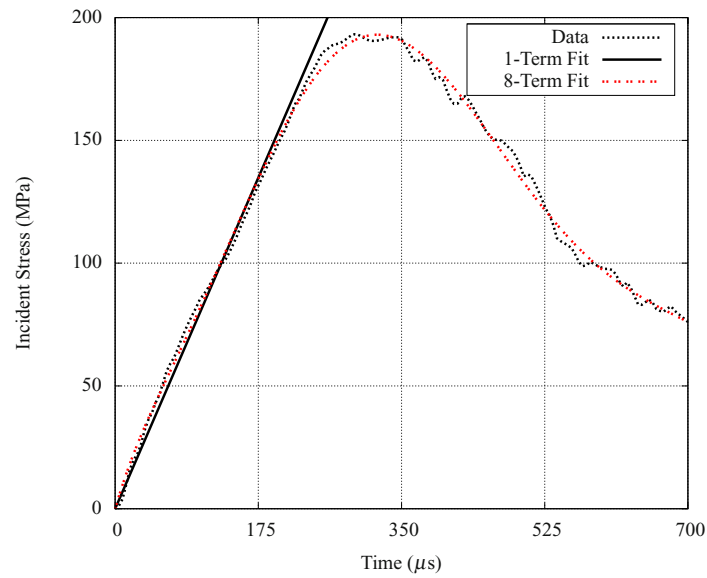


Fig. 7 Comparison of experimental incident pulse with 1-term and 8-term least square fits of data for Load Level 2

accelerometers was 92.88g. The curve fits of the incident pulse and the model predictions are shown in Figs. 5 and 6. The many subtle slope changes on the loading portion of the incident stress shown in Fig. 5 are not captured very well by a simple 2-term polynomial fit, hence the inaccuracy of the model prediction for the 2-term fit shown in Fig. 6. The 12-term fit does a much better job predicting the acceleration recorded at the quartz gage. The quartz gage actually records an integral stress traveling through the bar, therefore, the acceleration value shown in Fig. 6 is evaluated from Equation 9.

At Load Level 2, we approximate the incident stress by two curves as well. This time the incident stress rate is near linear during the loading portion of the curve, therefore, a 1-term or linear curve fit actually represents the data quite well. We also fit the incident stress with an 8-term polynomial which represents the unloading portion of the experimental stress pulse as well. The same procedure previously employed was used to make the model predictions at Load Level 2. The results are shown in Figs. 7 and 8.

Load Level 2 was a much higher loading rate as compared to Load Level 1, notice that the model fit curves had to be advanced in time in order for them to match the experimental data. When this is done, both the 1-term and the 8-term fits

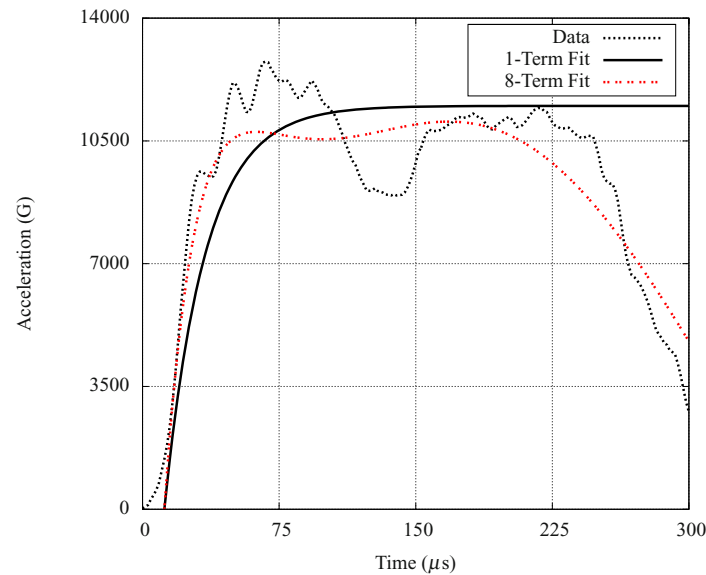


Fig. 8 Comparison of quartz crystal acceleration with 1-term and 8-term incident pulse fit model predictions for Load Level 2

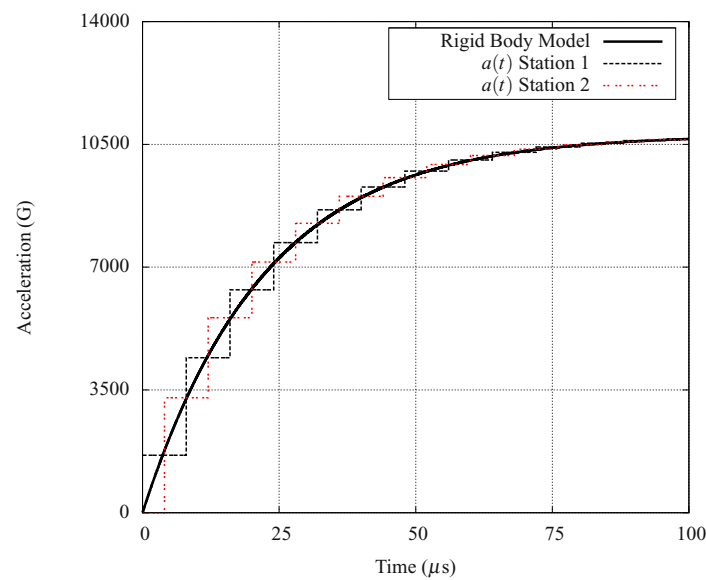


Fig. 9 Comparison of rigid body model acceleration to wave mechanics acceleration for 1-term fit at Load Level 2

predict the quartz gage acceleration quite well. The 1-term fit is representative of the data because the incident stress rate is very near linear and this slope dominates the acceleration of the tungsten disk. We can defend the advancement in time of the model fit curves by comparing the wave mechanics predicted acceleration of the tungsten disk at Stations 1 and 2 as shown in Fig. 1 to the rigid body model for a 1-term fit at Load Level 2. This is shown in Fig. 9. It is observed at this load level it takes some time for the wave mechanics solution to equilibrate. If we somewhat arbitrarily say that the sample is in equilibrium and the rigid body solution represents the wave mechanics solution when the accelerations of the two stations are each within 10% of the rigid body model, we can justify a 10 to 20 μs advancement in time of the rigid body model.

Finally, the modeling previously discussed was used to aide in the design-of-experiments for the evaluation of shock accelerometers. Two accelerometer models, the PCB 3991 and the Endevco 7270, each in both their 20 kG and 60 kG configurations were tested. The focus of this paper was to develop new and utilize existing methods to aid in the design-of-experiments for testing accelerometers, not to show a thorough evaluation these two suppliers accelerometers, therefore only a small sample of the entire test matrix is presented. Figure 10 shows a comparison of the Endevco 7270-60kG, the PCB 3991-60kG, and

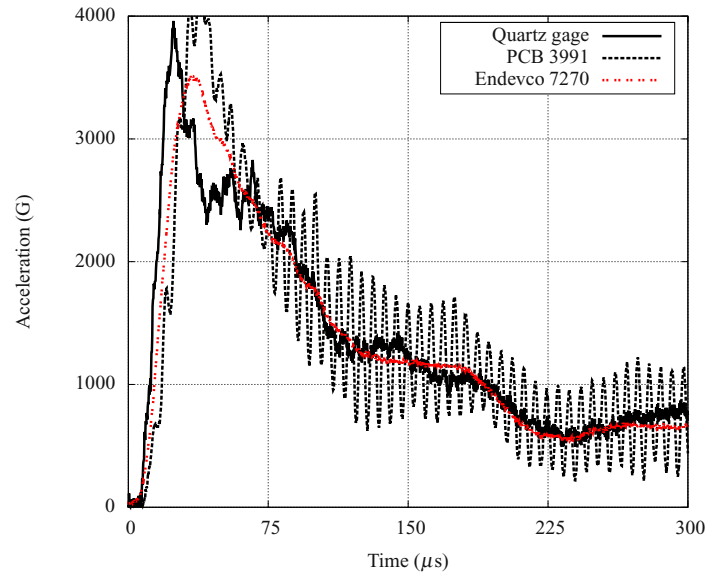


Fig. 10 Comparison of experimental data from quartz gage, PCB 3991-60kG, and Endevco 7270-60kG accelerometers at Load Level 1

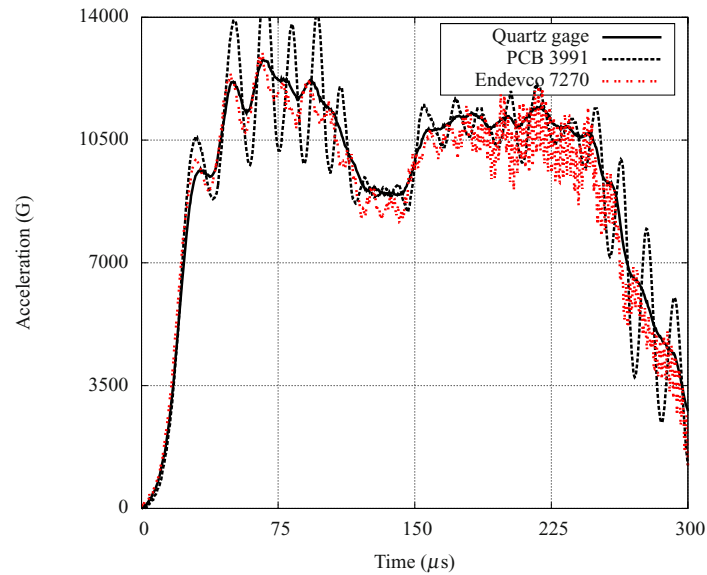


Fig. 11 Comparison of experimental data from quartz gage, PCB 3991-20kG, and Endevco 7270-20kG accelerometers at Load Level 2

the quartz gage acceleration. [Figure 11](#) shows a comparison of the Endevco 7270-20kG, the PCG 3991-20kG, and the quartz gage accelerations. This data was collected using an oscilloscope at 50MHz and subsequently digitally filtered using a 4-pole Butterworth lowpass filter with a 100kHz cutoff frequency. Conclusions on the performance of each suppliers accelerometer are left to the reader.

5 Summary

This paper presents a method to aide in the design-of-experiments for testing shock accelerometers on a Hopkinson pressure bar. Models for predicting the acceleration of a tungsten flyaway disk and accelerometers are presented and compared to experimental data with good results. Results from experiments at two distinct load levels are shown with comparisons of two

different manufactures shock accelerometers and a quartz gage.

6 Acknowledgement

This work was supported by the Joint DoD/DOE Munitions Program. Sandia is a mulitprogram laboratory operated by Sandia Corporation, a Lockheed Martin Company, for the United States Department of Energy under Contract DE-AC04-94AL85000.

REFERENCES

- [1] MJ Forrestal, DJ Frew, JP Hickerson, and TA Rohwer. Penetration of concrete targets with deceleration-time measurements. *International Journal of Impact Engineering*, 28(5):479–497, 2003.
- [2] DJ Frew, MJ Forrestal, and JD Cargile. The effect of concrete target diameter on projectile deceleration and penetration depth. *International Journal of Impact Engineering*, 32(10):1584–1594, 2006.
- [3] TC Togami, WE Baker, and MJ Forrestal. A split Hopkinson bar technique to evaluate the performance of accelerometers. *Journal of Applied Mechanics*, 63:353–356, 1996.
- [4] MJ Forrestal, TC Togami, WE Baker, and DJ Frew. Performance evaluation of accelerometers used for penetration experiments. *Experimental Mechanics*, 43(1):90–96, 2003.
- [5] D.J. Frew, M.J. Forrestal, and W. Chen. Pulse shaping techniques for testing brittle materials with a split Hopkinson pressure bar. *Experimental Mechanics*, 42(1):93–106, 2002.
- [6] D.J. Frew, M.J. Forrestal, and W. Chen. Pulse shaping techniques for testing elastic-plastic materials with a split Hopkinson pressure bar. *Experimental Mechanics*, 45(2):186–195, 2005.

Effect of residual stresses on spallation of the film under impact by coated bullet

Chen-Wu Wu *

Institute of Mechanics, Chinese Academy of Sciences, Beijing, PR China 100190

Abstract: The dynamic equilibrium equation was derived for the film under the test of impact by coated bullet (ICB) to include the effect of the residual stress. Then, the finite element modeling was carried through to investigate the impact responses of the film of different initial stress states. The preliminary results revealed that the residual stresses will influence both the film stress and interface stress of the sample under the ICB test.

Keywords: Film; impact by coated bullet (ICB); residual stress; spallation; interface

1. Introduction

The mechanical reliability of film/ substrate system is largely dominated by the bonding strength between the film and substrate. In order to evaluate the interface strength of film and substrate, many kinds of methods, either quasi-static or dynamic loading have been developed and applied successfully [1]. Among the methods of dynamic loading, both the methods of laser spallation [2, 3] and impact by coated bullet (ICB) [4] utilize the reflected tensile stress of the input compressive stress pulse to make the separation of film off the substrate.

The method of Impact with Coated Bullet (ICB) has been justified experimentally to be able to evaluate the interface adhesion of metallic coating and substrate [5]. By impacting the substrate with a front-end-coated bullet, a compressive stress pulse of short duration is initiated to propagate toward the film under test. After transmitting through the interface of the sample, the input compressive pulse is reflected on the free surface of the film. The tensile stress will arise around the film and substrate

* Corresponding author: Institute of Mechanics, Chinese Academy of Sciences, No. 15 Beisihuanxi Road, Beijing, PR China 100190. Tel.: +86 10 82544271. E-mail: wcu_on@yahoo.com.cn; chenwuwu@imech.ac.cn.

interface if the thickness of the bullet coat is appropriately chosen [4]. The propagation and evolution of the stress wave have been formulated for elastic system without considering the influences of the residual stresses [5, 6]. However, large residual stresses will inevitably be introduced into almost all kinds of films during deposition. These residual stresses shall contribute to the deformation of the surface layer and partly relax upon the separating of the film off the substrate, which will affect the fracture behaviors of the film and the film/ substrate interface. Such possible influences during the quasi-static loading experiments have drawn many attentions [7, 8]. In the present research, the effects of residual stresses on the spalling fracture of the films under the test of ICB are investigated. First, the dynamic equilibrium equation of the film was derived to include the contribution of the residual stress. Then, the finite element model was set up to simulate the impact responses of the film of different initial stress states. Finally, the influences of the residual stresses on the film stress and interface stress of the sample under ICB test were analyzed.

2. Theoretical description

Ideally, the spallation of the film on the substrate subjected to impact by fronted-end-coated bullet (ICB) can be schematically depicted in Fig.1.

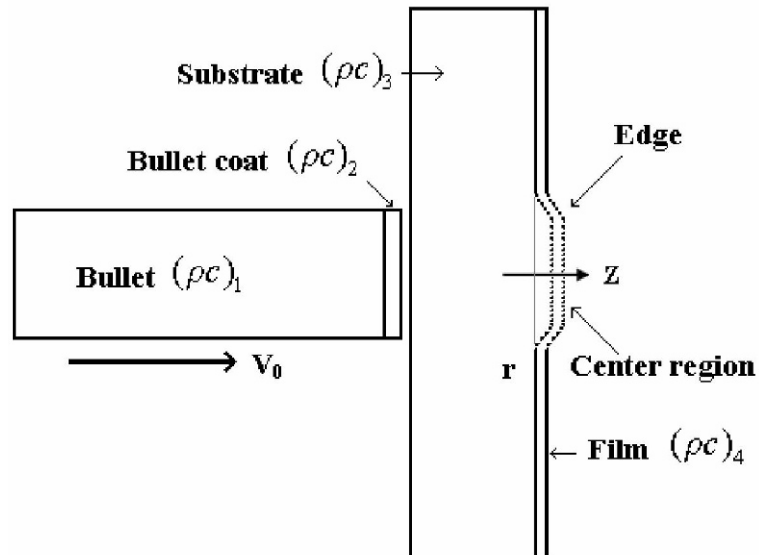


Fig.1 Sketch of spallation of the film under the ICB test

The deformation of the sample can be approximately described by uniaxial strain wave theory within the center region covered by the bullet cross-section. In fact, the experimental results also reveal that the planar features of the deformation and interface fracture are obvious under ICB test, in particular where far enough away from the edge of the impact region [6]. Of course, the uniaxial strain model should not be directly applied to the deforming pattern around the circular edge of impact, because wherein there is great deformation gradient. In other words, the edge effect should not be ignored near the edge of the region covered by the impacting bullet.

As far as the edge effect is taken into account, the theory of thin plate bending may be adopted to describe the dynamic deformation of the film.

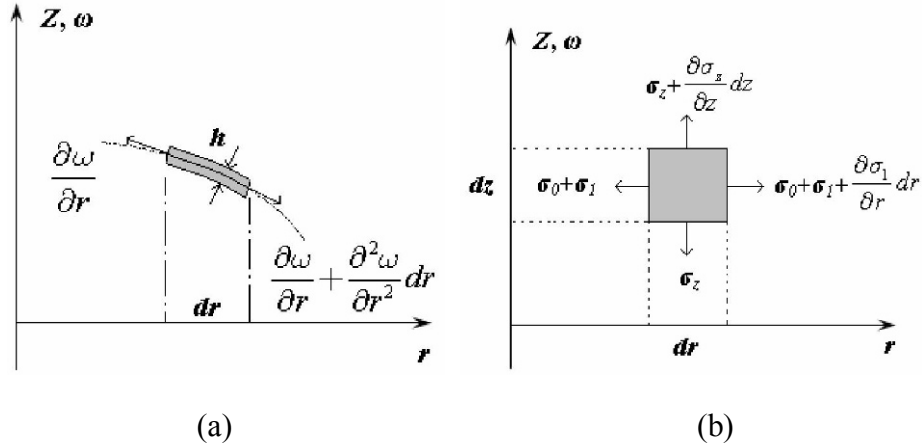


Fig.2 (a) Deformation of the infinitesimal section of total thickness and (b) Normal stresses acting on the infinitesimal ring of infinitesimal section

The deformation of a representative ring of infinitesimal length dr and height h of the film is illustrated in Figure 2 (a), and the normal stresses acting at the representative ring of square cross-section of infinitesimal dimensions are presented in Figure 2 (b).

By neglecting the shear stresses according to the theory of thin plates [9], the equilibrium equation for such representative ring can be written as

$$\begin{aligned} & \left(\sigma_z + \frac{\partial \sigma_z}{\partial z} dz \right) (2\pi(r + dr/2)) - (\sigma_z) (2\pi(r + dr/2)) \\ & \left(\sigma_0 + \sigma_1 + \frac{\partial \sigma_1}{\partial r} dr \right) \left(\frac{\partial w}{\partial r} + \frac{\partial^2 w}{\partial r^2} dr \right) (2\pi(r + dr) dz) + \\ & (\sigma_0 + \sigma_1) \frac{\partial w}{\partial r} (2\pi r dz) = \rho \frac{\partial^2 w}{\partial t^2} (2\pi(r + dr/2) dr dz) \end{aligned} \quad (1)$$

With eliminating the cancelable terms and neglecting the infinitesimal items of high orders, one can obtain the following control equation for the dynamic equilibrium of the film.

$$\rho \frac{\partial^2 \omega}{\partial t^2} - \frac{\partial \sigma_z}{\partial z} + (\sigma_0 + \sigma_1) \frac{\partial^2 \omega}{\partial r^2} + (\sigma_0 + \sigma_1) \frac{1}{r} \frac{\partial \omega}{\partial r} = 0 \quad (2)$$

By expressing the relationship between the stress and strain as

$$\sigma_z = \varepsilon_z \times \frac{d\sigma_z}{d\varepsilon_z} \quad (3)$$

and adopting the simplified treatment that

$$\varepsilon_z = \frac{\partial \omega}{\partial z} \quad (4)$$

, the equilibrium equation (2) can be further written as

$$\rho \frac{\partial^2 \omega}{\partial t^2} - \frac{d\sigma_z}{d\varepsilon_z} \frac{\partial^2 \omega}{\partial z^2} + (\sigma_1 + \sigma_0) \left(\frac{\partial^2 \omega}{\partial r^2} + \frac{1}{r} \frac{\partial \omega}{\partial r} \right) = 0 \quad (5)$$

As aforementioned, the uniaxial strain state can be assumed for the film and substrate away from the edge. By neglecting the radial deformation gradient, the equation (5) will reduce to

$$\rho \frac{\partial^2 \omega}{\partial t^2} - \frac{d\sigma_z}{d\varepsilon_z} \frac{\partial^2 \omega}{\partial z^2} = 0 \quad (6)$$

, which is identical to the one-dimensional wave equation [10]

$$\frac{\partial^2 \omega}{\partial t^2} - C_L^2 \frac{\partial^2 \omega}{\partial z^2} = 0 \quad (7)$$

where

$$C_L = \sqrt{\frac{1}{\rho} \frac{d\sigma_z}{d\varepsilon_z}} \quad (8)$$

represents the longitudinal wave velocity.

By assuming the linear elastic behaviors for the materials, the first peak tensile normal stress acting at the film/ substrate interface has been obtained as [6]:

$$\sigma_{itb} = T_{34} \times T_{23} \times [v_0(\rho c)_1 / 2] \quad (9)$$

when $r_{21}(\rho c)_3 + (\rho c)_2 \leq 0$

and

$$\sigma_{ib} = T_{34} \times T_{23} \times [v_0(\rho c)_1 / 2] \times (1 - T_{21} \times T_{23}) \quad (10)$$

$$\text{when } r_{21}(\rho c)_3 + (\rho c)_2 > 0$$

$$\text{Where } r_{ij} = ((\rho c)_j - (\rho c)_i) / ((\rho c)_j + (\rho c)_i) \text{ and } T_{ij} = 2(\rho c)_j / ((\rho c)_j + (\rho c)_i).$$

It is indicated in (9) and (10) that the residual stress has no contribution to the interface normal stresses at the center region of the linear elastic system under ICB test. However, once the nonlinear behaviors of materials are taken into account, the wave velocity, in particular in the surface layer should be influenced by the residual stresses [10]. This will influence the stress acting at the film/ substrate interface even around the center region away from the edge.

The deformation around the impact edge can be described by the equation (5), in which the in-plane stresses σ_1 will change with the stretching of the film. Thus σ_1 can be represented by some function $f(\omega)$ because that the stretch of the film is directly dependent on the magnitude of the off-plane displacement ω . Therefore the equation (5) can be further written as

$$\rho \frac{\partial^2 \omega}{\partial t^2} - \frac{d\sigma_z}{d\varepsilon_z} \frac{\partial^2 \omega}{\partial z^2} + (f_1(\omega) + \sigma_0) \left(\frac{\partial^2 \omega}{\partial r^2} + \frac{1}{r} \frac{\partial \omega}{\partial r} \right) = 0 \quad (11)$$

, which includes complex nonlinearity. As a preliminary attempt, we can assume that the circumferential strain is zero, that is

$$\varepsilon_\varphi = \frac{1}{E} (\sigma_\varphi - \nu \sigma_1) = 0 \quad (12)$$

Where σ_φ represents the hoop stress. Thus,

$$\sigma_\varphi = \nu \sigma_1 \quad (13)$$

By defining the radial strain as

$$\varepsilon_r = \left((dr)' - dr \right) / dr \quad (14)$$

which is related to the stresses by

$$\varepsilon_r = \frac{1}{E}(\sigma_1 - \nu\sigma_\varphi) \quad (15)$$

Approximately, one has

$$(dr)' = \sqrt{\left(dr \frac{\partial \omega}{\partial r}\right)^2 + (dr)^2} = dr \left(\sqrt{\left(\frac{\partial \omega}{\partial r}\right)^2 + 1} \right) = dr \left(2 \frac{\partial \omega}{\partial r} + 1 \right) \quad (16)$$

Therefore

$$\varepsilon_r = \left((dr)' - dr \right) / dr = 2 \frac{\partial \omega}{\partial r} \quad (17)$$

By substituting (13) and (17) into (15), one can obtain

$$\sigma_1 = \frac{E}{1-\nu^2} \varepsilon_r = \frac{2E}{1-\nu^2} \frac{\partial \omega}{\partial r} \quad (18)$$

Finally, the equation (11) can be written as

$$\rho \frac{\partial^2 \omega}{\partial t^2} - \frac{d\sigma_z}{d\varepsilon_z} \frac{\partial^2 \omega}{\partial z^2} + \left(\frac{2E}{1-\nu^2} \frac{\partial \omega}{\partial r} + \sigma_0 \right) \left(\frac{\partial^2 \omega}{\partial r^2} + \frac{1}{r} \frac{\partial \omega}{\partial r} \right) = 0 \quad (19)$$

The partial differential equation (18) involves at least the nonlinear items

of $\frac{2E}{1-\nu^2} \frac{\partial \omega}{\partial r} \left(\frac{\partial^2 \omega}{\partial r^2} + \frac{1}{r} \frac{\partial \omega}{\partial r} \right)$, which make the analytical solution is somewhat hard to

attain. For the sake of convenience, we use the finite element program *Ls-dyna* to analyze the impact responses of the sample herein.

3. Numerical model and computational results

3.1 Numerical model

The axisymmetric geometry model and the sketches of the mesh are shown in [Fig.3](#).

In [Fig.3](#), the X-axis starts from the symmetric axis and is parallel to the interface.

Perfect bonding are assumed for the film/ substrate interface, across which the continuity conditions can be interpreted as

$$u_n^+ = u_n^-, \quad \sigma_n^+ = \sigma_n^- \quad \text{and} \quad \sigma_\tau^+ = -\sigma_\tau^-$$

Where

Superscripts ‘+’ and ‘-’ denote the two sides across the interface,

u is the displacement,

σ_n is the interfacial normal stress,

σ_n is the interfacial shear stress.

The symmetric displacement constraints are applied at the nodes on the symmetry axis as the only boundary condition. The initial velocity of the bullet is 300 m/s in the computation.

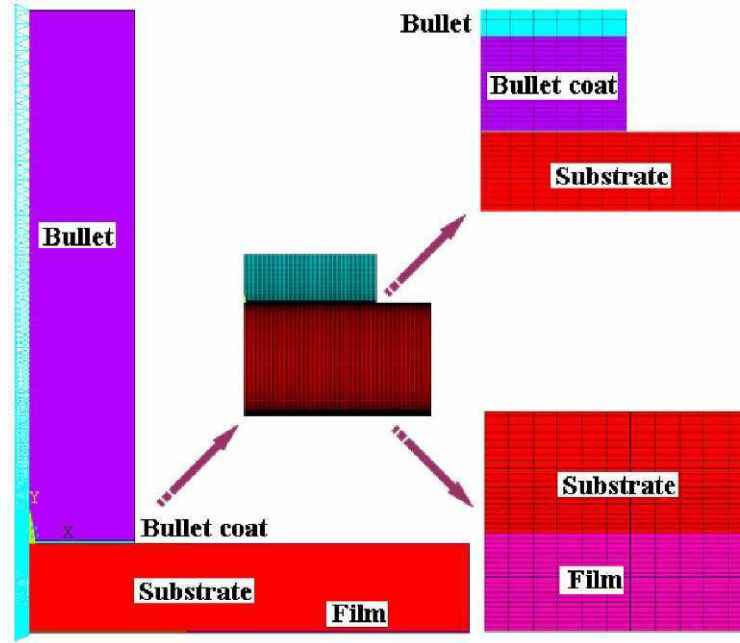


Fig.3 Finite element model of the bullet and sample

The rate-independent material model of bilinear isotropic plasticity is used in the computation, for which the main parameters are listed in Table1.

Table 1 Geometrical & mechanical parameters

	$t/ \text{ mm}$	$r/ \text{ mm}$	$\rho/ \text{ kg/m}^3$	$E/ \text{ GPa}$	ν	$\sigma_s/ \text{ MPa}$	$E'/ \text{ MPa}$
Bullet	30	6	1050	3.38	0.35	50	33.8
Bullet coat	0.1	6	7850	208	0.29	615	2080
Substrate	5	25	7850	208	0.29	900	2080
Film	0.1	25	8900	207	0.29	600	2070

In table 1,

t is the thickness of the bullet, bullet coat, film and the substrate,

r is the radius,

ρ is the density,

E is the elastic modulus,

ν is the Poisson's ratio,

σ_s is the yield stress,

E' is the tangent modulus.

The technique of virtual thermal expansion is utilized to realize the action of the residual stress, of which the magnitude is -1.73GPa in the initially compressed film and 1.73GPa in the initially tensioned film.

3.2 Computational results

The computation results reveal that the peak value of the first interface tensile pulse occurs at the moment of time $t=1\mu s$, therefore the deformation and stress distribution for the moment $t=1\mu s$ are discussed largely.

The deformation of the initially stress-free film at the moment $t=1\mu s$ is shown in Fig. 4, in which the displacements are magnified by 50 times. It is revealed that the deformation is uniform and close to the uniaxial strain state within the center region under impact, while the off-plane displacement gradient arises obviously around the edge region.

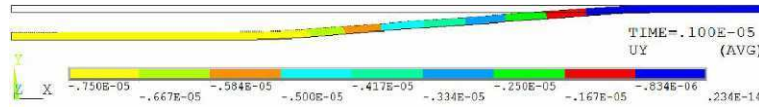


Fig.4 Deformation pattern at $t=1\mu s$ of the initially stress-free film

The off-plane displacements of the film mapped onto the path parallel to the interface are plotted in Fig. 5 for the three different initial stress states.

In Fig. 5, the symbol

$rs=0$ represents the initially stress-free state,

$rs=-$ represents the initially compressed state,

$rs=+$ represents the initially tensiled state,

r_b is the bullet radius.

The curves in Fig. 5 show that the residual compressive stress in the film will increase the off-plane displacements while residual tensile stress will decrease it. Moreover, it is indicated in Fig.5 that the off-plane displacements change in an almost linear law around the edge of the impact region.

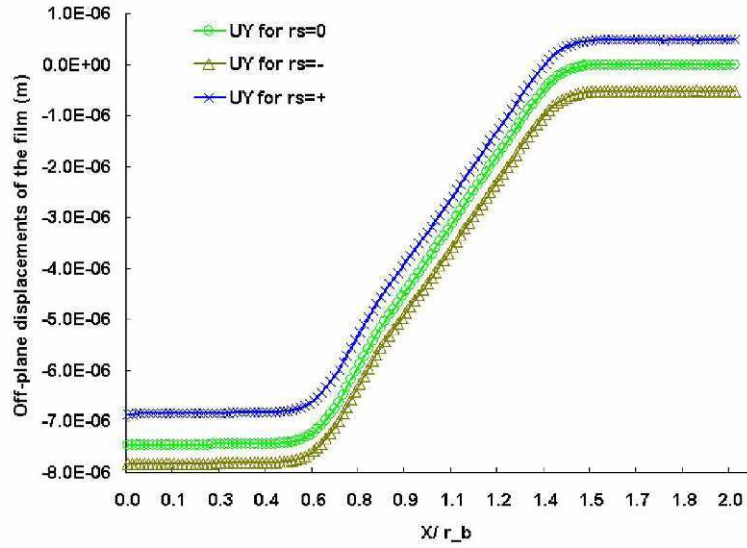


Fig. 5 Off-plane displacements at $t=1\mu\text{s}$ of films of different initial stress states

The contours of the radial stress component SX at time $t=1\mu\text{s}$ in the film of the three different initial stress states are further graphed in Fig. 6, in which the meanings of the symbols are identical to that in Fig. 5.

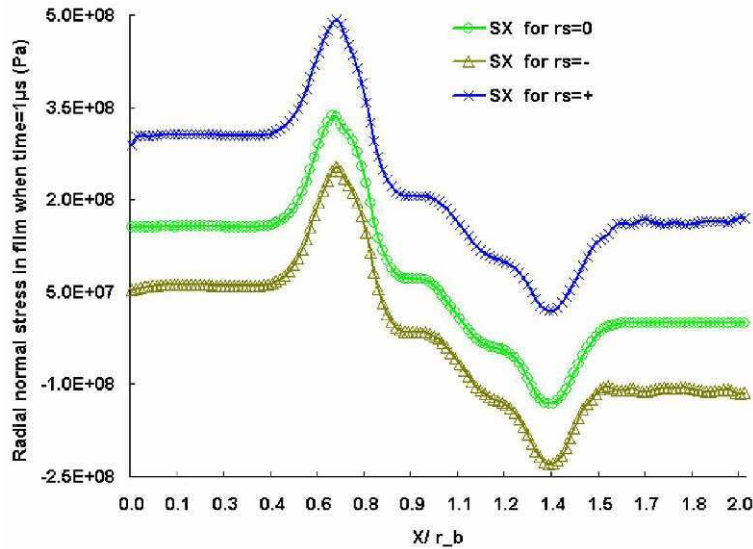


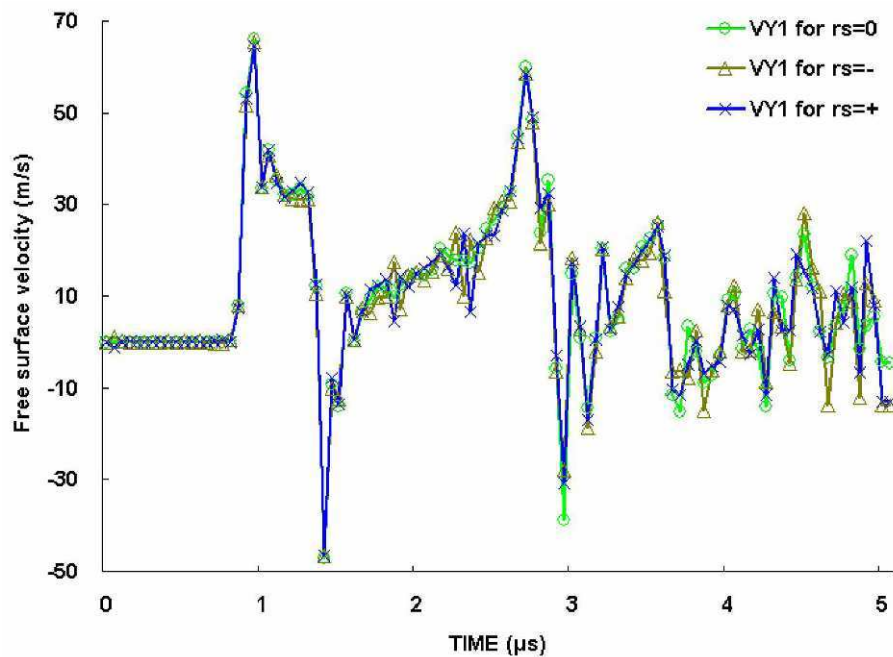
Fig.6 Radial normal stresses in the film at $t=1\mu\text{s}$

It is indicated in Fig. 6 that the film stress patterns are similar for all the three cases. Once again, the film stress is rather uniform within the center region under impact, while the obvious fluctuation arises around the edge regions as shown in Fig.6. It can also be noticed that in Fig. 6 that the maximum film stresses appear at the location about 0.7 times bullet radius distance from the center. Furthermore, just as one can

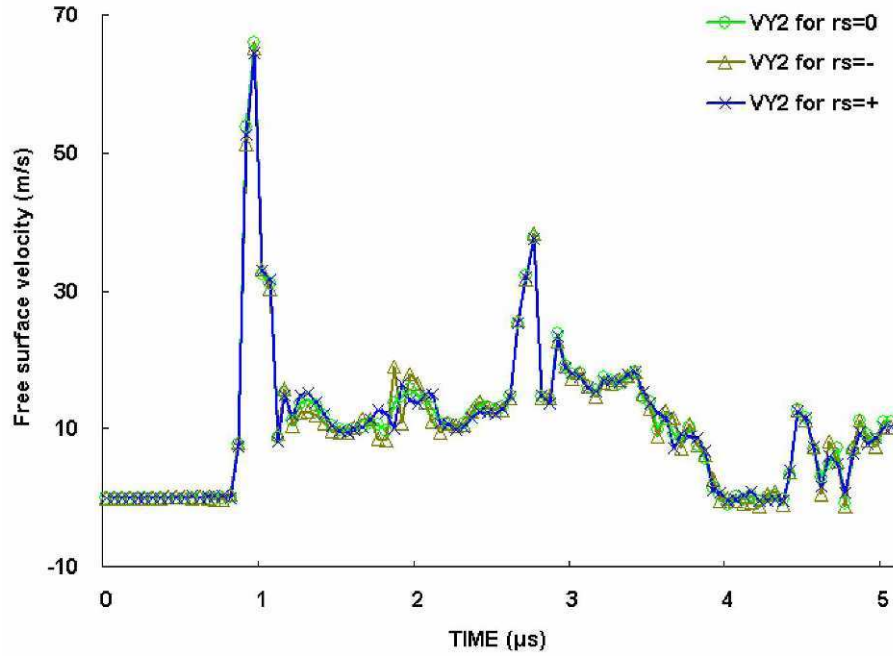
expect, it is revealed in Fig. 6 that the residual compressive stress will decrease the stress of the film while residual tensile stress will increase it. This means that the residual tensile stress will promote the cracking of the film under impact, while the residual compressive stress will hold back the film cracking if neglecting temporarily the buckling of a greatly compressed film.

The free surface velocity histories of the three positions, i.e. the locations of No. 1 at the center, No. 2 half bullet radius distance from the center and No.3 a bullet radius distance from the center along the X-axis are plotted in Figs. 7 (a), (b) and (c). In Fig.7, the positive velocity values represent that in the direction of the outer normal vector of the surface.

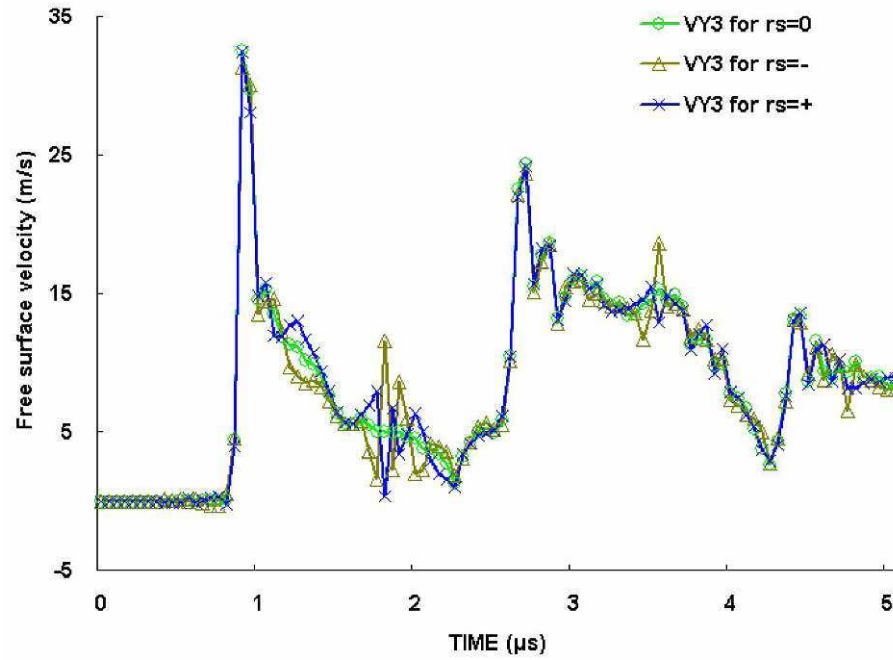
By comparing the outcome graphs in Figs. 7 (a), (b) and (c), one can find out that the effects of the residual stresses on the surface velocity gradually become more obvious when the observed positions move from the center toward the edge. However, both the results on the three positions as illustrated in Figs. 7 (a) and (b) show that the first maximum and the first minimum values of the velocity are seldom influenced by the residual stress states. This means that the residual stress in the film may not contribute greatly to the spall velocity, especially when measured around the center region, which is usually used to describe the spallation strength of the test interface.



(a)



(b)



(c)

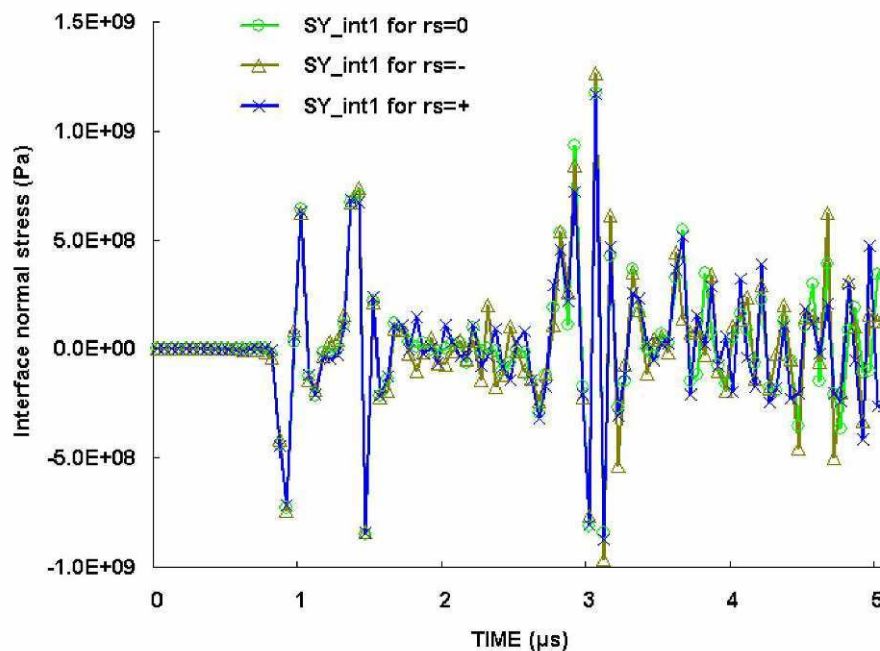
Fig.7 Surface velocity of the film at the (a) center, (b) half bullet radius and (c) a bullet radius distance from the center

The interfacial normal stress histories of the three positions, i.e. the locations of No. 1 at the center, No. 2 half bullet radius distance from the center and No.3 a bullet radius distance from the center along the X-axis are graphed in Figs. 8 (a), (b) and (c). Once again, one can find out in Fig. 7 (a), (b) and (c) that the effects of the residual stresses

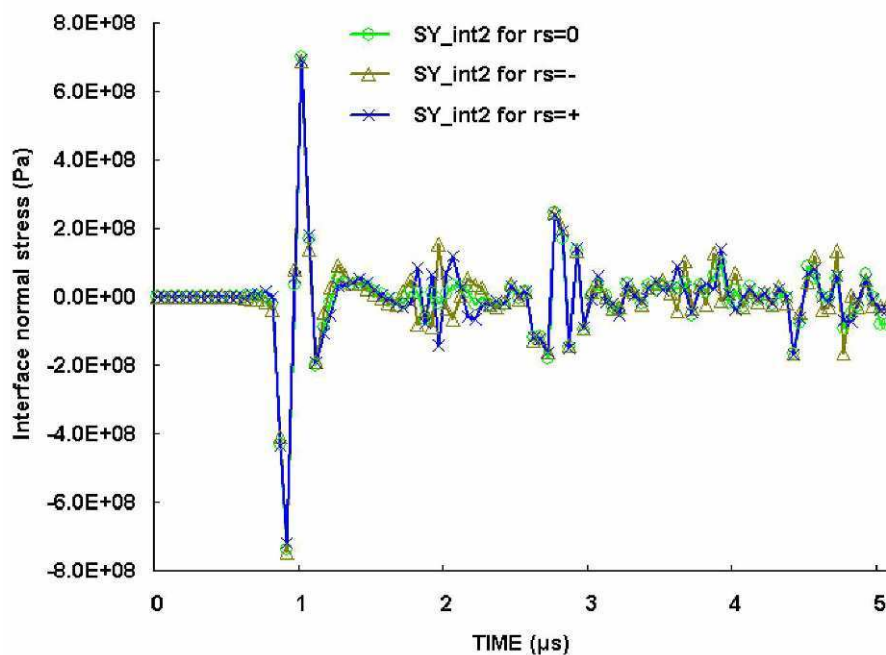
on the interfacial normal stress become gradually greater when the studied positions move from the center toward the edge.

It is also shown in Fig. 7 that the maximum interfacial normal stress is obviously changed by the residual stress states.

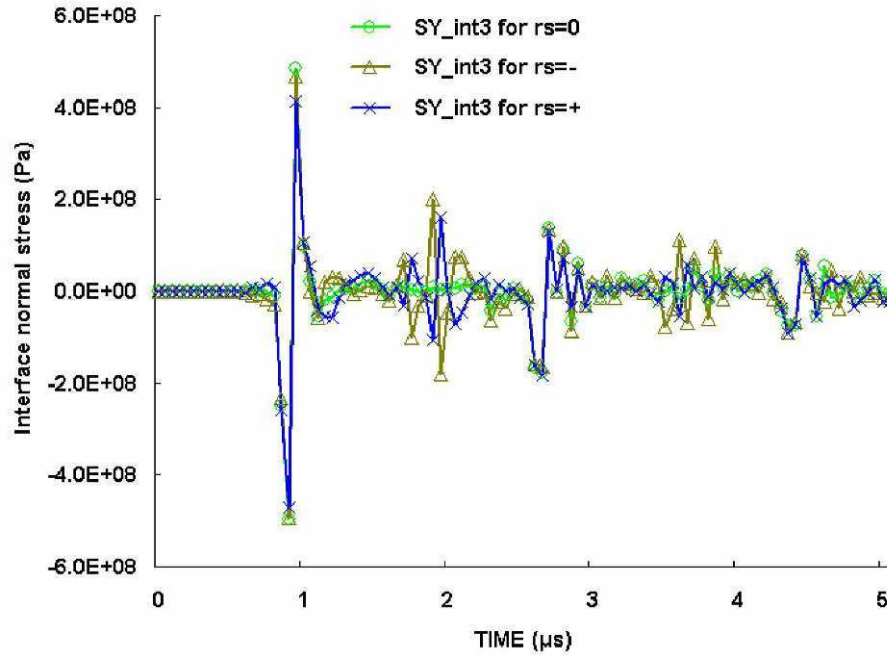
The results displayed in Fig.8 (a) show that the residual compressive stress in the film will increase the overall maximum interfacial tensile stress at the center position.



(a)



(b)



(c)

Fig.8 Normal stress on the film/ substrate interface at the (a) center, (b) half bullet radius and (c) a bullet radius distance from the center

It is further indicated in Fig.8 (c) that both the residual compressive and residual tensile stress will reduce the first peak value of the interfacial tensile stress at the position of one bullet radius distance from the center.

The results graphed in Figs. 8 (b) and (c) show that both the residual compressive stress and tensile stress in the film will increase the subsequent peaks of the interfacial normal stress at the locations of half or one bullet radius distances away from the center.

4. Conclusions

The residual stresses influence greatly the off-plane deformation and the film stress of the sample under ICB test, in detail the residual compressive stress will partly relax the tension of the film while the residual tensile stress enhance it.

The effects of the residual stress on the surface velocity and the interfacial normal stress histories become more prominent when the observed positions move from the center to the edge. The peaks of the interfacial normal stresses are changed to a certain extent by the residual stresses.

Acknowledgements

This work was supported by the National Natural Science Foundation of China (Grant No. 11002145).

References:

- [1] R. Lacombe, Adhesion Measurement Methods: Theory and Practice, CRC Press, London, 2006.
- [2] J.L. Vossen. Measurements of film–substrate bond strength by laser spallation. Adhesion Measurement of Thin Films, Thick Films and Bulk Coatings, American Society for Testing and Materials, ASTM STP 640 (1978):122–123.
- [3] Junlan Wang, Nancy R. Sottos and Richard L. Weaver, Tensile and mixed-mode strength of a thin film-substrate interface under laser induced pulse loading, Journal of the Mechanics and Physics of Solid 52 (2004): 999-1022.
- [4] Chen-Wu Wu, Zhi-Lin Wu, Kun Zhang and Guang-Nan Chen, Evaluation of film-substrate adhesion via impact using coated bullets, Journal of Mechanics of Materials and Structures, 10 (4) (2009) 1703-1709.
- [5] Zhi-Lin Wu, Chen-Wu Wu, Guang-Nan Chen and Kun Zhang, On a novel method of impact by a front-end-coated bullet to evaluate the interface adhesion between film and substrate, Progress in Organic Coatings, 68 (1-2) (2010) 19-22.
- [6] C.W. Wu, Z.L. Wu, C.G. Huang, Q. Zhang, L.R. He, K. Liu, G.N. Chen, Spallation of the thermal barrier coatings subjected to impact by coated bullet, submitted.
- [7] Thouless, M.D.and Jensen, H.M., The effect of residual stresses on adhesion measurements, Journal of Adhesion Science and Technology 8 (6) (1994): 579-586(8).
- [8] Pulin Nie, Yao Shen, QiuLong Chen and Xun Cai, Effects of residual stresses on interfacial adhesion measurement, Mechanics of Materials 41 (2009): 545–552.
- [9] S. Timoshenko and S. Woinowsky-Krieger, Theory of Plates and Shells, 2nd ed., McGRAW-HILL Book Company, New York, 1987.
- [10] Kolsky H., Stress Wave in Solids. Oxford: Clarendon Press, 1953.

Fracture Testing of Simulated FRP Repairs

Tanveer Chawla, Ph.D. Student, Department of Mechanical Engineering, University of North Dakota
tanveer.chawla@und.edu

M.N. Cavalli, Associate Professor and Chair, Department of Mechanical Engineering, University of North Dakota, 243 Centennial Drive, Stop 8359, Grand Forks, ND 58202-8359
matthewcavalli@mail.und.nodak.edu

ABSTRACT

Continuous fiber reinforcement in a polymer matrix can create a composite material with excellent strength-to-weight and stiffness-to-weight ratios. In a manufacturing environment, however, it is sometimes necessary to remove portions of the composite to repair defects like wrinkles and voids, particularly for complex part geometries. This results in a discontinuity of the reinforcement and the potential for the repaired portion to prematurely fail in service. The current work details an effort to optimize a resin for scarf repair of glass reinforced polyester composite structures. Results from Double Cantilever Beam (DCB) tests are presented along with details of micro-structural examination of the fracture surfaces. Additional optimization work to be carried out is discussed.

INTRODUCTION

Widespread use of composite materials in the defense, aerospace and alternative energy sectors has necessitated research in the field of composite repair [1]. Replacing damaged components, as is often done in the case of mechanically fastened metallic structures, proves to be costly [2] and difficult in these areas of application. Though these materials excel in performance and possess commendable strength-to-weight and stiffness-to-weight ratios, they are often subjected to damage which may occur as delamination, fiber failure, matrix failure or fiber matrix debonding [3]. The damaged component can degrade the integrity and cause failure of the whole structure of which it is a part [3]. Composite parts may get damaged not only due to conditions they are subjected to during their service life but also due to some inherent property of the manufacturing method used to make them. Whatever the cause may be, repairs become necessary and may be carried out using various techniques (e.g. patches, scarf joints, etc.) and different types of materials. Mechanically fastened repairs are not popular as the requirements involved, such as drilling holes [3], create undesirable areas of high stress concentration. Thus, considerable research has been and is being carried out to investigate the ultimate strength, stress states, etc. of composites repaired adhesively using a variety of repair parameters.

This paper details the experimental procedure and results obtained from work carried out to develop a high strength laminate repair system for glass fiber-reinforced wind turbine blades. A number of commercial suppliers were contacted and nine resins were selected for screening. Out of these, six were shortlisted for initial testing which was carried out in accordance with ASTM D 5528 (Test Method for Mode I Interlaminar Fracture Toughness of Unidirectional Fiber-Reinforced Polymer Matrix Composites) using Double Cantilever Beam (DCB) specimens. The fracture toughness values obtained from testing these repair resin candidates were compared to those obtained from the repair resin currently being used. The top three candidates were identified from the DCB testing. These three candidates will be further tested using modified tensile testing and fatigue testing to select the final repair resin.

SPECIMEN PREPARATION

The DCB specimens (Figure 1) consisted of two separate parts, the lower adherend (parent plate) representing the blade and the upper adherend (repair plate) simulating the flat part of a one-sided scarf repair. The lay-up and materials used for the upper and lower adherends are given in Table 1. For current repairs, a different polyester resin is used than is used to fabricate the main part of the blade. The parent plate of each DCB specimen was fabricated using the main blade resin. The

repair plate was fabricated using one of the candidate repair resins, including the current repair resin as a performance baseline.

Table 1. Specimen Lay-up and post curing details

2x Biaxial 806	Repaired Laminate: Hand Lay-up Repair Resin (Upper adherend)	Post curing: 24 hrs. at 60° C 3 hrs. at 95° C
8x Combi 1250 (CSM facing downwards)		
CSM 300		
Crack Initiator	Tape ($t \leq 13 \mu\text{m}$)	
8x Combi 1250 (CSM facing downwards)	Parent Laminate: VARTM Main Blade Resin (Lower adherend)	Post curing: 16 hrs. at 40° C
2x Biaxial 806		

The parent plate representing the blade was manufactured using VARTM (Vacuum Assisted Resin Transfer Molding) as shown in Figure 2. After being cured at room temperature for 24 hours, the parent plate was further post-cured at 60°C for 24 hours and then at 95°C for 3 hours to produce a low residual styrene content.

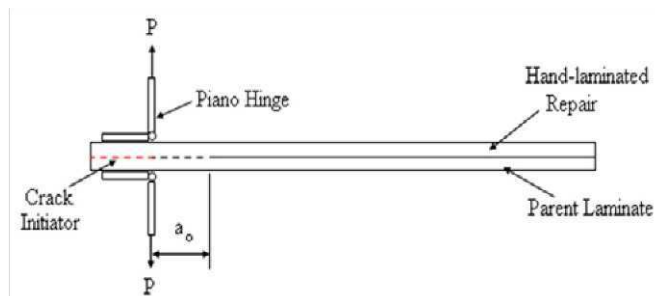


Figure1. DCB Specimen



Figure 2. VARTM set-up before infusion

Since the lay-up of the parent plate was not symmetric, some warpage was observed in the parent plates perpendicular to the 1-direction of the unidirectional fibers. The extent of warpage is depicted in Figures 3 and 4. The reading on the scale (depth of warp) in Figure 4 is 1.25 cm. The total width of the plate was 60 cm. As the specimens were to be cut along 1-direction, it was decided that the warpage would not have a significant effect on test results.



Figure 3. Straight rule along Combi1250 (0° direction)

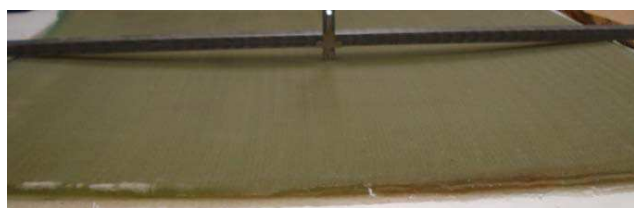


Figure 4. Straight rule along Combi1250 (90° direction)

The parent plate initially consisted of nine, 0.88 mm thick Combi 1250 plies (unidirectional fibers with a chopped strand mat attached on one side). Following curing of the parent plate, the top layer was completely ground off, resulting in an exposed layer of resin to serve as the repair surface. The repair was conducted by hand lay-up and after a cure of 24 hours at room temperature the whole sample was then post cured at 40° C for 16 hours. Certain parameters such as the gel time, peak exothermal temperature, peak time, Shore D hardness and ambient conditions were recorded to facilitate calculations for the degree of cure of the repair resin candidates. The specimens had a pre-crack of approximately 30 mm at the resin inlet side and the two adherends were pulled apart with the help of piano hinges which were glued with Araldite 2021 to the surfaces of the cut specimens. The final DCB specimen dimensions were 350 mm in length and 30 mm in width. The parent laminate adherend had a thickness of 7.7 ± 0.3 mm whereas the repair part was 10.2 ± 0.7 mm thick. Both edges of the specimens were coated with a water-based white typewriter fluid and thin lines were marked every 1 mm on either edge for a distance of 100

mm from the end point of the release tape. The coating and markings were added to aid in the observation of crack propagation during testing.

TESTING

Testing of the specimens was conducted on the Shimadzu AG-IS Universal Testing Machine under displacement control at a crosshead rate of 0.1 mm/min. The specimens were aligned and centered with the help of a level while mounting the hinges on the load grips. Crack propagation was monitored and recorded with the help of Retiga 1300 camera (Figure 5).



Figure 5. Experimental set-up for DCB testing

Load data was recorded using the Trapezium control software and images of the loaded samples were captured and analyzed using Vic-Snap digital image correlation software. Initial testing was conducted with the adherends of the specimen being pulled apart continuously. It was noticed that the crack growth was more of a run-arrest extension in which the delamination front jumped ahead abruptly rather than being a slow, stable extension. It was then decided to unload the specimens after a 15 mm crack growth increment, reduce the load by 30% and reload to continue the test; this procedure being repeated at least five times for each specimen. Five specimens were tested for each of the repair resin candidates to procure statistically significant data.

CALCULATIONS

Using the load data obtained from the Shimadzu UTM, along with values for the opening displacement recorded optically, the mode I critical strain energy release rate (interlaminar fracture toughness) for a built-in double cantilever beam can be calculated according to ASTM D5528 as

$$G_{Ic} = \frac{3P\delta}{2ba} \quad (1)$$

This expression is expected to overestimate the actual value of the material property due to incorrect boundary conditions. A corrected value, G_{Ic}' , can be calculated (ASTM D5528) as

$$G_{Ic}' = \frac{3P\delta}{2b(a + \Delta)} \quad (2)$$

where Δ corrects for beam rotation at the delamination front. The correction factor, Δ , is obtained from the least squares fit of a plot of the cube root of compliance of the DCB specimen as a function of the delamination length. The compliance of the beam can be calculated as the beam deflection at the point of applied load divided by the applied load, δ/P . This is a decreasing function of the crack length, a , measured from the point of applied load to the crack tip. Since the ratio of load point displacement to initial crack length, δ/a_0 , did not exceed 0.4, large deflection corrections were not required.

It should be noted that ASTM D5528 does not strictly apply to this test geometry. Despite the similar layup between the parent plate and the simulated repair, the hand lay-up process produces a significantly thicker top portion of the final plate. The ratio of the parent plate thickness to the hand-layup thickness, h_1/h_2 , is approximately 0.75 (averaged value). As a result,

the DCB specimens are not symmetric about the crack plane. This asymmetry leads to the presence of mode II (shear) loading at the crack front which is not present in a symmetric DCB specimen. Multiple approaches for calculating the overall strain energy release rate, G , and the mode I and mode II components, G_I and G_{II} , exist [e.g. 4-8]. For example, the method of Hutchinson and Suo [4] requires that the applied loading on the specimen be separated into several component moments. This requires either a modification to the experimental setup to measure additional loads or the use of complimentary numerical calculations. However, Mollon and co-workers [8] present a relationship to calculate the mode mixity that they found to work well over a range of material properties, Equations 3-6.

$$\alpha = \frac{1 - \frac{h_1^3}{h_2^3}}{1 + \frac{h_1^3}{h_2^3}} \quad (3)$$

$$b = 0.06\alpha + 0.35 \quad (4)$$

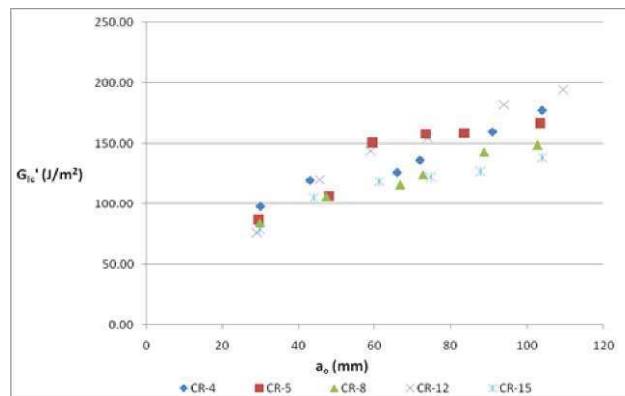
$$\frac{G_{II}}{G} = -b\sqrt{1 - \alpha^2} + b \quad (5)$$

$$\frac{G_I}{G} = 1 - \frac{G_{II}}{G} \quad (6)$$

Based on this analysis, G_{II}/G is approximately 0.030 ± 0.012 for the geometry tested in this work. Thus, the mode I analysis presented in ASTM D5528 should lead to an acceptable level of accuracy.

RESULTS AND DISCUSSION

The corrected values of interlaminar fracture toughness, G_{Ic}' , for each repair candidate were calculated using equation (2) and were plotted against a_o , the crack length at crack initiation. Figure 6 shows the resulting curve for the current repair resin and two of the potential candidates. G_{Ic}' values at a crack length of 100 mm for each repair resin were averaged for comparison. For baseline data the averaged value of G_{Ic}' for the repair resin currently in use, was found out to be 165 J/m^2 . From the plots it was observed that some specimens manufactured using resins AD, RH and RL had very high fracture toughness values. On examination of the surfaces of these specimens, it was noticed that the topmost plies of the parent plate had not been properly ground off to their full thickness and also the grinding was not uniform over the length of some specimens. In the case of these resins, the averaged G_{Ic}' values were calculated from the results obtained from specimens that had their parent plate surface ground properly.



(a)

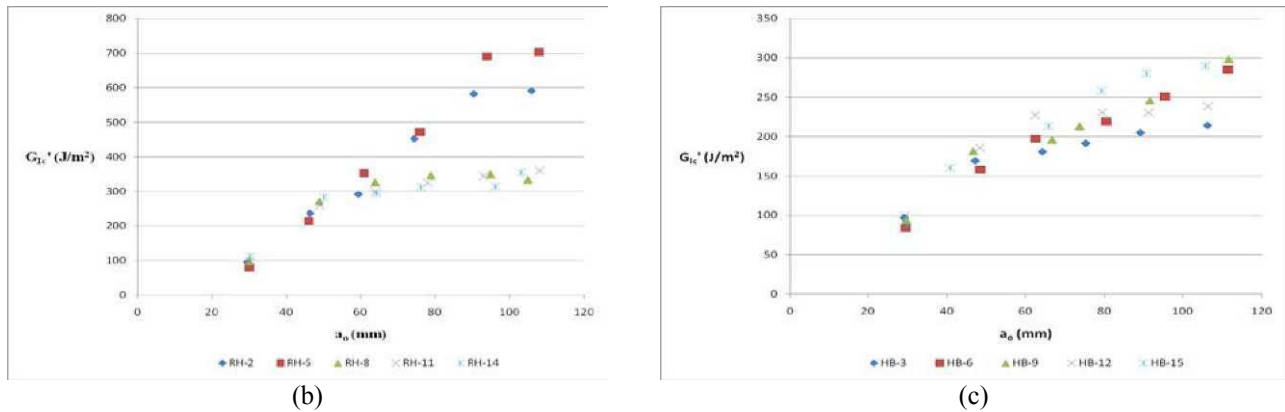


Figure 6. Fracture toughness values for DCB samples made with a) the current repair resin CR, b) resin RH, and c) resin HB.

The averaged corrected fracture toughness values at a crack length of approximately 100 mm for the selected repair resin candidates along with the baseline value are listed in Figure 7. From these numbers three resins RH, HB and AD have been chosen for further testing.

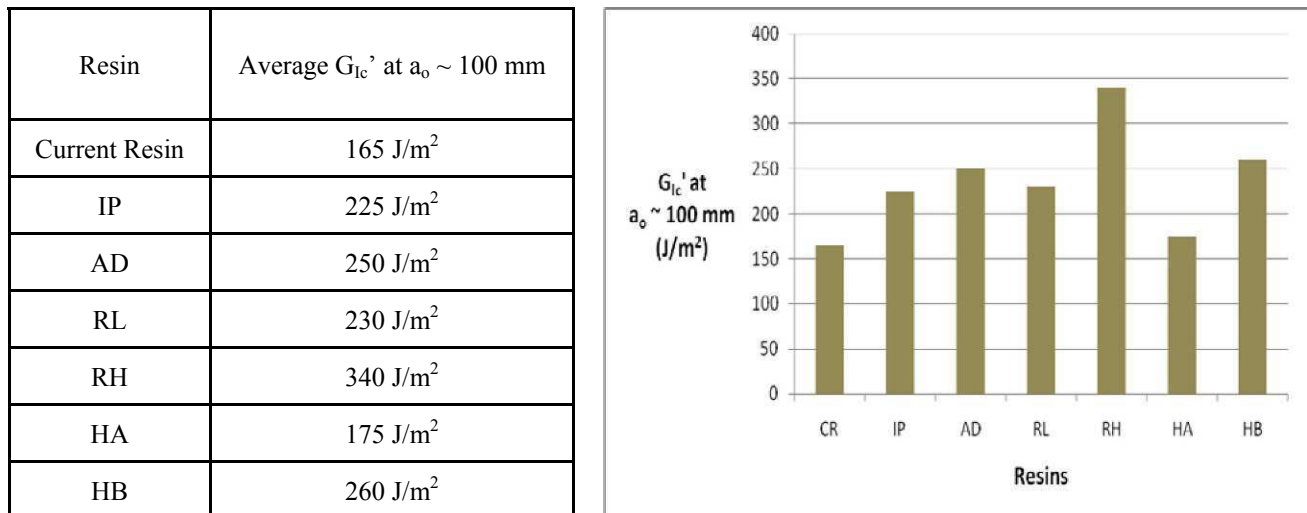


Figure 7. Consolidated DCB fracture testing results

The three chosen repair resin candidates RH, HB and AD along with the current repair resin will be tested under static tensile loading to choose the final repair resin. The specimen configuration is given in Figure 8.

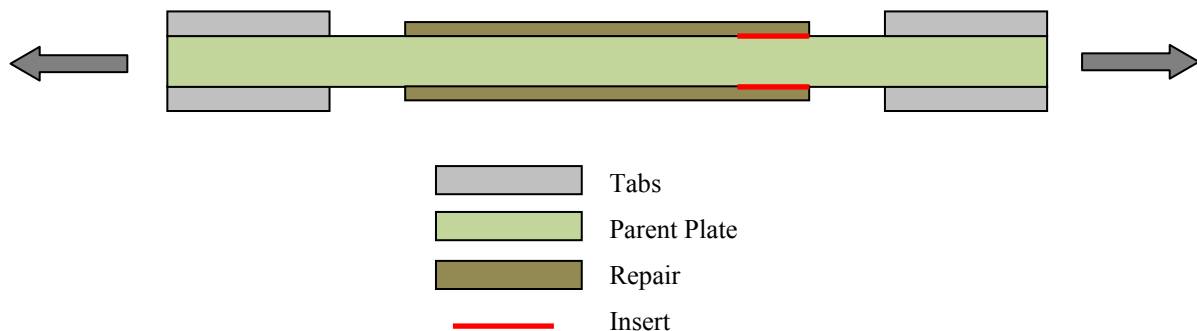


Figure 8. Static tensile test specimen configuration

CONCLUSIONS

DCB specimens with the lower adherend representing a part of a wind turbine blade and the upper adherend simulating a section of scarf repair were tested for Mode I fracture toughness in accordance with ASTM D 5528. Selected repair resin candidates were compared with the currently used repair resin. Examination of the results and the fractured specimens provided some interesting information. The new repair resins were able to almost double the fracture toughness of the repairs. In some specimens, the top ply was ground only partially and in these specimens a four times increase in the fracture toughness was observed. This implies that grinding of the top surface and the surface condition of the area of the composite part to be repaired affects fracture toughness values to a great extent. Three repair resin candidates have been chosen for further testing which will be carried out using static tension test and the final repair resin will be selected depending on results obtained. Regulations imposed by environmental and safety organizations will also govern the selection.

ACKNOWLEDGEMENTS

The authors acknowledge financial support of this work by LM Windpower and the UND Department of Mechanical Engineering.

REFERENCES

- [1] Breitzman T. D., Iarve E. V., Cook B. M., Schoeppner G. A., Lipton R. P., (2009) Optimization of a composite scarf repair patch under tensile loading. *Composites: Part A* (2009), *in press*
- [2] Harman Alex B., Wang Chun H., (2006) Improved design methods for scarf repairs to highly strained composite aircraft structure. *Composite structures* 75 (2006) 132-144
- [3] Tzetzis D., Hogg P. J., (2008) Experimental and finite element analysis on the performance of vacuum-assisted resin infused single scarf repairs. *Materials and Design* 29 (2008) 436- 449.
- [4] Hutchinson JW, Suo Z. Mixed mode cracking in layered materials (1992). *Advances in Applied Mechanics* 29. pp. 64 122.
- [5] F. Ducept, D. Gamby, P. Davies (1999). A mixed-mode failure criterion derived from tests on symmetric and asymmetric specimens, *Composites Science and Technology* 59(4). pp. 609-619.
- [6] Pereira, A.B., and A.B. de Moraes (2008). Mixed mode I and II interlaminar fracture of carbon/epoxy laminates. *Composites: Part A* 39. pp. 322-333.
- [7] Silva, A. and M.J. de Freitas (2003). Mixed-mode delamination growth of laminar composites by using three-dimensional finite element modeling. *Fatigue and Fracture of Engineering Materials and Structures* 26. pp. 543-549.
- [8] Mollon, V., J. Bonhomme, J. Vina, and A. Arguelles (2010). Theoretical and experimental analysis of carbon epoxy asymmetric dcb specimens to characterize mixed mode fracture toughness. *Polymer Testing* 29. pp. 766-770.

Hybrid Nano/Microcomposites for Enhanced Damage Tolerance

Isaac M. Daniel and Joel S. Fenner

Robert R. McCormick School of Engineering and Applied Science
Northwestern University
Evanston, IL 60208
imdaniel@northwestern.edu

ABSTRACT

The objective of this investigation was to develop, process, and test hybrid nano/microcomposites with nano-reinforced matrix and demonstrate an enhancement in thermomechanical properties, with emphasis on damage tolerance measured in terms of fracture toughness, impact damage, residual strength, and fatigue life. The material investigated was carbon fabric/epoxy with the matrix reinforced with multi-walled carbon nanotubes (CNTs). A solvent-based method with a dispersion enhancing block copolymer was used to prepare composites with and without CNTs. It was first shown that CNT reinforced composites have higher matrix dominated properties, such as compressive modulus and strength, in-plane shear modulus and strength, interlaminar shear strength, and interlaminar fracture toughness. The composite with 0.5 wt% of CNTs showed noticeably improved resistance to indentation damage by about 16 % and increased damage tolerance in terms of residual compressive strength by about 35 % over the composite without nanotubes. A significant enhancement was also shown under interlaminar fatigue testing with fatigue lives an order of magnitude longer than those of the reference material. The high increase in fatigue life was related to an increase in static interlaminar shear strength, the logarithmic dependence of the fatigue-life (S-N) curves, and an increase in interlaminar fracture toughness.

Introduction

Recent and ongoing research in nanoparticle-reinforced composites (nanocomposites) has shown significant enhancements in mechanical and other physical properties. In order to maximize the potential for scaled up industrial applications, such as wind turbine blades, it is desirable to incorporate the nanocomposite as a matrix in conventional continuous fiber composites to produce multiscale hybrid nano/microcomposites with enhanced properties, especially fracture toughness. Results obtained to date show enhancements in thermomechanical properties with some added functionalities by incorporating nanoparticles, such as carbon nanotubes, into the polymeric matrix of conventional fiber-reinforced composites [1-8].

Improvements in damage tolerance are expected from additional energy absorbing mechanisms introduced by the nanoparticles [2]. Addition of carbon nanotubes, for example, provides an additional source of energy absorption through nanotube pullout, stretching and fracture (Fig. 1). This behavior on the nanoscale is reflected in increased fracture toughness on the macroscale, improved impact damage tolerance, higher residual compressive strength, and extended fatigue life.

The objective of this study was to develop, process, and test hybrid multi-scale composite laminates and demonstrate and evaluate the enhancement in thermomechanical properties, with emphasis on fracture toughness, damage tolerance, and fatigue life.

Processing of Materials

The material investigated was carbon fabric/epoxy with the matrix reinforced with multi-walled carbon nanotubes (CNTs). The basic mechanical reinforcement was provided by a 5-harness satin carbon fabric perform (AS4 (AGP370-5H)). The matrix was an epoxy (DGEBA) reinforced with multi-walled carbon nanotubes (CNTs). These CNTs were 1 – 2 μm in length and 20 – 40 nm in outer diameter.

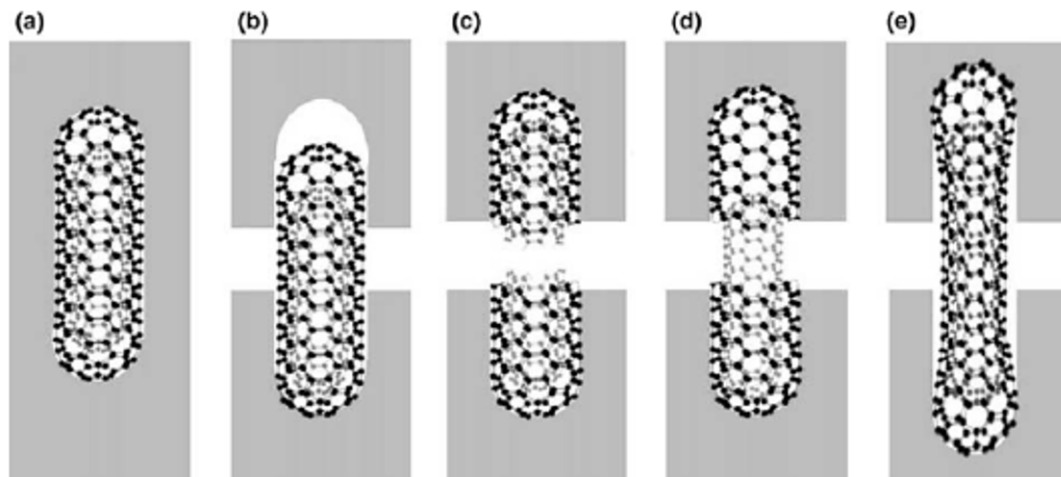


Figure 1. Possible energy absorbing mechanisms in CNTs. (a) initial state, (b) pullout following CNT/matrix debonding, (c) fracture of CNT, (d) telescopic pullout-fracture of outer layer and pullout of inner layer, (e) partial debonding and stretching [2].

A solvent-based method with a dispersion enhancing block copolymer was used as shown in Fig.2 [10, 11]. First, the block copolymer was dissolved in ethanol. CNTs were added to the solution, stirred and sonicated. A weighed amount of DGEBA was then added to the solution, followed by the hardener. After stirring, the ethanol was removed at an elevated temperature and the mixture was infused into the carbon fiber perform using a wet layup process. The impregnated preforms were placed in a vacuum oven to remove the ethanol. The prepreg layers were stacked and cured in the autoclave.

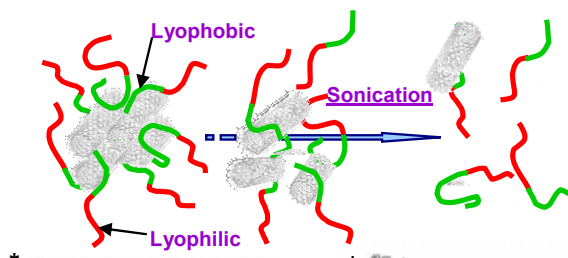


Figure 2. Process of CNT nanocomposite with dispersion enhancing block copolymer [10, 11].

Characterization

The neat and CNT- modified matrices were characterized by measuring their fracture toughness in both Modes I and II. The Mode I toughness was determined by means of a notched beam specimen under three-point bending (Fig. 3). The measured Mode I stress intensity factors for the neat resin and a nanocomposite with 0.5 wt% of CNTs, were

$$K_{Ic} (\text{neat resin}) = 0.79 \text{ MPa.m}^{1/2}$$

$$K_{Ic} (\text{nanocomposite}) = 0.95 \text{ MPa.m}^{1/2}$$

showing a 20 % increase for the nanocomposite. The calculated strain energy release rates for plane strain conditions, taking into account the increase in Young's modulus, are

$$G_{Ic} (\text{neat resin}) = 196 \text{ J/m}^2$$

$$G_{Ic} (\text{nanocomposite}) = 260 \text{ J/m}^2$$

showing a 33 % increase for the nanocomposite.

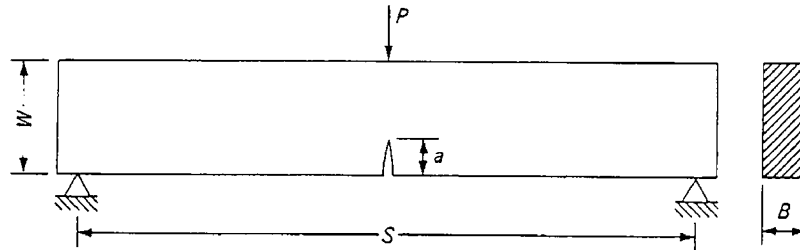


Figure 3. Three-point bending test of notched beam for determination of fracture toughness of neat resin and nanocomposite [13].

Properties relevant to energy absorption and damage tolerance in fiber composites are primarily the matrix dominated ones, such as the compressive modulus and strength, in-plane shear modulus and strength, interlaminar shear strength and fracture toughness. An example of mechanical enhancement in compressive strength as a function of CNT loading, with and without block copolymer dispersant, is shown in Fig. 4. It shows a nearly 40% increase in compressive strength for a 0.5 wt% CNT loading in the matrix with copolymer dispersant. The interlaminar shear strength was measured by means of short beam tests under three-point bending for the hybrid and the reference composite with and without the copolymer dispersant. An increase in interlaminar strength of approximately 15% was noted for the hybrid composite with 0.5 wt% CNTs and copolymer dispersant (Fig. 4).

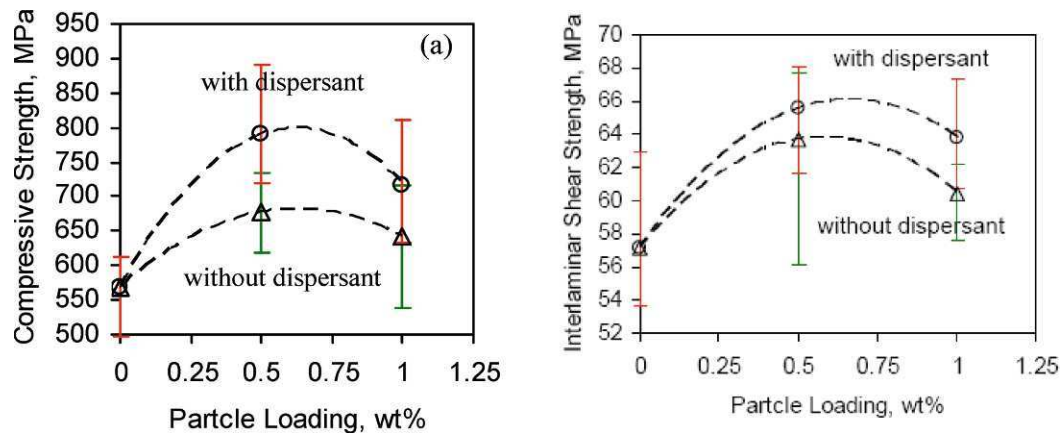


Figure 4. In-plane compressive and interlaminar shear strength of hybrid composite as a function of CNT concentration with and without block copolymer dispersant [10].

The Mode I energy release rate of the reference and hybrid composites was measured by means of the double cantilever beam (DCB) test [12]. Eight-ply laminates were prepared of the reference and hybrid composite with an embedded Teflon film strip along one edge. Coupons were machined so that the film strip served as a crack initiator at the loaded end of the beam. Figure 5 shows load-displacement curves obtained from such tests. Values of the interlaminar strain energy release rate were calculated by the area and compliance methods. It was found that the value for the hybrid composite was more than 100% higher than that of the reference composite.

Similar tests were conducted with end-notched flexure (ENF) beam specimens under three-point bending to determine the Mode II delamination fracture toughness [12]. Load-deflection curves obtained from these tests for the two composite materials tested are shown in Fig. 6. The strain energy release rates measured by these tests were:

$$G_{IIc}(\text{reference}) = 1080 \text{ J/m}^2$$

$$G_{IIc}(\text{hybrid}) = 1280 \text{ J/m}^2$$

a 36.5% increase for the hybrid composite

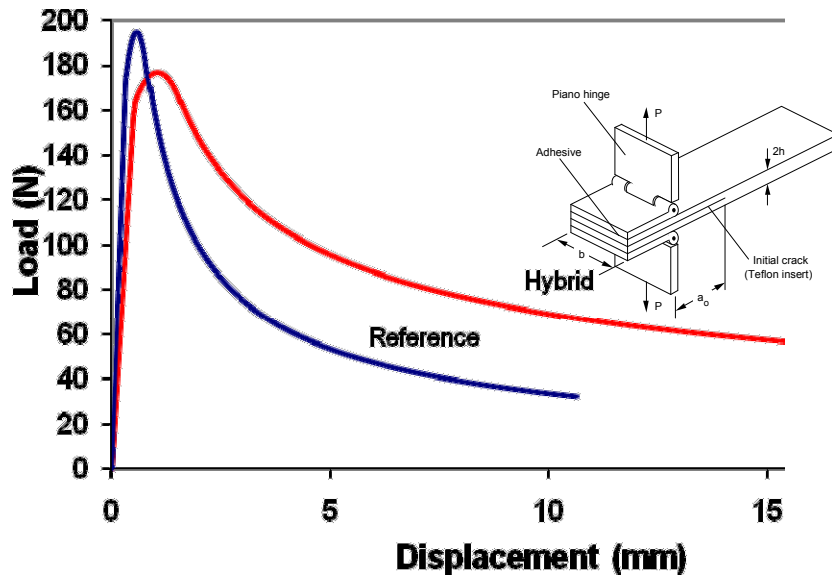


Figure 5. Load-displacement curves of DCB specimen for the reference and hybrid composites

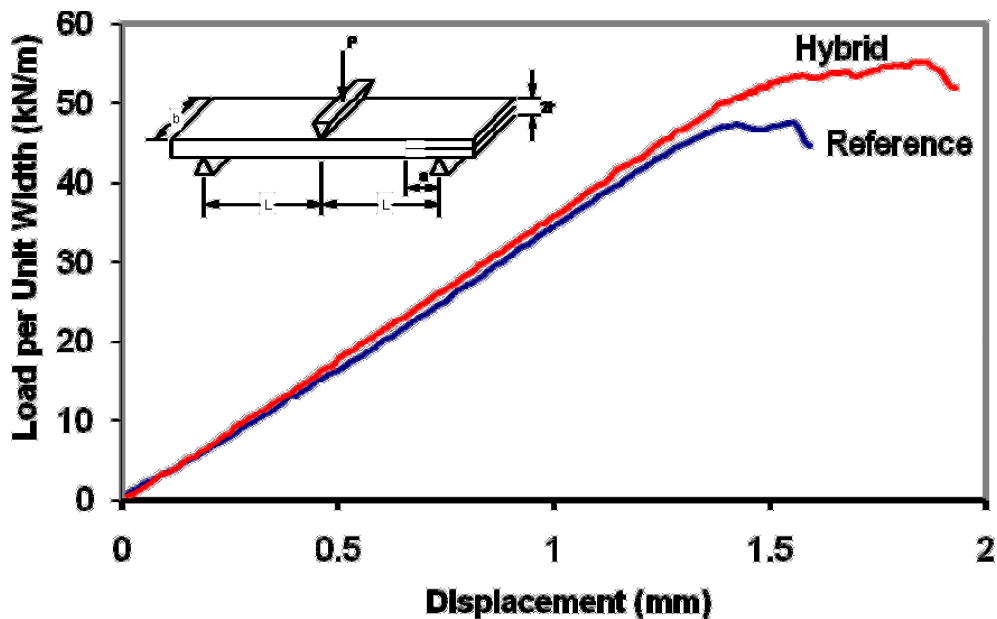


Figure 6. Load-deflection curves for end-notched flexure specimens of reference and hybrid composites

Resistance to Indentation Damage

Damage resistance of composites to a quasi-static indentation force is considered equivalent to low velocity impact damage. The indentation damage resistance of composites with and without CNTs was evaluated with the experimental set-up shown in [Figure 7](#). A ball indenter of 12.7 mm diameter was used for the test. Composite specimens 25.4 mm wide were supported on two steel rollers over a span length of 25.4 mm. Indentation testing was carried out at a machine crosshead rate of 0.127 mm/min until total indentation failure. Indentation displacement was measured with an extensometer mounted as shown in [Figure 7](#).

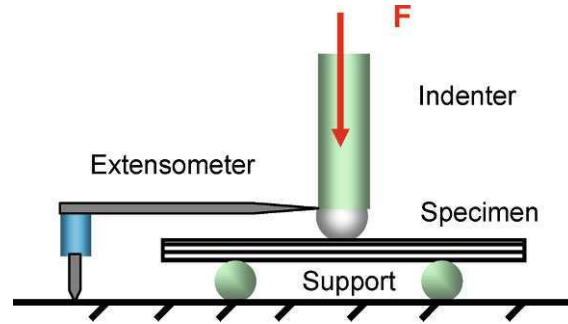


Figure 7. Experimental set-up for indentation damage resistance measurement.

Figure 8 shows typical indentation force-displacement curves of two composites with and without CNTs. There are two peaks in the figure. The first peak indicates damage initiation occurring on layers near the indented surface of the composite. The hybrid composites exhibited 13 % higher first peak load than the composite without CNTs. The second peak may be interpreted as the ultimate indentation resistance of the composite specimen. This indentation resistance was quantified by the energy absorbed in generating the damage. This energy was determined by integrating the indentation force-displacement curve. The indentation energy of the composite without CNTs was 4.4 J (average of four tests), and that of the hybrid composite was about 5.2 J, which represents a 16 % higher indentation damage resistance.

One generally accepted measure of impact, and by equivalence, indentation damage is the residual compressive strength following the damage. Following the indentation tests, direct compression tests to failure were conducted to determine the residual strength. These compression tests were conducted at a stroke rate of 0.254 mm/min. Figure 9 shows compressive stress-strain curves. It is seen that the compressive strength of the hybrid composite is about 35 % higher than that of the composite without CNTs, based on four tests. For a 4.4 J of applied indentation energy, the compressive strength of composites with and without CNTs was reduced by 69 % and 73 %, respectively.

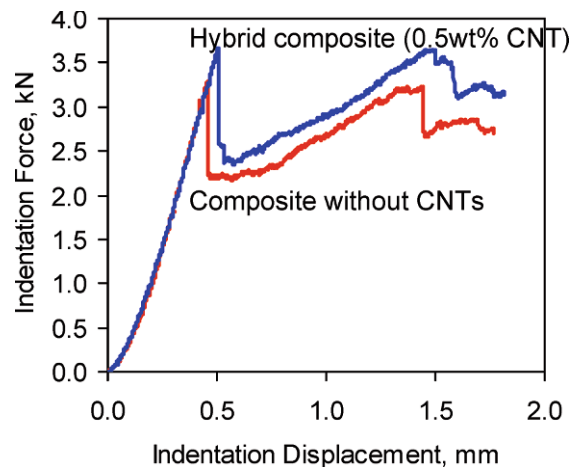


Figure 8. Indentation damage resistance; indentation force vs. displacement curves.

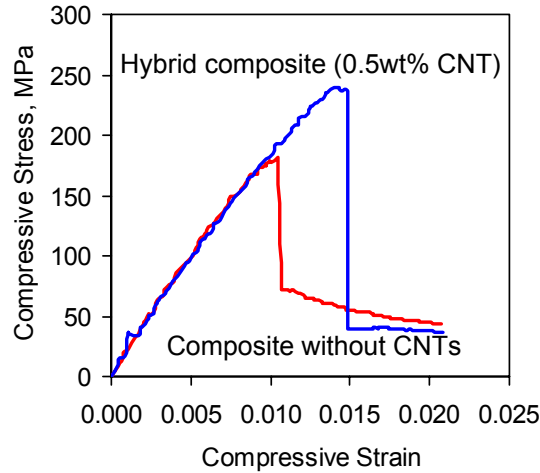


Figure 9. Compressive stress-strain curves of composites with/without CNTs after indentation.

Fatigue Behavior

Fatigue tests were conducted with short beams under cyclic three-point bending aimed at producing a cyclic interlaminar shear. Stress-life curves were produced for both the reference composite and the hybrid one containing CNTs. It can be seen that, at a given cyclic load amplitude, there is a significant difference of more than an order of magnitude in lifetimes between the two composite materials (Fig. 10). This can be attributed in part to a vertical shift due to the increased static interlaminar shear strength and in part to an increase in the Mode II interlaminar fracture toughness. The latter decreases the rate of material degradation during cyclic loading.

Guided by the Paris law, the experimental data were fitted by an empirical relation of the form

$$\sigma_{\max} = AN^{-1/m}$$

where σ_{\max} is the maximum cyclic stress, A is the static strength (at the first cycle), N the number of cycles to failure, and m a parameter related to the rate of material degradation. The parameters for the two materials tested were $A = 58.8$ MPa and $m = 20.47$ for the reference composite and $A = 66.2$ MPa and $m = 22.17$ for the hybrid composite. The difference in the stress parameter, A , is closely tied to the observed increase in static strength of the nanoparticle-enhanced material over the neat one. The difference in the slope parameter, m , is also significant, as it implies a more gradual fatigue life rate, resulting in further separation of fatigue life curves between the neat and nanoparticle-enhanced materials at higher numbers of cycles.

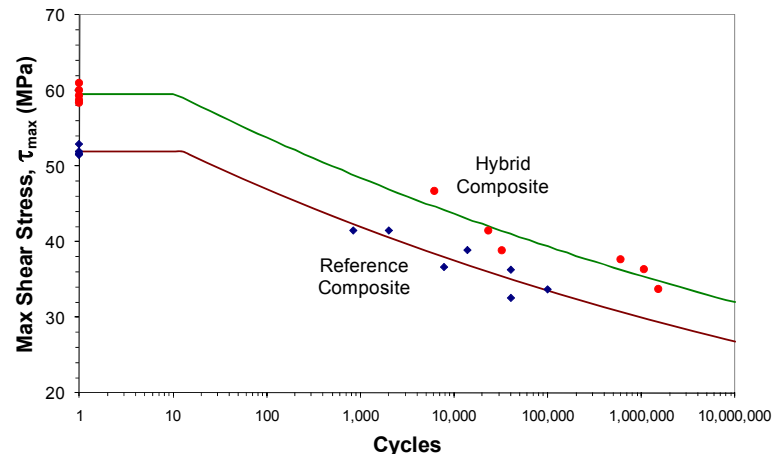


Figure 10. Stress-life curves for reference and hybrid composites under cyclic interlaminar shear

Conclusions

It was confirmed in this study that significant improvements in matrix dominated properties and energy absorption characteristics can be realized in hybrid nano/microcomposites with nano-reinforced matrix. It was demonstrated that such hybrid composites, with 0.5 wt% carbon nanotube reinforcement, have higher compressive and interlaminar shear strengths, higher delamination fracture toughness, increased indentation damage tolerance and residual strength. Composite laminates with 0.5 wt% of MWCNTs showed noticeably improved resistance to indentation damage by about 16 % and increased damage tolerance in terms of residual compressive strength by about 35 % over the composite without nanotubes. Fatigue lives extended by an order of magnitude.

References

- [1] Iwahori Y, S. Ishiwata, T. Sumizawa, and T. Ishikawa, "Mechanical properties improvements in two-phase and three-phase composites using carbon nano-fiber dispersed resin," *Composites Part A: Applied Science and Manufacturing*, **36**, 1430 (2005).
- [2] Gojny, F. H., M. H. G. Malte, B. Fiedler and K. Schulte, "Influence of different carbon nanotubes on the mechanical properties of epoxy matrix composites-A comparative study," *Comp. Scie. and Technology*, **65**, 2300-13 (2005).
- [3] Dean D, A. M Obore, S. Richmond, and E. Nyairo, , "Multiscale fiber-reinforced nanocomposites: Synthesis, processing and properties," *Composites Science and Technology*, **66**, 2135, (2006).
- [4] Subramaniyan A. K. and C. T. Sun, "Enhancing compressive strength of unidirectional polymeric composites using nanoclay," *Composites Part A: Applied Science and Manufacturing*, **37**, 2257 (2006).
- [5] Siddiqui, N. A, R. S. C. Woo, J. K. Kim, C. C. K. Leung and A. Munir, "Mode I interlaminar fracture behavior and mechanical properties of CFRPs with nanoclay-filled epoxy matrix," *Composites Part A: Applied Science and Manufacturing*, **38**, 449 (2007).
- [6] Cho J, J. Y Chen and I. M. Daniel, "Mechanical enhancement of carbon fiber/epoxy composites by graphite nanoplatelet reinforcement," *Scripta Materialia*, **56**, 685 (2007).
- [7] Qiu, J. J, C. Zhang, B. Wang and R. Liang, "Carbon nanotube integrated multifunctional multiscale composites," *Nanotechnology*, **18** (2007).
- [8] Bekyarova, E., E. T. Thostenson, A. Yu, H. Kim, J. Gao, J. Tang, H. T. Hahn, T. W. Chou, M. E. Itkis and R. C. Haddon, "Multiscale carbon nanotube-carbon fiber reinforcement for advanced epoxy composites," *Langmuir*, **23**, 3970 (2007).
- [9] Sun, L., R. F. Gibson, F. Gordaninejad and J. Suhr, "Energy absorption capability of nanocomposites: A review," *Composites Science and Technology*, **69**, 2392–2409 (2009).
- [10] Cho, J-M. and I. M. Daniel, "Reinforcement of carbon/epoxy composites with MWCNTs and dispersion enhancing block copolymer," *Scripta Materialia*, **58**, 533-536 (2008).
- [11] Daniel, I. M. and J-M. Cho, "Multiscale Hybrid Nano/Microcomposites-Processing, Characterization, and Analysis," Chapter 12, in R. Gilat and L. Banks-Sills (eds.), *Advances in Mathematical Modeling and Experimental Methods for Materials and Structures*, Springer, pp. 161-172, (2010).
- [12] Daniel, I.M. and O. Ishai, *Engineering Mechanics of Composite Materials*. 2nd ed. 2006, New York: Oxford University Press, Inc.
- [13] D2344/D2344M-00e1 AS. Standard Test Method for Short-Beam Strength of Polymer Matrix Composite Materials and Their Laminates. Annual Book of ASTM Standards 2002;15.03.

Drop-Weight Impact Studies of GLARE 5 Fiber-Metal Laminates

A. Seyed Yaghoubi, Y.X. Liu, B.M. Liaw

*Department of Mechanical Engineering, The City College of New York,
Convent Avenue and 138th Street, New York, NY 10031, USA*

ABSTRACT

Impact responses and damage induced by a drop-weight instrument on GLARE 5 fiber-metal laminates with different layup configurations and geometries were studied. The damage characteristics were evaluated using both the nondestructive ultrasonic and mechanical sectioning techniques. Only the contour of entire damage area could be obtained using ultrasonic C-scan whereas more details of damage were provided through the mechanical cross-sectioning technique. It was found that failure mode changed with varying stacking sequence. GLARE 5 made of unidirectional fibers had the worst impact resistance; followed by cross-ply and angle-ply configurations, while the quasi-isotropic lay-up showed the best resistance to impact. Finally, influence of different geometries was considered. The results show that by introducing circular geometry, damage patterns and impact behaviors were changed. This was especially apparent for panels with the quasi-isotropic layup configuration.

INTRODUCTION

GLARE 5 is a fiber-metal laminate (FML) made of alternating layers of 2024-T3 aluminum alloy sheets and S2-glass/epoxy laminates. FMLs combine the beneficial properties of metals and fiber-reinforced polymers, providing superior mechanical properties in comparison with conventional polymer matrix composites or aluminum alloys [1-3]. Liu et al. [4] investigated low velocity impact damage on ARALL 3 and various GLARE grades, i.e., GLARE 1, 2 and 3. They found that GLARE 1 with glass-epoxy prepreps possessed higher impact tolerance than ARALL 3 with aramid-epoxy prepreps. They also concluded that GLARE 3 with $[0^\circ/90^\circ]$ cross-ply glass-epoxy prepreps offered better impact resistance than GLARE 2, which is made of $[0_2]$ unidirectional glass-epoxy prepreps. Hitchen et al. [5] considered the effect of stacking sequence on impact damage in a carbon fiber-epoxy composite. They concluded that the stacking sequence influenced both the pre- and post-compression strengths and affected the impact damage in 16-ply carbon fiber toughened epoxy laminates. They also reported that the total delamination area was a function of the stacking sequence. Choi et al. [6] concluded that ply orientation and stacking sequence could significantly affect impact damage. They also found that impact damage was more sensitive to the change of stacking sequence than of thickness. The influence of lay-up configuration on graphite-epoxy composite material was studied by Guynn et al. [7]. They concluded that the difference in compression failure strain due to stacking sequence were small. Cantwell [8] studied geometrical effects in the low velocity impact response of GFRP. He drew a conclusion that tests on a range of circular and square plates had shown that the degree of damage within the structure was related to the force generated during the impact event.

In this study, the effect of stacking sequence and geometry were considered to evaluate the low velocity impact behavior of the GLARE 5 composite materials through drop weight tests. Optical imaging, ultrasonic C-scan and mechanical sectioning techniques were used to assess the impact damages.

EXPERIMENTAL PROCEDURES

All GLARE panels considered in this study consist of 2024-T3 aluminum alloy with a thickness of 0.305mm (0.012”) per layer and S2-glass/epoxy laminated layers, each with a thickness of 0.508 mm (0.020”). Each S2-glass/epoxy layer has a layup orientation according to [Table 1](#). Panels were cut into two different geometrical shapes: square and circular, with

dimensions of 101.6 mm x 101.6 mm (4" x 4") for the square specimens and 101.6 mm (4") in diameter for the circular specimens. The typical mechanical properties of constituents are described in Table 2 [9-11]. In Table 1, the term MVF represents metal volume fraction and is defined as the ratio of the sum of the thicknesses of all aluminum layers over the total thickness of the fiber-metal laminate [12]:

$$\text{MVF} = \frac{\sum t_{\text{aluminum}}}{t_{\text{FML}}} \quad (1)$$

Table 1. GLARE 5 panels tested in this study with different stacking sequences.

Lay-up Configuration (m/n)	Prepreg Plies & Orientation	Total Thickness	MVF
3/2	$[0_4]$ unidirectional	1.930mm (0.076")	0.474
	$[0^\circ/90^\circ/90^\circ/0^\circ]$ cross-ply		
	$[45^\circ/-45^\circ/-45^\circ/45^\circ]$ angle-ply		
	$[0^\circ/45^\circ/-45^\circ/90^\circ]$ quasi-isotropic		
The configuration notation <i>m/n</i> means the panel is composed of <i>m</i> aluminum-alloy layers interlaced with <i>n</i> fiber-reinforced epoxy layers.			

All impact tests were conducted using an Instron Dynatup 8250 pneumatic-assisted, instrumented drop-weight impact tester as shown in Fig. 1. The specimens were clamped circumferentially along a diameter of 76.2 mm (3") in the specimen fixture and impacted by a hemispherical steel impactor of diameter 16 mm with a mass of 6.14 kg. A pair of pneumatic breaks was also used to ensure no multiple strikes during impact test. The contact force history of impact was measured using a load cell located right above the impactor nose, and the impactor velocity was recorded by a pair of photoelectric-diodes attached to the base of the test machine. The time histories of the impactor position and the absorbed energy were obtained numerically by applying Newton's law and energy balance principle.

After each test, the specimen was carefully removed from the fixture for post-impact damage assessments. Figure 2 illustrates how the post-impact permanent central deflection was measured. Both nondestructive and destructive evaluation techniques were used to assess the impact damage inside the impacted panels. The impacted specimens were first scanned through an UltraPAC immersion ultrasound system for nondestructive damage evaluation, then carefully sectioned into two halves by a diamond saw through the impact center. Finally cross-sectional optical pictures were taken in order to reveal the more detailed damage inside the specimens. In this study a pair of 5 MHz ultrasonic transducers (one focused and another flat) in through-transmission mode was adopted to access the damage in the impacted specimens.

Table 2. Typical values of mechanical properties.

Mechanical property	Aluminum 2024-T3	UD S2 Glass/FM 94 Epoxy Prepreg
Tensile ultimate strength (MPa)	L 455	1900
	T 448	57
Tensile yield strength (MPa)	L 359	–
	T 324	–
Tensile modulus (Gpa)	L 72	54
	T –	9.4
Ultimate strain (%)	L 19	3.5
	T –	0.6
Compressive yield strength (MPa)	L 303	–
	T 345	–
Compressive modulus (GPa)	L 74	54.4
	T –	11
Density (g/cm ³)	2.79	2.00

The symbols, L and T, stand for longitudinal (the rolling direction for the metal) and transverse directions, respectively.

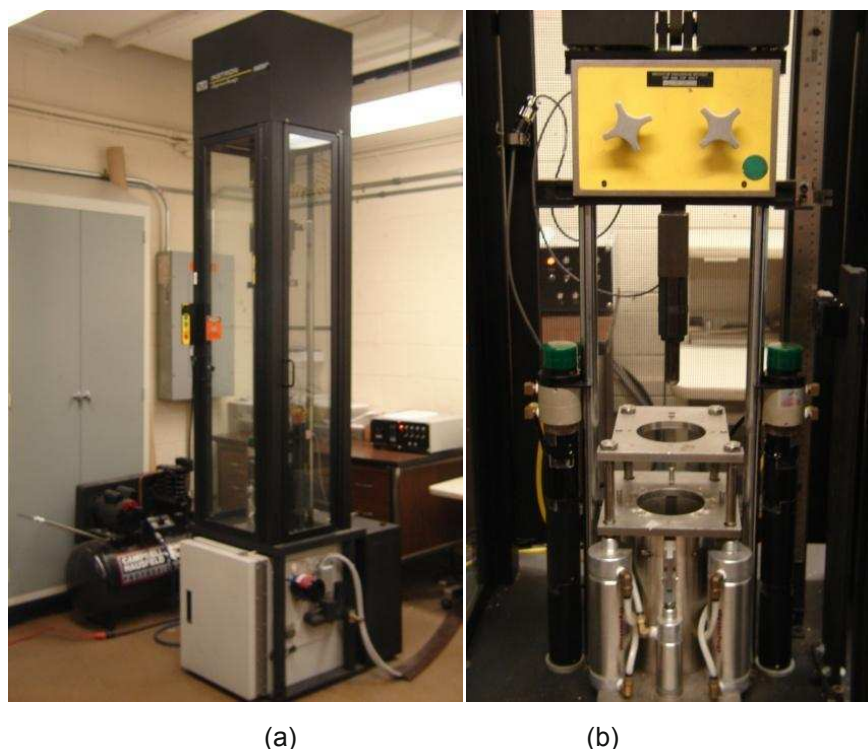


Figure 1. (a) Drop Weight impact tester, (b) The specimen fixture.

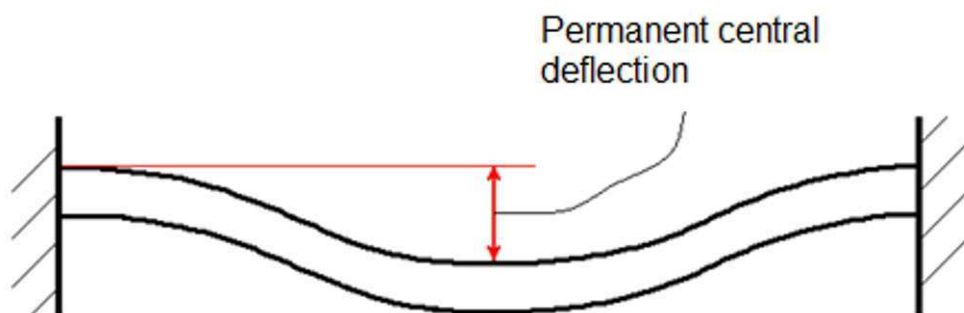


Figure 2. Measurement of the permanent central deflection.

RESULTS AND DISCUSSION

• SQUARE SPECIMENS

Stacking sequence effect was studied on GLARE 5 (3/2) specimens with different stacking sequences, namely: unidirectional, angle-ply, cross-ply and quasi-isotropic. Several drop-weight tests were conducted on GLARE 5 (3/2) with the cross-ply layup orientation, as a benchmark, in order to choose a proper impact energy to study and compare the impact responses and damage patterns of the GLARE 5 (3/2) of various stacking sequences. Based on the test results, 40J impact energy was chosen. Figure 3 shows the histories of absorbed energy, central displacement, contact force and contact stiffness for the square GLARE 5 (3/2) specimens with cross-ply $[0^\circ/90^\circ]_s$, unidirectional $[0^\circ_4]$, angle-ply $[+45^\circ/-45^\circ]_s$ and quasi-isotropic $[0^\circ/+45^\circ/-45^\circ/90^\circ]$ layup sequences. The corresponding C-scan results, back-side (non-impacted) views, as well as the cross-sectional views are shown in Figs. 4 and 5.

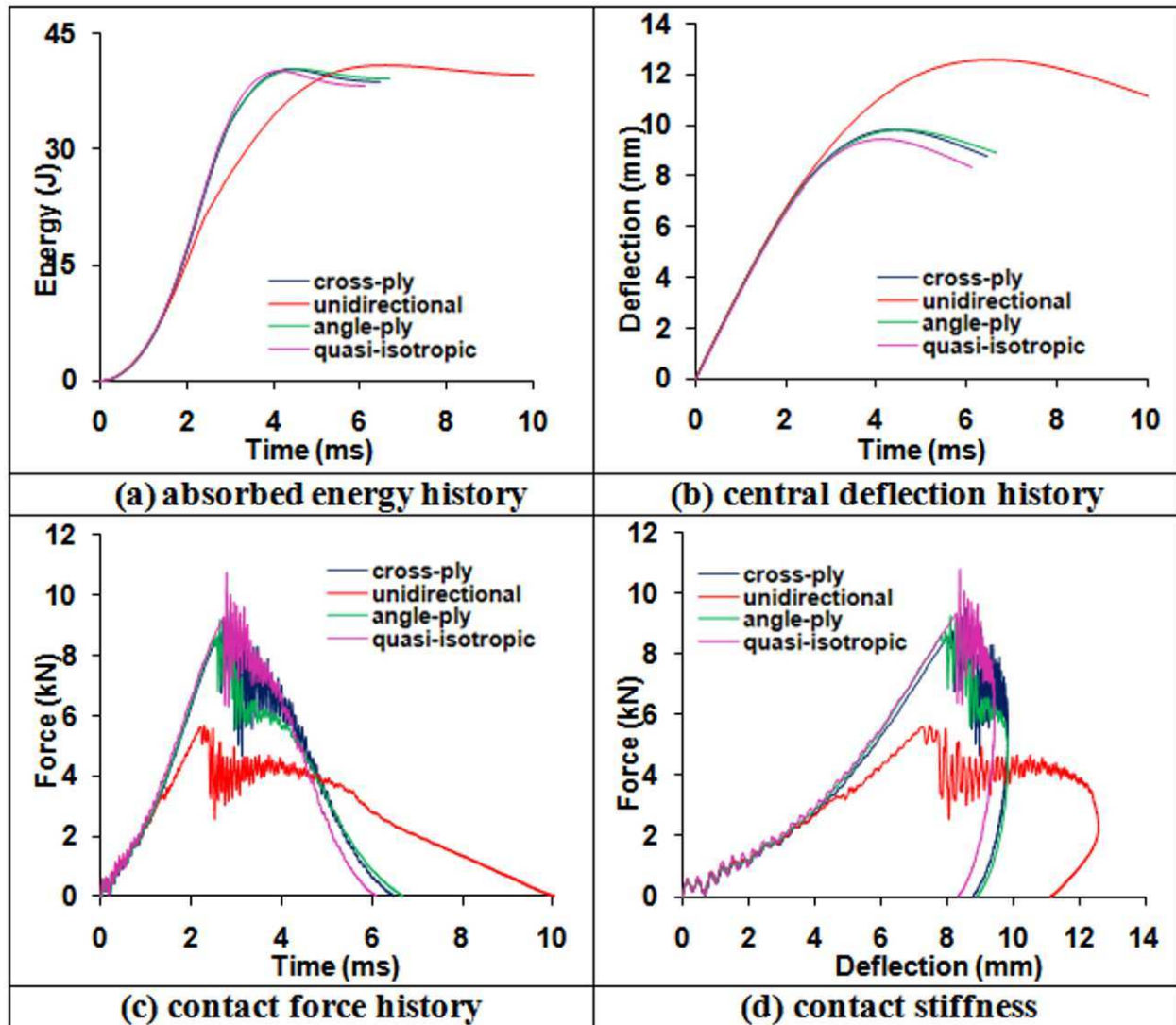


Figure 3. Impact responses of the cross-ply, unidirectional, angle-ply and quasi-isotropic GLARE 5 (3/2) square specimens under 40J impact energy.

The absorbed energy history revealed that under the same impact condition, unidirectional panel released less energy whereas quasi-isotropic panel released the most among the other type of panels. The peak value of central displacement history was the highest for the unidirectional panels while the lowest was for the quasi-isotropic panels. For the GLARE 5 (3/2) cross-ply and angle-ply, this peak was the same. Hence, the quasi-isotropic panels offered more resistance to the indentation than any other type of panels. The unidirectional panels were the worst panel to sustain the impact. By comparing the contact force histories, the unidirectional panels had the lowest peak contact force and the longest contact time duration. The quasi-isotropic panels offered the highest peak contact force among the other panel types. It is worth noting that although the patterns of contact force history for the GLARE 5 (3/2) panels with various layup configurations were similar, the damage patterns were different. From Fig. 3(d), it could be observed that contact stiffness curves started to deviate at time 1.16 ms, corresponding to 4.1 mm of the central deflection.

Mechanical-sectioning technique revealed that the major types of damage for the GLARE 5 (3/2) cross-ply panels were through-specimen crack, fiber breakage/splitting and delaminations (Figs. 4 and 5). The major delamination located between the non-impacted side aluminum layer and the adjacent glass-epoxy layer. Some small regional delaminations around the middle aluminum layer could also be found. A diamond-shaped damage zone was induced with major diagonal along 90°. For the unidirectional panels, long visible through-the-thickness cracks occurred, in which the cracks extended near the clamped edge. There was not much delamination besides fracture of aluminum layers and the splitting of the glass-epoxy

layers for the unidirectional panels. Since there was no bending stiffness mismatch in a unidirectional prepreg layer, no delamination was expected in the interface of the unidirectional prepreg layer. The fracture of aluminum in the non-impacted side resulted from bending while the stress concentration induced the crack in the impacted face. The damage zone observed from C-scan looked like a lip-shaped with the major axis aligned along the fiber direction. The damage pattern for the angle-ply panels was very close to the cross-ply panels except the damage contour for the angle-ply panels was smaller than the cross-ply panels (Fig. 4). Furthermore, from the C-scan results, the major diagonal, i.e. perpendicular to the fiber direction, was noticeably shorter for the angle-ply panels compared to the cross-ply panels. This means that the GLARE 5 (3/2) panels with the angle-ply stacking sequence resisted more to impact compared to the cross-ply lay-up with the same panel configuration. The reason for this is believed to be due to the fact that the angle-ply panels offered more shear stiffness than the cross-ply panels. For the quasi-isotropic panels, major damage were crack in the non-impacted side aluminum, damage in the bottom $[0^\circ/+45^\circ/-45^\circ/90^\circ]$ prepreg layer as well as significant delamination between the -45° and 90° layers. An approximately circular-shaped damage zone could be detected through ultrasonic C-scan for the quasi-isotropic panels. It is worth noting that under 40J impact energy, a visible crack appeared in all specimens on the non-impacted side. The crack was straight for the cross-ply, unidirectional and angle-ply GLARE 5 (3/2) specimens whereas it was not straight for the quasi-isotropic specimens.

Based on the discussion above, GLARE 5 (3/2) made of the unidirectional layup offered the worst impact resistance, followed by cross-ply and angle-ply layups, while quasi isotropic layup showed the best resistance to the impact. The reason for this is that the specimen stiffness decreased as layup configuration changed from quasi-isotropic layup to unidirectional. In other words, propagation of damage was alleviated and delayed as the bending stiffness mismatch decreased.

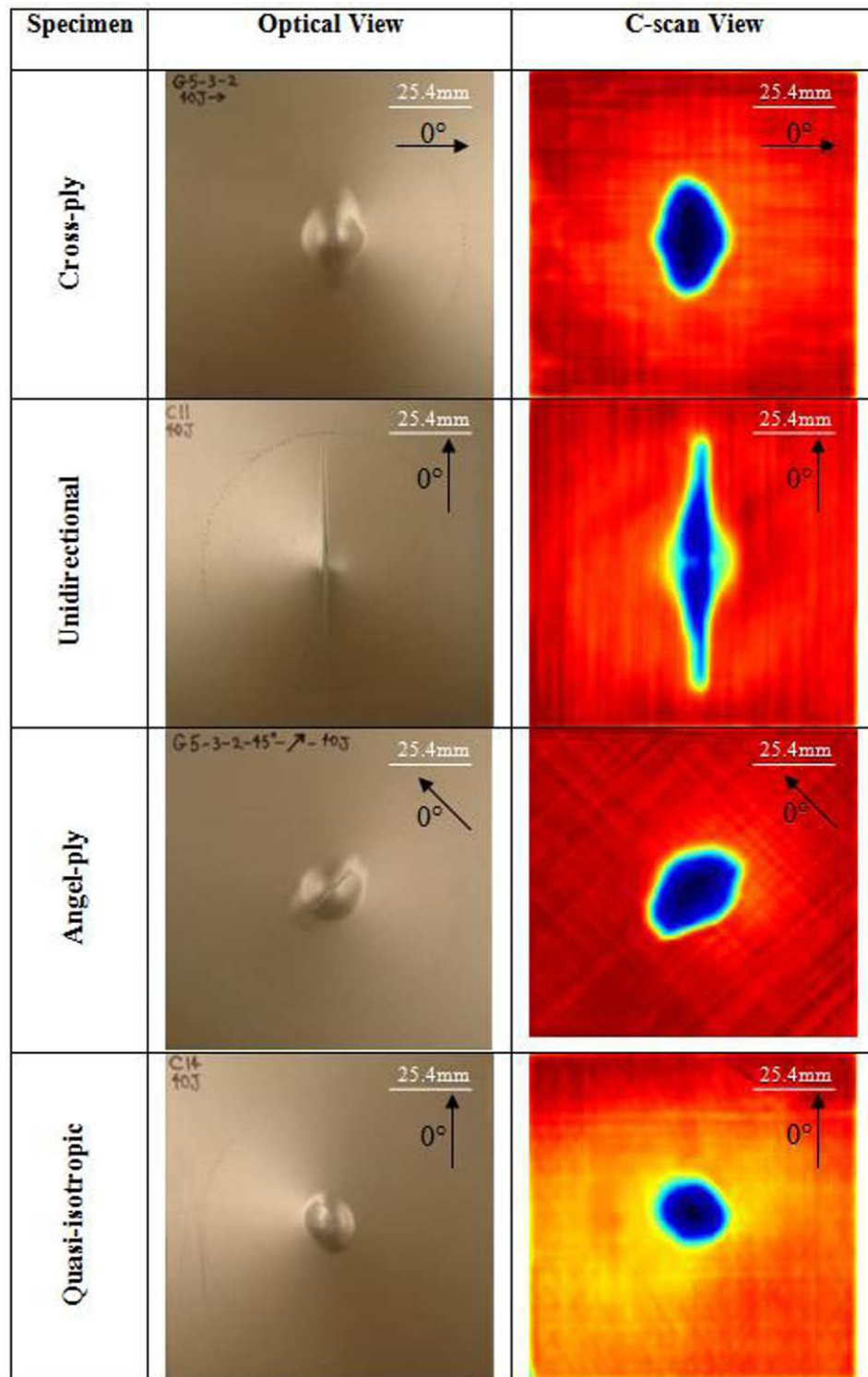


Figure 4. Back-side (non-impacted) view and corresponding C-scan view of the GLARE cross-ply, unidirectional, angle-ply and quasi-isotropic GLARE 5 (3/2) square specimens under 40J impact energy.

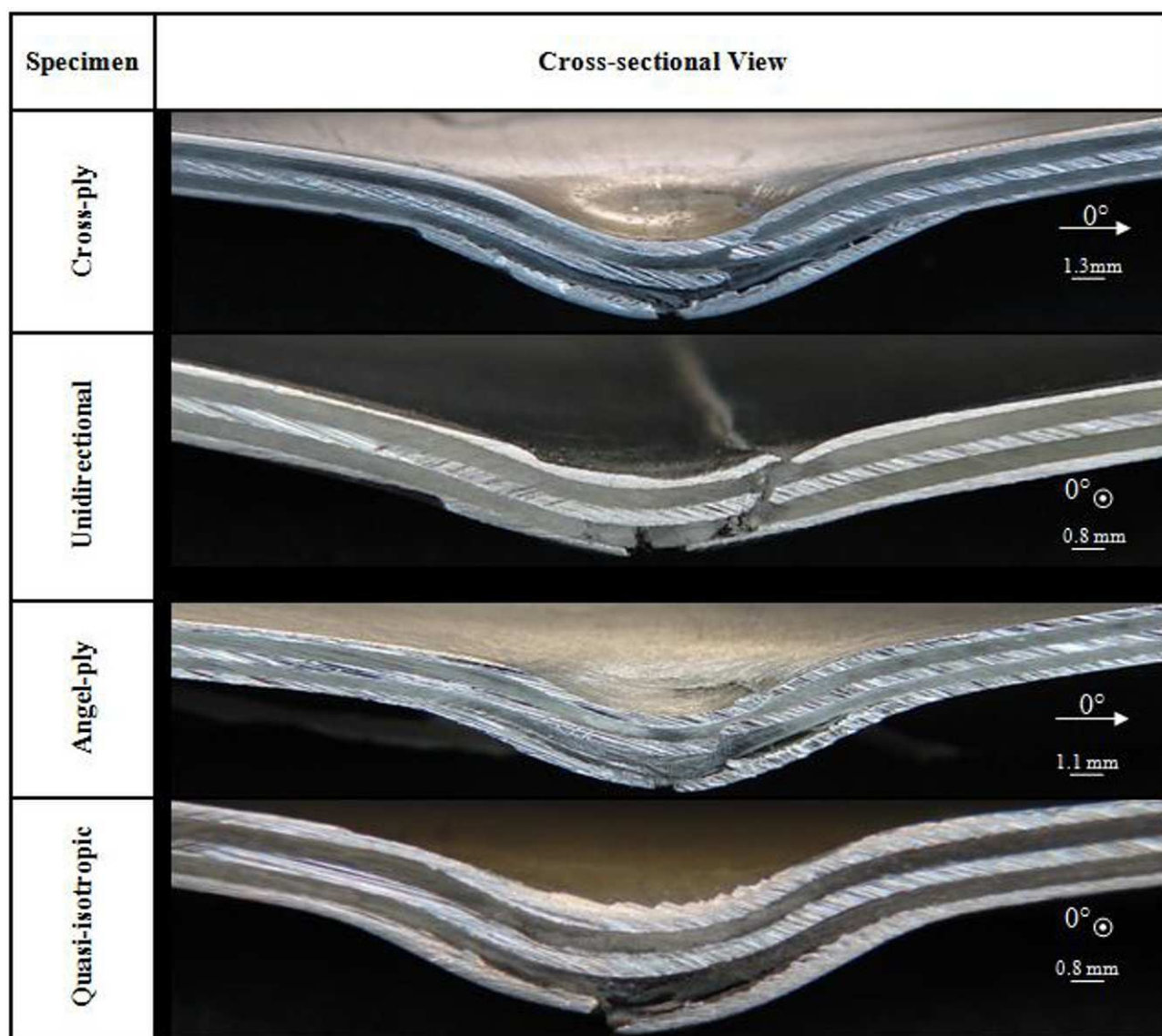


Figure 5. Cross-sectional view of the cross-ply, unidirectional, angle-ply and quasi-isotropic GLARE 5 (3/2) square specimens under 40J impact energy. The symbol \odot means that the fiber direction is perpendicular to the cross-sectional view picture.

• CIRCULAR VERSUS SQUARE SPECIMENS

Figure 6 shows histories of absorbed energy, central displacement, contact force, contact stiffness for the circular GLARE 5 (3/2) specimens with the cross-ply $[0^\circ/90^\circ]_s$, unidirectional $[0^\circ_4]$, angle-ply $[+45^\circ/-45^\circ]_s$ and quasi-isotropic $[0^\circ/+45^\circ/-45^\circ/90^\circ]$ layup sequences. Figures 7 and 8 depict corresponding C-scan results, back-side (non-impacted) views, as well as cross-sectional views of specimens of those configurations. Tables 3 summarizes experimental results of the impact-induced crack lengths measured on the impacted side (the top aluminum sheet) and the non-impacted side (the bottom aluminum sheet), respectively, along with the post-impact permanent central deflection in GLARE 5 (3/2) composite materials with different stacking sequences and geometries subjected to 40J impact energy. Comparing these results to those of the square specimens, the following remarks can be found.

The energy history curves were in a very close pattern to those of the square specimens. The central deflection curves for the circular unidirectional and quasi-isotropic specimens increased noticeably in comparison with the corresponding panels of

square specimens. This enhancement was very negligible for the cross-ply and angle-ply panels. The peak force values for the circular specimens were lower than those of the corresponding square specimens. The contact time was also raised by changing the geometry from square to circular. This difference was quite noticeable for the unidirectional and quasi-isotropic panels but it was relatively negligible for the cross-ply and angle-ply panels. The contact stiffness decreased by changing the geometry from square to circular. The effect of the above mentioned differences could be revealed by comparing the cross sectional, C-scan and back side views of the specimens with the ones for the square specimens. Comparing the cross-sectional views of the two different geometries for the cross-ply and angle-ply specimens, the overall damage patterns were similar except in circular geometry there was no debonding between the non-impacted aluminum and the adjacent prepreg layer. For the circular unidirectional specimen the induced damage pattern was different from the corresponding square specimen. Prepreg damages among the aluminum layers were noticeably increased. Also unlike the unidirectional square specimens, in which the prepreg close to the non-impacted side were broken into several pieces by through-the-thickness cracks, it did not happen for the circular specimen. The major differences in damage pattern were obvious for the circular quasi-isotropic specimen. By evaluating the cross-sectional views for the quasi-isotropic square and circular specimens, a dramatic change could be seen in the induced damages. Unlike the square specimen, which only the bottom aluminum damaged, all the aluminum layers failed for the quasi-isotropic circular specimen. It is worth noting that the impacted-side aluminum failed in two places. Another important difference was that the delamination was negligible for the circular specimens whereas it was relatively notable for the square specimens.

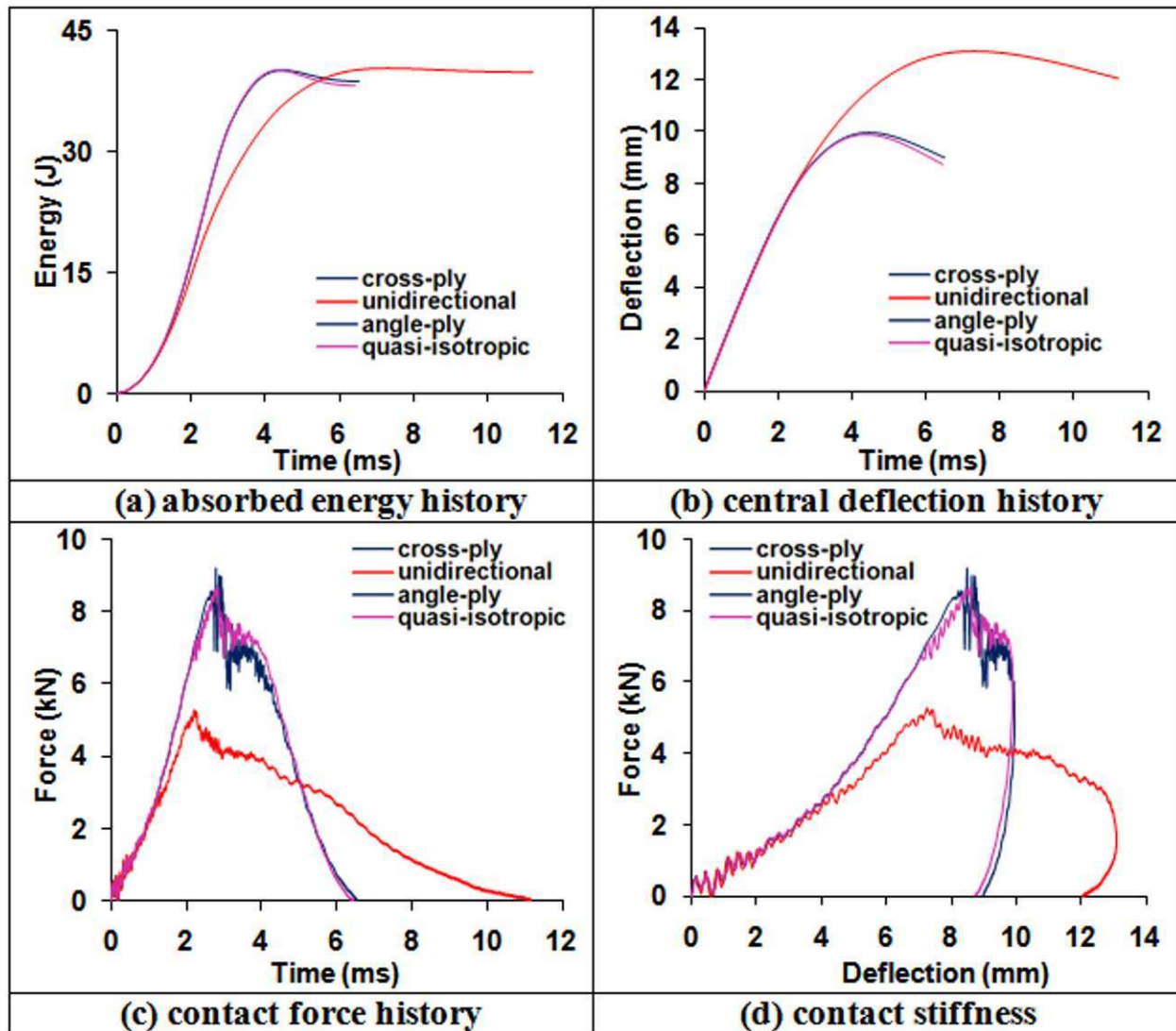


Fig.6. Impact responses of the cross-ply, unidirectional, angle-ply and quasi- isotropic GLARE 5 (3/2) circular specimens under 40J impact energy.

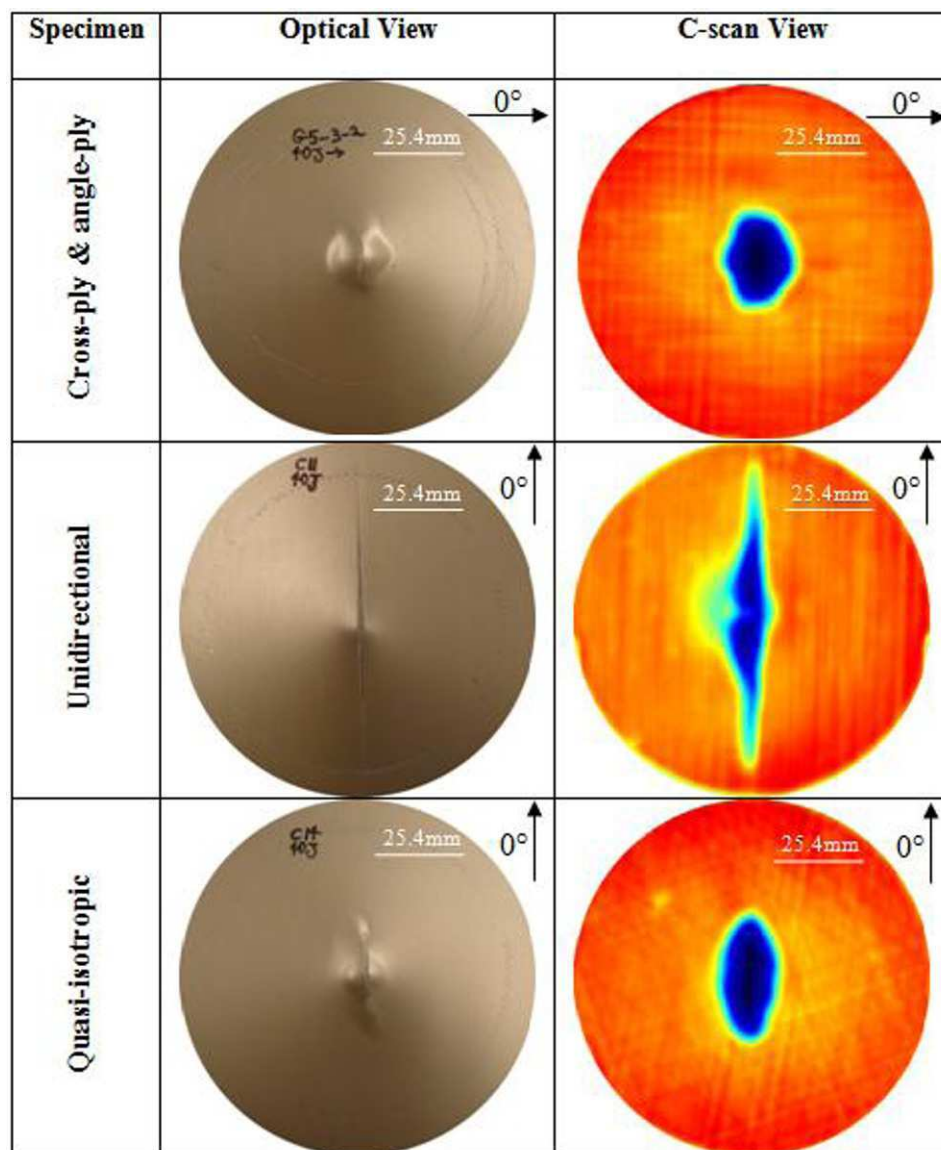


Fig.7. Back side (non-impacted) view and corresponding C-scan view of the cross-ply, unidirectional, angle-ply and quasi-isotropic GLARE 5 (3/2) circular specimens under 40J impact energy.

The C-scan results revealed that the damage contour decreased for the cross-ply and angle-ply circular specimens. For the unidirectional panels of the two geometries, the C-scan shapes were almost similar to each other with the exception that for circular geometry, the length of the damage along the 0° fiber direction was longer (Table 3, Figs. 4 and 7). In fact, the induced crack in the unidirectional circular specimens passed the grip area of the specimen. For the quasi-isotropic specimens, the crack at the non-impacted side of the circular specimen was noticeably longer than the square specimen. By transition from square to circular geometry, the damage contour changed from almost a circular shape to an elliptical shape with major axis along the 0° fiber direction. Due to change of the geometry, the central deflections were higher for the circular specimens compared to those of square specimens.

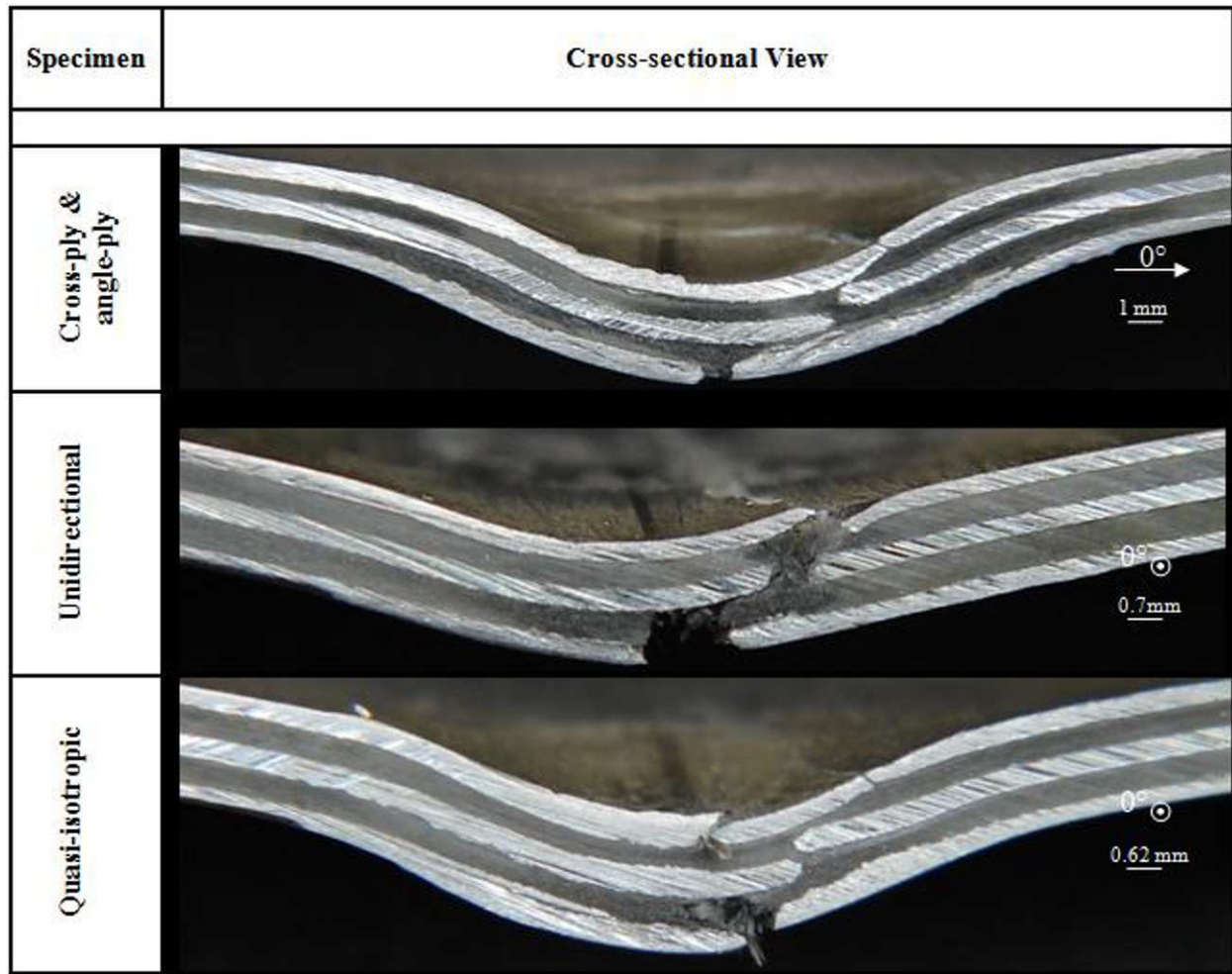










Fig.8. Cross-sectional view of the cross-ply, unidirectional, angle-ply and quasi-isotropic GLARE 5 (3/2) circular specimens under 40J impact energy. The symbol \odot means that the fiber direction is perpendicular to the cross sectional view picture.

Table 3. Crack lengths and permanent deflections of the cross-ply, unidirectional, angle-ply and quasi-isotropic GLARE 5 (3/2) under 40J impact energy.

Stacking Sequence & Geometry	Impact Energy (Joule)	Crack length in outer layer (mm)		Permanent Deflection (mm)
		Impacted side	None impact side	
Cross-ply 	40	9	18	6.75
Unidirectional 	40	69	75	7.65
Angle-ply 	40	7	16	6.65
Quasi-isotropic 	40	0	12	5.30
Cross-ply 	40	8.5	16	6.8
Unidirectional 	40	83	83	7.7
Angle-ply 	40	8.5	16	6.8
Quasi-isotropic 	40	7.5	20	5.80

CONCLUSIONS

This study presents an experimental investigation on the impact response of GLARE 5 (3/2) composite materials considering the effects of stacking sequence and geometry through using drop weight impact tester. The following remarks can be concluded from this study.

- GLARE 5 made of unidirectional fibers had the worst impact resistance; followed by cross-ply and angle-ply configurations, while the quasi-isotropic lay-up showed the best resistance to impact.
- By introducing circular geometry, damage patterns and impact behaviors were changed. This was very obvious for the panels with quasi-isotropic layup configuration, i.e. $[0^\circ/+45^\circ/-45^\circ/90^\circ]$.
- Only the profile of damage zone could be detected through the ultrasonic C-scan. The mechanical- sectioning technique must be adopted in order to get the details of damage inside the fiber-metal laminates. The drop-weight induced damage included indentation around impact center, delamination between aluminum and glass-epoxy composite, cracks in aluminum layers, and damage in composite layers. More severe damage occurred on the non-impacted side of fiber-metal laminates.

ACKNOWLEDGMENTS

This study was sponsored by NASA Faculty Award for Research (FAR) under Grant No. NAG3-2259 and by PSC-CUNY under Grants 61368-00 39 and 62209-00 40. Dr. Kenneth J. Bowles and Dr. John P. Gyekenyesi were the Technical Monitors of the NASA grant. Part of the equipment used in this investigation was acquired through Army Research Office Grant No. DAAD19-99-1-0366.

REFERENCES

1. Vlot, A., Glare-History of the development of a New Aircraft Material. Kluwer, Dordrecht: Kluwer Academic Publishers, 2001.
2. Vermeeren C.A.J.R., Beumler T., De Kanter, J.L.C.G., Van Der Jagt, O.C., Out, B.C.L., Glare design aspects and philosophies. Appl. Compos. Mater., 10, 257–276, 2003.

3. Lawcock G., Ye L., Mai Y.W., Novel fiber reinforced metal laminates for aerospace applications — a review: Part I — background and general mechanical properties. *SAMPE Journal*, 31, 23–31, 1995.
4. Liu Y., Liaw B., Effect of constituents and lay-up configuration on drop-weight tests of fiber-metal laminates. *Appl. Compos. Mater.*, 17 (1), 43-62, 2010.
5. Hitchen S.A., Kemp R.M.J., The effect of stacking sequence on impact damage in a carbon fiber/epoxy composite. *Composites*, 26, 207-214, 1995.
6. Choi H.Y., Wang H.S., Chang F.-K., Effect of laminate configuration and impactor's mass on the initial impact damage of graphite/epoxy composite plates due to line-loading impact. *Compos. Mater.*, 26 (6), 804-827, 1992.
7. Guynn E.G., O'Brien T.K., The influence of lay-up and thickness on composite impact damage and compression strength. AIAA-85-0646, Proceedings, 26th AIAA/ASME/ASCE/AHS Structures, Structural Dynamics, and Materials Conference. Orlando, FL., 1, 187-196, April 1985.
8. Cantwell W.J., Geometrical effects in the low velocity impact response of GFRP. *Compos. Sci. and Technol.*, 67, 1900-1908, 2007.
9. Data sheets. Aviation Equipment Structures, Inc., Costa Mesa, California, 1998.
10. QA Reports B0319B-2, B1008B-1, B0904A-3. Structural Laminates Company, New Kensington, Pennsylvania, 1994.
11. Alloy 7475 Plate and Sheet, ACRP-053-B. Alcoa Mill Products, Bettendorf, Iowa.
12. Vlot A., Gunnink J.W. (Eds.). *Fiber Metal Laminates, an Introduction*. Dordrecht, the Netherlands: Kluwer Academic Publishers, 2001.

Finite Element Modal Analysis of an Inflatable, Self-rigidizing Toroidal Satellite Component

M. Danesh Pazhooh, M.A. Dokainish, S. Ziada

McMaster University, Department of Mechanical Engineering, JHE 316, Hamilton, Ontario, Canada

ABSTRACT

Finite element analysis of an extremely flexible inflatable self-rigidizing torus (SRT) with regular pattern of hexagonal domes was carried out. Owing to the large number of hexagonal domes in the SRT, a simplified sub-structuring technique was proposed. In this method, each hexagonal dome was replaced with a statically equivalent flat hexagon with the same mass and stiffness as the hexagonal dome. Then the finite element modal analysis of the SRT was carried out for an equivalent torus made of flat film. The geometric nonlinearity and the effect of the follower load on the stiffness were included in the analysis. Natural frequencies and mode shapes determined by the finite element modal analysis were compared with those obtained from the earlier modal testing.

1. Introduction

The antenna design requirements for satellites drove their size to dimensions that could not be launched into space using current technology. This problem has introduced a revolutionary change in current satellite design. Instead of using large rigid antennas, new satellites may have inflatable ones. Inflatable satellites possess many advantageous properties such as ultra-lightweight, small stowage volume, high strength-to-mass ratio, low overall space program cost, on-orbit deployability, and low total system mass and deployment complexity [1].

The three main components of several gossamer communication or imaging satellites are inflatable struts, an inflatable torus as the structural support components and some sort of lens, aperture, or array housed inside the torus boundary. The circular or elliptical torus provides the boundary for any housed membrane or lens, and it ties together the satellite or craft supporting struts [2, 3]. While having many advantageous properties, the inflatable structures have additional challenges when compared to the rigid ones. Many traditional space structures have vibration problems. The harsh environment of space, i.e. intense temperature differentials and micrometeorite bombardment, most likely threatens the pressurized satellite components.

Addressing this issue, United Applied Technologies (Huntsville, AL, USA) has designed and manufactured a new thin film casting process for the toroidal satellite component. The membrane of the so called self-rigidizing torus, SRT, has a regular pattern of hexagonal domes. The inflated SRT, due to the additional stiffness provided by the pushed out hexagonal domes, can support its own structural shape even when there is no internal pressure.

The satellite structures are subjected to a variety of time-varying loadings, hence in order to design them, a study of dynamic behavior is important. The free vibration analysis is necessary in order to get the natural frequencies and mode shapes as basis for forced vibration analysis and control design.

Free vibration analyses of toroidal shells made out of flat sheets have been studied by many researchers [3-21]. While some experimental studies are available for the SRT [22-24], analytical structural dynamic studies of these types of structures lag behind the experimental one even for the inflatable pressurized smoothed-surface torus.

2. Self rigidizing torus

The structure, SRT, was an extremely flexible self-rigidizing inflatable torus, which ideally once inflated could support its own structural shape even when its internal pressure released. The 181cm ring diameter and 22 cm tube diameter torus was designed and manufactured at the United Applied Technologies (Huntsville, Alabama) of thin films of Kapton 300JP[®]. The flat 76 micrometers thin sheets of Kapton were formed into curved 46 micrometers thin films with regular pattern of hexagonal domes of 32.5 micrometers thickness, Fig. 1a. The top and bottom of the torus, which each were constructed from

seven joined segments at shear seams, were joined together at the inner and outer peel seams to form the complete torus, Fig. 1b. The "3M scotch-weld epoxy adhesive 2216 B/A translucent[®]" was used to join these 14 segments.

The physical properties of the SRT are listed in Table 1. The material properties of the Kapton 300JP[®] and the 3M scotch-weld epoxy adhesive 2216 B/A translucent[®] are listed in Table 2. The moduli of elasticity were measured at the Pulp of Paper Research Laboratory of McMaster University, Canada. Owing to the lack of first hand experimental data as well as manufacturer data, a Poisson's ratio of 0.34 was selected for both Kapton 300JP[®] and the epoxy.



Fig. 1 The self-stiffening inflatable torus, (a) Complete torus; (b) Peel and shear seams

Table 1 Geometric properties of the SRT

Property	Value
Film thickness	46×10^{-6} m
Ring radius	0.907 m
Tube radius	0.111 m
Average shear seam width	0.021 m
Average peel seam width	0.051 m
Average shear and peel seam thickness	2.88×10^{-4} m
Average overlapped shear and peel seam thickness	4.48×10^{-4} m
Hexadome width (major radius)	7×10^{-3} m
Hexadome height	3×10^{-3} m
Hexadome thickness	32.5×10^{-6} m
Gap between the adjacent hexadomes	1×10^{-3} m
Mass	0.560 kg

Table 2 Material properties

Parameter	Values
Kapton 300JP [®] Mass density, kg/m ³	1399.7
Kapton 300JP [®] Poisson's ratio	0.34
Kapton 300JP [®] Elastic modulus, GPa	2.98
Epoxy Mass density, kg/m ³	1042
Epoxy Poisson's ratio	0.34
Epoxy Elastic modulus, GPa	0.363

3. Finite element analysis

Due to the large number of hexagonal domes in the SRT shell, a simplified sub-structuring technique was used to replace each hexagonal dome with a statically equivalent flat hexagon with the same mass and stiffness as the hexagonal dome. Then the SRT was modeled by an equivalent torus with smooth surface. Such an approach combined accuracy and acceptable computational cost and made it possible to perform modal analysis of the structure using multi-purpose commercial software. This approach also allowed updating stiffness matrix and taking into account the large deformation under nonlinear static pressurization. Furthermore, the effect of the follower load on the stiffness was included in the analysis.

Using the commercial finite element software ANSYSTM, the 4 nodes SHELL181 element with six degrees of freedom at each node, translations in and rotations about the x, y, and z-axes, was used. SHELL181 was well suited for linear, large rotation and large strain nonlinear applications and suitable for analyzing thin to moderately thick-layered shell structures. It also accounts for the follower (load stiffness) effects of the distributed pressure.

The following steps were taken in the sub-structuring process. First, the geometry of one single hexagonal dome was built. This was done by pressurizing the central region of a hexagonal plate to match the actual dome shape. This step ended by updating the geometry of the model to form the hexagonal dome shape. Second, by modifying the thickness or density, a flat hexagon with the same width, mass and modulus of elasticity (Kapton 300JP[®]) of the hexagonal dome was selected. Third, through a tensile test and under a uniform displacement applied on the boundaries of models, the reaction forces of both hexagonal dome and hexagonal flat plate were calculated. The reaction forces were compared and the relative stiffness of the two models was calculated. Then, the stiffness of the SRT model was modified (changed) by the inverse ratio of the reaction forces of the hexadome to that of the flat plate. Thereafter, the SRT was modeled by a torus with smooth surface.

3.1. Equivalent Hexagonal Plate

In order to build the geometry of the dome, Table 1, a hexagonal plate with the major radius of 7.5 mm and thickness of 32.5 μm was constrained at a distant of 0.5 mm from each side. Hexagonal domes were separated from each other by 1mm flat film.

By applying sufficient normal pressure load on the plate, the un-constrained part of the hexagonal plate deformed to a dome shape with the desired height of 3 mm, as shown in Fig. 2. Then the geometry of the finite element model was updated to the deformed configuration.

In the sub-structuring process, each hexagonal dome was replaced with a statically equivalent flat hexagon of the same width, mass and stiffness. Three different flat hexagons with different thicknesses and densities were selected. First, a thickness of 32.5 μm (same as dome thickness) and then 46 μm (same as the SRT film thickness) was chosen. In both cases, in order to keep the mass constant, the density was modified. For the third case, the density was kept the same as of Kapton 300JP[®] and the thickness was modified. Thereafter, the tensile test modeling of the flat hexagons and the hexadome was undertaken. Their sides were stretched for an arbitrary uniform displacement of 0.01mm, as illustrated in Fig. 3.

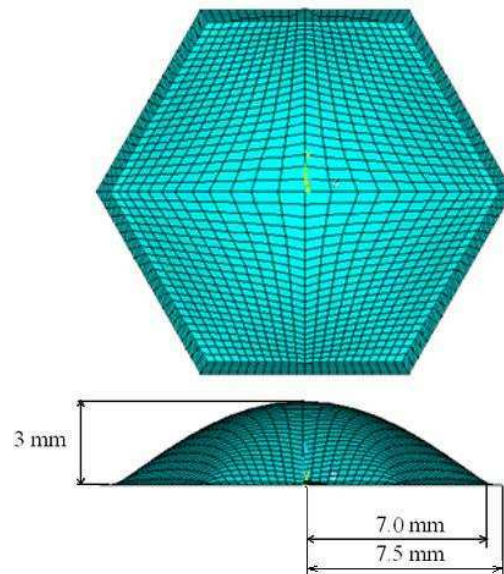


Fig.2 A hexadome

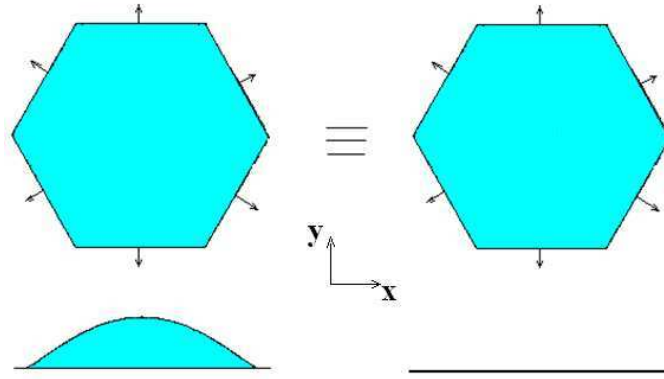


Fig. 3 Schematic of tensile test of hexadome and equivalent hexagon

Table 3 Reaction forces

Flat hexagon thickness (μm)	Flat hexagon density (kg/m^3)	$F_{flat_hexagon} _x$ (N)	$F_{hexadome} _x$ (N)	$F_{flat_hexagon} _y$ (N)	$F_{hexadome} _y$ (N)
32.5	1707	1.4670	0.1567	0.84492	0.0907
39.65	1399.7	1.7897	0.1567	1.0308	0.0907
46	1206	2.0764	0.1567	1.1959	0.0907

Table 4 Stiffness ratios

Flat hexagon thickness (μm)	Flat hexagon density (kg/m^3)	$\frac{E_{flat_hexagon}}{E_{hexadome}}$
32.5	1707	9.34
39.65	1399.7	11.39
46	1206	13.22

The thickness and density of the three cases as well as the reaction forces in the x and y directions on the boundary lines are listed in Table 3. Considering the fact that the displacement boundary conditions were equal, the ratio of reaction force to modulus of elasticity of both cases should have been equal. This ratio for the flat hexagon with the thickness of 32.5 μm in the x and y direction was found to be 9.362 and 9.315, respectively, with the average of 9.34. This means that the flat hexagon was 9.34 times stiffer than the hexadome. Henceforth, the torus with hexagonal dome could be simulated with a torus having a flat surface pending that the modulus of elasticity of the Kapton 300JP[®] film was reduced 9.34 times. This ratio for a 39.65 μm and 46 μm thick flat hexagons was 11.39 and 13.22, respectively. These ratios are listed in Table 4.

3.2. Finite element modal analysis of self-rigidized torus

In the vibration analysis of an inflated structure, the direct action of the pressure force, which is in addition to the pre-stress' effects, and accurate geometric nonlinearities was also considered. The finite element modal analysis was carried out based on the following assumptions:

1. a linear elastic and isotropic properties was assigned,
2. the internal pressure of 149.3 Pa (1.5 mm Water) equal to that used in the modal experiment study was applied to the torus and assumed to be constant during the static and modal FEA analyses,
3. geometric nonlinearity (large strain) was considered during the pre-stress analysis,
4. the effect of the follower load on the stiffness was included,
5. except for the internal pressure load, the other effects of the enclosed gas are ignored,
6. the effect of air damping was disregarded,
7. Free-free boundary conditions were considered.

Using the commercial finite element software package ANSYS[™], and SHELL181 element, a two-step approach was undertaken. First, a nonlinear static pressurization resulted in an updated stiffness matrix that took into account the large

deformation. Thereafter, through a restart procedure, the updated stiffness matrix was imported to a linear modal analysis section.

The geometry of the SRT and the material properties of Kapton 300JP[®] and 3M scotch-weld epoxy adhesive 2216 B/A translucent[®] were adopted from [Tables 1](#) and [2](#), respectively. The modulus of elasticity of the shear seam and peel seam was 1.35 GPa. For the section with the overlapped shear and peel seams, the modulus of elasticity was 0.966 GPa.

Once the modal analysis was carried out, it was observed that bonded regions added locally distributed masses to the structure and had higher stiffness than that of the toroidal membrane, which had to be accounted in the modeling of the torus, as well. The flaps constituted 35.5% of the SRT's total mass. When the peel seams, as shown in [Fig. 1.b](#), were added to the model, it was observed that numerous low frequency local modes of the flaps obscured the torus' modes of interest. Hence, for comparison purposes, two different models were developed. First, the peel seams (flaps) were added to the model and modal analysis was carried out. Second, instead of adding the peel seams to the model, structural mass elements MASS21 with the mass equal to the mass of the flaps were used at the nodes shared by the peel seams and the torus. That is, the mass of each peel seam, inner and outer, was distributed equally on the corresponding seam's nodes by the structural mass element.

Modal analysis was carried out for the three different combinations of thickness and density listed in [Table 3](#). Since the boundary conditions of the inflated torus were assumed free-free, the free vibration analysis should result in rigid-body motions. The present FEA study resulted in six approximately zero frequencies corresponding to six rigid body modes. This verifies that the element type is properly selected. Finite element analysis carried out by other researchers for an inflatable torus could not obtain six zero natural frequencies associated with the six rigid-body modes [16].

The mode shapes were mainly in two categories of in-plane and out of plane modes. The out of plane mode shapes resembled the bending modes of a free-free beam. In the in-plane mode, the structure symmetrically bended in plane of the torus and vibrated by making oval, triangular, square and pentagon shape for the first four modes, respectively. Both the in-plane and out of plane modes were obtained in pairs. The frequencies for both cases of lumped mass and peel seams are listed in [Tables 5 to 8](#) for the in-plane and out of plane modes, respectively. All three combinations of density and thickness resulted in the same frequencies and sequence of mode shapes.

Table 5 Frequencies for the in-plane modes for lumped mass application

Mode number	Frequency (Hz)		
	Thickness 32.5 μ m	Thickness 39.65 μ m	Thickness 46 μ m
1	3.54	3.54	3.54
2	7.66	7.67	7.67
3	9.90	9.91	9.92
4	11.23	11.25	11.26

Table 6 Frequencies for the in-plane modes for peel seam application

Mode number	Frequency (Hz)		
	Thickness 32.5 μ m	Thickness 39.65 μ m	Thickness 46 μ m
1	4.00	4.00	4.00
2	9.76	9.76	9.77
3	15.98	15.99	16.00
4	24.26	24.27	24.27

Table 7 Frequencies for the out of plane modes for lumped mass application

Mode number	Frequency (Hz)		
	Thickness 32.5 μ m	Thickness 39.65 μ m	Thickness 46 μ m
1	3.91	3.91	3.91
2	9.36	9.36	9.36
3	13.73	13.73	13.73
4	17.19	17.20	17.20

Table 8 Frequencies for the out of plane modes for peel seam application

Mode number	Frequency (Hz)		
	Thickness 32.5 μ m	Thickness 39.65 μ m	Thickness 46 μ m
1	3.60	3.63	3.65
2	11.26	11.36	11.46
3	15.77	15.79	15.82
4	19.06	19.09	19.11

By comparing the two cases of lumped mass and peel seams, we conclude that except for the first out of plane mode, the frequencies of the model with flaps are higher than the corresponding model with lumped mass. This means that the model with the flaps is stiffer than the model with no flaps. Adding the flaps increased the stiffness of the torus mainly in the in-plane direction, affecting the in-plane mode frequencies more than the out of plane ones. For the case of lumped mass, the mode shapes for the first four in-plane and out of plane modes are shown in Figs. 4 and 5. By reviewing the natural frequencies, one can conclude that the natural frequencies of the torus came in clusters.

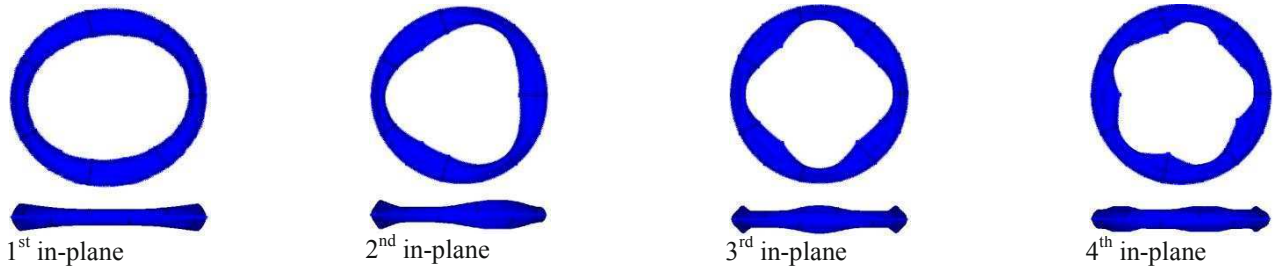


Fig. 4 The first four in-plane mode shapes

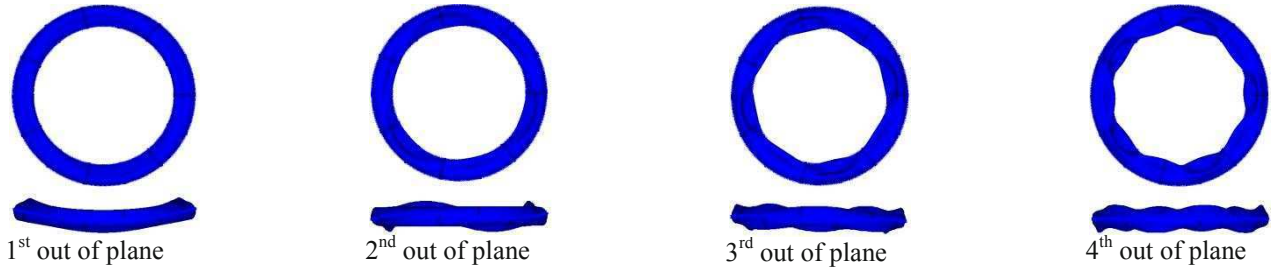


Fig. 5 The first four out of plane mode shapes

4. Discussion

The modal testing of the SRT model was recently studied [24]. Overall, a satisfactory agreement was found between the experimentally measured frequencies and those predicted in the finite element approach, Tables 9 and 10. The results indicate that in the out of plane direction, the FE models are slightly stiffer than the experimental model. While in the in-plane direction, except for the first mode, the experimental model is stiffer than the FE model with the lumped mass and is softer than the model with flap.

A few sources of discrepancies could be indentified in this approach explaining the aforementioned differences between experimental and predicted frequencies. In the modal testing, since maintaining the internal pressure was done manually, it is less likely to achieve the same pressure at all times. Variable pressure contributes to variable stiffness which alters the modal parameter of the structure. Owing to presence of very small punctures in the SRT, the air leakage made the distribution of pressure non-uniform in the torus. In the finite element model, the pressure was assumed to be constant in the entire torus.

Table 9 Frequencies for the in-plane modes

Frequencies (Hz)		
Experiment [24]	Lumped mass	Peel seams (flaps)
4.68 / 6.07	3.54	4.00
8.43 / 9.46	7.66	9.76
13.3	9.90	15.98
17.2	11.23	24.26

Table 10 Frequencies for the out of plane modes

Frequencies (Hz)		
Experiment [24]	Lumped mass	Peel seams (flaps)
3.21	3.91	3.60
8.12	9.36	11.26
12.8	13.73	15.77
17.5	17.19	19.06

Owing to the extremely small values of the film thickness, any increase in the thickness significantly affects the stiffness and mass of the structure and eventually the eigenvalues. For example, the average seams' thickness was above six times the shell film thickness. Furthermore, the method of fabrication, as well as the extensive repair that was done on the flaps, resulted in variations of the thickness of the joined regions. This contributed to non-uniform stiffness and mass distribution in both the torus and the flaps, affecting the modal parameters of the SRT. The flaps were not completely flat and had wrinkles at various locations. In the finite element study, the flaps were assumed to be flat with a uniform thickness equal to the average thickness of the inner and outer flaps.

To reduce the effect of the air tube's mass (to inflate the torus) on the SRT, the tube was suspended from a stand. However, since the plastic air tube was not soft enough, it might have constrained the torus which was not modeled in the finite element analysis.

In the modal testing, the torus was suspended at six points from the ceiling by very soft and long springs. The suspension frequencies were less than ten percent of the first natural frequency, 3.21 Hz, and should not affect the modal parameters directly. Though at the six suspension points, the outer flaps were inverted upward and their shape did not stay flat as it was assumed in the finite element analysis. These local deformations of flaps altered the stiffness of the structure and could affect the modal parameters.

While during the experiments all the air ventilation ducts of the lab were blocked and the air condition was turned off, still the effect of the air current disturbance over the SRT was observable. This disturbance and the effect of the air damping might be another cause of discrepancy between the experimental and predicted results. The impact of air current and damping were not included in the model. The uncertainty in the material properties might be another source of discrepancies.

Acknowledgments

Mitra Danesh Pazhooh would also like to thank NSERC for the scholarship.

References

- [1] Ruggiero, E.J., Jha, A., Park, G. and Inman, D.J., A Literature Review of Ultra-Light and Inflated Toroidal Satellite Components, The Shock and Vibration Digest, Vol.35, No.3, pp. 171-181, 2003.
- [2] Griffith, D.T., Main, J.A., Experimental Modal Analysis and Damping Estimation for an Inflated Thin-Film Torus, Journal of Guidance, Control, and Dynamics 25 (4), pp. 609-617, 2002.
- [3] Lewis, J.A., Inman, D.J., Finite Element Modeling and Active Control of an Inflated Torus Using Piezoelectric Devices, Journal of Intelligent Material Systems and Structures 12, pp. 819-833, 2001.
- [4] Jordan, P. F., Stresses and Deformations of Thin-Walled Pressurized Torus, Journal of Aerospace Science, Vol. 29, pp. 213-225, 1962.
- [5] Reissner, E., On Stresses and Deformations in Toroidal Shells of Circular Cross-Section Which Are Acted upon by Uniform Normal Pressure, Quarterly of Applied Mathematics, Vol. 21, 177, 1963.

- [6] Sanders, J. L., and Liepins, A. A., Toroidal Membrane under Internal Pressure, *AIAA Journal*, Vol. 1, No. 9, pp. 2105–2110, 1963.
- [7] Liepins, A. A., Flexural Vibrations of the Pres-stressed Toroidal Shell, NASA CR-296, September, No. 10, 1965.
- [8] Liepins, A. A., Free Vibrations of Pre-stressed Toroidal Membrane, *AIAA Journal*, Vol. 3, No. 10, pp. 1924–1933, 1965.
- [9] Jordan, P. F., Vibration and Buckling of Pressurized Torus Shells, in 4th Aerospace Science Meeting, Los Angeles, CA, AIAA Paper No. 66-445, 1966.
- [10] Jordan, P. F., Vibration Study of a Pressurized Torus Shell Part I – Experimental Study, NASA CR-884, 1967.
- [11] Liepins, A. A., Vibration Study of Pressurized Shell Part II-Development and Applications of analysis, NASA CR-885, 1967.
- [12] Colbourne, J. R., and Flügge, W., The Membrane Theory of the Toroidal Shell – A Singular Perturbation Problem, *International Journal of Nonlinear Mechanics*, Vol. 2, pp. 39–53, 1967.
- [13] Saigal, S., Yang, T. Y., Kim, H. W., and Soedel, W., Free Vibration of a Tire as a Toroidal Membrane, *Journal of Sound and Vibration*, Vol. 107, No. 1, pp. 71–82, 1986.
- [14] Leonard, J. W., *Tension Structures: Behavior and Analysis*, McGraw-Hill, New York, 1988.
- [15] Leigh, L., Hamidzadeh, H., Tinker, M. L., and Slade, K. N., Dynamic Characterization on an Inflatable Concentrator for Solar Thermal Propulsion, in 42nd AIAA/ASME/ASCE/AHS/ASC Structures, Structural Dynamics, and Materials Conference and Exhibit, Seattle, WA, March 15–19, 2001.
- [16] Jha, A.K., Vibration Analysis and Control of an Inflatable Toroidal Satellite Component Using Piezoelectric Actuators and Sensors, PhD Thesis, Virginia Polytechnic Institute and State University, Blacksburg, Virginia, 2002.
- [17] Jha, A. K., Inman, D. J., and Plaut, R. H., Free Vibration Analysis of an Inflated Torus, *Journal of Vibration and Acoustics*, Vol.124, pp. 387–396, 2002.
- [18] Park, G., Sausse, M., Inman, D.J., and Main, J.A., Vibration Testing and Finite Element Analysis of an Inflatable Structure, *AIAA JOURNAL*, Vol. 41, No. 8, pp. 1556-1563, 2003.
- [19] Ruggiero, E.J., Jha, A., Park, G. and Inman, D.J., A Literature Review of Ultra-Light and Inflated Toroidal Satellite Components, *The Shock and Vibration Digest*, Vol.35, No.3, pp. 171-181, 2003.
- [20] Jha, A.K, and Inman, D.J, Optimal Sizes and Placements of Piezoelectric Actuators and Sensors for an Inflated Torus, *Journal of Intelligent Material Systems and Structures*, Vol.14, pp. 563-576, 2003.
- [21] Jha, A. K. and Inman, D. J., Importance of Geometric Non-linearity and Follower Pressure Load in the Dynamic Analysis of a Gossamer Structure, *Journal of Sound and Vibration*, Vol.278, pp. 207–231, 2004.
- [22] Ruggiero, Eric J; Tarazaga, Plablo A.; Inman, Daniel J., Modal Analysis of an Ultra-Flexible, Self-Rigidizing toroidal Satellite Component, *Proceeding of IMECE04, ASME International Mechanical Engineering Congress and Exposition*, November 13-20, Anaheim, California, pp. 671-677, 2004.
- [23] Song, Haiping; Weaver Smith, Suzanne; Main, John A., Dynamic Testing of an Inflatable, Self-Supporting, Unpressurized Thin-Film Torus, *Journal of Guidance, Control, and Dynamics*, vol. 29, No. 4, pp. 839-845, 2006.
- [24] Danesh Pazhooh, Mitra, Dokainish, Mohammed, and Ziada, Samir, Modal Testing of an Inflatable, Self-Rigidizing Toroidal Satellite Component, *Proceedings of the International Conference on Noise and Vibration Engineering ISMA*, pp. 2467-2474, 2010.

Experimental and Finite Element Modal Analysis of the Flexible Wings of Micro Munition Vehicles

Uttam Kumar Chakravarty

National Research Council Postdoctoral Research Associate, Air Force Research Laboratory
Eglin Air Force Base, FL 32579, USA

ABSTRACT

Biologically inspired wings of micro munition vehicles are constructed with the pre-strained hyperelastic membrane, attached with composite reinforcing structures. Finite element models are developed for the modal characteristics of the flexible wings of micro munition vehicles and validated by experimental results. The effect of added mass, damping, and aerodynamic loads on the modal characteristics (natural frequencies and mode shapes) of the wings is investigated. The wings are vibrated in the vacuum and air environments for investigating the effect of added mass and damping on their modal characteristics. Aerodynamic loads are calculated from the wind tunnel test data where the angle of attack of the wings and free stream velocity of air are varied. Natural frequencies increase with mode, pre-strain level of the membrane, and aerodynamic loads but decrease in air from those in the vacuum environment due to the added mass of air. Damping of air is low and has minimal effect on the natural frequencies of the wings but helps to reduce the out-of-plane modal amplitude of vibration. The effect of added mass, damping, and aerodynamic loads on the mode shapes of the wings is also presented in the paper.

INTRODUCTION

The micro munition vehicles (MMVs) are small (wing span on the order of 100 mm) and fly at low flight speeds (up to 13 m/s) with low Reynolds number aerodynamics (10,000-100,000). The design and operation of MMVs of similar proportions to natural fliers emphasize the intricate but vital aeroelastic features mastered by the biological systems. A particular form of these enhanced flying abilities benefits from the use of flexible lifting surfaces: either fixed or flapping. Biologically inspired wings of MMVs (Fig. 1) are constructed by attaching pre-strained hyperelastic membrane with composite reinforced structures and the modal characteristics (natural frequencies and mode shapes) of the wings are controlled mainly by the pre-strained membrane due to lower stiffnesses than those of composite reinforced structures. The modal characteristics of the wings can be tuned by changing the pre-strain level of the membrane and also depend on the added mass, damping, and aerodynamic loads of surrounding air.

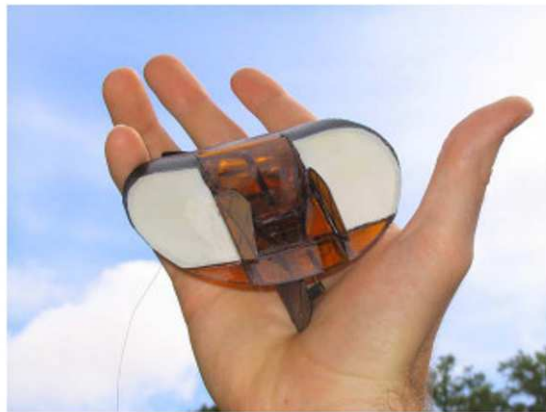


Fig. 1 MMV from the MAV Lab at the University of Florida, Gainesville, Florida, USA

Recently, there has been significant progress in the understanding of the aerodynamics of low Reynolds number artificial and natural flight [1], though the structural behavior is still under early numerical modeling efforts. The large amplitude of wing's deformation, the nonlinear interaction with the flow, and the lack of quantitative experimental results for validation limit the numerical models' applications. The aerodynamic models and flight control design of fixed [1] and flapping wings [2] must include the wing flexibility and structural dynamics, an area where very little experimental data

is available. Experimental modal analysis of the membrane has presented by Chakravarty and Albertani [3], Sewall et al. [4], Gaspar et al. [5], Jenkins and Korde [6]. Graves et al. [7] have conducted the dynamic deformation measurements of a MMVRIC-I semispan wing in a wind tunnel. Shape and strain measurements using visual image correlation (VIC) and aerodynamic coefficients evaluations for different configurations of the membrane MMV wings in the wind tunnel have been performed in steady conditions [8, 9]. Critical experimental work has shown the dependency of modal characteristics of microstructures with ambient pressure [10].

This paper presents the finite element (FE) models for evaluating the modal characteristics of an elliptical wing of MMVs. The FE modal analysis is validated by the experiment results. The elliptical wing is constructed by attaching the pre-strained membrane with a carbon/epoxy (T300/5208) elliptical ring. The wing is placed in a low speed wind tunnel, where the strain levels of the membrane due to aerodynamic loads are measured at different angles of attack and free stream velocities. FE models are developed for investigating the effect of added mass, damping of air, and aerodynamic loads on the modal characteristics (natural frequencies and mode shapes) of the wing.

EXPERIMENTAL SET-UP AND PROCEDURE

Test Specimen

An elliptical wing (Fig. 2) is considered for investigating the effect of damping, added mass, and aerodynamic loads on the modal characteristics. Pre-strained latex membrane (thickness = 0.15 mm) is attached with an elliptical ring (thickness = 1.5 mm) of major and minor inner radii (96, 46) and outer radii (100, 50) mm, respectively. The thickness and density of the latex membrane are 0.15 ± 0.01 mm and 980 kg/m^3 , respectively. Mooney-Rivlin material model [11, 12] is considered for the hyperelastic latex membrane. The Mooney-Rivlin material parameters of the membrane are $C1 = 18.088\text{E}4 \text{ Pa}$ and $C2 = 18.088\text{E}3 \text{ Pa}$. The ring is attached (symmetric to the minor axis) with a thin rectangular plate of dimension (100x3x10 mm with round of radius, 10 mm at a corner). Carbon/epoxy (T300/5208 prepreg plies of uniform thickness, 0.75 mm and $\pm 45^\circ$ orientation angles) is selected as the material of the ring and the plate. The Material properties of carbon/epoxy (T300/5208) unidirectional prepreg are provided in Table 1.

Table 1 Material properties of carbon/epoxy (T300/5208) unidirectional prepreg

Density	Young's moduli		Shear modulus	Poisson's ratios	
$\rho \text{ (kg/m}^3\text{)}$	$E_1 \text{ (GPa)}$	$E_2 \text{ (GPa)}$	$G_{12} \text{ (GPa)}$	ν_{12}	ν_{23}
1600	181	10.3	7.17	0.28	0.33

Membrane Deformation Measurement

The pre-strain level of the membrane is measured using a non-contact method, visual image correlation (VIC) technique [3]. The images are captured using two high speed cameras. Typical data results obtained from the VIC system consist of geometry of the surface in discrete coordinates (x , y , and z) and the corresponding displacements (u , v , and w). A post-processing option involves calculating the in-plane strains (ϵ_{xx} , ϵ_{yy} , and ϵ_{xy}). The strain level of the membrane of the elliptical wing is also calculated due to the aerodynamic loads using the VIC system during the low speed wind tunnel tests at different angles of attack and free stream velocities.

FINITE ELEMENT (FE) MODEL

FE models are developed for investigating the effect of added mass, damping, and aerodynamic loads at atmospheric pressure on the modal characteristics of the elliptical wing using FE analysis software, Abaqus 6.9[®] [13]. The aerodynamic in-plane strains of the membrane of the wing are calculated from the wind tunnel test data at different angles of attack and free stream velocities. These aerodynamic strains are added with the pre-strains of the membrane and provided in the FE models as input data. The pre-stresses of the membrane are calculated based on the hyperelastic Mooney-Rivlin material model. The damping is provided in the FE models as Rayleigh damping parameters. The FE models are developed using M3D6 (6-node quadratic triangular membrane) and SC6R (6-node triangular in-plane continuum shell wedge, general-purpose continuum shell, and finite membrane strains) type of elements for the membrane of the wing and the ring attached with plates, respectively.

RESULTS AND DISCUSSION

The FE modal analysis of an elliptical wing of MMVs is presented in the paper. Before presenting the FE modal analysis of the wing, the FE models for the modal analysis technique is validated by experimental results. For the validation process, pre-strained membrane is attached with a rigid circular ring. The pre-strain level of the membrane is measured using the VIC system. The rigid-circular-ring-membrane specimen is mounted on a shaker, placed inside a vacuum chamber, and vibrated at different ambient pressures of air. The three-dimensional dynamic deformation of the specimen is measured using the scanning laser Doppler vibrometer (LDV), and the natural frequencies are found from the fast Fourier transform of the out-of-plane deformation time histories of the selected points (LDV data) on the surface of the specimen. The mode shapes and damping ratios of the specimen are found from the experimental modal analysis. FE model of the circular membrane with clamped boundary condition (due to the attached circular rigid ring) is developed.

A good agreement is found between the experimental and FE results. The correlation between the experimental and FE results is not shown in this paper and can be found in Ref. [3]. The convergence of the natural frequencies of the circular membrane specimen is studied and it is found that the frequencies converge even at lower degrees of freedom (on the order of 1,000) [3].

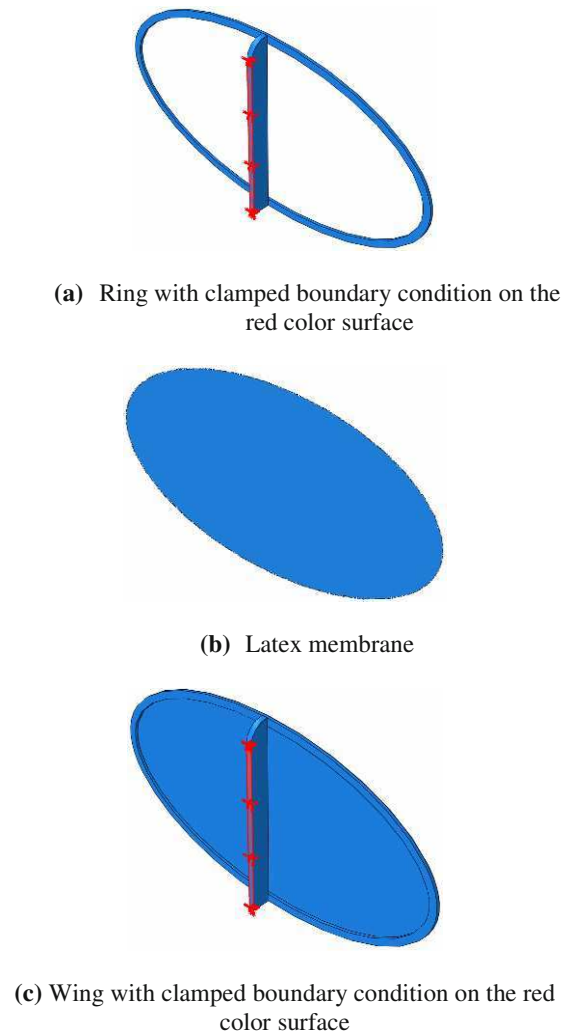


Fig. 2 Carbon/epoxy (T300/5208) ring, membrane, and wing

The wing is constructed by attaching the latex membrane of pre-strains, $\epsilon_{xx} = 0.0464$ and $\epsilon_{yy} = 0.0334$, with an elliptical ring (Fig. 2). The wing is placed inside the low speed wind tunnel and characterized at different angles of attack and free stream velocities. The in-plane strains (ϵ_{xx} and ϵ_{yy}) of the wing's membrane due to the aerodynamic loads are increased with the angle of attack and free stream velocity up to the stall of the wing and measured using the VIC system. The in-plane shear strain (ϵ_{xy}) of the membrane is small and neglected for this analysis. These in-plane strains with the pre-strains are provided as input data to the FE models for investigating the effect of added mass, damping, and aerodynamic loads on the modal characteristics of the wing. The effect of added mass of air on the membrane and elliptical ring (without the attached plate) is considered for the FE model.

The natural frequencies of the wing decrease in air from those in the vacuum environment due to the effect of added mass of air because the wing also needs to move the surrounding air during vibration [14]. Rayleigh damping parameters are computed by assuming the damping ratios are 0.5% based on the experimental modal analysis of the membrane [3] and provided in the FE model of the wing. The effect of damping on the natural frequencies is negligible due to low damping ratios but the damping helps to reduce the amplitude of vibration.

The first three natural frequencies and mode shapes of the wing from the FE model in air at atmospheric pressure are shown in Fig. 3 where the effect of aerodynamic loads is not considered. Natural frequencies of the wing increase with mode. The shape of the wing also changes with mode. The natural frequencies of the ring (for the first three modes: 90.038, 92.553, and 256.58 Hz) are higher than those of the membrane (for the first three modes: 51.053, 67.987, and

86.154 Hz). As a result, the natural frequencies and mode shapes of the wing are dominated by the membrane characteristics.

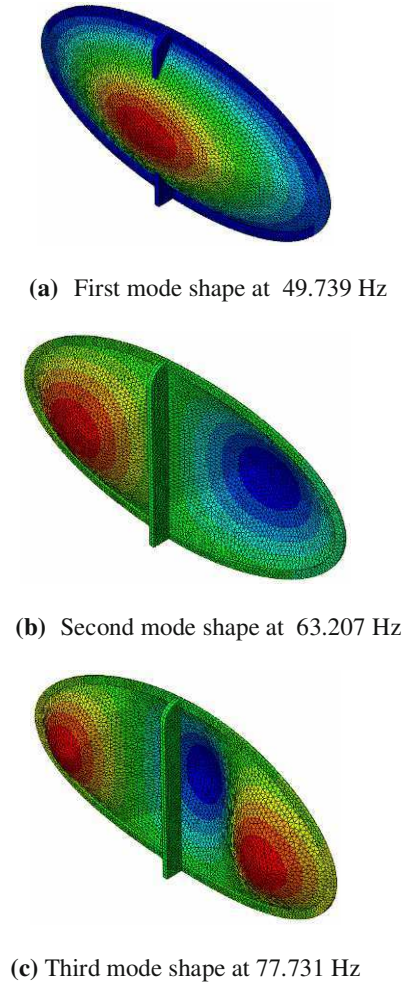


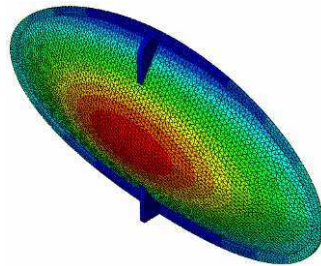
Fig. 3 Mode shapes of the wing for the membrane's pre-strains, $\epsilon_{xx} = 0.0464$ and $\epsilon_{yy} = 0.0334$ (no aerodynamic strain)

The first three natural frequencies and mode shapes of the wing from the FE model in air at atmospheric pressure are shown in Fig. 4 where the effect of strains due to the aerodynamic loads at free stream velocity, 13 m/s and angle of attack, 20° is considered. The natural frequencies of the membrane increase due to the increase of strain level for the aerodynamic loads from the previous case (Fig. 3), where the effect of aerodynamic loads is not considered. The influence of the ring on the modal characteristics increases with mode. The first natural frequency of the ring (90.038 Hz) is higher than that of the membrane (73.784 Hz). The first mode shape of the wing is similar to that of the membrane although the first natural frequency (68.215 Hz) decreases from that of the membrane due to minor deformation of the ring. The second and third natural frequencies of the wing (76.197 and 90.783 Hz, respectively) are less than those of the membrane (97.747 and 123.47 Hz, respectively) due to the deformation of the ring. (The second and third natural frequencies of the ring are 92.554 and 256.59 Hz, respectively.) The second mode shape of the wing shows a slight deformation of the ring but the third mode shape of the wing clearly depicts the deformation of the ring as well as the membrane.

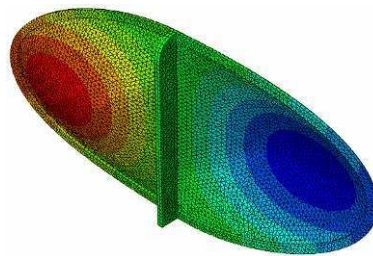
CONCLUSIONS

FE model is developed for investigating the modal characteristics of an elliptical wing of MMVs. The wing is constructed by attaching pre-strained membrane with an elliptical carbon/epoxy (T300/5208) ring. The pre-strain level of the membrane of the wing is measured using the VIC system before conducting any laboratory experiments. The wing is placed inside a low speed wind tunnel and the strains of the membrane due to the aerodynamic loads at different angles of attack and free stream velocities are also measured using the VIC system. These aerodynamic strains and the pre-strains of the membrane, added mass, and damping of air are considered for the modal characteristics of the wing. It is found that aerodynamic strains increase up to the stall of the wing and then decrease with the angle of attack. Natural

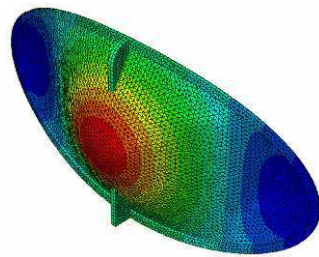
frequencies of the wing increase with mode and strain level of the membrane. The influence of the ring on the natural frequencies and mode shapes increases with the strain level of the membrane by increasing the aerodynamic loads (i.e., angle of attack and free stream velocity). The modal characteristics of the wing are dominated by the membrane at lower strain level of the membrane but ring also plays a significant role at comparatively higher strain level of the membrane.



(a) First mode shape at 68.215 Hz



(b) Second mode shape at 76.197 Hz



(c) Third mode shape at 90.783 Hz

Fig. 4 Mode shapes of the wing for the membrane's strains, $\epsilon_{xx} = 0.0947$ and $\epsilon_{yy} = 0.0781$ (pre-strains, $\epsilon_{xx} = 0.0464$ and $\epsilon_{yy} = 0.0334$ and aerodynamic strains, $\epsilon_{xx} = 0.0483$ and $\epsilon_{yy} = 0.0447$) for free stream velocity, 13.0 m/s and angle of attack, 20°

ACKNOWLEDGEMENTS

This research was performed while the author held a National Research Council Research Associateship Award at the Air Force Research Laboratory, Eglin Air Force Base, FL 32579, USA. The author would like to thank the experimental support from Mr. Joshua Martin and Dr. Roberto Albertani of the University of Florida, Research and Engineering Education Facility, Shalimar, FL 32579, USA.

REFERENCES

- [1] Lian, Y., Shyy, W., "Laminar-Turbulent Transition of a Low Reynolds Number Rigid or Flexible Airfoil," AIAA Journal, Vol. 45, pp. 1501–1513, 2007.
- [2] Ho, S., Nassef, H., Pornsinsirakb, N., Tai, Y., Ho, C., "Unsteady aerodynamics and flow control for flapping wing flyers," Progress in Aerospace Sciences, Vol. 39, pp. 635–681, 2003.
- [3] Chakravarty, U.K., Albertani, R., "Experimental and Finite Element Modal Analysis of a Pliant Membrane for Micro Air Vehicles Wings," 51st AIAA/ASME/ ASCE/AHS/ASC Structures, Structural Dynamics, and Materials Conference, Orlando, FL, AIAA Paper 2010-2710, 2010.
- [4] Sewall, J., Miserentino, R., Pappa, R., "Vibration Studies of a Lightweight Three-Sided Membrane Suitable for Space Applications," NASA Technical Paper, TP 2095, 1983.

- [5] Gaspar, J., Solter, M., Pappa, R., "Membrane Vibration Studies Using a Scanning Laser Vibrometer," NASA Technical Memorandum, TM 211427, 2002.
- [6] Jenkins, C., Korde, U., "Membrane vibration experiments: An historical review and recent results," *Journal of Sound and Vibration*, Vol. 295, pp. 602–613, 2006.
- [7] Graves, S., Bruner, A., Edwards, J., Schuster, D., "Dynamic Deformation Measurements of an Aeroelastic Semispan Model," *Journal of Aircraft*, Vol. 40, pp. 977–984, 2003.
- [8] Stanford, B., Sytsma, M., Albertani, R., Viieru D., Shyy, W., Ifju, P., "Static Aeroelastic Model Validation of Membrane Micro Air Vehicle Wings," *AIAA Journal*, Vol. 45, No. 12, pp. 2828-2837, 2007.
- [9] Albertani, R., Stanford, B., Hubner, J., Ifju, P., "Aerodynamic Coefficients and Deformation Measurements on Flexible Micro Air Vehicle Wings," *Experimental Mechanics*, Vol. 47, pp. 625–635, 2007.
- [10] Ozdoganlar, O., Hansche, B., Carne, T., "Experimental Modal Analysis for Microelectromechanical Systems," *Experimental Mechanics*, Vol. 45, pp. 498-506, 2006.
- [11] Mooney, M., "A Theory of Large Elastic Deformation," *J. Appl. Phys.*, Vol. 11, pp. 582–592, 1940.
- [12] Macosko, C. W., *Rheology: Principles, Measurement and Applications*, Wiley-VCH, NY, 1994.
- [13] Abaqus® 6.9 FEA software, SIMULIA, Rising Sun Mills, 166 Valley Street, Providence, RI 02909-2499, USA, 2009. <www.simulia.com>.
- [14] Azuma, A., *The Biokinetics of Flying and Swimming*, Second ed., American Institute of Aeronautics & Astronautics, Inc., Reston, VA, 2006.

Numerical analysis study of the failure mechanism of transparent materials during low velocity impact used in protective systems

C.G. Fountzoulas¹, R.E. Brennan², J.M. Sands³

U.S. Army Research Laboratory, WMRD, RDRL-WMM-B¹, RDRL-WMM-D², RDRL-WMM-A³, Aberdeen Proving Ground, MD 21005-5069

ABSTRACT

The rapid advancement of computing power and recent advances in numerical techniques and material models have resulted in accurate simulation of ballistic impacts into multi-layer transparent armor configurations. Transparent and opaque materials are used in protective systems for enhancing survivability of ground vehicles, air vehicles, and personnel. Transparent materials are utilized for face shields, riot gear, and vehicle windows, in addition to other applications for sensor protection, including radomes and electromagnetic (EM) windows. For both transparent and opaque protective systems, low velocity impact damage can compromise structural integrity and increase the likelihood of further damage or penetration from a high velocity impact strike. Modeling and simulation of material impact by various threat types has proven to be a significant analysis tool in the identification of damage mechanisms and the failure process. The impact of laminate targets consisting of a series of glass layers adhered to each other by polyurethane and backed by a polymeric backing layer, was modeled and simulated. The failure mechanism of laminate targets was studied by ANSYS/AUTODYN [1] commercial software and the results were compared to available experimental data from various nondestructive techniques. Successful output of this modeling effort will provide useful information for the mitigation of damage propagation through targets used in protective systems and it will help to establish an economical damage acceptance criterion for any future material prior to its fielding.

INTRODUCTION

The U.S. Army has invested heavily in the development of next generation materials, including ceramics, for military systems [2]. Among the potential ceramic materials considered for armor — sapphire, edge-form-growth sapphire, magnesium aluminate spinel, aluminum oxynitride — one was selected for the current pursuit, glass. Individual transparent materials used in protective systems typically consist of glass or other transparent materials, polymeric and/or ceramics, which were stacked and adhered by polymer interlayers to form interlayers to form transparent laminate protective systems [3]. In particular, glass is an appealing transparent material due to its availability and low cost. The presence of potentially harmful internal defects in these individual materials (pores, inclusions, secondary phases, etc.) and interlayer defects in the laminates (disbands, delamination, etc.) can reduce material properties but may not be visually detectable if index-matched [3].

Current strike face glasses used in transparent laminate protective systems are limited in how thin they can be fabricated before encountering durability issues. Lower density novel glass components have been developed that can be fabricated more than ten times thinner while maintaining their durability. By reducing the thickness and lowering

the density of the strike face glass, the overall weight will also be reduced. Weight reduction is desirable for vehicle systems to increase maneuverability and transportability while reducing operational costs [4].

Nondestructive bulk characterization techniques can be utilized in the pre-impacted state to detect material inhomogeneities and improve quality control for transparent materials before they are utilized in the field. They can also be used post-impact to detect resulting damage and a comparison of baseline and damaged states can be established to help determine critical impact conditions [4].

The damage resulting from standard projectile impact on a brittle target has been studied extensively over the past decades and it corresponds to the three stages [5-9]:

1. Crushing occurs in the high pressure compressive zone in the region of contact, which is associated with the onset of micro-cracking, the formation of interconnected cracks and fragmentation (loss of ceramic continuity).
2. The dynamic erosion at the interface between the ceramic and the projectile proceeds by a process of high pressure grinding and the mixture of target and impactor particles is accelerated and ejected from the front surface of the target.
3. The size distribution of the ceramic fragments is determined by the network of radial, transverse and spall cracks spreading from the contact zone determines. The constraint of the target is expected to affect mostly these failure processes.

The propagation of cracks in brittle solids, such as ceramics, results in their failure. Various defects in the ceramics such as, holes, inclusions, microcracks and surface scratches facilitate the nucleation and propagation of cracks by Ashby et al.[10]. Ashby and Sammis [9] reported that “the difference between compressive and tensile fracture is that in tension a single crack grows unstably (once started, it accelerates across the sample to cause failure) while in compression a population of small cracks extends stably, each growing longer as the stress is raised, until they interact in some cooperative way to give final failure. Because of this, the strength of a brittle solid in compression is usually greater, by a factor of ten or more, than that in tension”.

Finite element modeling has progressed substantially in the ability to predict failure of materials under extreme dynamic loading conditions. One of the limitations of predictive models is lack of a complete dynamic materials properties database which is needed for materials models for each of the materials in the simulations. In order to compensate for parameters whose dynamic values were extrapolated from their static or quasi-static properties, baseline experiments are often used to recalibrate the models [11, 12]. However, the recalibration method of modeling lacks many of the physical properties and failure mechanisms associated with real-world materials. Therefore, recalibrated models often lack the ability to predict within statistical error future failures over any substantial ranges due to the existence of defects, and materials substitutions often lead to new calibration requirements. The desired approach is to validate a fully characterized materials database with one calibration model, and subsequently apply the model to modified designs. However, despite its apparent problems, recalibration of existing materials models has been proven to be an effective tool in the hands of the modeler by minimizing the number of simulation iterations, resulting in more successful predictions. Regardless of methodology, finite element tools can be applied effectively to reduce the variability between impact tests and can be used to validate designs with fewer experimental failures, when robust models are created [11]. The result of the on-going investments is a critical understanding of ceramics strengths and weaknesses for military platforms.

EXPERIMENTAL

The transparent materials chosen for this study were four 14-inch by 14-inch laminate panels designated as 740 and 741 series. Each laminate consisted of a glass strike face, Glass A and Glass A' for 740 and 741 series, respectively, a central glass layer (Glass C), a polycarbonate backing and a polyurethane adhesive layer between the neighboring laminates. The total thickness of 740 and 741 series laminates was 23 mm and 17 mm respectively. The thickness and properties of strike face Glass A of laminate 740 were different than the corresponding ones of the face glass A' of 741-series. Both laminates were impacted by 4340 steel spheres of 19.05 mm and 5.56 mm diameter respectively. The laminates which were impacted by the 19.05 mm spheres were labeled as 740-1 and 741-1 respectively. The laminates which were impacted by the 5.56 mm sphere were labeled as 740-2 and 741-2 respectively.

Visual characterization, cross-polarization imaging, ultrasonic testing, x-ray digital radiography, and x-ray computed tomography (XCT) were used for the nondestructive characterization of the laminates. Details of the nondestructive techniques used can be found in reference [3].

MODELING

The ballistic behavior of all targets, which consisted of glass and polycarbonate backing, and were held together by polyurethane and impacted by steel spheres of 19 mm and 5.56 mm diameter, were simulated using the non-linear ANSYS/AUTODYN commercial package [1]. The geometry of the 2D and 3D axisymmetric modeled laminates was identical to the actual geometry of the laminates (Figure 1 and Figure 2). Smooth particle hydrodynamics (SPH) solver was used for the laminate and the impactor. The element size was 0.2 mm for 2D modeling and 0.5 mm for the 3D modeling. The polycarbonate was simply supported at the corners by applying zero velocity along the x-direction as a boundary condition. Results were obtained by simulating a projectile impacting the targets at constant velocity of 400 m/s and 30 m/s respectively. The material models used for all materials were obtained from the AUTODYN material library [1]. The polycarbonate (PC) was modeled using a shock equation of state (EOS), piecewise Johnson-Cook (JC) strength model, and a plastic strain failure criterion. The projectile steel was modeled using a shock EOS and a JC strength model. The glass was modeled using a polynomial EOS and Johnson-Holmquist (JH2) strength and failure models. The polyurethane was modeled using linear EOS, elastic strength model and principal stress tensile failure.

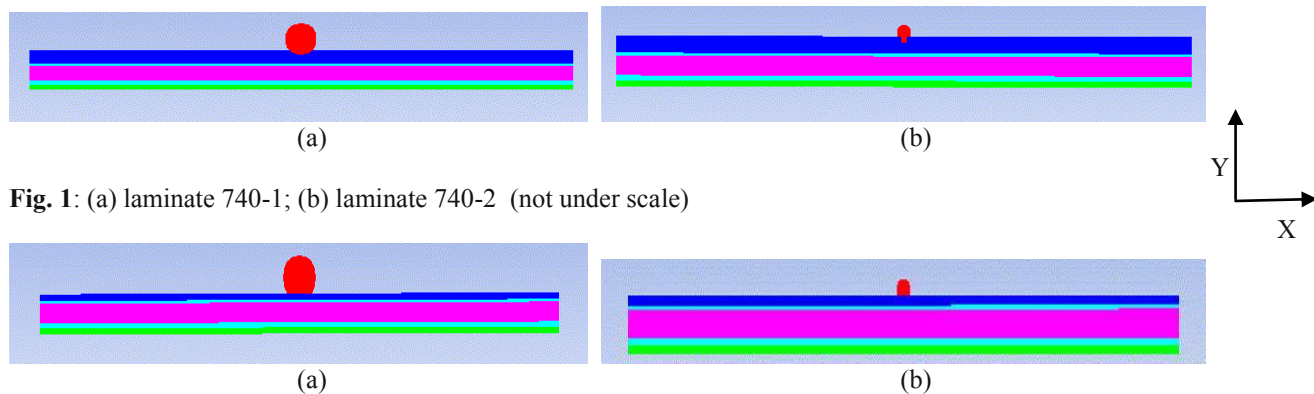


Fig. 1: (a) laminate 740-1; (b) laminate 740-2 (not under scale)

Fig. 2: (a) laminate 741-1; (b) laminate 741-2 (not under scale)

RESULTS

Figure 3 shows the XCT cross-section images of all four laminates prior and after the impact. Cone cracking appears in Glass C for 740-1 and 741-2 laminates. Simulations also showed similar cracking pattern for

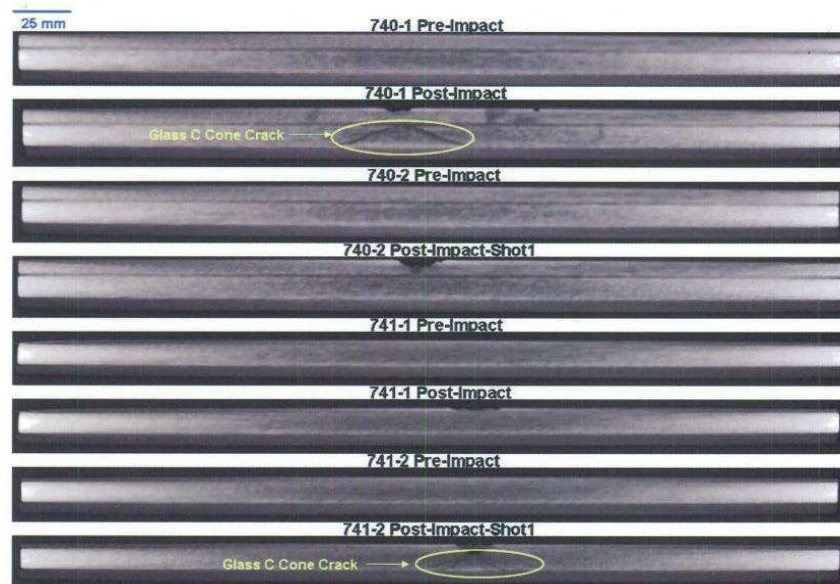


Fig 3 XCT cross section images of all laminates prior and after the impact (-1 designates impact by a 19.05 mm steel sphere, and -2 designates impact by a 5.56 mm sphere)

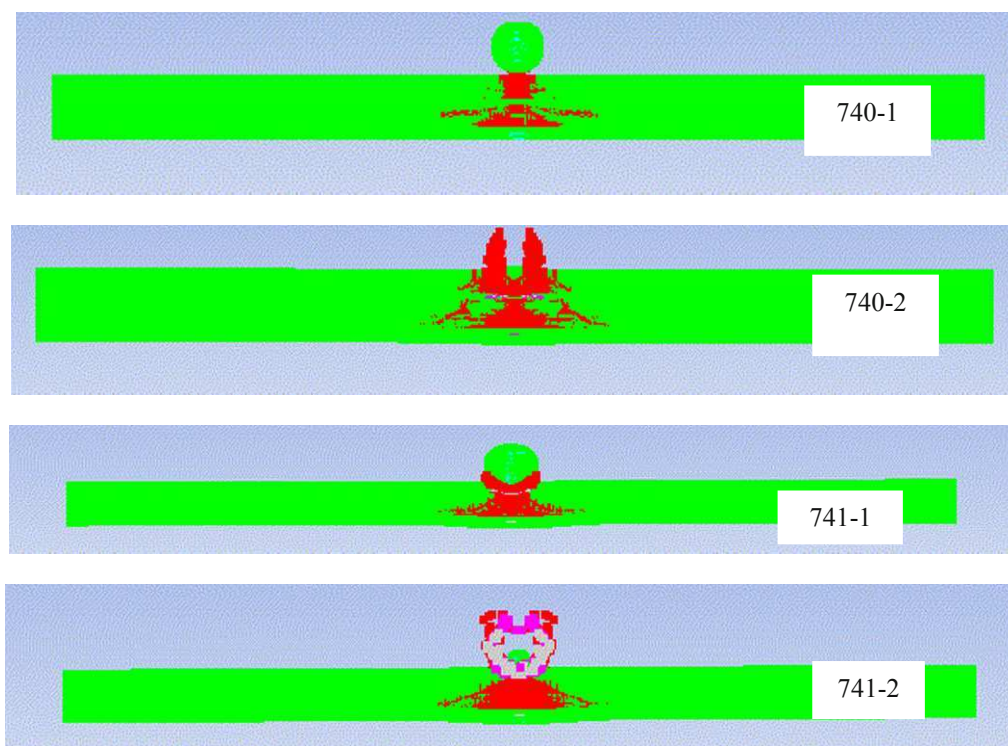


Fig. 4 2D simulated cross section images of all laminates after 50 μ s impact

the same laminates 740-1 and 741-2. Moreover, the characteristic comminuted zone below the center of impact and the tensile cracking of glass appears in all simulations. The simulation results agree with the experimentally

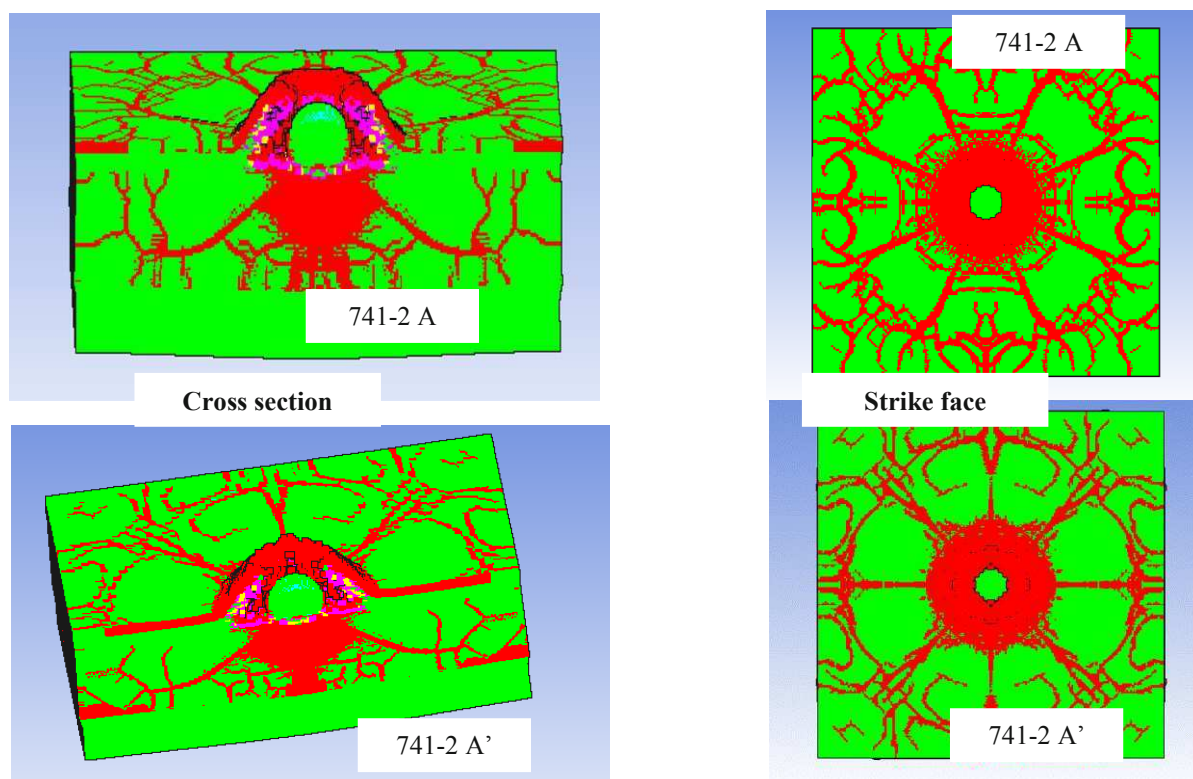


Fig. 5 Simulated damage for 741-2 geometry using Glass A and Glass A' as strike face after 30 μ s

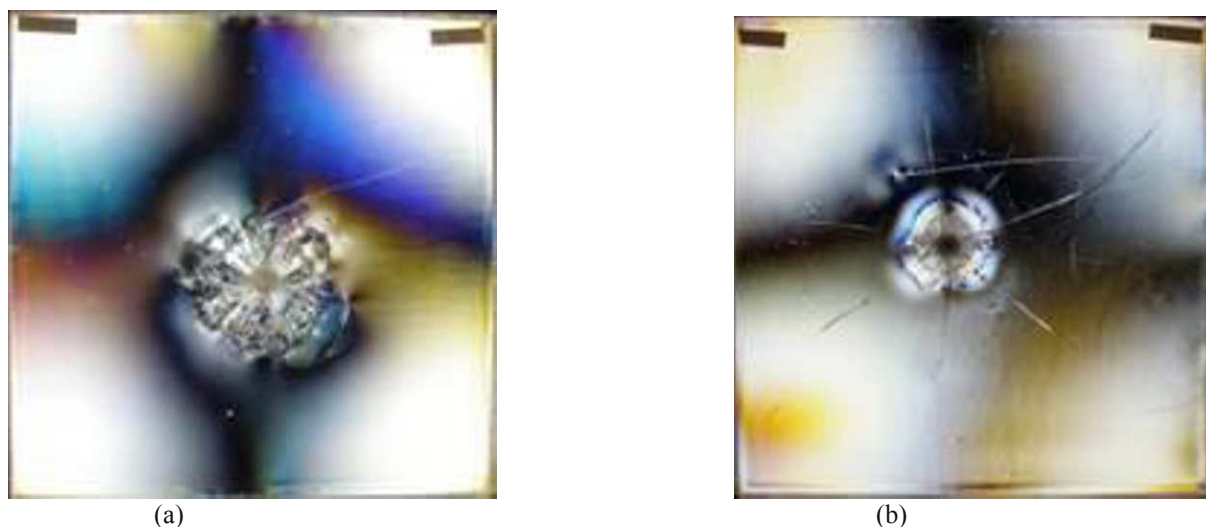


Fig. 6 Cross-polarized images of 740-2 (a) and 741-2 (b) laminate targets

observed data. The experimentally observed extension of the of the strike face damage into the central glass layers, was captured by all simulations. Careful examination of the cross-sections of the 2D simulations (Fig. 4) shows more cracking near the striking face of the 740-1 and 740-2 laminate targets than the cracking shown in 741-1 and 741-2 laminate targets. These simulation results agree well with the experimental results (Fig. 6). To further test the experimental observation that the 741-series transparent laminate system was the preferred choice due to the reduced average damage and less radial cracking that resulted in significant optical distortion [3], 3D impact simulations of 741-2 laminates were conducted. For this comparison, the Glass A' of the 741-2 target geometry was replaced by a similar thickness Glass A. After 30 μ s simulation, the cracking of the 741-2 target having Glass A as the striking face was more extensive than the cracking of 741-2 with Glass A' as the striking face. Moreover, the simulations showed higher density of tensile cracking at the periphery of the pulverized zone around the center of impact for the 741-2 (Glass A) case, in agreement with the experimental results shown in Fig. 6.

CONCLUSIONS

The failure mechanism of two different thickness laminate targets impacted at 30 m/s and 400 m/s by steel spheres was studied by 2D and 3D modeling and simulation. The results of the simulation compared well to the experimental data. The surface and interior failure of the laminate targets was observed experimentally by using a combination of various techniques such as visual characterization, cross-polarization image, ultrasonic testing, x-ray digital radiography, and x-ray computed tomography (XCT). The simulations replicated successfully the experimental surface and interior failure of the targets. Details of the failure of individual plies in the laminate target were observed and studied by simulation. It was shown that the damage of the surface is reflected in the central glass, an indication of the damage created by the propagating shock wave impact ahead of the penetrating projectile. In addition, the simulations replicated the bulging of the actual polycarbonate backing layer. The successful replication of the experimental data and the failure details of the laminate target suggest that modeling and simulation can be implemented as the initial decision making stage for examining current and future target architectures, thus decreasing the cost of the necessary experiments and NDE techniques.

REFERENCES

- ¹ ANSYS/AUTODYN Vol 11.0, Manual, Century Dynamics Inc., Concord, CA
- ² Gatti, A & Noone, M J, "Feasibility Study for Producing Transparent Spinel (MgAl_2O_4)", AMMRC-CR-70-8, February 1970.
- ³ Brennan R.E. and Green W.H., "Low Velocity Impact Testing and Nondestructive Evaluation of Transparent Materials", accepted for publication in *Advances in Ceramic Armor Annals VII*, Ceramic Engineering and Science Proceedings (2011)
- ⁴ Patel P.J., Gilde G.A., Dehmer P.G., and McCauley J.W., "Transparent Armor"; *AMPTI.ItG Newsletter*, 4, 3 (2000).

- 5 Brandon D.G., Baum L. and Sherman D., “Ballistic failure processes in alumina”, Colloque C8, supplement au Journal de Physique III, Volume 4, Septembre 1994
- 6 Brandon D.G. “Ceramic Armor”, Encyclopedia of Adv.Cer.Mat. (Pergamon 1991) pp.22
- 7 Laible R.C., 'Ballistic materials and penetration mechanics' **ed.** Laible R.C. (Elsevier Sci.Publ.1980) pp. 133
- 8 Wilkins M.L., Cline C.F. and Hondol C.A., Tech.Rep. UCRL-50694 (Lawrence Rad.Lab. 1969)
- 9 Wilkins M.L., 'Ballistic materials and penetration mechanics' **ed.** Laible R.C. (Elsevier Sci.Publ.1980) pp.225
- 10 Ashby, M.F. and Sammis, C.G., “The damage mechanics of brittle solids in compression”, Pure Appl. Geophy. Pp. 489-521, **133**(3) (1990)
- 11 Fountzoulas C.G., Cheeseman B.A., Dehmer P.G. and Sands J.M., “A Computational Study of Laminate Transparent Armor Impacted by FSP“, Proceedings of 23rd Inter, Ballistic Symp., Tarragona, Spain, 14-19 April 2007
- 12 Fountzoulas C. G., LaSalvia J.C., Cheeseman B.A., “Simulation of Ballistic Impact of a Tungsten Carbide Sphere on a Confined Silicon Carbide Target“, Proceedings of 23rd Inter, Ballistic Symp., Tarragona, Spain,

Effects of End Restraint on Eyebars in Bridges

David F. Mazurek, Ph.D., P.E.
Professor of Civil Engineering
U.S. Coast Guard Academy
Department of Engineering (dec)
27 Mohegan Avenue
New London, CT 06320-8101

ABSTRACT

Many steel truss railroad bridges use tension members consisting of eyebars. After years of service, these eyebars may exhibit significant wear at the pin holes, leading to the development of unequal tension stresses among eyebars within the same set. To restore bridge performance, eyobar tensions are often equalized through flame-shortening, where the tension in any eyobar is determined by measuring its fundamental natural frequency and then converting this frequency to the corresponding tension through a simple analytical model. In practice this model assumes that the ends of the eyobar are pinned; however, for transverse vibration about the minor axis, a significant degree of rotational restraint will often exist, potentially resulting in very inaccurate tension estimates. This paper presents the results of analytical studies, model testing, and field observations that focus on improving the prediction of eyobar tensions from observed natural frequencies. Besides supporting the flame-shortening process, the ability to achieve greater accuracy in tension measurements also provides for valuable applications to bridge rating.

INTRODUCTION

Older pin-connected truss bridges often use eyebars for tension members. Such a member will consist of multiple eyebars, and for optimal performance the tension in all eyebars that make up a particular member should be equal. After years of heavy traffic loads, especially those associated with railroad structures, it is possible for the eyebars to develop considerable variation in tension due to pin wear. To restore bridge performance, flame shortening of eyebars is often used to equalize stresses. A procedure for flame shortening is presented by AREMA [3]; to support this procedure, a simple technique is described for estimating eyobar dead load stress by observing the transverse fundamental flexural natural frequency (about the minor axis). A chart is provided by AREMA that enables this determination of dead load stress, the theoretical basis of which is a closed-form solution that relates tension stress to the observed natural frequency as given by Timoshenko [5]. While this solution assumes pinned ends, for vibrations about the minor axis it is apparent that a significant degree of fixity might generally be expected. However, a chart even for the extreme case of perfectly fixed ends has not been included in the AREMA procedure because a similar closed-form solution does not exist. This paper presents such a chart developed for the fixed-end case (obtained using a numerical solution), examines experimental work to both verify this new chart as well as study the effects of end fixity, and then considers the behavior of eyebars in actual bridge structures through field testing.

ANALYTICAL STUDY

The key parameters for the fixed-end eyobar model are shown in Fig. 1, and include the tension force, S , length, L , and thickness, t . The model assumes the eyobar to be prismatic, homogeneous, and linear-elastic, with the focus being on the first flexural mode. Using the equation of motion as developed by Timoshenko [5] (which disregards the effects of shear and rotary inertia), and applying boundary conditions for the fixed-end case, a numerical solution was completed as described in further detail by Mazurek [4]. The resulting chart that relates tension stress to the frequency of vibration for the first transverse flexural mode (about the minor axis) is presented in Fig. 2. This chart was developed using a similar range of eyobar lengths and thicknesses as given in the current AREMA procedure. To examine the differences between the fixed and pin-ended cases, Fig. 3 provides a comparison for the same range of lengths and a thickness of 50 mm. This figure shows that for longer eyebars of a given thickness, there is only a modest difference between the fixed and pinned cases, but as eyobar length decreases, the differences significantly increase. This reflects the general relation that as the L/t ratio decreases, the difference between the fixed and pin-ended cases increases, and this difference can be quite substantial.

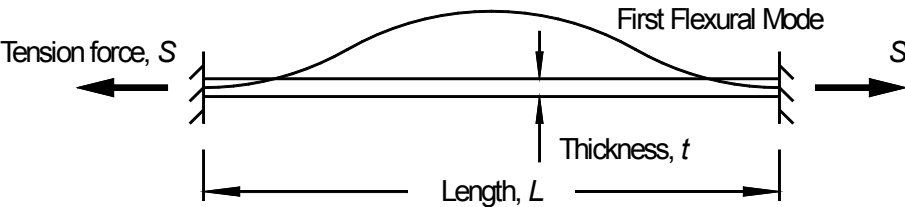


Fig. 1 Parameters of Fixed-End Eyebar

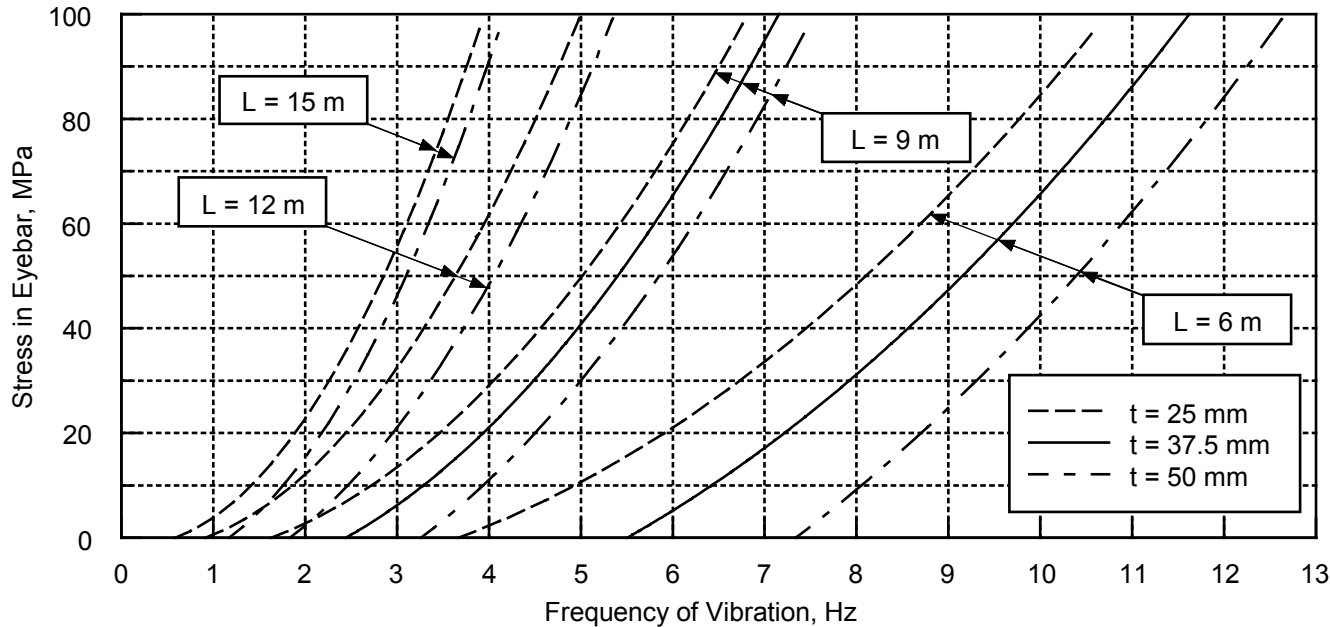


Fig. 2 Eyebar Stress Based on the Fixed-End Model

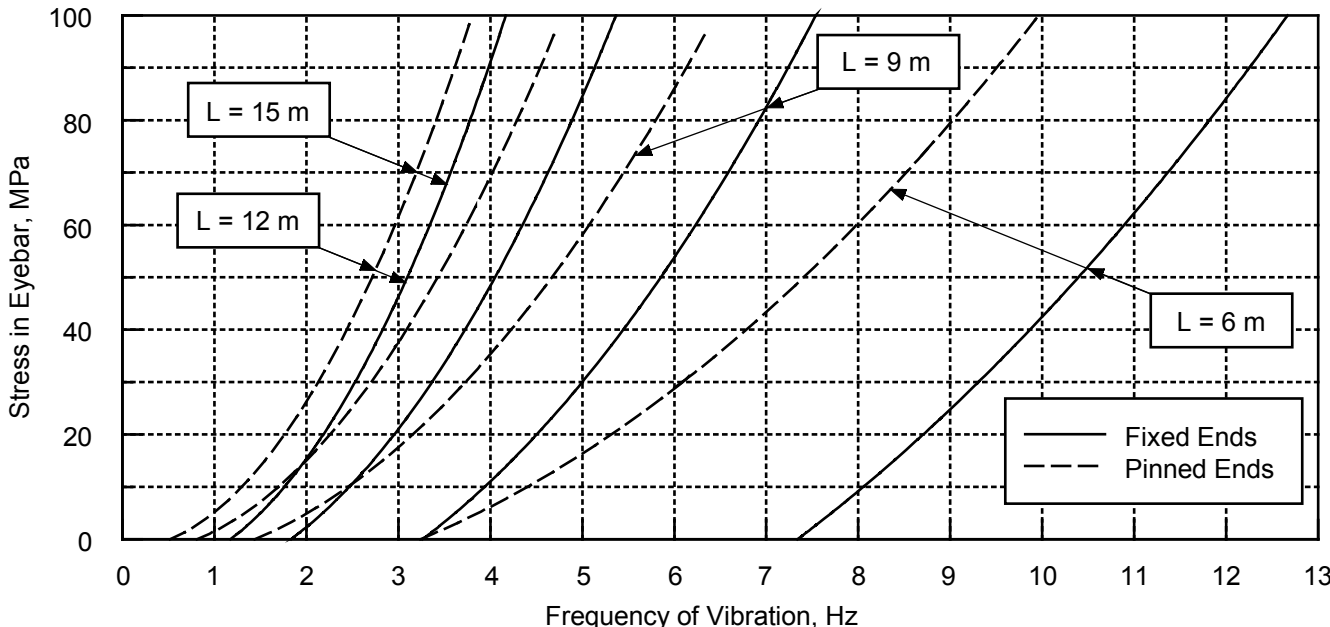


Fig. 3 Eyebar Stress for Thickness $t = 50\text{ mm}$

EXPERIMENTAL STUDY

In order to both validate the analytical model described in the previous section as well as to examine the effects of pinhole wear on the dynamic response of eyebars, an experimental study was completed using smaller-scale specimens suitable for laboratory testing. The eyebars were fabricated from 4.75-mm-thick ASTM A36 steel plate, and their key length attributes are illustrated in Fig. 4. The geometry of the heads satisfied the requirements of AREMA [1], and the heads were initially bored to accommodate a snug-fitting but free-to-rotate steel pin of 22.3-mm diameter. The AREMA procedure for determining dead load stress is not clear regarding what eyebar length is intended, but it is believed that the distance between pin centers is most commonly used, as this is the length typically given in construction drawings; for the laboratory specimen this is shown as the 1092-mm dimension. Using this length, the resulting L/t ratio for the eyebars is 230, which falls well within the range of 120 to 600 for the cases given in the AREMA procedure.

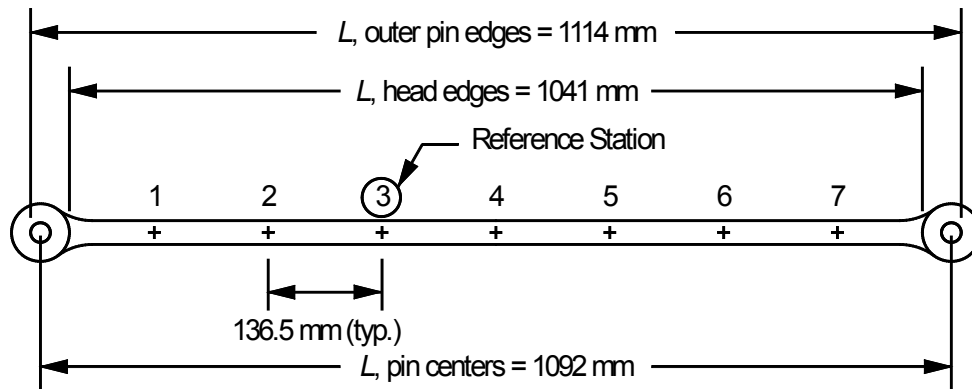


Fig. 4 Measurement Stations for Eyebar Laboratory Model

A universal testing machine was used to apply and measure tensile loads on the eyebars. For the results reported here, two load range settings were used, providing ranges of stress within the body of the eyebar of approximately 0 to 40 MPa (low load range) and 40 MPa to 90 MPa (high load range). Vibration measurements were collected using two accelerometers, each having a mass of about 2 g and a sensitivity of 100 mV/g, and a spectrum analyzer operating a frequency range of 4 to 104 Hz and a resolution of 0.125 Hz. Autospectra were collected at the measurement stations shown in Fig. 4, with the excitation consisting of a single impact with a plastic-tipped hammer. The fundamental flexural frequency was obtained by peak-picking from the raw autospectra, and mode shapes were obtained by scaling the corresponding autospectral amplitude at each station to that measured at the reference station (where one of the two accelerometers remained throughout the testing). Due to the nature of the hydraulically-driven testing machine, it was often difficult to maintain a constant tension over the course of a given set of data collection. Thus, to minimize the duration of each test, only 3 averages were collected, which still generally resulted in smooth autospectra. In addition, it permitted confirmation that the load was holding constant, as any significant shift in load was readily apparent by distortions in the autospectra, and any such measurements were then discarded. Based on the calibration and operating characteristics of the universal testing machine, the uncertainty of measured stress is estimated to be under 0.5 MPa for the low range and under 2 MPa for the high range.

Tests were first conducted to validate the fixed-end analytical model described in the previous section. In actual bridge applications, it is common for the multiple eyebars from members sharing the same pin to have firm contact between their heads and the overlapping heads of eyebars from adjacent members. This was emulated in the laboratory by placing washers (representing overlapping eyebar heads) on either side of each head, and clamping the pin-plate supports firmly about the washers. In this paper, this support condition will be referred to as a “packed joint”. Regarding the washers, their outer diameters were slightly (11%) less than the outer diameter of the eyebar heads. In theory, if the behavior of the joints emulates fixed-end conditions, the clear distance between overlapping eyebar head edges would be a suitable length to use in the fixed-end model; thus, in this study the length used in the analytical model was the clear distance between the washers, reflected by the 1041-mm dimension shown in Fig. 4. An example of a measured autospectrum is shown in Fig. 5; this was obtained at Station 3, with the eyebar stress being 22.0 MPa. Fig. 6 provides a comparison between the experimental results (tight pin, packed joint) and those predicted by the analytical model; here the correlation between the fixed-end specimen and the fixed-end analytical model using a length measured between overlapping eyebar heads (i.e., washers) is quite good, while the conventional analytical model assuming pinned ends and a length measured between pin centers deviates considerably. These results serve well to validate the fixed-end analytical model.

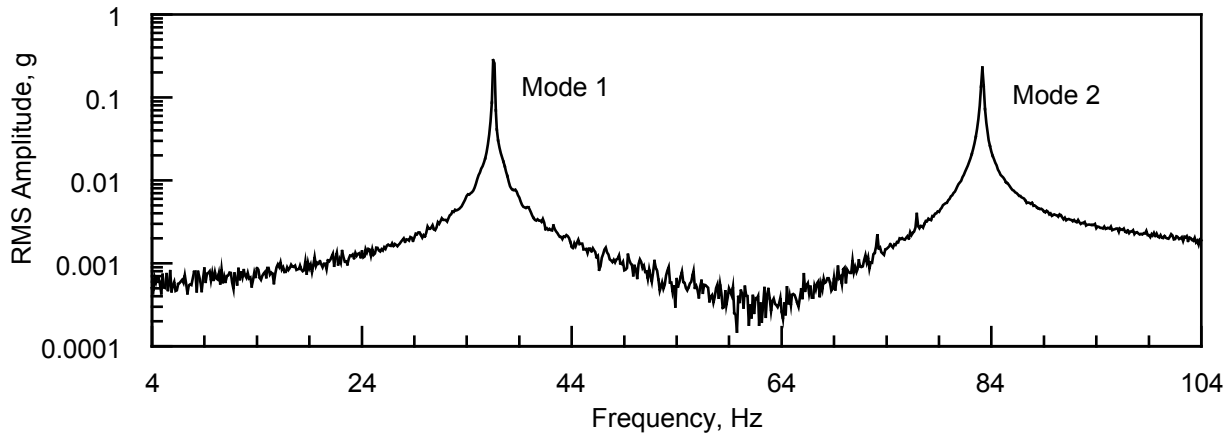


Fig. 5 Example Autospectrum for Fixed-Ended Eyebar (22.0 MPa)

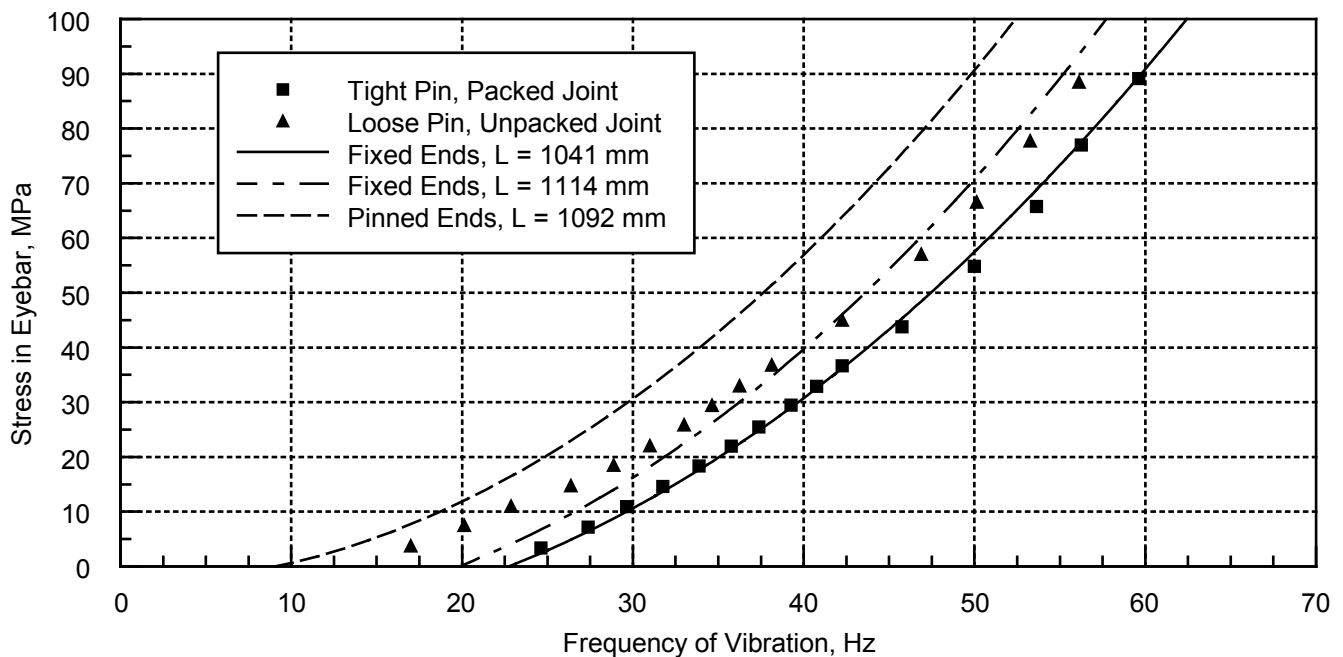


Fig. 6 Comparison of Experimental Eyebar Stresses with Analytical Models

Tests were then conducted to study the behavior of a very loose eyebar, that is, one that had sustained significant pinhole wear as well as having no lateral restraint of the head. The pinholes for an eyebar were reamed to result in an oversize of about 3% relative to the diameter of the pin. For comparison, AREMA [2] limits pin clearances in new construction to approximately 0.4% to 0.6%, depending upon pin diameter. In addition, there was a gap of approximately 20 mm between the eyebar head and the pin-plate support on either side; in this paper, this support condition will be referred to as an “unpacked joint”. Given the apparent looseness of the eyebar, it was hypothesized that the most appropriate length to use in either analytical model might be the outside distance between pins, or the distance between the primary points of bearing. This is reflected by the 1114-mm dimension shown in Fig. 4. The results of this experiment are shown in Fig. 6 (loose pin, unpacked joint). Observing the general trend that the experimental results drift from the pin-ended analytical model at low load levels to the fixed at higher load levels suggests that as the head “bites” into the pin under increasing load, the level of rotational restraint appears to increase. Further, once beyond the lowest levels of load, the experimental results follow reasonably close to the fixed-end analytical model using a length equal to the outer distance between pins (1114 mm). This increase in rotational restraint with load is also illustrated in Fig. 7, which shows the experimental modal amplitudes compared to the mode shapes obtained using the fixed-end analytical model (and a length of 1114 mm), where both have been normalized at the mid-length of the eyebar. Here, the right end of the eyebar in particular displays considerable rotation at low stress, but both ends quickly approach the fixed-end restraint exhibited by the analytical model at higher stress.

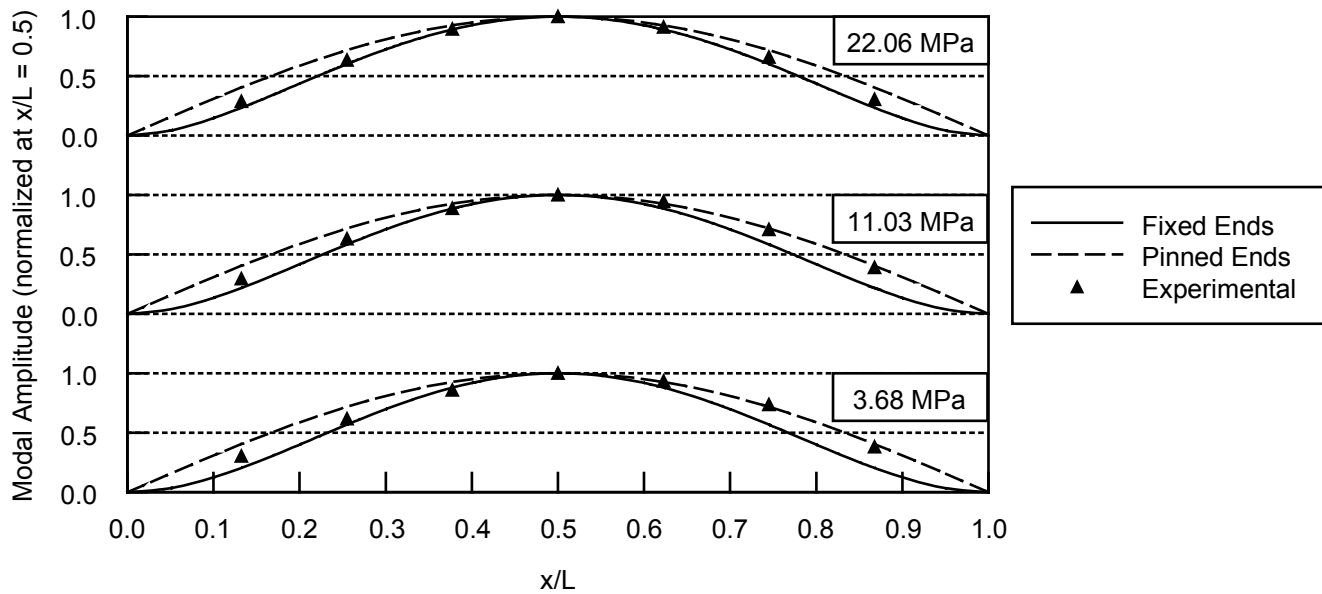


Fig. 7 Mode 1 for Unpacked, Worn Eyebars

ACTUAL BRIDGE PERFORMANCE

Case studies of eyebar behavior in two operational railroad bridges are now considered. Following an approach similar to the laboratory testing discussed in the previous section, measurement stations were marked off at the eighth-points for each eyebar that was studied. Excitation was applied by either using a single impact from a rubber mallet or just manually shaking and releasing the eyebar. Auto and cross-spectra were measured over a frequency range of 0-50 Hz and a resolution of 0.0625 Hz. The fundamental natural frequency was obtained by peak-picking from the raw autospectra, modal amplitudes were obtained by scaling autospectral amplitudes to a reference station, and cross-spectra were used to confirm phase relations.

The first study involves a bridge of the former Baltimore & Ohio Railroad's Philadelphia Branch in Canton, MD, now owned and operated by CSX Transportation. The bridge was built in 1885 and is a skewed, pin-connected, steel 12-panel Whipple through truss. Tests were conducted on the south truss and included lower chord member L9-L10, which consists of four eyebars, each with a 152-mm by 36.5-mm cross section. Visual observation indicated that the faces of overlapping eyebar heads were in firm contact with each other, and overall the joints appeared to be quite tight. In addition, the pins themselves were highly restrained against translation or rotation by heavy structure consisting of a floor beam as well as other members tied into the joint. Therefore, the length used in the fixed-end analytical model was the clear distance between overlapping eyebar heads, or 5420 mm. With an L/t ratio of approximately 150, this eyebar is at the low range of those considered in the AREMA procedure discussed earlier, where a greater difference in predicted eyebar stress would be anticipated between the pinned and fixed-end analytical models. The results obtained for the second eyebar are shown in Fig. 8, where excellent correlation between the fixed-end model and actual observed eyebar behavior is evident. This strong correlation was exhibited by the other three eyebars as well. As expected, the stress predicted by the fixed-end model (35.6 MPa) is considerably less than for the pinned model (75.4 MPa), where both values reflect a length equal to the clear distance between overlapping eyebar heads. If the length between pin centers is used instead for the pinned model, the disparity with the fixed becomes even worse with a predicted stress of 88.0 MPa. These results show that when firm contact exists between eyebar heads and the pins are restrained by heavy structure, the behavior of eyebars is very consistent with that predicted by the fixed-end model. Further details regarding the testing of this bridge and additional results are provided by Mazurek [4].

The second study involved a bridge over the Connecticut River on Amtrak's Springfield Line in Windsor, CT. Erected in 1904, this bridge of the former New York, New Haven, and Hartford Railroad is a skewed, pin-connected, steel 7-panel subdivided Pratt through truss. Tests were conducted on the north truss and focused on the diagonal member M5-L6, consisting of four eyebars, each with a 203-mm by 31.8-mm cross section. This member was selected in part because the first eyebar exhibited obvious looseness and very little tension, and when vibrated, its head was visibly rocking about the pin at mid-panel joint M5 (and about the minor axis of the eyebar). It was evident that the other three eyebars were under considerably more tension and appeared to have much more rotational resistance at this joint. At joint L6, all four eyebars displayed firm and tight contact between overlapping heads, and the pin itself was further restrained by a floor beam. A new analytical

model was developed that incorporated rotational springs of variable stiffness at each end, thereby permitting the study of eyebars with intermediate degrees of rotational end-restraint, as seemed apparent for this truss member. The details of this newer model will be presented in a future paper. Because of the significant looseness observed at the pin at one end of the first eyebar, based on the laboratory study it seemed appropriate to consider measuring the eyebar length to the far edge of the pin at this joint if using the fixed-end model. With the other end of the eyebar appearing to be fixed, the total length became the distance between the outer pin edge at the loose joint to the edge of the overlapping eyebar head at the tight joint. This length, being 6350 mm, reflects an L/t ratio of approximately 200, placing these eyebars in the lower range of those considered in the AREMA procedure.

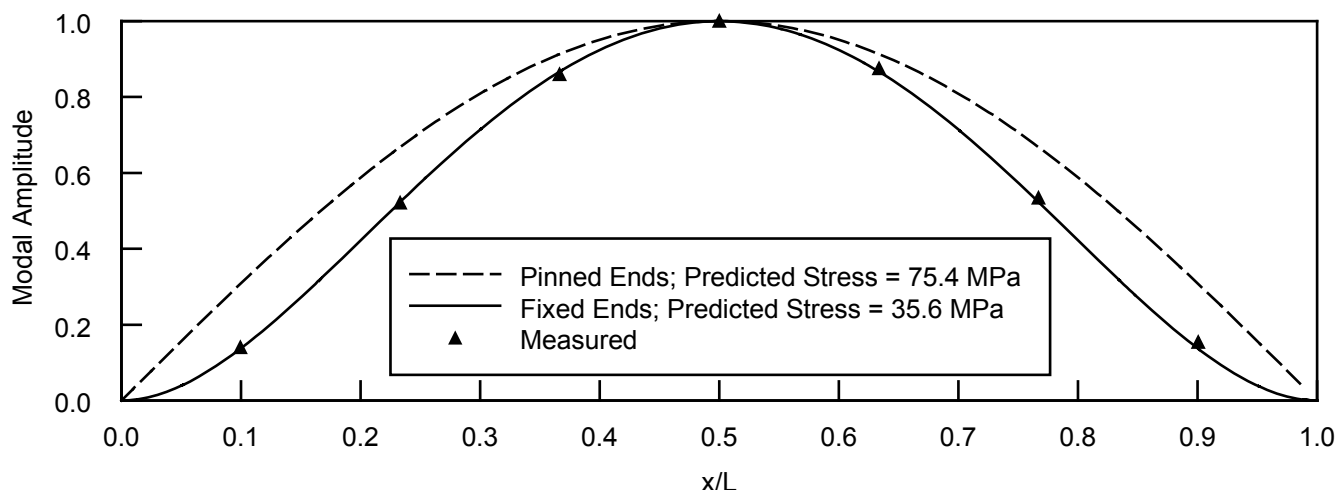


Fig. 8 First Flexural Mode for CSX Member L9-L10

The results for the first and fourth eyebars of member M5-L6 of the Amtrak bridge are shown in Fig. 9 and Fig. 10. Because of access limitations, measurements could only be obtained from joint M5 to the midpoint of each eyebar. When using the variable stiffness model, joint L6 was treated as fixed while the stiffness of the rotational spring at joint M5 was adjusted until the analytical model (labeled as “partial-fixed”) achieved a best fit with the measured response. The modal amplitudes in these figures have been adjusted so that the station possessing the peak value of measured response matches the partial-fixed model, and the amplitudes at the remaining stations scaled accordingly. For the first eyebar, the results of Fig. 9 confirm the visual observation that very little rotational resistance existed at joint M6. Not included in this figure is the conventional pin-ended model, which, when using a length measured between pin centers, resulted in a predicted stress of 9.79 MPa; this deviates considerably from the 0 MPa obtained for the best-fit partial-fixed model as shown in Fig. 9. Considering the fixed-end model, it was not surprising that it did not fit the modal amplitudes well, given the extremely low state of stress and observed looseness at joint M5; nonetheless, it also predicted a stress of 0 MPa. Though not shown, it should be noted that the variable stiffness model achieved a slightly better fit for the first eyebar if the length was taken to the center of the loose pin; even in this case, however, the predicted stress remained 0 MPa. Referring now to Fig. 10, the fourth eyebar displayed a high degree of rotational restraint at joint M6 along with higher predicted stresses, as anticipated by visual observations. In this case, the pinned-end model (not shown) provided a predicted stress of 49.4 MPa, which again differs greatly from the best-fit partial-fixed model result of 25.5 MPa, while the fixed-end model is much closer at 24.3 MPa. As observed in the laboratory study, this figure also shows that with the increase in tension, the fixed-end analysis fits much more closely with the observed modal amplitudes.

These results show that when ideal conditions are known to exist, such as both ends being fixed, a chart like that given in Fig. 2 can be used to quickly and accurately predict dead load stress in an eyebar from a single frequency measurement. Conversely, when partial rotational restraint exists at a joint, it may be possible to adjust a variable-stiffness spring model to obtain a similar measure of eyebar stress accuracy. In practice, however, this would not be conducive to performing a rapid assessment of eyebar behavior, as a number of measurements would be required for each eyebar in order to quantify the actual degree of rotational resistance. An alternate approach where full rotational restraint at an end appears to be lacking might be to continue to use the fixed-end model and chart of Fig. 2, along with a length measured to the far edge of the pin at this joint; both the laboratory and field results presented here show that this would provide for a close approximation.

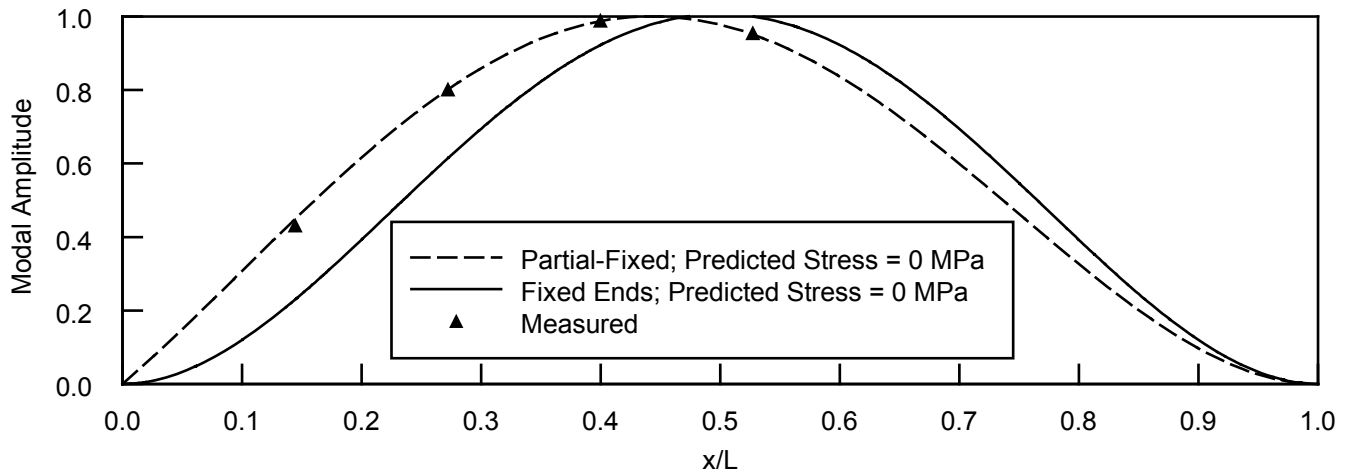


Fig. 9 First Flexural Mode for Amtrak Member M5-L6, Eyebars 1

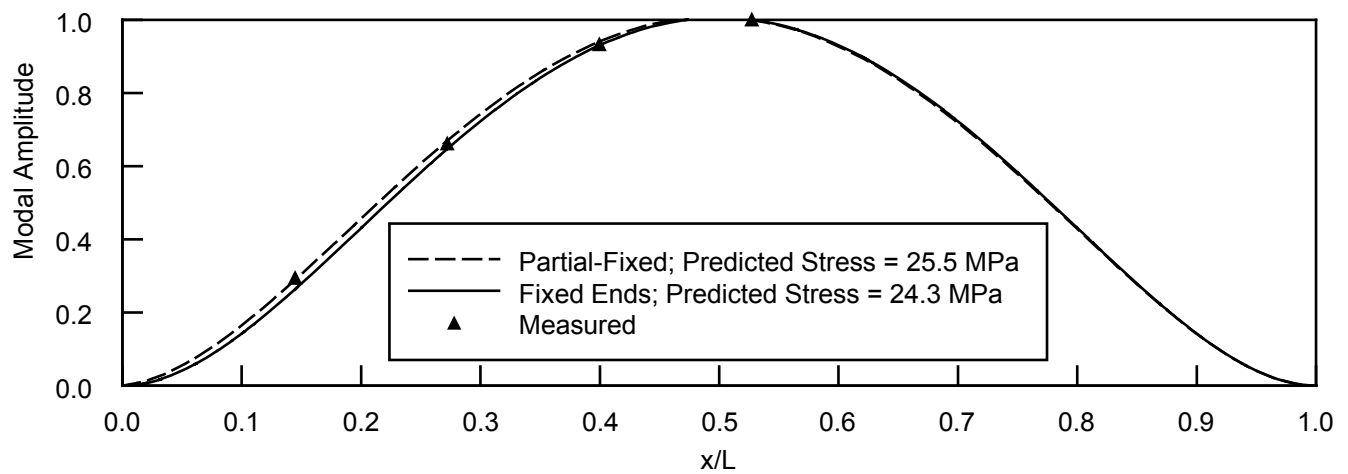


Fig. 10 First Flexural Mode for Amtrak Member M5-L6, Eyebars 4

CONCLUSIONS

An analytical model has been examined that enables the determination of stress from the observed fundamental flexural natural frequency in eyebars with fixed ends. It has been shown that using the pin-ended model as currently given by AREMA when fixed-end conditions actually exist can result in significant error, especially for eyebars with relatively low slenderness ratios. Laboratory test results were presented that served to validate the fixed-end analytical model, and field tests have also shown excellent correlation with this model when fixed-end conditions are apparent. It has been demonstrated that the appropriate length to use in this case is the clear distance between overlapping eyebar heads. Laboratory test results were also presented which considered the behavior of eyebars with significant pin-hole wear and with no lateral restraint of the heads. For all but the lowest levels of stress in this rather extreme situation, the eyebar response closely followed the fixed-end model when using a length equal to the distance between the far edges of the pins. Field tests of eyebars that displayed varying degrees of rotational stiffness at one end were examined to illustrate how an analytical model with variable-stiffness rotational springs might be used to accurately predict stresses in these situations. From a more practical standpoint, however, acceptable approximations might be obtained by using the fixed-end model with an eyebar length measured to the far edge of the pin at the end of reduced rotational restraint. The results of this research have potential applications well beyond supporting the flame-shortening process for eyebars. For example, the ability to quickly and accurately measure eyebar tensions in a bridge could provide valuable information relevant to bridge rating and performance assessments. Further, for bridges that are instrumented with strain gages to study live load behavior, the work presented here could be used to obtain dead load characteristics that, when combined with the strain gage results, would provide a complete picture of overall eyebar stress levels.

ACKNOWLEDGEMENTS

The author gratefully acknowledges the assistance provided by G. Davids and M. Brinck of the Federal Railroad Administration, R. Garro, J. Wallace, and S. Hardy of CSX Transportation, C. Yordy and J. Richter of Amtrak, and S. Harlacker and M. Hawkins of Hardesty & Hanover.

REFERENCES

1. American Railway Engineering and Maintenance-of-Way Association (AREMA), “Section 1.12: Pins and Pin-Connected Members”, *Manual for Railway Engineering*, 15-1-71, 2010.
2. American Railway Engineering and Maintenance-of-Way Association (AREMA), “Article 3.1.14: Pin Clearances”, *Manual for Railway Engineering*, 15-3-8, 2010.
3. American Railway Engineering and Maintenance-of-Way Association (AREMA), “Section 8.2: Method of Shortening of Eyebars to Equalize Stress”, *Manual for Railway Engineering*, 15-8-10 – 15-8-12, 2010.
4. Mazurek, D.F., “Evaluation of Common Method for Eyebars Tension Measurement”, *Proceedings of the 2010 Structures Congress*, American Society of Civil Engineers, 2010, 62-73.
5. Timoshenko, S., Young, D.H., and Weaver, W., *Vibration Problems in Engineering*, 4e, John Wiley & Sons, 453-454.

Three-Dimensional Mechanics of Microcellular Solids Using Scanning Confocal Microscopy

R.P. McCaffrey, P.B. Matthews and D.S. Gianola

*Department of Materials Science and Engineering
University of Pennsylvania
3231 Walnut Street, Philadelphia, PA 19104*

INTRODUCTION

Cellular solids are materials comprised of an interconnected network of solid ligaments or plates which form the edges and walls of cells^[1]. These types of materials are often considered in engineering applications because of their unique properties relative to their fully-dense counterparts, including elastic moduli, specific strength, and thermal conductivity^[1]. Classical cellular mechanics models, such as the Gibson-Ashby model, have been extensively used to describe the mechanical response and idealize the behavior of foam-like materials by modeling unit-cell level deformation. Scaling equations provided by such mechanics formulations allow for comparison between theory and experiment through readily measurable quantities such as relative density. These mechanics models are applied to cell sizes on the order of several micrometers or larger, and often to materials with random cell structures in the absence of a complete understanding of the mechanics governing local deformation. Direct experimental characterization of unit-cell level deformation has been scarce and generally limited to either two-dimensional or post-mortem analyses. Extensions to micro- and nanostructured systems are further complicated by size-dependent mechanical behavior where the constitutive response of the ligament material is not always known *a priori*.

To better experimentally characterize the mechanics of porous materials, we have developed a novel micromechanical testing technique that utilizes scanning confocal microscopy and digital volume correlation to provide three-dimensional deformation analysis of open-cell cellular solids. The testing system employs a piezoelectric actuator, a miniature load cell, and multi-axis alignment stages. Micromechanical testing is performed within a high frame rate confocal microscopy system, which utilizes a piezoelectric objective scanner to systematically alter depth of focus. Controlling depth of focus provides a way to achieve optical sectioning of transparent or porous structures, which results in full three-dimensional sample reconstruction and visualization (Fig. 1a). Laser scanning confocal microscopy provides enhanced focal plane resolution by placing a spatial pinhole along the optical axis to eliminate out-of-focus intensities. The planar confocal images of the optical sectioning are assembled into volume arrays. Using digital volume correlation, the volume arrays are correlated to provide local and full-field displacement and strain measurements to subvoxel accuracies in three dimensions.

This technique has been validated by tracking the deformations of 25.4 μm thick polyimide films in three dimensions during tension testing. 3 μm nominal diameter polystyrene beads are disbursed on the top and bottom surfaces of the transparent polyimide film to provide high-contrast markers for tracking. As the polyimide film is pulled in tension, the polystyrene markers, as well as other natural areas of high-contrast throughout the thickness of the film, are tracked. Full displacements (Fig. 1b) and strain fields are computed for every deformation increment, and in conjunction with the load measurement are used to measure Young's modulus and Poisson's ratio for three orthogonal directions.

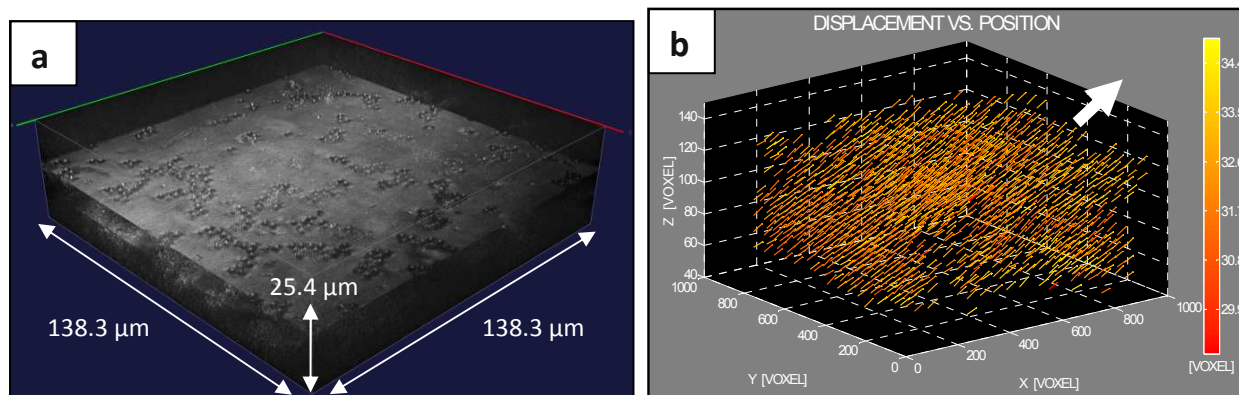


Fig. 1: (a) Three-dimensional specimen reconstruction of a polyimide film with polystyrene bead markers (note different vertical scale to show specimen thickness), and (b) a vector plot used to visualize three-dimensional displacements of discrete marker points within the sample (superimposed white arrow indicates pulling direction).

We have demonstrated a viable method to resolve in three dimensions the deformations of transparent structures. This experimental technique will be extended to study three-dimensional periodically ordered polymeric microcellular solids synthesized by multi-beam interference lithography (Fig. 2)^{[2],[3]}. In addition, other periodic elastomeric cellular solids have shown the ability to undergo pattern transformations triggered by deformation, which demonstrates the potential for mechanically-tunable photonic and phononic properties^[4]. Experimental testing of these structures will be compared to the theoretical predictions of the cellular mechanics models, and the influence of size-dependent effects on the properties and behavior of these materials will be explored at the microscale. Macroscopic mechanical behavior will be correlated with unit-cell level deformation. This experimental technique may also be applicable to characterizing unit-cell level deformations of other cellular systems, such as porous biological materials or periodically ordered multi-phase structures.

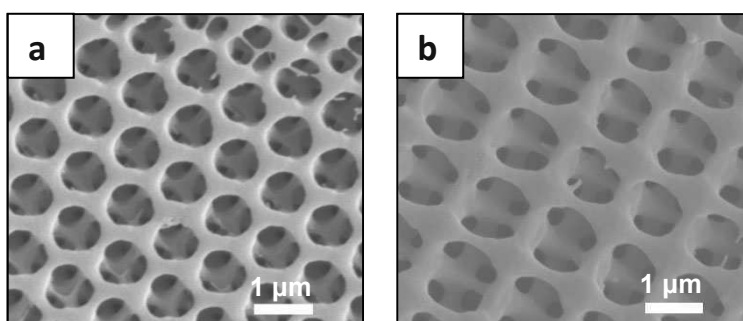


Fig. 2: Examples of three-dimensional periodically ordered polymeric microcellular solids: (a) SU-8 diamond like structure, and (b) POSS diamond structure. Images are courtesy of S. Yang and J. Li at University of Pennsylvania.

REFERENCES

- [1] Gibson, Lorna J., and Michael F. Ashby. *Cellular Solids*. Cambridge: Cambridge UP, 1997. Print.
- [2] Ullal, Chaitanya K., Martin Maldovan, Edwin L. Thomas, Gang Chen, Yong-Jin Han, and Shu Yang. "Photonic Crystals through Holographic Lithography: Simple Cubic, Diamond-like, and Gyroid-like Structures." *Applied Physics Letters* 84.26 (2004): 5434. Print.
- [3] Moon, Jun Hyuk, Jamie Ford, and Shu Yang. "Fabricating Three-dimensional Polymeric Photonic Structures by Multi-beam Interference Lithography." *Polymers for Advanced Technologies* 17.2 (2006): 83-93. Print.
- [4] Mullin, T., S. Deschanel, K. Bertoldi, and M.C. Boyce. "Pattern Transformation Triggered by Deformation." *Physical Review Letters* 99.8 (2007). Print.

Characterization of the Mechanical Properties of Surface Nanocrystallized Materials

Joshua D Gale
Graduate Student

Jeremy Marshall
Undergraduate Student

Ajit Achuthan
Assistant Professor

Department of Mechanical & Aeronautical Engineering,
8 Clarkson Avenue, Clarkson University, Potsdam, NY 13699

ABSTRACT

Recrystallization of the grain structure of metals into nano-sized grains by using mechanical means, has received wide attention in the last two decades. It is well known that materials with a fine-grain crystal structure have favorable properties compared to the same materials with coarse-grained crystal structure. Surface Mechanical Attrition Treatment (SMAT), a technique developed in the early part of this decade, has been successfully used to recrystallize the surface grains of metals into nanocrystals of the order of 10 to 100 nanometers from their original grain sizes on the order of 10 to 30 microns. Resulting enhancement in surface properties has quite interesting applications, varying from materials with improved fatigue resistance to medical devices. In this study, our focus is on experimental characterization of the enhancement in mechanical properties of surface nanocrystallized metals. Copper, Aluminum and Titanium samples are subjected to SMAT under different conditions followed by appropriate heat treatment. Microindentation and nanoindentation techniques are conducted to characterize various mechanical properties. Microindentation test shows significant improvement in surface hardness due to SMAT process on these samples. Our initial results from nanoindentation also show significant enhancement in materials surface properties. However, several other interesting characteristics obtained in the nanoindentation tests require further studies for verification.

1. Introduction

At low temperatures nanocrystallization is one of the few mechanical techniques that will increase strength and toughness without severely reducing ductility. The large number of grains and grain boundaries inhibit the movement of dislocations, and at low temperatures this strengthens the material. According to Hall Petch theorem, mechanical properties such as strength and hardness, will improve as grain sizes decrease until they are below the 10 nm size. Below 10 nm size the behavior is reverse, governed according to the inverse Hall Petch Theorem [1]. Nanocrystallization of a material is accomplished in various ways, such as electroplating [2], atomic layer deposition [3], severe plastic deformation (SPD) [4], inert gas condensation [13], and pulsed laser deposition [2]. In this experiment SPD is studied as the method for nanorecrystallization. SPD leading to nanorecrystallization can be enacted in several ways. Some popular techniques consist of equal angular channel pressing (ECAP) [5], high pressure torsion (HPT) [14], surface mechanical attrition treatment (SMAT) [7, 8], and hammer peening [9].

SMAT was chosen as in this study due to its relatively simplistic implementation and broad application for various materials. The surface of a material in most cases is where most of the fatigue and wear initiate, so improving the surface layer will improve the durability of the material as a whole. This is especially true in thin film applications, since the surface to volume ratio is very high. SMAT is accomplished by impregnating kinetic energy from an impulse into the surface of a material through strain hardening. The energy from the impact displaces and shifts dislocations in the materials crystal lattice. Frank Reed sources develop from the constant impact as dislocations continue to shift and combine. Shear bands and low energy dislocation structures form, storing strain energy from the impacts. These dislocation structures form into cells causing low

angle tilt boundaries that make up the basis for new grain formation. It has also been debated that a true nanocrystalline structure is not formed until the sample has been annealed allowing recrystallization and grain growth to occur [10]. The newly formed grains or dislocation cells range in size from 10 to 100 nm depending on the material and crystal structure.

In the present study, we characterized the improvement in the surface properties of bulk and thin foil material. Bulk copper samples were characterized by both microindentation and nanoindentation testing. We studied the improvement in properties through the thickness by cutting the sample and probing the cross-sectional face. Microindentation testing clearly shows significant improvement in hardness at the surface. Deeper into the sample this enhancement in properties reduces and eventually reaches the untreated sample value. Initial results from nanoindentation testing also shows significant improvement. However the overall behavior is inconclusive and requires further studies to confirm. Nanoindentation testing was also used to determine the improvement in surface properties for thin foil samples. Both Aluminum and Titanium samples were studied. In both cases, the reduced modulus was found to increase significantly, while hardness didn't show any significant improvement.

2. Experiment

2.1 Thick samples

Bar Stock of 25.4 mm diameter 99.99% alloy 101 Copper Alloy was utilized. The bar was cut into 12 mm pucks, polished and then annealed in a vacuum furnace at 700°C for one hour. Polishing consisted of varying grits of silicon carbide paper, 120, 300, 400, 600, 2400, and 4000 grit respectively. After rough polishing samples were diamond polished with a 3 and 1 μm Buehler Meta-Di diamond suspension. Annealing removed the effects of polishing and any prior mechanical deformation, as well promoted grain growth up to an average size of 40 μm . Prior to annealing, samples were cut transversely using a Buehler 20 HC diamond wafering blade and then polished. After each step the samples were then viewed using an Olympus PME optical microscope to document the change in microstructure. The samples were then treated to SMAT for 15 minutes. The SMAT process was accomplished by using a dome shaped vacuum sealed refractory chamber attached to a Labworks Inc. LW-139-40 Electrodynamical Shaker System. Each sample was clamped into the top of the dome refractory chamber and impacted with ten 6mm tungsten carbide balls at a frequency of 31 HZ. The pre cut cross sections were paired together at the spot of the cut and clamped to the top of the refractory chamber. Further details on the SMAT process have been documented in previous papers [9,10]. Tungsten balls were used in order to deter mechanical alloying of the balls into the specimen. One sample was left without treatment to be used as annealed control sample during testing.

Microindentation (hardness) test was used to confirm the existence of surface improvement with the use of a LECO M-400 Microindenter with a Vickers Tip. A series of 45 indents spaced 250 microns apart were performed down the cross section of a polished as annealed copper sample. The indents were produced with a force of 200 gf and a hold time of 15 seconds to account for thermal expansion and creep. The same method was repeated with the SMAT sample for comparison.

Nanoindentation was carried out on the same cross sections that microindentation had been performed on, for verification of results. A Hysitron Triboindenter 950 nanoindenter was used for indentation along with a Berkovich 150nm tip. The cross section of each sample was indented a total of 30 times laterally from the edge subjected to SMAT to the opposite untouched surface. Each indent lasted 15 seconds with a two second hold time to account for creep and thermal expansion. This process was repeated 3 times on each sample for validation of consistent results.

2.2 Thin samples

Foils of 10.1 micron thick Titanium and 12 micron thick Aluminum were treated using the same refractory chamber and vibration apparatus. In order to prevent excessive plastic deformation to the surface and eventual fracture of the thin foil a sacrificial aluminum puck was used. Each foil was held in between two 7068 alloy aluminum plates of 6 mm thickness and attached to the top of the refractory chamber. The aluminum plate allowed for transmittance of the strain inflicted by the impulse of the tungsten balls, but prevented the destruction of the foil. The foil was then tested with the use of a Hysitron Triboindenter 950 nanoindenter. The specimens were tested using a nanoindenter with a Berkovich 150 nm radius tip and a series of 25 indents. Both non treated and 30 minute SMAT samples were then compared based on change in reduced modulus and hardness (GPa).

3. Results and Discussion

3.1 Bulk Material

Results of the microhardness test conducted on SMAT treated and non treated samples are shown in [figure 1](#). Two sets of samples were tested both for untreated and treated cases. Results obtained shows that a large increase in hardness is achieved through SMAT process on the surface of the sample. The degree of enhancement in properties was similar for both the samples indicating a high level of repeatability of the sample preparation, SMAT and testing processes. The hardness decreases with depth as expected and reaches the hardness of the untreated sample at a depth of around 7mm. Improvement in properties for such a large depth has not been observed in previous studies [11,12,15]. Another interesting behavior is the enhancement in properties at the non-SMAT region. Considering the fact that these samples were not completely constrained laterally on that surface, the chances of property enhancement from the effect of residual stress build up is negligible. A modified setup with an even lower amount of constraint will be used in our future studies to investigate this property enhancement.

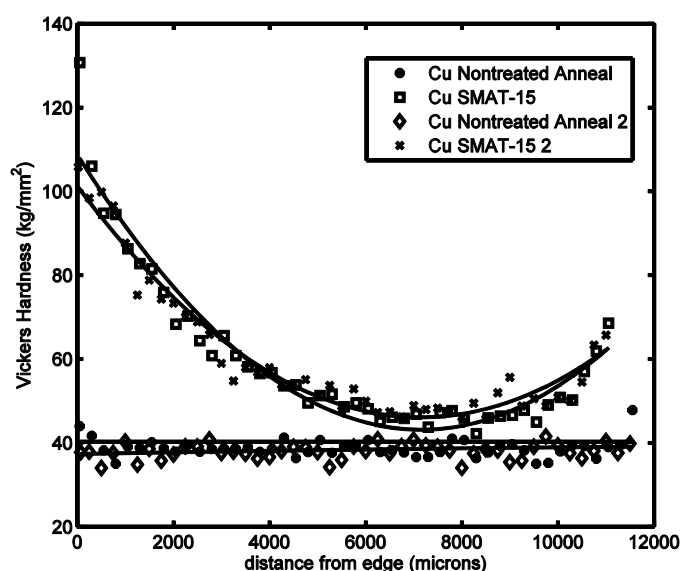


Fig. 1 Vickers hardness results of micro indentation on four cross sections of copper samples both as annealed and 15 minute SMAT. Hardness on SMAT sample is seen to decrease linearly from the edge of the sample

Results from the nanoindentation test of treated and untreated samples, two each, are shown in [figures 2 & 3](#). For each of the treated samples scanning was carried out at three different locations in order to verify the consistency of the result. Only one of the results is shown in the figure since all the three results match very well. SMAT treatment increased the reduced modulus almost two times that of the untreated values. Interestingly, the enhancement in modulus and the hardness did not show any significant variation through the thickness as we observed in the hardness behavior obtained using microindentation. Any enhancement in properties due to SMAT process is expected to vary with thickness since the induced plastic deformation due to ball impact should vary with the thickness. The uniform enhancement in properties as we observed in our result should result from a uniform attrition process, which in our case is polishing step conducted after SMAT. As per our result, this specimen preparation step for nanoindentation, appears to induce significant amount of plastic deformation resulting in significant property enhancement. However, this enhancement in property is only in a very thin volume of the material near the polished surface. In nanoindentation method, the indentation force and stress field are in a very small volume that the result obtained from this measurement is dominated by the effect of polishing. On the other hand, the hardness measurement obtained from the microindentation where indentation depth is much larger and hence the influence of polishing is relatively lower, clearly shows a variation in hardness values with thickness indicating the effect of SMAT. In order to investigate this further, one of the SMAT samples was annealed and measurements were repeated (not shown here). Annealing removed all the property enhancement, though the samples did not completely attained its original before-SMAT

values. Further studies will be conducted to quantify the effect of polishing in order to differentiate it from that obtained from SMAT process.

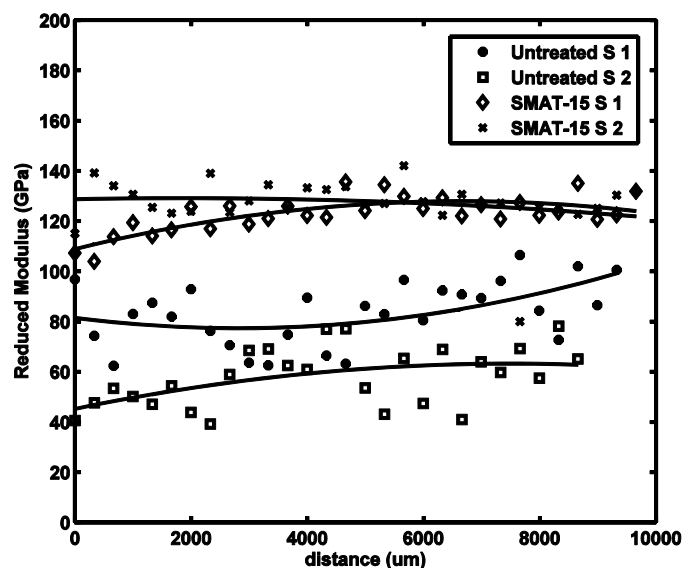


Fig. 2 Nanoindentation results of reduced modulus on both as annealed and 15 minute SMAT copper cross sections. A large increase in the coppers elastic modulus can be seen towards the middle of the sample

More than two times enhancement was also observed in hardness due to SMAT process is as shown in [Fig 3](#). As in the case of reduced modulus, the enhancement in the hardness of the SMAT sample was disappeared when the sample was subjected to annealing.

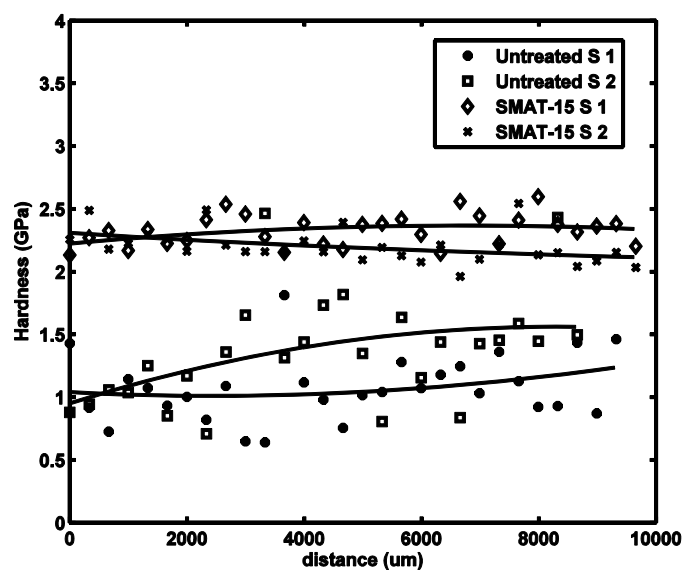


Fig. 3 Nanoindentation results of hardness on both as annealed and 15 minute SMAT copper cross sections. More than a 100% increase in hardness is seen throughout the sample

3.2 Thin foil

Nanoindentation results of aluminum foil samples are given in figures 4 and 5. Data obtained at different locations on the surface shows that there is roughly a 40% increase in the reduced modulus. This is quite significant considering the fact that for very thin samples enhancement in properties on the surface has higher influence on its macroscopic properties. However, the enhancement in the surface hardness is marginal. Since the variation observed in the hardness values obtained at different locations is significantly high, drawing a statistically meaningful conclusion is challenging.

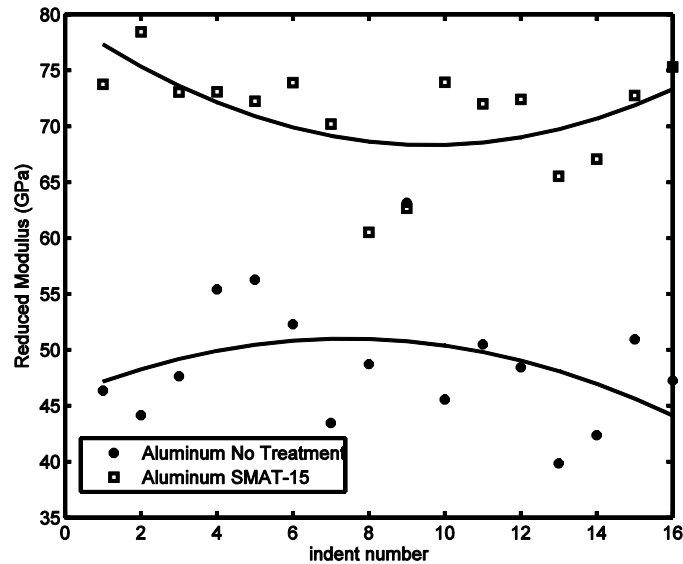


Fig. 4 Nanoindentation results of reduced modulus on both as received and 15 minute SMAT aluminum foil samples. An increase in the elastic modulus after a 15 minute SMAT treatment is shown.

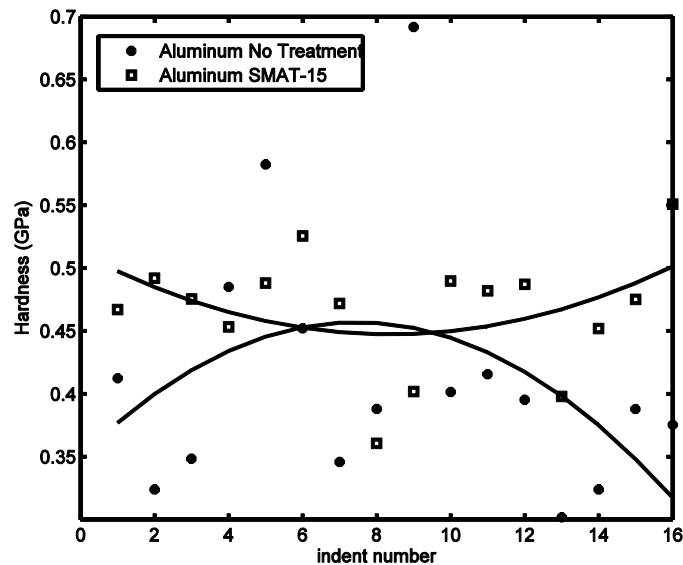


Fig. 5 Nanoindentation results of hardness on both as annealed and 15 minute SMAT aluminum foil samples. So far no real increase has been found in terms of hardness

Improvement in the reduced modulus was also observed in the titanium foil (figures 6 and 7). Improvement was relatively lower compared to that aluminum foil samples. This could be due to the fact that Titanium is a much stiffer and harder material, to obtain same amount of improvement in the property Titanium would require more SMAT energy. Currently we are testing Titanium under longer period of SMAT to investigate this effect. We have also made some modifications to the current set up in order to vary the impact energy. In the case of hardness, SMAT treatment did not make any improvement to the sample, similar to aluminum foil material.

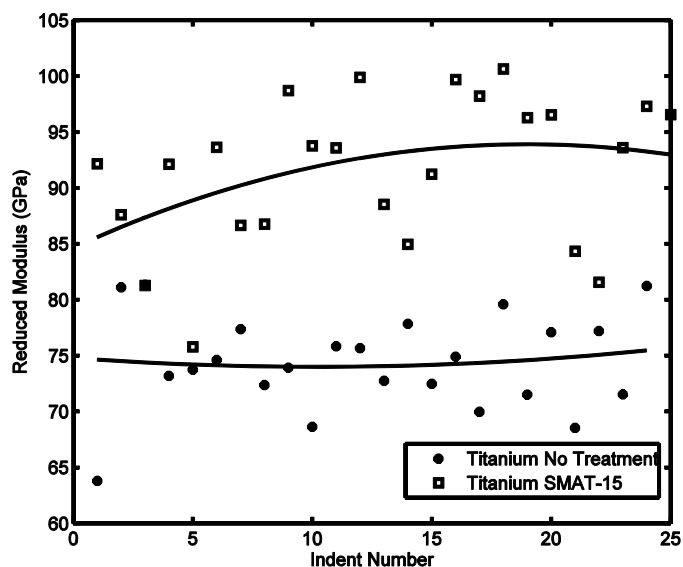


Fig. 6 Nanoindentation results of reduced modulus on both as received and 30 minute SMAT Titanium foil samples. An increase in the elastic modulus of the thin foil is seen in the SMAT sample

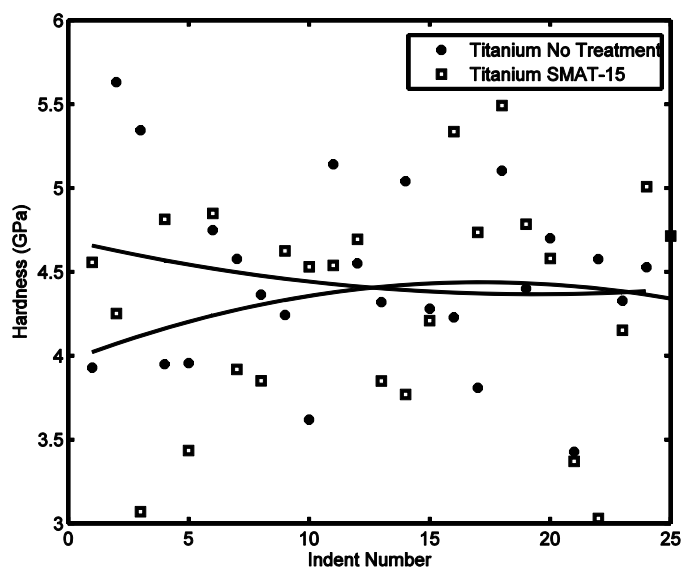


Fig. 7 Nanoindentation results of hardness on both as annealed and 15 minute SMAT Titanium foil samples. Similar to the aluminum sample no clear trend can be seen in terms of hardness increase between either sample

4. Conclusions

Improvement in mechanical properties due to surface mechanical attrition treatment (SMAT) was studied for bulk and thin foil samples. Enhancement in properties was determined by microhardness and nanoindentation tests. Microhardness tests clearly show significant improvement in the hardness properties. Improvement in surface hardness was achieved for as deep as 6 mm into the sample. This is significantly high compared to previous studies. Initial results from nanoindentation results are substantially different from those obtained from microhardness tests. The difference is mainly attributed to the difference in scale. Some of the interesting characteristics obtained in the nanoindentation test require further study to confirm the behavior and to provide explanation for such behavior. In the case of aluminum and titanium thin foil, significant enhancement in reduced modulus was obtained. However, hardness was not changed for the level of impact energy used in the current study.

Acknowledgements

The authors of this research would like to thank Arnold Magnetics for their donation of thin foil titanium specimens, as well as Center for Advanced Materials and Processing (CAMP) at Clarkson University for the use of their resources and facilities.

References

- [1] Aifantis, K. E., and Konstantinidis, A. A., 2009, "Hall–Petch Revisited at the Nanoscale," *Materials Science and Engineering: B*, **163**(3) pp. 139-144.
- [2] Bao, Q., Chen, C., Wang, D., 2005, "Pulsed Laser Deposition and its Current Research Status in Preparing Hydroxyapatite Thin Films," *Applied Surface Science*, **252**(5) pp. 1538-1544.
- [3] Erb, U., Aust, K.T., and Palumbo, G., 2007, "Nanostructured Materials (Second Edition)," William Andrew Publishing, Norwich, NY, pp. 235-292.
- [4] Fecht, H.J., and Ivanisenko, Y., 2007, "Nanostructured Materials (Second Edition)," William Andrew Publishing, Norwich, NY, pp. 119-172.
- [5] Iwahashi, Y., Horita, Z., Nemoto, M., 1998, "The Process of Grain Refinement in Equal-Channel Angular Pressing," *Acta Materialia*, **46**(9) pp. 3317-3331.
- [6] Klepper, K. B., Nilsen, O., and Fjellvåg, H., 2007, "Growth of Thin Films of Co₃O₄ by Atomic Layer Deposition," *Thin Solid Films*, **515**(20-21) pp. 7772-7781.
- [7] Lu, J., and Lu, K., 2003, "Comprehensive Structural Integrity," Pergamon, Oxford, pp. 495-528.
- [8] Lu, K., and Lu, J., 2004, "Nanostructured Surface Layer on Metallic Materials Induced by Surface Mechanical Attrition Treatment," *Materials Science and Engineering A*, **375-377** pp. 38-45.
- [9] Mao, X. Y., Li, D. Y., Fang, F., 2010, "A Simple Technique of Nanocrystallizing Metallic Surfaces for Enhanced Resistances to Mechanical and Electrochemical Attacks," *Materials Science and Engineering: A*, **527**(12) pp. 2875-2880.
- [10] Mao, X. Y., Li, D. Y., Fang, F., 2010, "Can Severe Plastic Deformation Alone Generate a Nanocrystalline Structure?" *Philosophical Magazine Letters*, **90**(5) pp. 349.
- [11] Ren, J., Shan, A., Zhang, J., 2006, "Surface Nanocrystallization of Ni₃Al by Surface Mechanical Attrition Treatment," *Materials Letters*, **60**(17-18) pp. 2076-2079.
- [12] Révész, Á., and Takacs, L., 2009, "Coating a Cu Plate with a Zr–Ti Powder Mixture using Surface Mechanical Attrition Treatment," *Surface and Coatings Technology*, **203**(20-21) pp. 3026-3031.
- [13] Sanders, P. G., Eastman, J. A., and Weertman, J. R., 1997, "Elastic and Tensile Behavior of Nanocrystalline Copper and Palladium," *Acta Materialia*, **45**(10) pp. 4019-4025.
- [14] Vorhauer, A., and Pippan, R., 2004, "On the Homogeneity of Deformation by High Pressure Torsion," *Scripta Materialia*, **51**(9) pp. 921-925.
- [15] Wang, K., Tao, N. R., Liu, G., 2006, "Plastic Strain-Induced Grain Refinement at the Nanometer Scale in Copper," *Acta Materialia*, **54**(19) pp. 5281-5291.

Variation of Compression of Seals in PEM Fuel Cells

Chi-Hui Chien^{*a}, Chih-Wei Lin^a, Yuh-Jin Chao^b

Cui Tong^c, John Van Zee^c and Ting-Hsuan Su^a

^a Department of Mechanical and Electro-Mechanical Engineering,
National Sun Yat-Sen University,
70, Lien-Hai Rd., Kaohsiung 804, Taiwan ROC

^b Department of Mechanical Engineering, University of South Carolina
300 S. Main Street, Columbia, SC 29208, USA

^c Department of Chemical Engineering, University of South Carolina
301 S. Main Street, Columbia, SC 29208, USA

* Corresponding Author, chchien@faculty.nsysu.edu.tw

ABSTRACT

Seals or gaskets under compressive stress are used in PEM fuel cells (PEMFC) or stacks to prevent leaking of the liquid and gas inside the cell. The fuel cells are normally assembled with bolts or a combination of bolts and springs. As the seal is typically made of polymers, the level of the compressive stress on the seal during long term operation of the fuel cell depends on the stress relaxation property and any potential chemical degradation of the seal materials. In addition, the amount of compression applied to the seal may vary due to temperature changes during the fuel cell operation which causes thermal expansion and contraction of all components in the cell. To understand the sealing force existed in a fuel cell during operation, all these factors must be fully understood.

In this study, the compression of the seal in a PEMFC was investigated experimentally. Specifically the compressive amount was measured in-situ, i.e. immediately after the assembly and during the normal operation of the PEMFC. The objective of this study is to gain an understanding of the variation of compressive strain applied to the seal as the temperature of the PEMFC changes and cycles. This information can then be used to estimate the sealing force in the cell and consequently the life prediction of the seal. Both the temperature and pressure are monitored during the tests.

An interesting observation is that both the gap spacing and the outside dimensions jumped initially and did not follow the cell temperature's later rise to a maximum of 80oC. It's effect by the first gas inlet pressure.

Keywords: Seals, PEMFC, Fuel cell stack, Durability

1. Introduction

There have been many studies on how the pressure applied to the GDL affects the electrical performance of PEMFC. Lee et al. [1] measured the power performance of PEMFC and found that each GDL has its optimal assembly pressure because of different mechanical properties and micro-porous characteristics. Chu et al. [2] proposed a mathematical model for the porous structure of the PEM GDL and studied its effects on cell performance. Because of the relatively thin dimensions (e.g. 20-200 μ m) and low mechanical strength of the GDL and membrane electrode assembly (MEA) versus sealant, bipolar plates and end plates, one important goal in the stack design and assembly is to achieve a proper and uniform pressure distribution. To achieve this goal, many stacking designs have been proposed [3–5]. Zhang et al. [6] employed hydro-pressure on the end plates to obtain uniform pressure. It is demonstrated that the cell performed better than the traditional nut and bolt point-load stacking design. Lee et al. [7] compared simulation results with experimental data at various levels of assembly pressures and analyzed the procedures for the fuel cell stacking assembly. The results obtained can help determine the proper stacking parameters such as bipolar plate thickness, sealing size and assembly pressure, and are important in obtaining a consistent fuel cell performance.

As the seal in PEMFC is typically made of polymeric materials, stress relaxation is inevitable which may eventually lead to leakage of the containments. In practice, performance of seals is required to be known over periods of years [8] and therefore accelerated testing is required from short term laboratory tests to predict long term behavior. Studies on the sealing of PEMFC is however scarce. Tan, et al [9-11] have studied chemical and mechanical degradation of sealing materials in PEMFC environment [12-14]. Burton et al. [15] made measurements for one year and applied an Arrhenius equation to predict the performance at the fifth years. Meier and Kuster [16] made measurements for up to 17 years in dry condition and found that at longer time the dominance of chemical relaxation could cause errors, but obtained some success in correlating results from short term tests by the method of reduced variables. Sprey [17] has demonstrated that predictions of compression set can be made from intermittent and continuous tension relaxation measurements. Derham [18] demonstrated the effects that arise from the cycling of temperature on a fluorocarbon elastomer and immersion in liquids on a EPDM and concluded that, while swelling of fluorocarbon elastomer could be adequately described by theory, temperature effects would need to be tested for each set of circumstances. In studying the sealing of PEMFC, a method for determining the torque applied to the bolts to achieve a desired compression of the elastomeric gasket in PEMFC is proposed by Tan, et al [19].

In this study, the compression of the seal in 25 cm² single PEMFC [20] was investigated experimentally. The thickness of the seal or the gap spacing in FC was measured *in-situ*, i.e. immediately after the assembly and during a thermal cycle of the PEMFC. The objective is to gain an understanding of the level of variation of the compressive strain applied to the seal as the temperature of the PEMFC changes and cycles. This information can be useful in estimating the sealing force in the cell and consequently the life prediction of the seal.

2. Experimental Procedures

2.1 Preparation of the PEMFC

A single PEM cell was assembled. As shown in the Fig. 1, the PEMFC contains two end plates, two current collecting plates, two flow channel plate, two gas diffusion layers, two sheets of gasket, and a membrane electrode assembly (MEA) in the middle. Table 1 shows the dimensions and materials of each component used in our test. The dimensions of the assembled cell are shown in Fig. 2.

The flow field channel and end plates were first cleaned. Dimensions and thickness of the gasket, MEA, and gas diffusion layer were measured and recorded. Two gaskets were cut from a large sheet into 76.3x76.3 mm and a square opening 50x50 mm in the center was made to accommodate the two carbon clothes (GDL) with a membrane sandwiched in-between. Eight nuts/bolts around the peripherals (see figure 1) were used to assemble the cell. A pre-load or pre-torque of 20kgf.cm was applied first to each bolt and a star sequence was then used to assemble the cell for a uniform distribution of the applied loads. A final torque 50kgf.cm was selected.

2.2 Operation of the PEMFC

A PEMFC testing station was used in the test. The station has heater, pipe, humidifier, electric controller and pressure gauge. A computer and software are used for control and continuous measurement. Following a typical operation of PEMFC, a break-in procedure was first applied for 72 hours. During the operation of the FC, the temperature at the center of the FC was measured with a thermocouple and recorded continuously. The temperature history in this test is shown in Fig. 3.

2.3 Measurement of gap spacing, outside cell dimensions and inlet gas pressure

The overall thickness of the cell and the gap spacing were measured occasionally during the test. As the flow pattern and temperature inside the cell are not uniform from place to place, these dimensional measurements were performed at four sides of the cell as shown in Fig. 4 and Fig. 5.

Fig. 4(a) shows the PEMFC cathode side flow field channel's shape. We can see the inlet and outlet holes and two pipes link with these holes. Fig. 4(b) shows the four measured gap spacing positions. On the upper position is No.1 and the bottom position is No. 3. The left and right side were No.2 and No. 4. No. 2 closed to inlet pipe and No.4 closed to outlet pipe. Fig. 5(a) shows the measuring value position. In the picture, we can see the inside gap spacing and the overall outside thickness measured position. Fig. 5(b) shows inside gap spacing before and after assembly thickness sketch graph. Note that in the FC assembly, two gaskets and a plastic sheet from the MEA are compressed together as the seal as shown in Fig. 5(b). The total thickness of the combined three-pieces before compression is $0.34 + 0.13 + 0.34 = 0.81$ mm. After assembly, there is a compressive strain to the combined seal.

A spark plug gap gauge, Mitutoyo 950-250 was used to measure the gap spacing, which accommodates the seal. This gauge has the range from 0.038 mm to 0.635 mm and the difference in thickness between two adjacent gauges or resolution is 0.0254 mm (0.001 in), which therefore provides

a tolerance or uncertainty of $\pm 0.0127\text{mm}$. A Mitutiyo digital slide caliper having the smallest scale of 0.01 mm was used to measure the outside or external dimensions of the cell. The uncertainty for this measurement is then $\pm 0.005\text{ mm}$. We installed two pressure gauges into anode and cathode gas inlet sides. A U.S. Gauge co. pressure gauge resolution is 0.1psi . The measure range is $0\text{ to }30\text{psi}$. When running the measure experiment, we should be careful about those measure tools conduct electricity.

Table 1. PEMFC dimensions (length (L), width (W) and height (H) or thickness) and materials

Component	End Plate	Current Collecting Plate	Flow Field Channel Plate	Gas Diffusion Layer	Gasket	MEA
Dimension (mm)	108* 108* 18.5	108*76.3*1.3	76.3* 76.3* 13	50* 50* 0.04	76.3*76.3*0.34 (outside)	50* 50*
L* W* H					50*50*0.34 (inside)	0.12
Material	Stainless steel	Copper	Graphite	Carbon Cloth	Saint-Gobain 1005	Gore 57

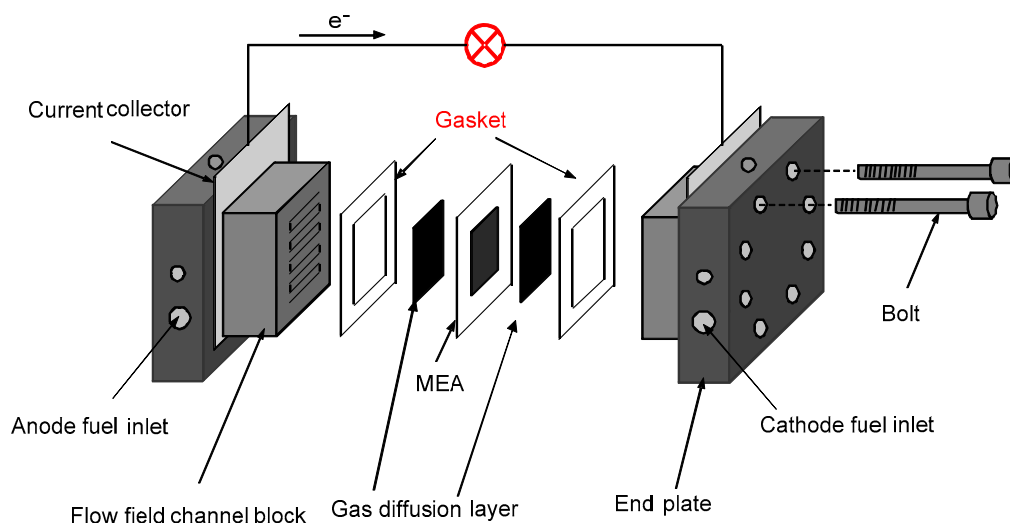
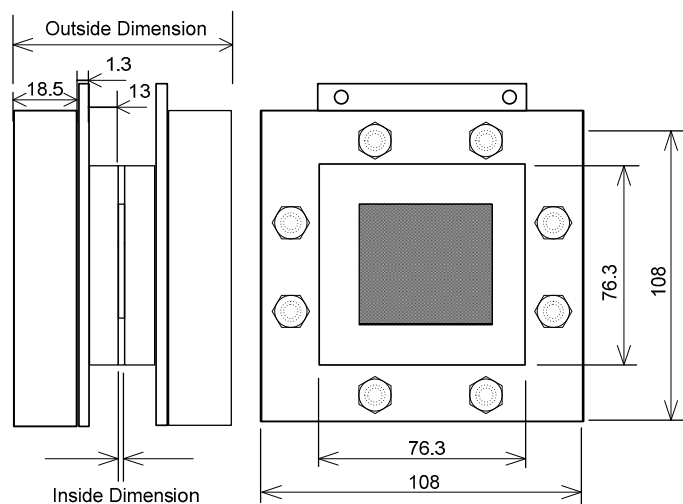


Fig. 1. Schematic of components in a PEM fuel cell



Unit:mm

Fig. 2. Assembled dimensions of the PEMFC tested.

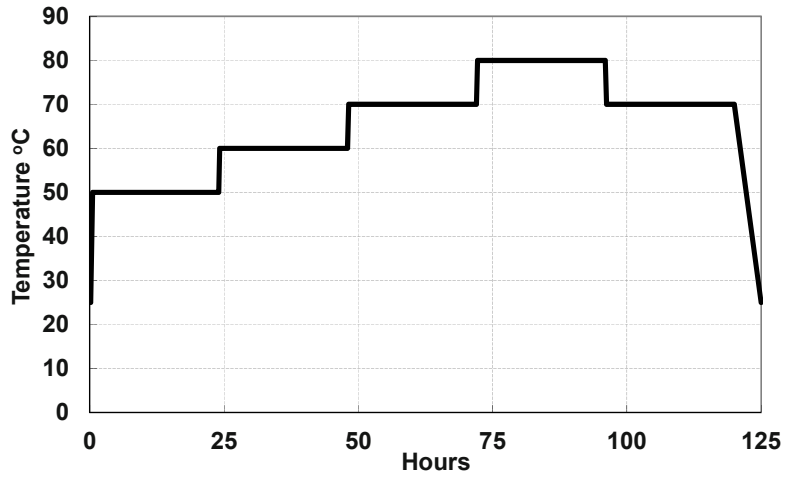


Fig. 3. Temperature history at the center of the fuel cell.

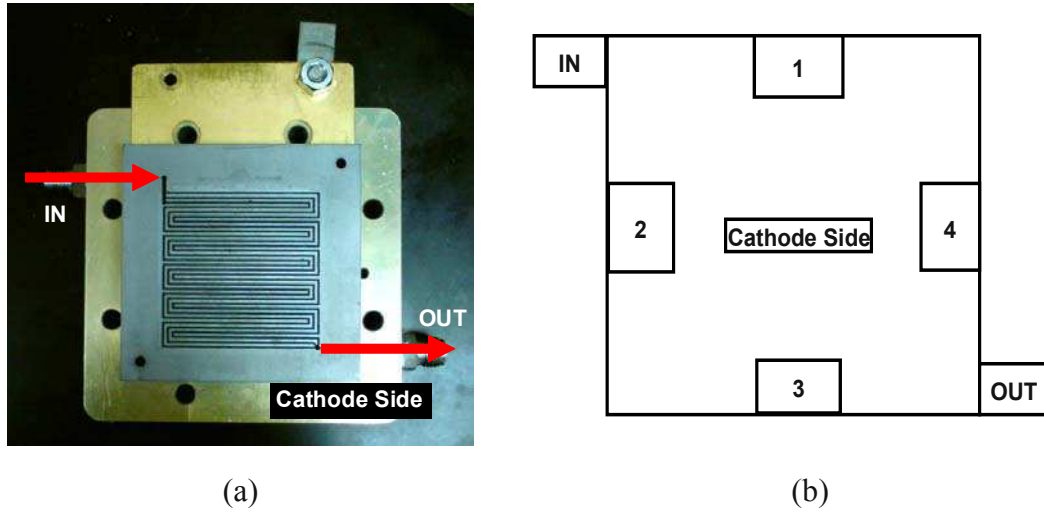


Fig. 4.(a)Front view and (b) the four sides of the PEMFC where the dimensions were measured.

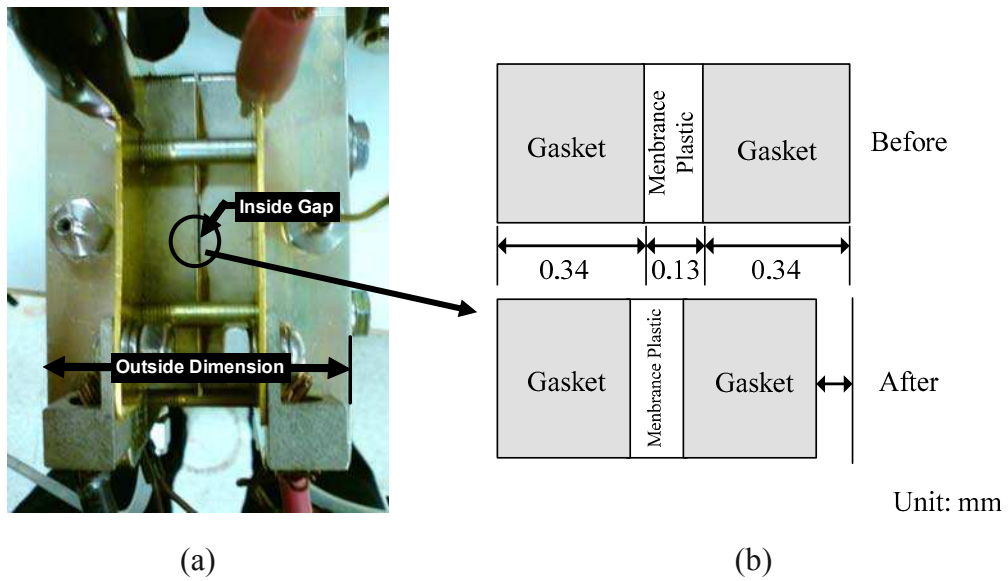


Fig. 5. (a) Side view of the PEMFC showing the locations where the inside gap spacing and the overall outside thickness of the FC were measured; (b) gap spacing before assembly.

3. Results and discussions

The gap spacing at the four sides of the FC during the thermal cycle is presented in Fig. 6 along with the temperature of the FC, Fig. 8(a) shows the time before 0.2 hr's four gaps spacing's variation. Fig. 6(b) shows the four gaps spacing's variations following the PEMFC running breaking procedure. Note that the initial gap spacing at the four sides, after the assembling but before the operation of the FC, are 0.47, 0.546, 0.4955, and 0.546 mm, respectively. They are non-uniform as typically seen in industrial operation. These four readings represent 42 %, 33 %, 39 %, and 33 % compression, respectively, that all exceed the 25 % industry standard for sealing. As shown in Fig. 6(a), the gap spacing at No.1-4 increased in the initial 10 minutes due to the applied humidity gas which is at 25 °C. No change is observed after that until shutdown. Fig. 6(b), the gap spacing No.3 changed during 48th hours. It is suspected that this is because No.3 is close to the exit (for air/water) and at the cell bottom which the air/water cumulating more than the other three. The maximum increase for all four gaps is about 0.0254 mm which is equivalent to a 3 % ($0.0254/0.81 \text{ mm} \times 100 \%$) reduction in compressive strain to the seal. Assuming a linear relation between the stress and strain, this implies that the sealing pressure/force is reduced by 3 % from the time just assembled to normal operation of the cell. Note this reduction of sealing force is purely from thermo-mechanical effect of the cell structure which is in addition to the inherent material stress relaxation behavior of the polymeric seal material.

In order to understand the input gas pressure's variation. We get the pipe of gas pressure rate from inlet of the cathode and anode side. Fig. 7 shows the fuel cell input gas pressure compared with gap spacing values. Fig. 7(a) shows the time before 0.2 hr's compare input gas pressure and four gap spacing's variation. Fig. 7(b) shows following the PEMFC breaking procedure running compare input gas pressure and four gap spacing's variation. In the graph, Fig. 7(a) was found the gap spacing rose immediately when the gas input. Follow procedure, it is suspected that the jump is due to the application of the inlet gas pressure which is in the range of 0.2 to 1.4 psig. For our group simulation study is 0.5~1 psi [21]. At the Fig. 7(b), the gap spacing No.3 was increasing when change the gas pressure. The No.3 was near the gas output and the end of the flow field channel. It's in the bottom and that has more gas and water accumulation. All of the gap spacing's deformation from the first inlet air pressure and No.3 was changed with increasing air/water pressure.

We found the inlet air flow rate in the anode and cathode side. Fig. 8 shows the flow rate's variation that compared with time and temperature. Fig. 8(a) shows the time before 0.2hr's compare inlet flow rate in the anode and cathode side's variation. Fig. 8(b) shows following the PEMFC breaking procedure running in the anode and cathode side's variation. At Fig. 8(a), it found the flow rate start at 0minute that we set 84ccm and 332ccm. After time at 10minute, the flow rate was going to 144 ccm and 570 ccm. After one day, the flow rate was going to 150 ccm and 600 ccm. The cell temperature was going to 60°C that the flow rate at 670 ccm and 170 ccm. The cell temperature was 70 °C that flow rate was growth to 720 ccm and 180 ccm. We try to up to 80 °C, but the flow rate was decreasing.

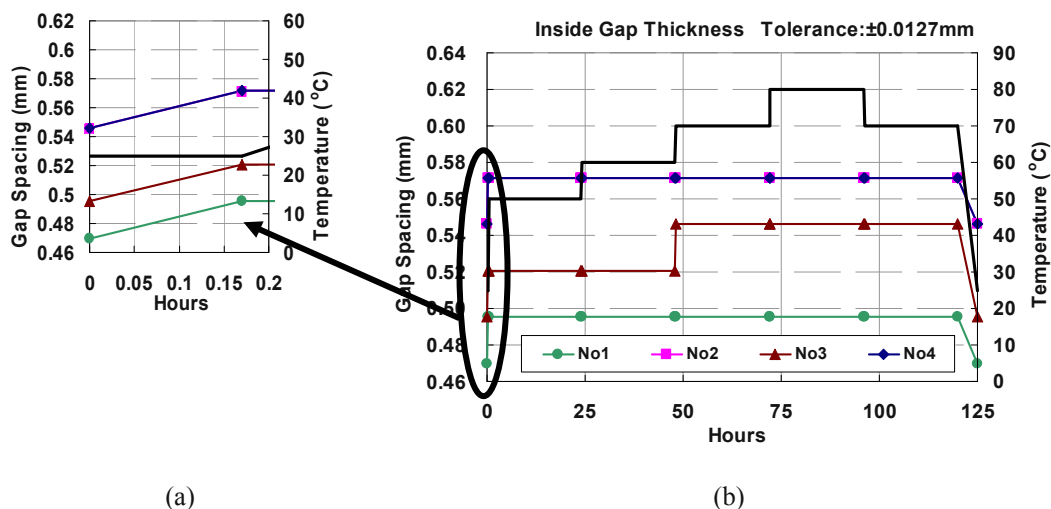


Fig. 6. The gap spacing's variation at four locations (the numbers were shown in [fig.5](#)). (a) the time before 0.2hr's four gaps spacing's variation. (b) the four gaps spacing's variations following the PEMFC running breaking procedure.

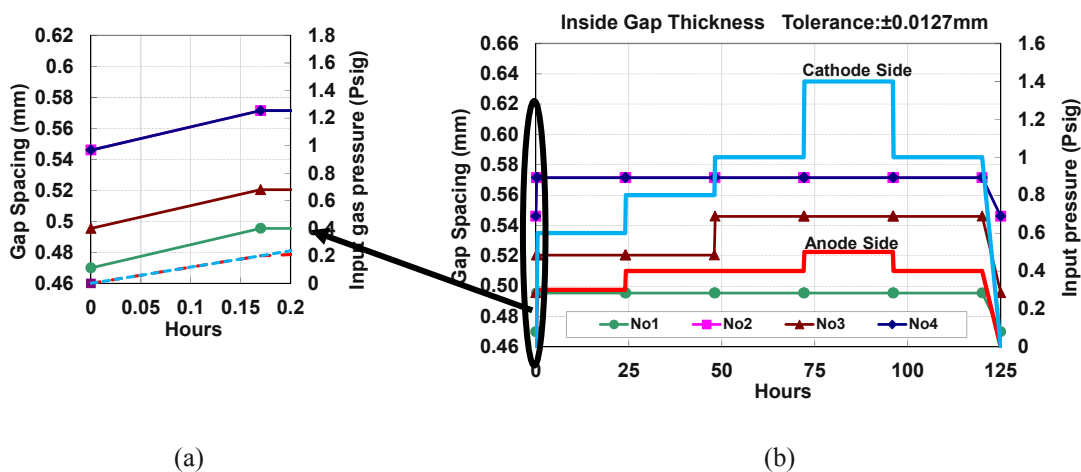


Fig. 7. Compare the gap spacing with input pressure and measured values. (a) The time before 0.2hr's compare input gas pressure and four gap spacing's variation. (b) Following the PEMFC breaking procedure running compare input gas pressure and four gap spacing's variation (Blue line is Cathode side pressure (Air), Red side is Anode side pressure (H₂)).

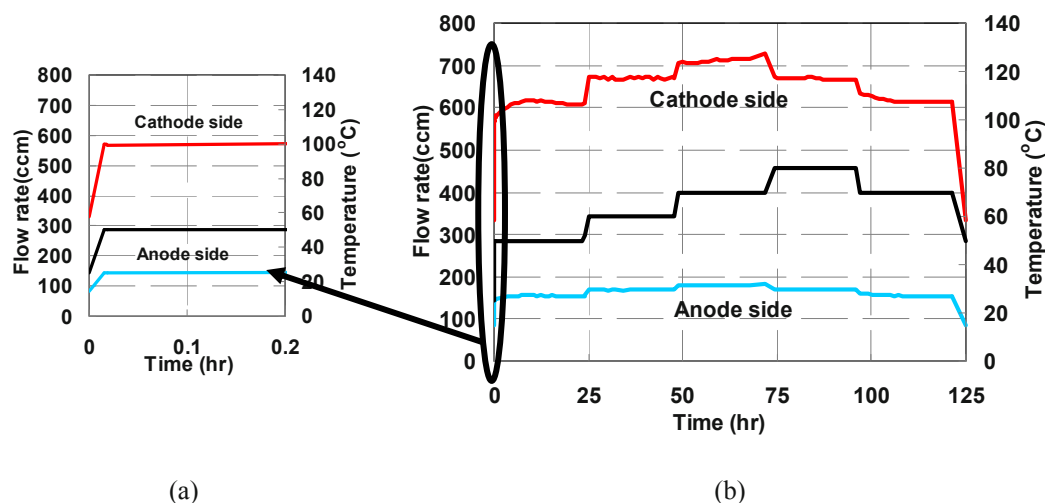


Fig. 8. Compare input flow rate values with time and temperate. (a) The time before 0.2hr's compare inlet flow rate in the anode and cathode side's variation. (b) Following the PEMFC breaking procedure running in the anode and cathode side's variation.

4. Conclusions

Variation of Compression of Seals in PEM Fuel Cells was studied in this paper.

The following conclusion can be made.

1. It appears that the change of gap spacing with temperature is relatively small, i.e. +3% maximum. That implies the sealing force is not affected much from the time assembled to operation, excluding the stress relaxation effect. It is largely because the operating temperature of PEMFC is low, i.e. less than 90°C. In addition, the change of all dimensions from thermal expansion is negligible.
2. An interesting observation is that both the gap spacing and the outside dimensions jumped initially and did not follow the cell temperature's later rise to a maximum of 80°C. It's effect by the first gas inlet pressure.
3. Gap spacing at No.3 was increasing when change the gas pressure. The No.3 in the bottom was near the gas output and the end of the flow flied channel. Here has more gas and more water accumulation.

5. Acknowledgements

This study is sponsored by National Science Council, Taiwan (Grants No. NSC 99-2221-E-110-020), Graduate Students Research Abroad Program (Grants No. NSC 97-2917-I-110-108) from National Science Council, Taiwan, and National Sun Yat-Sen University Study Abroad Scholarship Award. In addition, support from the US Department of Energy (DE-FC36-06G086041 and DE-FG36-08GO88116) to the University of South Carolina Research Foundation, the NSF Industry/University Cooperative Research Center for Fuel Cells at the University of South Carolina

(EEC-0324260 and IIP-0856055). YJ Chao also wants to thank the partial support from China 111 project (B08040) awarded to the School of Materials Science, Northwestern Polytechnical University, Xian, China.

6. References

- [1] W.K. Lee, C.H. Ho, J.W.V. Zee, M. Murthy, J. Power Sources, 1.84(1999)45–51.
- [2] H.S. Chu, C. Yeh, F. Chen, J. Power Sources, 123(2003)1–9.
- [3] D. Chu, R. Jiang, J. Power Sources, 83(1999)128–133.
- [4] S. Giddey, F.T. Ciacchi, S. P. S. Badwal, J. Power Sources, 125(2004)155–165.
- [5] R. Jiang, D. Chu, J. Power Sources, 93(2001)25–31.
- [6] B. Zhang, X. Wang, Y. Song, P, First International Conference on Fuel Cell Development and Deployment, 2005.
- [7] S.J. Lee, C.D. Hsu, C.H. Huang, J. Power Sources, 145(2005)353-361.
- [8] R P Brown, Physical Testing of Rubber, 2006.
- [9] Jinzhu Tan, Y. J. Chao, J. W. Van Zee and W. K. Lee, J. Material Science & Engineering A, 445-446(2007)669-675.
- [10] Jinzhu Tan, Y. J. Chao, Xiaodong Li and J. W. Van Zee, J. Power Sources, 172(2007)782-789.
- [11] Jinzhu Tan, Y. J. Chao, Min Yang, C. T. William, and J. W. Van Zee, J. Power Sources, 17(2007)785-792.
- [12] Jinzhu Tan, Y. J. Chao, J. W. Van Zee, Xiaodong Li, Xinnan Wang, Min Yang, J. Material Science & Engineering A, 496(2008)464-470.
- [13] Jinzhu Tan, Y. J. Chao, Xiaodong Li and J. W. Van Zee, J. Fuel Cell Science and Technology, 2009.
- [14] Jinzhu Tan, Y. J. Chao, Min Yang, Woo-Kum Lee and J. W. Van Zee, J. Hydrogen Energy, 2009.
- [15] T Burton, J L DeLanaye, C P Rader, Rubber and Plastic News, 1988.
- [16] U Meier, J Kuster and J F Mandell, Rubber, Chem. Technol. 57, No.2, 1984.
- [17] R. Sprey, Rubber World, 191, No. 1, 1984.
- [18] C J. Derham, IRC'96 Conf., Manchester, June 17-21, 1996.
- [19] Jinzhu Tan, Y. J. Chao, Woo-Kum Lee and J. W. Van Zee, Journal of Pressure Equipment and Systems, 5(1) 2007, 1-7.
- [20] Fuel Cell Technologies, Inc. <http://www.fuelcelltechnologies.com>
- [21] S. Shimpalee *, S. Greenway, J.W. Van Zee, J. Power Sources, 160(2006) 398-406.

Neutron emission evidences in natural materials under monotonic, cyclic, and vibrational loading

A. Carpinteri¹, G. Lacidogna¹, A. Manuello¹, O. Borla^{1,2}

¹*Politecnico di Torino, Department of Structural Engineering & Geotechnics
Corso Duca degli Abruzzi 24 – 10129 Torino, Italy*

²*Istituto Nazionale di Fisica Nucleare, INFN sez. Torino
Via Pietro Giuria 1 – 10125 Torino, Italy*

E-mail: alberto.carpinteri@polito.it

ABSTRACT

Neutron emission measurements, by means of ³He devices and bubble detectors, were performed during three different kinds of compression tests: (i) under monotonic displacement control, (ii) under cyclic loading, and (iii) by ultrasonic vibration. The material used for the tests was Green Luserna Granite. Since the analyzed material contains iron, our conjecture is that piezonuclear reactions involving fission of iron into aluminum, or into magnesium and silicon, should have occurred during compression damage and failure. This hypothesis is confirmed by the direct evidence of Energy Dispersive X-ray Spectroscopy (EDS) tests. It is also interesting to emphasize that the anomalous chemical balances of the major events that have affected the geomechanical and geochemical evolution of the Earth's Crust should be considered as an indirect evidence of the piezonuclear fission reactions.

INTRODUCTION

We deal with a new topic in the scientific literature: piezonuclear neutron emissions from brittle rock specimens under mechanical loading. The phenomenon is analyzed from an experimental point of view. In the scientific community some studies have been already conducted on the different forms of energy emitted during the failure of brittle materials. They are based on the signals captured by the acoustic emission measurement systems, or on the detection of the electromagnetic charge. On the other hand, only very recently piezonuclear neutron emissions from very brittle rock specimens in compression have been discovered [1-3].

In this paper, we present original experimental tests, using ³He neutron detectors and bubble type BD thermodynamic neutron detectors, performed on brittle rock test specimens. We carried out three different kinds of compression tests: (i) under monotonic displacement control, (ii) under cyclic loading, and (iii) by ultrasonic vibrations [4]. Similarly to the preliminary piezonuclear experiments presented in [1-3], the material used for the tests is non-radioactive Green Luserna Granite. In these new tests cylindrical specimens with different size and slenderness are used and not prismatic specimens as in the preliminary tests [1-3]. The compression tests were performed at the Fracture Mechanics Laboratory of the Politecnico di Torino, while the ultrasonic tests at the Medical and Environmental Physics Laboratory of the University of Torino.

For the specimens of larger dimensions characterized by a brittle behaviour, neutron emissions, detected by ³He, were found to be of about one order of magnitude higher than the ordinary natural background level at the time of the catastrophic failure. As regards test specimens with more ductile behaviour, neutron emissions significantly higher than the background level were also found. These emissions fully confirm the preliminary tests [1-3] and are due to piezonuclear reactions, which depend on the different modalities of energy release during the tests. For specimens with sufficiently large size and slenderness, a relatively high energy release is expected, and hence a higher probability of neutron emissions at the time of failure. Furthermore, during compression tests under cyclic loading, an equivalent neutron dose, analysed by neutron bubble detectors, about twice higher than the ordinary background level was found at the end of the test.

Finally, by using an ultrasonic horn suitably joined with the specimen, an ultrasonic test was carried out on a Green Luserna Granite specimen in order to produce continuing vibration at 20 kHz. Three hours after the beginning of the test, an equivalent neutron dose about three times higher than the background level was found. Moreover, Energy Dispersive X-ray Spectroscopy (EDS) was performed on different samples of external or

fracture surfaces belonging to specimens used in the preliminary piezonuclear tests [5]. For each sample, different measurements of the same crystalline phases (phengite or biotite) were performed in order to get averaged information of the chemical composition and to detect possible piezonuclear transmutations from iron to lighter elements. The samples were carefully chosen to investigate and compare the same minerals before and after the crushing failure. Phengite and biotite, that are rather common in the Luserna Granite (20% and 2%, respectively), were considered owing to the high iron concentration in their chemical compositions. The results of EDS analyses show that, on the fracture surface samples, a considerable reduction in the iron content (~25%) is counterbalanced by a nearly equal increase in Al, Si, and Mg concentrations.

Our conjecture is that piezonuclear reactions involving fission of iron into aluminum, or into magnesium and silicon, should have occurred during compression on the tested specimens. The present natural abundances of aluminum (~8%), and silicon (~28%) and scarcity of iron (~4%) in the continental Earth's crust are possibly due to the piezonuclear fission reactions considered above. These reactions would be activated where the environment conditions (pressure and temperature) are particularly severe, and mechanical phenomena of fracture, crushing, fragmentation, comminution, erosion, friction, etc., may occur.

From this point of view, piezonuclear reactions, induced by the sliding of faults and plate subduction phenomena at the Earth's crust scale, could imply the different mineral reservoir localizations on the Earth's surface and the most significant chemical element evolutions over the past 4.57 Gyrs (Earth's life time). The geomechanical and geochemical evidences shown in this paper involve the most abundant elements in the Earth's continental crust such as Si, Al, Mg, Fe, Ca, K, and Na. Therefore the plate tectonics, the related plate collisions, and the subduction phenomena are useful to understand not only the morphology of our planet, but also its compositional evolution [6].

NEUTRON EMISSION DETECTION TECHNIQUES

Since neutrons are electrically neutral particles, they cannot directly produce ionization in a detector, and therefore cannot be directly detected. This means that neutron detectors must rely upon a conversion process where an incident neutron interacts with a nucleus to produce a secondary charged particle. These charged particles are then detected, and from them the neutrons presence is deduced. For an accurate neutron evaluation, a ^3He proportional counter and a set of passive neutron detectors, based on the superheated bubble detection technique, insensitive to electromagnetic noise, were employed.

The ^3He detector used in the tests is a ^3He type (Xeram, France) with electronics of preamplification, amplification, and discrimination directly connected to the detector tube. The detector is powered with high voltage power supply (about 1.3 kV) via NIM (Nuclear Instrument Module) module. The logic output producing the TTL (through the lens) pulses is connected to a NIM counter. The logic output of the detector is enabled for analog signals exceeding 300 mV. This discrimination threshold is a consequence of the sensitivity of the ^3He detector to the gamma rays ensuing neutron emission in ordinary nuclear processes.

A set of passive neutron detectors insensitive to electromagnetic noise and with zero gamma sensitivity was used. The dosimeters, based on superheated bubble detectors (BTI, Ontario, Canada) (BUBBLE TECHNOLOGY INDUSTRIES (1992)) [7], are calibrated at the factory against an AmBe (Americium-Beryllium) source in terms of NCRP38 [8].

EXPERIMENTAL SET-UP

Compression tests under monotonic displacement control

Similarly to the preliminary piezonuclear tests presented in [1-3], the material used for the tests is non-radioactive Green Luserna Granite [4]. In these new experiments cylindrical specimens with different size and slenderness are used in order to assess neutron emissions related to specimens with very brittle or catastrophic failure [9,10]. Neutron emissions were measured on nine Green Luserna Granite cylindrical specimens, of different size and shape, denoted with P1, P2,..., P9. The tests were carried out by means of a servo-hydraulic press, with a maximum capacity of 1800 kN, working by a digital type electronic control unit. The management software was TESTXPRTII by Zwick/Roel (Zwick/Roel Group, Ulm, Germany), while the mechanical parts are manufactured by Baldwin (Instron Industrial Products Group, Grove City, PA, USA). The force applied was determined by measuring the pressure in the loading cylinder by means of a transducer. The margin of error in the determination of the force is 1%, which makes it a class 1 mechanical press. The specimens were arranged with the two smaller surfaces in contact with the press platens, without coupling materials in-between, according to the testing modalities known as "test by means of rigid platens with friction". The tests were performed under monotonic loading, with the planned displacement velocities ranging from 0.001 to 0.01 mm/s.

The ^3He neutron detector was switched on at least one hour before the beginning of each compression test, in order to reach the thermal equilibrium of electronics, and to make sure that the behaviour of the devices was

stable with respect to intrinsic thermal effects. The detector was placed in front of the test specimen at a distance of 20 cm and it was enclosed in a polystyrene case of 10 cm of thickness in order to avoid “spurious” signals coming from impact and vibration.

A relative measurement of natural neutron background was performed in order to assess the average background affecting data acquisition in experimental room condition. The ^3He device was positioned in the same condition of the experimental set-up and the background measures were performed fixing at 60 s the acquisition time, during a preliminary period of more than three hours, for a total number of 200 counts. The average measured background level is ranging from $(3.17 \pm 0.32) \cdot 10^{-2}$ to $(4.74 \pm 0.46) \cdot 10^{-2}$ cps (see Table 1).

Compression test under cyclic loading

A Green Luserna Granite specimen ($D=53\text{mm}$, $H=53\text{mm}$, $\lambda=1$) was used. The cyclic loading was programmed at a frequency of 2 Hz and with a load excursion from a minimum load of 10 kN to a maximum of 60 kN. With respect to the tests performed under monotonic displacement control, neutron emissions from compression test under cyclic loading were performed by using neutron bubble detectors. Due to their isotropic angular response, three BDT and three BD-PND detectors were positioned at a distance of about 5 cm, all around the specimen. The detectors were previously activated, unscrewing the protection cap, in order to reach the suitable thermal equilibrium, and they were kept active for all the test duration. Furthermore, a BDT and a BD-PND detector were used as background control during the test.

Ultrasonic test

A Green Luserna Granite specimen ($D=53\text{mm}$, $H=100\text{mm}$, $\lambda=2$) was connected to the ultrasonic horn by a glued screw inserted in a 5 mm deep hole. This kind of connection was made in order to achieve a resonance condition, considering the speed of sound in Luserna stone, and the length of the specimen. Ultrasonic irradiation of the specimen was carried out for 3 hours. After the switching on of the transducer, 10% of the maximum power was reached in 20 min. Successively, the transducer power increased to 20% after one hour, and next reached a maximum level of about 30% after 2 hours. Then, the transducer worked in the same power condition up to the end of the test.

TESTS ON CYLINDRICAL SPECIMENS: EXPERIMENTAL RESULTS

Compression tests under monotonic displacement control

Additional background measurements were repeated before each test, fixing an acquisition time of 60 s, up to the assessment of no significant variation in natural background. Neutron measurements of specimens P2, P3, P4, P7 yielded values comparable with the ordinary natural background, whereas in specimens P1 and P5 the experimental data exceeded the background value by about four times. On the other hand, for specimen P6, P8 and P9, the neutron emissions achieved values of about one order of magnitude higher than the ordinary background (see Table 1). In Fig. 1a-c the load vs. time diagram and the neutron count rate evolution for specimens P6, P8 and P9 are shown.

The preliminary experimental results described above and reported in [1-3] are confirmed by those obtained from compression tests on the cylindrical specimens. Neutron emissions related to specimens with very brittle or catastrophic failure result to be larger by about one order of magnitude than the ordinary background (see Fig. 1). The maximum neutron emissions were obtained from test specimens with a volume larger than a threshold value of about 360 cm^3 [4].

In addition, the experimental results seem to demonstrate that neutron emissions follow an anisotropic and impulsive distribution from a specific zone of the specimen. It is a matter of fact that the neutron flux and consequently neutron dose are inversely proportional to the square of the distance from the source. For these reasons, the ^3He device could have underestimated neutron flux intensity. A possible solution to avoid underestimated data acquisition is an experimental measurement by using more than one ^3He detector and more bubble dosimeters placed around the test specimen [4].

Compression test under cyclic loading

Droplets counting was performed every 12 hours and the equivalent neutron dose was calculated. In the same way, the natural background was estimated by means of the two bubble dosimeters used for assessment. The ordinary background was found to be $(13.98 \pm 2.76)\text{ nSv/h}$.

In Fig. 2 neutron equivalent dose variation, evaluated during the cyclic compression test, is reported. An increment of more than twice higher than the background level was detected at specimen failure. No significant variations in neutron emissions were observed before the failure. The equivalent neutron dose, at the end of the test, was $(28.74 \pm 5.75)\text{ nSv/h}$.

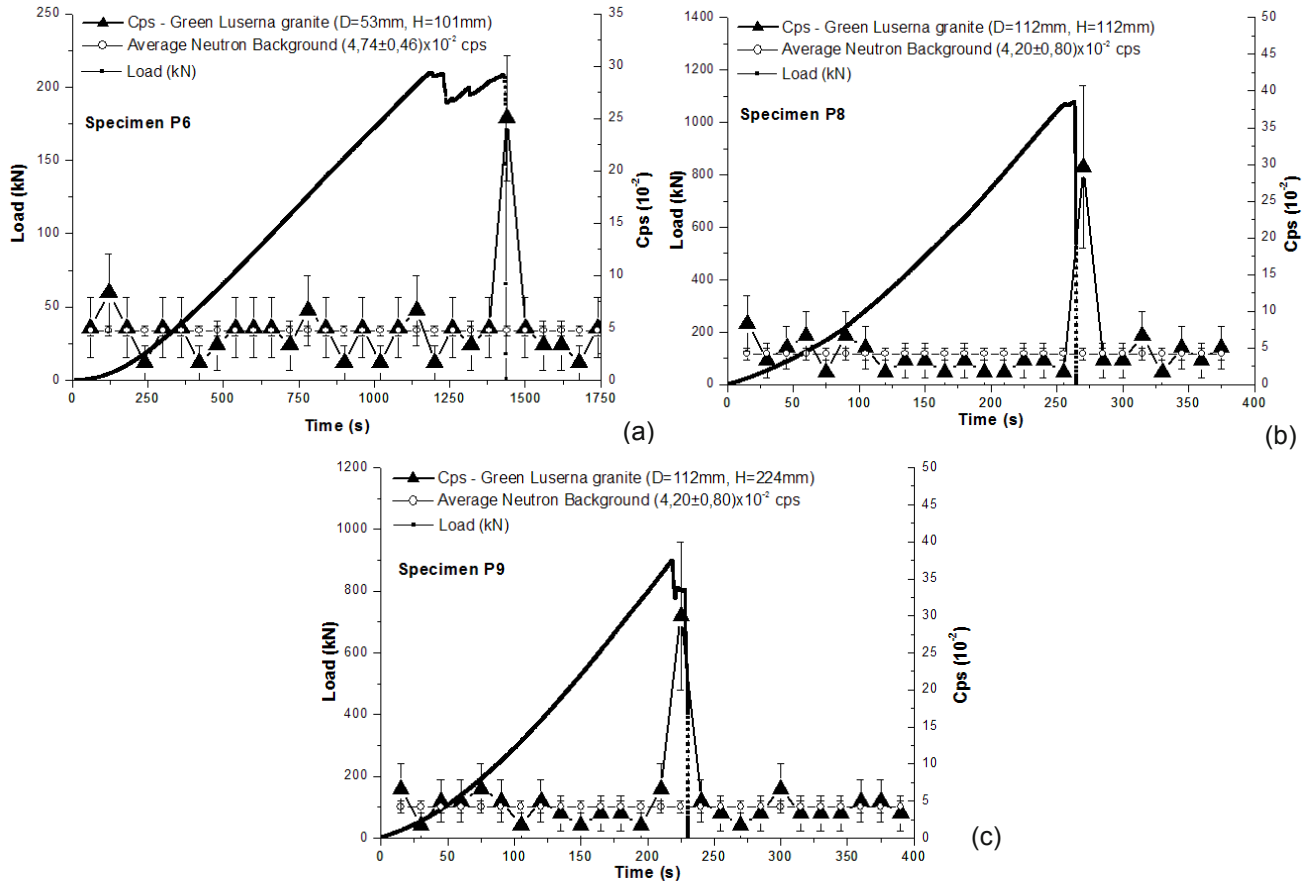


Fig. 1. Specimens P6, P8, P9. Load vs. time diagrams, and neutron emissions count rate

Table 1. Compression tests under monotonic displacement control. Neutron emissions experimental data on Green Luserna Granite specimens

Granite Specimen	D (mm)	$\lambda=H/D$	Average neutron background (10 ⁻² cps)	Count rate at the neutron emission (10 ⁻² cps)
P1	28	0.5	3.17±0.32	8.33±3.73
P2	28	1	3.17±0.32	background
P3	28	2	3.17±0.32	background
P4	53	0.5	3.83±0.37	background
P5	53	1	3.84±0.37	11.67±4.08
P6	53	2	4.74±0.46	25.00±6.01
P7	112	0.5	4.20±0.80	background
P8	112	1	4.20±0.80	30.00±11.10
P9	112	2	4.20±0.80	30.00±10.00

Ultrasonic test

Ultrasonic oscillation was generated by an high intensity ultrasonic horn (Bandelin HD 2200) working at 20 kHz. The device guarantees constant amplitude (ranging from 10% to 100%) independently of changing conditions

within the sample. The apparatus consists of a generator that converts electrical energy to 20 kHz ultrasounds, and of a transducer that switches this energy into mechanical longitudinal vibration at the same frequency.

The ultrasonic test on Green Luserna Granite specimen ($D=53\text{mm}$, $H=100\text{mm}$, $\lambda=2$) was carried out at the Medical and Environmental Physics Laboratory of Experimental Physics Department of the University of Torino. A relative natural background measurement was performed by means of the ^3He detector for more than 6 hours. The average natural background was of $(6.50 \pm 0.85) \cdot 10^{-3}$ cps, for a corresponding thermal neutron flux of $(1.00 \pm 0.13) \cdot 10^{-4} n_{\text{thermal}} \text{ cm}^{-2} \text{ s}^{-1}$. This natural background level, lower than the one calculated during the compression tests at the Fracture Mechanics Laboratory of the Politecnico of Torino, is in agreement with the location of the experimental Physics Laboratory, which is three floors below the ground level.

During the ultrasonic test, the specimen temperature was monitored by using a multimeter/thermometer (Tektronix mod. S3910). The temperature reached 50°C after 20 min, and then increased up to a maximum level of 100°C at the end of the ultrasonic test. In Fig. 3, the neutron emissions detected are compared with the transducer power trend and the specimen temperature. A significant increment in neutron activity after 130 min from the beginning of the test was measured. At this time, the transducer power reached 30% of the maximum, with a specimen temperature of about 90°C . Some neutron variations were detected during the first hour of the test, but they could be due to ordinary fluctuations of natural background. At the switching off of the sonotrode, the neutron activity decreased to the typical background value.

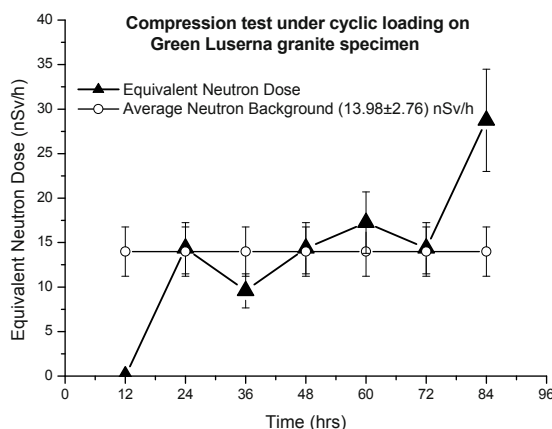


Fig. 2. Compression test under cyclic loading. Equivalent neutron dose variation on Green Luserna Granite specimen.

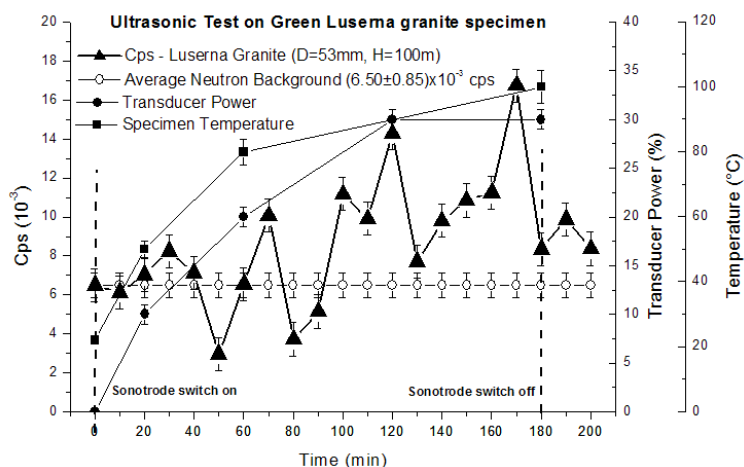


Fig. 3. Ultrasonic test. Neutron emissions compared with the specimen temperature, and with the transducer power trend.

COMPOSITIONAL AND MICROCHEMICAL EVIDENCE OF PIEZONUCLEAR FISSION REACTIONS IN THE ROCK SPECIMENS

Energy Dispersive X-ray Spectroscopy (EDS) was performed on different samples of external or fracture surfaces, belonging to the same specimens in Green Luserna Granite used in the preliminary piezonuclear tests by

Carpinteri et al. [1-3]. The tests were conducted in order to correlate the neutron emissions from the Luserna Granite with the variations in rock composition. These analyses lead to get averaged information of the mineral and chemical composition and to detect possible piezonuclear transmutations from iron to lighter elements. The quantitative elemental analyses were performed by a ZEISS Supra 40 Field Emission Scanning Electron Microscope (FESEM) equipped with an Oxford X-rays microanalyser. The samples were carefully chosen to investigate and compare the same crystalline phases both before and after the crushing failure. In particular, two crystalline phases, phengite and biotite, were considered due to their high iron content and relative abundances in the Luserna Granite (20% and 2%, respectively) [11].

In consequence of Luserna stone being a very heterogeneous rock, and in order to assess mass percentage variations in chemical elements such as Fe, Al, Si and Mg, the EDS analyses have been focused on two crystalline phases: phengite and biotite. These two minerals of granitic gneiss, that are quite common in the Luserna stone (20% and 2%, respectively), show a mineral chemistry in which the iron content is largely diffused. In Figs. 4a and 4b, two electron microscope images of phengite and biotite sites, the first on the external sample (thin section 1) and the second on the fracture surface (fracture surface 2), are shown.

EDS results for phengite and biotite

In Table 2, the results for the Fe concentrations obtained from the measurements on phengite crystalline phase are shown. Thirty measurements were carried out on the polished thin sections as representatives of the external surface samples, whereas other thirty measurements were carried out on fracture surfaces [5]. The distribution of Fe concentrations for the external surfaces has an average value (calculated as the arithmetic mean value) equal to 6.20%. The distribution of Fe concentrations on the fracture samples shows a significant variations. The mean value of the distribution of measurements performed on fracture surfaces is equal to 4.0% and it is considerably lower than the mean value of external surface measurements (6.20%) [5].

The iron decrease, considering the mean values of the distributions of phengite composition, is about 2.20%. This iron content reduction corresponds to a relative decrease of 35% with respect to the previous Fe content (6.20% in phengite). Similarly the Al mass percentage concentrations are considered in both the cases of external and fracture surfaces (see Table 2). For Al contents, the observed variations show a mass percentage increase approximately equal to that of Fe. The average increase in the distribution, corresponding to the fracture surfaces is about 2.00% of the phengite composition. The average value of Al concentrations changes from 12.50% on the external surface to 14.50% on the fracture surface. The relative increase in Al content is equal to 16%.

The evidence emerging from the EDS analyses, that the two values for the iron decrease (−2.20%) and for the Al increase (+2.0%) are approximately equal, is really impressive. This fact is even more evident considering the trends of the other chemical elements constituting the mineral chemistry (excluding H and O) in phengite, because no appreciable variations can be recognized between the average values (Table 2) [5].

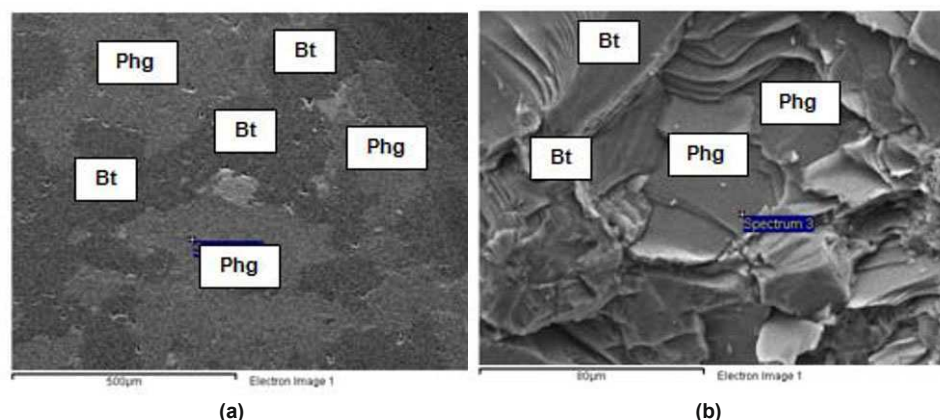


Fig. 4. FESEM images of phengite and biotite in the case of (a) external and (b) fracture sample.

In Table 3 the mean value for Fe, Al, Si and Mg concentrations measured on 30 acquisition points of biotite crystalline phase are shown. The measurements were selected on the polished thin sections as representatives of the uncracked material samples (15 measurements) and on fracture surfaces (15 measurements) [5]. It can be observed that the distribution of Fe concentrations for the external surfaces shows an average value (calculated as the arithmetic mean value) equal to 21.20%. On the other hand the distribution of Fe concentrations on fracture samples drops to 18.20%. In this case, the iron decrease, considering the mean values of the Fe distributions, is

about 3.00% (see Table 3). This iron content reduction (−3.00%) corresponds to a relative decrease of 14% with respect to the previous Fe content (21.20% in biotite). Similarly the Al mass percentage concentrations are considered in both cases of external and fracture samples. For Al contents the observed variations show an average increase of about 1.50% in the biotite composition (see Table 3). The average value of Al concentrations changes from 8.10% on the external surface to 9.60% on the fracture surface, with a relative increase in Al content equal to 18%. In Table 3 it is shown that, in the case of biotite, also Si and Mg contents present considerable variations. The mass percentage concentration of Si changes from a mean value of 18.40% (external surface) to a mean value of 19.60% (fracture surface) with an increase of 1.20%. Similarly, the Mg concentration distributions show that the mean value of Mg content changes from 1.50% (external surface) to 2.20% (fracture surface) (Table 3). Therefore, the iron decrease (−3.00%) in biotite seems to be counterbalanced by an increase in aluminum (+1.50%), silicon (+1.20%), and magnesium (+0.70%) [5].

Table 2: Phengite: Fe, Al, Si, Mg, and K weight percentage mean values on external and fracture surfaces. Variations with respect to the mineral (phengite) and to the same element

	External surface mean value (wt%)	Fracture surface mean value (wt%)	Increase/ decrease with respect to phengite	Increase/ decrease with respect to the same element
Fe	6.20	4.00	−2.20%	−35%
Al	12.50	14.50	+2.00%	+16%
Si	28.00	27.80	NO VARIATIONS	NO VARIATIONS
Mg	0.75	0.85	NO VARIATIONS	NO VARIATIONS
K	8.00	7.75	NO VARIATIONS	NO VARIATIONS

Table 3: Biotite: Fe, Al, Si, Mg, and K weight percentage mean values on external and fracture surfaces. Variations with respect to the mineral (biotite) and to the same element

	External surface mean value (wt%)	Fracture surface mean value (wt%)	Increase/ decrease with respect to biotite	Increase/ decrease with respect to the same element
Fe	21.20	18.20	−3.00%	−14%
Al	8.10	9.60	+1.50%	+18%
Si	18.40	19.60	+1.20%	+6%
Mg	1.50	2.20	+0.70%	+46%
K	6.90	7.10	NO VARIATIONS	NO VARIATIONS

PIEZONUCLEAR REACTIONS: FROM THE LABORATORY TO THE EARTH SCALE

From the results shown in the previous sections and the experimental evidence reported in recent papers [1-4,5], it can be clearly seen that piezonuclear reactions are possible in inert non-radioactive solids.

From the EDS results on fracture samples, the evidences of Fe and Al variations in phengite (Table 2) lead to the conclusion that the piezonuclear reaction:



should have occurred [1-4,5]. Moreover, considering the evidences for the biotite content variations in Fe, Al, Si, and Mg (Table 3), it is possible to conjecture that another piezonuclear reaction, in addition to (1), should have occurred during the piezonuclear tests [1-4,5]:



Taking into account that granite is a common and widely occurring type of intrusive, Sialic, igneous rock, and that it is characterized by an extensive concentration in the rocks that make up the Earth's crust (~60% of the Earth's crust), the piezonuclear fission reactions expressed above can be generalized from the laboratory to the Earth's crust scale, where mechanical phenomena of brittle fracture, due to fault collision and subduction, take place continuously in the most seismic areas. This hypothesis seems to find surprising evidence and confirmation from both the geomechanical and the geochemical points of view [6]. The neutron emissions involved in piezonuclear reactions can be detected not only in laboratory experiments, as shown in this paper, and in [1-4], but also at the Earth's crust scale [6]. Recent neutron emission detections by Kuzhevskij et al. [15,16] have led to consider also the Earth's crust, in addition to cosmic rays, as being a relevant source of neutron flux variations. Neutron emissions measured near the Earth's surface exceeded the neutron background by about one order of magnitude in correspondence to seismic activity and rather appreciable earthquakes [17]. This relationship between the processes in the Earth's crust and neutron flux variations has allowed methods for short-term prediction and monitoring of earthquakes to be developed [15,16]. Neutron flux variations, in correspondence to seismic activity, may be evidence of changes in the chemical composition of the crust, as a result of piezonuclear reactions. The present natural abundances of aluminum (~8%), silicon (~28%) and magnesium (~1.3%) and scarcity of iron (~4%) in the continental Earth's crust [18-20] are possibly due to the piezonuclear fission reactions expressed above [6]. In addition, considering the mass percentage concentrations of other chemical elements, such as Na (~2.9%), Ni (~0.01%), and Co (~0.003%), in the continental crust [18-24], it is possible to conjecture additional piezonuclear fission reactions that could have taken place in correspondence to plate collision and subduction [6]:



The large concentrations of granite minerals, such as quartz and feldspar (SiO_2 , Al_2O_3) in the Earth's crust, and to a lesser extent of magnesite, halite, and zeolite (MgO , Na_2O , Cl_2O_3), and the low concentrations of magnetite, hematite, bunsenite and cobaltite minerals (composed predominantly of Fe, Co, and Ni minerals), could be ascribed to piezonuclear reactions due to tectonic and subduction phenomena [6].

HETEROGENEITY IN THE COMPOSITION OF THE EARTH'S CRUST: Fe AND Al RESERVOIR LOCALIZATIONS

The localization of Al and Fe mineral reservoirs seems to be closely connected to the geological periods when different continental zones were formed [18-21, 25-28]. This fact would seem to suggest that our planet has undergone a continuous evolution from the most ancient geological regions, which currently reflect the continental cores that are rich in Fe reservoirs, to more recent or contemporary areas of the Earth's crust where the concentrations of Si and Al oxides present very high mass percentages [18]. The main iron reservoir locations (Magnetite and Hematite mines) are reported in Fig. 5a. The main concentrations of Al-oxides and rocky andesitic formations (the Rocky Mountains and the Andes, with a strong concentration of Al_2O_3 minerals) are shown in Fig. 5b together with the most important subduction lines, plate tectonic trenches and rifts [18,25]. The geographical locations of the main bauxite mines show that the largest concentrations of Al reservoirs can be found in correspondence to the most seismic areas of the Earth (Fig.5b). The main iron mines are instead exclusively located in the oldest and interior parts of continents (formed through the eruptive activity of the proto-Earth), in geographic areas with a reduced seismic risk and always far from the main fault lines. From this point of view, the close correlation between bauxite and andesitic reservoirs and the subduction and most seismic areas of the Earth's crust provides a very impressive evidence of piezonuclear effects at the planetary scale.

GEOCHEMICAL EVIDENCE OF PIEZONUCLEAR REACTIONS IN THE EVOLUTION OF THE EARTH'S CRUST ELEMENTS

Evidence of piezonuclear reactions can be also recognized considering the Earth's composition and its way of evolving throughout the geologic eras. In this way, plate tectonics and the connected plate collision and subduction phenomena are useful to understand not only the morphology of our planet, but also its compositional evolution [6].

From 4.0 to 2.0 Gyrs ago, Fe could be considered one of the most common bio-essential elements required for the metabolic action of all living organisms [29-38]. Today, the deficiency of this nutrient suggests it as a limiting factor for the development of marine phytoplankton and life on Earth [21,32]. Elements such as Fe and Ni in the

Earth's protocrust had higher concentrations in the Hadean (4.5–3.8 Gyr ago) and Archean (3.8–2.5 Gyr ago) periods compared to the present values [19,20,32,33, 39–42]. The Si and Al concentrations instead were lower than they are today [18–20].

The estimated concentrations of Fe, Ni, Al, and Si in the Hadean and Archean Earth's protocrust and in the present Earth's continental crust are reported in Fig. 6. The data for the Hadean period (4.5–3.8 Gyrs ago) are referred to the composition of Earth's protocrust, considering the assumptions made by Foing [35] and by Taylor and McLennan [19,20]. According to these authors, the Mars and Moon's crusts are considered to be representative of the composition of the early Earth's protocrust (Hadean Eon) that was strongly basaltic, with a composition similar to that of the proto-planets (chondrites) [19,20,35].

In the same Figure, for the Archean period (3.8–2.5 Gyrs ago) the data are referred to compositional analysis of Archean sediments [6,18–20, 24, 43, 44, 45, 46]. For the last period from 2.5 Gyrs ago to today, the mass percentage concentrations of Fe, Ni, Al and Si are referred to the present composition of Earth's continental crust [5,18–20,46,47].

A clear transition from a more basaltic condition (high concentrations of Fe and Ni) to a Sialic one (high concentrations of Si and Al) can be observed during the life time of our planet [18–20, 23, 24, 43, 43, 36–47].

The most abrupt changes in element concentrations shown in Fig. 6 appear to be intimately connected to the tectonic activity of the Earth. The vertical drops in the concentrations of Fe and Ni, as well as the vertical jumps in the concentrations of Si and Al, 3.8 Gyrs ago, coincide with the time that many scientists have pointed out as the beginning of tectonic activity on the Earth. The subsequent abrupt transitions 2.5 Gyrs ago coincide with the period of the Earth's largest and most intense tectonic activity [19,20].

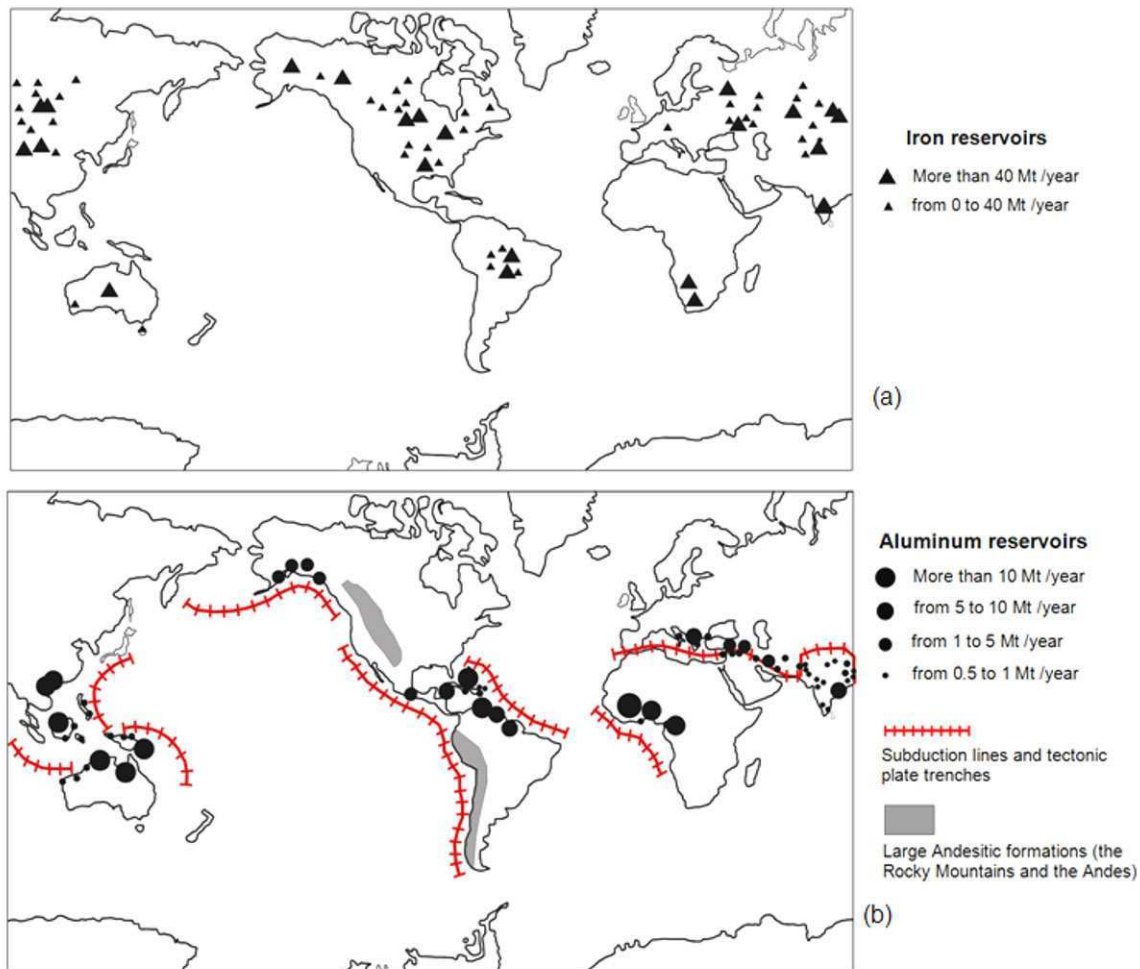


Fig. 5. (a) Locations of the largest iron mines in the world [25–28]. Iron ore reservoirs (Magnetite and Hematite mines) are located in geographic areas with reduced seismic risks and always far from fault lines. (b) The largest

aluminum (bauxite) reservoirs are reported together with the main Andesitic formations and most important subduction lines and plate tectonic trenches [18].

As shown in Fig. 6, the decrease in the mass concentration of iron and nickel is balanced by Al and Si increase and assuming an increase in Mg, according to reaction (2), equal to that of Si over the Earth's lifetime. In the same figure, a total decrease of ~7% in Fe and Ni concentrations and a relative increase of ~7% in the lighter chemical element concentrations (Si, Al and Mg) between the Hadean period (Hadean Eon, 4.5–3.8 Gyrs ago) and the Archean period (Archean Eon, 3.8–2.5 Gyrs ago) is shown. Similarly, a decrease of ~5% in the heavier elements (Fe and Ni) and a related increase (~5%) in the concentrations of lighter ones (Si, Al and Mg) can be considered between the Archean period (Archean Eon, 3.8–2.5 Billion years ago) and more recent times (Fig. 6). In particular, piezonuclear reactions (1,2,4) seem to be the cause of the abrupt variations shown in Fig. 6. Piezonuclear reaction (2) implies that not only the Si mass percentage should increase overall by about 4.0% but also that of Mg. However, the latter increase, due to piezonuclear reaction (2), cannot be revealed from geological data of sediments in the Earth's continental crust. The most probable explanation is that Mg is not only a resulting element, as shown by piezonuclear reaction (2), but can also be considered as a starting element of another possible piezonuclear reaction [6], like for example:



Reaction (6) could be very important for the evolution of both the Earth's crust and atmosphere, and considered as a valid explanation for the high level of CO₂ concentration (~15%) in the Archean Earth's atmosphere [48]. In addition, the large amount of C produced by Mg transformation (~4.0% of the Earth's crust) has undergone a slow but continuous diminishing in the CO₂ composition of the Earth's atmosphere, as a result of the escape which also involves other atmospheric gases like He and H [49].

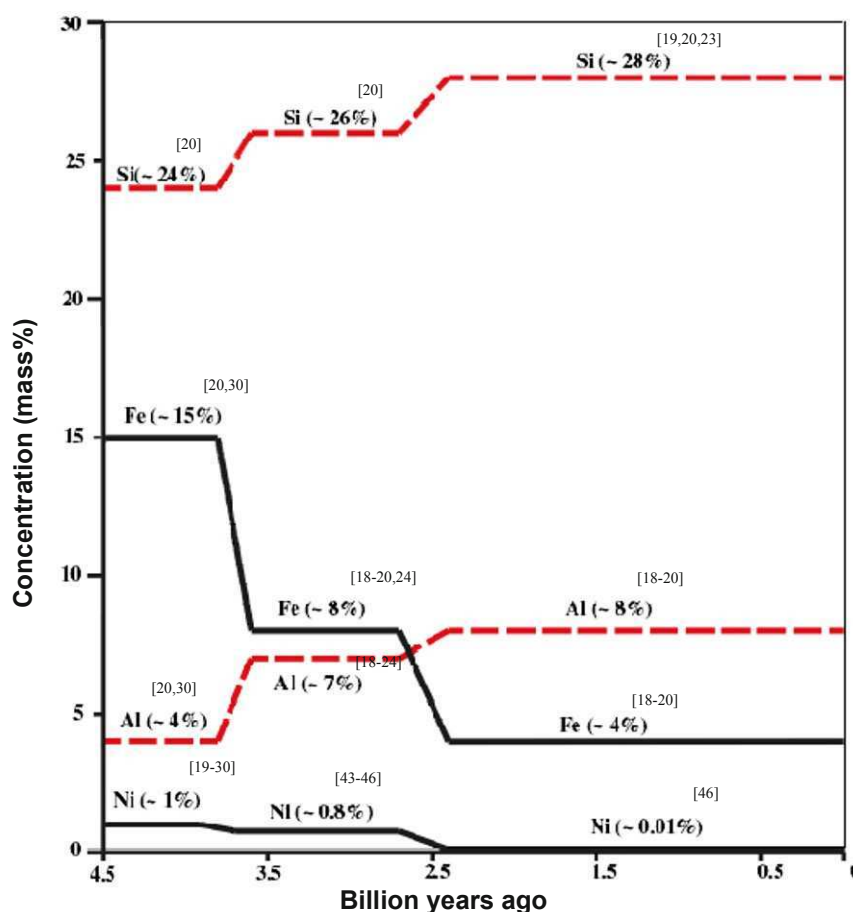


Figure 6: Estimated concentrations of Fe, Ni, Al, and Si in the Hadean and Archean Earth's protocrust and in the Earth's continental crust [18-20, 23, 30, 43-46].

Piezonuclear reaction (6) can also be put into correlation with the increase in seismic activity that has occurred over the last century [50]. Very recent evidence has shown CO₂ emissions in correspondence to seismic activity [51]: significant changes in the emission of carbon dioxide were recorded in a geochemical station at El Hierro, in the Canary Islands, before the occurrence of several seismic events during the year 2004. Appreciable precursory CO₂ emissions were observed to start before seismic events of relevant magnitude, and to reach their maximum values some days before the earthquakes [51].

Relation (6) is not the only piezonuclear reaction that involves Mg as a starting element. Like the considerations made for the concentrations of elements such as Fe, Ni, Al, and Si (Fig. 6), it is also possible to consider other elements such as Mg, Ca, Na, K, and O, which are involved in other piezonuclear reactions that have been assumed to occur in the chemical evolution of the Earth's crust [6].

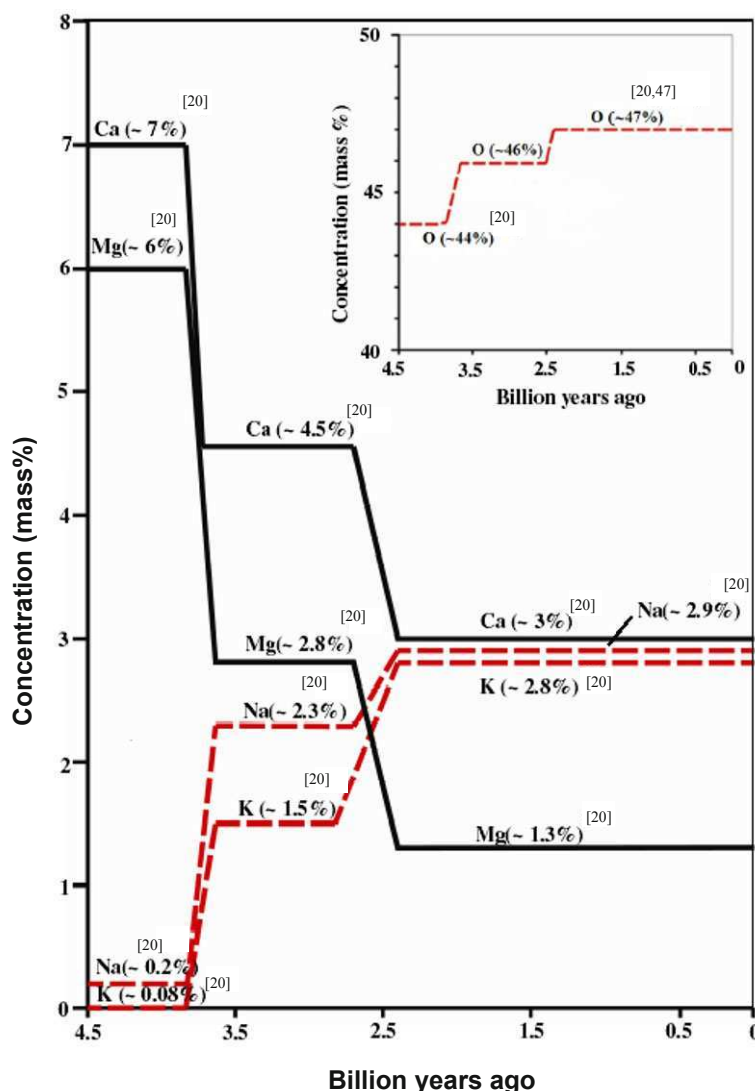


Figure 7: Variations in mass percentage concentration for Mg, Ca, Na, K, and O in the Hadean and Archean Earth's protocrust and in the Earth's continental crust [18-20, 47].

The variations in mass percentage for Mg, Ca, Na, K, and O in the Hadean and Archean Earth's protocrust and in the present Earth's continental crust are reported in Fig. 7, analogously to Fig. 6 [6, 18-20, 47]. The decrease in the mass concentrations of Mg and Ca has been balanced by the increase in Na, K, and O, during the Earth's lifetime. In particular, between the Hadean (4.5–3.8 Gyr ago) and the Archean (3.8–2.5 Gyrs ago) era, and between the latter and more recent times, it is possible to observe an overall decrease of ~4.7% for Mg and ~4%

for Ca. This decrease in the two alkaline-earth metals (Mg and Ca) seems to be nearly perfectly balanced by the increase in the concentrations of the two alkaline metals, Na and K (which have increased by 2.7% and 2.8%, respectively), and by a total increase (~3%) in O, which has varied from ~44% to ~47% (the latter being the present Oxygen concentration in the Earth's crust) (Fig. 7).

CONCLUSIONS

Neutron emission measurements were performed on Green Luserna Granite specimens during mechanical tests. From these experiments, it can be clearly seen that piezonuclear reactions giving rise to neutron emissions are possible in inert non-radioactive solids under pressure loading. In particular, during compression tests of specimens with sufficiently large size, the neutron flux was found to be of about one order of magnitude higher than the background level at the time of catastrophic failure. For test specimens with more ductile behaviour, neutron emissions significantly higher than the background were found. Neutron detection is also confirmed in compression test under cyclic loading and during ultrasonic vibration.

Our conjecture, also confirmed by the Energy Dispersive X-ray Spectroscopy (EDS) tests, is that piezonuclear reactions involving fission of iron into aluminum, or into magnesium and silicon, should have occurred during compression on the tested specimens. This hypothesis seems to find surprising evidence and confirmation at the Earth crust scale from both geomechanical and geochemical points of view. In this way, the piezonuclear reactions have been considered in order to interpret the most significant geophysical and geological transformations, today still unexplained. Finally, through experimental and theoretical studies of neutron emissions and piezonuclear fission reactions from brittle fracture, it will also be possible to explore new and interesting application fields, such as short-term prediction and monitoring of earthquakes.

REFERENCES

- [1] Carpinteri, A., Cardone, F. and Lacidogna, G. Piezonuclear neutrons from brittle fracture: Early results of mechanical compression tests. *Strain* 45: 332-339. (2009).
- [2] Cardone, F., Carpinteri, A. and Lacidogna, G. Piezonuclear neutrons from fracturing of inert solids. *Physics Letters A* 373: 4158-4163. (2009).
- [3] Carpinteri, A., Cardone, F. and Lacidogna, G. Energy emissions from failure phenomena: Mechanical, electromagnetic, nuclear. *Experimental Mechanics* 50: 1235-1243. (2010).
- [4] Carpinteri, A., Borla, O., Lacidogna, G. and Manuello, A. Neutron emissions in brittle rocks during compression tests: Monotonic vs cyclic loading. *Physical Mesomechanics* 13: 268-274. (2010).
- [5] Carpinteri, A., Chiodoni A., Manuello, A. and Sandrone, R. Compositional and microchemical evidence of piezonuclear fission reactions in rock specimens subjected to compression tests. *Strain*. doi: 10.1111/j.1475-1305.2010.00767.x. (2010).
- [6] Carpinteri, A. and Manuello, A. Geomechanical and geochemical evidence of piezonuclear fission reactions in the Earth's crust. *Strain*. doi: 10.1111/j.1475-1305.2010.00766.x. (2010).
- [7] Bubble Technology Industries Instruction manual for the Bubble detector, Chalk River, Ontario, Canada. (1992).
- [8] National Council on Radiation Protection and Measurements, Protection Against Neutron Radiation, NCRP Report 38. (1971).
- [9] Carpinteri, A. Cusp catastrophe interpretation of fracture instability. *J. of the Mechanics and Physics of Solids* 37: 567-582. (1989).
- [10] Carpinteri, A. A catastrophe theory approach to fracture mechanics. *Int. J. of Fracture* 44: 57-69. (1990).
- [11] Vola, G. and Marchi, M., Mineralogical and petrographic quantitative analysis of a recycled aggregate from quarry wastes. The Luserna stone case-study. *Proc. of the 12th Euroseminar on Microscopy Appl. to Building Mat.*, 15-19 September 2009, Dortmund, Germany (2009). (2009).
- [12] Sandrone, R., Cadoppi, P., Sacchi, R. and Vialon, P. The Dora-Maira Massif, in J.F Von Raumer and F. Neubauer (Eds.). *Pre-Mesozoic geology in the Alps*, Springer, Berlin, 317-325. (1993).
- [13] Compagnoni, R., Crisci, G. M. and Sandrone, R. Caratterizzazione chimica e petrografica degli "gneiss di Luserna" (Massiccio cristallino Dora-Maira, Alpi Occidentali) *Rend. Soc. It. Min. Petr.*, 38: 498. (1983).
- [14] Sandrone R., Colombo A., Fiora L., Fornaro M., Lovera E., Tunesi A., Cavallo A. Contemporary natural stones from the Italian western Alps (Piedmont and Aosta Valley regions), *Periodico di Mineralogia (Special issue)* 73: 211-226. (2004).
- [15] Kuzhevskij, M., Nechaev, O. Yu., Sigaeva, E. A. and Zakharov, V. A. Neutron flux variations near the Earth's crust. A possible tectonic activity detection, *Nat. Haz. and Earth System Sci.* 3: 637-645. (2003).
- [16] Kuzhevskij, M., Nechaev, O. Yu. and Sigaeva, E. A. Distribution of neutrons near the Earth's surface, *Nat. Haz. and Earth Syst.Sci.* 3: 255-262. (2003).

- [17] Volodichev, N.N., Kuzhevskij, B.M., Nechaev, O. Yu., Panasyuk, M.I., Podorolsky, A.N. and Shavrin, P.I. Sun-Moon-Earth connections: The neutron intensity splashes and seismic activity, *Astron. Vestnik* 34: 188-190. (2000).
- [18] Favero, G. and Jobstraibizer, P. The distribution of aluminum in the Earth: From cosmogenesis to Sial evolution. *Coord. Chem. Rev.* 149: 467- 400. (1996).
- [19] Taylor, S. R. and McLennan, S. M. The geochemical evolution of the continental crust, *Rev. of Geophys.*, 33: 241-265. (1995).
- [20] Taylor, S.R., and McLennan, S. M., Planetary Crusts: Their Composition, Origin and Evolution, *Cambridge University Press*, Cambridge. (2009).
- [21] Anbar, A. D. Elements and evolution. *Science* 322: 1481-1482. (2008).
- [22] Fowler, C. M. R. The Solid Earth: An Introduction to Global Geophysics. *Cambridge University Press*, Cambridge. (2005).
- [23] Doglioni, C. Interno della Terra, *Treccani, Enciclopedia Scienza e Tecnica*, 595-605, (2007).
- [24] Rudnick, R. L., Fountain, D. M. Nature and composition of the continental crust: A lower crustal perspective, *Rev. of Geophys.* 33: 267-309. (1995).
- [25] Roy, I., Sarkar, B. C. and Chattopadhyay, A. MINFO-a prototype mineral information database for iron ore resources of India, *Comp. and Geosciences* 27: 357-361. (2001).
- [26] World Iron Ore producers. Available at <http://www.mapsofworld.com/minerals/world-iron-ore-producers.html>
- [27] World Mineral Resources Map. Available at <http://www.mapsofworld.com/world-mineral-map.htm>;
- [28] Key Iron Deposits of the World. Available at <http://www.portergeo.com.au/tours/iron2002/-iron2002depm2b.asp>.
- [29] Lunine, J. I. E. Earth: Evolution of a Habitable World, *Cambridge Univ. Press*, Cambridge, New York, Melbourne. (1998).
- [30] Hazen, R. M. et al. Mineral evolution. *American Mineralogist* 93: 1693-1720. (2008).
- [31] Condie, K. C. Plate Tectonics and crustal evolution. *Pergamon Press, Elmsford*, New York. (1976).
- [32] Canfield, D. E. A new model for Proterozoic ocean chemistry. *Nature* 396: 450-453. (1998).
- [33] Holland, H. D. The oxygenation of the atmosphere and oceans. *Philos. Trans. R. Soc. London Ser. B* 361: 903-915. (2006).
- [34] Kholodov, V. N. and Butuzova, G. Y. Siderite formation and evolution on sedimentary iron ore deposition in the Earth's history. *Geology of Ore Deposits* 50: 299-319. (2008).
- [35] Foing, B. Earth's childhood attic. *Astrobiol. Mag.* Retrospection (on-line) February 23 (2005).
- [36] Sigman, D. et al. Polar ocean stratification in a cold climate. *Nature* 428: 59-63. (2004).
- [37] Galimov, E. M. Redox evolution of the Earth caused by a multistage formation of its core. *Earth and Plan. Sci. Lett.* 233: 263-276. (2005).
- [38] Yamaguchi, K. E. Evolution of the geochemical cycle of Fe trough geological time: iron isotope perspective. *Front. Res. on Earth E.* 2: 4-24. (2005).
- [39] Basile-Doelsch, I. Si stable isotope in the Earth's surface: a review. *J. of Geochem. Expl.* 88: 252-256. (2006).
- [40] Basile-Doelsch, I., et al. Another continental pool in the terrestrial silicon cycle. *Nature*. 433: 399-402. (2005).
- [41] De la Rocha, C. L., et al. A first look at the distribution of the stable isotopes of silicon in natural waters. *Geochim. et Cosmochim. Acta.* 64: 2467-2477. (2000).
- [42] Ragueneau, O., Tréguer, P., Leyneart, A. et al. A review of the Si cycle in the modern ocean: recent progress and missing gaps in the application of biogenic opal as a paleoproductivity proxy. *Global and Planetary Change* 26: 317-365. (2000).
- [43] Konhauser, K. O. et al. Oceanic nickel depletion and a methanogen famine before the Great Oxidation Event *Nature*. 458: 750-754. (2009).
- [44] Saito, M. A. Less nickel for more oxygen. *Nature* 458: 714-715. (2009).
- [45] Egami, F. Minor elements and evolution. *J. of Molecular Evol.* 4:113-120. (1975).
- [46] Natl Academy of Sciences Medical and Biological Effects of Environmental Pollutants: Nickel. *Proc. Natl Acad Sci.* Washington, DC. (1975).
- [47] Yaroshevsky, A. A. Abundances of chemical elements in the Earth's crust. *Geochem. Int.* 44: 54-62.
- [48] Liu, L. (2004) The inception of the oceans and CO₂-atmosphere in the early history of the Earth. *Earth and Planetary Sci. Lett.* 227: 179-184. (2006).
- [49] Catling, C. D. and Zahnle, K. J. The planetary air leak. *Scientific American*. 300: 24-31. (2009)
- [50] Aki, K. Strong motion seismology. In Earthquakes: Observation, Theory and Interpretation. (Kanamori, H. and Boschi, E. Ed), *North-Holland Pub. Co.*, Amsterdam. 223-250. (1983).
- [51] Padron, E., et al. Changes in the diffuse CO₂ emission and relation to seismic activity in and around El Hierro, Canary Islands. *Pure Appl. Geophys.* 165: 95-114. (2008).

Acoustic emission and electrical properties of quasi-brittle materials under compression

G. Lacidogna¹, A. Carpinteri¹, A. Manuello¹, G. Niccolini², A. Agosto², O. Borla^{1,3}

¹*Politecnico di Torino, Department of Structural Engineering & Geotechnics,
Corso Duca degli Abruzzi 24 – 10129 Torino, Italy*

²*Istituto Nazionale di Ricerca Metrologica INRIM
Strada delle Cacce 91 – 10135 Torino, Italy*

³*Istituto Nazionale di Fisica Nucleare sez. Torino
Via Pietro Giuria 1 – 10125 Torino, Italy*

E-mail: giuseppe.lacidogna@polito.it

ABSTRACT

Acoustic emission (AE), electromagnetic emission (EME) and electrical properties measurements have been performed during laboratory compression tests on Green Luserna Granite dry rock loaded with increasing pressure up to their failure. Using a servo-controlled testing machine (MTS) each compression test was carried out at constant displacement rate and under ordinary room conditions. AE signals were detected by applying to the sample surface a piezoelectric (PZT) transducer, sensitive in the frequency range from 50 to 500 kHz. EME signals were detected using a loop antenna (80.0 dB gain at 500 kHz). The time-dependent outputs of the PZT transducer and the electromagnetic tester were connected to a DL708 Yokogawa oscilloscope (10 MSa s⁻¹) in order to acquire simultaneously AE and EME signals associated with the same fracture event. Electrical properties, in terms of relative electrical resistance variation, were monitored by using copper electrodes coupled to specimens by conductive silver paint, and connected to a multimeter (Agilent model 34411A). The recorded AE, EME and electrical properties variation were related to the load vs. time diagram of the tested specimens. The experiments conducted in this research confirm that AE and EME are failure precursors in quasi-brittle materials, moreover EME signals and electrical property variations are related to sharp drops in stress vs. time diagram.

INTRODUCTION

It is possible to demonstrate experimentally that the failure phenomena, in particular when they occur in a brittle way, i.e. with a mechanical energy release, emit additional forms of energy related to the fundamental natural forces. In this work the authors have found increasing experimental evidence that energy emission of different forms occurs from solid-state fractures. The tests were carried out at the Laboratory of Fracture Mechanics of the Politecnico di Torino, Italy.

In the past, in addition of the studies on acoustic emission (AE), several analysis have been performed during fracture experiments on quasi-brittle materials to detect electromagnetic emission (EME) and variations in electrical properties [1-11]. Acoustic and electromagnetic emissions and electrical properties changes of materials during failure are analogous to the anomalies observed before major earthquakes [12-15] reinforcing the idea that these experimental methods can be applied as a forecasting tool for earthquakes.

While the mechanism of AE is fully understood, being provided by transient elastic waves due to stress redistribution following fracture propagation [16-21], the origin of EME from fracture is not completely clear and different attempts have been made to explain it.

An explanation of the EME origin was related to dislocation phenomena [22,23], which however are not able to explain EME from fracture in brittle materials where the motion of dislocations can be neglected [5]. The weakness of the “dislocation movement hypothesis” was confirmed in some experiments showing that the EME amplitude increased with the brittleness of the investigated materials [24].

Another EME explanation was initially given in terms of charge separation occurring across the fractures, even if no reasonable explanation is found for each crack face to obtain a net charge [3,25]. More recently, a model preserving the charge neutrality of crack surfaces, where lines of positive ions on both newly created

fracture surfaces oscillate around their equilibrium position in opposite phase to the negative ones, was proposed [5,8].

Regarding the electrical properties, most rocks, in particular silicates and carbonates, have very high specific resistivities ($> 10^9$ Ohm m) and for this reason are classified as *insulators*, materials with very large energy barriers between atoms such that electrons rarely become charge transport carriers. Studies on electrical properties of rocks have been demonstrated that their resistivity is highly dependent on the porosity [9-11]; a relationship referred to as Archie's law has been established between in-situ rocks porosity and electrical resistivity [26]. Electrical resistivity increases as microcracks open within the material failure and it appears that there should be a correlation between electrical resistivity and cumulative damage. The experimental relation between resistivity in water saturated crystalline rocks, and compressive stress was discovered by Brace's group [27-30]. Electrical resistivity of igneous rocks and limestone was measured in direction of the axial pressure saturating the rocks with tap water or salt solution. Changes in electrical resistivity were observed as a function of pressure in a variety of crystalline rocks subjected to confining pressure and pore pressure.

In this work we present preliminary compression tests, analyzed by acoustic and electromagnetic emissions, on four cylindrical Green Luserna Granite specimens characterized by different shape and size. Moreover further tests on the same type of rock specimens, simultaneously monitored by electrical resistance variation, and EME are presented. The novelty of this work is that the rocks electrical resistance was analyzed in dry and non-saturated conditions.

To obtain suitable tests on electrical properties of Green Luserna Granite specimens under stress, preliminary electrical resistance measurements were performed on *ad hoc* prismatic mortar specimens. These cementitious specimens are enriched with 10% of iron oxide in weight. Iron oxide, joined with a deposition of silver paint on the external specimen surfaces –in which the copper electrodes are applied– increases the mortar conductivity. Than the electrical conductivity of the granite specimens was also improved with a deposition of the same silver paint layers along the external surface of the specimens.

The mortar samples were tested in compression at a constant displacement rate, and analyzed only in terms of relative electrical resistance variation through a special multimeter detector. Instead Green Luserna Granite specimens were simultaneously monitored by EME and electrical resistance device.

PRELIMINARY AE AND EME TESTS

Crack growth is accompanied by AE ultrasonic waves and EME. We measured the magnetic field, given by the moving charges, in the low-frequency range during laboratory fracture experiments on granitic rocks specimens loaded up to failure [34,35].

Four cylindrical Green Luserna Granite specimens were examined (Fig. 1). The electromagnetic signals were detected using a device (Narda ELT-400 exposure level tester) calibrated according to metrological requirements. The adopted device works in the frequency range between 10 Hz and 400 kHz, the measurement range is between 1 nT and 80 mT, and the three-axial measurement system has a 100 cm^2 magnetic field sensor for each axis. This particular frequency range was chosen to avoid disturbances due to radio waves that operate on medium frequencies of 300-3000 kHz, or other electronic devices that generally operate on frequencies above 5-30 MHz.

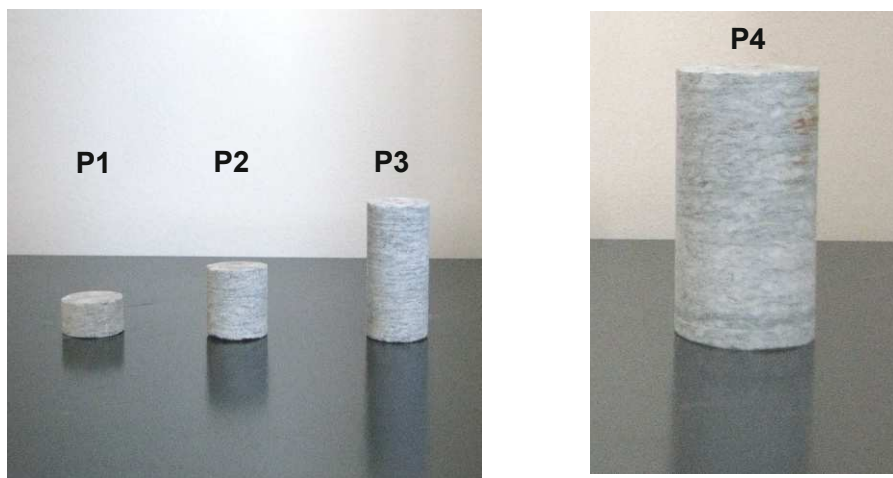


Fig. 1. The Cylindrical Luserna Granite Specimens P1,P2,P3 and P4 utilized for EM tests.

The tests were carried out by means of a servo-hydraulic press, with a maximum capacity of 1800 kN, working by a digital type electronic control unit. The management software was TESTXPERTII by Zwick/Roel

(Zwick/Roel Group, Ulm, Germany), while the mechanical parts are manufactured by Baldwin (Instron Industrial Products Group, Grove City, PA, USA). The force applied was determined by measuring the pressure in the loading cylinder by means of a transducer. The margin of error in the determination of the force is 1%, which makes it a class 1 mechanical press. The specimens were arranged with the two smaller surfaces in contact with the press platens, without coupling materials in-between, according to the testing modalities known as “test by means of rigid platens with friction”. During the compression tests Narda ELT-400 device was placed 1 m away from the specimens. Specific tests were conducted to assess the potential EM environmental noise, and what affecting the EM signals due to the MTS test machine electronic control. In particular, the EM probe was used to detect the EM background noise for about five hours before the beginning of each compressive test. The background noise was estimated at about 40 nT in the frequency range 10 Hz - 400 kHz. Data acquisition of the EME signals was triggered when the magnetic field exceeded the threshold fixed at 0.2 μ T, after the preliminary measurements to filter out the magnetic noise in the laboratory.

All the shapes and sizes of all the tested specimens, and the employed piston velocity are listed in Table 1. The selected piston velocity, reported in the table, is in the authors' experience the most suitable value to evaluate AE and EME activity in quasi-brittle materials such as concrete and rocks [34-37].

Specimen	Material	Diameter [mm]	Height [mm]	Slenderness $\lambda=H/D$	Piston velocity [m s ⁻¹]
P1	Granite	28	14	0.5	1.0×10^{-6}
P2	Granite	28	28	1	1.0×10^{-6}
P3	Granite	28	56	2	1.0×10^{-6}
P4	Granite	53	100	2	2.0×10^{-6}

Table 1: Geometry of the Green Luserna Granite specimens, and compression test piston velocities.

As can be seen from Table 1, the first three specimens (P1-P3) have the same diameter (28 mm) with a different slenderness λ , respectively of 0.5, 1 and 2, specimen P4 has a diameter equal to 53 mm and slenderness $\lambda=2$. During the compression tests all the specimens have shown a brittle response, with a rapid decrease in load-carrying capacity beyond the peak load. In Figs. 2-5, the load vs. time diagrams and the EM signals are reported for specimens P1-P4. As shown in Figs. 2-5, the specimens mechanical behaviour is characterized by a complex load vs. time diagram. This is due to the composition of Green Luserna Granite, which is a natural and heterogeneous material.

Specimen P1 presents a more ductile behaviour (Fig. 2) characterized by the descending branch of the load vs. time diagram. During the compression test three EM signals, with constant peak amplitude of 1.2 μ T, were detected at 180s, 500s and 750s (see Fig. 2a). All these signals were anyway detected at stress-drops, in Fig. 2b also the amplitude and FFT analysis of the first EME signal of the test on specimen P1 are shown. During the post-peak stage, i.e., the softening branch in the load vs. time diagram, no further EME signals were detected. In fact, at the peak load the fracture is completely formed and the subsequent stages are characterized only by opening of the fracture surfaces. According to the model proposed by [5] and [8], this means that no newly broken atomic bonds can contribute to EME. In Fig. 2b the FFT analysis for signal 1 is shown. The main detected frequency is close to 160 kHz according to the working frequency range of the Narda ELT-400.

Otherwise, specimens P2 and P3 show a very brittle behaviour, characterized by abrupt stress drops after reaching the peak load. The experimental results are reported in Figs. 3 and 4. Five EM signals were detected during the specimen P2 test. In specimen P3 four EM signals were observed. Only in the case of specimen P2 the signal amplitudes (in μ T) seem to be proportional to the stress-drop values, as reported in [7]. Specimen P4 presents a very high amplitude EME (16 μ T) in correspondence of a stress drop localized at 1420 s after the beginning of the test. In this case, a very brittle behaviour is observed and the EME is localized in correspondence of the failure of the specimen. Also the cumulated number of AE is detected during the compression test (see Fig. 5). The experimental results obtained in the described test are in good agreement with those obtained in [34,35].

Based on the authors' experience gained in numerous laboratory tests, it is interesting to note that, despite their different mechanical behaviour, all the specimens composed by brittle or quasi-brittle materials, as rocks or concrete, generate EME only during sharp drops in stress [7,34,35]. These sharp stress drops are due to a rapid decay of the material mechanical properties, generated by the formation of new micro-cracks during the loading process. Indeed, as it has been shown by Carpinteri [38-41] and by Hudson et al. [42], the energy release modalities during compressive tests depend on the intrinsic brittleness of the material of the test specimens, as well as on test specimen dimensions and slenderness. This evidence enables the investigation EM signals as collapse precursors in materials like rocks and concrete. Furthermore, the

observed electromagnetic activity from laboratory experiments looks very promising for effective applications at the geophysical scale [1,3].

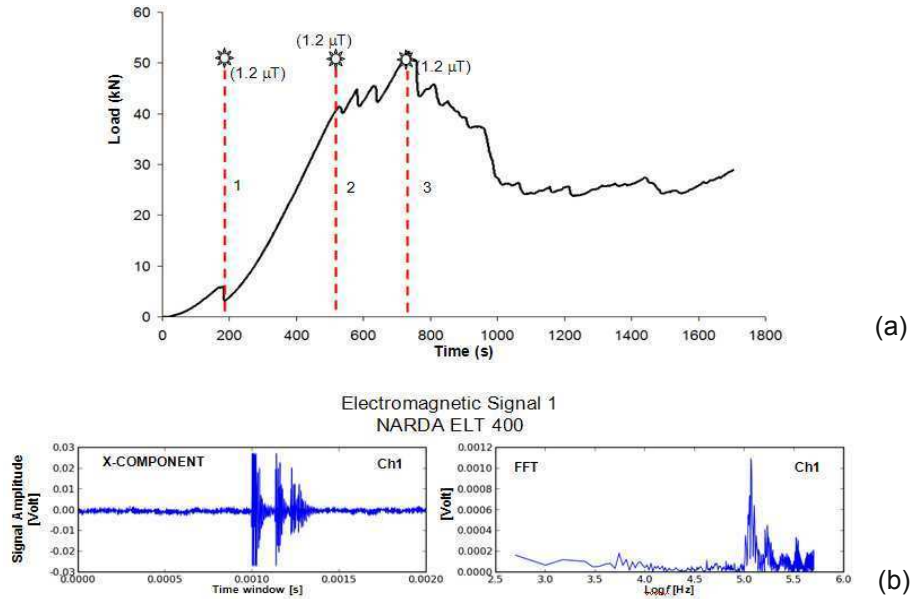


Fig. 2. (a) Load vs. time diagram of the Luserna Granite specimen P1. (b) Amplitude and FFT analysis for the detected signal 1.

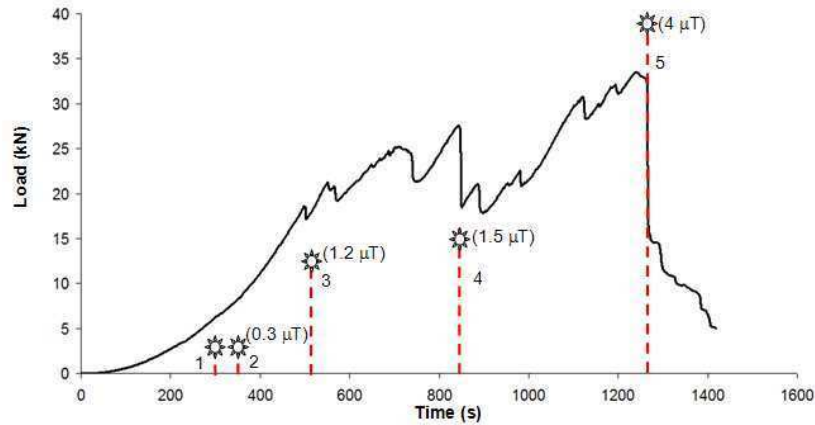


Fig. 3. Load vs. time diagram of the Luserna Granite specimen P2. Five EM signals were detected during the test.

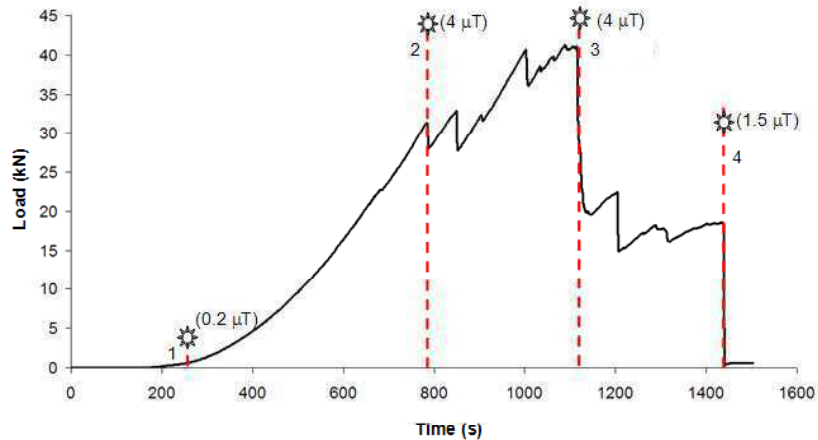


Fig. 4. Load vs. time diagram of the Luserna Granite specimen P3. Four EM signals were detected during the test.

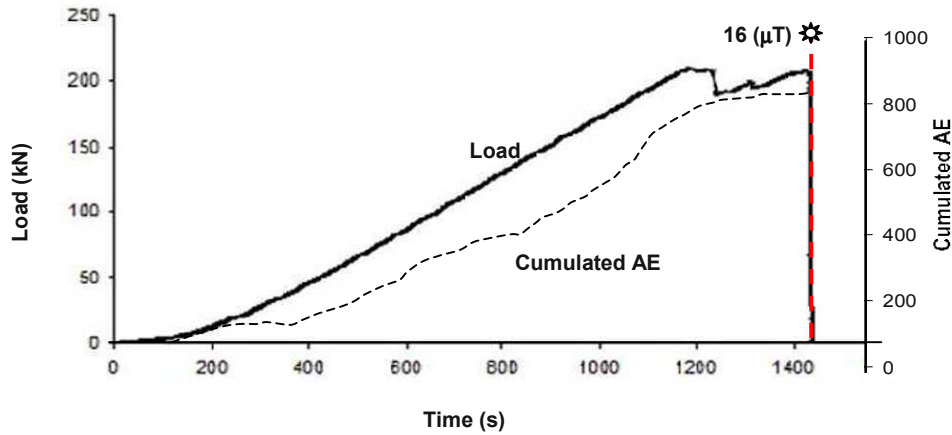


Fig. 5. Load vs. time diagram and AE cumulated number (dashed line) for specimen P4. A signal of 16 μT is detected in correspondence to the peak load.

EME AND RELATIVE ELECTRICAL RESISTANCE VARIATIONS TESTS

Three further cylindrical specimens made of Green Luserna Granite, and four prismatic cementitious mortar specimens, enriched with 10% of iron oxide in weight, were examined to analyze the relative electrical resistance variations in compression (Fig. 6). The geometric characteristics of the specimens and the employed piston velocity are listed in Table 2. To obtain electrical contacts, copper electrodes joined with silver paint, were connected on two opposite faces, parallel to the vertical load axis, and positioned symmetrically at the half height of the specimens. The electrical resistance was monitored by means of constant-voltage method using an Agilent model 34411A multimeter detector. By this device the electrical resistance is automatically detected. The multimeter was programmed in order to acquire experimental data every 0.1 s in real-time measurement.

For all the specimens, at the beginning of each compression test, the initial electrical resistance R_0 was evaluated. Afterwards the resistance variation R was monitored until the final collapse, calculating the relative ratio R/R_0 .

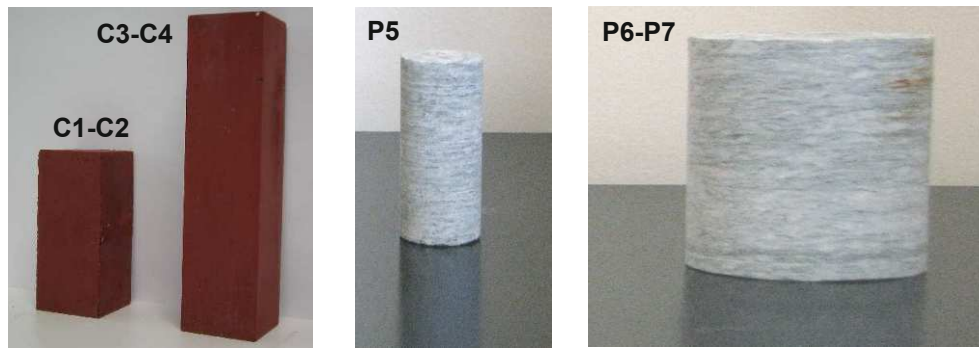


Fig. 6. Prismatic mortar specimens C1-C4 and cylindrical granite specimens P5-P7.

Specimen	Material	Side [mm]	Height [mm]	Slenderness $\lambda=H/S$	Piston velocity [m s ⁻¹]
C1	Mortar	40	80	2	2.0×10^{-6}
C2	Mortar	40	80	2	2.0×10^{-6}
C3	Mortar	40	160	4	2.0×10^{-6}
C4	Mortar	40	160	4	2.0×10^{-6}
Specimen	Material	Diameter [mm]	Height [mm]	Slenderness $\lambda=H/D$	Piston velocity [m s ⁻¹]
P5	Granite	28	56	2	1.0×10^{-6}
P6	Granite	53	50	1	1.0×10^{-6}
P7	Granite	53	50	1	1.0×10^{-6}

Table 2: Geometry of mortar and granite specimens, and compression test piston velocities.

The four mortar specimens (C1-C4), analyzed during the preliminary electrical resistance tests, have the same section ($40 \times 40 \text{ mm}^2$) and different slenderness λ , respectively of 2 (C1-C2) and 4 (C3-C4). All the specimens present a very brittle behaviour, characterized by abrupt stress-drops after reaching the peak load. **Figures 7a-7d** illustrate the relation between applied stress level and electrical resistance variation for specimens C1-C4. As can be seen from **Figs. 7a-7d** the mechanical behaviour of the specimens is characterized by an almost linear load vs. time diagram up to failure. For specimens C1 and C2, at about 30% of the peak load a moderate increment in electrical resistance variation was observed. Successively a plateau appeared in which the electrical resistance remained almost constant until the 90% of the peak load. An intense electrical resistance variation was detected at final stress-drop. The significant variation of the electrical resistance that precedes the final collapse clearly represents a precursor of specimen failure. Excepting of the moderate increase of the resistance at 30% of the peak load, similar behaviour was observed for specimens C3 and C4.

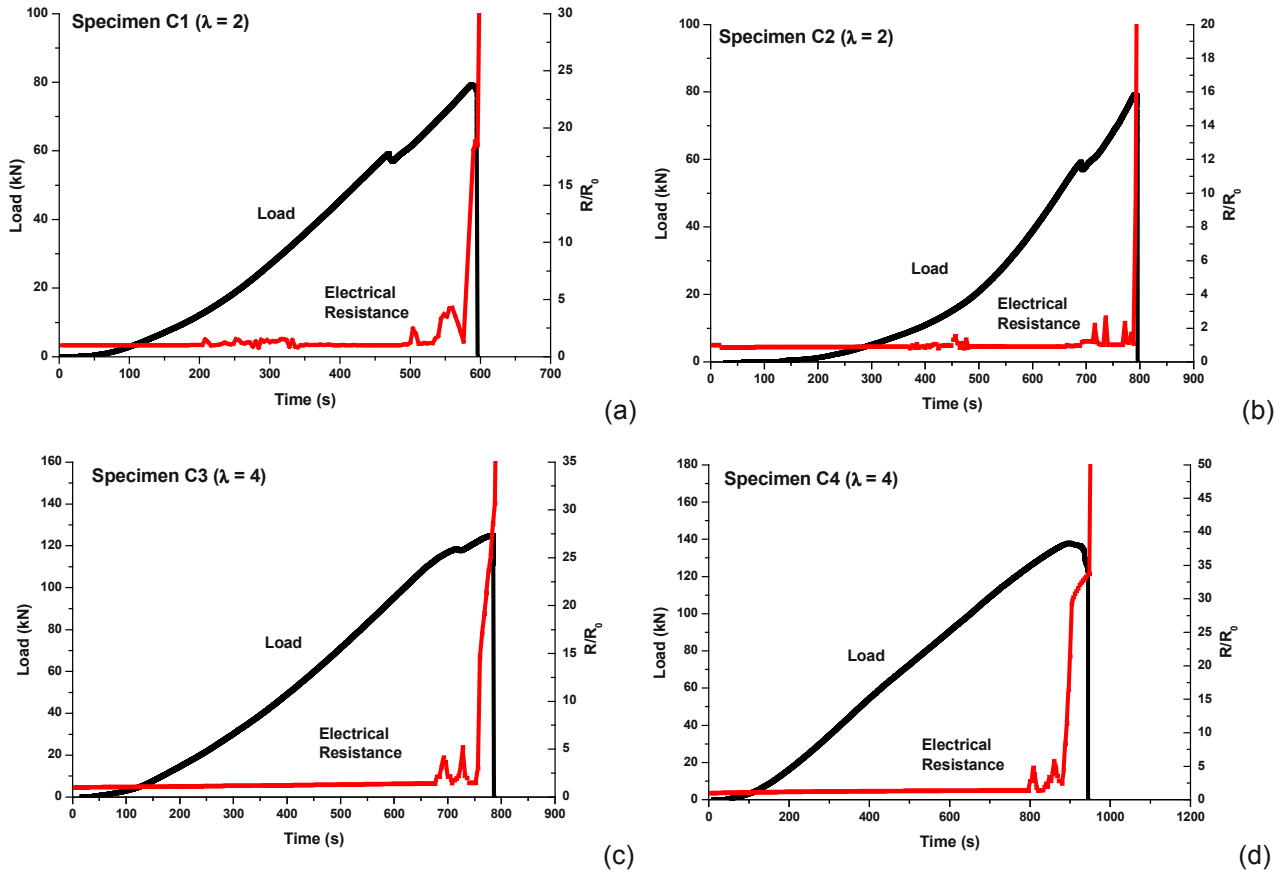


Fig. 7. Load vs. time diagram and relative electrical resistance (R/R_0) variation for specimens C1 (a), C2 (b), C3 (c) and C4 (d).

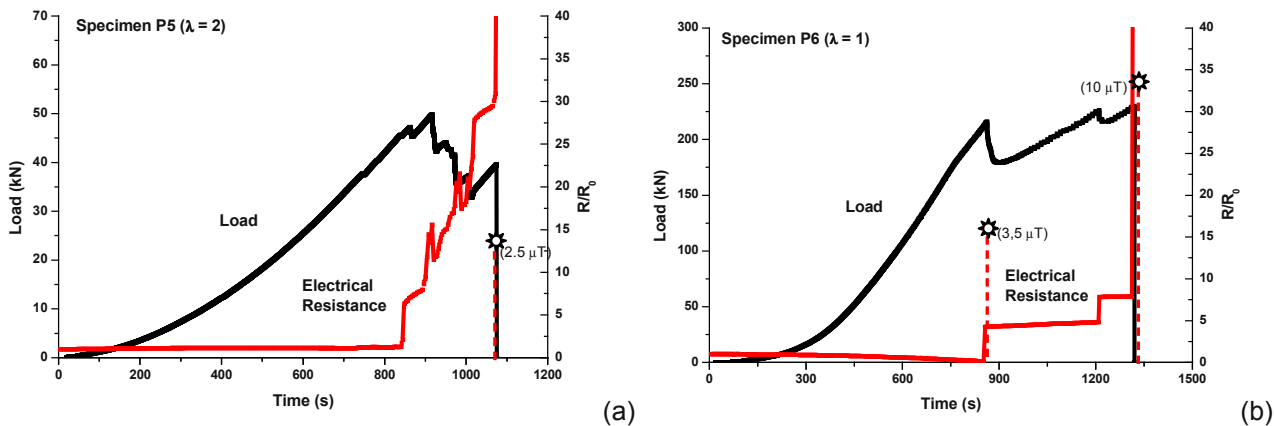


Fig. 8. Load vs. time diagram and relative electrical resistance (R/R_0) variation for specimens P5 (a) and P6 (b).

In Figs. 8a and 8b, the load vs. time diagrams, and the relative electrical resistance variations are reported for Green Luserna Granite specimens P5-P6. These samples are characterized by different diameters (28 mm and 53 mm) and different slenderness ($\lambda=2$, $\lambda=1$), see Table 2. The brittle mechanical behaviour of these samples is characterized by a more complex load vs. time diagram with respect to the mortar specimens. This is due to the composition of Green Luserna Granite that, as previously reported, is a natural and more heterogeneous material. Electrical resistance maintains constant values until the first stress-drop, then significant variations occurred at each successively load vs. time steps. Also in this case, as for mortar specimens, it is evident the correlation between electrical resistance changes and cumulative damage. Similar behaviour was observed for the specimen P7. As can be observed from Figs. 8a and 8b, specimen P5 presents an EM signal (2.5 μT) in the failure correspondence. For the specimen P6 two EM signals were detected, the first (3.5 μT) at 850 s starting from the beginning of the test, the second (10 μT) at the final failure.

As can be seen from Figure 8a and 8b, the EME signals, related to the sharp stress-drops, take place instantaneously, while the electrical resistance changes, connected to the size evolution and different orientations of the fracture planes, take place first gradually and then in a very sudden way, reaching very high R/R_0 values at the final specimen collapse.

CONCLUSION

By subjecting Green Luserna Granite rocks, to compression tests, it was observed AE, EME signals, and resistance variations during the damage evolution, suggesting electrical charges redistribution. These experiments confirm AE and EME as failure precursors in quasi-brittle materials. Moreover, EME signals are related to sharp stress-drops, while electrical property variations are linked to the size and orientations of the fracture planes. These signals are analogous to the anomalies observed before major earthquakes, reinforcing the idea that these experimental methods can be applied as a forecasting tool for earthquakes.

ACKNOWLEDGEMENTS

The financial support provided by Regione Piemonte (RE-FRESCOS project) is gratefully acknowledged. We are grateful to Prof. M. Parvis of the Politecnico of Torino for his valuable suggestions and for providing the electrical resistance measurement device.

REFERENCES

- [1] Warwick, J.W., Stoker, C. and Meyer, T.R. (1982) Radio emission associated with rock fracture: Possible application to the great Chilean earthquake of May 22, 1960, *J. Geophys. Res.*, 87, 2851-2859.
- [2] Ogawa, T., Oike, K., and Miura, T. (1985) Electromagnetic radiation from rocks. *J. Geophys. Res.*, 90, 6245-6249.
- [3] O'Keefe, S. G. and Thiel, D. V. (1995) A mechanism for the production of electromagnetic radiation during fracture of brittle materials, *Phys. Earth Planet. Inter.*, 89, 127-135.
- [4] Lolajicek, T. and Sikula, J. (1996) Acoustic emission and electromagnetic effects in rocks, *Progress in Acoustic Emission VIII*, 311-314.
- [5] Frid, V., Rabinovitch, A. and Bahat, D. (2003) Fracture induced electromagnetic radiation, *J. Phys. D.*, 36, 1620-1628.
- [6] Hadjicontis, V., Mavromatou, C. and Nonos, D. (2004) Stress induced polarization currents and electromagnetic emission from rocks and ionic crystals, accompanying their deformations, *Nat. Hazards and Earth System Science*, 4, 633-639.
- [7] Fukui, K., Okubo, S. and Terashima, T. (2005) Electromagnetic radiation from rock during uniaxial compression testing: The effects of rock characteristics and test conditions, *Rock Mech. Rock Eng.*, 38, 411-423.
- [8] Rabinovitch, A., Frid, V. and Bahat, D. (2007) Surface oscillations. A possible source of fracture induced electromagnetic oscillations, *Tectonophysics*, 431, 15-21.
- [9] Russell, J. E. and Hoskins E. R. (1969) Correlation of electrical resistivity of dry rock with cumulative damage, *The 11th U.S. Symposium on Rock Mechanics (USRMS)*, June 16 - 19, 1969, Berkeley, CA
- [10] Laštovičková M. Laboratory measurements of electrical properties of rocks and minerals *Surveys in Geophysics Volume 6, Numbers 1-2*, 201-213, DOI: 10.1007/BF01454001
- [11] Beblo, M. Electrical conductivity (resistivity) of minerals and rocks at ordinary temperatures and pressures. Angenheister, G. (ed.). SpringerMaterials - The Landolt-Börnstein Database (<http://www.springermaterials.com>). DOI: 10.1007/10201909_42
- [12] Gokhberg, M.B., Morgunov, V.A., Yoshino, T. and Tozawa, I. (1982) Experimental measurement of electromagnetic emissions possibly related to earthquakes in Japan, *J. Geophys. Res.*, 87, 7824-7828.
- [13] Nagao, T., Enomoto, Y., Fujinawa, Y. et al. (2002) Electromagnetic anomalies associated with 1995 Kobe earthquake, *Journal of Geodynamics*, 33, 401-411.

- [14] Karamanos, K., Dakopoulos, D., Aloupis, K. et al. (2006) Preseismic electromagnetic signals in terms of complexity, *Physical Review E*, 74, 016104.
- [15] Mazzella A. and Morrison H. F. (1974) Electrical Resistivity Variations Associated with Earthquakes on the San Andreas Fault Science 6 September 1974: Vol. 185 no. 4154 pp. 855-857
- [16] Kaiser, J. (1950) An investigation into the occurrence of noises in tensile tests, or a study of acoustic phenomena in tensile tests. Ph. D. dissertation, Munich (FRG), Technische Hochschule München.
- [17] Pollock, A.A. (1973) Acoustic emission-2: Acoustic emission amplitudes, *Non-Destructive Testing*, 6, 264-269.
- [18] Ohtsu, M. (1996) The history and development of acoustic emission in mortar engineering, *Magazine of Mortar Research*, 48, 321-330.
- [19] Carpinteri, A., Lacidogna, G. and Pugno, N. (2007) Structural damage diagnosis and life-time assessment by acoustic emission monitoring, *Engineering Fracture Mechanics*, 74, 273-289.
- [20] Carpinteri, A., Lacidogna, G. and Manuello, A. (2007) Damage mechanisms interpreted by acoustic emission signal analysis, *Key Engineering Materials*, 347, 577-582.
- [21] Carpinteri, A., Lacidogna, G., Niccolini, G. and Puzzi, S. (2008) Critical defect size distributions in mortar structures detected by the acoustic emission technique, *Meccanica*, 43, 349-363.
- [22] Misra, A. (1977) Theoretical study of the fracture-induced magnetic effect in ferromagnetic materials, *Physics Letters*, 62A, 234-236.
- [23] Misra, A. (1978) A physical model for the stress-induced electromagnetic effect in metals, *Applied Physics*, 16, 195-199.
- [24] Jagasivamani, V. and Iyer, K.J.L. (1988) Electromagnetic emission during the fracture of heat-treated spring steel, *Mater. Lett.*, 6, 418-422.
- [25] Miroshnichenko M and Kuksenko V 1980 Study of electromagnetic pulses in initiation of cracks in solid dielectrics. *Soviet Physics-Solid State* 22: 895-896.
- [26] Archie, G.E., 1942, The electrical resistivity log as an aid in determining some reservoir characteristics: *Petroleum Transactions of AIME (Am. Inst. Min. Metall. Eng.)*, v. 146, p. 54-62.
- [27] W.F. Brace, A.S. Orange and T.R. Madden, The effect of pressure on the electrical resistivity of water-saturated crystalline rocks. *J Geophys Res* 70 22 (1965), pp. 5669-5678.
- [28] W.F. Brace and A.S. Orange, Electrical resistivity changes in saturated rocks during fracture and frictional sliding. *J Geophys Res* 73 4 (1968), pp. 1433-1445.
- [29] W.F. Brace and A.S. Orange, Further studies of the effects of pressure on electrical resistivity of rocks. *J Geophys Res* 73 16 (1968), pp. 5407-5420.
- [30] W.F. Brace, Dilatancy-related electrical resistivity changes in rocks. *Pure Appl Geophys* 113 (1975), pp. 207-217.
- [31] Carpinteri, A., Lacidogna G. and Manuello, A. (2009) The b-value analysis for the stability investigation of the ancient Athena Temple in Syracuse, Strain, doi: 10.1111/j.1475-1305.2008.00602.x.
- [32] Lacidogna, G., Manuello, A., Durin, G., Niccolini, G., Agosto, A. and Carpinteri, A. (2009). Acoustic and magnetic emissions as precursor phenomena in failure processes, *Proc. of SEM Annual Conference & Exposition on Experimental and Applied Mechanics*, Albuquerque, 1-4 June 2009, Paper No. 540.
- [33] Schiavi, A., Niccolini, G., Tarizzo, P., Lacidogna, G., Manuello, A. and Carpinteri, A (2009) High and low frequency elastic wave propagation in brittle materials under compression, *Proc. of SEM Annual Conference & Exposition on Experimental and Applied Mechanics*, Albuquerque, 1-4 June 2009, Paper No. 539.
- [34] Lacidogna G, Carpinteri A, Manuello A, Durin G, Schiavi A, Niccolini G and Agosto A 2010 Acoustic and electromagnetic emissions as precursor phenomena in failure processes. *Strain*. doi: 10.1111/j.1475-1305.2010.00750.x.
- [35] Carpinteri A, Lacidogna G, Manuello A, Niccolini G, Schiavi A, Agosto A 2010 Mechanical and electromagnetic emissions related to stress-induced cracks. *Exp.Tech*. In print.
- [36] Carpinteri A, Lacidogna G and Pugno N 2006 Richter's laws at the laboratory scale interpreted by acoustic emission. *Mag of Mortar Res*. 58: 619-625.
- [37] Carpinteri A, Lacidogna G, and Niccolini G 2006 Critical behaviour in mortar structures and damage localization by acoustic emission. *Key Eng. Mat.* 312: 305-310.
- [38] Carpinteri A 1986 *Mechanical Damage and Crack Growth in Concrete: Plastic Collapse to Brittle Fracture*. Dordrecht: Martinus Nijhoff Publishers.
- [39] Carpinteri A 1989 Cusp catastrophe interpretation of fracture instability. *J. of the Mechanics and Physics of Solids*. 37: 567-582.
- [40] Carpinteri A 1990 A catastrophe theory approach to fracture mechanics. *Int. J. of Fract.* 44: 57-69.
- [41] Carpinteri A 1994 Scaling laws and renormalization groups for strength and toughness of disordered materials. *Int. J. of Solids and Struct.* 31: 291-302.
- [42] Hudson J A, Crouch S L and Fairhurst C 1972 Soft, stiff and servo-controlled testing machines: A review with reference to rock failure. *Eng. Geol.* 6: 155-189.

Temperature Effect on Tensile Testing of Hybrid and Non-Hybrid Composites*

Yougashwar Budhoo ^{a*}, Feridun Delale ^b, Benjamin Liaw ^b

^a *Department of Engineering and Technology, Vaughn College of Aeronautics and Technology, 86-01, 23 Ave, East Elmhurst, Queens, NY 11369, USA*

^b *Department of Mechanical Engineering, The City College of New York, Convent Avenue and 138th Street, New York, NY 10031, USA*

ABSTRACT

Monotonic tensile tests were conducted following ASTM Standards D3039 (Standard Test Method for Tensile Properties of Polymer Matrix Composite Materials) and D3518 (Standard Test Method for In-Plane Shear Response of Polymer Matrix Composite Materials by Tensile Test of a $\pm 45^\circ$ Laminate), on hybrid and non-hybrid plain weave composite materials. Strips of non-hybrid IM-7 Graphite/SC-79 epoxy called GR for short, non-hybrid S-2 Glass/SC-79 epoxy called GL for short, hybrid GR/GL/GR and hybrid GL/GR/GL specimens were tensile tested. The tests were conducted at -60°C , -20°C , room temperature, 75°C and 125°C . The rule of mixtures was used to predict the Young's moduli of GL/GR/GL and GR/GL/GR using the experimental values obtained from the stress-strain curves of the GL and GR specimens. The predicted Young's moduli of GL/GR/GL and GR/GL/GR were then compared to those obtained experimentally. It was found that the calculated Young's and shear moduli match closely (within 6 %) to those obtained experimentally.

INTRODUCTION

Tensile testing has been the most fundamental test in obtaining the mechanical properties of a particular material. The limitation of obtaining mechanical properties from tensile testing using an MTS machine is that only low strain rates results can be obtained, therefore only material properties under quasi-static loading can be determined. Material properties under high strain rates require different types of tests such as tests using the Split Hopkinson Pressure Bar Test (SHPB) [1]. Several analytical models have been developed to predict the material properties and behavior of woven hybrid and non hybrid composites under tensile loading. Many of these models also incorporate the effect of moisture and temperature; however most of these models assume the properties of each individual constituent as being constant. For example, most of these models assume that the thermal expansion coefficient is temperature independent. Analytical models tend to provide a cost effective method to determine the effects of several parameters on the mechanical properties. These parameters include fabric weight, constituent volume fraction, yarn undulation, weave style and properties of the constituent materials. Several micro mechanical models based on the classical thin laminate theory have been developed. Scida [2] developed a model called MESOTEX to predict the elastic behavior of composites reinforced with hybrid and non-hybrid weaves. A model which study the failure behavior of plain weave fabric laminates under on-axis uniaxial tensile loading was done by Naik and Ganish [3-5]

*Corresponding author. Tel.: +1 646 496 6102; Fax: +1 718 429 6339.

E-mail address: yougashwar.budhoo@vaughn.edu (Y. Budhoo).

Ishakawa and Chou [6-10] have presented three models (mosaic, crimp and bridging) for the analytical and numerical prediction of the thermo-mechanical properties of woven composites (plain, twill and satin weaves).

Maybe the most common agent other than force that may adversely affect composites is temperature. Some research has been done to study the effect of temperature on composite materials. High-performance thermo-plastic matrices used in composite materials need to be processed at high temperatures; therefore, thermal residual stresses arise due to the mismatch of thermal expansion coefficients of the fibers and the thermoplastic matrix. Since residual stresses are inherently present in virtually all composite materials and influence the properties of the composite structure, it is important to take them into consideration in the event that they are significant. Parlevliet, Bersee and Beukers [11-13] did a study of the literature focusing on the formation of residual stresses due to manufacturing, experimental techniques in quantifying these residual stresses and also the effect of these residual stresses.

In this study, the effect of temperature on the unidirectional tensile behavior of the composites will be studied experimentally.

EXPERIMENTAL PROCEDURE

Materials:

The individual constituent materials combined to form the composite material used in this research are, IM-7 graphite (IM7-GP 6000) and S2-glass (S2-4533 6000) woven fabrics placed in SC-79 toughened epoxy resin matrix. The IM-7 graphite woven fabric and SC-79 epoxy matrix form the non-hybrid composite called GR. The S2-Glass woven fabric and SC-79 epoxy matrix form the non-hybrid laminate called GL. A GL laminate will be sandwiched between two GR layers to form the hybrid laminate called GR/GL/GR. Finally the fourth layup is formed by a GR layer sandwiched between two GL layers to form the second hybrid laminate called GL/GR/GL. S2-glass fabrics and IM7-graphite fabrics were supplied by the Hexcel Corporation. The matrix, SC-79 toughened epoxy resin, which has Part A (Batch number: SC79A012307) and Part B (Batch number: SC79B012507), was supplied by Applied Poleramic Inc. The manufacturing of the composite was done by EDO Fiber Innovations. The vacuum assisted resin transfer molding (VARTM) technique was used to stack the plain woven fabrics together. The specimens were cured at 177° C. Fiber volume fraction for all types were 55%.

Experimental setup:

Strip specimens of dimensions 6.35mm×25.4mm×254mm with four different lay-ups were tested under uniaxial tension at 125 °C, 75 °C, room temperature (R.T), -20 °C and -60 °C. The desired temperatures were achieved using an environmental chamber, where each specimen was allowed to soak at the required temperature for thirty minutes before testing. The chamber utilizes a heating coil for achieving high temperatures and liquid nitrogen for low temperatures. During this soaking period, one end of the specimen was clamped while the other end was free; this was done in order to allow the specimen to elongate freely. The tests were conducted using a universal testing machine also known as MTS while specimens were still in the environmental chamber. Both loading and elongation histories were recorded using a National Instruments (NI)-DAQ based Lab View data acquisition system. The longitudinal and shear modulus of each specimen were calculated from the acquired data. Due to the woven fiber structure, the transverse (in-plane) modulus of the composites was assumed to be the same as the longitudinal (in-plane) modulus. Thus, tensile tests for transverse direction were not carried out. For each lay-up configuration a minimum of three tests were conducted.

EXPERIMENTAL RESULTS

In [Figure 1](#) the longitudinal stress-strain curves of GL are shown at the five different temperatures. Each specimen in the tests didn't exhibit the identical stress-strain relationship; however the curves were very close to each other especially in the elastic range. In order to avoid clustering of data, only a representative curve is plotted along with an error bar which represents the range of results obtained from the tests.

It is seen that at low temperatures the effect of temperature is less pronounced than at higher temperatures. At high temperatures, the stress-strain curves become more non linear. [Figure 4.2](#) shows the stress-strain curves for GL specimens with ± 45 fiber orientation. The results indicate that temperature has a significant effect on the shear properties of GL specimens.

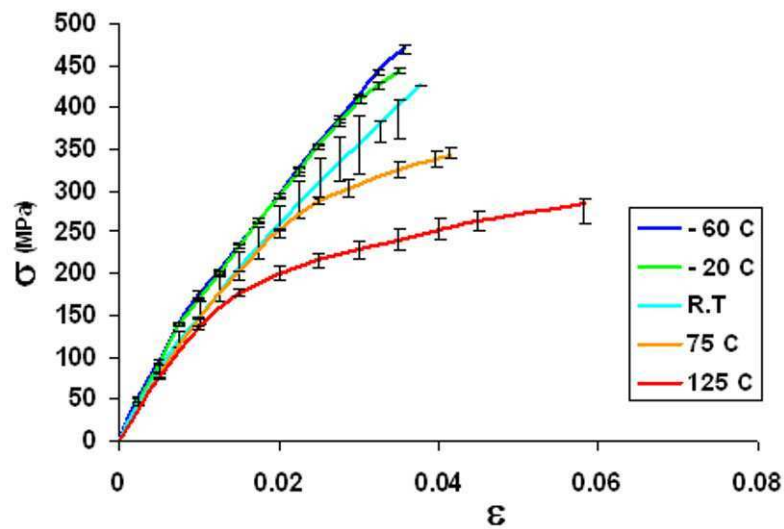


Figure 1 Longitudinal and transverse stress-strain curves for GL specimens at 125 °C, 75 °C, R.T, -20 °C and -60 °C

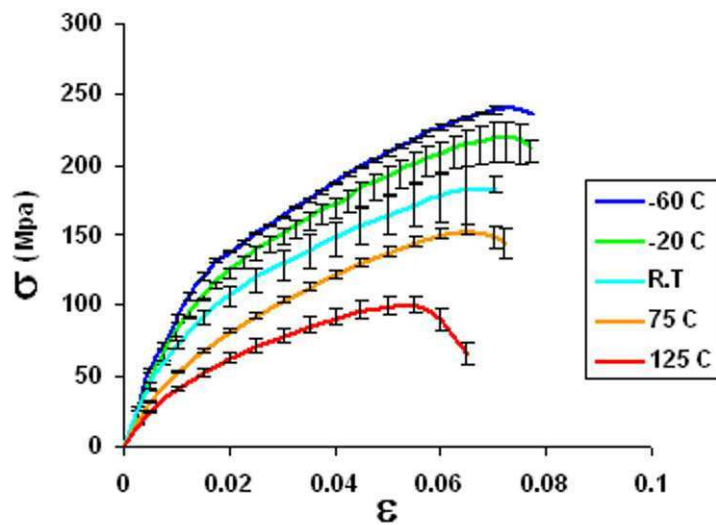


Figure 2 Stress-strain relations for ± 45 GL specimens at 125 °C, 75 °C, R.T, -20 °C and -60 °C

Figure 3 shows the longitudinal stress-strain curves for hybrid GR/GL/GR specimens. The curves can be divided into three portions. The first portion is almost linear at all test temperatures followed by a mostly nonlinear portion. Then the material had a sudden drop in stress due to the fracture of the graphite part of the hybrid specimen. However, the glass part in the hybrid composite was still undamaged, providing some strength which constitutes the third portion of the curve.

Figure 4 shows the stress strain curves of the GR/GL/GR specimen with $\pm 45^\circ$ fiber orientation. Here, there is no drop before failure. This is due to the fact that the graphite and glass layers failed together. It is observed that all the curves are non-linear. Also at higher temperatures the specimens did not totally fracture.

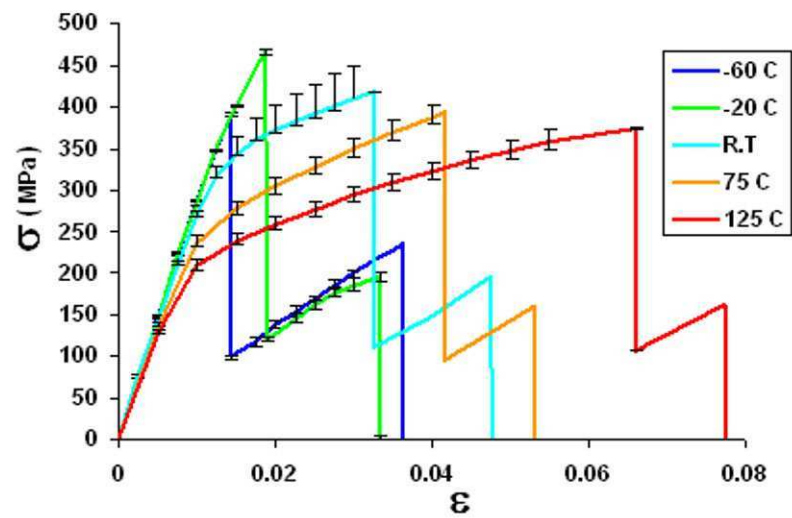


Figure 3 Longitudinal and transverse stress-strain curves for GR/GL/GR specimens at 125 °C, 75 °C, R.T, -20 °C and -60 °C.

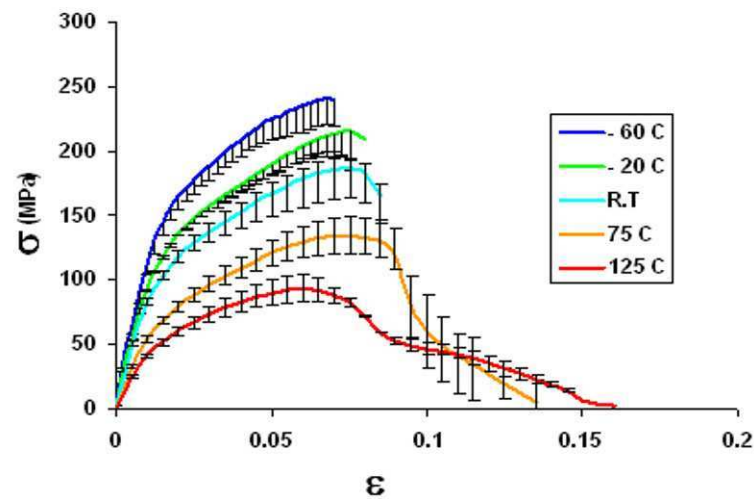


Figure 4 Stress-strain relations for ± 45 GR/GL/GR specimens at 125 °C, 75 °C, R.T, -20 °C and -60 °C

In [Figures 5](#) and [6](#), the stress strain behavior of hybrid GL/GL/GR specimens is seen to be similar to that of the hybrid GR/GL/GR specimens described above.

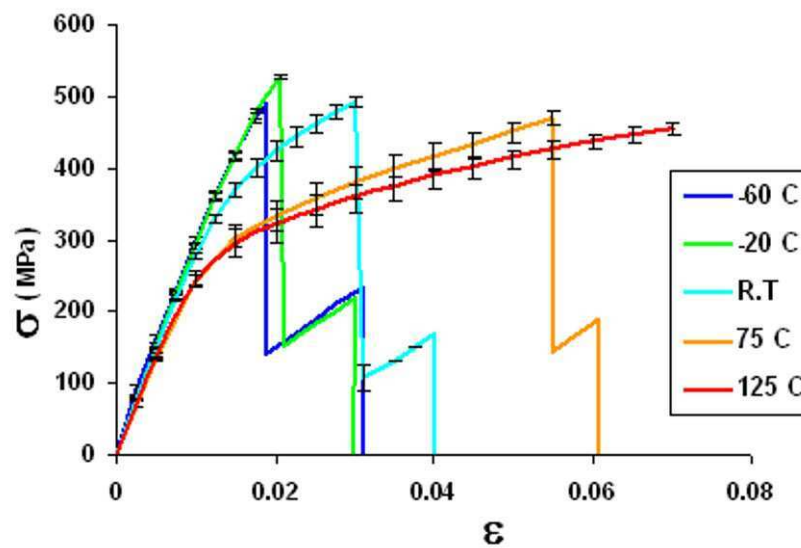


Figure 5 Longitudinal and transverse stress-strain curve for GL/GR/GL specimens at 125 °C, 75 °C, R.T, -20 °C and -60 °C

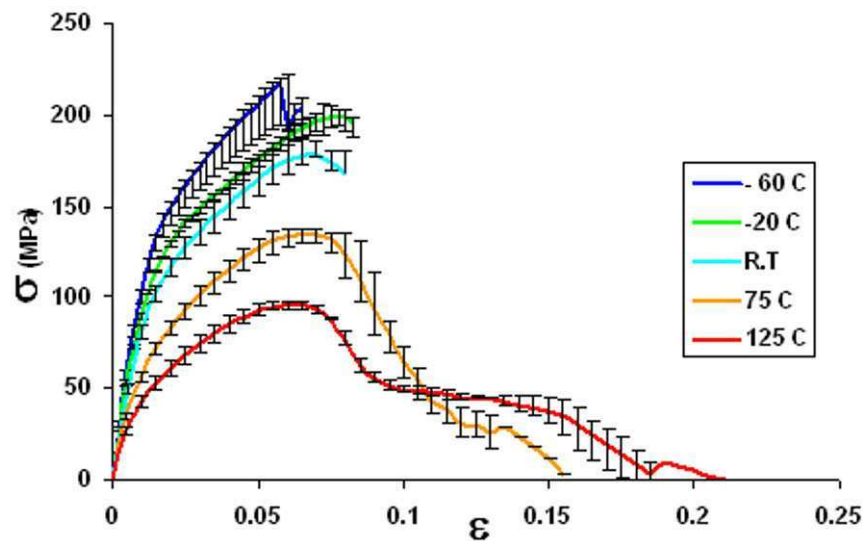


Figure 6 Stress-strain curve for $\pm 45^\circ$ GL/GR/GL specimens at 125 °C, 75 °C, R.T, -20 °C and -60 °C

Figure 7 shows the longitudinal stress-strain relation of the GR composite specimens. Tests conducted at each test temperature were very consistent with each other.

The GR specimens are shown to have higher failure strengths than all the other specimens at a given test temperature. The stress-strain relations for $\pm 45^\circ$ GR specimens are shown in [Figure 4.8](#). All the specimens exhibit a linear behavior followed by a non-linear portion. At higher temperatures again the specimens did not fracture completely.

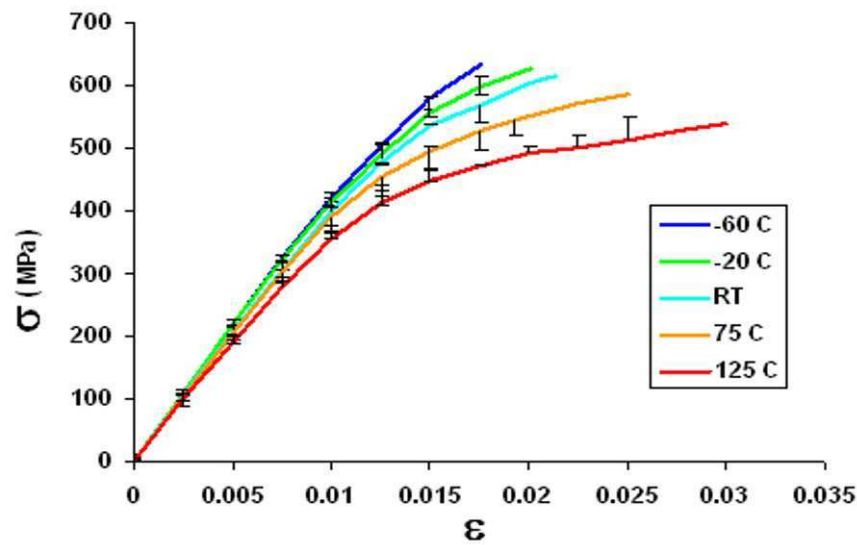


Figure 7 Longitudinal and transverse stress-strain curves for GR specimens at 125 °C, 75 °C, R.T, -20 °C and -60 °C

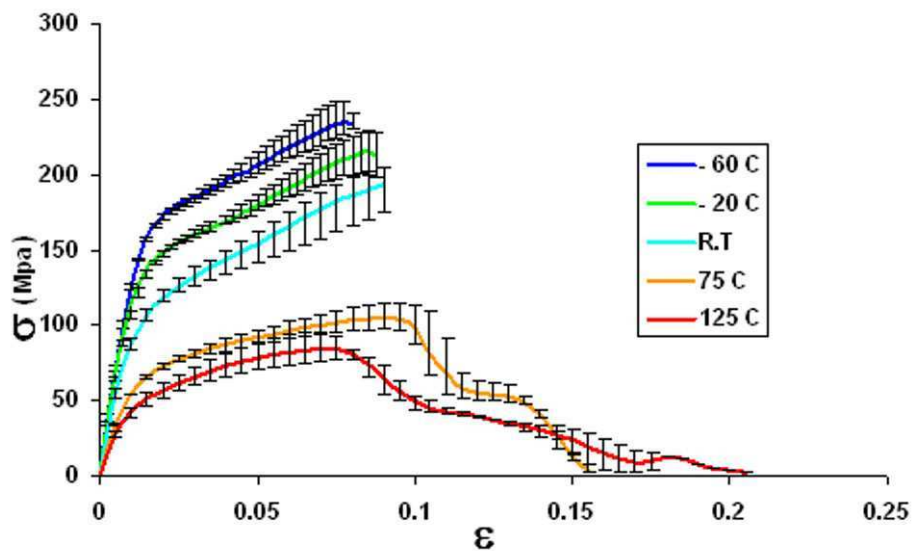


Figure 8 Stress-strain curves for ± 45 for GR specimens at 125 °C, 75 °C, R.T, -20 °C and -60 °C

Tables 1 and 2 show the summary of material properties obtained from the uniaxial tension tests. GR at -60 °C has the highest Young's modulus (43.8 GPa) and ultimate stress (633 MPa) compared to all specimens at all temperature values. Overall it is also seen that GR exhibits the highest stiffness and strength while GL exhibits the lowest. The hybrid specimens have material properties which are intermediate between those of GR and GL. It can also be seen that as the temperature increases the stiffness of the material decreases.

Table 1 Material properties for 0°/90° plain weave composites

Composite	Test Temperature	$E_1=E_2$ (GPa)	σ_{max} (MPa)	ϵ_{max} (%)
Non- Hybrid GL	-60 °C (-76 °F)	19.395	469	3.56
	-20 °C (-4 °F)	18.927	443	3.46
	R T (R T)	17.047	427	3.76
	75 °C (167 °F)	16.139	342	4.13
	125 °C (257 °F)	15.038	286	5.81
Hybrid GL/GR/GL	-60 °C (-76 °F)	31.985	489	1.90
	-20 °C (-4 °F)	30.285	529	2.05
	R T (R T)	29.036	493	3.08
	75 °C (167 °F)	27.102	470	5.50
	125 °C (257 °F)	26.894	459	8.10
Hybrid GR/GL/GR	-60 °C (-76 °F)	31.460	388	1.43
	-20 °C (-4 °F)	30.725	466	1.87
	R T (R T)	30.305	418	3.26
	75 °C (167 °F)	27.208	393	4.15
	125 °C (257 °F)	25.912	374	6.59
Non- Hybrid GR	-60 °C (-76 °F)	43.820	633	1.76
	-20 °C (-4 °F)	43.715	628	2.01
	R T (R T)	42.559	614	2.13
	75 °C (167 °F)	41.497	586	2.54
	125 °C (257 °F)	40.392	544	3.60

Table 2 Material properties for ±45° plain weave composites

Composite	Test Temperature	E_{xy} (GPa)	σ_{max} (MPa)	ϵ_{max} (%)
Non- Hybrid GL	-60 °C (-76 °F)	10.118	239.50	7.8
	-20 °C (-4 °F)	9.474	219.34	7.7
	R T (R T)	8.667	182.43	7.0
	75 °C (167 °F)	6.288	152.12	7.2
	125 °C (257 °F)	4.940	100.27	6.5
Hybrid GL/GR/GL	-60 °C (-76 °F)	12.117	216.05	5.9
	-20 °C (-4 °F)	10.872	198.62	8.3
	R T (R T)	9.794	178.41	8.0
	75 °C (167 °F)	6.571	135.03	8.0
	125 °C (257 °F)	5.275	95.67	7.8
Hybrid GR/GL/GR	-60 °C (-76 °F)	12.782	240.70	7.0
	-20 °C (-4 °F)	11.177	214.57	8.1
	R T (R T)	9.939	186.38	8.5
	75 °C (167 °F)	6.604	133.44	9.0
	125 °C (257 °F)	5.070	92.89	9.2
Non- Hybrid GR	-60 °C (-76 °F)	13.96	233.41	8.0
	-20 °C (-4 °F)	12.906	213.20	8.7
	R T (R T)	10.739	193.05	9.0
	75 °C (167 °F)	6.765	104.86	10.3
	125 °C (257 °F)	5.481	49.40	11.0

Figure 9 shows the change in elastic moduli as the test temperature changes for all layups. It is a summary of table 1 for the variation of elastic moduli.

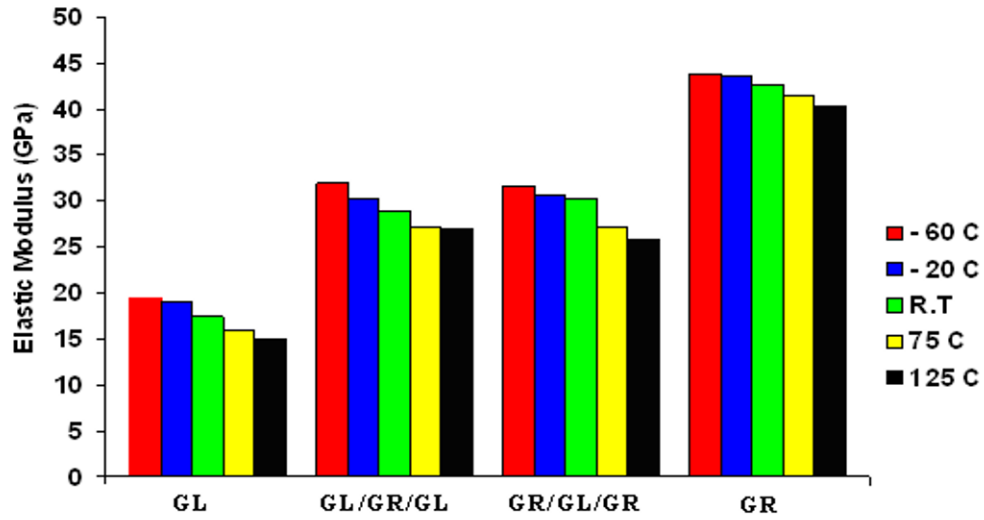


Figure 9 Elastic Moduli of all layups at different test temperatures

Using the Rule of Mixtures to determine the Young's Modulus of Hybrid Composites:

Using the rule of mixtures (RoM), the Young's moduli for the hybrid composites were calculated and then compared with those obtained experimentally from the uniaxial tensile tests. The rule of mixtures for fiber reinforced composites can be written as:

$$E_c = V_f E_f + V_m E_m$$

where E_c , E_f , E_m are the Young's moduli of the composite, fiber, and matrix, respectively, and V_f , V_m are the fiber and matrix volume fractions. To obtain the Young's modulus of the hybrid composite, the formula was applied to the laminae,

$$E_c = V_{GR/E} E_{GR/E} + V_{GL/E} E_{GL/E}$$

where $V_{GR/E}$, $V_{GL/E}$ are the volume fractions of the GR and GL laminae of the hybrid GR/GL/GR and GL/GR/GL laminates, and $E_{GR/E}$, $E_{GL/E}$ are the Young's moduli of the GR and GL specimens respectively, obtained from the tensile tests.

Table 3 Material properties for 0°/90° composites from experiments and applying RoM

Composite	Test Temperature	Young' Modulus from Experiment	Young's Modulus from RoM
Hybrid GL/GR/GL	-60 °C (-76 °F)	31.985	31.61
	-20 °C (-4 °F)	30.285	31.32
	R T (R T)	29.036	29.80
	75 °C (167 °F)	27.102	28.82
	125 °C (257 °F)	26.894	27.71
Hybrid GR/GL/GR	-60 °C (-76 °F)	31.460	31.61
	-20 °C (-4 °F)	30.725	31.32
	R T (R T)	30.305	29.80
	75 °C (167 °F)	27.208	28.82
	125 °C (257 °F)	25.912	27.71

Table 4 Material properties for $\pm 45^\circ$ composites from experiment and applying RoM

Composite	Test Temperature	Young' Modulus From Experiment	Young' Modulus from RoM
Hybrid GL/GR/GL	$-60^\circ\text{C} (-76^\circ\text{F})$	12.117	12.04
	$-20^\circ\text{C} (-4^\circ\text{F})$	10.872	11.19
	R T (R T)	9.794	9.70
	$75^\circ\text{C} (167^\circ\text{F})$	6.571	6.53
	$125^\circ\text{C} (257^\circ\text{F})$	5.275	5.21
Hybrid GR/GL/GR	$-60^\circ\text{C} (-76^\circ\text{F})$	12.782	12.04
	$-20^\circ\text{C} (-4^\circ\text{F})$	11.177	11.19
	R T (R T)	9.939	9.70
	$75^\circ\text{C} (167^\circ\text{F})$	6.604	6.53
	$125^\circ\text{C} (257^\circ\text{F})$	5.070	5.21

From Tables 3 and 4 it can be seen that there is good correlation between experimental results and those obtained using RoM. The RoM provides a better prediction for the Young's modulus of the $\pm 45^\circ$ laminates than of $0^\circ/90^\circ$ composite specimens.

Determination of material properties:

Based on the experimental data, some of the material constants can be obtained, i.e. Young's modulus in longitudinal direction (E_1), transverse Young's modulus (E_2) and in plane Shear modulus (G_{12}). E_1 and E_2 were assumed to be same due to the woven structure of the composites and were obtained from tensile tests. Following the ASTM Standard D-3518, the corresponding shear stress, shear strain and in-plane shear modulus were calculated using the relations:

$$\tau_{12} = \frac{\sigma_x}{2}, \gamma_{12} = \epsilon_x - \epsilon_y, \text{ and } G_{12} = \frac{E_x}{2(1 + \nu_{xy})}, \text{ respectively. Here } \sigma_x = \left(\frac{P}{A}\right) \text{ is the axial stress, } \epsilon_x \text{ and } \epsilon_y \text{ are the}$$

axial and transverse strains, respectively ($\epsilon_y < 0$) and $\nu_{xy} = -\frac{\epsilon_y}{\epsilon_x}$ is the associated

Poisson's ratio obtained in the ASTM D-3518 $\pm 45^\circ$ laminate tensile test while E_x is the initial slope of the stress-strain curve obtained from that test. As verification G_{12} was also calculated by taking the initial slope of the τ_{12} vs. γ_{12} curve, where the results closely match those obtained using the ASTM D-3518 standard. The shear moduli in the remaining two planes were

$$\text{obtained through the relations } G_{13} = G_{23} = \frac{E_z}{2(1 + \nu_{xz})}.$$

Details of the Poisson's ratio can be found in [14]. Figs. 10 and 11 depict the temperature-dependent shear stress-shear strain curves of the GL and GR composites, respectively, from high to low temperatures. The slopes of these curves give the shear moduli of the material. The nonlinear behavior of the curves is due to damage as well as temperature effect.

Table 5 gives a summary of the key in-plane material properties obtained for the composite for all the test temperatures.

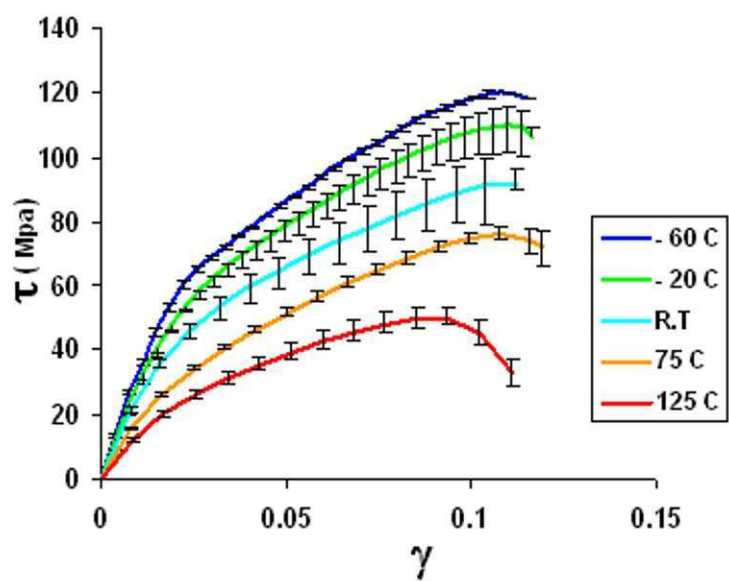


Figure 10 In-plane shear stress-strain curves with their slopes representing shear moduli for GL at 125 °C, 75 °C, R.T, -20 °C and -60 °C

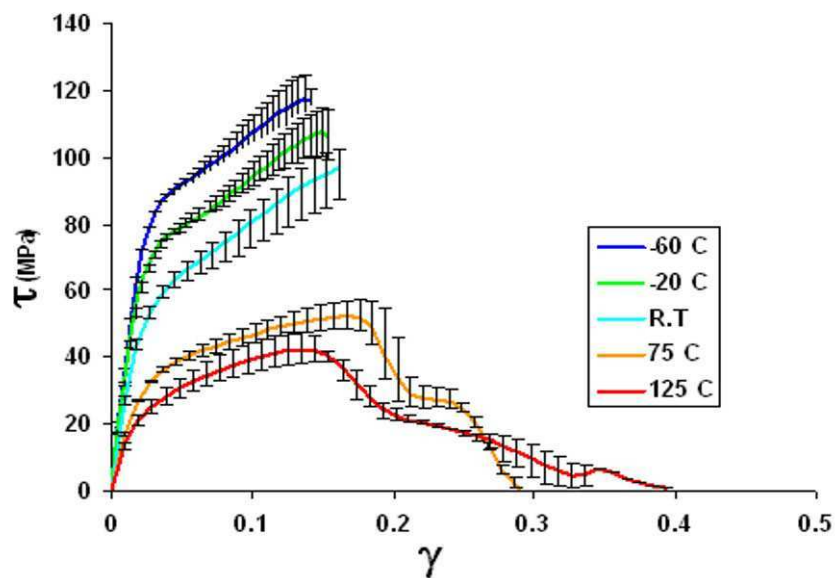


Figure 11 In-plane shear stress-strain curves with their slopes representing shear moduli for GR at 125 °C, 75 °C, R.T, -20 °C and -60 °C

Table 5 Mechanical properties of woven GL and GR composites

		$E_1=E_2(\text{GPa})$	$G_{12}(\text{GPa})$	ν_{12}	$\rho (\text{kg/m}^3)$
Glass	-60 °C	19.39	2.98	0.152	1766
	-20 °C	18.92	2.78	0.145	1761
	R.T	17.04	2.74	0.130	1755
	75 °C	16.13	1.89	0.128	1750
	125 °C	15.03	1.44	0.121	1744
Graphite	-60 °C	43.82	3.97	0.140	1392
	-20 °C	43.71	3.93	0.129	1387
	R.T	42.55	3.08	0.121	1381
	75 °C	41.49	1.99	0.116	1375
	125 °C	40.39	1.67	0.099	1370

CONCLUSION

- As the test temperature increases, the elastic modulus of the material tends to decrease. It can also be seen that the modulus of toughness (This may be calculated as the entire area under the stress-strain curve from the origin to rupture.) of the material increases with an increase in temperature.
- The over-all mechanical properties of hybrid composites were between those of GL and GR composites.
- The rule of mixture can be used successfully to predict the elastic and shear moduli of hybrid composites.

REFERENCES

- [1] N.K. Naik, P. Yernamma, N.M. Thoram, R. Gadipatri, V.R. Kavala, "High strain rate tensile behavior of woven fabric E-glass/epoxy composite", Polymer Testing, Volume 29, Issue 1, February 2010, Pages 14-22.
- [2] Scida D., Aboura Z., Benzeggagh M. L. and Bocherens E., "Prediction of the elastic behavior of hybrid and non-hybrid woven composites", Composites Science and Technology, Volume 57, Issue 12, 16 January 1998, Pages 1727-1740
- [3] Ganesh V.K. and Naik N.K., "Failure behavior of plain weave fabric laminates under on-axis uniaxial tensile loading: I- Laminate Geometry". Journal of Composite Material. 1996, 30(16), 1748-1778.
- [4] Ganesh V.K. and Naik N.K., "Failure behavior of plain weave fabric laminates under on-axis uniaxial tensile loading: II- Analytical Geometry". Journal of Composite Material. Volume 30, Issue 16, 1996, 1779-1782.
- [5] Ganesh V.K. and Naik N.K., "Failure behavior of plain weave fabric laminates under on-axis uniaxial tensile loading: III- Effect of fabric Geometry". Journal of Composite Material, Volume 30, Issue 16, 1996, 1823-1856.
- [6] Ishakawa T. and Chou T.W., "Stiffness and strength behavior of woven fabric composites". Journal of Material Science. Volume 17, 1982, Pages 3211-3220.
- [7] Ishakawa T. and Chou T.W., "Elastic behavior of woven hybrid composites". Journal of Composite Materials, Volume 16, 1982, Pages 2-19.
- [8] Ishakawa T. and Chou T.W., "One dimensional micromechanical analysis of woven fabric composites". AIAA J., , Volume 21, Issue 12, 1983, Pages 1714-1721.
- [9] Ishakawa T. and Chou T.W., "In-plane thermal expansion and thermal bending coefficients of fabric composites". Journal of Composite Materials. Volume 17, 1983, Pages 92-104.
- [10] Ishakawa T., Matsushima M., Hyashi Y., and Chou T.W., "Experimental confirmation of the theory of elastic moduli of fabric composites". Journal of Composite Materials. Volume 19, 1985, Pages 443-458.
- [11] Patricia P Parlevliet, Harald E.N. Bersee and Adriaan Beukers, "Residual stresses in thermoplastic composites- A study of the literature-Part 1: Formation of residual stresses", Applied Science and Manufacturing, Volume. 37, 2006, Issue 11, Pages 1847-1857
- [12] Patricia P Parlevliet, Harald E.N. Bersee and Adriaan Beukers, "Residual stresses in thermoplastic composites- A study of the literature-Part 11: Experimental techniques", Volume. 37, 2006, Issue 11, Pages 1847-1857
- [13] Patricia P Parlevliet, Harald E.N. Bersee and Adriaan Beukers, "Residual stresses in thermoplastic composites- A study of the literature-Part 111: Effects of residual stresses", Volume. 37, 2006, Issue 11, Pages 1847-1857
- [14] Budhoo, Yougashwar. Delale, Feridun and Liaw, Benjamin. "Effect of temperature on the Poisson's ratio of woven composites". To be published (SEM 2011 Annual Conference & Exposition on Experimental and Applied Mechanics)

Studies on Fracture Performance of Bio-fiber-Silica-glass Fiber Reinforced Epoxy Hybrid Composites

Arun Kumar Chaudhary¹, Prakash Chandra Gope², Vinay Kumar Singh²

¹Assistant Professor

¹Department of Production Engineering

²Department of Mechanical Engineering

College of Technology,

G. B. Pant University of Agriculture & Technology, Pantnagar-263145

Udham Singh Nagar, Uttarakhand, India

*E mail: pcgope@rediffmail.com, aruncdme@gmail.com

ABSTRACT

In the present investigation, fibers from banana stem and Bagasse are used in addition to low wt% of silica to cast bio composites. Extraction of the banana fibers, Bagasse fibers and preparation of both banana and Bagasse fibers were carried out as explained elsewhere in literature. The lengths of the fibers are kept between 180 to 425 micrometer. Composites, containing lower fiber content of Bagasse and banana (10 wt %) and higher fiber content (20 wt %) were used with silica (2 wt%) and mixed with epoxy CY 230 epoxy resin. Different mechanical properties such as tensile, compressive, impact, flexural, fracture strength etc are discussed and characterized.

Introduction

With growing environmental awareness, ecological concerns and new legislations, bio-fiber-reinforced plastic composites have received increasing attention during the recent decades. The composites have many advantages over traditional glass fiber or inorganic mineral-filled materials, including lower cost, lighter weight, environmental friendliness, and recyclability. In addition, use of their composites have established comparable performance with those of glass fiber composites with possibility for their use as structural components as well [1-3]. When such materials are used in composites, developing countries, which produce these, become part of global composite industry as developer and manufacturer leading to increased revenues and creation of jobs [4]. In view of the above, many attempts have been made to characterize the lignocellulosic fibers either individually [5-6], or as part of their composites research [7].

Sugarcane is one of the most abundant agro fiber resources whose worldwide annual production of 1200 million metric tones per year. Bagasse (BaG) is a byproduct from sugarcane processing. The composition of bagasse is approximately 50% cellulose, 25% hemicellulose, and 25% lignin [8]. Currently the main use of bagasse is for energy in the sugarcane industry through burning, but their caloric value is relatively low compared to other fuel resources [9].

Banana fiber (BaN) is extracted from the waste product of banana cultivation. Due to high cellulose content and comparatively low microfibrillar angle, it has superior mechanical properties, especially tensile strength and modulus [10-13]. It is thus considered as a promising candidate for replacing conventional glass fibers in the fiber-reinforced composites. Earlier studies showed that BaN provided good reinforcement for various thermosetting resins such as unsaturated polyester [14-18], phenol formaldehyde (PF) [19-20], and epoxy [21].

This paper presents mechanical and fracture behavior aspects of two different types of lignocellulosic fibers of India namely, fiber from bark (banana) and fiber from agro waste (sugarcane bagasse). It is hoped that such attempts would lead to the better utilization of these fibers through composite technology leading to a low cost eco friendly composite materials for many automotive parts, household equipments, and also as packing and insulating materials.

Experimental Aspects

Materials

Two types of fibers, namely banana fibers (*Musa sapientum*) obtained from the pseudostem of the plant and sugarcane (*Saccharum officinarum*) bagasse fibers obtained from a nearby sugar mill in the state of Uttarakhand, India were used in this study. Banana fibers were extracted from the pseudostem (average diameter of 150 mm) of the banana plant. The leaf sheaths from the pseudostem were cut in parts of about 300 mm length using long knife and then dried outdoors exposing the fibers to the sun for about two to three weeks. They were then dried in a hot air oven at 65^o C until constant mass was observed. They were then further cut in a knife mill to get fibers of 3–5 mm length. The banana fibers were cleaned with 5% sodium hypochlorite before they were maintained at 100^o C for 1 h in an autoclave followed by drying at 65^o C for 72 h to maintain constant moisture content. The sugarcane fiber also known as Bagasse fiber (here after called as Bagasse and denoted as BaG) used in the present study are collected from the nearby sugar industry. No fiber preparation was required in this case since the Bagasse fiber received was in the fiber form (not extracted from the stem/stalk as described for banana fiber), except cutting them to random size using a suitable cutter and conditioning them by keeping the fibers for 12 h at 65^o C to maintain constant moisture content. The fibers obtained from banana and Bagasse (Fig. 1) were then grinded in ball mill to obtain relatively finer particles. The sizes of the fibers were controlled by using sieves (ASTM 18 and 40). Silica is another reinforcing element used in the present investigation. In the present investigation nano sized silica powder (<142 nm) procured from M/s DEGUSSA INDIA Pvt. Limited, New Delhi have been used in the ratio of 0.5%, 1%, and 2.0% wt/wt. Silica powder is directly mixed in resin and stirred mechanically by means of a high speed mechanical stirrer while casing the composites.

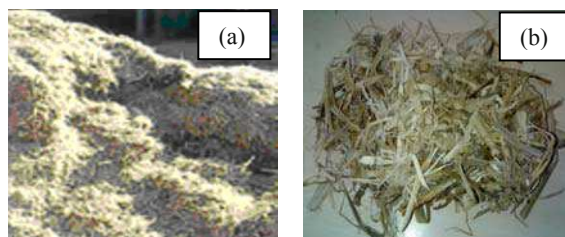


Fig. 1 (a) Bagasse and (b) banana fiber

Results and Discussion

Tensile stress-strain behavior

The tensile stress-strain curve for unfilled epoxy resin (8 wt% HY-951 hardener and rest CY-230 resin) and hybrid composite materials containing 20wt% Bagasse fiber, 20wt% bagasse+2 wt% silica reinforced composite and banana + Bagasse (10wt% each) reinforced composite is shown in figure 1. All tests are conducted as per ISO in 100 kN servo hydraulic universal testing machine under displacement mode of control.

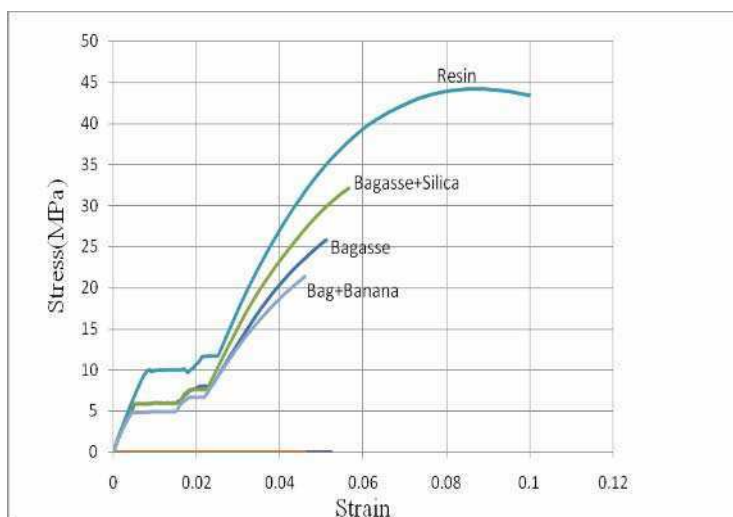


Fig. 2 Stress-strain diagram for different composite materials at 0.1 mm/min crosshead speed

Table 1 shows the mechanical properties of the hybrid composites containing different wt % of Bagasse, banana and silica.

Table 1 Tensile properties of the composite materials and epoxy resin.

Property	BaG fibre	BaG fibre+ Si	BaN	BaN+Si	BaG+ BaN fibre	Epoxy
E (GPa)	1.268 \pm 0.121	1.357 \pm 0.10	1.34 \pm 0.14	1.46 \pm 0.18	1.523 \pm 0.06	1.359 \pm 0.124
UTS (MPa)	28.397 \pm 2.342	28.297 \pm 3.888	22.26 \pm 5.55	24.62 \pm 4.94	22.663 \pm 2.36	35.790 \pm 7.767
Yield Stress (MPa)	5.41 \pm 0.791	5.57 \pm 1.137	4.15 \pm 2.99	4.43 \pm 1.36	4.93 \pm 0.81	9.82 \pm 0.629
Strain Energy (Joule)	19.135 \pm 3.865	20.652 \pm 9.176	23.79 \pm 10.28	37.41 \pm 8.45	30.388 \pm 7.642	597.54 \pm 42.48

Remarkable differences can be seen on the mechanical properties of the hybrid composite material having different reinforcing materials. It can be noticed that Bagasse fiber reinforced material is having higher strength as compared to banana fiber composites. Use of silica as additional filler material has little effect on the mechanical properties. However, if the material is to be used as energy storing device, banana fibre based composites is more suitable as compared to Bagasse based composites. From the results it is evident that moderate increase in tensile strength occurred upon filling the polymer matrix with BaG fibers, indicating a considerable reinforcing effect from these fibers. The possible reasons proposed for this kind of behavior may be the improved interfacial adhesion between the matrix and BaG fibers as compared to BaN fibre.

Compressive Strength

The results of the compressive test are shown in figure 3 and mean values are tabulated in table 2.

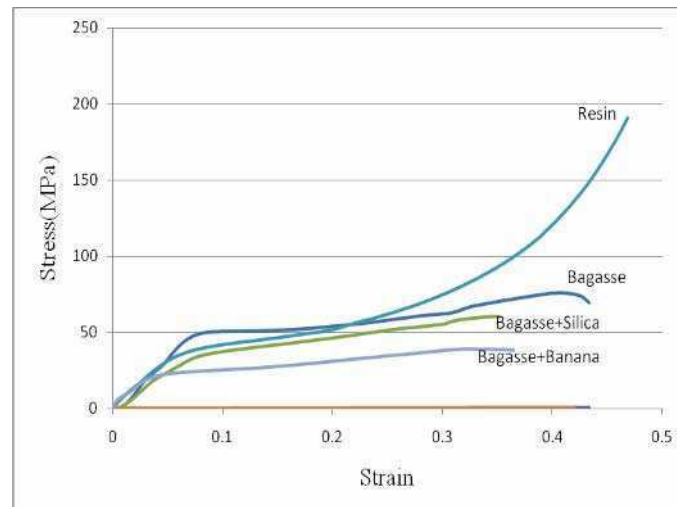


Fig. 3 Stress-strain diagram for different composite materials

Table 2 Compressive properties of the composite materials and epoxy resin

Property	BaG	BaG + Si	BaN	Ban+Si	BaG+ BaN	Epoxy
E (GPa)	0.512 \pm 0.156	0.754 \pm 0.110	0.564 \pm 0.25	1.67 \pm 0.27	1.235 \pm 0.113	0.736 \pm 0.136
Comp. strength (MPa)	76.621 \pm 4.35	60.691 \pm 2.184	49.86 \pm 4.23	63.28 \pm 15.75	35.770 \pm 5.672	175.283 \pm 37.679
Yield Stress(MPa)	48.9 \pm 2.3	36.3 \pm 3.21	10.17 \pm 2.02	13.07 \pm 6.28	10.1 \pm 2.166	13.5 \pm 2.18
Strain Energy(Joule)	21.401 \pm 8.136	21.670 \pm 2.164	31.26 \pm 9.03	11.32 \pm 1.57	62.829 \pm 28.395	50.899 \pm 27.581

The load bearing capacity in compression is more incase of Bagasse based composites as compared to banana based composites.

Impact Strength

The results obtained from Charpy test are presented in [table 3](#).

Table 3 Impact strength

S. No.	BaG (Nm)	BaG + Si (Nm)	BaN (Nm)	BaN+Si (Nm)	BaG+ BaN (Nm)	Epoxy (Nm)
Mean	24.53	20.44	20.42	23.68	24.50	22.07
S D	2.45	1.42	2.83	1.42	2.45	2.45

It is seen that Bagasse fibres shows maximum impact strength amongst all hybrid composites studied. Addition of banana with Bagasse has insignificant effect on the impact strength where as silica decreases the impact strength. From the present observations it can be concluded that banana and bagasse fibres shows same impact strength when they added individually or as combined with equal weight percentage. Addition of silica particle as filler material decreases the impact strength. The probably causes may be due to localized stress concentration due to angularities in the regions of silica particle corners and would, therefore facilitate failure under impact conditions. Therefore, silica is causing decrease in impact strength of bagasse or banana based composites.

Bending

The Bending strength properties of the Bagasse, Bagasse+silica and Bagasse+banana filled epoxy resin hybrid composite materials were determined by 100 kN ADMET make servo controlled universal testing machine at 0.1mm/min strain rate under displacement control mode. The results are presented in [Table 4](#).

Table 4 bending strength properties for resin and composite materials

Property	BaG	BaG+ Si	BaN	BaN+Si	BaG+ BaN	Epoxy
E (GPa)	0.799+0.098	1.189+0.3105	1.25+0.42	0.697+0.298	0.901+0.462	0.801+0.254
Flexural stress(MPa)	30.716+5.779	36.622+6.308	32.62+5.78	29.67+5.84	31.311+5.97	51.254+7.171
Flexural Strain	0.048+0.014	0.038+0.008	0.04+0.006	0.043+0.005	0.047+0.022	0.091+0.026

As depicted by the test data, amongst the composite materials developed the 20 wt% Bagasse+2 wt% silica reinforced composite shows the best results with regards to the modulus of elasticity (1.189 GPa against 0.801 GPa of epoxy resin) and also it is better than 20 wt% Bagasse, 20 wt% banana reinforced composites.

Toughness Test - K_{Ic} Test

Linear-elastic plane-strain fracture toughness K_{Ic} of metallic materials is most often tested according to ASTM E 399 specifications. The K_{Ic} test is used to determine the fracture toughness of metallic materials. Thirty numbers of tests are conducted according to the standard procedure described in ASTM E 399. The specimens used are shown in [Figure 4](#) and the results are presented in [Fig. 5](#) with mean and standard value in [table 5](#).



Fig.4 K_{Ic} test specimen before and after fracture

Table 5 Toughness test values for resin and composite materials

Composites	BaG	BaG+Si	BaN	BaN+Si	BaN+BaG	Epoxy
Mean, $MPa \sqrt{m}$	49.56	55.28	20.39	48.64	20.12	57.39
SD	9.29	11.53	5.65	12.22	9.63	11.96

The probability distribution of the test results are shown in Figure 5. The result shows that mostly they follow normal distribution. The mean and standard deviation of the test results are shown in table 5. Addition of silica seems to be beneficial. Bagasse fiber shows higher fracture strength as compared to banana fibre.

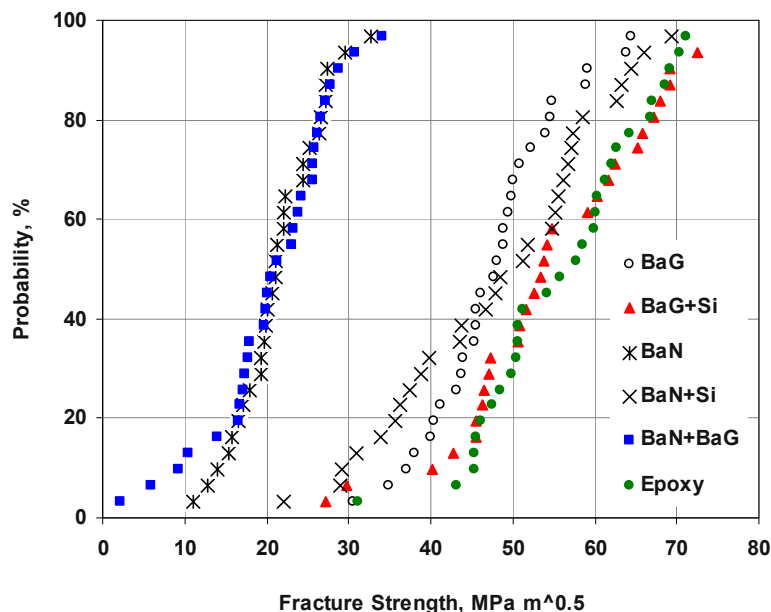


Fig.5 Probability distribution of fracture strength, K_{IC} , $\text{MPa}\sqrt{m}$

Conclusions

The term bio-composite is now being applied to a staggering range of materials derived wholly or in part from renewable biomass resources. This concept of bio-based materials has now become of key importance due to the need to preserve our environment. Present study shows that Biofibres like banana and Bagasse shows improved strength when they are mixed with different volume fraction. This study has experienced an explosion of interest, particularly with regard to its comparable properties to glass fibres within composites materials.

References

1. Burgueno R., Quagliata, M.J. Mohanty, A.K., Mehta G., Drzal L.T., Misra M, Load-bearing natural fiber composite cellular beams and panels. Composite: Part A 35 (6), 645–656, 2004.
2. Dweib M.A., Hu B., O'Donnell A., Shenton H.W., Wool R.P, All natural composite sandwich beams for structural applications. Composite Struct. 63 (2), 147–157, 2004.
3. Satyanarayana K.G., Agrobased fibers of Brazil and their composites—An overview, In: Rajesh Anandjiwala, Hunter, L. (Eds.), Textiles for Sustainable Development. Ryszard Kozlowski and Gennady Zaikov, Nova Publishers, USA, pp. 247–261 (Chapter 1) v.1, ISBN: 1-60021-559-9, 2007.
4. Rijswijk I.V., Brouwer W.D., Benefits of composites made of locally grown natural fibers. In: Mattoso, L.H.C., Leão, A.L., Frollini, E. (Eds.), Proceedings of the from Fourth International Symposium on Natural Polymers and Composites. Publishers: Embrapa Agricultural Instrumentation, São Paulo University (USP), São Paulo State University (UNESP), São Carlos, SP, Brasil, pp. 422–428, ISNaPol- 2002, ISBN: 85-86463-10-8, 2002.
5. Chand N., Sood S., Rohatgi P.K., Satyanarayana K.G., Resources, structure, properties and uses of natural fibres of Madhya-Pradesh. J. Sci. Ind. Res. 43 (9), 489–499, 1984.

6. Satyanarayana K.G., Ravikumar K.K., Sukumaran K., Mukherjee P.S., Pillai S.G.K., Kulkarni A.G., Structure and properties of some vegetable fibers. Part 3. Talipot and palmyrah fibers. *J. Mater. Sci.* 21 (1), 57–63, 1986.
7. Jacob M., Thomas S., Varughese K.T., Mechanical properties of sisal/oil palm hybrid fiber reinforced natural rubber composites. *Composite Sci. Technol.* 64(7–8), 955–965, 2004.
8. Pandey A., Soccol C.R., Nigam P., Soccol V.T., Biotechnological potential of agro-industrial residues. I: sugarcane bagasse. *Bioresource Technology* 74, 69–80, 2000.
9. Vazquez A., Dominguez V.A., Kenny J.M.J., Bagasse fiber–polypropylene based composites. *Journal of Thermoplastic Composite Materials* 12 (6), 477–497, 1999.
10. Idicula M., Neelakantan N.R., Oommen Z., Joseph K., Thomas S., A study of the mechanical properties of randomly oriented short banana and sisal hybrid fiber reinforced polyester composites. *J. Appl. Polym. Sci.* 96 (5), 1699–1709, 2005a.
11. Idicula M., Malhotra S.K., Joseph K., Thomas S., Dynamic mechanical analysis of randomly oriented intimately mixed short banana/sisal hybrid fiber reinforced polyester composites. *Compos. Sci. Technol.* 65 (7–8), 1077–1087, 2005b.
12. Idicula M., Malhotra S.K., Joseph K., Thomas S., Effect of layering pattern on dynamic mechanical properties of randomly oriented short banana/sisal hybrid fiber-reinforced polyester composites. *J. Appl. Polym. Sci.* 97 (5), 2168–2174, 2005c.
13. Idicula M., Boudenne A., Umadevi L., Ibos L., Candau Y., Thomas S., Thermophysical properties of natural fiber reinforced polyester composites. *Compos. Sci. Technol.* 66 (15), 1719–1725, 2006.
14. Pothan L.A., Thomas S., Neelakantan N.R., Short banana fiber reinforced polyester composites: mechanical, failure and aging characteristics. *J. Reinf. Plast. Compos.* 16 (8), 744–765, 1997.
15. Pothan L.A., Oommen Z., Thomas S., Dynamic mechanical analysis of banana fiber reinforced polyester composites. *Compos. Sci. Technol.* 63 (2), 283–293, 2003.
16. Pothan L.A., Thomas S., Polarity parameters and dynamic mechanical behaviour of chemically modified banana fiber reinforced polyester composites. *Compos. Sci. Technol.* 63 (9), 1231–1240, 2003.
17. Pothan L.A., Thomas S., Groeninckx G., The role of fiber/matrix interaction on the dynamic mechanical properties of chemically modified banana fiber/polyester composites. *Compos. Part A: Appl. Sci. Manuf.* 37 (9), 1260–1269, 2006.
18. Sreekumar P.A., Albert P., Unnikrishnan, Joseph K., Thomas S., Mechanical and water sorption studies of eco-friendly banana fiber-reinforced polyester composites fabricated by RTM. *J. Appl. Polym. Sci.* 109 (3), 1547–1555, 2008.
19. Mishra S., Naik J.B., Patil Y.P., The compatibilizing effect of maleic anhydride on swelling and mechanical properties of plant-fiber-reinforced novolac composites. *Compos. Sci. Technol.* 60 (9), 1729–1735, 2000.
20. Joseph S., Sreekala M.S., Oommen Z., Koshy P., Thomas S., A comparison of the mechanical properties of phenol formaldehyde composites reinforced with banana fibres and glass fibers. *Compos. Sci. Technol.* 62 (14), 1857–1868, 2002.
21. Naleque M.A., Belal F.Y., Sapuan S.M., Mechanical properties study of pseudo-stem banana fiber reinforced epoxy composite. *Arabian J. Sci. Eng.* 32 (2B), 359–364, 2007.

Mechanical Behavior of Bio-inspired Sandwich Composites

Sandip Haldar, Jachimike K. Imo and Hugh A. Bruck
Department of Mechanical Engineering, Univ. of Maryland, College Park, MD 20742

Abstract

Nature is a popular source of inspiration for the development of new materials and structures. Palmetto wood has been found to be a potential bio-inspiration due to its historically successful mechanical performance to develop materials with enhanced mechanical properties. To understand the basis of mechanical performance of Palmetto wood, its failure mechanism and energy absorbing capacity is elucidated at multiple length scales. The quasi-static and dynamic three-point bend tests has been used to reveal the leading failure mechanisms like shear dominated debonding and pore collapse. The damage evolution under quasi-static and dynamic impact is determined. The sandwich material systems are yet to be investigated in detail to utilize its potential in advanced engineering applications. We present some work on development of sandwich composites with improved mechanical behavior using Palmetto wood as a biological template. The quasi-static and dynamic characterization of nano-enhanced sandwich materials is presented. The leading failure mechanism in Palmetto wood are found to be shear dominated delamination at the macrofiber-matrix interface caused by shear strain concentration and shear cracking in the porous cellulose matrix caused by pore collapse. Reinforcement in the bio-inspired core and the nano-enhancement in the adhesive increase the mechanical properties of the sandwich structure.

I. Introduction

Palmetto wood has attracted the attention as a potential bio-inspiration to develop bioinspired energy-absorbent sandwich structures for its successful usage in the protective structures in the Civil and Revolutionary wars. Palmetto wood exhibited excellent mechanical strength and dynamic behavior under the impact of bullets and calls for detail study of the basis of its mechanical behavior to replicate its properties in advanced composite materials with enhanced mechanical behavior and damage tolerance. To understand the mechanical behavior of the Palmetto wood, the hierarchical structure of the fibers and its relationship to the mechanical behavior of the fibers has been characterized at multiple length scales and related to the mechanical behavior of the fibers [1]. Characterizing the inelastic behavior of Palmetto wood at multiple length scales is very important to improve the understanding of the mechanisms that give rise to its extraordinary energy absorbing capacity. Therefore, to understand the inelastic behavior and failure mechanism of Palmetto Wood to provide the foundation for developing polymer composites with similar properties, an appropriate mechanical characterization technique have been established to elucidate on the deformation process at different length scales [2]. The quasi-static mechanical behavior of Palmetto wood under three-point bend test has been characterized at multiple length scales. The images of the specimen were captured during the deformation to characterize and quantify the load transfer mechanism and the response of the porous cellulose matrix and the reinforced macrofibers to the bending load. Digital Image Correlation (DIC), a widely-used optical deformation measurement technique has been employed to the images captured during the test to quantify the strains. DIC being non-contact, full-field deformation measurement technique has been well accepted in the experimental mechanics for the deformation measurement at several length scales, materials like wood, concrete, metal, polymers as well as to capture non-uniform deformation fields, crack tip singularities [2, 3, 4, 5, 6, 7]. The DIC technique correlates the undeformed and deformed images through the grey scale of the image and tracks the local deformation through the subset, a finite area that is repeated over the full images during the correlation. The image correlation calls for a random speckle pattern to track the deformation. Several literatures are available detailing the evolution and applications of DIC [8, 9]. In the present investigation, images of deformed specimen were captured at several magnifications achieved by lenses and at several location of the specimen with respect to the global loading. The natural texture of the wood was found to be sufficient for image correlation. Motivated by the excellent mechanical behavior of Palmetto wood, bioinspired foam-core sandwich materials have been developed to achieve enhanced mechanical as well as energy absorbent behavior. The sandwich materials have been fabricated by closed cell foam as core and epoxy-carbon laminate as facesheets. Even though the core of a sandwich material is assumed to act as a separator between the facesheets and to increase the energy absorption by compressive deformation, the core is used to increase the strength and stiffness of the sandwich by reinforcement in the foam core. Carbon rods have been used as macroscale reinforcement in the foam core in longitudinal direction. The hierarchical structure has been employed using nano-enhancement at lower length scale to increase the interface strength. The sandwich materials fabricated in the preliminary investigation has been characterized under quasi-static three-point bend test.

In this paper, the characterization of the failure mechanism Palmetto wood is reported. The failure mechanisms in the Palmetto wood were elucidated to investigate the failure initiation and energy absorbing mechanism. The leading failure mechanism was found to be shear-dominated delamination at the macrofiber and porous cellulose matrix interface. The macrofibers being mechanically stronger deforms lesser than the porous cellulose matrix leading to a deformation mismatch at the interface, which again leads to accumulation of shear strain. It has been found that the macrofibers carry the axial load and the cellulose matrix transfers the loads to the macrofiber. The pore collapse mechanism helps to absorb the high strain energy as well as leads to the potential sites. The detail of fabrication and preliminary results of the mechanical characterization of the sandwich structures with bio-inspired core have been reported.

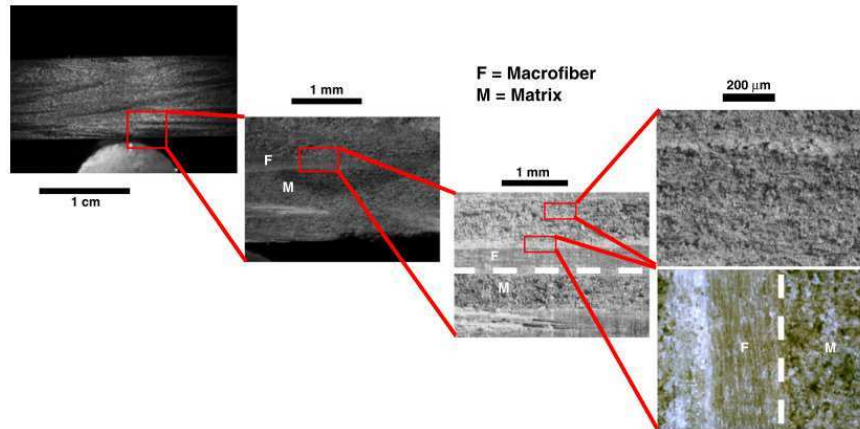


Figure 1. Characterization of mechanical behavior and failure mechanism in Palmetto wood at multiple length scales [2]

2. Experimental mechanical characterization technique

Quasi-static three-point bend test has been used to characterize the mechanical behavior of the Palmetto wood and the sandwich material with bio-inspired core at multiple length scales as depicted in [Figure 1](#). The Palmetto wood specimens were prepared from a harvested palmetto tree of the size of around 10 cm x 9 mm x 9 mm. Tests were performed in an Imada model MX 500 load frame with a Z2H-440 2 kN load cell with resolution of 0.1 kg. Supports for the three-point bend test fixture were 62.5 mm apart, and the specimen was loaded with the fibers oriented transverse to the loading direction ([Figure 2](#)). The quasi-static bending was performed under displacement control at a macroscale flexural strain rate 1.6×10^{-4} /sec. The Palmetto wood surface texture was good enough for the image correlation at all length scales waiving off any artificial speckle pattern. The images of the specimen undergoing bending and illuminated by MI-150 high intensity fiber optic illuminator from Edmund Industrial Optics was captured by FL2-14S3C Point Grey high speed camera aided with the required lenses for magnification. The DIC analysis was performed using a commercially available package known as Vic-2D from Correlation Solutions Inc. (Columbia, SC). The optimum subset size and strain filter was chosen for the image correlation to determine the deformation in the specimen.

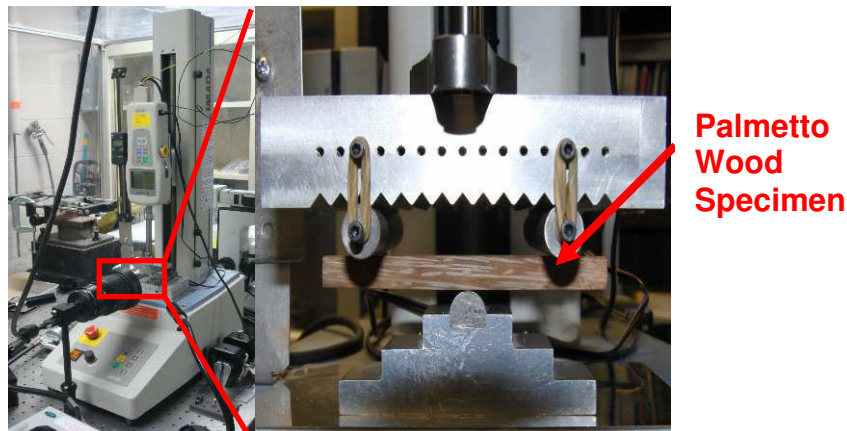


Figure 2. Quasi-static three-point bend test set-up and test configuration

The dynamic response of the Palmetto wood was performed at low velocity impact test at three-point bend configuration. The specimen was impacted by a 12.6 gm cylindrical projectile at a velocity of about 30 m/s leading to a strain rate of around 450 s^{-1} . The images were captured by a high speed Phantom camera under the illumination by high intensity illuminators.

3. Fabrication of sandwich structure with bio-inspired core

The bio-inspired sandwich specimens were prepared from soft closed-cell foam as core and epoxy-carbon composites from The Composite Store. Carbon rods of diameter of 0.027" from The Composite Store have been used as reinforcement in the soft foam. Epoxy resin 105 and slow hardener 206 from West System have been used as the adhesive in the interfaces between facesheet – core and carbon rod reinforcement – foam core. Two types of adhesives were prepared, namely, pure-epoxy based and nano-enhanced epoxy. West system epoxy resin 105 with 206 slow hardener has been mixed by 5:1 ratio by weight. Nano-enhancement was achieved by mixing 1 wt % PR-19 grade low density carbon nanofiber (LDCNF) that was obtained from Applied Sciences. The pure epoxy adhesive was prepared by hand-mixing of the epoxy resin and hardener for 3 – 5 minutes, with a subsequent degassing for 5 minutes at a vacuum chamber with 22 mm Hg vacuum pressure. The nano-enhanced adhesive was prepared by a hand-mixing of epoxy resin and LDCNF for 3 – 5 minutes followed by 90 minutes of sonication and a degassing of 3 – 5 minutes in the vacuum chamber with 22 mm Hg vacuum pressure. These pure epoxy and nano-enhanced epoxy based adhesives have been used as adhesives to glue the soft foams, and facesheets of carbon strips. The foam and facesheets were manually attached by the adhesives detailed above. For another class of specimen, reinforcement of Carbon rods have been used by penetrating the carbon rods in the soft foam core after dipping them in the adhesive to achieve better adhesion with the foam. The glued and reinforced specimens were cured in a closed chamber at 80 C for 30 hrs under a dead weight. The bio-inspired sandwich structures fabricated for this investigation are depicted in [Figure 3](#).

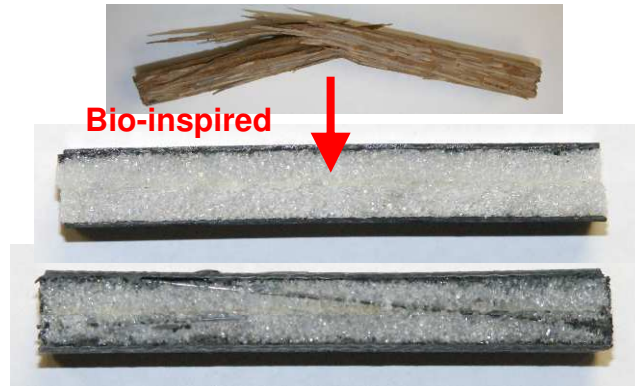


Figure 3. Representative sandwich specimen with bio-inspired foam-core

4. Characterization of Palmetto wood

A representative flexural response of the Palmetto wood specimen under quasi-static three-point bending is depicted in [Figure 4\(a\)](#). A fit of a Weibull distribution for the failure response of a bundle of fibers is found to fit well with the flexural response of the Palmetto wood. For these specimen dimensions, the cross-sectional area is nearly 400 times the cross-sectional area of an individual fiber in the macro-fiber bundle, so the global behavior should be considered macroscopic. The bulk flexural modulus of this representative specimen was determined to be approximately 500 MPa, and the specimen failed at approximately 4% elongation with a corresponding nominal stress of about 10 MPa. The Weibull distribution of the failure response for a bundle of fiber is given by:

$$\sigma = E\varepsilon \exp \left[- \left(\frac{\varepsilon}{\varepsilon_0} \right)^\beta \right], \quad (1)$$

where ε_0 and β are the Weibull parameters and E is elastic modulus. The Weibull parameters are chosen as $\varepsilon_0 = 0.05$ and $\beta = 1.5$ for the present response with elastic modulus (E) as 500 MPa.

At the macroscale, the vertical displacement and strain field obtained by DIC in [Figure 4\(b\), \(c\)](#) resembles to that of a homogeneous isotropic response. The symmetric displacement field indicates that the macroscopic behavior of the wood appears to be homogeneous. Slight asymmetry in the strain field with respect to the loading point was assumed to arise due to inhomogeneity from the macro-fiber distribution in the wood along the specimen length.

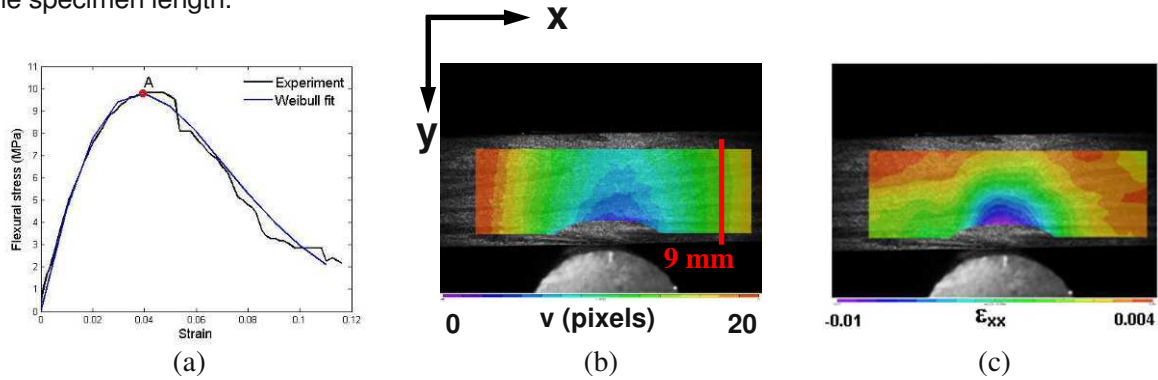


Figure 4. (a) Representative quasi-static macroscopic flexural-stress strain curve for Palmetto wood with a fit indicating that the failure response conforms to Weibull failure distribution, (b) vertical displacement and (c) axial strain field in Palmetto wood before the onset of failure (point A) indicating macroscopically homogeneous behavior [2].

Strain fields at the microscale elucidate high strain accumulation at the macrofiber-matrix interface as depicted in [Figure 5](#). The strain fields indicate high shear and normal strain at the macro-fiber-matrix interface. It is apparent that the high interfacial strains make the wood prone to cell collapse near the macro-fibers, which increases shear loading and initiates the shear dominated debonding. Pore collapse mechanism is captured from the deformation in the porous cellulose matrix as shown in [Figure 6](#). Due to the normal compression and shear, cells collapse and coalesce at the micro-scale and gives rise to shear cracking.

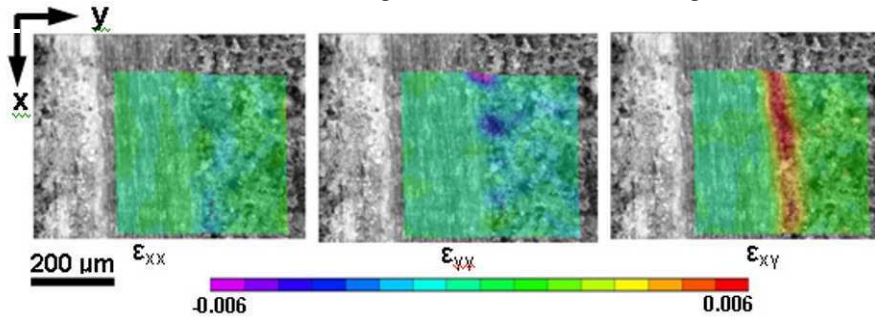


Figure 5. Interfacial strains measured 200 μm into matrix at microscale indicating concentration of shear strains very close ($\sim 0.25d_f$) to the fiber-matrix interface with associated pore collapse which may allow the shear strain to build up at the interface [2].

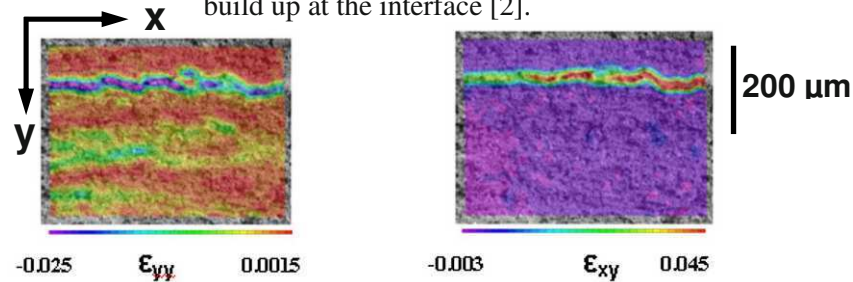


Figure 6. Shear cracking in cellulose material. The pores collapse and coalesce together due to compressive normal strain (left) which causes shear strain to accumulate (right) leading to macroscopic crack formation. The pore collapse mechanism helps for load absorption [2].

The flexural response of Palmetto wood under low velocity impact is depicted in [Figure 7\(a\)](#) and compared to that under the quasi-static loading. The Palmetto wood exhibits a higher stiffness and failure initiation load under impact as compared to characterization. The preliminary results show that the macrofiber volume fraction has significant role in the elastic behavior as well as the failure mode of the Palmetto wood. Specimens were prepared from several locations of the Palmetto stem with different macrofiber volume fraction

indicated by the bulk density. The effect of macrofiber distribution in the bulk Elastic modulus is depicted in [Figure 7\(a\)](#). As evidenced by [Figure 7\(b\)](#), higher macrofiber volume fraction increases the Elastic modulus of the Palmetto wood. Under the quasi-static loading the Elastic modulus is noted to increase by around 45% for an increase in macrofiber volume fraction by 8%, whereas, this increment under dynamic load is found to be around 25%.

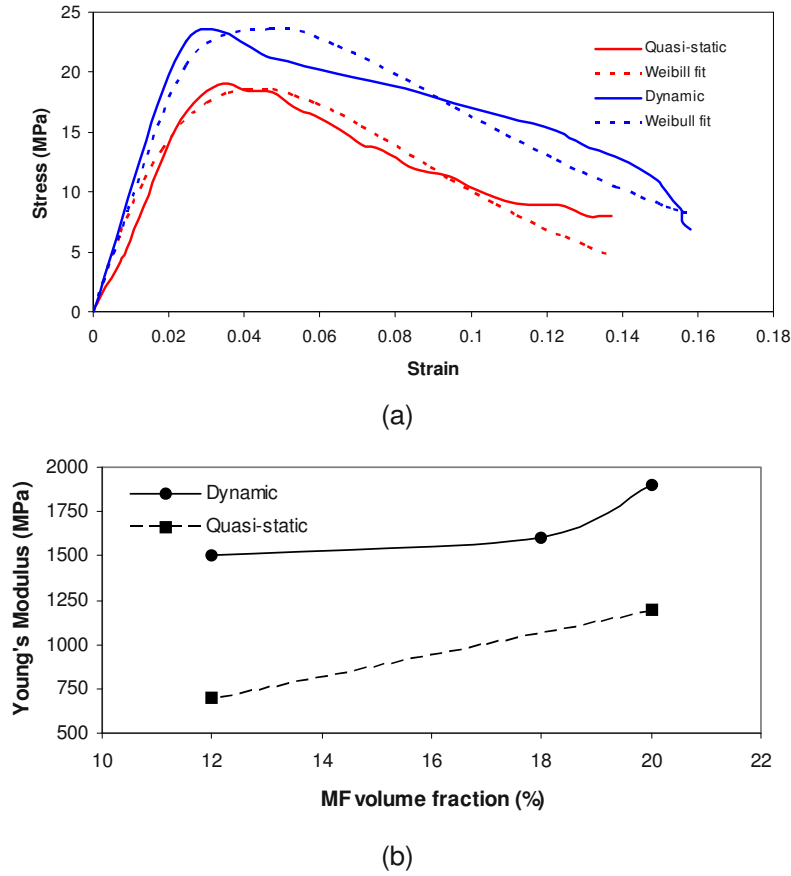


Figure 7. (a) Flexural response of Palmetto wood under low velocity impact and comparison with quasi-static flexural response (b) effect of macrofiber distribution on the bulk Elastic modulus of palmetto wood

The damage evolution of palmetto wood under quasi-static bending and low velocity impact is quantified. The Damage parameter is determined by $D = 1 - (E/E_0)^2$ and the Palmetto wood is found to exhibit a slower damage evolution under dynamic load than under quasi-static load as depicted in [Figure 8](#). A regression fit using progressive damage evolution given by $D_e = 0.9 \{1 - \exp[-A(\varepsilon - 0.034)]\}$ is used to estimate the damage evolution parameters [10]. As depicted in [Figure 8\(a\)](#), the damage acceleration rate is 80% less under dynamic bending. The evolution of plastic strain was determined by $\varepsilon_p = \varepsilon_t \left[1 - \exp\left\{-a(\varepsilon - \varepsilon_y)^p\right\} \right]$ with appropriate parameters from the regression fit. The Palmetto wood was found to exhibit a slower evolution of damage and plastic strain under the dynamic load than that under quasi-static bending.

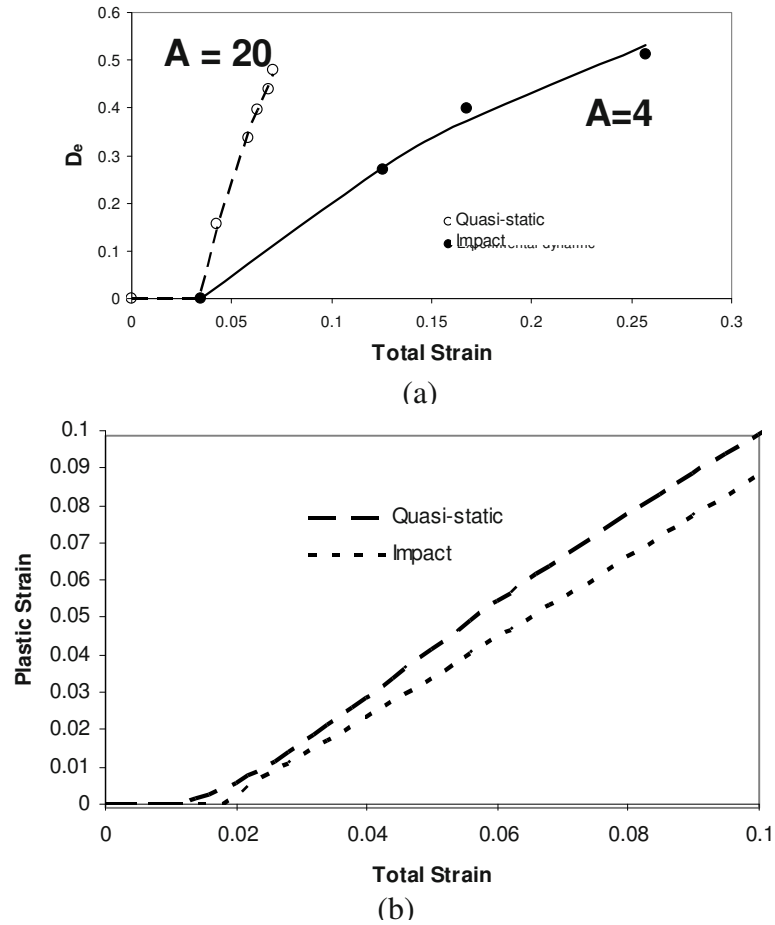


Figure 8. (a) Damage evolution in palmetto wood and (b) evolution of plastic strain under quasi-static and dynamic load

5. Characterization of sandwich material with bio-inspired core

Motivated by the mechanical benefits of hierarchical structure in the Palmetto wood to resist failure, we developed a reinforced sandwich material system as shown in [Figure 3](#) to replicate and investigate the strength and energy absorbing capabilities. The sandwich specimens have been characterized under quasi-static three-point bend and low velocity impact as discussed earlier. The sandwich specimens have been fabricated (1) with pure epoxy as adhesive and no reinforcement, (2) with pure epoxy as adhesive and carbon rod reinforcement and (3) with nano-enhancement in epoxy and carbon rod reinforcement. The quasi-static response of several sandwich specimens has been depicted in [Figure 9](#). The nano-enhancement at the facesheet-core and carbon rod – foam interfaces increases its stiffness as well as energy absorbance.

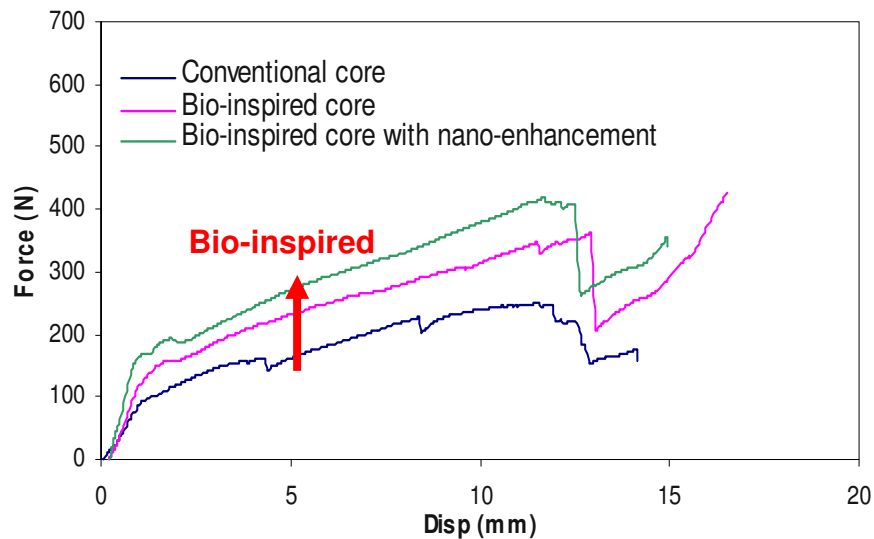


Figure 9. Flexural response of the conventional sandwich and sandwich with bio-inspired core under quasi-static three-point bend test.

The dynamic response of the sandwich specimen with palmetto wood as core was measured under low velocity impact (~ 34 m/s) and compared with that of a specimen with the bio-inspired core of similar dimensions (*Figure 9*). From the impact force-time curves, the behavior of the two specimens is remarkably similar. The force is higher in the bio-inspired core, peaking around 2750 N shortly after initial impact while the Palmetto wood core specimen peaks around 2050 N about 0.15 ms after impact. While the bio-inspired specimen exhibits a load drop after initial impact, the Palmetto wood core specimen is able to sustain its load. Furthermore, the Palmetto wood core specimen tends to accumulate load approximately twice as quickly as the bio-inspired specimen upon initial impact, which would be indicative of a greater initial stiffness. It has been seen that the bio-inspired core enhances the impact resistance and energy absorbance of the specimen in a manner that is similar to the Palmetto wood. The strain fields under low velocity impact test of sandwich specimen with bio-inspired core are also depicted in *Figure 9*. The flexural response of the sandwich beam specimens under low velocity impact and quasi-static loading as they become more bio-inspired through the use of 15 wt. % carbon fibers and with CNF coating of the fibers is also shown in *Figure 9*. It is found that the carbon rod reinforced nano-enhanced foam core has the maximum impact resistance and energy absorbing capability.

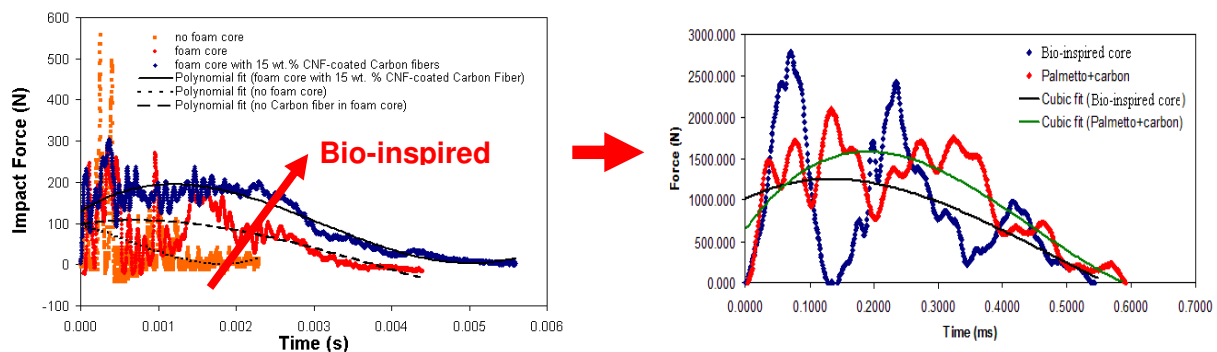


Figure 9. (left) Effects of using new bio-inspired core on sandwich specimens on flexural response under impact, and (right) comparison of dynamic response of sandwich specimens with Palmetto wood and a bio-inspired structure as core under low velocity impact.

6. Conclusions

The mechanical behavior of Palmetto wood, a potential bio-inspiration to develop advanced materials has been characterized under quasi-static and dynamic bending. The study has been performed in the elastic and inelastic deformation regime to elucidate the load transfer and failure initiation. The DIC technique has been employed at multiple length scale to elucidate failure mechanisms. Palmetto wood has been found to exhibit higher stiffness and energy absorbance under dynamic impact than the quasi-static bending. The deformation measurement in the inelastic regime at multiple length scale revealed that the shear dominated delamination occurs at the macrofiber-matrix interface due to accumulation of high shear strain caused by the difference in mechanical properties of macrofiber and porous cellulose matrix. The shear cracking in the porous matrix has been captured at lower length scale occurring following the pore collapse and coalescence. The damage evolution under dynamic loading is found to be slower than under quasi-static bending. The damage modeling of palmetto wood based on a progressive damage model revealed the slower plastic strain evolution under dynamic load.

Sandwich specimens have been developed based on closed-cell soft-foam as core and carbon-epoxy laminates as facesheet. Reinforcement of carbon rod has been used in the soft foam core to mimic the structure of palmetto wood. Using the hierarchical structure of Palmetto wood as template, nano-enhancement was employed in the epoxy based adhesive used in the facesheet-foam and reinforcement-foam interfaces. The preliminary quasi-static and dynamic characterization of the sandwich materials shows that the nano-enhancement increases the stiffness and energy absorbance of the sandwich material.

ACKNOWLEDGEMENTS

This work was supported by ONR award number N000140910640.

REFERENCES

1. A.L. Gershon, H.A. Bruck, S. Xu, M.A. Sutton, and V. Tiwari, "Multiscale mechanical and structural characterizations of Palmetto wood for bio-inspired hierarchically structured polymer composites", *Materials Science and Engineering C*, 30: 235–244 (2010).
2. S. Haldar, N. Gheewala, J. Grande-Allen, M. A. Sutton, and H. A. Bruck, "Multi-scale Mechanical Characterization of Palmetto Wood as a Template for Biologically-inspired Polymer Composite", *Experimental Mechanics*, DOI: 10.1007/s11340-010-9422-7 (2010).
3. Samarasinghe S, Kulasiri D, Nicolle K (1997) Study of mode-I and mixed-mode fracture in wood using digital image correlation method. *Proceedings of International Wood Engineering Conference*, Louisiana, USA
4. Forsberg F, Sjodahl M, Mooser R, Hack E, Wyss P (2010) Full Three-Dimensional Strain Measurements on Wood Exposed to Three-point Bending: Analysis by Use of Digital Volume Correlation Applied to Synchrotron Radiation Micro-Computed Tomography Image Data. *Strain* 46(1): 47-60
5. Choi S, Shah SP (1997) Measurement of deformations on concrete subjected to compression using image correlation. *Experimental Mechanics* 37(3): 307-313
6. Wang Y, Cuitiño AM (2002) Full-field measurements of heterogeneous deformation patterns on polymeric foams using digital image correlation. *International Journal of Solids and Structures*, 39(13-14): 3777-3796
7. Tong W (1997) Detection of plastic deformation patterns in a binary aluminum alloy. *Experimental Mechanics* 37(4): 452-459
8. Pan B, Qian K, Xie H, Asundi A (2009) Two-dimensional digital image correlation for in-plane displacement and strain measurement: a review, *Measurement Science and Technology*: 20(6):
9. Hild F and Roux S (2006) Digital Image Correlation: from Displacement measurement to Identification of Elastic Properties – a Review, *Strain*, 42(2): 69 – 80
10. Chow CL, Lu TJ (1989) On evolution law of anisotropic damage, *Engineering Fracture Mechanics*: 34(3): 679-701

Characterization of Mechanical Behavior of Kevlar 49 Fabrics

Deju Zhu¹, Barzin Mobasher², S.D. Rajan³

¹ Postdoctoral fellow, Department of Mechanical Engineering, McGill University, Montreal, QC, Canada, E-mail: Deju.Zhu@mail.mcgill.ca

² Professor, Ph.D., P.E., Department of Civil, Environmental and Sustainable Engineering, Arizona State University, Tempe, AZ, 85287, corresponding author, E-mail: Barzin@asu.edu

³ Professor, Ph.D., Department of Civil, Environmental and Sustainable Engineering, Arizona State University, Tempe, AZ, 85287, E-mail: S.Rajan@asu.edu

ABSTRACT

Woven fabrics are used in many applications, including ballistic armors, propulsion engine containment systems and fabric reinforced composites. In order to facilitate the design and improvement of such applications, this paper presents the experimental programs of quasi-static uniaxial tension, biaxial tension and picture frame test to obtain the material properties of Kevlar[®] 49 fabric. This study discusses the stress-strain response in both the warp and the fill directions of the fabric under uniaxial tension, the effective Poisson's ratio and the in-plane shear response, and also investigates the possible effect of specimen size on the responses of the fabric. The results show that the fabric exhibits non-linear and orthogonal behavior in tension, and can deform up to 20% before the complete failure. The effective Poisson's ratio is a nonlinear function of strain. The shear response is nonlinear to the shear angle, but not dependent upon the specimen size after normalization. Images were used to demonstrate the deformation and failure behavior of the fabric. All these results are very important for the numerical modeling of the Kevlar[®] 49 fabric used in engine fan containment systems and other ballistic protection.

Keywords: Woven fabric; Stress-strain response; Poisson's ratio; Shear behavior

1. Introduction

High strength woven fabrics are ideal materials for use in structural systems where large deformations and high energy absorption are required. Their high strength per weight ratio and ability to resist high speed impacts enable them to be very efficient compared to metals. Fabrics are highly anisotropic and the behavior in one direction is coupled to the behavior in the other in a nonlinear manner. Even under uniaxial loading, the response of a fabric is often nonlinear due to its woven structure and to nonlinearities in the material response. In addition, many applications of fabric involve large rotations and deformations. Various deformation mechanisms, i.e. yarn stretch, uncrimping, crimp interchange, locking, trellising and yarn slip, determine the mechanical response of a woven fabric [1].

Research on the mechanics properties of aramid yarns has been reported by some authors, but little on aramid woven fabrics. Schwartz et al. [2] carried out quasi-static tensile tests on single fibers of Kevlar[®] 29 and 49 taken from various locations within a spool and production lots. An increased strength for fibers at shorter gage lengths, but no increased variability at longer lengths was observed. Amaniampong and Burgoyne [3] studied the effect of gage length and strain rate from 3×10^{-4} to 0.003 s^{-1} on the failure stress and failure strain of Kevlar[®] 49 yarns. Yarn strength decreases slightly as the gage length increases; whereas the failure strain of the Kevlar[®] 49 yarns was independent of the gage length, however decreased slightly as the strain rate increased. Zhu et al. [4-7] conducted dynamic tensile testing on Kevlar[®] 49 single yarn and fabrics using a servo-hydraulic high speed machine [8-14] and found that the Young's modulus, tensile strength, maximum strain and toughness increased with increasing strain rate over a range of 20 to 170 s^{-1} . Naik et al. [15] studied the quasi-static properties of Kevlar[®] 49 and Zylon fabrics in tension at a strain rate of $1.4 \times 10^{-4} \text{ s}^{-1}$ and the load-deflection response of single layer and multiple layers in static penetration test.

Determination of biaxial nature of interaction between yarns in two dimensional woven fabrics is among the fundamental characteristics of textile materials. This interaction characterizes important mechanical characteristics for a woven fabric, and affects the response in many applications which incorporate textile fabrics as structural elements. This process is known as crimp interchange which is similar to a Poisson's effect, although it is nonlinear, so the effective Poisson's ratio evolves as the fabric is deformed. This mechanism represents an important difference between fabrics and other anisotropic materials because it permits the two families of reinforcing structures to interact in a nonlinear manner [1]. While the significance of the effects of Poisson's ratios on fabric drape and other behaviors is well recognized, their values were mostly estimated, based on those for ordinary solid materials, for fabric modeling and simulations.

Another important material property required for the finite element models of the fabric is the response of the fabric under shear deformation. During shear deformation, the fabric yarns experience large angular variation between warp and fill yarns. Three experimental approaches can be used to characterize the shear properties: the simple shear [16], bias extension test [17] and the picture-frame shear test [18]. The bias extension approach usually brings out a complex combination of shear and tension, which makes it difficult to isolate the shear deformation in the test and hence complicates the characterization of pure shear behavior. In the picture-frame shear test, a fabric sheet is clamped within a square frame hinged at each corner. The two diagonally opposite corners are then displaced using a mechanical testing machine. It can produce a quite uniform shear deformation state in the fabric or composite sheet [19]. In the picture-frame shear test, in-plan shear deformation is limited by local wrinkling, when yarns reach the so-called "locking angle". And corner cut-off is typically needed to allow rotations of the hinges and prevent immediate wrinkling.

This paper presents a comprehensive experimental study of Kevlar[®] 49 fabric subjected to quasi-static uniaxial tension, biaxial tension and in-plane shear. The first section of this paper presents detailed experimental programs to characterize the orthotropic stress-strain relationships by uniaxial tension test, the effective Poisson's ratio by biaxial test, and the shear properties by picture-frame shear test. The second section discusses the results and the possible effects of specimen size and pre-loading on the mechanical properties. Images captured during loading process have been used to study the deformation and failure mechanism of the fabric. The last section summarizes the results and makes some conclusions. It is expected that the results will improve the modeling of the fabric used in aircraft engine fan containment systems [20] and other ballistic protection.

2. Experimental Program

The plain-woven Kevlar[®] 49, a high performance fabric for ballistic protection application, made by El du Pont de Nemours & Co., is used in this study. It is about five times stronger than steel on an equal weight basis, yet it is more flexible and light weight. The Kevlar[®] 49 fabric is manufactured using a plain weave of 17x17 yarns (per linear inch) each consisting of hundreds of filaments. The bulk density and linear density are 1.44 g/cm³, 1.656(10⁻³) g/cm, respectively. The cross-sectional area of each yarn was calculated as 1.15(10⁻³) cm² by dividing the linear density of the material by its bulk density [5].

2.1 Uniaxial Tensile Test

The tests were performed in a 90 kN INSTRON machine operated under closed-loop displacement control with the displacement rate of 2.5 mm/min. Digital data acquisition was used to collect data at a sampling rate of 2 Hz. The test was continued until complete failure of the specimen was achieved. The overall specimen deformation was measured by the stroke movement. To create a strip of specimen, the fabric was first cut into rectangular strips, and then a number of yarns along the fabric length are removed from both sides of the fabric width, thereby producing a sample without yarn crossovers along the edges. This step is necessary to ensure that the effects of edge defects are minimized and that the loaded yarns will not slip out of the cross yarns during the test. The fabric was cut into strips with a length of 250 mm and two sets of width-30 mm and 60 mm. In each set, yarns are removed from both sides of the strip such that the samples are left with 17 and 34 longitudinal yarns, respectively. The initial gage length was 200 mm. The total cross-sectional area of a specimen was defined as the cross-sectional area per yarn multiplied by the number of yarns per width of the specimen. Five tests were conducted on each specimen size in both the warp and the fill directions, and the deformation and failure behavior of the specimens were recorded by a CCD camera.

2.2 Biaxial Tension Test

The test setup comprises of two actuators which are capable of applying displacement velocity and measuring displacement of test specimen in two orthogonal directions independently, two load cells with capacity of 90 and 225 kN which are used for force measurement, a grip assembly to hold the specimen, a sliding block (super pillow) on a steel roller which is mounted on ground, and connecting bars and universal joints, as shown in Figure 1(a). The load cell with capacity of 90 kN was used to measure the force in vertical direction, and the other was used to measure the force in horizontal direction. An edge-clamped fabric holding fixture was developed to hold the fabric specimen. The clamping of the fabric edges is accomplished through wrapping with a notch. The grip assembly can hold specimens with size up to 150 mm x 150 mm. The original fabric is 250 mm wide and was cut into different specimen sizes with corner cut-off. The arm parts were clamped to the fixture. Figure 1(b) shows the specimens of 100 mm x 100 mm with corner cut-off. The clamped specimens were pre-loaded in vertical direction for each specimen size at 4.5 N/mm, and kept vertical direction stationary after pre-loading, and then applied displacement in horizontal direction at a loading rate of 5 mm/min.

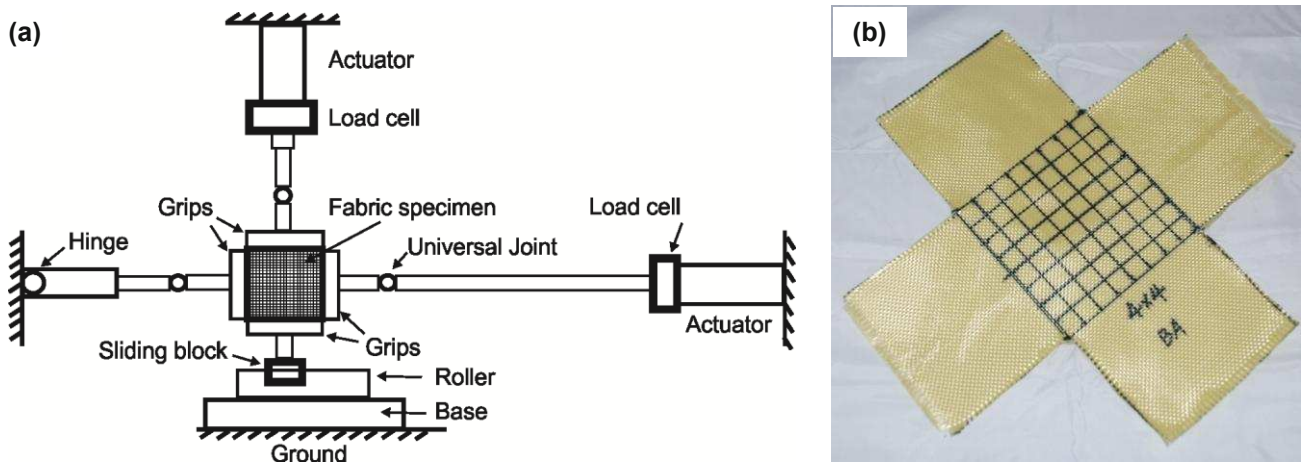


Fig. 1 (a) Schematic diagram of biaxial test setup and (b) cruciform specimens of 100 mm x 100 mm

2.3 Picture Frame Test

All the tests were conducted in a servo-hydraulic test frame (MTS) operated under closed-loop displacement control. Data were acquired at a sampling rate of 2Hz. A CCD monochrome camera was used to capture the images during loading process. A schematic diagram of the picture frame is shown in Figure 2(a). The frame consists of five basic parts namely bearings, clamping plates, multiplier links, a long plate with a 88.9 mm slot and two connecting fixtures (for connecting to the top and bottom crosshead mount). The side length of the frame (L_{frame}) is 165 mm, and the side length of the amplifier (L_a) is 70 mm. The fabric was wound over the circular rod and placed in the circular slot in the top part of the clamping plate. The tightened set screws at the top of the plates kept the assembly intact and prevented the fabric slipping through the application of uniform mechanical pressure. Before the start of the test the multiplier links are orthogonal to each other. The top crosshead mount remains stationary while the stroke moves down at a rate of 5 mm/min. In order to minimize the marginal restriction due to the joints of the fixture, four corners of a square fabric sheet are cut off to generate a test sample with smaller size than clamped in the picture frame. However, the fringe yarns still rotate and make contribution to immediate wrinkling. One way to eliminate the contribution from the edge parts, thus provide an accurate material characterization, is removing some yarns in each arm part. The inner areas of constructed specimens have three different sizes, i.e., 75x75 mm, 100x100 mm and 125x125 mm. Before experiment, four unidirectional-yarn parts are clamped tightly into the two plates on the fixture with screws, as shown in Figure 2(b). When clamped into the fixture, the specimen is kept exactly loose in order to avoid pre-tension in both directions of the fabric.

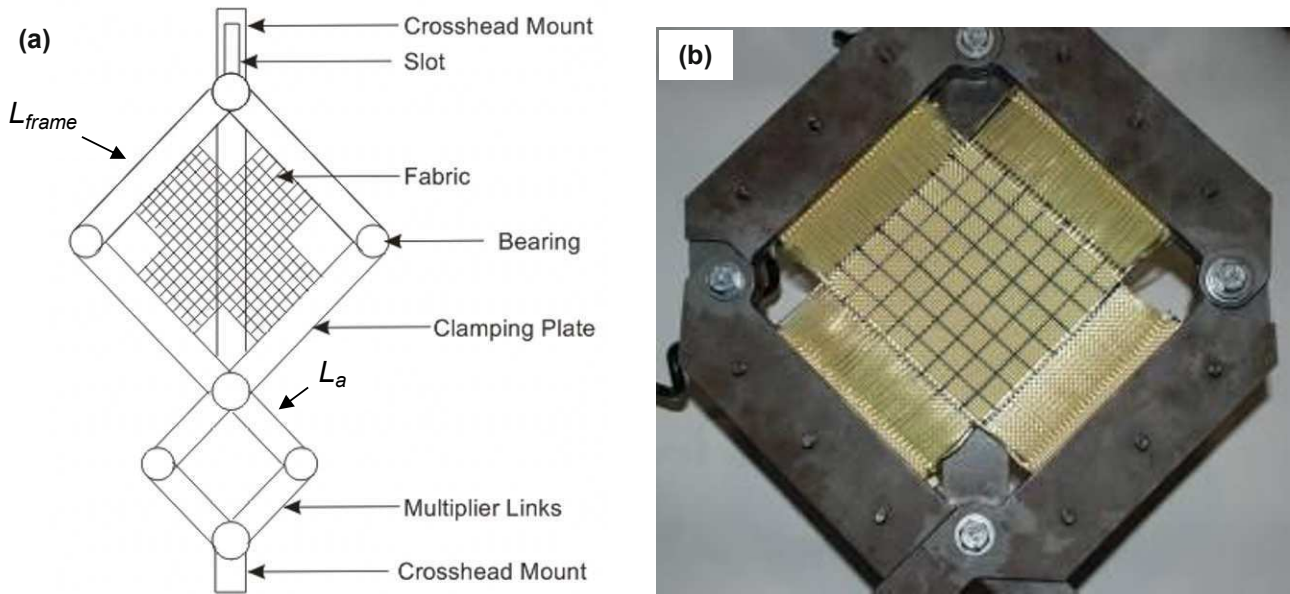


Fig. 2 (a) Schematic diagram of the picture frame and (b) specimen clamped into fixture

The picture frame tests were conducted by following procedure which is similar to the procedure in the reference by Zhu et al. [18]. The shear angle, shear force and shear stress were determined using the same method as discussed by Cao et al. [19]. To compare the results of different specimen sizes or the tests conducted on different fixtures, Harrison et al. [21] proposed a method for normalization which uses the frame length based on an energy method. Their assumption was that the frame length was equal to the fabric length. However, as there is no standard ratio for the length of a test sample to the length of the frame, this method is not the best method for normalization. The investigation continued by comparing the data when normalized by the fabric area as discussed by Peng et al. [22]. Here, the fabric area was defined as the inner square area of the sample, i.e., the arm areas were neglected. The fabric area is directly related to the number of crossovers in the material. A larger sample would have more yarns resulting in more crossovers between the yarns. With an increased number of yarns and crossovers, a larger force is required to shear the sample. The normalization by the inner fabric area is quite straightforward and reasonable if part of the yarns in the arm area is removed so that no shear occurred in the arm area. In the present study, as some of the yarns in the arm area are removed before the tests, it is reasonable to normalize the shear force by the inner fabric area, and normalize the shear stress by the length (width) of the inner area.

3. Experimental Results and Discussion

3.1 Uniaxial Tensile Behavior

Figure 3 shows the typical stress versus strain (time) relationship, the fabric deformation and failure mechanism under uniaxial tension. There are four distinct regions in the stress-strain behavior: crimp region, linear pre-peak region, linear post-peak region and non-linear post-peak region. In the undeformed state ($t = 0$ second), the warp and fill yarns are orthogonal to each other and free of any stretch. In the crimp region, the stress increase is relative low due to the straightening of the woven structure of the fabric. As the strain is increased, the yarns in the loading direction are extended and become compacted. When the yarns in the loading directions are fully straightened, or in some cases, until cross yarns wrap around the loaded yarns and thereby prevent them from extending [23], the fabric exhibits a linear response and there is no visible failure of the fabric. The Young's modulus is defined by the slope of the stress-strain curve in this region. When the stress level reaches the strength of the constituent yarns, the yarns in the loading direction start to fail, resulting in a dramatic decrease in the fabric load-carrying capacity until reaching a transition point which is about 200 MPa (the end of linear post-peak region). After that the stress decreases gradually to almost zero when the strain increases up to about 0.2 mm/mm, representing the nonlinear post-peak region where the failed yarns slip away out of the fabric ($t = 200$ to 800 second). The strain energy of stretched yarns and the energy dissipated through frictional sliding play key

roles in the energy absorption ability of the fabric. The toughness is defined by the area under the entire stress-strain curve.

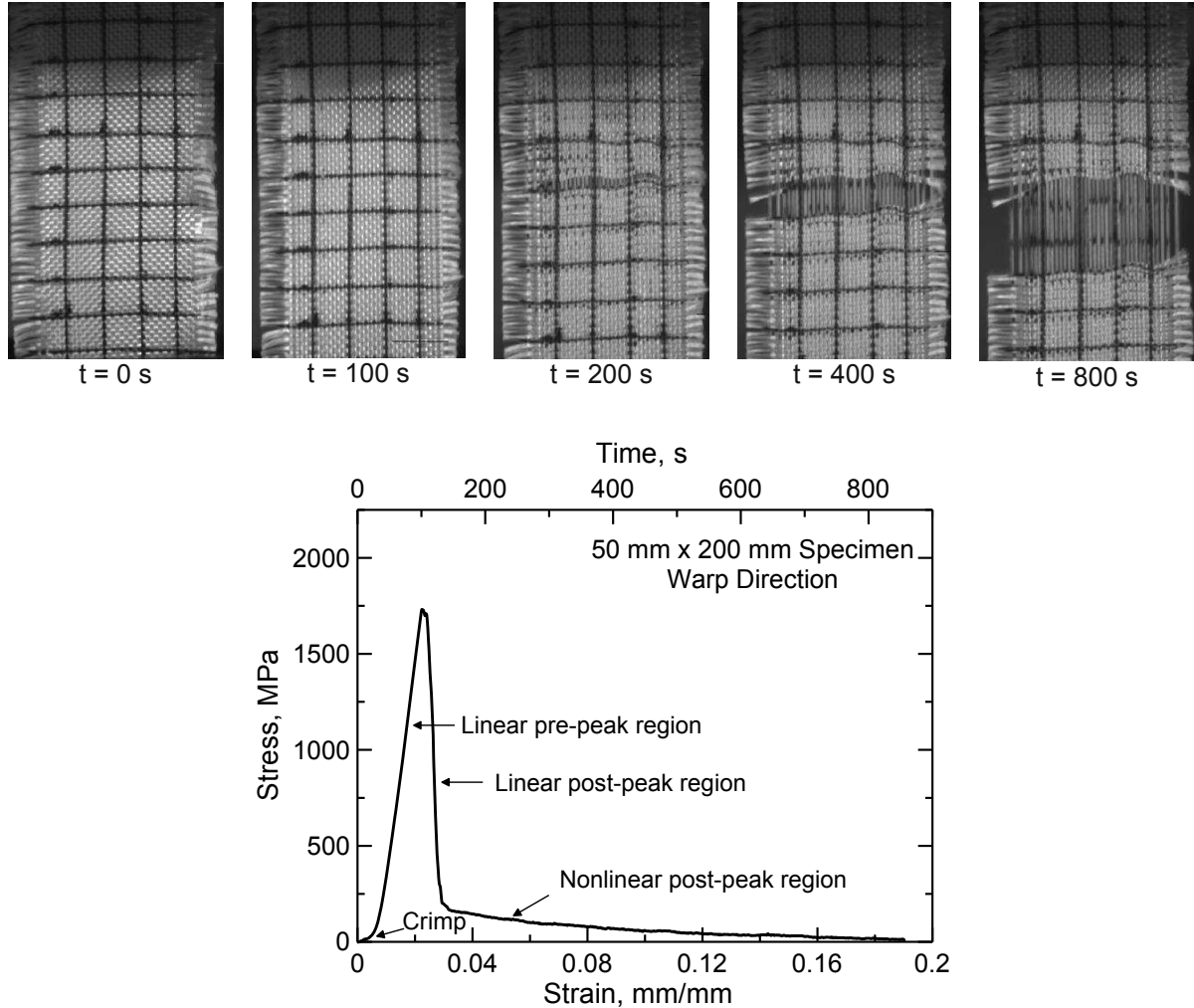


Fig. 3 Typical stress-strain relationship and fabric deformation under uniaxial tension

Tables 1 summarizes the tensile properties of both specimen sizes in warp and fill directions. The tensile strength in warp direction is approximately 10-15% lower than that in fill direction, while the ultimate strain in warp direction is approximately 7-12% higher than that in fill direction. The elastic stiffness in pre-peak region of warp direction is almost identical to that of fill direction. Although the tensile strengths of 50 mm wide specimen are slightly lower (2-6%) than those of 25 mm wide specimens in both warp and fill direction, the Young's modulus, toughness and ultimate strain are almost identical to each other, indicating the tensile properties of the fabric are independent with the width-to-length ratio for the considered range of configuration.

Table 1 Summary of Tensile Properties of Kevlar 49 Fabric in Warp and Fill Directions

Specimen Size (Width x Length, mm)	Direction (Warp/Fill)	Tensile Strength (MPa)	Young's Modulus (GPa)	Toughness (MPa)	Ultimate Strain (mm/mm)
50x200	Warp	1748 ± 56	117.2 ± 3.3	32.4 ± 3.0	0.0223 ± 0.0012
	Fill	2013 ± 44	117.1 ± 3.0	33.9 ± 1.3	0.0201 ± 0.0010
25x200	Warp	1859 ± 109	117.9 ± 2.5	32.9 ± 1.4	0.0215 ± 0.0015
	Fill	2055 ± 72	119.7 ± 4.0	33.2 ± 1.2	0.0200 ± 0.0009

3.2 Effective Poisson's Ratio

Figures 4(a) and 4(b) show the effective Poisson's ratio of the specimens with pre-loading of 4.5 N/mm. The effective Poisson's ratio first increases with increasing strain very quickly at the beginning, then decreases gradually, leveling off before the specimen fails for all the specimen sizes and pre-loading conditions. For the 50 mm x 50 mm specimens, the maximum value of Poisson's ratio varies between 0.35 and 0.57. When the fabric fails at the strain value of 0.025, the effective Poisson's ratio decreases to approximately 0.15 (average value). For the 100 mm x 100 mm specimens, the maximum value of Poisson's ratio is in the ranges of 0.48 to 0.63. And the average Poisson's ratio is also approximately 0.15 when the fabric fails.

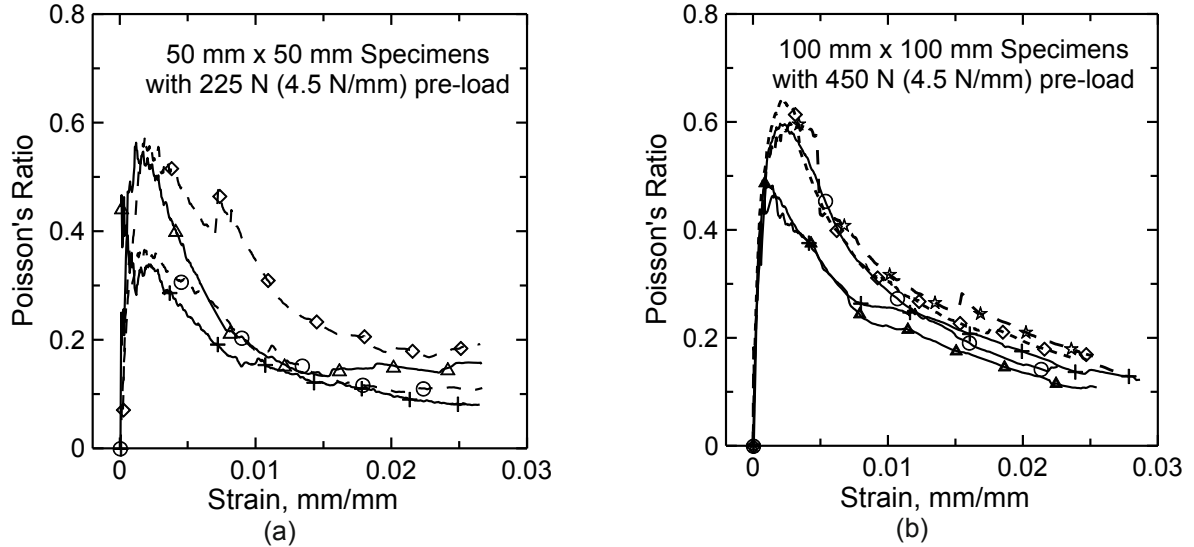


Fig. 4 Effective Poisson's ratio of (a) 50 mm x 50 mm and (b) 100 mm x 100 mm specimens

3.3 In-plane Shear Behavior

The shear response of woven fabric is different from that in metals and other homogeneous material sheets due to the fabric unique woven structure. In particular, the in-plane shear response of fabric is dominated by the relative rotation of the two yarn families. This behavior is responsible for many distinct features observed during shear deformation of woven fabrics. Figure 5 shows the images captured during the shear deformation of the 125 mm x 125 mm specimen. Grid pattern was applied on the specimen surface before the test for image analysis. One should notice that all the specimens undergo fairly uniform shear deformation.

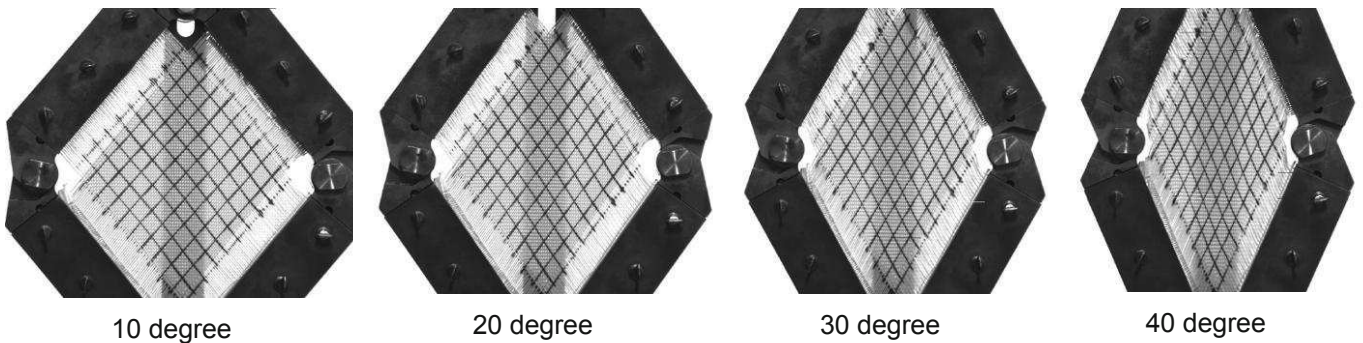


Fig. 5 Shear deformation of the 125 mm x 125 mm specimen at different shear angles

The initial portion of the Figures 6(a) and 6(b) depicts a linear response corresponding to the elastic rotation, following with a region where the yarns undergo dissipative rotation at the yarn crossover points. In dissipative rotation region (shear angle from 2 to 30 degree), both the shear force and the shear stress slightly increase with shear angle. As the yarns are compressed (shear angle between 30 and 40 degree), shear stiffness in the fabric

increases, providing higher shear resistance. The shear force and the shear stress increase much faster in this region. When the yarns cannot be compacted further and the in-plane movements of the yarns are prohibited, the level of shear deformation is commonly referred to as the fabric's shear locking angle. The last portion of the curves (shear angle above 40 degree) is dominated by shear locking effects.

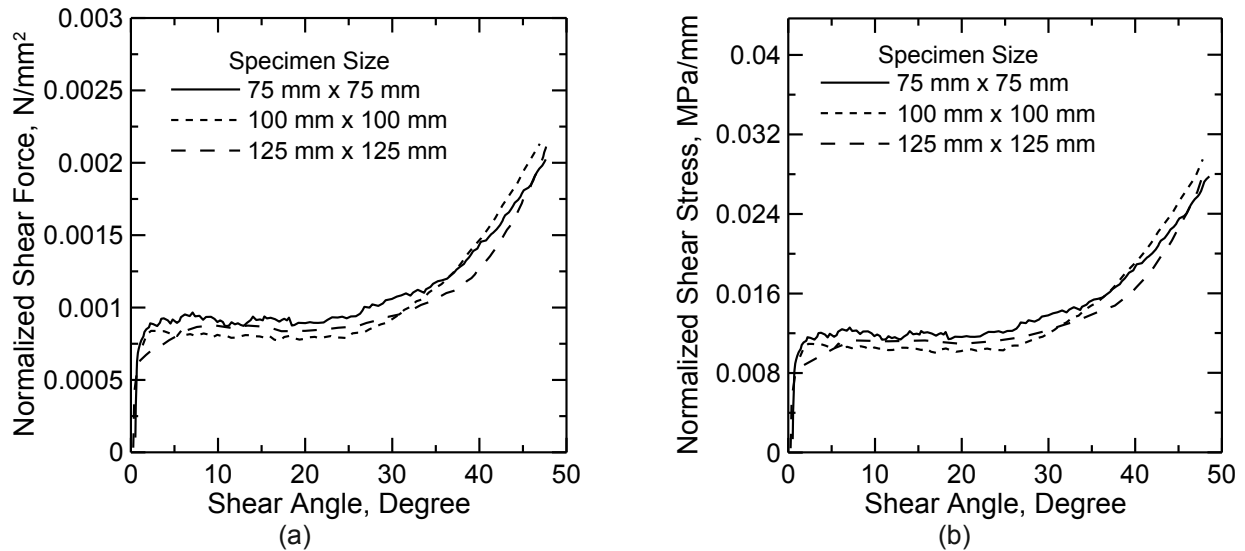


Fig. 6 Normalized (a) shear force and (b) shear stress versus shear angle

4. Conclusions

The present study focuses on the experiment and characterization of uniaxial, biaxial tension, and in-plane large shear deformation on the Kevlar 49 fabric, and analyzes the non-linear stress-strain relationship in warp and fills directions, effective Poisson's ratio as a function of strain, and the shear response. The following conclusions can be reached:

- (1) The stress-strain response of Kevlar 49 fabric exhibits non-linear and orthogonal behavior in warp and fill directions, and can deform up to 20% before the complete failure. The tensile strength in warp direction is approximately 10-15% lower than that in fill direction, while the ultimate strain in warp direction is approximately 7-12% higher than that in fill direction. The elastic stiffness in pre-peak region of warp direction is almost identical to that of fill direction.
- (2) The effective Poisson's ratio is a nonlinear function of strain values. It first increases with increasing strain very quickly at the beginning, then decreases gradually, leveling off before the specimen fails. The maximum value of the effective Poisson's ratio varies between 0.35 and 0.63, and when the fabric starts to fail it is approximate 0.15.
- (3) The normalized shear response is independent with the specimen size. The normalized shear force and stress versus shear angle curves consist of several regions: linear elastic rotation region, dissipative rotation region, yarn compression region and shear locking region.

Acknowledgements

The authors wish to thank William Emmerling, Donald Altobelli and Chip Queitzsch of the Federal Aviation Administration's Aircraft Catastrophic Failure Prevention Research Program for their support and guidance. Funding for this effort was provided by the FAA.

Reference

- [1] King MJ. A Continuum constitutive model for the mechanical behavior of woven fabrics including slip and failure. Ph.D. dissertation, Massachusetts Institute of Technology, 2006.

- [2] Schwartz P, Wagner HD and Phoenix SL. A study of statistical variability in the strength of single aramid filaments. *Journal of Composite Material*, 18(4), 312-338, 1984.
- [3] Amaniampong G and Burgoyne, CJ. Statistical variability in the strength and failure strain of aramid and polyester yarns. *Journal of Material Science*, 29, 5141-5152, 1994.
- [4] Zhu D, Mobasher B and Rajan SD. Experimental study of dynamic behavior of Kevlar 49 single yarn. *Society for Experimental Mechanics - Annual Conference & Exposition on Experimental and Applied Mechanics*, v3, p. 542-547, 2010.
- [5] Zhu D, Mobasher B and Rajan SD. Dynamic tensile testing of Kevlar 49 fabrics. *ASCE Journal of Materials in Civil Engineering*, 2010, in press, [http://dx.doi.org/10.1061/\(ASCE\)MT.1943-5533.0000156](http://dx.doi.org/10.1061/(ASCE)MT.1943-5533.0000156).
- [6] Zhu D, Mobasher B and Rajan SD. High Strain Rate Testing of Kevlar 49 Fabric. *Society for Experimental Mechanics - 11th International Congress and Exhibition on Experimental and Applied Mechanics*, v1, p.34-35, 2008.
- [7] Zhu D, Mobasher B and Rajan SD. Image Analysis of Kevlar 49 Fabric at High Strain Rate. *Society for Experimental Mechanics - 11th International Congress and Exhibition on Experimental and Applied Mechanics*, v2, p.986-991, 2008.
- [8] Zhu D, Rajan SD, Mobasher B, Peled A and Mignolet M. Modal analysis of a servo-hydraulic high speed testing machine and its application to dynamic tensile testing at an intermediate strain rate. *Experimental Mechanics*, 2010, in press, <http://dx.doi.org/10.1007/s11340-010-9443-2>.
- [9] Zhu D, Mobasher B and Rajan SD. Characterization of dynamic tensile testing using aluminum alloy 6061-T6 at intermediate strain rates. *ASCE Journal of Engineering Mechanics* 2010 (accepted).
- [10] Zhu D, Peled A and Mobasher B. Dynamic tensile testing of fabric-cement composites. *Construction and Building Materials*, 25(1), 385-395, 2011.
- [11] Zhu D, Mobasher B, Silva FA and Peled A. High Speed Tensile Behavior of Fabric-Cement Composites. *International Conference on Material Science and 64th RILEM Annual Week, Proceedings pro075: Material Science - 2nd ICTRC - Textile Reinforced Concrete - theme 1*, p. 205-213, 2010.
- [12] Silva FA, Zhu D, Mobasher B, Soranakom C and Toledo Filho RD. High speed tensile behavior of sisal fiber cement composites. *Materials Science and Engineering: A*, 527(3), 544-552, 2009.
- [13] Silva FA, Butler M, Mechtcherine V, Zhu D and Mobasher B. Strain rate effect on the tensile behaviour of textile-reinforced concrete under static and dynamic loading. *Materials Science and Engineering: A*, 528(3), 1727-1734, 2011.
- [14] Mechtcherine V, Silva FA, Butler M, Zhu D, Mobasher B, Gao S and Mäder E. Behaviour of strain-hardening cement-based composites under high strain rates. *Journal of Advanced Concrete Technology*, 9(1), 51-62, 2011.
- [15] Naik D, Sankaran S, Mobasher B, Rajan SD and Pereira JM. Development of reliable modeling methodologies for engine fan blade-out containment analysis. Part I: experimental studies. *Int J Impact Eng.*, 36(1), 1-11, 2009.
- [16] Kothari VK and Tandom SK. Shear behavior of woven fabrics. *Textile Research Journal*, 59(3), 142-150, 1989.
- [17] Potter KD. The influence of accurate stretch data for reinforcements on the production of complex structural moldings. Part I: deformation of aligned sheets and fabrics. *Composites*, 10(3), 161-167, 1979.
- [18] Zhu B, Yu TX and Tao XM. An experimental study of in-plane large shear deformation of woven fabric composite. *Composites Science and Technology*, 67, 252-261, 2007.
- [19] Cao J, et al. Characterization of mechanical behavior of woven fabric: experimental methods and benchmark results. *Composites Part A*, 39, 1037-1053, 2008.
- [20] Stahlecker Z, Mobasher B, Rajan SD and Pereira, JM. Development of reliable modeling methodologies for engine fan blade-out containment analysis. Part II: finite element analysis. *Int J Impact Eng.*, 36(3), 447-459, 2009.
- [21] Harrison P, Cliffod MJ and Long AC. Shear characterization of viscous woven textile composites: a comparison between picture frame and bias extension experiments. *Composites Science and Technology*, 64, 1453-1465, 2004.
- [22] Peng XQ, Cao J, Chen J, Xue P, Lussier DS and Liu L. Experimental and numerical analysis on normalization of picture frame test for composite materials. *Composites Science and Technology*, 64, 11-21, 2004.
- [23] Jearanaisilawong P. Investigation of deformation and failure mechanisms in woven and nonwoven fabrics under quasi-static loading conditions. M.S. Thesis, Massachusetts Institute of Technology, 2004.

Identification of the Tensile Properties of Composite Material Under Variable Strain Rates

V. K Singh*, P.C. Gope & Manish Tewari

*Associate Professor, Department of Mechanical Engineering
College of Technology, G B Pant University of Agril. & Tech., Pantnagar -263 145 (INDIA)
Mail Id: vks2319@yahoo.co.in

ABSTRACT

In recent years, there has been a large increase in the use of polymers in engineering applications. Silica-styrene-butadiene rubber filled hybrid composites is a material designed with different weight % of silica and styrene-butadiene rubber. Five crosshead speeds (0.01 mm/min, 0.1 mm/min, 1mm/min, 10mm/min and 100mm/min) are considered in this study. The results showed that yield stress and elastic modulus decreased with decreasing crosshead speed. An artificial neural network model is presented to predict the mechanical properties. The result of the analysis of variance (ANOVA) shows a good interaction between filler materials and testing condition by 99% confidence level. In the present investigation Scanning Electron Microscope studies has been done to see the dispersion of silica and styrene-butadiene rubber particles in resin.

INTRODUCTION

Polymers are materials composed of long chain-like molecules in which the atoms are bound together by strong covalent bonds. Polymers exist in nature in such forms as wood, cotton, silk, hair and flesh. In addition, there are countless man-made or synthetic polymers being used in more traditional applications such as clothing, packing and various household items. However, in recent years these synthetic polymers are being increasingly used in engineering applications related to the automotive and aerospace industries, civil engineering applications, gas and liquid transport systems, paints and coatings, and electronics industries.

Silica is one of the most applied fillers in polymer composites. Epoxy resin reinforced with silica particles having submicron dimensions represents one of the most studied systems. Already published results[1] evidenced that well dispersed silica nanoparticles can effectively enhance the comprehensive properties of epoxy-based nano- composites, which are unique and different from any other current conventional micro composite with typical filler amounts of less than 5 wt %. Various investigators reported that mechanical properties of silica particle/polymer nanocomposites are significantly enhanced even at very low particle volume fraction [2, 3].

Styrene rubber resembles natural rubber in processing characterization as well as quality of finished product. It has been reported that silica particles dispersed uniformly within the rubber matrix [4] and enhances the mechanical properties of the hybrid composite significantly. The interaction between the rubber and the filler has been studied to determine the effects on failure of the compounds by many researchers [5, 6]. The tensile properties of polymers are specified with parameters of yield stress, elastic modulus and ultimate strength. For many polymeric materials, the simple stress strain test is employed for the characterization of these parameters. The tensile properties are highly sensitive to the strain rate. The data derived from tensile tests is essential for material selection during design of engineering components.

MATERIAL

In the present investigation CY-230 purchased from M/s CIBATUL Limited, India has been used as matrix material. Hardener HY-951 purchased from M/s CIBATUL Limited, India has been used as curing agent. In the present investigation 8 % wt/wt has been used in all material developed. It is reported [7] that silica partials are uniformly dispersed in to the matrix

of parent material and there is no chemical reaction between silica and resin matrix. In the present investigation nano sized silica powder (<142 nm) procured from M/s DEGUSSA INDIA Pvt. Limited, New Delhi have been used in the ratio of 0.5%, 1%, and 2.0% wt/wt. Silica powder is directly mixed in resin and stirred mechanically by means of a high speed mechanical stirrer. In the present investigation synthetic rubber is also used as secondary filler material in order to improve the abrasion resistance & load bearing capacity and resilience.

RESULT AND DISCUSSION

SCANNING ELECTRON MICROSCOPE (SEM)

The state of dispersion of nano particles into the resin matrix plays a significant role on the mechanical properties of the composite. Various methods such as SEM, TEM etc can be used to evaluate the particle dispersion in the composite. In the present investigation SEM was carried out for hybrid composite containing different weight percentage of silica and styrene-butadiene rubber to evaluate the particle size, particle matrix interface and dispersion of the silica particle and styrene-butadiene rubber in the epoxy resin matrix. Figure 1-2 shows the SEM photographs of different hybrid composite material investigated in the present work. Figure 2 shows the SEM photograph of composite containing 1 wt% of silica respectively. It is seen from the figures that silica particles are well dispersed in the epoxy resin matrix in a preferred orientation. The absence of any voids around the particle indicates a good adhesion between silica particle and epoxy matrix. From the above figures it is also evidence that there is no chemical reaction between silica-rubber and epoxy resin. It is estimated that average size of the silica nano particles are $132\text{nm} \pm 12\text{ nm}$. Hence, from the above micrographs it is can be concluded that due to uniform dispersion of nano sized silica particle in the epoxy resin, a remarkably affect on the mechanical properties may be obtained.

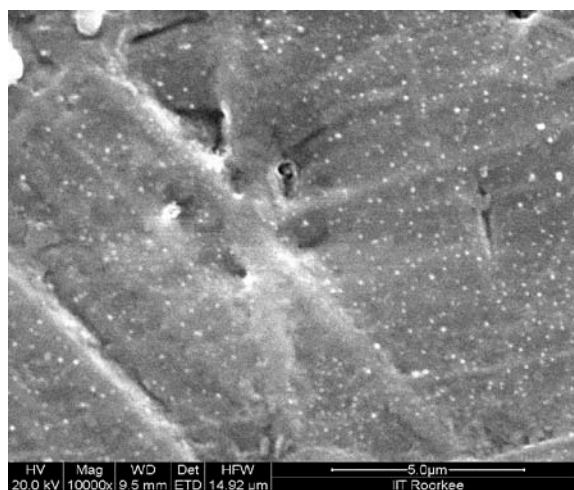


Figure 1: Scanning electron micrograph for 2wt% Silica reinforced composite material at magnification 10000x.

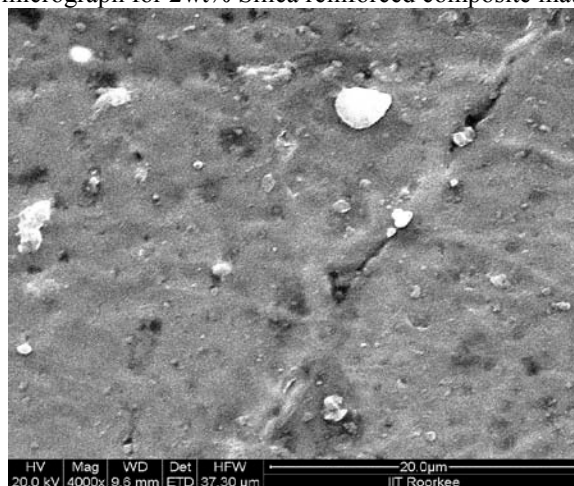


Figure 2: Scanning electron micrograph of 1 wt% Silica & 1.5 wt% rubber hybrid composite material at magnification 4000x.

TENSILE STRENGTH

The mechanical properties of the silica-styrene-butadiene rubber filled epoxy resin hybrid composite material were determined by 100 kN ADMET make servo controlled universal testing machine at different strain rates under displacement control mode. Remarkable differences can be seen in the stress-strain behavior due to addition of silica and styrene-butadiene rubber in epoxy resin matrix. Significant improvement in tensile strength, modulus of elasticity and % elongation has been seen due to addition of silica and styrene-butadiene rubber in the epoxy matrix. Tensile tests were carried out at different strain rates of 0.01 mm/min, 0.1 mm/min, 1 mm/min, 10 mm/min and 100 mm/min. The results of modulus of elasticity obtained from stress-strain test data are presented in [table 1](#). The modulus of elasticity of pure epoxy (8%HY-951 hardener and rest CY-230) is found to be 0.443 GPa at slow strain rate of 0.01 mm/min. At higher strain rate of 10 mm/min it reduces to 0.309 GPa.

Table 1: Modulus of elasticity (MPa) of base material at different strain rates

S.N	Strain rate (mm/min)	Modulus of elasticity (MPa)
1	0.01	443.34
2	0.10	388.32
3	1.00	368.00
4	10.00	309.00

[Figure 3-6](#) shows the effect of strain rate on ultimate strengths and % elongation for different composite material containing 1wt% silica with 0.25, 0.50, 1.0 and 1.5 wt% of styrene-butadiene rubber. [Figures 3-4](#) indicate that ultimate strength increases for 0.25, 0.50, 1.00 and 1.50 where as decreases in case of pure silica base nano-composite as increases strain rate. This indicates increases in ultimate strength due to addition of styrene-butadiene rubber in silica hybrid composite material; the material is expected to behave less elastically throughout practically at lower strain rate. Its entire strength range under higher strain rate condition, where as sharp increase in ultimate strength, the hybrid material containing silica and styrene-butadiene rubber is, expected to behave plastically throughout its entire strength range under higher strain rate. Hence, it can be concluded that silica-styrene-butadiene rubber mixed hybrid composite has decreased elastic region and ductility, a higher plastic region as compared to base material as shown in [figure 5-6](#).

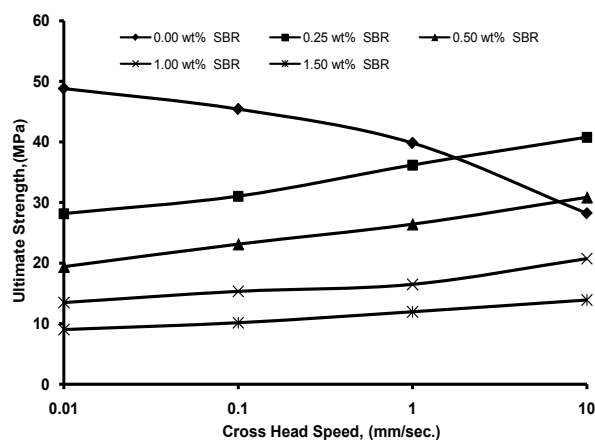


Figure 3: Effect of strain rate on ultimate strength of 1 wt% of silica filled hybrid composite

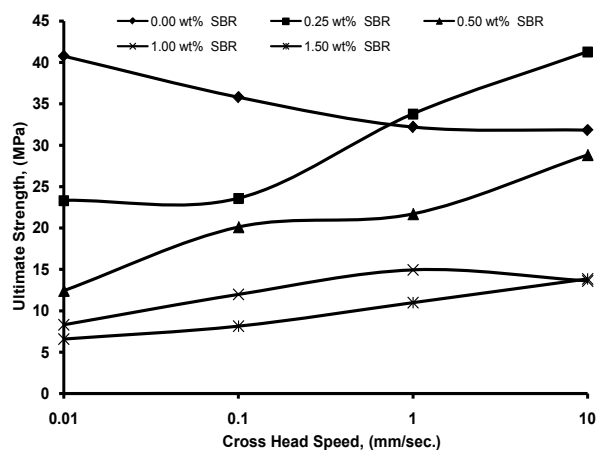


Figure 4: Effect of strain rate on ultimate strength of 2 wt% of silica filled hybrid composite

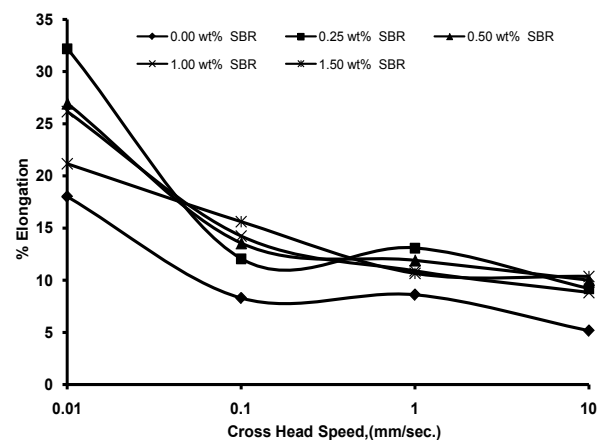


Figure 5: Effect of strain rate on % elongation of 1 wt% of silica filled hybrid composite

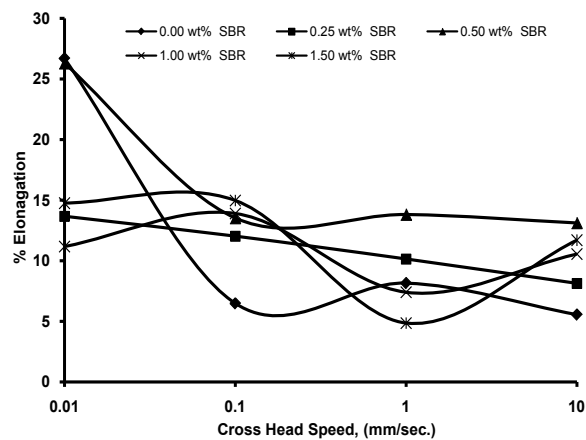


Figure 6: Effect of strain rate on % elongation of 2 wt% of silica filled hybrid composite

HARDNESS

As known, hardness implies a resistance to indentation, permanent or plastic deformation of material. In a hybrid composite material, filler weight fraction significantly affects the hardness value of the hybrid composite material. The effect of weight percentage of silica and styrene-butadiene rubber on the hardness values of hybrid composite are shown in figure 8. It is found that hardness of neat epoxy resin (CY-230+ 8 wt% of HY-951) is 85 HRR. The hardness of the fabricated composite made of epoxy resin and 0.5, 1.0 and 2 wt% of the silica are 99.56, 120.17 and 120.98 respectively. The hardness increases with the amount of silica reflecting the reinforcement formed in the hybrid composite. It is seen from the figure 7 that the beyond of 1 wt% of silica, the improvement in the hardness value of the hybrid composite is insignificant. This shows that the optimum value of silica wt% is about 1 wt% which increases about 40% of hardness as compared to base material. In the contrast, the addition of styrene-butadiene rubber to silica filled composite decreases the surface hardness. It is seen that addition of 0.5 wt% of styrene-butadiene rubber to 1 and 2 wt% of silica filled composite yields the hardness value of 82.27 and 83.85 HRR, respectively, which is just equal to the hardness of pure epoxy resin composites. Hence, it can be concluded that use of styrene-butadiene rubber as additional filler material in silica filled resin composite decreases the hardness values. An amount of 0.5 wt% of styrene-butadiene rubber may be used in the silica filled composite to get the reasonable mechanical properties including hardness. Beyond the value of 0.5-1.0 wt%, it decreases the hardness drastically. The variation of the hardness with the ultimate tensile strength of hybrid composite is shown in figure 8. Figure 8 illustrates that the hardness value follows a linear relation with ultimate strength of the silica-styrene-butadiene rubber hybrid composite material. An attempt has been made to correlate hardness with the ultimate strength. Following correlation has been obtained from the least square analysis.

$$\sigma_u = \left(\frac{\pi}{10} \right) \times (HRR) \quad (1)$$

With correlation coefficient of 0.866 with 50 % reliability, where σ_u is in MPa and hardness in Rockwell ‘R’ scale.

Figure 9 is drawn to see the effectiveness of the present model. Figure shows that most of the data except one falls within the scatter bond of 1. This illustrates the effectiveness of the proposed model to estimate the ultimate strength from the hardness. The correlation coefficient value of 0.886 indicates a good correlation between hardness and ultimate strength and a direct relation between them. The student’s test results is found to be 4.582, ($t_{7,0.01} = 3.0$), which confirm the correlation between the factors hardness and ultimate strength with probability $p \leq 0.01$. Hence, there is a linear relation between ultimate strength and hardness exists in the present investigation.

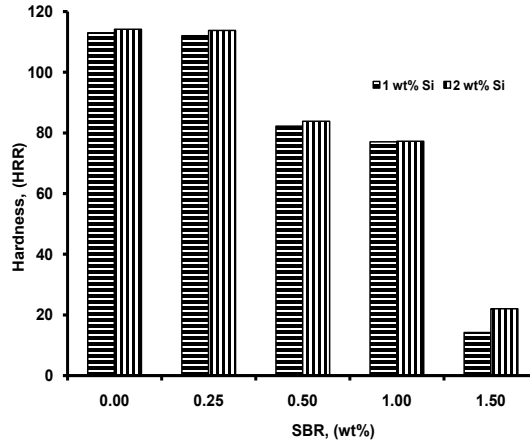


Figure 7: Effect of styrene-butadiene rubber (wt %) on Hardness

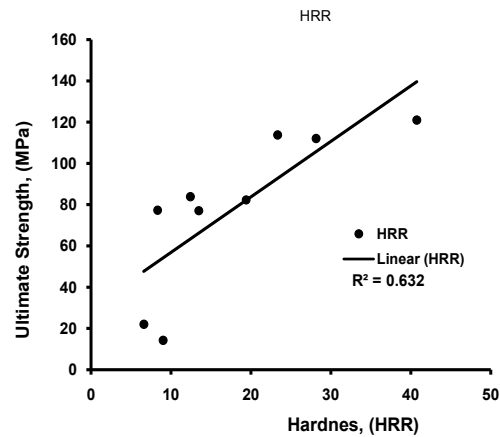


Figure 8: Variation of hardness with ultimate tensile strength

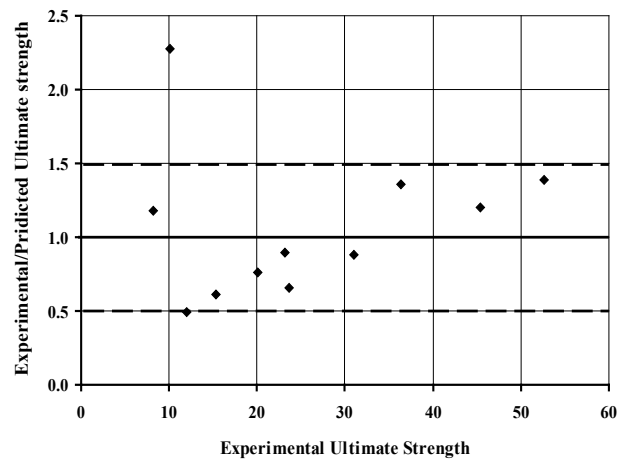


Figure 9: Effectiveness of predicted ultimate strength by model

ANOVA

From the above discussions it is evident that the silica and rubber as filler material and strain rate as test condition has significant effect on ultimate strength. To find out the effect of silica, styrene-butadiene rubber content and strain rate as individual and for their interactions three-way analysis of variance (ANOVA) have been performed. The results are presented in [tables 2](#). Numbers of replications are determined as per the procedure given for ANOVA in statistical book [8]. Three numbers of replicates are selected from the experimental data provided in the Appendix F & G for three-way analysis of variance for tensile strength, randomly. Results shown in [Table 2](#) reveals that the effect of styrene-butadiene rubber seems to be more as compared to the silica content and strain rate on the ultimate strength.

Table2: Result obtained from ANOVA analysis for ultimate tensile strength

S N	Source of Variation	Sum of squares (SS)	DF	Mean-square ratio MS (SS/DF)	Mean-square ratio (MSR)	Min MSR required for Confidence		
						90%	95%	97.5%
1.	Among the rubber (wt%)	8212.89	3	2737.63	524450.50	2.15	2.73	3.28
2.	Among the strain rate	298.39	1	298.39	57163.51	2.77	3.96	5.22
3.	Among the silica (wt%)	3168.58	4	792.15	151752.06	2.02	2.49	2.95
4.	rubber (wt%)- strain rate interaction	39.78	3	13.26	2540.04	2.15	2.73	3.28

5.	strain rate - silica (wt%) interaction	538.04	12	44.84	8589.37	1.64	1.88	2.11
6.	rubber (wt%)- silica (wt%) interaction	36.19	4	9.05	1733.28	2.02	2.49	2.95
7.	rubber (wt%)- strain rate - silica (wt%) interaction	137.21	12	11.43	2190.45	1.64	1.88	2.11
8.	Residual Error	4.18	80	0.05				

PREDICTION OF MECHANICAL PROPERTIES BY ARTIFICIAL NEURAL NETWORK (ANN)

In the present investigation single hidden layered neural network is used in the prediction of mechanical properties of the hybrid composite material. The ANN structure used in the present investigation is shown in [Figure 10](#). Back propagation algorithm is used in training. The training of ANN by back propagation involved three stages: the feed forward of the input training pattern, the calculation and back propagation of the associated errors and the adjustment of the weights. [Figure 11](#) shows the training and testing output of the selected ANN structure. Figures indicate that most of the outputs are very close to the experimental data. The prediction of ultimate strength from hardness value is compared with prediction made by ANN in [table 3](#) and [figure 12](#).

Table 3: Ratio of experimental values to predicted values from the hardness data and ratio obtained from experimental and ANN.

Composition		HRR	σ_u (MPa)			Experimental /Predicted from Hardness	Experimental /Predicted by ANN
Silica (wt %)	Rubber (wt %)		Experimental	Predicted by Hardness	Predicted by ANN		
1.0	0.00	120.17	45.40	37.73	37.99	1.20	1.20
1.0	0.25	112.06	31.04	35.19	34.97	0.88	0.89
1.0	0.50	82.27	23.12	25.83	24.59	0.90	0.94
1.0	1.00	80.26	15.33	25.20	12.60	0.61	1.22
1.0	1.50	14.22	10.15	04.47	11.67	2.27	0.87
2.0	0.00	120.98	35.79	37.99	36.93	0.94	0.97
2.0	0.25	113.77	23.59	35.72	30.23	0.66	0.78
2.0	0.50	83.85	20.12	26.33	18.17	0.76	1.11
2.0	1.00	77.06	11.98	24.20	12.61	0.50	0.95

[Table 3](#) shows that ratio of experimental values to predicted values from the hardness data lies between 0.61 to 2.27 as compared to 0.78 to 1.22 ratio obtained from experimental and ANN. [Figure 12](#) shows that data set except one falls outside the scatter band of 1.0, illustrating the suitability of equation 4.6 to the predict the ultimate tensile strength only from the hardness values.

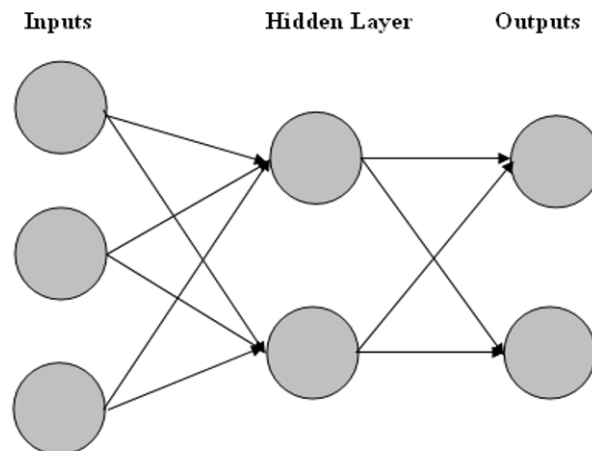


Figure 10: ANN model for tensile strength

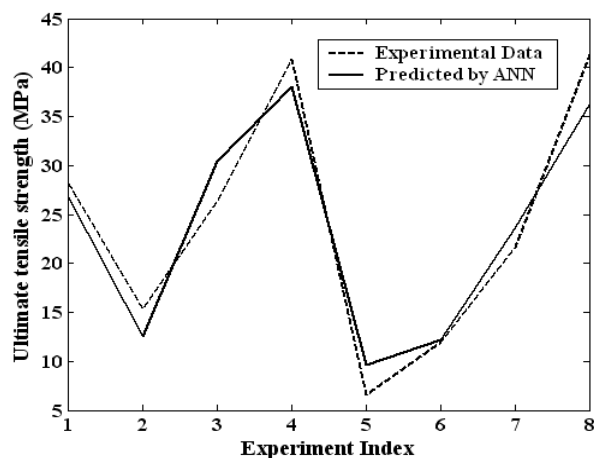


Figure 11: Comparison between Calculated and Target Ultimate Strength for testing data

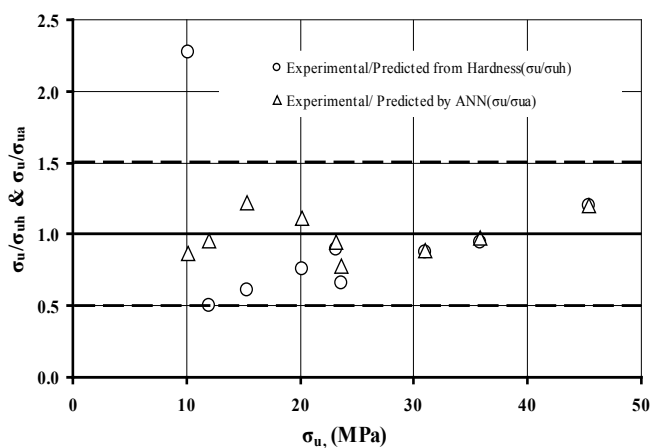


Figure 12: Effectiveness of Predicted ultimate Strength by model and ultimate Strength by ANN

REFERENCES:

- [1] Perminov V. P., Modyanova A. G., Ryabkov Y. I., Sevbo O. A., Gailyunas I. A., Kuchin A. V. Russian J of Applied Chemistry (Translation of Zhurnal Prikladnoi Khimii), 75, 636, 2002.
- [2] Ou, Y., Yang, F., Yu, Z. Z., New conception on the toughness of nylon 6/silica nanocomposite prepared via in situ polymerization. J. Polym. Sci. B: Polym. Phys. 36, 789–795, 1998.
- [3] Wetzel B., Hauptert F., Zhang M. Q., Epoxy nanocomposites with high mechanical and tribological performance. Compos. Sci. Technol. 63, 2055–2067, 2003.
- [4] Bandyopadhyay Abhijit, Bhowmick Anil K, Sarkar Mousumi De., Synthesis and characterization of acrylic rubber/silica hybrid composite prepared by sol gel technique. J. of Applied polymer Sci, vol. 93; pp 2579-2589, 2004.
- [5] Neogi C., Basu S. P., Bhowmick A. K., Analysis of Rubber-Filler Interaction at High Temperature by Using Strain Amplification Factor. Plastics and Rubber Processing and Applications, 12, pp. 147-151, 1989.
- [6] Wang M. J., Effect of Polymer-Filler and Filler-Filler Interactions on Dynamic Properties of Filled Vulcanizates. Rubber Chemistry and Technology, 71, pp. 520-589, 1998.
- [7] Hyung Jin Kim, Sung Wi Koh, Jae Dong Kim and Byung Tak Kim., Materials Science Forum Vols. 544-545 pp 267-270, 2007.
- [8] Lipson and Seth, Text book of Stastical design and analysis of engineering experiments, pp 194-219, 1973.
- [9] Lefebvre J. M., Micromechanics-based modeling of stiffness and yield stress for silica/polymer nanocomposites. International Journal of Solids and Structures, Volume 46, Pages 1716-1726, 2009.

Compression/Shear Response of Honeycomb Core

Michael W. Czabaj, W.R. Tubbs, Alan T. Zehnder,
Mechanical and Aerospace Engineering
Cornell University, Ithaca, NY 14853
atz2@cornell.edu

Barry D. Davidson
Mechanical and Aerospace Engineering
Syracuse University, Syracuse, NY 13244

ABSTRACT

Composite sandwich structures find applications in many aerospace systems due to their lightweight and high strength. However, these structures are susceptible to low energy impact damage. Our studies of the damage resistance and tolerance of honeycomb core sandwich structures shows that the performance of the core plays a key role. Thus we have undertaken a study of the compressive and shear behavior of the aluminum honeycomb cores used in several space systems. The study consists of uniaxial and compression/shear tests of the core. Using a novel ring specimen loaded in compression and torsion, we can load along any line in compression/shear stress space in order to map out the core's yield surface and its evolution. Results from the experiments are used to validate computational models that are part of a larger simulation of the compression after impact strength of honeycomb core composites.

INTRODUCTION

The compression after impact strength of composite honeycomb core structures has been the subject of a great deal of experimental^{1,2}, analytical³ and computational⁴ research. Past modeling approaches to the prediction of CAI strength relied on explicitly prescribing the state of impact damage state as part of the computational model⁵. The response of the underlying core is modeled with a set nonlinear springs. Such approaches limit the models to cases where the damage state is already known. To bypass this limitation we are developing an approach that simulates the impact event and predicts the compression after impact strength.

Work to date indicates that the response of the core must be captured with high fidelity in order to make accurate predictions of damage and residual strength.⁶ Both a continuum model⁷ and an explicit model⁶ in which the core geometry is represented by shell elements are being explored. To validate the explicit model and to provide inputs to the continuum model a series of compression and compression/shear experiments are underway.

MATERIALS AND SAMPLE PREPARATION

All tests were performed using HexWeb® CR-III, 3.2 mm cell size, 5052-H39 aluminum honeycomb core. In all tests the samples are bonded to aluminum blocks using an epoxy based 3M™ AF-555 film adhesive. Prior to cure the honeycomb core was primed using a 3M™ EW-5000 adhesive primer. Two different densities of 25.4 mm thick cores were used; C1: 49.7 kg/m³ and C3: 72.1 kg/m³.

COMPRESSION TESTS

The flatwise tension-compression test seen in [Figure 1](#) was used to measure the tensile and compressive response of the honeycomb s in the thickness direction. The test specimen consisted of 50.8 × 50.8 mm

square honeycomb core bonded to aluminum loading blocks using the AF-555 film adhesive. The specimen deformation measured between the two loading blocks was performed using an MTS LX-500, non-contact laser extensometer. The deformation in the elastic region was measured with the extensometer range set to 2.54 mm, while the large deformation during core crushing was done with the range set to 25.4 mm.

Example data from a tension-compression test of a C1 core are presented in [Figure 2](#). In this test, the specimen was first loaded in tension at a rate of 0.0237 mm/s to a stress level approximately equal to 2.1 MPa. The particular tensile stress level was chosen to prevent debonding between the core and the loading blocks. Next, the loading direction was reversed and the specimen was compressed at the same rate until the peak compressive stress was reached, followed by sudden softening of the material, and core crushing at an approximately constant stress level. Once this stress plateau was reached, the test was halted, and the range of the extensometer switched to 25.4 mm. The compressive loading was next reinitiated and the specimen was crushed to roughly 40% of its initial thickness. Data for full compression tests of cores C1 and C3 core are presented in [Figure 3](#).



Figure 1, Flatwise compression/tension test setup with C1 honeycomb core.

Examining the data in [Figure 2](#), the difference between the tensile and compressive moduli is approximately 0.3 GPa. The measured tensile modulus was approximately 0.1 GPa larger than the theoretically predicted modulus of 1.3 GPa, while the measured compressive modulus was approximately 0.2 GPa smaller than theoretically predicted. The difference between the experimentally measured tensile and compressive moduli can be related to initial cell wall waviness of most core specimens. During tension, the applied load partially straightens the cell walls, and tensile modulus gradually approaches the theoretically predicted value. During compression, however, the cell walls become increasingly distorted, and the elastic compressive response becomes increasingly softer. As the load increases, the cell walls undergo finite lateral deformation, and trigger the onset of wall collapse, resulting in the sudden softening response.

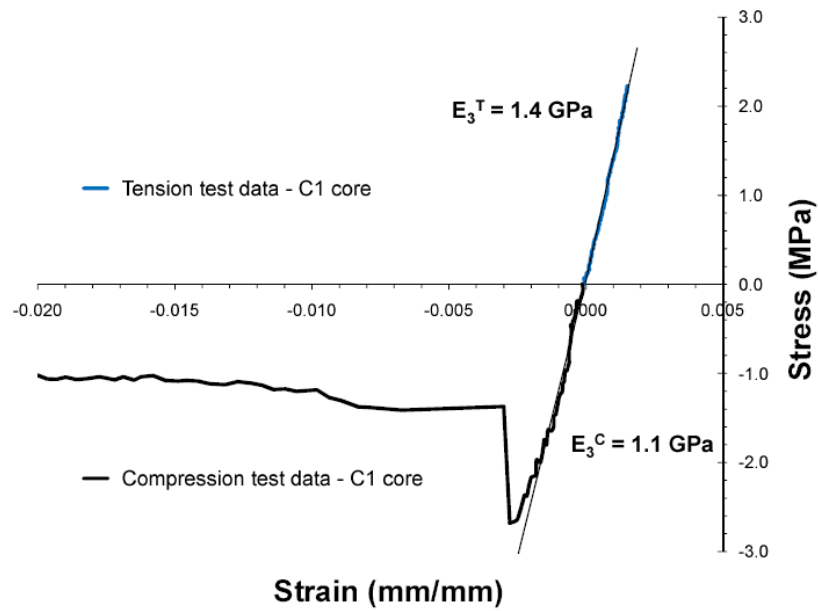


Figure 2, Flatwise tension/compression test data for C1 core.

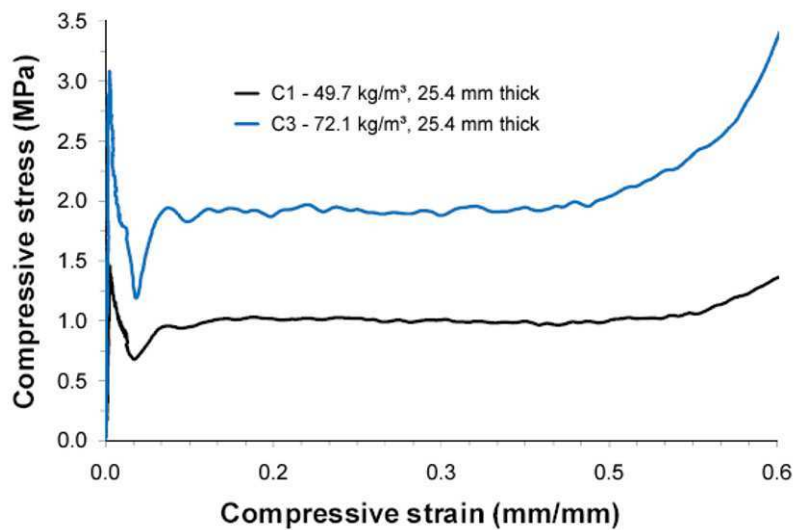


Figure 3, Flatwise compression test data for C1 and C3 cores.

COMPRESSION/SHEAR TESTS WITH RING SAMPLE

In this study a new test was developed using an existing axial-torsion load frame to provide any combination of out-of-plane shear and thickness-wise compression. The test is based on axial/torsional loading of a cylindrical sample of core, shown in [Figure 4](#). The cylinder has inner and outer radii of 50.8 and 63.5 mm, respectively. The specimen geometry was chosen such that when twisted, the ratio of the minimum and maximum values of shear stress across the wall thickness remained near unity, while keeping the specimen wide enough to measure the out-of-plane shear across several cell units. The specimen was then loaded in an axial-torsional load frame. The compression strain was measured using a non-contact,

MTS LX-500, laser extensometer, while rotation was measured using a rotary variable differential transformer (RVDT) built into the axial-torsion load frame system.

In the tests pure shear was achieved by twisting the specimen in rotation control, while simultaneously enforcing zero axial force. The enforcement of zero axial force minimized the tensile stresses that can develop in the honeycomb walls at large angles of rotation. A pure compression test was done in the same way as the previously mentioned flatwise compression test. Tests performed at a fixed ratio of shear to axial stress were performed in rotation and displacement control to ensure test stability in the post yield, softening loading regime. Preliminary experiments in which the shear and axial compliances were measured were used to determine the relative rates of rotation and axial motion needed to attain a given shear to normal stress ratio.

As in the compression tests, deformation localizes in the core during shearing as shown in the sequence given in Figure 5. Repeating such tests for a mix of shear to compressive stress ratios the yield surface in compression/shear is mapped out as shown in Figure 6. Similar to results from other compression/shear experiments⁸ the initial collapse envelope is approximately elliptical, similar to the yield surface of a polycrystalline metal.

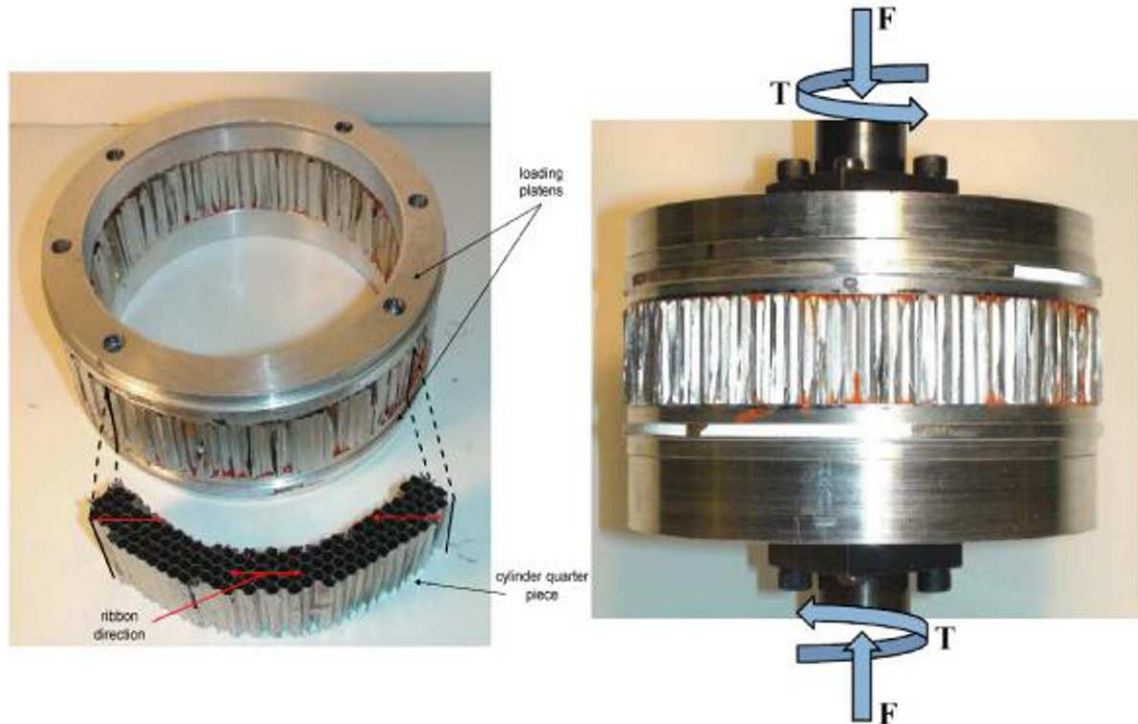


Figure 4, Compression/shear test of honeycomb core

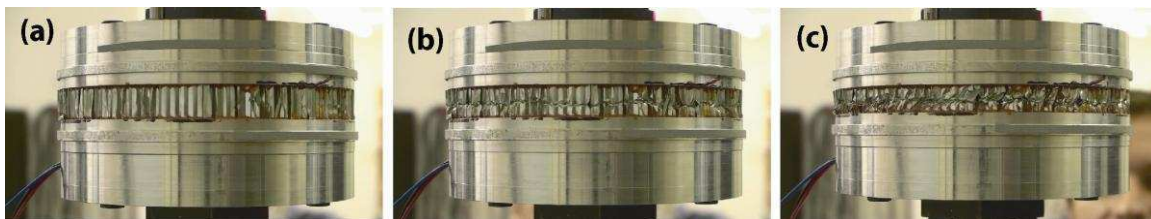


Figure 5, Progression of core deformation during a pure shear test.

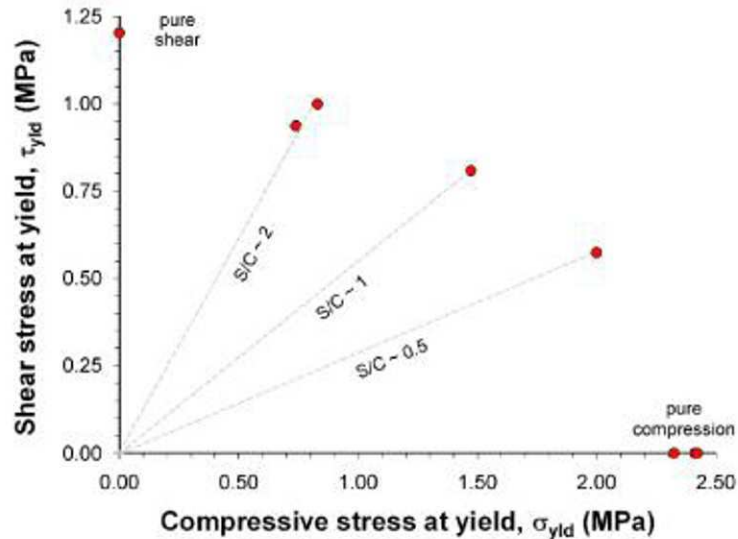


Figure 6, Yield surface for C1 core. S is the ratio of shear stress to the shear yield strength. C is the ratio of compressive stress to compressive yield strength.

SUMMARY

As part of a larger study of the damage due to low energy impact on composite sandwich structures, two studies of the behavior of aluminum honeycomb core have been performed. Results from these tests are being used to provide parameters to a phenomenological, continuum model of the core. The tests are also used to validate explicit representation finite element models of the core based on thin shells with elastic-plastic material behavior and geometric imperfections.

ACKNOWLEDGEMENTS

This study was funded through the NASA Constellation University Institutes Project, under grant NCC3-989 with Claudia Meyer, project manager and by the NASA Exploration Technology Development Program / Advanced Composite Technologies Project, Mark Shuart, Project Manager. Experiments made use of the Shared Experimental Facilities of the Cornell Center for Materials Research, an NSF MRSEC (DMR-0520404).

REFERENCES

- ¹ Nettles, A., Jackson, J., "Compression After Impact Testing of Sandwich Composites for Usage on Expandable Launch Vehicles." *Journal of Composite Materials*, 44, 707-738, (2010).
- ² Moody, C., Vizzini, A.J., "Damage Tolerance of Composite Sandwich Structures." Final Report, Federal Aviation Administration Report, DOT/FAA/AR-99/91, 2000.
- ³ Minguet, P.J., "Model for predicting the behavior of impact-damaged minimum gauge sandwich panels under compression," AIAA-91-1075-CP (1991).
- ⁴ Aminanda, Y., Castanie, B., Barrau, J.J. and Thevenet, P., "Experimental and numerical study of compression after impact of sandwich structures with metallic skins," *Composites Science and Technology*, 69, 50-59 (2009).
- ⁵ Ratcliff, J.G. and Jackson, W.C., "A finite element analysis for predicting the residual compressive strength of impact-damaged sandwich panels," NASA/TM 2008 215341 (2008).

⁶ Michael Czabaj, “Damage and damage tolerance of high temperature composites and sandwich composite structures,” Ph.D. thesis, Cornell University, (2010).

⁷ Xue, Z., and Hutchinson, J.W., “Constitutive model for quasi-static deformation of metallic sandwich cores,” *International Journal for Numerical Methods in Engineering*, 61, 2205-2238, (2004).

⁸ Mohr, D., and Doyoyo, D., “Experimental investigation on the plasticity of hexagonal aluminum honeycomb under multiaxial loading,” *Journal of Applied Mechanics*, 71, 375-385 (2004).

Light Guide Component in Efficiency Enhancement of DSSC

Chi-Hui Chien^{a,*}, Ming-Lang Tsai^a, Chi-Chang Hsieh^b, Yan-Huei Li^a, Ting-Hsuan Su^a,
Fang-I Su^a, Yu-Lin Chung^a, Chang-I Chen^a, Chih-Wei Lin^a

^aDepartment of Mechanical and Electro-Mechanical Engineering
National Sun Yat-Sen University

70, Lien-Hai Road, Kaohsiung 80424, Taiwan ROC

^bDepartment of the Mechanical and Automation Engineering
National Kaohsiung First University of Science and Technology

2, Jhuoyue Road, Nanzih, Kaohsiung 81164, Taiwan ROC

* Corresponding Author, chchien@faculty.nsysu.edu.tw

ABSTRACT

In this study, a light guide component for enhancing light harvesting efficiency of dye-sensitized solar cell (DSSC) was designed and developed through both optical simulated and experimental approaches. The light guide component is capable of being disposed on a photo electrode of DSSC to turn the light toward a dye covered nanoporous TiO₂ film (D-NTF). The optical simulation results show that the light harvesting efficiency of DSSC can be effectively improved and the experimental power conversion efficiency can be enhanced as high as 39.78% for active area of 0.25 cm².

Keywords: light guide component; dye-sensitized solar cell; light harvesting efficiency; power conversion efficiency

1. Introduction

Dye-sensitized solar cells (DSSCs) have been intensively investigated in past few years [1-3], driven by their promises for future, cost-effective, easily mass production. DSSCs were comprised by four key components, which are respectively said photo electrode [4,5], said platinum (Pt) counter electrode [4-7] disposed opposite to the photo electrode, said electrolyte solution [5,6] contained iodide/tri-iodide redox couple between the photo and counter electrodes and said sealing spacer [8,9] for spacing the photo and counter electrodes and sealing the electrolyte solution. In general, the photo electrode was formed by a dye covered nanoporous TiO₂ film (D-NTF) fabricated on a transparent conducting substrate and designated to perform the light-to-electricity operation. When the light illuminates the D-NTF of the photo electrode, the dye will be excited by the light, thereby leading to a fast injection of electrons into the conduction band of TiO₂ and further movement toward the transparent conducting substrate. However, the light also illuminates the sealing spacer, then penetrates the sealing spacer and finally departs from the cell. This means that the light illuminated on the D-NTF could be effectively used. On the contrary,

the light illuminated on the sealing spacer would be wasted, said phenomenon could be strongly observed in grid type DSSCs [10,11]. Lee et al. [10] and Ramasamy et al. [11] used many sealing spacers to separately seal each of the cells, so it could be anticipated that a lot of illuminated light would penetrate the sealing spacers incapable of being used. In other words, the light harvesting efficiency of DSSCs would be enhanced if the light could be turned toward the D-NTF before illuminating the sealing spacer. Therefore, we present a light guide component (LGC) and illustrate how this component turns the light toward the D-NTF and further improves photovoltaic performance of DSSCs.

2. Simulation and Experiment

2.1 LGC Simulation

Figure 1 shows a sketch of the light illuminated on a DSSC. It could be clearly observed that one part of the light directly arrives at the D-NTF of the photo electrode (PE) and absorbed by the dye. Another part of the light penetrates the photo electrode (PE), the sealing spacers (SS) and the counter electrode (CE) in order and finally departs from the cell. This interprets that the light illuminated on the sealing spacer was wasted.

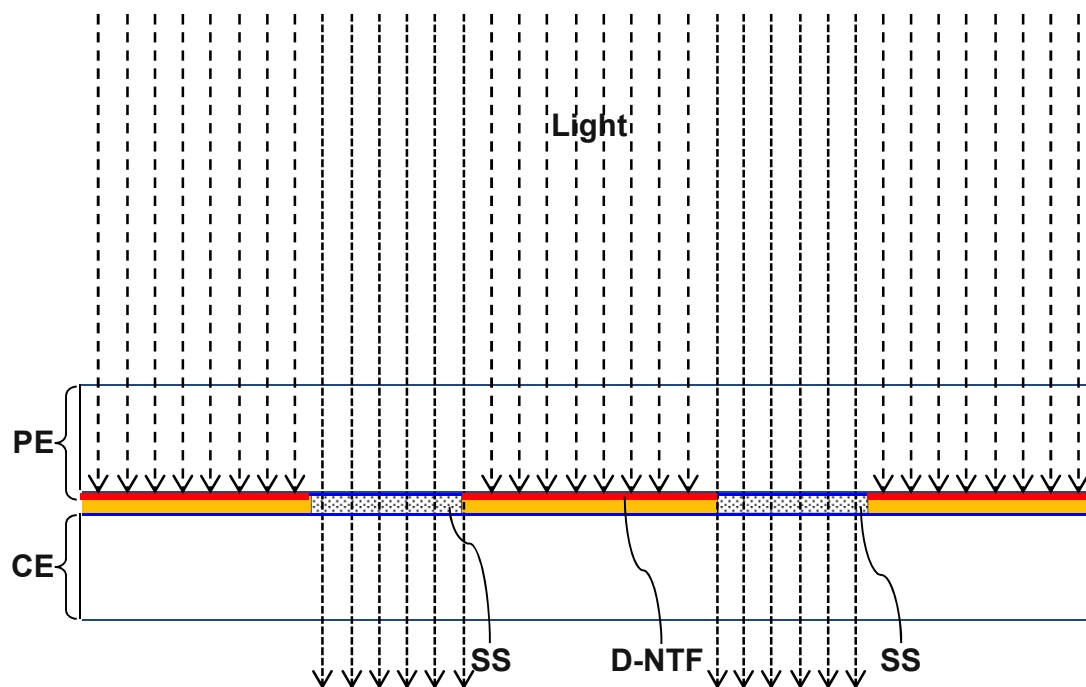


Figure 1: Schematic illustration of the light illuminated on a DSSC.

In order to obtain a high light harvesting efficiency, a light guide component (LGC) made of a transparent medium was proposed to turn the light toward the D-NTF. For a design of the LGC, it is very important to minimize the optical loss in all trajectories of turning the light toward the D-NTF in order to ensure that the light arrived at the D-NTF can achieve a maximum intensity. Therefore, two conditions of the normal incidence and the total internal

reflection (TIR) were applied to the LGC. The normal incidence condition was used to ensure that the light travels from medium 1 into medium 2 with a minimum reflection loss. The TIR condition was used to ensure that the light travels from medium 1 into medium 2 without any transmission loss. According to the above conditions, a suitable LGC structure was proposed as shown in [Figure 2](#).

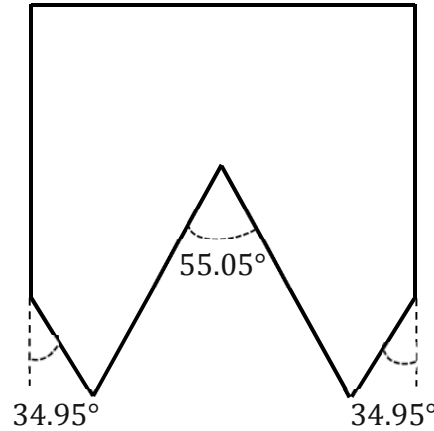


Figure 2: LGC structure.

In order to verify the effect of the LGC for enhancing the light harvesting efficiency, a ray-trace simulation for a DSSC with the LGC was performed. In this study, the LGC was used to turn the light toward the D-NTF of the photo electrode, which means that the analysis of the light harvesting efficiency could be focused at the D-NTF. Therefore, the simulation model for DSSC could be simplified as only the photo electrode. The software TracePro based on Monte-Carlo ray tracing method was applied to computer modeling of the photo electrode (PE) with the LGCs. The simulation model as shown in [Figure 3](#), it was only consider geometrical optics and do not consider diffraction and polarization effects.

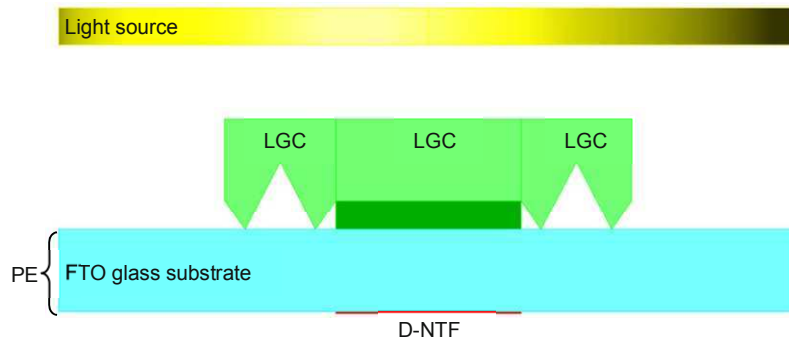


Figure 3: Simulation model for the photo electrode (PE) with the LGCs.

The light source has a wavelength range between 400 nm and 800 nm. The wavelength step was 1 nm, and a ray of 80000 number was randomly generated with a total power of 0.18 W. In general, the photovoltaic performances

of DSSC were measured under one sun illumination of 100 mW/cm^2 and the simulated light generated by the solar simulator illuminates normal to the DSSC. This means that the angular distribution of the light in ray-trace simulation should be set at normal to the DSSC to ensure the simulation work with the same conditions as that in the experiment.

2.2 LGC fabrication

In order to fabricate the LGC, we made choice of acrylic as the material of the LGC. The acrylic has a refractive index of 1.496 at wavelength of 400 nm. Besides, the LGC was defined in a size of 3 mm (width) x 3 mm (height) x 100 mm (length), wherein the width of the LGC is regarded as the width of the sealing spacer. Based on the LGC structure as shown in Figure 2, the LGC mold could be fabricated by using a wire-cut machining method, and furthermore a mirror-like polishing was also applied to the LGC mold. Figure 4 shows the photographs of the LGC mold. It was clearly from this figure that the machining error of the LGC mold was very small.

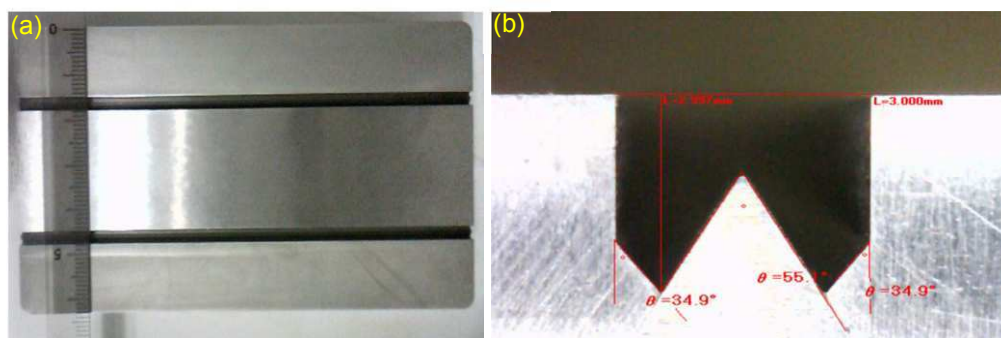


Figure 4: Photographs of the LGC mold viewed from top (a) and in cross-section (b).

An acrylic gel was infused into the LGC mold, and then the LGC mold was disposed within a vacuum chamber to remove the air bubbles inside the gel. Afterword, a glass plate was covered onto the top of the LGC mold to level the acrylic gel. After hardening the acrylic gel, the first removes the glass plate and the second removes the LGC from the mold. In order to meet the area of the D-NTF, the LGC must be cut into several sections as shown in Figure 5.

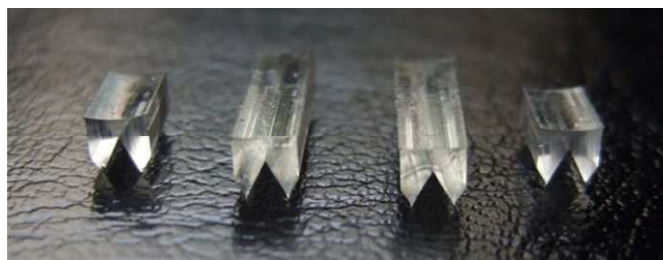


Figure 5: Photograph of the LGCs.

2.3 Fabrication and measurements of DSSC

The photo electrode was fabricated by the procedures described below. First, an acetic solution was prepared by mixing 2 g citric acid, 0.08 mL acetylacetone, 0.2 mL Triton X-100 and 0.2 mL tetrabutyl orthotitanate in 3 mL purified water and stirring for 30 min. Then, a TiO_2 paste was prepared by mixing 1 g TiO_2 nanopowder (P25, Degussa) with the acetic solution and stirring for 1 h. The nanoporous TiO_2 film was obtained by coating the TiO_2 paste on an FTO glass substrate (Hartford Glass Co., USA, fluorine-doped SnO_2 overlayer, sheet resistance: $7 \Omega/\text{sq}$) using a doctor-blade method and then sintered at 450°C for 30 min. After sintering, the thickness of the nanoporous TiO_2 film was about $15 \mu\text{m}$ measured using an Alpha-Step profilometer and the active area was $0.5 \times 0.5 \text{ cm}^2$.

Then the photo electrode was soaked in a dye solution of 0.3 mM N719 dye in ethanol for 24 h at room temperature. The photo electrode and the Pt counter electrode were sandwiched with $60 \mu\text{m}$ thick (before melting) surlyn polymer foil (Solaronix) as a sealing spacer. Sealing was done by keeping the structure in a hot-pressing at 100°C for few seconds. An electrolyte solution consisting of 0.05 M iodine, 0.1 M lithium iodide, 0.5 M 4-tert-butylpyridine (TBP) and 0.3 M 1,2-dimethyl-3-propylimidazolium iodide (DMPII) in 3-methoxy propionitrile (MPN) was introduced into the cell gap to complete the fabrication of DSSC. In order to investigate the performance variation of DSSCs with and without the LGC, four LGCs were disposed on the DSSC as shown in Figure 6. The photovoltaic performances of DSSC were measured using a computer-controlled digital source meter (Keithley, Model: 2400) under one sun illumination of $100 \text{ mW}/\text{cm}^2$ (AM 1.5 simulated light radiation).

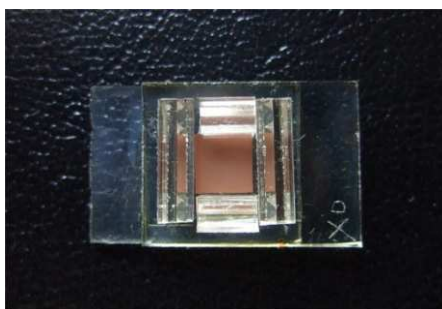


Figure 6: Photograph of DSSC with four LGCs.

3. Results and discussions

3.1 Simulation results

Figure 7 shows the ray tracing of the photo electrode (PE) with the LGCs, it could be observed that the light illuminated normal to the DSSC could be effectively turned toward the D-NTF via the LGCs. Figure 8 shows the simulation results of the photo electrodes with and without the LGC. As shown in Figure 8a, the photo electrode without the LGC has a total flux of 13.511 mW in the D-NTF with an active area of 0.25 cm^2 . The result as shown in Figure 8b was the case of the photo electrode with one LGC, it could be found that the total flux in the D-NTF was

improved to 16.678 mW as an increase in light harvesting efficiency by 23.44%. When the amount of the LGC was increased to two and four respectively, the total flux in the D-NTF could be improved to 19.158 mW and 26.126 mW respectively as shown in [Figures 8c and 8d](#). This also means that the light harvesting efficiency could be increased by 41.8% in case of two LGCs and 93.37% in case of four LGCs.

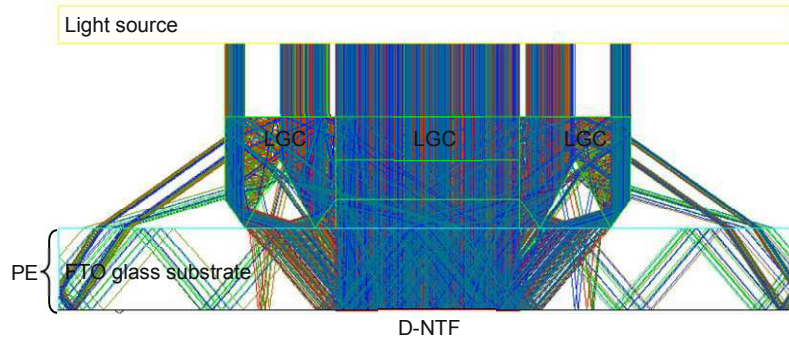


Figure 7: Ray tracing of the photo electrode (PE) with the LGCs.

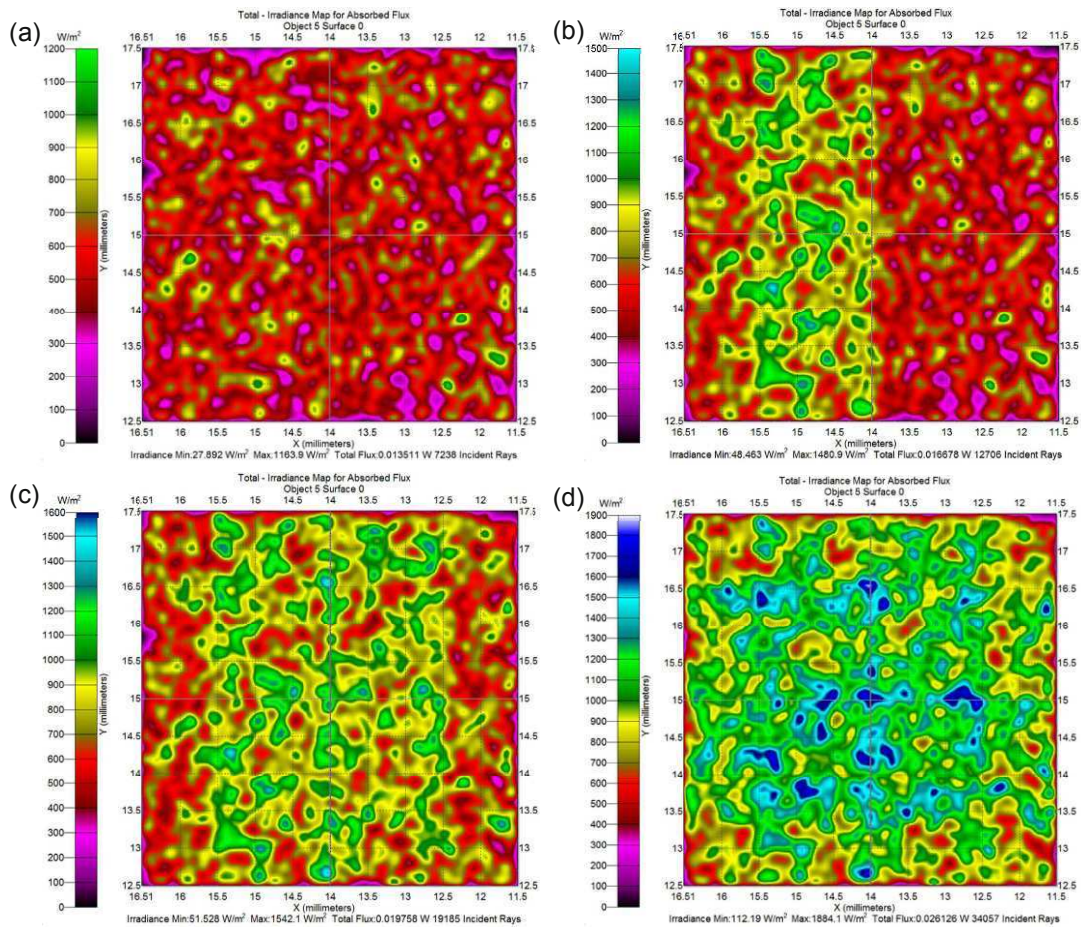


Figure 8: Simulation results of the photo electrode without LGC (a), with 1 LGC (b), with 2 LGCs (c), and with 4 LGCs (d).

3.2 Photovoltaic performances of DSSC with LGC

Figure 9 shows the photographs of DSSC with and without the LGC under one sun illumination of 100 mW/cm^2 (AM 1.5). Photovoltaic performances of DSSCs with and without the LGC were presented in Table 1 and the photocurrent density versus voltage characteristic curves were shown in Figure 10. As the results, the DSSC without the LGC has an open-circuit voltage (V_{oc}) of 0.685 V, short-circuit current density (J_{sc}) of 6.90 mA/cm^2 , fill factor (FF) of 0.591, and power conversion efficiency (η) of 2.79%. In the case of the DSSC with one LGC, J_{sc} and η were improved to 8.04 mA/cm^2 and 3.16% respectively, as J_{sc} increased by 16.52% and η increased by 13.26%. In other case of the DSSC with two LGCs, J_{sc} and η were improved to 9.53 mA/cm^2 and 3.49% respectively, as J_{sc} increased by 38.12% and η increased by 25.09%. When the amount of the LGC was increased to four, J_{sc} and η were improved as high as 10.83 mA/cm^2 and 3.9% respectively, as J_{sc} increased by 56.96% and η increased by 39.78%. In comparison to the simulation work, it could be found that the light harvesting efficiency increases as the photocurrent density increases and the power conversion efficiency increases. It was also demonstrated that the improvement of light harvesting efficiency strongly affect the photocurrent density of the DSSC.

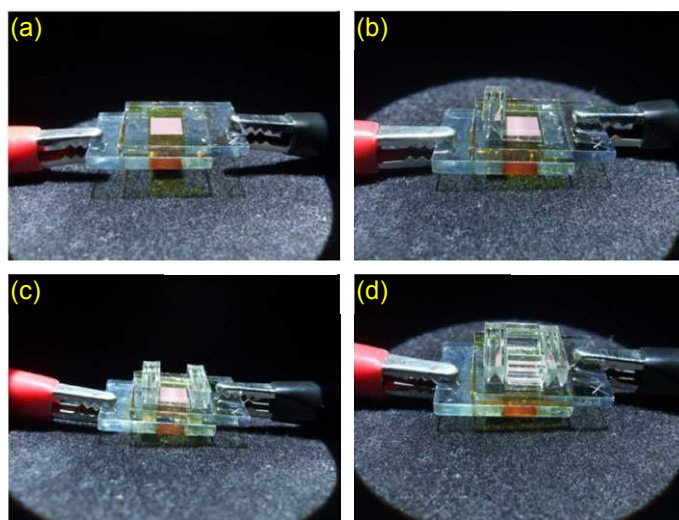


Figure 9: Photographs of DSSC without LGC (a), with 1 LGC (b), with 2 LGCs (c), and with 4 LGCs (d). Under one sun illumination of 100 mW/cm^2 (AM 1.5).

Table 1: Photovoltaic performances of DSSCs with and without LGC.

DSSCs	J_{sc} (mA/cm^2)	V_{oc} (V)	FF	η (%)
without LGC	6.90	0.685	0.591	2.79
with 1 LGC	8.04	0.676	0.581	3.16
with 2 LGCs	9.53	0.687	0.533	3.49
with 4 LGCs	10.83	0.723	0.498	3.90

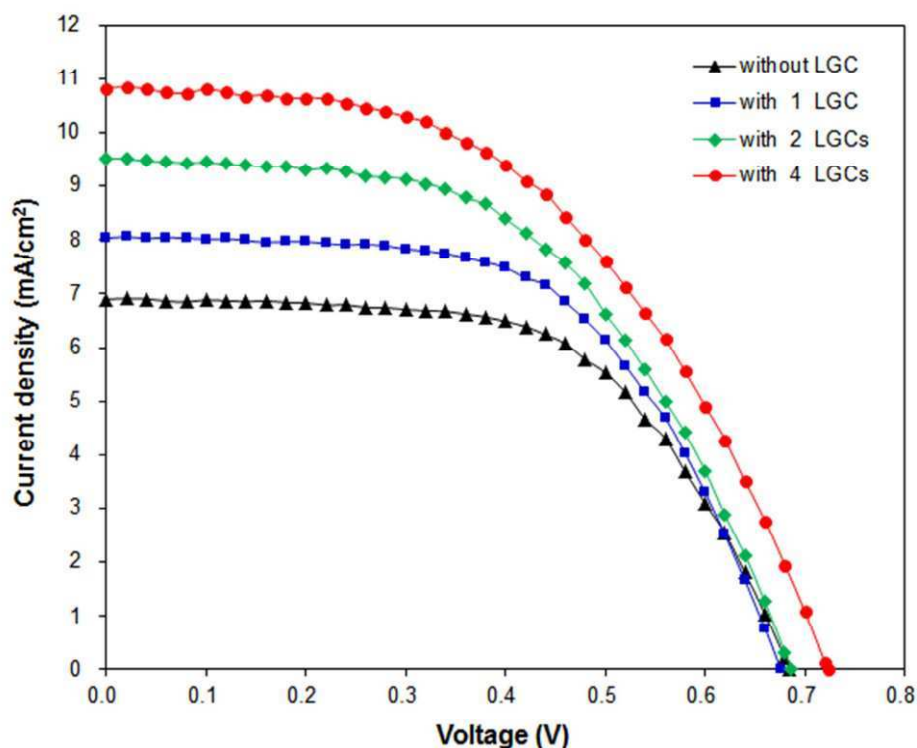


Figure 10: Photocurrent density-voltage curves of DSSC without LGC (\blacktriangle), with 1 LGC (\blacksquare), with 2 LGCs (\blacklozenge), and with 4 LGCs (\bullet).

4. Conclusion

We have presented a comparison of DSSCs with and without the light guide component (LGC) in simulated and experimental works. The results show that the LGC could effectively turn the light toward the dye covered nanoporous TiO_2 film (D-NTF) of the photo electrode and enhance the light harvesting efficiency, thereby improving the photocurrent density and the power conversion efficiency of DSSCs.

5. Acknowledgements

This study is sponsored by the National Science Council of Taiwan, R.O.C. (Grants No. NSC 99-2221-E-110-020).

6. References

- [1] McConnell, R. D., Assessment of the dye-sensitized solar cell, *Renewable and Sustainable Energy Reviews*, Vol. 6, Iss. 3, pp. 273-295, 2002.
- [2] Marsh, G., Can dye sensitised cells deliver low-cost PV?, *Renewable Energy Focus*, Vol. 9, Iss. 5, pp. 58-62, 2008.
- [3] Wang, P., Klein, C., Humphry-Baker, R., Zakeeruddin, S. M., and Grätzel, M., Stable 8% efficient nanocrystalline dye-sensitized solar cell based on an electrolyte of low volatility, *Applied Physics Letters*, Vol.

86, Iss. 12, 123508, 2005.

- [4] Oda, T., Tanaka, S., and Hayase, S., Differences in characteristics of dye-sensitized solar cells containing acetonitrile and ionic liquid-based electrolytes studied using a novel model, *Solar Energy Materials & Solar Cells*, Vol. 90, Iss. 16, pp. 2696-2709, 2006.
- [5] Hauch, A. and Georg, A., Diffusion in the electrolyte and charge-transfer reaction at the platinum electrode in dye-sensitized solar cells, *Electrochimica Acta*, Vol. 46, Iss. 22, pp. 3457-3466, 2001.
- [6] Bay, L., West, K., Winther-Jensen, B., and Jacobsen, T., Electrochemical reaction rates in a dye-sensitized solar cell—the iodide/tri-iodide redox system, *Solar Energy Materials & Solar Cells*, Vol. 90, Iss. 3, pp. 341-351, 2006.
- [7] Fang, X., Ma, T., Guan, G., Akiyama, M., Kita, T., and Abe, E., Effect of the thickness of the Pt film coated on a counter electrode on the performance of a dye-sensitized solar cell, *Journal of Electroanalytical Chemistry*, Vol. 570, Iss. 2, pp. 257-263, 2004.
- [8] Okada, K., Matsui, H., Kawashima, T., Ezure, T., and Tanabe, N., 100mm × 100mm large-sized dye sensitized solar cells, *Journal of Photochemistry and Photobiology A: Chemistry*, Vol. 164, Iss. 1-3, pp. 193-198, 2004.
- [9] Kubo, W., Sakamoto, A., Kitamura, T., Wada, Y., and Yanagida, S., Dye-sensitized solar cells: improvement of spectral response by tandem structure, *Journal of Photochemistry and Photobiology A: Chemistry*, Vol. 164, Iss. 1-3, pp. 33-39, 2004.
- [10] Lee, W. J., Ramasamy, E., Lee, D. Y., and Song, J. S., Grid type dye-sensitized solar cell module with carbon counter electrode, *Journal of Photochemistry and Photobiology A: Chemistry*, Vol. 194, Iss. 1, pp. 27-30, 2008.
- [11] Ramasamy, E., Lee, W. J., Lee, D. Y., and Song, J. S., Portable, parallel grid dye-sensitized solar cell module prepared by screen printing, *Journal of Power Sources*, Vol. 165, Iss. 1, pp. 446-449, 2007.

Sign Support Structures Tested by means of Guided Waves

Xuan “Peter” Zhu¹, Piervincenzo Rizzo^{1,*}, Jerry Bruck²

¹ University of Pittsburgh, Department of Civil and Environmental Engineering, Pittsburgh, PA, USA

*Corresponding Author: 942 Benedum Hall, 3700 O’Hara St., Pittsburgh, PA, 15261, Tel. (412) 624-9575;

E-mail pir3@pitt.edu

² Pennsylvania Department of Transportation, Clearfield, PA, USA

ABSTRACT

In the last few years the use of guided ultrasonic waves (GUWs) for the health monitoring of engineering structures increased rapidly, with the most recent studies focusing on the application of GUWs to complex structures or to simple structures under varying environmental conditions. Monitoring complex structures is challenging as reflections, scattering, and mode conversion arise. In addition, sensitivity to temperature and surface wetting can degrade the performance of a GUW-based structural health monitoring system. This paper presents the results of an experimental investigation where GUWs were used for the health monitoring of a truss, that was part of a highway variable message structure removed from service. The monitoring strategy proposed here combines the advantages of GUWs with the extraction of defect-sensitive features to perform a multivariate diagnosis of damage. The effectiveness of the proposed approach was tested by monitoring the propagation of waves along one of the main chords of the truss and detecting the presence of two artificial cracks located around the welds that join two diagonal angular members to the chord.

1. INTRODUCTION

Sign and variable message support structures are ubiquitous in any Nation road transportation system. For they contain welds, these structures are prone to damage due to defects at both welds’ surface and subsurface. In truss structures where weld is used to connect diagonal members to the chords, cracks are usually found propagating within the leg of a fillet weld or at the toe. Depending upon the amount of time the cracks have to grow, they can propagate in the main supporting member and lead to damage, which ultimately leads to faults. In the United States, in-service sign support structures are inspected using visual inspection and when indications of possible damage are identified conventional nondestructive evaluation methods such as dye penetrants, magnetic particles, or ultrasonic testing are employed [1].

This paper describes a method based on Guided Ultrasonic Waves (GUWs) to detect cracks in sign support structures. The approach exploits the waveguide geometry that most of the members composing the structure have. The advantage of GUW inspection/monitoring is the capability to probe long lengths, locating cracks and notches from a few monitoring points, while providing full coverage of the pipe’s cross-section [2-7]. The work presented here extends that of [8] and presents the results of an experimental investigation on the use of GUWs to detect two notches localized at the welded joint of a dismantled overhead sign structure truss. An array of eleven Lead Zirconate Titanate (PZT) transducers was attached to the

structure. Each transducer acted either as an actuator or receiver, and it was automatically controlled via a National Instruments-PXI running under LabView. Statistical signal features and damage indexes as introduced by Rizzo and co-authors [9-12], were applied to the health monitoring of a welded joint. The algorithm and the weld geometry being investigated are different from the ones proposed recently for the inspection of welds [13-16]. Indeed, the inspection/monitoring scheme described here utilized a set of defect-sensitive features to construct a damage index vector that represented the input vector of an outlier analysis (OA) algorithm. OA is a novelty detection method that establishes whether a new configuration of a given system is discordant or inconsistent from the baseline configuration which consists of an existing set of data or patterns that describe the normal operative conditions [17].

In the present paper it is demonstrated that the method is effective to detect the onset and growth of damage and to provide an indirect insight about the location of damage. The novel contribution of this study is the application of the GUWs and the associated OA algorithm to a complex structure such as a truss. The role of the transducers' locations on the performance of the signal processing constitute another contribution of the study.

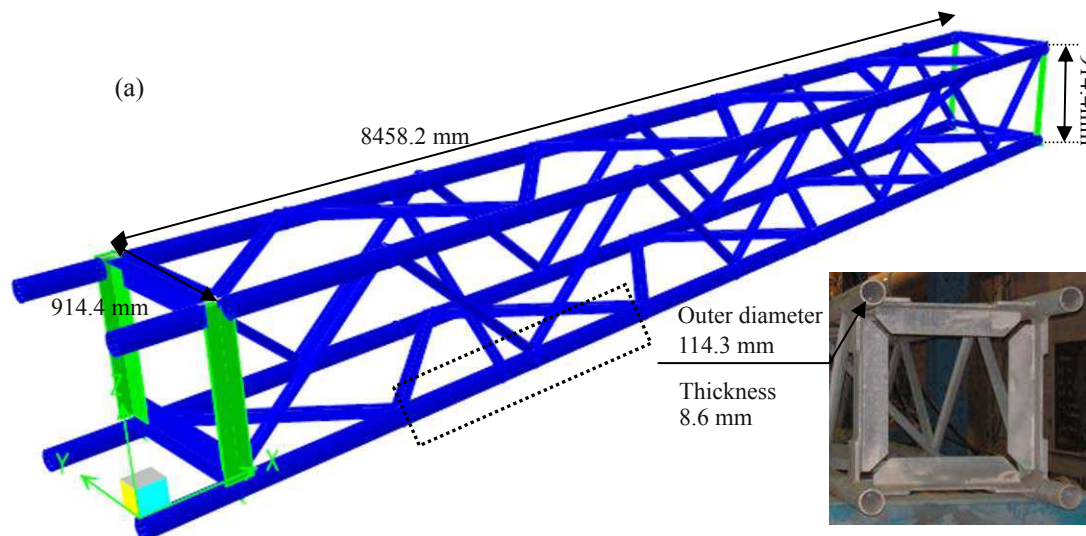


Figure 1 - (a) 3-D rendering of the tested truss. (b) Photo of the side view.

2. EXPERIMENTAL SETUP

The tested truss was part of a variable message support structure located in Pennsylvania, USA [1,18]. The center to center bearing span of the original truss was 17.4 m, with the bearings located on the vertical support columns. The chord is made from ASTM A-53 steel. The scheme and the dimensions of the truss are presented in Figs. 1a and 1b.

Eleven PKI-502-Navy type II PZT transducers from Piezo-Kinetics were employed to monitor the portion of the truss boxed in Fig. 1a. They were attached to the structure at the positions shown in Fig. 2a. For convenience, the transducers are sequentially identified as S0, S1, ..., S10. A National Instruments PXI unit running under LabView, integrated with a reed relay matrix switch module PXI 2530, and combined with TB 2643 and SCB 264X as terminal block, was employed for signal generation, detection, and acquisition. Guided waves were excited using a 5-cycle 10 V peak-to-peak toneburst, modulated with a Gaussian window.

The detected signals were amplified 20-fold by a linear amplifier, sampled at 10 MHz, averaged 10 times to increase the signal-to-noise ratio, and stored for post-processing analysis. A LabView program was designed *in-house* to operate the

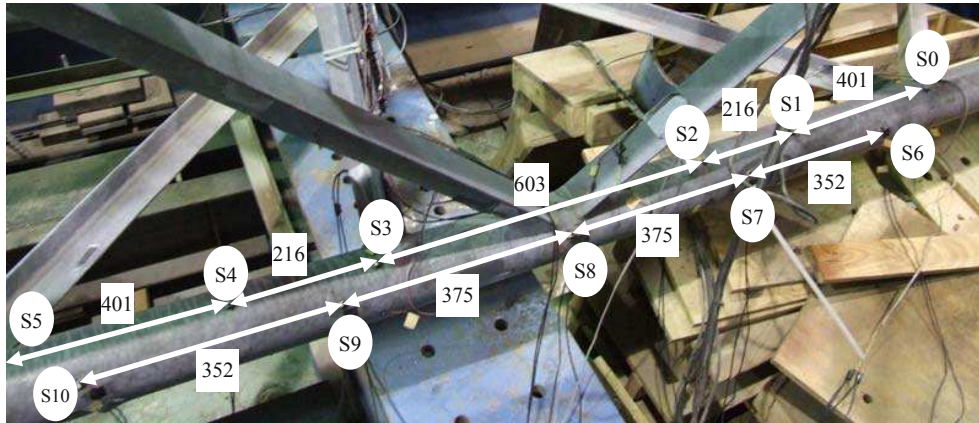


Figure 2 - Location and relative distances of the transducers' array. Dimensions are expressed in mm.

switch so that every PZT could act as a transmitter or as a receiver. For instance, when PZT S0 was transmitting the toneburst, S1-S10 acted as sensors. Then PZT S1 was switched into an actuator and PZTs S0, S2-S10 acted as receivers. The operation was repeated for every PZT. To simulate steady-state vibrations induced by wind or traffic-induced gusts, a 1 Hz sinusoidal cyclic load was induced onto the structure. The loading setup consisted of a 1290 mm-long steel beam that distributed over two joints the force generated by a hydraulic actuator. The load was cycled from 8.9 kN to 125 kN, resulting in a load range of 116 kN. Following every few thousand cycles the steady-state loading was paused and a static load of 66.7 kN was applied.

To investigate the capability of GUWs to detect crack initiation and growth, two artificial notches were machined and progressively increased in size using a Dremel MultiPro machine. The first defect was devised near the weld toe at one of the diagonal members connected to the portion of the chord under monitoring. The position and orientation of the notch are shown in Fig. 3a. While the dynamic load was paused, the size of the crack was measured, ultrasonic data from the PZTs were collected, and the notch size was increased. The load history of the crack, i.e. the crack size as a function of the number of cycles, is presented in Fig. 3b. The area of the crack is approximately the length of the notch along the surface multiplied by the depth. The dots in Fig. 3b indicate the moment at which the crack size was measured. Ultrasonic measurements were also taken during the active cyclic loading. A total of 192 acquisitions associated with the presence of this first notch only were taken. The acquisition number as a function of the number of load cycles is superimposed in Fig. 3b. It should be observed that the loading after 40,000 cycles had a limited effect on the crack growth. The modest scatter of the crack area value above 50,000 cycles is likely related to the variability of the manual measurement.

The second crack was devised near the weld toe of the other diagonal member concurring at the same joint. Similarly to Test 1, the crack was progressively machined and its position and orientation are shown in Fig. 3c. The load history of the crack is presented in Fig. 3b. As Test 2 followed Test 1, the cycle number count associated to Test 2 is considered starting at cycle 180,001. During the first 150,000 load cycles (cycles' range 180,001-330,000) the notch size was increased manually. During this range the 1 Hz sinusoidal load spanned from 8.9 kN to 151.2 kN. Following every 5,000 cycles the dynamic loading was paused and a static load of 80 kN was applied. Under this constant load, the size of the crack was measured, data from the PZTs were collected, and damage size was increased. The circles in Fig. 3b indicate the moment at which the crack size was measured. Measurements were also taken during the active cyclic loading. A total of 124 acquisitions were taken.

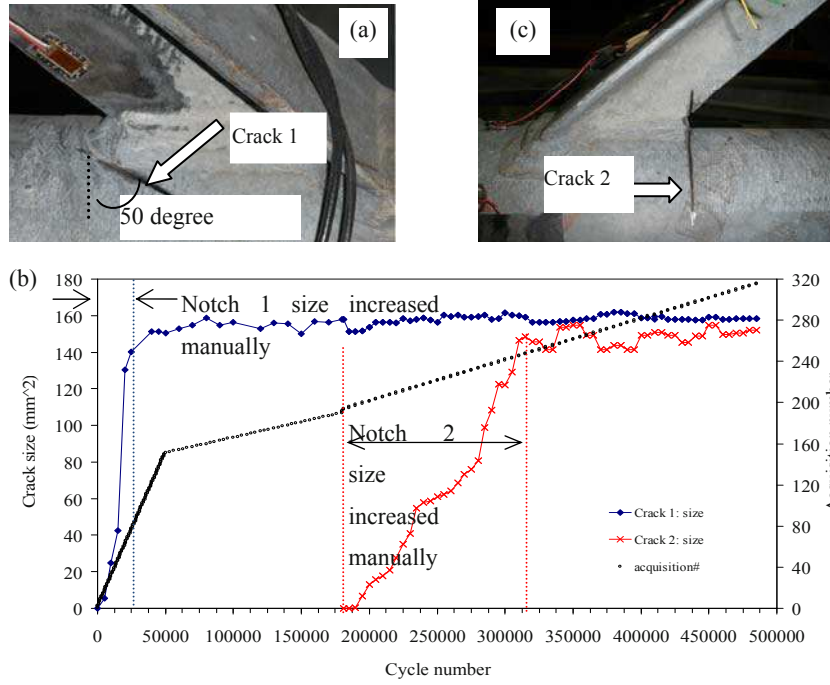


Figure 3 (a) Close-up view of the first notch machined along the weld between the chord and one angular diagonal member. (b) Crack size and acquisition number as a function of cycle loading number. The vertical lines representing the interval during which the size of the cracks was increased by using a Dremel Pro machine. (c) Close-up view of the second notch machined along the weld between the chord and one angular diagonal member.

3. SIGNAL PROCESSING ALGORITHM

Among all the actuator-sensor pairs activated by the NI-switch, only a subset of waveform paths were selected in the study presented here. This selection considered those paths where the transducers were the farthest ($S0 \Rightarrow S5$), or those paths that were expected to be affected by one crack only ($S0 \Rightarrow S8$, $S5 \Rightarrow S8$) or unaffected at all ($S5 \Rightarrow S4$). The first step of the damage detection algorithm was to retain the portion of the signal containing the corresponding to the first three or four wave packets observed at each detected baseline waveform. Such a strategy aimed at investigating the effect of damage on the fastest mode and at neglecting the contribution of the slow modes. Following the strategy adopted in previous studies, statistical features were extracted from the time-windowed waveforms. Here maximum (max) amplitude, peak-to-peak (ppk) amplitude, variance (var), root mean square (rms), kurtosis (krt), crest factor (cf), and k-factor (kf) were selected.

The next step of the algorithm was to compute a Damage Index (D.I.) defined as the ratio between a certain statistical feature $F_{a \Rightarrow b}$ and the same feature $F_{a \Rightarrow d}$:

$$D.I._{ab/ad} = \frac{F_{a \Rightarrow b}}{F_{a \Rightarrow d}} \quad (1)$$

where subscripts a , b , or c identify one of the eleven PZTs. The denominator was introduced to normalize the feature associated with waveform path $a \Rightarrow b$ with respect to the wave path that was expected not to be affected by the presence of damage. In the context of this study, the aim was to mitigate or eliminate any operational disturbance that might have affected the actuators. The D.I.s were then used to feed an unsupervised learning algorithm, based on the multivariate OA. An outlier is a datum that appears inconsistent with the baseline, i.e. a set of data that describes the normal condition of the structure under investigation. A new datum is an outlier if the corresponding value of the Mahalanobis Squared Distance

(MSD) D_ζ , calculated as:

$$D_\zeta = (\{x_\zeta\} - \{\bar{x}\})^T \cdot [K]^{-1} \cdot (\{x_\zeta\} - \{\bar{x}\}) \quad (2),$$

falls above a set threshold.

In Equation (2), where $\{x_\zeta\}$ is the potential outlier vector, $\{\bar{x}\}$ is the mean vector of the baseline, $[K]$ is the covariance matrix of the baseline, and T symbolizes the transpose operation. Both vectors $\{x_\zeta\}$ and $\{\bar{x}\}$ are p -dimensional, whereas $[K]$ is a square matrix of the order p . In the present study, the baseline was computed from the first 18 time histories that according to Fig. 3b were collected within the first 5,000 cycles. Once the values of D_ζ of the baseline distribution were determined, the threshold value was taken as the usual value of 3σ , equal to 99.73% of the Gaussian confidence limit.

4. EXPERIMENTAL RESULTS

The MSD for each measurements associated with the onset and growth of the defects was computed. Figure 4 shows the results of the single combination of the 7-dimensional vector formed by the statistical features applied to the following features' ratios: $S9 \Rightarrow S6/S9 \Rightarrow S8$, $S9 \Rightarrow S1/S9 \Rightarrow S8$, $S5 \Rightarrow S6/S5 \Rightarrow S4$, $S5 \Rightarrow S1/S5 \Rightarrow S4$, $S0 \Rightarrow S4/S0 \Rightarrow S2$, $S0 \Rightarrow S5/S0 \Rightarrow S1$, $S0 \Rightarrow S4/S0 \Rightarrow S1$, and $S5 \Rightarrow S0/S5 \Rightarrow S4$ against cycle number respectively. As the abscissas range from 0 to 480,000, the plots present the results associated with both Test 1 (0 – 180,000) and Test 2 (180,001 - 380,000). It is evident that certain waveform paths outperform other paths in terms of crack growth detection. For figures (a), (b), (c) and (d), the MSD values increased during the first 180,000 cycles and stay relatively constant from 180,000 to 485,000. For instance, the wave path $S5 \Rightarrow S6/S5 \Rightarrow S4$ increased dramatically at the first 25,000 cycles in which crack 1 was artificially increased, and then remained constant as the second crack was 'shadowed' by the welding joints. In Figs. 4e, 4f and 4g an increasing trend could be observed from 180,000 to 330,000 cycles, which suggests the crack growth along this period. Thus, different behaviors of one PZT wave path in different tests and of different PZT wave path in same test suggest the possibility of crack growth detection and crack localization.

It must be remarked that the cluster of data observed in Figs. 4a, 4b, and 4c and located between 295,000 and 340,000 cycles are related to an accidental connection loss that occurred to sensors 6, 7, and 8. After the connection was re-established a slight shift of MSD values is observed.

5. DISCUSSION and CONCLUSIONS

This paper presents a crack detection technique for truss welded joints using low-cost, non invasive PZT transducers. Specifically, the study focused on the detection of the onset and growth of cracks induced on the weld fillet of a truss' joint. The technique is based on the propagation and detection of ultrasonic guided waves processed through a multivariate analysis. Ultrasonic waves were generated through a PZT-wafer connected to a NI-PXI, used to excite a sinusoidal-modulated toneburst. The propagating waves, detected by identical PZT-wafer sensors, were digitized through the same NI-PXI. An array of eleven PZTs was used. The PZTs were used in actuator-sensor pair mode and the performance of several pairs in terms of damage detection sensitivity was investigated. The time waveforms were processed to generate a set of relevant damage sensitive features used to construct a multi-dimensional damage index. The damage index was fed to an unsupervised learning algorithm, aimed at detecting anomalous conditions of the structure and in particular the presence of cracks around welded joints that are, according to owners and inspectors, the most critical part of sign support structures.

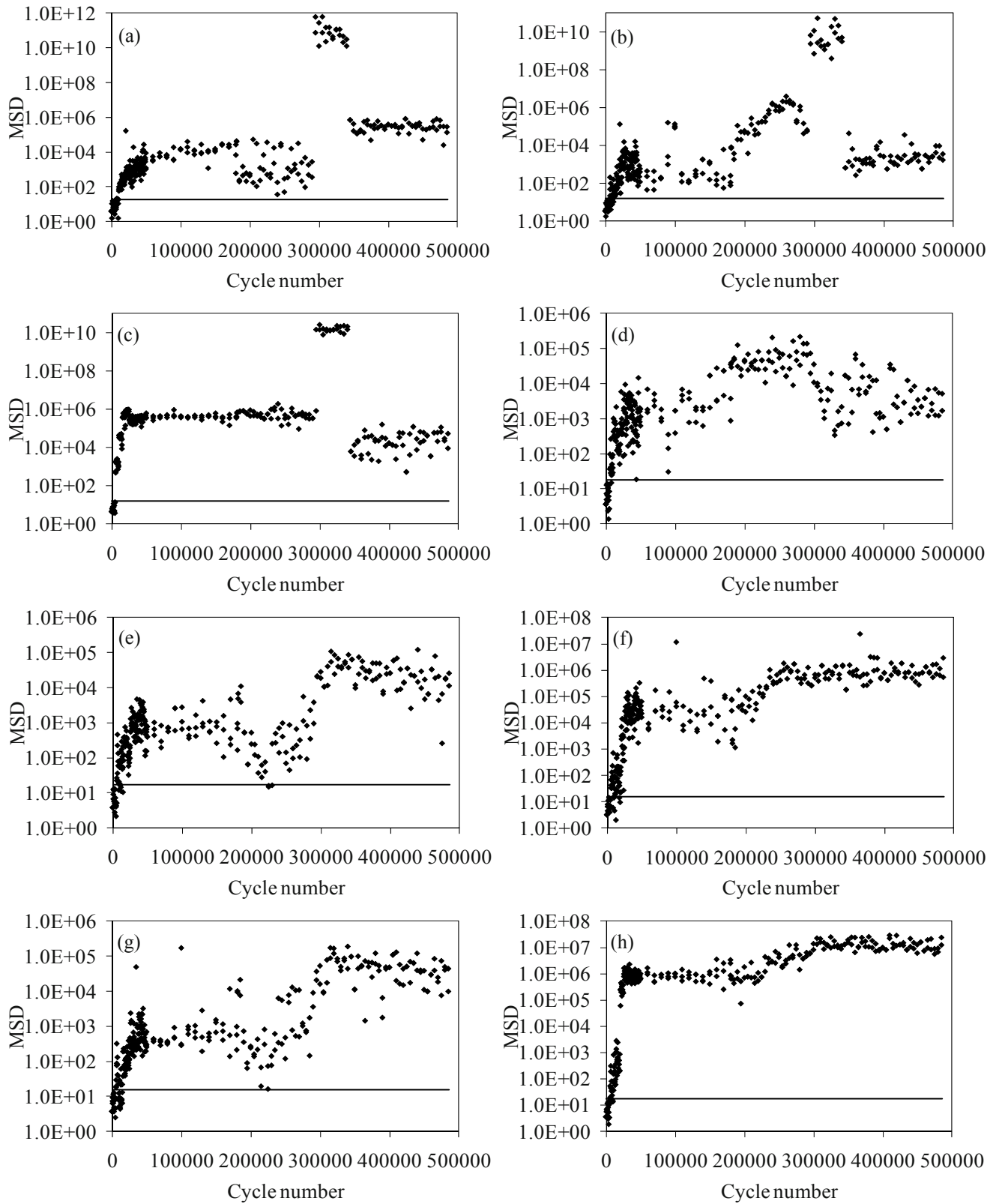


Figure 4 - Mahalanobis squared distances as a function of the measurement number for the actuator-sensor pairs considering all 7 features: (a) $S6 \Rightarrow S9/S6 \Rightarrow S7$; (b) $S6 \Rightarrow S8/S6 \Rightarrow S7$; (c) $S5 \Rightarrow S6/S5 \Rightarrow S4$; (d) $S5 \Rightarrow S1/S5 \Rightarrow S4$; (e) $S0 \Rightarrow S4/S0 \Rightarrow S2$; (f) $S0 \Rightarrow S5/S0 \Rightarrow S1$; (g) $S0 \Rightarrow S4/S0 \Rightarrow S1$; (h) $S5 \Rightarrow S0/S5 \Rightarrow S4$.

It was shown that by exploiting the response of the Mahalanobis squared distance, it is possible to assess qualitatively the defect growth. By comparing the performance of the multivariate analysis for the detection of two different defects, it was found that the optimal wave paths are dependent upon the position of damage with respect to the actuator-sensor pair and the orientation of the crack with respect to the waves' direction of propagation. This can be exploited such that the proposed approach not only serves for damage detection and damage growth assessment, but it serves as damage location as well.

It is believed that the health monitoring strategy presented here can be extended to other sign support structures provided the geometry of the waveguides forming the structure are known, and therefore the dispersive behavior of the guided waves can be predicted. An ongoing study is evaluating the data collected from the field and associated to two sign supported structures.

It must be remarked that, as sign support structures can be very large, any coherent strategy for instrumenting this type of structure must account for a tradeoff between full coverage and reasonable number of transducers. The outcomes from this paper seem to suggest that for the type of structure under consideration as few as five transducers, namely S0, S5, S8, S4, and S1 (the latter two being used for *normalization* purposes) are sufficient to monitor a joint with two concurrent members. It might be argued that similar configuration can be used for other geometries.

ACKNOWLEDGEMENTS

This research was supported by the Pennsylvania Department of Transportation under contract 10601-PIT 008. The authors are grateful to Mr. Mahdi Tajari for providing Fig. 1a and to Dr. K. Harries for useful technical comments and discussion in the preparation of the loading setup.

REFERENCES

1. Rizzo, P., and Zhu, X. (2010). *Sensing Technology for Damage Assessment of Sign Supports and Cantilever Poles*, Final Report # FHWA-PA-2010-010-PIT008.
2. J. J. Ditri, Utilization of guided elastic waves for the characterization of circumferential cracks in hollow cylinders, *Journal of the Acoustical Society of America* 96 (1994) 3769-3775.
3. H. Kwun, S.Y. Kim, G.M. Light, Improving Guided Wave Testing of Pipelines with Mechanical Attachments, *Materials Evaluation* 68(8) (2010) 927-932.
4. J. L. Rose, D. Jiao, and J. Spanner, Ultrasonic guided wave NDE for piping, *Materials Evaluation* 54 (1996) pp 1310–1313.
5. M. Lowe, D. Alleyne, P. Cawley, The mode conversion of a guided wave by a part-circumferential notch in a pipe, *Journal of Applied Mechanics* 65 (1998) 649–656.
6. D. Alleyne, M. Lowe, P. Cawley, The reflection of guided waves from circumferential notches in pipes, *Journal of Applied Mechanics* 65 (1998) 635–641.
7. W.B. Na, T. Kundu, Underwater pipeline inspection using guided waves, *Journal of Pressure Vessel Technology* 124(2) (2002) 196-201.
8. X. Zhu, P. Rizzo, A. Marzani, J. Bruck, Ultrasonic Guided Waves for NDE/SHM of Trusses, *Measurement Science and Technology* 21 (2010) 045701, doi: 10.1088/0957-0233/21/4/045701.
9. P. Rizzo, M. Cammarata, D. Dutta, H. Sohn, K.A. Harries, Unsupervised learning algorithm for fatigue crack detection in waveguides, *Smart Materials and Structures* 18 (2009) 025-016, doi:10.1088/0964-1726/18/2/025016.
10. P. Rizzo, F. Lanza di Scalea, Wavelet-based unsupervised and supervised learning algorithms for ultrasonic structural

- monitoring of waveguides, Progress in Smart Materials and Structures Research, Ch.8 Ed. Peter L. Reece, NOVA publishers (2007) 227-290.
11. P. Rizzo, E. Sorri, F. Lanza di Scalea, E. Viola, Wavelet-based outlier analysis for guided wave structural monitoring: application to multi-wire strands, *Journal of Sound and Vibration* 307 (2007) 52-68.
 12. P. Rizzo, I. Bartoli, M. Cammarata, S. Coccia, Digital signal processing for rail monitoring by ultrasonic guided waves, *Insight - NDT & Condition Monitoring* 49(6) (2007) 327-332.
 13. P.B. Nagy, L. Adler, Ultrasonic NDE of solid-state bonds: inertia and friction welds, *Journal of Nondestructive Evaluation* 7(3/4) (1988) 199-215.
 14. G. Tong, L. Aiqun, L. Jianhui, Fatigue Life Prediction of Welded Joints in Orthotropic Steel Decks Considering Temperature Effect and Increasing Traffic Flow, *Journal of Structural Health Monitoring* 7(3) (2008) 0189–14.
 15. N. Juluri, M.J.S. Lowe, P. Cawley, The guiding of ultrasound by a welded joint in a plate, *Review of Progress in QNDE* 26 (2007) 1079-1086.
 16. Z. Fan, M.J.S. Lowe, Propagation of feature guided waves in a plate with a welded joint, *Review of Progress in QNDE* 28 (2009) 185-192.
 17. V. Barnett, T. Lewis, *Outliers in statistical data*, New York: John Wiley & Sons (1994).
 18. Connor, R.J., Draft Final Report - Results of the Investigation into the Cause of the Observed Cracking on VMS Support Structures in Penn DOT District 4-0, (2008).

RELIABILITY-BASED DESIGN OF STRUCTURES UNDER SEISMIC LOADING: APPLICATION TO TIMBER STRUCTURES

Hassen RIAHI, Rostand MOUTOU PITTI, Philippe BRESSOLETTE,
Alaa CHATEAUNEUF, Eric FOURNRLY.

Clermont Université, Université Blaise Pascal, Laboratoire de Mécanique et Ingénieries, EA
3867, BP 206, 63000 CLERMONT FERRAND, France.

hassen.riahi@polytech.univ-bpclermont.fr

ABSTRACT. A reliability approach applied to wood structures under seismic excitation is proposed in this paper. This approach is based on First Order Reliability Method (FORM). The mechanical model which represents a timber roof truss used in individual housing, is detailed and the mechanical nonlinear behavior of the timber joints is defined by hysteresis elements. The uncertainties are taken into account in the numerical model through random variables representing the stiffness parameters at timber joints. The reliability analysis allows us to compute the failure probability and their sensitivity to various random parameters. Numerical examples show the performance and the efficiency of the proposed method.

1. Introduction

Due to the advantages provided by its mechanical behaviour under seismic and fire loadings, to its aesthetic and environmental effects, timber is commonly employed in building and civil engineering structures. In most cases of industrial and individual buildings, the timber structures are composed of wood members joint with connectors made of steel plates. From the mechanical point of view, the combination of the nonlinear behaviour of wood and the ductility of steel components inevitably generate energy dissipation phenomena [1] during the seismic loading. Unfortunately, this major advantage (i.e. dissipation capacity) of the wood material is omitted in most design codes, because it is not appropriately taken into account in the calibration of the safety factors. Mostly, the failure of the wood material is considered to occurs due to brittle fracture. Unfortunately, the mechanical behaviour of timber joints is highly nonlinear mainly due to the metal plate fasteners which ensure the connection between the timber members. In spite of the important scientific work devoted in this context, the mechanical behaviour of timber joints is still misunderstood. Contrary to the approximations made in considering the timber joints either completely rigid or flexible, the behaviour of punched metal plate fasteners is now described by semi-rigid behaviour law. In this way, several nonlinear models have been developed including those in [2, 3, 4]. Although, these models have been widely used, the obtained predictions are conservative since the parameters of the behaviour law have been considered as deterministic. However, probabilistic approaches must be used in order to take into account the variability observed in material properties, fluctuations of seismic excitation and uncertainties in geometrical properties. In this context, several works already took into account these uncertainties [5, 6, 7, 8]. In the present work, an alternative to these approaches is proposed on the basis of reliability analysis. The mechanical behaviour under seismic loading is simulated by nonlinear finite element model, the parameters defining the stiffness of the timber joints in the roof truss are considered as random variables and the probability of failure against a prescribed failure mode is estimated using the First Order Reliability Method (FORM). This paper is organized in three sections: in the first one, we describe the methodology adopted to construct the finite element model dealing with timber roof truss under seismic excitation. In section 3, we describe the method for coupling mechanical and reliability computations. The performance of the proposed approach is depicted in section 4, based on numerical applications. Finally, conclusions based on the obtained results and some prospects for a further work are presented.

2. Finite element model of timber roof truss

In this study, we consider a timber roof truss without attic. Figure 1 gives the geometrical proprieties of the timber members and the punched metal plates ensuring the connection between those members. We note that this typical configuration of timber roof truss is widely used in timber housing all over the world as in Europe, North

America, New Zealand and Australia. In these countries, timber housing represents more than 90% of the market of the private housing. In France, there are more and more interest to use this configuration of timber roof trusses in individual housing. Indeed, for this reason, this typical configuration is already planned to be studied in the scope of the French research project SISBAT [9].

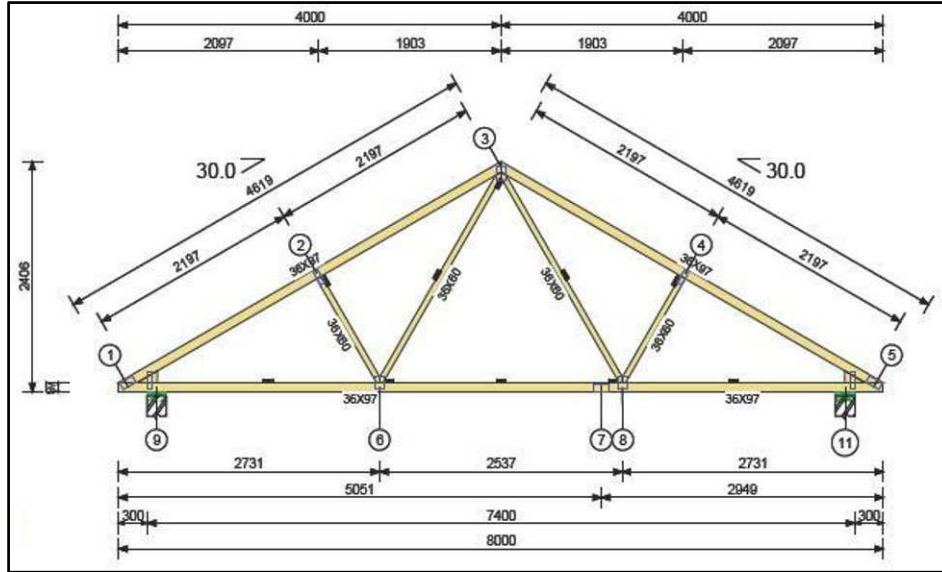


Figure 1 : Truss wood structure

The industrialized timber roof truss is composed by several timber members connected with punched metal plate fasteners. Due to the complexity of the geometrical configuration of the timber roof truss and to the nonlinear behaviour of the metal joints, a finite element model is developed [10] to analyze the mechanical response induced by seismic excitation. The adopted mesh is illustrated in figure 2.

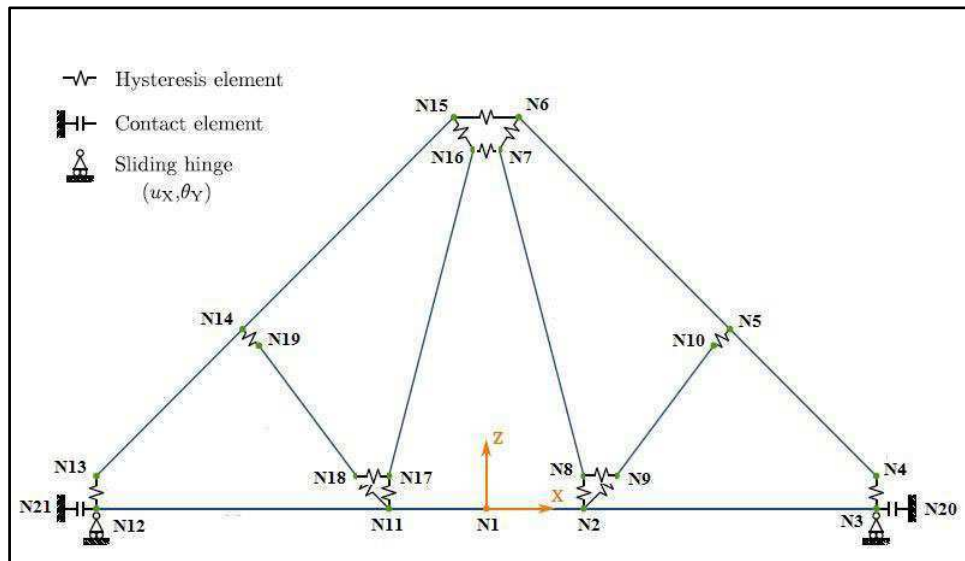


Figure 2 : Nodes mesh

The finite element model is composed of beam elements modelling the timber members connected with hysteresis elements modelling the punched metal plates. Additional contact elements and sliding hinges are used for the boundary conditions. We assume that the nonlinearity is not due to the geometrical configuration of the timber roof truss but mainly induced by the behaviour of the metal fasteners. Consequently, the behaviour of the timber members is assumed to be linear elastic with Young's modulus $E_w = 12.5 \text{ MPa}$. This value is chosen as the lower bound of the range given by the mechanical grading of timber members achieved in experimental tests. We note that the orthotropy of the wood is not taken into account, as the beam elements are slender, thus the load remains collinear to the principal beam's direction and shear loads in wood are limited. The wood density ρ_w is chosen equal to 350 kg/m^3 based on experimental measurements.

The finite element model is composed of 14 hysteresis elements modeling the punched metal plate fasteners. The metallic joints connect two nodes. We define 7 locations corresponding to 7 metal plates in the timber roof truss. At each location, one or more hysteresis elements are used, depending on the number of connected timber beams. This modelling allows us to ensure a better compromise between simplicity and accuracy. The choice of the parameters used for each joint is based on experimental tests on metallic joints. The developed finite element model allows us to obtain the displacement fields at each node during the seismic excitation. In this study, the seismic excitation corresponds to Kobe earthquake in Japan which occurred in January 17, 1997. Figure 3 illustrates the recorded ground acceleration. We note that, the dynamic computations are performed using incremental scheme. The seismic excitation is applied in the direction \overrightarrow{OX} (see figure 2). Figure 4 illustrates the displacement in the nodes related to metallic joints at the top and the supports of the truss.

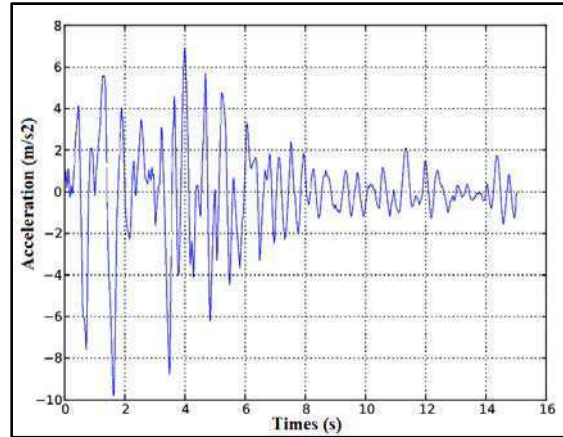


Figure 3 : *Kobe earthquake accelerogram*

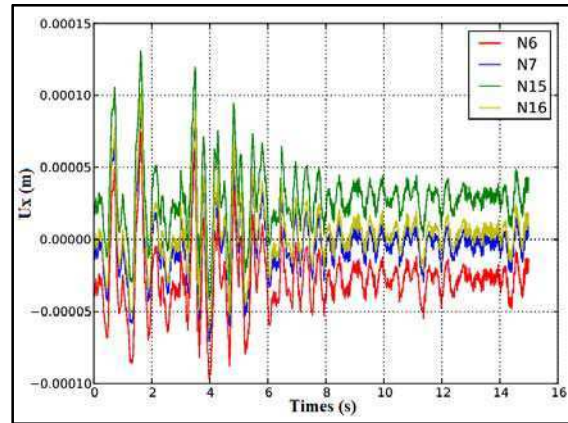


Figure 4 : *Displacement in the direction of the applied seismic excitation in the nodes N_6 , N_7 , N_{15} and N_{16}*

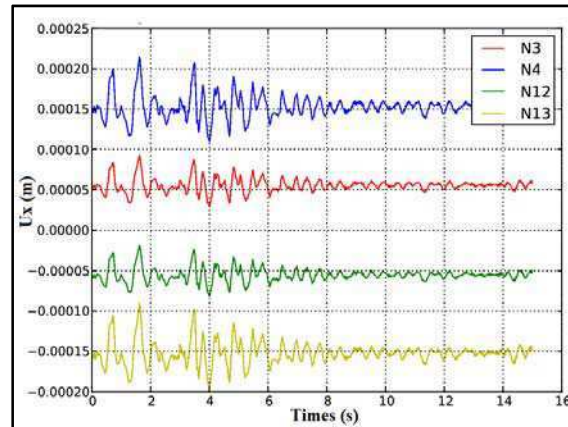


Figure 5 : *Displacement in the direction of the applied seismic excitation in the nodes N_3 , N_4 , N_{12} and N_{13}*

As it can be seen in figures 4 and 5, the obtained displacement in the nodes defining the same punched metallic plate fasteners takes different values. This can be explained by the nonlinear semi-rigid behaviour of the metallic connection (i.e. the use of hysteresis elements at the same connection).

2. Reliability computation method

2.1. Failure criterion and probability of failure

The main objective of the structural reliability analysis is to compute the probability of failure P_f of a mechanical system regarding a prescribed failure criterion which takes account for uncertainties arising from the geometry, the material parameters and applied load. The failure criterion concept can be defined as the conflict between two fundamental quantities namely the “Demand” and the “Capacity” of the system. In the mechanical engineering context, the “Demand” is defined as the action effects which induce a realization of a mechanical state such as stress or displacement. The “Capacity” is represented by the material strength which defines a limit state that should be respected such as ultimate stress or critical displacement, to avoid the failure of the structure. Mathematically speaking, the failure criterion is represented by a limit state function G , defined in terms of the vector of uncertain parameters $\mathbf{X} = \{X_1, X_2, \dots, X_n\}^T$, such that, $G(\mathbf{X}) > 0$ denotes the safe domain and $G(\mathbf{X}) \leq 0$ denotes the failure domain. The limit state surface corresponds to the points verifying the condition $G(\mathbf{X}) = 0$, in other word, it defines the boundary between the safe and the failure domains as shown in figure 6.

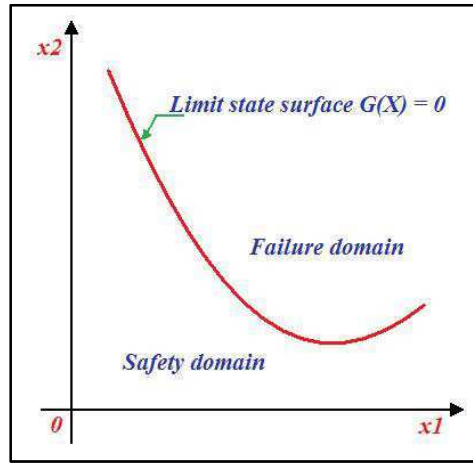


Figure 6 : Limit state surface in the random physical space

The probability of failure P_f of the structure corresponding to the prescribed limit state function $G(\mathbf{X})$ can be defined by:

$$P_f = \text{Prob}(G(\mathbf{X}) \leq 0) = \int_{G(\mathbf{X}) \leq 0} f(\mathbf{x}) d\mathbf{x} \quad (1)$$

where $f(\mathbf{x})$ is the joint probability density function associated to the vector of uncertain parameters $\mathbf{X} = \{X_1, X_2, \dots, X_n\}^T$.

2.2. Computation of the probability of failure

In practical applications, the evaluation of the integral (1) is not a trivial task, because the reliability problems involve a very large random space dimension (i.e. large number of uncertain parameters) and the value of the probability of failure is often represented by a very small quantity. For these reasons, the first order and the second order reliability methods FORM/SORM have been proposed [11]. The main idea of these approaches is to approximate the limit state function $G(\mathbf{X}) = 0$ to provide an estimation of the probability of failure P_f (Figure 7). Generally, in the FORM/SORM approaches, the approximation of the limit state surface is carried out in the standard random space, where the set of uncertain input parameters $\mathbf{X} = \{X_1, X_2, \dots, X_n\}^T$ are represented by independent standard Gaussian random variables denoted by the vector $\mathbf{U} = \{U_1, U_2, \dots, U_n\}^T$. The passage from the physical random space \mathbf{X} to standard random space \mathbf{U} is established by the mean of probabilistic transformation, such that:

$$\mathbf{X} = T(\mathbf{U}) \quad (2)$$

The function T can be represented by either Rosenblatt's [12] or Nataf's [13] probabilistic transformations.

The limit state function $G(\mathbf{X})$ is defined in the standard random space as:

$$G(\mathbf{X}) = G(T(\mathbf{U})) \equiv H(\mathbf{U}) \quad (3)$$

and the probability of failure P_f is written as:

$$P_f = \text{Prob}(H(\mathbf{U}) \leq 0) = \int_{H(\mathbf{U}) \leq 0} \phi_n(\mathbf{u}) d\mathbf{u} \quad (4)$$

where ϕ_n is the probability density function of n -dimensional Gaussian random variable.

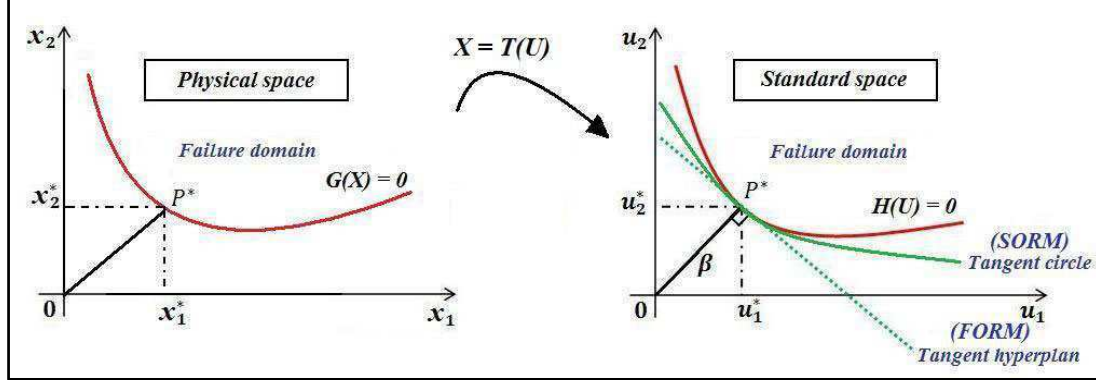


Figure 7 : FORM/SORM reliability analysis methodology

The first order reliability method (FORM) is based on the concept of the reliability index β to estimate the probability of failure P_f . As a geometrical interpretation, the reliability index is the distance defined by the closest point on the limit state surface $H(\mathbf{U}) = 0$ to the origin of the standard random space. This point is called the most likely failure point \mathbf{P}^* , its coordinates in the standard random space are denoted by the vector \mathbf{u}^* .

Based on the above interpretation, finding the reliability index β is an optimization problem under one constraint:

$$\begin{cases} \beta = \min \|\mathbf{u}^*\| \\ \text{under the constraint } H(\mathbf{U}) \leq 0 \end{cases} \quad (5)$$

This problem can be easily solved by the use of the optimization algorithm developed by Rackwitz and Fiessler [14]. Once, the reliability index is obtained, the first order estimation of the probability of failure is given as:

$$P_f \approx \Phi(-\beta) \quad (6)$$

where Φ is the standard Gaussian cumulated distribution function.

We note that, the estimation of the probability of failure P_f using Eq. (6) is exact only when the limit state surface is linear in the standard random space. However, the approximation is widely approved for mechanical systems.

2.3. Dynamic reliability problem

Generally, when dealing with dynamic reliability problem, the failure is defined as the maximum displacement response exceeding a critical threshold d_{crit} during the seismic excitation $\gamma(t)$. Thus, the limit state function is defined in this context as:

$$G(\mathbf{X}) = d_{crit} - \max_{t \in [0, T]} \{ |d(\mathbf{X}; t)| \} \quad (7)$$

where d is the displacement response computed by the finite element model of the truss structure and \mathbf{X} is the random vector representing the uncertain parameters. The critical threshold displacement d_{crit} is defined as the displacement recorded when the yield stress is achieved. It is obtained through a static analysis.

4. Numerical application : timber roof truss

As indicated above, the timber roof truss is composed of several timber members connected with punched metal plate fasteners, as depicted in figure 8. The connections are represented in the two dimensional finite element model by hysteresis elements where the behaviour is defined by three parameters namely the horizontal stiffness K_x , the vertical stiffness K_z and the rotational stiffness K_θ . In order to assess the structural reliability of the timber roof truss under seismic loading, we consider the stiffness $K = f(K_x, K_z, K_\theta)$ of each connection as uncertain parameters which are modeled as lognormal random variables having a mean value $\mu = 20 \text{ kNmm}^{-1}$

and a coefficient of variation $C_V = 10\%$. In order to reduce the dimension of the random space, we assume perfect correlation between the horizontal stiffness K_x , the vertical stiffness K_z and the rotational stiffness K_θ . We note that for this later (ie. the rotational stiffness), the mean value is translated by deterministic quantity $\Delta K = 40$. Hence, the random variable representing the rotational stiffness is defined as $K_\theta = \Delta K + X_i$, where X_i is the random variable defining the joint uncertainties.

Based on the experimental tests presented in [10], the failure mode of the timber roof truss is composed of wood fracture on the top chord, as well as an anchor failure on the bottom chord.

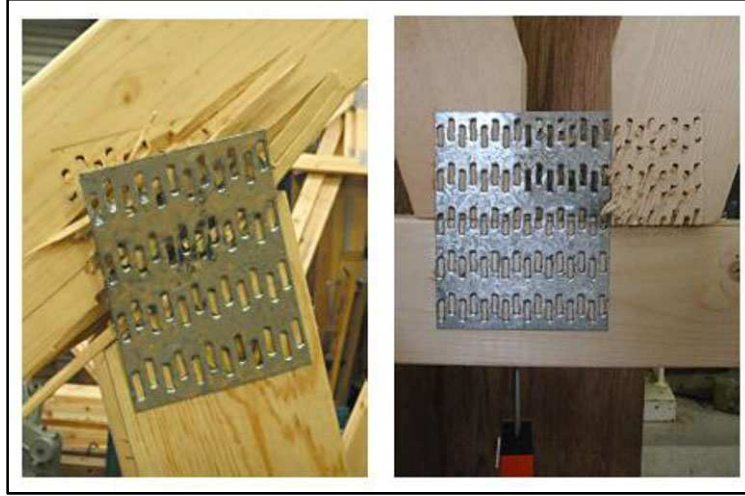


Figure 8 : Failure modes of the timber roof truss

Firstly, we are interested by the first failure mode (i.e. wood fracture on the top chord). The mechanical response is defined by the displacements of the nodes N_{14} and N_{19} in the direction \vec{OX} (see figure 2). The limit state function is defined as stated by equation (7) and the critical displacement is $d_{crit} = 1,8 \cdot 10^{-4} m$. The results of the reliability analysis are presented in table 1.

Table 1 : Results of the reliability analysis of the first failure mode

Reliability index	4,297
Failure probability	$8,651 \cdot 10^{-6}$
Number of iterations	10
Number FEM calls	99

As it can be seen, the employed reliability method is not time consuming since the convergence of the reliability index is well achieved. For a precision level of 10^{-4} , we need only 10 iterations which correspond to 99 finite element analysis. For instance, the target probability of failure suggested by the design code is about 10^{-5} . We can observe that the estimated probability of failure is lower than the target value. Thus, the timber roof structure can safely performs its function.

We are interested now by the second failure mode (i.e. anchor failure of the bottom chord). The mechanical response is represented by the displacements of the nodes N_{11} , N_{17} and N_{18} in the direction \vec{OX} (see figure 2). As previously, the limit state function is defined by equation (7). The obtained results concerning the reliability analysis for different values of the critical displacement d_{crit} are summarised in table 2.

Table 2 : Results of the reliability analysis of the second failure mode

	$d_{crit} = 5.5 \cdot 10^{-5} m$	$d_{crit} = 6.1 \cdot 10^{-5} m$	$d_{crit} = 6.8 \cdot 10^{-5} m$	$d_{crit} = 7.5 \cdot 10^{-5} m$
Reliability index	0.691	1.818	3.102	4.301
Failure probability	$2.446 \cdot 10^{-1}$	$3.447 \cdot 10^{-2}$	$9.607 \cdot 10^{-4}$	$8.469 \cdot 10^{-6}$
Number of iterations	5	15	12	10
Number FEM calls	45	154	129	103

We can observe that the reliability index increases fastely when the critical displacement increases. Obviously, the critical displacement represents the capacity of the timber roof structure to resist the seismic excitation. From the obtained results, we can conclude that the risk of anchorage failure on the back truss is more important than the failure by the fracture of wood on the front truss. Those information collected trough the reliability analysis can help the engineers to take better decision concerning the choice of the convenient technological solution for the connection elements.

5. Conclusions

The reliability analysis methodology proposed in this paper can be used to predict the probability of failure of timber roof truss subject to earthquake events. This approach is based on coupling the numerical model stemming from the finite element modeling of timber roof truss and the First Order Reliability Method. The finite element model has been based on the assumption that the main nonlinearity is due to the punched metal plate fasteners employed in the timber joints (i.e. connection between the timber elements). The behaviour of these joints has been simulated using hysteresis elements. The stiffness parameters of these hysteresis elements have been considered as random. Based on experimental results, the failure mode of the timber roof truss is composed of wood fracture on the top chord, as well as an anchor failure of the bottom chord. These two failure modes have been considered in the reliability analysis and the probability of failure against the failure criteria has been estimated. We have shown that the risk of anchorage failure on the back truss is more important than the failure by fracture on the top chord. We have also shown that the proposed methodology is not time consuming since the convergence of the quantities of our interest (i.e. reliability index, reliability of failure) is well achieved using a limited number of finite element analysis. The ongoing research aims to develop a coupling method able to deal with higher order reliability problems.

6. References

- [1] Lam, F. et al. Performance of timber buildings under seismic load. Part I: experimental studies. *Prog. Struct. Engng Mater.* 4: 276–285, 2002.
- [2] Foschi, R.O. Analysis of wood diaphragms and trusses. Part one: Diaphragms. *Can. J. of Civil Engrg., NRC*, 4(3): 345-352, 1977.
- [3] Yasumura, M. and Yasui. Pseudodynamic tests and earthquake response analysis of timber structures I: plywood-sheathed conventional wooden walls with opening. *J.Wood Sci.* 52: 63-68, 2006.
- [4] Richard, N. et al. Prediction of seismic behaviour of wood-framed shear walls with openings by pseudodynamic test and FE model. *J. Wood Sci.* 49: 145-151, 2003.
- [5] Foliente, G.C. Earthquake performance and safety of timber structures – Chapter: Modeling and analysis of timber structures under seismic loads: State-of-the-art. *Forest products society, Madison, USA*, 55-73, 1997.
- [6] Li, Y., Ellingwood. Reliability of woodframe residential construction subjected to earthquakes. *Structural Safety.* 29: 294-307, 2007.
- [7] Der Kiureghian, A. Structural reliability methods for seismic safety assessment: a review, *Engineering structure.* 18(6). 412-424, 1996.
- [8] Gao W., Random seismic response analysis of truss structures with uncertain parameters, *Engineering structure*, 29, 1487–1498, 2007.
- [9] SISBAT. Analyse probabiliste de la vulnérabilité sismique de l'habitat avec toiture en charpentes industrialisées en bois - Couplage modélisation probabiliste /experimentation (in French). ANR RiskNat 2008, project ref. ANR-08-RISK-008, 2009-2013.
- [10] Humbert J., Caractérisation du comportement des structures bois à assemblages métalliques sous sollicitations sismiques : Essais experimentaux , Modelisation numerique, Analyse de sensibilité. Thesis, Grenoble, France 2010.
- [11] Madsen HO. Omission sensitivity factors. *Struc Safe.* 35-45, 1988.
- [12] Rosenblatt M. Remarks on a multiformation. *Ann Math Statist.* 23:470-472, 1952.
- [13] Nataf A. Determination des distributions dont les marges sont données. *Comptes Rendus de l'Académie des Sciences.* 225:42-43, 1962.
- [14] Rackwitz R, Fiessler B. Structural reliability under combined load sequences. *Comput Struct.* 9:489-494, 1978.

Progress in developing a standard for dynamic strain analysis

Erwin Hack¹, George Lampeas², John Mottershead³, Eann Patterson³, Thorsten Siebert⁴ and Maurice Whelan⁵

¹ Laboratory of Electronics & Metrology, EMPA Duebendorf, Ueberlandstrasse 129, CH-8600 Duebendorf, Switzerland. erwin.hack@empa.ch

² Department of Mechanical Engineering and Aeronautics, University of Patras, 26500 Rion, Patras, Greece labeas@mech.upatras.gr

³ School of Engineering, University of Liverpool, Liverpool, UK. J.E.Mottershead@liverpool.ac.uk & eann.patterson@liverpool.ac.uk

⁴ Dantec Dynamics GmbH, Kaessbohrer Str. 18, D 89077 Ulm, Germany. thorsten.siebert@dantecdynamics.com

⁵ Institute for Health and Consumer Protection, European Commission DG Joint Research Centre, 21021 Ispra (VA), Italy. maurice.whelan@jrc.it

ABSTRACT

Previous work has led to the publication of a standard guide for the calibration of optical instruments for making full-field measurements of in-plane strain in pseudo-static cases. A consortium of international organizations drawn from across the innovation process is engaged in extending this earlier work to allow the calibration of instruments capable of making full-field measurements of in-plane and out-of-plane deformations resulting from time-varying loading that may or may not be repetitive or cyclic. Preliminary designs for a reference material have been completed and are being tested in a round robin exercise. Calibration of the system employed for performing measurements in experiments allows the associated uncertainty to be defined which is an important step in the validation of computational models. However no recognized procedures exist for performing validations of simulations with full-field data from experiments. The consortium is developing appropriate validation procedures based on using image decomposition to enable comprehensive and quantitative comparisons between data sets for strain from experiments and simulations. Progress will be reported and the direction of planned work will be discussed to allow input from the user-community.

INTRODUCTION

Structural analysis is an essential part of the design process for any engineering artefact whose function includes the bearing or transmission of loads. Most analyses are performed using computational models of prototype designs. The verification and validation of these models is a critical step in ensuring the safe and reliable operation of engineering components. A guideline [1] exists that describes the key components for verification and validation; however there are no guidelines or standards for performing a validation. In 2008 a consortium of international organizations [2] was formed to develop appropriate validation procedures for dynamic analyses based on optical measurements of deformation. The work programme agreed by this consortium represented a continuation and extension of the pre-normative research performed by an earlier collaboration, known as SPOTS (Standardisation Project for Optical Techniques of Strain measurement) [3]. The objectives of the new programme, known as ADVISE (Advanced Dynamic Validations using Integrated Simulation and Experimentation) are as follows:

- development of reference materials that allow traceability and calibration of full-field optical methods of deformation measurement in cyclic, transient and non-linear dynamic events;
- optimisation of methodologies for both optical measurement and computational modelling and simulation of non-linear, transient dynamic events;
- contributions to standardisation activity for experimental validation of dynamic simulations.

The planned output arising from the last objective is anticipated to be the first attempt to provide a unified approach to experimental validation of engineering simulations of primary structures; while, the first objective is expected to extend the work in SPOTS for static measurements into the realm of dynamic events. This paper provides a brief status report on the three-year funded programme of ADVISE which at the time of writing had slightly under twelve months remaining.

CALIBRATION

Calibration involves making comparisons with a known, recognized criterion or reference material which has been compared via a continuous chain of comparison to an international standard. The motivation for performing a calibration is usually two-fold: to establish the minimum uncertainty in future measurements made with the calibrated instrument and to provide confidence in the quality of the instrument and the results generated with it. The latter is important in a regulatory environment such as the aerospace industry; while the former is important when performing validations based on the experimental data. The SPOTS programme designed a reference material, which consisted of a beam loaded in four-point bending via a monolithic frame, for use in the calibration of optical systems for measuring in-plane static, or pseudo-static strain distributions [4]. It was deemed impractical to extend the loading range of the SPOTS reference material to include out-of-plane and dynamic loading; so the development of new designs was initiated using the same process of consultation with the user-community that was employed successfully by the SPOTS consortium. The ADVISE consortium identified a set of attributes for the new reference material and then invited members of the user-community to grade the importance of the attributes and to suggest any that may have been omitted. The results are summarised in figures 1 and 2 for the physical attributes of the reference material and for the attributes of the gauge section, respectively. Those attributes which were graded most highly were designated as essential attributes that must be possessed by any design in order for it to be viable; while the remainder of the attributes were considered desirable and were used for ranking candidate designs.

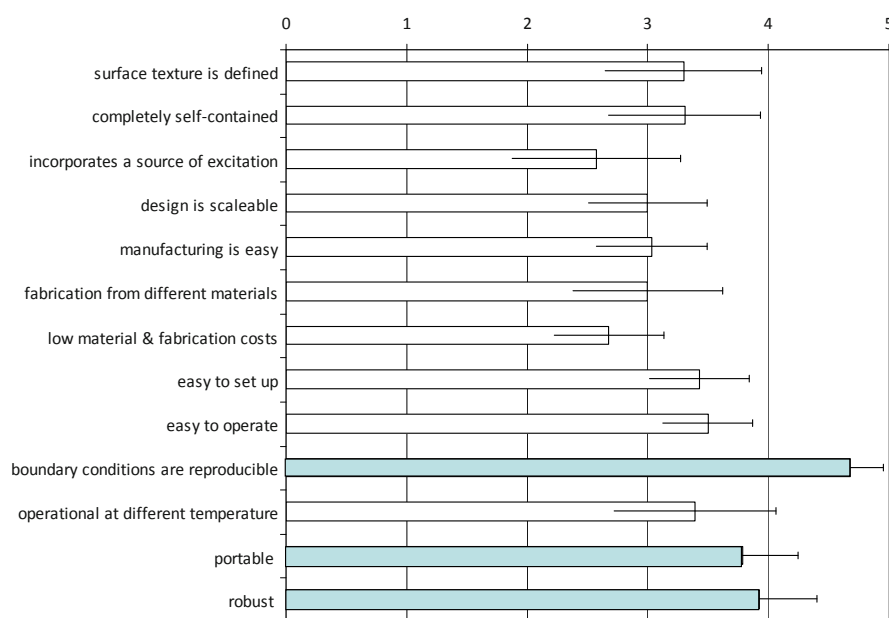


Fig 1 Physical attributes of the reference material and the average grades assigned by the user-community (from 5=essential to 0= not required) with those designated as essential highlighted in blue.

The ADVISE consortium used brainstorming to generate a large number of candidate designs and subsequently rejected those that did not possess the essential attributes. The remaining candidate designs were evaluated based on the degree to which they possessed the desirable attributes. This procedure is based on the rational decision making process [5] which had been used in the design of the SPOTS reference material [4]. At the conclusion of this evaluation, two candidate designs were identified for further investigation and detailed embodiment; namely, a membrane manufactured in a monolithic cylinder and a cantilever beam shaped from a monolithic block as shown in figure 3. Prototypes of these designs have been constructed and, at the moment, are being tested in cyclic loading via a round robin with the ADVISE consortium. In the future, the prototypes will be assessed to determine whether they can be used for calibrating instruments designed to measure transient and non-linear deformation. The goal is to extend the SPOTS guidelines for the calibration of optical systems of strain measurement to include dynamic loading cases and the use of the new reference material. The principles of operation will be similar since the connection to the international standard for length is via a calibrated transducer used to measure the displacement of the reference material at a defined point. A known distribution of deformation will be compared with the measured distribution and the level of uncertainty in the calibration established using the same concepts as those expounded in the SPOTS guidelines. This procedure will allow confidence levels to be established for the data subsequently acquired with the calibrated instrument and will provide assurance of the fitness for purpose of the instrumentation.

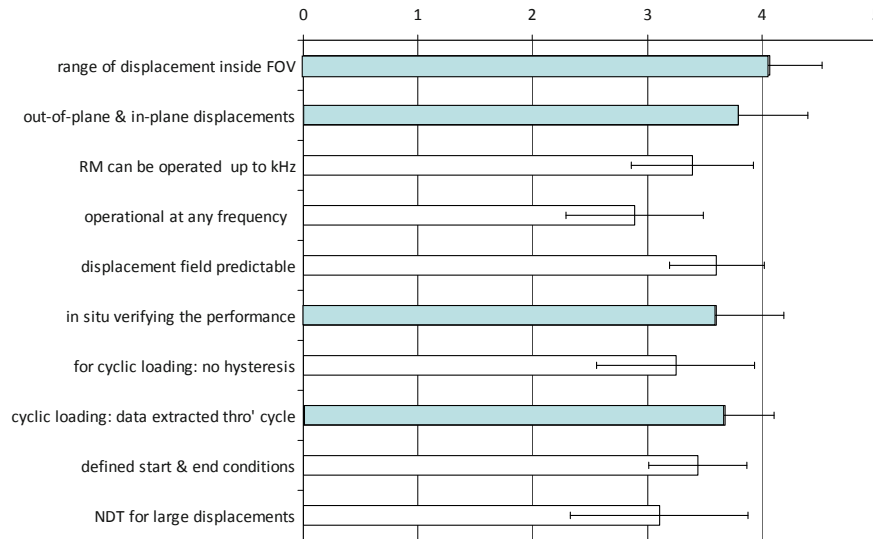


Fig 2 Attributes of the gauge-section in the reference material and the average grades assigned by the user-community (from 5=essential to 0= not required) with those designated as essential highlighted in blue.

VALIDATION

Verification is associated with identifying and quantifying the errors of logic and programming in the code used for modelling, whereas validation involves assessing the extent to which the model is an accurate representation of the real-world. ASME guide [1] recommends that experiments should be designed and performed specifically for the purpose of validation but goes no further in providing direction for their conduct. It is common practice to identify locations of high stress in a component, known as 'hot-spots', using the computational model and to compare the stress with data obtained from strain gauges placed in the corresponding locations in a physical prototype. This approach is flawed because 'hot-spots' that occur at locations other than those identified by the model could lead to unexpected failure of the component. Even worse, efforts to reduce the weight of a component could lead to catastrophic failure through removal of material at locations predicted by the model to be experiencing low or zero strain but actually subject to significant strain. The advent of powerful, digital optical techniques for measuring strain distributions over the entire surface of a component rendered it unnecessary and inappropriate to consider strains only at single points. These techniques can provide maps of displacement and strain for an array with the order of 10^6 locations or nodes on the surface of a component, which is comparable to the nodal density in computational models. However, it is not straightforward to make quantitative comparisons of strain distributions from computation and experimentation that each consist of about 10^6 data points; particularly when the data may not be in the same coordinate system, at the same scale or in the same orientation.

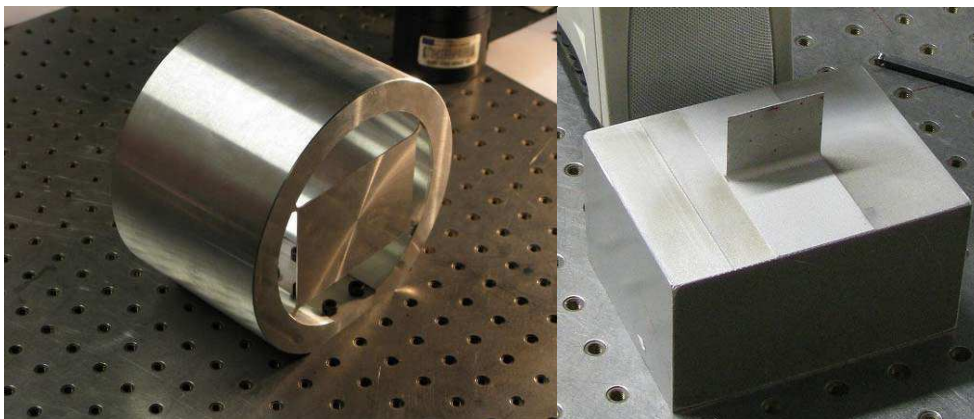


Fig 3 Prototype reference materials: membrane in monolithic cylinder (*left*) and a cantilever protruding from a monolithic block (*right*).

Research in the ADVISE consortium has focused on treating strain distributions as images and using of image decomposition methods to enable the strain data to be represented by a less than a hundred geometric moments that are invariant to rotation, scaling and translation [6]. These techniques have been used previously for iris and finger print recognition and their use in validating strain maps provides an elegant means of comparing data-rich maps of strain from simulations and prototypes. Geometric moments, such as Zernike and Tchebichef, are information-preserving moments that can be used to describe detailed images by fitting orthogonal polynomials to the digital image data. The result is a relatively small number of moment values from which the original image can be reconstructed and that can be used for comparative purposes in place of the original data-rich map of strain. An example of Zernike moments, the reconstruction obtained from them and the original strain map obtained from digital image correlation performed on a plain, undamaged composite tie-bar loaded in tension [7] is shown in figure 4.

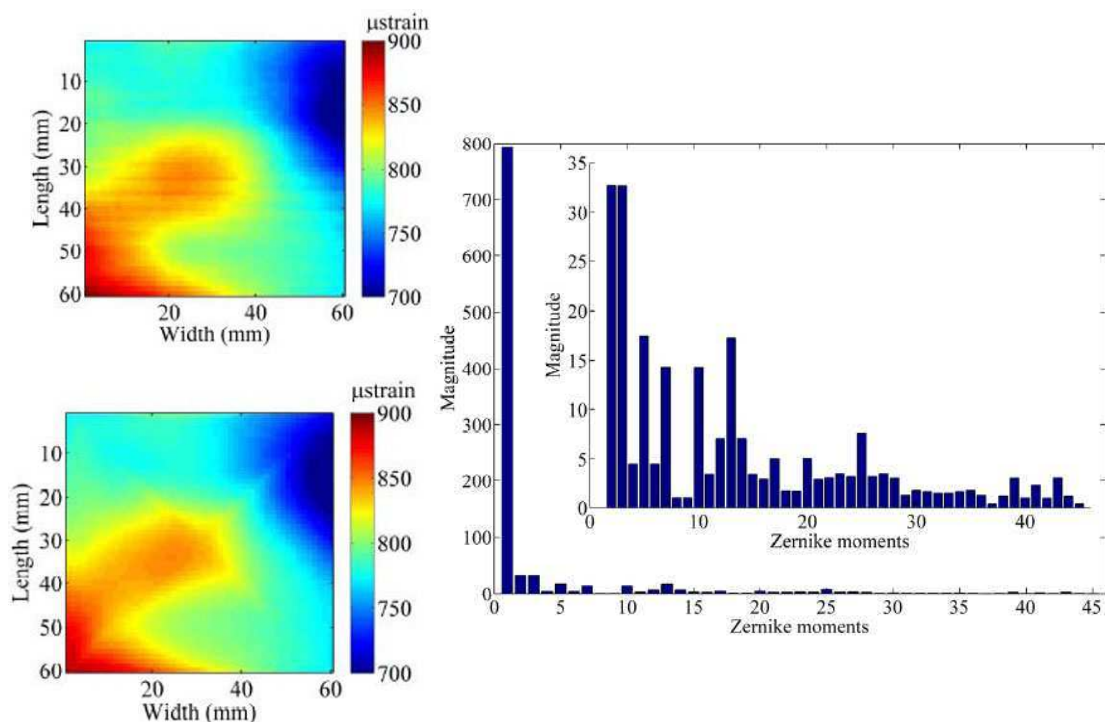


Fig 4 Maximum principal strain map obtained from digital image correlation (*top left*); its Zernike moment descriptors (*right*) with the inset showing the same data but without the first moment; and the reconstructed strain map from the moments (*bottom left*) for a plain undamaged composite tie-bar (from [7])

The geometric moments obtained from maps of strain derived from simulation and experiment can be compared by using relatively simple statistical approaches, such as the Pearson correlation coefficient, Euclidean distance or cosine similarity. Work is in progress to develop this final step in the process that would allow a quantitative measure of the extent of correlation between results from a computational model and experiments with a prototype. Figure 5 shows an example of the change in these measures with mesh density for a simple finite element model of a aluminium plate loaded in tension compared to the results obtained using digital image correlation to obtain the strain distribution in a corresponding laboratory specimen [7]. A value of unity for the Pearson correlation coefficient and the cosine similarity would represent perfect agreement between the results from experiment and computation.

DISCUSSION AND CONCLUSIONS

A brief overview and status report of the pre-normative research programme being pursued by the ADVISE consortium has been described. The goal of the programme is two-fold: (a) to extend the existing guidelines for the calibration of optical systems for the measurement of in-plane, static maps of strain [4] to include systems capable of handling out-of-plane, dynamic deformation; and (b) to develop a methodology for using the data from such instruments in the validation of computational models. A rational decision making process [5] has been used to incorporate input from the user-community into the design of a new reference material for the extension of the calibration process. A large number of candidate designs were identified and evaluated against a set of attributes. Two designs have been retained for further evaluation via round robin with the consortium and more detailed embodiment, namely a cantilever attached to a monolithic block and a

membrane attached to a cylinder. A protocol for the use of the final design for calibrating optical systems for measuring strain will be developed and published as an extension or supplement to current guidelines [4]. In parallel, novel work is underway to establish an efficient and effective way of comparing quantitatively two data-rich maps of strain so that validation of computational solid mechanics models can be performed relatively straightforwardly using maps of strain data obtained from calibrated optical instruments. The use of geometric moments to achieve a substantial reduction in dimensionality of the data has been explored and combined with common statistical measures to provide a simple indicator of the level of correlation between the results from models and experiments. It is planned to develop a guideline for validation based on this preliminary work.

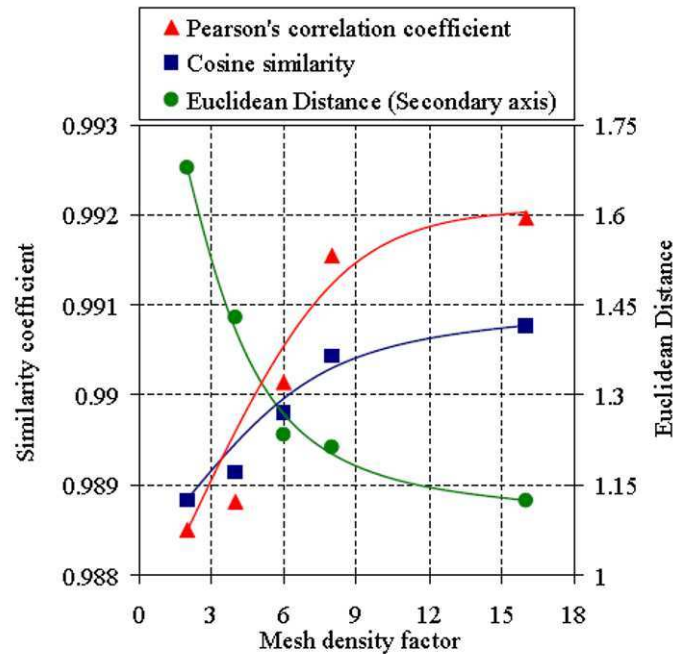


Fig 5 Pearson's correlation coefficient, Cosine similarity and Euclidean distance between results from a computational model and an experimental prototype based on geometric moment representation of the strain maps and plotted as a function of the mesh density in the model

REFERENCES

- [1] ASME V&V 10-2006, *Guide for verification & validation in computational solid mechanics*, American Society of Mechanical Engineers, New York.
- [2] ADVISE, *Advanced Dynamic Validation through Integrated Simulations and Experimentation*, www.dynamicvalidation.org.
- [3] Patterson, E.A., Hack, E., Brailly, P., Burguete, R.L., Saleem, Q., Seibert, T., Tomlinson, R.A., Whelan, M., 'Calibration and evaluation of optical systems for full-field strain measurement', *Optics and Lasers in Engineering*, 45(5):550-564, 2007.
- [4] *Guidelines for the Calibration and Evaluation of Optical Systems for Strain Measurement*, SPOTS, www.opticalstrain.org, 2010.
- [5] Cross, N., *Engineering Design Methods*, John Wiley & Sons, London, 1989.
- [6] Wang W, Mottershead JE, Sebastian CM, Patterson EA, Shape features and finite element model updating from full-field strain data, *Int. J. Solids Struct.* (2011), doi:10.1016/j.ijsolstr.2011.02.010.
- [7] Patki A, *Advances in structural damage assessment using strain measurements and invariant strain descriptors*, PhD thesis, Michigan State University, East Lansing, MI, USA, 2010.

Polymers in Biaxial States of Stress at Various Loading Rates

Nils G. Ohlson

Professor

Department of Solid Mechanics
The Royal Institute of Technology
SE-100 44 Stockholm, Sweden
moja.jernvag@telia.com

ABSTRACT

Previous uniaxial tests have shown that the viscoplastic behaviour of several polymers can be accurately described by means of the Rabotnov-Suvorova integral equation for materials with memory, for a wide range of loading rates in tension. Prediction of deformation can also be made in creep and relaxation. Present investigation concerns biaxial states of stress, achieved by simultaneously applying tensile force and torsional moment to thin-walled tubes. Results show that this constitutive equation, whose parameters were determined from uniaxial tensile tests at three different loading rates, also predicts the biaxial behaviour quite well until the torque comes close to the buckling load of the specimen. As a second verification, creep tests of a polyoximethylene membrane, subjected to hydrostatic pressure, were carried out. The validity of the equation is again confirmed.

INTRODUCTION

Thermoplastic materials are sometimes used in engineering applications at load levels where large strains are expected and the influence of time-dependence must be considered. Uniaxial tests have shown that the hereditary behaviour of many polymers can be described by an equation of type

$$\varphi(\varepsilon) = \sigma(t) + \int_0^t \frac{k}{(t-\tau)^\alpha} \sigma(\tau) d\tau \quad (1)$$

as suggested in [1], which takes the loading history into account. Here, φ denotes the instantaneous stress-strain curve of the material, k and α are material constants. Both these and φ may be determined in uniaxial tests, preferably by means of tensile tests at several loading rates, as outlined in [2], or by evaluating creep tests at several stress levels, which was described in [3]. Given the load history $\sigma(t)$, the strain ε can always be calculated by means of (1), provided the material characteristics are known.

SCOPE OF INVESTIGATION

In many applications, multiaxial states of stress prevail. An extension of (1) to such states is then needed. The relevance of this extension was examined by tests.

APPROACH TO MULTI-AXIAL STATES OF STRESS

In time-independent plasticity, it is assumed that the plastic strain increments are proportional with the corresponding component of the stress deviator,

$$d\epsilon_{ij} = d\lambda s_{ij} \quad (2)$$

Normally, the total strain cannot be obtained by direct integration. For the case of proportional loading, however, the total strain can be shown to depend only on the final stress. One obtains

$$\epsilon_{ij}^p = \frac{3}{2} \frac{\epsilon_e^p}{\sigma_e} s_{ij} \quad (3)$$

where index e denotes effective stress and strain. In analogy with this, it is assumed in our case that the plastic strain components should depend in the same way on the deviatoric components, while the effective strain may be calculated from (1), with uniaxial stress and strain duly replaced by effective values. The right hand side of (1) thus contains two terms: one for the instantaneous stress value and one from the hereditary type integral along the load path.

The effective strain may be computed, under some simplifying assumptions, for stress which increases linearly with time (loading) and for constant stress (creep), as follows.

$$\text{loading} \quad \varphi(\epsilon_e^p) = \dot{\sigma} t \left(1 + \frac{k}{(1-\alpha)(2-\alpha)} t^{1-\alpha} \right) \quad (4a)$$

$$\text{creep} \quad \varphi(\epsilon_e^p) = \sigma \left(1 + \frac{k}{1-\alpha} t^{1-\alpha} \right) \quad (4b)$$

Denoting strain from tension by ϵ and shear from torsion by γ , and assuming incompressible material, one obtains

$$\epsilon_e^p = \int \sqrt{\frac{2}{3}} d\epsilon_{ij} d\epsilon_{ij} = \sqrt{\frac{2}{3}} \epsilon_{ij}^p \epsilon_{ij}^p = \sqrt{\frac{1}{3}} (4\epsilon^2 + \gamma^2) \quad (5)$$

(The special case of pure tension is not fully correct, for reasons that may be left aside at the moment.) This approach also agrees with the generalization of Norton's law for stationary (secondary) creep in multiaxial states of stress, proposed by Odqvist, [4], which states that

$$\epsilon_{ij}^c = \frac{3}{2} \frac{\dot{\epsilon}_0}{\sigma_c} \left(\frac{\sigma_e}{\sigma_c} \right)^{n-1} t s_{ij} \quad (6)$$

The creep strain is proportional with the corresponding deviatoric component, and with time t, the factor of proportionality thereby containing the effective stress. For long-term creep one may write, if the present material model is valid, that

$$\varphi(\epsilon_e^p) = \sigma_e \left(1 + \frac{k}{1-\alpha} t^{1-\alpha} \right) \quad (7a)$$

$$\epsilon_{ij}^p = \frac{3}{2} \frac{\epsilon_e^p}{\sigma_e} s_{ij} \quad (7b)$$

MATERIALS AND METHODS

Biaxial experiments were carried out, using thin-walled tubes (length 42 mm, inner diameter 19, wall thickness 1.5 mm) subjected to simultaneous tension and torsion. Force, moment, tensile strain and torsional shear were recorded as functions of time. Tests were made in an MTS servohydraulic testing machine under controlled force and moment conditions, so that load history was prescribed and deformations measured.

Polyoximethylene POM and a polyamide PA were investigated. Ratios of normal stress to shear stress were 0.5, 1.0, and 2.0, with some variation of effective stress,

$$\sigma_e = \sqrt{\sigma^2 + 3\tau^2} \quad (8)$$

As a second test, a circular membrane (diameter $2c=620$ mm, thickness $h=1$ mm) made from a POM sheet was subjected to hydrostatic pressure p . Pressure was increased stepwise and evaluation can be performed according to the formulas given above for strain.

Strains were calculated from experimental parameters in two ways: by taking direct measurements from strain gages attached to the membrane surface in circumferential and radial directions, and also by measuring the deformation of the membrane, using an LVDT at the center. Denoting this displacement by d , the length of the arc from the apex to the edge along the surface by b , and the radius of curvature by R , one has

$$c/R = 2cd/(c^2 + d^2) \quad (9a)$$

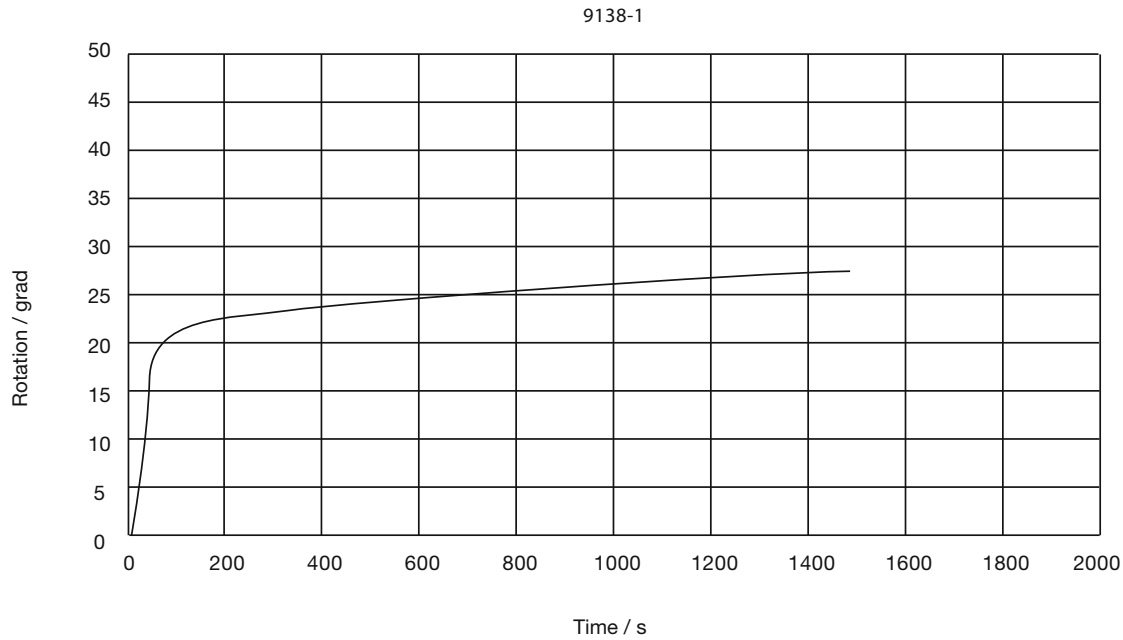
$$\sigma_\varphi = \sigma_g = pR/2h \quad (9b)$$

$$\varepsilon_\varphi = (b - c)/c = d^2/2c^2 \quad (9c)$$

RESULTS

Tension-torsion tests

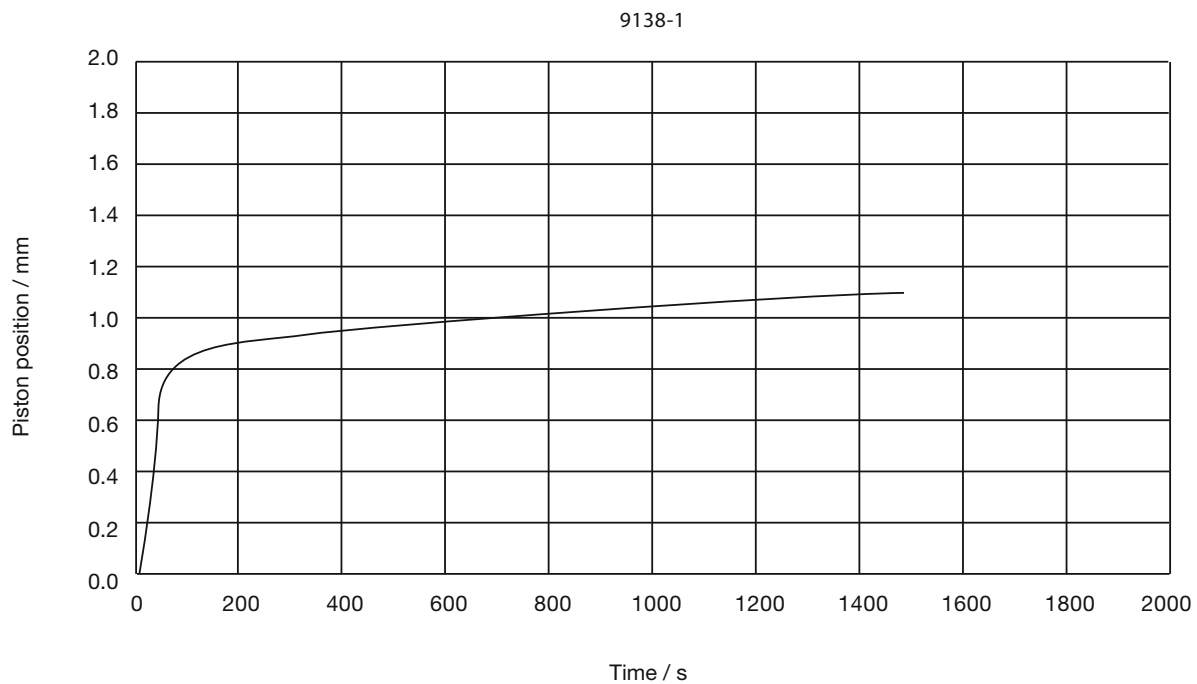
For POM, parameter values were obtained from previous tensile tests, see [Figure 1](#), whereas for PA, for comparison, these values were derived by direct curve-fitting of the equation for the function φ . [Figure 2 a & b](#) shows the recorded displacements versus time for POM. The loading stage was 50 s and then creep at constant load sets in. [Figure 3](#) shows the corresponding displacements for PA, at two different values of the effective stress, 24 and 35 MPa, respectively, duly normalized. [Figure 4](#) shows the computed effective strain for PA specimens and the fitted curves for the appropriate material model. [Figure 5](#) shows the loading stage strains as computed by means of the model for PA. It gives excellent agreement with the recorded strain values at the end of the loading stage.



2002-08-27

 $\sigma = 0,5 \times \tau$ to 68 MPa at 1,55 MPa/s (von Mises)

Fig 1 Instantaneous stress-strain curve for POM (1), curves for three different loading rates (2,3,4), linearized curves (5,6,7). Dashed lines are curves predicted by theory, bold lines are experimental curves. From [2].



2002-08-27

 $\sigma = 0,5 \times \tau$ to 68 MPa at 1,55 MPa/s (von Mises)

Fig 2a Elongation of POM specimen as function of time, at prescribed axial stress.

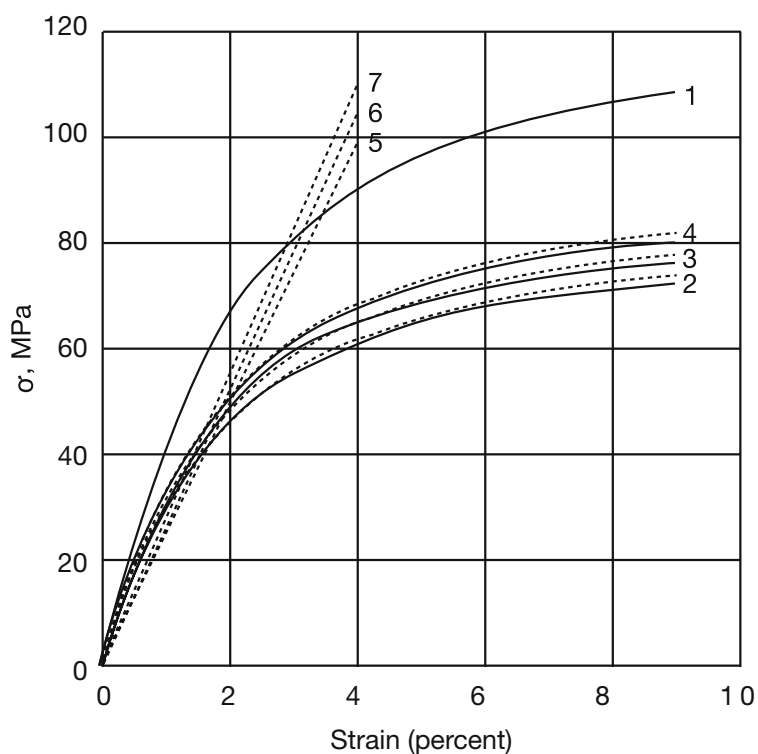


Fig 2b Angle of rotation of POM specimen (degrees) as a function of time. Loading for 50 s, followed by creep.

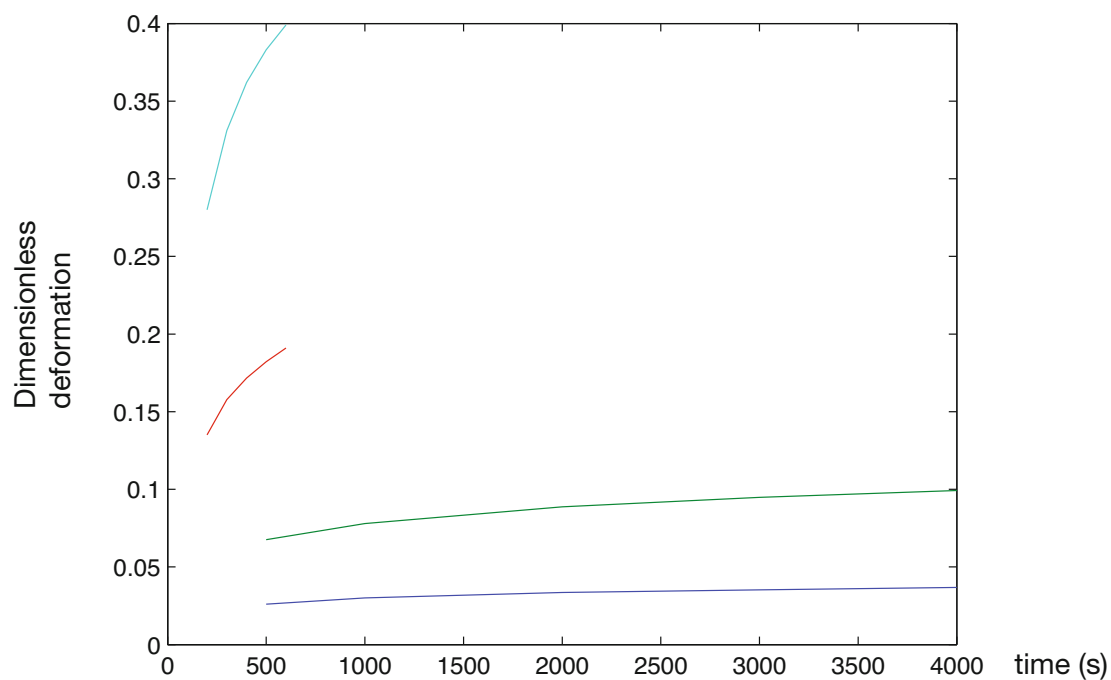


Fig 3 Relative deformation for PA at effective stress 35 MPa (upper two curves, the lower of the two, red, is elongation, the other is torsion) and at 24 MPa (lower of the two, blue, elongation, the other is torsion). It is seen that although stresses are in constant proportion, deformations are not.

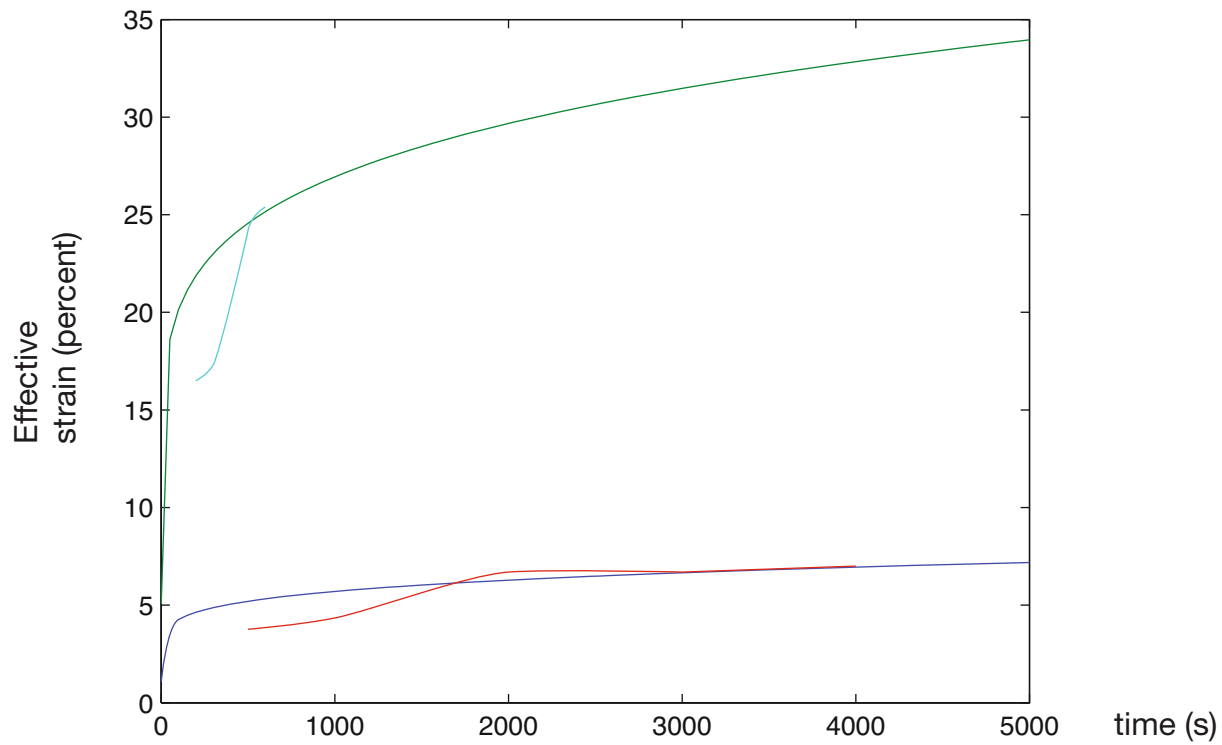


Fig 4 Results from tests of PA at 35 MPa effective stress (upper curves) and at 24 MPa (lower curves). The smooth curves ranging from 0 to 5000 s are predicted curves (green and violet), the other two are based on test results (turquoise and red).

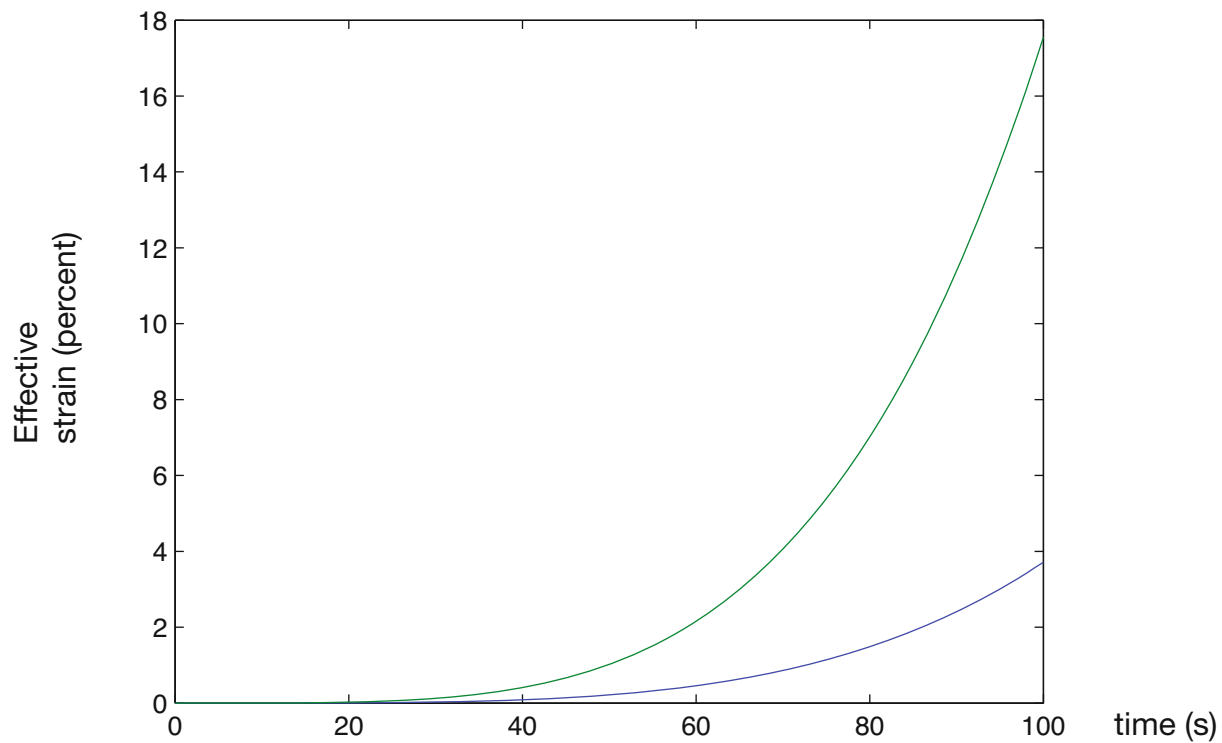


Fig 5 Predicted strain during loading stage for PA. Upper curve (green) at effective stress 35 MPa. Lower curve (blue) at effective stress 24 MPa.

Results for POM are presented in [Table 1](#). All tests were made at effective stress 65 MPa. Strains are in percent, presented as axial strain/shear strain.

Table 1

Test	σ MPa	τ MPa	Time s	Experiment	Theory
1	51	23	500	11.4/10.3	15.9/10.9
			1500	13/12.2	16.8/11.5
2	19	38	500	2.3/9.1	2.4/7.3
			1500	2.6/9.9	2.6/8.0
3	34	31	500	5.3/9.9	5.9/8.3
			1500	6.0/11	6.3/8.8

Membrane tests

Pressure load in bars as a function of time is presented in [Figure 6](#). Measured and computed strains are shown in [Figure 7](#). Lower curve (green) was obtained from strain gage measurements. Upper curve (blue) are strains computed from displacements. Middle curve (red) shows results according to theory.

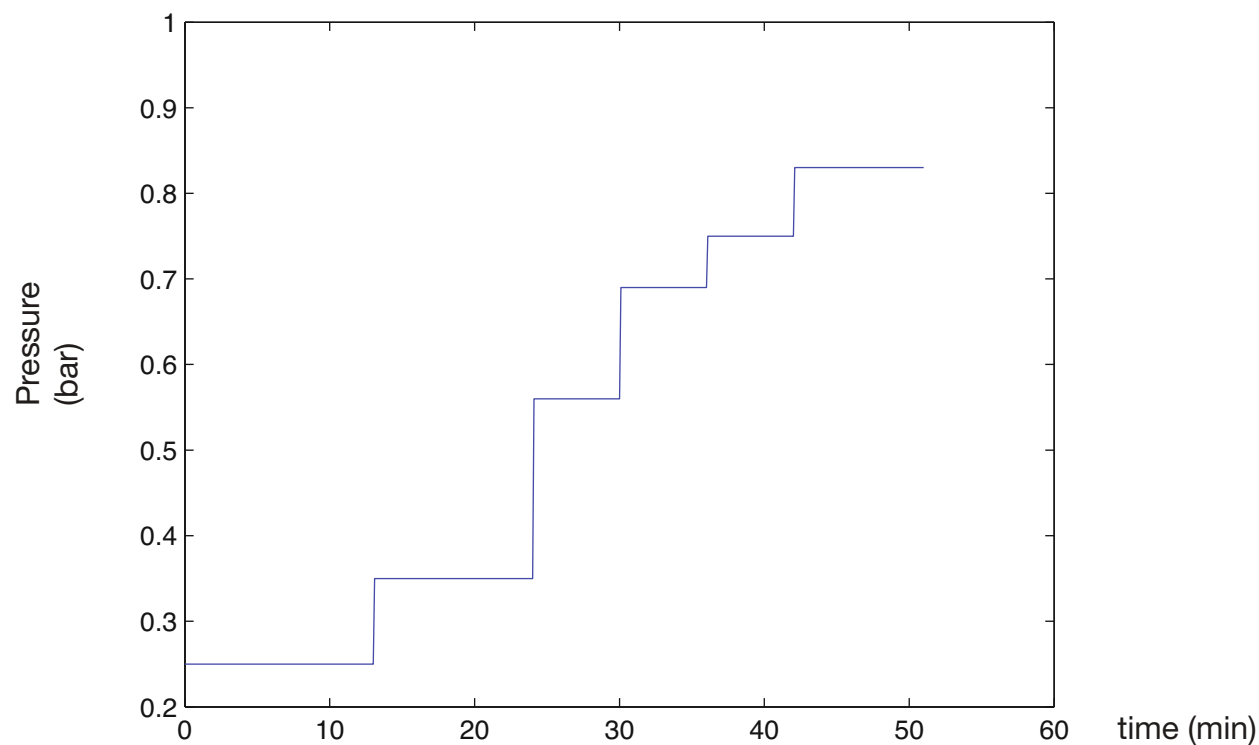


Fig 6 Pressure load of POM membrane, applied in steps.

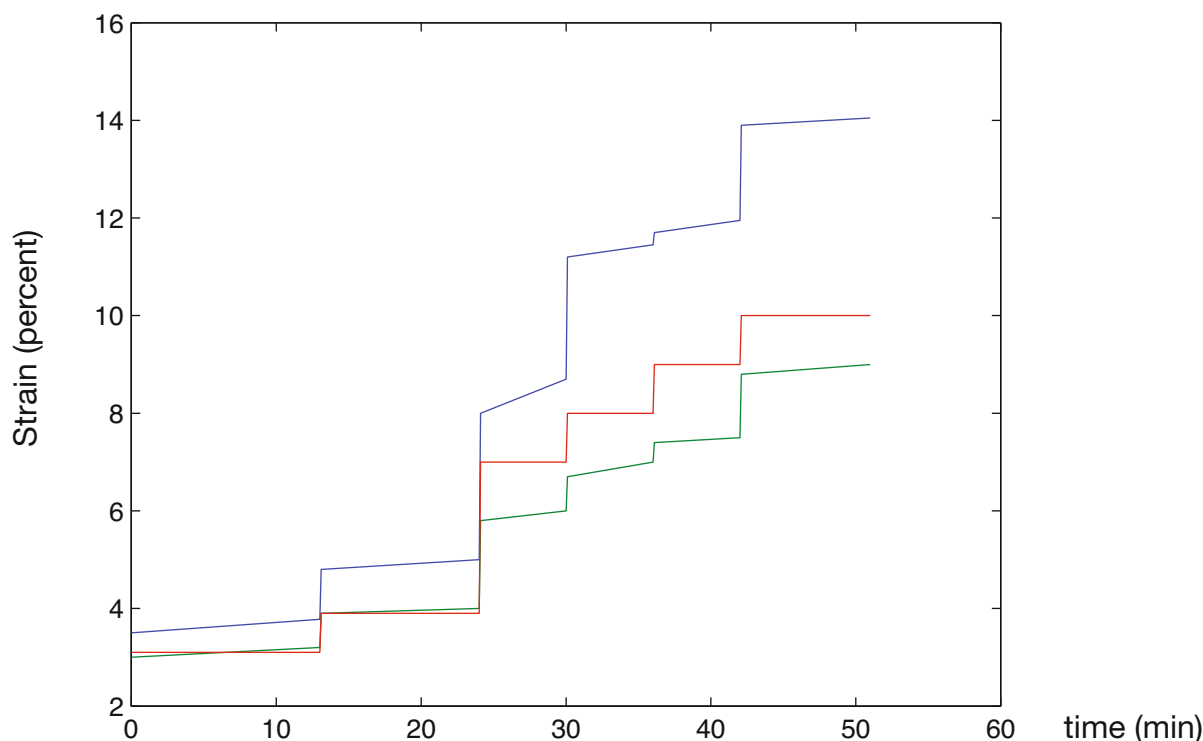


Fig 7 Membrane strain at apex. Green and blue curves are measured strains, see text, and red curve is predicted strain.

DISCUSSION

Biaxial testing is often connected with many trivial problems in the test set-up, like slip in specimen clamping, and precision in measurements of displacements and their conversion to strains. Presented results are average values taken over about three specimens subjected to the same treatment. Scatter in these tests are within 10 percent. Experiments agree quite well with test values, taking into account the rather strict assumptions that must be made, e.g. concerning incompressibility. Corrections may be made with respect to elastic deformation but it seems to be unnecessary and would complicate the model.

Buckling was observed for POM in most specimens. The tube began to "swell" almost symmetrically, as if it had been subjected to interior pressure, an unexpected kind of behaviour. Finally, normal buckling with a pattern of two buckles emerged. Especially for high biaxiality, material appeared to be "brittle" and failed by brittle fracture, a large number of fragments being created. Obviously, the hereditary theory is unable to predict such changes in material behaviour, which instead may be caused by some change in molecular structure of the polymer.

CONCLUSION

One concludes that the Rabotnov-Suvorova theory for hereditary materials can predict plastic deformation of the polymers tested in monotonous biaxial loading with constant ratio between loads as a function of time, both at applied loading and at constant load. The strength of the singularity in the integral equation (represented by parameter α) must be accurately determined for obtaining good results for long-term creep.

REFERENCES

- [1] Rabotnov, Yu.N., & Suvorova, J.V. The non-linear hereditary-type stress-strain relation for metals. *Int. J. Solids Structures*, 14, pp 173-185, 1978.
- [2] Suvorova, J.V., Ohlson N.G. & Alexeeva, S.I. An approach to the description of time-dependent materials. *Materials and Design*, 24, pp 293-297, 2003.
- [3] Ohlson, N.G. Use of viscoplastic models for prediction of deformation of polymer parts. *Proc. SEM annual conf.*, 2010, paper no. 234.
- [4] Odqvist, F.K.G. In *Proc. 4th Int Congress Appl. Mech.*, Cambridge, p 228, 1934.

Parametric study to optimize aluminum shell structure under various conditions

F. Ayari ^{1,2,*}, E. Bayraktar ²

¹ Laboratory of Mechanics, College of Science and Technology, 1008 Montfleury, Tunis, Tunisia

² Supméca/LISMMA (EA2336)-Paris, School of Mechanical and Manufacturing Engineering France

* Corresponding author. E-mail address: fayza_20002000@yahoo.com

Abstract:

The horizontal stabilizer is a fixed wing section; it's a key element to provide flight stability for the aircraft, to keep it flying straight. Most of horizontal stabilizers are equipped with elevators which are a movable surfaces intended to vary the amount of force generated by the tail surface and are used to generate and control the pitching motion of the aircraft. The most important requirement expected from the horizontal stabilizer is to be reliable, easy maintainable, and operable at any condition which might occur during standard flight. The main goal in this paper is to perform a static analysis for the structure of the stabilizer assembly using ABAQUS CAE to simulate and predict the behavior of the structure under various external critical loads.

Keywords: horizontal stabilizer; *FEM*, *parametric study*

1.Introduction

The production of the light aircraft becomes more and more important nowadays, considering the primordial need for these types of aircraft in several fields such as pilot training, agricultural chemical treatments, topographic pictures, and so many other useful field of our everyday developed way of life. The invention of the airplane and numerical drawing and analysis are one of the most important technical developments of the twentieth century [1-10]. Nowadays, the most critical issues for airplane constructors are to find new methods and technologies to make the aircraft lighter and also find design and testing processes at the lowest cost, the answer to these issues came with the appearance and the development of new mathematical and computational tools that allow the development of the virtual drawing, simulation and testing software. Even if most of the work on simulation and design of aircraft structural component is directed towards large commercial aircraft engineering [11-12], there is also considerable interest in developing design of small aircrafts type A and B. Essentially, recently a large amount of structural design research papers have been the focus of intensive investigations, due to the powerful world commerce of this industrial field. As far as experimental tests of aircraft structure during design process are extremely expensive and time consuming and in order to reduce the number of costly prototype tests, a reliable analytical tool is necessary to accurately predict the structural responses and to avoid failure. This work consists on a parametric finite element simulation of a full horizontal light aircraft stabilizer structure, under various critical loading conditions. In order to improve the design and performances of this key structural aircraft component, under critical loading conditions, the ABAQUS software package is used to carry out this study. It is worthy important to perform a static analysis for the structure of the stabilizer assembly using ABAQUS CAE to simulate and predict the behavior of the structure under various external critical loads. In this investigation, the structure was modeled with a 3D full model with geometry similar to a commercial STORM RG aircraft. A realistic and accurate description is done via figures 1 and 2 as it seen below. This study has been very constructive and useful, so that it has allowed us to define the best appropriate geometric parameters under critical boundary conditions. The methodology proposed in this study can also be used to optimize the foremost aircraft components. The first section explains the three-dimensional pressure distribution over the horizontal stabilizer. The second section was devoted to describe a simple variable cross

section beam extension using finite element method (FEM) analysis, on which the FEM software packages are based to make the numerical analysis. The third section illustrates the numerical analysis of the horizontal stabilizer, the main wing spar using ABAQUS FEM [13] software package and CATIA CAD (computer aided design) software. A discussion and conclusions are presented at the last section to evaluate these case studies.

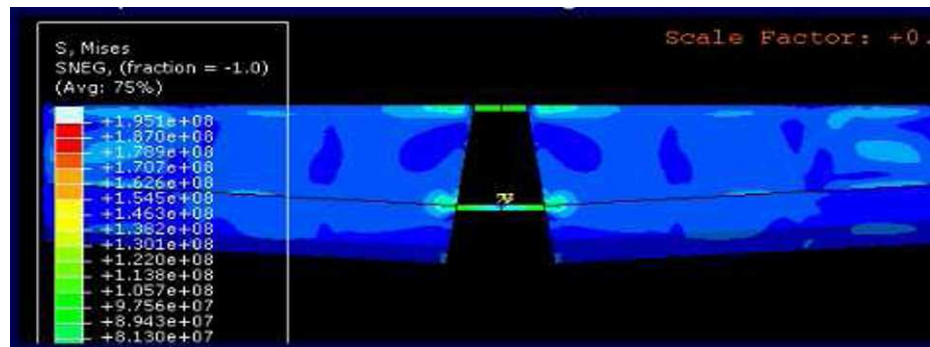


Figure.1 skin of the stabilizer

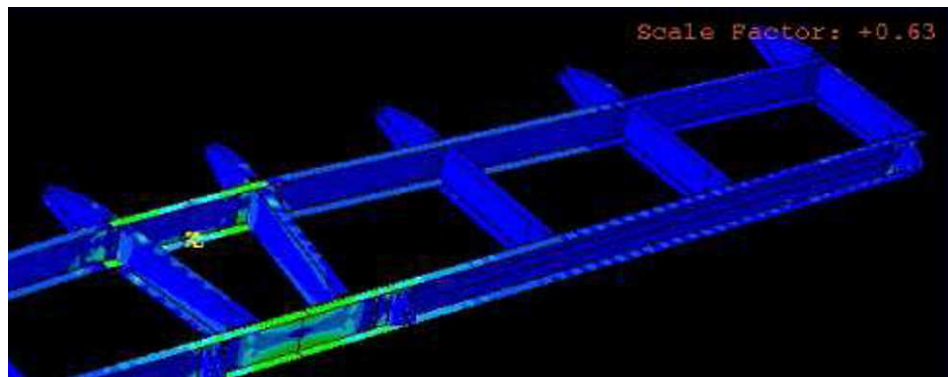


Figure.2 Internal stiffeners of the stabilizer

2. Experimental conditions and pressure distribution

Initially, the plate materials with a thickness of 2 and 3mm were made of special continuous casting by our objective in this report is to justify that the wings and the empennage are well dimensioned. So we will be interested at the worst (limit) conditions to which of the aircraft flight, by mean of the limit values of VNE (Speed to Never Exceed) of 310km/hour as IAS (indicated air speed) at 5000ft and simultaneously 13000ft altitude with no gust wind. Following to the Storm RG Manual, limit testing should be done at altitudes of at least 5000 ft. So the Altitude domain at which we got to justify our wings and empennage structure is between 5000ft and 13000ft. in the fooling subsections we will justify the geometric and loading parameters.

2.1 Loading parameters evaluation

As it is shown by the [figure 3](#), the maximum thickness of the empennage are measured and then presented in [figure 3](#). Thickness located at 22.2 cm from the leading edge which represent 30% of the empennage length (74 cm), is about 8.9 cm. Then, the maximum percentage thickness to the empennage tip chord is equal to $\frac{8.9}{74} * 100 = 12\%$. It is noted that the empennage airfoil is symmetric; the airfoil of the empennage is a NACA 0012.

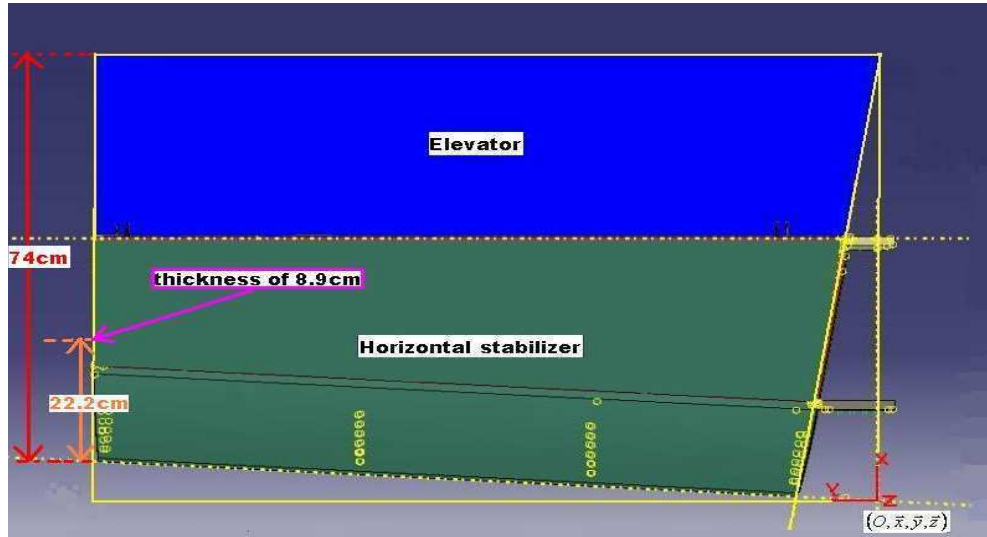


Figure.3 the maximum thickness to the empennage tip chord

2.2 Calculation of the Mach and Reynolds numbers at the limit conditions

For both of case, 5000 ft altitude with IAS speed of 310km/hour and 13000 ft altitude with IAS 310km/hour, we have to estimate the Mach number and the Reynolds number.

$$IAS \approx EAS \text{ (Equivalent Air Speed)} \approx \sqrt{\frac{\rho}{\rho_0}} * TAS = \sqrt{\sigma} * TAS \quad (1)$$

So $TAS \approx IAS/\sqrt{\sigma}$

Where ρ is the air density, and $\rho_0=1.225 \text{ kg/m}^3$ is the air density at zero meter altitude, and σ is the relative density $\sqrt{\frac{\rho}{\rho_0}}$ given by the International Standard Atmosphere (ISA) table [14] as a function of the altitude Z (in feet).

$$Mach = \frac{TAS}{a} = \frac{TAS}{\sqrt{\gamma RT}} \quad (2)$$

Where $a = \sqrt{\gamma RT}$ is the local speed of sound and it is function of the temperature T , $R = 287.05 \text{ J/kg/K}$ and $\gamma = 1.4$. The Reynolds number is given by the following formulation:

$$Re = \frac{\rho * TAS * L}{\mu} \quad (3)$$

Where ρ the air density at 5000ft, TAS is the true air speed equal to 99.9317 m/s, L is the empennage average chord length, it is equal to 0.773 meter, and μ is air viscosity at 5000ft. using the Sutherland law the air viscosity is done by equation (4):

$$\mu = \frac{1.4586 * T^{3/2}}{110.4 + T} * 10^{-6} \quad (4)$$

Taking into account these equations; the Mach number is then equal to $0.2988 \approx 0.3$ at 5000ft and the Reynolds number is about $4.6 * 10^6$. Similarly, at 13000 ft Mach number of 0.32 and a Reynolds number of about $4.0 * 10^6$.

2.3 Determination of the lift coefficient C_L and the drag coefficient C_D for the NACA0012 at the limit conditions.

The lift coefficient C_L for this empennage NACA0012 and the empennage attack angle $\alpha = -4^\circ$ when the aircraft is at a straight level flight. C_L represents the proportion of total dynamic pressure converted to lift force. The following graphs presented in figure 4 a, draw the C_L coefficient vs the empennage attack angle α , simultaneously the blue curve is done by the reference [15], while the green and red graphs have been determined using two airfoil prediction codes [16] Xfoil and Javafoil.

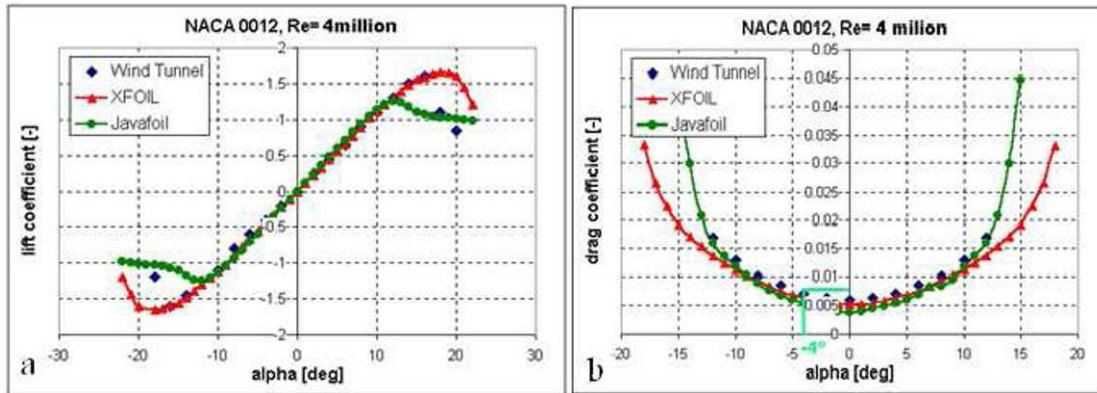


Figure 4 (a) NACA0012 lift coefficient vs. angle of attack at $Re=4 \cdot 10^6$, (b) NACA 0012 drag coefficient vs. angle of attack at $Re=4$ million

We can see that the three curves overlap between -12° and 12° of incidence, -4° is incidence in the linear domain of these curves with a slope $dC_L / d\alpha$ of 0.11, so that the C_L coefficient corresponding to the incidence $\alpha = -4^\circ$ is $C_L(-4^\circ) = -0.449$. The coefficient C_{d0} of the NACA0012 according to the McCroskey correlation function is done by the relation (5).

$$C_{d0} = 0.0044 + 0.018 Re^{(-0.15)} \quad (5)$$

According to equation (5) C_{d0} is equal to 0.006168. The figure 4b presents the drag coefficient C_d vs the empennage attack angle α according to the XFOIL and Javafoil prediction codes; we are closer to the blue wind Tunnel curve. Graphically our drag coefficient for -4° is 0.008, so in the two cases we will take $C_D(-4^\circ) = 0.008$.

2.4 Determination of the 2-dimensional pressure distribution of the empennage airfoil at the limit conditions.

We have seen that the pressure over an airfoil is not uniformly distributed, and we know that the pressure distribution depends of the airfoil shape, the angle of attack, the Mach number, the Reynolds number. To have a realistic pressure distribution over this NACA0012 airfoil empennage in the two limit configurations (5000ft and 13000 ft), we have used NASA report [15]. In this report tests were conducted in the two dimensional test section of the Langley 0.3 meter transonic cryogenic tunnel on a NACA 0012 airfoil to obtain aerodynamic data as a part of the Advanced Technology Airfoil Test (ATAT) program. The test program covered a Mach number range of 0.30 to 0.82 and a Reynolds number range of $3.0 \cdot 10^6$ to $45.0 \cdot 10^6$. The stagnation pressure was varied between 1.2 and 6.0 atmospheres and the stagnation temperature was varied to obtain these test conditions. This will give us the answer about how the pressure is distributed for our two cases.

It has been shown in the McCroskey report, that for the NACA 0012, at a Mach 0.3, the variation of the Reynolds numbers from 3 to 9 million have mostly no effect on the lift coefficient C_L and variation of 10% on the drag coefficient C_D (C_D is evaluated in our case at a hundred percent of C_L). So if the impact from 3 to 9 million of the Reynolds number is so small, the impact of a 1.5 million in that domain is negligible (between 4 million and 4.6 million). Thus, we can assume that for both of cases we have a unique pressure distribution function and an average Mach number of 0.31.

According to reference [16], it is deduced that the closest Reynolds number is equal to 3.1 million, the closest Mach number is equal to 0.3053, and the closest angle of attack, α is equal to -4.01° . We are interested here for this specific configuration to study the pressure coefficients C_p of the upper and lower surface which will give us the shape of the 2-D pressure distribution over the lower and upper surfaces of our NACA0012 airfoil empennage. So we will extract for the lower and upper surfaces the coefficients of pressure C_p corresponding to a particular position of X/C in %. A 2-D pressure function, $C_p = f(X/C)$ is drawn using interpolation via Math Lab.

A polynomial interpolation technique is used to identify the pressure distribution function on the upper and lower surfaces. Using the `polyfit(x,y,n)` function in matlab package, we have

rise up the polynomial function until the best approximation was found. For both surfaces the best approximation degree function is obtained with degree 6 as it is shown by figure.6a and Figure.6b

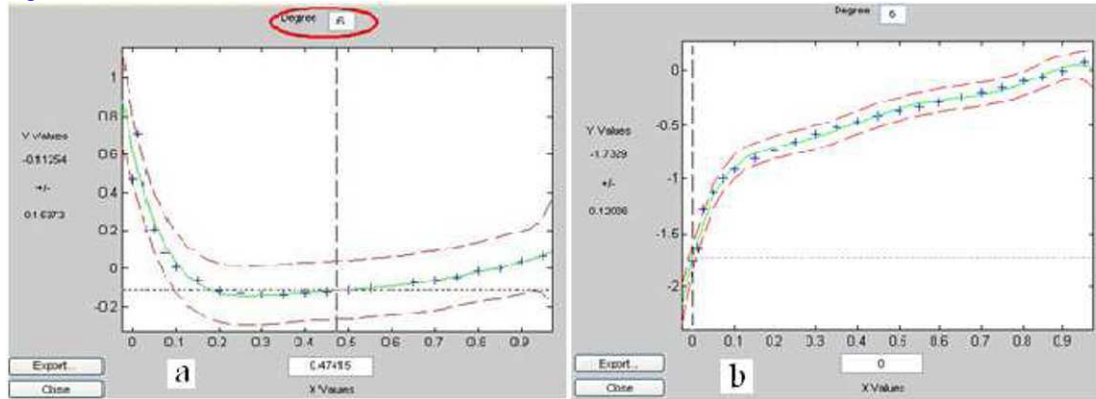


Figure.6 polynomial function for the pressure distribution $C_p=f(X/C)$, best fit interpolation with degree “6” from polytool(x,y) (a) upper surface, (b) lower surface of the empennage

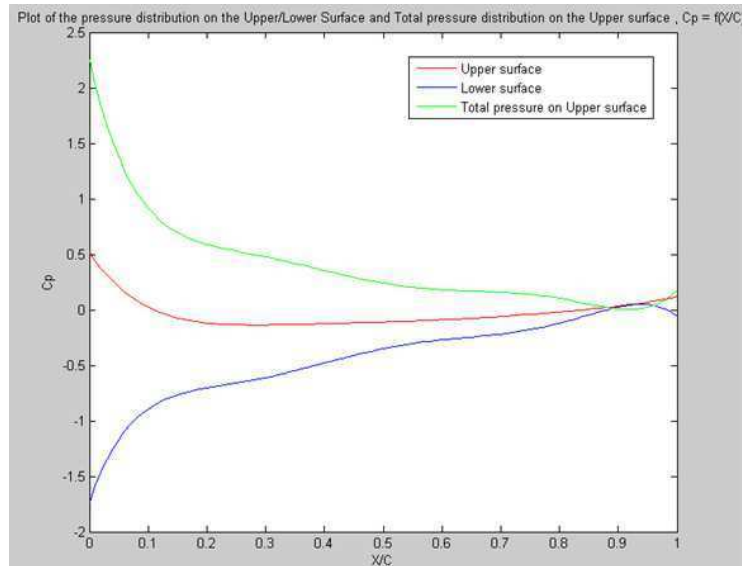


Figure.7 Pressure distribution on the upper/lower surface and the total pressure distribution on the upper surface $C_p=f(X/C)$

The green curve is representing the total pressure distribution over the upper surface which gives us the total down lift on the empennage, the red curve is representing the upper surface pressure distribution function and the blue curve is representing the lower surface pressure distribution function.

In order to get the 3-D pressure distribution from the last 2-D pressure distribution function we have to consider the geometry shape of the empennage, thus we consider that the orthogonal projection of the empennage profile is rectangular with a constant chord of 0.815 m and a span of 1.229 m. an adequate transform is applied to the 2D pressure function to get the 3D pressure distribution as it is shown by the figure 8. This function is too close to the real pressure distribution applied to the empennage according to the limit flight defined previously. Taking into account that IAS is 310km/hour = 86.11 m/s, the magnitude of the pressure distribution function over the empennage area “S” is done with equation 6:

$$\begin{aligned}
 R &= \frac{1}{2} \left(\rho_0 * \sigma(5000 ft) \right) \left(\frac{V_{IAS}}{\sqrt{\sigma(5000 ft)}} \right)^2 * S * \sqrt{C_L^2 + C_D^2} \\
 &= \frac{1}{2} \left(\rho_0 * \sigma(13000 ft) \right) \left(\frac{V_{IAS}}{\sqrt{\sigma(13000 ft)}} \right)^2 * S * \sqrt{C_L^2 + C_D^2}
 \end{aligned} \quad (6)$$

So far, the load over the empennage is then equal to 1822.146 Newton and our final pressure distribution function is given by the following plots [figure.8](#).

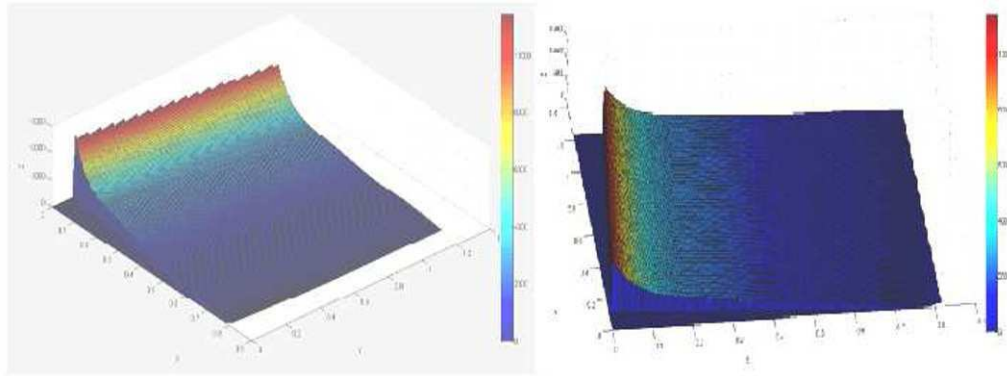


Figure.8 Plot of the 3-D pressure distribution function over the whole empennage

2.4 Punctual loads on the elevator hinge brackets at the limit conditions

An algorithm was build with mat lab package to provide the volume function of the pressure distribution over the empennage sections. Then, we can obtain the plot of the pressure distribution function over the horizontal stabilizer. The plot of the pressure distribution over the horizontal stabilizer given via [figure.9 b](#)

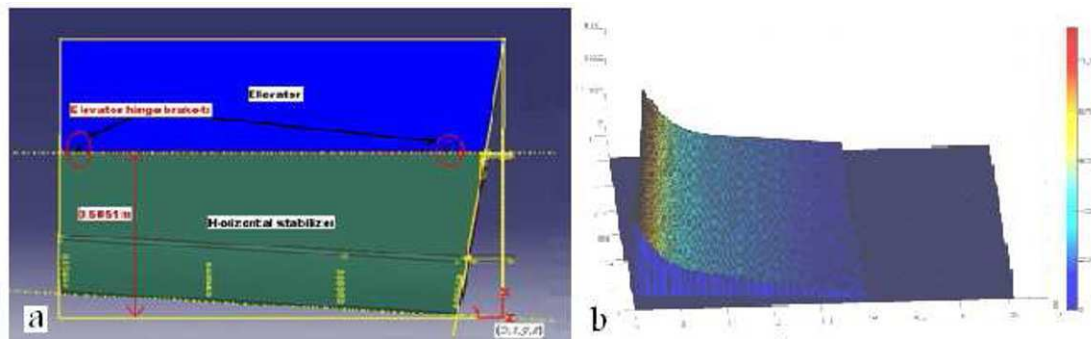


Figure.9 (a) Storm RG empennage and (b) the upper view of the pressure distribution over the horizontal stabilizer

It is easy so to deduce the elevator loads and the lift and drag over the elevator can be calculated then. As it is shown via [figure 10](#), the horizontal stabilizer has two elevator hinge brackets, and at this stage, it is possible to get the over load distribution on the different parts of the empennage. It is noticed that we haven't take vortices effect into account, because their effect is to reduce the load pressure on the empennage tip, this fact lead artificially to overestimate a bit the load on our empennage and so to justify safely those boundary conditions.

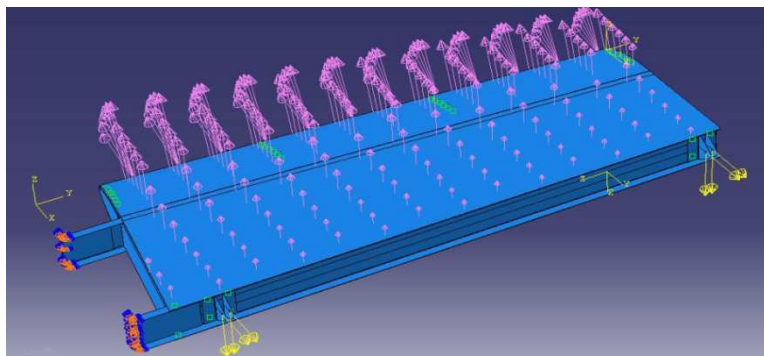


Figure.10 View of the pressure distribution function on the horizontal stabilizer and the loads on every elevator hinge bracket

3. FEM numerical study of the horizontal stabilizer.

The horizontal stabilizer is a fixed wing section; it's a key element to provide flight stability for the aircraft keeping its flying straight. Most of horizontal stabilizers are equipped with elevators which are a movable surfaces intended to vary the amount of force generated by the tail surface and are used to generate and control the pitching motion of the aircraft. The most important requirement expected from the horizontal stabilizer is to be reliable, easy maintainable, and operable at any condition which might occur during standard flight. Experimental tests of aircraft structure during design process are extremely expensive and time consuming. In order to reduce the number of costly prototype tests, a reliable analytical tool is necessary to accurately predict the structural responses/failures.

3.1 FEM modeling

Our task consists of performing a numerical analysis for the horizontal stabilizer using Abaqus software package. The horizontal stabilizer was modelled in a 3D space and its geometry was very realistically and accurately described as it can be seen in [Figure.11](#). A 3D model was produced using CATIA V5. In [figure 12 a and b](#), it is shown that all component are created as parts to be assembled with a geometry that is parameterized. A 3D model was imported to ABAQUS as a 3D shell structure. 4SR elements are used to model the skin and the shell structural components. Riveting is done with fasteners elements. Connection between layers in the skin is done with fastening points using either connector elements or BEAM MPC. Each fastening point is connected to the surface using a distributing coupling constraint that couples the displacement and rotation of each fastening point to the average displacement and rotation of the nearby nodes. The number of fasteners generated over the structure was up to 500 fasteners. [Figure 12 c](#) illustrates clearly the model after fastening, and also the number of features and sets under the assembly module in the model tree. Fastening is among the most delicate and time consuming operation since each region of a part must be fastened independently.

Based on the information provided by the constructor, we assume that the material is isotropic, linearly elastic and the load is transferred symmetrically to both halves of the structure, so only one half of the structure needs to be analyzed during the process of numerical calculation as shown by [figure13](#) and [14](#). The material used for construction is aluminum alloy. [Table 1](#) below illustrates the material properties used in all structural components. [Figure 13](#) show the boundary and loading conditions and [Figure 14](#), illustrates the dynamic modal response of the different assembly components tested up to 260 modes. After performing this analysis we can obviously make sure that all the parts are well fixed and well positioned.

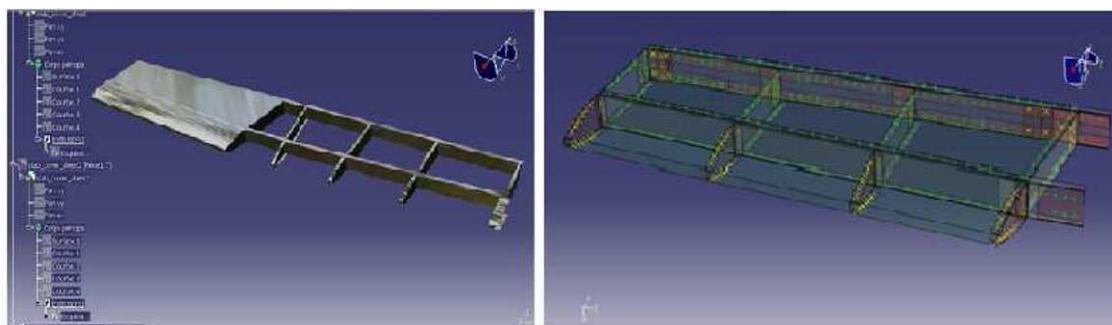


Figure.11 3D presentation of the model using Abaqus

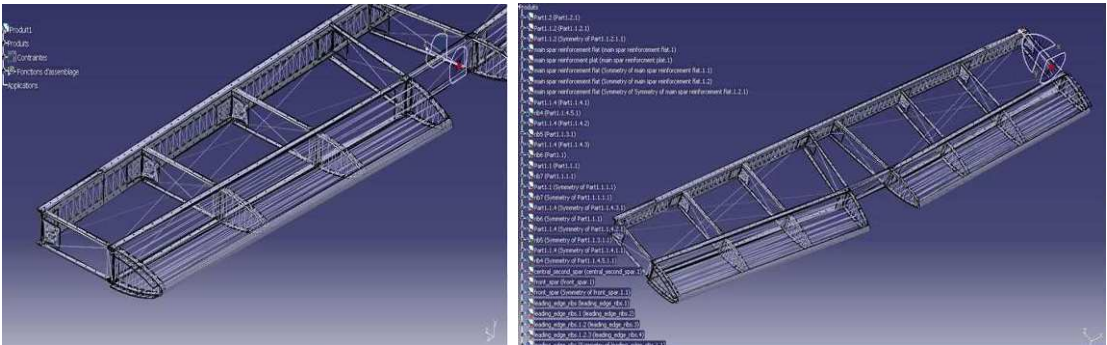


Figure.12 a 3D presentation of the internal components using catia v5

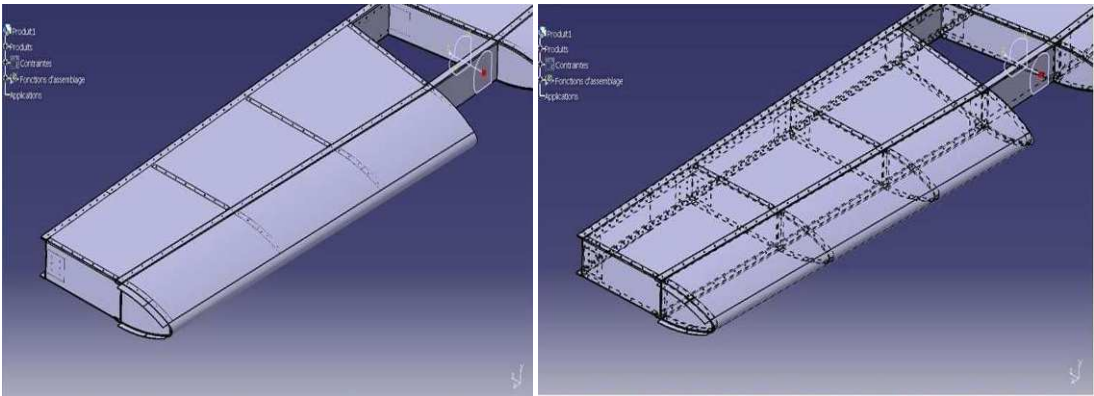


Figure.12 b 3D presentation of the skin and flanges using catia v5

Table.1. structural material properties

Material category	Density (kg/m3)	Young's modulus (Gpa)	Poisson's ratio	Parts involved
6082-T6	2700	69	0.33	Skins(coversheets)
6061-T6	2850	70	0.33	Rib stiffening
2024-T3	2780	73.1	0.33	Beams and spars

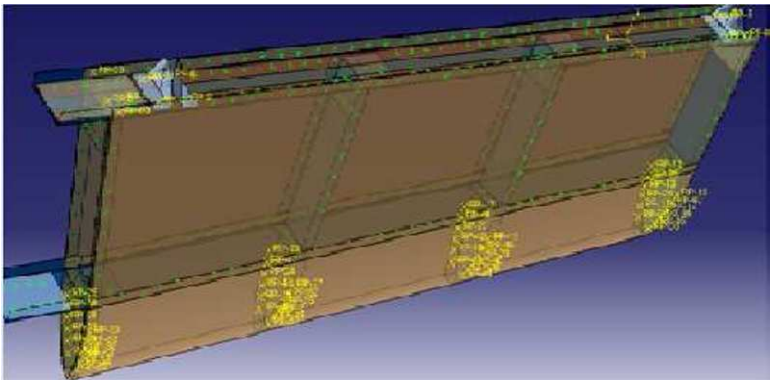


Figure.12 c 3D FEM model using Abaqus

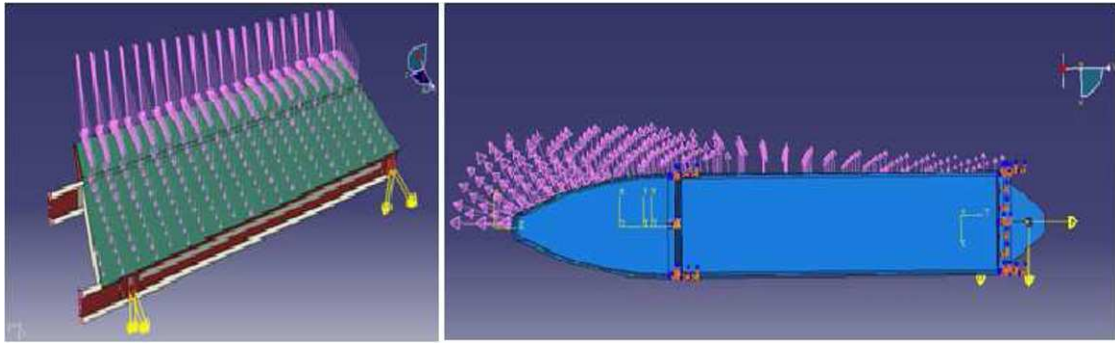


Figure.13 3D FEM model using Abaqus

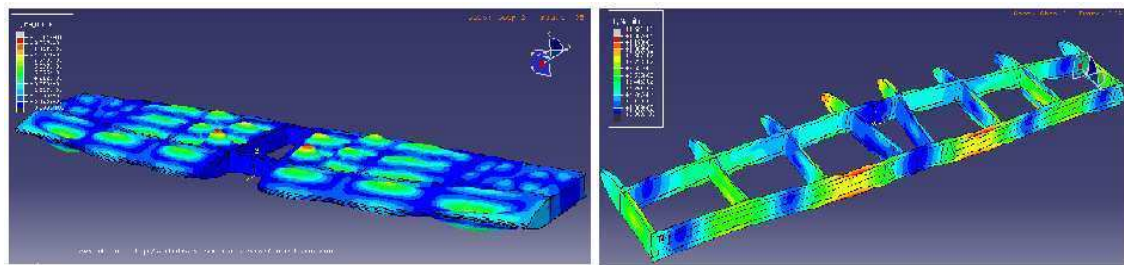


Figure.14 3D FEM model using Abaqus

4 Results and Discussion

The maximum displacement of the horizontal stabilizer in the x-direction is 20 mm, the figure 15.a and 15b below illustrate displacements of the main wing spar.

The maximum principal stress in the model, reported in the contour legend, is 195,123 MPa located in the attachment zone of the horizontal stabilizer, although the mesh in this model is fairly refined and, thus the extrapolation error should be minimal. The maximum stress value doesn't reach the yield strength of material which is 483 MPa. Figure 16.a and 16 b below show the stress distribution using contour plots and the zone of maximum stress in the model.

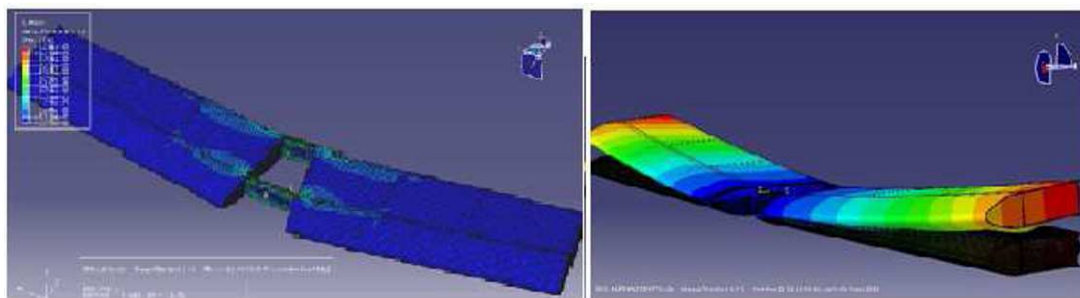


Figure.15 (a) mesh details of the model, (b) displacement contour of the deformed model of the horizontal stabilizer

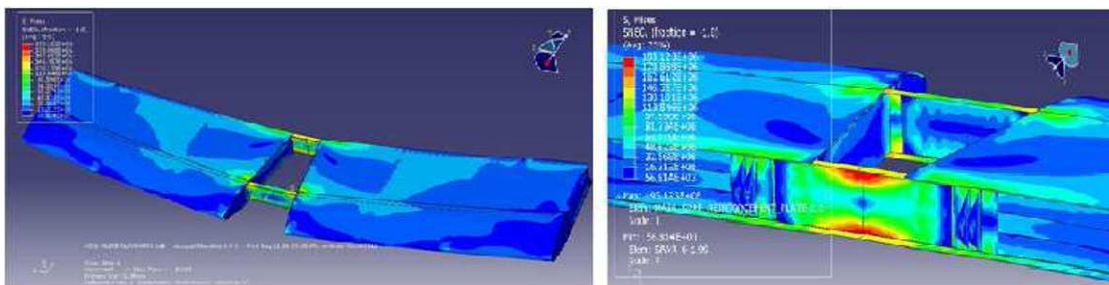


Figure.16 (a) stress distribution of the model, (b) stress details at the end step.

The central spar is a 2024T3 aluminium alloy with tensile yield strength of 345 Mpa. The maximum principal stress in the main spar, reported in the contour legend is 162 Mpa located in the attachment zone, the maximum stress value show that the structure is already under the yield strength of material which is 345 Mpa.

4.1 Stress distribution in the main spar reinforcement plate

The main spar reinforcement plate is a 6061T6 aluminium alloy with tensile yield strength of 276 Mpa. The maximum principal stress [figure 17](#) in the part reported in the contour legend is 195 Mpa located in the attachment zone, the maximum stress value reached show that the structure is already under the yield strength of material which is 276 Mpa.

The regions distinguished by a high stress distribution are subjected to a high shear stress when two or more parts are riveted together where the appropriate type, size and mechanical characteristics of rivets must be chosen. The size, material, and mechanical properties of rivets near the maximum stress zone must be higher than other regions. The [figure 17](#) below shows the location of rivets in the model.

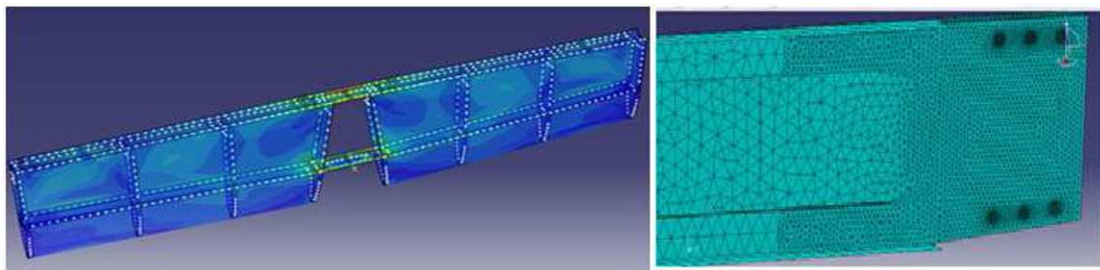


Figure.17 (a) stress distribution of the model, (b) mesh details at the rivets vicinity.

4.3 Main wing spar

The main wing spar is the essential part where every wing piece (main landing gear, ribs, etc.) is attached to make up the entire wing of the aircraft. The main wing spar is also the critical part of the wing that will withstand the great proportion of the external load effect applied on the wing.

This approach of geometry and meshing simplification made by the aircraft engineer might be a way to reduce the computational cost of the simulation when the machine memory and processing is limited, however it will reduce the accuracy of the simulation result and give rise to a high error rate which will entails to make a rough and even wrong observations and result confirmations. The right way to have accurate results is to make the model with maximum details so as to be geometrically close to the real model since the model geometry has a direct connection with its behaviour under load effect. The zone of maximum stress corresponds with the first series of vertical holes that join and attach the main wing spar to the wing box of the fuselage. The same result was found with the constructor simulation which lead us to confirm the behavior of the main wing spar under the same principal definitions which are: The distribution of stress over the model implements also a distribution of shear stress between parts that are riveted together. This phenomenon enables the resizing of rivets by modifying materials or dimensions according to local stress values.

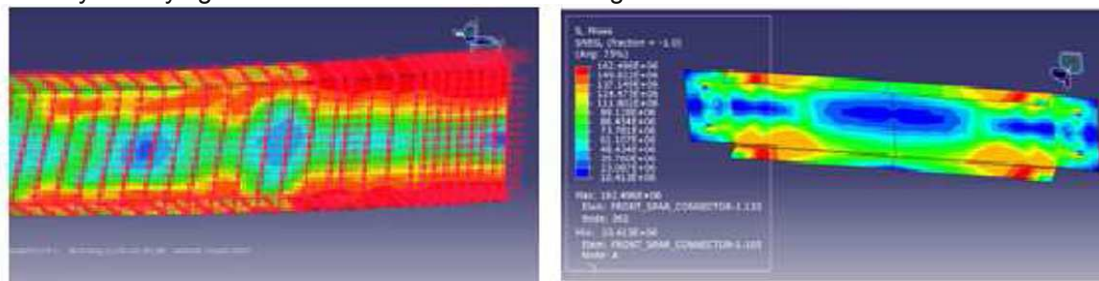


Figure.18 (a) stress distribution of the wing and their orientation, (b) stress details of the wing spar

The [figure 18](#) shows stress simulation, the maximum principal stress in the model, reported in the contour legend, is 324 MPa located in the first row of joint holes, although the mesh in this model is fairly refined and, thus the extrapolation error should be minimal. The maximum stress value reached show that the structure is already under the yield strength of material which is 483 MPa. If we compare our simulation result with the other simulation we see a difference in the maximum principal stress as well as the stress distribution, the maximum value reached by the other simulations is about 336 MPa.

5. Conclusions

Aircraft stabilizers are complex assemblies of thousands of components and as a result simulation models are highly idealized. In the typical design process, a coarse FE model is used to determine loads within the structure. The size of the model and number of load cases necessitates that only linear static behavior is considered. This paper reports on the development of a modeling approach to increase the accuracy of the global model, accounting for variations in loading.

To summarize we might say that over the past few years, many aeronautical engineers are asked to use commercial FEM software packages to simulate and find quantity of interest for engineering systems that are generally described by pictures. Numerous drawings and charts are used to describe important concepts and theories; this is very important and definitely is welcomed by readers, especially those from non-engineering background. One thing must be kept in mind that the finite element method doesn't gives us the exact solution but an approximate one with more or less degree of accuracy, but simulations are very necessary to report a synthesis of the structural behavior under the most limits cases of flight. The numerous steps performed to get accurate results are imperative because they lead to important decisions in designing engineering systems. It is to be noted that many other simulations might be done such as dynamic analysis, virtual crash test, computational fluid dynamics (CFD), and safety analysis are important approaches toward integrated.

References

- [1] FLEURY C., W.H. ZHANG - Selection of appropriate approximation schemes in multidisciplinary engineering optimization, OPTI 95 Conference, Miami, September 95. Published in Computer Aided Optimum Design of Structures IV, Structural Optimization, pp 11-18, Editors Hernandez, El-Sayed and Brebbia, Computational Mechanics Publications
- [2] ZHANG, W.H. and FLEURY C. et al., A generalized method of moving asymptotes (GMM) including equality constraints, WCSMO-1, Goslar, Germany, 1995.
- [3] I-Deas Solid Modeling User Manual, SDRC Corporation. 2000 Eastman Drive, Mildford, Ohio 45150, USA, 1990.
- [4] Jean-Paul Baillon & Jean-Marie Dorlot, Des matériaux, 3rd edition, presse international polytechnique, 2005.
- [5] Li, Q., Steven, G. P., Xie, Y.M., "A Simple Checkerboard Suppression algorithm for evolutionary structural optimization," Structural Optimization, Vol22, 2001, pp. 230-239.
- [6] Bendsoe, M.P., Sigmund, O, Topology Optimization Theory, Methods and Applications, Springer, New York, 1995, pp. 1-158
- [7] Kim, W-Y., Grandhi, and R.V., Haney, M., "An Evolutionary Optimization method for designing a Thermal Protection System for Dynamics," International Journal of Mechanics Based Design of Structures and Machines (Submitted 2005).
- [8] Penmetsa, R.C., Grandhi, R.V., Haney, M., "Topology Optimization for an Evolutionary Design of a Thermal Protection System," AIAA Journal of Space Craft and Rockets, 2004 (Submitted)
- [9] Li, Q., Steven, G.P., Querin, O.M, and Xie, Y.M., "Optimization of thin shell structures subjected to thermal loading," Structural Engineering and Mechanics, vol7, 1999, pp. 401-412.
- [10] Blosser, M. L., "Investigation of Fundamental Modeling and Thermal Performance Issues for A Metallic Thermal Protection System Design," 40th Aerospace Sciences Meeting & Exhibit, Jan 2002, Nevada.
- [11] Iqbal LU, Sullivan JP, Application of an integrated approach to the UAV conceptual design. AIAA 2008-144. Reno, Nevada, USA; January 7–10 2008.

- [12] Alonso JJ, LeGresley P, Pereyra V. Aircraft design optimization. *Math Comput Simulat* 2009; 79:1948–58.
- [13] Abaqus” user’s manual”, volumes I, II and III, version 6.9-3: Hibbitt, Karlsson & Sorensen, Inc., 2009.
- [14] Murray R.Spiegel & Larry J.Stephens, *Statistiques*, 3rd edition, Schaum’s, McGraw-Hill.
- [15] N.F Crasnov, *Fundamentals of theory. Aerodynamics of an airfoil and a wing*, first published 1985.
- [16] W.J.MCroskey, NASA technical memorandum nbr:100019, “Critical assessment of wind tunnel results for NACA 0012 Airfoil”, published by the NASA Ames research center and US Army aviation systems command, in 1987.
- [17] Charles L.Ladson, Acquilla S.Hill & William G.Johnson Jr. NASA technical memorandum nbr:100526, “pressure distributions from high Reynolds number transonic tests of NACA 0012 airfoil in the Langley 0,3-meter transonic cryogenic tunnel” published by NACA published research center. 1987.

A Force Domain Analog-to-Digital Converter Applied in Micro and Nanoscale Tensile Tests

Wu-Feng Yeh and Junlan Wang

Department of Mechanical Engineering, University of Washington, Seattle, Washington, USA

ABSTRACT

Mechanical characterization of sub-micron thin films or similar small scale structures have been a continuous challenge to the mechanics community due to the difficulty in accurately quantizing the applied load and resulted deformation. In this work, a new Force Domain Analog-to-Digital Converter (F-D ADC) is adopted to perform thin film tensile tests. The key component of the F-D ADC is a quantizer-array of microfabricated buckling beams of pre-determined length. During the testing, the applied force is quantized using the critical load of the increasing number of buckling beams and the deformation of the specimen is controlled by the loading stage. The resolution and accuracy of the current method can be significantly improved by increasing the number of buckling beams.

INTRODUCTION

With the rapid development of MEMS technology, more and more thin-film materials are applied in the MEMS fields. Mechanical properties such as Young's modulus, tensile strength, Poisson's ratio, etc. are very important for designing MEMS devices and also directly linked to their performance and reliability. However, the mechanical properties of thin-film materials are quite different from bulk materials because of the difference in scale and fabrication process. Therefore, measuring mechanical properties of thin-film materials has become an essential research topic in MEMS fields.

In general, to measure the mechanical properties of materials in micro- or nano-scale, the method must be able to: (1) fabricate and manipulate test specimens, (2) measure geometric scales of test specimens, (3) apply force or displacement to deform test specimens, (4) measure the force applied to test specimens, and (5) measure the deformation of test specimens [1]. Various testing methods such as nano-indentation [2], surface acoustic wave [3], resonant frequency [4], bending test [5], have been developed to measure the mechanical properties. However, tensile test is still the most common and direct method. To perform the tensile test on thin films or micro-structures, MEMS technology provides a promising platform on which test specimens can be fabricated and tested. Therefore, MEMS based tensile test is very popular for characterizing the mechanical

properties with high accuracy and reliability.

Although MEMS technology already presents significant advantage in fabrication and alignment, difference in force/displacement application and measurement mechanism greatly affects the accuracy of the tensile test. In literature, a few research groups have developed several outstanding techniques in MEMS based tensile testing field. Sharpe et al. [6-9] adopted an interferometric strain/displacement gage (ISDG) technique to measure the deformation of the test specimen and used a commercial load cell to record the applied tensile force. Tsuchiya et al. [10] applied electrostatic force to a probe for gripping test specimens and measure the tensile force with a strain gauge on the probe. The testing was performed in an SEM chamber and also monitored by SEM to determine the deformation. Chasiotis and Knauss [11, 12] also adopted electrostatic force to grip test specimens but monitored the local deformation with an atomic force microscope. An inchworm actuator was used to provide displacement to test specimens, and the induced tensile force was measured by a load cell. Saif and Haque [13-19] proposed an in-situ tensile test in SEM/TEM. The experimental setup consists of a test chip and a piezoelectric actuator which provides displacement/force to the test chip. The applied tensile force was measured by the force sensing beam while the deformation was measured by SEM/TEM. Espinosa [20, 21] also developed a tensile testing system for in-situ SEM/TEM testing. A thermal actuator provides force/displacement to the test specimen. A load sensor was used to measure the applied tensile force, and SEM/TEM was employed to monitor the deformation. Ruoff [22] imported the force sensing beam to measure the tensile force exerted by a thermal actuator. The deformation of the test specimen was also monitored by SEM/TEM.

In this paper, a new force sensor, Force Domain Analog-to-Digital Converter (F-D ADC), is invented and applied to a MEMS based tensile test. F-D ADC proposes an innovative method to quantize the magnitude of the applied tensile force with a quantizer-array instead of measuring the deformation of force sensing beam under high resolution microscopes. The most significant feature of F-D ADC is that the accuracy of the tensile test can be greatly improved by increasing the number of quantizer-array instead of improving the resolution of microscopes. In theory, F-D ADC can even exceed existing high resolution microscopes by selecting proper geometric scales and substrate material for high-numbered quantizer-array.

CONCEPT OF FORCE DOMAIN ANALOG-TO-DIGITAL CONVERTER

I. Flash ADC vs. F-D ADC

The concept of F-D ADC comes from the theory of analog-to-digital converter (ADC) in electric and electronic circuits [23]. An electronic ADC converts a continuous-time and continuous-amplitude signal to a discrete-time and quantized-amplitude signal. There are many ways to implement an electronic ADC such as flash ADC, sub-ranging ADC, two-step ADC, time-interleaved ADC, successive approximation ADC, pipeline ADC, delta-sigma ADC, etc. Among these various ADCs, flash ADC is the fastest and one of the simplest ADCs. Figure 1(a) illustrates the architecture of an n-bit flash ADC. The n-bit flash ADC performs $2^n - 1$ level quantization on input voltage, V_{in} , with $2^n - 1$ comparators. The reference voltage of each comparator is generated by using a resistor ladder connected between V_{REF} and ground, which determines the full scale range of quantization. Each tap at the resistor ladder is connected to one comparator which generates logical “0” or “1”

depending on whether the input voltage is above or below the reference voltage of each resistor tap. Gathering of all the comparator outputs forms a 2^{n-1} -bit code which is converted to an n-bit binary code after a digital encoder.

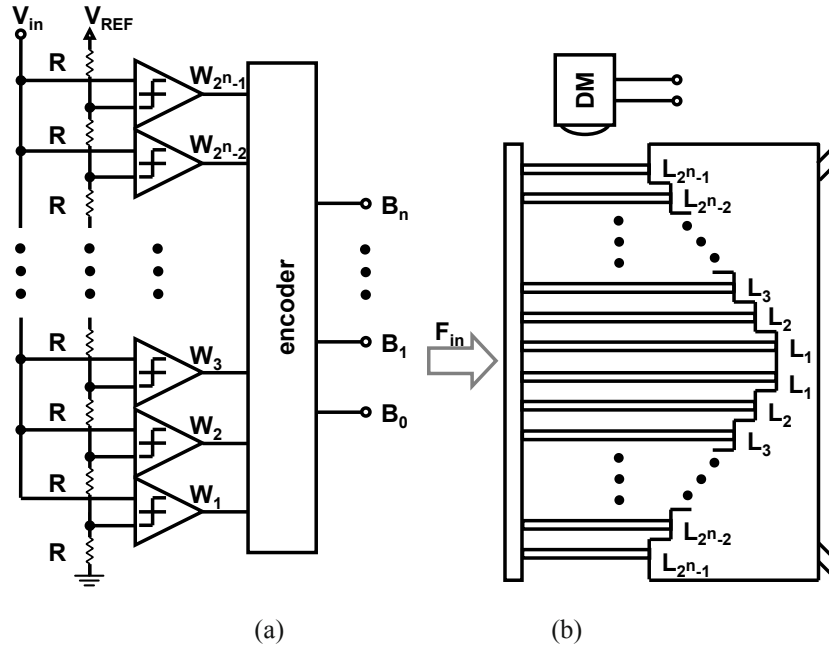


Figure 1. (a) n-bit flash ADC, and (b) n-bit F-D ADC.

Based on the concept of flash ADC, F-D ADC is created to convert continuous force input to discrete buckling responses. Figure 1(b) shows the architecture of an n-bit F-D ADC which consists of $2^n - 1$ pre-determined length beams connected in-parallel and a digital microscope. The length of each beam is determined by the critical buckling length. The pre-determined length beams are compressed by the input force, F_{in} , and the magnitude of the input force is identified as buckled beams and unbuckled beams by comparing the input force to critical buckling load. In this research, the pre-determined length beams are also called quantization beams, buckling beams, or quantizer-array of F-D ADC. The symmetric architecture of F-D ADC is designed for the stabilization of the whole structure. In contrast to flash ADC, the beam arrays corresponds to the comparators while the digital microscope corresponds to the encoder.

II. Proposed F-D ADC Tensile Test

In this paper, the concept of F-D ADC is demonstrated by applying F-D ADC as a force sensor to a tensile test. The architecture of a 2-bit F-D ADC tensile tester is illustrated in Figure 2. As the tensile force, P , is exerted to the tensile tester, P goes through the test specimen and then compresses the quantization beams. Therefore, the tensile force of test specimen is equal to the compressive force of the quantization beams. In other words, the tensile force is quantized by the quantization beams. If distributed compressive force in beam #1 is smaller than the critical buckling load, P_{cr1} , P is equal to the sum of the elastic reactive forces in beam #1, #2, and #3 (i.e. $P = P_{e1} + P_{e2} + P_{e3}$). If distributed compressive force in beam #1 is greater than P_{cr1} while in beam #2 and beam #3 are smaller than P_{cr2} and P_{cr3} , P is equal to the sum of P_{cr1} , P_{e2} , and P_{e3} (i.e. $P = P_{cr1} + P_{e2} + P_{e3}$). If distributed compressive forces in beam #1 and beam #2 are greater than P_{cr1} and P_{cr2}

while in beam #3 is smaller than P_{cr3} , P is equal to the sum of P_{cr1} , P_{cr2} , and P_{e3} (i.e. $P = P_{cr1} + P_{cr2} + P_{e3}$). If distributed compressive forces in beam #1, beam #2, and beam #3 are greater than P_{cr1} , P_{cr2} , and P_{cr3} , P is equal to the sum of P_{cr1} , P_{cr2} , and P_{cr3} (i.e. $P = P_{cr1} + P_{cr2} + P_{cr3}$) [see Figure 2].

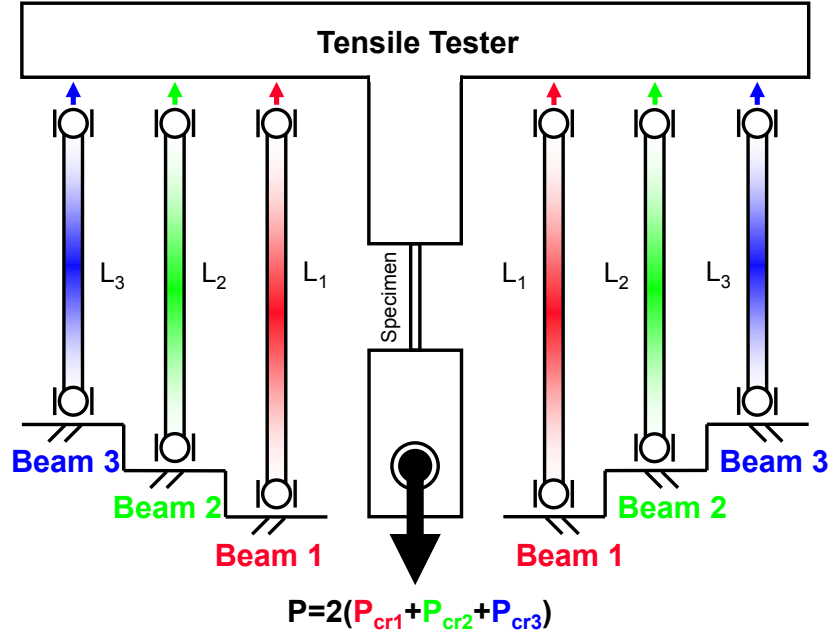


Figure 2. 2-bit F-D ADC tensile test when beam #1, #2, and #3 progressively buckle.

The configuration of an F-D ADC tensile test chip is illustrated in Figure 3. The structure includes two circular holes, two U-springs, 3 pairs of support beams, a C-grip, a transmission beam, a set of test specimens, a T-beam, and a quantizer-array. The two circular holes at the two ends are designed for applying tensile force with two pins and allow the test chip automatically align with the applied force direction. The two U-springs provide enough displacement for the deformation of the test specimen. 3 pairs of support beams suspend the transmission beam which transmits the applied force to both the test specimens and the quantizer-array. The C-grip is designed to avoid unexpected disturbance during fabrication or testing. The T-beam transfers the applied force from tensile to compressive force exerting to the quantizer-array. The quantizer-array quantizes the magnitude of applied force with unbuckling and buckling beams.

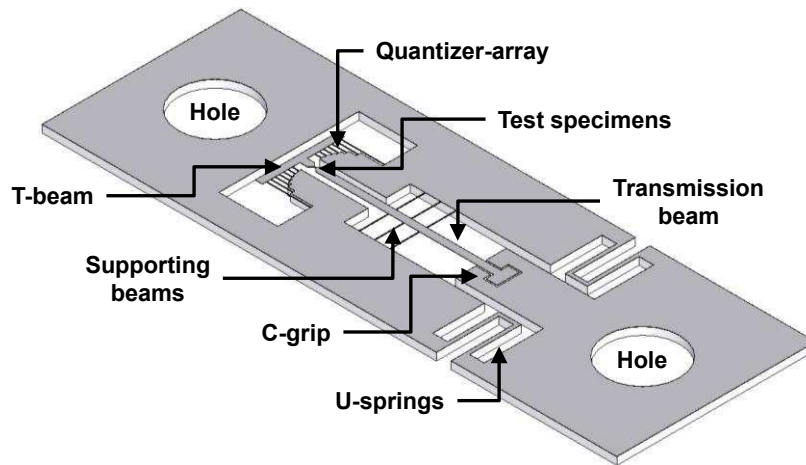


Figure 3. Schematic of F-D ADC tensile test chip.

III. Post-Buckling Behavior

In the F-D ADC, the quantizer-array is composed of numbers of different-length beams to take the compressive load generated by the applied force. Once the compressive load in the longest beam reaches the critical load, the longest beam starts to buckle and laterally deform while the rest of beams remain concentrically compressed by the applied force. After the first buckling occurs in the longest beam, the applied force keeps increasing till the next buckling occurs in the second longest beam. During the first to the second buckling, the longest buckling beam is under the condition of post-buckling. With the increase of the applied force, all beams buckle and then enter post-buckling state one by one. The post-buckling behavior of a fixed-fixed micromechanical beam generated by thermal expansion has been studied by Lindberg et al. in 1993[24] and Chiao et al. in 2000 [25] and the one generated by residual stress has been studied by Fang in 1994 [26]. The general theoretical analysis of the post-buckling behavior in fixed-fixed beam is also derived by Saif in 2000 [27]. The ratio of the post-buckled and pre-buckled axial stiffness is $(\pi^2/6)(t/L)^2$, where t and L are the thickness and length of the buckling beam respectively. Since the ratio in our test is 0.00097 which is very small and can be neglected, the post-buckling effect is neglected in this study.

FABRICATION OF F-D ADC TENSILE TEST CHIP

The tensile test chip is fabricated by means of bulk micromachining in Washington Technology Center at the University of Washington. Figure 4 represents the process flow of fabricating the tensile test chip. First, a 200 μm thick and double side polished silicon wafer is utilized as substrate. Second, a 1.5 μm thick photoresist (AZ1512) is spun onto the front side of the substrate and patterned with mask #1 by mask aligner. After 100 $^\circ\text{C}$ hard baking for 1 hour, 25 μm deep trenches are etched by deep reactive ion etcher (DRIE). Next, another 5 μm thick photoresist (AZ4620) is spun onto the backside of substrate and patterned with mask #2 by mask aligner again. After hard baking for another 1 hour at 100 $^\circ\text{C}$, the final release of the structure is achieved by etching through the substrate with DRIE again. Figure 5 shows the SEM pictures of 2-bit, 3-bit, 4-bit, 5-bit F-D ADC tensile test chips, C-grip, and supporting beams.

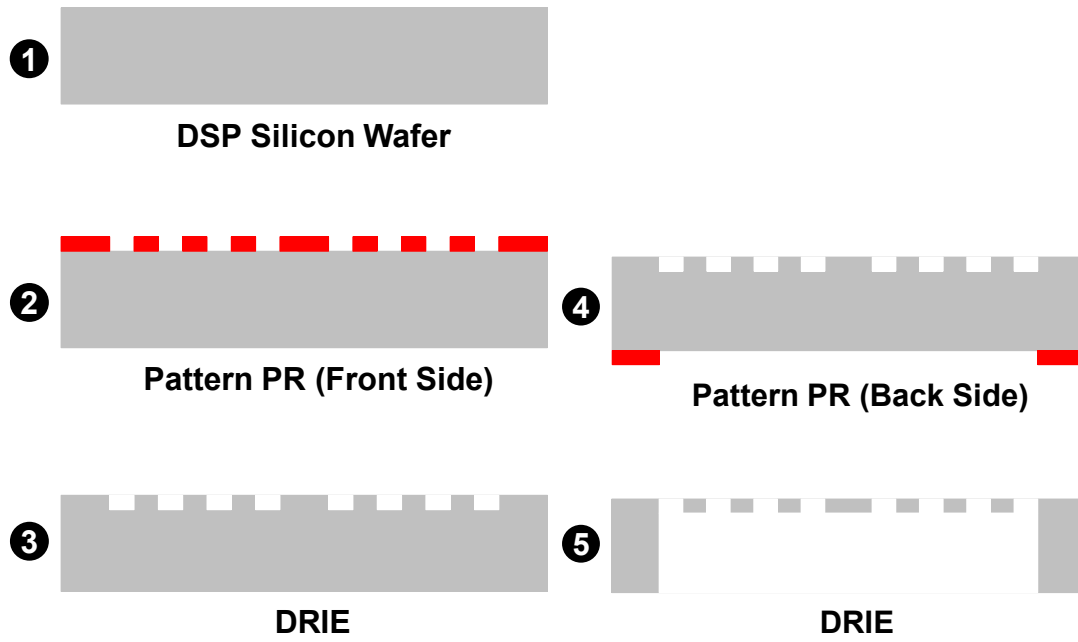


Figure 4. Process flow of F-D ADC tensile test chip.

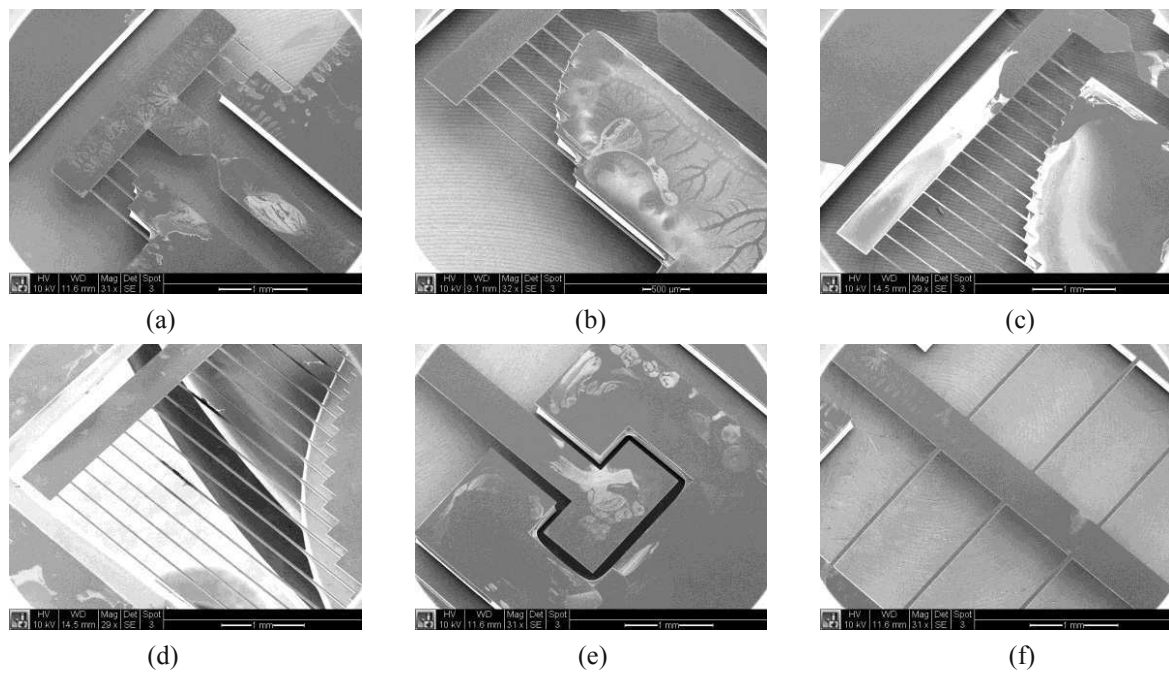


Figure 5. SEM pictures of (a) 2-bit, (b) 3-bit, (c) 4-bit, (d) 5-bit F-D ADC tensile test chip, (e) C-grip, and (f) supporting beams.

EXPERIMENTAL MEASUREMENT

Figure 6 shows the experimental setup for the F-D ADC tensile test including both the test chip and the measurement system. The test chip is positioned by matching the two circular holes to two pins on the piezoelectric actuator (P-841.20, PI) and single-axis linear stage (DM-13, Newport). A digital microscope (AD413T, Dino-Lite) is mounted above the test chip to monitor the testing process. The piezoelectric actuator is used to supply voltages to induce force/displacement to the test chip while the tensile force of the test specimen is derived from monitoring the buckling behavior of the quantizer-array. A single-axis linear stage is used to preload the test chip by adjusting the transmission beam to contact with the edge of C-grip. The deformation of the test specimen is obtained by subtracting the deformation of the quantizer-array from the travel distance of the piezoelectric actuator. The deformation of the quantizer-array is obtained from determining which beam is buckled and then tracing back to its buckling deformation.

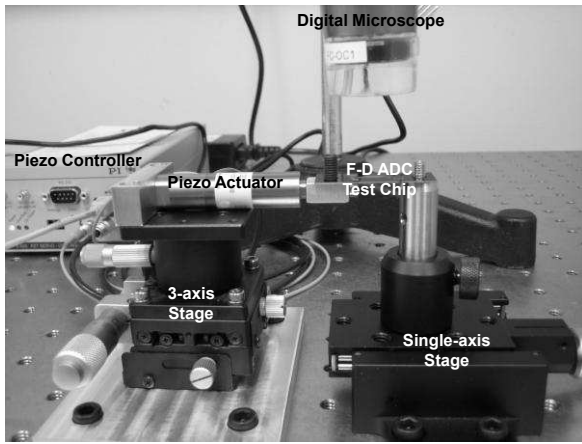


Figure 6. Measurement system setup.

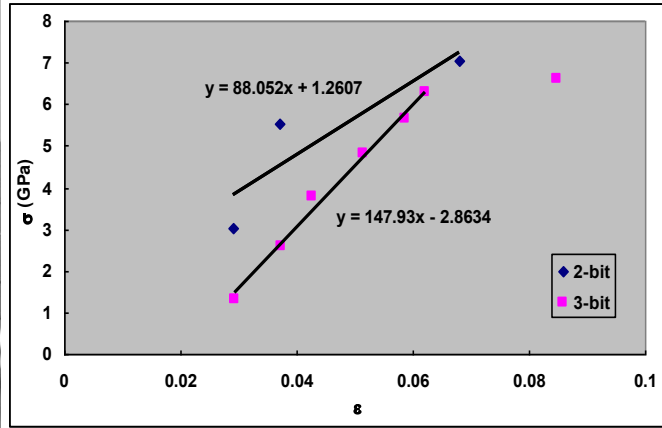


Figure 7. Measurement results of the 2-bit and 3-bit test chips.

The preliminary measurement results of the 2-bit and 3-bit test chips are shown in Figure 7. By linear regression and skipping of non-linear data points on measured stress-strain curves, the slope which represents Young's modulus is estimated around 88 GPa and 148 GPa from the 2-bit and 3-bit chips respectively. Comparing to the theoretical Young's modulus of silicon of 169 GPa, the 3-bit testing result has a smaller error around 12%.

CONCLUSIONS

This study reports a new method to measure the mechanical properties of thin films and microscale structures based on the concept of force-domain analog-to-digital converter. While the displacement is provided by a piezoelectric actuator, the force is sensed by an array of beams of varying lengths based on a progressive buckling phenomena. Although the fabrication of the 2-bit, 3-bit, 4-bit, and 5-bit F-D ADC were all completed, preliminary testing results were only obtained from the 2-bit and 3-bit chips. The 4-bit and 5-bit chips failed prematurely during the testing due to fabrication defects. Current effort is being devoted to the optimization of the fabrication process so high bit number chips can be fabricated and tested successfully. In the future, this new test method will be applied to the testing of various known and new materials to further

confirm its validity. The concept of F-D ADC can be further applied to many other fields which require accurate force measurement.

REFERENCES

1. Sharpe, W.N., J. Bagdahn, K. Jackson, and G. Coles, *Tensile testing of MEMS materials - recent progress*. Journal of Materials Science, 2003. **38**(20): p. 4075-4079.
2. Pharr, G.M. and W.C. Oliver, *Measurement of Thin-Film Mechanical-Properties Using Nanoindentation*. Mrs Bulletin, 1992. **17**(7): p. 28-33.
3. Neubrand, A. and P. Hess, *Laser Generation and Detection of Surface Acoustic-Waves - Elastic Properties of Surface-Layers*. Journal of Applied Physics, 1992. **71**(1): p. 227-238.
4. Kieseewetter, L., J.M. Zhang, D. Houdeau, and A. Steckenborn, *Determination of Young Moduli of Micromechanical Thin-Films Using the Resonance Method*. Sensors and Actuators a-Physical, 1992. **35**(2): p. 153-159.
5. Osterberg, P.M. and S.D. Senturia, *M-TEST: A test chip for MEMS material property measurement using electrostatically actuated test structures*. Journal of Microelectromechanical Systems, 1997. **6**(2): p. 107-118.
6. Sharpe, W.N., *Interferometric Strain Gage*. Experimental Mechanics, 1968. **8**(4): p. 164.
7. Sharpe, W.N., *Applications of the Interferometric Strain Displacement Gauge*. Optical Engineering, 1982. **21**(3): p. 483-488.
8. Sharpe, W.N., B. Yuan, and R.L. Edwards, *A new technique for measuring the mechanical properties of thin films*. Journal of Microelectromechanical Systems, 1997. **6**(3): p. 193-199.
9. Sharpe, W.N., K.T. Turner, and R.L. Edwards, *Tensile testing of polysilicon*. Experimental Mechanics, 1999. **39**(3): p. 162-170.
10. Tsuchiya, T., O. Tabata, J. Sakata, and Y. Taga, *Specimen size effect of tensile strength of surface-micromachined polycrystalline silicon thin films*. Journal of Microelectromechanical Systems, 1998. **7**(1): p. 106-113.
11. Chasiotis, I. and W.G. Knauss, *A new microtensile tester for the study of MEMS materials with the aid of atomic force microscopy*. Experimental Mechanics, 2002. **42**(1): p. 51-57.
12. Knauss, W.G., I. Chasiotis, and Y. Huang, *Mechanical measurements at the micron and nanometer scales*. Mechanics of Materials, 2003. **35**(3-6): p. 217-231.
13. Haque, M.A. and M.T.A. Saif, *Microscale materials testing using MEMS actuators*. Journal of Microelectromechanical Systems, 2001. **10**(1): p. 146-152.
14. Haque, M.A. and M.T.A. Saif, *In-situ tensile testing of nano-scale specimens in SEM and TEM*. Experimental Mechanics, 2002. **42**(1): p. 123-128.
15. Haque, M.A. and M.T.A. Saif, *Application of MEMS force sensors for in situ mechanical characterization of nano-scale thin films in SEM and TEM*. Sensors and Actuators a-Physical, 2002. **97-8**: p. 239-245.
16. Haque, M.A. and M.T.A. Saif, *Mechanical behavior of 30-50 nm thick aluminum films under uniaxial tension*. Scripta Materialia, 2002. **47**(12): p. 863-867.
17. Haque, M.A. and M.T.A. Saif, *A review of MEMS-based microscale and nanoscale tensile and bending testing*.

- Experimental Mechanics, 2003. **43**(3): p. 248-255.
18. Haque, M.A. and M.T.A. Saif, *In situ tensile testing of nanoscale freestanding thin films inside a transmission electron microscope*. Journal of Materials Research, 2005. **20**(7): p. 1769-1777.
 19. Haque, M.A. and M.T.A. Saif, *Thermo-mechanical properties of nano-scale freestanding aluminum films*. Thin Solid Films, 2005. **484**(1-2): p. 364-368.
 20. Zhu, Y., N. Moldovan, and H.D. Espinosa, *A microelectromechanical load sensor for in situ electron and x-ray microscopy tensile testing of nanostructures*. Applied Physics Letters, 2005. **86**(1): p. 013506 1-3.
 21. Zhu, Y., A. Corigliano, and H.D. Espinosa, *A thermal actuator for nanoscale in situ microscopy testing: design and characterization*. Journal of Micromechanics and Microengineering, 2006. **16**(2): p. 242-253.
 22. Lu, S.N., D.A. Dikin, S.L. Zhang, F.T. Fisher, J. Lee, and R.S. Ruoff, *Realization of nanoscale resolution with a micromachined thermally actuated testing stage*. Review of Scientific Instruments, 2004. **75**(6): p. 2154-2162.
 23. Maloberti, F., *Data Converters*. 2007, Dordrecht, The Netherlands: Springer.
 24. Lindberg, U., J. Soderkvist, T. Lammerink, and M. Elwenspoek, *Quasi-buckling of micromachined beams*. Journal of Micromechanics and Microengineering, 1993. **3**(4): p. 183-186.
 25. Chiao, M. and L. Lin. *Microactuators based on electrothermal expansion of clamped - clamped beams*. in 1997 ASME International Mechanical Engineering Congress and Exposition, Proceedings of Micro-Electro-Mechanical Systems(MEMS). 1997. Dallas, Texas.
 26. Fang, W. and J.A. Wickert, *Post buckling of micromachined beams*. Journal of Micromechanics and Microengineering, 1994. **4**(3): p. 116-122.
 27. Saif, M.T.A., *On a tunable bistable MEMS - Theory and experiment*. Journal of Microelectromechanical Systems, 2000. **9**(2): p. 157-170.

Distributed Fiber Optic Strain Measurement Using Rayleigh Scatter in Composite Structures

Eric E. Sanborn, Director, Engineering and Production

Alex K. Sang, Engineering Services Manager

Luna Technologies, 3157 State Street, Blacksburg, VA 24060

sanborne@lunatechnologies.com

Ed Wesson, Engineering/R&D Manager

Non-Metallic Resources (RPS), 8375 Zeigler Blvd. Mobile, AL 36608

Donald E. Wigent III, Product Manager

3TEX Inc., 109 MacKenan Drive, Cary N.C. 27511

Gregory Lucier, Laboratory Manager

North Carolina State University, Constructed Facilities Laboratory,

2414 Campus Shore Dr., Raleigh, NC 27695

Abstract: This paper presents the use of distributed fiber optic sensing to achieve centimeter level resolution strain data along the entire length of a large composite beam. A 6.5 meter long composite beam, designed for use in a corrosive flue gas desulfurization (FGD) unit, was instrumented. A section of optical fiber was embedded into a fiberglass rope, which in turn was embedded into the composite beam during the manufacturing process. The beam was experimentally tested in four-point bending at the North Carolina State University Constructed Facilities Laboratory, and the strain profile along the entire length was measured using the embedded optical fiber. Strains of up to 6500 microstrain were measured at over 300 unique positions along the span by monitoring changes in the spectral shift of the Rayleigh scatter in the optical fiber using optical frequency domain reflectometry (OFDR). The fiber used in this test was optically equivalent to standard telecommunication fiber, allowing for low-cost, high-density strain measurements on large structures. The experiment confirms the potential of embedded fiber optic distributed sensing to be used for real-time health monitoring, or as a process feedback in an instrumented structural system. Benefits of employing distributed fiber optic sensing in structures such as the composite FGD unit include the ability to monitor and detect deterioration and damage, minimize the chance of unplanned downtime or failure, and limit exposure to consequences such as environmental contamination.

1. Introduction

Common methods traditionally used to inspect composite structures are not conducive to online, continuous structural health monitoring. Traditional inspection techniques are often time consuming and labor-intensive, and rely heavily on visual inspections and manual measurements. Large, complex, specialty structures, like the composite flue gas desulfurization (FGD) units described in this paper, can be difficult to inspect fully using current methods. One possible solution is fiber optic distributed sensing, a method which uses a glass fiber sensing element to provide a continuous strain profile along a beam or other structural element over the life of the system. This paper examines the implementation of this method to capture hundreds of simultaneous strain readings along the length of a 6.5 meter long glass fiber reinforced polymer (GFRP) composite beam. This sensing method is based around an embedded optical fiber, commonly known as single mode fiber, which is continuously interrogated using a technique known as Optical Frequency Domain Reflectometry (OFDR). This highly distributed measurement technique [1-13] can be used to identify localized manufacturing defects or isolated damage sustained in service. Defects can be detected that would likely be missed if a series of point measurements, such as electrical resistance strain gauges or conventional Fiber Bragg Grating (FBG) fiber optic sensors, were used. In addition to the benefits of continuous measurement, the small size of the fiber optic sensor allows it to be embedded in a structure without affecting the strength. The sensor cost can also be kept low by using common-grade optical fiber typically used for telecommunication infrastructure.

In this paper, fiber optic distributed sensing was applied to a full-scale composite beam designed for use in a flue gas desulfurization (FGD) unit, commonly referred to as an exhaust scrubber. FGD is the process of removing sulfur-dioxide (SO_2) from the emissions of coal-fired power plants. The chemicals formed in the process are highly corrosive, and the process elements and byproducts are extremely abrasive. Thus, special materials must be used in the construction of the building-sized FGD structures. The conventional solution relies on specialized metallic alloys and coatings, which are extremely expensive. A new approach, developed by Non-Metallic Resources of Mobile, AL, relies entirely on glass-fiber reinforced polymer (GFRP) composites. The experimentally tested beam is a full-size production component of the composite scrubber. The beam was designed for a long service life in the harsh FGD application using composite materials and a special abrasion-resistant coating. The addition of fiber optic distributed sensing allows for the health of this critical structure to be monitored over its entire life.

2. Measurement Method

Fiber optic distributed sensing measures strain and temperature by processing spectral shift in the Rayleigh backscatter of optical fibers embedded in a structure. Rayleigh backscatter in optical fiber is caused by small variations in the index of refraction in the amorphous structure of the glass, and creates a pattern that is random, but stable. The instrument used to monitor this phenomenon relies on a tunable laser source and an interferometer to resolve small fluctuations down the length of the fiber at intervals of fractions of one mm. In general, the instrument is connected to one end of the embedded optic fiber, sends a laser signal into the fiber, and measures the light that is reflected back. The optical network shown in [Figure 1](#), presents the process in more detail. The tunable laser source (TLS) sends light through a coupler, splitting the light between the measurement and reference arms of an interferometer. The measurement arm is connected to the fiber under test (FUT), here the fiber embedded in the structural component. A polarization controller in the reference arm is used to evenly divide the light in the reference arm into two orthogonal polarization states. The returning light is recombined with the light from the reference arm and directed through a polarizing beam splitter to two detectors. In this way, a consistent interference signal can be obtained regardless of the polarization state of the light returning from the FUT. The signals from the S and P detectors are digitized and sent to an instrument controller for processing. These detector signals are processed through a Fourier transform to calculate the Rayleigh scatter as a function of position along the entire fiber. References [14-15] provides additional information on this process.

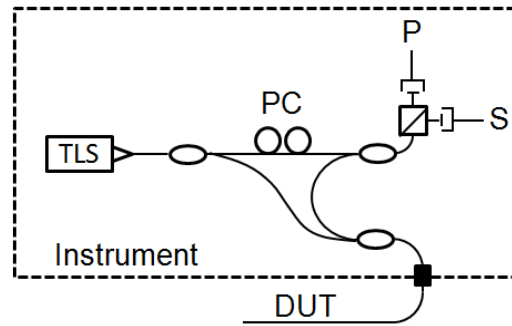
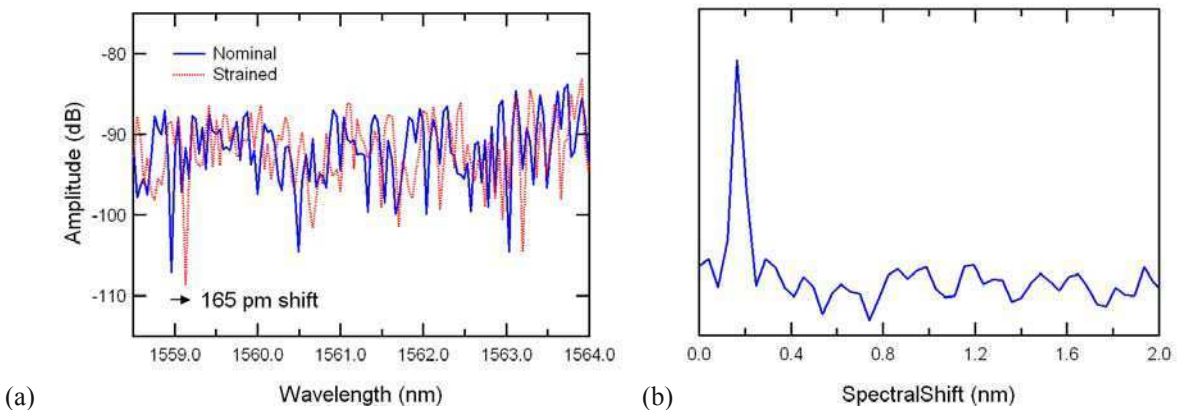


Figure 1 Optical network diagram for measurement of Rayleigh Backscatter

Figure 2 (a) shows the reflected spectrum of a segment of scatter from a piece of standard single mode telecommunication fiber (SMF-28), calculated by windowing a segment of scatter data in the distance domain and performing an inverse Fourier transform. Changes in temperature or strain shift the reflected spectrum of the scatter in the fiber at the location of the disturbance. Finding the frequency shift of the scatter spectrum is accomplished by performing a cross-correlation of the scatter spectrum from a measurement data set with that from a reference data set taken with the FUT in some nominal temperature or strain state. Figure 2 (b) shows the cross-correlation of a reference scatter spectrum with one that was perturbed by external strain. The correlation peak is shifted from center by a frequency shift resulting from the strain change. This process is repeated for segments of scatter along the entire length of the fiber to yield temperature or strain as a function of distance.



**Figure 2 (a) Rayleigh scatter spectra along a 5 mm fiber segment for a reference (dotted) and strained (solid) scan
(b) Cross-correlation of the two spectra**

Strain is measured by either bonding the fiber to the surface of the structure to be measured, or in the case of composites, integrating the fiber into the structure. For measuring temperature, the fiber must first be installed inside a low friction tube. This isolates the fiber from strain, so all dimensional changes in the fiber can be attributed to temperature. Small Teflon tubing etched on the outside diameter to facilitate bonding was used in this application. While this paper focuses on strain sensing, temperature testing was conducted prior to the presented strain testing.

3. Sensor Integration

Distributed fiber sensors can be implemented in a number of ways, the simplest of which is surface bonding. This approach is similar to that used for conventional bonded electrical resistance foil strain gauges. While surface bonding is a fast and effective method, it leaves the fiber exposed to the external environment. To avoid external exposure and the potential for physical damage, optical fiber can instead be integrated during the manufacture of glass or carbon fiber fabrics [16], however, this technique may require at least some special considerations or extra care during manufacture. The approach taken in this

paper is an intermediate technique. The optical sensing fiber was integrated into a 3D braided glass rope, which was bonded to the exterior surface of the completed beam. This technique allowed the sensor to be applied with methods familiar to composite producers, protected the optic sensing fiber from the external environment, and did not require any special fabric. The FilletBraid 3D braided rope used to house the sensing fiber can be formed in various cross-section shapes, tailored to work with joints and gaps in the structure. The rope was specially designed so as not to constrain the sensing fiber. A large portion of the internal glass fibers in the braided rope was processed to disorient and spread them apart. These internal lofted fibers appear almost as cotton balls, surrounded by non-lofted angled fibers. The off-axis orientation of the surrounding angled fibers allows for both elongation and diameter change by shear, much like a finger trap. The combination of angled outer fibers and lofted inner fibers provides a soft and compliant cross section, which can accommodate variable gaps or grooves [17]. Thus, deformations of the optical sensors inside the rope are driven by the stiffer and stronger structure to which the rope is applied. Additionally, the particular FilletBraid used for this work was produced with boron-free fiber to reduce susceptibility to corrosion by the sulfuric acid present in the service environment of a coal gas desulfurization system.



Figure 3 Sensing rope prior to installation in composite structure

The optical fiber used was a polyimide coated single mode fiber with an outside diameter of 0.155 mm. Two such fibers were integrated into the braided fiberglass rope. One was directly incorporated into the core of the rope, and the other was first installed in a Teflon tube to allow for temperature sensing. Polyimide coated fiber was selected in place of more conventional acrylate coating due to its high strain transfer performance, wider temperature range, smaller size, and high durability. This type of fiber is produced using the same methods used to mass produce standard telecommunications fiber kilometers at a time. Unlike some fiber optic strain measurement systems that utilize discrete wavelength FBGs, the system presented here used the sensing fiber as drawn. This feature eliminates post-production operations that can significantly weaken the sensing fiber. The completed sensing rope is shown in [Figure 4](#).



Figure 4 Sensing rope prior to installation in composite structure (diagram indicates lofted, bias, and optical fiber locations in cross section).

4. Experimental Test Setup

The optical fiber distributed sensing system was installed on a 6.5 m full-scale rectangular composite beam that was load tested. Sensing ropes were pre-installed by composite fabricators using standard resin and common tools. A V-groove was milled in the top and bottom surfaces of the beam using a die grinder. The fiberglass rope was then placed in the V-groove along the entire length of the beam, and resin was applied using brushes and rollers and allowed to cure. By first installing the optical fiber sensors in the fiberglass rope, the sensing fiber was protected during and after installation, as the beam was transported to the laboratory, and set in the testing rig. Figure 5 shows the sensor rope installed in the lower surface of the beam, along with a diagram of the beam cross-section.

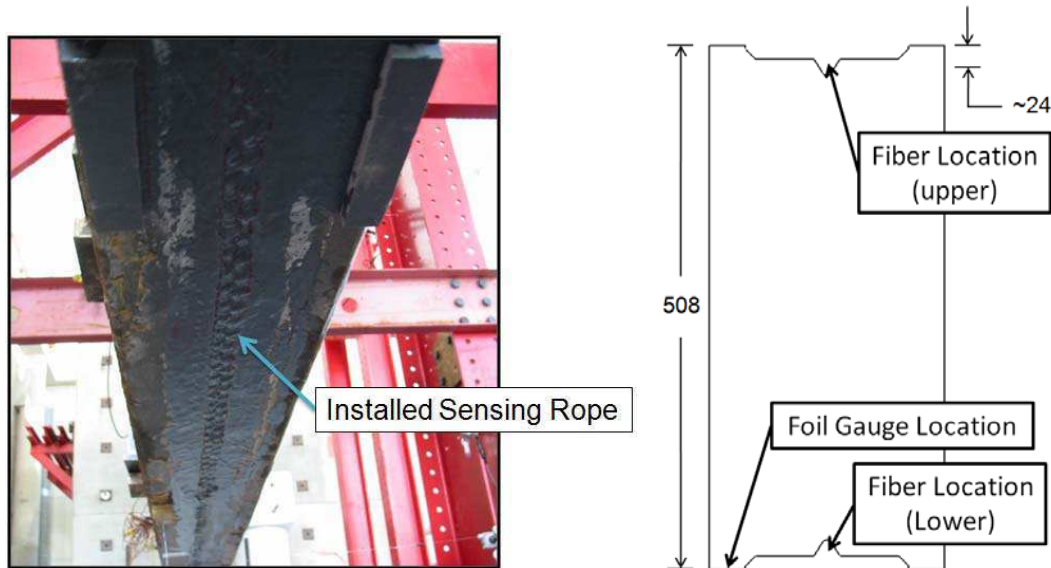


Figure 5 (a) Sensing rope installed the full length of the composite beam (b) Schematic of beam construction

The instrumented beam was tested in four point bending. The beam was supported on a simple 6 m span, 0.25 m from each end. Steel plates and rollers resting on concrete blocks served as supports. The supports allowed for rotation and horizontal translation, but prevented vertical motion. Two hydraulic actuators, each with an 1800 kN capacity, were centered on the beam, spaced 1.8 m apart. The actuators were configured to apply matching loads as they pressed down on the top surface of the beam at a rate of approximately 13 mm per minute. In addition to the fiber-optic sensing data, the applied loads were measured with load cells integrated into the actuators and deflections were measured with potentiometers at several locations. In addition, a foil gauge was mounted on the bottom beam surface at midspan, adjacent to the fiber optic sensing rope. Data from the conventional instrumentation were collected by an electronic data acquisition system at a rate of one Hz. Data from the optical sensors were acquired by a separate system at a rate of one scan every 10 seconds, and were synchronized to the conventional data during post processing. The instrument available to interrogate the fiber was a single channel system, therefore only the fiber on the top surface of the beam was monitored in the tests presented here. Figure 6 shows the beam instrumented and ready for testing in the laboratory at NC State University.



Figure 6 Beam installed at NC State's Constructed Facilities Laboratory

5. Results

Two load tests are described here. For the initial test, the beam was displaced approximately 22 mm to verify that all systems were working as expected. This displacement required a combined applied load of 258 kN, corresponding to the service load. For the second test, the actuators were extended approximately 140 mm with a total combined applied load of approximately 1650 kN, corresponding to a severe overload condition. For both runs, the measured data was processed to provide strain readings every 20 mm along the entire length of the beam; however, a much finer interval could be selected if necessary. For the tested beam, the 20mm interval resulted in continuous strain measurements at over 300 individual points along the span.

Theoretical Result

Evaluating the experimental results requires a review of the loading of beams in the elastic range, a well-documented behavior. Of greatest interest to engineers is usually the shear force and bending moment. Both can be determined from the locations of the loads and supports, and the load magnitudes. A shear diagram can be constructed from the loading, support, and span conditions, and a bending moment diagram can be constructed from the shear diagram. The strain profile in an elastic beam is directly proportional to the bending moment diagram. [Figure 7](#) shows the shear and moment diagrams for four point bending.

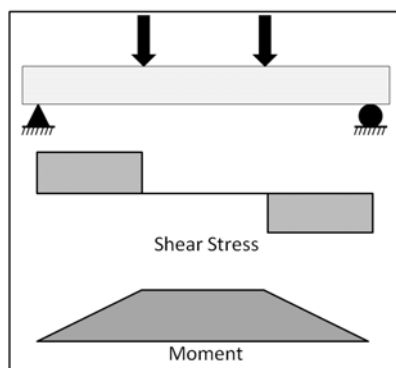


Figure 7 Shear and moment diagrams for four point bending

The stress on the top beam surface is theoretically equal to the product of the applied moment (M) and the distance from the neutral axis of the beam (y), divided by the second moment of area (I_x), as shown in Equation (1). The proportional relationship between stress and strain can then be used to relate strain and moment in Equation (2). As y , I_x , and E are all constants for an uncracked, symmetric, elastic beam, strain is proportional to moment and the shape of the strain profile

should match the shape of the moment diagram in Figure 7. Since the top surface of the beam is in compression along its length, strain will be negative.

$$\sigma = \frac{My}{I_x} \quad (1)$$

$$\varepsilon = \frac{My}{I_x E} \quad (2)$$

As noted in Figure 5(b) the sensing fiber was embedded approximately 24 mm closer to the neutral axis of the beam than the foil gauge. This yields a distance to the neutral axis about 10% smaller for the fiber optic sensor. Equation (2) shows that the fiber optic sensor should measure 10% lower strain relative to the foil gauge.

Experimental Results: Initial Test

The initial test corresponds to the usual load in service for the composite beam. A measured strain profile along the length of the beam is presented in Figure 8 for a selected moment approximately halfway through the service load test. The strain data show the expected inverted trapezoidal shape discussed above. All strain data recorded during the test are plotted in Figure 9 verses both time and position. The distance along the beam runs left to right while time moves from the back of the graph to the front. As the figure shows, distributed sensing can provide a detailed map of the measured strain for all positions and all times during a test run. Such data would not be practical or cost effective to generate using electrical strain gauges. Figure 9 does utilize interpolation to generate the surface plot, but the graph contains over 22,000 individual data points.

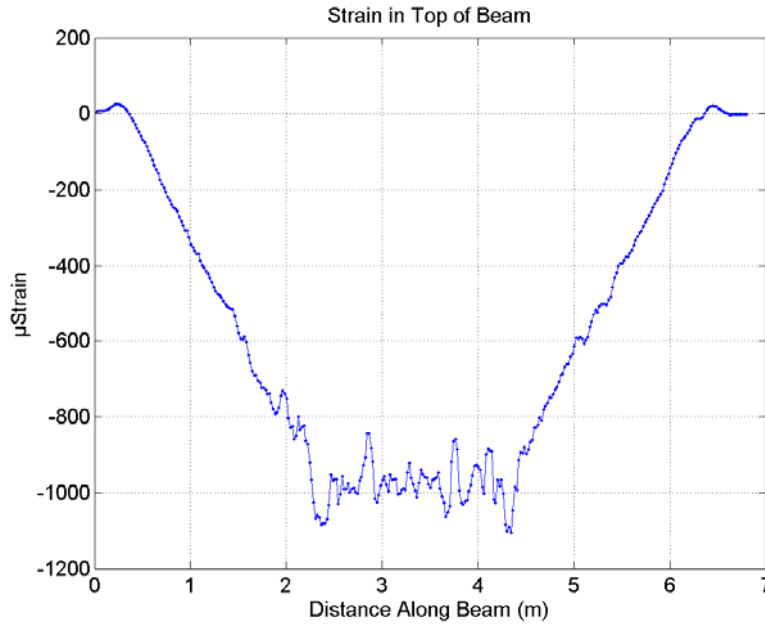


Figure 8 Single scan of strain data during Run 1

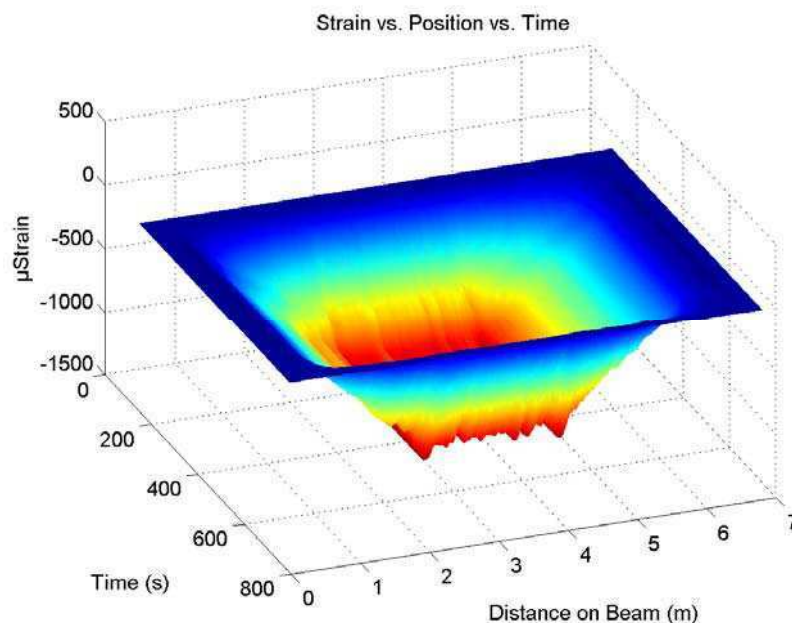


Figure 9 Strain verses position and time for Run 1

One measurement point in the fiber optic sensor at the center of the beam was selected and plotted with the foil gauge verses time. [Figure 10](#) shows the differences in magnitude of the measurements. The fiber optic sensor measured approximately 15% lower strain magnitudes compared to the foil gauge. As discussed earlier, a difference of about 10% is expected. This result indicates an additional 5% error that is unaccounted for and may be due to several factors. First, it is possible that the cross-section of the composite beam contains enough variation that the strain levels between the top and bottom of the beam could be slightly out of balance. Second, the sensing rope developed for this test was larger than necessary, resulting in more distance between the sensing fiber and the uni-axial fibers carrying the load in the top of the beam. This is analogous to mounting a foil gauge with a thick adhesive layer. The result is reduced strain transfer performance with the fiber sensor measurement lagging the actual structural strain. Another possible contributor to the unexplained error is the manufacture of this specific sensing rope, as the sensing fiber wandered slightly through the rope core. Methods to improve the manufacturing process have been identified, but were not available at the time of this experiment. It is believed that this wandering also contributed to some of the variation seen in the horizontal portion of the strain profile in [Figure 8](#).

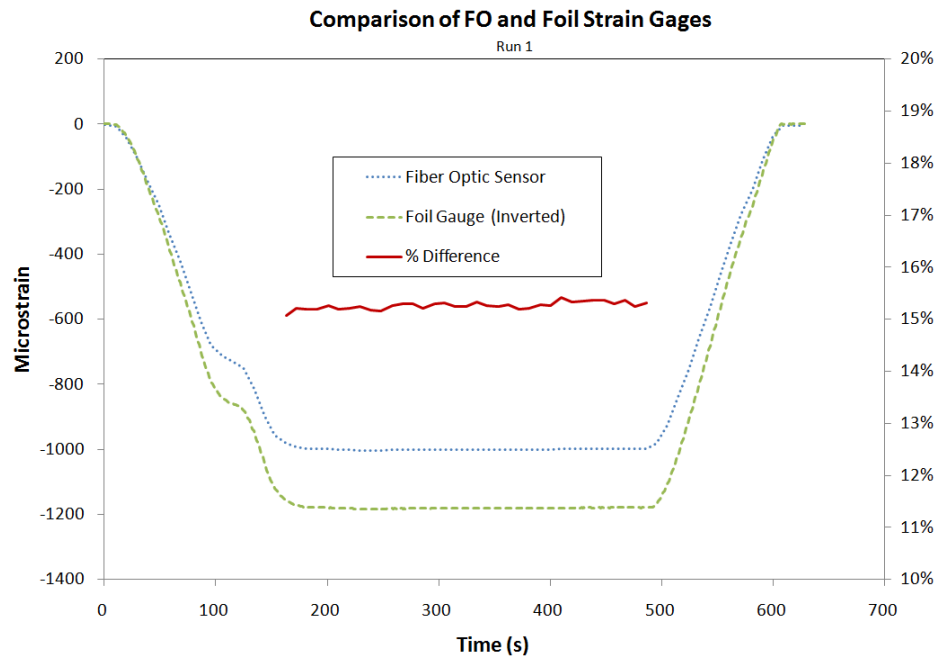


Figure 10 Comparison of fiber optic sensor at the center of the beam with foil gauge for Run 1 (not corrected for distance to neutral axis)

Experimental Results: Second Test

For the second experimental run, the beam was tested well beyond the service load. The same inverted trapezoidal profile is apparent in the strain profile data, as in the initial test. The measured strains, as would be expected, were much higher reaching a peak of approximately 6800 microstrain in compression. The same form that was apparent in [Figure 8](#) and [Figure 9](#) can be seen in [Figure 11](#), but becomes more pronounced at the higher strain levels.

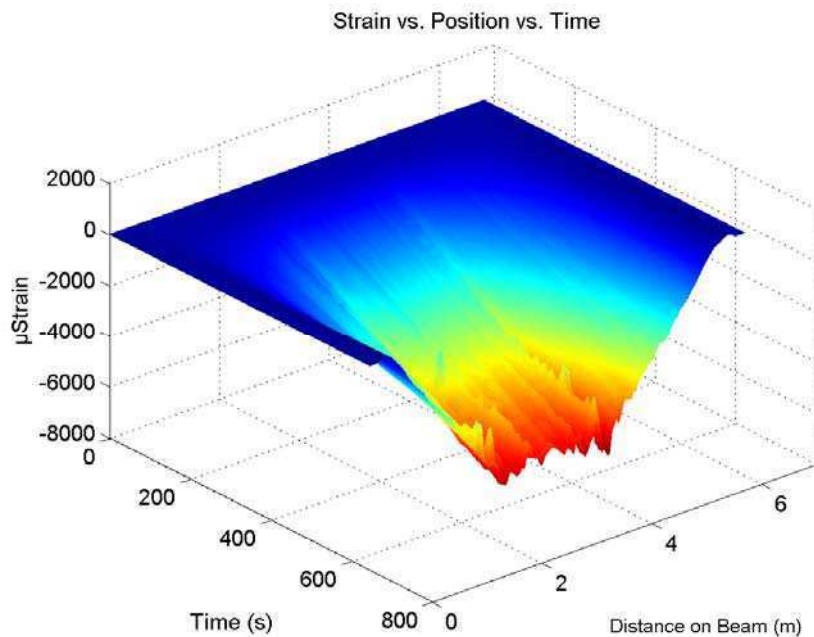


Figure 11 Strain profile along beam plotted verses time

6. Conclusions

Strain was measured along the length of a composite beam measuring 6.5 meters in length using single mode optical fiber. Over 300 measurement points were collected with each scan, although the system could be used to collect far more points if desired. Fiber optic measurements were collected once every 10 seconds while the beam was physically loaded in four point bending. Two experimental tests were performed; one to the service load rating and one to an extreme overload condition. The distributed strain measurements performed well throughout the test, and matched the expected theoretical shape.

The methods presented here can be applied to large structures and high strain levels. Sensor installation during construction by embedment, or after construction by surface bonding with or without a protective fiber rope, provides a wide range of usage options. Embedded sensing facilitates continuous structural health monitoring while structures are in service. This technique is particularly useful in critical specialty applications like flue gas desulfurization systems, as conventional inspection methods would require costly system outages, and would necessitate inspectors work in a very hazardous environment. Other composite applications where failure is costly or dangerous like wind turbine blades and aircraft structures would also benefit. The use of off-the-shelf telecommunications rated fiber keeps sensor cost low, and insures a durable, long lasting health monitoring system.

7. References

- [1] Mark E. Froggatt, Turan Erdogan, "System and method for measuring the transfer function of a guided wave device", Patent 6376830, Apr 23, 2002
- [2] Mark E. Froggatt, Brooks A. Childers, "High precision wavelength monitor for tunable laser systems", Patent 6426496, Jul 30, 2002
- [3] Mark E. Froggatt, "Apparatus and method for the complete characterization of optical devices", Patent 6856400, Feb 15, 2005
- [4] Mark E. Froggatt, "Apparatus and method for correcting errors generated by a laser with non-ideal tuning characteristics", Patent 6900897, May 31, 2005
- [5] Mark E. Froggatt, "Apparatus and method for the complete characterization of optical devices including loss, birefringence and dispersion effects", 7042573, May 9, 2006
- [6] W. Eickhoff and R. Ulrich, "Optical frequency domain reflectometry in single-mode fiber," *Appl. Phys. Lett.*, vol.39, pp. 693–695, 1981
- [7] U. Glombitza and E. Brinkmeyer, "Coherent frequency domain reflectometry for characterization of single-mode integrated optical waveguides," *J. Lightwave Technol.*, vol. 11, pp. 1377–1384, 1993
- [8] B. J. Soller, D. K. Gifford, M. S. Wolfe and M. E. Froggatt, "High resolution optical frequency domain reflectometry for characterization of components and assemblies," *Optics Express*, vol. 13, issue 2, p. 666-674, 2005
- [9] D.K. Gifford, A.K. Sang, S. T. Kreger, M. E. Froggatt, "Strain measurements of a fiber loop rosette using high spatial resolution Rayleigh scatter distributed sensing," *Proc. SPIE*, vol. 7653, paper 765333, Sept. 2010
- [10] M. Froggatt and J. Moore, "High resolution strain measurement in optical fiber with Rayleigh scatter," *Applied Optics*, vol. 37, pp.1735-1740, 1998.
- [11] B. J. Soller, D. K. Gifford, M. S. Wolfe, M. E. Froggatt, M. H. Yu, and P. F. Wysocki, "Measurement of localized heating in fiber optic components with millimeter spatial resolution," *OFC Technical Digest*, paper OFN 3, 2006.
- [12] D. K. Gifford, B. J. Soller, M.S. Wolfe, M. E. Froggatt, "Distributed fiber-optic temperature sensing using Rayleigh backscatter," *ECOC Proceedings*, vol. 3, pp. 511-512, Sept. 2005.
- [13] S. Kreger, D. K. Gifford, M. E. Froggatt, B. J. Soller, and M. S. Wolfe, "High resolution distributed strain or temperature measurements in single- and multi-mode fiber using swept-wavelength interferometry," *OFS 18 Technical Digest*, Paper ThE42, 2006
- [14] B. J. Soller, M. S. Wolfe, and M. E. Froggatt, "Polarization resolved measurement of Rayleigh backscatter in fiber-optic components," *OFC Technical Digest*, paper NWD3 (Los Angeles, March, 2005).
- [15] Mark E. Froggatt, "Calculation of birefringence in a waveguide based on Rayleigh scatter", Patent 7330245, Feb 12, 2008
- [16] Wigent III, Donald E., Bogdanovich, Alexander E., Whitney, Thomas. J., "Strain Monitoring of 3-D Woven Composites Using Integrated Bragg Grating Sensor Arrays", *SAMPE* 2004, May 2004.
- [17] D. Mungalov, P. Duke, and A. Bogdanovich, "High Performance 3-D Braided Fiber Preforms: Design and Manufacturing Advancements for Complex Composite Structures," *SAMPE Journal*, 2007, Vol. 43, No. 6, November/December, pp. 53-60.

Diamond Sensors with Silicon Technologies for Sensing in Harsh Environments

Tom. Sanders and Glenn. Hess, AET, Inc., 1900 S. Harbor City Blvd., Suite 225, Melbourne FL, 32901
Jim Davidson and W.P. Kang, Vanderbilt University, 5617 Stevenson Center, Nashville TN, 37235
Teng Ooi, Missile Defense Agency, Redstone Arsenal, Huntsville AL, 35806
Aaron Corder, Missile Defense Agency, 196 Jeff Rd., Suite 1501, Huntsville AL, 35806

ABSTRACT

This paper presents the results of a research program aimed at developing passive and active circuit components to be used in air vehicle applications. The team of Advanced Engineering Technology (AET, Inc.) and Vanderbilt University is developing diamond sensors that will be integrated with a silicon-based integrated circuit for incorporation into air vehicles. Specifically, the team is developing the technology necessary to integrate chemical vapor deposited (CVD) diamond films with the silicon integrated circuit.

INTRODUCTION

The primary objective of this program is the development of manufacturing technologies for passive and active circuit components to be used in air vehicles multifunctional skin applications. Specific advantages of the miniaturization of electronic circuits and components in air vehicles lie in the potential to integrate these devices into surface layers or sub-surface layers without impacting structural integrity or aerodynamics.

Advanced fabrication processes and manipulation at the nanoscale promise smart skin technology with numerous possibilities. Preferred functions are manufacturing of devices that, due to size, can be integrated into both structural and flexible components. Examples of nanodevice integration into components include insertion into aircraft parts or skin to measure structural state as well as integrated onto surfaces to perform the signal processing for conformal antennas.

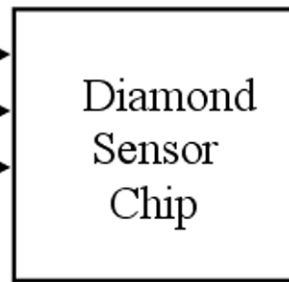
This seamless integration allows for multifunctional skins that combine sensing, actuation and control while at the same time supporting load-bearing, self-healing, conformal or morphing functionality. Advantages to diamond device skin integration also include increased payload, increased internal real-estate as well as concealment. A smart skin would be one that localizes sensing, actuation and control functions.

SENSOR CHIP CONCEPT

AET is developing diamond sensors that will be integrated into a silicon chip so that the information coming to the computer on-board the air vehicle can accurately process the data. To achieve this we are developing a system concept as illustrated in [Figure 1](#). As seen here, the stimulus for the Diamond Sensor Chip can be any information from the environment including temperature, radiation, pressure, etc. Actually, this includes anything that can be detected by a sensor on-board Diamond Sensor Chip. The output of the Diamond Sensor Chip is a digital signal that goes to the aircraft computer. To implement this Nanoscale Sensor System, we propose the circuit concept shown in [Figure 2](#). The temperature and radiation sensors will be a diamond resistive element that will be integrated with the monolithic silicon integrated circuit that makes up the primary part of the Nanoscale Sensor Chip. Researchers at Vanderbilt University will fabricate the diamond structures.

Environmental Stimulus

- Temperature
- Radiation
- Other



Output
to system
computer

Fig 1 System Block Diagram

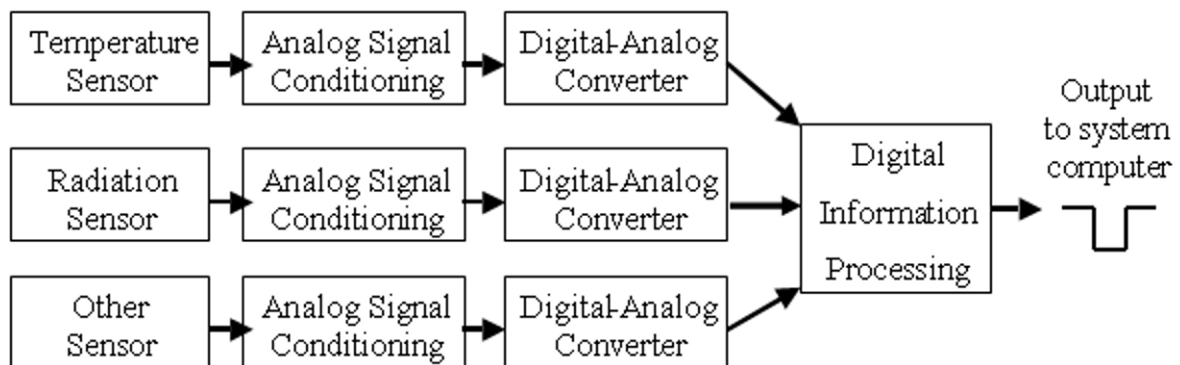


Fig 2 Diamond Sensor Chip Block Diagram

DIAMOND TECHNOLOGY

Diamond is generally recognized as a principal candidate for advanced semiconductor devices. The applications for diamond, more specifically in this case, CVD (chemical vapor deposited) diamond layers, include microelectronic devices, sensors, micromechanical systems, and high power structures. Major advantages for the use of diamond technology are its superior nuclear survivability and operation at much higher temperatures, high breakdown voltage, high electron saturation velocity, high carrier mobility, and large thermal conductivity.

Examination of the critical paths to useable advanced technology for SHM will invariably lead to the sensors at the edge of the networks. Certainly the network design is important - intelligent formulation will lead to faster/appropriate response and better SHM predictive behavior - but unless the data *in* is extensive, robust, fast and true, there is no real *system* monitoring.

The fundamental problem with existing sensor technology begins and ends with the sensor *material*. Obviously, by virtue of precedent, silicon is the established sensor material, but because of its (relative) narrow band gap and the semiconductor physics approach to sensing, it is *fundamentally* limited by temperature, pressure, radiation exposure and most other variables of interest/stress to system health. In fact, silicon and related materials lose their useful sensing properties *well before* many system health extremes (yellow/red zone range) are reached. This leads to either overdesign, dangerous extrapolative techniques, compromised remote sensor placement and/or undermonitored systems.

The need for sensors that will operate at significantly broader extremes (temp., radiation, etc.) and be economical and embedded (emplaced with no effect on system) is apparent and essential for next-generation systems. As discussed below,

superior sensors will come from superior material and that material is diamond. First of all, diamond processing/deposition coating has become a commodity operation. It has become deployed routinely and “in production”. This form of diamond is neither expensive nor exotic. Most importantly, it will extend the range_of sensing viability by many times as illustrated in Table I.

TABLE I. COMPARISON OF SILICON AND DIAMOND FOR SHM SENSOR PROPERTIES

Parameter	Silicon Sensor Limits	Diamond Sensor Limits
Maximum Operating Temp.	~ 150 C	> 500 C
Minimum Operating Temp.	~ -55 C	< -270 C
Junction Rectification	~ 0.7 V	~ 0.1 V
Pressure “Strength”	1	>10X
Radiation Tolerance	~ 1 MRad	> 10 MRad
Chemical Susceptibility	Not Inert	Inert

As shown in Table I, silicon devices are more sensitive to temperature than are diamond devices. For example, as a thermistor, the thermal coefficient of resistance of diamond is well behaved [1].

TECHNOLOGY INTEGRATION

The researchers have developed a process flow for combining silicon integrated circuit structures and diamond sensors on the same chip. This flow utilizes all existing processes at Vanderbilt University and allows the use on a number of different silicon integrated circuit fabrication facilities. In addition, this flow is compatible with several different silicon technology types, including both standard CMOS and SOI-CMOS. The silicon process will proceed normally through circuit processing and nominally three metal layers and the passivation layer. The final step to be performed by the SOI foundry will be to open the bond pads in the passivation layer. This final topology is represented conceptually per a mask pattern for an IC chip as shown in Figure 3.

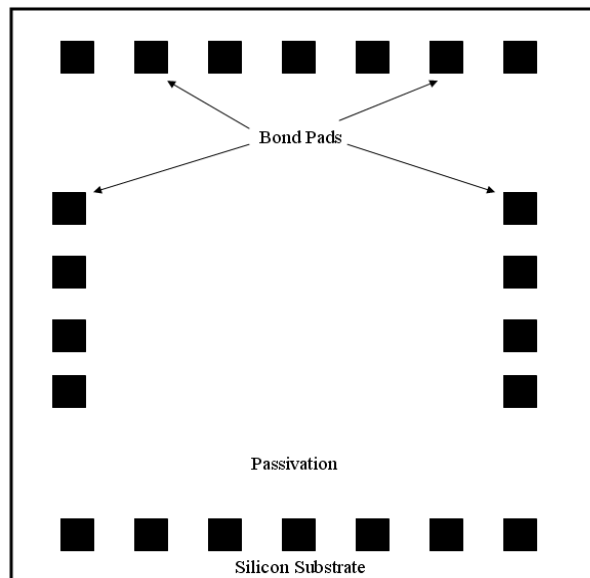


Fig 3 Die Topology After CMOS Processing

The wafers will then be transferred to Vanderbilt University for the processing steps to achieve diamond sensors. A 2-3 micron thick diamond film will be deposited at a temperature low enough to be compatible with the IC wafer (less than 450C). The diamond processing conformity will cover the topology typical of such CMOS wafers and will not require fine geometry photoresist.

The first step performed in the creation of the diamond sensor is to deposit a lift-off layer comprised of SiO₂ 'glass' which may be applied by several techniques. The liftoff layer is then patterned and etched as shown in [Figure 4](#).

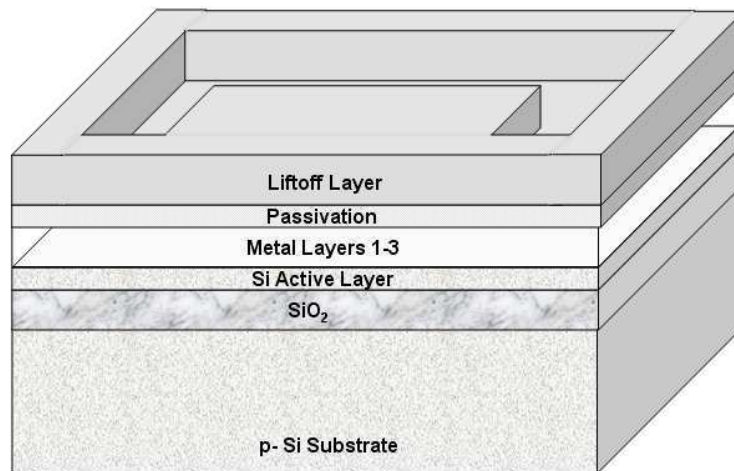


Fig 4 Mask/Photoresist Define Lift-Off Layer

The diamond is then deposited at a low temperature (less than 450C). The optimum process to do this will be evaluated during the development phase, determining, for example whether the CVD or hot filament technique provides superior performance. The excess diamond is then 'lifted off' and the diamond sensor is delineated as shown in [Figure 5](#). A liftoff procedure is presently preferred to achieve more benign conditions for the IC wafer substrate.

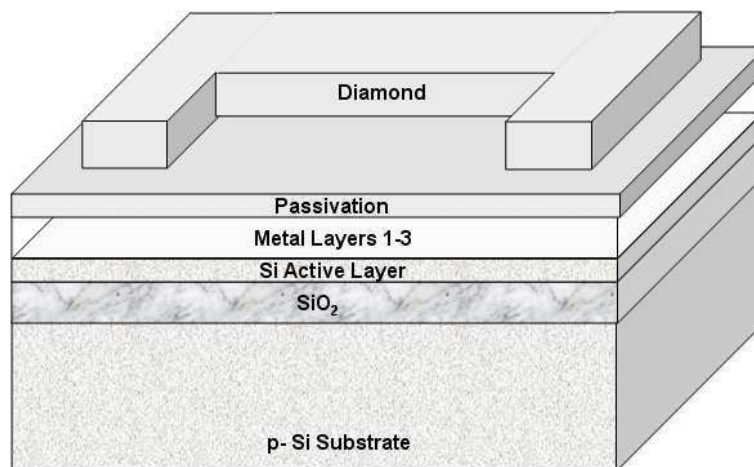


Fig 5 Lift-Off Excess Diamond

The metalization for contact to the diamond will be deposited and defined at Vanderbilt. The metal lies completely on the diamond, avoiding step coverage issues. We do not anticipate the need for a passivation layer over the diamond and metal layers at this time. Contact between the diamond sensor(s) and the SOI circuitry will be made with bond wires. The final topology is shown in [Figure 6](#).

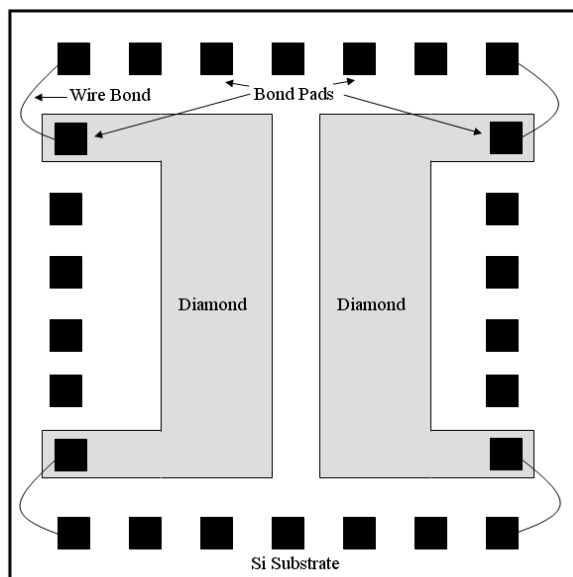


Fig 6 Die Topology after Diamond Contact Metal Deposition

CONCLUSIONS

AET and Vanderbilt University have developed an integrated circuit manufacturing process flow that combines both diamond and silicon technologies on a single IC chip. This chip will contain a variety of diamond sensors along with silicon CMOS readout circuitry. The application for the chip is to be embedded in the skin of air vehicles to improve the structural health monitoring of the system.

REFERENCES

1. P. Hamari, P. Taylor, J. L. Davidson, W. P. Kang, "Thermal Properties of Freestanding Diamond Resistors", Proceedings of ICNDST/ADC 2006 Joint Conference, pp. 65, May 15-18, 2006, Research Triangle Park, NC, USA.
2. K. Subramanian, Y. M. Wong, W.P. Kang, J.L. Davidson, B.K. Choi, and M. Howell, "Nanocarbon Field Emission Devices", Proceedings of SBDD XI, paper 10.2, February 22-24, 2006, Hasselt, Belgium.
3. W.P. Kang, T. Fisher, and J. L. Davidson, "Diamond Microemitters – The New Frontier of Electron Field Emissions and Beyond," New Diamond and Frontier Carbon Technology, Vol. 11, No. 2, pp. 129-146, 2001. (Invited)
4. J. L. Davidson, D. R. Wur, W. P. Kang, D. L. Kinser, and D. V. Kerns, "Polycrystalline Diamond Pressure Microsensor", Diamond and Related Materials, pp. 86-92, 1996.

The Influence Of Restraint Systems On Panel Behavior

Dawn C. Jegley

NASA Langley Research Center, Mail Stop 190, Hampton, VA 23681-2199

E-mail dawn.c.jegley@nasa.gov

ABSTRACT

When a panel is tested in uniaxial compression in a test machine, the boundary conditions are not quite the same as they would be if it were part of a complete structure. A restraint system may be used to simulate conditions found in a complete vehicle. Quantifying the quality of the restraint with only point-measurement devices can leave an inadequate characterization of the out-of-plane behavior. However, today's full-field displacement monitoring techniques allow for much more accurate views of the global panel deformation and strain, and therefore allow for a better understanding of panel behavior. In the current study, the behavior of a hat-stiffened and two rod-stiffened carbon-epoxy panels is considered. Panels were approximately 2 meters tall and 0.76 to 1.06 m wide. Unloaded edges were supported by knife edges and stiffeners were attached to a support structure at selected locations to restrain out-of-plane motion. A comparison is made between test results based on full-field measurements and analyses based on assumptions of boundary conditions of a completely rigid edge restraint and the absence of any edge restraint. Results indicate that motion at the restrained edges must be considered to obtain accurate test-analysis correlation.

INTRODUCTION

When a panel is tested in uniaxial compression in a test machine, the boundary conditions are not quite the same as they would be if it were part of an entire wing or fuselage structure. The panel is usually supported by a restraint system which may be representative of the support found in an aircraft structure. Quantifying the quality of the restraint with only point-measurement devices can leave an inadequate characterization of the out-of-plane behavior. However, today's full-field displacement monitoring techniques allow for much more accurate views of the global and local panel deformation.

The ends of a composite compression panel are usually encased in a potting compound which is surrounded by a steel support to prevent end brooming. The unloaded edges are often supported by metallic knife edges to restrain the panel from deforming in a global single half-wave mode, and to prevent the free edge of a thin skin region from buckling into shorter wavelengths. Analytically, these supports are often approximated by restraining all degrees for freedom except axial shortening for the entire potted region, and restraining all out-of-plane motion along the unloaded edge. In addition, a restraint system is also often included to restrain the panel from out-of-plane motion. A support structure is attached to panel stiffeners, where the connection points are assumed to fully restrain out-of-plane motion but allow in-plane motion. The validity of these assumptions is considered in this paper for three carbon-epoxy panels. One hat-stiffened and two rod-stiffened panels loaded in axial compression are discussed herein. In this case, "hat-stiffened" refers to hat-stiffeners in the loading direction and "rod-stiffened" refers to stiffeners with pultruded carbon rods in the stiffeners in the loading direction. Each panel was fabricated by the Boeing Company and provided to NASA Langley Research Center for testing.

TEST ARTICLES AND ARRANGEMENT

Each panel had stringers in the loading direction and frames perpendicular to the stringers, as shown in [figure 1](#). The hat-stiffened panel was 1.885 m tall and 76.2 cm wide, and contained three hat-stringers and two blade-frames. The hat-stiffener spacing was 25.4 cm and the frame spacing was 61 cm. The rod-stiffened panels were 2.032 m tall and 1.067 m wide, and contained seven rod-stringers and four hat-frames. The stringer spacing was 15.24 cm and the frame spacing was 50.8 cm. The hat-stringers and hat-frames were supported by Rohacell foam on the inside of the hats. All three panels were fabricated from dry components that were infused with resin using high temperature and vacuum pressure. Skins, flanges, tear straps and webs were composed of layers of graphite material forms that were prekitted into multi-ply stacks using Hercules, Inc. AS4 fibers. Each nine-ply stack had a $[45/-45/0_2/90/0_2/-45/45]_T$ stacking sequence of approximately 0.132 cm thickness. Several stacks of the prekitted material were used to build up the desired thickness and configuration. Stringer and frame flanges were stitched to the skin using Vectran fibers; no mechanical fasteners were used for joining. Panels were infused with HexFlow VRM-34 epoxy resin using a VARTM process as described in reference 1.

In the hat-stiffened panel, the skin and hats were composed of two stacks of material with a total approximate thickness of 0.264 cm. The blade-frames were composed of four stacks with a total approximate thickness of 0.528 cm. The hats and blades were 5.5 and 5.0 cm tall, respectively. Sketches of the hat stiffener and frame cross sections are shown in figures 2a and 2b, respectively. For both of the rod-stiffened panels, the sides of the hat frames and the stringer webs were each composed of two stacks with a total approximate thickness of 0.264 cm. The rod-stiffeners contained pultruded rods with a diameter of 0.95 cm which were surrounded by one stack of material. The rod-stiffeners were 3.78 cm tall and the frames were 15.2 cm tall. The skin of one rod-stiffened panel was one stack thick and the skin of the other was two stacks thick. These panels will be referred to herein as the thin-skinned and thick-skinned rod-stiffened panels, respectively. Sketches of the rod-stiffener and hat-frame cross sections are shown in figures 3a and 3b, respectively.

Each of the three panels considered in this study had potted loaded ends, metal edge restraints along the unloaded edges, and a steel support structure attached to the frames. The edge restraints and support structure were intended to prevent out-of-plane motion in the form of a single half-wave along the panel length. The edge restraints are shown in figure 1.

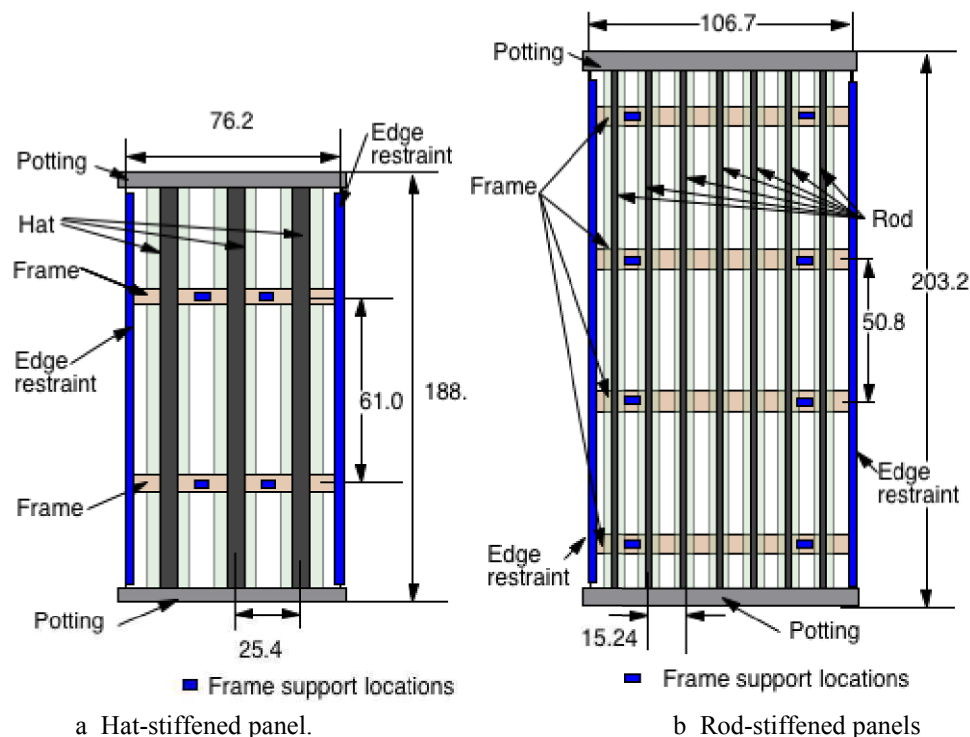


Fig 1 Panel geometry. Dimensions are in cm.

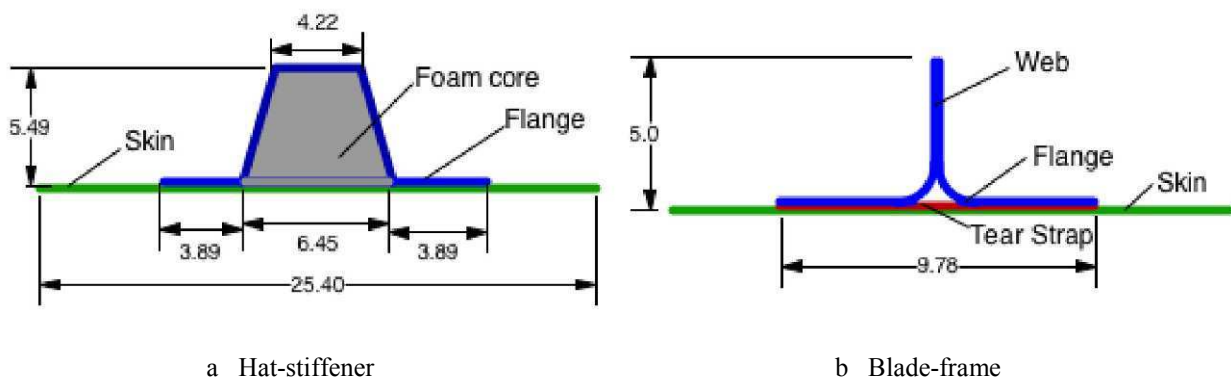


Fig 2 Stiffeners in hat-stiffened panel. Dimensions are in cm.

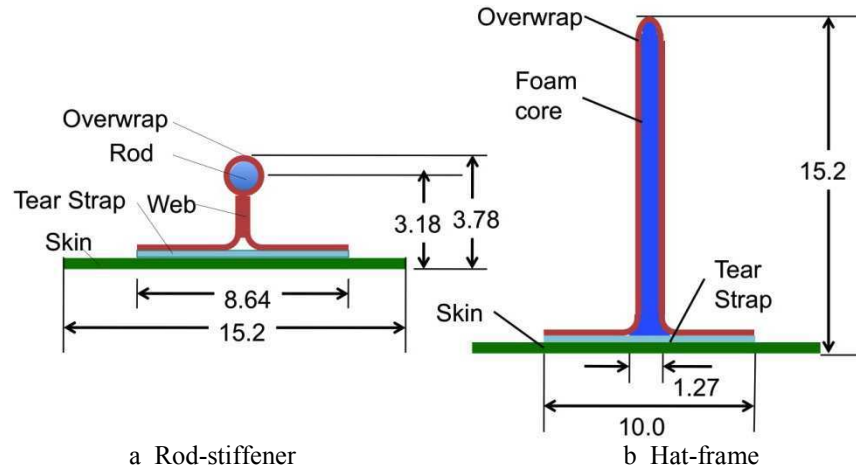


Fig 3 Stiffeners in rod-stiffened panels. Dimensions are in cm.

The dimensions of the steel tube edge restraints for the three panels are shown in [figure 4](#). The steel tube was slightly shorter than the length of the panel between the potting to allow for axial shortening during the test. A slot was cut through the wall thickness for the full length of each tube so that the tube could slide over the panel skin. However, since the frames extended to the panel edges, cutouts in the tubes at each frame location were required to accommodate the frames. The edge restraints were required to just touch the surface of the panel. Small fasteners were inserted through holes in the tubes so the fasteners could be used to close the slot to match the skin thickness after the tube was in position. Teflon tape was placed between the panel surface and the restraint so that the panel would not bind up on the restraint during shortening. The edge restraints for the thick-skinned rod-stiffened panel was the same as for the hat-stiffened panel except for the different spacing for the cutouts for the frames, as indicated in the figure. The tubes for the thin-skinned rod-stiffened panel had a larger diameter and wall thickness than for the other two panels.

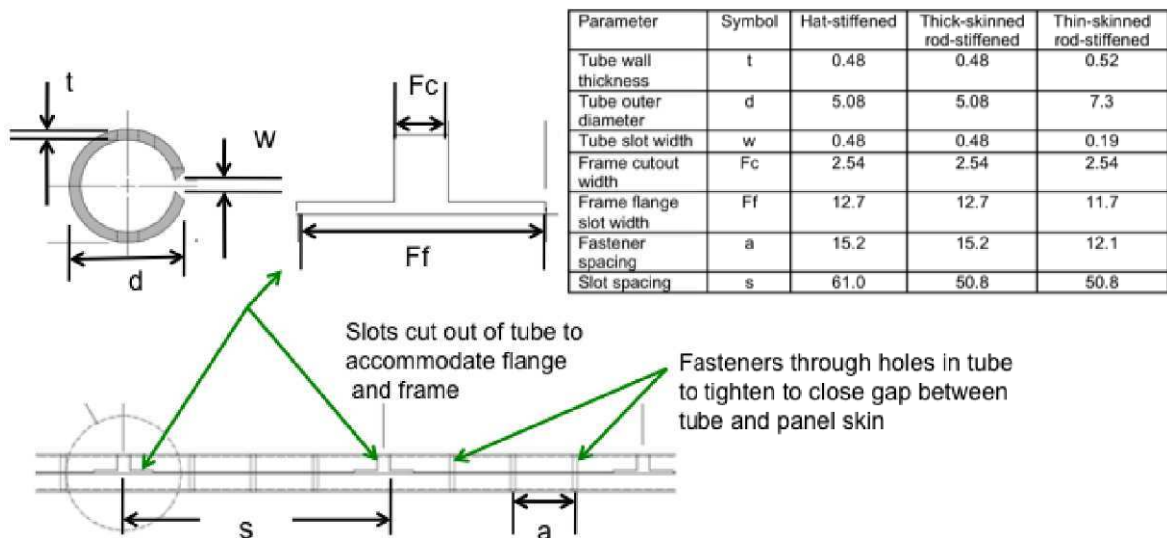


Fig 4 Edge restraints with dimensions in cm.

Additionally, since the frames would not be totally free to move in a real structure, a support structure was used on all panels to prevent out-of-plane motion at two locations on each frame, as shown in [figure 5](#). Steel channel arms were attached to clips on the frames and the arms were attached to uprights behind the panel. The uprights were attached to a steel I-beam sitting on the floor. These arms were pinned to the clips and to the uprights so the restraints did not restrict rotation of the frames during loading, as shown in the close-up in [figure 5d](#). However, the frame support structure was not attached to the floor or test machine during loading for the hat-stiffened or thick-skinned rod-stiffened panel. The floor I-beam was attached

to the floor and angle bars were attached between the frame support and the floor during the test of the thin-skinned rod-stiffened panel as shown in [figure 5c](#). In addition, lateral supports connecting the midlength position of the edge supports to the frame support assembly were added for the thin-skinned panel test to ensure that the tubes could not move out-of-plane during loading. These features are noted in [figure 5c](#). Shims were also added to take up tolerances where the arms were pinned to the uprights in the frame restraint system.

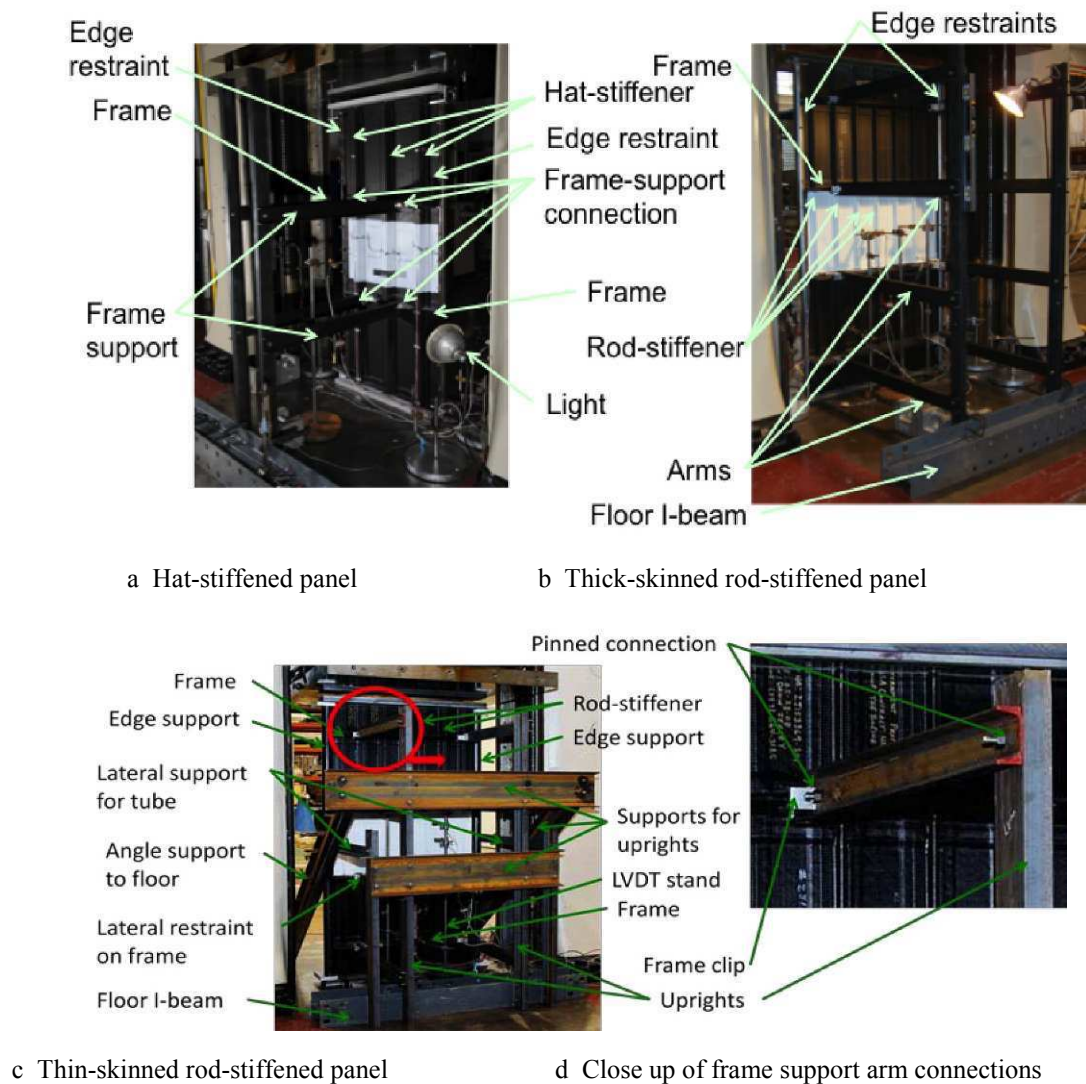


Fig 5 Panels in test machine

INSTRUMENTATION AND TEST PROCEDURE

Each panel was monitored during loading using approximately 80 strain gages, 8 LVDTs and a full-field optical measurement system. The optical measurement or Vision Image Correlation (VIC) system [2] was used to obtain full field displacement and strain results for the unstiffened side of the panel skin during the loading of each specimen. The VIC system required a black and white speckle pattern be painted on the specimen surface, and used two cameras positioned at different angles to the specimen surface to simultaneously photograph the specimen at set intervals during the test. In these tests, the specimen was photographed every 2 to 5 seconds, resulting in approximately 150 time steps of data. The VIC system also recorded the load from the test machine so images could be related to the corresponding load. The VIC system compared the photographic images and produces three-dimensional displacements and strains. For each panel, the section between the centermost frames was monitored using the VIC system. A typical VIC arrangement is shown in [figure 6](#).

Photographs of the hat-stiffened, thick-skinned and thin-skinned rod-stiffened panels in the test machine are shown in figures 5a, 5b and 5c, respectively. The stiffened surface was painted white to improve the video images and was not monitored using VIC since restraints, instrumentation and shadows would limit the clear vision area of a VIC image.

Each panel was loaded in a series of tests at a load rate of between 100 and 200 kN/min. Even though each panel was subjected to barely-visible impact damage prior to loading, these impacts did not significantly affect the panel behavior and are not visible in the VIC data, so this damage is not considered in the current paper.

FINITE ELEMENT ANALYSIS

An analytical evaluation of each panel was conducted using the computer code STAGS [3]. The finite element model for the hat-stiffened panel is shown in figure 7. The others used a similar mesh with similar numbers of elements. The hat-stiffened panel model included 13,656 quadrilateral shell elements representing the skin, flanges, hats, and frames. The foam inside the hats in all three panels was modeled as part of the shell elements representing the hat tops and webs. This assumption was adequate since the foam carried a negligible amount of load but restrained buckling of the hat webs. For all three panels, the material properties are based on the compression properties for a stack of material [1], such that the stack axial stiffness is 63.6 GPa, the lateral stiffness is 32.1 GPa, the shear stiffness is 15.6 GPa, and Poisson's ratio is 0.397. In addition, the pultruded rods were modeled as beam elements with axial stiffness 124 GPa for both rod-stiffened panels.

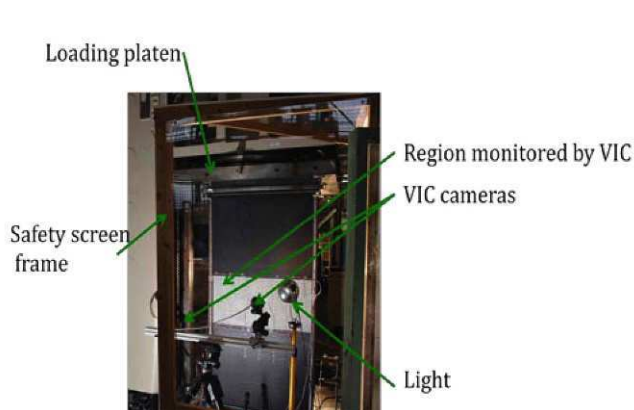


Fig 6 Vision Image Correlation System.

13,981 nodes
14,193 elements
83,886 DOF

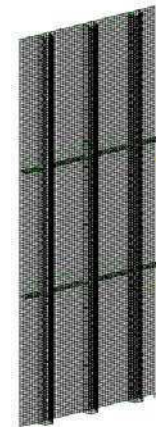


Fig 7 Finite element model of the hat-stiffened panel.

The loaded ends of each panel inside the potting were restrained by forcing all lateral and out-of-plane displacements to be zero inside the potted region. Frame supports were not included as restraints in the analyses since test data indicates that the frames moved out-of-plane during loading. Two types of edge restraint assumptions were used for each panel. First, the unloaded edges were restrained such that no out-of-plane motion was permitted but all other degrees of freedom were allowed. Second, no edge restraint was included, allowing the unloaded edge to deform in any direction.

RESULTS AND DISCUSSION

The experimental full-field deformation in the center region between frames for the hat-stiffened panel is shown in figure 8 for a load level of approximately 640 kN, which is immediately prior to the failure load of 641.7 kN. The edges of the panel display an out-of-plane deformation of approximately 0.9 cm despite the presence of the edge restraints. Lines of data for out-of-plane motion near the left edge, and midbay between hats were extracted from the VIC data and plotted in figure 9 as a function of vertical position. Frame locations are indicated by the light black dashed lines. Out-of-plane deformations along the left edge and midbay between hats from test and the two analyses of the hat-stiffened panel are shown in figure 9a for the full panel length, and in figure 9b for the center section between frames, for a load of approximately 640 kN. The analytical results show the full panel length and are represented by solid lines, while test results were only obtained between two center frames and are shown as dashed lines. Panel edge deformations are shown in green lines, and left and right midbay

deformations are shown in red and blue lines, respectively. Since the panel is symmetric, the analysis indicates that the two midbay deformations are the same, so only blue and green lines for analysis are seen in the plot.

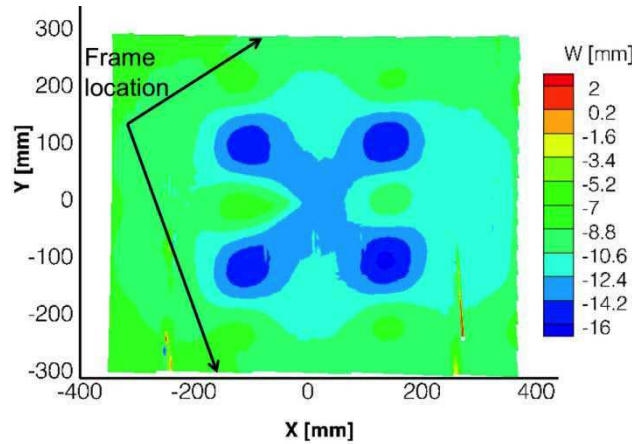


Fig 8 Experimental full-field out-of-plane deformation in center region of hat-stiffened panel at 99.8% of failure load.

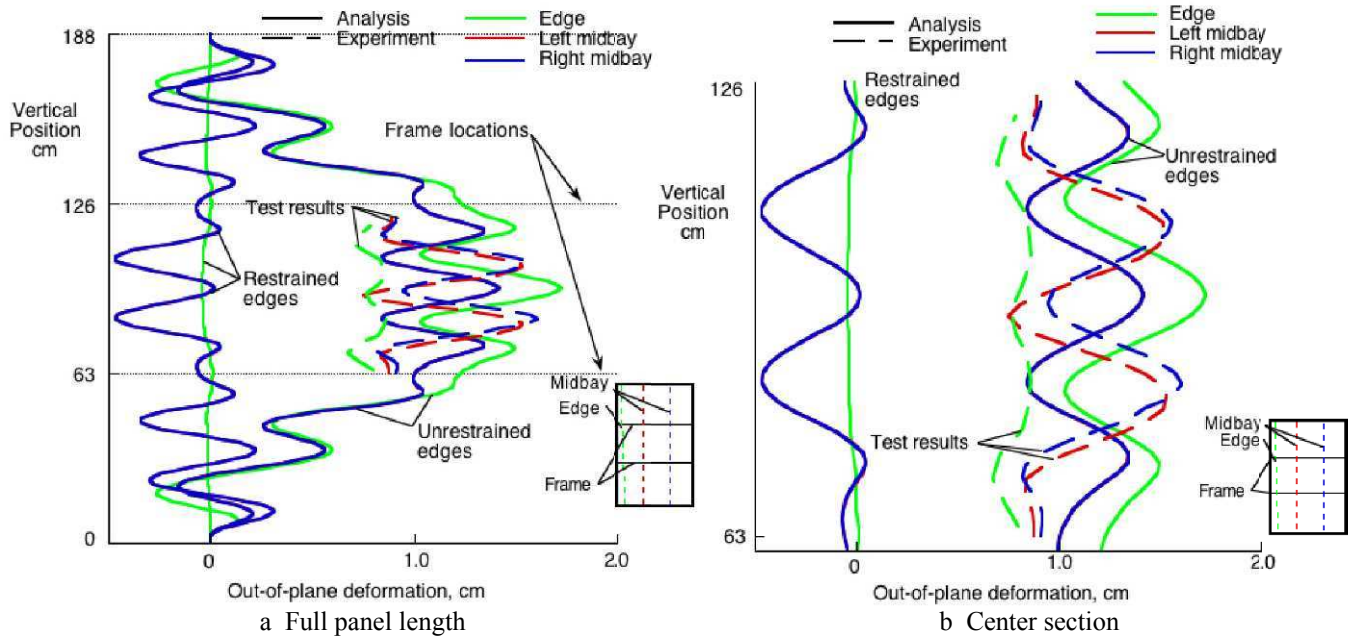


Fig 9 Out-of plane deformation of the hat-stiffened panel at approximately failure load.

Significant deformation is seen for all three locations in the test results. Even at the restrained edges and frame locations, the panel is not fully restrained for this load level. At this load level the relatively uniform edge and frame deformations indicate that the edges and frames have moved out-of-plane by approximately 0.76 cm at the frame locations despite the presence of the restraints. A comparison of the edge deformation and the midbay deformation, with the knowledge that the loaded ends of the panel could not move out-of-plane, imply that the panel is taking on a single half-wave mode shape along the panel length with an amplitude of approximately 0.9 cm while the midbay measurements indicate that a local deformation with an amplitude of approximately 0.5 cm is superposed on this global mode.

The predicted out-of-plane motion of the unstiffened side of the hat-stiffened panel resulting from the assumptions of the restrained and unrestrained unloaded edges are shown in [figure 10](#) for a load of approximately 640 kN. These boundary conditions result in the same local buckling pattern, but the global behavior differs. The midbay deformation between the stiffeners shows the same pattern as the test data, but the amplitudes are different. When no restraint is included on the unloaded edge, the 0.264-cm thick skin buckles along the free edge but edge buckles are not seen in the test data. The hat-stiffened panel supported its Design Ultimate Load of 600.5 kN by carrying load after the skin buckled locally, so the unanticipated edge deformations along the frames and edges had no major impact on the test results.

A similar process of evaluation was completed for the rod-stiffened panels. The only difference between the two rod-stiffened panels is the thickness of the skin. The experimental full-field out-of-plane deformations are shown in [figure 11](#) for a load of approximately 915 kN for the thick-skinned panel and 885 kN for the thin-skinned panel, which are slightly less than the failure loads of 918.6 and 889.6 kN, respectively.

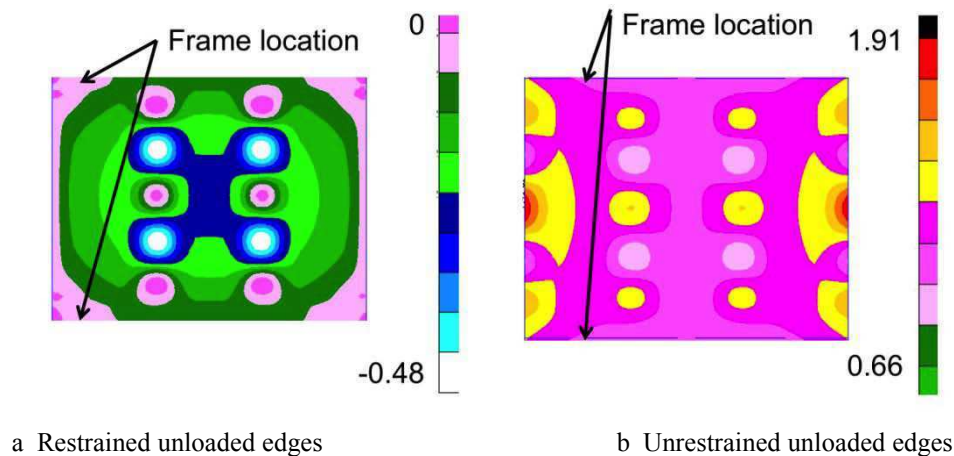


Fig 10 Predicted out-of-plane deformation of the unstiffened surface of the hat-stiffened panel at a load level near failure.

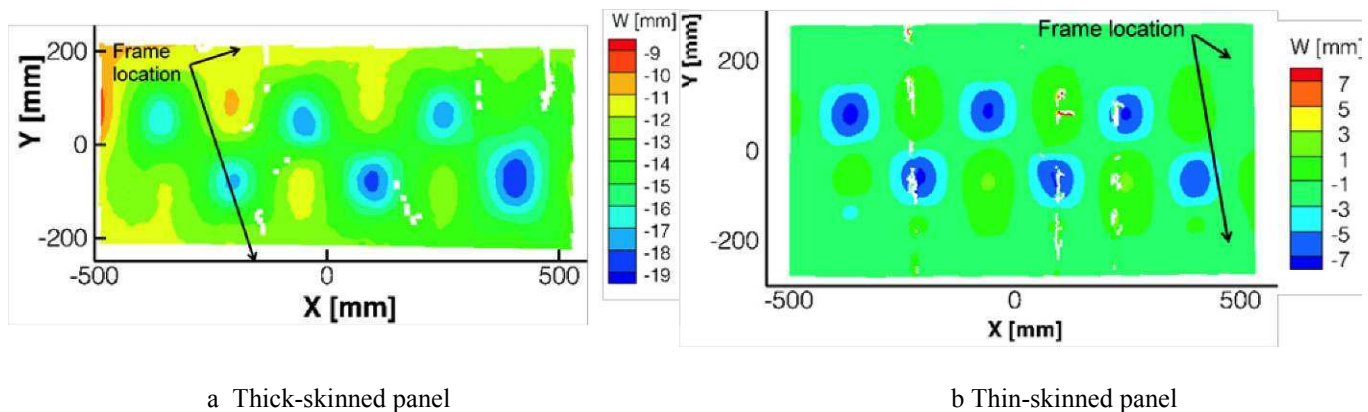


Fig 11 Experimental full-field out-of-plane deformation in center region of rod-stiffened panels at approximately 99% of failure load.

Out-of-plane deformations at a load level just prior to failure along the left edge, midbay location nearest the center of the panel, and midbay location one bay away from the center are shown in [figure 12](#) for the thick-skinned panel and [figure 13](#) for the thin-skinned panel. The analytical results show the full panel length and are represented by solid lines, while test results were only obtained between two center frames and are shown as dashed lines. The edge is shown in green and the midbay locations are shown in red and blue. Frame locations are indicated by light black dashed lines. These results show that the edges and frame locations again deform out-of-plane. Test results show that in the thick-skinned panel, one edge of the panel moved out-of-plane by approximately 1.2 cm, shown in [figure 12b](#), while the thin-skinned panel moved out-of-plane

approximately 0.20 cm, shown in figure 13b. The thick-skinned panel failed at a load of 918.6 kN while the thin-skinned panel failed at a load of 889.6 kN. The modifications to the support structure reduced the out-of-plane motion for approximately the same load level and allowed the thin-skinned panel to support almost as much load as the thick-skinned panel. Both panels display local buckling between the stiffeners. Notice that the edge in both unrestrained edge cases shows a global single half-wave deformation shape along the panel length, while the midbay locations show local deformations between the frames superposed on the global shape. Buckling mode shapes of several half-waves occur between the stiffeners and add to the global deformation. In the thick-skinned panel, the test data indicates a larger amplitude of the global buckle than either of the analysis cases, and local buckle amplitudes which are approximately the same as seen in the unrestrained edge case. In the thin-skinned panel the test results show little global deformation and local buckle amplitudes which are close to what is predicted for the unrestrained edge case.

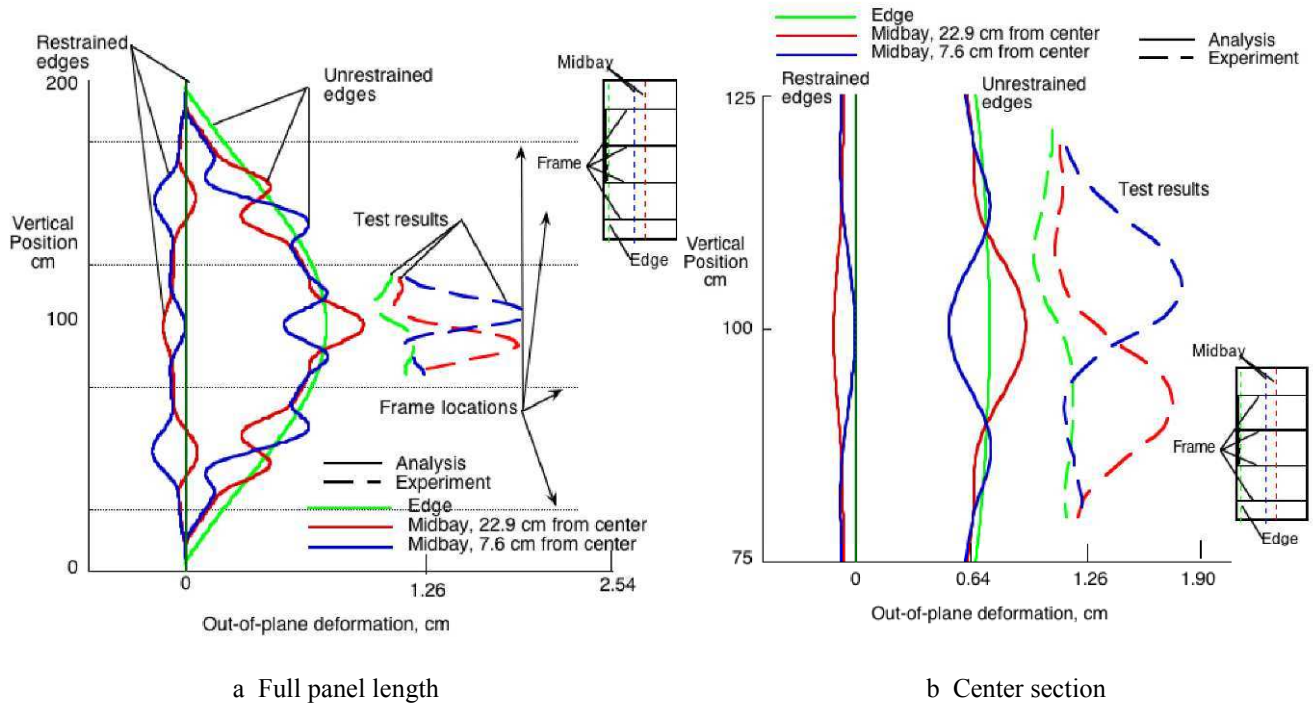


Fig 12 Out-of-plane deformation of thick-skinned rod-stiffened panel at a load of approximately the failure load.

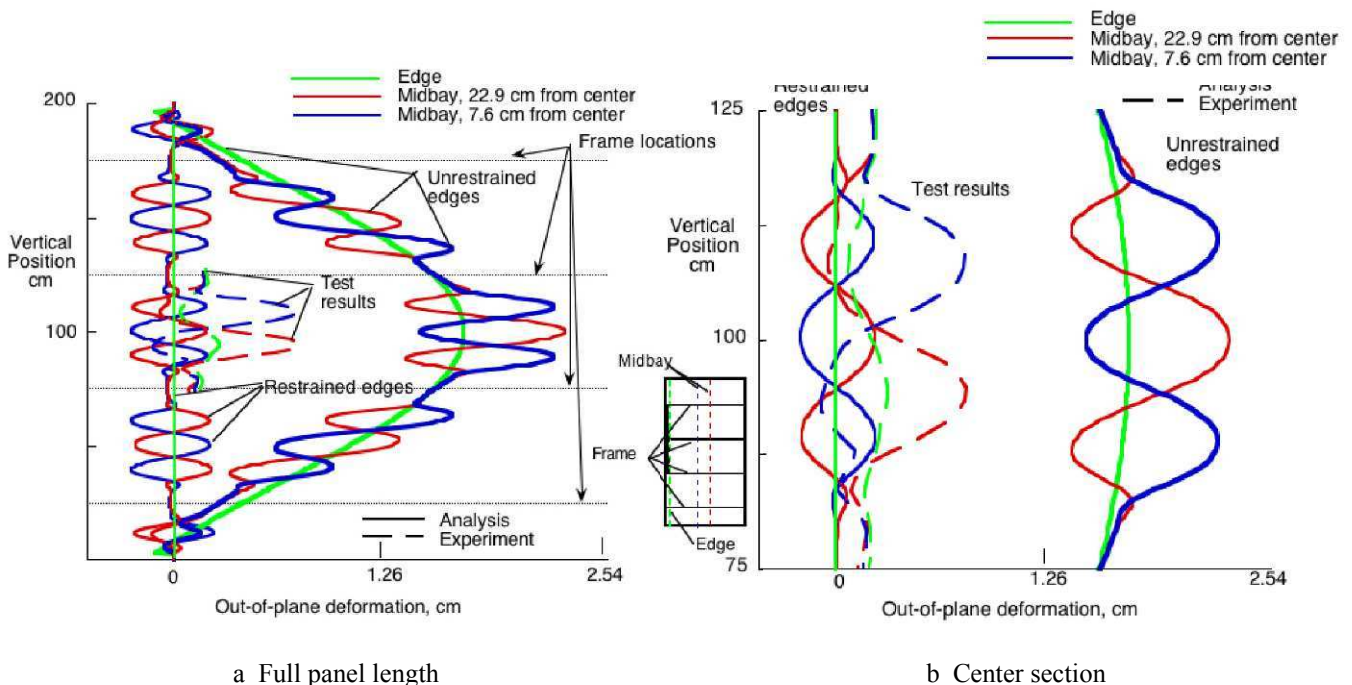


Fig 13 Out-of-plane deformation of thin-skinned rod-stiffened panel at a load of approximately the failure load.

The out-of-plane motion of the unstiffened side of the rod-stiffened panels resulting from the assumptions of the restrained and unrestrained unloaded edges are shown in figures 14 and 15. Analytical result for the thick-skinned rod-stiffened panel for the restrained and unrestrained conditions at a load of 890 kN are shown in figure 14a and 14b, respectively. Analytical result for thin-skinned panel with restrained edges at a load of 934 kN is shown in figure 15a. Analytical result for thin-skinned panel with unrestrained edges at a load of 778 kN is shown in figure 15b. The deformation patterns are similar but not identical to the test data shown in figure 11. The thick-skinned and thin-skinned rod-stiffened panels support 70 and 97 percent of their Design Ultimate Loads, respectively. The lack of adequate edge restraints appears to have contributed to the premature failure.

For all three panels, the VIC system was critical to understanding the effect of the restraint system. Test results indicated that the restraint system for the hat-stiffened panel did not fully constrain the panel as intended. However, the panel design limited the global buckling and allowed local buckling to occur. The global buckling was not significant enough to prevent the panel from meeting its design requirements. The restraint system for the thick-skinned rod-stiffened panel did not fully constrain the panel as intended, which led to global buckling and premature failure. The modified restraint system for the thin-skinned allowed small deformations at the restraint points, however the panel displayed the expected local buckling and supported 97 percent of its design load.

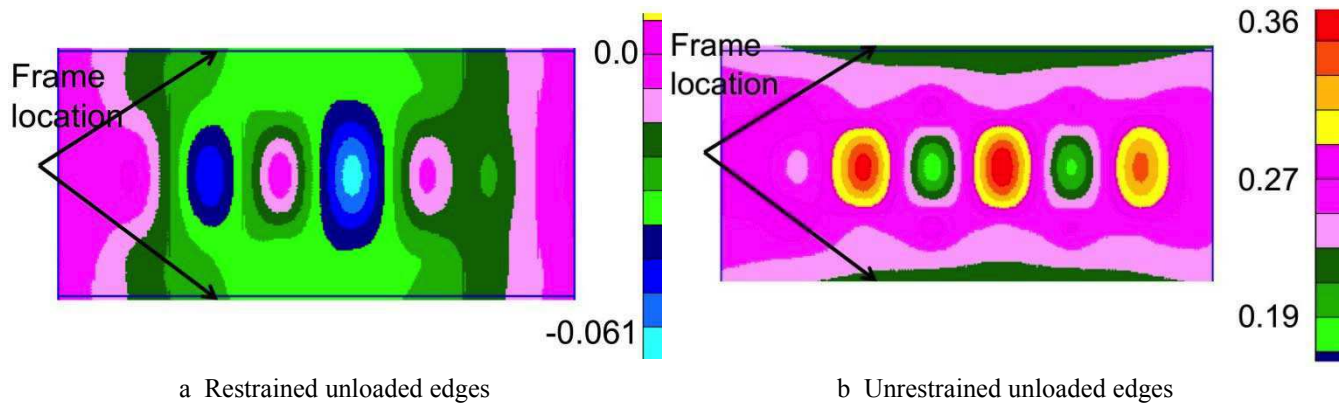


Fig 14 Analytical predictions of out-of-plane deformation the thick-skinned rod-stiffened panels at a load of approximately failure load.

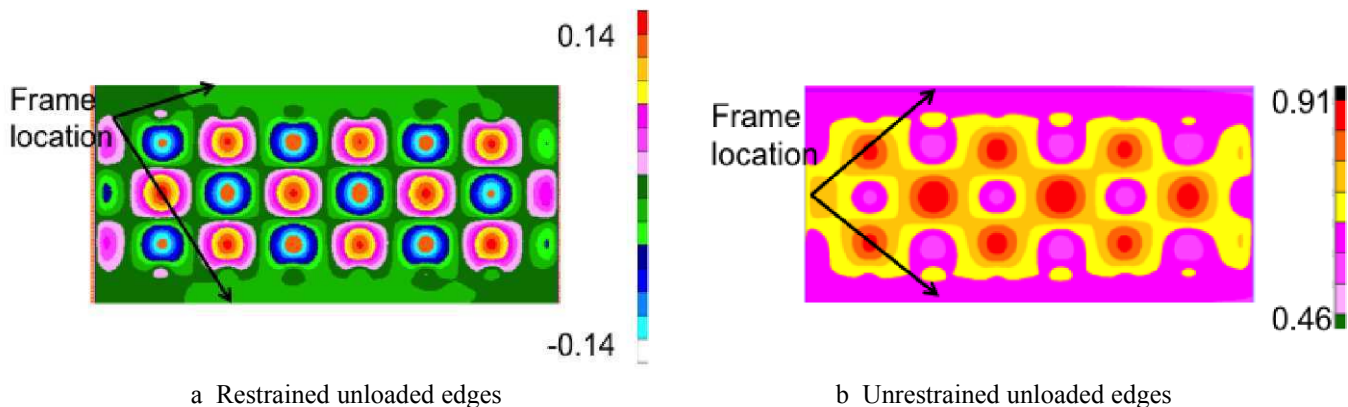


Fig 15 Analytical predictions of out-of-plane deformation the thin-skinned rod-stiffened panels at a load of approximately failure load.

CONCLUDING REMARKS

Three composite panels were loaded to buckling and failure in axial compression. In each case, the panel deformation was a combination of a global one-half wave deformation shape and a local multi-wave shape between stiffeners. The amplitude of the global wave was dependent upon the edge restraint system. Both test and analyses indicate that the restraint system did not fully restrain the edges of the panels during testing. Without the measurements at the panel edges provided by the full field measurement system, the edge behavior would not have been quantified. An improved restraint system was used for the thin-skinned rod-stiffened panel because, by the time of that test, it was understood that the prior restraint systems were not limiting out-of-plane motion as well as had been assumed. This understanding of the limitations of the restraint system relied upon the data provided by the full-field measurement system.

REFERENCES

- [1] Velicki, Alex, "Damage Arresting Composites for Shaped Vehicles, Phase I Final Report, NASA CR-2009-215932, September 2009.
- [2] McGowan, David M., Ambur, Damodar R., and McNeil, Stephen R. 2003. "Full-field Structural Response of Composite Structures: Analysis and Experiment," presented at the 44th AIAA/ASME/ASCE/AHS Structures, Dynamics and Materials Conference, AIAA 2003-1623, Norfolk, VA, April 2003.
- [3] Rankin, C. C., Brogan, F. A., Loden, W. A., and Cabiness, H. D. 2001. "STAGS User Manual, Version 4.0." Lockheed Martin Missiles and Space Company, Incorporated.

Burst Strength of Pipeline Test Specimens Containing Longitudinal or Circumferential Corrosion Defects

José L. F. Freire, Pontifical Catholic University of Rio de Janeiro, Brazil, jlfreire@puc-rio.br

Adilson C. Benjamin, PETROBRAS R&D Center, Rio de Janeiro, Brazil,

acbenjamin@petrobras.com.br

Ronaldo D. Vieira, Pontifical Catholic University of Rio de Janeiro, Brazil, rdvieira@puc-rio.br

Jorge L. C. Diniz, Fluke Engineering, Macaé, Brazil, jorge.diniz@flukeengenharia.com.br

ABSTRACT

The elastic and plastic strain data of tubular specimens undergoing rupture under internal pressure tests are presented and analyzed. Six tubular specimens were tested. The specimens were cut from longitudinally welded tubes made of API 5L X80 steel with a nominal outside diameter of 457.2 mm (18 in) and a nominal wall thickness of 7.93 mm (0.312 in). Each of the six specimens had one external longitudinal or circumferential corrosion defect that had been machined using spark erosion. Tensile specimens and impact test specimens were tested to determine material properties. Post-yielding electrical resistance strain gages were used to measure the elastic and plastic strains. The failure pressures measured in the laboratory tests were compared with those predicted by four assessment methods: the B31G method, the RSTRENG 085dL method, the DNV RP-F101 method for single defects and by the Kastner equation. The paper also discusses the strength of the pipe segments used in the tests under the assumptions of following the Tresca and von Mises rupture criteria.

1. Introduction

General or localized corrosion represents a threat to pipeline strength because it produces a reduction in the pipe wall thickness. In order to evaluate the remaining strength of a corroded pipe segment it is necessary to know at least the following parameters: the outside diameter of the pipe D_e , the wall thickness of the pipe t , the yield strength of the pipe material σ_{yield} or the ultimate tensile strength of the pipe material σ_{ult} , the remaining wall thickness in the defect t^* or the maximum defect depth d ($d = t - t^*$), the defect length L and the defect width w .

Over the past decade over forty full scale burst tests have been conducted by PETROBRAS and the Pontifical Catholic University of Rio de Janeiro with the objective of investigating the failure behavior of pipelines containing corrosion defects. Several types of corrosion defects have been tested, namely: short and long longitudinal defects (respectively defects in which L is smaller or larger than $\sqrt{20 D_e t}$), uniform depth defects, non uniform depth defects, simulated defects (machined using spark erosion), real defects (removed from service) and colonies of defects. Most of these tests have already been published and are referenced in Table 1 of reference [1] and also in [2-8].

In this paper the burst tests of six tubular specimens loaded with internal pressure (presented in [1] and [9]) are analyzed in terms of strain distributions determined by strain gages located inside the corrosion patches and in terms of the adequacy of failure pressure predictions based on simple equations existing in the literature for corrosion geometries that are localized in a transition zone where they can be classified as short longitudinal defects or long circumferential defects.

The specimens were cut from a longitudinal welded tube made of API 5L X80 steel with a nominal outside diameter of 457.2 mm (18 in) and a nominal wall thickness of 7.93 mm (0.312 in). Each of the six specimens had one external short length uniform depth corrosion defect, machined using spark erosion. Measurements were carried out in order to determine the actual dimensions of each tubular specimen and its respective defect. Tensile specimens and impact test specimens were tested to determine material properties.

The failure pressures measured in the laboratory tests were compared with those predicted by four methods, three of them used in the assessment of longitudinal defects, namely: the B31G method [10], the RSTRENG 085dL method [11], the DNV RP-F101 method for single defects [12], and the fourth of them being based on the Kastner equation [13], which is used for the assessment of circumferential defects. Strain data collected with post-yielding strain gages that were bonded to surface locations inside the corrosion patches were analyzed to determine differences in the strain distributions caused by the proposed geometries of corroded defects.

2. Theoretical Background

Assuming that the pipeline is a thin shell (ratio of the pipeline's outside diameter D_e to the pipeline's wall thickness t is greater than twenty ($(D_e/t) \geq 20$)), the radial stress σ_r at any point of the pipe wall is negligibly small. Consequently there are only two stresses at any point of the pipe wall: the hoop or circumferential stress σ_h and the longitudinal stress σ_L . The hoop tensile stress σ_h and the longitudinal tensile stress σ_L are related to the internal pressure p by equations (1-2) for points of the thin pipe located in nominal regions, i.e., located far away from the defect patches and from the pipe caps.

$$\sigma_h = \frac{p \cdot D}{2t} \quad (1)$$

$$\sigma_L = n \cdot \sigma_h \quad (2)$$

where $n = 0.5$ or $n = \nu = 0.3$ respectively, are associated to longitudinally unrestrained pipe or to longitudinally restrained pipe, ν being the Poisson coefficient.

In a pipeline subjected only to internal pressure, the nominal hoop stress σ_h and the nominal longitudinal stress σ_L are positive (tensile stress). Thus, the equations of the Tresca failure criterion are:

$$\sigma_h = \sigma_{flow} \cdot (f_R)_h \quad (3)$$

or

$$\sigma_L = \sigma_{flow} \cdot (f_R)_L \quad (4)$$

and the equation of the von Mises failure criterion is:

$$\left(\sigma_L^2 / (f_R)_L^2 + \sigma_h^2 / (f_R)_h^2 - (\sigma_L / (f_R)_L) \cdot (\sigma_h / (f_R)_h) \right)^{1/2} = \sigma_{flow} \quad (5)$$

where σ_{flow} is the material flow stress, and $(f_R)_h$ and $(f_R)_L$, respectively, are the reduction strength factors in the hoop and longitudinal directions caused by the corrosion defect's geometry. The reduction factor in the hoop direction $(f_R)_h$ is given by equation (6). Table 1 presents the equations adopted by three selected methods to calculate flow stress σ_{flow} , pipe diameter D , geometric factor α_{area} and bulging factor M . Other variables in these equations are maximum depth of corrosion d and length and width of the corrosion patch, given respectively by L and w .

$$(f_R)_h = \frac{1 - \alpha_{area} (d/t)}{1 - \alpha_{area} (d/t) M^{-1}} \quad (6)$$

The reduction factor in longitudinal direction $(f_R)_L$ was derived by Kastner [13] and is given in equation (7). Angle β is the half angle width of the circumferential defect.

$$(f_R)_L = \frac{\left(1 - \frac{d}{t}\right) \left(\pi - \beta \frac{d}{t}\right)}{\pi \left(1 - \frac{d}{t}\right) + 2 \frac{d}{t} \sin \beta} \quad (7)$$

The burst pressure based on the hoop stress is given by equation (8). It is generally accepted that the best equation to represent the longitudinal stress in a corroded pipe at failure is the Kastner equation [13] given by equation (9).

$$(p_f)_h = \sigma_{flow} \frac{2t}{D} \frac{1 - \alpha_{area} (d/t)}{1 - \alpha_{area} (d/t) M^{-1}} \quad (8)$$

$$(p_f)_L = \sigma_{flow} \frac{1}{n} \frac{2t}{D_e} \frac{\left(1 - \frac{d}{t}\right) \left(\pi - \beta \frac{d}{t}\right)}{\pi \left(1 - \frac{d}{t}\right) + 2 \frac{d}{t} \sin \beta} \quad (9)$$

Application of the Tresca and Mises criteria for a given specimen is accomplished by using equations (10) and (11).

$$(p_f)_{TRESCA} = \min((p_f)_h, (p_f)_L) \quad (10)$$

$$(p_f)_{MISES} = \left[\frac{1}{(p_f)_h^2} + \frac{1}{(p_f)_L^2} - \frac{1}{(p_f)_h (p_f)_L} \right]^{-1/2} \quad (11)$$

Table 1 – Parameters adopted by the three selected methods to predict the rupture caused by the hoop stresses

Method	σ_{flow}	D	α_{area}	M
B31G ($L \leq \sqrt{20D_e t}$)	$1.1 \sigma_{yield}$	D_e	$2 / 3$	$\left[1 + 0.8 \frac{L^2}{D_e t} \right]^{1/2}$
B31G ($L > \sqrt{20D_e t}$)	$1.1 \sigma_{yield}$	D_e	1	∞
085dL ($L \leq \sqrt{50D_e t}$)	$\sigma_{yield} + 69 \text{ MPa}$	D_e	0.85	$\left[1 + 0.6275 \frac{L^2}{D_e t} - 0.003375 \left(\frac{L^2}{D_e t} \right)^2 \right]^{1/2}$
085dL ($L > \sqrt{50D_e t}$)	$\sigma_{yield} + 69 \text{ MPa}$	D_e	0.85	$3.3 + 0.032 \frac{L^2}{D_e t}$
DNV RP-F101 (Part B)	σ_{ult}	$D_e - t$	1	$\left[1 + 0.31 \frac{L^2}{D_e t} \right]^{1/2}$

3. Experimental Methods

3.1. Material Characterization

The raw material used in this research was composed of one longitudinally welded tube made of American Petroleum Institute API 5L X80 steel [14]. The length of this pipe was approximately 12m. The nominal outside diameter and the nominal wall thickness of the pipe were 457.2mm (18in) and 7.93mm (0.312in), respectively, with actual dimensions being 459mm and 8.1mm, respectively. This pipe was named Tube 3.

A summary of the tension test results for the transverse tensile specimens, cut from the Tube 3, is presented in Table 2. The yield strength measured as the stress required to produce a plastic deformation of 0.2% presented a mean value 13% greater than the specified minimum yield strength SMYS of API 5L X80 steel (SMYS = 551.6MPa). The mean ultimate strength was 19% greater than the specified minimum ultimate strength SMTS of API 5L X80 steel (SMTS = 620.6MPa).

The results of the Charpy V-notch impact tests at a temperature of 0°C for 2/3 thickness specimens cut from the Tube 3 are also presented in Table 2. This table also presents the impact energy equivalent for full thickness specimens. The mean value of the full thickness impact energy is equal to 80J, the minimum all-heat average full-size absorbed energy value required by product specification level 2 (PSL 2) of API Specification 5L for pipe size 18 and grade X80 [14].

3.2 Manufacture of the Tubular Specimens

Three tubular specimens 1.7 m long with circumferential defects and three tubular specimens 1.9 m long with longitudinal defects were manufactured. Each of the six specimens had one external uniform depth corrosion defect that had been machined using spark erosion. These defects were machined opposite the tube seam weld at a centralized position in relation to the ends of the specimens. The corrosion defects were smooth rectangular defects, i.e., the shape of the longitudinal area of metal loss was rectangular with smooth edges. These edges were made with a small radius equal to 4.4mm for the

circumferential and longitudinal defects, except for specimen RDTS 1, which was 3.2mm. The tubular specimens were closed by specially designed plane heads with crossed reinforcements that were welded on after the defects were machined. The actual dimensions of each tubular specimen and its respective defect are presented in Table 3. Using the values of ratios $L^2/(D_e t)$, one can see that all the corrosion defects are short according to the ASME B31G method [10] (defects in which $L \leq \sqrt{20 D_e t}$).

Table 2 – Tension test and Charpy impact test results

Tension test results for the transverse tensile specimens				Charpy impact test results		
Tensile specimen	σ_{yield} (MPa)	σ_{ult} (MPa)	$\frac{\sigma_{yield}}{\sigma_{ult}}$	Impact specimen	Impact energy for 2/3 thickness specimens (J)	Impact energy transformed to full thickness specimens (J)
T3T1	645.0	738.0	0.87	CHT31	48	72
T3T6	607.0	736.0	0.82	CHT32	51	76
mean value	626.0	737.0	0.85	CHT33	62	93
				mean value	54	80

Table 3 – Actual dimensions of the tubular specimens and of the machined defects

Specimen	t^* (mm)	$d=t-t^*$ (mm)	L (mm)	w (mm)	β (°)	$\frac{d}{t}$	$\frac{L^2}{D_e t}$	$D_e = 459\text{mm}$ $t = 8.1\text{mm}$
CDTS 1	2.84	5.28	40.3	147	37	0.65	0.44	
CDTS 2	2.51	5.62	40.0	296	74	0.69	0.43	
CDTS 3	2.05	6.01	40.0	445	111	0.74	0.43	
RDTS 1	5.74	2.36	208	32.1	4.0	0.29	11.7	
RDTS 2	4.05	4.05	208	32.1	4.0	0.50	11.7	
RDTS 3	2.41	5.69	208	32.1	4.0	0.70	11.7	

3.3 Pressure Tests

The tubular specimens were loaded with internal pressure only. The pressurizing system used an oil pump with a maximum capacity of 40MPa. The tubular specimens were filled with de-aired water and an extra pressure vessel located between the pump and the tubular specimens separated the oil and water pressure fluids. Pressure rates were kept to a maximum of 0.17MPa/min up to the beginning of yielding of the most-strained pipe wall in the defect region. From this point up to rupture, the pressure rate was decreased and followed the volume injection rate of water, which was kept to a maximum of $2 \times 10^{-7} \text{m}^3/\text{min}$. Pressure was monitored by two pressure transducers. The volume of the water injected into the tubular specimen was monitored by a specially constructed direct reading device.

Each tubular specimen was instrumented with high elongation strain gage rosettes (5mm gage length) that were bonded to the external pipe surface with an adhesive appropriate for high strains. The strain gage rosettes were bonded at pre-selected hot locations on the outside surface of the tubular specimen, mainly along and inside the corrosion defect.

4. Results and Discussion

The second column of Table 4 presents the failure pressures $(p_f)_{\text{test}}$ measured during the burst tests of the six tubular specimens. Depending on the dimensions of a circumferential corrosion defect (d , L and w), its failure will be governed either by the hoop stress or by the longitudinal stress. For this reason a failure criterion based on the Tresca yield criterion was adopted to be compared with the experimentally determined burst pressures. The Mises criterion was also used for comparison purposes. In terms of failure pressures, both criteria are represented by Equations (10) and (11).

Each method used for longitudinal failure prediction, represented by equation (7) and information given in Table 1, was combined with the single version of Equation (8), resulting in a pair of equations for which two values of failure pressures were calculated: $(p_f)_h$ and $(p_f)_L$. The lesser pressure $(p_f)_{\min}$ is the Tresca's pressure and was selected to be the predicted failure pressure. These selected predicted pressures are depicted in Table 4 by light grey shaded cells. The flow stress in the hoop direction was also adopted to calculate the flow stress in the longitudinal direction.

The DNV-Kastner pair of equations was verified to be the one with minimum deviation from the actual test pressures. Table 5 repeats the data of Table 4 in terms of the results obtained for the pair DNV-Kastner and included the Tresca and Mises predictions given by equations (10) and (11). Fig. 1 presents the results of Table 5 in the form of a plot showing that both criteria represent reasonably well the test pressures, the Tresca predictions being more conservative (5 out of 6 results).

Table 4 – Actual (test) and predicted (pair longitudinal – circumferential) failure pressures

Specimen	$(p_f)_{\text{test}}$ (MPa)	Pair B31G-Kastner		Pair 085dL-Kastner		Pair DNV-Kastner	
		$(p_f)_h$ (MPa)	$(p_f)_L$ (MPa)	$(p_f)_h$ (MPa)	$(p_f)_L$ (MPa)	$(p_f)_h$ (MPa)	$(p_f)_L$ (MPa)
CDTS 1	25.25	21.95	33.00	21.49	33.30	23.74	35.31
CDTS 2	23.29	21.73	22.32	21.11	22.53	23.27	23.89
CDTS 3	20.51	21.42	14.93	20.57	15.07	22.54	15.98
RDTs 1	22.73	20.85	47.42	20.25	47.86	21.71	50.76
RDTs 2	17.36	18.08	46.02	16.62	46.45	17.25	49.25
RDTs 3	9.94	15.13	43.30	12.56	43.70	11.70	46.34

Table 5 – Actual (test) and predicted (DNV-Kastner Pair) failure pressures

Specimen	$(p_f)_{\text{test}}$ (MPa)	DNV-Kastner Pair			
		$(p_f)_h$ (MPa)	$(p_f)_L$ (MPa)	$(p_f)_{\text{TRESCA}}$ (MPa)	$(p_f)_{\text{MISES}}$ (MPa)
CDTS 1	25.25	23.74	35.31	23.74	26.886
CDTS 2	23.29	23.27	23.89	23.27	23.573
CDTS 3	20.51	22.54	15.98	15.98	17.94
RDTs 1	22.73	21.71	50.76	21.71	24.983
RDTs 2	17.36	17.25	49.25	17.25	19.639
RDTs 3	9.94	11.70	46.34	11.70	13.003

Fig. 2 presents a plot of points that correspond to the ratios of the actual failure pressure $(p_f)_{\text{test}}$ to the failure pressure predicted by the DNV-Kastner pair of assessment results given in Tables 4 and 5. The Tresca criterion for the first quadrant (positive stresses) is also depicted in the figure. The data point falling in the right extreme of the plot is related to specimen CDTS 3 and it clearly predicts that fracture will occur along the longitudinal direction, i.e., it is determined by the longitudinal stress. Tables 4 and 5 and Fig. 1 show that the Tresca predicted failure pressures are conservative, i.e., the ratios are less than or equal to the unity, except for specimen RDTs 3. An observation about this result is made in the last paragraph of this section.

Fig. 3 presents photographs of the defects of specimens CDTS and RDTs after failure. The longitudinal orientation of the fracture suffered by the defects of specimens RDTs 1-3 and CDTS 1-2 suggests that these failures were governed by the hoop stress. On the other hand, the circumferential orientation of the fracture suffered by the defect of the specimen CDTS 3 suggests that its failure was governed by the longitudinal stress.

Strains along the longitudinal and circumferential directions measured by the strain gage rosettes for points located at or near the center of the corrosion patches are shown in Fig. 4 for specimens RDTs 1 and CDTS 3. The plots shown in the Fig. depict the circumferential and longitudinal strains varying with the internal pressure. It is possible to separate the strain distributions into two types of behaviors. One shows very large circumferential plastic strains and very small longitudinal strains and is connected to the defects characterized as longitudinal defects (specimens named RDTs 1 to 3 with large ratio $L^2/(D_e t) \cong 12$ and small angle β). The reason for this behavior is the high hoop stress compared to the longitudinal stress. These stresses cause the fracture of the specimens and generate the fracture path along the longitudinal axis. The second type of behavior is presented by the specimens named CDTS 1 to 3, which present wide β angles and very small values for ratio $L^2/(D_e t) \cong 0.4$. In this case the longitudinal and circumferential strains are of the same order. Specifically, the circumferential strain was much greater than the longitudinal strain for specimen CDTS 3.

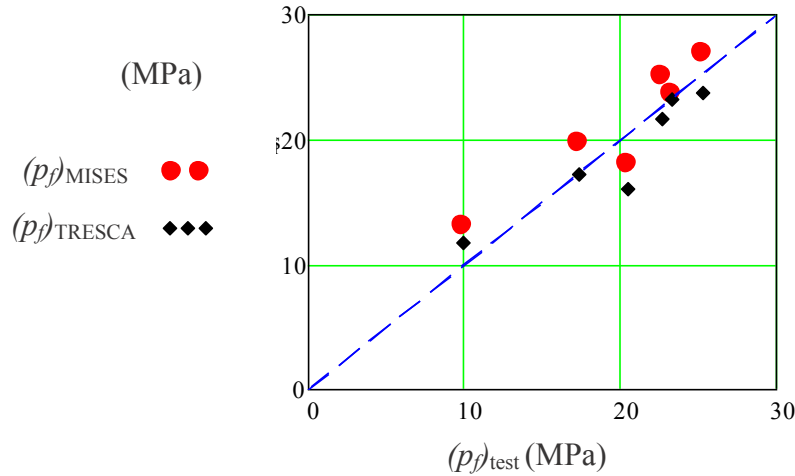


Fig. 1 Burst pressures calculated with Mises and Tresca criteria using the DNV-Kastner pair of equations compared with the actual burst test pressures

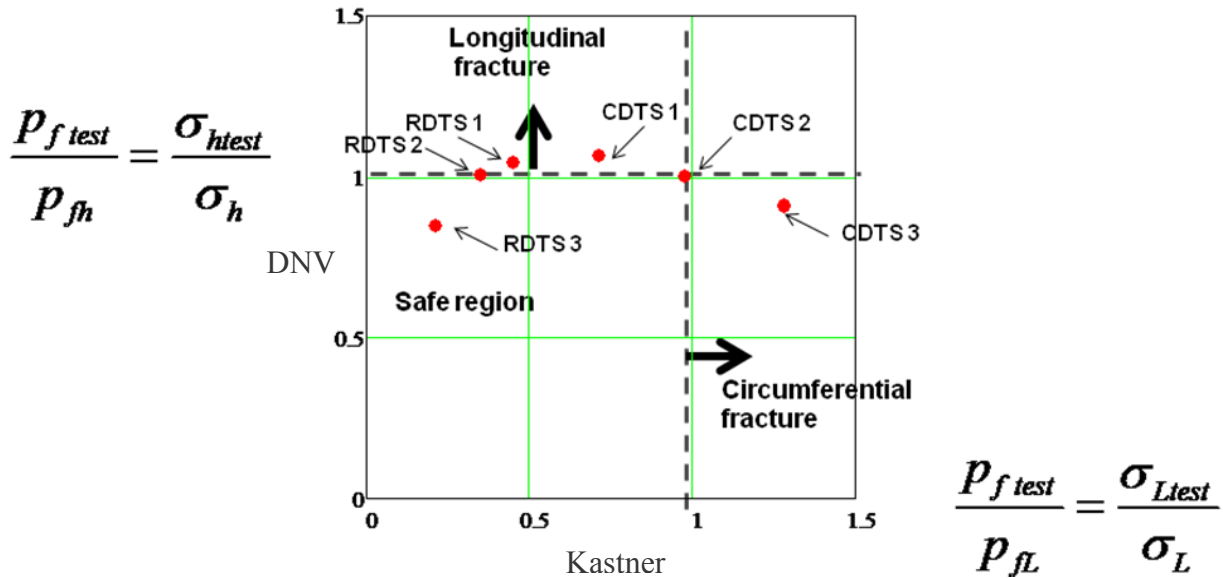


Fig.2 Normalized plot of fracture data points for the pair of DNV-Kastner equations

According to the results presented in [Tables 4](#) and [5](#) and in [Fig. 1](#), the DNV method applied to specimens RDTs 1 and RDTs 2 led to conservative predictions while non conservative predictions were met for the specimen RDTs 3. The good performance of specimens RDTs 1 and RDTs 2 is useful for ruling out two possible causes of the poor performance of RDTs 3: the generation of the artificial corrosion (the same process was used to machine the defect) and the material properties (specimens came from the same tube). Moreover, small error measurements in the order of 0.5mm in the remaining thickness can propagate errors as high as 20% in the predicted failure pressure for specimens such as the one named RDTs 3 due to its small thickness (about 2mm along the defect region). An investigation is underway to acquire own and selected published data to look for any extraneous behavior of specimens that present very thin remaining ligaments (less than 2.5mm in large diameter pipes) and that belong to corrosion regions with lengths greater than 50mm.

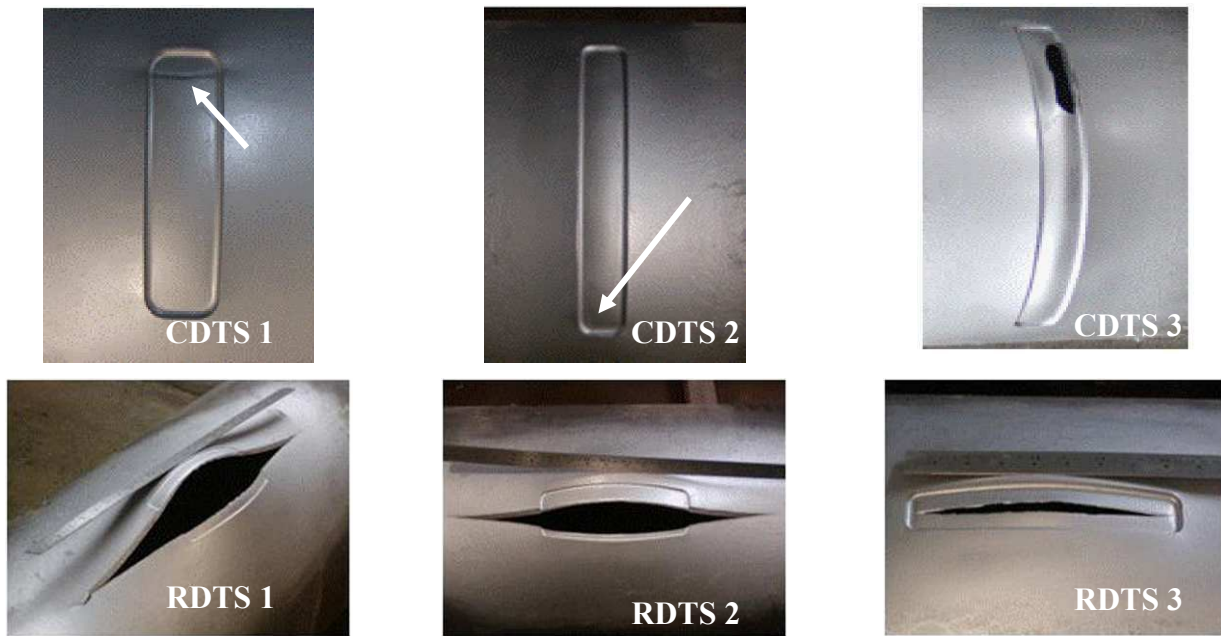
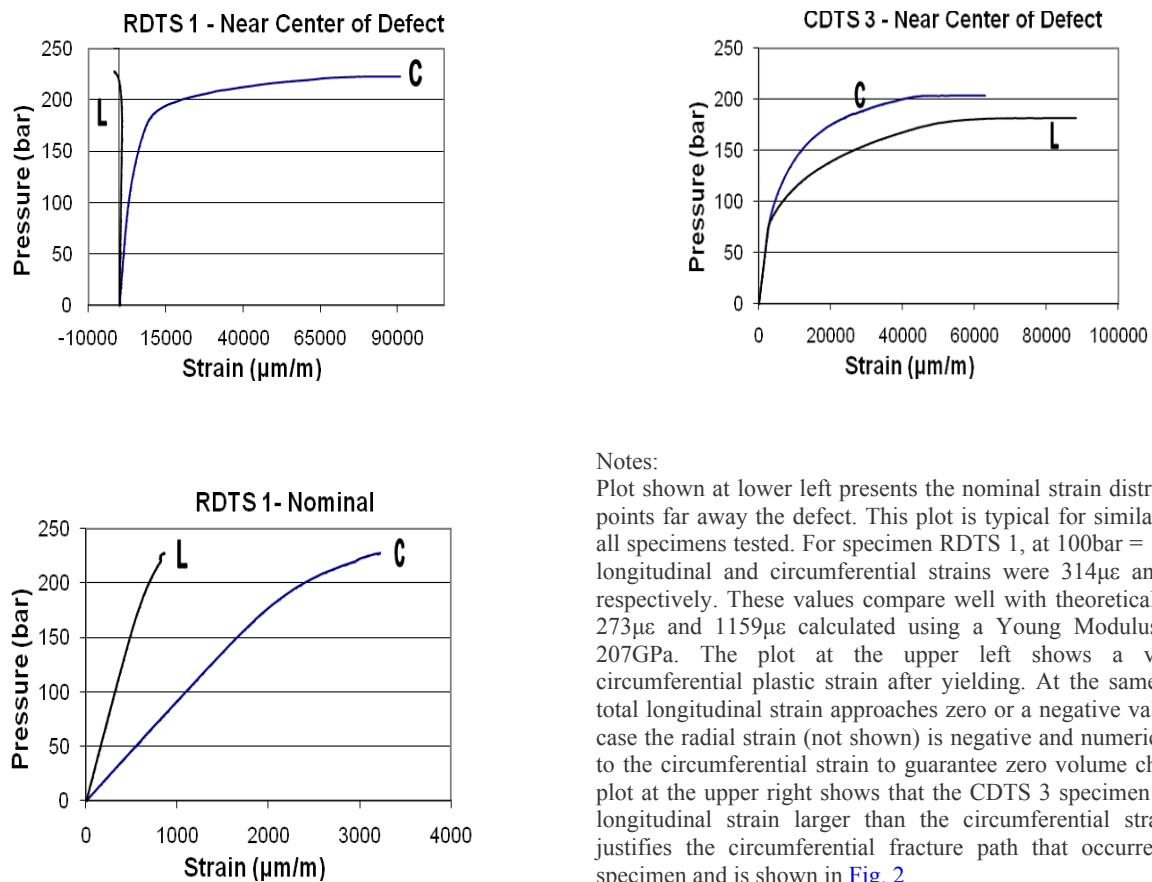


Fig. 3 Fracture path inside the defect patches for the circumferential defects (CDTS) and longitudinal defects (RDTS); arrows indicate fractures for specimens CDTS 1 and 2.



Notes:

Plot shown at lower left presents the nominal strain distribution for points far away the defect. This plot is typical for similar points of all specimens tested. For specimen RDTS 1, at 100bar = 10MPa the longitudinal and circumferential strains were $314\mu\epsilon$ and $1085\mu\epsilon$, respectively. These values compare well with theoretical values of $273\mu\epsilon$ and $1159\mu\epsilon$ calculated using a Young Modulus equal to 207GPa. The plot at the upper left shows a very large circumferential plastic strain after yielding. At the same time, the total longitudinal strain approaches zero or a negative value. In this case the radial strain (not shown) is negative and numerically equal to the circumferential strain to guarantee zero volume change. The plot at the upper right shows that the CDTS 3 specimen presents a longitudinal strain larger than the circumferential strain. This justifies the circumferential fracture path that occurred for this specimen and is shown in [Fig. 2](#)

Fig. 4 Strain distribution of specimens RDTS 1 and CDTS 3 varying with internal pressure.

5. Conclusions

Test results confirmed that, depending on the dimensions of a corrosion defect (d , L and w), its failure will be governed by the hoop stress or by the longitudinal stress. The longitudinal orientation of the fracture suffered by the defects of specimens RDTs 1 to 3 and CDTS 1 and CDTS 2 suggests that their failures were governed by the hoop stress. The circumferential orientation of the fracture suffered by the defect of specimen CDTS 3 suggests that its failure was governed by the longitudinal stress. The Tresca criterion using the DNV RP-F101 and Kastner equations was shown to predict the fracture path correctly, i.e., whether it would follow a longitudinal or circumferential direction inside the corrosion patch. The strain distributions measured for points inside the corrosion patches also indicated the same trend: the much larger circumferential strains implied longitudinal fractures, and the much larger longitudinal strain implied a circumferential fracture.

Acknowledgments

The authors would like to thank PETROBRAS for permission to publish this paper and to Eng. Byron Goncalves de Souza Filho (PETROBRAS) for his valuable comments in the early stage of this research.

References

- [1] - Benjamin, A.C., Freire, J.L.F., Vieira, R.D. and Diniz, J.L.C., 2010 "Burst Tests on Pipeline Containing Circumferential Corrosion Defects," International Pipeline Conference, IPC2010-31445, (2010).
- [2] - Freire, J.L.F., Vieira, R.D., Castro, J.T.P. and Benjamin, A.C., "Burst Tests of Pipeline with Extensive Longitudinal Metal Loss," Experimental Techniques, Nov.- Dec., Vol. 30, No. 6, 60-65, (2006).
- [3] - Souza, R.D., Benjamin, A.C., Vieira, R.D., Freire, J.L.F., and Castro, J.T.P., "Rupture Tests of Pipeline Segments Containing Long Real Corrosion Defects," Experimental Techniques, Jan.- Feb., Vol. 31, No. 1, 46-51, (2007).
- [4] - Freire, J.L.F., Vieira, R.D., Castro, J.T.P. and Benjamin, A.C., "Rupture Tests of Pipeline Containing Complex-Shaped Metal Loss Defects," Experimental Techniques, March-April, Vol. 31, No. 2, 57-62, (2007).
- [5] - Benjamin, A. C., Freire, J.L.F., Vieira, R.D., "Analysis of Pipeline Containing Interacting Corrosion Defects," Experimental Techniques, May-June, Vol. 31, No. 3, 74-82, (2007).
- [6] - Freire, J.L.F., Vieira, R.D., and Benjamin, A.C., "Experimental Strain Analysis of Metal Loss Defects in Pipeline," Experimental Techniques, September-October, Vol. 30, No. 5, 42-47 (2006).
- [7] - Benjamin, A.C., Franzoi, A.R., Leal C., J.J, Freire, J.L.F., Vieira, R.D. and Diniz, J.L.C., 2010 "Additional Test Results of Pipeline With Corrosion – Irregular Shaped Defects," Experimental Techniques, September-October., Vol. 34, No. 5, 68-75, (2010).
- [8] - Diniz, J.L.C., Vieira, R.D., Castro, J.T., Benjamin, A.C., and Freire, J.L.F., "Stress and Strain Analysis of Pipelines with Metal Loss," Experimental Mechanics, December, Vol. 46, No. 6, 765-775, (2006).
- [9] - Benjamin, A.C., Freire, J.L.F., Vieira, R.D. and Diniz, J.L.C., 2009 "Burst Tests on Pipeline Containing Short Uniform Depth Corrosion Defects," Rio Pipeline Conference 2009, IBP1105-09, 2009.
- [10] - Anon, "ASME-B31G - Manual for Determining the Remaining Strength of Corroded Pipelines – A Supplement to ANSI/ASME B31 Code for Pressure Piping," The American Society of Mechanical Engineers, New York, 1991.
- [11] - Kiefner, J.F. and Vieth, P.H., "A Modified Criterion for Evaluating the Remaining Strength of corroded Pipe," Final Report on Project PR 3-805, Pipeline Research Committee, American Gas Association, 1989.
- [12] - DNV-RP-F101, "Corroded Pipelines," Det Norske Veritas, Norway, 2004.
- [13] - Kastner, W., Rohrich, E., Schmitt, W. and Steinbuch, R., "Critical crack sizes in ductile piping," International Journal of Pressure Vessel & Piping, Vol. 9, pp. 197-219, 1981.
- [14] - "Specification for Line Pipe," American Petroleum Institute, Upstream Segment, API Specification 5L, Forty Third Edition, December, 2004.

A Comparative Analysis of Two Full-Scale MD-500 Helicopter Crash Tests

Justin Littell

ATK Space Systems, NASA Langley Research Center MS 495, 12 W. Bush Rd, Hampton Virginia 23681

Justin.D.Littell@nasa.gov

ABSTRACT

Two full scale crash tests were conducted on a small MD-500 helicopter at NASA Langley Research Center's Landing and Impact Research Facility. One of the objectives of this test series was to compare airframe impact response and occupant injury data between a test which outfitted the airframe with an external composite passive energy absorbing honeycomb and a test which had no energy absorbing features. In both tests, the nominal impact velocity conditions were 7.92 m/sec (26 ft/sec) vertical and 12.2 m/sec (40 ft/sec) horizontal, and the test article weighed approximately 1315 kg (2900 lbs). Airframe instrumentation included accelerometers and strain gages. Four Anthropomorphic Test Devices were also onboard; three of which were standard Hybrid II and III, while the fourth was a specialized torso. The test which contained the energy absorbing honeycomb showed vertical impact acceleration loads of approximately 15 g, low risk for occupant injury probability, and minimal airframe damage. These results were contrasted with the test conducted without the energy absorbing honeycomb. The test results showed airframe accelerations of approximately 40 g in the vertical direction, high risk for injury probability in the occupants, and substantial airframe damage.

Introduction

The Landing and Impact Research Facility (LandIR) at NASA Langley Research Center (LaRC) has a long history of aircraft and spacecraft impact testing. The 73 m (240 ft) high, 122 m (400 ft) long steel gantry structure was originally built in 1965 as a training facility for astronauts to practice landing on the moon during the Apollo program [1]. It has since been converted for use as a full-scale aircraft crash test facility [2]. Since the mid 1970s, over 150 vehicles comprising a mix of general aviation aircraft, helicopters, and fuselage subsections have been tested at LandIR [3]. Currently, the facility supports NASA's Constellation and Subsonic Rotary Wing Crashworthiness research programs for Orion crew module landing and rotorcraft impact testing. The LandIR is shown in [Figure 1](#).



Fig. 1 LandIR Facility at NASA LaRC

Research in aircraft crashworthiness has mainly been focused on the attenuation of impact loads and ultimately the mitigation of crew or occupant injury. External airframe airbags are a common external energy absorbing concept, which have been evaluated for crash attenuation [4-5] in the past. Similar to an automotive airbag system, these deploy immediately before impact and offer attenuation through active or passive venting systems. One design challenge with airbags is the high shear forces seen from horizontal velocities, which can make them unstable and unreliable during impacts involving high forward velocities.

At NASA LaRC, a program has been implemented to demonstrate a novel Deployable Energy Absorbing (DEA) composite honeycomb concept [6-8] as an alternative to the conventional airbag system. Originally developed for evaluation on NASA's Orion spacecraft, the DEA was also considered for aircraft as a potential device to attenuate crash loads transmitted to crew members and to alleviate occupant injuries. The DEA structure was fabricated from Kevlar/epoxy composite sheets and then assembled to form hexagonal cell walls. The DEA featured a flexible hinge design at the junctions of each individual hexagonal cell which allows the entire structure to lay flat until deployment. A mechanism deploys the DEA such that the cells open and form their honeycomb shape oriented normal to the airframe and impact surface. [Figure 2](#) shows a sample DEA test article used in a subscale crush test so that the reader can familiarize themselves with the concept. Note these photos do not depict the actual DEA used in the full scale test.

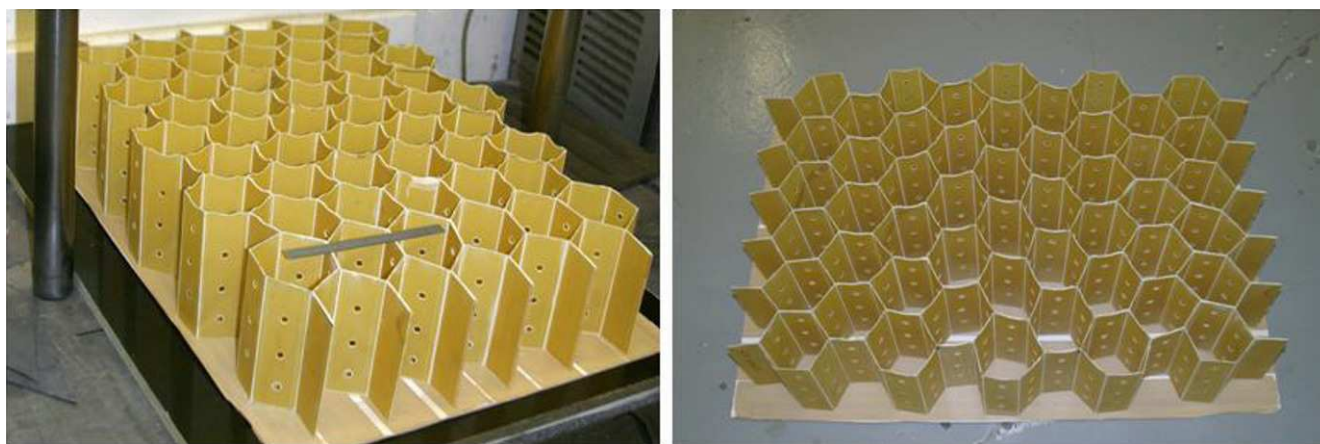


Fig. 2 An example DEA used in subscale testing. Isometric view (left) and top view (right)

As a demonstration of concept, engineers at NASA LaRC conducted two tests on a small MD-500 helicopter which enabled an evaluation of the DEA concept on an actual airframe under realistic crash conditions. In the two full-scale impact tests conducted, the first test included the DEA structure externally attached to the airframe while the second was a baseline test that did not include the DEA structure. Identical initial conditions, with the exception of the presence of the DEA, were present for both tests such that the performance of the DEA could be evaluated using metrics including airframe accelerations and loads, human occupant injury thresholds and limits, and airframe deformation.

Test Article Description

The MD-500 is a derivative of the Hughes OH-6 helicopter and over 5,000 airframes have been built since 1982. The latest civilian utility variant is the MD-500E. The military derivative of the helicopter is the Defender series that is currently in service in the US Army. Currently, the MD-500E is used as a general-purpose utility and executive transport helicopter. Maximum gross weight is 1,360 kg (3,000 lb), with an empty weight of 703 kg (1,550 lb). The total length of the airframe is 9.4 m (30.84 ft) and the tail height is 2.7 m (8.9 ft). The as-received test article weighed approximately 227 kg (500 lb), and is shown in [Figure 3](#). Components not included in the as-delivered helicopter were the engine and gear box, main rotor, rear tail and tail rotor, avionics, fuel tanks, seats, restraints and doors.



Fig. 3 As-Received MD-500 Helicopter Test Article

Modifications were necessary to prepare the MD-500 helicopter for the tests. Major modifications included:

- 1 – Damaged aluminum skin near helicopter tie down points and acrylic windshield panels were replaced or repaired.
- 2 – Original oleo-pneumatic skid gear struts were replaced with crushable energy absorbing struts. [9]
- 3 – The test which included the DEA only: Four layers of 0.25 mm (0.010 in) thick graphic/epoxy fabric were added to the belly to enhance the load carrying capability due to the expected loading from the DEA crushing.
- 4 – Aluminum straps were added to each side of the helicopter at the exterior water line level to serve as DEA tie down attachment points.
- 5 – Box beams were added to the front and rear bulkheads to serve as LandIR cabling system attachment points.
- 6 – Ballast mass, in the form of lead blocks, was placed in locations representing major structural and mechanical components of the aircraft, such as the engine and transmission, main rotor, tail rotor, doors, and instrument panel.
- 7 – Sand bags were placed in the rear sub-floor to represent fuel ballast.
- 8 – Original skid gear was replaced with new gear. New skid gear was installed for each test.
- 9 – New front bucket and rear bench seats were installed for each test.

The airframe was tested in the modified configuration for both tests, even though only a small number of the modifications were directly involved with the DEA and DEA attachment hardware. For example, the aluminum straps added to the water line of the airframe for the DEA attachment tie-down locations were left on the airframe for the test without the DEA to generate comparable test data. The test weight for the MD-500 with DEA test was 1329 kg (2930 lb), while the test weight for the MD-500 without DEA test was 1318 kg (2906 lb). The 9 kg (24 lb) difference was due to the removal of the DEA between tests. The weight and center of gravity (CG) of the airframe stayed within realistic limits. [10]

The helicopter was instrumented with 160 channels of instrumentation to collect strain, acceleration, load and Anthropomorphic Test Device (ATD) occupant response data. Accelerometers were placed on critical components of the airframe, ballast locations, floors and subfloors, while strain gages were placed on the bulkheads, keel beam, and skid gear. Four ATD occupants were onboard the helicopter for both tests. The pilot (front left) was a Hybrid III 50th percentile ATD. However, instead of the standardized curved spinal column, the spinal column was replaced with an FAA approved straight spinal column [11]. The co-pilot (front right) and rear passenger (rear right) were a standard Hybrid II 50th percentile ATD, which normally includes a straight lumbar spinal column. The left rear was a specialized human surrogate torso model (HSTM), designed to measure the internal loads on a human torso [12]. The HSTM torso was attached to a standard Hybrid III pelvis and lower extremities. The front pilot and co-pilot were seated in mesh cloth bucket seats. The rear occupants sat on a mesh bench seat. [Figure 4](#) shows the pre impact configuration of the helicopter before each test.

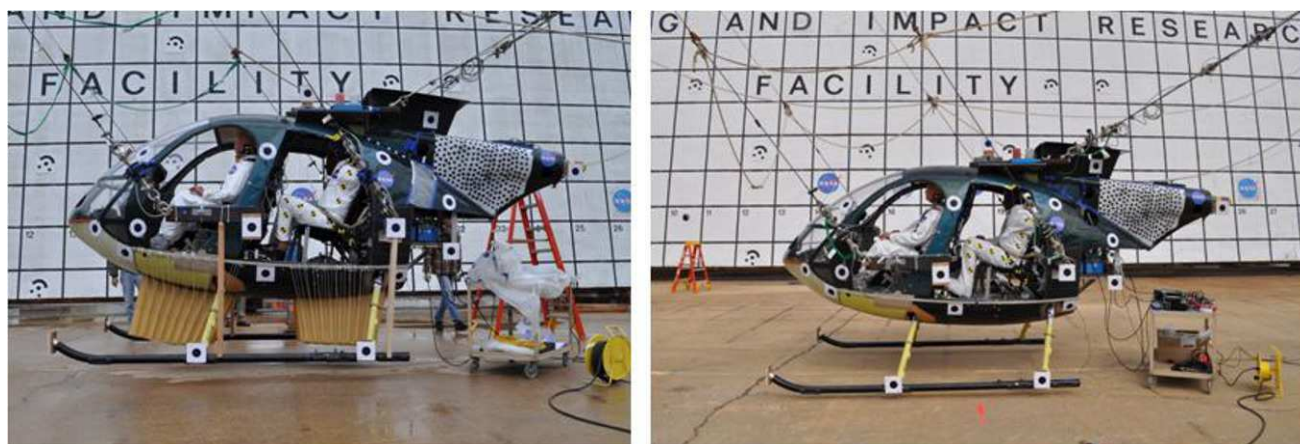


Fig. 4 Pre test configurations of the MD-500 helicopter: DEA configuration (left); baseline configuration (right)

The aircraft was also covered with black and white targets for use in a photogrammetric imaging system. These targets were 7.6 cm (3 in) diameter black dots mounted on specific locations on the airframe to determine impact velocities and orientations, and post-impact structural integrity of the airframe. The numbering scheme of the targets for the test which included the DEA is shown in [Figure 5](#). Note that the target numbering scheme was identical for both tests.

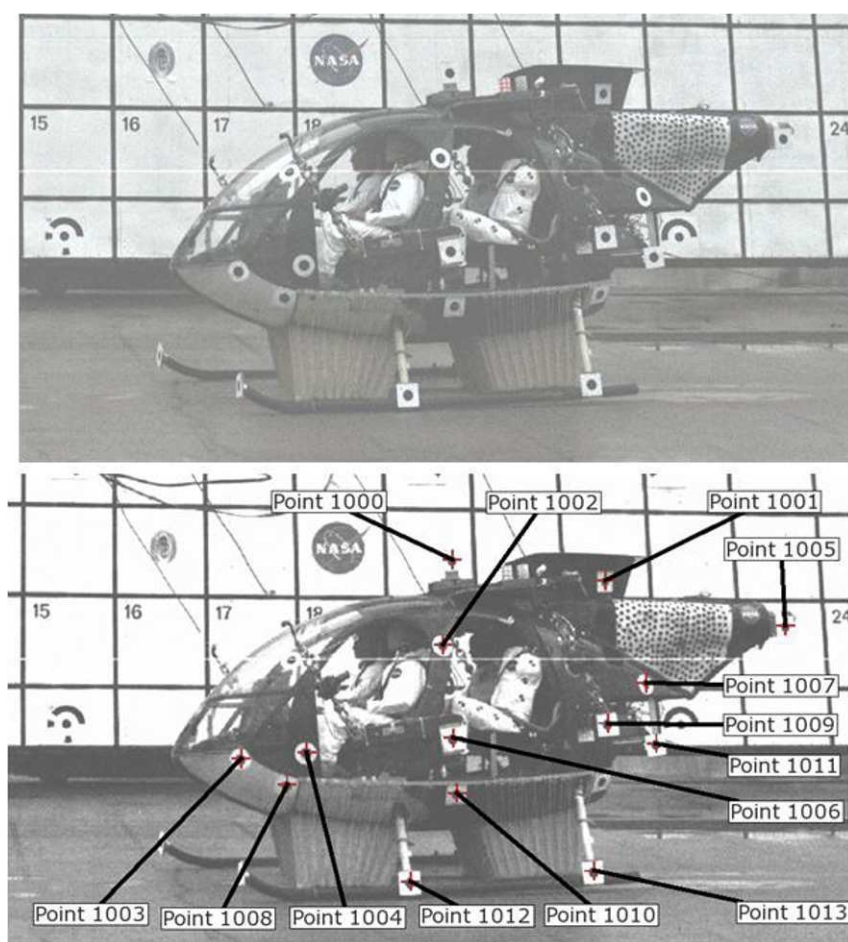


Fig. 5 Frame of video from MD-500 with DEA test (top) and identified target locations (bottom)

The nominal impact conditions for the full-scale crash tests were 12.19 m/s (40 ft/sec) horizontal and 7.92 m/s (26 ft/sec) vertical velocities giving a resultant velocity of 14.54 m/s (47.7 ft/sec) at a 33 degree glide angle for both tests. The impact surface was concrete. The particular velocities were chosen to represent a severe, but survivable crash, and not explicitly based on any particular crashworthiness standard such as MIL-STD-1290A [13]. The impact conditions were achieved by swinging the helicopter through a pendulum style fashion using LandIR cabling equipment and hardware. This was achieved through two sets of parallel swing cables, located on either side of the vehicle, and a pullback cable. The pullback cable lifted the vehicle to the specified drop height and was then pyrotechnically cut at the beginning of the test, allowing the vehicle to swing toward the ground via the swing cables. Immediately before impact, pyrotechnics severed the swing cables such that free fall impact conditions were present immediately prior to impact. Figure 5, above, shows the helicopter immediately after the swing cables have separated.

Results

The measured impact conditions were determined through photogrammetric techniques by tracking the rigid body motion of the vehicle through the final portion of the swing. All tracked points were averaged to achieve a final impact velocity. For angle and angular rate measurements, the photogrammetric software tracked projected angles between the vehicle and the stationary photogrammetric backboard. For a complete description of photogrammetric techniques used, see reference 14. Table 1 lists the velocity, attitude, and angular rates recorded from each test.

The three translation velocities between tests match well and are only slightly different from the nominal 12.2 m/s (40 ft/sec) forward, 7.9 m/s (26 ft/sec) vertical and 0 m/s (0 ft/sec) lateral velocity conditions. The lower-than-anticipated forward and vertical velocities can be attributed to air resistance and friction in the cabling systems, while the non-zero lateral velocity can be attributed to prevailing wind conditions pushing the test article off center. The pitch down attitude present in both tests was attributed to the CG of the vehicle being slightly forward of the midpoint for the LandIR parallel swing cabling system. There was a higher-than-normal amount of roll and yaw present for the test which included the DEA. These high values were attributed to misalignment of the LandIR cabling pullback harness. This issue was only identified during post-test data analysis. The harness was modified for the baseline test, and both the roll and yaw conditions were much closer to nominal at approximately 2 degrees. The pitch rate stayed approximately the same between tests, which was assumed to be constant since the longitudinal location of the CG did not change. The yaw rate was especially high for the test which included the DEA as the uneven pullback harness created cable preload misalignments. The change in pullback harness also corrected the rate results for the baseline test.

Table 1 – Impact Conditions

Impact Parameter	MD-500 with DEA	MD-500 without DEA
<i>Linear velocity - m/s (ft/sec)</i>		
Forward	11.8 (38.8)	11.9 (39.1)
Vertical	7.8 (25.6)	7.3 (24.1)
Lateral	0.2 (0.5)	0.2 (0.6)
Resultant	14.2 (46.5)	14.0 (45.9)
<i>Attitude (deg)</i>		
Pitch	-5.69	-6.2
Roll	7.04	1.9
Yaw	9.3	2.1
<i>Angular Velocity (deg/sec)</i>		
Pitch Rate	0.44	0.54
Roll Rate	1.11	0.68
Yaw Rate	4.82	1.65

Figures 6 and 7 show still-frame side views from the high speed camera for each test. The figures depict four images each. These four images represent the MD-500 helicopter before impact, at first ground contact, at maximum vertical deflection, and during post-impact rebound. Figure 6 shows a picture of the MD-500 test which included the DEA, while Figure 7 shows a picture of the baseline test.

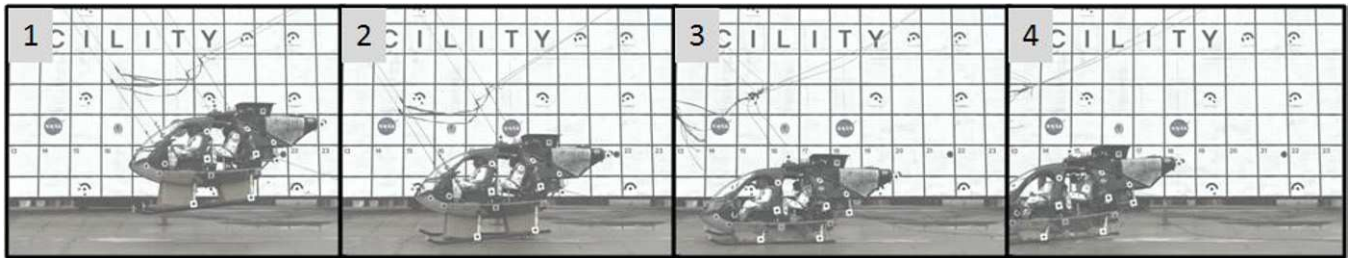


Fig. 6 MD-500 test which included the DEA - Image Sequence

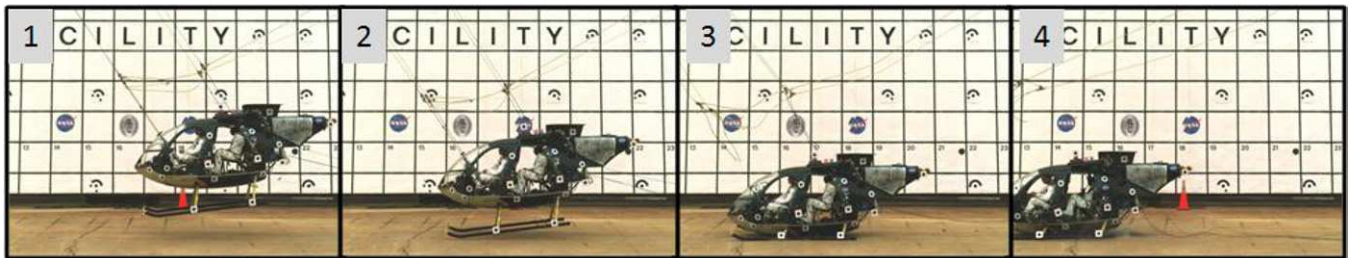


Fig. 7 MD-500 baseline test - Image Sequence

In Figure 6, picture 1 (left) shows the helicopter approximately 30 ms before impact, pitched down and with some slight yaw. The yaw can be seen by noting the difference in horizontal position in the near and far skid gear. Picture 2 (left center) shows the helicopter at the point of right skid gear impact. Picture 3 (right center) shows the point of maximum DEA crushing stroke, and picture 4 (right) shows a post-impact rebound, again noting that the vehicle's nose has pitched down. At the point of maximum crush deflection (picture 3), the helicopter straightened out to show almost no pitch. After the point of maximum crush, the nose pitched forward on the rebound, presumably due to friction between the DEA and the impact surface. An analogous sequence is shown in Figure 7 for the MD-500 test which did not include the DEA.

In Figure 7, picture 1 (left) shows the helicopter before impact. Note that due to the minimal roll and yaw present, the tips of the near and far skid gears were approximately at the same longitudinal position. Picture 2 (left center) shows the helicopter at the point of first skid gear impact. As before, for the MD-500 baseline test, the far (right) gear impacted the ground first which was due to the minor amount of yaw and roll present. Picture 3 (right center) shows the point of maximum vertical displacement, noting that the helicopter still had a down pitch orientation. Picture 4 (right) shows a post-impact rebound. After the point of maximum vertical deflection, the nose pitched forward on the rebound, presumably due to the downward pitch of the nose at impact. Post test photographs document some of the differences in the helicopter after the completion of each test, and are included to show the damage incurred. Figure 8 shows the post impact position of the helicopter immediately after each test.

Due to the presence of some yaw in both tests, the helicopter turned to the left during the post-impact slide out. The slide out distance for the test which included the DEA was 13.86 m (45 ft 6 in). The slide out distance for the baseline test was 15.57 m (51 ft 1 in). The slide out difference is attributed to the friction contact between the DEA and the impact surface. The MD-500 with DEA turned a greater distance, presumably due to the greater amount of yaw and yaw rate. Finally, it is noted that all of the onboard occupants for both tests are leaning to their right, presumably from the helicopter turning to the left.

Further inspections were completed after the helicopter was moved from the impact area. Figure 9 shows the condition of the front bucket and rear bench seats after the baseline test. Pictures of the test which included the DEA are not shown because the seats remained intact during that test. However, Figure 9 shows the front bucket seats buckled in multiple places, one of which is highlighted in Figure 9(a), while much of the rear seat failed, as shown in Figure 9(b). The rear support beam sheared from its connection points, while the front beam and the side beams have sheared and split at their attachment point junctions.

The seats and occupants were removed from the airframe and deformations of the supporting seat box structure were examined. Figure 10 shows the structure in the vicinity of the front seat box for the MD-500 baseline test. The post test photographs show extensive damage around the seat box area for the baseline test. The buckling of the front bucket seats caused the occupants to directly impact and dent the seat box cover. The seat box was cracked and the seat box support structure buckled. Figure 11 shows pictures looking further down below the seat box and into the subfloor.



Fig. 8 Post test impact position of the MD-500 with DEA (left) and baseline (right)

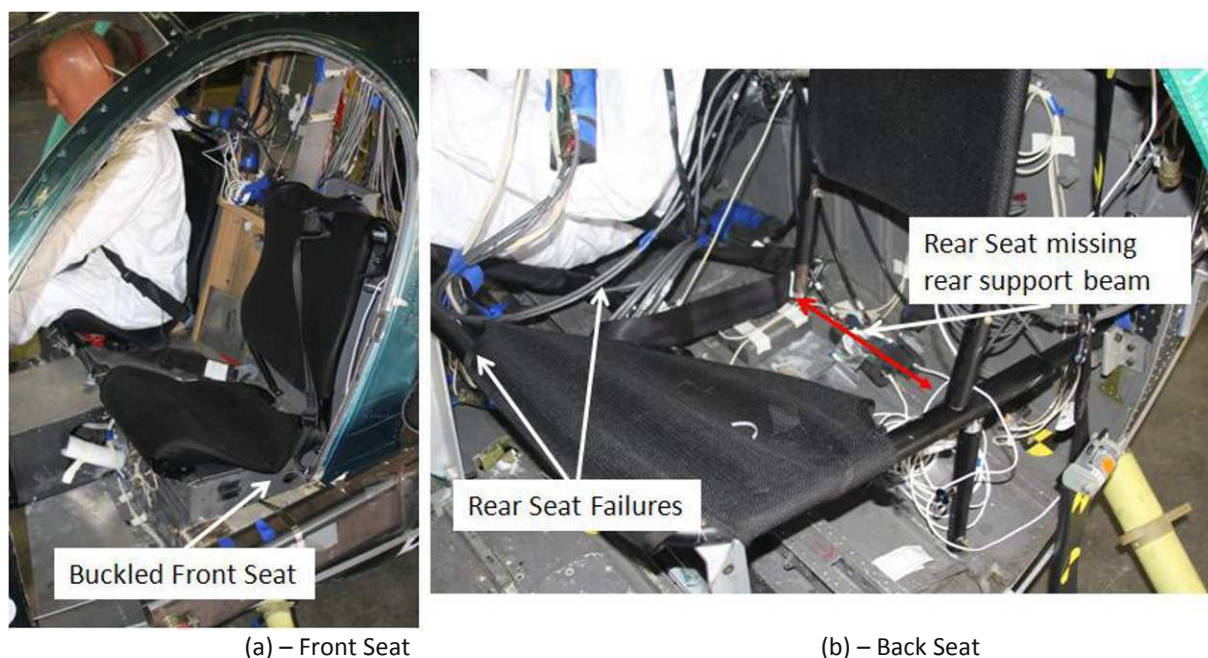


Fig. 9 Seat failures in MD-500 baseline test

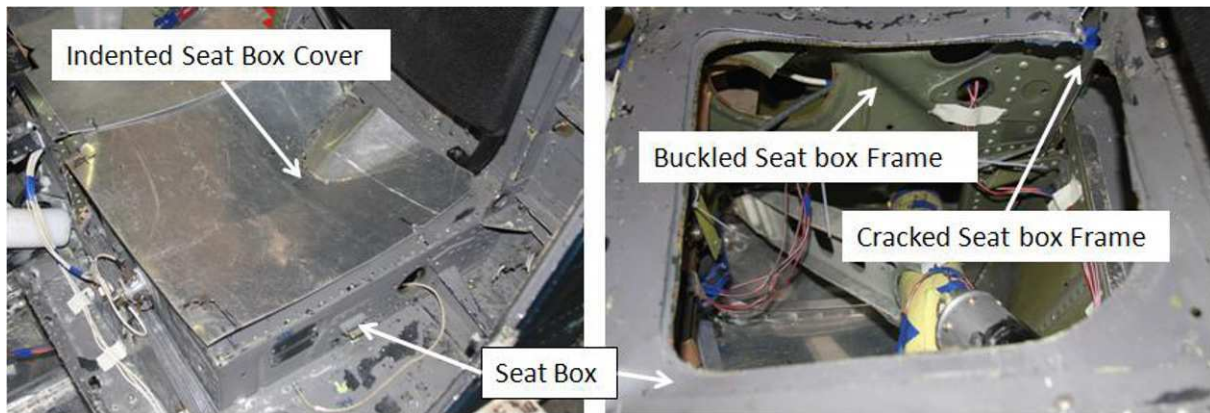


Fig. 10 Front seat box structural deformations

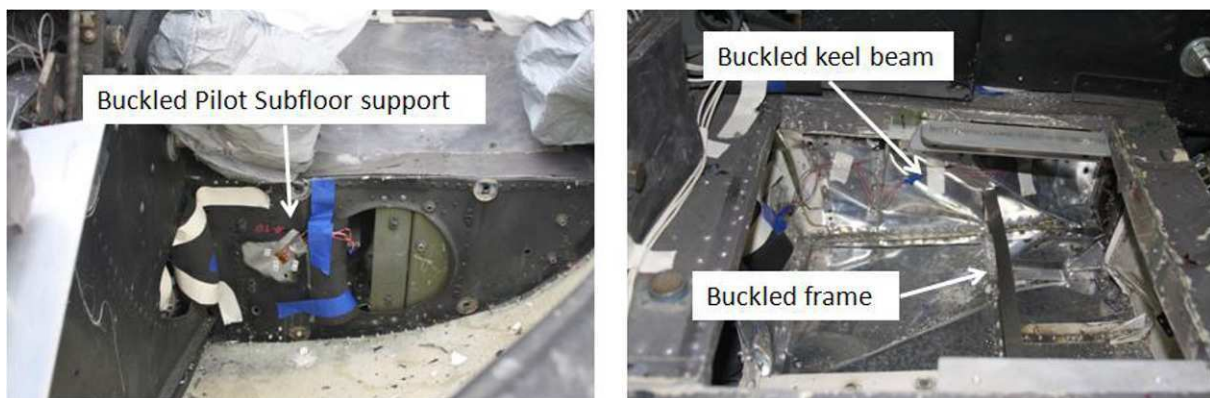


Fig. 11 Forward structural failures in MD-500 baseline test

Areas below the seat box under the pilot and copilot showed extensive buckling. The subfloor support showed signs of damage, while the middle keel beam and co-pilot frame also buckled. [Figure 12](#) shows the damage from the keel beam under the rear occupants for the baseline test. As [Figure 12](#) shows, major structural damage is seen in the rear keel beam. Cracks and buckled regions (not shown) were present under the rear floor, indicating major damage to the bottom section of the airframe. These failures are in contrast to the test which included the DEA, where the airframe did not show any signs of damage.

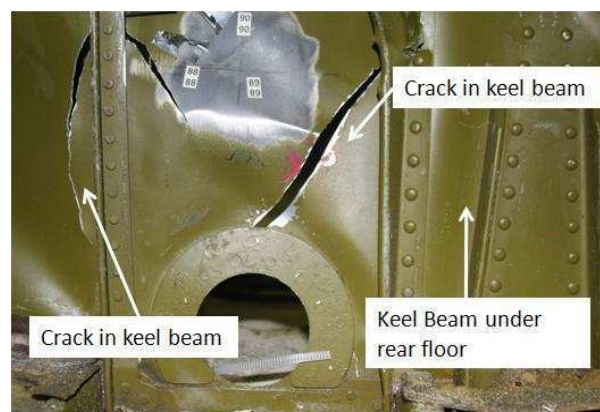


Fig. 12 Rear Keel Beam failure in MD-500 without DEA test

Impact loads and accelerations which caused the major damage were next examined. Figure 13 shows the front floor vertical (z) accelerations for both the left and right sides. Figure 14 shows vertical accelerations from the rear of the cabin, both on the floor and on the rear bulkhead. In both Figures 13 and 14, all accelerations were filtered with a four-pole, low-pass Butterworth filter with a 60 Hz cutoff frequency.

The left front floor acceleration peaks at approximately 45 g on the left and 55 g on the right for the baseline test, and approximately 15 g for both the left and right for the test which did include the DEA. For the baseline test, the front right floor experienced the highest acceleration levels of the entire airframe. This was due to the downward pitch and high yaw in the test, in which the front right portion of the helicopter impacted the surface first.

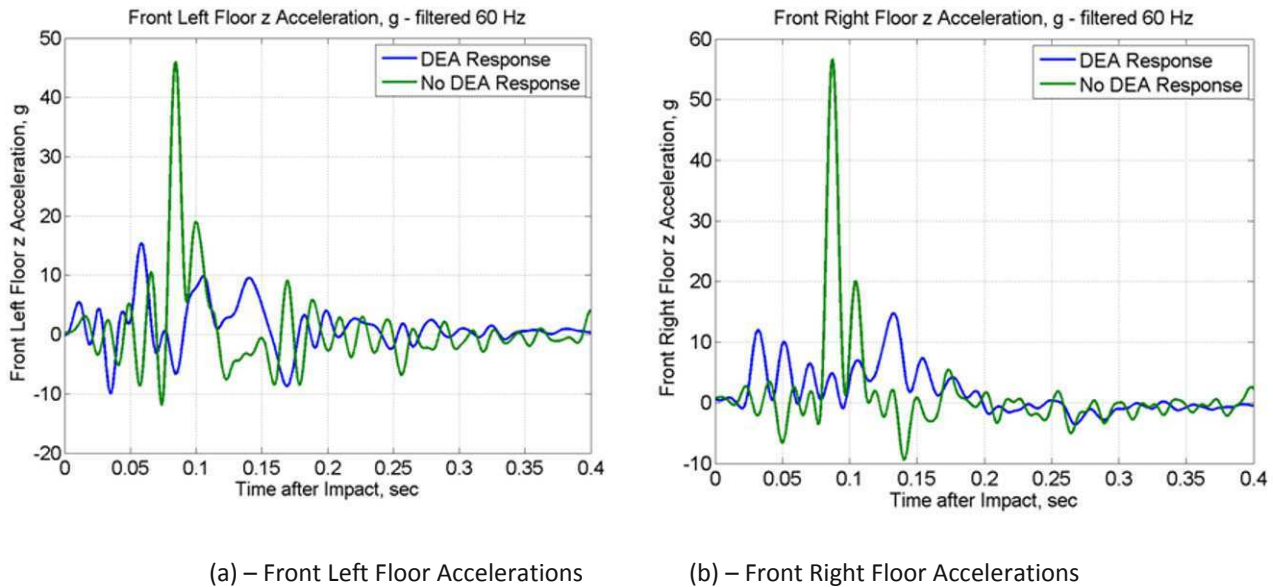


Fig. 13 Front floor accelerations

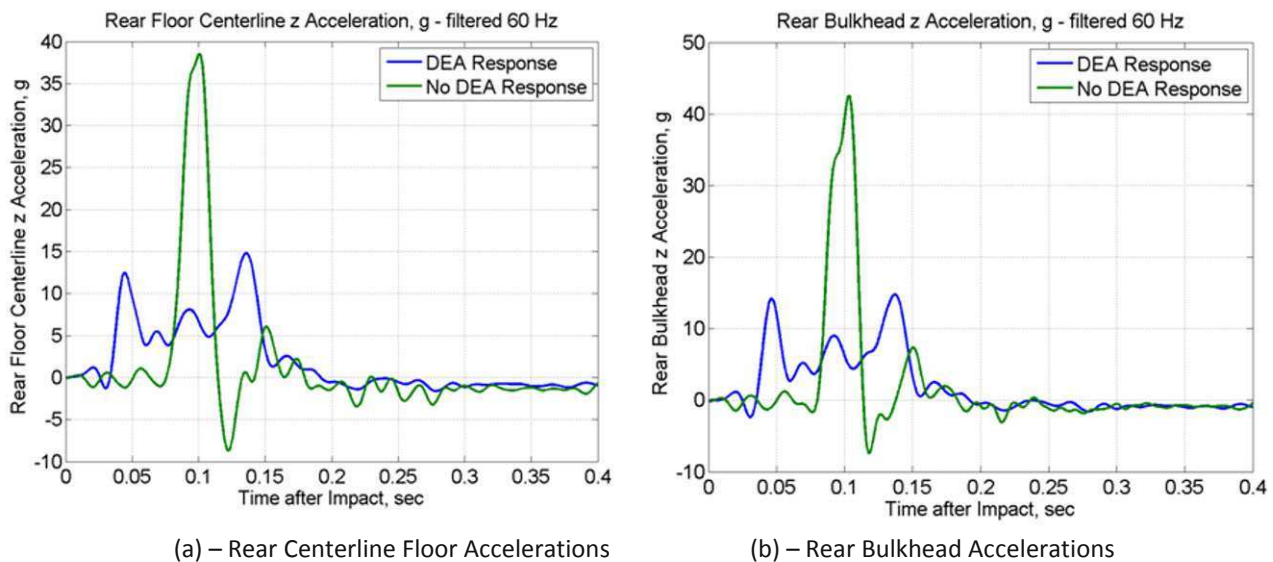


Fig. 14 Rear floor and bulkhead accelerations

In Figure 14, the rear floor experienced a peak acceleration of approximately 40 g, while the rear bulkhead experienced approximately 42 g for the baseline test. The accelerations which did include the DEA showed peaks of approximately 15 g. One major difference between the two tests is the time history of the accelerations. The baseline test shows a large spike at approximately 0.1 seconds after impact, lasting approximately 40 ms. The test which included the DEA showed two peaks of less magnitude at either end of a longer pulse. The peak value at the beginning of the pulse is from the initial contact between the DEA and impact surface and the peak value at the end of the pulse is from bottoming out of the DEA. The length of the pulse was approximately 120 ms. The DEA effectively changed the shape of the impact pulse from a high magnitude, low duration pulse to a low magnitude, high duration pulse. This shape change is important when examining occupant injury. For occupant injury protection, since both the magnitude and the duration of the input pulse have an effect on occupant response [15], acceleration traces from the onboard occupants were examined next.

Three of the four onboard occupants had instrumentation recording translational accelerations in three dimensions for the head, chest and pelvis, along with lumbar load values in the spine. Figure 15 shows the head accelerations from both tests for the pilot. The baseline test is shown in Figure 15(a), while the test which included the DEA is shown in Figure 15(b).

The results in Figure 15 show that the DEA attenuated the vertical (z) accelerations of the pilot's head from approximately 30 g to approximately 10 g, or by a factor of 3. The test which included the DEA also showed lower horizontal (x) accelerations as well, with magnitude attenuation of a factor of 2. The test which included the DEA, however, did show higher lateral (y) accelerations, presumably from the large amount of airframe yaw present in the impact conditions described previously. This lateral acceleration had effectively been removed for the baseline test. The data corresponds well with the photogrammetric impact condition data. Figure 16 shows the chest acceleration responses of the pilot for both tests. The baseline test is shown in Figure 16(a), while the test which included the DEA is shown in Figure 16(b).

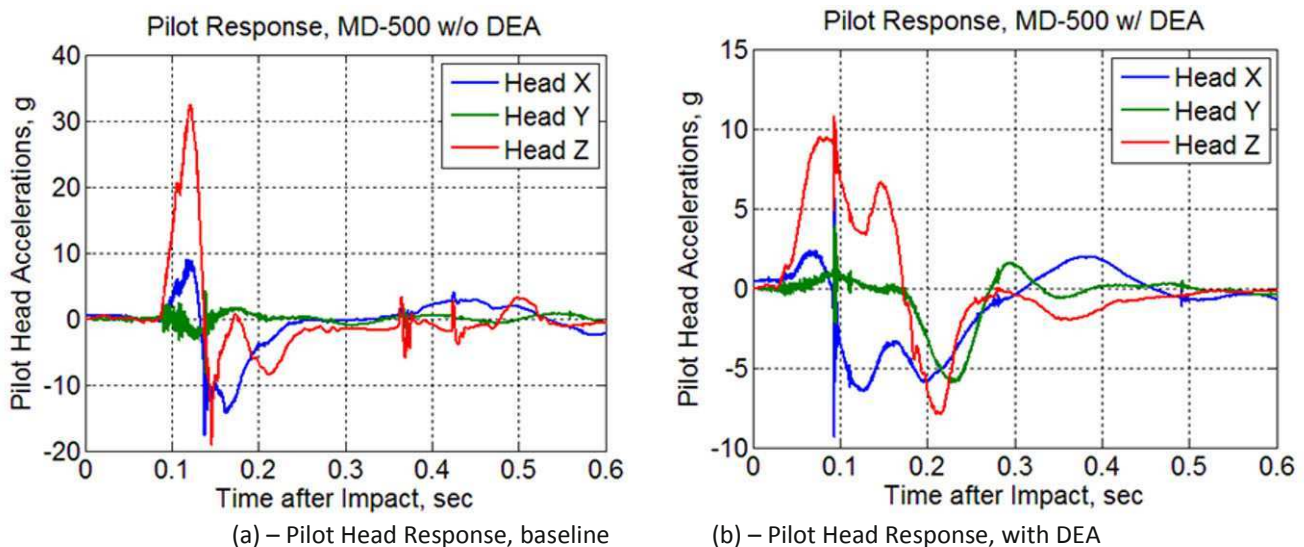


Fig. 15 Head Accelerations for the pilot

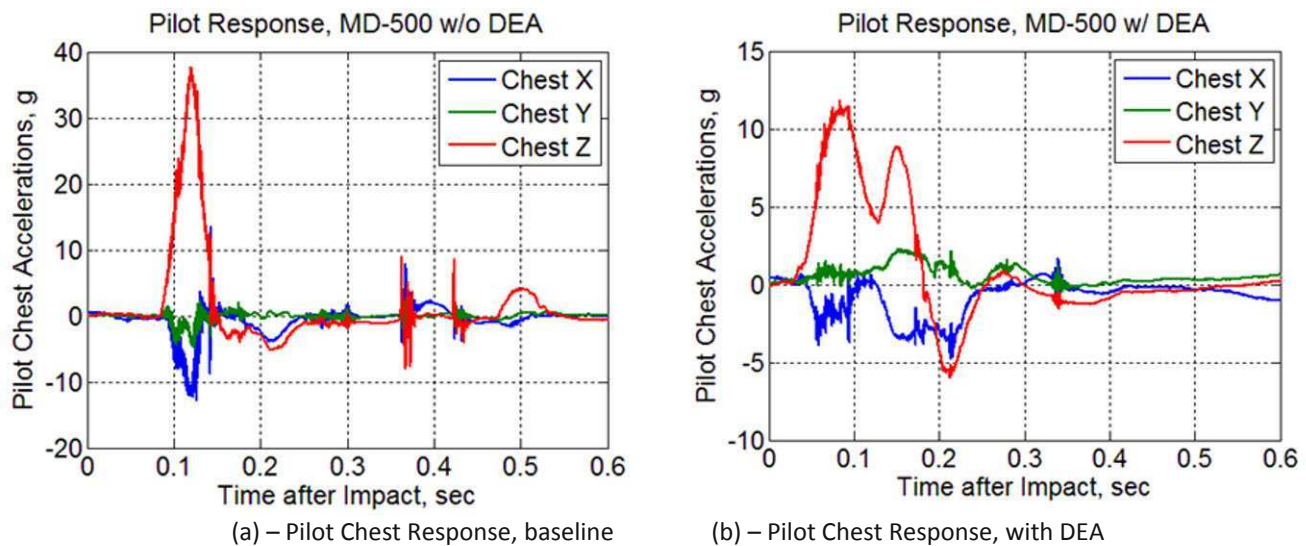


Fig. 16 Chest Accelerations for the pilot

The results in [Figure 16](#) show that the DEA attenuated the vertical (z) accelerations for the pilot's chest from approximately 35 g to approximately 12 g, or by a factor of 3, which is similar to the results seen for the pilot's head. As with the head results, the test which included the DEA also showed lower horizontal (x) accelerations, but higher lateral (y) accelerations. This finding is attributed to the large amount of yaw present in the impact conditions for the test which included the DEA. Next, [Figure 17](#) shows the acceleration responses from the pelvis of the pilot. The baseline test is shown in [Figure 17\(a\)](#), while the test which included the DEA is shown in [Figure 17\(b\)](#).

Pelvis accelerations matched trends seen for the occupant's head and chest. The pilot's pelvis experienced vertical (z) accelerations of approximately 40 g for the baseline test, while experiencing only 10 g in the test which did include the DEA. The test which included the DEA also attenuated the pilot's horizontal accelerations by a factor of two. The head, chest and pelvic results all show an attenuation of between 2 and 4 for vertical accelerations and approximately 2 for horizontal accelerations for the occupant representing the pilot of the helicopter. The other occupant acceleration time history results showed similar trends with similar magnitudes and, for brevity, are not shown. However, the occupant lumbar load values for all three occupants containing a lumbar load cell were examined. Lumbar load responses are reported in [Figure 18](#).

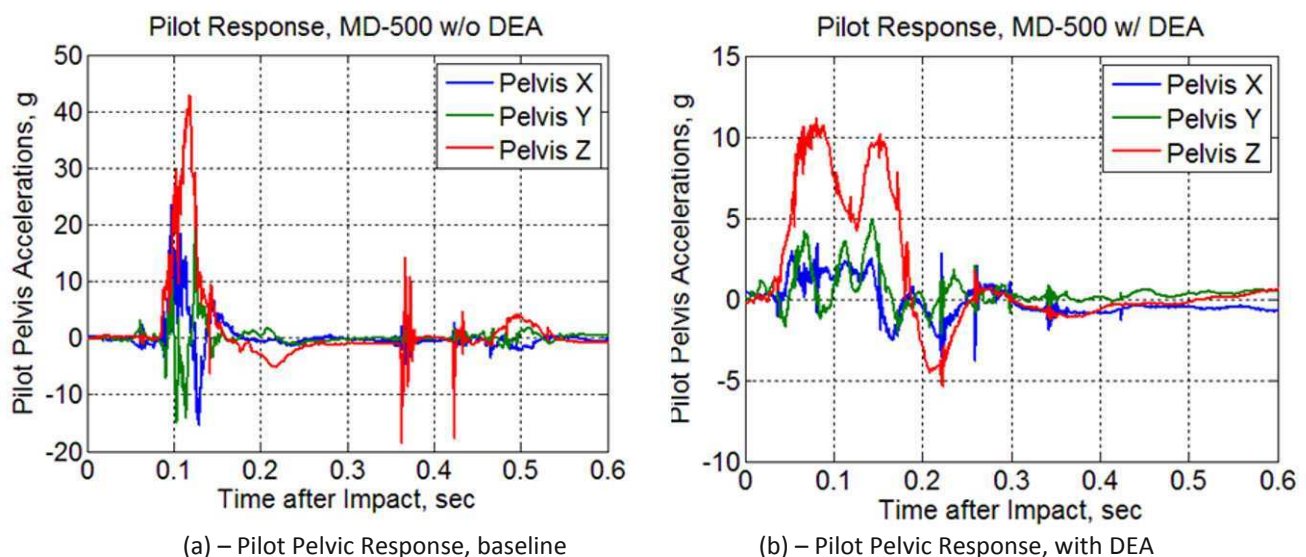


Fig. 17 Pelvic accelerations for the pilot

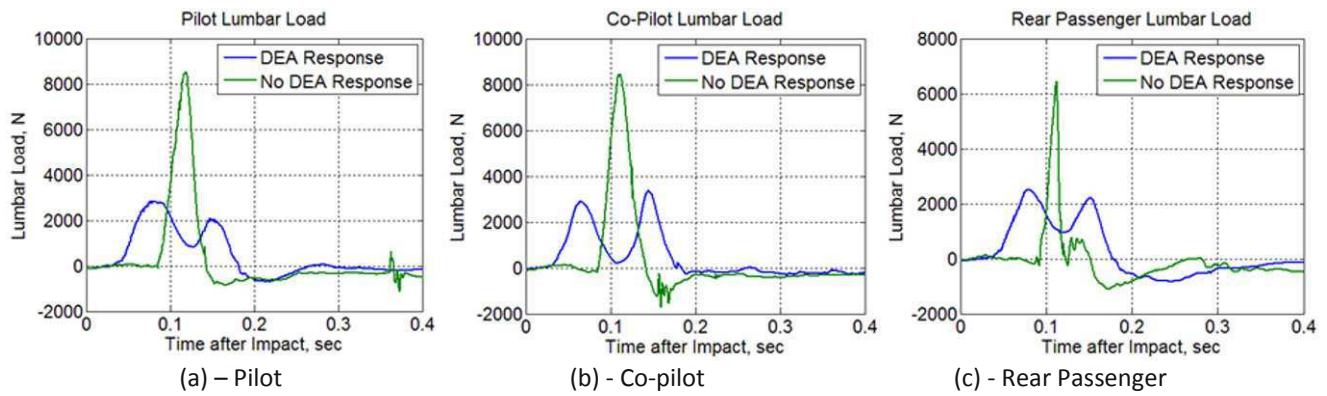


Fig. 18 Lumbar loads

The pilot and co-pilot's compressive lumbar loads reached similar magnitudes and durations for each test, presumably because they were seated in similar mesh bucket seats. The rear passenger's time history is slightly different due to its position on a bench seat. Comparing results between tests, the compressive lumbar load values were approximately 3860, 3372, and 2518 N (643, 758, and 566 lb) for the pilot, co-pilot and rear passenger, respectively, during the test which included the DEA; and 8536, 8461, and 6445 N (1919, 1902, and 1449 lb) for the pilot, co-pilot and rear passenger respectively for the test which did not include the DEA. The data was filtered using SAE CFC 600 with accordance to SAE J211 [16]. When evaluating potential for injury, FAR Part 27.562 (c) [17] establishes a lumbar limit of 6,672 N (1,500 lb) as being injurious. The loads incurred in the occupants were well below this limit for the test which included the DEA, but were over the limit for the front occupants for the test which did not include the DEA. This result indicated that, when examining the lumbar load data, the DEA protected the occupant sufficiently enough to avoid injury.

The pilot, co-pilot and rear passenger seat pan accelerations were input into the Brinkley model [18], which is used to evaluate the risk of injury in a variety of aircraft and spacecraft systems [19-20]. The Brinkley model estimates the likelihood of injury using a spring/mass/damper lumped parameter representation of the body for each axis (x – chest to back direction, y – sideways direction, and z – vertical or spinal direction) of the occupant. The coefficients of these lumped parameters in the mathematical formulation are based on experiments conducted on volunteers from the U.S. Army and Navy.

Seat pan acceleration time history pulses in all three directions were input into the Brinkley model. The output result from the Brinkley model is the beta value, which is an index taking into account responses from all three axes. The value of beta is given for three risk categories (low, medium and high), and a beta value greater than one in a particular category pushes the injury probably into the next higher category. Table 2 lists the beta values for all occupants for both tests, with careful attention being paid to the values in *italic*.

The Brinkley responses show a high probability of injury for the pilot and copilot and show a medium probability of injury for the rear passenger for the baseline test. The Brinkley values confirm the results previously obtained for the lumbar loads: Both the pilot and co-pilot had a high probability of injury while the rear passenger was only slightly under high probability of injury, and very close to the limit for lumbar load and 0.01 over the limit for medium injury in the Brinkley results. For the test with the DEA, all injury probabilities were low.

Table 2 – Beta values from Brinkley Model

Position	Beta Low		Beta Med		Beta High	
	<i>w/o DEA</i>	<i>DEA</i>	<i>w/o DEA</i>	<i>DEA</i>	<i>w/o DEA</i>	<i>DEA</i>
Pilot	<i>1.87</i>	0.70	<i>1.56</i>	0.59	<i>1.22</i>	0.46
Co-Pilot	<i>1.78</i>	0.62	<i>1.49</i>	0.52	<i>1.17</i>	0.41
Rear Passenger	<i>1.24</i>	0.86	<i>1.01</i>	0.72	0.81	0.57

Finally, along with providing the six degree-of-freedom impact conditions for both tests, photogrammetry was used to examine relative deflections between the target locations identified on the helicopter. Areas of large relative deflection on the aircraft suggested possible compromises in structural integrity and damage. Figure 19 shows visually the locations chosen for the examination of relative deflections between targets while Table 3 shows the results obtained from both tests.

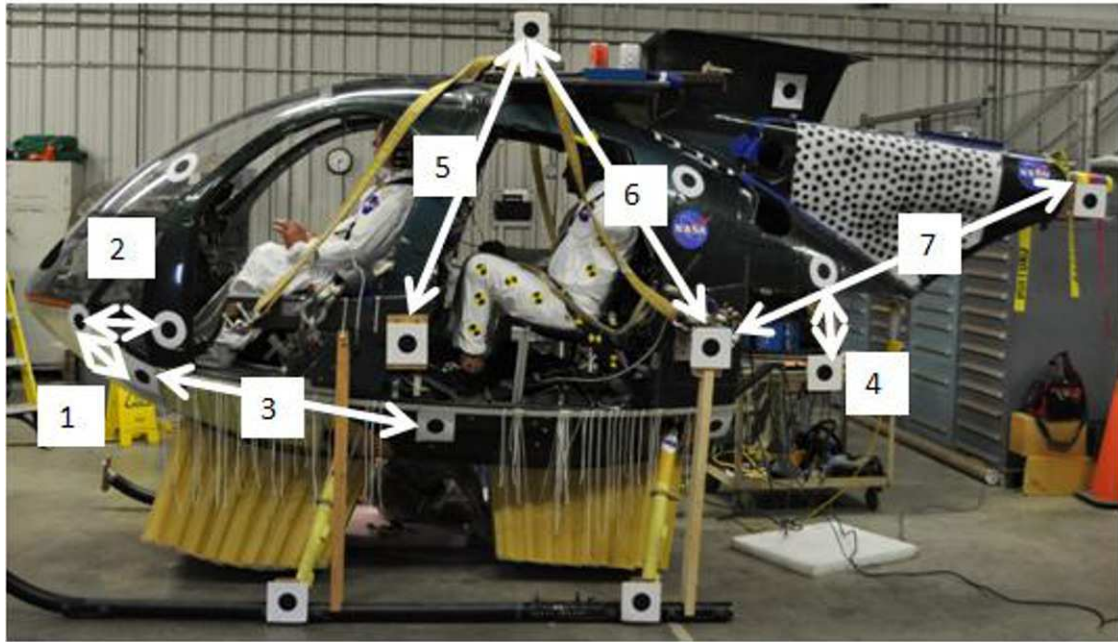


Fig. 19 MD-500 Photogrammetric Structural Deformation Locations

Table 3 – Deformations from both MD-500 helicopter tests

Vehicle Position (ID # - Figure 19)	MD-500 without DEA (Relative deformation, /)	MD-500 with DEA (Relative deformation, /)
Nose to Water Line (1)	0.28	0.85
Seat Line (2)	0.43	0.47
Water Line (3)	0.16	0.17
DAS Shelf Support (4)	2.78	0.98
Top Mass to Front Lifting fixture (5)	0.77	0.32
Top Mass to Rear Lifting fixture (6)	0.69	0.34
Tail to Rear Lifting fixture (7)	1.65	0.24

Table 3 shows that the highest relative displacements occurred in the front of the vehicle and near the rear at Position 4, for the test which included the DEA. The relative displacements in the front occurred when the nose impacted the surface first due to the pitched down orientation of the helicopter at impact. The large deformations from the DEA crushing upon impact pushed the front targets upward while the ballast mass in the nose continued downward. However, the photogrammetry results also showed that no permanent deflection occurred. The other area of high relative deflection was near the rear of the helicopter, under the tail support, in position 4. Position 4 measured the relative deflection on a

bar which connected the aircraft frame to a metal plate which held the onboard data acquisition system, acting as the ballast mass for the engine. The plate and data acquisition system weighed approximately 69 kg (150 lb) total, and was attached to brackets located on the tail. During impact, the inertial load into the tail due to the large amount of ballast mass in combination with the large amount of compliance in the tail caused the surrounding airframe to deform. However, the deformation was elastic in nature and the structure rebounded to its pre-impact position. All other areas examined exhibited low deflection, and confirmed the findings from the visual inspections that the airframe was relatively undamaged.

Large relative deformations were seen for the test which did not include the DEA, and confirmed the findings seen in [Figures 8 through 12](#). The common trend in the photogrammetry data showed that the areas which had large amounts of ballast mass produced the areas of largest displacement. Ballast mass for the main rotor affected both Position 5 and 6, ballast mass for the engine affected position 4 and ballast mass for the tail rotor affected position 7. These inertial loads were not absorbed by the DEA structure since it was not included in the second crash test, which deformed the airframe the greatest amount. These photogrammetric results, along with acceleration profiles and visual inspections post-test showed that the airframe was unusable after the test.

Summary

Two full scale crash tests were conducted on an MD-500 helicopter airframe to examine, in part, the performance of a deployable energy absorbing (DEA) concept. In the first test, the DEA was attached to the bottom of an instrumented MD-500 helicopter, which impacted a concrete surface at a resultant velocity of 14.2 m/s (46.5 ft/s). The response data shows that the airframe experienced a peak acceleration of approximately 15 g in the vertical and 8 g in the horizontal directions. Airframe deflection data from photogrammetry measurements suggested that the airframe survived the impact relatively undamaged after the impact. The occupant data was processed through various injury criteria's, all of which showed no injury.

These results are in contrast to a second test which was conducted as a baseline to evaluate the DEA performance. The test which did not include the DEA showed vertical airframe accelerations of approximately 40 g. The various injury criteria showed a medium to high risk of injury for the onboard occupants. The test program demonstrated that the DEA can be a valuable energy absorbing or attenuation mechanism for aircraft, and can be modified to applications for future aircraft or spacecraft.

References

- [1] O'Bryan, Thomas C., and Hewes, Donald E., "Operational Features of the Langley Lunar Landing Research Facility," NASA Technical Note, TN D-3828, February 1967.
- [2] Vaughan, Jr., Victor L. and Alfaro-Bou, Emilio, "Impact Dynamics Research Facility for Full-Scale Aircraft Crash Testing," NASA Technical Note, TN D-8179, April 1976.
- [3] Jackson, K.E., et al, "A History of Full-Scale Aircraft and Rotorcraft Crash Testing and Simulation at NASA Langley Research Center," NASA TM 20040191337, 2004.
- [4] Shane, J.S., "Design and Testing of an Energy-Absorbing Crewseat for the F/FB-111 Aircraft," NASA CR-3916, August 1985.
- [5] Tutt, B., et al, "A Summary of the Development of a Nominal Land Landing Airbag Impact Attenuation System for the Orion Crew Module," 20th AIAA Aerodynamic Decelerator Systems Technology Conference, Seattle, WA, 4-7 May 2009.
- [6] Kellas, S., "Deployable Rigid System for Crash Energy Management," US Patents 6,755,453, June 29, 2004; 6,976,729, December 20, 2005; and 7,040,658, May 9 2006.

- [7] Kellas, S. and Jackson, K. E., "Deployable System for Crash-Load Attenuation," Proceedings of the 63rd AHS Annual Forum, Virginia Beach, VA, May 1-3, 2007.
- [8] Kellas, S. and Jackson, K.E., "Multi-Terrain Vertical Drop Tests of A Composite Fuselage Section," Proceedings of the 64th Annual AHS Forum, Montreal, Canada, April 29-May 1, 2008.
- [9] Kellas, S., et al, "Full Scale Crash Test of an MD-500 Helicopter with Deployable Energy Absorbers," Proceedings of the 66th AHS Annual Forum, Phoenix, AZ, May 11-13, 2010.
- [10] MD Helicopters. MD-500E Rotorcraft Flight Manual Revision 14. CSP-E-1. 1982.
- [11] Gowdy, V. et al, "A Lumbar Spine Modification to the Hybrid III ATD for Aircraft Seat Tests", SAE 1999-01-1609. 1999.
- [12] Roberts, J., et al, "Computational and Experimental Models of the Human Torso for Non-Penetrating Ballistic Impact", Journal of Biomechanics, Vol. 40, pp. 125-136, 2007
- [13] Military Standard, MIL-STD-1290A (AV), Light Fixed- and Rotary-Wing Aircraft Crash Resistance, Department of Defense, Washington DC, 20301, 26 September 1988.
- [14] Littell, J.D. "Large Field Photogrammetry Techniques in Aircraft and Spacecraft Impact Testing," Proceedings from the Society of Experimental Mechanics Annual Conference, Indianapolis, IN, June 7-10, 2010.
- [15] Eiband, A.M., "Human Tolerance to Rapidly Applied Accelerations: A Summary of the Literature," NASA Memorandum 5-19-59E, June 1959.
- [16] Society of Automotive Engineers (SAE). "Recommended Practice: Instrumentation for Impact Test – Part 1, Electronic Instrumentation," SAE J211/1, March 1995.
- [17] Code of Federal Regulations. Federal Aviation Regulations for Aviation Maintenance Technicians FAR AMT, Part 27 Airworthiness Standard: Normal Category Rotorcraft, 27.562 Emergency Landing Dynamics.
- [18] Brinkley, J.W., Specker, L.J., and Mosher, S.E., "Development of Acceleration Exposure Limits for Advanced Escape Systems," NATO AGARD Proceedings, AGARD-CP-472, February 1990.
- [19] Jackson, K.E., et al, "Occupant Responses in a Full-Scale Crash Test of the Sikorsky ACAP Helicopter," Journal of the American Helicopter Society, Vol 49, No. 2, April 2004.
- [20] Lawrence, C., et al, "The Use of Vehicle Acceleration Exposure Limit Model and a Finite Element Crash Test Dummy Model to Evaluate the Risk of Injuries During Orion Crew Module Landings," NASA TM 2008-215198, 2008.

Structural Integrity Assessment of blade's subcomponents using Acoustic Emission Monitoring

Dimitrios Zarouchas^a, Alexandros Antoniou^b, Florian Sayer^b,
Danny Van Hemelrijck^a, Arno van Wingerde^b

^aFree University of Brussels, Faculty of Engineering,
Department of Mechanics of Material and Constructions (MeMC),
Pleinlaan 2, B 1050 Brussels, Belgium

^bFraunhofer Institut für Wind Energy and Energy System Technology,
Bremerhaven, Germany

ABSTRACT

Since the power generation capacity of a wind turbine has a direct correlation with increased blade length there is a general trend in the wind industry to move towards larger blades. Critical design issues associated with larger blades are: weight, strength and blade stiffness, reliability, manufacturing, installation and service costs and testing. Definitely, full scale testing becomes quite expensive. Therefore, testing components reduced in size and containing critical parts like adhesive bond lines seems to be an interesting alternative. As the adhesives are one of the main load carrying materials in many modern wind turbine blades, the bond line strength investigation is of vital importance. Recently, linking the gap between coupon size material characterization and the material performance on a blade structure, a lot of effort has been invested in the development of sub-component tests for structural evaluation prior to the construction of a prototype. In the present study, two GFRP I-beams are loaded incrementally to failure. The particular subcomponents simulate the complex stress state developed in the adhesive bonding between the spar cap and the shear web connection of a blade. The bond line has a thickness of 5 mm. Typical Acoustic Emission (AE) load-hold proof tests are performed at intermediate loading stages, in order to locate and characterize damage processes at relatively low loads.

INTRODUCTION

During the last decade the size of the Wind Turbine Rotor Blade has increased to over 60m and is expected to reach 90m within the next years. The load carrying components are made from materials that have a high weight and cost-specific strength as well as stiffness. For the same reason Wind Turbine Rotor Blades are adhesively bonded structure. Structural evaluation under realistic stress fields will contribute to optimize the blade design and reduce costs. As the adhesives are one of the main load carrying materials in many modern Wind Rotor Turbine Blades, the bond lines are often of great importance. Lately, a lot of effort has been invested in the development of sub-component tests for material evaluation and possible certification prior to the construction of a prototype blade. The investigation of the sub-components mechanical behavior can be beneficial for the structural characterization under realistic stress field in terms of damage initiation and propagation mechanisms [1-2].

Non Destructive Testing (NDT) techniques are widely used to assess damage accumulation in tested materials, components or systems. Particularly, Acoustic Emission NDT technique has been already implemented to monitor Wind Turbine Rotor Blades during static and fatigue tests [3-8].

Acoustic Emission (AE) is defined in E 1316, Terminology for Nondestructive Examinations, as the class of phenomena whereby transient elastic waves are generated by the rapid release of energy from localized sources within a material. An AE sensor (usually piezo-electric based) mounted onto the component, detects the high frequency mechanical shock wave and converts it into an electronic signal that is amplified by a preamplifier and processed by the AE instrument. AE is generally transient, occurring in discrete bursts. AE systems process these bursts as AE “hits” by analyzing various aspects of the waveforms associated with each hit.

The AE system is very sensitive and can detect much weaker signals than those normally audible. The signals can be characterized in terms of their features such as Amplitude, Energy, rise time etc. Their on-line or post analysis can reveal failure location and damage processes taking place in the structure. AE monitoring can also be used to determine damage severity [9-10].

AE events can be located in different ways. The simplest one is zonal location, in which the event is picked up by one sensor. Linear Location means the location is calculated between two sensors using the difference in time of arrival of the AE waves. Planar location means the location is calculated using the difference in time of arrival of the AE wave on three different sensors providing the x-y coordinates.

In the present study, two I-beams, representing the adhesive loading of the spar cap to web bonding are loaded incrementally to failure. The I-Beam assembly comprises two flanges of a multidirectional layup made of GFRP (upper and lower), a shear-web sandwich-like structure with a polymer foam core and GFRP skins and a 5 mm thick epoxy bonding paste joining flanges with shear web. The first I-Beam is incrementally loaded up to failure in order to measure the Ultimate Strength (US). During the test the structure is monitored with AE. The second I-Beam is subjected to intermediate loading stages while typical AE load-hold proof tests are performed in order to locate and characterize damage processes at relatively low loads.

I-BEAM DESIGN

Two different Beam geometries are tested. One with a symmetric and one with an asymmetric web design. The height of the beams is 110mm and the bond line height 5mm. The bond line width is 13mm for the symmetric and 19mm for the asymmetric beam. The length of both beams is 1 meter. The I-beam consists of three different materials. The flanges and the skin of the sandwich shear-web are made of glass/epoxy. The lay-up of the flanges is $[\pm 45, 0_4]_2$. The thickness of the 45° lamina is 0.325mm and the thickness of the 0° lamina is 0.7426mm. That leads to a nominal thickness of 5.25mm for each flange. The lay-up of the shear web's skins is $[\pm 45]_2$, with average thickness 2.6mm. The core of the shear web is a closed cell, cross-linked polymer foam that combines high specific stiffness and strength. The thickness of the web core is 10mm. A thick bonding paste is used to glue together the three parts, the two flanges and the shear-web. The adhesive is a solvent free epoxy based bonding paste. The system is hot thixotropic and particularly suitable for bonding laminates.

TEST PROCEDURE AND INSTRUMENTATION

Two cantilever I-Beam tests are performed. Four aluminum pieces are glued, using the commercial adhesive Araldite 420A/B on the two sides of the upper flange and the bottom side of the lower flange. The aluminum pieces are used in order to adjust the I-Beams to the loading frame. A piece of the shear web is removed in order to increase the section modulus (the further the material of a structure is from its neutral axis the larger the section modulus becomes and the larger the section modulus the larger the bending moment resistance). Finally, two wooden blocks are placed between the load introduction point and the I-Beam in order to protect the flange and avoid local damage. Figure 1 illustrates how the I-beams are adjusted to the loading frame.



FIG 1. The adjustment of the I-Beam to the loading frame.

The first I-Beam is incrementally loaded up to failure while the second I-beam is loaded in steps. The load level of each step is defined according to the US of the I-Beam measured in the first experiment.

The two I-Beams are instrumented with one LVDT, positioned in the center, measuring the deflection during the uniaxial bending test. A PAC SPARTAN system, PCI-DSP4 (4 channels) is used while surface mounted AE sensors, R15 with 40dB internal preamplifier, monitor the activity. The sensors are located in such a way to perform Linear Location. At the start of each test, lead break tests are performed to check the mounting of the sensors, as specified in standard ASTM E976-94 [11]. The I-Beams are loaded in the flapwise direction in displacement control using rate 2.5mm/min. In addition to the aforementioned instrumentation, Digital Image Correlation (DIC) is used in order to measure the resulting strain field in the bonding paste. Results of the DIC will not be discussed in this paper.

Figure 2a,b presents the set up of the two experiments. In the first experiment, the transducers are positioned on the shear web while in the second one on the upper flange, for safety reasons. Figure 3 depicts the load hold test profile which consists of four blocks. The first block is a triple loop of a loading up to 20% of the US, holding for 60 sec and unloading. The second block is a double loop of a loading up to 40% of the US, holding for 30 sec and unloading. The third block is two single loops of a loading up to 60% of the US, holding for 20 sec, unloading and reloading up to 80% of the US, holding for 10 sec and unloading. Finally the fourth block is a single loop up to 90% of the US holding for 10 sec unloading and reloading up to failure. The first and the second block are named 'nominal operating load', the third block 'examination load' and the forth block 'maximum test load'.

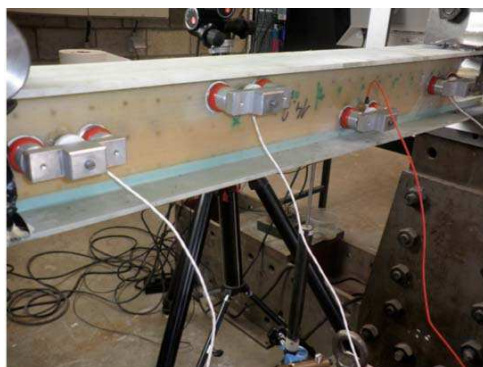


FIG 2. The position of the transducers during the first (a) and the second test (b).

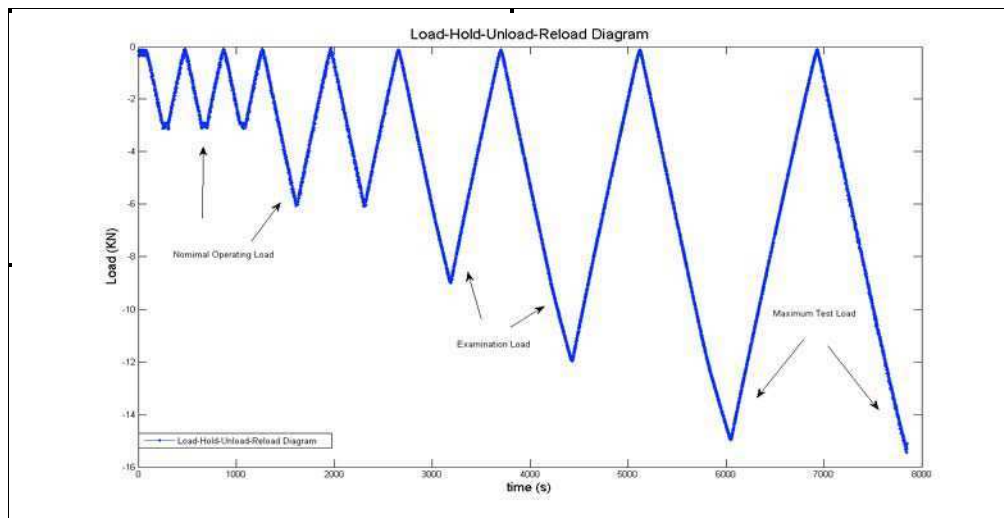


FIG 3. The Load Hold Unload Reload test Profile.

RESULTS

The first I-Beam fails at 17.1kN. [Figure 4](#) presents a 3D bar distribution graph of the hits versus time per channel. [Figure 5](#) presents a 3D bar distribution graph of the planar event location (counts to peak are selected to be plotted for each event). [Figure 6](#) depicts the position of the four transducers along the shear web. Useful information can be extracted by examining [figures 4,5](#). The first and the second transducer record events which might originate from the friction between the two wooden blocks and the loading piston. A hits peak (transducer number 3) at 500 sec indicates the existence of a defect approximately located at $x=0.5\text{m}$ and $y=0.075\text{m}$. However this defect does not seem critical for the structural integrity of the I-Beam.

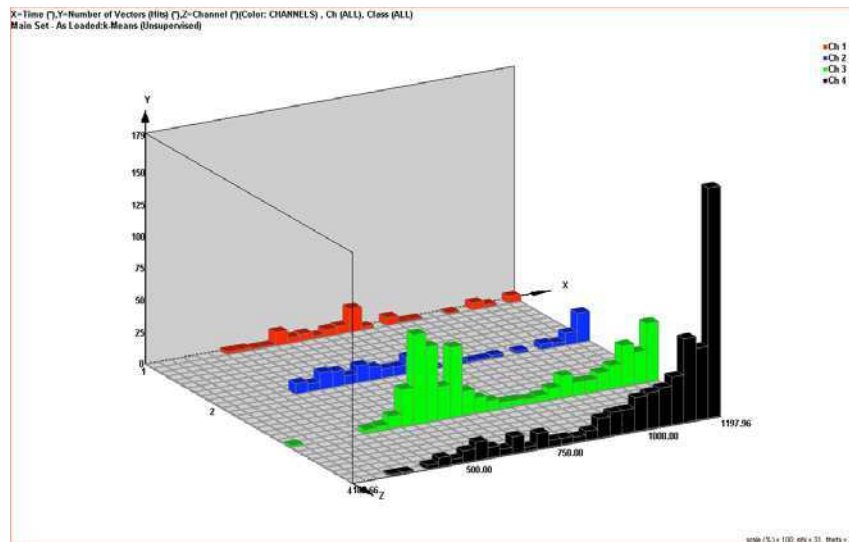


FIG 4. A 3D bar distribution graph of the hits versus time for each channel.

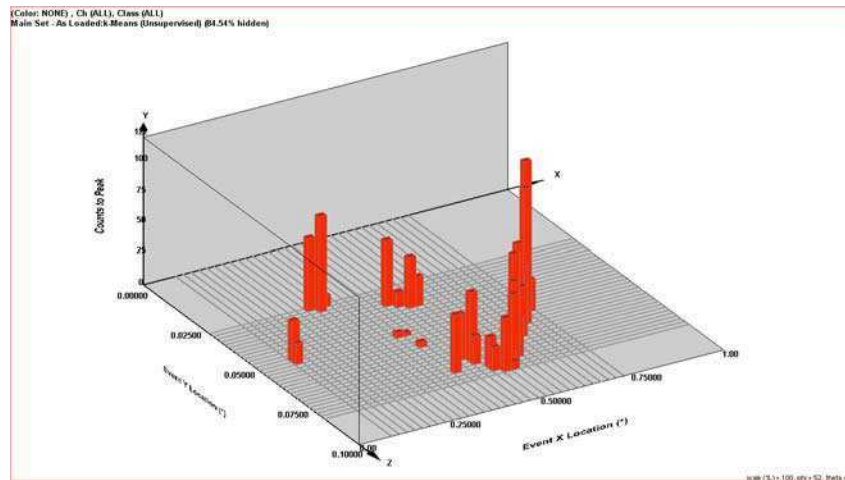


FIG 5. 3D distribution bar graph of the planar event location (counts to peak are selected to be plotted for each event)

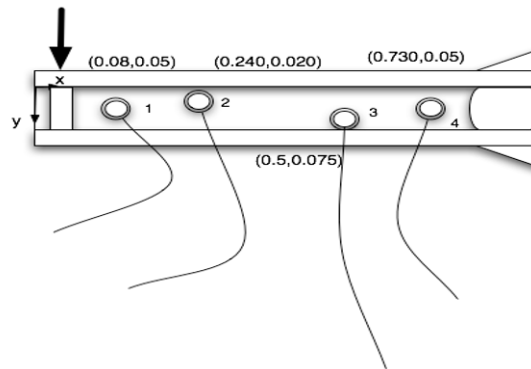


FIG 6. The position of the four transducers in the shear web.

Post failure analysis of the I-Beam may confirm the previous observation. Figure 7a,b illustrates the damaged I-Beam. Although the failure is sudden, it can be observed that the damage is initiated at the bonding paste of the I-beam's lower part, close to the clamped region. A crack is propagating across the adhesive, then into the adherent, where it propagated in an interlaminar mode, producing joint separation and causing severe damage to the flange.



FIG 7. The damaged I-beam

The second I-Beam is subjected to a load-hold proof test. This test is appropriate so as to investigate in which load level the damage might be critical for the I-Beam's structural integrity. Figure 8 presents the recorded hits during the whole period of the proof holding test while a more detailed view of the events follows in figure 8. Almost zero activity is recorded during the first block - upper left graph of figure 9. During the first loop of the second block the activity starts at 3.26 KN and keeps on during the holding period. That might be an indication of damage initiation. On the other hand, during the second loop of this block there is no significant activity in the holding and unloading phase, correlating the activity of the first loop with cracks coming from the Araldite 420 A/B paste. Moreover, during the third block the felicity ratio is 0.97 which proves that the structure withstands the 'examination load'.

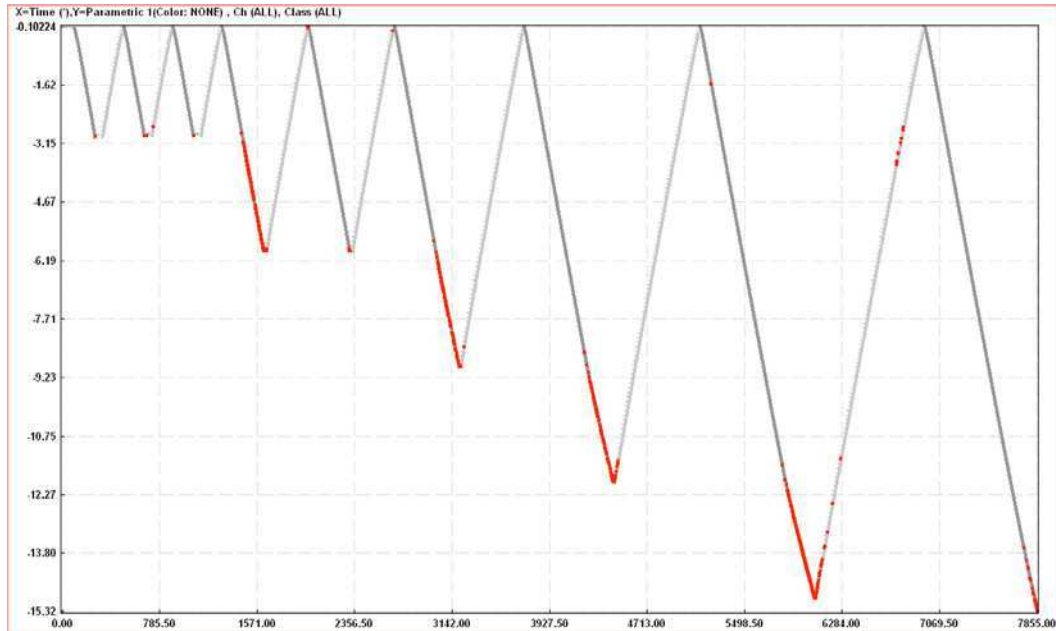


FIG 8. The recorded hits during the proof holding test.

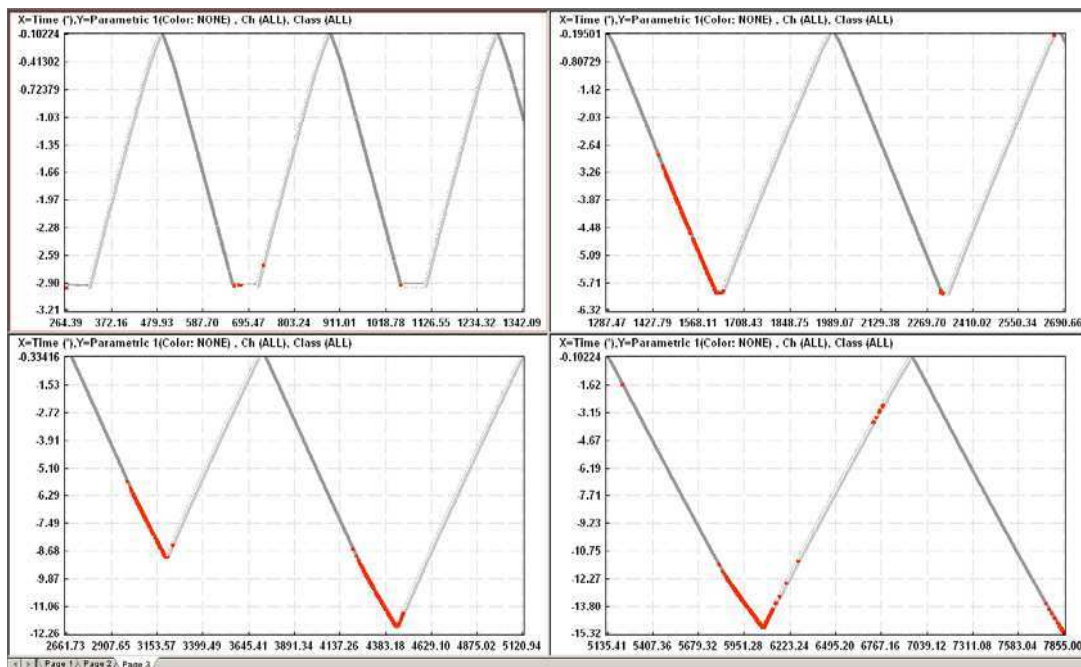


FIG 9. A detailed view of the four blocks.

Finally, the events, occurring during the unloading period of the forth block and the felicity ratio of 0.897 which is calculated in the reloading phase of the forth block, prove the existence of severe damage. The second I-Beam fails at 16.1 KN. Although the failure seems similar to the first I-Beam's failure, it is hard to conclude if it is caused due to shear web buckling or due to failure at the bonding paste, see [figure 10](#).

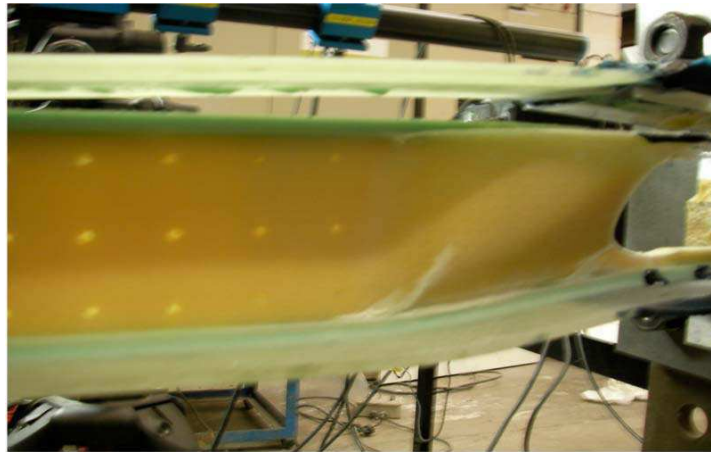


FIG 10. The damaged I-Beam

CONCLUSIONS

Two I-Beams, simulating the adhesive complex stress field of the spar cap to web bonding were loaded incrementally up to failure. The first one was incrementally loaded measuring the US while the second was loaded in steps performing load-hold proof tests. Acoustic Emission technique was used trying to locate and evaluate the damage process. Examining the results of the first test, one can notice that the AE technique succeeded to locate a defect early in the loading procedure. However, the defect did not seem critical for the I-Beams structural integrity. This observation might be confirmed by the results of the second test. These results showed that severe damage to the I-Beam appeared at almost 90% of the US.

However, in order to comprehend better the results and confirm firmly their validity, more tests and an advanced analysis of the Acoustic Emission's recordings are needed.

REFERENCES

- [1] Povl Brondsted, Hans Lilholt, Aage Lystrup, 'Composite materials for Wind Power Turbine Blades' Annual Review of Materials Research, 2005, 35,508-538
- [2]F.Sayer, N.Post, A.Van Wingerde, H.G. Busmann, F.Kleiner, W. Fleischmann, M. Gansow, 'Testing of adhesive joints in the wind industry. Proceedings European Wind Energy Conference, 2009, Marseille'
- [3] Chia Chen Ciang, Jung-Ryul Lee and Hyung-Joon Bang Structural health monitoring for a wind turbine system: a review of damage detection methods. Measurement Science and Technology, vol. 19 2008.
- [4] Mark A. Rumsey, Joshua A. Paquette 'Structural Health Monitoring of Wind Turbine Blades'. Sandia Report
- [5]P. A. Joosse, M. J. Blanch, A. G. Dutton, D. A. Kouroussis, T. P. Philippidis, P. S. Vionis 'Emission Monitoring of Small Wind Turbine Blades'
- [6]Beattie, A.G., 1997, 'Acoustic Emission Monitoring of a Wind Turbine Blade During the Fatigue Test' 1997 AIAA Aerospace Sciences Meeting.
- [7]Sutherland, H., Beattie A.G., Hansche, B., Musial, W., Allread, J., Johnson, J., and Summers, M., 1994, 'The Application of Non-destructive Techniques to the Testing of a Wind Turbine Blade' Report SAND93-1380, Sandia National Laboratory.
- [8]Vionis, P.S., Anastassopoulos, A.A., Kolovos, V.K., and Kouroussis, D.A., 1999, 'Non-Destructive Testing of Full Scale w/t Blade by Means of Acoustic Emission Monitoring During Controlled Static Loading,' Paper PB9.23, Proc.EWEC 1999, E.L. Petersen and P.H. Jensen, James & James Ltd., London, pp. 691–694.

- [9] Patrick O. Moore, Ronnie K. Miller, Eric v.K. Hill 'Non Destructive Testing Handbook, vol. 6 Acoustic Emission Testing', American Society for Nondestructive Testing, Third Edition.
- [10] Adrian A. Pollock 'Acoustic Emission Inspection', Physical Acoustics Corporation, Technical Report TR-103-96-12/89.
- [11] ASTM E976-10. Standard Guide for Determining the Reproducibility of Acoustic Emission Sensor Response.

Measurement of Cohesive Parameters of Crazes in Polystyrene Films

Chaitanya K. Desai, A.S. Kumar, S. Basu, V. Parameswaran*

Mechanical Engineering Department, Indian Institute of Technology Kanpur,

Kanpur-208016, Uttar Pradesh, India.

*Corresponding author: venkit@iitk.ac.in

ABSTRACT

Crazing is one of the dominant failure mechanisms in amorphous polymers. The micro-mechanics of crazing is often incorporated by embedding Cohesive Zone Models (CZM) into continuum models. In CZM, a traction separation law for the cohesive zone is specified with a maximum traction and a critical opening as the parameters. The main focus of the present study is to determine the cohesive parameters of craze in thin polystyrene films. Polystyrene granules were dissolved in Toluene on a glass slide which was then transferred to a spin coater. By changing the spinning speed, polystyrene films of the desired thickness were prepared. Single Edge Notch Tension (SENT) specimens were cutout of the prepared sheets and fracture tests were conducted inside a Scanning Electron Microscope (SEM) using a tensile tester at a loading rate of 0.1 mm/min. The critical opening of the cohesive zone was directly measured from the SEM images while the J -Integral was calculated from the load-displacement curve. The opening traction was calculated by differentiating the J -Integral with the measured critical craze opening.

1. Introduction

Glassy amorphous polymers are attractive materials for many engineering applications because of their low density, excellent optical clarity and ease of fabrication. They are also used as matrices in fiber composites. However, the tendency of these materials to fracture in a brittle manner and their relatively low fracture toughness have somewhat limited their applicability. Fracture in glassy polymers involves two mechanisms of localized deformation: shear yielding and crazing. Shear yielding involves plastic deformation in the form of shear bands. Shear bands are formed in polymers which exhibit strain softening in their stress-strain response. Upon further deformation, the material hardens due to molecular orientation and this leads to multiplication and propagation of shear bands. The deformation zone formed during shear yielding does not have any voids or premature cracks. Crazing is another mechanism which starts with the formation of micro voids in region of stress concentrations and primarily normal to the maximum principle stress. These voids do not coalesce to form cracks since highly stretched molecular chains (fibrils) stabilize this process to create crazes. However further craze widening leads to the breakdown of fibrils and eventually to the formation and propagation of a crack. [Figure 1](#) shows both deformation processes observed during the fracture of glassy polymers (polycarbonate and polystyrene).

Unlike cracks, crazes are load bearing with the craze surfaces bridged by large number of thin polymers fibrils. Usually crazes eventually generate into a crack by the breakdown of craze fibrils. Therefore, controlling crazing is a viable way of increasing the fracture toughness of polymers. The plastic work required to create crazes ahead of the growing crack appears as the major contribution to the fracture toughness G_{Ic} .

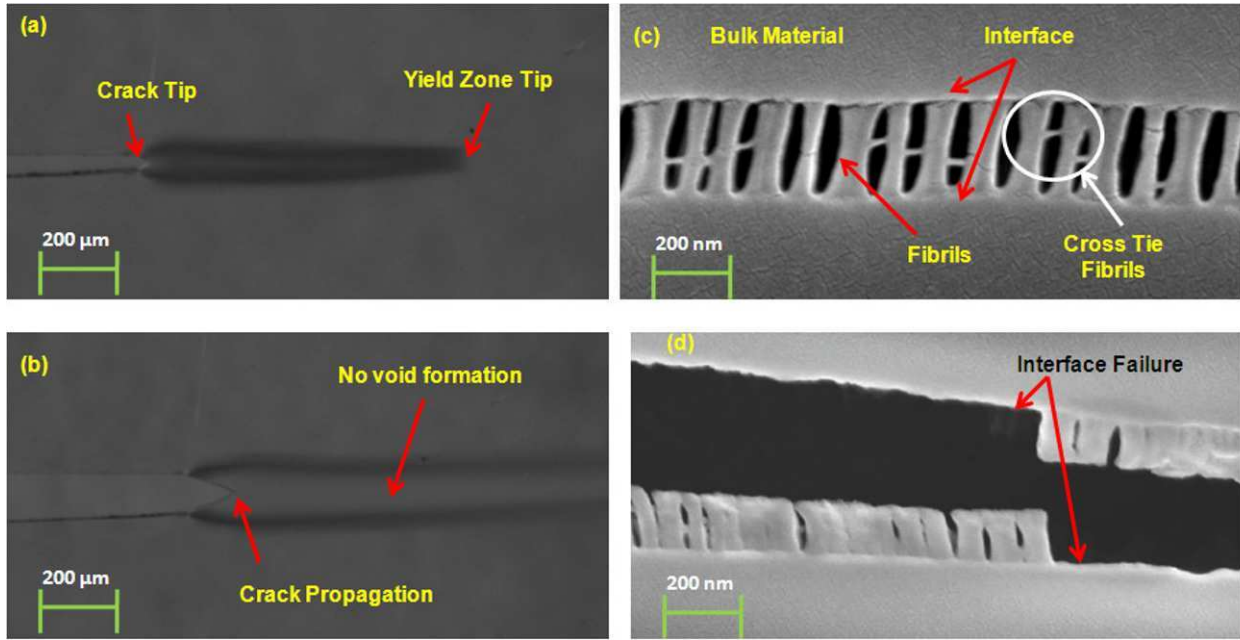


Fig. 1 Shear yielding in 0.5 mm thick sheet of polycarbonate (a) before crack propagation (b) after crack propagation and crazing in 800 nm thick polystyrene film (c) fibril formation (d) fibril breakage

The earliest works on crazing can be found in Rabinowitz and Beardmore [1], Kambour [2] and Gent [3]. The first authoritative experimental work on crazing was reported by Lauterwasser and Kramer [4]. They determined the stress distribution around the craze surface using the craze displacement profile determined experimentally. To this end they employed a Fourier transform method due to Sneddon [5].

Generally, the phenomena of crazing proceeds in three steps namely, craze nucleation, craze widening and craze breakdown. Many authors have proposed different models for different aspects of crazing. Argon and Hannoosh [6] assumed that the critical event in the craze nucleation is the formation of a critical level of porosity in the material. Sternstein and Ongchin [7] proposed a simple empirical relation for the craze initiation. Craze growth is associated with two important aspects, namely craze tip advance and craze widening. Donald and Kramer [8], Kramer [9] and Kramer and Berger [10] performed systematic experiments and proposed a criterion for craze widening. William [11] postulated that craze breakdown and subsequent crack advance occurs when a critical craze opening displacement is reached. From fracture experiments on various glassy polymers (Doll [12], Doll and Konczol [13]), indeed such a critical constant craze maximum opening has been observed.

Various authors (Estevez R. [14], Tijssens MGA [15], Van der Giessen [16], Saad Gouider [17], Basu *et al.* [18] and others) have studied the crazing phenomena in glassy polymers using numerical techniques like Finite Element Analysis (FEA) with Cohesive Surface Modeling. The success of a CZM depends on how faithfully the traction separation behaviour mimics the actual micromechanical processes of initiation, widening and breakdown. To this end, critical opening, maximum stress and the energy release rate (area under the traction-separation curve) are the critical parameters. These parameters have to be carefully determined from the experiments in order to successfully apply the CZM in FEA. The main focus of the present study is to determine the cohesive parameters of crazes in thin polystyrene films. The paper is organized as follows: In the next section we discuss the experimental methods which include the preparation of the polystyrene (PS) film and measurement of cohesive parameters. Results obtained from experiments and final conclusions are drawn in the last section.

2. Experimentation

2.1 Sample preparation

PS in the form of beads was procured from the Gail Petrochemicals, India. The molecular weight of the material was measured using Gel Permeation Chromatography (GPC). The measured molecular weights were $\overline{M}_w = 1.88 \times 10^5$ and $\overline{M}_n = 4.15 \times 10^4$, where \overline{M}_w and \overline{M}_n are the weight average and number average molecular weights. PS beads of 50 % by weight were dissolved in Toluene solution by continuous stirring and then filtered using vacuum filtration technique. The films were prepared using the spin coating technique. For that, the solution of PS was transferred to a glass slide which was mounted on the spin coater and by changing the speed of the spin coater; films of desired thickness were prepared. For the present study, a PS film of 52 μm thickness was used.

2.2 Testing

The films so formed could be easily peeled off from the glass slides and cut into the desired dimensions. The width (W) and length (Z) of the films were 15 mm and 30 mm respectively. Crack of 5 mm length (a) was cut using a razor blade. Fig 2a shows the schematic diagram of the specimen used for in situ experiments. Since PS is an insulator it tends to get charged up by the electron beam of the SEM and images tend to become blurred at high magnifications. Hence it is required to gold coat the PS film before testing under an SEM.

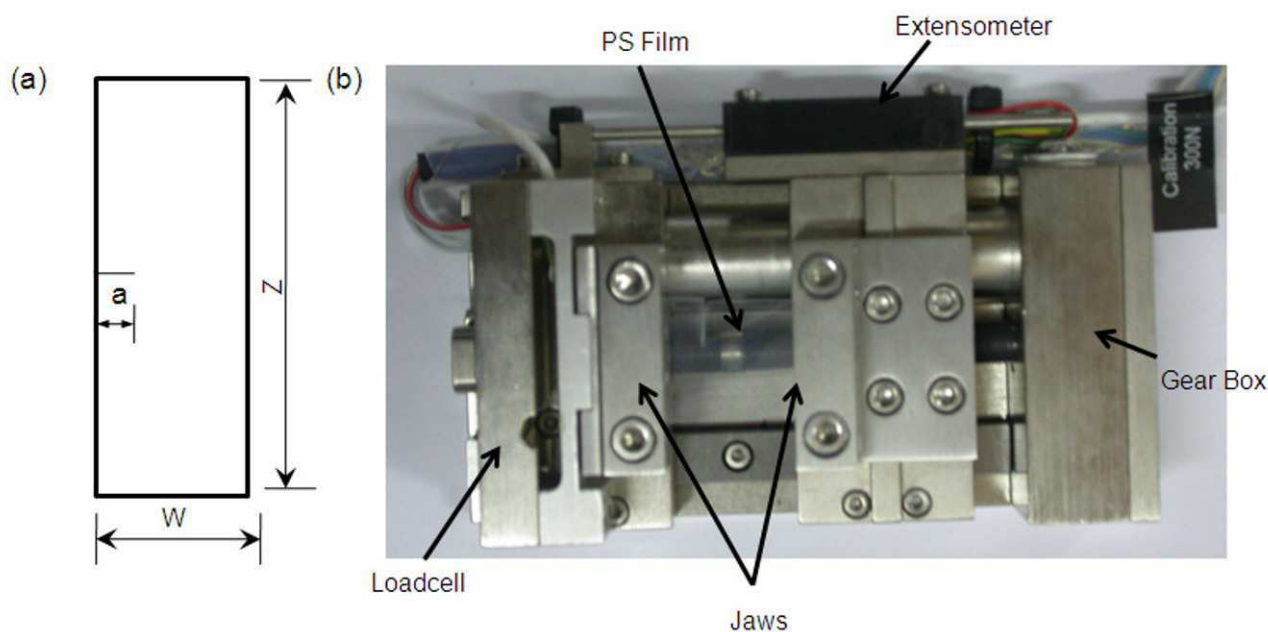


Fig 2 (a) Specimen geometry (b) micro tensile testing machine.

The sample was fixed on the micro tensile machine (Deben UK Ltd, UK) after gold coating using flat jaws which was then mounted on a mobile stage of FESEM (Field Emission Scanning Electron Microscope). The imaging parameters used are given in Table 1. The micro tensile machine was operated through a separate data port which could be connected to the computer. Figure 2b shows the micro tensile machine used for experiments clearly indicating the jaws for holding the specimen. The micro tensile machine was connected to the digital computer via a controller unit. The function of the controller unit is to give power supply to the micro tensile machine and to transfer the test data to the digital computer. The micro tensile machine had a load cell of capacity 300 N. The specimen was then subjected to tensile loading at a slow loading rate of 0.1 mm/min. Successive micrographs of the events occurring at the crack tip was recorded at regular intervals. The load corresponding to each micrograph was also noted. This helped to record the evolution of the craze from the crack tip as the load was increased. Further analysis of these micrographs helped in finding various parameters associated with crazing.

Table 1 Parameters for single scan imaging

Imaging Properties	Zeiss SUPRA 40VP
Magnification	500X
Electron detector	In lens
Working distance (mm)	9
Vacuum mode	High Vacuum
Accelerating voltage (kV)	10
Image size	1022 x 685
Recording pixel shape	Square
Image quantization	8

3. Results

3.1 In situ observations

Figure 3 shows the successive micrographs of events happening at the crack tip during the fracture test. The micrographs clearly show the nucleation, growth and final breakdown of a craze at the tip of a crack. It can be observed that during loading, a fibrillated zone formed ahead of the crack tip. In Fig 4a, the crack tip and the incipient craze are clearly seen.

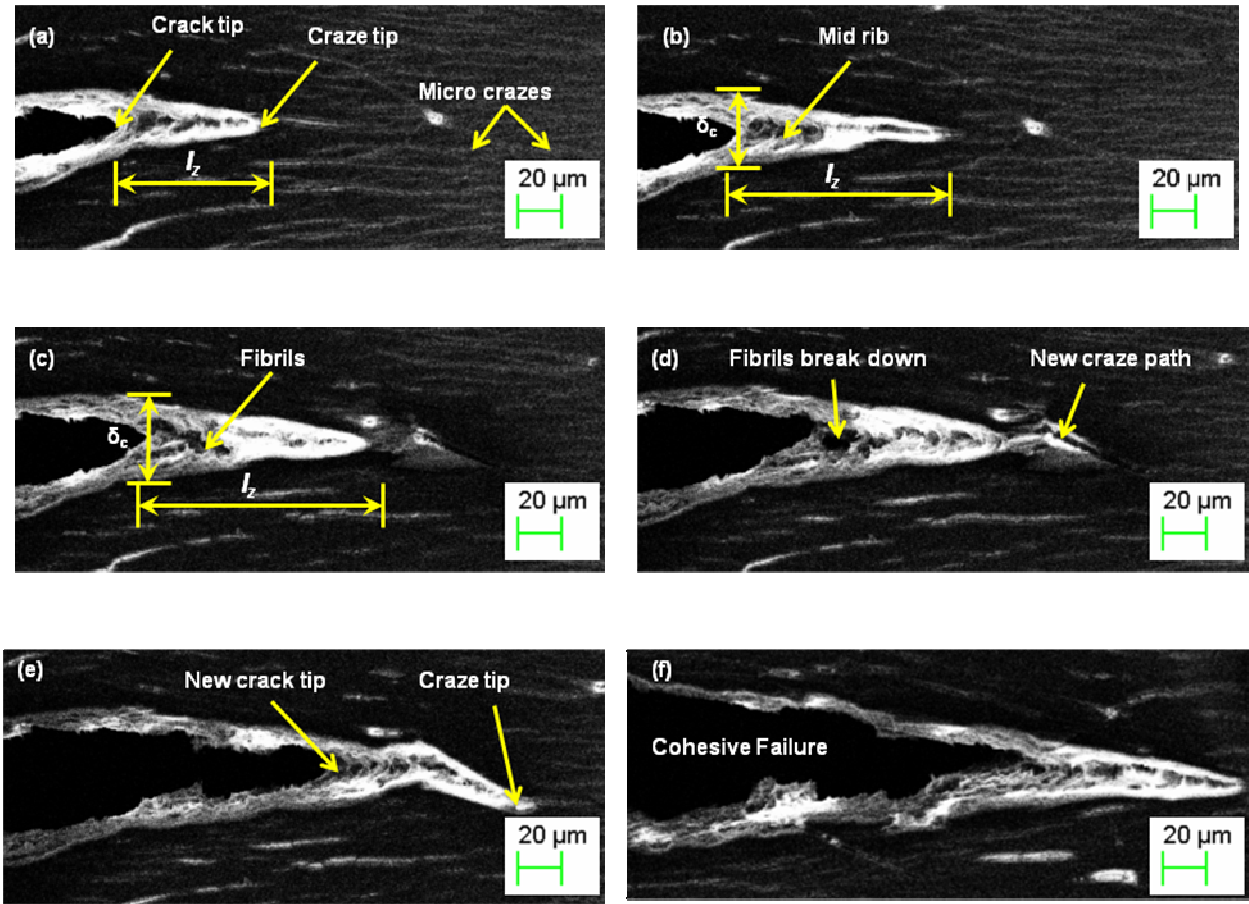


Fig. 3 Deformation stages of the PS film at various load levels.

The distance between the crack tip and the craze tip is marked as l_z , length of the craze. The craze evolved gradually with applied load. Fibrils in the craze elongated till a critical load after which they broke down at the midrib. Critical opening and the length of the cohesive zone during loading were directly measured from the SEM images.

Figure 4 shows the global load-displacement curve measured during the fracture test. The curve shows an initial linear portion followed by a plateau before dropping to zero. Points marked (a) – (f) on the load displacement curve corresponds to the SEM images marked (a)-(f) in Fig. 3. The craze opening (δ) as a function of the craze length (l_z) measured from the SEM images at different load intervals is shown in Fig. 4b. The craze opening was measured at the crack tip. It can also be seen from Fig. 4b that the craze opening was constant with applied load but the length of the craze changes. The opening at the crack tip is known as the critical opening of the craze which should be constant and can be treated as a material property. The critical opening was measured to be $30\ \mu\text{m}$.

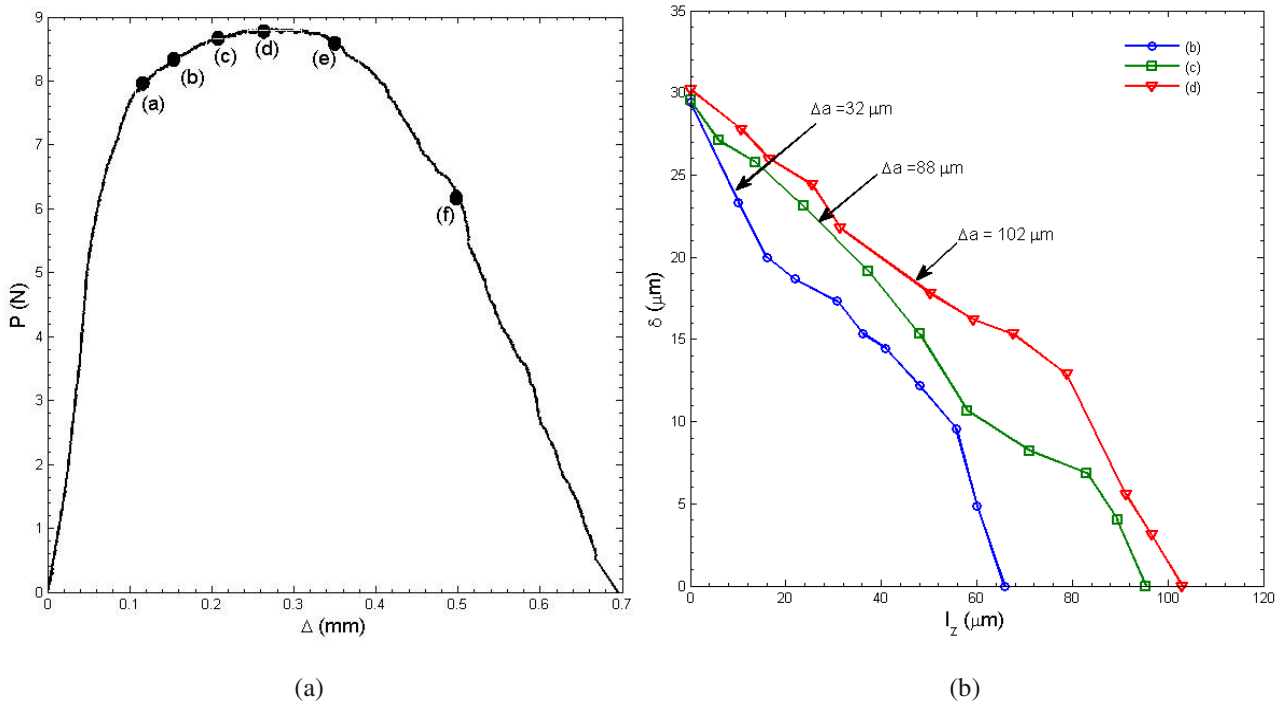


Fig. 4 (a) Load-displacement curve for SENT specimen made of PS ($B = 52\ \mu\text{m}$) (b) opening profile of craze

3.2 Determination of Traction-Separation Law (TSL)

To determine the cohesive law or TSL, the J -integral approach was used. The relation between the J -integral and strain energy release rate which is valid for Linear Elastic Fracture Mechanics (LEFM) was used. LEFM can be applied when the material remains elastic except in the small damage zone forming ahead of the crack tip. The length of the damage zone should be smaller than the initial crack length ($l_z < a$). Here the maximum length of the cohesive zone was $100\ \mu\text{m}$ before crack propagation which is much smaller than the initial crack length ($a = 5.93\ \text{mm}$). In LEFM, the J -integral is correlated to the energy release rate, G , and can be calculated from the load displacement curves shown in Fig. 4a.

$$J = \frac{\eta_e U_e}{B(W - a)}, \quad (1)$$

where U_e is elastic component of the strain energy, η_e is the elastic work factor and B is the thickness of the specimen. The elastic work factor can be evaluated for a given specimen geometry from the LEFM shape factor, $Y(a/W)$. For SENT specimen geometry, η_e is given by [18-19] as

$$\eta_e = \frac{(W-a)Y^2a}{\int Y^2ada + (ZW/2)}, \quad (2)$$

where

$$Y = 1.99 - 0.41(a/W) + 18.7(a/W)^2 - 38.48(a/W)^3 + 53.84(a/W)^4, \text{ and} \quad (3)$$

Z is the gauge length. For the present case, $Z = 30$ mm and $a/W = 0.39$. For the given geometric dimensions, the value of elastic work factor was 1.85. To determine the cohesive law, the J -integral was determined experimentally using eq. (1) and the crack tip opening (δ) was directly measured from SEM images. The cohesive stress was calculated by numerically differentiating the measured J -integral with the measured crack tip opening as

$$\sigma(\delta) = \frac{\partial J(\delta)}{\partial \delta}. \quad (4)$$

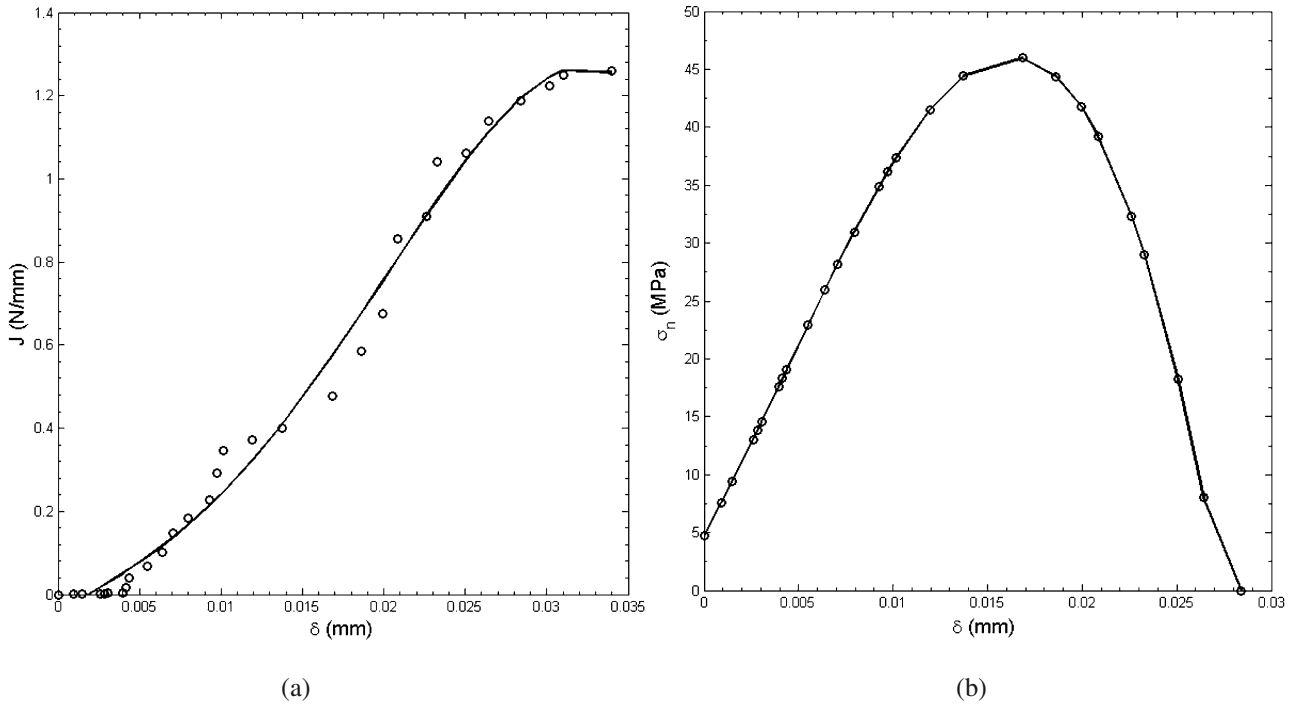


Fig. 5 (a) J -integral as a function of crack tip opening (b) Traction Separation Curve

The calculated J -integral as a function of crack tip opening is shown in Fig. 5a while the TSL obtained from eq. (4) is shown in Fig. 5b. Figure 5b shows that the normal traction increases with crack tip opening, reaches its maximum value at approximately 15 μm , then decreases and eventually vanishes when fibrils break and the crack propagates. The critical opening (corresponding to zero traction) is 28.5 μm . The energy release rate measured from the TSL was 0.83 N/mm. Also the opening of the craze zone was measured during crack extension and it can be observed from the Fig. 6 that the maximum opening remains constant during crack propagation. The average critical opening measured directly from the SEM images is in good agreement with that shown in figure 5(b).

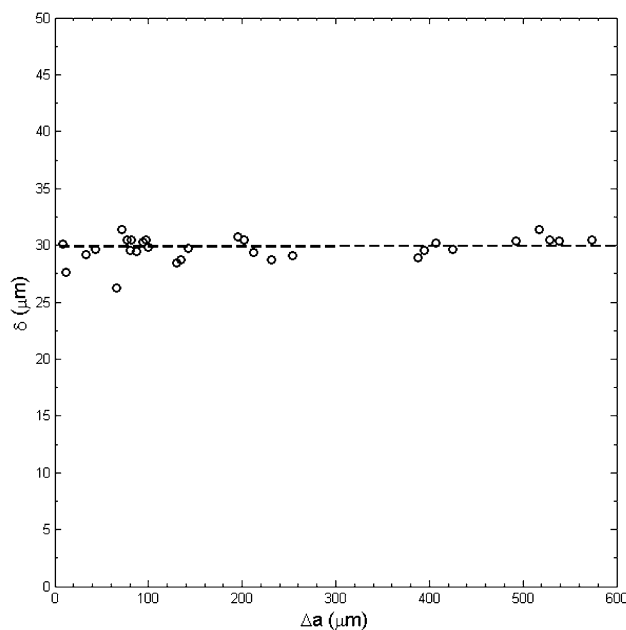


Fig. 6 Critical opening as a function of a crack extension

Conclusions

In-situ fracture experiments were performed inside an SEM on PS film using the SENT geometry. The nucleation, growth and final breakdown of the craze at the tip of the crack was captured in real-time. The critical opening before crack propagation was measured directly from the SEM images. The J -integral was calculated from load-displacement diagram. This J -integral was numerically differentiated by the opening at the crack tip which was measured from SEM images to obtain the traction. The maximum traction before crack propagation was determined as 46 MPa. The critical opening at which the stresses are zero was 28.5 μm . The critical energy release rate (area under the TSL) was calculated as 0.83 N/mm. It was also observed that the critical opening, directly measured from SEM images, at different crack lengths remained essentially constant.

Acknowledgement

The authors acknowledge the financial support of Department of Science and Technology through project SR/S3/MREC/085/2008, Dr. Dinesh Deva and Ms. Barkha Awasthi of Nanoscience center of IIT Kanpur for providing the SEM facilities and helping during experiments and Dr. Dwibendu Bagh at DMSRDE for measuring the molecular weights of PS.

References

- [1] Kambour. A review of crazing and fracture in thermoplastics, J. Polym. Sci, Macromolecular Reviews **7**, pp. 1–154, 1973.
- [2] Gent AN. Hypothetical mechanism of crazing in glassy plastics, Journal of Material Science **5**, 925–932, 1970.
- [3] Lauterwasser BD, Kramer EJ. Microscopic mechanisms and mechanics of craze growth and fracture. Phil. Mag. A **39** 4, pp. 469–495, 1979.
- [4] Sneddon JN, Fourier Transform, Mc. Graw Hill, 1951.
- [5] Argon AS, Hannoosh, JG. Initiation of crazes in polystyrene. Phil. Mag. **36**, 5, pp. 1195–1216, 1977.
- [6] Sternstein, SS, Ongchin, L. Yield criteria for plastic deformation of glassy high polymers in general stress fields. Polymer preprints **10**, 2, pp. 1117–1124, 1969.

- [7] Donald AM, Kramer, E.J. The mechanism of craze-tip advance in glassy polymers. *Phil. Mag. A* 43, 4, pp. 857–870, 1981.
- [8] Kramer H.H. Microscopic and molecular fundamentals of crazing. *Adv. Polym. Sc.* 52, pp. 1–56, 1983.
- [9] Kramer HH, Berger LL. Craze growth and fracture. *Adv. Polym. Sc.* 91, pp. 1–68, 1990.
- [10] Williams JG. *Fracture Mechanics of Polymers*, Ellis Horwood, 1984.
- [11] Döll W. Optical interference measurements and fracture mechanics analysis of crack tip craze zones. *Adv. Polym. Sc.* **52**, pp. 105–168, 1983.
- [12] Döll W, Könczöl, L., Micromechanics of fracture: optical interferometry of crack tip craze zone. *Adv. Polym. Sc.* **91**, pp. 138–214, 1990.
- [13] R. Estevez, MGA. Tijssens, E. Van der Giessen. Modeling of the competition between shear yielding and crazing in glassy polymers. *Journal of the Mechanics and Physics of Solids*, 48, 2585–2617, 2000.
- [14] Tijssens MGA, Van der Giessen, E, Sluys, L.J. Modeling of crazing using a cohesive surface methodology. *Mech. Mat.* **32**, pp. 19–35, 2000.
- [15] Van der Giessen, E. Localized plastic deformations in glassy polymers. *Eur. J. Mech. A/Solids* **16**, pp. 87–106, 1997.
- [16] Saad-Gouider N, Estevez R, Olagnon C, Seguela R, Calibration of a viscoplastic cohesive zone for crazing in PMMA, *Eng. Frac. Mech.* 73, 2503-2522, 2006.
- [17] Sumit Basu, Erik Van der Giessen, A thermo mechanical study of mode I, small scale yielding crack tip fields in glassy polymers, *Journal of plasticity*, 18, 1395-1423, 2002.
- [18] Turner CE. The ubiquitous η factors. *Frac. Mech.* 12th conference, ASTM-STP 700, 314-337, 1980.
- [19] Towers OL. Tests for fracture toughness and fatigue assessment: a compilation of stress intensity, compliance and elastic η factors. The Welding Institute, Abington, 1985.

Delamination Growth Using Cohesive Zone Model for Adhesive Bonding Under Compression

M. M. Islam
Graduate Research Assistant, Engineering Science and Mechanics
Virginia Tech
Blacksburg, VA, 24061

Rakesh K. Kapania
Mitchell Professor, Aerospace and Ocean Engineering
Virginia Tech
Blacksburg, VA, 24061

ABSTRACT

Adhesive bonding of aircraft primary structures has been in use for many years. For example, joining the stringers to skins of fuselage and wing structures, metallic honeycomb to the skins of elevators, ailerons, tabs, and spoilers constitute the main uses of adhesives in aircraft structures. Due to this increasing use of bonded structures in recent years, for weight saving, considerable work has been done in the fracture testing of different types of adhesive joints. However, most previous work on adhesive bonded joints deals mostly with Mode I fracture, and very little work appears to have been done on compressive delamination of adhesive joints. The Chow and Ngan test, consisting of two slender beams with a blister at the centre of each, which were bonded together and loaded in compression, is an exception. In the present work, a cohesive finite element model was developed for this blister test-piece, and the geometric non-linearity was incorporated in the strain/displacement relations. The crack propagation in the adhesive joint under compression for the proposed test-piece was found to agree with the available experimental observation. Most importantly, the delamination in adhesive joint under compression for different constrained cases was studied by cohesive finite element with different interface mesh densities. Stronger adhesive joint was achieved for less constrained Double Cantilever Beam (DCB) specimen.

1. Introduction

Adhesive bonding has been used in the fabrication of primary aircraft fuselage and wing structures for many years [1]. For example, joining the stringers to skins of fuselage and wing structures, metallic honeycomb to skins of elevators, ailerons, tabs, and spoilers constitute the main uses of adhesives in aircraft structures. Adhesive bonded aircraft structures are stable and durable, and, hence, this construction method has a good potential for future design programs. However, application of a new technology needs corresponding development of design and assessment methods. In industry, the earlier analytical design procedures have been replaced by the Finite Element Method (FEM) so that the complete structure including adhesive bonds can be simulated and assessed. The detailed FEM computations are based on detailed understanding of all relevant material behaviors including adhesives in joined or layered materials.

Delamination is one of the most common failure modes in layered materials, which may result from joint imperfections, edge effects, and various loadings. The presence of delamination can cause significant reduction in stiffness and strength of a joined structure and leads to a failure; hence a clear understanding of the failure behavior of the joined structure under shear/tension/compression is extremely important. Considerable work has been done in the compression delamination of composite structures [2-9], Mode-I fracture of adhesive joints [10-14], and mixed mode fracture [15-21]; however, very little work appears to have been done on compressive delamination of adhesive joints.

Besides, different constrained ends of adhesive joints might change the fracture properties of the adhesive layer. In experimental study, capturing end constrained effects on fracture properties of the adhesive under compression requires proper complicated models of adherents and adhesive. On the other hand, the cohesive zone model can be introduced to describe the response of the adhesive layer and to simulate fracture process under compression for different constrained end cases.

The objective of this paper is, therefore, to study the delamination and growth of adhesively bonded joint under compression for different constrained end cases. Although most of the previous simulations of delamination growth were either for composite laminates or for the peel fracture of an adhesive joint, simulation for adhesively bonded joint under compression having different constrained ends is equally important. Chow and Ngan [22] proposed a test consisting of two slender beams with a blister at the centre of each and which were bonded together and loaded in compression. Simulation of this test along with those for the various constrained end effects on an adhesive joint under compression can be performed by using interface cohesive finite elements.

In the present work, a finite thickness interface cohesive element model is used to simulate the progressive delamination in adhesive joints under compressive in-plane loads for different constrained end conditions. For validation of the delamination model, a cohesive finite element model is developed for the blister test-piece, and the geometric non-linearity is incorporated in the strain/displacement relations. In addition, cohesive finite element model is validated with available literature [23]. Finally, the delamination in adhesive joint under compression for different constraint cases is studied by cohesive finite element with different mesh densities of the interface.

2. Crack Propagation on Bonded Joint Under Compression

Chow and Ngan [22] proposed a test consisting of two slender beams with a blister at the centre of each and which were bonded together and loaded in compression. The geometry of the test-piece is depicted in Fig. 1, which consists of two slender beams bonded together with adhesive and loaded in compression. In Fig. 1, u is axial displacement, v is lateral displacement, a is the half crack length, q is quarter of the maximum distance between the curved beams, and P is the axial load. A blister arrangement is made at the centre of the beam simulating the bonding flaw, and the load displacement relationship is formulated.

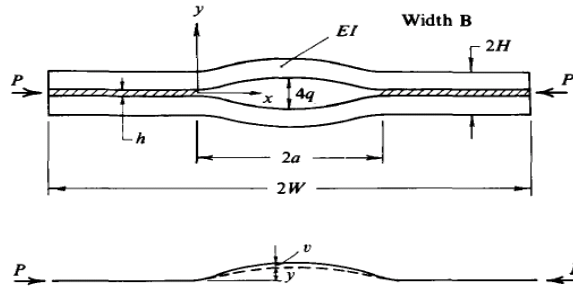


Fig. 1 Slender beams with a blister at the center [22]

The load, P , and displacement, u , relationship at constant crack area can be obtained by assuming that the length of the curved strut is not affected by application of the load P . The axial displacement, u , is given as

$$u = 2 \int_0^a \left[\sqrt{1 + \left(\frac{dy}{dx} \right)^2} - \sqrt{1 + \left(\frac{dy}{dx} + \frac{dv}{dx} \right)^2} \right] dx \quad (1)$$

For small initial curvature and small deflection, both the $(dy/dx)^2$ and $(dv/dx)^2$ are much smaller than unity. From the first approximation of binomial expansion [22],

$$u = 2 \int_0^a \frac{1}{2} \left[\left(\frac{dy}{dx} \right)^2 - \left(\frac{dy}{dx} + \frac{dv}{dx} \right)^2 \right] dx \quad (2)$$

Assuming $y = q(1 - \cos \pi x/a)$ and $v = \{q\mu^2 a^2 / (\pi^2 - \mu^2 a^2)\}(1 - \cos \pi x/a)$, where $\mu = (P/2EI)^2$,

$$u = \frac{\pi^2 q^2}{2a} \cdot \frac{\left(\frac{pa^2}{2EI} \right) \left\{ 2\pi^2 - \left(\frac{pa^2}{2EI} \right) \right\}}{\left\{ \pi^2 - \left(\frac{pa^2}{2EI} \right) \right\}^2} \quad (3)$$

where E is the modulus of elasticity, and I is the second moment of the area of the beam. Although the load displacement relationship is nonlinear for a constant a , for small P , Eq. (3) becomes linear.

$$u = \frac{a q^2}{2EI} \cdot p \quad (4)$$

3. The Cohesive Model

The idea for the cohesive model goes back to the strip yield models of Dugdale [24] and Barenblatt [25]. Instead of letting stresses become singular, finite stresses are introduced in a cohesive zone ahead of at the crack tip, which are assumed to be same as the yield stress for a plane stress state [24] or as some function of the distance to the crack tip [25]. This model has become very useful for practical applications, when numerical methods are used to solve nonlinear problems. The cohesive stresses or tractions have been introduced as functions of the local separation, $\delta = [u] = u^+ - u^-$, of the material. This local separation is a vector having three components in mutually perpendicular directions for the selected orthogonal coordinate system. The cohesive model for crack propagation analysis of ductile materials is introduced by Needleman [26].

The interface element for cohesive finite element is an isoparametric element with a very small thickness as shown in Fig. 2. The thickness of the element is about 1/50 of the adherent thickness, and it is inserted as a numerical layer between the adherent layers. The strain vector, ϵ , and the traction vector, t , are calculated in a local coordinate system (s, t, n) , which is located on the element midplane. The local separation, δ , is calculated as the relative movement of the two surfaces from this midplane. The strain is then transformed to the global matrix, (x, y, z) , to calculate the nodal reaction forces. The displacement vector, u , and the strain vectors are defined by

$$u = \begin{Bmatrix} u \\ v \\ w \end{Bmatrix}; \epsilon = \begin{Bmatrix} \epsilon_{sn} \\ \epsilon_{tn} \\ \epsilon_{nn} \end{Bmatrix} \quad (5)$$

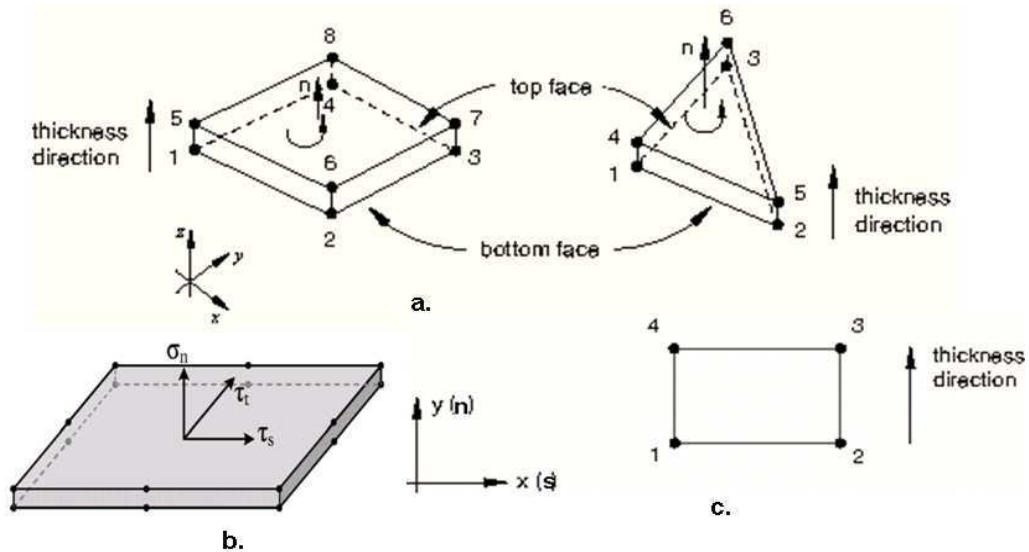


Fig. 2 Cohesive elements: a) 3D cohesive element, b) local coordinates direction, c) 2D cohesive element [27]

In an elastic region, if the deflection is large, nonlinearity is assumed to be for geometric nonlinearity and not due to a nonlinear stress-strain relationship. The strain displacement relationship for geometrically nonlinear case with respect to the reference coordinate system can be written as

$$\varepsilon_{ij}^{\pm} = \frac{1}{2} (u_{i,j}^{\pm} + u_{j,i}^{\pm} + u_{k,i}^{\pm} u_{k,j}^{\pm}) \quad (6)$$

Here i, j , and k run from 1 to 3, and Einstein's summation rule is used for repetitive indices. The indices 1, 2, and 3 represent the local s , t , and n directions respectively. The superscript \pm represents the top/bottom surfaces with respect to the midplane. The comma between subscripts represents the partial derivative. From Eq. (6) replacing notation for local coordinate system, the strain displacement relationship for non-linear case is

$$\begin{Bmatrix} \varepsilon_{sn}^{\pm} \\ \varepsilon_{tn}^{\pm} \\ \varepsilon_{nn}^{\pm} \end{Bmatrix} = \frac{1}{2} \begin{Bmatrix} u_{s,n}^{\pm} + u_{n,s}^{\pm} + u_{k,s}^{\pm} u_{k,n}^{\pm} \\ u_{t,n}^{\pm} + u_{n,t}^{\pm} + u_{k,t}^{\pm} u_{k,n}^{\pm} \\ u_{n,n}^{\pm} + u_{n,n}^{\pm} + u_{k,n}^{\pm} u_{k,n}^{\pm} \end{Bmatrix} \quad (7)$$

where k runs from 1 to 3.

The material separation and thus damage to the structure is described by interface elements at the boundaries of the undamaged continuum elements. Thus, the mechanical behavior of the material is split into two parts, the damage-free continuum with an arbitrary constitutive law, and the cohesive zone specifying material damage and separation. Interface elements open according to some decohesion law and finally lose their stiffness so that the adjacent continuum elements get disconnected.

4. Constitutive Equation

A bilinear constitutive law is chosen which is based on the 2-D cohesive model. This constitutive law relates the stresses to strains for any pure fracture or loading mode. In the case of mixed mode loading, the constitutive law relates the effective stresses to the effective strains, as shown in Fig. 3.

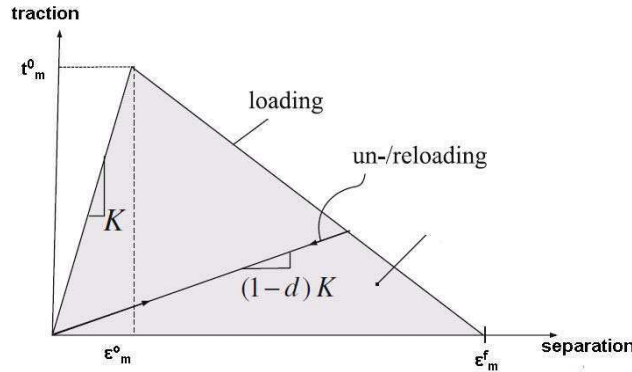


Fig. 3 Bilinear constitutive relationship

These quantities are defined as follows: The effective strain is a positive continuous quantity and when there is not any compressive normal strain, it is equal to the norm of strain vector and is defined by

$$\varepsilon_m = \sqrt{\langle \varepsilon_{nn} \rangle^2 + \varepsilon_{sn}^2 + \varepsilon_{tn}^2} \quad (8)$$

where $\langle \rangle$ means if the inside parameter value of that is negative, it will be considered as zero. This constitutive law consists of three different parts [27]:

- i) If the effective strain is less than ε_m^0 (Fig. 3), the interface material behaves as linear elastic, and no damage is presented in the element.
- ii) If the effective strain reaches ε_m^0 , the interlaminar damage initiates. After this point, the interface stresses decrease linearly.
- iii) Strain ε_m^f refers to complete decohesion.

It is also necessary to specify the strains corresponding to initiation and completion of damage. The delamination initiation is predicted by the quadratic failure criterion. Damage is assumed to initiate when a quadratic interaction function involving the nominal stress ratios reaches a value of one. This criterion can be represented as

$$\left(\frac{\langle t_n \rangle}{t_n^0}\right)^2 + \left(\frac{t_s}{t_s^0}\right)^2 + \left(\frac{t_t}{t_t^0}\right)^2 = 1 \quad (9)$$

where t_n^0 , t_s^0 , t_t^0 are the Mode I, Mode II, and Mode III strengths respectively. The constitutive equation for the elastic behavior can then be written as [27]

$$t = \begin{Bmatrix} t_n \\ t_s \\ t_t \end{Bmatrix} = \begin{bmatrix} K_{nn} & K_{ns} & K_{nt} \\ K_{ns} & K_{ss} & K_{st} \\ K_{nt} & K_{st} & K_{tt} \end{bmatrix} \begin{Bmatrix} \varepsilon_{nn} \\ \varepsilon_{sn} \\ \varepsilon_{tn} \end{Bmatrix} = K \varepsilon \quad (10)$$

where n , s , and t are the local coordinate directions, and K is the stiffness matrix. This elasticity matrix (stiffness matrix, K) provides fully coupled behavior among all components of the traction and separation vectors. It is required to set the off-diagonal terms in the elasticity matrix to zero if uncoupled behavior between the normal and shear components is desired.

5. The Interface Properties

From Eq. (10), uncoupled constitutive behavior is defined as

$$t = \begin{Bmatrix} t_n \\ t_s \\ t_t \end{Bmatrix} = \begin{bmatrix} K_{nn} & 0 & 0 \\ 0 & K_{ss} & 0 \\ 0 & 0 & K_{tt} \end{bmatrix} \begin{Bmatrix} \varepsilon_{nn} \\ \varepsilon_{sn} \\ \varepsilon_{tn} \end{Bmatrix} = K \varepsilon \quad (11)$$

The elasticity components for particular cases: (i) $K_{nn} = K_{ss} = K_{tt} = 0$ means complete debonding between adherents, (ii) $K_{nn} = K_{ss} = K_{tt} = \alpha$ means perfect bonding between adherents.

If the (interface thickness/adherent thickness) $\ll 1$, an approximation of stiffness values can be given by [28]

$$k_{nn} = \frac{E_3}{\rho}; k_{ss} = \frac{2G_{13}}{\rho}; k_{tt} = \frac{2G_{23}}{\rho} \quad (12)$$

where E_3 , G_{13} , and G_{23} are homogenized adherent moduli, and ρ is the interface thickness.

6. Cohesive Zone Modeling Validation

Double Cantilever Beam (DCB) Tests for Validation of Cohesive Zone Modeling

The DCB test specimen is generally used for the characterization of Mode-I fracture. The geometry and the loading conditions of the DCB configuration is shown in Fig. 4, and the finite element mesh is shown in Fig. 5. One layer of linear quadrilateral, type CPS4R (continuum plane stress 4 nodes reduced integration), elements are used for adherents, and one layer of linear quadrilateral, #508 COH2D4 (cohesive 2-dimensional 4 nodes), elements is used for the adhesive. The experiment consists of a load that is applied at the end blocks attached to the DCB specimen. The geometrical properties are the length $L=203\text{mm}$, the arm thickness $h=6.35\text{mm}$, and width $B=25.4\text{mm}$. The initial crack length a_0 is about 55mm. The mechanical properties of the DCB specimen are $E=69\text{ GPa}$, $\nu=0.3$, $G_C=1.6\text{ N/mm}$ [23].

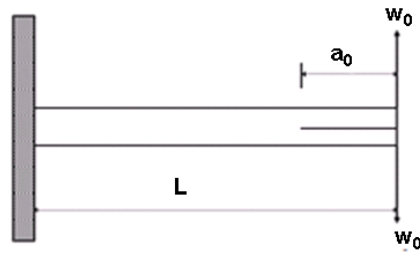


Fig. 4 DCB configuration [23]

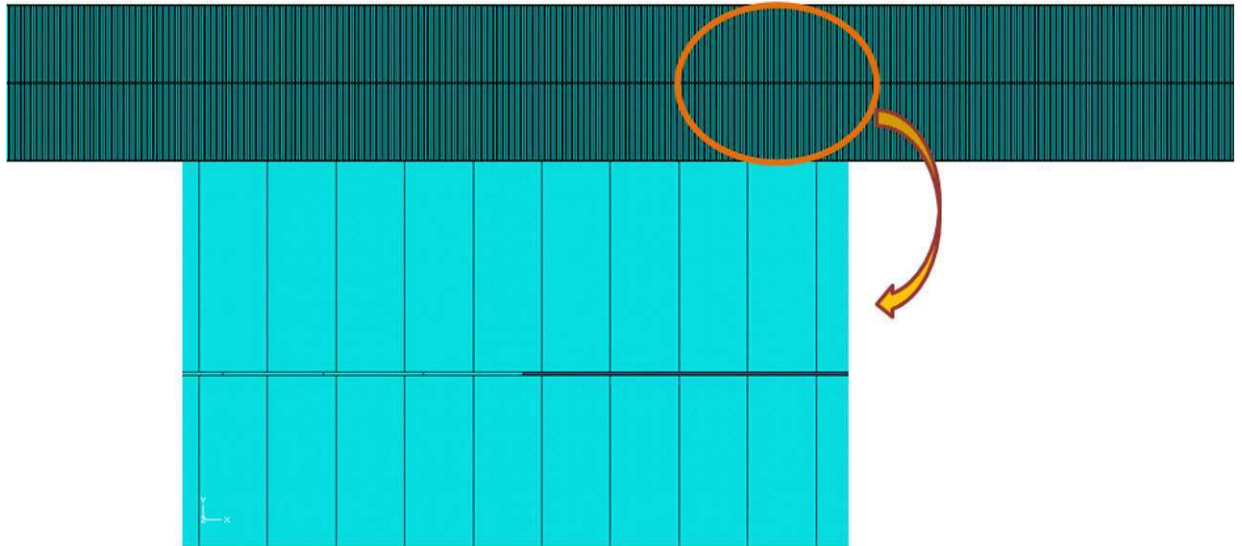


Fig. 5 Finite element model of the DCB configuration

The load history from the finite element simulation is compared to the experimental result of this DCB configuration tested at a cross head speed of 0.1mm/min. The corresponding load–displacement curves of the DCB tests are shown in Fig. 6. For the quasi-static loading, the model result was in excellent agreement with the experimental result [23].

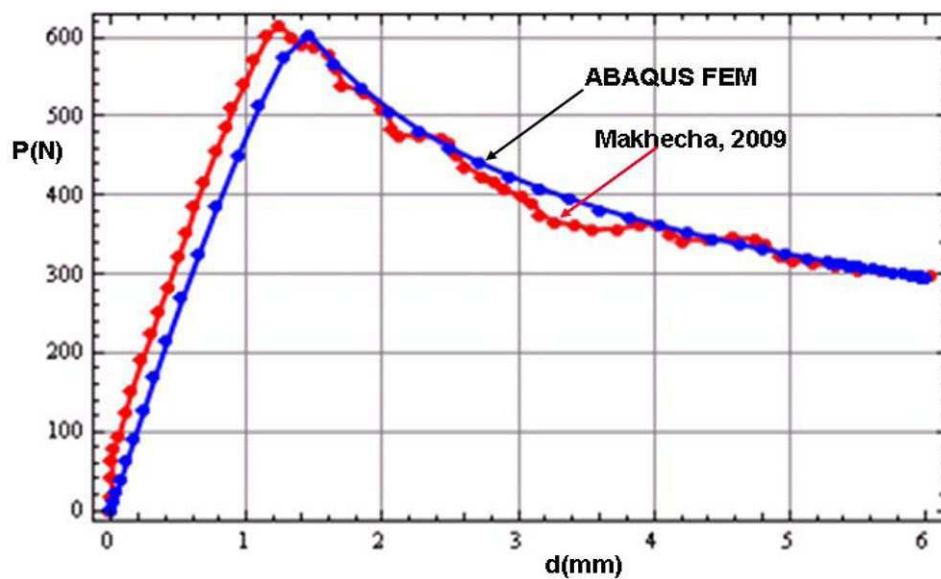


Fig. 6 Load–displacement curves using the nominal interface strength 40 MPa for a DCB test

Compression Delamination Model

Since we have experimental results for compression delamination test for Aluminum adherents with initial crack at the center point along the longitudinal distance of the adhesive [22], we developed compression delamination model following the exact shape of the experimental set-up for proper validation of the model response. The finite element model of the system and the boundary and loading conditions is shown in the Fig. 7. The left end is fixed, and the x -directional displacement is applied at the right end. Three layers of linear quadrilateral, type CPS4R (continuum plane stress 4 nodes reduced integration), elements are used for Aluminum, and one layer of linear quadrilateral, type COH2D4 (cohesive 2-dimensional 4 nodes), elements is used for the adhesive. The geometrical and mechanical properties of the system: adherent thickness=6 mm, joint length on each side = 80 mm, $E = 150$ GPa, $\nu = 0.25$, and $G_c = 0.352$ N/mm.

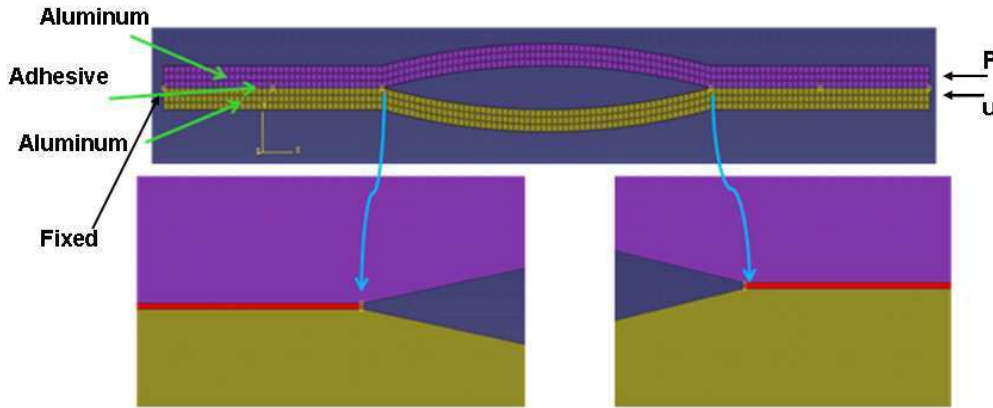


Fig. 7 Finite element model of the compression delamination test

The linear relationship between the reaction force and free end displacement was observed (Fig. 8) before the crack started to propagate. Reaction force had linearly increased to a certain peak, where the crack started to propagate. The simulation result showed similar response to that given by Chow [22].

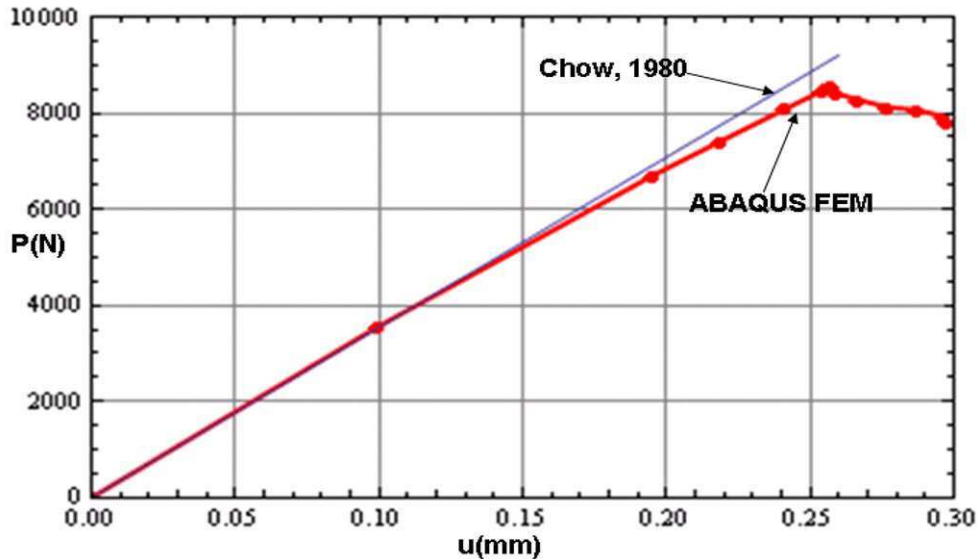


Fig. 8 Reaction force profile

7. Compression Delamination Under Different Constrained End Conditions

In this work, the DCB-specimen is studied under compression. The adhesive layer is modeled using cohesive elements. The effect of the compression and different constrained ends on the fracture is studied for different mesh densities of the cohesive interface. The geometry and the loading conditions of the DCB configurations are shown in Fig. 9 for fixed end and Fig. 10 for the top adherent with free end. The geometrical properties are the length $L=100$ mm; the arm thickness $t_1 = 2$ mm, $t_2 = 4$ mm, width $B = 4$ mm, and the initial crack length $a_0 = 50$ mm. The material properties for adherents are $E_1 = E_2 = 200$ GPa, $\nu = 0.3$, and for adhesive are ultimate strength = 35 MPa, and fracture energy = 0.7 N/mm.

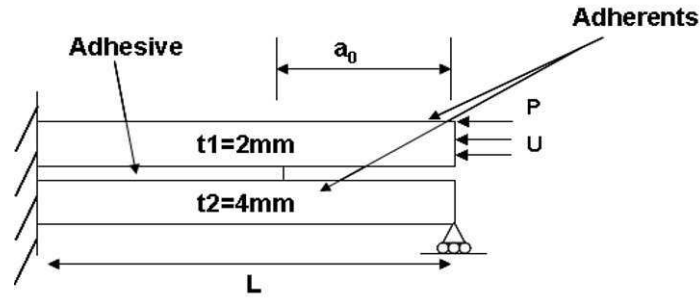


Fig. 9 DCB configuration for fixed end

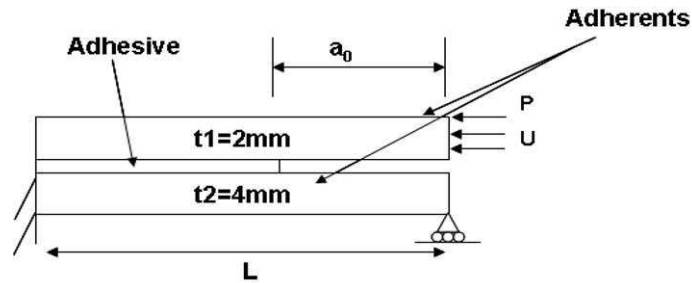


Fig. 10 DCB configuration for the top adherent with free end

The result of the delamination under compression for constrained end for different mesh densities of the cohesive interface is shown in Fig. 11. The reaction force continued to increase to a certain peak before the delamination started to propagate. The reaction force gradually decreased after the peak, since the delamination occurred like the peel delamination. After the reaction force rises to a certain peak, crack propagates until the entire interface fails. Fig. 12 shows the delamination characteristics for different mesh densities of the cohesive interface for the DCB configuration under compression with top adherent free. The reaction force had increased to a certain peak before the delamination suddenly propagated. The reaction force rapidly decreased after the peak, since the delamination occurred in the entire interface, at the same time, after the maximum tolerable deformation. Since for the free end case, the entire layer failed at a certain peak (with no gradual decrease), the reaction force was larger in the free end case.

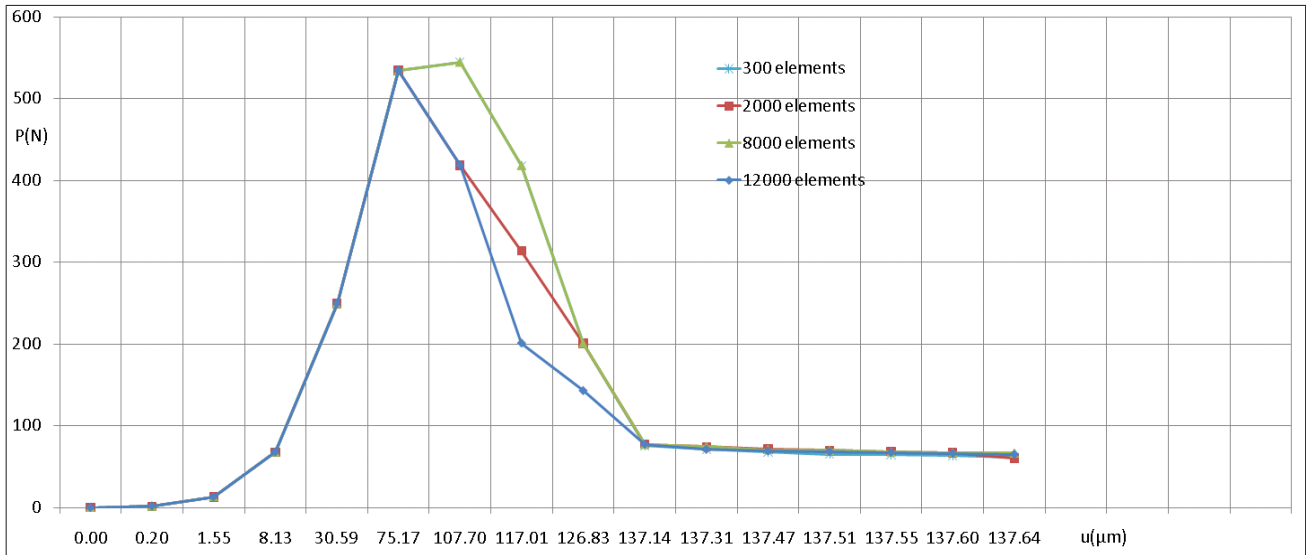


Fig. 11 Load displacement profile for fixed end DCB specimen with different mesh densities of the cohesive interface

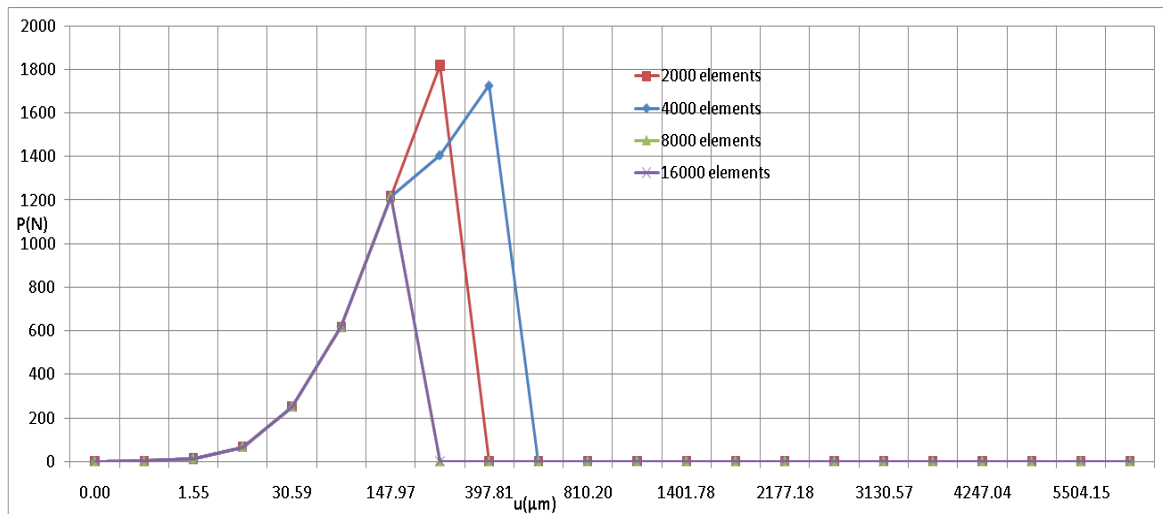


Fig. 12 Load displacement profile for free end DCB specimen with different mesh densities of the cohesive interface

However, in such trends inertia effect might be significant. For this reason, future work would be the study of effect of constrained ends on the delamination in adhesive joint under compression in dynamic case.

8. Conclusions

The delamination under compression in the adhesive joint was numerically investigated in this study. The delamination growth caused by compressive loads was modeled via softening behavior of cohesive interface elements. The effect of compression in crack propagation was studied and found to be in satisfactory agreement with experimental observations. A cohesive finite element model was developed for this blister test-piece, and the geometric non-linearity was incorporated in the strain/displacement relationship. The crack propagation through the adhesive joint under compression for the proposed test-piece was found to agree with the available experimental observation.

The effect of end constrained on the fracture resistance of the DCB specimen under compression was investigated. The numerical observations showed that for the fixed end DCB configuration, the reaction force had increased to a certain peak before the delamination started to propagate gradually. For the free end condition, on the other hand, the reaction force had increased to a certain peak before the delamination propagated rapidly. Since for the free end case the entire layer failed at a certain peak (with no gradual decrease), the reaction force was larger in the free end case.

References

- [1] Higgins, A., Adhesive Bonding of Aircraft Structures, *Int. J. of Adhesion & Adhesives*, 20, 367-376, 2000
- [2] Tafreshi, A., and Oswald, T., Global Buckling Behavior and Local Damage Propagation in Composite Plates With Embedded Delaminations, *Int. J. Press. Vessels Piping*, 80, 9-20, 2003.
- [3] Withcomb, J.D., and Shivakumar, K.N., Strain Energy Release Rate Analysis of Plates With Postbuckled Delaminations, *J. Comp. Mat.*, 23, 714-734, 1989.
- [4] Riccio, A., Perugini, P., and Scaramuzzino, F., Modelling Compression Behaviour of Delaminated Composite Panels, *J. Comp. and Struc.*, 78, 73-81, 2000.
- [5] Chai, H., Babcock, C. D., and Knauss, W. G., One Dimensional Modelling of Failure in Laminated Plates by Delamination Buckling, *Int. J. Solids Structures*, 17 (11), 1069-1083, 1981.
- [6] Gaudenzi, P., On Delamination Buckling of Composite Laminates Under Compressive Loading, *J. Comp. Struc.*, 39 (1-2), 21-330, 1997.
- [7] Hwang, S. F., and Mao, C. P., Failure of Delaminated Carbon/Epoxy Composite Plates Under Compression, *J. of Comp. Mat.*, 35 (18), 1634-1653, 2001.
- [8] Kim H., and Kedward, K. T., A Method for Modeling the Local and Global Buckling of Delaminated Composite Plates, *J. Comp Struc.*, 44, 43-53, 1999.
- [9] Kapania, R. K., and Wolfe, D. R., Buckling of Axially Loaded Beam Plate With Multiple Delaminations, *J. Press. Vess. Technol.*, 111, 151-158, 1989.

- [10] Yuan, H., and Xu, Y., Computational Fracture Mechanics Assessment of Adhesive Joints, *Computational Mat. Sc.*, 43, 146–156, 2008.
- [11] Plausinis, D., and Spelt, J. K., Designing for Time-Dependent Crack Growth in Adhesive Joints, *Int. J. Adhesion & Adhesives*, 15, 143-154, 1995.
- [12] Tvergaard, V., and Hutchinson, J. W., On the Toughness of Ductile Adhesive Joints, *J. Mech. Phys. Solids*, 44 (5), 789-800, 1996.
- [13] Katnam, K. B., Sargent, J. P., Crocombe, A. D., Khoramishad, H., and Ashcroft, I. A., Characterization of Moisture-Dependent Cohesive Zone Properties for Adhesive Joints, *J. Engg Frac. Mech.*, 77, 3105-3119, 2010.
- [14] Ameli, A., Papini, M., Schroeder, J. A., and Spelt, J.k., Fracture R-Curve Characterization of Toghened Epoxy Adhesives, *J. Engg Frac. Mech.*, 77, 521-534, 2010.
- [15] Yang, Q. D., and Thouless, M. D., Mixed-Mode Fracture Analysis of Plastically Deforming Adhesive Joints, *Int. J. of Frac.*, 110, 175-187, 2001.
- [16] Madhusudhana, K. S., and Narasimhan, R., Experimental and Numerical Investigations of Mixed Mode Crack Growth Resistance of a Ductile Adhesive Joint, *J. Engg. Frac. Mech.*, 69, 865-883, 2002.
- [17] De-Morais, A. B., and Pereira, A. B., Mixed Mode II+III Interlaminar Fracture of Carbon/Epoxy Laminates, *J. Composites Sc. and Tech.*, 68, 2022-2027, 2008.
- [18] Szekrenyes, A., Delamination Fracture Analysis in the G_{II} - G_{III} Plane Using Prestressed Transparent Composite Beams, *Int. J. of Solids and Struc.*, 44, 3359-3378, 2007.
- [19] Marannano, G. V., Mistretta, L., Cirello, A., and Pasta, S., Crack Growth Analysis at Adhesive-Adherent Interface in Bonded Joints Under Mixed Mode I/II, *J. Engg. Fract. Mech.*, 75, 5122-5133, 2008.
- [20] Guo, Y. J., and Weitsman, Y. J., A Modified DCB Specimen to Determine Mixed Mode Fracture Toughness of Adhesives, *J. Engg Frac. Mechanics*, 68, 1647-1668, 2001.
- [21] Sun, C., Thouless, M. D., Waas, A. M., Schroeder, J. A., and Zavattieri, P. D., Rate Effects for Mixed-Mode Fracture of Plastically-Deforming Adhesively-Bonded Structures, *Int. J. of Adhesion & Adhesives*, 29, 434-443, 2009.
- [22] Chow, C. L., and Ngan, K. M., Method of Fracture Toughness Evaluation of Adhesive Joints, *J. of Strain Analysis*, 15(2), 97-101, 1980.
- [23] Makhecha, D. P., Kapania, R. K., Johnson, E. R., Dillard, D. A., Jacob, G. C., and Starbuck, M. J., Rate-Dependent Cohesive Zone Modeling of Unstable Crack Growth in an Epoxy Adhesive, *Mechanics of Adv. Mat. and Struc.*, 16, 12-19, 2009.
- [24] Dugdale, D. S., Yielding of Steel Sheets Containing Slits, *J. Mech. Phys. Solids*, 8, 100-104, 1960.
- [25] Barenblatt, G. I., The Mathematical Theory of Equilibrium Crack in the Brittle Fracture, *Advances in Applied Mechanics*, 7, 55-125, 1962.
- [26] Needleman, A., An Analysis Decohesion Along an Imperfect Interface, *Int. J. Fracture*, 42, 21-40, 1990.
- [27] ABAQUS User Manual, Version 6.9, ABAQUS, Inc., Providence R.I.
- [28] Daudeville, L., Allix, O., and Ladeveze, P., Delamination Analysis by Damage Mechanics: Some Applications, *J. Composites Engg.*, 5(1), 17-24, 1995.

Simulation of Stable Tearing Crack Growth

Using the Cohesive Zone Model Approach

Xin Chen¹, Xiaomin Deng², Michael A. Sutton³

1. Graduate Research Assistant, Department of Mechanical Engineering, University of South Carolina

2. Professor and Corresponding author, Department of Mechanical Engineering, University of South Carolina.

Tel: 803-777-7144; Email: deng@cec.sc.edu

3. Professor, Department of Mechanical Engineering, University of South Carolina

Abstract

A cohesive zone model (CZM) based approach is applied with 3D finite element method to simulate stable tearing crack growth events in Arcan specimens made of 2024-T3 aluminum alloy. The CZM parameter values are calibrated for a triangular cohesive law under Mode I condition. Simulation prediction of the load-crack extension curve compares reasonably well with experimental data. With the same set of CZM parameter values, simulations are performed for mixed Mode I/II stable tearing crack growth events as well. A good agreement is also reached between the simulation predictions and the experimental results. The CTOD variation with crack extension is also checked under both Mode I and mixed-mode I/II conditions. The results suggest that CZM based simulations can predict the critical CTOD value, which conventionally is used as an input in CTOD based stable tearing simulations and is obtained from experimental measurements. The findings of the current study establish a connection between CTOD and CZM based simulation approaches.

Keywords: Cohesive zone modeling; Finite element analysis; Crack growth; Mixed-mode fracture; Stable tearing

1. Introduction

The analysis of stable crack growth events plays an important role in assessing the structural integrity and residual strength of critical engineering structures such as aircraft frames. In practice, fracture criteria based on the concept of crack tip opening displacement/ angle (CTOD/CTOA) have been shown to be effective in stable crack growth simulations. Computational studies under Mode I (e.g. [1]) and mixed-mode (e.g. [2]) conditions have been performed to assess the viability of a CTOD/CTOA based fracture criterion for simulations of stable tearing crack growth. As an alternative approach, the cohesive zone model (CZM) [3-5] represents the behavior of the fracture process zone and describes the relationship between cohesive tractions and separations across the cohesive crack surfaces. The CZM approach has been used to simulate fracture processes in a wide range of material systems and at multi-length scales[6]. The current study aims at investigating the applicability of the CZM based approach in simulating mixed-mode stable tearing crack growth events in ductile materials. The CZM parameter values will be calibrated by trial & error based on certain physical considerations of Mode I stable tearing crack growth. Predictions of mixed-mode I/II tearing crack

growth will be performed using the same CZM parameter values. The variation of CTOD with crack extension and the load-crack extension curve will be examined under both Mode I and mixed-mode I/II conditions and compared with experimental measurements. An effort will be made to establish a connection between the CZM approach and the CTOD approach.

2. Arcan fixture and specimen for stable tearing crack growth tests

The Arcan fixture and specimen are designed to facilitate stable tearing crack growth tests under the mixed-mode loading conditions ranging from pure mode I to pure mode II [7]. The Arcan fixture, which is shown in Fig. 1a, is made of stainless steel and has a Young's modulus of 207 GPa, a Poisson's ratio of 0.3, and an initial yield stress of 1,724 MPa. The test specimen, as shown in Fig. 1b, is made of 2024-T3 aluminum alloy and has a Young's modulus of 71.7 GPa, a Poisson's ratio of 0.3, and an initial yield stress of 345 MPa. Both the steel and the aluminum alloy exhibit a strain-hardening behavior. A single-edge crack with a 6.35 mm length is introduced on one side at the mid-section of the specimen. The Arcan specimen is loaded by gradually pulling apart the grips of the fixture at a pair of grip holes on the opposite sides of a radial line. When the loading angle, Φ , is zero, the specimen is under Mode I condition, while Φ equals to 90° , the specimen is under Mode II condition. Between the two angles, the mixed-mode loading conditions are obtained by changing the pair of loading holes.

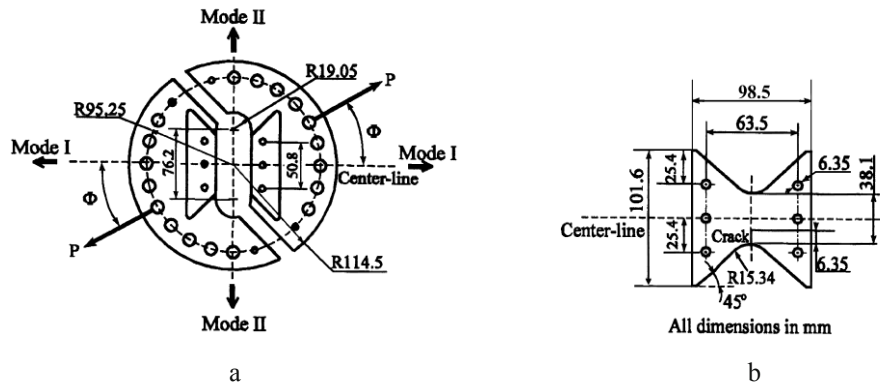


Fig. 1 A schematic of: a. the Arcan test fixture and b. test specimen

3. Finite element modeling

CZM simulations are carried out using the commercial software ABAQUS. The fixture and the specimen are meshed with 8-node hexahedral elements, C3D8R, while the cohesive zone is meshed with 8-node quadrilateral cohesive interface elements, COH3D8. A layer of cohesive elements is placed along the experimentally measured Mode I crack path, starting from the initial crack tip (at the left edge of the specimen) to the right edge of the specimen. At the right end of this layer, a few cohesive elements along the crack path are removed and node pairs above and below the crack path are tied together at the location of the removed elements. This will prevent the penetration between the top and bottom cohesive surfaces due to the overall bending of the specimen as the crack grows and becomes sufficiently long. Based on the result of convergence study, the mesh in the specimen region is divided into eight layers through the thickness and the cohesive elements have a uniform length 0.05mm. Fig. 2 shows the 3D mesh (Fig. 2a) and a zoomed-in view of the cohesive interface elements (Fig. 2b) for the Mode I case.

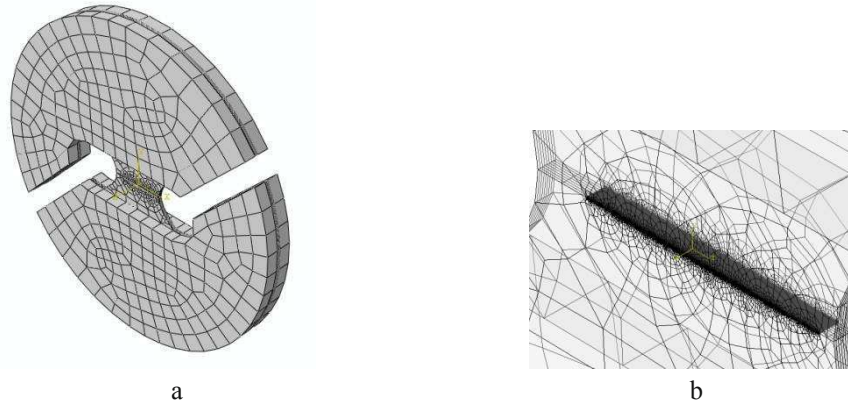


Fig. 2 a. 3D mesh of the Arcan fixture-specimen system for the Mode I case; b. a zoomed-in view of the mesh showing the cohesive interface elements

4. Calibration of triangular cohesive law parameter values

The triangular traction-separation cohesive law, as shown in [fig. 3](#), was used in this study. The triangular cohesive law contains two critical parameters: the cohesive strength T_{\max} (the maximum traction the interface can endure) or the separation length δ_{sep} , and the cohesive energy Π which is the area of the triangle. As such, the two parameters T_{\max} and δ_{sep} can be chosen as the two input parameters. It is a common practice to let the cohesive energy Π equal the energy fracture toughness of the material, ϕ_c . Thus, $\delta_{\text{sep}} = 2\phi_c / T_{\max}$.

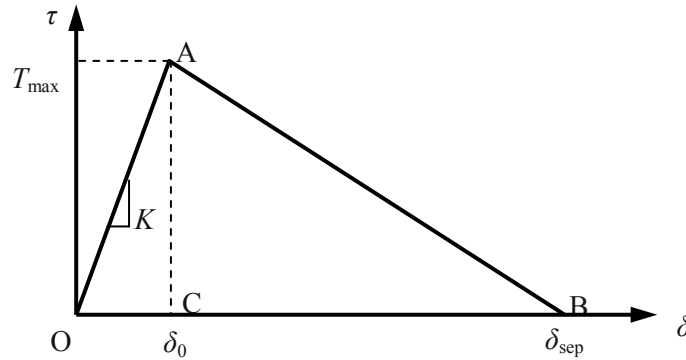


Fig. 3 The triangular cohesive traction-separation law

The cohesive parameter values for TL oriented aluminum alloy 2024-T3 will be selected by trial and error based on the values used in the literature[6,8,9], through matching simulating predictions of the Mode I load-crack extension curve with experimental data. From the fracture toughness $K_{IC}=35 \text{ MPam}^{1/2}$ for AL2024-T3 thin sheet specimens, ϕ_c was set as 17 KJ/m^2 for exponential cohesive law in [9]. Since the traction in the exponential CZM approaches 0 at infinite separation, the area under the cohesive curve (the cohesive energy) is larger than that of the triangular CZM. Thus, the cohesive energy for the triangular CZM here is taken to be 95% of the value for the exponential CZM. The cohesive strength T_{\max} is chosen from the range of $1.0\sigma_y$ to $2.5\sigma_y$, where σ_y is the initial yield stress of AL2024-T3.

5. Results and discussions

5.1 Load-crack extension curve

The load-crack extension curve is an important curve in structural integrity and residual strength analyses, describing the variation of the load carrying capability of a cracked specimen or structure with the amount of crack extension during

stable tearing crack growth. In the simulations, the load corresponding to a certain amount of crack extension is computed by finding the reaction force at the fixed points.

After a range of trials for the Mode I case, a proper set of CZM parameter values is found as $T_{\max} = 2.2\sigma_y = 759\text{MPa}$ and $\delta_{\text{sep}} = 0.0426\text{mm}$. A comparison of computer simulation results with experimental measurements is shown in [fig. 4](#), the simulating results of traction-crack extension relation agree with the experimental data reasonably.

The prediction of the load-crack extension curve has often been made using a fracture criterion based on the crack tip opening displacement (CTOD) [10]. In the case of the Mode I stable tearing crack growth in an Arcan specimen, good agreement between experimental data and simulation predictions based on the CTOD criterion have been demonstrated using both a 2D model [11] and a 3D model [2]. The simulation prediction[2] of the load-crack extension curve using CTOD approach is also compared in [fig. 4](#). It is shown that the CZM and CTOD approaches lead to similar predictions, showing good agreement with the experimental data.

5.2 Variation of CTOD with crack extension

To understand if there exists any connection between CZM and CTOD based simulations, it is important to examine the CZM simulation prediction of the CTOD value at the same distance away behind the current crack as in the experimental measurement of CTOD.

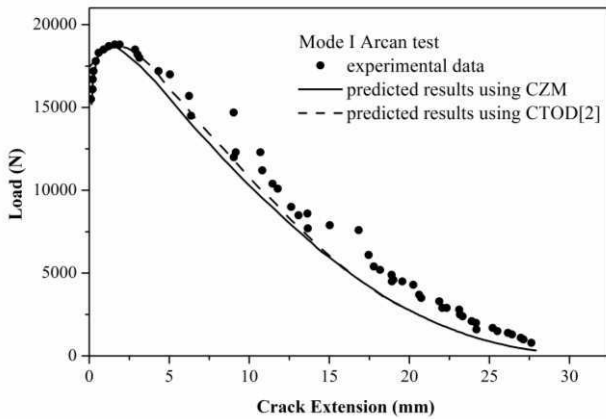


Fig. 4 Comparison of simulation prediction of the Mode I load-crack extension curve using CZM ($T_{\max} = 759\text{ MPa}$, $\delta_{\text{sep}} = 0.0426\text{ mm}$) with experimental measurements[7,12] and predicted results[2] using CTOD approach

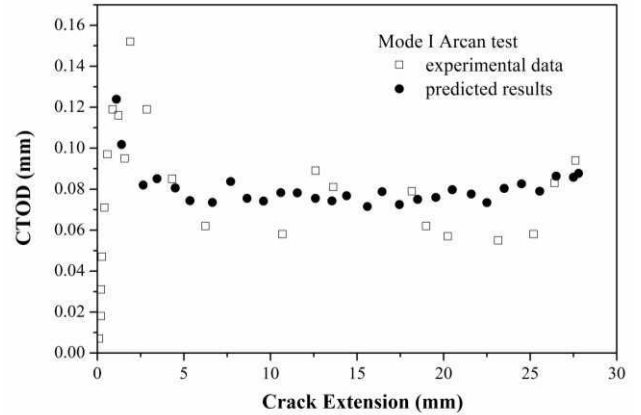


Fig. 5 Comparison of CZM prediction for CTOD at 1mm behind the crack tip with experimental measurements[7,12]

In a CTOD based simulation, a critical CTOD value used as input to control the crack growth process. This critical CTOD value is determined based on experimental measurement at a fixed distance behind the crack front. If this value can be predicted using the CZM approach, then a connection between the CTOD and CZM approach is established. In the current study, since the distance of 1.0 mm was used in the experimental measurement of CTOD, this distance is also employed in the simulations when CTOD is computed. In [Fig. 5](#), with the CZM approach, Mode I predictions of CTOD variation with crack extension are compared with the experimental measurements. The predictions lay in the range of the experimental data. Thus, it can be argued that there exists an equivalence or connection between the CZM and CTOD approaches and both types of simulations lead to good predictions of the load-crack extension curve.

6 Prediction of mixed Mode I/II of tearing crack using CZM

The simulations of mixed-mode I/II stable tearing crack growth events are performed using 3D finite element models based on the discussion of mode I models. The only difference is that the predefined crack paths are modified to those measured from experiments in the mixed-mode I/II conditions. With the same set of CZM parameter values obtained for the Mode I case, the load-crack extension curves and the CTOD variation with crack extension are predicted for two different mixed-mode conditions, corresponding to the 15° and 45° loading cases.

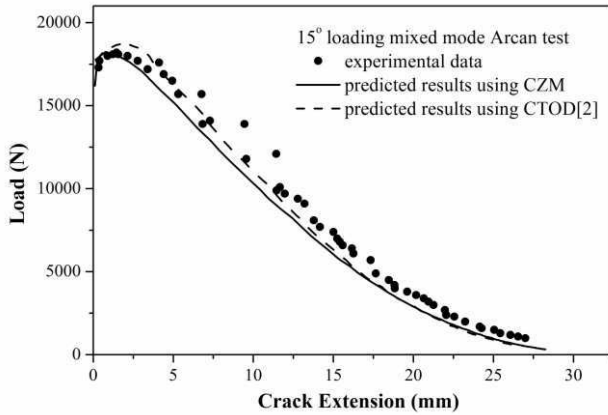


Fig. 6 Comparison of prediction of the load-crack extension curve using CZM with experimental measurements[7,12] and predicted results[2] using CTOD (15° loading)

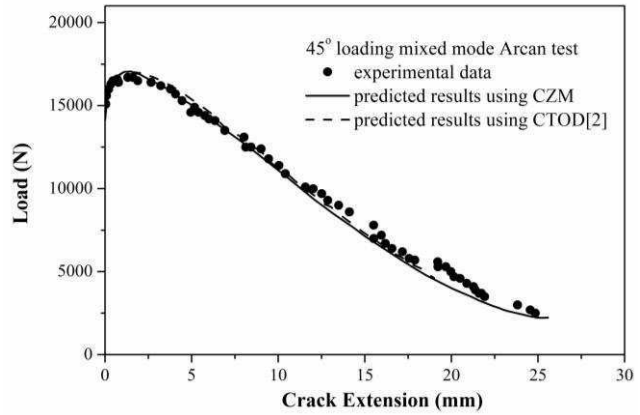


Fig. 7 Comparison of prediction of the load-crack extension curve using CZM with experimental measurements[7,12] and predicted results[2] using CTOD (45° loading)

As shown in [fig. 6](#) and [fig. 7](#), the CZM approach can be successfully applied to evaluate stable tearing crack growth under mixed-mode I/II loading conditions. The predicted results of load-crack extension responses using both the CTOD and CZM approaches agree well with the experimental measurements. CTOD variations with crack extension at 1mm behind the crack front are obtained for two mixed-mode loading cases. The predicted results, including the ones for the Mode I case, are compared with the experimental measurements [7,12] in [fig. 8](#). For all of the three loading conditions, the predicted results locate in the range of the corresponding experimental measurements. The average values are

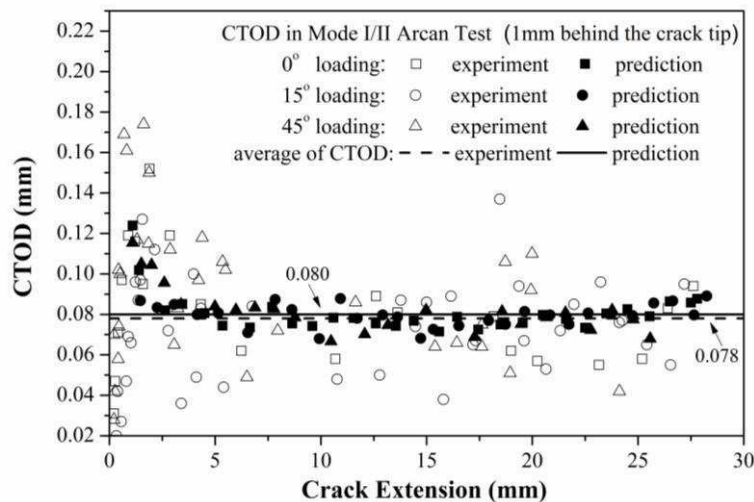


Fig. 8 Comparison of predicted and measured CTOD variation with crack extension under Mode I and mixed-mode I/II conditions

calculated for the predictions and the experimental data, respectively, and are plotted in [fig. 8](#) as well. Two average values reasonably match with each other. The experimental average is the critical CTOD value employed in the CTOD based simulations. The fact that the measured and CZM-predicted critical CTOD values match explains why both the CZM and CTOD based simulations lead to the same good predictions of the load-crack extension curve. Again this demonstrates a certain equivalence or connection between the CZM and CTOD based simulation approaches.

7. Conclusions

A cohesive zone model (CZM) based approach is applied to simulate mixed-mode stable tearing crack growth events in Arcan specimens made of 2024-T3 aluminum alloy. 3D finite element models are developed in Abaqus employing the triangular CZM law. From the current study, the CZM based approach can be successfully applied to simulate stable tearing crack growth events in ductile materials under both of Mode I and mixed-mode I/II loading conditions. A proper set of CZM parameter values is reached for Mode I case and is used for the mixed-mode cases. Both the CZM and CTOD based approaches lead to same simulation predictions of the load-crack extension curve that compare well with experimental measurements. The critical CTOD value used in CTOD based simulations, which is conventionally taken from experimental data, can be predicted using the CZM based approach, which establishes certain equivalence or connection between the CZM and CTOD based simulation approaches.

References

- [1] Newman JC Jr, Dawicke DS, Bigelow CA. Finite element analyses and fracture simulation in thin sheet aluminum alloy. NASA, TM-107662, 1992.
- [2] Lan W, Deng X, Sutton MA. Three-dimensional finite element simulations of mixed-mode stable tearing crack growth experiments. *Eng Fracture Mechanics*; 74:2498-2517, 2007.
- [3] Barenblatt GI. The formation of equilibrium cracks during brittle fracture. General ideas and hypothesis. Axially-symmetric cracks. *Prikl. Matem. I mekham*; 23: 434-444, 1959.
- [4] Barenblatt GI. Mathematical theory of equilibrium cracks. In: *Advances in Applied Mechanics*, vol. 7. Academic Press, New York, pp. 55-125, 1962.
- [5] Dugdale DS. Yielding of steel sheets containing slits. *J. Mech. Phys. Solids*; 8: 100-108, 1960.
- [6] Shet C, Chandra N. Analysis of Energy Balance When Using Cohesive Zone Models to Simulate Fracture Processes. *J Eng Materials Tech*; 124:1-11, 2002.
- [7] Amstutz BE, Sutton MA, Dawicke DS, and Newman JC Jr.. An Experimental Study of CTOD for Mode I/modelII Stable Crack Growth in Thin 2024-T3 Aluminum Specimens. *Fracture Mechanics*, STP 1256 American Society for Testing and materials; 256-271, 1995.
- [8] Roychowdhury S, Yamuna DAR, Doddds RH Jr. Ductile tearing in thin aluminum panels: experiments and analyses using large-displacement, 3-D surface cohesive elements. *Eng Fracture Mechanics*; 69: 983-1002, 2002.
- [9] Li W, Siegmund T. An analysis of crack growth in thin-sheet metal via a cohesive zone model. *Eng Fracture Mechanics*; 69(18): 2073-2093, 2002.

- [10] Sutton MA, Deng X, Ma F, Newman JC Jr. and James M. Development and application of a crack tip opening displacement-based mixed mode fracture criterion. *Int. J of Solids and Structures*; 37: 3591-3618, 2000.
- [11] Deng X, Newman JC Jr.. A study of some issues in stable tearing crack growth simulations. *Eng Fracture Mechanics*; 64: 291-304, 1999.
- [12] Amstutz BE, Sutton MA, Dawicke DS, Boone ML. Effects of mixed mode I/II loading and grain orientation on crack initiation and stable tearing in 2024-T3 aluminum. *ASTM STP 1296 on Fatigue and Fracture Mechanics*, 27:105-126, 1997.

Experimental and Numerical Results for Diffusion Bonded Joints

A.H.M.E. Rahman, Ph.D. Student, Department of Mechanical Engineering
University of North Dakota

M.N. Cavalli, Associate Professor and Chair, Department of Mechanical Engineering
University of North Dakota, 243 Centennial Drive, Stop 8359, Grand Forks, ND 58202-8359
matthewcavalli@mail.und.nodak.edu

ABSTRACT

Commercially pure Fe and Ni have been diffusion bonded. Pure Cu (99.999%) and Au-20Sn eutectic alloys have been used to bond Fe while Cu has been used to bond Ni. Fe bonded using Cu at 1071°C for 10 h showed ~20 μm thick residual Cu in the bond centerline. However, at 1100°C bonding temperature for 10 h the residual Cu disappeared and the Cu content of the joint centerline was ~7wt.%. Although Sn forms intermetallics with both Fe and Au, no intermetallics were found when Au-20Sn eutectic was used to bond Fe at 600-650°C for 10h. Ni bonded at 1071°C for 10h contained 40 wt.% Cu in the joint centerline with the Cu content decreasing gradually with increasing distance from the bondline. Cu content in the bond centerline decreased to 35wt.% at 1100°C for 10 h. The concentration profiles of Cu in a Ni-Cu diffusion couple were simulated with DICTRA/Thermocalc. The simulated profiles were comparable to the experimental profiles. The ultimate tensile strengths obtained for Fe-Cu system were 245 and 276 MPa at 1085 \pm 1 and 1090 \pm 1°C for 10 h, respectively.

INTRODUCTION

To enhance overall efficiency, the operating temperatures of aero-engines and power generation turbines are continuously increasing. Higher operating temperatures result in increased effects from creep, fatigue and corrosion causing rapid degradation of the components. This damage requires the repair of these components in order to extend their total life and to keep the material costs to a minimum. Two material families that are often used in hot sections of aero-engines and power generation turbines are nickel-based superalloys and stainless steels. Since these alloys are exposed to severe operating conditions, they require resistance to high temperature creep, sufficient tensile strength and corrosion resistance [1]. For example, stainless steels are generally used in process plants, petrochemical industries, aero-engine hot section components, pump and valve shafts, steam generators, expansion joints, super-heaters, re-heaters, etc. because of their high strength, ductility, resistance to creep and resistance to corrosion at elevated temperatures [2].

The most widely used repair process for metals and alloys is the fusion welding process, which typically involves relatively large scale melting at the joint line and the introduction of a filler metal. Depending on the material chemistry, borides and silicides can be formed during fusion welding. These phases are brittle and detrimentally affect the mechanical properties of the joints [3-5]. Also, weldability of nickel-based superalloys largely depends on the Ti and Al content. Precipitation-hardened nickel-based superalloys containing high Al and Ti are susceptible to heat affected zone (HAZ) cracking during welding and post-weld heat treatment [6-8]. Different stainless steels also show intergranular cracks in the HAZ during fusion welding. Fusion welding disrupts the ferrite-to-austenite ratio in duplex stainless steels [9]. In contrast to fusion welding, diffusion bonding is a joining process in which bonding is primarily due to atomic diffusion between base metals and filler materials (if any). Melting may occur, as in the case of transient liquid phase (TLP) bonding in which a filler metal or alloy with a relatively low melting temperature is used. Joints may also remain solid throughout the diffusion bonding process if a phase with a higher melting temperature forms before reaching the bonding temperature. Acceptable joint morphology depends on proper control of the thermodynamics and kinetics of the materials involved in the joining process. Transient liquid phase bonding (TLP), or diffusion brazing, has become a preferred method of joining for both nickel-based superalloys and stainless steels [10]. Optimum joint quality requires proper control of parameters which includes temperature, time, filler alloy composition and thickness.

To simulate diffusion-controlled transformations, two steps are required: (1) calculation of the thermodynamic quantities, and (2) modeling of the kinetics of the transformation. Thermocalc, developed at the Royal Institute of Technology in Stockholm, can predict the correct equilibrium state in multi-component alloy systems [11]. DICTRA (Diffusion Controlled TRAnsformation), can simulate the diffusion controlled transformation in multi-component systems [12]. DICTRA is a finite difference code and uses a Newton-Raphson iteration technique to solve the multi-component diffusion equation. In solving the diffusion equation, DICTRA uses kinetic databases and recalls thermodynamic quantities from Thermocalc. The accuracy of DICTRA simulations depends on the accuracy of the thermodynamic and kinetic data and can be verified by comparison with experimental results.

In the present investigation, commercially pure iron and nickel are diffusion bonded using different interlayers. The ultimate goal of the work is to optimize bonding conditions, including temperature, bonding time, interlayer type and thickness, with respect to the resulting joint strength. Joint microstructures and chemical compositions are reported. The concentration profiles of the diffusing species in a diffusion couple are simulated using DICTRA/Thermocalc software and compared with experimental results.

EXPERIMENTAL METHOD

Initial studies of the diffusion bonding joint morphology were performed using base metal rods with a diameter of 6.35 mm, 8 mm long. After cutting, the samples were polished to a 1200 grit finish and cleaned in an ultrasonic bath using isopropyl alcohol. The interlayer foils were cut the same diameter as the base metal rods. Immediately after cleaning, the samples were placed in a jig and put in a tube furnace. The tube was repeatedly evacuated and purged with argon gas. All bonding was done under vacuum. The bonding jig was made of Kovar to minimize the thermal expansion mismatch. Following morphology studies, the tensile specimens were fabricated. The specimens had a gauge length of 59 ± 0.5 mm and diameter of 9.0 ± 0.1 mm. These specimens were also polished to a 1200 grit finish and cleaned in ultrasonic bath. The sample geometries are shown in Fig. 1.

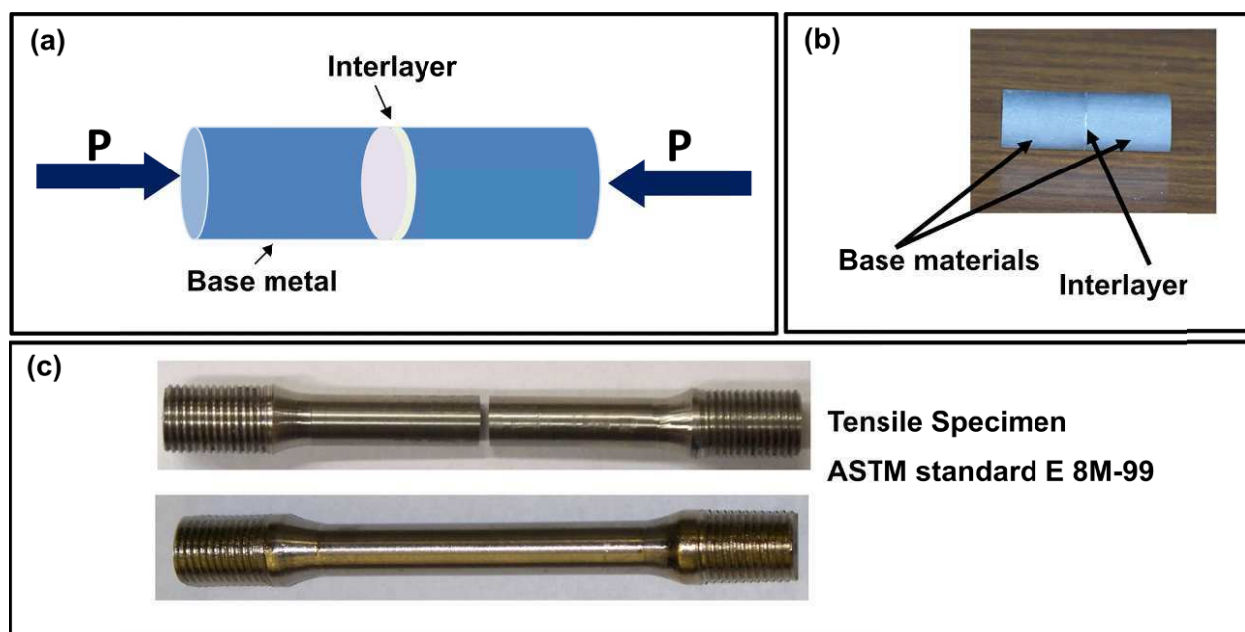


Fig. 1 (a) Schematic of diffusion bond geometry, (b) diffusion bonded sample and (c) tensile specimen before and after diffusion bond

Cu interlayer was used for bonding both commercially pure Fe and Ni while Au-20Sn interlayer was used for Fe only. Cu foil has been selected because it does not form any intermetallics with either Fe or Ni and it has a melting temperature less than either of the base metals. The thicknesses were 100 and 25 μm for Cu interlayers and 100 μm for Au-20Sn interlayers. The bonding temperatures were 1050°C to 1100°C for Cu interlayers. For Au-20Sn interlayers, 600-650°C temperatures were used. Following bonding, the morphology samples were mounted in epoxy and polished perpendicular to the bondline to prepare for metallography. The morphology of the bonded samples was examined using a Hitachi S-3400N scanning electron microscope and the composition and different phases in the bond area were determined by energy dispersive spectrometry.

(EDS). The strength of the tensile specimens were measured using a Shimadzu AG-IS 50kN universal testing machine. Samples were tested under a cross-head speed of 1mm/min.

For the numerical simulation, only half of the joint was used modeled due to symmetry. The integration points were assumed to be linearly distributed throughout the Fe-Cu diffusion couple. The input parameters were bonding temperature, bonding time, heating and cooling rate, compositions and phases of the diffusion couple. To initiate the calculation, the Cu region was set with a 'seed' of 0.001 wt.% Ni in it and Ni region was set with a 'seed' of 0.1 wt.% Cu in it.

RESULTS AND DISCUSSION

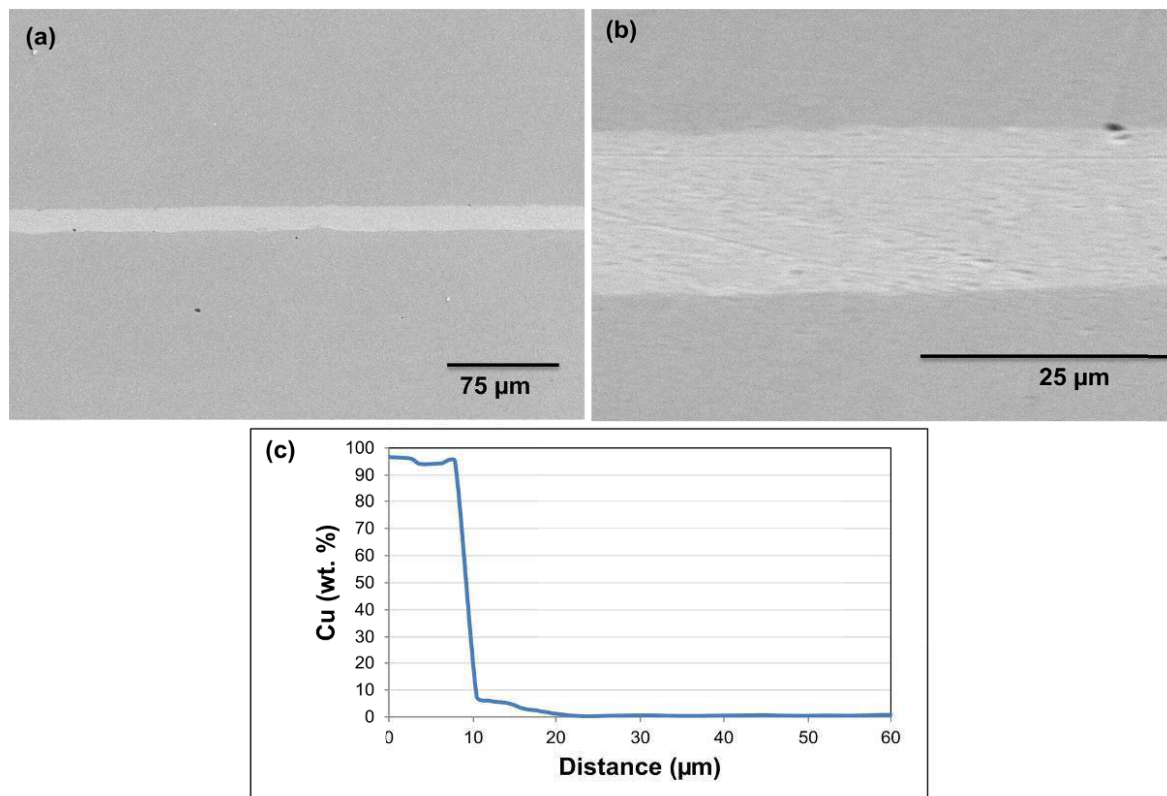


Fig. 2 (a) SEM images of diffusion bonded Fe using Cu interlayer (25 μm) at 1071°C for 10h, (b) magnified image of (a) and (c) Concentration profile of Cu from the bond centerline to the interior of base metal

Initially, 1050°C and 100 μm C foil was used for bonding Fe, but the interdiffusion was negligible. The temperature was then increased to 1071°C and the foil thickness was decreased to 25 μm. Fig. 2 shows (a) SEM images of diffusion bonded Fe using Cu interlayer (25 μm) at 1071°C for 10h, (b) magnified image of (a) and (c) concentration profile of Cu from the bond centerline to the interior of base metal. A significant amount of Cu remained at the centerline of the joint. The thickness of the residual Cu was ~20μm (the foil thickness was 25 μm). The concentration profile indicates that the Cu concentration suddenly dropped just after interface and gradually decreased after that. The Fe content in the residual Cu was ~3 wt.%. According to the Fe-Cu phase diagram (Figure 3) γ-Fe can dissolve ~ 7.2 wt.% Cu at 1100°C and ε-Cu can dissolve ~ 4.15 wt.% Fe at the same temperature [13]. So, to enhance the inter-diffusion, the bonding temperature was increased to 1100°C.

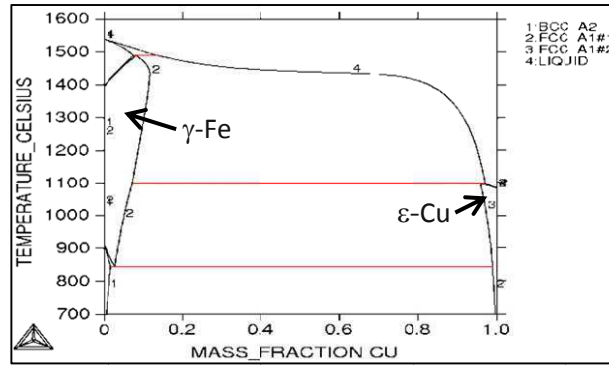


Fig. 3 Phase diagram of Fe-Cu generated using Thermocalc software [11]

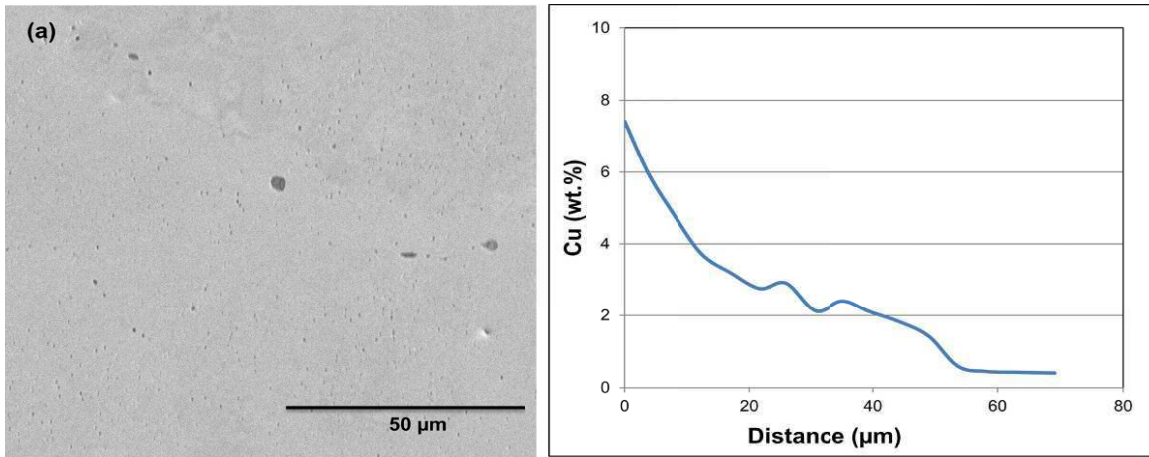


Fig. 4 (a) SEM images of diffusion bonded Fe using Cu interlayer (25 μm) at 1100°C for 10h and (b) the concentration profile of Cu taken from the bond centerline to the interior of the base metal

Fig. 4 shows (a) SEM images of diffusion bonded Fe using Cu interlayer (25 μm thick) at 1100°C for 10h and (b) the concentration profile of Cu taken from the bond centerline to the interior of the base metal. The bond centerline contains only ~ 7.4 wt.% Cu. In diffusion bonding it is necessary for the interlayer to diffuse into the base metal as completely as possible so that the bond strength remains close to that of the base metal. However, some micro-pores appeared in the joint area. This might be due to the fact that γ-Fe gets supersaturated at 7.2 wt.% Cu while ε-Cu gets supersaturated at 4.15 wt.% Fe at 1100°C; this may create an atomic flux imbalance. Investigations into this phenomenon are ongoing.

Fig. 5 shows SEM images of diffusion bonded Fe using Au-20Sn interlayer (100 μm thick) (a) at 600°C for 10h, (b) magnified image of (a) and (c) at 650°C for 10h. After holding at 600°C for 10 h, almost all interlayer has been diffused into the base metal. The thickness of the residual interlayer was less than a micrometer with a composition of 40-45 wt.% Au and 19-21 wt.% Sn. The joint area away from the residual interlayer contains a maximum of 4 wt.% Au and 0.2 wt.% Sn and decreased gradually. No intermetallics were found in the joint area. After increasing the bonding temperature to 650°C, the residual interlayer disappeared. Fast diffusion occurred at such a low temperature because the Au-20Sn eutectic alloy has a melting temperature of 277°C.

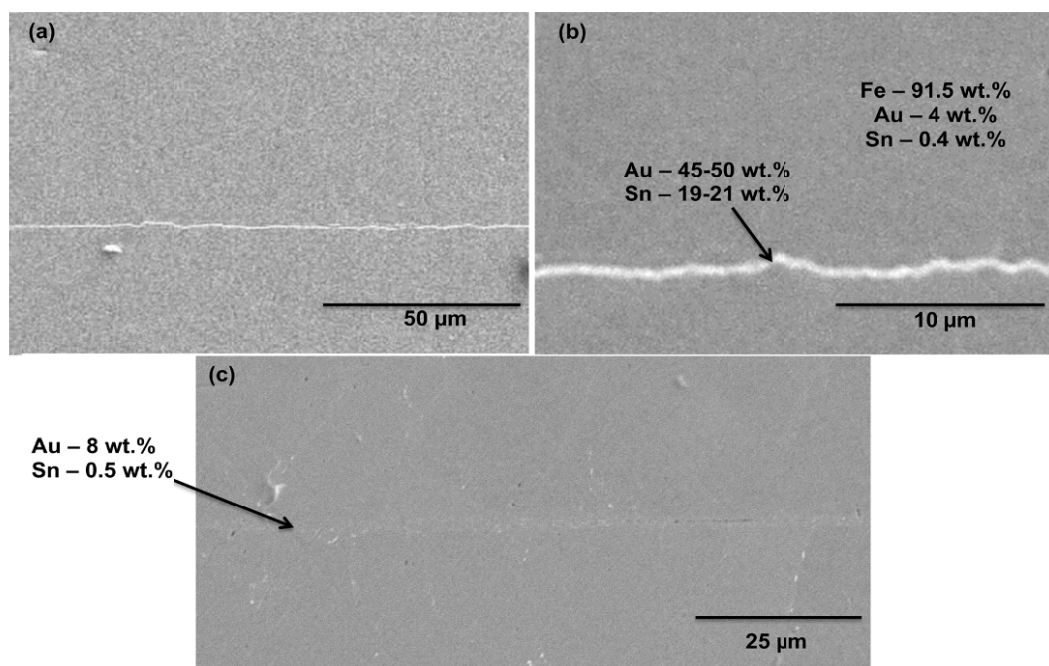


Fig. 5 SEM images of diffusion bonded Fe using Au-20Sn interlayer (100 μm) (a) at 600°C for 10h, (b) magnified image of (a) and (c) at 650°C for 10h

Fig. 6 shows (a) SEM image of diffusion bonded Ni using Cu interlayer (25 μm thick) at 1071°C for 10 h and (b) measured and predicted (DICTRA) concentration profiles of Cu from the bond centerline to the interior of base metal. The microstructures of the base metal and the joint area were not distinguishable because Cu and Ni form a complete solid solution in any composition range. The composition of the bond centerline was ~ 40 wt.% Cu and the Cu content decreased gradually away from the bond centerline. DICTRA was able to capture the diffusion behavior of the system quite well.

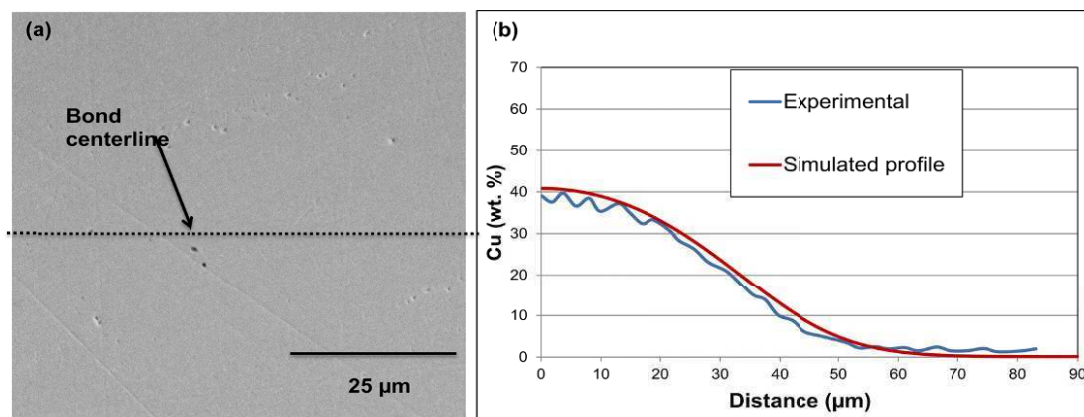


Fig. 6 (a) SEM image of diffusion bonded Ni using Cu interlayer (25 μm) at 1071°C for 10 h and (b) concentration profile of Cu from the bond centerline to the interior of base metal

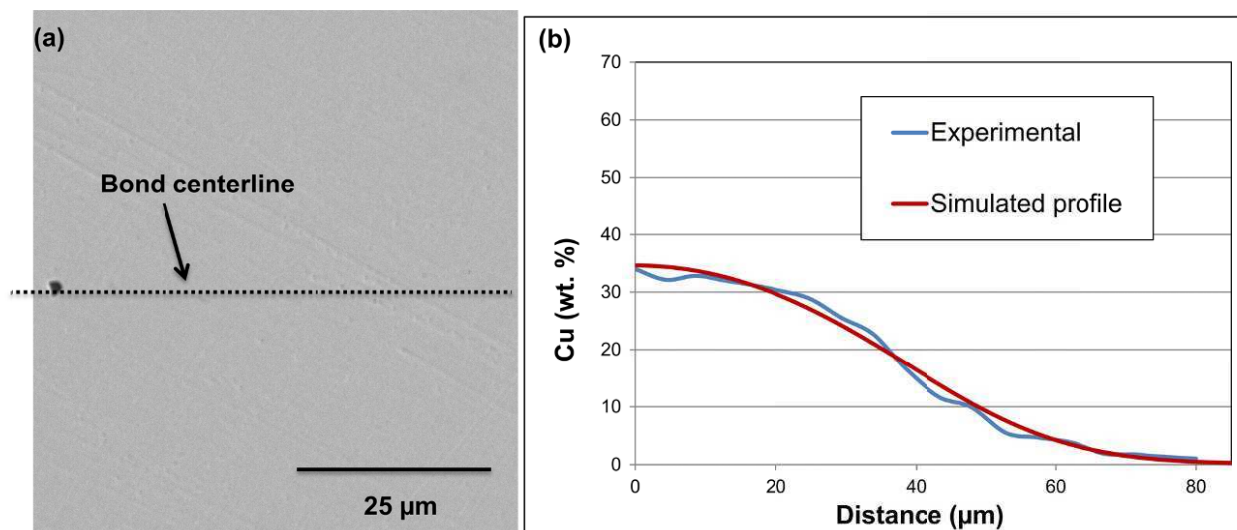


Fig. 7 (a) SEM image of diffusion bonded Ni using Cu interlayer (25μm) at 1100°C for 10 h and (b) concentration profile of Cu from the bond centerline to the interior of base metal

Fig. 7 shows (a) SEM image of diffusion bonded Ni using Cu interlayer (25μm thick) at 1100°C for 10 h and (b) measured and predicted concentration profiles of Cu from the bond centerline to the interior of base metal. At the 1100°C bonding temperature, the Cu content at the bondline decreased to ~ 35 wt.% and gradually decreased with distance from the centerline, as found in the previous condition. Cu also diffused farther from the bondline than before. In **Fig. 6** and **Fig. 7**, the centerline of the joint is shown with a broken line. The DICTRA-simulated profile agreed well with the experimental profile for this condition.

The average tensile strength for commercially pure Fe is 495 MPa and for annealed Cu is 240 MPa. The Fe-Cu joint bonded at 1085±1°C for 10 h had a measured strength of 245 MPa and the strength increased to 276 MPa when bonded at 1090±1°C. Under both of these bonding conditions, residual Cu remained in the joint area. The measured joint strength was slightly higher than that of pure Cu. The strength increased beyond Cu strength because of solid solution effect as the residual Cu contained small percentage of Fe (~3 wt.%). The strength of Fe-Cu system is yet to be optimized while the strengths of other systems (Fe-(Au-20Sn), Ni-Cu) have yet to be determined.

CONCLUSION

Fe was diffusion bonded using Cu and Au-Sn interlayers without forming any intermetallics. However, residual Cu of approximately 20 μm thick was found in the joint centerline at 1071°C for 10 h. At 1100°C for 10 h of bonding, the Cu content in the bond centerline was ~7.15 wt.%, but some micro-pores appeared in the joint area which could potentially decrease the strength of the joint. Au-20Sn eutectic interlayers allowed bonding Fe at 650°C for 10 h without having any residual interlayer material at centerline. Ni bonded at 1071°C for 10 h contained 40 wt.% Cu and at 1100°C for 10 h contained 35 wt.% Cu at the centerline. The simulated profiles using DICTRA/Thermocalc software for Ni-Cu system agreed well with the profiles obtained experimentally. The strengths found for Fe-Cu joint were 245 and 276 MPa at 1085±1 and 1090±1°C, respectively.

ACKNOWLEDGEMENTS

The authors would like to thank the National Science Foundation (Award #DMR-0907616) for their financial support of this work.

REFERENCES

- [1] Ekrami, A. Moeinfar, S. Kokabi, A.H., Microstructure development during transient liquid phase bonding of GTD-111 nickel-based superalloy, *Mater. Sci. Eng. A* 456 (2007) 93-98.
- [2] Arafin, M.A. Medraj, M. Turner, D.P. Bocher, P., Effect of alloying elements on the isothermal solidification during TLP bonding of SS 410 and SS 321 using a BNi-2 interlayer, *Mater. Chem. Phys.*, 106 (2007) 109-119.
- [3] Campbell, C.E. Boettinger, W.J., Transient liquid-phase bonding in the Ni-Al-B system, *Metall. Mater. Trans. A* 31 (2000) 2835-2847.
- [4] Sakamoto, A. Fujiwara, C. Hattori, T. Sakai, S., *Weld. J.* 68 (1989) 63-71.

- [5] Tung, S.K. Lim, L.C. Lai, M.O. Wu, H., *Mater. Sci. Technol.* 13 (1997) 1051.
- [6] Duvall, S.D. Owczarski, W.A., *Weld. J.* 46(9) (1967) 423s–432s.
- [7] Haafkens, M.H. Matthey, G.H., *Weld. J.* 61(25) (1982) 25–30.
- [8] Ojo, O.A. Richards, N.L. Chaturvedi, M.C., *Scripta Mater.* 50 (2004) 641–646.
- [9] Khan, T.I. Kabir, M.J. Bulpett, R., Effect of transient liquid-phase bonding variables on the properties of a micro-duplex stainless steel, *Mater. Sci. Eng. A* 372 (2004) 290.
- [10] Duvall, S.D. Owczarski, W.A. Paulonis, D.F., *Weld. J.* 53(4) (1974) 203–214.
- [11] Saunders, A: Thermotech Ltd., Guildford, Surrey United Kingdom, personal communications, 1997.
- [12] Andersson, J.O. Hoglund, L. Jonsson, B. Agren, J., *Fundamentals and Applications of Ternary Diffusion*, G.R. Purdy ed., Pergamon Press, New York, NY 1990, pp. 153–63.
- [13] Caro, A. Caro, M. Lopasso, E.M. Turchi, P.E.A. Farkas, D., Thermodynamics of Fe-Cu alloys as described by a classic potential, *Jr. Nucl. Mater.* 349 (2006) 317–326.

Modeling of Stable Tearing with Crack Tunneling in Specimens of Different Thickness

Junhui Yan, Michael A. Sutton and Xiaomin Deng

Department of Mechanical Engineering, University of South Carolina, Columbia, SC 29208

ABSTRACT: Stable tearing with crack tunneling in ductile materials has been commonly observed, but a quantitative understanding of the 3D complicated crack tunneling phenomena is very limited. In particular, the correlation between the driving force and fracture toughness during stable tearing with crack tunneling has not been well evaluated. In the current study, modeling efforts have been made to simulate stable tearing events with crack tunneling and slanting under remote tension in A2024-T3 plate specimens of two thickness values (2.286mm and 6.35mm). It is observed that values of CTOD, stress constraint and the Lode stress parameter vary in the specimen thickness direction. For the thinner specimen, a higher stress constraint and a lower CTOD in the midsection of the crack front are found, and the critical CTOD decreases approximately linearly with an increasing constraint and is weakly dependent on the Lode stress parameter. The variations of CTOD, the stress constraint and the Lode parameter in the two plate specimens in the thickness direction are very similar, but the magnitudes of these parameters near the midsection of the crack front increase significantly in the thicker specimen. The approximate linear correlations in the two specimens between constraint and CTOD are not identical, probably due to the coupled effects of constraint and the Lode stress parameter in this midsection region of the crack front.

1. Introduction

Crack tunneling has been observed in stable tearing experiments in ductile materials under tension or combined tension torsion loading [1-5]. For a specimen containing a through-thickness crack with an initially straight crack front, as the specimen is loaded monotonically, the midsection of the crack front will advance first and then the rest of the crack front will grow, leading to the formation of thumbnail shaped crack-front profiles [1, 3, 6]. In addition to tunneling, slant crack growth may also occur in ductile materials [3, 4].

As can be seen, stable tearing is a complicated three-dimensional fracture process. One important subject of stable tearing fracture investigation is to understand the mechanism for the crack growth in ductile materials and to develop a general fracture criterion to predict the three-dimensional fracture process (for both the instant and direction of crack growth) [6]. Due to the complexity of the fracture process accompanied by large deformation and large-scale yielding that develops in ductile materials under stable tearing, there is currently no general fracture criterion available for crack growth in ductile materials. Of the various approaches available [7-13], a generalized mixed-mode I/II crack tip opening displacement (CTOD) has been shown to be a viable crack growth parameter for ductile materials (e.g., 2024-T3 aluminum alloy) under combined tension (mode I) and in-plane shear (mode II) loading conditions.

From the point of view of fracture mechanics, crack tunneling might occur first in a specimen's center section due to a lower fracture toughness and/or a higher driving force in the specimen's center section (relative to the specimen surface) so that the operating fracture criterion is satisfied first in the middle portion of the crack front. For example, a higher stress triaxiality (also called the stress constraint) in the specimen's center section promotes void nucleation, growth and coalescence, leading to a lower fracture toughness there and thus crack growth first in the interior of the specimen instead of at the specimen surface [6, 14].

Recent work by Zuo et al. [6] has shown that the critical CTOD is a strong function of the stress constraint or triaxiality (ratio of the mean stress to the von Mises effective stress). Using a custom simulation code, CRACK3D, and the measured slant fracture surface and tunneled crack front shapes in a 2.3mm thick 2024-T3 specimen under tension loading, they obtained the through-thickness variations of constraint along crack fronts and established a relationship between constraint and critical COD for the crack growth process, which can be approximated by a straight line for the range of observed constraint values. The reduction in the critical CTOD near the specimen centerline suggests that crack growth occurs first near the specimen centerline, with the specimen surfaces lagging behind due to a lower constraint in this region. Using the obtained CTOD vs.

constraint relationship, the shape of tunneled flaws during stable tearing in a thin, 2024-T351, LT specimen undergoing nominally Mode I loading was successfully predicted.

Mahmoud and Lease [15] investigated the effect of specimen thickness on the surface CTOA in 2024-T351 aluminum alloy with thicknesses of 2.3, 6.35, 12.7, and 25.4 mm. The critical CTOA was shown to decrease with increasing specimen thickness and appears to possibly be approaching a lower limiting value. However, there is very limited quantitative investigation in the open literature on the variation of the constraint with specimen thickness and on the validation of the correlation between CTOD and constraint when the specimen thickness changes. In addition to the work by Zuo et al [6], the only work in this area can be found by Johnston and James [16]. They investigated the relationship between constraint and the critical crack tip opening angle (CTOA) (which is equivalent to CTOD) in a 6.35mm thick 2024-T351, LT plate under tensile loading, where the measured load and FLAT fracture (no slanting) tunneling data were used as input for the finite element analysis. Similar to the results by Zuo et al [6], an inverse linear relationship between the constraint and CTOA was observed. They also found that the angle along the crack front monotonically increases from the centerline to the surface for a given amount of surface crack growth, however, no through thickness variations of constraint were provided [16].

Although similar relationships between constraint and critical CTOD or CTOA were observed in 2024-T351 specimens with different thickness ($T=2.3\text{mm}$ by Zuo et al [6] and $T=6.35\text{mm}$ by Johnston et al [16]), a careful comparison of the results by Zuo et al [6] and those by Johnston et al [16] reveals that a) both $T=2.3\text{mm}$ and $T=6.35\text{mm}$ specimens have almost the same constraint range from 0.5 to 1.3 for tunneled cracks, instead of a higher constraint for $T=6.35\text{mm}$ specimen; b) the maximum CTOA (corresponding to a surface CTOA) in the $T=6.35\text{mm}$ specimen obtained in [16] is about 14° , which is much greater than the averaged experimental measurement of 5.17° [15]. As can be seen, whether and how constraint and CTOD (or CTOA) vary along tunneled crack fronts in ductile specimens with different thicknesses need to be further clarified. A particular question that needs to be answered is whether the constraint-critical CTOD (or CTOA) relation depends on the plate thickness. If yes, then the critical CTOD must depend on not only constraint but also some other stress state parameters, such as the Lode parameter (which is related to the 3rd stress invariant and reflect the role of the 2nd principal stress [17]).

The objective of this paper is to investigate (a) the variations of constraint and CTOD along tunneled crack fronts in specimens with different thicknesses, (b) the effect of constraint on CTOD in different thickness specimens, and (c) the effect of the Lode stress parameter on the critical CTOD.

2. Experimental conditions and crack tunneling measurement

Fig.1 presents the major dimensions of tension torsion loading specimens for $T=2.286$ and 6.35mm thick AA2024-T3 sheets. The pre-crack length for $T=2.286\text{mm}$ and 6.35mm specimens are respectively 12.7mm and 25.4mm . The specimen has an LT orientation, i.e., the loading direction is along the longitudinal rolling direction and the crack is along the transversal direction.

The engineering tensile curves for AA2024-T3 plates with different thickness are shown in Fig.2. No significant difference was observed for tensile curves from different thicknesses of AA2024-T3 plates (from 2.286 mm to 12.7mm).

Experimental measurement results for crack tunneling in $T=2.286\text{mm}$ and 6.35mm thick AA2024-T3 plates under pure tension loading ($ST/SP=0$) are presented in Fig.3, where the corresponding load levels for each crack front are also shown. The experimental procedure to assess the crack tunneling can be found in reference [1, 3].

It should be pointed out that slant fracture surfaces were observed in all these experiments. The three-dimensional digital image correlation technique [3,10] was used to measure the three-dimensional profiles for the slant fracture surfaces including tunneled crack fronts, which were used as input for the finite element analysis (reference to Fig.5).

3. Finite element simulation procedures

To analyze and understand the fracture behavior around the actual 3D crack fronts, the experimentally measured fracture surface and crack front profiles are built into finite element models. A custom finite element simulation code, CRACK3D [6, 18, 19], developed at the University of South Carolina, is used to simulate the crack growth process during stable tearing. Pre-processing and post-processing are done in an ANSYS environment. The nodal release option in CRACK3D is used. CRACK3D performs displacement controlled loading in small increments and evaluates the resulting load at each loading interval. At specified loading levels corresponding to experimentally observed crack fronts, the node pairs between the current and next crack fronts are released sequentially in accordance with experimental load versus crack front data. The detailed procedures were outlined in ref. [6].

To reduce the loading step and thus help the crack growth simulation run smoothly, interpolated crack fronts were obtained and built into the finite element models. Fig.4 shows measured (solid lines) and interpolated (dashed lines) crack fronts for finite element models in $T=2.286\text{mm}$ and 6.35mm thick AA2024-T3 plates under pure tension loading ($ST/SP=0$). The corresponding load levels for the interpolated crack fronts are also obtained by interpolation.

Fig.5 presents the geometry models for T=2.286mm and 6.35mm AA2024-T3 plates under pure tension loading (ST/SP=0), into which the experimentally measured slant fracture surfaces with tunneled crack fronts are built.

Values of fracture parameters, such as the generalized CTOD (which is the magnitude of the vector formed by the differences of the displacement components of the upper and lower crack surfaces at a certain fixed distance behind the crack front), the stress constraint and the Lode stress parameter at the actual 3D crack fronts are evaluated right before the nodal release. In the analysis, suppose σ_1 , σ_2 , and σ_3 (in decreasing order) are the principal stresses, then the stress constraint is defined by the ratio σ_m/σ_e , where σ_m is the mean stress and σ_e is the von Mises effective stress, and the Lode stress parameter is defined by $\mu = - (2\sigma_2 - \sigma_1 - \sigma_3) / (\sigma_1 - \sigma_3)$. As discussed in ref [6], integrated average values for stress constraint are obtained by integrating the stress constraint over a small distance of 0.3mm ahead of the crack front, in the direction normal to the crack front for interior nodes, within the plane of the crack surface; for nodes on the specimen surfaces, numerical integration is along the specimen surfaces. Integrated average values for the Lode stress parameter are also obtained similarly. For CTOD in this study, it is chosen to be computed at 0.3mm behind the crack front along a line normal to the crack front for interior nodes and along the specimen surface for surface nodes. As can be seen from the crack profiles shown in Fig.3, the crack was tunneled so severely in the middle region of a crack front especially for thicker specimen, a point at a distance greater than 0.3mm behind a severely tunneled crack front along a line normal to the crack front may be too close to other parts of the crack front, making this point inappropriate for getting accurate CTOD values (in general the location where CTOD is computed should not be too close to the crack front in order to avoid using extremely small elements to achieve CTOD convergence [6]).

4. Results and Discussion

Two meshes are used to perform the mesh convergence study for the crack growth in T=2.286 thick AA2024-T3 plate under pure tension loading: Mesh I with 20,215 nodes and 11,326 elements and Mesh II with 45,302 nodes and 27,141 elements (as shown in Fig.5 (a)). Mesh II are obtained by bisection each edge of elements in 3D space near the crack surface region of mesh I. Fig.6 shows comparisons of through-thickness variations of constraint (A_m), the Lode stress parameter and CTOD (@0.3mm behind crack front) for measured crack Front 4 from Mesh I (with an element size of 0.2 mm around the crack front) and refined Mesh II (with an element size of 0.1 mm around the crack front) in T=2.286mm thick AA2024-T3 plate under pure tension loading (ST/SP=0). As can be seen, very close results from Mesh I and refined Mesh II are obtained respectively for stress constraint (A_m), the Lode stress parameter and CTOD (@0.3mm behind crack front). Similar mesh convergence study is also performed for T=6.35mm thick specimen under tension loading and converged results are obtained.

Fig.7 shows through thickness variations and averages of constraint (A_m), the Lode stress parameter and CTOD for measured crack fronts in T=2.286mm thick AA2024-T3 plate under pure tension loading (ST/SP=0). As can be seen, the CTOD through thickness variation for Crack Front 3 is somehow different from those for Crack Fronts 4, 5 and 6. For Crack Front 3 CTOD increases from the minimum at the mid-thickness location to its maximum at the free surfaces of the specimen, while for the rest of the crack fronts, CTOD increases as the location from the mid-plane to the free surface reaches its maximum at about $|z|=0.8\text{mm}$ and then decreases. The difference might be related to the crack front profiles as shown in Fig.4, where Crack Front 3 profile is different from those of Crack Fronts 4, 5 and 6, but the reasons behind this behavior need to be further investigated.

The following trends can be observed from the averaged variation of constraint, CTOD and Lode's stress parameter, a) constraint varies along a crack front from a higher value at the mid-plane region to a lower value near the crack surfaces, b) CTOD along the crack front increases from the mid-plane ($z=0\text{mm}$) to $|z|=0.8\text{mm}$, and then reaches a plateau or drops slightly near the surface regions, c) the averaged Lode's stress parameter along crack front oscillates from $|z|=0$ to 0.15mm, with its minimum near $|z|=0.7\text{mm}$ and maximum near $|z|=0.25\text{mm}$. The observed trends for constraint and CTOD are consistent with the results published in ref. [6].

Fig.8 shows the through-thickness variations and the averages of constraint (A_m), Lode's stress parameter and CTOD (@0.3mm behind crack front) for measured crack fronts in 6.35mm thick AA2024-T3 plate under pure tension loading (ST/SP=0). A comparison of Fig.8 with Fig.7 reveals that the through-thickness variations of constraint, CTOD and Lode's stress parameter in both T=2.286mm and T=6.35mm thick specimens are, respectively, very similar.

Shown in Fig.9 is a comparison of through-thickness variations of averaged constraint (A_m), Lode's stress parameter and CTOD in 2.286mm thick and 6.35mm thick AA2024-T3 plates under pure tension loading, where the normalized thickness is used. As stated in Section 3, the calculation of constraint and Lode's parameter should be along the normal direction of the crack front at that node, but for nodes on and near the specimen surfaces, the normal direction at that node is usually towards outside of the specimen, so there is no data there to obtain the numerical integration. As such, the integration directions for these nodes on or near the specimen surfaces were along the specimen surfaces. To reduce the numerical errors due to this assignment, the two data points near each surface should be removed. The solid lines in Fig.9 reflect this consideration. The following observations can be made:

a) The variation shapes of constraint along specimen thickness direction in both specimen thickness ($T=2.3\text{mm}$ and 6.35mm) are very similar, with a higher constraint in the crack mid-point region and a lower constraint near the crack surfaces. However, the overall constraint value for a given point along the crack front increases with increasing specimen thickness, for example, the mid-plane constraint increases significantly from 1.22 in $T=2.3\text{mm}$ to 1.78 in $T=6.35\text{mm}$ specimen (about 45% increase).

b) The overall trend in the through-thickness variation of Lode's stress parameter in the thicker specimen is generally similar to that in the thinner specimen except that there is a shallow minimum in the mid-point for thinner specimen. The value of Lode's stress parameter near the surfaces in both specimen thicknesses oscillates around 0, but when the normalized length varies from -0.4 to 0.4, the amplitude of Lode's stress parameter in the thicker specimen rises rapidly to 0.422, much greater than 0.154 in thinner specimen (about 174% increases).

c) For both specimen thickness ($T=2.3\text{mm}$ and 6.35mm), CTOD varies along a crack front from a lower value in the mid-section region to a higher value near the crack surfaces. The averaged through-thickness CTOD values near the specimen surface regions (-0.8 to -0.4 and 0.4 to 0.8 in normalized length) are almost identical for $T=6.35\text{mm}$ and $T=2.3\text{mm}$ thick specimens. This is consistent with the experimental results for surface CTOA in 2024-T351 specimens with different thickness [15]. CTOD in the mid-plane region increases about 18% (from 0.0272mm to 0.0320mm) with increasing specimen thickness.

d) By comparing the through-thickness variations of CTOD, constraint and Lode's stress parameter in Fig.9, it is revealed that the increase of constraint near the crack surface regions (-0.8 to 0.4 or 0.4 to 0.8 for normalized thickness) in the thicker specimen does not bring up much CTOD changes in this region, while the increase of CTOD in the midsection (-0.4 to 0.4 for normalized thickness) of the crack front in the thicker specimen is well correlated with the increase of Lode's stress parameter. This implies that in the thicker specimen, in addition to constraint, the Lode's stress parameter also has an effect on the fracture toughness.

Based on the results (with two data points near crack surfaces was removed) shown in Fig.9, the effect of constraint and Lode's stress parameter on the critical CTOD in specimens with $T=2.3\text{mm}$ and 6.35mm are obtained and plotted in Fig.10. As can be seen for $T=2.286\text{mm}$, the critical CTOD decreases almost linearly with increasing stress constraint (A_m), but weakly depends on the Lode's stress parameter (LSP). The linear fitting equations for $T=2.286\text{mm}$ are respectively,

$$\text{CTOD}=0.0949-0.0574A_m \quad (R^2 = 0.9035) \quad (1)$$

$$\text{CTOD}=0.0461-0.1255 \text{ LSP} \quad (R^2 = 0.4926) \quad (2)$$

For $T=6.35\text{mm}$, the linear fitting equations are:

$$\text{CTOD}=0.0787-0.0282A_m \quad (R^2 = 0.8395) \quad (3)$$

$$\text{CTOD}=0.0411-0.0313 \text{ LSP} \quad (R^2 = 0.628) \quad (4)$$

Equations (1) to (4) and results in Fig.9 indicate that for a thin specimen, the effect of constraint on CTOD is dominant where the effect of the Lode's parameter is low; when the specimen's thickness is increased, the Lode's stress parameter in the midsection region increases dramatically and its effect on CTOD also increases. This implies that, for a thicker specimen where the second principal stress is important, constraint alone may not be sufficient to describe the stress state and other stress state parameters, such as the Lode's stress parameter, should be taken into consideration.

5. Conclusions

Modeling efforts have been made to simulate stable tearing events with crack tunneling and slanting under pure tension for 2.286mm and 6.35mm thick AA2024-T3 plates by using the custom simulation code CRACK3D along with pre-processing and post-processing in ANSYS. Experimentally measured crack fronts, fracture surfaces and load-crack extension curves are used as simulation input data. The nodal release option in CRACK3D is used to control the crack growth process. Fracture parameter values, such as the generalized crack tip opening displacement (CTOD), the stress constraint and the Lode's stress parameter, at actual 3D crack fronts are evaluated right before the crack growth. The through thickness variations of these parameters and the effect of stress constraint and Lode's stress parameter on critical CTOD have been established for the two simulation cases. The following conclusions can be made:

- 1) Values of CTOD, stress constraint and the Lode stress parameter ahead of the crack front vary in the specimen thickness direction.
- 2) For different thicknesses, the variation of CTOD, stress constraint or the Lode stress parameter along the thickness direction is very similar.
- 3) Critical CTOD decreases with increasing stress constraint. In thin specimen, the effect of constraint on CTOD is dominant.

4) The effect of Lode's stress parameter on CTOD is weak for thin specimen and increases for thicker specimen.

Acknowledgments

The authors gratefully acknowledge the support of the NASA Langley Research Center.

References:

- [1] D.S. Dawicke and M.A. Sutton, "CTOA and Crack Tunneling Measurements in Thin Sheet 2024-T3 Aluminum Alloy", *Experimental Mechanics*, 34 (4), 357-369 (1994).
- [2] Boone, M. L., 1999, "Characterization of Stable Tearing in Thin Sheet of 2024-T3 Aluminum Alloy under Tension-Torsion Loading Conditions," MS thesis, University of South Carolina, Columbia, SC.
- [3] Sutton M.A., Helm J.D. and Boone M.L. 2001. Experimental Study of Crack Growth in Thin Sheet Material under Tension-Torsion Loading, *International Journal of Fracture* 109 285-301
- [4] James, M. A., and Newman, J. C., Jr., 2003, "The Effect of Crack Tunneling on Crack Growth: Experiments and CTOA Analysis," *Eng. Fract. Mech.*, 70, pp. 457-468.
- [5] B.E. Amstutz, M.A. Sutton and D.S. Dawicke, "Experimental Study of Mixed Mode I/II Stable Crack Growth in Thin 2024-T3 Aluminum", *ASTM STP 1256*, 26, 256-273 (1995).
- [6] J. Zuo, X. Deng, M.A. Sutton, and C-S Cheng, Three-Dimensional Crack Growth in Ductile Materials: Effect of Stress Constraint on Crack Tunneling, *ASME Journal of Pressure Vessel Technology* 130, 031401.1 -8 (2008).
- [7] Hutchinson, J. W., and Paris, P. C., 1979, "Stability Analysis of J-Controlled Crack Growth, Elastic-Plastic Fracture," *ASTM STP 668*.
- [8] Chao, Y. J., and Sutton, M. A., 1994, "On the Fracture of Solids Characterized by One or Two Parameters: Theory and Practice," *J. Mech. Phys. Solids*, 42, pp. 269-647.
- [9] Ma, F., Deng, X., Sutton, M. A., and Newman, J. C., Jr., 1999, "A CTOD Based Mixed-Mode Fracture Criterion," *ASTM STP 1359*.
- [10] J.-H. Yan, M. A. Sutton, X. Deng, Z. Wei and Pablo Zavattieri. Mixed-mode crack growth in ductile thin-sheet materials under combined in-plane and out-of-plane loading. *Int J Fract* (2009) 160:169-188
- [11] Sutton, M. A., Deng, X., Ma, F., Newman, J. C., Jr., and James, M., 2000, "Development and Application of a Crack Tip Opening Displacement-Based Mixed Mode Fracture Criterion," *Int. J. Solids Struct.*, 37, pp. 3591-3618.
- [12] Dawicke, D. S., Sutton, M. A., Newman, J. C., Jr., and Bigelow, C. A., 1993, "Measurement and Analysis of Critical CTOA for an Aluminum Alloy Sheet," NASA Langley Research Center, NASA TM 109024.
- [13] F. Ma, X. Deng, M.A. Sutton, "Plane Strain Mixed Mode Crack-Tip Stress Fields Characterized by A Triaxial Stress Parameter and A Plastic Deformation Extent Based Characteristic Length", *Journal of the Mechanics and Physics of Solids*, 49, 292-2953 (2001).
- [14] Weiming Lan, Xiaomin Deng, Michael A. Sutton. Investigation of crack tunneling in ductile materials. *Engineering Fracture Mechanics* 77 (2010) 2800-2812
- [15] Samer Mahmoud and Kevin Lease, The effect of specimen thickness on the experimental characterization of critical crack-tip-opening angle in 2024-T351 aluminum alloy, *Engineering Fracture Mechanics* 70 (2003) 443-456
- [16] William M. Johnston and Mark A. James. A Relationship between Constraint and the Critical Crack Tip Opening Angle. NASA/CR-2009-215930, 2009
- [17] R.A.C. Slater, *Engineering Plasticity: Theory and Application to Metal Forming Processes*, MacMillan, London, 1977.
- [18] J. Zuo, M.A. Sutton and X Deng, "Basic studies of ductile failure processes and implications for fracture prediction", *Fatigue and Fracture of Engineering Materials*, , 27, 231-243 (2004).
- [19] J. Zuo, X. Deng and M. A. Sutton, "Computational Aspects of 3D Crack Growth Simulations", Paper # IMECE 2004-60699, Proc. of 2004 ASME International Mechanical Engineering Congress, Nov. 13-20, 2004, Anaheim, CA.

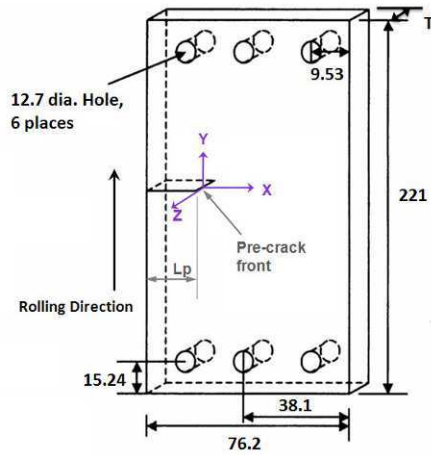


Fig.1 Tension torsion test specimen with thickness of $T=2.286\text{mm}$ and 6.35mm . All dimensions in mm. For $T=2.3\text{mm}$ and 6.3mm thick specimens, pre-crack length L_p are respectively 12.7mm , and 25.4mm

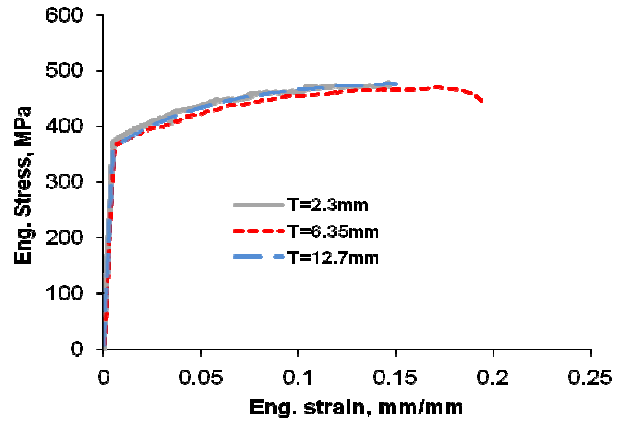


Fig.2 Engineering tensile curves for $T=2.286\text{mm}$, 6.35mm and 12.7mm thick AA2024-T3 plates

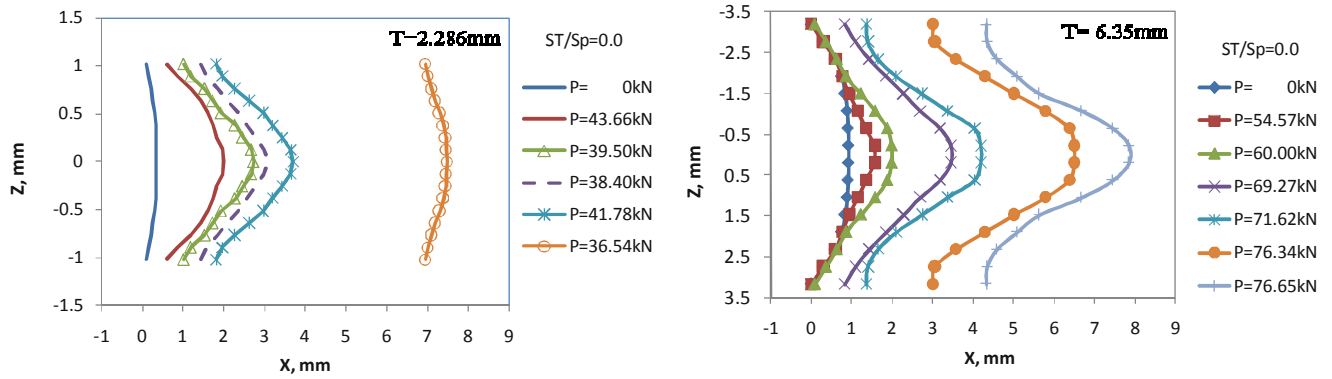


Fig.3 Experimental measurement results for crack tunneling in $T=2.286$ and 6.35mm thick AA2024-T3 plate under pure tension loading ($ST/SP=0$)

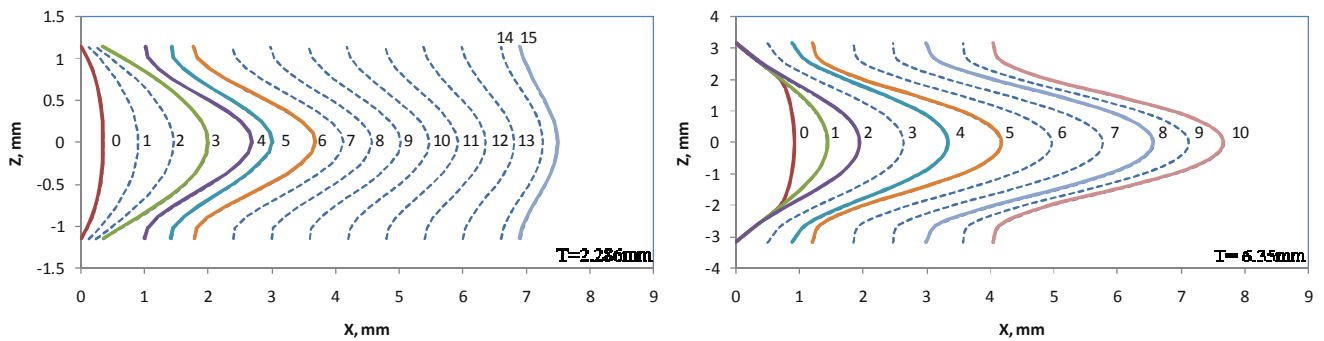
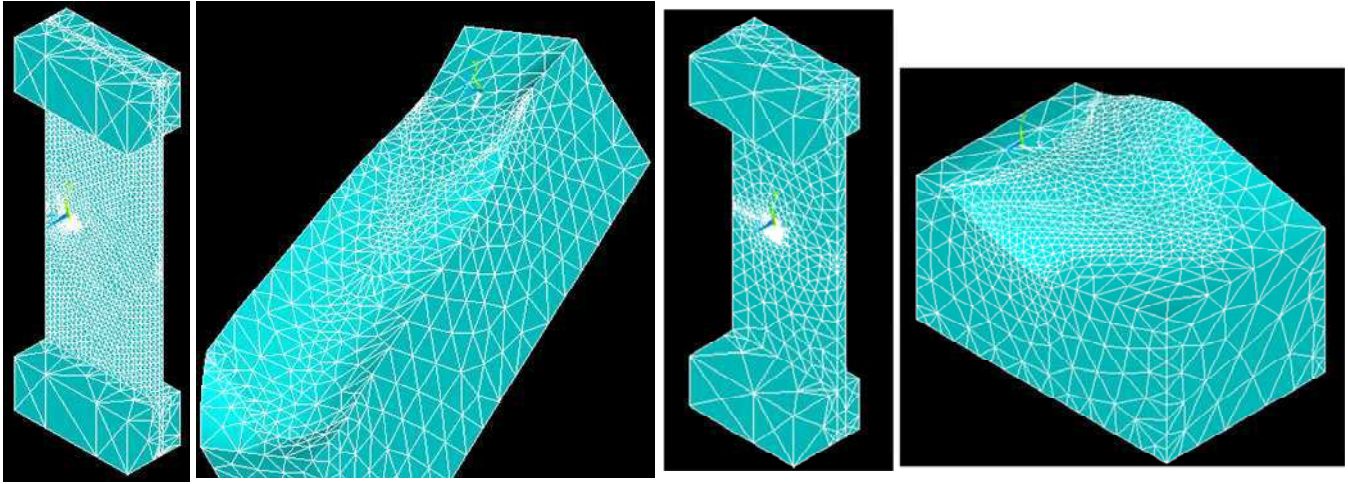


Fig.4 Crack fronts (solid lines for measured ones and dashed lines for interpolated ones) used in the modeling in $T=2.286\text{mm}$ and 6.35mm thick AA2024-T3 plate under pure tension loading ($ST/SP=0$).



(a) $T=2.286\text{mm}$ with 45302 nodes and 27141 elements

(b) $T=6.35\text{mm}$ with 46651 nodes and 30734 elements

Fig.5 Geometry models for (a) $T=2.286\text{mm}$ and (b) $T=6.35\text{mm}$ AA2024-T3 plate under pure tension loading ($ST/SP=0$) showing crack tunneling and slanting

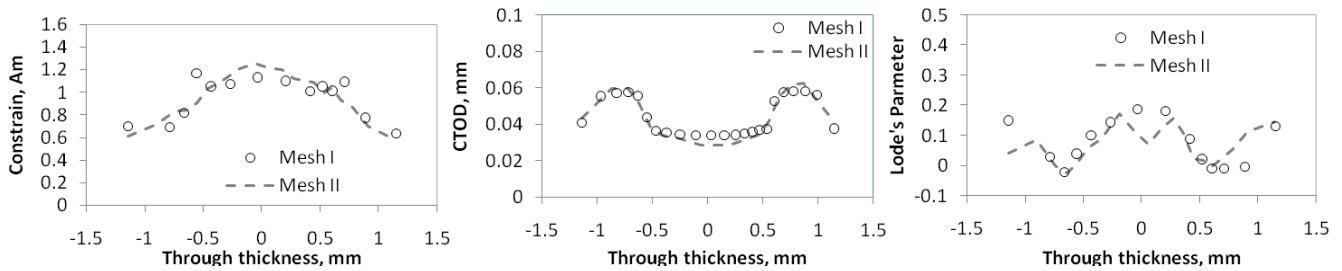


Fig.6 Through thickness variations of constraint (A_m), Lode's stress parameter and CTOD (@0.3mm behind crack front) for measured crack front 4 from Mesh I and refined Mesh II in $T=2.286\text{mm}$ thick AA2024-T3 plate under pure tension loading ($ST/SP=0$).

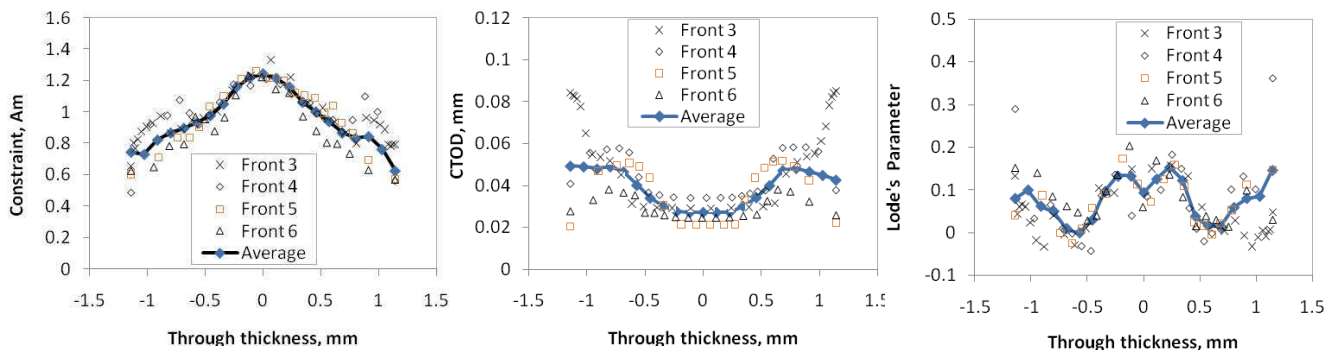


Fig.7 Through thickness variations and averages of constraint (A_m), Lode's stress parameter and CTOD (@0.3mm behind crack front) for measured crack fronts from coarse mesh and refined mesh in $T=2.286\text{mm}$ thick AA2024-T3 plate under pure tension loading ($ST/SP=0$)

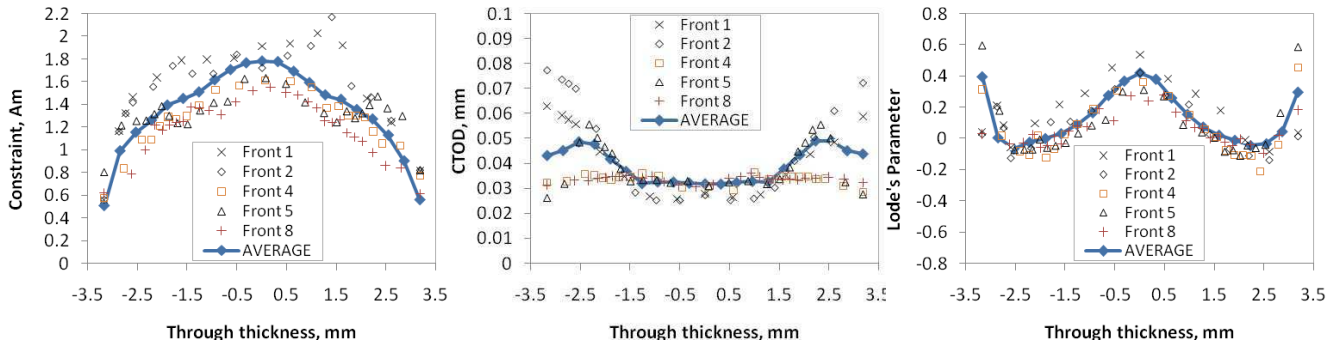


Fig.8 Through thickness variations and averages of constraint (A_m), Lode's stress parameter and CTOD (@0.3mm behind crack front) for measured crack fronts from coarse mesh and refined mesh in $T=6.35\text{mm}$ thick AA2024-T3 plate under pure tension loading ($ST/SP=0$)

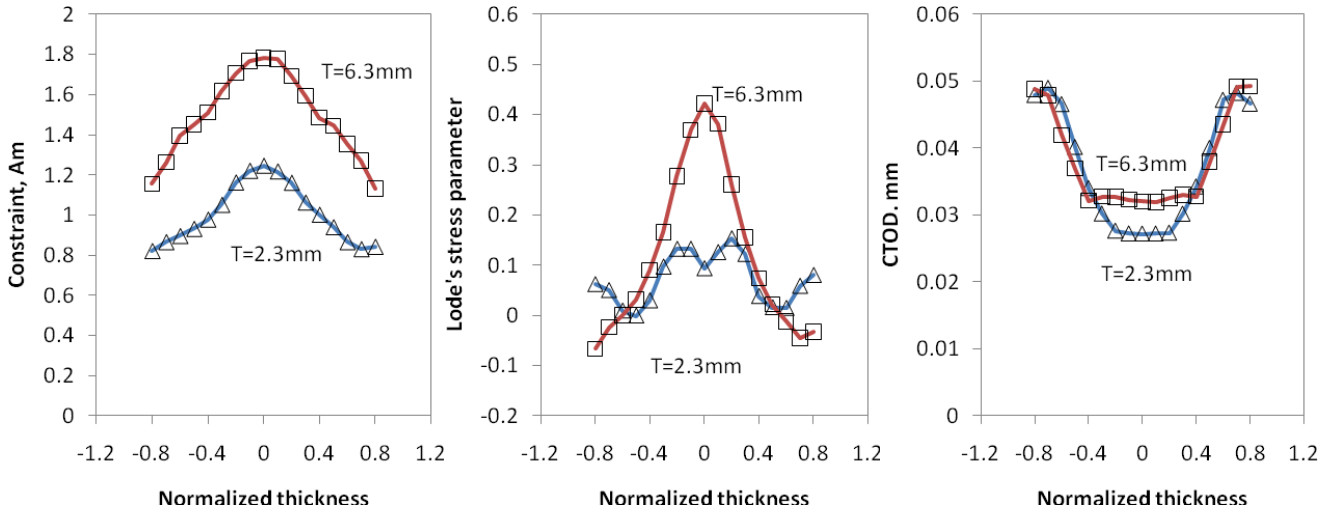


Fig.9 Comparison of through thickness variations of (a) averaged constraint (A_m), (b) Lode's stress parameter and (c) CTOD (at 0.3mm behind crack front) in 2.286mm thick and 6.35mm thick AA2024-T3 plate under pure tension loading ($ST/SP=0$)

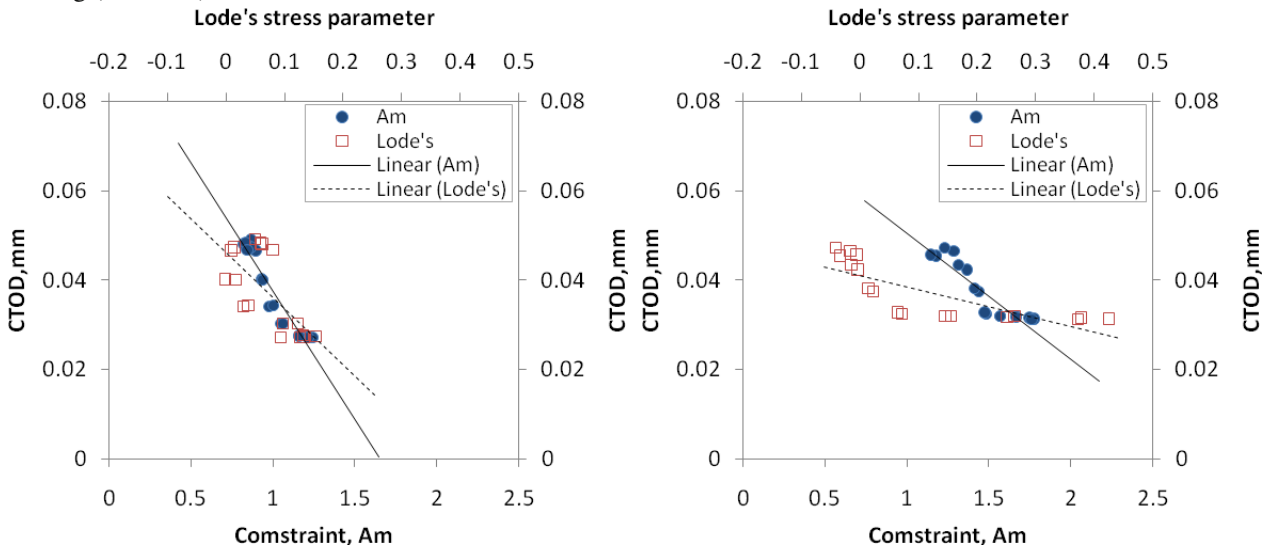


Fig.10 Effect of constraint (A_m) and Lode's stress parameter on CTOD in (a) 2.286mm thick and (b) 6.35mm thick AA2024-T3 plate under pure tension loading ($ST/SP=0$). The correlations were obtained by removing the two data points near each surface as shown in Fig. 9

Fatigue Modeling of Collagenous Soft Tissue

Caitlin Martin and Wei Sun

Tissue Mechanics Laboratory
Biomedical Engineering and Mechanical Engineering
University of Connecticut, Storrs

ABSTRACT

In this study, a phenomenological tissue damage model has been developed to describe the fatigue-induced stress softening and permanent set of biological tissues. Since damage evolution is an irreversible dissipative process, following thermodynamic principles, an equivalent strain proportional to the strain energy of the material is employed as the damage criterion. The maximum equivalent strain represents the value necessary to cause complete sample failure during one loading cycle, while the minimum equivalent strain is the value required to elicit the onset of fatigue damage. The damage parameter evolves from zero (below minimum equivalent strain) to one at maximum equivalent strain as a function of both the equivalent strain and number of loading cycles. The permanent set evolves as a function of the peak strain in the principal directions. The damage model is implemented into ABAQUS via a user defined material (UMAT) in conjunction with the nonlinear orthotropic Fung-elastic model. For the purpose of this study, glutaraldehyde-treated bovine pericardium (GLBP), a collagenous tissue traditionally used for fabricating bio-prosthetic heart valve (BHV) leaflets, is utilized as a representative collagenous tissue due to its limited durability in BHV applications.

INTRODUCTION

Biologically derived, chemically-treated collagenous tissues are extensively utilized in a broad spectrum of medical applications including cardiovascular grafts and bio-prosthetic heart valves (BHV), as well as ligament, tendon, cartilage, sclera, and hernia repair and replacement. However, despite their widespread use, similar to devices made of metallic and polymeric materials, fatigue-induced degradation, wear and tearing have been identified as some of the major problems associated with collagenous tissue implant failure.

Fatigue is an especially critical issue for the application of BHVs. Today, the only effective, long-term treatment for valvular heart disease (VHD) is open-chest cardiac valve repair or replacement surgery. BHVs fabricated from glutaraldehyde-treated bovine pericardium (GLBP) have been used to treat VHD for over three decades¹, and continue to be one of the dominant replacement valve modalities, either as a conventional prosthetic valve design or more recently for minimally invasive percutaneous delivery^{2,3}. BHVs display superior hemodynamics to mechanical valves, and they eliminate the need for anticoagulant therapy. Regardless of the specific design, long-term fatigue resilience remains the major limitation in the durability of the GLBP tissue leaflets (10-15 years) and the mechanisms governing this process are largely unknown.

There are many challenges associated with fatigue testing of BHV materials. The experimental methods can be very time consuming, involving complex testing instruments. The current FDA requirement mandates new BHV designs to be tested up to 200 million cycles to evaluate the fatigue performance using accelerated wear testers⁴. Although, accelerated wear testers can approximate the *in vivo* hemodynamics, it remains difficult to determine the specific effects of different fatigue modalities (tensile, compressive, bending, etc.) on the leaflet material properties when using this technique. To address this drawback, several groups have conducted isolated material tests in order to determine for instance, the effects of uniaxial cyclic loading on GLBP material properties^{5,6} and collagen fiber orientation⁶. Others have investigated the effects of cyclic bending fatigue on the leaflet flexural rigidity⁴. These studies, however, are limited to less than 100 millions of cycles of fatigue.

There is a lack of constitutive models for describing the damage process in soft biological tissues, which can arise from the plastic deformation or fracture of the fibers or tearing of the matrix⁷⁻⁹. In 1987, Simo⁷ introduced the concept of a fully three-dimensional (3D) finite-strain viscoelastic damage model, based on irreversible thermodynamics with internal variables. This pioneering work served as the basis for several soft tissue models⁸⁻¹⁰. Each of these models can be utilized to model damage induced by cyclic stretching with increasing magnitude; however, damage in these models is dependent only upon the strain history and not on the number of loading cycles, which limits the applicability of such models to study long-term fatigue damage in BHVs.

In this study, we propose a phenomenological damage model to describe the overall fatigue damage of GLBP due to the strain history and number of loading cycles for the purpose of investigating the fatigue damage process of BHVs. The model incorporates descriptions of the fatigue-induced stress softening and permanent set of biological tissues. The damage model is implemented into ABAQUS via a user defined material (UMAT) in conjunction with the nonlinear orthotropic Fung-elastic model, and is utilized in a tissue biaxial fatigue loading simulation and a BHV fatigue simulation.

METHODS

Un-fatigued State Tissue Properties

Glutaraldehyde-treated bovine pericardium is assumed to be anisotropic, nonlinear, hyperelastic material per Sun et al.¹¹. Therefore, the in-plane second Piola Kirchhoff stress (S^0) at the un-fatigued state can be computed by Eq. 1, where E represents the Green-Lagrangian strain tensor and W^0 is a strain energy function.

$$S_{ij}^0 = \frac{\partial W^0}{\partial E_{ij}} \quad i, j = 1, 2 \quad (1)$$

Furthermore, because this tissue is assumed to be incompressible and planar, the generalized Fung-type strain energy function for the planar biaxial response of soft biological tissues given by the following equations was used for subsequent calculations¹²:

$$W^0 = \frac{c}{2}(e^Q - 1) \quad (2)$$

$$Q = A_1 E_{11}^2 + A_2 E_{22}^2 + 2A_3 E_{11} E_{22} + A_4 E_{12}^2 + 2A_5 E_{11} E_{12} + 2A_6 E_{22} E_{12} \quad (3)$$

where c and A_i are material parameters.

The elasticity tensor C is given by Eq. 4.

$$C = \frac{\partial S_{ij}}{\partial E_{ij}}, \quad i, j = 1, 2 \quad (4)$$

Damage Evolution

The stress-strain response of collagenous soft tissues have 3 distinct regions: the toe region where the collagen fibrils extend, the quasi-linear region as the collagen fibrils uncrimp as they bear load causing the tissues stiffness to greatly increase, and the damage region as the strain exceeds a specific limit and collagen fibrils and interfibrillar bonds progressively break down, and the material stiffness decreases until the tissue fails¹³. Here it is assumed that material damage is related to the maximum distortional energy, independent of hydrostatic pressure⁷.

Equivalent Strain

In order to establish the law of tissue damage evolution, we first define an equivalent strain ε_t ⁷, a scalar quantity proportional to the strain energy at time t ,

$$\varepsilon_t(\bar{E}(t)) := \sqrt{2W^0(\bar{E}(t))} \quad (5)$$

where $\bar{E}(t)$ is the deviatoric Green strain tensor at time $t \in [0, T]$ and W^0 is the isometric strain energy of the un-fatigued tissue. In an effort to reduce computational time, the damage criterion were only evaluated at the peak of each sinusoidal loading cycle. Therefore, we introduce a peak equivalent strain ε_n^{peak}

$$\varepsilon_n^{peak} = \varepsilon_{t=(n+\frac{1}{2})f}, \quad n = 0, 1, 2, 3, \dots, N \quad (6)$$

where f is the loading frequency and n is the number of loading cycles.

Fatigue Induced Stress Softening

The stress softening caused by cyclic fatigue damage is a function of both equivalent strain and the number of loading cycles. The parameters ψ_{min} and ψ_{max} are employed to describe the accumulation of damage. A specimen cyclically loaded to an equivalent strain of ψ_{max} will completely fail during the first loading cycle. A specimen loaded to an equivalent strain of ψ_{min} will be able to endure a maximum number, n_{max} , of loading cycles before complete failure. Therefore, ψ_{min} represents the minimum equivalent strain to elicit the accumulation of fatigue damage, while ψ_{max} represents the tissue equivalent strain limit. Here we chose $n_{max} = 368$ million loading cycles as an upper bound because this translates to approximately 10 patient years considering a heart rate of 70 beats per minute. Therefore, the number of cycles until failure (n_{tot}) is given by the following novel equation:

$$n_{tot}(\varepsilon_n^{peak}) = \begin{cases} \infty & \text{if } \varepsilon_n^{peak} < \psi_{min} \\ \frac{\beta(n_{max}-1)}{\varepsilon_n^{peak} - \psi_{min} + \beta} \left(\frac{1 - \exp\left(\alpha \left(1 - \frac{\varepsilon_n^{peak}}{\psi_{max}}\right)\right)}{1 - \exp\left(\alpha \left(1 - \frac{\psi_{min}}{\psi_{max}}\right)\right)} \right) + 1 & \text{if } \psi_{min} \leq \varepsilon_n^{peak} \leq \psi_{max} \\ 1 & \text{if } \varepsilon_n^{peak} > \psi_{max} \end{cases} \quad (7)$$

where n_{max} represents the number of cycles required to completely damage a specimen loaded successively to an equivalent strain of ψ_{min} , while α and β represent the rate of damage accumulation as a function of ε_n^{peak} . These parameters should be measured experimentally.

Assuming further that at a set equivalent strain, an equal amount of damage is accumulated during each loading cycle, the rate of damage accumulation is given by

$$\frac{dD_1}{dn} = \frac{1}{n_{tot}}, \quad \text{if } \psi_{min} \leq \varepsilon_n^{peak} \leq \psi_{max}. \quad (8)$$

Therefore the total amount of damage after N tensile loading cycles is given by

$$D_1(\varepsilon_n^{peak}) = \begin{cases} 0 & \text{if } \varepsilon_n^{peak} < \psi_{min} \\ \sum_{n=1}^N \frac{n}{n_{tot}} & \text{if } \psi_{min} \leq \varepsilon_n^{peak} \leq \psi_{max} \\ 1 & \text{if } \varepsilon_n^{peak} > \psi_{max} \end{cases} \quad (9)$$

Fatigue Induced Permanent Set

Tissue damage is associated with permanent tissue elasticity loss. Therefore, when the elastic limits of the tissue are exceeded, a permanent set is exhibited upon unloading. A negative stress at zero deformation is equivalent to a permanent set (deformation) at zero stress; therefore, we employ a plastic stress S_p to ensure this condition¹⁴.

$$Sp_{ij} = (1 - D_2) \frac{\partial N}{\partial E_{ij}} \quad (10)$$

$$D_2 = \frac{\tanh\left[\left(\frac{\varepsilon_t}{\varepsilon_n^{peak}}\right)^{J+K\varepsilon_n^{peak}}\right]}{\tanh(1)} \quad (11)$$

where D_2 is a function of the equivalent strain which governs the contribution of S_p to the overall tissue response throughout loading and unloading and N is a pseudo-energy function following the theory of pseudo-elasticity of Dorfmann and Ogden¹⁴. We chose N in the form of a modified Fung energy function, which is dependent upon the maximum strain achieved in each principal direction. This modified Fung-type strain energy function enforces a negative stress at zero deformation which is necessary to capture the permanent set. Thus, N is given by the following relations

$$N = \frac{C_2}{2} (e^{Q_2} - 1) \quad (12)$$

$$Q_2 = B_1(E_{11p} - E_{11})^2 + B_2(E_{22p} - E_{22})^2 + 2B_3(E_{11p} - E_{11})(E_{22p} - E_{22}) \quad (13)$$

where E_{11p} and E_{22p} are the strains along the principal axes at the peak of the loading curve, and C_2 , B_1 , B_2 , and B_3 are material parameters.

Fatigued State Tissue Properties

The inclusion of D_1 and D_2 provides a means of changing the form of the energy function, which is no longer elastic, as a response to cyclic loading. Assuming that D_1 and D_2 are independent of E , the second Piola-Kirchoff stress tensor for the matrix may be expressed in the following form:

$$S(n) = (1 - D_1) \frac{\partial W^0}{\partial E} + (1 - D_2) \frac{\partial N}{\partial E} \quad (14)$$

Therefore, the deviatoric elasticity tensor in the material description may be expressed in the following form:

$$C(n) = (1 - D_1) \frac{\partial^2 W^0}{\partial E^2} + (1 - D_2) \frac{\partial^2 N}{\partial E^2} \quad (15)$$

RESULTS

Determination of Damage Parameters

The model parameters for the un-damaged GLBP tissue (Eqn. (2)) were obtained using the biaxial mechanical testing data reported previously by Sun et al.¹⁵. Typical equi-biaxial testing data of GLBP is illustrated in Figure 1a. The damage criterion, ψ_{min} and ψ_{max} , were chosen based upon the biaxial data of GLBP. Illustrated in Figure 1b, is the contour plot of the equivalent strain. In this study, we assumed that $\psi_{min} = 9$ and $\psi_{max} = 65$, within which marks the damage evolution region. The maximum number of loading cycles, n_{max} , was set to 368 million cycles. However, to reduce computational cost, in the simulation, n_{max} , was proportionally scaled from 368 million to 36 cycles, reflecting an accelerated accumulation of damage.

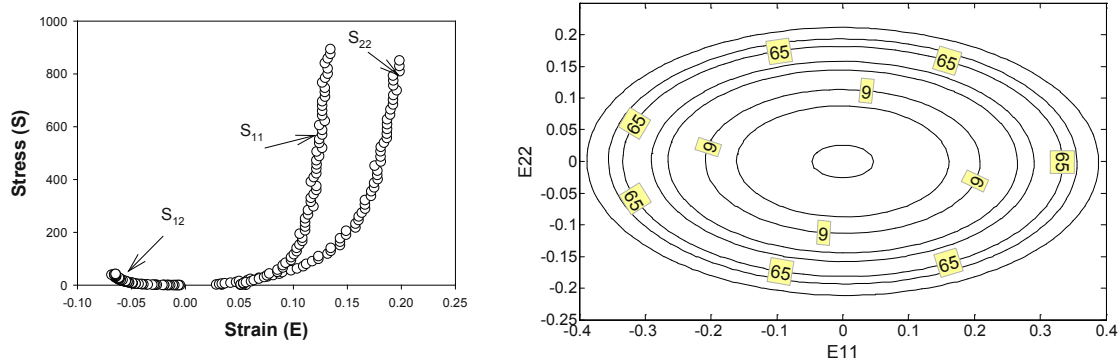


Fig.1 - Contour plot of equivalent strain with $\psi_{min} = 9$ and $\psi_{max} = 65$ marking the damage evolution region.

The effects of varying α and β in Eqn. (9) on the tissue damage factor are illustrated in Figure 2. It can be seen (Fig. 2a) that an increase in α results in a more gradual accumulation of damage, whereas an increase in β accelerates the rate of damage (Fig. 2b). The corresponding effects of varying α and β on the number of cycles to failure are illustrated in Fig. 2c&d.

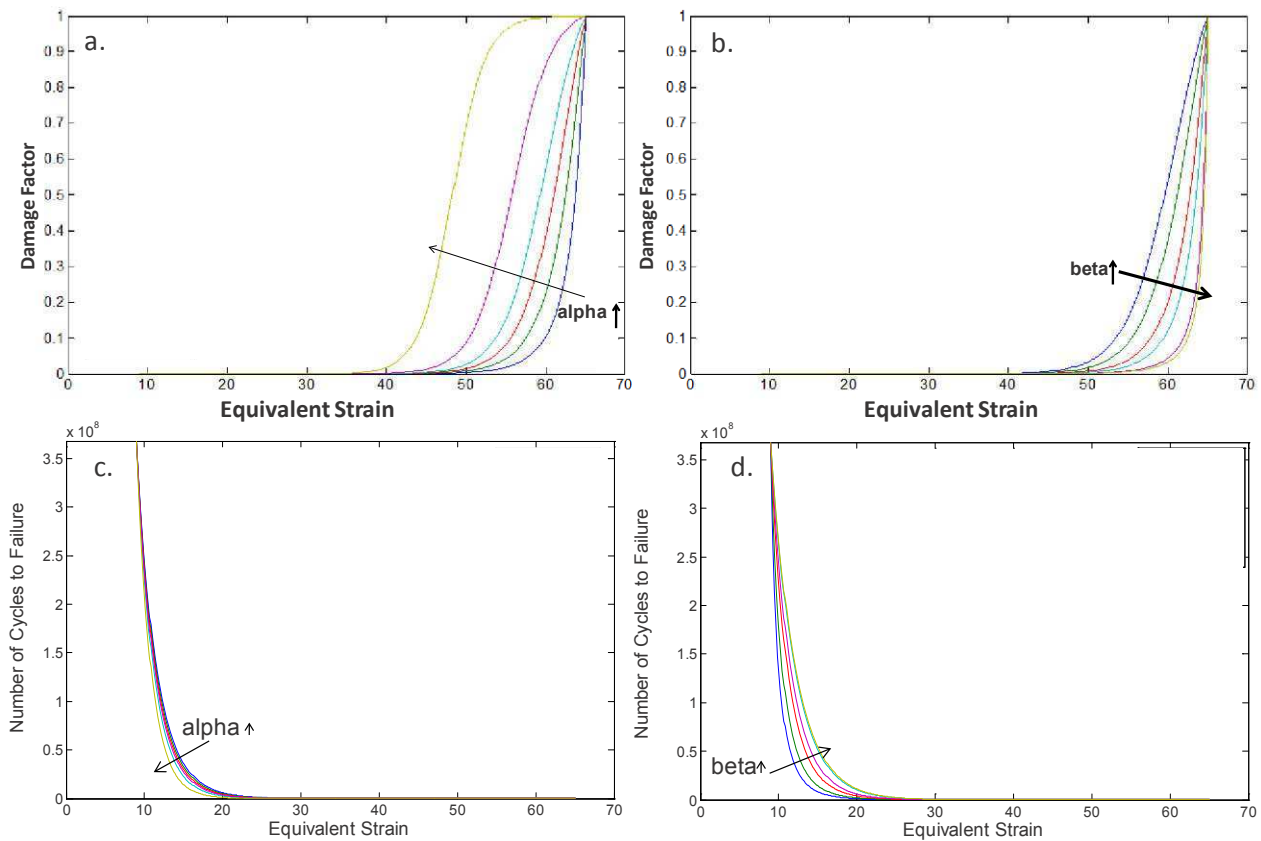


Fig.2 - Illustration of the effects of parameters α and β on the (a&b) rate of damage evolution and the (c&d) number of cycles to failure as a function of equivalent strain.

Fatigue biaxial loading simulation

The fatigue damage model of Eqn. (14) was incorporated in the finite element software ABAQUS via the user subroutine UMAT. To evaluate model effects, a finite element model of a biaxial test specimen was constructed and subjected to simulated equi-biaxial cyclic loading. The biaxial testing simulation model consisted of 400 plane stress elements to allow for test specimen geometry of 25 mm x 25 mm x 0.4 mm (Fig. 3a). Four evenly spaced node forces, with 5 mm between two adjacent nodes and 2.5 mm inside the specimen edge, were imposed on each side (Fig. 3a). Each node force was 2.5 N, imposing a net total 1 MPa Lagrangian stress on each edge. Similar to the actual biaxial testing experiments^{15,16}, only the central region was used for stress-strain measurements. This was accomplished by averaging the stress and strain tensor components for sixteen elements located in the center of the FE model, delimiting a 5 mm x 5 mm region. Details of the constitutive model implementation into ABAQUS have been previously presented^{11, 17}.

The biaxial test fatigue simulation demonstrated the altered mechanical properties of the tissue specimen in response to cyclic loading. As illustrated in Fig. 3c, the equi-biaxial stress-strain curves exhibited progressive tissue softening and increased permanent deformations throughout the cycles. A redistribution of the maximum principal stress throughout the central 16 elements of the tissue specimen model is evident during the progression of damage (Fig. 3d-f).

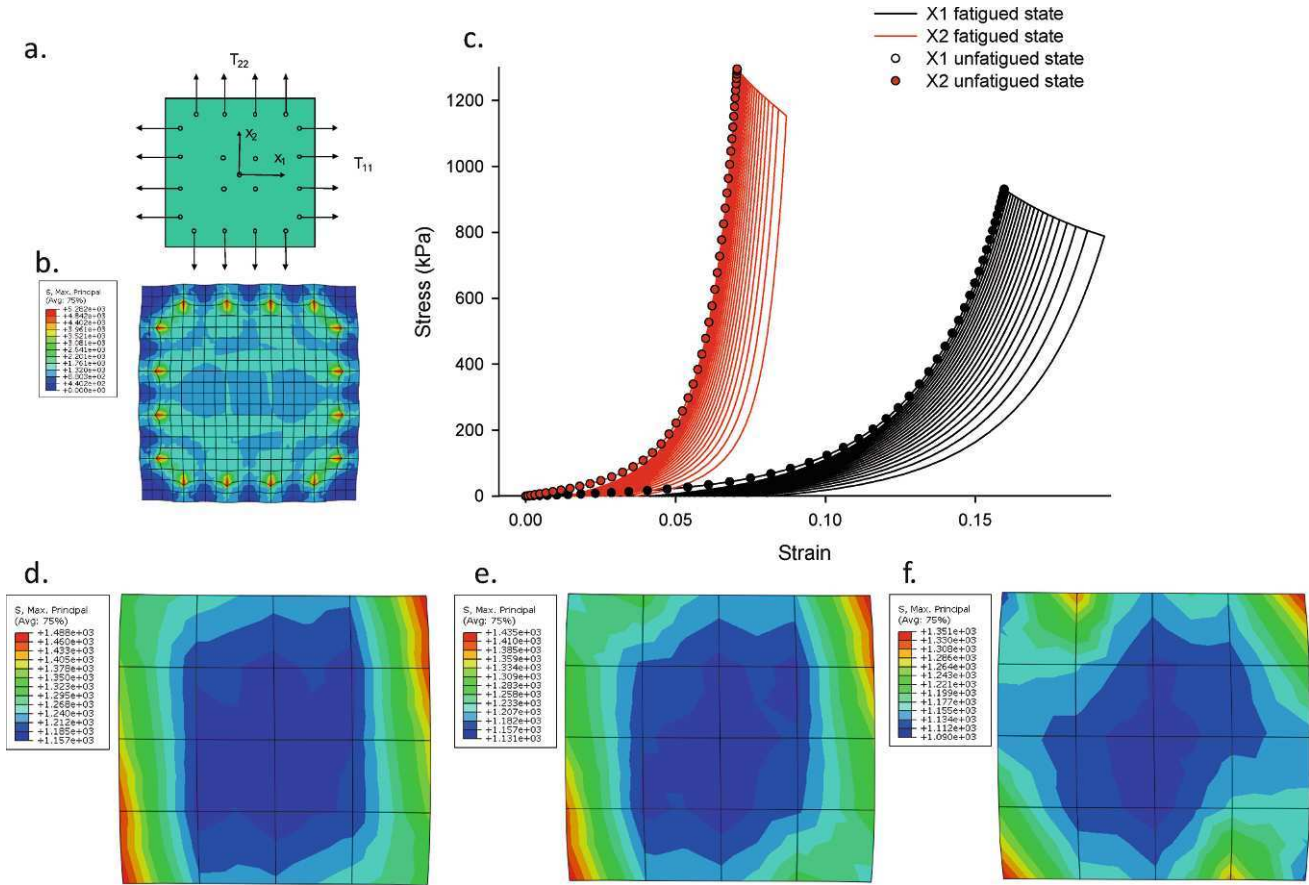


Fig.3 - (a) Loading conditions for simulated biaxial test specimen, and (b) the max principal stress contour plot for the simulated specimen under maximum tension. (c) The average stress-strain response of the central 16 elements throughout loading cycles. Fatigue response of simulated biaxial test specimen subjected to cyclic loading cycles. The max principal stress at peak loading of the 16 central elements at the (d) un-fatigued state, the (e) moderately fatigued state, and the (f) highly fatigued state.

Fatigue BHV simulation

The BHV finite element model was developed previously by Sun et al.¹⁸. Briefly, the tri-leaflet valve is fabricated from GLBP sheets that are die-cut to form leaflets, which are then mounted onto a metal frame. In the finite element model the wireframe was modeled using beam elements. The nominal material properties of the wireframe were taken from the material properties of Elgiloy with a Young's modulus of 2.33×10^7 kPa and Poisson ratio of 0.3. The leaflets were attached to the wire frame and modeled using large strain shell elements. Each leaflet had its own local coordinate system for material property definitions that are fully defined by the constitutive law Eq. (14). It was assumed that each leaflet can be modeled with one set of material parameters¹⁸. The leaflets were also assumed to have uniform thickness, which has been verified for pericardial tissue that is selected for valve fabrication. The valve model was cyclically loaded from a stress-free position to a fully loaded configuration by applying a uniform pressure to the aortic side of the leaflet. The contact between two leaflets was modeled using a master-slave contact pair (an option in ABAQUS). The leaflet that was stiffer in the radial direction was assigned as the master surface while the other was specified as the slave surface.

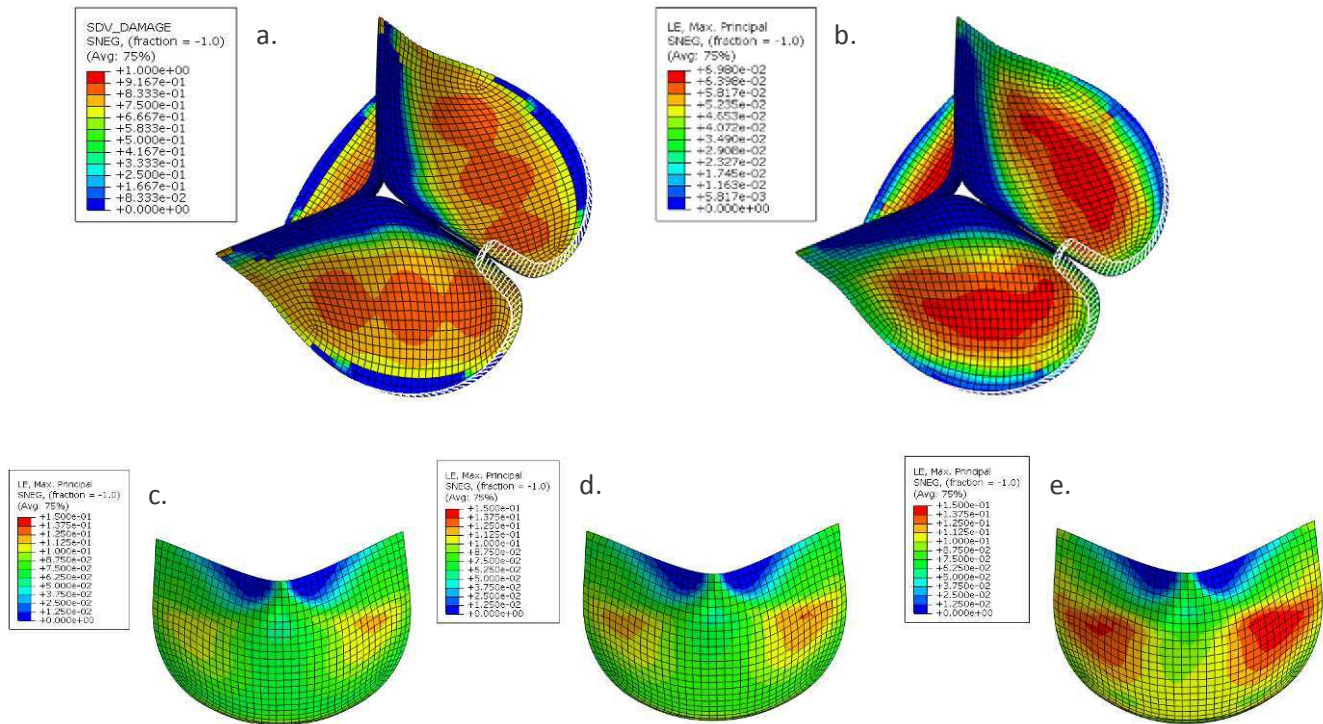


Fig.4 - (a) Damage contour plot and (b) residual strain contour plot of an unloaded (zero stress) BHV model after cyclic loading. Strain contour plot of a BHV leaflet at the un-fatigued state, the (b) moderately fatigued state, and the (c) highly fatigued state under ~ 120 mmHg of pressure.

The valve simulation demonstrated the model capability to describe the fatigue-induced effects of GLBP leaflets subjected to cyclic loading cycles of 120mmHg pressure. A contour plot of the damage factor (Fig.4a) reveals high damage in the belly region of the leaflets, and a contour plot of the logarithmic strain (Fig.4b) shows residual strains in the damaged regions at the zero-stress state. As the leaflets become more damaged, they achieve higher strains at loading as evident from the strain contour plots of a GLBP leaflet at different fatigue states in Fig.3c-e.

DISCUSSION

In this study, we developed a theoretical and computational framework to model soft tissue damage that incorporates the long-term fatigued-induced stress softening and permanent set phenomena exhibited by biological tissues under cyclic loading. We demonstrate the feasibility of this approach by simulating tissue fatigue damage under biaxial loading conditions as well as for BHV applications. The distinguishing characteristic of our approach with respect to that of others^{7-9,19}, is that our focus is on long-term fatigue effects. Unlike previous damage models for fibered composites^{7-9,19} we considered an incremental accumulation of damage at a set equivalent strain, whereas other models considered an accumulation of damage only when the previous maximum equivalent strain had been exceeded. Our approach was also unique to other models that consider residual strain^{14,20}, because our focus was not to model the hysteresis effect upon each unloading cycle, rather the progressive permanent change in specimen geometry due to long-term loading cycles, and thus our D_1 and D_2 functions are active during both loading and unloading cycles at the onset of damage. Therefore, our framework is not intended for the accurate fitting of each loading and unloading curve, rather we assume uniform damage accumulation to model the transition from a zero-state to a fatigued state with long-term (100+ million) loading cycles.

One of the limitations of this study is that we assume a linear progression of damage at a given equivalent strain as a function of loading cycles, whereas the damage may be more dramatic during the initial cycles. Also, the damage parameters used in simulations may not be representative of actual experimental fatigue data of GLBP tissue.

ACKNOWLEDGEMENT

Research for this project was funded in part by the CT DPH grant #2010-0085 and an AHA SDG grant #0930319N.

REFERENCES

1. Brewer R, Mentzer R, Deck J, Ritter R, Trefil J, Nolan S. An in vivo study of the dimensional changes of the aortic valve leaflets during the cardiac cycle. *Journal of Thoracic and Cardiovascular Surgery* 1977;74:645-650.
2. Munt B, Webb J. Percutaneous valve repair and replacement techniques. *Heart*. 2006;92(10):1369-72. Epub 2005 Dec 9.
3. Webb J, Pasupati S, Humphries K, Thompson C, Altwegg L, Moss R, Sinhal A and others. Percutaneous transarterial aortic valve replacement in selected high-risk patients with aortic stenosis. *Circulation* 2007;7(116):755-763.
4. Mirnajafi A, Brett Z, Michael SS. Effects of cyclic flexural fatigue on porcine bioprosthetic heart valve heterograft biomaterials. *Journal of Biomedical Materials Research Part A* 2010;94A(1):205-213.
5. Sun W, Sacks M, Fulchiero G, Lovekamp J, Vyavahare N, Scott M. Response of heterograft heart valve biomaterials to moderate cyclic loading. *J Biomed Mater Res* 2004;69A(4):658-69.
6. Sellaro TL, Hildebrand D, Lu Q, Vyavahare N, Scott M, Sacks MS. Effects of collagen fiber orientation on the response of biologically derived soft tissue biomaterials to cyclic loading. *Journal of Biomedical Materials Research Part A* 2007;80A(1):194-205.
7. Simo JC. On a fully three-dimensional finite-strain viscoelastic damage model: Formulation and computational aspects. *Computer Methods in Applied Mechanics and Engineering* 1987;60(2):153-173.
8. Calvo B, Pena E, Martinez MA, Doblaré M. An uncoupled directional damage model for fibred biological soft tissues. Formulation and computational aspects. *International Journal for Numerical Methods in Engineering* 2007;69(10):2036-2057.
9. Rodríguez JF, Cacho F, Bea JA, Doblaré M. A stochastic-structurally based three dimensional finite-strain damage model for fibrous soft tissue. *Journal of the Mechanics and Physics of Solids* 2006;54(4):864-886.
10. Li D, Robertson AM. A Structural Multi-Mechanism Damage Model for Cerebral Arterial Tissue. *Journal of Biomechanical Engineering* 2009;131(10):101013-8.
11. Sun W, Sacks MS. Finite element implementation of a generalized Fung-elastic constitutive model for planar tissues. *Biomechanics and Modeling in Mechanobiology* 2005;4(Nov.,(2-3)):190-9.
12. Fung YC. *Biomechanics: Mechanical Properties of Living Tissues*. New York: Springer Verlag; 1993. 568 p.
13. Natali AN, Pavan PG, Carniel EL, Dario P, Izzo I. Characterization of soft tissue mechanics with aging. *IEEE Engineering in Medicine and Biology Magazine* 2008;27(4):15-22.
14. Dorfmann A, Ogden RW. A constitutive model for the Mullins effect with permanent set in particle-reinforced rubber. *International Journal of Solids and Structures* 2004;41(7):1855-1878.
15. Sun W, Sacks MS, Sellaro TL, Slaughter WS, Scott MJ. Biaxial mechanical response of bioprosthetic heart valve biomaterials to high in-plane shear. *Journal Biomechanical Engineering* 2003;125:372-380.
16. Sacks MS, Sun W. Multiaxial Mechanical Behavior of Biological Materials. *Annu Rev Biomed Eng* 2003.
17. Sun W, Chaikof E, Levenston M. Numerical approximation of tangent moduli for finite element implementations of nonlinear hyperelastic material models. *Journal of Biomechanical Engineering* 2008 130(6):20-27.
18. Sun W, Abad A, Sacks MS. Simulated bioprosthetic heart valve deformation under quasi-static loading. *J Biomech Eng* 2005;127(6):905-14.
19. Alastrué V, Rodríguez JF, Calvo B, Doblaré M. Structural damage models for fibrous biological soft tissues. *International Journal of Solids and Structures* 2007;44(18-19):5894-5911.
20. Wan WK, Campbell G, Zhang ZF, Hui AJ, Boughner DR. Optimizing the tensile properties of polyvinyl alcohol hydrogel for the construction of a bioprosthetic heart valve stent. *Journal of Biomedical Materials Research* 2002;63(6):854-861.

An *in-situ* experimental-numerical approach for interface delamination characterization

J.P.M. Hoefnagels¹, M. Kolluri^{1,2}, J.A.W. van Dommelen¹, M.G.D. Geers¹

¹ Eindhoven University of Technology, Dept. of Mechanical Engineering,
Den Dolech 2, 5612AZ, Eindhoven, The Netherlands.

³ Materials Innovation Institute (M2i),
P.O.Box 5008, 2600GA, Delft, The Netherlands.

E-mail: j.p.m.hoefnagels@tue.nl

ABSTRACT

Interfacial delamination is a key reliability challenge in composites and micro-electronic systems due to (high density) integration of dissimilar materials. Predictive finite element models are used during the design and optimization stage to minimize delamination failures, however, they require a relevant interface model to capture the (irreversible) crack initiation and propagation behavior observed in experiments. Therefore, a set of experimental-numerical tools is presented to enable accurate characterization of delamination mechanism(s) and prediction of the interface mechanics.

First, a novel Miniature Mixed Mode Bending (MMMB) delamination setup is presented that enables in-situ SEM characterization of interface delamination mechanisms while sensitively measuring global load-displacement curves for the full range of mode mixities. Accurate determination of the critical energy release rate from the global load-displacement curve requires, however, identification and separation of bulk plastic contributions from the measured total energy dissipation; to this end, an analytical procedure is presented. Finally, a cohesive zone model suitable for mixed mode loading with realistic coupling is presented that can capture the range of interface failure mechanisms from damage to plasticity, as observed in-situ with SEM, as well as a parameter identification procedure. The set of experimental-numerical tools is validated on delamination measurements of a glue interface.

INTRODUCTION

In the past century, the ever increasing demand from the aerospace industry for lightweight structures with superior mechanical and physical properties has led to the development of several composite materials with many different combinations of matrix and reinforcement materials. On the other hand, the demand for continuous miniaturization and multi-functionality of electronic devices led to the development of new packaging technologies like "system in packages" in which multiple, thin, stacked layers manufactured using different materials and processes are integrated in a single package to achieve multi-functionality. The common feature in both systems (composites and electronic package) is that superior properties come along with a high density of interfaces that are formed between dissimilar materials. Therefore, interface integrity is inherently crucial for the reliability and performance of these systems. In spite of many efforts [1, 2] to improve the mechanical properties of these interfaces, interface delamination is often identified as the prominent failure mechanism in many of the modern interface structures ranging from micro-electronic packages [3–5], advanced aerospace composite structures [6–8] to the adhesive joints in honeycomb sandwich structures [6, 9] and wind turbine blades [10]. [Figure 1](#) shows the examples of delamination failures observed in a typical lead frame based micro-system package and a composite material. Delamination occurs mainly due to significant stresses generated at these interfaces during thermal cycling, triggered by the mismatch of the coefficient of thermal expansion (CTE) and the Poisson's ratio of the adherent layers or by mechanical loading of the structure. No adequate methodologies are currently available for the proper characterization and prediction of

interfacial failure in these systems. As a consequence, the industry is still heavily depending on trial-and-error methods for product/process development. Predictive finite element models are required to minimize delamination failures during the design and optimization of these materials and systems. Successful prediction, however, requires a relevant interface model that can capture the observed (irreversible) crack initiation and propagation behavior in experiments.

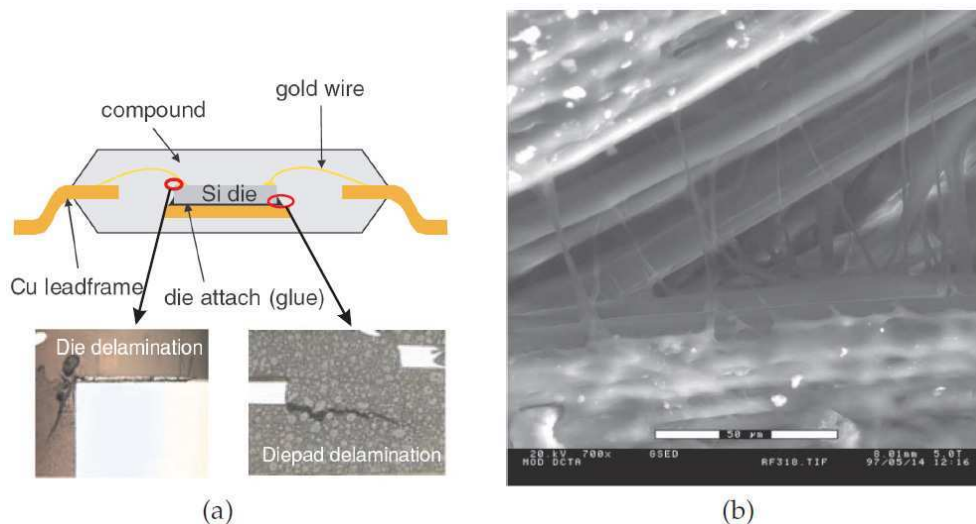


Figure 1. Example of delamination failures in (a) lead frame based package [3] and (b) 0°/90° ultra high molecular weight polyethylene composite [6].

To minimize the delamination failures and to improve the design rules of these products a generic experimental-numerical methodology that can accurately characterize and predict interface delamination is needed. Therefore, the aim of this work was to develop an experimental-numerical methodology for characterization and prediction of interface delamination in dissimilar multi-layer systems. To achieve this goal, (i) an experimental setup suitable to characterize delamination in dissimilar bi-layer material systems was designed and realized, (ii) a numerical model that can simulate the irreversible loading-delamination-unloading behavior of the interface was formulated and (iii) a procedure to extract the relevant parameters of the interface from the delamination experiments was developed. In this proceeding, the methods, analyses, results and conclusions of this work are briefly summarized.

RESULTS AND DISCUSSION

A miniature mixed mode delamination setup for in-situ microscopic interface failure analyses

The development of the experimental setup started with a literature review to evaluate the suitability of existing experimental setups for characterization of delamination and to identify the requirements for the new setup. Experimental methods based on linear elastic fracture mechanics (LEFM) approaches [11–25] are widely used in the literature for delamination studies. The critical load for delamination together with information about the crack length are the only values required from the experiment to obtain the interface toughness using existing LEFM approaches (assuming the geometry and material properties of the adherent layers are known). Unfortunately, this approach might fail for cases where the interface exhibits a relatively large fracture process zone (compared to the crack length) for at least two reasons: (i) validity of LEFM solutions for interface toughness is questionable, and (ii) quantification of interface behavior with only one parameter is insufficient. Therefore, detailed characterization of fracture process zone is needed to quantify the behavior of such interfaces. Cohesive zone (CZ) models, where the shape of the constitutive law is a priori assumed and is parameterized with at least two parameters (e.g. interface toughness and characteristic fracture length scale), are widely used to describe the behavior of such interfaces. This means that apart from the interface toughness, additional parameters that quantify the fracture processes within the process zone are needed from the delamination experiments. Moreover, the setup should allow for the measurement of interface toughness without any LEFM solutions. Many reports in the literature [26–31] have shown that the interface fracture toughness varies significantly with mode mixity. Therefore, the interface toughness should be evaluated over the full range of mode mixities. Although several experimental setups for mixed-mode delamination characterization are available in the literature [20–24], they are not suitable for in-situ visualization of the delamination process under a

microscope which is mandatory for the evaluation of details of the process zone (e.g. local crack opening displacement fields at the delamination front) to quantify the input parameters needed for CZ models.

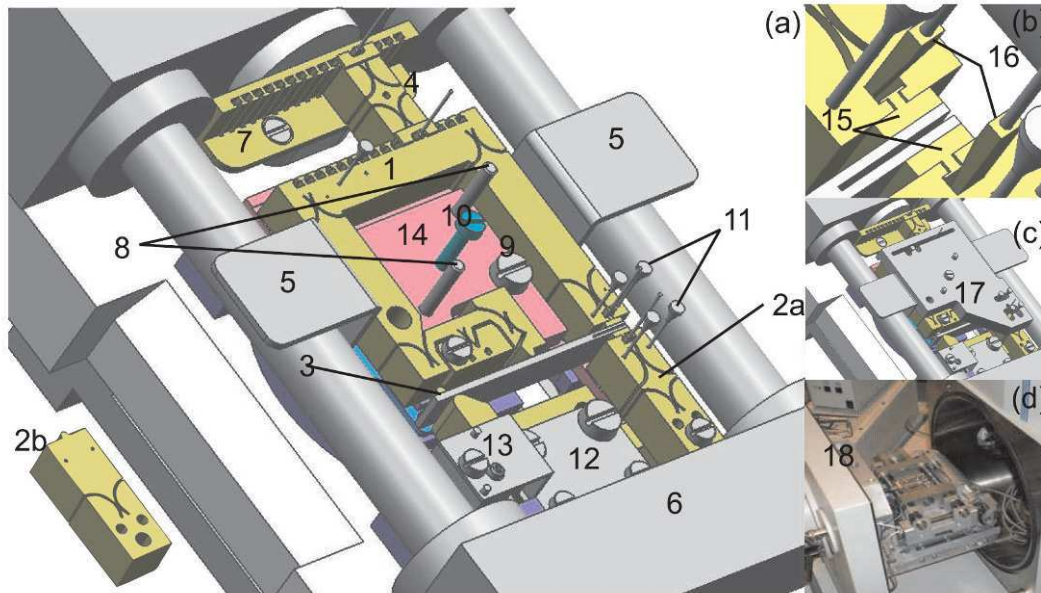


Figure 2. (a) the improved MMBB setup mounted in the micro-tensile stage: (1) main loading mechanism, (2a,2b) bottom hinges, (3) sample, (4) position selector; (5) handling plate, (6) micro-tensile stage, (7) position bar; (8) guiding rods, (9) set screw, (10) screw lock, (11) alignment pins, (12) sample height adjuster, (13) alignment screw, (14) bottom plate. (b): (15) new tapered dovetail connectors and, (16) wedge locking tools that remove any clearance in the connectors. (c): (17) top supporting plate (to lock the device during insertion and removal of the wedges) and (d): improved MMBB setup mounted in (18) SEM chamber [32,33].

Therefore, a novel Miniature Mixed Mode Bending (MMBB) delamination setup, capable of in-situ characterization of interface delamination in miniature multi-layer structures, was designed and realized [32,33], see Fig. 2. An inventive loading configuration in combination with friction free elastic hinges is employed in the setup to sensitively measure global load-displacement delamination curves for the full range of mode mixities from which the interface toughness or Critical Energy Release Rate (CERR) can be determined. The setup was designed to work in a horizontal plane with sufficiently small dimensions to fit in the chamber of a scanning electron microscope or under an optical microscope allowing visualization of the detailed real-time fracture process during delamination. Finite element analysis of the setup proved the capability of the new setup to achieve a full range of mode mixities, with a constant mode angle as a function of the crack length and crack opening displacement, see Fig. 3. Analysis of the loading configuration revealed that the conventional end notch flexure test (ENF) may not be a good representation of mode II delamination, because the friction (resulting from the compressive normal stresses) between the two layers in the cracked region during the ENF test can lead to overestimation of the mode II interface toughness. This problem can be circumvented in the new MMBB setup by performing a delamination test in a pure mode II loading configuration.

It was found that the setup exhibits (i) a wide application range of interface systems because of its large maximum accessible load (50N) and large stroke (the maximum achievable displacement depends on the geometry and the material properties of the adherents) for all mode mixities, (ii) high accuracy in measuring the load-displacement response, as demonstrated from experiments on validation samples, which showed negligible hysteresis (Fig. 4(a)), (iii) excellent experimental reproducibility characteristics due to the specially designed alignment tools.

The measurement concept of the new MMBB setup was successfully validated by testing homogeneous bilayer samples with a glue interface system over the full range of mode mixities. It was also demonstrated that the crack length can be measured with high precision (Fig. 5(a)) and the delamination mechanism (crack bridging) can be visualized in detail by performing in-situ delamination tests (Fig. 5(b) and 5(c)).

The setup was employed for testing industrially relevant (coated) copper lead frame – molding compound epoxy (CuLF-MCE) samples in the full range of mode mixities (Fig. 4(b)). As explained earlier, loading-delamination-unloading tests performed were used to calculate the CERR at different mode mixities (Fig. 4(c)). In addition to the CERR measurements, real-time microscopic visualization allowed for the identification of the difference in the crack growth behavior between

different mode mixity tests and the correlation of the observed behavior with the measured CERR. A relatively brittle cleavage type of fracture was observed for the investigated CuLF-MCE samples, although at high magnification, limited crack bridging was observed (Fig. 5(d)).

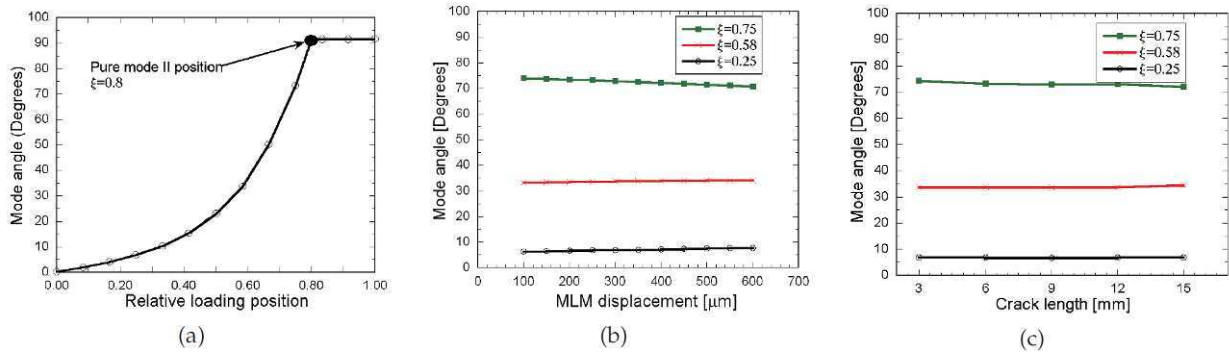


Figure 3. Mode angle obtained by FEM analysis as a function of (a) relative loading position (ξ) for a crack length of 6 mm at 400 μm MLM displacement, (b) displacement applied to MLM for three loading positions for a 6mm crack length specimen, and (c) crack length for three loading positions at 400 μm MLM displacement.

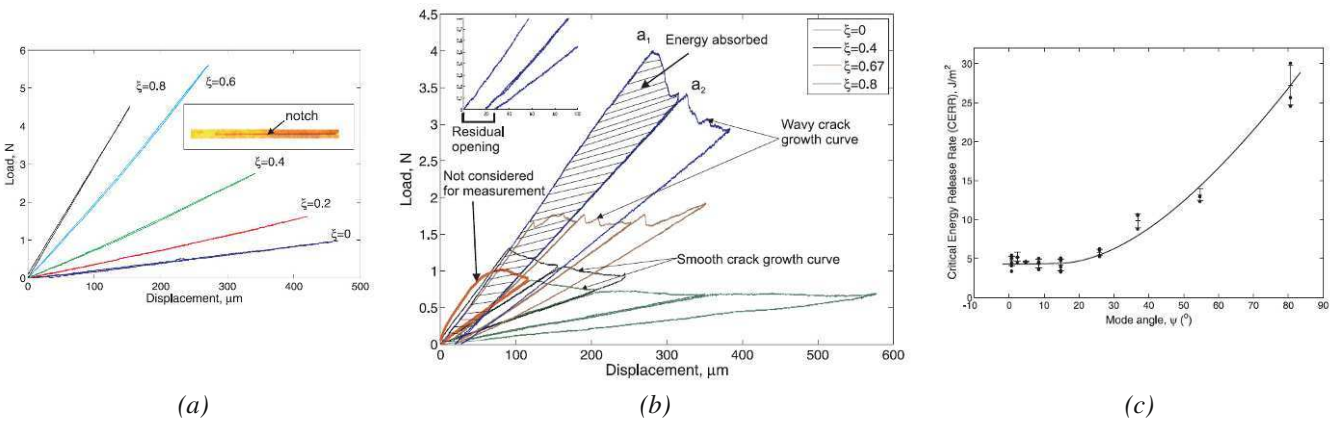


Figure 4. (a) Load-displacement results for loading-unloading cycles with the 12 mm validation sample at different loading positions (indicated by ξ); the inset shows the notched extremity of a validation sample used for mode I to pure mode II tests $\xi = 0 - 0.8$. (b) Comparison of load-displacement plots of a mode I ($\xi = 0$) and mixed mode ($\xi = 0.4, 0.67, 0.8$) experiments conducted on CuLF-MCE samples; the inset shows a magnification around the origin of the $\xi = 0.8$ curve illustrating the residual opening after unloading to zero load. (c) Critical energy release rate with standard deviation band width as a function of mode angle for the CuLF-MCE samples.

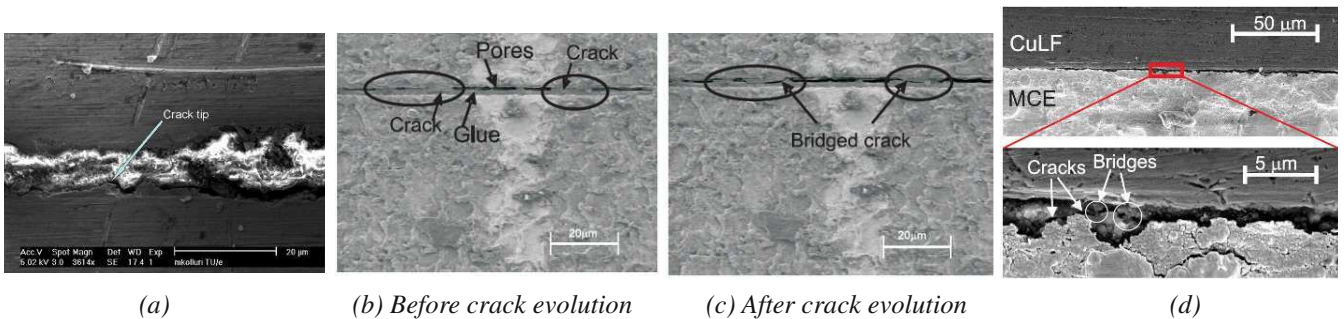


Figure 5. (a) SEM micrograph showing the precise crack tip location. (b,c) SEM micrographs of the glue interface samples showing the mechanism of delamination: bridging of the small cracks into a main crack. (d) SEM micrographs of the CuLF-MCE samples showing small cracks and a limited number of bridges at the interfaces.

Modeling and characterization of irreversible mixed mode interface delamination using a cohesive zone with combined damage and plasticity

In the delamination growth experiments conducted in this work, the energy dissipated in one loading-delamination-unloading cycle (i.e. the area under the load displacement curve) is divided by the corresponding increase in crack length during that cycle and the sample width to obtain the interface fracture toughness. This procedure for determination of the interface toughness is valid for any size of fracture process zone and only assumes that (i) the size and shape of (a fully developed) process zone remain constant during the crack growth, (ii) the energy supplied to trigger delamination growth is stored elastically in the specimen structure, without any plastic dissipation in the adherent layers (an assumption that is also employed for LEFM approaches). Consequently, the interface toughness can be straightforwardly obtained from the measured load-displacement response of delamination growth experiments when there is no plasticity in adherent bulk layers. However, there is much evidence in the literature showing that plasticity often does occur in the adherent (bulk) layers, particularly, if the layers forming the interface are ductile and the interface is strong. Consequently, it has been reported that large errors in the measurement of the interface fracture toughness can occur if these bulk plastic dissipations are neglected. Moreover, in-situ SEM observation of delamination on different interface structures revealed failure mechanisms ranging from interface damage to interface plasticity (Figs. 4 and 5). However, identification and separation of bulk plasticity from the total dissipated energy during a delamination experiment is not trivial, particularly in the presence of interface plasticity which is part of the interface fracture toughness. To be able to understand the individual contribution of bulk and interface plasticity to the total energy dissipated during a delamination experiment and to the global retained opening of the sample after complete unloading (inset of Fig. 4(b)), a numerical model that can incorporate both damage and plasticity behavior of the interface along with bulk plastic behavior was developed.

For this purpose, a combined plasticity-damage cohesive zone model that allows for modeling of irreversible unloading behavior with partial damage and partial plasticity and is suitable for mixed mode loading with a coupling between different modes was implemented [34], which is summarized here and is illustrated in Fig. (6). The combined plasticity-damage formulation is generic in the sense that it can be applied irrespective of the shape of CZ law used. In the current research, it was implemented based on the improved mixed-mode Xu-Needleman CZ law (Fig. 6(a,b)). The combined plasticity-damage behavior is accomplished by altering the ratio of the plastic energy and the total energy of the separation with one additional parameter called the plastic limit, $\delta_{n,pl}$, in addition to the standard CZ parameters (such as the interface toughness and critical displacement) that characterize the loading behavior of the traction-separation law used. The plastic limit was defined such that until the effective maximum separation of the cohesive zone reaches the plastic limit, the cohesive zone behaves fully elasto-plastic, as schematically shown in Fig. 6(c,d). Once the effective maximum separation passes the plastic limit, the plastically deformed cohesive zone damages with further separation (Fig. 6(c)). It was demonstrated that by varying the plastic limit from 0 to ∞ , the irreversible interface behavior of the CZ can be varied from full damage to a mixture of damage and plasticity to full plasticity (Fig. 6(d)). The CZ with a plastic limit (and without plasticity in adherent layers) provides a way to model the global retained opening due to only interface plasticity for mode I and mixed mode situations (Fig. 7).

A hybrid approach was proposed and demonstrated to determine all parameters of the mixed mode CZ law for a glue interface system. In this approach, first, Andersson and Stigh's method [35] is applied to extract mode I parameters (Fig. 8(a)). Then, the mode II interface strength, $T_{t,max}$, is determined using the fracture toughness values obtained from mixed mode tests performed at different mode angles from mode I to mode II (Fig. 8(b)). Finally, the plastic limit is determined from an analysis of displacement field maps obtained with digital image correlation (Fig. 8(c)).

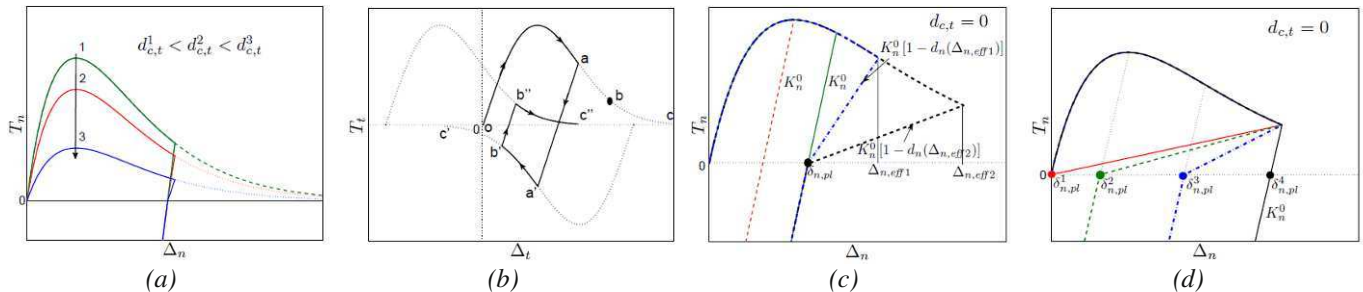


Figure 6. Schematic illustration of the combined plasticity-damage cohesive zone interface model (a) Influence of the coupled damage ($d_{c,t}$) term on the normal traction separation law with fully plastic unloading. (b) The yielding behavior of the tangential traction-separation law when the loading direction is reversed (at a and b'). The equivalent curve oabc shows the response when the CZ is loaded monotonically in one direction. (c) The unloading behavior of the new combined plasticity-damage CZ in normal opening above and below the plastic limit ($\delta_{n,pl}$). (d) The influence of $\delta_{n,pl}$ on the unloading behavior of the new combined plasticity-damage CZ in normal opening.

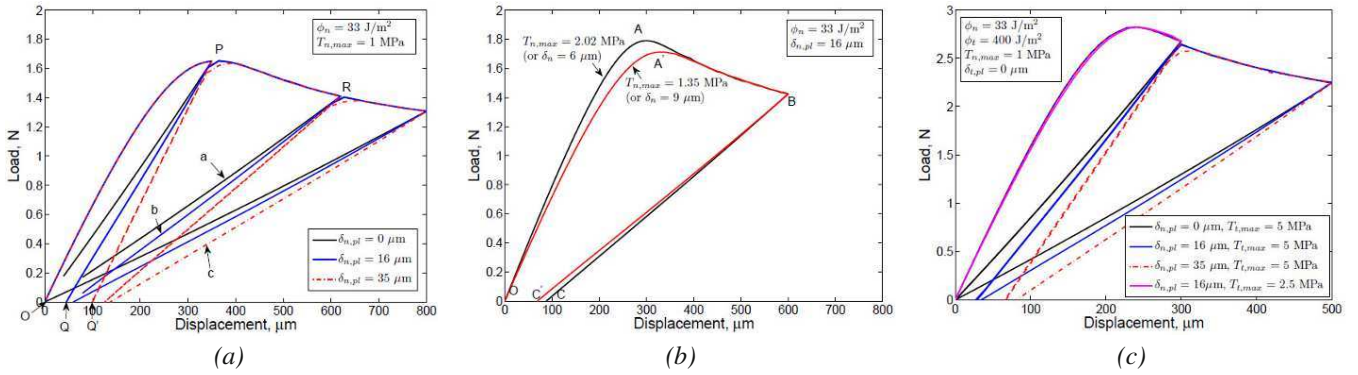


Figure 7. Global load-displacement response of mode I and mixed mode delamination simulations using the combined plasticity-damage cohesive zone interface model. (a) Influence of plastic limit on unloading-reloading behavior in mode I test. (b) Influence of $T_{n,max}$ on the mode I response. (c) Results of mixed mode simulation ($\psi = 20^\circ$) at different $\delta_{n,pl}$ and $T_{t,max}$.

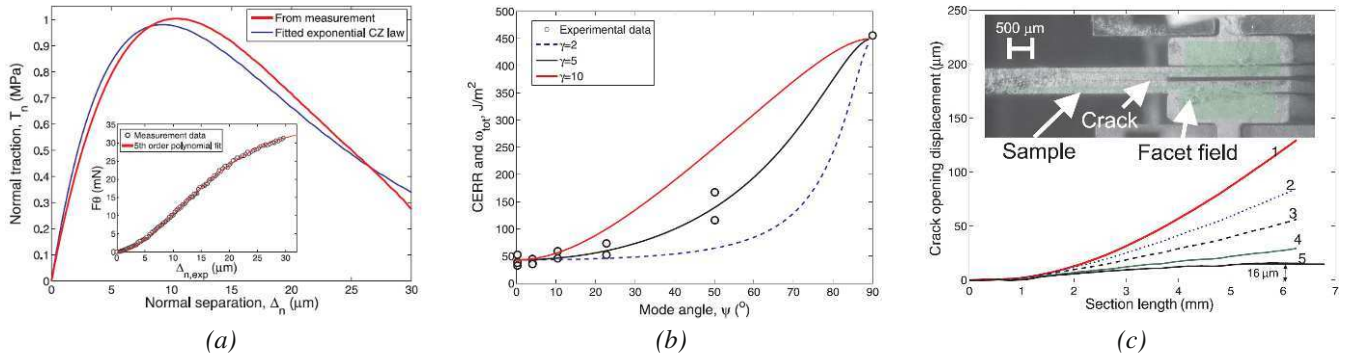


Figure 8. (a) Mode I traction-separation law of the glue interface system experimentally determined using Andersson and Stigh's approach (red line), shown together with the best-fit exponential CZ law using δ_n and ϕ_n as fitting parameters while taking $\Delta_t = 0$ (blue line); the inset shows the experimental $F\theta$ data as a function of opening of the interface at the crack tip, $\Delta_{n,exp}$ fitted with a 5th order polynomial with an R^2 value of 0.9996. (b) Experimentally measured critical energy release rates and the total work of separation of the cohesive zone model, ω_{tot} , as a function of the mode angle, ψ , for different values of $\gamma = T_{t,max} / T_{n,max}$. (c) Experimentally obtained unloading crack opening displacement profiles close to zero load showing the plateau with a value of $\delta_{n,pl} = 16 \text{ μm}$; the inset shows a micrograph of the edge of the sample (on the pre-cracked side) with the digital image correlation (DIC) facet overlay in green.

A semi-analytical approach for separation of interfacial toughness and bulk plastic dissipation in a delamination experiment

Finally, a semi-analytical approach is proposed that can be used as a data analysis tool to account for plasticity in the adherent (bulk) layers to obtain an accurate value for the interface fracture toughness from a mode I experiment [34]. This approach is based on reconstructing the force-displacement curve equivalent to the plasticity free case from the measured force-displacement response by identifying the individual contributions of bulk and interface plasticity to the total retained opening after complete unloading of the sample. This was achieved by assuming (for a given crack length) that (i) both the structural unloading stiffness and (ii) the critical load for delamination remain constant with and without bulk plasticity. The partitioning of the individual contributions of bulk plasticity and interface plasticity to the total retained opening is obtained by using retained crack opening profiles of the sample together with the assumptions that (iii) the size and shape of the process zone are constant and (iv) the bulk deforms plastically only in the region surrounding the process zone. The proposed approach and underlying assumptions were numerically verified by employing a finite element model with the combined damage-plasticity cohesive zone elements at the interface. An experimental assessment performed on CuLF-MCE samples with different thicknesses of the CuLF layers demonstrated that the correction of the interface fracture toughness due to bulk plasticity, resulting from this approach, was more than a factor of 2, see Fig. 9. Finally, this approach was developed such that it is generally applicable for most of the existing delamination growth experiments, as it only requires the determination of the crack opening displacement profile before and after the delamination test. Moreover, the approach does neither require any analytical solution or numerical simulation nor the constitutive behavior of the adherents.

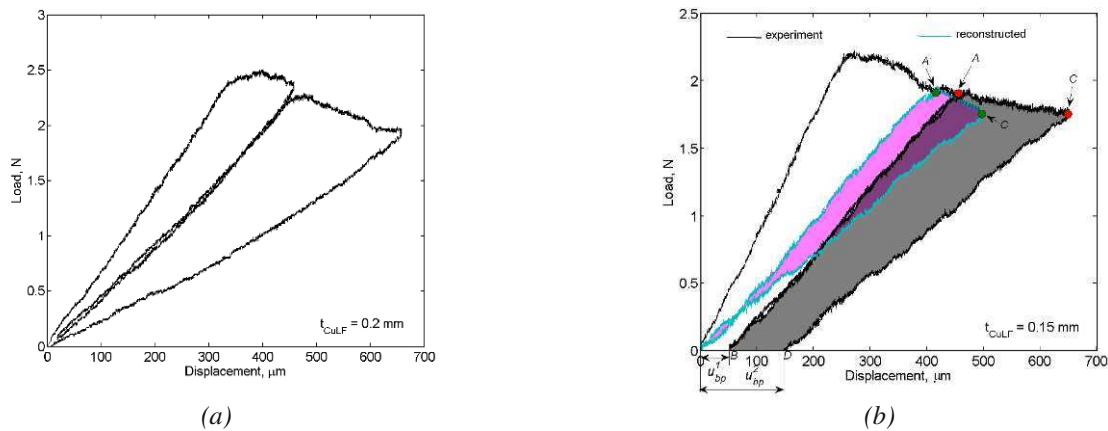


Figure 9. Load-displacement response of a mode I delamination experiment conducted on (a) a thick CuLF(0.2 mm)-MCE(0.5 mm) bilayer sample showing negligible retained opening after complete unloading yielding $CERR = 36 \text{ J/m}^2$, and on (b) a thin CuLF(0.15 mm)-MCE(0.5 mm) bilayer sample of exactly the same interface, which exhibits a significant retained bulk plasticity. The shaded grey area (ACDB) shows the total energy spent during loading-unloading cycle 2, corresponding to an apparent $CERR$ of 73 J/m^2 . The reconstructed curve with enclosed magenta filled area (OA'C') shows the delamination energy in cycle 2 after separation of the bulk plastic contribution by applying the semi-analytical approach, yielding a corrected $CERR$ value of 31 J/m^2 which agrees within measurement uncertainties.

SUMMARY

In summary, the combined application of in-situ MMB experiments, the analytical procedure to determine the CERR, and the cohesive zone model with a parameter identification procedure allows for accurate characterization of delamination mechanism(s) and prediction of interface mechanics.

REFERENCES

1. N. Srikanth, L. Chan, and C. J. Vath-III. Adhesion improvement of EMC-lead frame interface using brown oxide promoters. *Thin Solid Films*, 504:397–400, 2006.
2. K. Bose, P. A. Mataga, and P. P. Castaneda. Improved impact and delamination resistance through interleaving. *Journal Key Engineering Materials*, 37:317–348, 1991.
3. O. van der Sluis, C. A. Yuan, W. D. van Driel, and G. Q. Zhang. *Nanopackaging*. Springer US, 2009.
4. O. van der Sluis, R. A. B. Engelen, R. B. R. van Silfhout, W. D. van Driel, and M. A. J. van Gils. Efficient damage sensitivity analysis of advanced Cu/low-k bond pad structures by means of the area release energy criterion. *Microelectronics Reliability*, 47:1975–1982, 2007.
5. W. D. van Driel, M. A. J. van Gils, R. B. R. van Silfhout, and G. Q. Zhang. Prediction of delamination related IC and packaging reliability problems. *Microelectronics Reliability*, 45:1633–1638, 2005.
6. S. A. Taylor and D. J. Carr. Post failure analysis of 00/900 ultra high molecular weight polyethylene composite after ballistic testing. *Journal of Microscopy*, 196:249–256, 1999.
7. A. Todoroki, M. Tanaka, and Y. Shimamura. Electrical resistance change method for monitoring delamination of CFRP laminates: effect of spacing between electrodes. *Composites Science and Technology*, 65:37–46, 2005.
8. G. A. O. Davies, D. Hitchings, and J. Ankersen. Predicting delamination and de-bonding in modern aerospace composite structures. *Composites Science and Technology*, 66:846–854, 2006.
9. R. Okada and M. T. Kortschot. The role of the resin fillet in the delamination of honeycomb sandwich structures. *Composites Science and Technology*, 62:1811–1819, 2002. Nix, W. D., "Mechanical properties of thin films," *Metall. Trans. A.*, 20, 11, pp. 2217–2245, 1989.
10. C. C. Chiang, J.-R. Lee, and H.-J. Bang. Structural health monitoring for a wind turbine system: a review of damage detection methods. *Measurement Science and Technology*, 19(122001):1–20, 2008.
11. A. G. Evans, M. Ruhle, B. J. Dalgleish, and P. G. Charalambides. The fracture energy of bimaterial interfaces. *Material Science and Engineering*, A126:53–64, 1990.
12. G. Dreier, M. Meyer, S. Schmauder, and G. Elssner. Fracture mechanics studies of thermal mismatch using a four-point bending specimen. *Acta Metallurgica et Materialia*, 40:S345–S353, 1992.

13. V. Gupta and A. Pronin. New technique to measure the toughness of thin-film interfaces. *Journal of American Ceramic Society*, 78(5):1397–1400, 1995.
14. A. A. Volinsky, J. B. Vella, and W. W. Gerberich. Fracture toughness, adhesion and mechanical properties of low-k dielectric thin films measured by nanoindentation. *Thin Solid Films*, 429:201–210, 2003.
15. W. Li and T. Siegmund. An analysis of the indentation test to determine the interface toughness in a weakly bonded thin film coating - substrate system. *Acta Materialia*, 52:2989–2999, 2004.
16. L. Banks-Sills, V. Boniface, and R. Eliasi. Development of a methodology for determination of interface fracture toughness of laminate composites - the $0^\circ/90^\circ$ pair. *International Journal of Solids and Structures*, 42:663–680, 2005.
17. Jy-An. J. Wang, I. G. Wright, M. J. Lance, and K. C. Liu. A new approach for evaluating thin film interface fracture toughness. *Material Science and Engineering A*, 426:332–345, 2006.
18. I. Ocăna, J. M. Molina-Aldareguia, D. Gonzalez, M. R. Elizalde, J. M. Sánchez, J. M. Martinez-Esnaola, J. Gil Sevillano, T. Scherban, D. Pantuso, B. Sun, G. Xu, B. Miner, J. He, and J. Maiz. Fracture characterization in patterned thin films by cross-sectional nanoindentation. *Acta Materialia*, 54:3453–3462, 2006.
19. Yu-Fu Liu, Y. Kagawa, and A. G. Evans. Analysis of a barb test for measuring the mixed-mode delamination toughness of coatings. *Acta Materialia*, 56:43–49, 2008.
20. J. R. Reeder and J. R. Crews. Mixed mode bending method for delamination testing. *AiAA Journal*, 28(7):1270–1276, 1990.
21. W. O. Soboyejo, G. Y. Lu, S. Chengalva, J. Zhang, and V. Kenner. A modified mixed-mode bending specimen for the interfacial fracture testing of dissimilar materials. *Fatigue and Fracture of Engineering Materials and Structures*, 22:799–810, 1999.
22. C. C. Merrill and P. S. Ho. Effect of mode mixity and porosity on interface fracture of low-k dielectrics. In *Materials Research Society Symposium Proceedings*, volume 812, 2004.
23. N. Blanco, E. K. Gamstedt, J. Costa, and D. Trias. Analysis of the mixed-mode end load split delamination test. *Composite Structures*, 76:14–20, 2006.
24. J. Thijssse, O. van der Sluis, J. A. W. van Dommelen, W. D. van Driel, and M. G. D. Geers. Characterization of semiconductor interfaces using a modified mixed mode bending apparatus. *Microelectronics Reliability*, 48:401–407, 2008.
25. J. D. Gunderson, J. F. Brueck, and A. J. Paris. Alternate test method for interlaminar fracture toughness of composites. *International Journal of Fracture*, 143:273–276, 2007.
26. J. W. Hutchinson and Z. Suo. Mixed mode cracking in layered materials. *Advances in Applied Mechanics*, 29:63–191, 1992.
27. M. S. Hu and A. G. Evans. The cracking and decohesion of thin films on ductile substrates. *Acta Metallurgica*, 37(3):917–925, 1989.
28. L. Banks-Sills, Nahum Travitzky, and Dana Ashkenazi. Interface fracture properties of a bimaterial ceramic composite. *Mechanics of Materials*, 32:711–722, 2000.
29. A. Kuhl and J. Qu. A technique to measure interfacial toughness over a range of phase angles. *Journal of Electronic Packaging*, 122:147–151, 2000.
30. X. Q. Shi, X. R. Zhang, and J. H. L. Pang. Determination of interface fracture toughness of the adhesive joint subjected to mixed-mode loading using finite element method. *International Journal of Adhesion and Adhesives*, 26:249–260, 2006.
31. S. Tang, T. F. Guo, and L. Cheng. Rate dependent interface delamination in plastic IC packages. In *9th Electronics packaging technology conference*, pages 680–685, 2007.
32. M. Kolluri, M. H. L. Thissen, J. P. M. Hoefnagels, J. A. W. van Dommelen, and M. G. D. Geers. In-situ characterization of interface delamination by a new miniature mixed mode bending setup. *International Journal of Fracture*, 158:183–195, 2009.
33. M. Kolluri, J. P. M. Hoefnagels, J. A. W. van Dommelen, and M. G. D. Geers. An improved miniature mixed mode delamination setup for in-situ microscopic interface failure analyses. *Journal of Physics D: Applied Physics*, 44:1–13, 2011.
34. M. Kolluri, An *in-situ* experimental-numerical approach for interface delamination characterization, PhD thesis, Eindhoven University of Technology, 2011, in press.
35. T. Andersson and U. Stigh. The stress-elongation relation for an adhesive layer loaded in peel using equilibrium of energetic forces. *International Journal of Solids and Structures*, 41:413–434, 2004.

Interface Integrity in Stretchable Electronics

Jan Neggers¹ (j.neggers@tue.nl), Johan Hoefnagels¹, Olaf van der Sluis², O. Sedaghat¹ and Marc Geers¹

1) Eindhoven University of Technology, Department of Mechanical Engineering, Den Dolech 2, 5612 AZ Eindhoven, Netherlands

2) Philips Applied Technologies, High Tech Campus 7, 5656 AE Eindhoven, Netherlands

ABSTRACT

Stretchable electronic devices enable numerous futuristic applications. Typically, these devices consist of a (metal) interconnect system embedded in a stretchable (rubber) matrix. This invokes an apparent stretchability conflict between the interconnect system and the matrix. This conflict is addressed by shaping the interconnects in mechanistic patterns that bend and twist to facilitate global stretchability. Metal-rubber type stretchable electronic systems exhibit catastrophic interface delamination, which is investigated in this research. The fibrillation process occurring at the delamination front of the metal-rubber interface is investigated through *in-situ* SEM imaging of the progressing delamination front of peel tests of rubber on copper samples. Results show that the interface strength is dependent on the delamination rate and the interface roughness. Additionally, the fibril geometry seems highly dependent on the interface roughness, while being remarkably independent on the delamination-rate.

INTRODUCTION

To allow electronic devices to be used close to or inside the human body, the devices need to be able to comply with the body. Since the body is very flexible, and locally even stretchable it is desired that these electronic devices are also stretchable. These devices typically consist of rigid or flexible functional electronic components, embedded in a elastomeric (rubber) matrix material [1-3]. These functional islands then need to be connected, and for the interconnect design two paths can be followed; (i) start with a stretchable, typically non-conductive, material and add conductivity, or (ii) start with conductive, typically non-stretchable, material and add stretchability. Designs following the first path mostly use elastomers for the interconnect material filled with conductive particles, or even nanotubes [4]. These interconnects are often very stretchable but the conductivity is low which limits frequency of the electronic signals. Designs following the second path mostly use metals for the interconnects adding stretchability by structuring the interconnects in mechanistic patterns which locally reduce the deformation, when they are stretched globally, similar to a helical telephone cord [5-7]. Although, both design paths have reliability issues, this paper focuses mainly on issues related to the second design path.

In previous research is shown that interface delamination between the elastomer matrix and metal interconnect is a precursor to failure [8-9]. After delamination the device has not yet failed, but the matrix material no longer distributes the load over the metal structure, thereby causing localization in the delaminated part of the interconnect, which then quickly leads to failure. Improving the interface will also improve the stretchability and reliability of the device and thereby may reduce the requirements on the mechanistic design or even render it obsolete. The amount of energy an interface can dissipate before delamination determines the toughness of the interface. Previous research indicated to the rubber fibrillation which occurs at the delamination front as the dominant dissipative mechanism. Therefore in this research the fibrillation is investigated further focusing on the dependence of the interface delamination on the interface roughness and on the delamination rate.

EXPERIMENTAL SETUP

The interface delamination is investigated by means of a T-peel test, which is an established method for testing interface delamination properties [10]. In a T-peel test, the two layers of an interface are separated at an angle of 90° using a tensile stage (Figure 1). From the force measured at the steady-state part of the peel-force displacement curve the work of separation can be calculated as

$$G_c = \frac{U_e}{A} = \frac{2uF}{bu} = \frac{2F}{b}, \quad (1)$$

where U_e is the mechanical energy supplied to the system, A the peeled area, F the force measured on the load-cell, u the displacement of the clamps and b the width of the peel front.

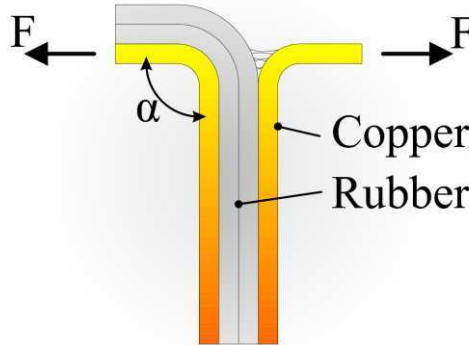


Fig. 1 Schematic illustration of the sample layout, and loading conditions

For this research a Kammrath-Weiss micro-tensile stage is used which is especially designed for use in combination with optical or electron microscopes. The stage is fitted with a 100N load-cell and can operate at clamp displacement velocities between 0.1μm/s and 100μm/s. This tensile stage fits inside the vacuum chamber of the FEI Quanta 600, Environmental Scanning Electron Microscope (ESEM), thereby allowing for high magnification *in-situ* observation of the real-time progressing delamination front (Figure 2). The possibility to visualize the delamination front *in-situ* is proven to be invaluable for observing the fibrillation process, because the fibrils quickly relax when the experiment is stopped. Consequently, imaging the peel front in a paused or interrupted experiment would not have shown the correct fibril geometry. The same ESEM is also used to image both the new surfaces created by the peel-test experiment, where for the rubber side the Environmental mode was essential, due to the non-conductive nature of the material.

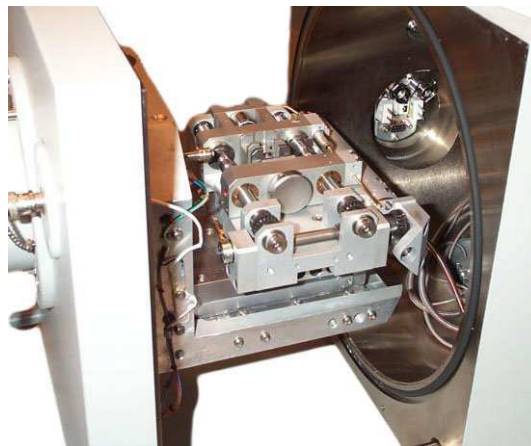


Fig. 2 The micro-tensile stage, placed in the vacuum chamber of the environmental scanning electron microscope

SAMPLES

The samples used in the test were provided by the TU-Berlin, courtesy of Thomas Löher. The samples consist of a 50 μm thick layer of TPU¹ laminated on a 35 μm thick layer of TW-YE grade printed circuit board copper, which is delivered with the interface side roughened, exhibiting a 3–5 μm deep fractal surface (Figure 3b). This combination of materials is chosen because it is actually used in current stretchable electronic prototypes. To create a T-peel-test sample two of such (bi-layer) samples are laminated back to back, with the TPU in the center at a processing temperature of 200°, where a small part of the sample is not laminated to create a pre-crack. This effectively creates a 3 layer sample with on the outsides the copper layers and in the middle a 100 μm thick TPU layer with a pre-crack in the middle of the layer. This pre-crack is not at the correct interface, therefore before starting the “real” experiment, the sample is first peeled until the crack has propagated to either one of the two copper-TPU interfaces. To test the dependence of the interface delamination properties on the interface surface roughness the smooth side of the copper was treated with a chemical roughening step to create a 1 μm deep fractal surface (Figure 3a), from this point onwards called “smooth”, the TPU was then laminated to this surface in the same way as for the rough surface, which is from this point onwards called “rough”.

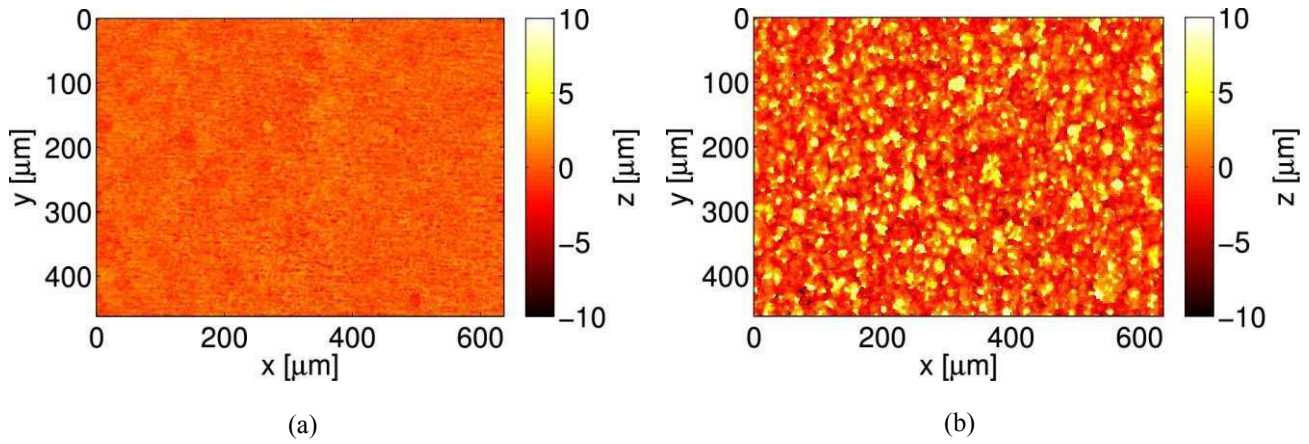


Fig. 3 Surface height maps measured with optical confocal profilometry for (a) the “smooth” sample type, and (b) the “rough” sample type

SURFACE ROUGHNESS DEPENDENCY

First the influence of the interface surface roughness on the fibrillation mechanics is investigated. The surface roughness is quantified by measuring “clean” pre-laminated copper surfaces of both sample types using a Sensofar plμ4200 optical confocal surface profilometer (Figure 3). From the surface height maps of both sample types the root mean squared roughness is calculated

$$R_q = \sqrt{\frac{1}{N} \sum_{i=1}^N (z_i - \bar{z})^2}, \quad (2)$$

where N is the number of data points (i.e. pixels) in the surface height map, z is the height and \bar{z} is the mean height of the entire measurement. Before calculating the roughness, the surface height map is leveled with a 3rd order plane, fitted through the data, to correct for any large scale deviations. The two sample types measured a roughness of 0.52 μm and 2.46 μm for the “smooth” and the “rough” sample respectively.

¹ Thermo-Plastic Urithane, walopur by Epurex

The peel-force displacement curves of peel-tests performed for both samples revealed that the “smooth” interface is a lot weaker than the “rough” interface (Figure 4). This is expected and already shown in [9], the reasons for a rougher interface to be stronger are threefold, a rougher interface (i) has a larger area to chemically bond to, (ii) increases the amount of delamination mode-mixity, caused by the various angles of the local interface with respect to the peel-front opening angle, and (iii) the extreme asperities can also mechanically interlock the elastomer. However, the effect on the fibrillation process was not discussed in [9]. From the *in-situ* imaging of the progressing delamination front the fibrillation process can be visualized (Figure 5). From these micrographs can clearly be seen that the fibrils for the “rough” sample are much larger than the fibrils for the “smooth” sample. Furthermore, for the “rough” samples the fibrils seem to remain connected to the copper longer in the “valleys” of the copper roughness, while for the “smooth” sample no clear correlation is seen between the roughness pattern and the fibril pattern.

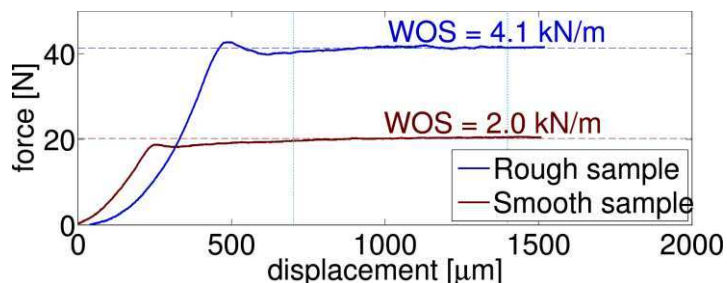


Fig. 4 Typical force displacement curves obtained from two peel tests for samples with different roughness, each curve consists of an initiation part, where the sample is loaded and starts to delaminate until a steady state peel-force is reached where the delamination rate is in balance with the loading rate, this is where the work of separation is determined.

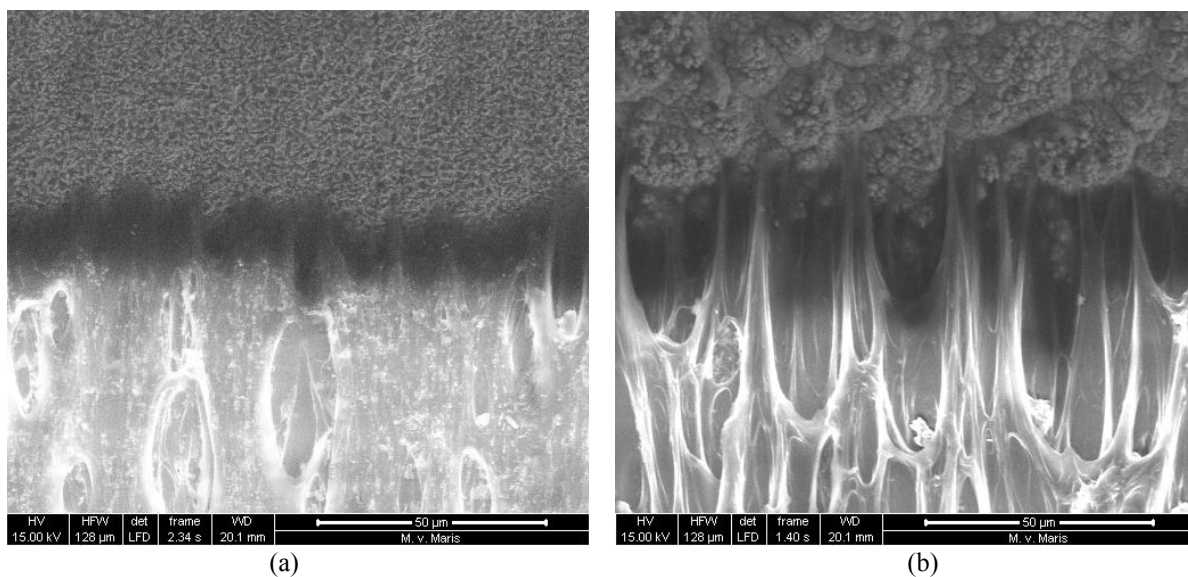


Fig. 5 ESEM micrographs captured of the progressing delamination front for (a) the “smooth” sample and (b) the “rough” sample type, with copper shown on top and TPU shown on the bottom side. Note that for the “smooth” sample the fibrils are located in the darker band at the peel-front.

Movies were made from the *in-situ* ESEM images, which allows for further analysis of the fibrils. By evaluating the movies backwards an estimation of the average fibril length is acquired by measuring each fibril in the movie just before it fractures. This method is performed for both sample types and the measured fibril lengths are approximately $12 \pm 3 \mu\text{m}$ and $23 \pm 3 \mu\text{m}$ for the “smooth” and “rough” sample respectively (Figure 6).

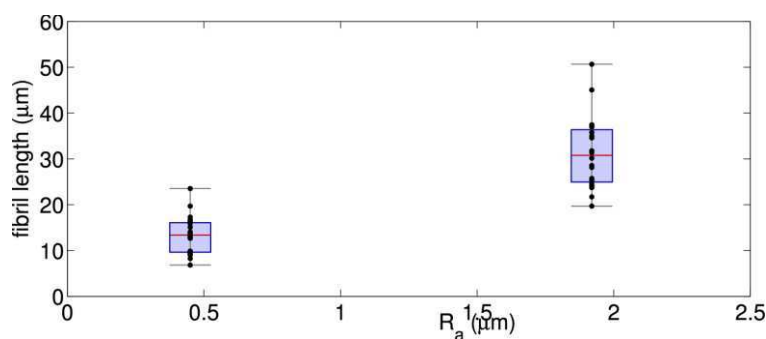


Fig. 6 A quantitative comparison of the fibril length as measured from movies, taken from both the “smooth” and “rough” sample

PEEL RATE DEPENDENCY

To investigate the rate dependency of the interface delamination, the peel-test experiments, using the “rough” copper surface sample type, were performed at various peel-rates. Where the peel-rates were chosen logarithmically over a regime as large as possible with the current setup, resulting in four peel-rates 0.1, 1, 10 and 100 $\mu\text{m/s}$. For the fastest peel-rate it was impossible to capture useful *in-situ* ESEM images due to the too low acquisition rate compared to the movements within an image.

Figure 7a shows typical peel-force displacement curves measured at all four peel-rates, showing that for increasing peel-rate the work of separation also increases. To reduce the scatter between different series of measurements, each measurement set is normalized with the 10 $\mu\text{m/s}$ measurement of the set. Interestingly, if the normalized work of separation is plotted against the logarithm of the peel-rate, a linear relation is shown (Figure 7b).

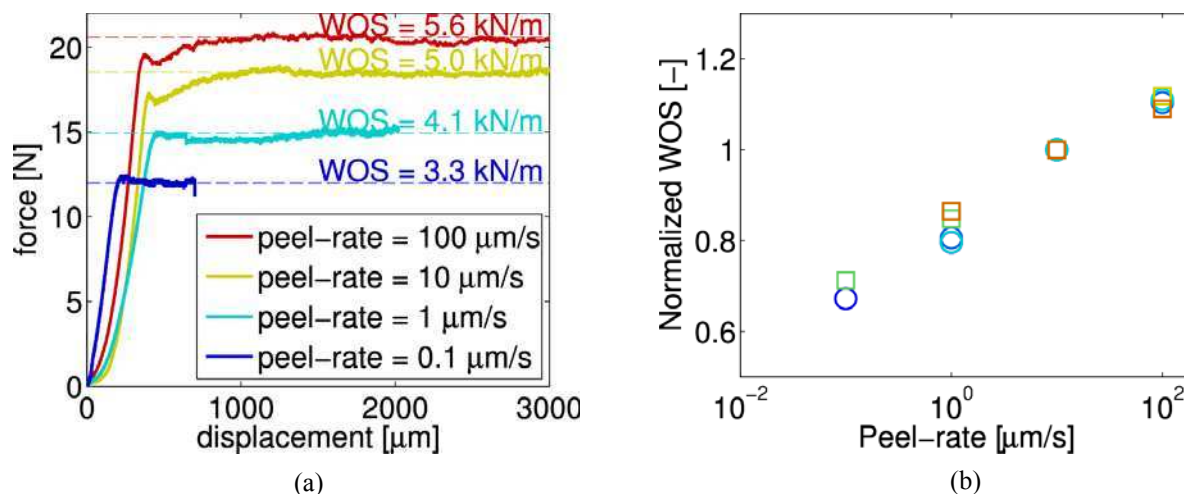


Fig. 7 (a) Four typical force displacement curves obtained from peel tests performed at four different peel-rates. **(b)** Plotting the work of separation, normalized with the 10 $\mu\text{m/s}$ measurement of that measurement set, against the logarithmic peel-rate reveals a linear peel-rate dependency.

Using the same method as described above to measure the fibril length, gives an approximation of the average fibril length for each peel-rate (Figure 8). From these fibril length measurements can be concluded that the fibrils remain remarkably constant over three decades of peel-rates (Figure 9). This indicates that while the peel-rate affects the interface strength, it does not affect the delamination micro-mechanisms. Therefore, to understand these mechanisms better, the surfaces created by the peel test can be investigated. The interface delamination can be subdivided in three failure modes, where the interface can fail

(i) in the copper, leaving copper behind on the rubber surface and (ii) in the fibril, leaving rubber behind on the copper surface, (iii) at the interface.

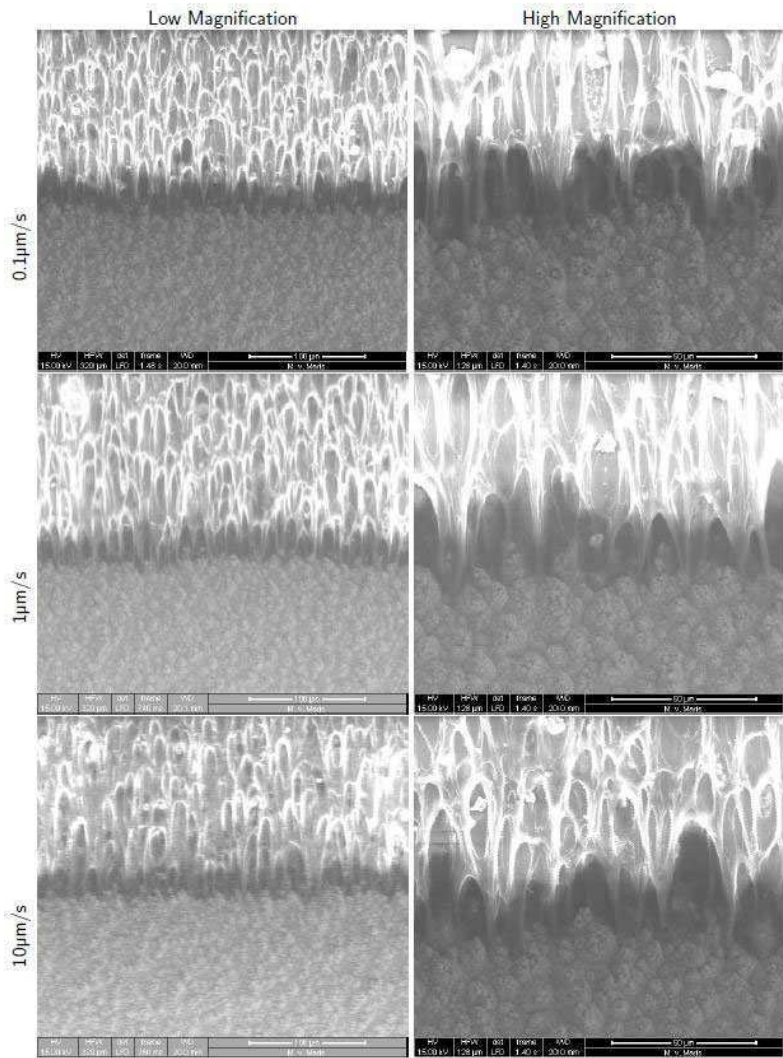


Fig. 8 ESEM *in-situ* micrographs of the fibrillation process for various peel-rates, note that the fibril geometry is remarkably similar for all peel-rates

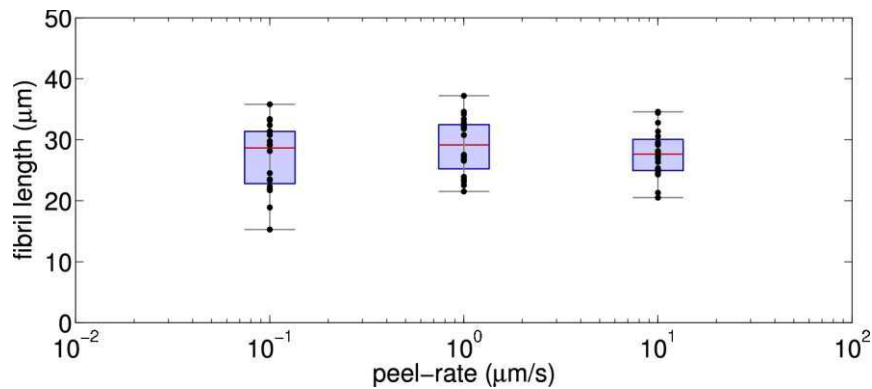


Fig. 9 A quantitative comparison of the fibril length as measured from movies, taken from both three different peel-rates

Figure 10 shows typical ESEM micrographs of the rubber surface after peeling for three peel-rates, each showing small copper particles on the rubber surface, confirmed with Energy-dispersive X-ray spectroscopy. From the area created by the peel test experiment for each respective peel-rate, five images are taken. For each image the amount of copper left behind on the rubber surface is quantified by means of segmentation, and plotted in figure 11, showing that there is an increasing trend for the amount of copper for increasing peel-rate. The “rough” copper surface is created by adding an extra electroplating step to the TW-YE grade copper foil. Resulting in a surface covered with various size (and strength) asperities. Consequently, it can be assumed that if more copper asperities are torn off the copper surface by the fibrils, that in the distribution of torn-off asperities, some were stronger. Following this reasoning, we can assume that the forces in these fibrils are also larger. Figure 8 shows that the fibril geometry does not change significantly as a function of peel-rate, leading to the conclusion that if the number of copper particles for a given peel-rate is larger, that then the stresses at the interface must also have been larger. However, it must be noted that the fibril geometry is actually very difficult to quantify or compare, therefore this conclusion must be taken lightly.

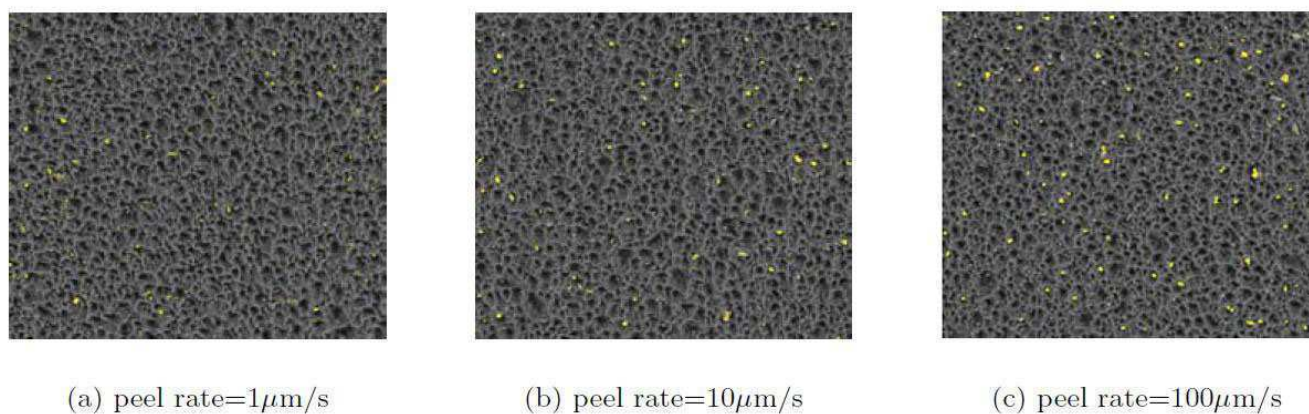


Fig 10 ESEM images of the rubber surface created by the peel-test experiment, the bright spots are copper particles torn off the copper surface.

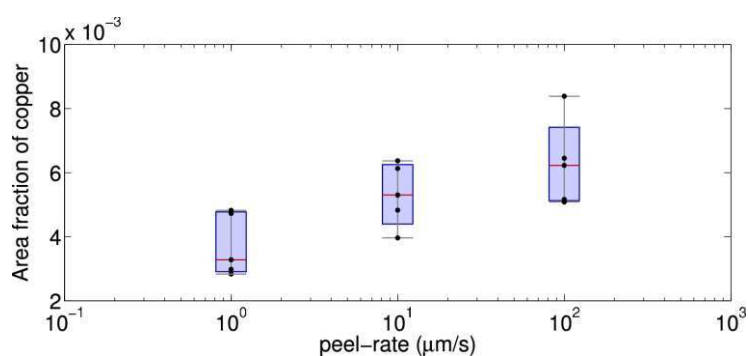


Fig 11 The measured area of copper on the rubber surface after peeling for various peel-rates

Likewise, the copper area after peeling is also investigated, where rubber fibril fracture will leave rubber patches on the copper surface. For all four peel rates, 10 SEM images are taken from the area created by the peel-test for the respective peel-rates. Similarly to the rubber surface analysis the area covered with rubber is quantified using a threshold technique. The obtained rubber area fractions are compared in figure 12, which, due to large scatter, show an unclear trend between the rubber area fraction and the peel-rate. For all investigated copper surfaces the rubber area fraction was significant, which by itself shows that the rubber fracture mechanism plays a significant role in the delamination process, and thus possibly also in the peel-rate dependency.

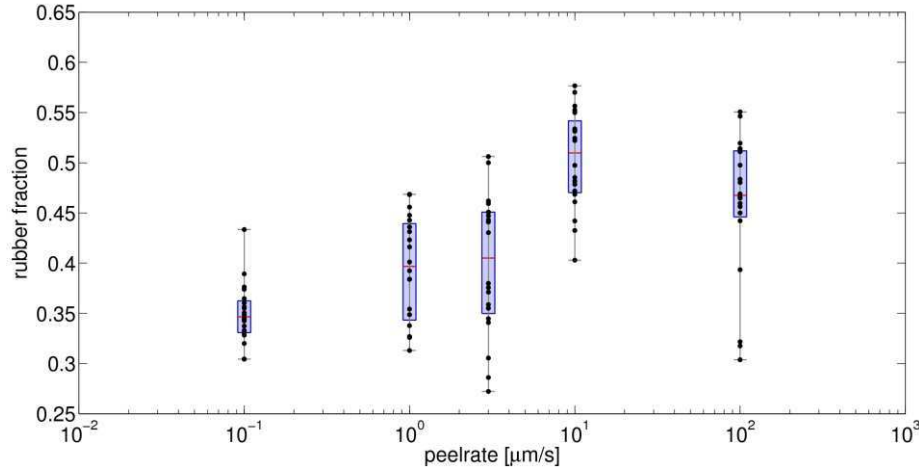


Fig 12 The measured area of rubber on the copper surface after peeling for various peel-rates

CONCLUSIONS

In-situ visualizations are a powerful tool for investigating the real-time progressing delamination front, because it allows the visualization of the real fibrillation process. Due to the fast relaxation of the fibrils they are impossible to visualize for a paused experiment or after the experiment. The *in-situ* visualization shows that the fibril geometry depends strongly on the copper surface roughness, which can be expected since the onset of a fibril is a void in the interface which will probably occur in the weakest spot in the interface, which is determined by the micro-shape of the interface. This is confirmed by the measured work of separation which is larger for the rougher sample. Remarkably, the *in-situ* visualization also shows that the fibril geometry does not change significantly between different peel-rates, while the work of separation, or interface strength does depend logarithmically on the peel-rate.

Three interface failure modes are identified, (i) failure in the copper near the interface, (ii) failure in the rubber fibril, (iii) failure at the interface. Analysis of the rubber surface created by the peel-test revealed that for increasing peel-rates more copper fracture occurs, indicating that the fibril stresses are higher for faster peel-rates, which is in contrast with the apparent insignificant changes in fibril geometry for different peel-rates. Analysis of the copper surface after peeling showed that fibril fracture occurs frequent indicating that it will probably have a significant role in the rate-dependency of the interface. It remains a question if the observed constant fibril length is due to the fact the fibril fracture strain is actually constant, or that the fibrils are stronger for higher peel-rates, and therefore, pull in more bulk rubber material, where-after they fracture at a lower (local) strain.

Finally, these interfaces are typically modeled using Cohesive Zone (CZ) elements in a Finite Element Method (FEM) model. Such CZ elements model the traction response of the interface as a function of opening, using a Traction Separation Law (TSL), for which typically three parameters are required, (i) the maximum traction, (ii) the critical opening, and (iii) the work of separation. The work of separation can easily be determined from the peel-force displacement curve, and through the TSL

all three are coupled, so only one more parameter is required to characterize the interface. Considering that the fibrils did not show significant geometrical changes for changes in peel-rate, indicates that if only one of the two remaining parameters would be time dependent it would probably be the maximum traction, since the critical opening of an interface is related to the maximum opening of an interface which is where the fibrils are imaged.

REFERENCES

- [1] D.-H. Kim et al., *Adv Mater* 20, (2008) 4887-4892
- [2] V.J. Lumelsky et al., *IEEE Sensors*, vol.1 no.1 (2001)
- [3] S. Wagner et al., *Physica E* 25 (2004) 326-334
- [4] T. Sekitani et al., *Science* 321, (2008) 1468
- [5] D. Brosteaux et al., *IEEE Electr. Device. L* 28, 7 (2007) 552-554
- [6] S.P. Lacour et al., *Appl. Phys. Lett.* 82, 15 (2003) 24004-2406
- [7] A. Ostmann et al., 3rd International Microsystems, Packaging, Assembly and Circuits Technology Conference (2008)
- [8] O. van der Sluis et al., *Key Eng. Mater.* (2010) 417-418
- [9] J.P.M. Hoefnagels, et al., *Scripta Mater*, 63 (2010) 875-878
- [10] K.-S. Kim et al., *Int. J. Solids Struct.* 24, 4 (1988) 417-435

A miniaturized contactless pure-bending device for in-situ SEM failure analysis

J.P.M. Hoefnagels¹, C.A. Buizer¹, M.G.D. Geers¹

¹ Eindhoven University of Technology, Dept. of Mechanical Engineering,
Den Dolech 2, 5612AZ, Eindhoven, The Netherlands.

E-mail: j.p.m.hoefnagels@tue.nl

ABSTRACT

Flexible electronic devices (flexible displays, solar cells) are subjected to large bending loads during manufacturing and use, making delamination in the underlying thin-film structure a major reliability concern. To investigate such failures, a new miniature contactless, frictionless pure-bending device is presented that enables highly sensitive moment-curvature measurements and simultaneous in-situ SEM failure analysis. Bending tests are of particular interest as they apply non-uniform loads without geometrical instabilities (necking, buckling, etc.). Most standardized bending tests (3-point, 4-point or cantilever bending) are contact-based, however, therefore they: cannot straightforwardly impose (large amplitude) cyclic or reversed loading; may introduce local deformations (indentations); typically obstruct the field of view at top or bottom surface; and typically introduce ill-defined parasitic frictional forces and moments. Contact and friction contributions particularly form a problem for cyclic testing or miniaturization and significantly complicate experimental-numerical material model identification. The here presented miniature pure-bending device overcomes these limitations. Contactless pure bending is realized through the relative rotations of two clamps, while active piezo control is used to eliminate axial and normal clamp forces and keep the area of interest in field of view for continuous SEM observation.

INTRODUCTION

Thin film technology has become indispensable over the last few decades. It is already been widely used in many industrial applications and its potential is still enormous. Applications can be found in Integrated Circuits (IC), data storage devices, fuel cells etc. Frequently, thin film technology is also used in flexible applications. For instance, flexible organic light emitting diode displays is an example of thin film technology in such an application. Flexibility and ruggedness is obtained by using a polymer substrate. Although advantageous for flexibility, the properties of polymeric materials seldom match with all requirements set by display processing usage, either mechanically (e.g. scratch resistance), chemically (e.g. chemical resistance) or physically (e.g. water permeability). Therefore, multiple layers are stacked on top of the polymer substrate to improve the properties of the total film. The individual layers are manufactured using different materials and processes.

Flexible displays are frequently subjected to bending, which results in both tensile and compressive stresses in these products. Brittle and stiff layers can crack or buckle as a result of these stresses. In both cases this may lead to interfacial delamination of the stacked layers. Therefore, tensile failure and compression failure are mentioned to be the most common failure modes of flexible displays [1]. The same trends can be observed in flexible electronics which are subjected to both static and (large amplitude) cyclic bending [2, 3].

In order to improve the design rules for manufacturing and the reliability during service of flexible displays and electronics, bending induced failure needs to be researched in these products. To this end, a novel miniature bending test is presented. In the following, first the requirements of this bending test are specified in detail, after which these requirements are worked out into practical design criteria. Finally, the concept of the bending test is presented.

REQUIREMENTS OF THE BENDING TEST

A transverse load, an eccentric load and a moment load or a combination of these three loads can induce bending of a material. Transverse and eccentric loads results in the simultaneous presence of shear forces and an inhomogeneous bending moment in the material. On the other hand, when solely a bending moment is imposed to a material, it is purely bended. The bending moment will be constant over the material indicating that the loading condition at every part of the material is well-defined. Therefore, pure bending is a commonly preferred loading condition in both numerical and experimental tests to characterize bending behavior of materials. Hence, the most important requirement of the bending setup is that it applies to the specimen a pure bending moment, i.e. all parasitic loads should be eliminated. This bending should also be known, therefore, it must be measured by the setup. With the requirement of pure bending in mind, existing bending setups can be investigated.

A wide range of bending setups has been proposed to perform experimental bending tests. The three- and four-point bending tests are well-known techniques to characterize bending behavior of materials. The working principle of three- and four-point bending is based on a sample posing on two supports and one or two bars which impose a concentrated force on the sample resulting in pure bending for small loads. The bar(s) cause(s) local effects due to contact with the sample. Local effects (e.g. indentations, slip, rupture,...) near the contact areas are described in detail by Zineb et al. [4]. Moreover, reversed loading and large amplitude, cyclic, pure bending tests can not straightforwardly be performed by three- or four-point bending tests. Yoshida et al. [5] developed a large-amplitude, cyclic, bending setup with the possibility to apply reversed loadings. This last ability can be used for the experimental examination of phenomena like the Bausschinger effect or elastic springback. Unlike three-point and four-point bending tests, Yoshida's setup uses a non-contact principle to induce bending. The bending is realized by relative rotations of two clamps that are mounted on sliders. The friction of the sliders, however, induces a parasitic load to the bended sample, causing the state of pure bending to be lost. The presence of friction in a setup generally introduces hysteresis in cyclic tests which is usually not trivial to calibrate. On top of that, the influence of friction on a measurement increases if the setup is miniaturized e.g. to test samples in combination with microscopy. Boers et al. [6] replaced Yoshida's sliders for frictionless air bearings, enabling their setup to perform large amplitude, cyclic, pure bending in a contactless and frictionless fashion. Boers et al. also notes that in general, influences of contact and friction are not included in numerical tests. Therefore, contact and friction effects should also not be present in experimental setups in order to give a fair judgment on numerical tests.

Setups for the *in situ* Scanning Electron Microscope (SEM) characterization of mechanical behavior of materials are another class of experimental devices. The microscopic information obtained from these experiments is used for the research on mechanical behavior at the microscale. Kolluri et al. [7] reports an example of the relevance of such an investigation with a miniaturized mixed-mode delamination setup, with which quantitative delamination characteristics can be measured while simultaneously the delamination mechanisms can be observed during real-time *in situ* SEM visualization. Wiklund et al. [8], Frei et al. [9] and Buchanan et al. [10] already performed *in situ* bending tests in a SEM, relying on the four-point bending principle. Crack propagation due to bending was examined by all of them at the microscopic level. For the here presented bending setup *in-situ* SEM observation of bending failure during the bending test is also an important requirement, as it will greatly enhance the possibilities to unravel the underlying physical origin of the bending failure.

A contactless, frictionless pure bending setup for large amplitude, cyclic loading was developed by Boers et al. [6] which can be used to achieve the first two points listed above. However, simply miniaturizing the contactless, frictionless pure bending setup developed by Boers et al. such that it fits SEM is not trivial. Air bearings that were used by Boers et al. can not be used since the setup should be able to operate in vacuum circumstances. Furthermore, magnetic fields may affect the electron beam in the SEM causing a disturbance during visualization. Therefore, strong magnetic fields should be avoided. When focusing on a certain region of interest, it should stay in the field-of-view. The constant observation of a microscopically small area which can undergo large amplitude cyclic displacements is another mayor problem which is also not trivial to solve.

The bending setup presented here, is developed for the bending of flexible thin films, because they are widely used, frequently fail and their potential is still enormous. However, the setup should not only extend the pure bending of flexible thin films, but also other materials like metal foils, laminar composites and paper. Consequently, quick and easy modifications should be allowed to make this possible. The setup should be usable for a range of sample dimensions and testing conditions should be well-defined and reproducible. Beside all of this, the setup should enable to investigate time-dependent pure bending behavior like relaxation and creep. Relaxation can be measured by prescribing a fixed bending angle and monitoring the bending moment over time. Creep tests on the other hand, can be performed by prescribing a fixed bending moment and monitoring the resulting bending angle over time.

In conclusion, the goal of this project is to develop a large-amplitude, cyclic, pure bending setup for *in situ* SEM characterization.

DESIGN CONCEPT

The proposed basic concept for the bending setup is based on the analytical description of the kinematics of a homogeneous, elastic, purely bended beam. Frictionless and contactless pure bending is imposed by prescribing the movement of the clamped sides of the beam with the aid of a combination of displacement and force driven manipulators. This concept is introduced in this chapter.

Analytical kinematics description

At first, we consider the perfect case where samples have a uniform composition and behave in an either orthotropic or isotropic, elastic manner over their full length. In the case of pure bending of a homogeneous, elastic beam, see Figure 1, the clamp positions can be determined analytically, therefore, a purely displacement driven setup can be designed based on mathematical positions. The sample in Figure 1 is fixed in space at point O in the middle of the beam. This point O represents the region of interest that will be examined in the SEM. The beam should be uniformly curved as a result of the pure bending. The facts that there is fixed point and that the beam is uniformly curved, enable us to analytically describe the kinematics of the purely bended beam. Fixed point O is also the origin of a Cartesian coordinate system with coordinates x and y .

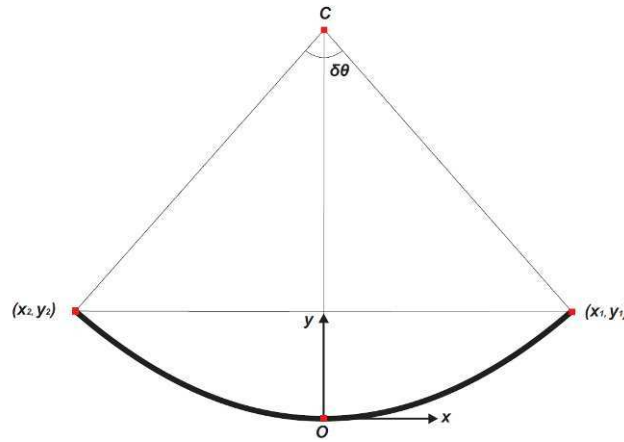


Figure 1. Model to describe the kinematic behavior of homogeneously bend beam.

(x_1, y_1) and (x_2, y_2) are the coordinates which represent the location of the right and left clamped sides of the beam (i.e. the clamps) with respect to the fixed point O. (x_1, y_1) and (x_2, y_2) can be written as:

$$x_1 = -x_2 = \frac{L}{\delta\theta} \sin\left(\frac{\delta\theta}{2}\right) \quad (1)$$

and

$$y_1 = y_2 = \frac{L}{\delta\theta} \left(1 - \cos\left(\frac{\delta\theta}{2}\right)\right) \quad (2)$$

The position of both sides of the sample can be written in terms of the bending angle $\delta\theta$ and the length L of the sample. The length of the sample is considered to be constant. Manipulators can use this information to precisely position the clamps correctly with respect to each other such that the sample will be in the state of pure bending. Multiple strategies to realize this are discussed next.

Strategies to prescribe clamp movement

The first concept is based on the use of two linear and one rotation stage for the actuation of each individual clamp. The linear manipulators should position the clamps to positions (x_1, y_1) and (x_2, y_2) while the rotation stages should rotate the clamps under the bending angle $\delta\theta$ with respect to each other. Detailed study on this concept showed, however, that the space inside the SEM was too limited for the realization of this proposal.

A second strategy is based on the description of the clamp movement by a circle. As shown in figure 2, circles can be

characterized by a center at coordinate (a_1, a_2) and a radius b . In this concept, each individual clamp should be located at a distance b from a point (a_1, a_2) and rotate around it, such that a simple circular movement for each clamp would suffice to follow the analytically determined path.

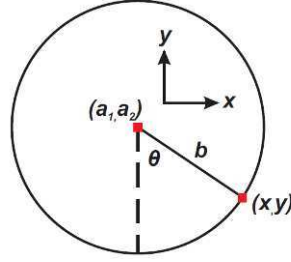


Figure 2. Circular path description model.

Every point (x, y) of the circle shown in figure 2 can be mathematically determined by the following equations:

$$x = a_1 + b \sin(\theta) \quad (3)$$

and

$$y = a_2 - b \cos(\theta) \quad (4)$$

From (1) and (2), we can recognize $a_1 = 0$, $a_2 = \pm L / \delta\theta$ and $b = L / \delta\theta$. The parameter a_2 and the radius b are dependent on the bending angle and thus not constant. The clamp movements can therefore not perfectly be described by circles. Besides, the circular path is described with an angle θ while the clamps rotate with an angle $\delta\theta/2$ with respect to the zero-bending-angle-condition. Therefore, simple circular movements of the clamps as described here do not suffice.

The third concept is actually a continuation of the second concept. Bouten [28] introduced another model to describe the movement of the sample sides in pure bending with simple circular movements and already concluded that these would not suffice to describe the clamp kinematics. Bouten's model describes the movement of the clamped sample sides with two rotational point at a distance a from each other and two end-plates to clamp the sample. These end-plates clamp the sample at a distance b from the rotational points. An extension to this model was made by the introduction of extra degrees of freedom and the restriction that the region of interest, located in the middle of the sample, is fixed in space. This extended model is schematically presented in figure 3.

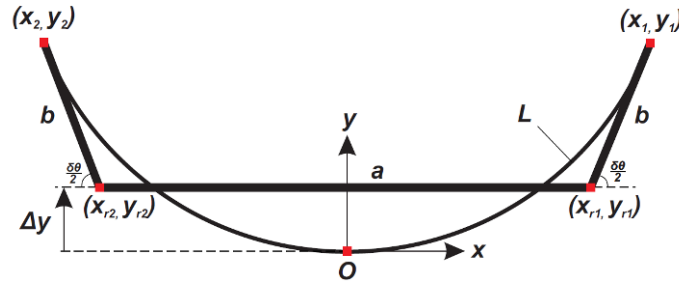


Figure 3. Extended path description model.

The origin of the introduced Cartesian coordinate system O corresponds with the fixed region of interest. (x_1, y_1) and (x_2, y_2) are the coordinates of the clamped sides of the samples. Coordinates (x_{r1}, y_{r1}) and (x_{r2}, y_{r2}) are the coordinates of the rotation points. Positions (x_1, y_1) and (x_2, y_2) in the drawing can be calculated by:

$$x_1 = -x_2 = \frac{a}{2} + b \cos\left(\frac{\delta\theta}{2}\right) \quad (5)$$

and

$$y_1 = y_2 = \Delta y + b \sin\left(\frac{\delta\theta}{2}\right) \quad (6)$$

Equations (5) and (6) should be equal to the outcomes of equations (1) and (2) respectively. This lead to a system of equation which can be rephrased in a matrix form as:

$$\begin{bmatrix} \frac{1}{2} & 0 & \cos(\frac{\delta\theta}{2}) \\ 0 & 1 & \sin(\frac{\delta\theta}{2}) \end{bmatrix} \begin{bmatrix} a \\ \Delta y \\ b \end{bmatrix} = \begin{bmatrix} \frac{L}{\delta\theta} \sin(\frac{\delta\theta}{2}) \\ \frac{L}{\delta\theta} (1 - \cos(\frac{\delta\theta}{2})) \end{bmatrix} \quad (7)$$

One extra equation is required to solve this system of equations for the full bending angle range. In order to describe the movements of the clamps, restrictions can be put on the degrees of freedom of the movement of the rotation points in space. We can allow only movement in x-direction (i.e. varying a), only movement in y-direction (i.e. varying Δy), full freedom of movement in both x- and y-direction or no movement at all. Besides, we can consider a fixed and a varying length b . In total, eight different cases can be considered. Only three of those cases are suitable to solve equation (7): the case in which solely y-movement of the rotation points and variation in distance b are allowed, the case where solely x-movement of the rotation points and variation in distance b are allowed and the case in which both x- and y-movement of the rotation points and no variation of distance b are allowed. The system is over- or underconstraint in all other conditions. The case in which both x- and y-movement of the rotation points and no variation of distance b are allowed is similar to the first concept discussed in this section, so it will not be considered any further. In case no linear actuator which can move in the x-direction is used, symmetry around the y-axis is required to keep the region of interest at a fixed point in space. The case in which solely x-movement of the rotation points and variation in distance b are allowed, requires two actuators to move both rotation points in synchronous, opposite direction for the realization of symmetry. The case in which solely y-movement of the rotation points and variation in distance b is allowed (and a is kept constant), only requires one. Consequently, this last case is used as a starting point for the actual design of the setup.

Setup kinematics

This section explains how the proposed motion pattern is realized in the setup. Before this is done, it should be noted that distance a between the rotation points is chosen to be zero, resulting in a single rotation point. Because the samples are small, two rotation points would be located closely together possibly causing inconveniences in the construction. When $a = 0$ is postulated in equation (7), expressions for b and Δy can be obtained:

$$b = \frac{L}{\delta\theta} \tan(\frac{\delta\theta}{2}) \quad (8)$$

and

$$\Delta y = \frac{L}{\delta\theta} \left(\frac{-1 + \cos(\frac{\delta\theta}{2})}{\cos(\frac{\delta\theta}{2})} \right) \quad (9)$$

The setup consists of two individual clamps which are attached on top of two bars. These bars with a length $L1$ can rotate around the single fixed joint J1. By using two push/pull rods attached to the bars with joints at point J2 and J3, synchronous rotation of the bars is accomplished. The pull/push rods have a length $L2$ and they are linearly actuated at joint J4. The actuator at this point is referred to as the rotation stage. The distance between the clamps and the fixed joint J1 equals the half of the length of the sample in zero-bending-angle condition. This condition is drawn in [figure 4](#).

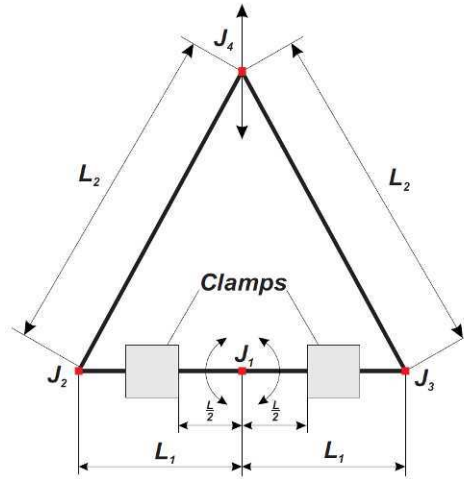


Figure 4. Rotation mechanism of the setup.

Equation (8) shows that distance b should vary over the full range of bending angles. The clamps should therefore move along the longitudinal direction of the bars. Mechanical bearings can not be used for this clamp movement since friction in the bearings cause parasitic loading of the sample. Air bearings can not be used, because the setup will be used in (low) vacuum circumstances. In case magnetic levitation would be used, the strong magnetic fields will disturb the electron beam of the SEM and thus the real-time visualization. Free movement of the clamps by attaching them to very low-stiffness leaf springs causes problematic dynamic behavior. Finally, a solution can be found in the use of simple linear actuators. Two actuators will move the clamps synchronously in the axial direction of the sample with a magnitude $\Delta b = b - L/2$. The entire setup is positioned on top of another linear actuator to keep the region of interest in the field-of-view. The movement of this field-of-view stage represents the Δy -movement as described by equation (9). Figure 5 shows the implementation of the two synchronous linear actuators and the mechanism to keep the region of interest in the field-of-view.

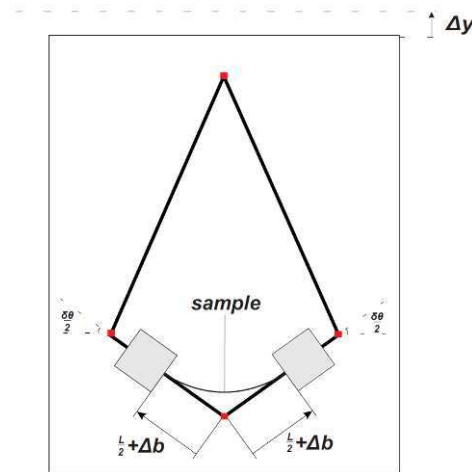


Figure 5. Integration of axial actuators and field-of-view mechanism in the basic concept.

Active feedback

So far, we considered the perfect case where samples had a uniform composition and behaved in an either orthotropic or isotropic, elastic manner over their full length. This allowed to devise a purely displacement driven setup based on mathematical positions. In reality this perfect case does not exist because of failure, plastic deformation, material defects, variation in geometric properties, etc. These phenomena and artifacts have a significant effect of the deformation of a sample in pure bending. They will cause diversion from the perfect pure bending path, so a correction needs to be made for the inhomogeneity of samples and for the case that samples behave in a non-elastic fashion. The position of the clamps should be

determined by the position and angle of the ends of the sample and not the other way around, otherwise the clamps will apply undesired parasitic (axial, transverse, shear) forces on these samples. However, the undesired forces can be used for active feedback control of actuators. These forces can be sensitively measured and they can be used to steer the movement of actuators. Therefore, very small parasitic loads are allowed to act on the sample. However, these loads should be negligibly small in comparison to the bending moment which is applied on the sample. Moreover, the sample should move freely, so the loads should be measured according to a contactless and thus frictionless principle. Figure 6 represents this idea in case of correction of the (actual or transverse) force. A clamp holds a sample and is attached to a base plate by two leaf springs. These leaf springs have a low stiffness in the direction in which the force of the sample is supposed to be sensed. When the sample starts to get off the pure bending track, it will push or pull the clamp and load the leaf springs with a force F . The displacement of the clamp Δx caused by this loading is sensed by a sensitive displacement sensor (it was found that a Linear Variable Differential Transformer (LVDT) is best suited for the present purpose considering resolution versus range). The clamp is attached to the core of the LVDT, which slides free of contactless through the LVDT. When the sample does not induce a resultant force, the distance between the LVDT and the clamp is x_0 . The signal measured by the LVDT is used to determine the movement of an actuator which is located underneath the base plate. The actuator will move till the distance between the clamp and the LVDT is x_0 again (i.e. the leaf springs are unloaded).

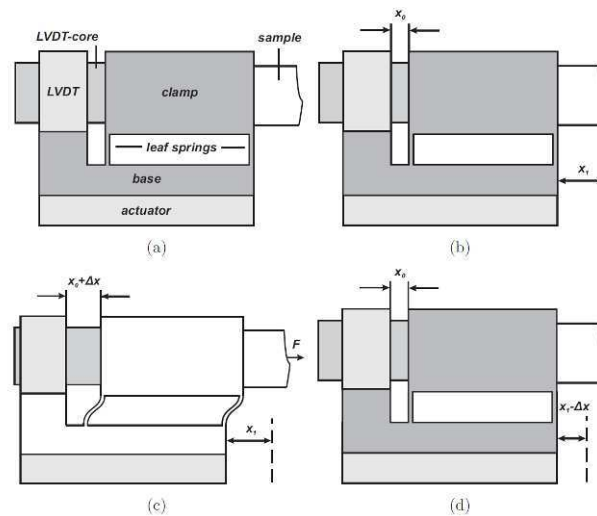


Figure 6. (a) Schematic overview of the active feedback control system (b) Initial condition (c) Condition of the system when the sample pulls it (d) Condition of the system after a feedback was carried out.

As mentioned earlier in this section, the clamps positions should be fully determined by the (position and angles of the) edges of the sample. To realize this, all the linear and rotational positions of the clamps other than the rotation around the bending axis should be controlled with the aid of a feedback system. So, forces and torsion in five directions need to be measured and actuated. Besides, the setup should be able to be driven by the bending moment and to characterize the bending behavior. Thus, a bending moment measurement needs to be done as well. Consequently, loads in six directions need to be measured. The realization of this is difficult since space is limited and load measurements of all the loads according to the described principle (Fig. 6) are complex. The dynamic behavior of the complete setup with multiple leaf springs will be problematic and loads tend to interfere with the measurements of other loads. Moreover, use of many actuators lead to an increase of complexity in the control scheme of the setup.

In order to simplify the problem, the number of directions in which load is measured and actuation is provided, should be decreased. First, geometrical errors (e.g. twist) of samples are not incorporated in numerical tests. They should be very small for a fair judgment of these numerical simulations. We limit the use of arbitrarily samples by allowing only very small twists in the sample such that torsion (after straightening of the sample during clamping) is minimal. Second, actuation and force measurement in the width direction of the sample is not necessary, since the position of the clamps in width (vertical) direction should remain constant during the bending (in horizontal plane). Moreover, care is taken to clamp the sample only from side in the thickness direction, thus not exerting any forces in vertical direction during clamping.

After simplifying the problem, still feedback in the horizontal plane needs to be implemented in the basic concept. This means that forces in the axial and transverse direction of the sample are measured and used for feedback control. As can be seen in figure 7 just one more stage, which moves in the transverse direction of the sample is to be integrated in the basic concept discussed above. This additional stage corrects for asymmetry in the sample.

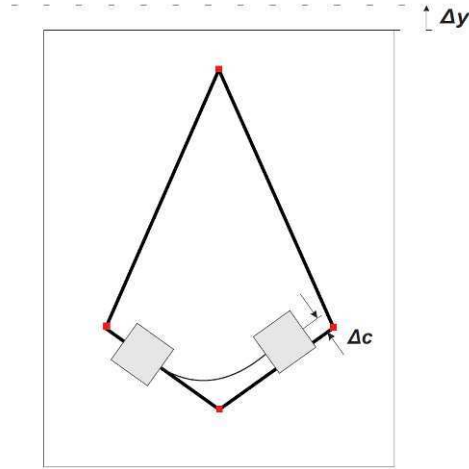


Figure 7. Final basic concept with transverse correction actuator.

We accept the fact that symmetry of the setup is lost, since solely small movements in the transverse direction are expected (i.e. small asymmetry in the sample). It is noted that the setup is underconstraint if symmetry would be obtained by adding two transverse correction actuators rather than one.

An advantageous property of the transverse stage is its ability to correct for non-synchronous movement of the two axial actuators (Δb). In case of pure bending of a homogeneous, elastic beam, non-synchronicity causes the clamps to force the sample to a certain position. This induces a parasitic load on the sample. The transverse actuator however, can correct for this incorrect positioning. Though, movement of the transverse actuator causes the region of interest to shift in lateral direction. This is further clarified by [figure 8](#) in which a homogeneous, elastic beam is purely bended. A difference of the displacement between both axial actuators Δs is introduced. This non-synchronicity leads to a shift Δx of the region of interest. The positions of the depicted clamps can be mathematically described. These clamp positions should match with those determined in equation (1) and (2).

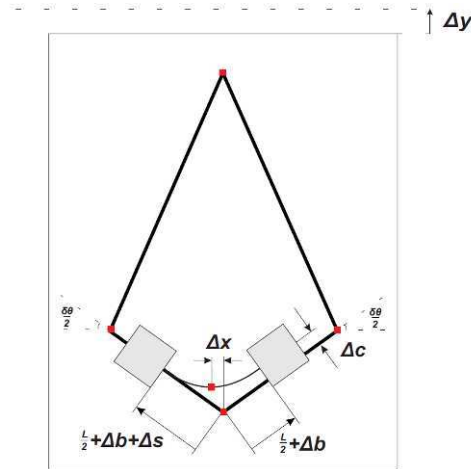


Figure 8. Shift of the region of interest due to non-synchronicity of the axial actuators.

Again, a system of equations can be formulated and solved, leading to an expression for the shift Δx :

$$\Delta x = \frac{\Delta s}{2 \cos\left(\frac{\delta\theta}{2}\right)}, \quad (10)$$

which shows that the shift as a result of non-synchronicity Δx remains below half the displacement mismatch Δs . This mismatch should be less than 100 μm , assuming that the region of interest is at the center of the 100 μm ×100 μm field-of-view.

Finally, synchronicity of the two axial actuators (Δb) can be realized in either a mechanical or a mechatronic manner. It is not trivial to integrate a mechanism in the basic concept to obtain synchronicity mechanically for the full range of bending angles. Furthermore, space is already limited, so synchronicity is obtained mechatronically. This is needed as non-synchronicity can easily be obtained due to misalignment of the actuators or slip in the driving mechanism etc.

FINAL DESIGN

The resulting design of the cyclic, pure bending setup for *in situ* SEM characterization is given and explained in Figure 9.

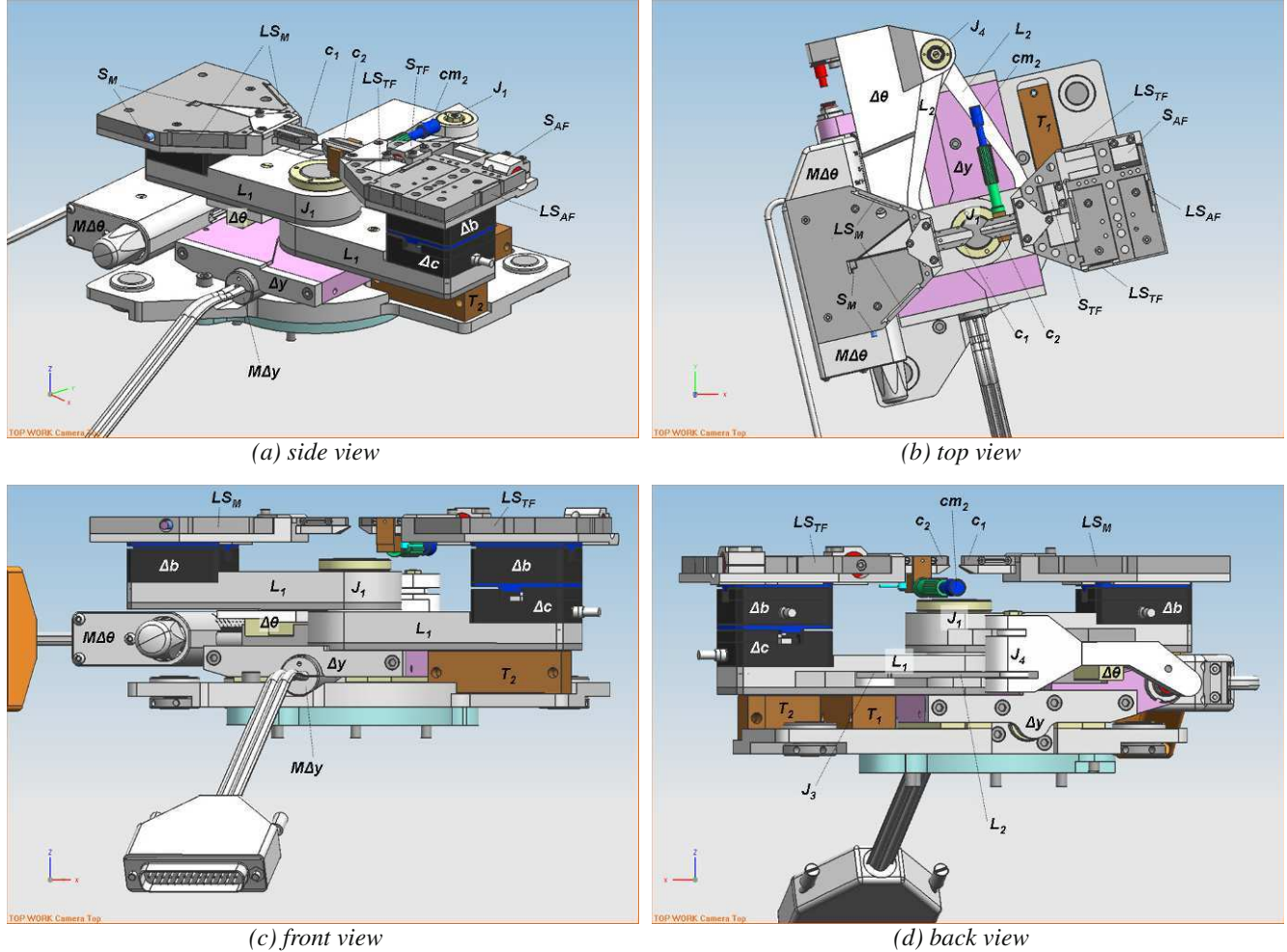


Figure 9. Final design of the large amplitude, cyclic, pure bending setup for *in situ* SEM characterization. The sample (not shown) is placed in the clamps (c_1 and c_2) and each clamp is closed in a highly controlled concentric manner using a clamping mechanism (only cm_2 is shown). The clamps are rotated by a rotation mechanism as explained in Fig. 4, where J_1 , J_2 , J_3 , and J_4 are the rotation points and L_1 and L_2 are the (length of the) beams, while $\Delta\theta$ is the linear actuator with motor $M\Delta\theta$ that moves rotation point J_4 . The resulting moment applied to the sample is measured with a leaf spring mechanism LF_M which displacement is measured with very high resolution using a capacitive sensor S_M . The axial force in the sample pulls leaf spring LS_{AF} out of equilibrium, which displacement is measured with LVDT sensor S_{AF} ; subsequently, the two linear actuators Δb move the clamps synchronously in the axial direction of the sample to reduce the axial force below its setup point value (explained in Fig. 6). The transverse force in the sample pulls leaf spring LS_{TF} out of equilibrium, which displacement is measured with LVDT sensor S_{TF} and linear actuators Δc moves clamp c_2 to reduce the transverse force below its setup point value (explained in Fig. 7). Δy is the linear actuator with motor $M\Delta y$ that moves the complete setup to keep the region of interest in the field-of-view (explained in Fig. 5). T_1 and T_2 are sensitive tilt sensors that allow to position the rotation axis J_4 exactly vertically, and thus leaf spring mechanism LF_M , LF_{AF} , LF_{TF} exactly horizontal.

SUMMARY

Bending tests are of particular interest as they apply non-uniform loads without geometrical instabilities (necking, buckling, etc.). Here, a novel concept has been presented for a contact-less, (large-amplitude) cyclic, pure bending test setup that can be employed under *in-situ* scanning electron microscopic visualization. Care has been taken to installed measures that reduce to negligible levels all ill-defined parasitic axial, transverse, shear, and frictional forces in order to apply a well-defined pure bending moment to the sample. This allows for the measurement of (cyclic) bending test, either controlled from the applied clamp angle or from the (highly sensitive) measurement of the applied moment. Such tests can be directly and accurately compared with conjugant bending simulations, which allows for straightforward experimental-numerical material model identification. The ability to perform *in-situ* optical microscopic or scanning electron microscopic visualization allows following the ongoing deformation behavior and resulting failure mechanism (delamination, cracking,...) during the well-defined bending test. *In-situ* visualization has been assured by (i) reducing the size of all mechanisms and components, (ii) using only vacuum-compatible materials and elements, (iii) by using applying only actuator and (feed-back) mechanisms that do not influence SEM operation with magnetic or electric field, (iv) by keeping free open access from the top of the (bended) sample, and (iv) by installing an extra actuator that keeps the region of interest stationary in the field-of view. The measurement concept will be validated on cyclic bending tests of flexible electronic samples.

REFERENCES

1. G. P. Crawford, Flexible flat panel displays. Chichester, England: John Wiley and Sons Ltd, 2005.
2. J. Zheng, M. B. Tucker, and L. Teng, "Failure mechanics of organic-inorganic multilayer permeation barriers in flexible electronics," *Composite Science and Technology*, vol. 71, pp. 365–372, 2010.
3. B. Cotterel and Z. Chen, "Buckling and cracking of thin films on compliant substrates under compression," *International Journal of Fracture*, vol. 104, pp. 169–179, 2000.
4. T. B. Zineb, A. Sedrakian, and J. L. Billoet, "An original pure bending device with large displacements and rotations for static and fatigue tests of composite structures," *Composites Part B*, vol. 34, pp. 447–458, 2003.
5. F. Yoshida, M. Urabe, and V. V. Toropov, "Identification of material parameters in constitutive model for sheet metals from cyclic bending tests," *International Journal of Mechanical Science*, vol. 40, pp. 237–249, 1998.
6. S. H. A. Boers, M. G. D. Geers, and V. G. Kouznetsova, "Contactless and frictionless pure bending," *Experimental Mechanics*, vol. 50, no. 6, pp. 683–693, 1999.
7. M. Kolluri, J. P. M. Hoefnagels, J. A. W. van Dommelen, and M. G. D. Geers, "An improved miniaturize mixed-mode delamination setup for in situ microscopic interface failure analysis," *Journal of Physics D: Applied Physics*, vol. 44, 2011.
8. U. Wiklund, M. Bromark, M. Larson, P. Hedenquist, and S. Hogmark, "Cracking resistance of thin hard coatings estimated by four-point bending," *Surface and Coatings Technology*, vol. 91, pp. 57–63, 1997.
9. H. Frei and G. Grathwohl, "Development of a piezotranslator-based bending device for in situ sem investigations of high-performane ceramics," *Journal of Physics E: Scientific Instruments*, vol. 22, pp. 589–593, 1989.
10. M. Buchanan, J. W. Provan, and J. E. Gruzleski, "An apparatus for four-point-bending fatigue testing of materials in a scanning electron microscope and its application to nodular cast iron," *Metallography*, vol. 20, pp. 125–143, 1987.

Study of Propagation of a Pre-Existing Crack under Different Boundary Conditions for Fatigue Loading

*Maneesh Tewari, V. K. Singh & Arun K. Chaudhary

*Assistant Professors, Deptt. of Production Engineering
College of Technology, G. B. P. U. A & T, Pantnagar- 263145
E. Mail: vks2319@yahoo.co.in

ABSTRACT

To better design structures and machines, understanding of flaws and failures is essential. Stresses in the vicinity of a crack tip can be characterized by Stress Intensity Factor. The effective methods of experimentally determining the stress intensity factor for a body containing a crack is to analyze the isochromatic pattern obtained from a photoelastic model. The effect of biaxial load factor, crack angle, Crack length/width of specimen and length of specimen/width of specimen were studied and a regression model was developed for geometry correction to predict stress intensity factor for tearing mode and intensity factor for shearing mode. This approach is being used to predict crack growth trajectory under biaxial cyclic loading by assuming that the crack may grow in a number of discrete steps using the vectorial method. MTS criterion (Maximum Tangential Stress criterion) is used for prediction of crack initiating angle. The crack growth trajectory has been determined by cycle by cycle simulation procedure.

INTRODUCTION

The strength of a structure could be severely affected by presence of crack like defects or pre-existing cracks and the defects are unavoidable in a cost effective manufacturing process. Since there are limitations on minimum size of the defects that can be detected, one needs to know the relation between the defect size and the strength of a structure. Fracture mechanics provide a methodology through which a quantitative relationship between the applied stress on a structure, defects size present, inherent properties of material and the fracture resistance characteristics of structure may be obtained. In the middle 1950 Irwin and co-workers laid the foundations for what has since become known as fracture mechanics [1]. The most important contribution of this development has been to introduce and experimentally determined material constant called the stress intensity factor (K) that characterizes the significance of the defects present in a material from the point of view of brittle crack growth. The effective methods of experimentally determining the stress intensity factor for a body containing a crack is to analyze the isochromatic pattern obtained from a photoelastic model. Measurements of the fringe order N and position parameters r and θ , which locate number of points on a fringe loop, are sufficient to permit the determination of K_I and K_{II} . The Irwin method for SIF extraction from photoelastic patterns was the accepted method for analysis for many years. In this method the positional coordinates and fringe order for a specific point that satisfies the criteria is used for evaluating K_I and K_{II} . The crack usually initiates at the surface of the specimen and propagate slowly at first into the interior. This is called as micro crack growth. The Material will continue the neck down, the crack is found to nucleate at brittle particle. A particle is said to have nucleated, when it becomes stable and will not disappear due to thermal fluctuation. Once the particle has attained this stage, it can grow further with a continuous decrease in energy. If fracture initiate at pore in the crack region, then the voids are already present. The voids grow with increasing deformation and ultimately reach sizes of the order of millimeter. This is called as macro crack growth. All some critical stage, the crack propagation becomes rapid culminating in fracture. With the recent advances in computation technology, researchers around the globe are working to simulate the crack propagation under different loading conditions. One can predict the crack propagation path if crack initiation and subsequent crack extension (initiation) angles are known. The problem needs to be studied in mixed mode since in mixed mode loading both crack initiation angle and hence crack growth rate varies during subsequent growth process. Prediction of initial fracture angle of mixed mode problem allows for the determination of the crack trajectory based on strain energy density factor. Several studies related to the prediction of the initial fracture crack angle and crack trajectories under mixed mode loading conditions were performed for uniaxial loadings as well as for biaxial loadings. The strain energy density criterion has used to predict the crack trajectory by approximating the developed crack by new crack angle and a fictitious crack length under uniaxial loading. Later, this

approach is being used to predict crack growth trajectory under biaxial cyclic loading by assuming that the crack may grow in a number of discrete steps using the vectorial method.

ANALYSIS OF THE PROBLEM

The stress optic law relates the fringe order N and principal stresses σ_1 and σ_2 as:

$$\frac{Nf_\sigma}{t} = \sigma_1 - \sigma_2 \quad (1)$$

Where, f_σ is the material fringe value and t is the model thickness. For a plane stress problem the principal stresses are:

$$\sigma_1, \sigma_2 = \frac{\sigma_x + \sigma_y}{2} \pm \sqrt{\frac{(\sigma_x - \sigma_y)^2}{4} + (\tau_{xy})^2} \quad (2)$$

For the purpose of mixed mode study, the stresses in the local neighborhood of a crack tip ($r/a < 1$) can be approximated by Westergaard Stress component σ_{ij} in an increasing order power series as follows [2]:

$$\begin{aligned} \sigma_x = & \sigma_{xx} + \frac{K_1}{2\sqrt{\pi a}} \left\{ \left(\frac{r}{2a} \right)^{-1/2} \cos \frac{\theta}{2} \left(1 - \sin \frac{\theta}{2} \sin \frac{3\theta}{2} \right) + \right. \\ & \frac{3}{2} \left(\frac{r}{2a} \right)^{1/2} \cos \frac{\theta}{2} \left(1 + \sin^2 \frac{\theta}{2} \right) + \sum_{n=1}^{\infty} \left(\frac{r}{2a} \right)^{n+1/2} C_n \left[\cos \left(n + \frac{1}{2} \right) \theta - \left(n + \frac{1}{2} \right) \right. \\ & \left. \sin \theta \sin \left(n - \frac{1}{2} \right) \theta \right] \left. \right\} + \frac{K_{11}}{2\sqrt{\pi a}} \left\{ - \left(\frac{r}{2a} \right)^{-1/2} \sin \frac{\theta}{2} \left(2 + \cos \frac{\theta}{2} \cos \frac{3\theta}{2} \right) + \right. \\ & \frac{3}{2} \left(\frac{r}{2a} \right)^{1/2} \sin \frac{\theta}{2} \left(2 + \cos^2 \frac{\theta}{2} \right) + \sum_{n=1}^{\infty} \left(\frac{r}{2a} \right)^{n+1/2} C_n \left[2 \sin \left(n + \frac{1}{2} \right) \theta + \left(n + \frac{1}{2} \right) \right. \\ & \left. \left. \sin \theta \cos \left(n - \frac{1}{2} \right) \theta \right] \right\} \end{aligned} \quad (3)$$

$$\begin{aligned} \sigma_y = & \frac{K_1}{2\sqrt{\pi a}} \left\{ \left(\frac{r}{2a} \right)^{-1/2} \cos \frac{\theta}{2} \left(1 + \sin \frac{\theta}{2} \sin \frac{3\theta}{2} \right) + \frac{3}{2} \left(\frac{r}{2a} \right)^{1/2} \cos^3 \frac{\theta}{2} + \right. \\ & \left. \sum_{n=1}^{\infty} \left(\frac{r}{2a} \right)^{n+1/2} C_n \left[\cos \left(n + \frac{1}{2} \right) \theta + \left(n + \frac{1}{2} \right) \sin \theta \sin \left(n - \frac{1}{2} \right) \theta \right] \right\} + \\ & \frac{K_{11}}{2\sqrt{\pi a}} \left\{ \left(\frac{r}{2a} \right)^{-1/2} \sin \frac{\theta}{2} \cos \frac{\theta}{2} \cos \frac{3\theta}{2} - \frac{3}{2} \left(\frac{r}{2a} \right)^{1/2} \sin \frac{\theta}{2} \cos^2 \frac{\theta}{2} - \right. \\ & \left. \sum_{n=1}^{\infty} \left(\frac{r}{2a} \right)^{n+1/2} C_n \left(n + \frac{1}{2} \right) \sin \theta \cos \left(n - \frac{1}{2} \right) \theta \right\} \end{aligned} \quad (4)$$

$$\begin{aligned} \sigma_{xy} = & \frac{K_1}{2\sqrt{\pi a}} \left\{ \left(\frac{r}{2a} \right)^{-1/2} \sin \frac{\theta}{2} \cos \frac{\theta}{2} \cos \frac{3\theta}{2} - \frac{3}{2} \left(\frac{r}{2a} \right)^{1/2} \sin \frac{\theta}{2} \cos^2 \frac{\theta}{2} \right. \\ & \left. - \sum_{n=1}^{\infty} \left(\frac{r}{2a} \right)^{n+1/2} C_n \left(n + \frac{1}{2} \right) \sin \theta \cos \left(n - \frac{1}{2} \right) \theta \right\} + \frac{K_{11}}{2\sqrt{\pi a}} \left\{ \left(\frac{r}{2a} \right)^{-1/2} \right. \\ & \cos \frac{\theta}{2} \left(1 - \sin \frac{\theta}{2} \sin \frac{3\theta}{2} \right) + \frac{3}{2} \left(\frac{r}{2a} \right)^{1/2} \cos \frac{\theta}{2} \left(1 + \sin^2 \frac{\theta}{2} \right) + \\ & \left. \sum_{n=1}^{\infty} \left(\frac{r}{2a} \right)^{n+1/2} C_n \left[\cos \left(n + \frac{1}{2} \right) \theta - \left(n + \frac{1}{2} \right) \sin \theta \sin \left(n - \frac{1}{2} \right) \theta \right] \right\} \end{aligned} \quad (5)$$

where,

$$C_n = (-1)^n \frac{(2n+3)1 \times 3 \times \dots \times (2n-1)}{(2n+2)2 \times 4 \times \dots \times 2n}$$

where r and θ are polar co-ordinates with the origin defined at the crack tip.

The maximum in-plane shear stress (τ_m) is related to the Cartesian components of stress by:

$$(2\tau_m)^2 = (\sigma_y - \sigma_x)^2 + (2\tau_{xy})^2 \quad (6)$$

$$\text{or} \quad (\sigma_1 - \sigma_2)^2 = (\sigma_y - \sigma_x)^2 + (2\tau_{xy})^2 \quad (7)$$

Substituting Equation (1) in above equation

$$\text{or} \quad \left(\frac{Nf_\sigma}{t} \right)^2 = (\sigma_y - \sigma_x)^2 + (2\tau_{xy})^2 \quad (8)$$

Substituting Equation (3 to 5) into (8), we get

$$\begin{aligned}
 \left(\frac{N \cdot f \sigma}{t} \right)^2 = & \frac{K_I}{2\sqrt{\pi a}} \left\{ \left(\frac{r}{2a} \right)^{-1/2} \cos \frac{\theta}{2} \left(2 \sin \frac{\theta}{2} \sin \frac{3\theta}{2} \right) + 3 \left(\frac{r}{2a} \right)^{1/2} \cos^3 \frac{\theta}{2} - \right. \\
 & 3 \left(\frac{r}{2a} \right)^{1/2} \cos \frac{\theta}{2} + \sum_{n=1}^{\infty} \left(\frac{r}{2a} \right)^{n+1/2} C_n \left[2 \left(n + \frac{1}{2} \right) \sin \theta \sin \left(n - \frac{1}{2} \right) \theta \right] \Big\} + \\
 & \frac{K_{II}}{2\sqrt{\pi a}} \left\{ \left(\frac{r}{2a} \right)^{-1/2} \left(2 \sin \frac{\theta}{2} \cos \frac{\theta}{2} \cos \frac{3\theta}{2} \right) + \left(\frac{r}{2a} \right)^{-1/2} 2 \sin \frac{\theta}{2} - \frac{3}{2} \right. \\
 & \left. \left(\frac{r}{2a} \right)^{1/2} 2 \sin \frac{\theta}{2} \cos^2 \frac{\theta}{2} - \frac{3}{2} \left(\frac{r}{2a} \right)^{1/2} 2 \sin \frac{\theta}{2} \right. \\
 & \left. - \sum_{n=1}^{\infty} \left(\frac{r}{2a} \right)^{n+1/2} C_n \left[2 \sin \left(n - \frac{1}{2} \right) \theta \right] - \sigma_{ox} \right\}^2 + \\
 & \frac{K_{I1}}{2\sqrt{\pi a}} \left\{ \left(\frac{r}{2a} \right)^{-1/2} \sin \frac{\theta}{2} \cos \frac{\theta}{2} \cos \frac{3\theta}{2} - \frac{3}{2} \left(\frac{r}{2a} \right)^{1/2} \sin \frac{\theta}{2} \cos^2 \frac{\theta}{2} \right. \\
 & \left. - \sum_{n=1}^{\infty} \left(\frac{r}{2a} \right)^{n+1/2} C_n \left(n + \frac{1}{2} \right) \sin \theta \cos \left(n - \frac{1}{2} \right) \theta \right\} + \frac{K_{II1}}{2\sqrt{\pi a}} \left\{ \left(\frac{r}{2a} \right)^{-1/2} \right. \\
 & \left. \cos \frac{\theta}{2} \left(1 - \sin \frac{\theta}{2} \sin \frac{3\theta}{2} \right) + \frac{3}{2} \left(\frac{r}{2a} \right)^{1/2} \cos \frac{\theta}{2} \left(1 + \sin^2 \frac{\theta}{2} \right) + \right. \\
 & \left. \sum_{n=1}^{\infty} \left(\frac{r}{2a} \right)^{n+1/2} C_n \left[\cos \left(n + \frac{1}{2} \right) \theta - \left(n + \frac{1}{2} \right) \sin \theta \sin \left(n - \frac{1}{2} \right) \theta \right] \right\}
 \end{aligned} \tag{9}$$

The N-K relation given in Equation (9) is non-linear in term of the three unknowns K_I , K_{II} and σ_{ox} . In the present analysis these three points deterministic approach have been used.

In this approach data is selected from three arbitrary points (r_1, θ_1) , (r_2, θ_2) and (r_3, θ_3) . The Newton-Raphson method [3] is applied to the solution of three simultaneous non-linear equations.

THE DETERMINATION OF DIRECTION OF CRACK INITIATION

MTS-criterion is the simplest off all, and it states that direction of crack initiation coincides with the direction of the Maximum Tangential Stress along it constant radius around the crack tip. It can be stated mathematically as,

$$(\partial \sigma_{\theta} / \partial \theta)_{\theta=\theta_0} = 0 \tag{10}$$

$$(\partial^2 \sigma_{\theta} / \partial \theta^2) < 0 \tag{11}$$

Using then stress field in polar co-ordinates and applying the M.T.S.-criterion, we get the following equations

$$\tan^2(\theta/2) - (\mu/2) \tan(\theta/2) - 0.5 = 0 \tag{12}$$

$$(-3/2)[\{(1/2)\cos^3(\theta/2)\cos(\theta/2)\sin^2(\theta/2)\} + \{(1/\mu)\sin^3(\theta/2)\} \tag{13}$$

$$- (7/2)\sin(\theta/2)\cos^3(\theta/2)\} < 0$$

Where μ is defined as,

$$\mu = (K_I / K_{II}) \tag{14}$$

If the value of θ is equal to the β , the solution of above equation will give the value of crack initiation angle (β_0).

To solve the equations for the crack initiation angles defined above, we need to have expressions for the stress intensity factors for the angled crack problem for different loading conditions.

Where σ_n and τ_n are the normal and tangential stress to the crack plane respectively, to obtain expressions for σ_n and τ_n for slant crack problem, the most general loading case is considered [figure2](#).

$$\sigma_n = \sigma_x \cos^2 \beta + \sigma_y \sin^2 \beta - \tau_{xy} \sin 2\beta \tag{15}$$

$$\tau_n = ((\sigma_x - \sigma_y) / 2) \sin 2\beta - \tau_{xy} \cos 2\beta \tag{16}$$

The crack growth rate da/dN can be expressed as a function of strain energy density range similar to Paris's law[5] of model 1 cyclic loading and is given by

$$(da / dN) = C(\Delta S)^n \tag{17}$$

$$= 2.98 \times 10^{-10} (\Delta S)^{1.15} \quad \text{for } 750 < \Delta S < \Delta S_{cr}$$

$$= 1.88 \times 10^{-18} (\Delta S)^{3.98} \quad \text{for } \Delta S < 750$$

where C and n are material properties to be determined experimentally, The strain energy density factor range, ΔS , can be expressed as:

$$\Delta S = b_{11}K_I^2 + 2b_{12}K_I K_{II} + b_{22}K_{II}^2 \quad (18)$$

Where Coefficients b_{11} , b_{12} and b_{22} are given by

$$b_{11} = (1/16G)[(1 + \cos \beta)(k - \cos \beta)] \quad (19)$$

$$b_{12} = (1/16G) \sin \beta [2 \cos \beta - (k - 1)] \quad (20)$$

$$b_{22} = (1/16G)[(k + 1)(1 - \cos \beta) + (1 + \cos \beta)(3 \cos \beta - 1)] \quad (21)$$

Where

$$k = (3 - 5\nu) \quad \text{for plane strain} \quad (22)$$

$$k = (3 - \nu)/(1 + \nu) \quad \text{for plane stress} \quad (23)$$

Strain Energy Density range was found to be a convenient parameter for predicting fatigue crack growth under complex loading. Using crack geometry, the crack angle and the corresponding crack length at i^{th} state of cycle can be expressed in terms of initial fracture crack angle and the incremental crack length given in figure 2 as follows:

New crack inclination angle (after crack propagation)

$$\beta_i = \beta + \tan^{-1}[(\Delta a \sin \beta_0)(a + \Delta a \cos \beta_0)] \quad (24)$$

New half crack length (after crack propagation)

$$a_i = \sqrt{[(\Delta a \sin \beta_0)^2 + (a + \Delta a \cos \beta_0)^2]} \quad (25)$$

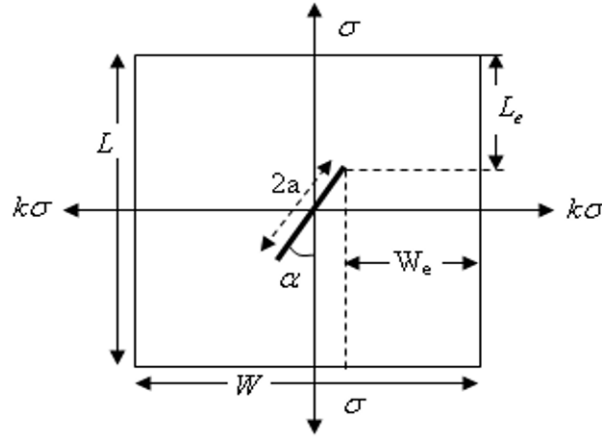


Figure 1: Effective length and effective width in the specimen

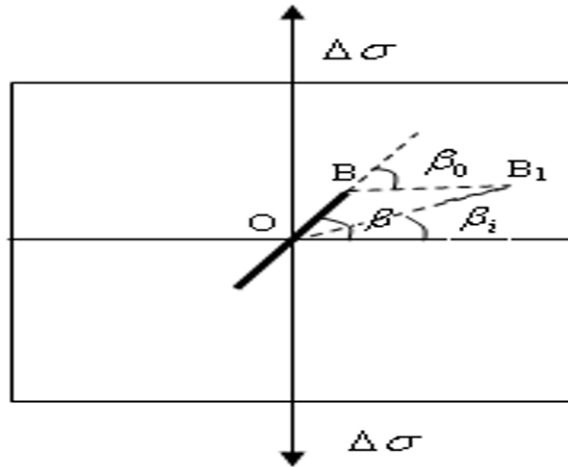


Figure 2: Direction and crack growth

RESULT & DISCUSSION

STRESS INTENSITY FACTOR K_I

The effect of biaxial load factor k , crack angle a/W ratio on stress intensity factor (K_I) is shown in Figure 3(a-c) for different crack length and crack angles. Figure 3 shows that K_I increases as k increases. This may be due to increase in plastic zone size produced ahead of the crack-tip. Figure 4 shows that K_I decreases as crack angle α increases for all values of k values. This may be due to the change of crack position for minimum loading direction (σ -axis) to maximum loading direction ($k\sigma$ -axis). K_I increases when a/W increases shown in figure 5.

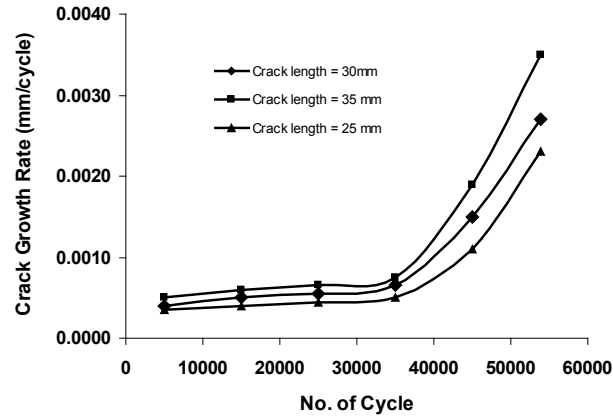


Figure 3: Variation of crack growth rate with number of cycles under different crack length

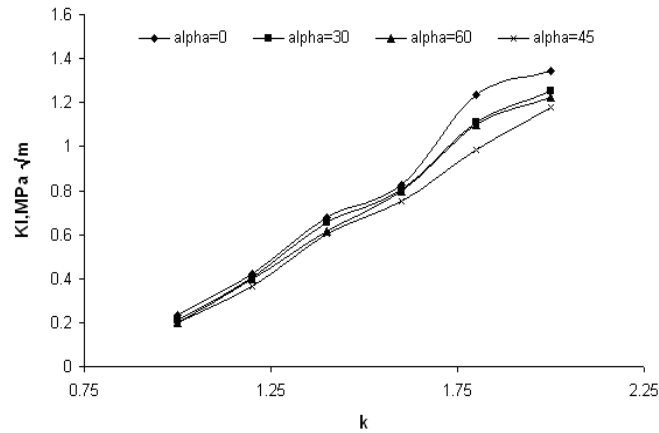


Figure 3(a): Effect of biaxial factor on stress intensity factor K_I for $a/W = 0.08$

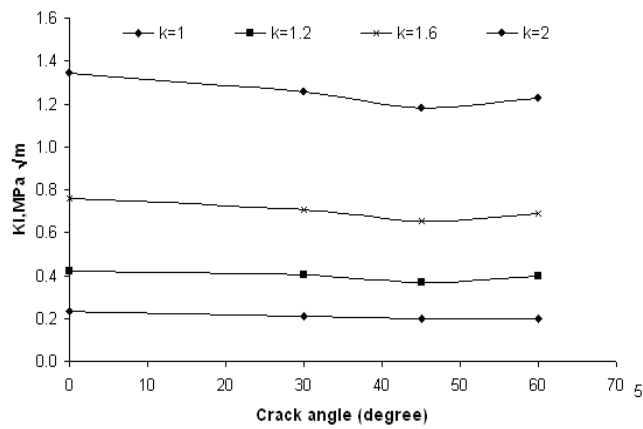


Figure 3(b): Effect of crack angle on stress intensity factor K_I for $a/W = 0.06$.

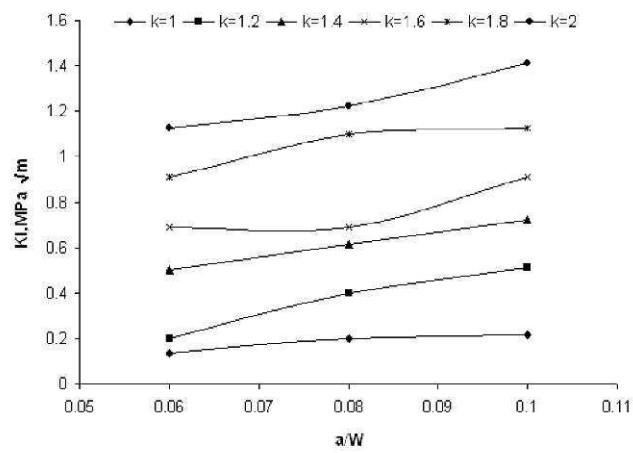


Figure 3(c): Effect of (a/W) ratio on stress intensity factor K_I , for $\alpha = 60^\circ$

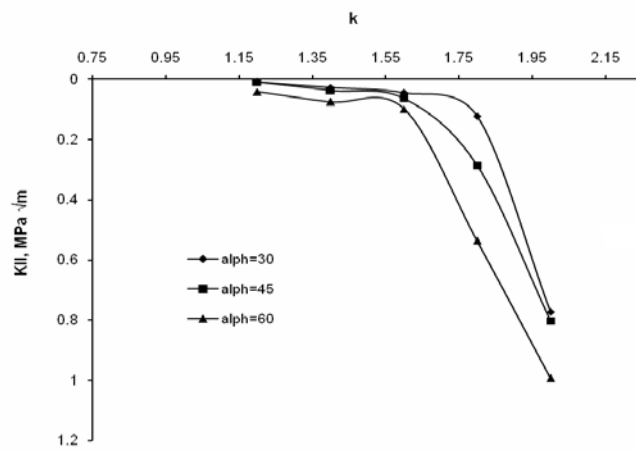


Figure 4(a): Effect of biaxial factor on stress intensity factor K_{II} for $a/W = 0.08$

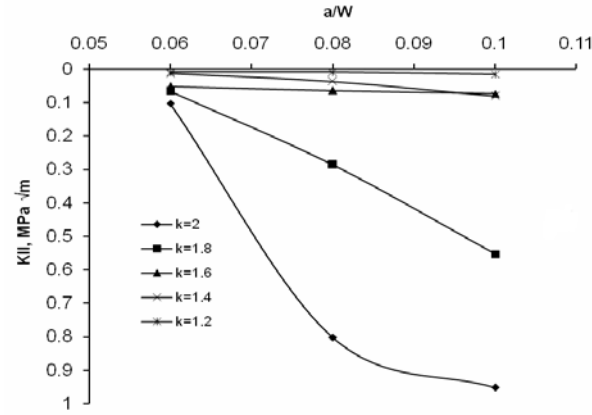


Figure 4(b): Effect of a/W on stress intensity factor K_{II} for $\alpha = 45^\circ$

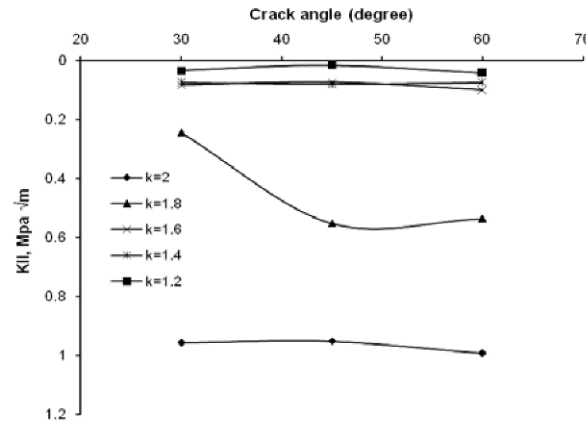


Figure 4(c): Effect of crack angle on stress intensity factor K_{II} for $a/W = 0.08$

The theoretical relation available for K_I is written as:

$$K_I = \frac{\sigma\sqrt{\pi a}}{2} \{ (1+k) - (1-k)\cos 2\alpha \} \quad (26)$$

This relation is based on assumption of infinite plate with remote loading conditions, i.e. $L_e/W_e = 1$ for all α values. So that K_I is independent of (L_e/W_e) ratio in above relation. Liebowitz [6] have proposed analytically and numerically that stress intensity factor, depends on the (L/a) and (W/a) , where L is the length of specimen and W is the width of the specimen. In the present investigation it is seen that K_I depends upon crack angle, biaxial load factor, constant stress term and geometry factor (a/W) and (a/L) . Hence an attempt has been made to correlate these parameter to K_I and following from is presented.

$$K_I = \sigma\sqrt{\pi a} \{ (1+k) - (1-k)\cos 2\alpha \} f_1 \left(\frac{L_e}{W_e} \right) \quad (27)$$

Where $L_e = L/2 - a \cos \alpha$ and $W_e = W/2 - a \sin \alpha$,

where the function $f_1 (L_e/W_e)$ is obtained from regression analysis and found as :

$$f_1 \left(\frac{L_e}{W_e} \right) = \left[a_1 + a_2 \left(\frac{L_e}{W_e} \right) + a_3 \left(\frac{L_e}{W_e} \right)^2 + a_4 \left(\frac{L_e}{W_e} \right)^3 + a_5 \left(\frac{L_e}{W_e} \right)^4 \right] \quad (28)$$

The coefficient $(a_1$ to $a_5)$ are shown in Table (1) for various biaxial factor. L_e and W_e are defined in figure 1.

Table 1: The coefficient of Equation (28)

k	Coefficients				
	a ₁	a ₂	a ₃	a ₄	a ₅
1.0	2958.13	-12319.36	19224.87	-13324.242	3460.51
1.2	4537.08	18372.43	27972.43	-18972.07	4837.87
1.4	15558.09	-64654.20	100712.02	-69686.75	18072.87
1.6	25511.84	-105574.57	163730.04	-112775.23	29110.39
1.8	13629.04	-56212.08	87054.91	-59991.82	15522.33
2.0	42527.06	-175971.91	272858.97	-187899.41	48486.72

The correlation coefficient in all cases are found to be greater than 0.90.

STRESS INTENSITY FACTOR, K_{II}

It reveals for the Figure (6-8) that K_{II} depends on α , k and (W and L). The magnitude obtained from experiments are also quite different from the theoretical solutions for same boundary conditions and loading. This is due to the geometry constraint. Hence a geometry factor is derived for K_{II} and presented in following form.

$$K_{II} = \frac{\sigma\sqrt{\pi a}}{2} f_2\left(\frac{L_e}{W_e}\right) \quad (29)$$

where the function $f_2 (L_e/W_e)$ is obtained from regression analysis and found as :

$$f_2\left(\frac{L_e}{W_e}\right) = \left[a_{21} + a_{22}\left(\frac{L_e}{W_e}\right) + a_{23}\left(\frac{L_e}{W_e}\right)^2 + a_{24}\left(\frac{L_e}{W_e}\right)^3 + a_{25}\left(\frac{L_e}{W_e}\right)^4 \right] \quad (30)$$

The coefficient (a_{21} to a_{25}) are shown in Table (2) for various biaxial factor.

Table 2: Coefficient of Equation (30)

k	Coefficients				
	a ₂₁	a ₂₂	a ₂₃	a ₂₄	a ₂₅
1.0	0.023338	-0.006552	0.0149691	-0.103077	0.026600
1.2	166886.09	-484369.54	751914.84	-518243.74	133810.83
1.4	52169.22	-215980.16	334828.70	-230670.93	59558.42
1.6	5040.72	-22239.70	36592.78	-26637.27	7234.41
1.8	8273.014	-34264.72	53203.89	-36704.137	9492.012
2.0	2974206.00	-12400926.00	19376463.00	-13446820.00	3497075.30

A detailed analysis has been done under fatigue loading. Maximum Tangential Stress (MTS) criterion has been used for the prediction of crack initiating angle. The crack growth trajectories have been determined by cycle by cycle simulation procedure. For determination of instantaneous crack angle and instantaneous crack length equations (24) and (25) has been used. A computer programme in C++ has been developed to solve the various equations to find out the life and to study the effect of various parameters on fatigue life. The results obtained from the simulation are presented in figures 9. Figure 9 shows a graph between crack growth rate and number of cycles for a constant inclination angle (30°) at different initial crack length. Figure shows that for crack length, initially crack grows slowly and beyond a cycle of 5×10^4 it increases rapidly. It is observed that as the crack length increases the growth rate also increases beyond the cycle of 5×10^4 . It is concluded that the life of component depends upon the initial crack length and crack inclination angle and stress intensity factors. According to the equation 17 & 18 crack growth rate increases as the stress intensity factors increases. Stress intensity factors are depended upon the initial crack length, crack angle, biaxial factor k and a/W as shown in figure (3-5) and figure (6-8). It is concluded that the life of component depends upon the initial crack length, crack inclination angle biaxial factor k and a/W . As the crack inclination angle increases the crack growth rate increases and the life of component becomes less. Similarly as the crack length increases the crack growth rate increases and the life of components decreases. On increasing the value of crack inclination angle the value of new crack length increases for a constant initial crack length.

REFERENCES

- [1] Irwin, G.R. , Analysis of Stress Strains near the end of a Crack Traversing Plate, Trans. ASME, J. Appl. Mech., 24(3): 361-364, 1957.
- [2] Sih, G.C. , A Special Theory of Crack Propagation Methods of Analysis and Solution of Crack Problems, Mechanics of Fracture, Vol.1, Edited by G.C. Sih, pp XXI-XLV, Noordhoff Int. Pub. Leyden, Amsterdam, 1973.

- [3] Kelley, L.G. , Handbook of Numerical Method and Applications. Addison-Werly, Reading Mass. p. 99, 1991.
- [4] Stephens, Stephens, R. I., Fatemi, A., Stephens, R. R., Fuchs, H. O., Metal "Fatigue in Engineering", 2nd Edition, John Wiley & Sons, Inc., New York, 2001.
- [5] Paris, P. C., and Erdogan, A critical analysis of crack propagation laws, *J. Bas. Engng, Trans. ASME*, Ser D 85, 528-533, 1963.
- [6] Liebowitz, H.; Lee, J.D. and Eftis, J. ,Biaxial Load Effects in Fracture Mechanics, *Engg. Frac. Mech.*, 10 : 315-335, 1978.
- [7] Khan, Shafique M.A., and Khraisheh, M.K., Analysis of Mixed Mode Crack Initiation Angle under Various Loading Conditions, Elsevier science Ltd., pp. 1-10, 2000.

Stochastic model for estimation of probability-confidence bounded a - N curves

Prakash Chandra Gope

Mechanical Engineering Department, College of Technology, G. B. Pant University of Agriculture & Technology, Pantnagar-263145, Uttarakhand, India

Email address: pcgope@rediffmail.com, Tel: +91 9411159916; fax: +91 5944 233338

ABSTRACT

Based on the crack opening displacement, fatigue crack growth model is expressed as a function of mechanical properties. The effect of material non-homogeneity is included in the model through a random process parameter of Gaussian type. The model is validated through the experimental and predicted results from several data sets. All experimental data are taken from literature.

Nomenclature

a	: Crack size
B	: Thickness of the specimen
E	: Modulus of elasticity, GPa
N or N_f	: Number of cycles to failure, or fatigue life, cycles
W	: Width of the specimen
ϖ	: Degree of material non-homogeneity
μ	: Population mean
a_0	: Initial crack length
a_f	: Final crack length
a/w	: Crack aspect ratio
K_I	: Mode I stress intensity factor, $MPa\sqrt{m}$
K_{\max}	: Maximum stress intensity factor, $MPa\sqrt{m}$
K_{\min}	: Minimum stress intensity factor, $MPa\sqrt{m}$
K_{op}	: Opening stress intensity factor
K_{th}	: Fatigue threshold, $MPa\sqrt{m}$
K_{IC}	: Fracture toughness, $MPa\sqrt{m}$
ΔK_I	: Stress intensity factor range, $MPa\sqrt{m}$
da/dN	: Crack growth rate
$s(\dots)$: Standard deviation of parameter (.)
σ_y	: Yield strength, MPa
$\mu(\dots)$: Population mean of parameter (.)

Introduction

All structural component experiences cyclic stresses of sufficient magnitude during their life span. Under fluctuating load condition the physical mechanisms leading to crack formation and failure is very complicated and difficult to model. However, several deterministic crack growth models are available in literature. It is widely recognized that the fatigue crack growth is fundamentally a stochastic phenomenon. The two main reasons for the randomness in fatigue crack growth

behaviour are the random material resistance or inhomogeneous material properties and the random loading. During the last three decades, the probabilistic aspect of fatigue crack growth has been addressed by many researchers [1-7]. These studies are based on Markov chain model, random process model or random variable model. Most of the stochastic crack growth models are based on the inclusion of a suitable stochastic random process either of stationary and ergodic process of Gaussian type or non Gaussian type in the deterministic crack growth model. Mostly the deterministic part of the model is based on Paris-Erdogan, Elber or polynomial models. Keeping in view these aspects, the present study is aimed at the development of a stochastic crack growth model and estimation of confidence and probability bounded crack growth relation (a - N) curve) coupled with stationary Gaussian random process. In the model the statistical scatter of the material properties between the specimens and the microstructural stochastic non-homogeneity of the material within a specimen are well addressed. The validity of the model is demonstrated through the comparison with an extensive amount of the published crack growth data. The probability-confidence bounded prediction of a - N curves presented in this paper will be extremely helpful for the reliability assessment of structure.

Stochastic Crack Growth Model

On the basis of energy release and crack opening stress, author has developed the following crack growth model [8]

$$\frac{da}{dN} = \frac{0.63(1-\nu^2)(\Delta K_{eff})^m}{(\alpha E \sigma_y)} \frac{1}{1 - \left(\frac{K_{max}}{K_{IC}}\right)^2} \quad (1)$$

where α is plastic zone correction factor, $\Delta K_{eff} = K_{max} - K_{op}$ and this K_{op} is the crack opening stress.

It is now, possible to consider the following functional dependence for the phenomenon of fatigue crack growth as:

$$\frac{da}{dN} = f(E, \sigma_y, \Delta K_{IC}, \Delta K_{th}, \Delta K_{op}; K_{max}, R; a_0, W, B) \quad (2)$$

f in Eq. (2) denotes function. Making groups of the similar properties, Eq. (2) can be expressed as:

$$\frac{da}{dN} = f(\psi, C, a) \quad (3)$$

where ψ is vector of geometry parameters, C is the experimentally determined function of monotonic and cyclic strength and $a = a(N)$, the crack length at cycle N . With the randomization of material and geometry parameters, $a - N$ curves similar to experimental observations can be obtained and it can be interpreted as crack growth model for generating the sample crack growth curves. Hence, Eq. (1) in terms of mean values can be expressed as:

$$N(a) = \int_{a_0}^a \frac{\alpha(\mu_E)(\mu_{\sigma_y})}{0.63(1-\nu^2)} \left(\frac{1}{\mu \Delta K_{eff}} \right)^2 \left(\frac{1}{\mu K_{IC}} \right)^2 \left(\mu K_{IC}^2 - \left\{ \psi \sigma_{max} \sqrt{\pi a} \right\}^2 \right) da \quad (4)$$

Eq. (4) can be solved for each crack increment Δa and the required cycles to reach the crack length can be obtained. Sum of these cycles will be the cycles required to grow the crack from a_0 to a . Let the cycles obtained at each crack increment be denoted by $N(\Delta a)$. The total cycles required to grow the crack from a_0 to a is

$$N(a) = \sum_{a_0 + \Delta a}^a N(\Delta a) \quad (5)$$

From the results of Eq. (5) $a - N$ curve can be drawn. The $a - N$ curve thus obtained explains only the variability due to the material properties and specimen geometry. Hence, the variability due to material non-homogeneity is to be incorporated to account this effect on the growth process.

Consider a random process, $X(a)$ as:

$$X(a) = \left\{ \bar{X} + \sigma_X \cdot \zeta(a) \right\} \quad (6)$$

where

$\zeta(a)$ is the standard Gaussian white noise and

$E[\zeta(a)] = 0$ and $Co Var[\zeta(a'), \zeta(a'')] = \delta(a'' - a')$, $\delta(\cdot)$ as the Dirac function.

\bar{X} and σ_X^2 denotes mean and variance of $X(a)$. ϖ is the degree of non homogeneity factor and it can be assumed that $0 < \varpi \leq 1.0$. The random factor $X(a)$ now is added to the each normalized life data (normalized between -1 and 1) obtained for each crack increment from Eq. (5) to account the material non-homogeneity effect.

Validity of the model

Equation (5) and (6) are solved with the initial parameters as given by Virkler et al [3] and model predictions are compared in Fig 1. The predicted a-N curve seems to be very close to the experimental results of Virkler data.

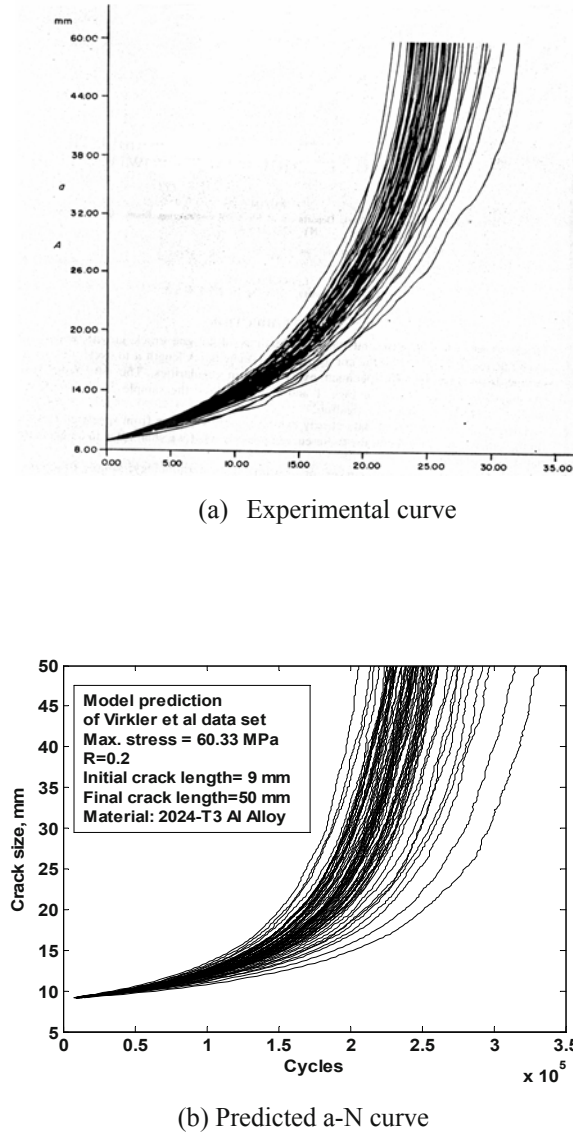


Fig. 1 Comparison of experimental and predicted crack propagation curves (a) Experimental curve taken from Virkler et al a - N data set [3] (b) Model prediction of Virkler et al a - N data set

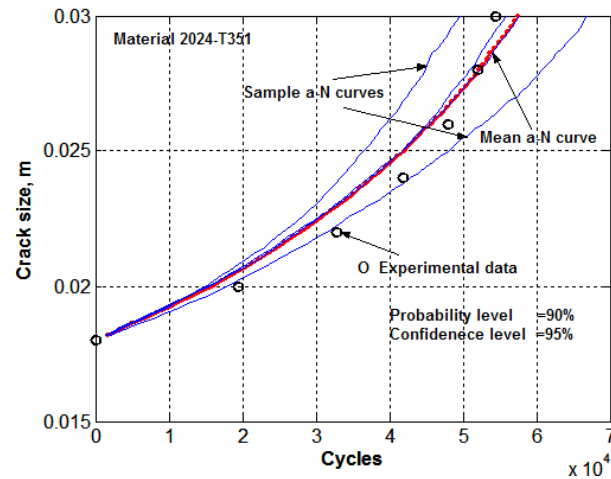


Fig. 2 Prediction of mean $a - N$ curve from the four generated sample curves at 90% probability and 95% confidence level within an error of 5%. Mean experimental life data are taken from Wu & Li [5]

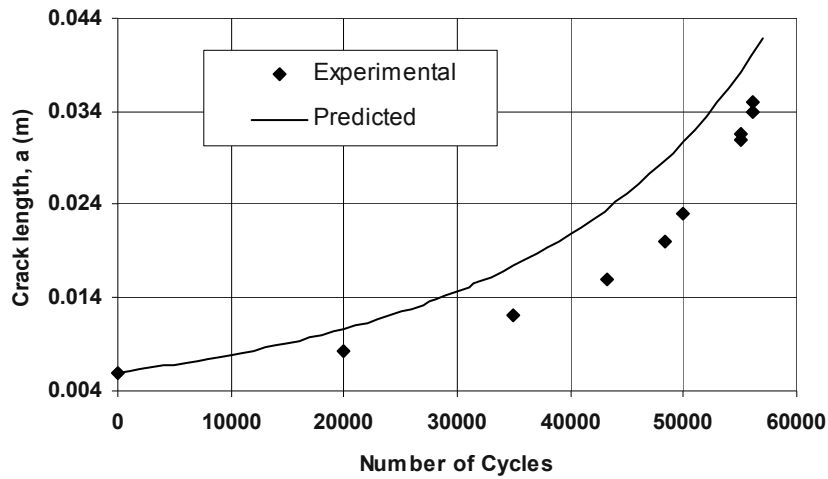


Fig. 3 Predicted and experimental growth behaviour of Aluminum alloys. Experimental data are taken from [9-10]. $R=0.1$

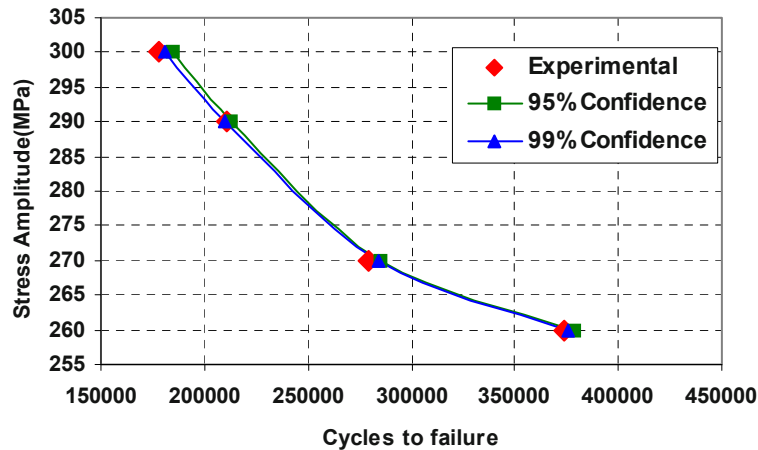


Fig. 4 S-N curve for 0.26% carbon steel at 50% Probability and different confidence level, $R=-1$ [11]

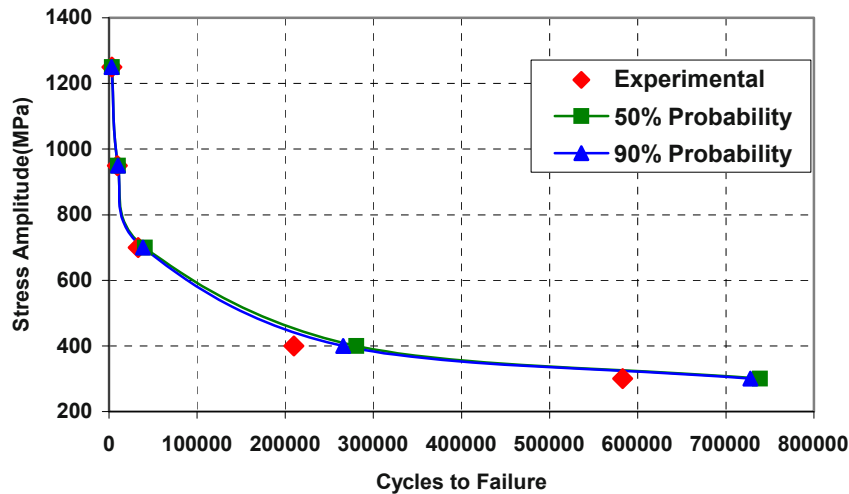


Fig. 5 S-N curve for 4340 steel at 90% confidence level and different probability, R=-1 [12]

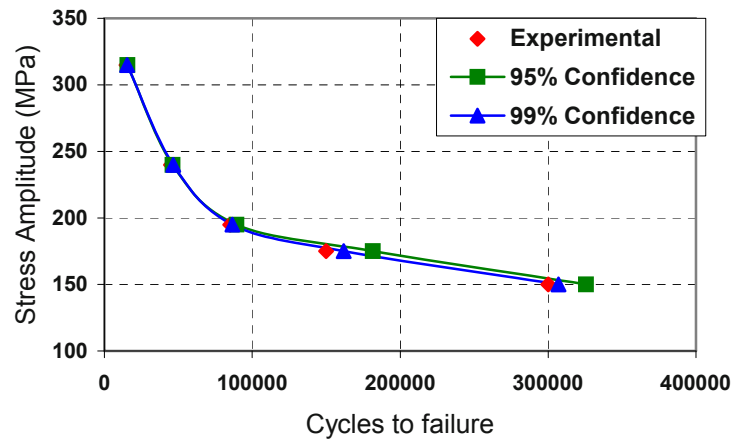


Fig. 6 S-N curve for 7075-T6 Aluminum alloy at 50% Probability and different confidence level, R=-1 [12]

Fig. 2 shows the predicted $a-N$ curve from the four generated sample curves at 90% probability and 95% confidence level within an error of 5%. Mean experimental life data are taken from Wu & Li [5]. Fig. 4-6 shows the predicted mean S-N curve along with the experimental data for different materials. The results shown in figures are very close to the experimental results which show the capability of the model presented in this study.

Conclusions

The stochastic crack growth model based on crack opening and random process parameter for the effect of material non-homogeneity is found to be suitable for crack growth prediction. The model is validated through available experimental results.

References

- [1] W.F. Wu, C.C. Ni., Probabilistic models of fatigue crack propagation and their experimental verification. Probabilistic Engineering Mechanics, 19:247-257, 2004.
- [2] Elber W., Fatigue crack closure under cyclic tension. Engng Fract Mech, 2:37-45, 1970.

- [3] Virkler DA, Hillberry B M, Goel P K., The statistic nature of fatigue crack propagation. ASME J Engng Mater Technol, 101:148–53, 1979.
- [4] Ghonem H, Dore S., Experimental study of the constant probability crack growth curves under constant amplitude loading. Engng Fract Mech., 27:1–25, 1987.
- [5] Wu W F, Ni C. C., A study of stochastic fatigue crack growth modeling through experiment data. Probab Engng Mech., 18:107–18, 2003.
- [6] Wu WF, Ni C. C., Statistical aspect of some fatigue crack growth data. Engineering Fracture Mechanics.,74:2952-2963, 2007.
- [7] Gope P. C., Bhatt S. , Pant M., Geometry and material property uncertainty model for fatigue life predictions, Proc of the SEM 2007 Annual conference and Exposition 2007; Springfield: Massachusetts USA. Paper No 119, 2007.
- [8] Gope P. C., Probabilistic model of fatigue crack propagation and estimation of probability-confidence bounded a-N curves, submitted for publication, 2011.
- [9] Kumar Raghuvir, Pandey A. K. Investigation of fatigue crack growth under constant amplitude loading, Int. J. Pres. Ves & Piping, 41:179-192, 1990.
- [10] Kumar Raghuvir, Garg S. B. L. A study of effective stress range ratio in programmed loading. Int. J. Pres. Ves. & Piping, 37: 331-343, 1989.
- [11] Parida N., Das S. K., Gope P. C., Mohanty O. N., Probability, confidence, and sample size in fatigue testing. J. Testing & Evaluation, 18(6):385–389, 1990.
- [12] Bhatt Sandeep, Specimen geometry and material property uncertainty model for probabilistic fatigue life predictions, M. Tech Thesis, G.B. Pant University of Agriculture and Technology, Pantnagar, India, 2006.

Waveforms and frequency spectra of elastic emissions due to macrofractures in solids

A. Schiavi¹, G. Niccolini¹, P. Tarizzo¹, A. Carpinteri², G. Lacidogna², A. Manuello²

¹ INRiM - National Institute of Metrological Research, Strada delle Cacce 91, 10135 Torino, Italy.

² Politecnico di Torino, Department of Structural Engineering & Geotechnics,
C.so Duca degli Abruzzi 24, 10129 Torino, Italy

ABSTRACT

This paper investigates the waveforms and frequency spectra of elastic emissions (ELE), or quasi-rigid body vibration pulses, due to the formation of macrofractures in perfectly brittle, quasi-brittle and ductile materials subjected to uniaxial compression. Elastic emissions, differently from acoustic emissions, are detected in a low frequency range (i.e. below 15-10 kHz) and are characterized by high levels of released energy. Approaching to the large fractures and the final collapse of the material bursts of ELE are observed indicating the solid elastic-mechanical properties degradation and its irreversible plastic deformation.

Through waveform and time-frequency analysis of the ELE spectra, measured by calibrated transducers, it is possible to provide quantitative information on the damage evolution and the strain energy released during each ELE event.

INTRODUCTION

The brittle fracture of materials is a complex phenomenon which occurs according to two broadly defined scenarios. In the first one, failure occurs by sudden propagation of a single fracture without appreciable precursors. In the latter, failure occurs as the culmination of progressive damage. The phenomenon of damage from a physical point of view represents surface discontinuities in the form of cracks, or volume discontinuities in the form of cavities due to decohesion between inclusions, debonding between fibers and matrix in composite materials, delamination, corrosion and other disruptive phenomena.

The most advanced method of quantitative non-destructive evaluation of damage progression is the acoustic emission (AE) technique. Since many years the expression “acoustic emission” (AE) is used to mean a class of phenomena in which transient elastic waves are generated by the rapid release of energy from localised sources, typically developing cracks, within a material. AE waves, whose frequencies typically range from kHz to MHz, propagate through the material towards the surface of the structural element, where they can be detected by sensors which turn the released strain energy packages into electrical signals.

Traditionally, in AE testing a number of parameters are recorded from the signals, such as cumulate number, occurrence and amplitude. The condition of the specimen is determined from these parameters.

Over the years, through more sophisticated analysis techniques, many spectral analysis of acoustic emissions generated by fracture in many typologies of materials were carried out. However, in general, the analysis are limited in frequency range greater than 100 kHz, regardless the signals in the audible range, and are mainly focused on the counting of events in time.

More in deep analysis of the waveform and frequency on spectra of AE, allow to identified additional informations carried by elastic waves, such as the quantification of the energy released in the evolution of damage. The amplitude level increasing, the variation in frequency and the cumulative rate over time are signature of the damage evolution, from micro-crack to the meso- and macro-crack until to the collapse of the material.

SHORT BACKGROUND

The first analytical studies on the AE signals are due to Egle and Tatro in 1967 [1]; the authors have discriminate the AE due to longitudinal waves by AE due to flexural waves, providing the first estimation of energy released for each AE event.

Pollock [2], in 1971, had highlighted the question of broad-band spectrum of the acoustic emission claiming that these emissions source wave carries appreciable energy at low frequency. The analysis of the energy content and the frequency spectrum of the AE allows to provide relevant information on the fracture and on its evolution from the diffusion of microfractures to macrofractures in different materials experience evolving damage.

In 1990 Bocca and Carpinteri [3] have shown that in rock and concrete specimens, with very high strength, the catastrophical failure gives rise to the release of a remarkable amount of energy quantifiable through a negative impulse produced by the specimen in the time interval immediately following the achievement of peak load.

Bruneau and Potel [4], through a statistical analysis of the energy content of AE, showed the evolution of fracture in composite materials. AE signals, approaching to fracture, are characterized by different higher distribution and rate. Depending on the energy level of the signals two main stages of damage are classified: matricial-cracks and interfacial decohesion.

Aggelis *et al.* [4] have also used the AE parameters to monitor the transition of the damage mechanism from transverse cracking to delamination of cross ply laminates degradation, through an analysis of the signal amplitudes and frequencies in a range between 100 kHz and 500 kHz, of acoustic emissions.

Recently a spectral analysis of acoustic emission signals at very low frequency, i.e. between 1 kHz and 20 kHz has been proposed [6]. The evolution of the fracture has been investigated in a frequency range such as to exclude all AE due to purely vibration modes of the specimen. Actually, these emissions, defined elastic emissions (ELE), are quasi-rigid body vibrations resulting from the specimen flexibility and the constraints (specimen-platen contact with friction). In the next stages of the fracture, until to the final collapse, ELE with wavelengths much greater than the maximum size of the solid under consideration are detected.

The hypothesis is that the formation of macrocrack generate pulses in the volume of the solid, which excite not only the vibration modes of the body (whose wavelengths, depending on the speed of elastic wave propagation in solid, are less than the size of the solid tested), but also actual dislocation of the entire parts of the solid.

ELASTIC EMISSIONS

An ELE event would imply a rigid vibration of the body, while high-frequency AE are pure vibration modes of the body, including longitudinal (P-), shear (S-) and surface (Rayleigh) waves, due to micro-crack growth.

Taking into account that the Rayleigh superficial waves velocity, c_R , is about 0.92 of the S waves velocity c_S and, at least, $c_S \approx c_L / \sqrt{3}$, the propagation velocity c_R of the Rayleigh superficial waves in the tested materials has been estimated to be roughly $0.531 \cdot c_L$, from the measured c_L of the longitudinal elastic waves. On the basis on this restrictions, for the typology of the material and for the size, i.e. that the half-wavelengths λ_{ELE} of detected signals fulfil the relationship $\lambda_{ELE} \geq 2 \cdot d_{MAX}$, the upper limit for the ELE frequencies is defined as:

$$f_{ELE} \leq \frac{c_R}{2 \cdot d_{MAX}} \approx \frac{0.92 \cdot c_L}{2 \cdot \sqrt{3} \cdot d_{MAX}} \approx 0.265 \frac{c_L}{d_{MAX}} \quad (1)$$

In order to verify that ELE were actually fracture phenomena and not random or spurious signals, such as extraneous noise and background vibration statistical analysis for specific this type of phenomenon has been carried out. All ELE were subjected to the Gutenberg-Richter and Omori laws [7]. These statistical methods show that the space-time organization of events of fracture (from seismic macro-scale to faintest acoustic emissions), is governed by well-defined scaling laws, as shown in some recent works.

This result, comforted by other evidences, such as increase of rate and amplitude in time [8], allow the hypothesis that ELE are actually precursors of plastic deformation and irreversible damage in volume of the solid under compression to be confirmed. Besides a simple method to quantify the released energy in terms of kinetic energy of ELE has been also proposed [9].

However these emissions can be considered as precursor of large fractures or collapse, even if no change in slope can be recognized in the classical stress-strain curve. This consideration implies that, even if the material is undergoing a yielding or damage, for certain values of load, the elastic modulus does not seem to vary.

EXPERIMENTAL SET UP AND TESTED MATERIALS

The test is performed in displacement control at constant piston velocity of $0.5 \cdot \mu\text{m/s}$, using a servo-hydraulic press with a maximum capacity of 500 kN, equipped with control electronics. The specimen adheres to the press platens without any coupling material (specimen-platen contact with friction). The applied force is determined by measuring the pressure in the loading cylinder by means of a transducer. The margin of error in the determination of the force is 1%. The stroke of the press platen in contact with the test specimen is controlled by means of a wire type potentiometric displacement transducer. Two kind of “delta shear” accelerometers, with respectively the upper frequency limit of 10 kHz and 20 kHz, for detection of ELE events are used, depending on the typology and size of specimen tested. The events are characterized by the output response of the calibrated transducers (charge sensitivity 9.20 pC/m s^{-2} and 0.33 pC/m s^{-2}), expressed in mm/s^2 . The accelerometer transducers are rigidly (fixed) coupled to the specimens in order to detect the surface acceleration. In order to filter out environmental background noise, we set appropriate detection thresholds for acquisition systems, i.e. 60 dB (referred to $1 \mu\text{m/s}^2$) for ELE signals and a pass-high filter in order to filter out any residual background vibration under 1 kHz. Tested materials are two specimen of concrete (with different features) and one specimen of Green Luserna Granite. As shown in Table 1, the physical quantities of interest

(specimen size, longitudinal wave velocity) indicate that the adopted transducer, working in the range of 1 to 10 kHz or in the range of 1 to 20 kHz, properly detects only ELE events.

Table I. Tested materials and features

Specimen	Material	Density [kg/m ³]	Mass [kg]	Max size [m]	Longitudinal wave speed [m/s]	f_{ELE} [kHz]
1	Concrete	2500	0.146	$5.3 \cdot 10^{-2}$	4270	21.3
2	Luserna gran.	2480	0.580	$10.6 \cdot 10^{-2}$	2950	7.4
3	Concrete	2200	2.200	10^{-1}	~ 4500	11.9

EXPERIMENTAL RESULTS

We analyzed the energy (in terms of global level amplitude) and frequency spectra of ELE during compression tests on three materials with different failure modes: ductile (concrete 1), quasi-brittle (Luserna 2) and perfectly brittle (concrete 3). In previous works such investigations were restricted to high-frequency AE. The increase of AE amplitudes as failure is approached were experimentally observed in [4]. Variation of AE frequencies during damage evolution has been studied in [10]. It has been observed that AE frequencies, as a function of increasing load, tend to decrease during “pre-failure” and “post-failure” stage, while tend to increase after the main fracture. These stages are separated by the so-called “seismic calm” stage, in which AE activity can be detected only in the MHz range. The behaviour of AE frequencies can be described through a “s-shape” curve, as shown in Fig.1. In this work analogous analysis on ELE spectra has been carried out.

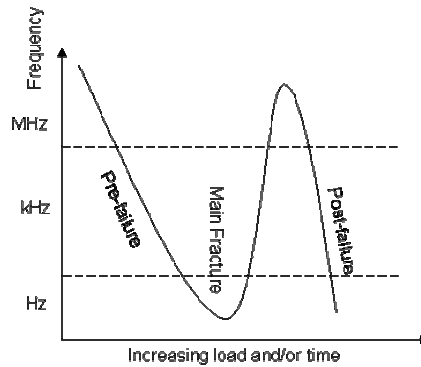


Fig. 1: S-shape curve of AE during failure of rock specimen

Here, all ELE events detected during a compression test are shown as a function of time, amplitude and frequency. These 3D-graphs provide exhaustive information on the ELE activity. Each point represents the global level of a single ELE experimentally measured, and the frequency value is related to the peak of greatest amplitude in the considered spectrum. As an example, Fig. 2 shows the spectrum related to a single point in the time - energy - frequency diagram, where the X-axis represents the time in seconds, the Y-axis is the frequency in hertz, and the Z-axis is the amplitude in dB referred to $1 \mu\text{m/s}^2$.

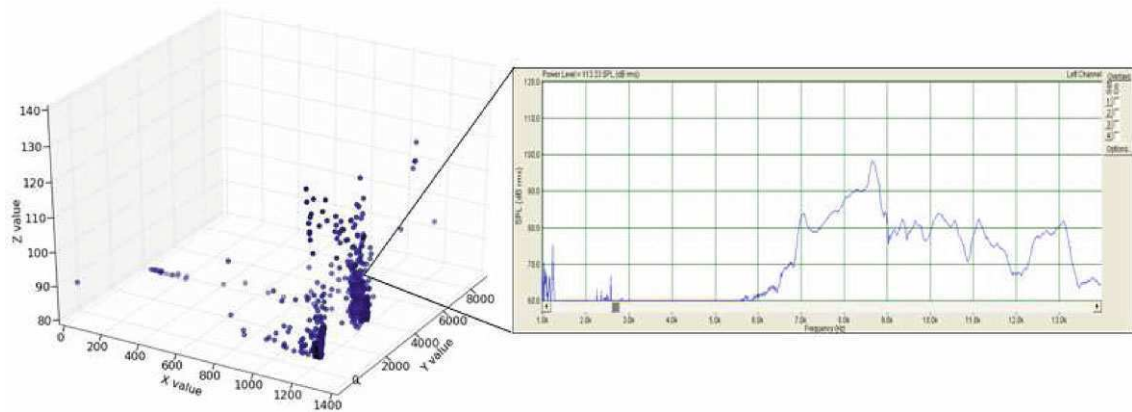


Fig. 2: Example of spectrum extrapolated from the 3D-graph of a single ELE (detected on concrete 3 at 1209 s). Global level 113 dB, frequency peak 8.6 kHz.

Ductile fracture

The duration of compression test on concrete-1 was 1600 s, with a change in the slope of the stress/strain curve 760 s since the beginning of the test. The failure behaviour of the specimen is ductile. In the graph a sporadic ELE activity at the beginning of the test and during the failure is detected. The ELE energy is spread over a range of about 15 dB. Frequency peaks are located around 4.5 kHz, both before and after the collapse of the sample. However, ELE activity both in pre-failure and in post-failure stages may be mainly due to frictional phenomena within the specimen. Failure occurs as the culmination of progressive damage without propagation of large fractures within the bulk of material. Therefore, ELE do not play as failure precursors in the specimens which exhibit ductile behaviour. In Fig. 3 distribution of ELE activity during compression test and distribution of amplitude/frequency are shown.

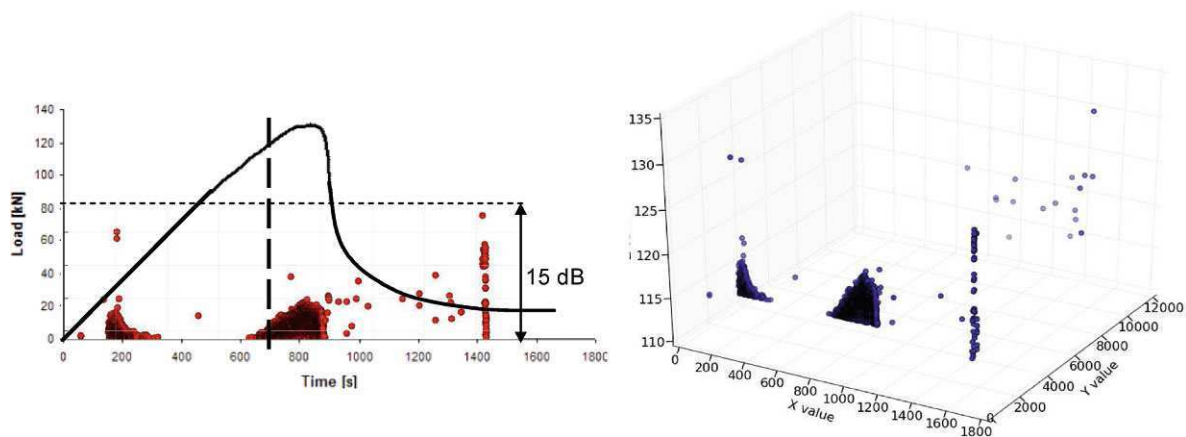


Fig. 3: ELE activity in ductile fracture on concrete 1.

Quasi brittle fracture

The duration of compression on the granite Luserna specimen was 1420 s, and ELE activity started 600 s since the beginning of the test. ELE events concentrated when load drops occur. A burst of ELE activity can be recognized at about 1000 s, before the first significant load drop occurred at 1180 s. Although the slope of the stress/strain curve didn't exhibit any significant variation between 600 s and 1180 s, the presence of ELE with high energy content (between 105 dB and 125 dB) indicated the growth of meso-and macro-fractures. Moreover, the range of signal amplitudes, i.e. 30 dB, was greater than the ductile specimen.

Later on, between 1200 and 1400 s, the ELE rate increased with bursts of activity at each load drop. While in the stages shortly afterward each load drop (e.g. between load drops 3 and 4) no significant ELE bursts were detected, similarly to the AE "seismic calm".

The ELE frequencies of ELE were generally at 3.5 kHz, between 600 s 1200 s, while in the final stage, after 1200 s, ELE peaks appear at 1.9 kHz, 4.5 kHz and 6 kHz, as shown in the 3D diagram of Fig.4.

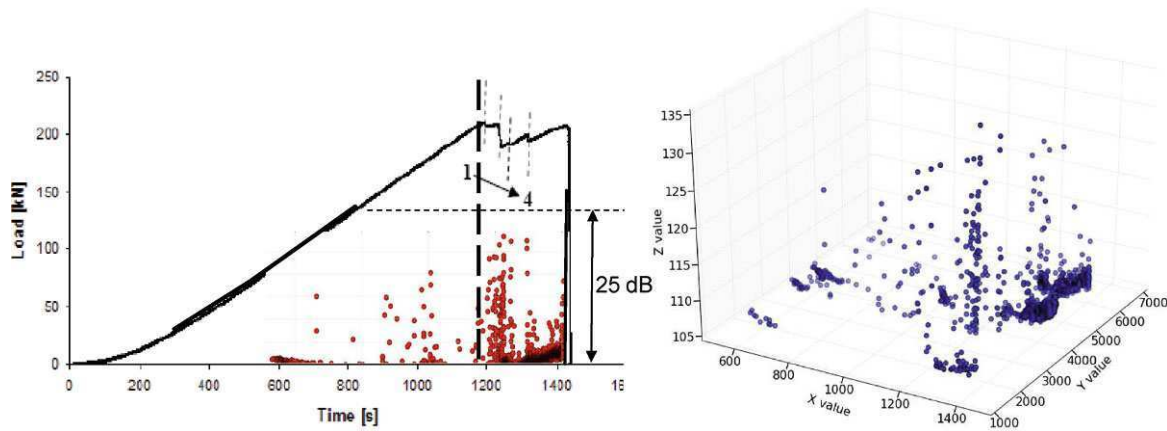


Fig. 4: ELE activity in quasi-fragile fracture on granite 2.

Perfectly brittle fracture

The ELE activity, during the compression test on concrete-3 (high resistance concrete) was detected during all the test, although a significant increase was revealed after 1000 s. In this specimen a significant increase in the ELE amplitudes, and a concomitant decrease of peak frequencies can be detected, as shown in Fig. 5.

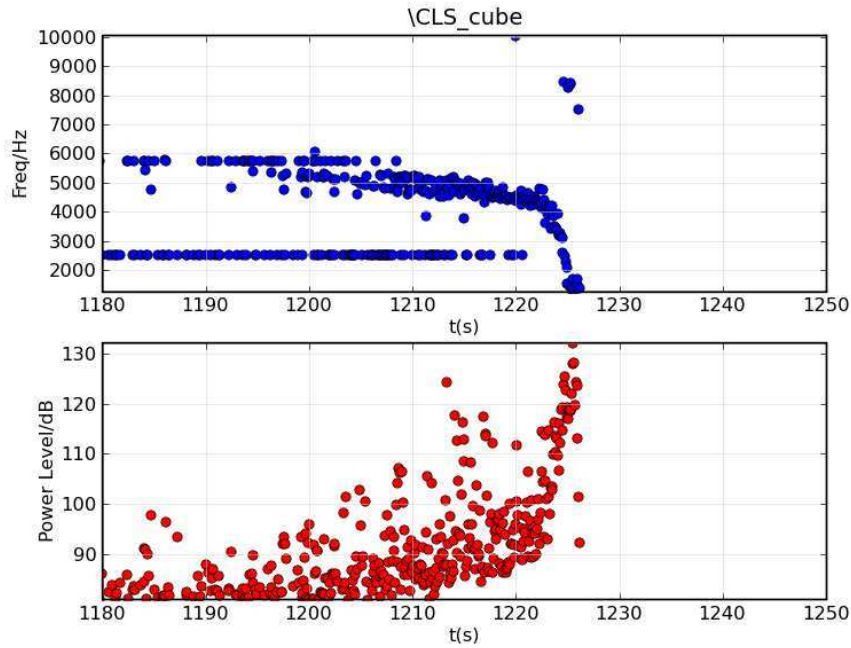


Fig.5: zoom selection of ELE activity (frequency in blue and amplitude in red) in the proximity of fracture.

Between 900 s and 1200 s, as the slope of stress/strain curve didn't change appreciably, the ELE activity played a significant role both as a fracture precursor and as indicator of plastic deformation (or irreversible deformations). Moreover, ELE were detected in a very wide range of amplitude, extending approximately over 50 dB.

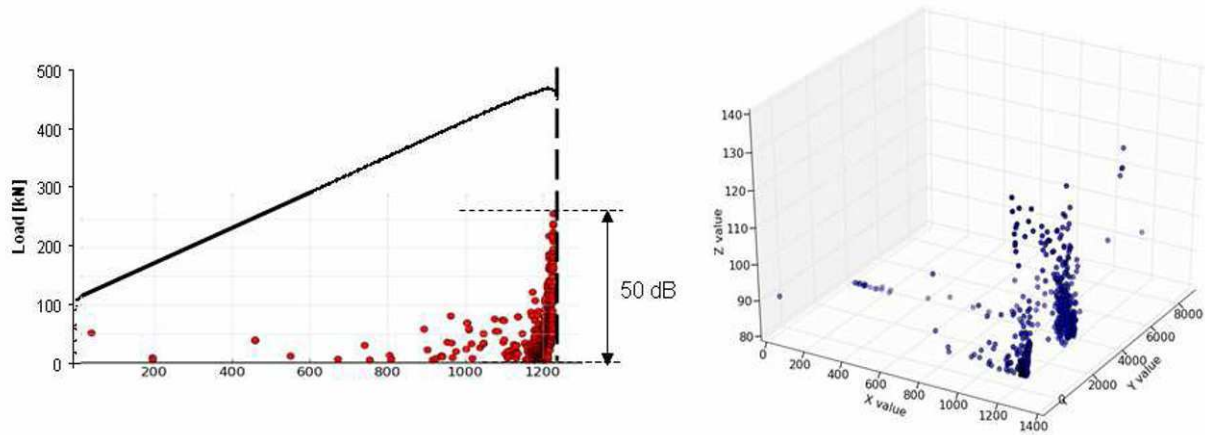


Fig. 6: ELE activity in perfectly brittle fracture on concrete 3.

CONCLUSIONS

In this work the analysis of waveforms and frequency spectra of ELE has been proposed. Each spectrum (including the energy content as a function of frequency) was experimentally determined using calibrated accelerometers. A

quantitative analysis of the global level of acceleration (or velocity) of vibration can be carried out for all detected ELE events. The spectrum shape in the frequency region of interest and the energy released were measured as well.

The variation of energy content and ELE frequency depend on the failure behaviour of the examined solids. In perfectly brittle materials, ELE energy increase is correlated with a frequency decrease until the specimen failure. In the case of brittle materials (such as granite) burst ELE seemed to show a random distribution of frequencies, although it is still possible to highlight significant increases in amplitude approaching the drop-load and the main fracture. In these materials, after the drop-load, the phenomenon of so-called “seismic calm” can be observed. At this stage it is assumed that AE are probably still present at frequencies too high to be detected with instruments used in these tests, but ELE are completely absent. Finally, in materials with ductile behaviour ELE events are due to internal frictional phenomena and appear during progressive damage until failure occurrence.

ACKNOWLEDGEMENTS

The financial support provided by “Regione Piemonte” Re-Frescos project, is gratefully acknowledged.

REFERENCES

- [1] Egle, D. M., Tatro, C. A., Analysis of acoustic emission strain waves, *J. Acoust. Soc. Am.* 41 (2), 1967.
- [2] Stephens, R. W. B., Pollock, A. A., Waveforms and frequency spectra of acoustic emissions, *J. Acoust. Soc. Am.* 50 (3) part 2, 1971.
- [3] Bocca, P., Carpinteri, A., Snap-back fracture instability in rock specimens: experimental detection through a negative impulse, *Engineering Fracture Mechanics*, Vol. 35, n. 1/2/3, 1990.
- [4] Bruneau, M., Potel, C., *Materials and Acoustic Handbook*, ISTE Ltd., London/John Wiley & Sons, Inc., Hoboken, NJ, 2009, Chap. 24.
- [5] Aggelis, D. G., Barkoula, N. M., Matikas, T. E., Paipetis, A. S., Acoustic emission monitoring of degradation of cross ply laminates, *J. Acoust. Soc. Am.* 127 (6), 2010.
- [6] Schiavi, A., Niccolini, G., Tarizzo, P., Lacidogna, G., Manuello, A., Carpinteri, A., Analysis of acoustic emissions at low frequency in brittle material under compression, *Proceedings of the SEM Annual conference 2009*, Albuquerque, New Mexico, USA.
- [7] Niccolini, G., Schiavi, A., Tarizzo, P., Carpinteri, A., Lacidogna, G., Manuello, A., Scaling in temporal occurrence of quasi-rigid body vibration pulses due to macrofractures, *Physical Review E*, 82, 2010.
- [8] Schiavi, A., Niccolini, G., Tarizzo, P., Carpinteri, A., Lacidogna, G., Manuello, A., Acoustic emissions at high and low frequencies during compression tests in brittle materials, *Strain*, 2010, doi: 10.1111/j.1475-1305.2010.00745.x.

- [9] Schiavi, A., Niccolini, G., Tarizzo, P., Lacidogna, G., Manuello, A., Carpinteri, A., Analysis of energy released by elastic in brittle material under compression, Proceedings of the SEM Annual conference 2010, Indianapolis, Indiana, USA.
- [10] Kukalov, G. I., Yakovitskaya, G. E., Acoustic Emission and stages of the crack-formation process in rock, Mining Institute, Siberian Branch, Russian Academy of Sciences, Novosibirsk 2, 111 (1993).

Failure Characteristics of Spot Welds of AHSS under Quasi-static Conditions

J. Ha¹⁾ · H. Huh^{*1)} · H. Lee²⁾ · K. S. Kim²⁾

¹⁾ School of Mechanical, Aerospace & System Engineering, Korea Advanced Institute of Science Technology, 291 Dachak-ro, Yuseong-gu, Daejeon, 305-701 Korea

²⁾ POSCO Global R&D Center, 180-1, Songdo-dong, Yeonsu-gu, Incheon, 406-840, Korea

ABSTRACT

This paper is concerned with the failure characteristics and the failure load of spot welds of AHSS under combined axial and shear loading conditions. A testing fixture and a specimen are newly designed to impose the pure-shear load acting on a spot weld. The testing fixture and the specimen proposed by Song *et al.* [1] are used to impose the combined axial and shear load at the loading angle from 0° to 75° on a spot weld. Using those testing fixtures and specimens, failure tests of the spot weld of TRIP590 1.2t, DP780 1.0t, and DP980 1.2t are conducted with seven different conditions of combined loading. Based on the experimental results, failure loads and failure behaviors of a spot weld of AHSS are investigated with respect to the different loading angles. Failure loads of the spot weld obtained from failure tests are interpolated to construct the Song and Huh's failure model [2], which facilitates the failure description of a spot weld in the macroscopic finite element analysis of auto-body crashworthiness.

INTRODUCTION

Improvement of crashworthiness becomes one of the challenging issues in auto industries together with the light weight design. Actual crash test cost to evaluate the crashworthiness of the auto-body structure become larger due to tighten regulation for a car crash. Thus, computer simulation as an alternative method to evaluate the crashworthiness of the auto-body structure is widely used in the automotive industry [3]. In order to estimate the crashworthiness of the auto-body structure properly, the correct failure prediction of a spot weld is indispensable for the crash simulation [4], [5]. Rupture of a spot weld is likely to occur prior to failure of the base metal when a large load is applied to the auto-body structure since extremely high stress is concentrated at the interface between the nugget and the base metal [6]. Because the impact load transferred from one part to another part through a spot weld is abruptly changed after the spot weld fails, deformation behaviors of the auto-body structure usually reveal large discrepancies between the experiment and the finite element analysis after joined components are separated.

Research on the failure characteristics of a spot weld has been investigated over the past few decades. Especially, it is necessary to estimate the strength of spot welds under various loading modes in order to provide a failure criterion of a spot weld for the structural analysis or crashworthiness assessment of the auto-body structures using the finite element analysis. Lee *et al.* [7], Barkey and Kang [8], Madasamy *et al.* [9] and Langrand and Combescure [10] proposed testing fixtures to provide various loading conditions including pure axial, mixed axial/shear, or pure shear loads on a spot-welded specimen through changing the position of the fixture. The failure strengths of the spot weld under combined loading conditions were utilized to provide the failure criterion. The coefficients that constitute a force-based failure criterion were determined by a regression analysis from the failure strength data of the spot weld. Similarly, Lin *et al.* [11], [12] proposed a test methodology with a different type of test fixture. They analyzed and clarified the failure mechanism of spot welds in square-cup specimens made from the mild steel and the HSLA steel under combined loading conditions. After failure tests of the spot-welded specimens using four fixture sets designed by them, an engineering failure criterion was proposed to be in quadratic form in terms of the normalized axial and shear loads with consideration of the sheet thickness and the nugget radius under combined loading conditions. Although the testing fixtures proposed by previous researchers could impose various combinations of axial and shear loads on the spot weld efficiently by changing the loading position of the fixtures, it is impossible to consider the change of load histories acting on the spot weld due to the rotation of the nugget during the failure tests. Since the rotation

of the nugget during the failure tests alters the ratio of the axial load and the shear load acting on the spot weld, the change of the load histories by the rotation of the nugget have to be considered when the ratio of the axial load and the shear load is calculated using the failure load.

In order to construct a reasonable failure model of a spot weld for crash analyses of an auto-body, Song *et al.* proposed testing fixtures and specimens for failure tests of spot welds under combined loading conditions. Failure contour of a spot weld was constructed using the failure loads obtained from the experiment at seven different loading angles of 0°, 15°, 30°, 45°, 60°, 75° and 90°. The parameters that construct the failure criterion of a spot weld in mild steel and HSS were directly calculated using the regression analysis of the axial load and the shear load at the initiation of failure in the experiments. Their failure criterion took the shape of a β -norm failure contour. In general case of a failure model for a spot welded mild steel and HSS, they suggested that the β value of 1.45 with the axial failure load and the shear failure load obtained from cross-tension tests and pure-shear tests could be used for the construction of a failure. But the characteristics of spot welds of AHSS steel sheets are different from mild steel and HSS because AHSS contain more carbon than mild steel and HSS. Therefore, the failure characteristics and the failure model proposed by Song and Huh of a spot weld of AHSS may be different from those of mild steel and HSS.

This paper proposes a failure criterion of spot welds of TRIP590 1.2t, DP780 1.0t and DP980 1.2t based on the Song and Huh's model. In order to construct the failure model by determining the coefficients, failure tests of spot welds of TRIP590 1.2t, DP780 1.0t and DP980 1.2t were carried out under combined loading conditions. Testing fixture and specimen were proposed newly for failure tests at loading angle 90° to obtain the more reasonable pure-shear failure load of spot weld. Finite element analyses for deformation of a spot weld were first carried out in order to design a testing fixture and a specimen to prevent the rotation of a spot weld and concentrate plastic deformation around a spot weld during the test. Failure tests of the spot weld were then conducted at seven different loading angles of 0°, 15°, 30°, 45°, 60°, 75° and 90° with test fixtures and specimens proposed by Song *et al.* and this paper. Failure contours of a spot weld of TRIP590 1.2t, DP780 1.0t and DP980 1.2t were constructed using the failure load obtained from tests. Failure criterion was constructed in order to describe the failure contour of a spot weld for numerical simulations in engineering applications. The coefficients that constitute the failure criterion were calculated using the regression analysis of the axial load and the shear load at the onset of failure in the experiments.

DESIGN OF THE TESTING FIXTURE AND SPECIMEN FOR THE PURE-SHEAR TEST

In order to examine the failure load of a spot weld under combined axial and shear loads, the maximum loads measured in the experiment were decomposed into the two components along the axial and shear directions. Decomposed axial and shear loads are plotted in the force domain, which shows that a typical failure criterion can be constructed in terms of the axial and shear load to describe the failure contour obtained in the experiment. Song and Huh's failure criterion is constructed to describe the failure contour of spot welds in the finite element analysis of auto-body components [2]. The failure criterion proposed by Song and Huh is expressed as Eq. (1).

$$\left(\frac{f_n}{F_N}\right)^2 + \beta \left(\frac{f_n}{F_N}\right) \left(\frac{f_s}{F_S}\right) + \left(\frac{f_s}{F_S}\right)^2 = 1 \quad (1)$$

Here, F_N and F_S are the axial failure load and the shear failure load of a spot weld, respectively. The variable β is a failure parameter. The coefficients that constitute their failure model are obtained using the least square method to minimize the discrepancy between the experimental data and interpolated one. Song and Huh's failure model of a spot weld under the combined loading condition is used to describe the failure contour of spot welds of AHSS.

Song *et al.* [1] performed the pure-shear test to obtain the failure load at loading angle of 90° using the pure-shear test specimen which was fabricated with three sheets stacked. Three-sheet spot-welded specimen is not practical at loading angle of 90° because of difficulties in making pure-shear specimens with the same welding conditions of two-sheet spot weld. In order to obtain the more reasonable pure-shear failure load of spot weld, this paper newly proposed testing fixture and specimen for failure tests at loading angle 90° as shown Fig. 1. Main purposes of this fixture and specimen are to prevent the rotation of a spot weld and concentrate the plastic deformation around a spot weld during the failure test. The proposed fixture is composed of four parts which are the fixture body, the gap controller, the holder and the keeper. The holder that is assembled to the fixture body like Fig. 1(b) is used to clamp the fixture and the specimen not to move the specimen during the failure test. And the keeper that is assembled to the fixture body like Fig. 1(c) is used to prevent the rotation of a spot weld during the failure test. The shape of the pure-shear test specimen is designed similar to a dog born shape like a tensile

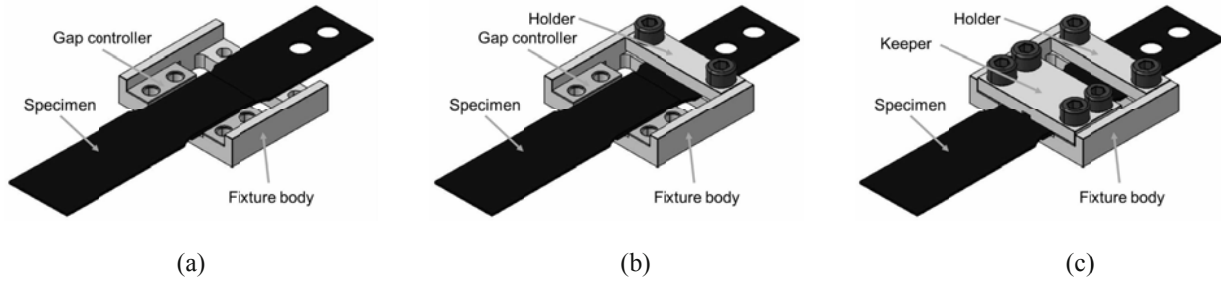


Fig. 1 Schematic design of the fixture set for the failure test of a spot weld under pure-shear loading condition: (a) assemble the fixture body and specimen; (b) clamp the specimen with the holder; (c) assemble the keeper to prevent the rotation of a spot weld.

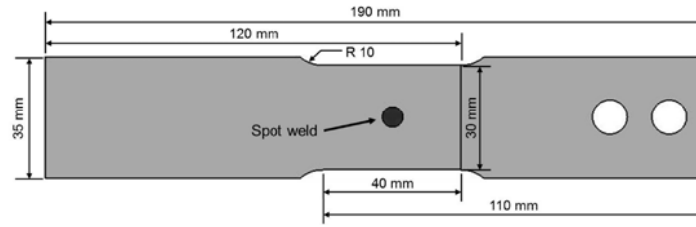


Fig. 2 Specimen shape for the failure test of a spot weld under pure-shear loading condition.

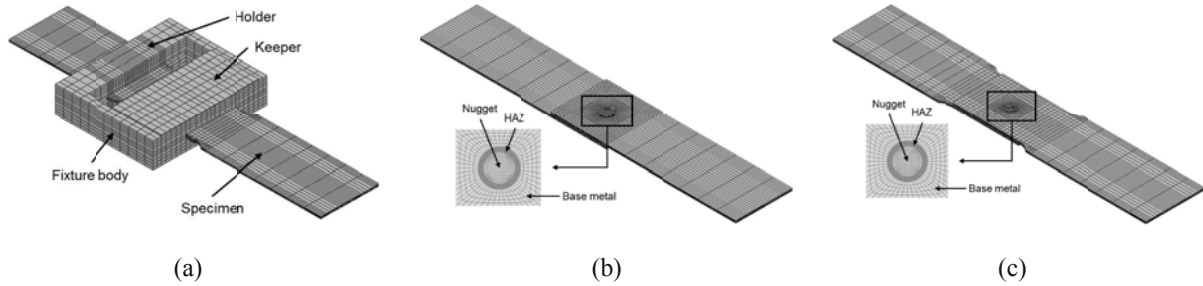


Fig. 3 Finite element model for the analysis of the proposed fixture and the specimen: (a) assembled testing fixture with the specimen; (b) lap-shear test specimen; (c) proposed pure-shear test specimen.

test specimen as shown Fig. 2. In order to concentrate the plastic deformation around a spot weld, the width of the spot-welded region is designed smaller than other.

Finite element analyses of the proposed fixture and the specimen were carried out to examine the loading histories and confirm the main purposes of those. In order to investigate the rotation angle of a spot weld and the plastic deformation of a specimen, finite element analyses results are compared with the cases of using the lap-shear shape specimen and the proposed pure-shear test specimen. The proposed fixture is described as a simplified finite element model, and the specimen is discretized as a full model as shown in Fig. 3. Refined finite element models are utilized to describe the shape of the nugget and the heat-affected zone (HAZ) to maintain reasonable aspect ratios of the three-dimensional brick elements. The material used for the specimen was an advanced high strength steel of TRIP590 with a thickness of 1.2 mm. The flow stress of the steel sheet is expressed as $\bar{\sigma} = 1151.1(0.0147 + \bar{\epsilon})^{0.287}$ MPa whose value is obtained from tensile tests performed following Huh *et al.* experiment procedure [13]. The shape of the nugget is assumed to be cylinder with the diameter of 5.8 mm and the shape of the HAZ is assumed to be hollow cylinder with the thickness of 1.0 mm. Those dimensions are determined from the failed specimen. The material properties of the welded nugget and the HAZ are estimated using the determination method of Ha *et al.* [14] and the hardness distribution method originally proposed by Zuniga and Sheppard [15]. Kinematic constraints are imposed on the nodes around the holder of the fixture and the specimen in order to describe the clamping condition between two components. Contact condition is imposed on the surface around the keeper of the fixture, the fixture body and the specimen in order to describe the sliding behavior between two components. The upper part of the specimen is fixed and a displacement boundary condition is imposed on the lower part of the specimen. Finite element analyses were carried out using the commercial implicit code Abaqus/Standard [16].

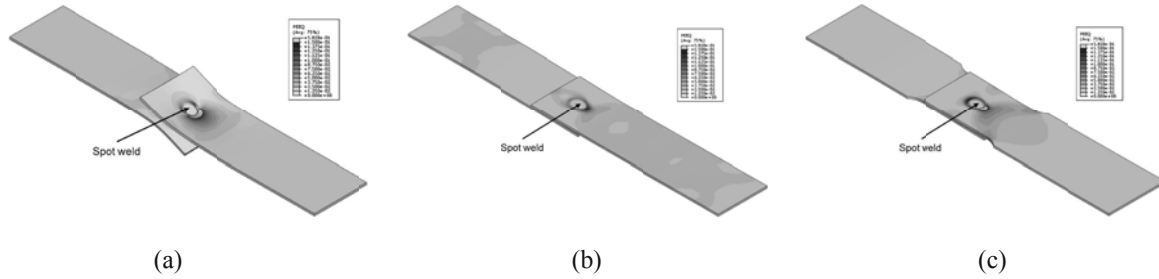


Fig. 4 Numerical results with respect to the testing method to obtain the pure-shear failure load: (a) only lap-shear test; (b) pure-shear test attaching the proposed fixture on the lap-shear test specimen; (c) pure-shear test attaching the proposed fixture on the proposed specimen.

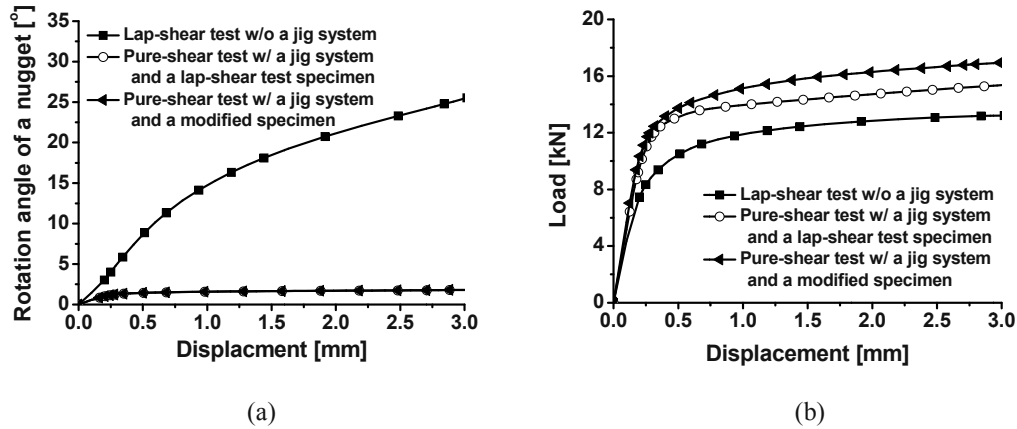


Fig. 5 Rotation angle of a nugget and load-displacement curve with respect to the testing method to obtain the pure-shear failure load: (a) rotation angle of a nugget; (b) load-displacement curve.

Fig. 4 shows the deformed shape of the specimens with respect to the testing method to obtain pure-shear failure load of a spot weld. It is impossible to obtain the pure-shear failure load using only lap-shear test specimen due to the rotation of a nugget during failure test. If pure-shear test is carried out using the proposed fixture attaching on the lap-shear test specimen or the proposed pure-shear test specimen, it is possible to prevent the rotation of a nugget during the failure test. The rotation angle of a nugget and the reaction force acting on the spot weld are plotted in Fig. 5. The rotation angles of a nugget with respect to the testing method without or with the proposed fixture for the pure-shear test are about 25° and 2° as shown in Fig. 5(a), respectively. Therefore, the testing fixture for the pure-shear test is more effective to prevent the rotation of a nugget. However, even if the testing fixture is used for the pure-shear test, the reaction force acting on the spot weld is measured differently as shown in Fig. 5(b). This difference of the reaction force is deduced from the type of the specimen for the failure test. When the lap-shape test specimen is used for the test, plastic deformation occurs all of specimen as shown in Fig. 4(b) because the width of the specimen is the same. However, when the modified specimen is used for the test, plastic deformation is concentrated around the spot weld as shown in Fig. 4(c) because the width of the spot-welded region is smaller than other part. Therefore, the reaction force of the modified specimen is higher than the other's one.

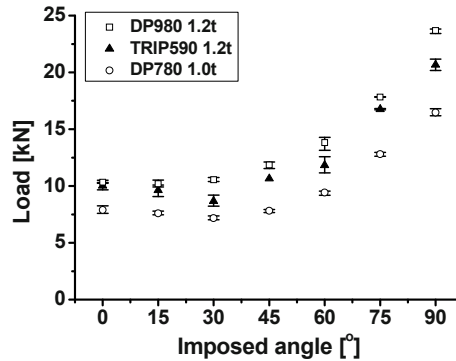
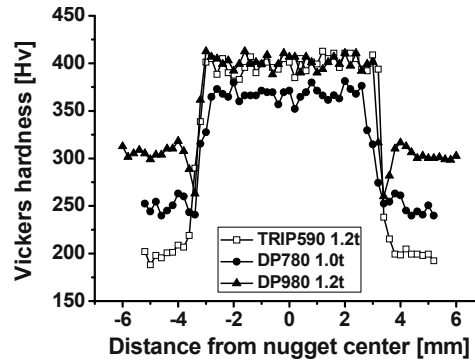
FAILURE TESTING CONDITIONS AND EXPERIMENTAL RESULTS

Spot welds in TRIP590 1.2t, DP780 1.0t and DP980 1.2t are considered to obtain the failure loads of spot welds in this paper. These materials are selected to construct the failure contour of a spot weld of AHSS. Spot welding was performed using a static spot/projection welding machine. The welding schedules shown in Table 1 were determined after several U-tension tests with the aid of industry standards to guarantee a nugget diameter of about $5\sqrt{t}$ and a button-type failure.

Using the fixtures and specimen proposed by Song *et al.* [1], failure tests of the spot weld were conducted at six different loading angles of 0°, 15°, 30°, 45°, 60° and 75°. And the pure-shear test at loading angle of 90° was carried out using the proposed fixture and specimen in this paper. Failure tests were conducted using an INSTRON 4206 device with a cross-head speed of 3.0 mm/min until the spot weld failed and the specimen separated into two components. The load and the

Table 1. Welding schedule of steel sheets tested

Material	Squeeze Time [cycles, 1/60 sec]	Weld Time [cycles]	Hold Time [cycles]	Current [kA]		Force [kN]
				Base metal	Base metal & guide plate	
TRIP590 1.2t	20	17	17	7.0	7.8	4.0
DP780 1.0t	18	13	13	6.8	7.8	3.5
DP980 1.2t	20	17	17	7.4	8.2	4.0

**Fig. 6** Average maximum loads of spot-welded specimens at various loading angles.**Fig. 7** Vickers hardness distributions of a spot weld in each material.

displacement were measured simultaneously during each test. The load was measured with the load cell in the testing machine and the displacement was calculated from the relative movement of the two pull bars. With these testing conditions, failure tests were carried out at seven different loading angles to investigate the failure load and the failure behavior of the spot-welded specimen. Failure tests were carried out up to five times at each loading angle, and then reproducible three data of those were used for constructing the failure model of a spot weld. Fig. 6 shows the average maximum loads obtained from the failure tests with the different loading angles. In case of TRIP590 1.2t, it was difficult to obtain the reproducible experiment data because the failure of a spot weld was easily initiated at the nugget.

The maximum load decreases a little as the loading angle increases when the loading angle is less than 30°, whereas the maximum load increases dramatically as the loading angle increases at the interval from 45° to 90° as shown in Fig. 6. The maximum load of TRIP590 1.2t and DP980 1.2t is similar to each other at the loading angle of 0°. Generally, a spot weld is failed in the interface between the HAZ and the base metal. Therefore, the failure loads is determined by the strength of a base metal. However, the spot weld of AHSS is failed at the HAZ or the nugget easily because of the HAZ softening phenomenon and the increased brittleness of a nugget. When the Vickers hardness was measured after a spot weld of TRIP590 1.2t, DP780 1.0t and DP980 1.2t, the HAZ softening phenomenon was found in the spot weld of DP780 1.0t and DP980 1.2t as shown in Fig. 7. Therefore, the initial crack of a spot weld of AHSS is generated at the HAZ. The maximum

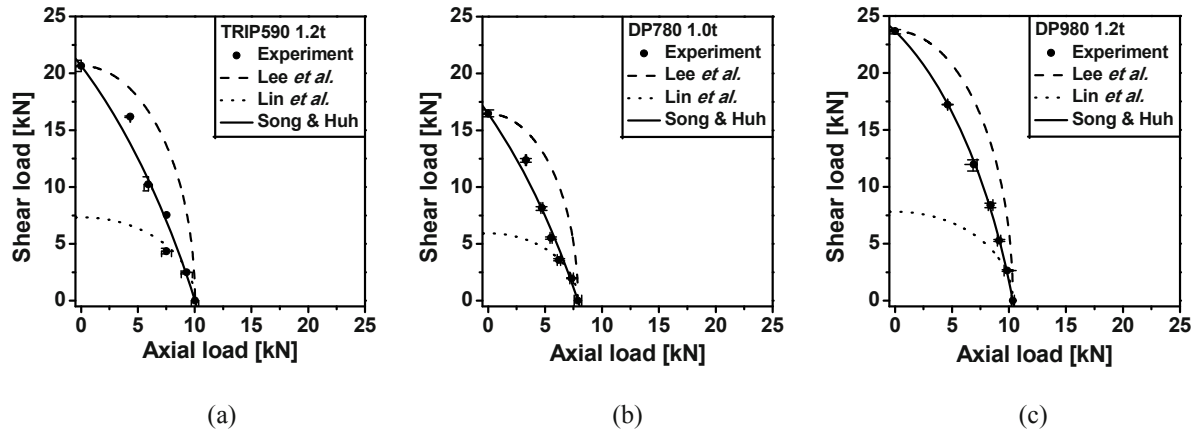


Fig. 8 Failure contours and interpolation of those of spot welds using Song and Huh's failure model: (a) TRIP590 1.2t; (b) DP780 1.0t; (c) DP980 1.2t.

Table 2. Coefficients of the Song and Huh's failure model of a spot weld

Material	Axial load (F_N) [kN]	Shear load (F_S) [kN]	Failure parameter (β)
TRIP590 1.2t	10.04	21.41	1.52
DP780 1.0t	7.87	16.92	1.46
DP980 1.2t	10.41	23.70	0.88

load of TRIP590 1.2t, DP780 1.2t and DP980 1.2t is determined by the strength of a base metal at the loading angle of 90° due to failed at the base metal.

FAILURE CRITERION OF A SPOT WELD OF AHSS UNDER COMBINED LOADING CONDITIONS

In order to examine the failure load of a spot weld under combined axial and shear loads, the maximum loads measured in the experiment were decomposed into the two components along the axial and shear directions. Decomposed axial and shear loads are plotted in the force domain as shown in Fig. 8, which shows that a typical failure criterion can be constructed in terms of the axial and shear load to describe the failure contour obtained in the experiment. Failure contours from the tests were interpolated with a failure criterion. The coefficients that constitute the failure model shown in Table 2 are obtained using the least square method to minimize the discrepancy between the experimental data and interpolated one. Fig. 8 shows the comparison among the proposed failure model and the conventional models by Lee *et al.* [7] and Lin *et al.* [12] as well as the experimental results. The comparison indicates that the conventional failure criterions are inadequate to describe the failure load of a spot weld under combined loading conditions. On the other hand, the Song & Huh's failure criterion with the value of β in Table 2 provides a relatively good description of the failure contour obtained from the experiment since the axial load and shear failure load are coupled in a bi-linear form with the failure parameter β . The failure models of a spot weld in SPCUD 1.0t, SPRC340R 1.2t and DP590 1.0t were interpolated with the β value of 1.42, 1.35 and 1.57, respectively [2]. Therefore, the value of a failure parameter β could be approximated as 1.45 for a spot weld in SPCUD 1.0t, SPRC340R 1.2t and DP590 1.0t. The β values of TRIP590 1.2t and DP780 1.0t are similar to their experiment result. But the β value of DP980 1.2t is smaller than others because the failure load of the spot weld of DP980 1.2t is smaller than expectation at the loading angle of 0° . There is a transition point of a failure parameter β between DP780 and DP980. The failure characteristics and the failure contours of a spot weld of AHSS are different from mild steel and HSS because of the high carbon containing.

CONCLUSION

This paper investigates the failure characteristics and the failure criterion of a spot weld of AHSS and determines the coefficients of the Song & Huh's failure model. In order to acquire the correct failure load under the pure-shear loading condition with a spot weld fabricated by the same welding condition between two sheets, test fixtures and a specimen were newly designed and prepared with the information from finite element analyses at the loading angle of 90° . The apparatus

proposed prevents both the rotation of a spot weld and the plastic deformation of a specimen at some distance from a spot weld during the failure test at the loading angle of 90°. The tests are also carried out at the loading angle ranging from 0° and 90°. From the experimental data, failure criterion has been constructed for AHSS to describe the failure behavior of spot welds for numerical simulation of car crashes. According to the Song & Huh, the value of β -norm is confined to a certain value from 1.4 to 1.6. The value of β for DP980 1.2t is, however, determined as much lower value of 0.88. This phenomenon can be explained with different failure behavior which shows lower failure load under the axial loading condition, as well as high carbon contents which results in a brittle at the weldment after welding.

REFERENCE

- [1] J.H. Song, H. Huh, J.H. Lim and S.H. Park, "Effect of tensile speed on the failure load of a spot weld under combined loading conditions", *International Journal of Modern Physics B*, Vol. 22, pp. 4169–1474, 2008.
- [2] J.H. Song and H. Huh, "Failure characterization of a spot weld under combined axial–shear loading conditions", *International Journal of Materials Sciences*, Submitted for publication.
- [3] M. van Schaik, D.C. Martin and S. Denner, "ULSAB Advanced Vehicle Concepts – The Latest Steel Demonstration for Automotive", SAE 2000-01-1545, 2000.
- [4] K. Sato, A. Yoshitake, Y. Hosoya and H. Mikami, "FEM Simulation to Estimate Crashworthiness of Automotive", SAE 982356, 1998.
- [5] T. Inoue and E. Nakanishi, "A Crash Simulation Analysis which Consider the SPOTWELD Rupture", *JSAE*, No. 88-00, pp. 5–7, 2000.
- [6] H. Zhang and J. Senkara, "Resistance welding–fundamentals and application", CRC press, Florida, 2006.
- [7] Y.L. Lee, T.J. Wehner, M.W. Lu, T.W. Morrisett and E. Pakalns "Ultimate strength of resistance spot welds subjected to combined tension and shear", *Journal of Testing and Evaluation*, Vol. 26, No. 3, pp. 213–219, 1998.
- [8] M.E. Barkey and H. Kang, "Testing of spot welded coupons in combined tension and shear", *Experimental Techniques*, Vol. 23, No. 5, pp. 20–22, 1999.
- [9] C. Madasamy, T. Tyan, O. Faruque and P. Wung, "Methodology for testing of spot-welded steel connections under static and impact loadings", SAE 2003-01-0608, 2003.
- [10] B. Langrand and A. Combescure, "Non-linear and failure behavior of spotwelds: a "global" finite element and experiments in pure and mixed modes I/II", *International Journal of Solids and Structures*, Vol. 41, pp. 6631–6646, 2004.
- [11] S.-H. Lin, J. Pan, S.-R. Wu, T. Tyan and P. Wung, "Failure loads of spot welds under combined opening and shear static loading conditions", *International Journal of Solids and Structures*, Vol. 39, pp. 19–39, 2002.
- [12] S. -H. Lin, J. Pan, T. Tyan and P. Prasad, "A general failure criterion for spot welds under combined loading conditions", *International Journal of Solids and Structures*, Vol. 40, No. 21, pp. 5539–5564, 2003.
- [13] H. Huh, J. H. Lim and S. H. Park, "High speed tensile test of steel sheets for the stress-strain curve at the intermediate strain rate", *International Journal of Automotive Technology*, Vol. 10, No. 2, pp. 195-204, 2009.
- [14] J.W. Ha, J.H. Song, H. Huh, J.H. Lin and S.H. Park, "Dynamic material properties of the heat-affected zone (HAZ) in resistance spot welding", *International Journal of Modern Physics B*, Vol.22, No.31/32, pp.5800~5806, 2008.
- [15] S. Zuniga and S.D. Sheppard, "Resistance spot weld failure loads and modes in overload conditions", *ASTM STP 1296*, pp. 469–489, 1997.
- [16] AbaqusTM, 2007. User's manual-Vers.6.7. Hibbitt, Karlsson & Sorensen, Pawtucket, RI, USA.

Characterization of Adaptive Reinforced Concrete Structures

Kirk R. Biszick
Director of Engineering
Optechnology, Inc.
5000 Allendale Drive
Huntsville, AL 35811

John A. Gilbert
Professor of Mechanical Engineering
Department of Mechanical and Aerospace Engineering
University of Alabama in Huntsville
Huntsville, AL 35899

Houssam Toutanji
Professor of Civil Engineering
Department of Civil and Environmental Engineering
University of Alabama in Huntsville
Huntsville, AL 35899

Thomas Lavin
President
Soems, Inc.
Watchung, NJ 07069

Michael T. Britz
Department of Mechanical and Aerospace Engineering
University of Alabama in Huntsville
Huntsville, Alabama 35899

Ravi K. Bommu
Department of Mechanical and Aerospace Engineering
University of Alabama in Huntsville
Huntsville, Alabama 35899

ABSTRACT

This paper discusses the research, development, and design considerations used to produce a Structural Information System (SIS) capable of characterizing the behavior of an adaptive reinforced concrete structure designed to withstand reverse loadings. The SIS consists of a collection of surface mounted and embedded sensors connected to a portable computer. The composite structure is reinforced with hollow carbon fiber tendons equipped with embedded strain gages and the work includes theoretical arguments, polymer concrete mix design, concrete testing, reinforcement selection and placement, sensor selection and placement, and structural testing and analysis. The primary objective is to insure that the stress in the materials remains within the elastic range so that damage does not occur. A finite element model is developed to accurately

characterize the structural response in the elastic range and a hybrid approach is suggested in which displacement, strain, and stress can be obtained with a rudimentary SIS consisting of a single embedded sensor. The ability to characterize failure, once it occurs, is also demonstrated by analyzing data obtained from displacement-controlled tests. Results indicate that splices in the tendons and slippage between the tendons and the concrete help to prevent sudden failure and allow the structure to withstand relatively high service loads despite appreciable deformation.

INTRODUCTION

Today's common advanced composite materials are made of continuous fibers, either graphite or Kevlar®, suspended in a polymeric matrix, typically an epoxy of some type. The technology underlying these materials has been developed over the past sixty years and the materials have been widely used in numerous civil and aerospace applications primarily due to their high strength-to-weight and/or stiffness-to-weight ratio. While advances in such composite materials have been steady, there have been relatively few revolutionary changes of late. But the investigation and development of a new breed of cementitious composite materials with matrices based on a unique hybrid blend of inorganic and organic components has the potential to revolutionize structural design.

The designs associated with this technology are based on the strength and position of the materials in the composite section but the overall design strategy relies mainly on the large difference in stiffness between the constituents in the composite section to drive the internal stress from the matrix to the reinforcement [1]. Since it is possible to produce a cementitious matrix that is more flexible than the polymeric matrices currently used to construct most advanced composite materials, these so-called "STARS" (Strategically Tuned Absolutely Resilient Structures) offer structural and aerospace engineers more design flexibility.

The evolution of STARS began with the production of thin, lightweight, and structurally efficient panels capable of resisting stresses produced by reverse bending [2]. The study showed that a very efficient composite structure could be fabricated by placing a flexible polymer-enhanced cementitious matrix having a relatively low elastic modulus over two layers of a rigid steel wire mesh having a relatively high elastic modulus. Materials were placed symmetrically to form an "adaptive" section that reacted similarly when bending couples were reversed. Since the compressive strength of the cementitious material was less than its tensile strength [3], it was the modulus of elasticity and tensile strength of the cementitious matrix, as well as the bond strength between the matrix and the reinforcement, that impacted the design most.

A modified transform section theory was developed to determine the deflections and stresses in these highly compliant cementitious structures [4] and the method was applied to study graphite-reinforced composites. Multi-layered composite beams were analyzed by incorporating material properties established from standard tests and finite element modeling was used to verify results.

The work fueled another investigation that quantified the dynamic characteristics of laminated plates [5]. In this study, an analytical dynamic finite element model was developed to evaluate the natural frequencies and mode shapes for structures subjected to different boundary conditions. This model was subsequently applied to study the dynamic performance of a larger structure [6]. Numerical results compared favorably with experimental impact hammer test data. As a result, it was concluded that the classical laminated plate theory developed for composite materials could be applied to quantify the dynamic behavior of highly compliant composite structures made from cementitious materials.

Research performed on stiffer concretes showed that material deficiencies caused by impact could be overcome by introducing a stiff weave-like reinforcement [7], and tests were performed to characterize the impact properties of STARS [8,9]. Recent improvements were made in cementitious matrices by capitalizing on the atomic and molecular interaction that occurred between constituents [10-12].

Although research in this area has progressed, most of the investigators mentioned above relied on layers of continuous graphite fiber mesh to reinforce their sections. However, there is merit associated with embedding rebar, especially if it can be outfitted with sensors capable of monitoring the overall performance of the reinforced cementitious structure.

Many studies have been performed by placing strain gages directly on the surface of rebar. In these cases, the lead wires are typically wrapped around the rebar and fed to the measuring instrument. As such, the wires are embedded in the surrounding matrix making them susceptible to lead wire effects.

In recent studies, strain gages have been installed within hollow steel rebar and sister bars. The rebar is embedded directly

into the matrix for structural purposes while the sister bar is strapped to a reinforcing element [13]. Several bars can be joined by screwing them together.

Other vibrating wire sister bar strain meters have been used in concrete structures such as piles, diaphragm/slurry walls, bridge abutments, tunnel lining, dams, and foundations [14]. Gages have even been embedded within a membrane to monitor the effects associated with waterproofing roof systems of large buildings [15].

This paper discusses the research, development, and design considerations used to produce a Structural Information System (SIS) capable of characterizing the behavior of an adaptive reinforced concrete structure designed to withstand reverse loadings. The SIS consists of a collection of surface mounted and embedded sensors connected to a portable computer. The composite structure is reinforced with hollow carbon fiber tendons equipped with embedded strain gages and the work includes theoretical arguments, polymer concrete mix design, concrete testing, reinforcement selection and placement, sensor selection and placement, and structural testing and analysis.

REINFORCED CONCRETE BEAM DESIGN

As mentioned previously, the evolution of STARS included a transition from steel to graphite mesh. This was done primarily because graphite is ten times stronger and five times lighter than steel; graphite is also less susceptible to corrosion. Similarly, an alternative to producing instrumented steel rebar is to manufacture discrete instrumented hollow carbon fiber reinforced polymer (CFRP) tendons that have strain gages mounted within them. But, before these structural elements could be embedded within a cementitious matrix to form an adaptive structure, it was necessary to characterize their material properties and structural response [16,17].

The design of the reinforced concrete beams used to demonstrate the SIS began with determining their dimensions. In order to comply with ASTM C78/C78M-10 [18], the standard for determining flexural strength of concrete in third-point loading, the height and width of the beam were made 8.9 cm. The total length of the reinforced concrete section was established at 53.3 cm. This allowed a third-point test to be conducted over a 45.72 cm long span comprised of three equally distant sections that were 15.24 cm long. The central span constitutes the constant moment section of the beam where measurements were taken.

As illustrated in Fig. 1, an adaptive section was constructed by placing two instrumented tendons symmetrically in the section. The carbon tendons had an inner diameter of 1.59 cm and a wall thickness equal to 1.02 mm.

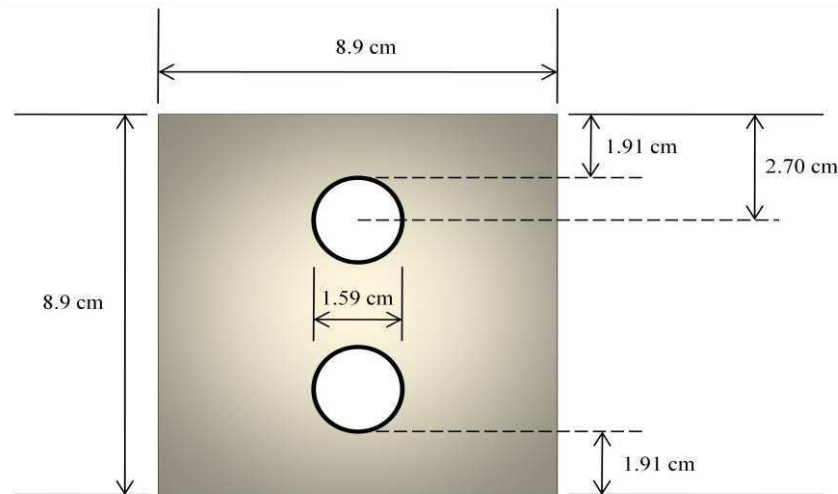


Fig. 1 Typical cross section of the reinforced concrete beam

Each reinforcing element consisted of two equal length tendons sections spliced together at center span in order to facilitate strain gage placement. The 5.08 cm long splice had an inner diameter of 1.4 cm and an outer diameter of 1.54 cm.

A strain gage was placed on the inner surface of each reinforcing element adjacent to the splice before the sections were joined. The elements were rotated so that these gages were located at the furthest distance from the centroid of the beam.

The tendons were suspended within a wooden mold and the concrete mix, described in Table 1, was placed over them. After the beams had cured, strain gages were placed at mid span on the upper and lower surfaces of the beam.

Table 1 Acrylic SBR mix table

	SBR mix	Proportion
Cement	10.08 kg	710.1 kg/m ³
B-79	3.84 kg	270.5 kg/m ³
Metakaolin	0.6 kg	42.27 kg/m ³
Water	0.36 kg	25.36 kg/m ³
Sika	0.12 kg	8.45 kg/m ³
Acrylic SBR latex	4.8 kg	338.1 kg/m ³

TEST SETUP

Figure 2 shows a photograph of the test apparatus. The upper roller extensions were placed 15.24 cm apart, and the lower roller extensions were placed 45.7 cm apart. The strain gage wires from the gages placed within the tendons and on the free surfaces of the beam were inserted into separate channels of a data acquisition system. Wires from two linear variable differential transformers (LVDT's) were also inserted into separate channels to ascertain the central deflection of the beam but the deflection of the crosshead was ultimately used to establish this parameter.

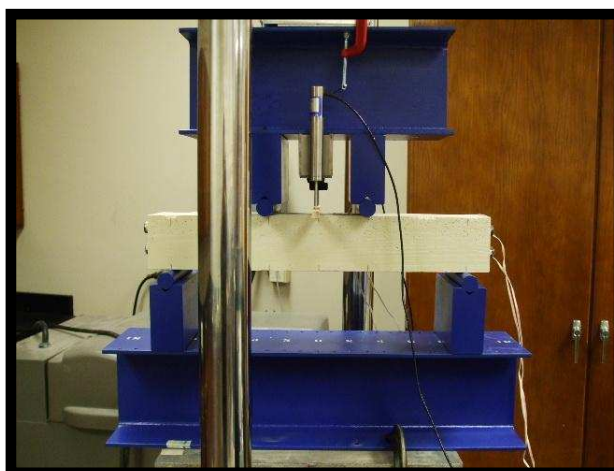


Fig. 2 Beam situated within test apparatus

During the tests, the bottom of the platen moved upwards. Displacement control was used to apply load to the beam at a rate of 1.27 mm/min. Wires from a load cell, located directly above the upper platen, were also fed into the data acquisition system.

RESULTS AND DISCUSSION

A total of four beams were tested. Figure 3 shows plots corresponding to strain vs. deflection data taken from the strain gages placed within the tendons in beam 1; a load vs. deflection plot is superimposed. Note that the ordinate values correspond to both strain ($\mu\epsilon$) and load (N). Since the test was conducted in a deflection controlled manner, the abscissa reflects the time expended during the test. In this case, the duration was 12 minutes (15.14 mm/1.27 mm/min).

Figure 4, on the other hand, shows plots corresponding to strain vs. deflection data taken from the strain gages mounted on

the upper and lower surfaces of beam 1; the load vs. deflection plot is also superimposed.

In this case, the beam remained intact until a crack developed in the central span at the lower surface of the beam. The first crack occurred when the load reached 11.64 kN. The crack is detected by the gages and can be seen as jump discontinuities in the load and strain plots for both the tendons (see Fig. 3) and the surface mounted gages (see Fig. 4).

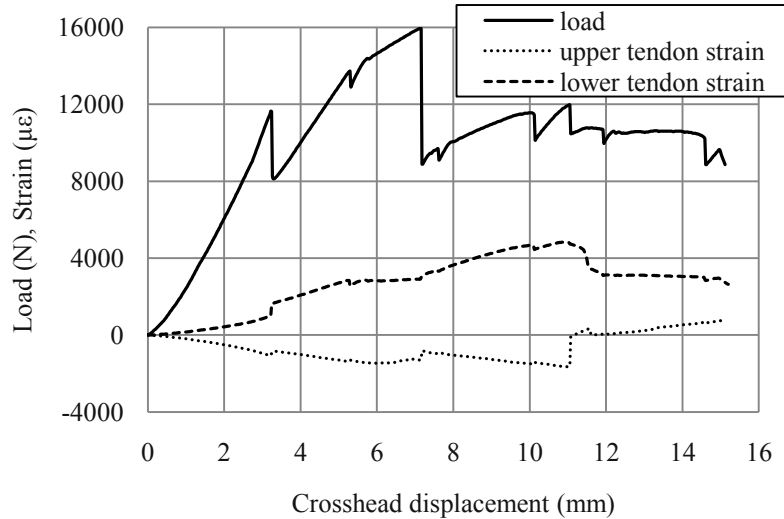


Fig. 3 Beam 1 load and tendon strain plotted as a function of crosshead displacement

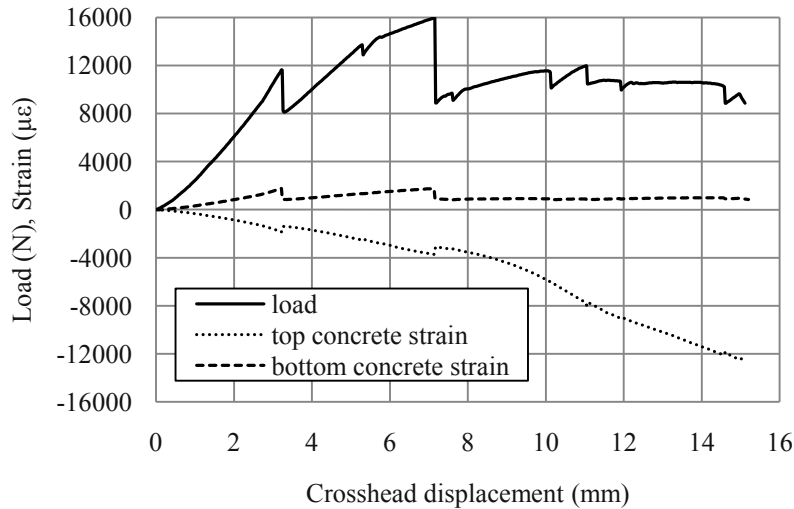


Fig. 4 Beam 1 load and concrete strain plotted as a function of crosshead displacement

Prior to cracking, the strains increase monotonically and fairly linearly with load. The strains in the upper tendon and top gage are compressive while those in the lower tendon and bottom gage are tensile. The magnitudes of the strains in the tendons are nearly equal; the same holds true for the magnitudes of the strains measured on the surface. Up until this point, the material behavior can be construed as linearly elastic.

Referring to the plots shown in Figs. 3 and 4, immediately after the first crack occurred, the load dropped from 11.64 kN to 8.12 kN. The strain in the upper tendon decreased slightly from $-1074\mu\epsilon$ to $-851\mu\epsilon$, whereas that in the lower tendon significantly increased from $1004\mu\epsilon$ to $1646\mu\epsilon$. At the same time, the strains on the upper and lower surfaces both decreased, slightly more on the lower surface.

The distinct shape changes which occurred in the strain plots reflected the stress transfer from the weakened concrete, located

in the tension zone, to the lower tendon. When this happened, the neutral axis of the beam moved upward toward the top of the beam but remained below the inside top portion of the upper tendon where the strain gage was located.

Remarkably, once this stress transfer occurred, the load continued to increase significantly to a peak value of 15.94 kN, at which point a second crack was observed. This crack occurred in the central span on the right side about 2.54 cm inside the right upper roller. The second crack extended up to the top of the upper tendon, and as time went on, propagated lengthwise toward the center of the beam.

During the time between the occurrences of the first and second cracks, the magnitudes of the strains in the tendons and on the surfaces increased, except for a slight glitch observed approximately midway through the cycle. This anomaly was later attributed to slippage of the lower tendon within the concrete matrix.

Following the drop in load to 8.88 kN, created by the onset of the second crack, the load increased to 11.96 kN as the crack on the right side continually widened. During this time, the compressive strains in the upper and lower tendons increased; from $-823\mu\epsilon$ to $-1646\mu\epsilon$ and from $2901\mu\epsilon$ to $4825\mu\epsilon$, respectively.

At this point, the lower tendon began to fracture which resulted in a decrease in strain from $4825\mu\epsilon$ to $3096\mu\epsilon$. But the failure did not happen instantly; since the tendon continued to sustain a tensile strain. When the fracture occurred, the compressive strain in the upper tendon dropped from $-1646\mu\epsilon$ to $-112\mu\epsilon$ (compressive) before gradually changing to $321\mu\epsilon$ (tensile, and finally increasing to $795\mu\epsilon$ when the test was halted; after 12 minutes when the crosshead deflection was 15.24 mm. During this portion of the loading cycle, the strain on the bottom surface remains fairly constant at about $950\mu\epsilon$, since the central section was completely segmented. At the same time, the strain on the top surface became progressively higher and increased to $-12,380\mu\epsilon$ as the stresses were transferred to this region.

The change in sign of the strain that occurred in the upper tendon indicated that, when the lower tendon fractured, the neutral axis shifted even further towards the top of the beam, beyond the inside portion of the upper tendon where the gage was located. At this point, both tendons were in tension; albeit the lower tendon had already fractured. The minor glitches in the strain plots extracted from the tendons were later attributed to lateral movement (slippage) which occurred as the bonds between the tendons and the concrete matrix broke.

It is significant to note that the beam sustained a load only slightly less than that which corresponded to the first crack (11.64 kN) despite appreciable deformation and readily observable damage that was observed. This remarkable performance was attributed mainly to the symmetrical distribution of the tendons in the section and partly to the expansion joints created by placing the splices in them. The result was so unexpected that a decision was made to extend the duration of the next three tests to see how much deformation a beam could really take before it was readily apparent that it would collapse.

Figure 5 shows a superposition of load vs. deflection plots corresponding to the four beams tested.

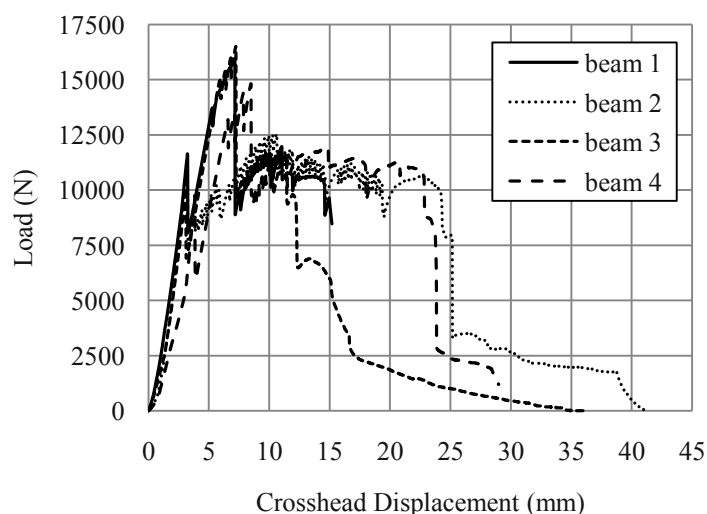


Fig. 5 Load vs. crosshead displacement of the four beams

It is readily apparent that these curves provide a measure of structural integrity as well as valuable clues regarding how damage took place and progressed. A similar conclusion can be reached regarding the output from the sensors in the structural information system. It is also apparent that the structural performance of these reinforced concrete beams is nearly the same up to the first crack but it may be very different after that. The discussions included below show that it is possible to produce a finite element model that accurately characterizes the structural behavior and, as a result, a structural information system containing a single sensor is all that is required to completely define the displacement, strain, and stress for every point in the structure.

FINITE ELEMENT ANALYSIS (FEA) OF REINFORCED CONCRETE BEAMS: CONCRETE

A finite element model was developed to quantify the structural behavior of the beams while they remained within the elastic range. The analysis was performed using NX Nastran and Patran 2010. The model was developed using FEMAP, imported into Patran, solved in Nastran, and then post processed in Patran. The beam section was made 45.7 cm long. It was simply supported on the bottom at both ends along the direction of the width. This corresponded to the position of the bottom rollers of the loading frame used to test the beams. In order for the model to successfully run, a single fixed point was required to be placed somewhere along the bottom roller. This was done at the center of the right roller for reasons of symmetry and convenience.

The finite element model utilized the material properties gleaned from the concrete tests and the tendon tests. For the concrete, modeled as an isotropic material, $E_c = 3.82$ GPa and $\nu = 0.255$. For the nominal portion of the fused tendon, $E_L = 98.6$ GPa, $E_T = 13.03$ GPa. For the fused portion of the same tendon, $E_L = 103.2$ GPa, $E_T = 20.9$ GPa. A Poisson's ratio of 0.27 was used for both portions of the fused tendon.

Since the model was developed in tandem with structural testing, deflections and strains are presented for a simulated load case of 11.12 kN. To simulate the loads placed at the upper rollers at the 15.24 cm center span, a 5.56 kN load was distributed along the width of the beam at the position of each of the rollers. These two loads when added together constitute the 11.12 kN load. This load case was selected because it approximated the load value to the first crack of the first two beams tested. Comparisons are made with test results by multiplying the analytical results by a scale factor of 0.953 that reflects the average load to the first crack for beams 1 through 4 which was 10.61 kN.

A linear elastic constitutive model was used, because it was assumed that the deflections occurred within the linear elastic range. The mesh element used to simulate the carbon fiber tube was a 2D quadrilateral shell (or plate) element called CQUAD4. The elements were assigned a thickness of 0.89 mm, corresponding to the thickness of the carbon fiber in the 1.59 cm diameter tube.

In the 5.08 cm long region of the fused piece, elements were assigned a thickness of 1.73 mm. This accounts for the thickness of the 0.89 mm tube plus that of the 0.84 mm splice. The rest of the fused tube was correctly aligned by assigning the material orientation $\langle 0, 1, 0 \rangle$, which aligned the tube with the local Y axis coordinate system.

The solid elements used for the concrete in the model were a solid hexagonal element called CHEXA8. Locations of node points of the concrete elements in the region of the tendons were joined with the nodes from the tendons so that the model would perform correctly.

Figure 6 shows a contour plot of the strain in the concrete beam. The beam model is oriented so that the strain on the top of the beam can be more easily identified. By inspecting the contour plot, the color of the top of the beam can be matched with the color key identifying the corresponding range of strain in the model. In the small region over which the gage was placed, strains range from $-1170\mu\epsilon$ to $-1910\mu\epsilon$.

In order to more precisely determine the strain in the top of the concrete, maximum and minimum ranges of the color key are modified during post-processing. In this case, $-1170\mu\epsilon$ to $-1910\mu\epsilon$ are inserted and results obtained. Then the process is repeated for a smaller range. This produces a rendition in which the contour plot is isolated to the upper surface of the beam between the load points (see Fig. 7). Based on the contour plot in Fig. 7, the strain at the very center of the span ranges from $-1795\mu\epsilon$ to $-1806\mu\epsilon$, with an average of $-1800.5\mu\epsilon$. This value is compared to the test results of the beams.

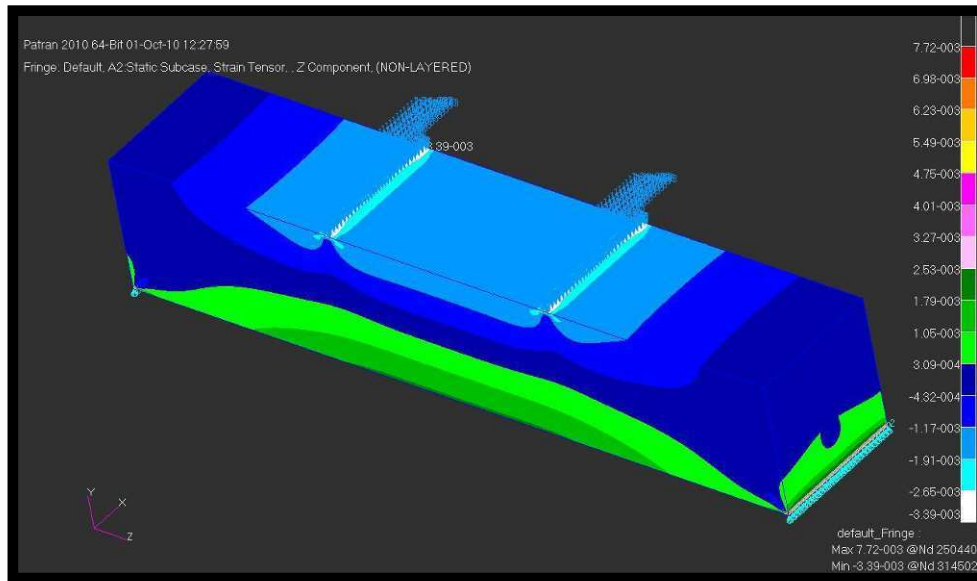


Fig. 6 Concrete strain, oriented to show strain on top

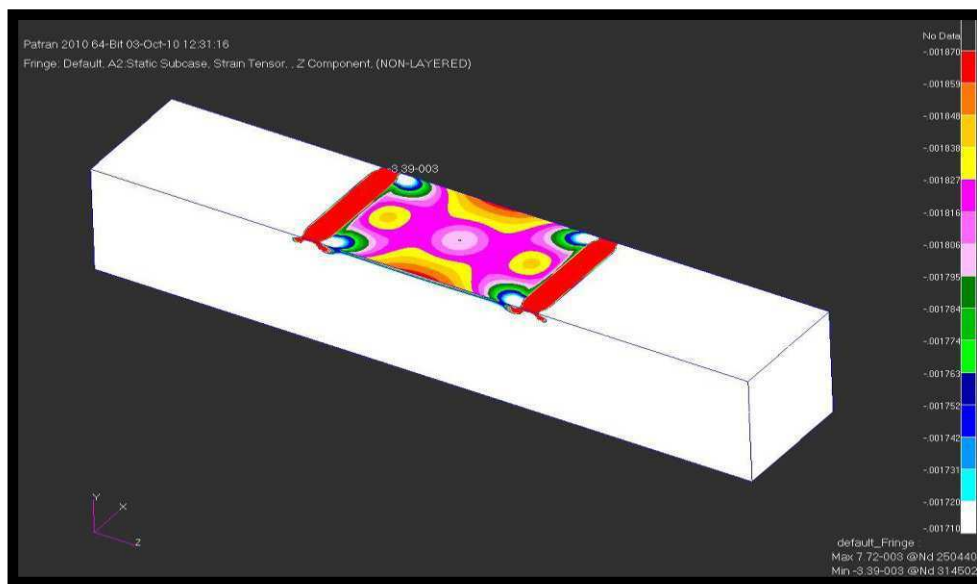


Fig. 7 Concrete strain on top, with strains isolated between the load points

FINITE ELEMENT ANALYSIS (FEA) OF REINFORCED CONCRETE BEAMS: TENDONS

Figure 8 shows a contour plot of the strain in the tendons. The beam model is oriented so that the strain on the top of the upper tendon can be more easily identified. By inspecting the contour plot, the color of the top of the tendon can be matched with the color key identifying the corresponding range of strain in the model. This shows the strain range in the top of the upper tendon in the region where the gage was placed. Those values range from $-900\mu\epsilon$ to $-1100\mu\epsilon$. The contour plot is of the maximum strains in the tendons, so the figure most accurately interprets the strains on the outside of the tendon. Note that the strain gage was placed on the inside of the tendon.

In order to more precisely determine the strain in the top of the upper tendon in the region where the strain gage was placed, maximum and minimum ranges of the color key are again modified during post-processing. In this case, $-550\mu\epsilon$ to $-1100\mu\epsilon$ are inserted and results obtained. This produces a picture where the contour plot is isolated to a portion of the upper surface of the tendon (see Fig. 9). The contour plot in Fig. 9 is of the inner strains in the tendons, so the figure most accurately interprets the strains on inside of the upper tendon. Based on the contour plot, the strain in the region of the upper gage

indicates the strain ranges between $-1063\mu\epsilon$ and $-1100\mu\epsilon$, with an average of $-1082\mu\epsilon$. This value is compared to the test results of the beams. Close inspection of the contour plots in Figs. 8 and 9 shows that there is a longitudinal strain gradient along the length of the tendon, highest in the region just beyond the center of the fuse piece.

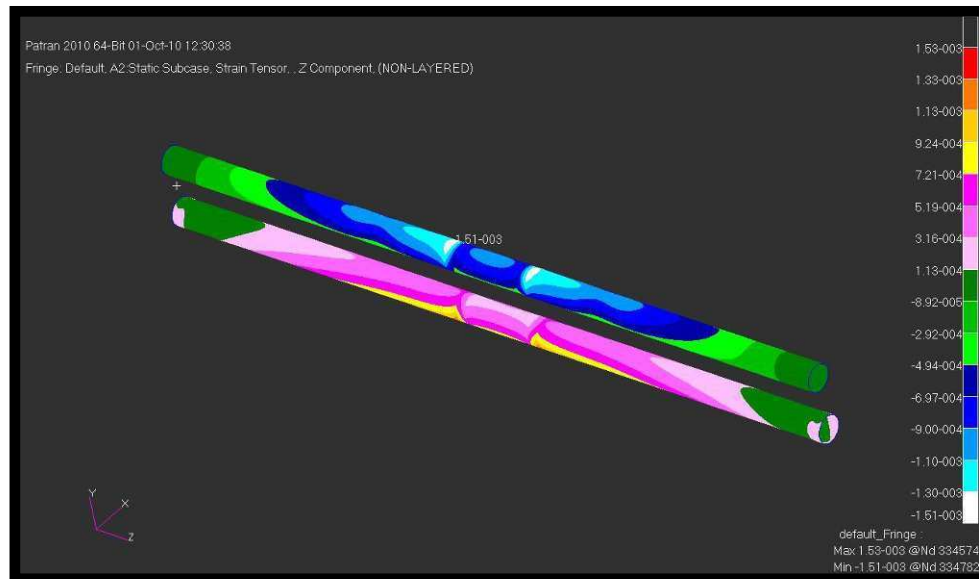


Fig. 8 Tendon strain, oriented to show outer strain in the top of the upper tendon

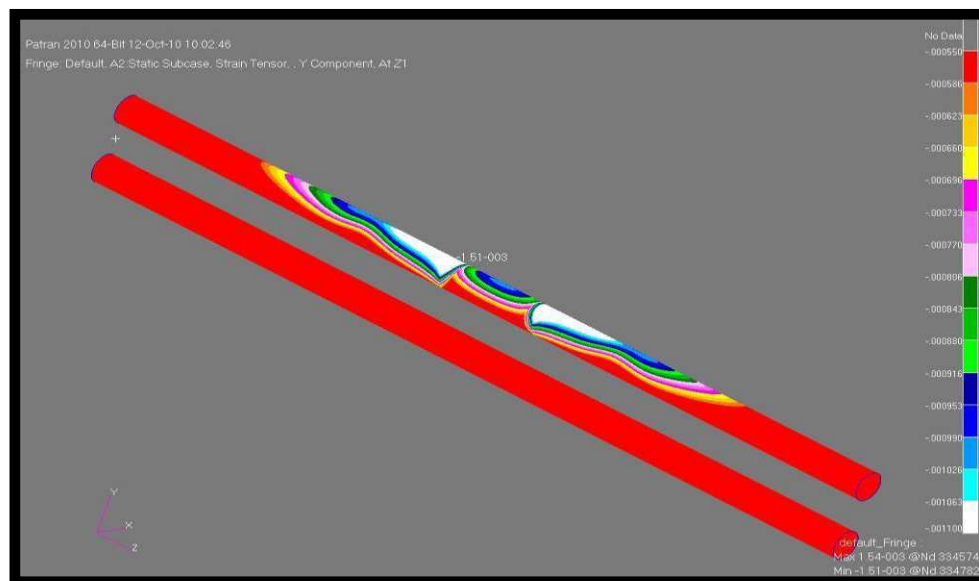


Fig. 9 Tendon strain, oriented to show inner strain isolated in the top of the upper tendon

COMPARISON OF FEM AND SIS RESULTS

The finite element model was designed to characterize the elastic behavior of the concrete reinforced beams. A comparison of the results of the four beams corresponding to the point at which the first crack occurred was performed to verify the model. The average load to the first crack for the beams was 10.61 kN. The finite element model was developed in tandem with structural testing; deflections and strains were presented for a simulated load case of 11.12 kN. Thus, comparisons can be made with the test results by multiplying the analytical results by a scale factor of 0.953.

Figure 10 shows plots corresponding to strain vs. deflection data taken from the strain gages placed within the upper and lower tendons, respectively. The results are presented for all four beams and only up to the point at which the first crack

occurred. The average value of the strain in the upper tendon is $-1011\mu\epsilon$, whereas the average value in the lower tendon is $871.5\mu\epsilon$. The strains predicted by the model on the inner surfaces (see Fig. 9) were equal to $-1082\mu\epsilon$ and $1135\mu\epsilon$, respectively. When multiplied by the scale factor, strains of $-1031\mu\epsilon$ and $1082\mu\epsilon$, respectively, are predicted. Assuming that the model is correct, the percentage errors are 1.9 and 19.5%, respectively.

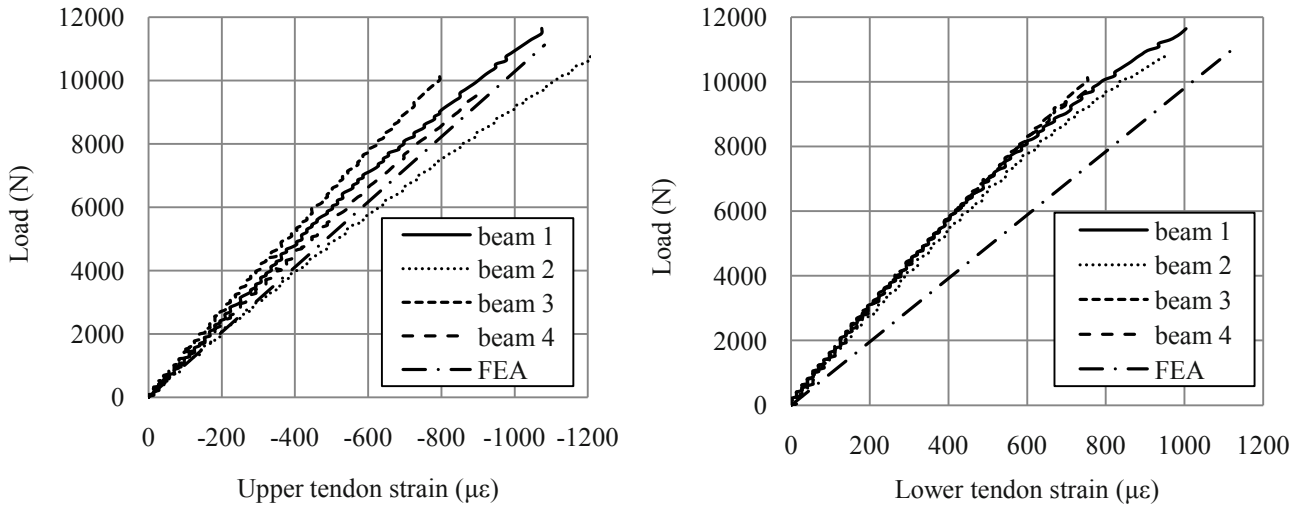


Fig. 10 Load vs. upper tendon strain (left) and lower tendon strain (right) in the four beams, to first crack

Figure 11 shows plots corresponding to strain vs. deflection data taken from the strain gages placed on the upper and lower surfaces, respectively. The results are presented for all four beams and only up to the point at which the first crack occurred. The average value of the strain on the upper surface is $-1537.5\mu\epsilon$, whereas the average value on the lower surface is $1736\mu\epsilon$. The strains predicted by the model on the upper and lower surfaces (see Fig. 7) were equal to $-1800.5\mu\epsilon$ and $1861\mu\epsilon$, respectively. When multiplied by the scale factor, strains of $-1716\mu\epsilon$ and $1774\mu\epsilon$, respectively, are predicted. Assuming that the model is correct, the percentage errors are 10.4 and 2.1%, respectively.

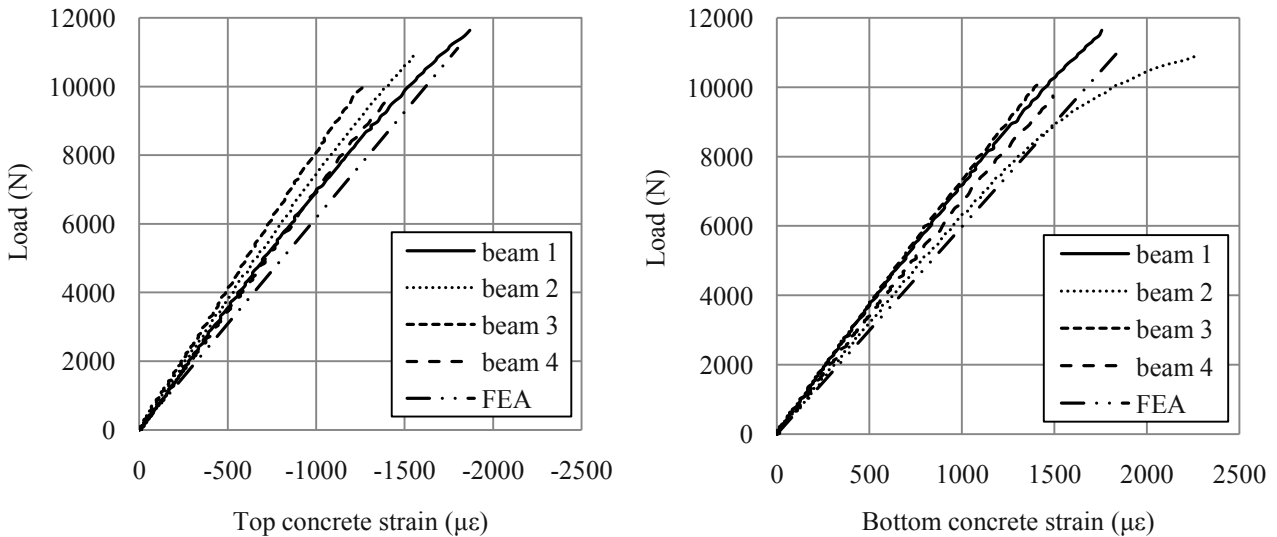


Fig. 11 Load vs. top concrete strain (left) and bottom concrete strain (right) in the four beams, to first crack

The average value of the tensile stress on the lower surface was 6.63 MPa. The tensile stress predicted by the model is 7.58 MPa. When multiplied by the scale factor, a tensile stress of 7.23 MPa is predicted. Assuming that the model is correct, the percentage errors are 10.4 and 2.1%, respectively.

Table 2 summarizes the load, strain, and stress to the first crack in the beams, and compares them to the results obtained from the FEA. Considering that there are deviations in the strain plots from beam to beam and that the strain response is somewhat non-linear just before the beams crack, the model predicted the structural behavior quite well. If the beams were placed more consistently, the model may have done even better.

Table 2 First crack summary of beams 1 through 4, with test results compared to FEA

	Beam 1	Beam 2	Beam 3	Beam 4	Beam average	FEA result
Load	11.64 kN	10.88 kN	10.12 kN	9.75 kN	10.60 kN	10.60 kN
Upper tendon strain	-1074 $\mu\epsilon$	-1255 $\mu\epsilon$	-795 $\mu\epsilon$	-920 $\mu\epsilon$	-1011 $\mu\epsilon$	-1031 $\mu\epsilon$
Lower tendon strain	1004 $\mu\epsilon$	976 $\mu\epsilon$	753 $\mu\epsilon$	753 $\mu\epsilon$	871.5 $\mu\epsilon$	1082 $\mu\epsilon$
Top concrete strain	-1869 $\mu\epsilon$	-1576 $\mu\epsilon$	-1269 $\mu\epsilon$	-1436 $\mu\epsilon$	-1537.5 $\mu\epsilon$	-1716 $\mu\epsilon$
Bottom concrete strain	1757 $\mu\epsilon$	2259 $\mu\epsilon$	1436 $\mu\epsilon$	1492 $\mu\epsilon$	1736 $\mu\epsilon$	1774 $\mu\epsilon$
Bottom concrete stress	6.72 MPa	8.63 MPa	5.49 MPa	5.70 MPa	6.63 MPa	7.23 MPa

There is also a possibility of tuning the model with the data extracted from the structural information system or making the model more sophisticated by incorporating an iterative procedure to account for things like changes in the elastic modulus with strain.

HYBRID ANALYSIS

Provided that an accurate model can be developed, it should be possible to monitor the strain at any location and by scaling the reading, predict the displacements, strains and stresses at every point in the structure. Although this approach is only valid while the structure is in the elastic range, it has the potential to change the way in which structural monitoring is currently performed and could significantly lessen the associated work and cost.

CONCLUSIONS

This paper showed that a structural information system can be developed to monitor an adaptive structure designed to resist reverse loadings. The primary objective was to insure that the stress in the materials remained within the elastic range so that damage did not occur.

A finite element model was developed to accurately characterize the structural response in the elastic range and a hybrid approach was suggested in which displacement, strain, and stress could be obtained with a rudimentary SIS consisting of a single embedded sensor.

The ability to characterize failure, once it occurred, was also demonstrated by analyzing data obtained from displacement-controlled tests. Results indicated that splices in the tendons and slippage between the tendons and the concrete helped to prevent sudden failure and allowed the structure to withstand relatively high service loads despite appreciable deformation.

ACKNOWLEDGMENTS

The authors would like to thank the United States Army Research, Development, and Engineering Center (AMRDEC) of the Research, Development, and Engineering Command (RDECOM) at Redstone Arsenal in Huntsville, Alabama, for supporting this research under the Department of Defense (DOD) Small Business Innovative Research (SBIR) Phase I, Phase I Option, and Phase II contract no. W31P4Q-05-C-R103. Portions of the work were also funded by the U.S. Department of Commerce under NOAA SBIR Phase I and Phase II contract no. WC133R-09-CN-0108. The authors would also like to thank Dr. Bo Xu for his contribution to the PVB concrete development and Mr. Rajesh Vuddandam for his contribution to beam testing with the data acquisition system. Any opinions, findings, conclusions or recommendations expressed in this publication are those of the authors and do not necessarily reflect the views of the funding agencies previously mentioned.

REFERENCES

- [1] Biszick, K.R., Toutanji, H.A., Gilbert, J.A., Marotta, S.A., Ooi, T.K., "Evolution of strategically tuned absolutely resilient structures (STARS)," Proc. of SEM Annual Conference & Exposition on Experimental and Applied Mechanics, Saint Louis, Missouri, Paper No. 32, 7 pages, 2006.
- [2] Biszick, K.R., Gilbert, J.A., "Designing thin-walled, reinforced concrete panels for reverse bending," Proc. of the SEM Spring Conference on Theoretical, Experimental and Computational Mechanics, Cincinnati, Ohio, pp. 431 - 434, 1999.
- [3] Brara, A., Klepaczko, J.R., "Experimental characterization of concrete in dynamic tension," CNERIB, Algeria and Laboratory of Physics and Mechanics of Materials, Ile de Saulcy, France, 2005.
- [4] Vaughan, R.E., Gilbert, J.A., "Analysis of graphite reinforced cementitious composites," Proc. of the SEM Annual Conference and Exposition, Portland, Oregon, pp. 532-535, 2001.
- [5] Ooi, T.K., Gilbert, J.A., Bower, M.V., Vaughan, R.E., Engberg, R.C., "Modal analysis of lightweight graphite reinforced silica/polymer matrix composite plates," Experimental Mechanics, 45(3), pp. 1-5, 2005.
- [6] Ooi, T.K., Engberg, R.C., Gilbert, J.A., Vaughan, R.E., Bower, M.V. "Modal testing of a lightweight cementitious structure," Experimental Techniques, November/December, pp. 37-40, 2004.
- [7] Badr, A., Ashour, A.F., Platten, A.K., "Statistical variations in impact resistance of polypropylene fibre-reinforced concrete," International Journal of Impact Engineering, 32(11), pp. 1907-1920, 2006.
- [8] Binek, L.A., Gilbert, J.A., Ooi, T.K., Bower, M.V., Biszick, K.R., "Ballistic testing of STARS," Proc. of SEM Annual Conference & Exposition on Experimental and Applied Mechanics, Springfield, Massachusetts, Paper No. 196, 10 pages, 2007.
- [9] Xu, B., Toutanji, H., Gilbert, J.A., "Impact resistance of poly(vinyl alcohol) fiber reinforced high-performance organic aggregate cementitious material," Cement and Concrete Research, 40, pp. 347-351, 2010.
- [10] Lavin, T., Toutanji, H., Xu, B., Ooi, T.K., Biszick, K.R., Gilbert, J.A., "Matrix design for strategically tuned absolutely resilient structures (STARS)," Proc. of SEM XI International Congress on Experimental and Applied Mechanics, Orlando, Florida, Paper No. 71, 12 pages, 2008.
- [11] Toutanji, H., Xu, B., Gilbert, J.A., Lavin, T., "Properties of poly(vinyl alcohol) fiber reinforced high-performance organic aggregate cementitious material: converting brittle to plastic," Construction and Building Materials, 24(1), pp. 1-10, 2010.
- [12] Xu, B., Toutanji, H.A., Lavin, T., Gilbert, J.A., "Characterization of poly(vinyl alcohol) fiber reinforced organic aggregate cementitious materials," Polymers in Concrete, 666, pp. 73-83, 2011.
- [13] Instrumented rebar and sister bar, Model IRHP and IRCL, RockTest Limited company (Ltd.) Telemac subsidiary data sheet, Saint-Lambert, Quebec, Canada, available on the web at <http://www.roctest-group.com/sites/default/files/datasheets/products/IRHP-E50138-W.pdf>, pp. 1-2, 2005.
- [14] Encardio-rite: Excellence through ingenuity: Model EDS-12V vibrating wire sister bar strain meter product sheet, Encardio-rite Electronics, Lucknow, India, available on the web at: http://encardio.com/strain_gage.asp, pp. 1-2, 2008.
- [15] Sanchez, J., Andrade, C., Fulla, J., "Hydrothermal monitoring using embedded sensors of the actual roof system of the Prado Museum," Construction and Building Materials, 24(12), pp. 2579-2589, 2010.
- [16] Bommu, R.K., Development of instrumented tendons for embedment in a structural information system, Master's Thesis, Department of Mechanical and Aerospace Engineering, University of Alabama in Huntsville, 2010.
- [17] Biszick, K.R., Design of a Structural Information System (SIS) for Strategically Tuned Absolutely Resilient Structures (STARS), Ph.D. Dissertation, Department of Civil and Environmental Engineering, University of Alabama in Huntsville, 2010.
- [18] ASTM C78/C78M-10, Standard test method for flexural strength of concrete (using simple beam with third-point loading), technical committee document, American Society for Testing and Materials (ASTM) Committee C09.61, West Conshohocken, Pennsylvania, 2010.

Bulk Waves for the Nondestructive Inspection of Immersed Structures.

Elisabetta Pistone (Department of Civil and Environmental Engineering, University of Pittsburgh, 963L Benedum Hall, 3700 O'Hara Street, Pittsburgh, PA 15261).

Piervincenzo Rizzo*, Ph.D., Assistant Professor (Department of Civil and Environmental Engineering, University of Pittsburgh, 942 Benedum Hall, 3700 O'Hara Street, Pittsburgh, PA 15261 Tel: 412-624-9575; Fax: 412-624-0135; E-mail: pir3@pitt.edu).

Paul Werntges (Department of Civil and Environmental Engineering, University of Pittsburgh, 963L Benedum Hall, 3700 O'Hara Street, Pittsburgh, PA 15261).

* Contact author.

Abstract.

Laser-generated ultrasonic guided and bulk waves are increasingly considered for the nondestructive testing (NDT) and structural health monitoring of engineering systems. Methods based on the use of pulsed laser or continuum laser are ideal when a non-contact approach for the generation and detection of stress waves is desired.

This paper presents the initial progresses of an ongoing study where pulsed laser is used to generate stress waves in underwater structures. In particular, in this paper we show the results of few experiments where stress ultrasonic waves are generated in an aluminum block. Owing to the geometry of the specimen, ultrasonic bulk waves are generated and detected by means of either a dry or an immersion transducer. The study presented here aims at investigating the effect of certain water parameters on the ultrasonic energy propagating through the specimen. The results of three experiments are presented. In the first experiment the effect of water level on the signal-to-noise ratio of laser generated bulk waves was evaluated. Then, the effect of laser energy was studied. Finally, the effect of water temperature on the amplitude of the bulk waves was investigated. With the exception of the latter experiment, we used laser pulses at 1064 nm and 532 nm wavelengths.

1. Introduction.

Reliable and efficient nondestructive testing (NDT) techniques are needed to ensure the performance and the proper response of engineering systems, avoiding failures as well as keeping maintenance costs at a minimum. Among all the available methods, laser ultrasonic testing (LUT) have been used during the past two decades years to perform material characterization and to assess the integrity of structures. LUT involves the generation of mechanical waves through the focusing of a laser beam on the surface of the specimen under investigation [1]. Monchalin and Scruby demonstrated that a duration pulse in the order of few nanoseconds can excite a very broad frequency spectrum which is in the DC-20 MHz range [2, 3, 4]. Furthermore, LUT is extremely useful in all those NDT applications that require non-contact generation and detection of stress waves, easy scanning, accurate displacement calibration, broad- or narrow-band signal generation, wideband measurement, and applicability to curved surfaces [5].

Although the use of laser ultrasonic in dry surface application is known and widespread, and the investigation of liquid/solid interface waves with laser has been carried out by few researchers [6, 7, 8], very little attention has been given to the application of laser ultrasonic techniques for the NDT of immersed structures [9]. When laser travels through water, it is subjected to absorption which is dependent on the laser wavelength. Theisen-Kunde et al studied the effect of water temperature on water absorption in the 1920-1940 nm wavelength range [10]. Han et al successfully detected different types of laser-generated waves at liquid solid interface using the 532 nm wavelength [11].

In this paper, we present the results of three series of experiments. First, we studied the effect of water absorption on laser-generated bulk waves at 1064 nm and 532 nm wavelengths. Then, the effect of laser energy is investigated for both wavelengths. Finally, the effect of water temperature is studied for the 532 nm wavelength. For all the experiments, we used a Q-switched Nd:YAG pulsed-laser operating either at 1064 nm or at 532 nm to generate stress waves. The laser beam was focused on the surface of the specimen in order to deliver a point-source of one millimetre. In order to achieve this, we used a mirror and a plano-convex lens (PCX) with an effective focal length of 350 mm. In all the experiments, an aluminum block with dimension 255 x 150 x 50 mm was used. The longitudinal speed velocity was considered equal to 6.32 mm/ μ sec [1]. The time waveforms were digitized using an oscilloscope (LeCroy 44Xi 400 MHz) and post-processed using Matlab. The long-term scope of our research is to develop an innovative NDT technique based on laser ultrasound to assess the integrity of underwater structures.

1. Effect of water level

Figure 1 shows the set-up used to investigate the effect of water level on the signal-to-noise (SNR) of the laser-induced stress waves. In particular, a plastic pipe 50.8 mm in diameter was glued on the aluminum block and filled with water at a temperature of 22 °C. The water level was progressively raised from 12.7 mm to 203.2 mm at 12.7 mm increments. By means of the mirror and the PCX lens, the laser beam was delivered through the column of water on the surface of the aluminium block. An ultrasonic transducer (resonance frequency equal to 1 MHz) was attached on the opposite surface of the block to detect the bulk longitudinal waves generated by the laser pulses.

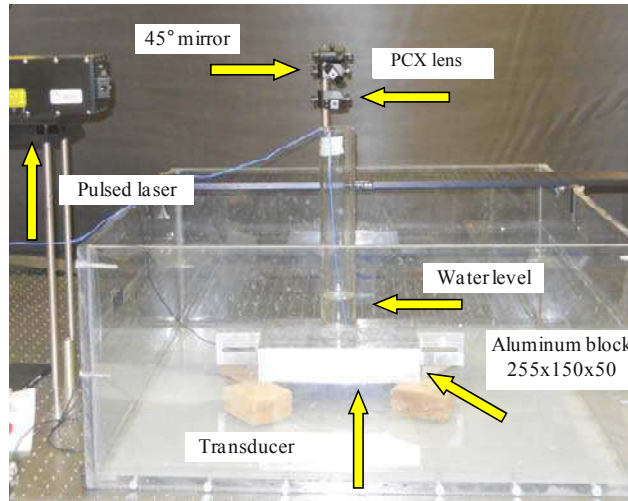


Fig. 1 Experimental set-up used in the water-level test. Photo of the laser, PCX lens, aluminum block and pipe filled with water

1.1 Effect of water level - Results.

We repeated five times all the measurements for each water level in order to assess the repeatability of the set-up. This procedure was used both for the case of the 1064 nm and for the case of the 532 nm wavelength. The correspondent level of energy was chosen for the two wavelengths in order to properly compare the results. In particular, we chose an energy level equal to 170 mJ.

Figure 2 shows two typical time waveforms detected at a water-level equal to 12.7 mm. In particular, figure 2a shows the time waveform excited with the 1064 nm wavelength and figure 2b shows the time waveform excited with the 532 nm wavelength. In both cases, the bulk longitudinal waves are perfectly detectable and their time of arrival is consistent with the expected one, i.e., 7.9 μ sec. The low frequency components that are visible in both time waveforms are still under investigation. Nevertheless, it was possible to detect and distinguish the arrival of the longitudinal waves with remarkable precision. The peak-to-peak amplitude of the longitudinal waves was extracted and plotted as a function of the water level. Fig. 3a shows that the amplitude of the longitudinal waves decays with a quasi-exponential behaviour in the case of the 1064

nm wavelength. By contrast, Fig. 3b shows that the amplitude of the longitudinal waves remains almost stable in the case of the 532 nm wavelength.

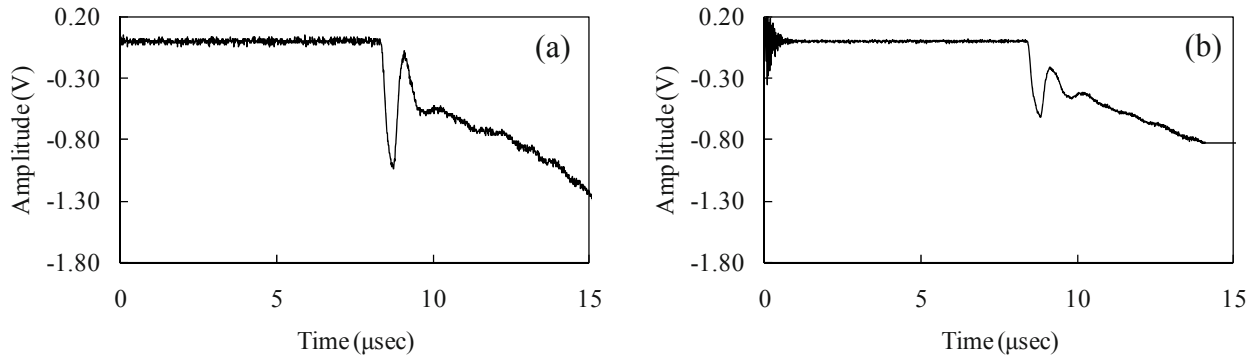


Fig. 2 Laser-generated time waveforms registered at 12.7 mm water level. (a) 1064 nm (b) 532 nm

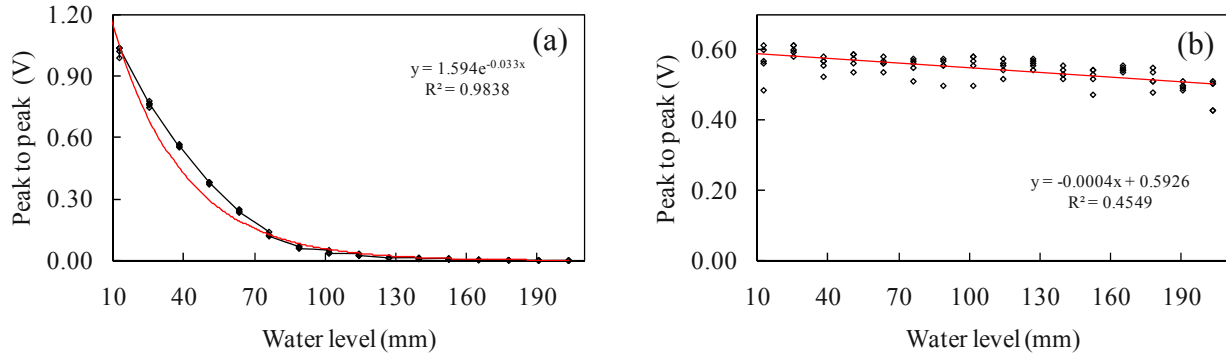


Fig. 3 Peak-to-peak amplitude as a function of the water level. Effect of the water level on the SNR of the laser-induced bulk waves. (a) 1064 nm and (b) 532 nm

In the first case, as the water level increases, the peak-to-peak amplitude of the bulk wave decreases almost exponentially. This is mainly explained by water absorption because at 1064 nm wavelength the optical absorption coefficient of water is approaching unity. However, a non perfect exponential decay suggests that other phenomena beside water absorption can occur at this wavelength. The plot also clearly shows a good repeatability of the test. In the second case, the water absorption has little effect on the propagation of the mechanical waves. In fact, the peak-to-peak amplitude is almost constant due to the fact that the optical absorption coefficient of water at 532 nm wavelength is very small. The graph shows that an amplitude-drop occurs, even though the decrease in amplitude is almost insignificant. This outcome can be positively exploited in the NDT of underwater structures. The plot also shows a significant repeatability of the results.

2. Effect of laser energy for a fixed water level

The same set-up described in the previous section was adopted to investigate the effect of laser energy on the peak-to-peak amplitude of laser-generated bulk waves. In this series of experiments, we fixed the water level and we tested the system with the 1064 nm wavelength and with the 532 nm wavelength. In fact, the level of the water column in the pipe was kept constant at 50.8 mm and the water was at a temperature of 22°C. We chose four values of laser energy for the 1064 nm wavelength and we adopted the correspondent energy level for the 532 nm wavelength in order to compare the results. In particular, the energy levels were equal to 160 J, 170 J, 180 J, 190 J. Figure 4 plots the energy level versus the peak-to-peak amplitude of the laser-generated bulk waves. Specifically, figure 4a presents the case of 1064 nm wavelength and figure 4b presents the case of 532 nm wavelength. In both tests a good repeatability was proven. The increase of amplitude is very small for the case of the 1064 nm wavelength. It is argued that the absorption of water plays a key role in this case. Even a

significant increase in the laser-energy level will not increase the amplitude of the signal detected. However, this will not happen in the case of the 532 nm wavelength.

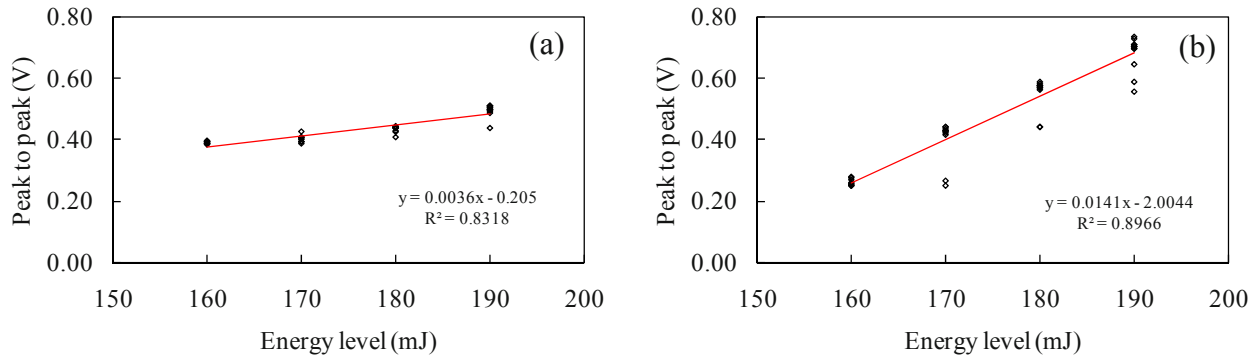


Fig. 4 Peak-to-peak as a function of the laser energy level. (a) 1064 nm and (b) 532 nm

In fact, it can be noticed that a significant increase in amplitude occurs as the energy intensity increases. This can be mainly explained with the fact that water absorption does not interfere with the propagation of bulk waves at 532 nm. Therefore, a higher laser energy level will result into higher peak-to-peak amplitude of the signal. It can also be noticed that at 160 mJ the amplitude for the 532 nm wavelength is smaller than the amplitude at the 1064 nm wavelength. However, as the energy level increases, the amplitude for the 532 nm increases significantly. In particular, at 190 mJ the amplitude at 532 nm is much larger than the amplitude at 1064 nm. Therefore, as the level of energy increases, the amplitude of the signal increases more for the 532 nm wavelength than for the 1064 nm wavelength. This can be particularly useful for the NDT investigation of underwater structures by means of laser ultrasound because the 532 nm wavelength can be suitable for this type of applications.

3. Effect of water temperature on bulk waves-532nm.

In this chapter we studied the effect of water temperature on laser-induced bulk waves. In order to achieve this, two experiments were designed. In the first test, the surface of the specimen was in contact with air except for the small portion in contact with the water that was contained in the pipe. Therefore, thermal equilibrium was reached between the column of water and the portion of the specimen surrounding the water pipe. In the second test, we wanted to mitigate the thermal difference between the column of water in the pipe and the whole specimen. Therefore, we filled in a tank with water and we placed the aluminium block in the tank. The level of water was such that the upper surface of the aluminium block was minimally covered.

3.1 Test 1

Figure 5 shows the setup adopted to estimate the effect of water temperature on the ultrasonic signal strength.

In particular, a plastic pipe 50.8 mm in diameter was glued on the aluminum block and filled up to 50.8 mm with water. The temperature of the water-column in the pipe was initially equal to 68.3 °C. Measurements were continuously taken until the water reached the thermal equilibrium with the ambient at 22.8 °C. By means of the mirror and the PCX lens, the laser beam was delivered through the column of water on the surface of the aluminium block. An ultrasonic transducer (resonance frequency equal to 1 MHz) was attached on the opposite surface of the block to detect the bulk longitudinal waves generated by the laser pulses. The aluminium block was placed on four wood blocks in order to be placed at a height that could have been exploited in the second test where we were planning to use an immersion transducer. Based on the previous experiment, the level of energy was equal to 170mJ.

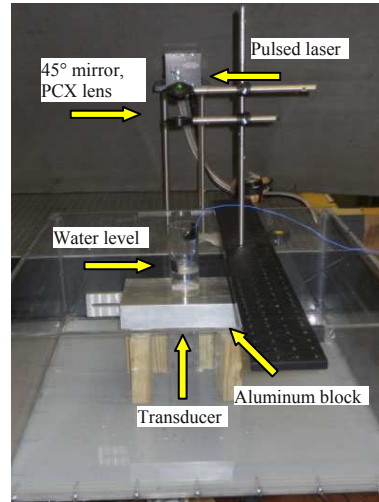


Fig. 5 Experimental set-up used in test 1. Photo of the laser, PCX lens, aluminum block and pipe filled with water

Figure 6 presents the peak-to-peak value of the signals as a function of the water temperature. As the water temperature decreases, the amplitude of the bulk waves slightly increases but there is not a significant change in the peak-to-peak value. It is argued that thermal equilibrium was only reached between the column of water and the portion of the specimen illuminated by the laser. Therefore, we wanted to mitigate the thermal difference between the column of water in the pipe and the whole specimen. In fact, we considered this latter case as the one that better represents the effect of water temperature on the amplitude of laser-generated bulk waves.

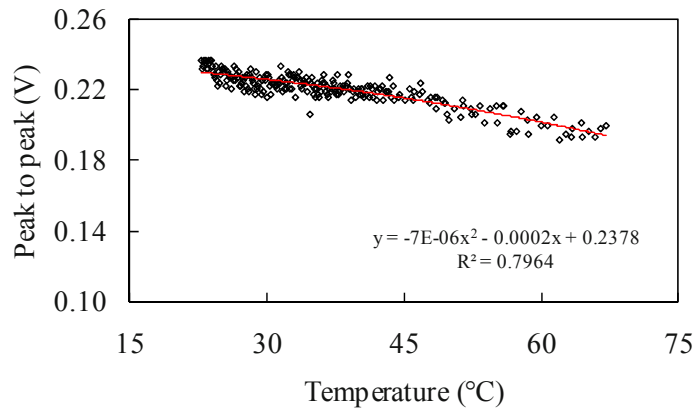


Fig. 6 Test 1: peak-to-peak amplitude as a function of the temperature for the 532 nm wavelength

3.2 Test 2

On the basis of the previous considerations, a different test was conducted. Figure 7 shows the setup adopted for test two. In particular, we filled in a tank with water at a temperature of 15°C. The level of water was such that the upper surface of the aluminium block was minimally covered. After few hours, the temperature of the aluminium block was measured to be the same as the temperature in the tank. A plastic pipe 50.8 mm in diameter was glued on the aluminum block and filled up to 50.8 mm with water. The temperature of the water-column in the pipe was initially equal to 70.8°C. Measurements were continuously taken until the water reached the thermal equilibrium with the whole aluminium block. By means of the mirror and the PCX lens, the laser beam was delivered trough the column of water on the surface of the aluminium block. An immersion piezoelectric transducer (resonance frequency equal to 1 MHz) was placed beneath the aluminum block with a lift off distance of 10 mm. Then, a preamplifier set at 40dB was employed to improve the SNR. Finally, the level of energy was equal to 170mJ.

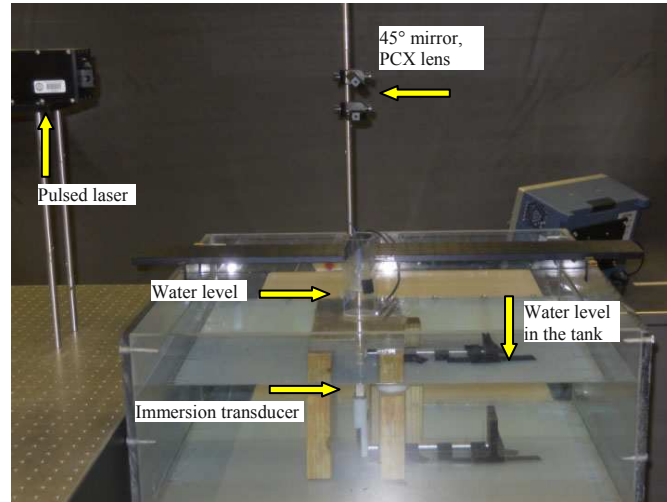


Fig. 7 Experimental set-up used in test 2. Photo of the laser, PCX lens, aluminum block, immersion transducer and pipe filled with water

Figure 8 presents the peak-to-peak value as a function of the water temperature. In this case, the trend of the time waveforms is substantially different from the one observed in test one. In fact, as the water temperature decreases, the amplitude of the bulk waves almost stays constant. In particular, the trend line can be approximated as a polynomial of order two. It is argued that a better thermal equilibrium was reached between the whole specimen and the column of water. Therefore, this case can be representative of the effect of water temperature on the amplitude of laser-generated bulk waves. On the basis of this experiment, we can say that the temperature does not affect the peak to peak amplitude of laser-generated bulk waves for the case of the 532 nm wavelength.

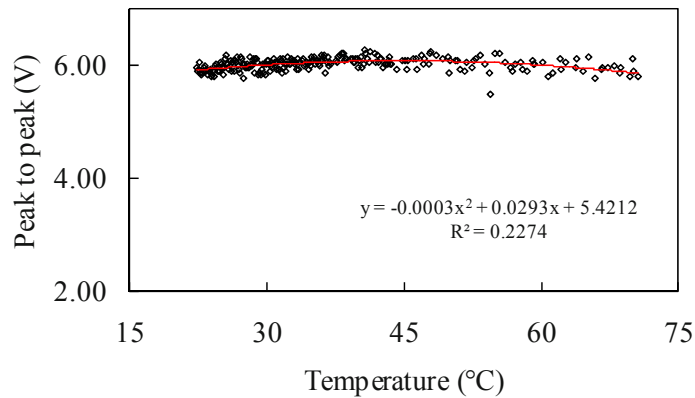


Fig. 8 Test 2: peak-to-peak amplitude as a function of the temperature for the 532 nm wavelength

4. Conclusions

This paper represents the experimental phase of a project aimed to develop a new NDE technology for the inspection of underwater structures. We proved that the 532 nm wavelength is suitable for the scope while the 1064 nm wavelength is not. In fact, in the latter case, water absorption strongly affects the propagation of laser-generated bulk waves. We observed a quasi-exponential amplitude decay of the signal as the water level increased. On the other hand, this phenomenon does not occur for the 532 nm wavelength. In fact, the amplitude stayed almost stable as the water level increased. Furthermore, a significant increase in amplitude can be achieved by employing higher energy levels for the case of the 532 nm wavelength. This results in an additional advantage for the use of this specific wavelength in underwater inspection. Another important outcome is the fact that water temperature does not significantly affect the SNR of the laser-induced stress waves. In fact, the

amplitude of the signals almost stayed stable as the water temperature decreased approaching the thermal equilibrium between the specimen and the environment.

Acknowledgements

This work is supported by the National Science Foundation under grant number CMMI 1029457, Dr. M.P. Singh program director.

5. References

- [1] Shull, P.J. "Nondestructive Evaluation: theory, techniques, and applications", Marcel Dekker Ed., New York, 2002.
- [2] Monchalin, J-P. "Optical detection of ultrasound", *IEEE Transactions on Ultrasonics, Ferroelectrics, and Frequency Control*, Vol. 33, No 5, pp. 485-499, 1986.
- [3] Monchalin, J-P., Neron, C., et al. "Laser-Ultrasonics: From the Laboratory to the Shop Floor," *Advanced Performance Materials*, Vol. 5, pp. 7-23, 1998.
- [4] Scruby, C., and Drain, L. *Laser Ultrasonics: Techniques and Applications*, Adam Hilger, New York, NY.
- [5] Achenbach, J. D. "Quantitative nondestructive evaluation," *International Journal of Solids and Structures*, Vol. 37 pp. 13-27, 1990, 2000.
- [6] Han, Q., Qian, M., Wang, H. "Investigation of liquid/solid interface waves with laser excitation and photoelastic effect detection," *Journal of applied physics* 100, 093101, <http://dx.doi.org/10.1063/1.2365377> , 2006.
- [7] Ko, S., Ryu, S. et al. "Laser induced short plane acoustic wave focusing in water," *Applied physics letters* 91, 051128, <http://dx.doi.org/10.1063/1.2768192> , 2007.
- [8] Glorieux, C., Van de Rostyne, J. et al. "Shear properties of glycerol by interface wave laser ultrasonics," *Journal of applied physics* 99, 013511, 2006.
- [9] Rizzo, P., Han, J., and Ni, X. "Structural Health Monitoring of Immersed Structures by Means of Guided Ultrasonic Waves," *Journal of Intelligent Materials and Structures*, Vol. 21, pp. 1397-1407, doi:10.1177/1045389X10384170, 2010.
- [10] Theisen-Kunde, Dirk, Danicke, Veit et al. "Temperature dependence of water absorption for wavelengths at 1920 nm and 1940 nm", *IFMBE Proceedings, 4th European Conference of the International Federation for Medical and Biological Engineering - ECIFMBE 2008*, November 23-27, 2008, 22, pp. 2228-2229, 2008.
- [11] Han, Q., Wang, H. et al. "Liquid-solid interface waves with laser ultrasonic and mirage effect", *Chinese Physical Letters*, Vol. 22, No. 12, pp. 3104-3106, 2005.

Assault Rifle Bullet-Experimental Characterization and Computer (FE) Modeling

Leopoldo Carbajal, Jovan Jovicic, Helga Kuhlmann

DuPont Engineering Research & Technology – Engineering Mechanics

DuPont Company

Chestnut Run Bldg 701/Rm 104

4417 Lancaster Ave.

Wilmington, DE 19880-0701

ABSTRACT

This paper describes the development of a finite element model for the 7.62x39 mm mild steel core (MSC) bullet. The derivation of the numerical model is based on results of compression testing performed on bullet components and bullets. The material constants needed are obtained using an iterative approach, where numerical models of the compression tests are carried out to match the force displacement response of the tested structures. Later, these set of constants are refined by comparing predicted deformed shapes against those observed during ballistic impact experiments. Numerical simulations of the 7.62x39 mm MSC bullet impacting a semi-infinite rigid plate are carried out over a range of impact velocities, and the predicted deformed shapes compared to experimental shapes obtained with the help of high speed photography. Soft recovery of cores and jackets are also used to perform comparisons with predicted results. It was found that our constitutive and damage models, implemented in ABAQUS Explicit, were able to accurately predict deformed shapes and failure modes without any predefined defects in the element mesh.

KEYWORDS

ABAQUS Explicit, AK-47 Kalashnikov bullet, Assault rifle bullets, Ballistics, Explicit Finite Elements Models, Johnson-Cook plasticity model, Johnson-Cook strength model, Johnson-Cook constants for steel, Johnson-Cook constants for lead, Material properties for lead, Material properties for steel, Nonlinear Finite Elements Models, Taylor impact test, 7.62x39 mm Mild Steel Core bullet, 7.62x39 mm MSC bullet.

INTRODUCTION AND OBJECTIVES

This paper covers the work done to obtain a physical – mathematical representation of small arms ammunition identified as critical for the successful design of helmet, based on results of mechanical experiments, and validated by ballistic testing. The projectile selected is the one fired from the AK-47 Kalashnikov assault rifle. The reason for selecting this bullet is the immense popularity of the AK-47 Kalashnikov assault rifle around the world [1, 2].

Among the factors affecting the penetration resistance of an armor system are the characteristics of the projectile, mass, geometry (length, shape and caliber), materials (stiffness, strength, and density), and initial impact conditions, striking velocity, and impact angle. The goal of this study is to characterize the response of one type of bullets fired by the AK-47 assault rifle. Objectives included obtaining the geometrical shapes of each bullet components, hardness, and material constants at low (1 s^{-1}) medium (100 s^{-1}) and ballistic strain rates.

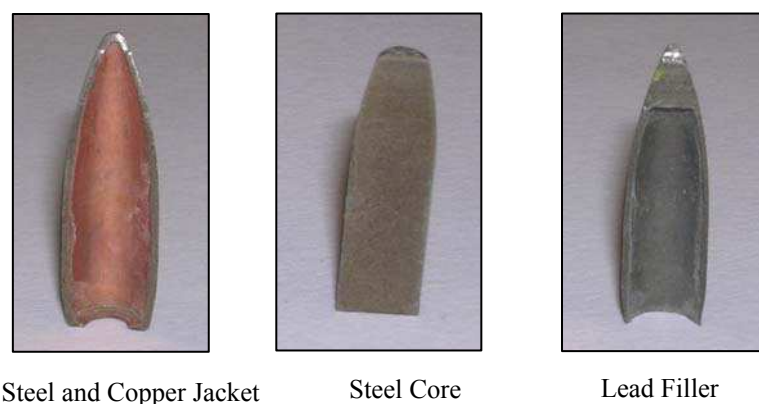


Fig. 1 AK-47 Kalashnikov assault rifle bullet components

To obtain geometrical shapes, bullets were cut in half, using water jets and wire EDM techniques (Figure 1). For each bullet component, geometric profiles were recorded 5 times using a profilometer (Figure 3), and then an average profile was obtained for each of them. Figure 4 shows the averages profile for the core, the filler and the jacket. As it can be shown in Figure 4, the steel core is flat at the top, instead of being machined to a point as it is the case with Armor Piercing rounds (AP-Armor Piercing, a bullet intended to penetrate without deformation).

Hardness measurements were conducted at several locations for each bullet component (Figure 2), and the average results are summarized in Table 1 [3].

Table 1 Rockwell Hardness for 7.62x39mm MSC components

Component	Hardness
Copper plated Steel Jacket	92 HRB
Steel Core	23HRC

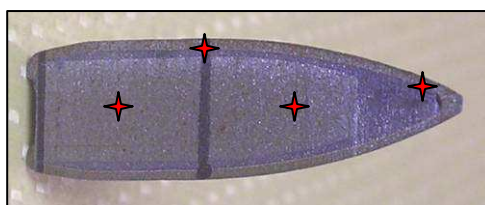


Fig. 2 AK-47 Hardness measurements of bullet components

The average mass of whole bullet is determined to be 7.93 g, steel core has a mass of 3.58 g, while copper plated steel jacket's mass is 2.15 g. The lead filler has a mass of 2.2 g.

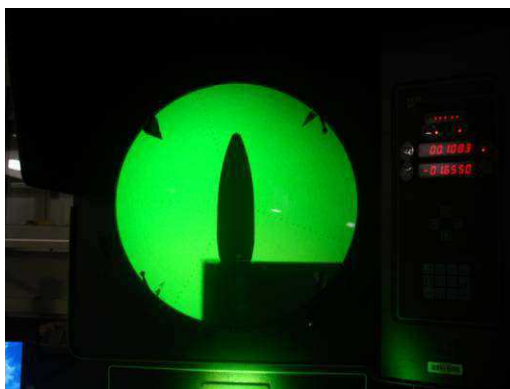


Fig. 3 Bullet jacket on profilometer

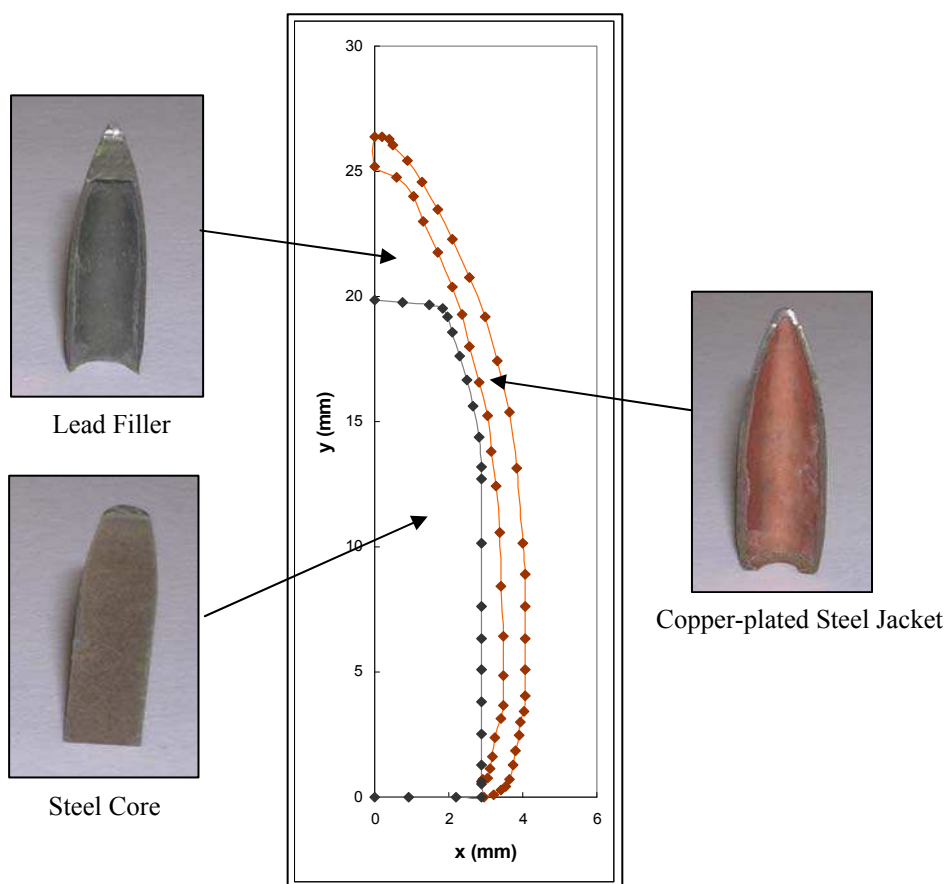


Fig. 4 Projectile composition

EXPERIMENTAL

Compression Test

In order to obtain material properties of both copper plated steel jacket and steel core, bullets were cut, with high precision, by water jet (Figure 5) into cylindrical test samples, as shown on Figure 5.

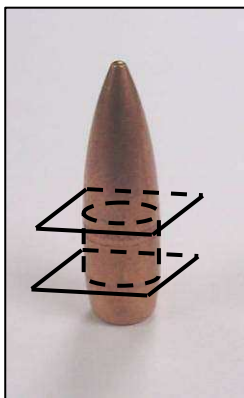


Fig. 5 The way bullets are cut

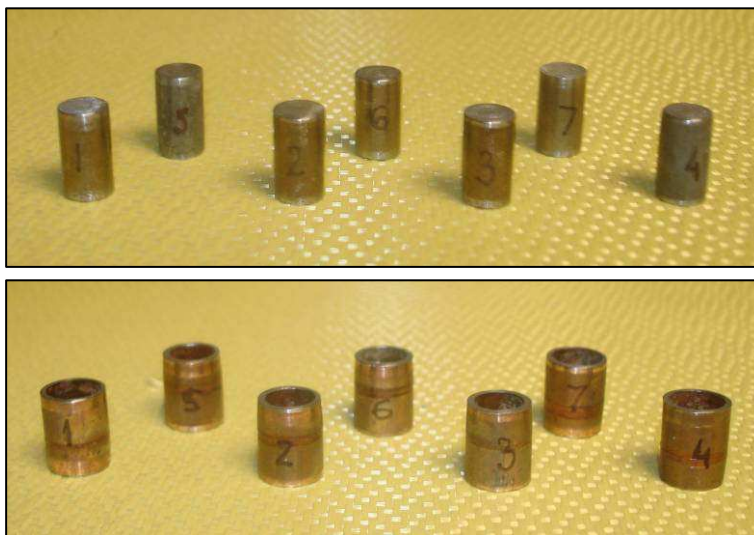


Fig. 6 Core and jacket compression test samples

The average mass of the cylindrical core test samples is 2.08 g, while cylindrical jacket samples have a mass of 1.01 g.

Quasi-static Compression test results

First set of compression tests are performed under very low strain rate of 1 s^{-1} on samples freely positioned between flat platens (Figure 7).

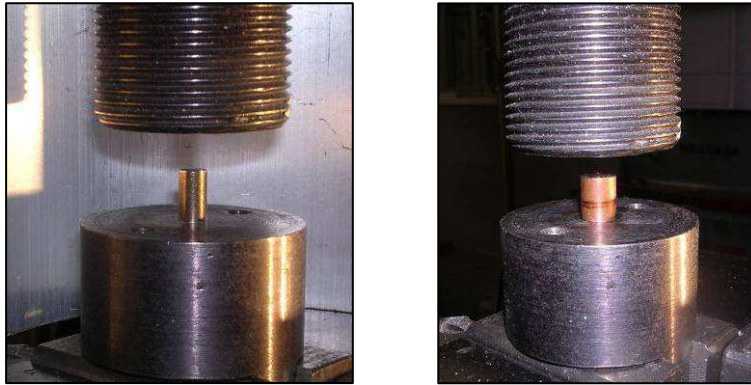


Fig. 7 Quasi-static compression test setup

Figure 8 shows the average, base on five repetitions, load-displacement and approximate stress-strain responses for the bullet steel core cylinders under compression.

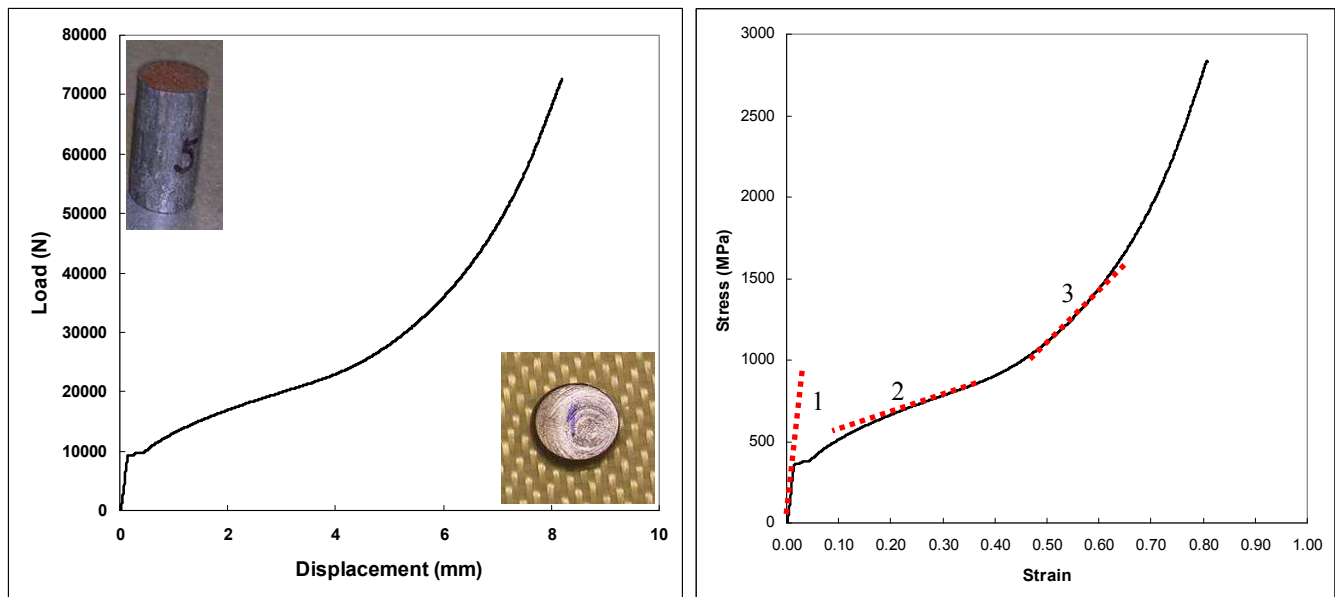


Fig. 8 Steel Core Compression Test Result

From the graph, three different regimes of material's response to compression can be distinguished. After first, elastic response, with the modulus of elasticity of $E_1=31.72$ GPa, and yield point of $\sigma_y=362$ MPa, there are two strain hardening zones with stiffness of $E_2=1.24$ GPa and $E_3=3.45$ GPa, respectively, ending by load increase due to platen to platen compression.

Figure 9 represents copper plated steel jacket compression test results. Jacket showed to be stiffer, having Young's modulus of $E=42.5$ GPa as well as higher yield strength of $\sigma_y=603.3$ MPa, then steel core. During compression, cylindrical test sample, after reaching the Yield point, gets crushed including two buckling modes, indicated by two peaks on the graph.

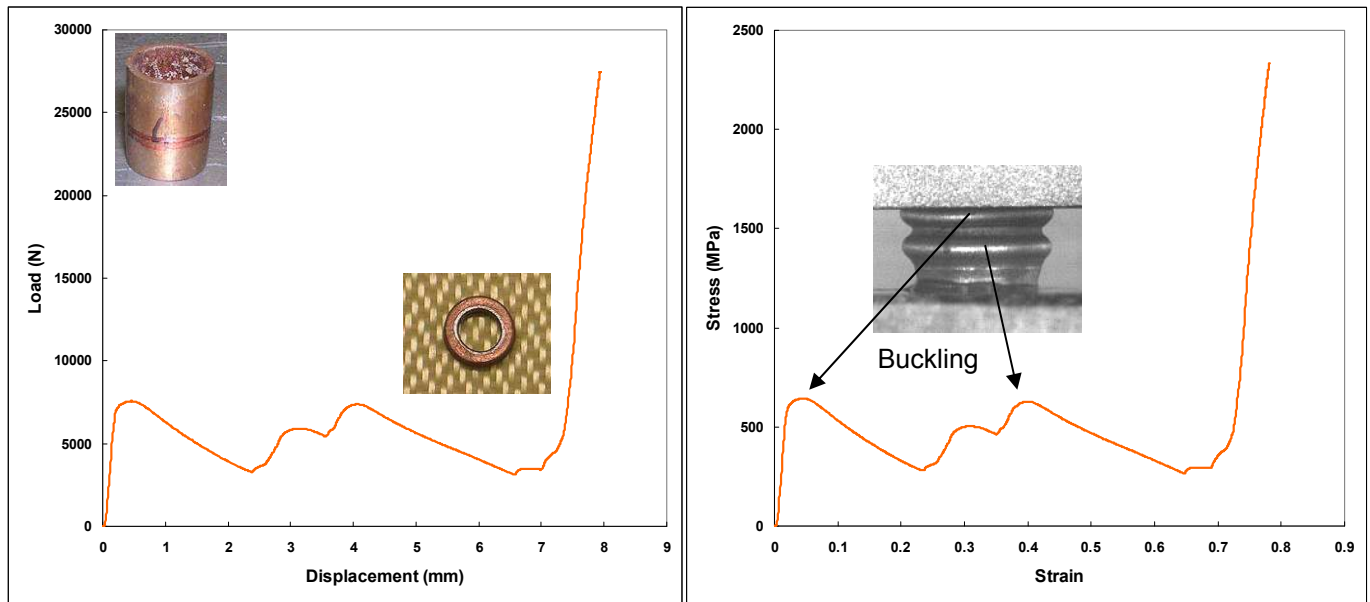


Fig. 9 Steel Jacket Compression Test Result

Moderate strain rate compression test

The moderate strain rate compression test is performed on MTS machine with the load limit of 30 kN, and speed range up to 17 m/s (Figure 10).

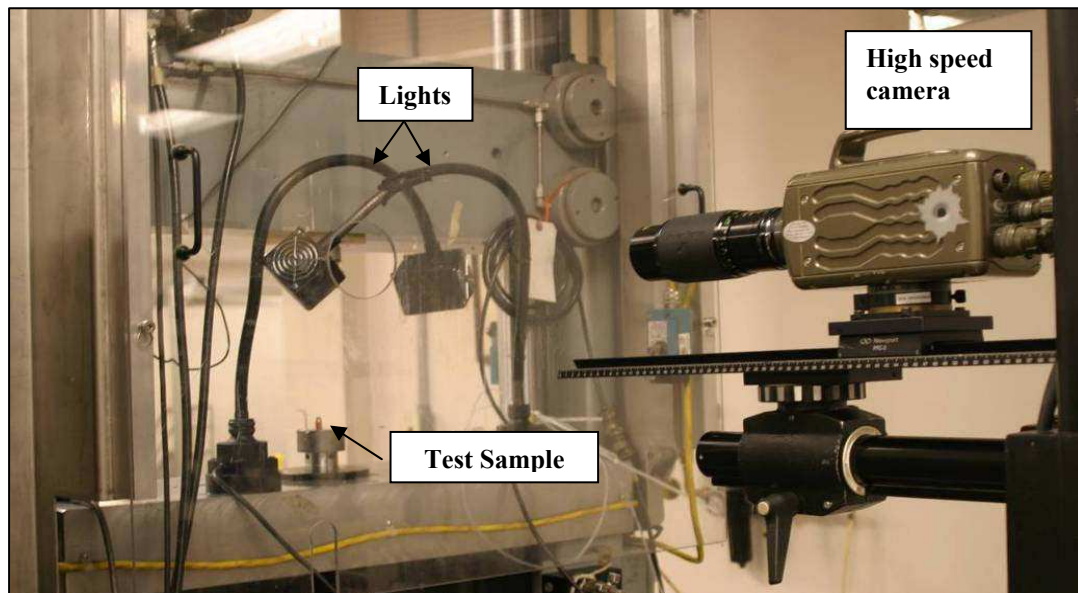


Fig. 10 High strain rate test setup

Note that because the MTS machine was not been able to maintain the loading rate, high strength steel core was able to compress only to a certain point, when the test would stop. Therefore the results on Figure 11 are valid only up to 0.5 mm displacement (shown with the arrow). After that point, the strain rate would change due to the deceleration of the test. On the other hand, the test of steel jacket results in full compression of the sample, with two buckling modes, as shown on a Figure 12.

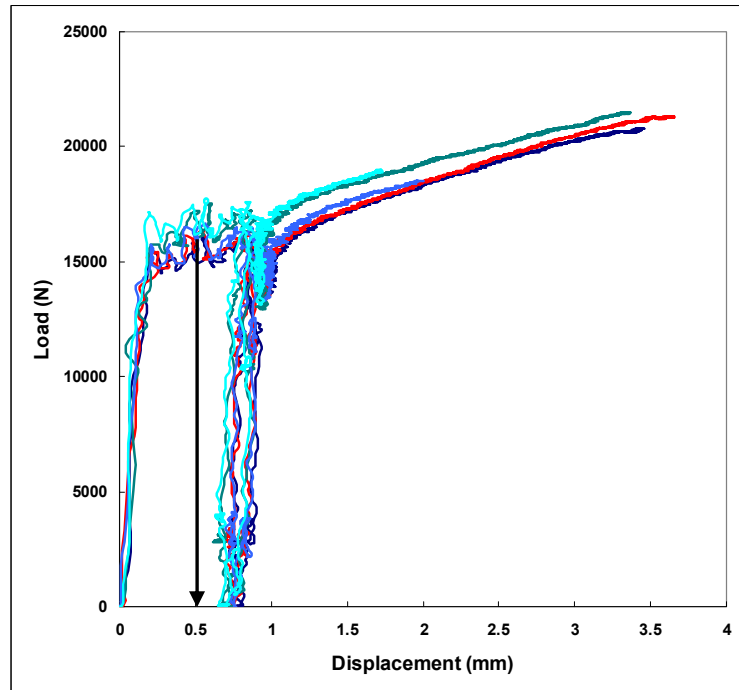


Fig. 11 Moderate strain rate compression test results of a steel core

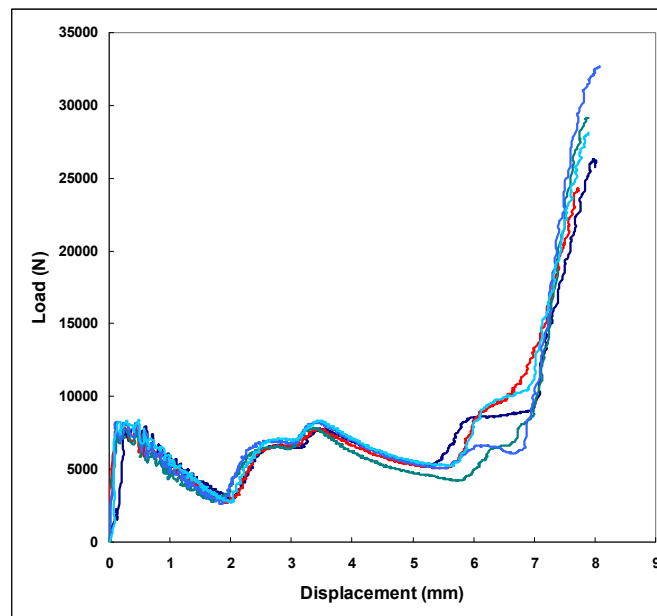


Fig. 12 Moderate strain rate compression test results of a steel jacket

Compared, quasi-static and moderate strain rate compression results, for both bullet core and jacket (Figure 13), show initially stiffer response (marked on graphs) of both core and jacket at higher strain rate. However, it has to be noted that

even moderate strain rate of 100 s^{-1} (that was set by machine limitation) is still much lower than strain rates that projectile materials experience during ballistic event, which are in order of $10,000 \text{ s}^{-1}$.

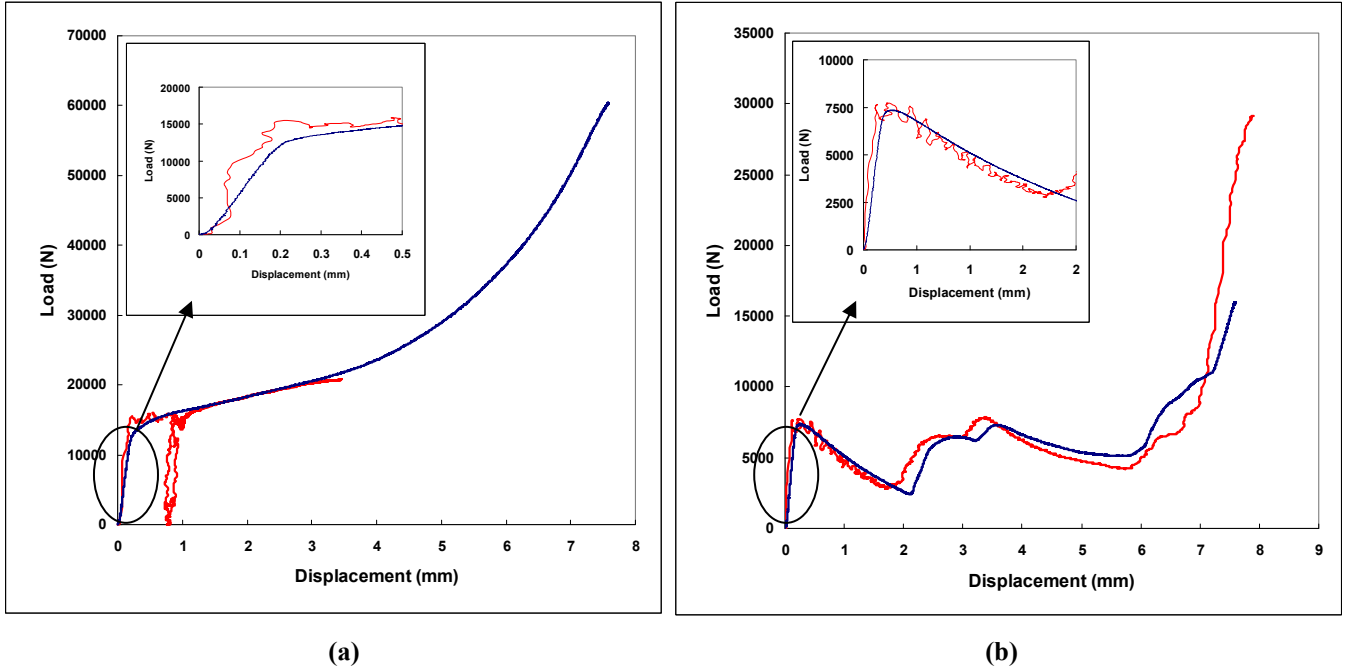


Fig. 13 Test strain rate comparison: (a) Core, (b) jacket

Bullet deformation during ballistic impact (semi - infinite steel plate impact test)

The objective of this experiment is to capture bullet dynamic deformation while impacting a hardened steel block (Taylor test) [6]. The test setup consists of a light source illuminating the projectile's side, while impacting the steel block, and two high speed cameras capturing images of the projectile deformation during the impact. Figure 14 shows a schematic of the experimental set up. While back camera serves to ensure straightness of the impacted bullet (Figure 15), side camera images (shown in Model validation paragraph, Figures 20 and 21) are used to determine projectile deformation during the impact.

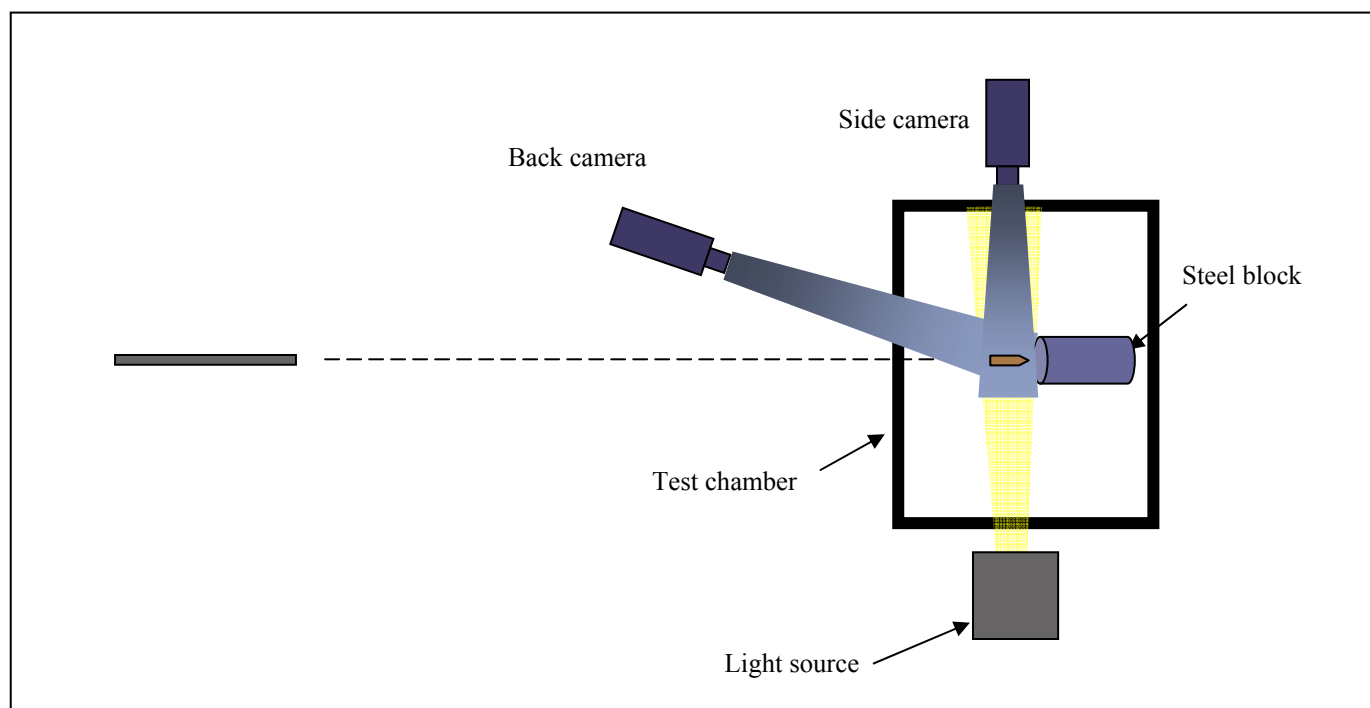


Fig. 14 Test setup

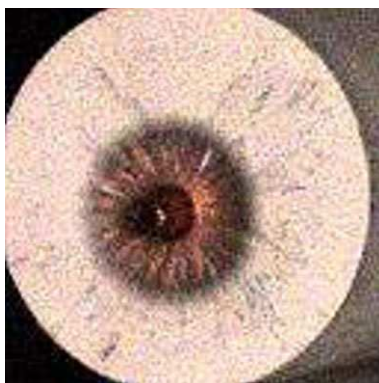


Fig. 15 Back camera view of a bullet impacting steel block

NUMERICAL

To determine the elastic and inelastic material properties of the material, numerical simulations of the quasi-static (1 s^{-1} strain rate) and moderate strain rate (100 s^{-1}) compression tests of bullet components (core and jacket) were performed using ABAQUS/Explicit.

The jacket model was compressed between two flat rigid plates that represent the boundary condition in the compression test. The ABAQUS/Explicit general contact algorithm was employed. The bottom plate was fixed in space and the bottom of the component was in contact with the bottom plate. The top plate moved slowly, compressing the specimen, to simulate the strain rate of 1 s^{-1} and 100 s^{-1} . A similar modeling approach was used to simulate the core and bullet compression tests (Figures 16 and 17). Initial literature values for common material were used and load-deflection curve from the simulation were compared to the experimental load-displacement curve. The material properties were determined through an iteration process in which the load-deflection curve of the model with the best fit for the experimental load-displacement curve was chosen.

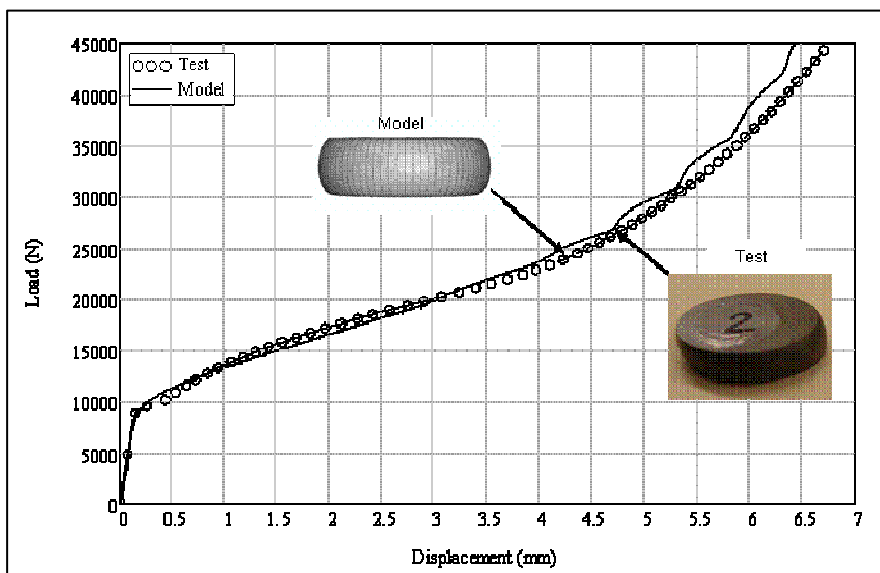


Fig. 16 Test and Model – Core

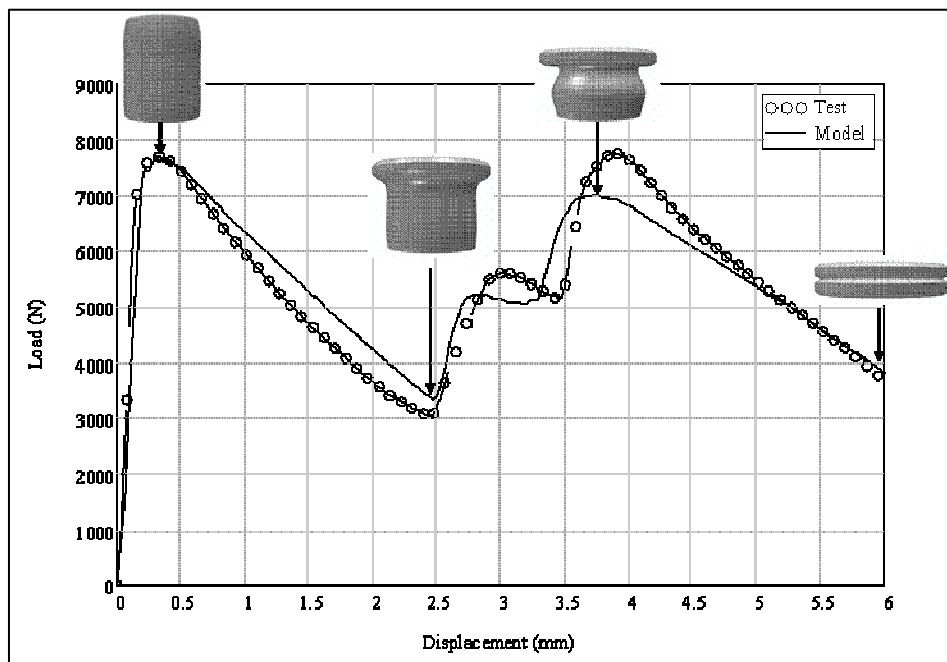


Fig. 17 Test and Model-Jacket (with the model deformation modes)

The second set of simulations included the model of a whole bullet under quasi-static (1s^{-1}) and moderate (100s^{-1}) strain rate (MSR) compression test using the material properties developed with the numerical simulation of the individual bullet components (Figure 18). Note that comparison of the test and model is not valid after 14mm of compression. After that point

tested bullets would start to buckle, therefore assumed perfect symmetry of the model is not applicable any more. The objective was to refine the constitutive and damage models for the materials and the structural response of bullet.

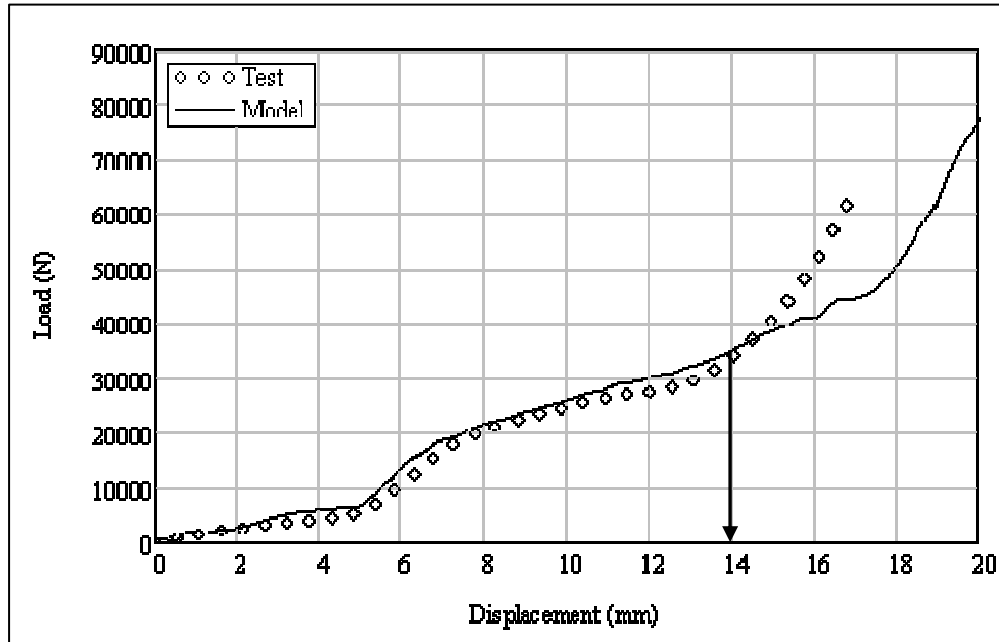


Fig. 18 Force-Displacement MSR Test and Model

The final numerical simulation was of bullets impacting a semi-infinite rigid plate over a range of impact velocities. The predicted failure modes and deformed shapes were compared to the experimental results. The objective was to obtain an accurate representation of bullet response during ballistic impact.

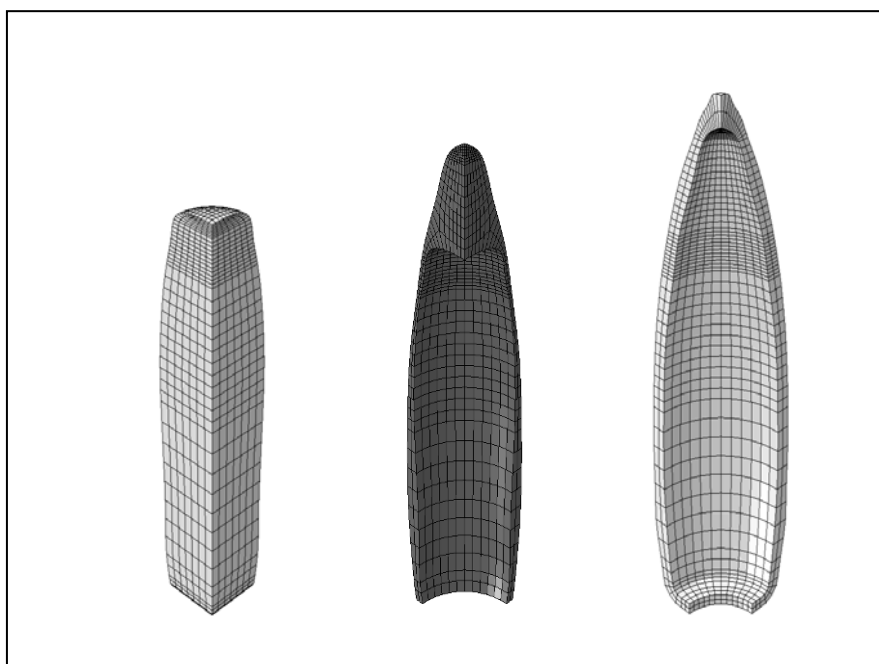
Description of the model

A numerical simulation of the compression test requires a 3D model of the bullet. Three-dimensional linear brick elements with reduced integration were used. FE model characteristics are listed in Table 2. The bullet and bullet components are symmetrical. Consequently, only a quarter of the specimen tested with a symmetric boundary was considered. The component models represent the exact dimensions, geometry and loading conditions as the specimen tested.

Table 2 7.62x39mm MSC FE Model characteristics

Element Type		C3D8R
Number of elements	jacket	2487
	core	2148
	filler	1704
Adaptive mesh		Yes
Hourglass control		Enhanced
Bulk Viscosity		0
Kinematic formulation		Orthogonal

The bullet geometry determined by the coordinates on profilometer ([Figure 3](#) and [4](#)) was used to create the non-linear finite element model of the jacket, filler and core of the bullet ([Figure 19](#)).

**Fig. 19 Bullet Model (core, filler and shell)**

Material Constitutive Model

In general, the response of material under high-speed impact involves consideration of the effect of strain, strain rate and temperature.

The Johnson-Cook material model with strain rate dependence [4] was used in the simulation to define the inelastic behavior of the bullet materials.

The static yield stress, σ_0 , is assumed to be of the form

$$\sigma^0 = \left[A + B \left(\bar{\epsilon}^{pl} \right)^n \right] \left(1 - \hat{\theta}^m \right) \quad (1)$$

Where $\bar{\epsilon}^{pl}$ is the equivalent plastic strain and A, B, n and m are material parameters measured at or below the transition temperature $\theta_{transition}$. $\hat{\theta}$ is the non-dimensional temperature defined as

$$\hat{\theta} = \begin{cases} 0 \rightarrow \theta < \theta_{transition} \\ \frac{(\theta - \theta_{transition})}{(\theta_{melt} - \theta_{transition})} \rightarrow \theta_{transition} \leq \theta \leq \theta_{melt} \\ 1 \rightarrow \theta > \theta_{melt} \end{cases} \quad (2)$$

Where θ is the current temperature, θ_{melt} is the melt temperature and $\theta_{transition}$ is the transition temperature defined as the one at or below which there is no temperature dependence on the expression of the yield stress.

The Johnson-Cook strain rate dependence assumes that

$$\bar{\sigma} = \sigma^0 \left(\bar{\epsilon}^{pl}, \theta \right) R \left(\dot{\bar{\epsilon}}^{pl} \right) \quad (3)$$

And

$$\dot{\bar{\epsilon}}^{pl} = \dot{\epsilon}_0 \exp \left[\frac{1}{C} (R - 1) \right] \quad \text{for } \bar{\sigma} \geq \sigma^0 \quad (4)$$

Where

$\bar{\sigma}$: yield stress at nonzero strain rate

$\dot{\bar{\epsilon}}^{pl}$: equivalent plastic strain rate

$\dot{\epsilon}_0$: reference strain rate

C: material parameters measured at or below the transition temperature

$\sigma^0(\bar{\epsilon}^{pl}, \theta)$: is the static yield stress

$R(\dot{\bar{\epsilon}}^{pl})$: is the ratio of the yield stress at nonzero strain rate to the static yield stress (so that $R(\dot{\epsilon}_0) = 1.0$)

The elastic behavior of the material was defined with a hydrodynamic material model, in which the pressure is defined as a function of the density and the internal energy.

Two different dynamic failure models were used in the numerical simulation.

The ABAQUS/Explicit Johnson-Cook dynamic failure model was used for the lead material, since the filler of the 7.62x39 mm Mild Steel Core (MSC) bullet are made out of lead.

The ABAQUS/Explicit progressive damage and failure model was used for the steel material, in order to simulate the core and jacket of the 7.62x39 mm Mild Steel Core (MSC) bullet that are made out of steel.

Dynamic Failure Model for Lead Material

The Johnson-Cook dynamic failure model [5] which is suitable for high-strain rate deformation of metals was used to define the lead failure in the high speed ballistic impact simulation. This dynamic failure mode is available in ABAQUS/Explicit.

The model assumes that the equivalent plastic strain at the onset of damage, $\bar{\epsilon}^{pl}$, is a function of stress triaxiality and strain rate. The failure is assumed to occur when the damage parameter exceeds 1. The damage parameter, ω , is defined as

$$\omega = \sum \left(\frac{\Delta \bar{\epsilon}^{pl}}{\bar{\epsilon}_f^{pl}} \right) \quad (5)$$

Where $\Delta \bar{\epsilon}^{pl}$ is an increment of the equivalent plastic strain, $\bar{\epsilon}_f^{pl}$ is the strain at failure, and the summation is performed over all increments in the analysis. The strain at failure, $\bar{\epsilon}_f^{pl}$, is assumed to be dependent on a non-dimensional plastic strain rate, $\frac{\dot{\bar{\epsilon}}^{pl}}{\dot{\bar{\epsilon}}_0}$; a dimensionless pressure-deviatoric stress ratio, p/q , where p is the pressure and q is the Mises stress; and the non-dimensional temperature $\hat{\theta}$. The dependencies are of the form

$$\bar{\epsilon}_f^{pl} = \left[d_1 + d_2 \exp \left(d_3 \frac{p}{q} \right) \right] \left[1 + d_4 \ln \left(\frac{\dot{\bar{\epsilon}}^{pl}}{\dot{\bar{\epsilon}}_0} \right) \right] (1 + d_5 \hat{\theta}) \quad (6)$$

Where d_1 to d_5 are failure parameters measured at or below the transition temperature.

Dynamic Failure Model for Steel Material

ABAQUS/Explicit offers a general capability to predict progressive damage and failure. The capability supports the specification of damage initiation criteria and damage evolution.

The Johnson-Cook damage criterion was used in the simulation, which is defined in equation (7).

The damage evolution was based on effective plastic displacement, which is defined with the evolution equation

$$\dot{u}^{pl} = L \dot{\bar{\epsilon}}^{pl} \quad (7)$$

where L is the characteristic length of the element

Table 3 Bullet Material Properties

Johnson - Cook Plasticity Material Model					
Bullet Component	A [MPa]	B [MPa]	n	m	C
7.62x39mm MSC-core	234.4	413.8	0.25	1.03	0.00333
7.62x39mm MSC-jacket	448.2	303.4	0.15	1.03	0.00333
Lead-filler	10.3	41.3	0.21	1.03	0.00333

Johnson - Cook Dynamic Failure Model					
Bullet component	d ₁	d ₂	d ₃	d ₄	d ₅
Steel core	5.625	0.3	-7.2	-0.0123	0
7.62x39mm MSC-jacket	2.25	0.0005	-3.6	-0.0123	0
Lead filler	0.25	0	0	0	0

Damage Evolution Type displacement =0.0001

Mie-Grüneisen Equation of State (used on all the materials)

$c_0 = 4.569 \text{E}6 \text{ mm/s}$

$s = 1.4$

$\Gamma_0 = 1.93$

Linear Elastic Shear Modulus $G = 9.446 \text{E}3 \text{ MPa}$

Validation of Numerical Model

A series of high speed ballistic impact test simulations were performed for bullets with velocities ranging from 120 m/s to 600 m/s. The ABAQUS/Explicit general contact was employed to simulate contact between the projectile and the plate. This contact algorithm was also used to simulate the interaction between the different bullet components, such as the interaction between the core and jacket and/or interaction between core, filler and jacket. During the bullet impact, the petals that developed bend until they come into contact with the hardened steel plate. The self-contact algorithm was used to consider this interaction.

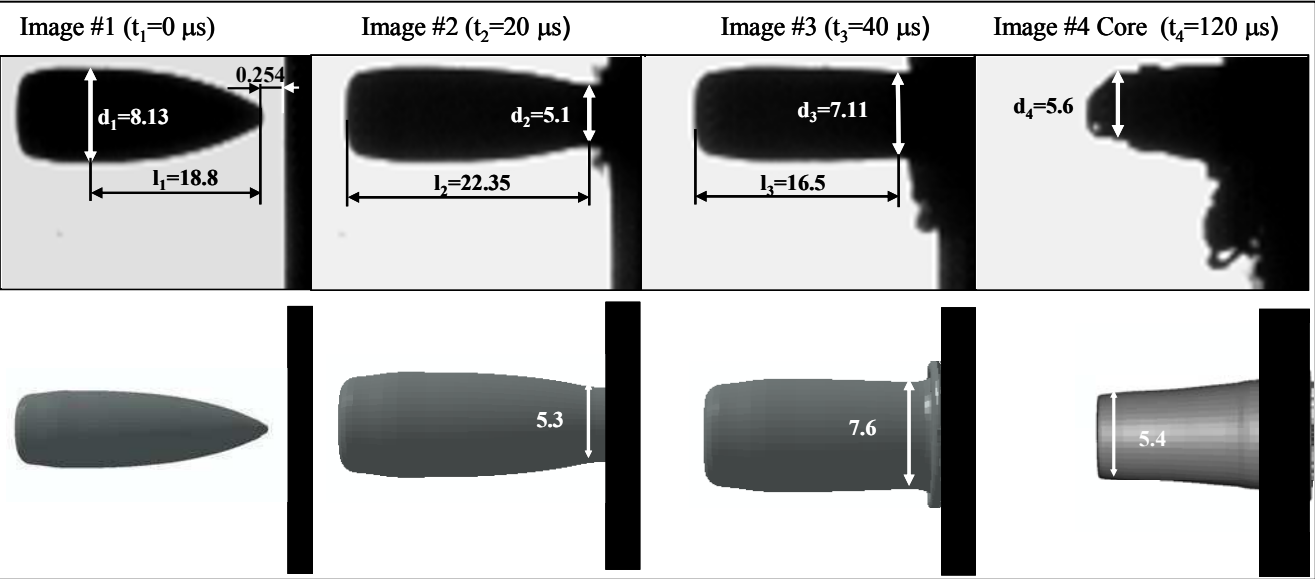


Fig. 20 A comparison of projectile side view impact and numerical simulation of an MSC Bullet traveling at 253 m/s and impacting a hardened steel plate (all dimensions in mm)

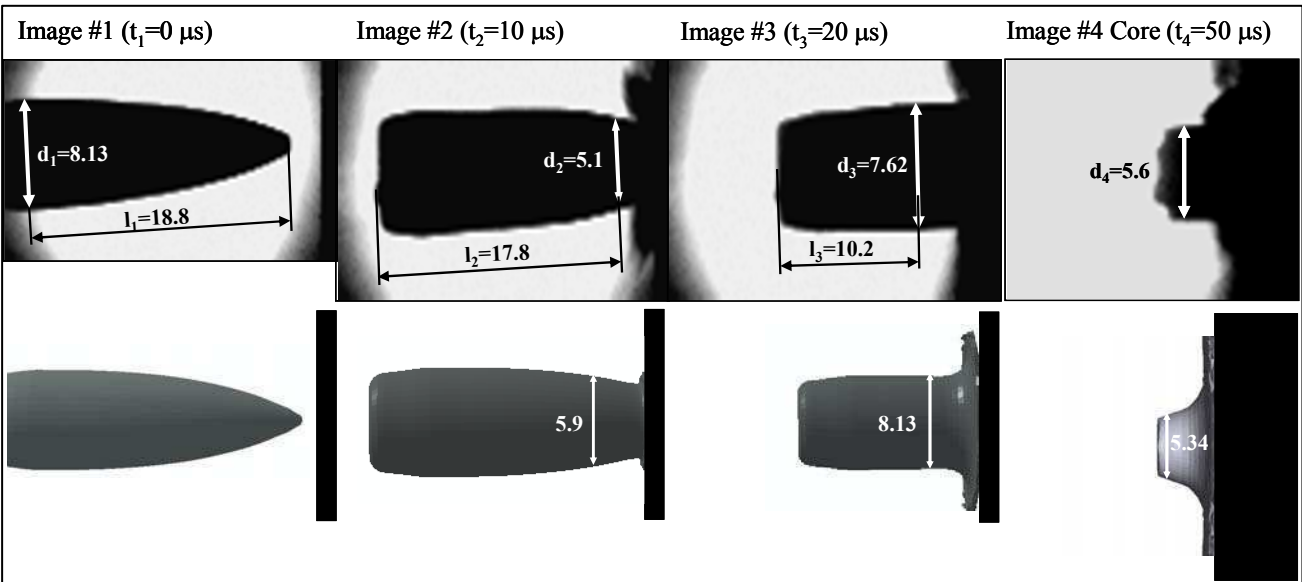


Fig. 21 A comparison of projectile side view impact and numerical simulation of an MSC Bullet traveling at 562 m/s and impacting a hardened steel plate (all dimensions in mm)

Figures 20 and 21 show a comparison between the experiment and the model of a bullet impacting steel plate at 253 m/s and 562 m/s, respectively. It can be seen that the model accurately represents deformed shapes and failure modes.

The predicted versus actual bullet diameter change for a range of velocities are plotted on Figure 22. Again, the predicted bullet deformations are in good correlation with the measured diameter change.

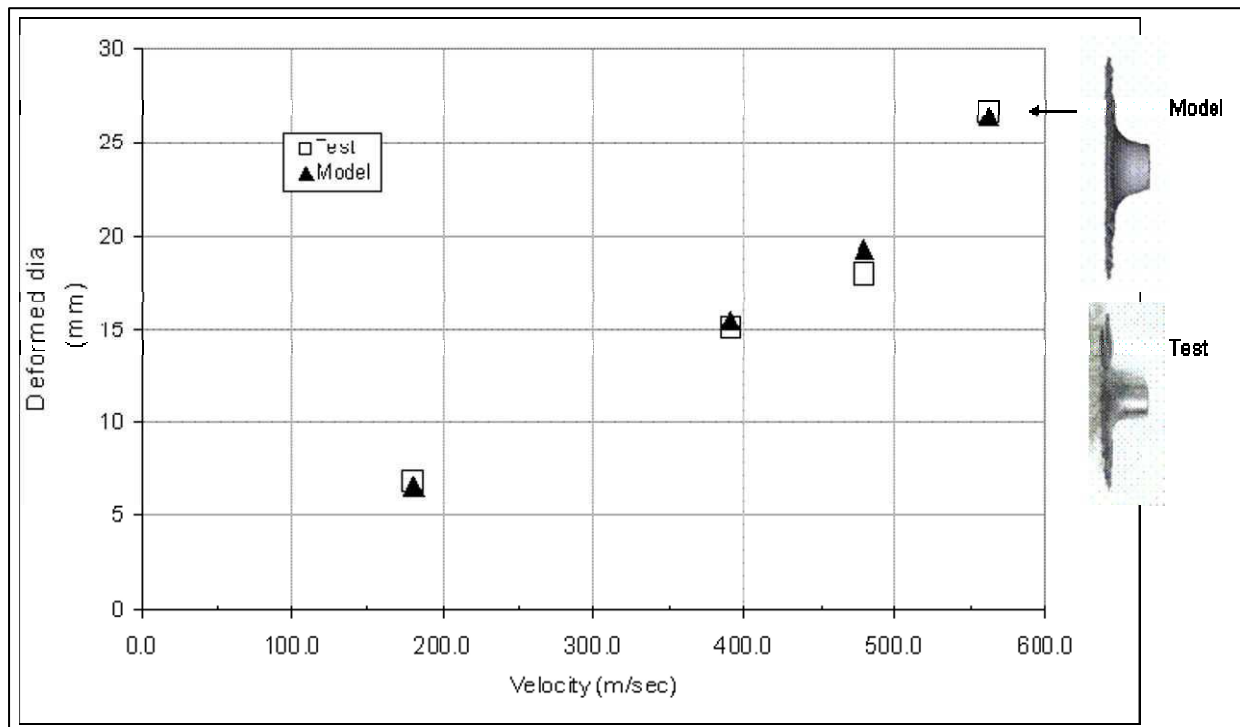


Fig. 22 A comparison of maximum deformed diameter of bullet after impacting a hardened steel plate and numerical simulation of an MSC bullet traveling at various velocities and impacting a hardened steel plate

CONCLUSION

In order to develop a constitutive and damage models of 7.62x39 mm mild steel core (MSC) bullet for nonlinear FE analysis, series of mechanical experiments are performed on bullet and bullet components, including quasistatic and moderate strain rate compression tests. Exact geometry and dimensions of each bullet's component is obtained using profilometer. Numerical simulations of a bullet impacting a semi-infinite rigid plate are carried out over a range of impact velocities, and the predicted failures modes and deformed shapes compared to experimental results obtained using high speed cameras. It was found that the models, implemented in ABAQUS Explicit, were able to accurately predict deformed shapes and failure modes without any predefined defects in the element mesh. These validated models form part of a growing set of tools within DuPont to study energy absorption and dissipation mechanisms during the ballistic impact of fibrous armor. This in turns should help with the design of better armor structures such as helmets, small arm protection inserts and vehicle armor.

ACKNOWLEDGMENT

The authors would like to acknowledge William Briers (DuET) for his high speed photography work during the first "Taylor" impact test at the DPT Spruance Range. Also, we want to thank Dave Mellen (DuET) for the development of a shadowgraph, and Gregory Oldham and Randy Kendzierski (DuET) for helping with the mechanical testing work, and James Marek (DuET) for helping with data acquisition. We want to thank William Nichols and Patrick Fitzgerald (DPT) for their help during all "Taylor" test impacts.

REFERENCES

- [1] J. Boutwell and M.T. Klare: "Light weapons and civil conflict: controlling the tools of violence". ISBN 0-8476-9485-2., 1999.
- [2] Phillip Killicoat: "Weaponomics: The Global Market for Assault Rifles". World Bank Policy Research Working Paper 4202, April 2007.
- [3] M.B. Karamis, A.A. Cerit and Fehmi Nair: "Surface characteristics of projectiles after frictional interaction with metal matrix composites under ballistic condition". Wear 261, Issues 7-8, Pages 738-745, 20 October 2006.
- [4] G.R. Johnson and W.H. Cook: "A constitutive model and data for metals subjected to large strains, high strain rates and high temperatures. In Proceedings of the 7th International Symposium on Ballistics, pp. 541-547. The Hague, The Netherlands, April 1983.
- [5] G.R. Johnson and W.H. Cook: "Fracture characteristics of three metals subjected to various strains, strain rates, temperatures and pressures". Engineering Fracture Mechanics Vol. 21, No 1, pp. 31-48, 1985.
- [6] Sir Geoffrey Taylor, FRS: "The use of flat-ended projectiles for determining dynamic yield stress. I Theoretical considerations". Proceedings of the Royal Society of London. Series A, Mathematical and Physical Sciences. Vol. 194. 2 September 1948.
- [7] ABAQUS/Explicit User Manuel